sustainability

Special Issue Reprint

Advances in Rock Mechanics and Geotechnical Engineering

Volume II

Edited by
Mahdi Hasanipanah, Danial Jahed Armaghani and Jian Zhou

mdpi.com/journal/sustainability

MDPI

Advances in Rock Mechanics and Geotechnical Engineering—Volume II

Advances in Rock Mechanics and Geotechnical Engineering—Volume II

Editors

Mahdi Hasanipanah
Danial Jahed Armaghani
Jian Zhou

MDPI

Basel • Beijing • Wuhan • Barcelona • Belgrade • Novi Sad • Cluj • Manchester

Editors

Mahdi Hasanipanah
Institute of Research and Development
Duy Tan University
Da Nang, Vietnam

Danial Jahed Armaghani
School of Civil and Environmental Engineering
University of Technology Sydney
Sydney, Australia

Jian Zhou
School of Resources and Safety Engineering
Central South University
Changsha, China

Editorial Office
MDPI
St. Alban-Anlage 66
4052 Basel, Switzerland

This is a reprint of articles from the Special Issue published online in the open access journal *Sustainability* (ISSN 2071-1050) (available at: https://www.mdpi.com/journal/sustainability/special_issues/advances_rock_mechanics_geotechnical_engineering).

For citation purposes, cite each article independently as indicated on the article page online and as indicated below:

Lastname, A.A.; Lastname, B.B. Article Title. *Journal Name* **Year**, *Volume Number*, Page Range.

Volume II
ISBN 978-3-0365-9774-4 (Hbk)
ISBN 978-3-0365-9775-1 (PDF)
doi.org/10.3390/books978-3-0365-9775-1

Set
ISBN 978-3-0365-9762-1 (Hbk)
ISBN 978-3-0365-9763-8 (PDF)

© 2023 by the authors. Articles in this book are Open Access and distributed under the Creative Commons Attribution (CC BY) license. The book as a whole is distributed by MDPI under the terms and conditions of the Creative Commons Attribution-NonCommercial-NoDerivs (CC BY-NC-ND) license.

Contents

About the Editors . . . . . **ix**

Xuesong Zhang, Biao He, Mohanad Muayad Sabri Sabri, Mohammed Al-Bahrani and Dmitrii Vladimirovich Ulrikh
Soil Liquefaction Prediction Based on Bayesian Optimization and Support Vector Machines
Reprinted from: *Sustainability* **2022**, *14*, 11944, doi:10.3390/su141911944 . . . . . **1**

Saeed Aligholi, Reza Khajavi, Manoj Khandelwal and Danial Jahed Armaghani
Mineral Texture Identification Using Local Binary Patterns Equipped with a Classification and Recognition Updating System (CARUS)
Reprinted from: *Sustainability* **2022**, *14*, 11291, doi:10.3390/su141811291 . . . . . **17**

Engin Özdemir
Investigation of Some Property Changes of Light-Colored Turkish Natural Stones after High-Temperature Treatments
Reprinted from: *Sustainability* **2022**, *14*, 10298, doi:10.3390/su141610298 . . . . . **37**

Muhammad Nasir Khurshid, Ammad Hassan Khan, Zia ur Rehman and Tahir Sultan Chaudhary
The Evaluation of Rock Mass Characteristics against Seepage for Sustainable Infrastructure Development
Reprinted from: *Sustainability* **2022**, *14*, 10109, doi:10.3390/su141610109 . . . . . **53**

Naseer Muhammad Khan, Kewang Cao, Qiupeng Yuan, Mohd Hazizan Bin Mohd Hashim, Hafeezur Rehman, Sajjad Hussain, et al.
Application of Machine Learning and Multivariate Statistics to Predict Uniaxial Compressive Strength and Static Young's Modulus Using Physical Properties under Different Thermal Conditions
Reprinted from: *Sustainability* **2022**, *14*, 9901, doi:10.3390/su14169901 . . . . . **73**

Hongxin Xie, Qiangling Yao, Liqiang Yu and Changhao Shan
Study on Damage Characteristics of Water-Bearing Coal Samples under Cyclic Loading–Unloading
Reprinted from: *Sustainability* **2022**, *14*, 8457, doi:10.3390/su14148457 . . . . . **101**

Zhenghu Li, Junhui Zhang, Hui Chen, Xiuzhi Shi, Yanyang Zhang and Yanjun Zhang
A Safe and Efficient Mining Method with Reasonable Stress Release and Surface Ecological Protection
Reprinted from: *Sustainability* **2022**, *14*, 5348, doi:10.3390/su14095348 . . . . . **117**

Mohamed Elgharib Gomah, Guichen Li, Changlun Sun, Jiahui Xu, Sen Yang and Jinghua Li
On the Physical and Mechanical Responses of Egyptian Granodiorite after High-Temperature Treatments
Reprinted from: *Sustainability* **2022**, *14*, 4632, doi:10.3390/su14084632 . . . . . **129**

Fhatuwani Sengani and Dhiren Allopi
Accuracy of Two-Dimensional Limit Equilibrium Methods in Predicting Stability of Homogenous Road-Cut Slopes
Reprinted from: *Sustainability* **2022**, *14*, 3872, doi:10.3390/su14073872 . . . . . **151**

Niaz Muhammad Shahani, Xigui Zheng, Xiaowei Guo and Xin Wei
Machine Learning-Based Intelligent Prediction of Elastic Modulus of Rocks at Thar Coalfield
Reprinted from: *Sustainability* **2022**, *14*, 3689, doi:10.3390/su14063689 . . . . . **177**

Shuai Li, Zheng Yu, Haoxuan Yu and Xinmin Wang
The Recent Progress China Has Made in High-Concentration Backfill
Reprinted from: *Sustainability* **2022**, *14*, 2758, doi:10.3390/su14052758 . . . . . **201**

Huaming An, Shunchuan Wu, Hongyuan Liu and Xuguang Wang
Hybrid Finite-Discrete Element Modelling of Various Rock Fracture Modes during Three Conventional Bending Tests
Reprinted from: *Sustainability* **2022**, *14*, 592, doi:10.3390/su14020592 . . . . . **219**

Hai Wu, Qian Jia, Weijun Wang, Nong Zhang and Yiming Zhao
Experimental Test on Nonuniform Deformation in the Tilted Strata of a Deep Coal Mine
Reprinted from: *Sustainability* **2021**, *13*, 13280, doi:10.3390/su132313280 . . . . . **245**

Qun Yu, Masoud Monjezi, Ahmed Salih Mohammed, Hesam Dehghani, Danial Jahed Armaghani and Dmitrii Vladimirovich Ulrikh
Optimized Support Vector Machines Combined with Evolutionary Random Forest for Prediction of Back-Break Caused by Blasting Operation
Reprinted from: *Sustainability* **2021**, *13*, 12797, doi:10.3390/su132212797 . . . . . **259**

Qinqiang Guo, Haoxuan Yu, Zhenyu Dan and Shuai Li
Mining Method Optimization of Gently Inclined and Soft Broken Complex Ore Body Based on AHP and TOPSIS: Taking Miao-Ling Gold Mine of China as an Example
Reprinted from: *Sustainability* **2021**, *13*, 12503, doi:10.3390/su132212503 . . . . . **275**

Ruichong Zhang, Shiwei Wu, Chenyu Xie and Qingfa Chen
Study on the Geological Condition Analysis and Grade Division of High Altitude and Cold Stope Slope
Reprinted from: *Sustainability* **2021**, *13*, 12464, doi:10.3390/su132212464 . . . . . **289**

Xingkai Wang, Leibo Song, Caichu Xia, Guansheng Han and Zheming Zhu
Nonlinear Elasto-Visco-Plastic Creep Behavior and New Creep Damage Model of Dolomitic Limestone Subjected to Cyclic Incremental Loading and Unloading
Reprinted from: *Sustainability* **2021**, *13*, 12376, doi:10.3390/su132212376 . . . . . **307**

Sen Yang, Guichen Li, Ruiyang Bi, Bicheng Yao, Ruiguang Feng and Yuantian Sun
The Stability of Roadway Groups under Rheology Coupling Mining Disturbance
Reprinted from: *Sustainability* **2021**, *13*, 12300, doi:10.3390/su132112300 . . . . . **323**

Jinjin Ge, Ying Xu, Wei Huang, Haibo Wang, Rongzhou Yang and Zhongyi Zhang
Experimental Study on Crack Propagation of Rock by Blasting under Bidirectional Equal Confining Pressure Load
Reprinted from: *Sustainability* **2021**, *13*, 12093, doi:10.3390/su132112093 . . . . . **341**

Chia Yu Huat, Seyed Mohammad Hossein Moosavi, Ahmed Salih Mohammed, Danial Jahed Armaghani, Dmitrii Vladimirovich Ulrikh, Masoud Monjezi and Sai Hin Lai
Factors Influencing Pile Friction Bearing Capacity: Proposing a Novel Procedure Based on Gradient Boosted Tree Technique
Reprinted from: *Sustainability* **2021**, *13*, 11862, doi:10.3390/su132111862 . . . . . **359**

Qingliang Chang, Yifeng Sun, Qiang Leng, Zexu Liu, Huaqiang Zhou and Yuantian Sun
Stability Analysis of Paste Filling Roof by Cut and Fill Mining
Reprinted from: *Sustainability* **2021**, *13*, 10899, doi:10.3390/su131910899 . . . . . **383**

Yan Li, Fathin Nur Syakirah Hishamuddin, Ahmed Salih Mohammed, Danial Jahed Armaghani, Dmitrii Vladimirovich Ulrikh, Ali Dehghanbanadaki and Aydin Azizi
The Effects of Rock Index Tests on Prediction of Tensile Strength of Granitic Samples: A Neuro-Fuzzy Intelligent System
Reprinted from: *Sustainability* **2021**, *13*, 10541, doi:10.3390/su131910541 . . . . . **397**

Yuantian Sun, Guichen Li, Junfei Zhang, Junbo Sun, Jiandong Huang and Reza Taherdangkoo
New Insights of Grouting in Coal Mass: From Small-Scale Experiments to Microstructures
Reprinted from: *Sustainability* **2021**, *13*, 9315, doi:10.3390/su13169315 . . . . . **419**

Chenxi Zhang, Diyuan Li, Shunchuan Wu, Long Chen and Jun Peng
Study on Evolution Mechanism of Structure-Type Rockburst: Insights from Discrete Element Modeling
Reprinted from: *Sustainability* **2021**, *13*, 8036, doi:10.3390/su13148036 . . . . . **437**

Carlos Efrain Contreras Inga, Gabriel Walton and Elizabeth Holley
Statistical Assessment of the Effects of Grain-Structure Representation and Micro-Properties on the Behavior of Bonded Block Models for Brittle Rock Damage Prediction
Reprinted from: *Sustainability* **2021**, *13*, 7889, doi:10.3390/su13147889 . . . . . **463**

Aman Tiwari, Nitin Dindorkar and Suneet Kaur
Bibliometric and Knowledge Network of Global Research on Pile Foundations: A Review of Recent Developments
Reprinted from: *Sustainability* **2023**, *15*, 11108, doi:10.3390/su151411108 . . . . . **491**

Huaming An, Yuqing Fan, Hongyuan Liu, Yinyao Cheng and Yushan Song
The State of the Art and New Insight into Combined Finite–Discrete Element Modelling of the Entire Rock Slope Failure Process
Reprinted from: *Sustainability* **2022**, *14*, 4896, doi:10.3390/su14094896 . . . . . **507**

About the Editors

Mahdi Hasanipanah

Dr. Mahdi Hasanipanah obtained his BSc degree in Mining Engineering from the University of Kashan, Iran, in 2008; his MSc degree in Mining Engineering from the Islamic Azad University—South Tehran Branch, Iran, in 2010; and his PhD in Mining Engineering from University of Kashan, Iran, in 2020. His research interests include rock blasting, rock mechanics, machine learning methods, and optimization algorithms. He has cooperated in a large number of projects in Iran and Malaysia. He is also the chief Guest Editor of *Sustainability* (MDPI)'s Special Issue "Advances in Rock Mechanics and Geotechnical Engineering". His citation and H-index are 5600 and 49, respectively, which indicate the significant impact and influence of his research in the academic and scientific communities. He was among the top 2% of scientists for two consecutive years, including 2022 and 2023, according to Stanford University.

Danial Jahed Armaghani

Dr. Danial Jahed Armaghani is a prominent researcher in the field of civil and geotechnical engineering. His work has made significant contributions to the understanding and mitigation of geotechnical and geological hazards, earning him a reputation as an excellent researcher in his field. Dr. Danial's research focuses on a wide range of topics, including slope stability analysis, rock mechanics, tunnel construction, surface and deep excavations, and applying machine learning models and optimization algorithms to solve various geotechnical problems. Dr. Danial obtained his MEng (2012) and PhD (2015) in the area of Civil-Geotechnics, from Universiti of Teknologi Malaysia (UTM), Malaysia. He is currently working as a Postdoctoral Research Fellow at the School of Civil and Environmental Engineering, University of Technology Sydney (UTS), Australia. He published more than 300 articles in well-established ISI and Scopus journals and at national and international conferences. His published works have received more than 19,000 citations, which indicate the significant impact and influence of his research in the academic and scientific communities. He was among the top 2% of scientists for four consecutive years from 2020 to 2023, according to Stanford University.

Jian Zhou

Assoc. Prof. Jian Zhou obtained his BSc degree (2008) and PhD (2015) from Central South University (CSU), China, and was a visiting scholar with Mine Design Laboratory at McGill University from 2013 to 2014. Currently, he is an associate professor in the School of Resources and Safety Engineering at CSU, China. His current research interests include geological and geotechnical hazards prediction and mitigation, applying predictive models in rock mechanics, and mining engineering. Dr. Zhou is the Highly Cited Researcher in the field of Cross-Field (Clarivate); a Highly Cited Chinese Researcher in the field of Mining Engineering (Elsevier); one of the World's Top 2% Scientists according to Stanford University; and a recipient of the Distinguished Young Scholars Fund of Hunan Province, China. He has published more than 180 papers in international journals on mining and geotechnical issues and has received China's 100 Most Influential International Academic Papers Award, the *Journal of Rock Mechanics and Geotechnical Engineering's* Best Paper Award, and the *Journal of Central South University's* Best Paper Award. His citation and H-index are 9600 and 55, respectively.

sustainability

MDPI

Article

Soil Liquefaction Prediction Based on Bayesian Optimization and Support Vector Machines

Xuesong Zhang [1,*], Biao He [2], Mohanad Muayad Sabri Sabri [3,*], Mohammed Al-Bahrani [4] and Dmitrii Vladimirovich Ulrikh [5]

[1] College of Pipeline and Civil Engineering, China University of Petroleum (East China), Qingdao 266580, China
[2] Department of Civil Engineering, Faculty of Engineering, Universiti Malaya, Kuala Lumpur 50603, Malaysia
[3] Peter the Great St. Petersburg Polytechnic University, 195251 St. Petersburg, Russia
[4] Air Conditioning and Refrigeration Techniques Engineering Department, Al-Mustaqbal University College, Babylon 51001, Iraq
[5] Department of Urban Planning, Engineering Networks and Systems, Institute of Architecture and Construction, South Ural State University, 76 Lenin Prospect, 454080 Chelyabinsk, Russia
* Correspondence: snowpiner@upc.edu.cn (X.Z.); mohanad.m.sabri@gmail.com (M.M.S.S.)

Abstract: Liquefaction has been responsible for several earthquake-related hazards in the past. An earthquake may cause liquefaction in saturated granular soils, which might lead to massive consequences. The ability to accurately anticipate soil liquefaction potential is thus critical, particularly in the context of civil engineering project planning. Support vector machines (SVMs) and Bayesian optimization (BO), a well-known optimization method, were used in this work to accurately forecast soil liquefaction potential. Before the development of the BOSVM model, an evolutionary random forest (ERF) model was used for input selection. From among the nine candidate inputs, the ERF selected six, including water table, effective vertical stress, peak acceleration at the ground surface, measured CPT tip resistance, cyclic stress ratio (CSR), and mean grain size, as the most important ones to predict the soil liquefaction. After the BOSVM model was developed using the six selected inputs, the performance of this model was evaluated using renowned performance criteria, including accuracy (%), receiver operating characteristic (ROC) curve, and area under the ROC curve (AUC). In addition, the performance of this model was compared with a standard SVM model and other machine learning models. The results of the BOSVM model showed that this model outperformed other models. The BOSVM model achieved an accuracy of 96.4% and 95.8% and an AUC of 0.93 and 0.98 for the training and testing phases, respectively. Our research suggests that BOSVM is a viable alternative to conventional soil liquefaction prediction methods. In addition, the findings of this research show that the BO method is successful in training the SVM model.

Keywords: liquefaction potential; prediction; Bayesian optimization; support vector machines; optimization

Citation: Zhang, X.; He, B.; Sabri, M.M.S.; Al-Bahrani, M.; Ulrikh, D.V. Soil Liquefaction Prediction Based on Bayesian Optimization and Support Vector Machines. *Sustainability* **2022**, *14*, 11944. https://doi.org/10.3390/su141911944

Academic Editors: Mahdi Hasanipanah, Danial Jahed Armaghani and Jian Zhou

Received: 4 July 2022
Accepted: 15 September 2022
Published: 22 September 2022

Publisher's Note: MDPI stays neutral with regard to jurisdictional claims in published maps and institutional affiliations.

Copyright: © 2022 by the authors. Licensee MDPI, Basel, Switzerland. This article is an open access article distributed under the terms and conditions of the Creative Commons Attribution (CC BY) license (https://creativecommons.org/licenses/by/4.0/).

1. Introduction

Solid-to-liquid transitions in granular materials are known as liquefaction, and may be caused by a growth in pore water pressure [1,2]. Seismic liquefaction of saturated soils, which occurs as a result of earthquakes, is one of geotechnical engineers' most pressing problems. This is because the lateral expansion of soil mass might represent a significant hazard to civil engineering works in the area if it occurs [1–3]. As an example, after the Wenchuan earthquake of M 8.0 which struck China in 2008, both surface buildings and subsurface utilities were damaged by liquefaction [1,2,4]. Consequently, estimating the soil liquefaction potential is a significant issue, and must be considered when building civil engineering structures [5–10]. Soil liquefaction potential may be measured in a variety of ways, as described in the scientific literature (e.g., [11–13]). Since in situ observations can only be made in regions where testing may be done on site, most approaches rely

on separating non-liquefaction sections from liquefaction components (e.g., the shear wave velocity (Vs) technique and flat dilatometer tests (DMTs)) [2,14]. Due to the great uncertainty in both soil properties and earthquake scenarios, it is difficult to find a single effective empirical formula for regression analysis. This is why scientists are working to develop scientific predictive methods that are simpler, more intuitive, and more accurate than the typical empirical models that were previously used to analyze soil liquefaction.

Liquefaction potential may be accurately predicted using artificial neural networks (ANN)-based models, the most extensively used of all (e.g., [15–19]). In fact, ANNs have been shown to be more efficient than statistical approaches, but they also display several shortcomings, such as slow convergence speed, over-fitting, falling into local minima, poor generalization, and so forth. Using post-liquefaction cone penetration test (CPT) and standard penetration test (SPT) data, Muduli and Das [20,21] created the multi-gene genetic programming (MGGP) technique to assess the ability of the soil to be liquefied. It was discovered that a new instrument for assessing liquefaction could be marketed and supported efficiently. Particle swarm optimization (PSO) was used to improve a neuro-fuzzy GMDH model created by Javdanian et al. [22]. This model was shown to be acceptable and reliable in this area. PSO was also hybridized with a kernel extreme learning machine (KELM) to evaluate liquefaction potential [23]. To forecast the likelihood of the soil liquefaction, Hoang and Bui [24] used a least squares support vector machine (LSSVM) and a kernel Fisher discriminant analysis. Their findings demonstrated that the suggested model is both acceptable and reliable in this domain. Soil liquefaction was also predicted using the ensemble group method of data handling (EGMDH) [25]. The EGMDH model was shown to be more accurate than the standard GMDH model in forecasting soil liquefaction. Rahbarzare and Azadi [26] proposed an improved fuzzy support vector machine (FSVM) based on PSO and a genetic method. According to the researchers, FSVM performance was improved by using PSO and genetic algorithms (GAs). It seems that machine learning models are able to solve liquefaction potential problems with an acceptable level of accuracy. It is important to note that such models have been successfully applied in different areas of civil engineering, as reported by many scholars [27–49]. Some studies also employed Bayesian models to model the liquefaction triggers [50–52].

SVM models have been frequently utilized to forecast soil liquefaction. This method has been hybridized with different optimization techniques, including genetic algorithms (GAs), differential evolution (DE), grey wolf optimization (GWO), and kernel Fisher discriminant analysis (KFDA) [24,53]. However, to the best of our knowledge, no study to date has hybridized SVM with the Bayesian optimization (BO) technique, which is one of the most effective optimization techniques. Thus, in order to forecast soil liquefaction potential, this research develops a hybrid intelligence model (BOSVM). The remainder of the paper is organized as follows: Section 2 explains the mechanics of soil liquefaction. Section 3 goes on to describe the SVM and BO frameworks, as well as the datasets that were employed in this investigation. The results and discussion are described in Section 4. Finally, Section 5 gives a summary of this study.

2. Process of Soil Liquefaction

Saturated cohesionless soils liquefy when pore pressure rises, causing a loss in firmness that may lead to cracking and crumbling [1]. More specifically, Sladen et al. [54] describe the process of soils losing their shear resistance when subjected to cyclic, monotonic, or shock loadings; subsequently, the soil flows like a liquid until the shear stresses that operate on its mass are equal to or lower than its lowered resistance. In a broader sense, liquefaction is a transition from solidity to fluidity that happens when the pore pressure and the functional stresses are increased or decreased [1]. When soils are subjected to shearing forces, they have a propensity to shrink in volume, which can lead to the process known as liquefaction. After being sheared, saturated loose soil tends to compact into tighter particles that take up fewer pore spaces, analogous to the way that water is driven out of pores when trapped in them. Penetrating shear loads may cause pore water pressures to increase over time if the

drainage system is blocked. When this occurs, stress is transferred from the soil mass to the pore water, reducing the soil's shear resistance and its effective stress [1]. Liquidity occurs when the soil's shear resistance is less than its static, driving shear stress, allowing the soil to undergo structural damage. True liquefaction occurs only when the flow of soil is greater than the undrained residual shear resistance of a contracting soil under a static shear stress, according to Castro's most restrictive description [55]. It is worth remembering that both cyclic and monotonic shear stresses may lead to the liquefaction of cohesionless, loose soil.

3. Method

Soil liquefaction was predicted using a hybrid of the SVM model and the BO algorithm. Input selection, data splitting, model construction, and evaluation were all part of the procedure. A flowchart of this study is shown in Figure 1.

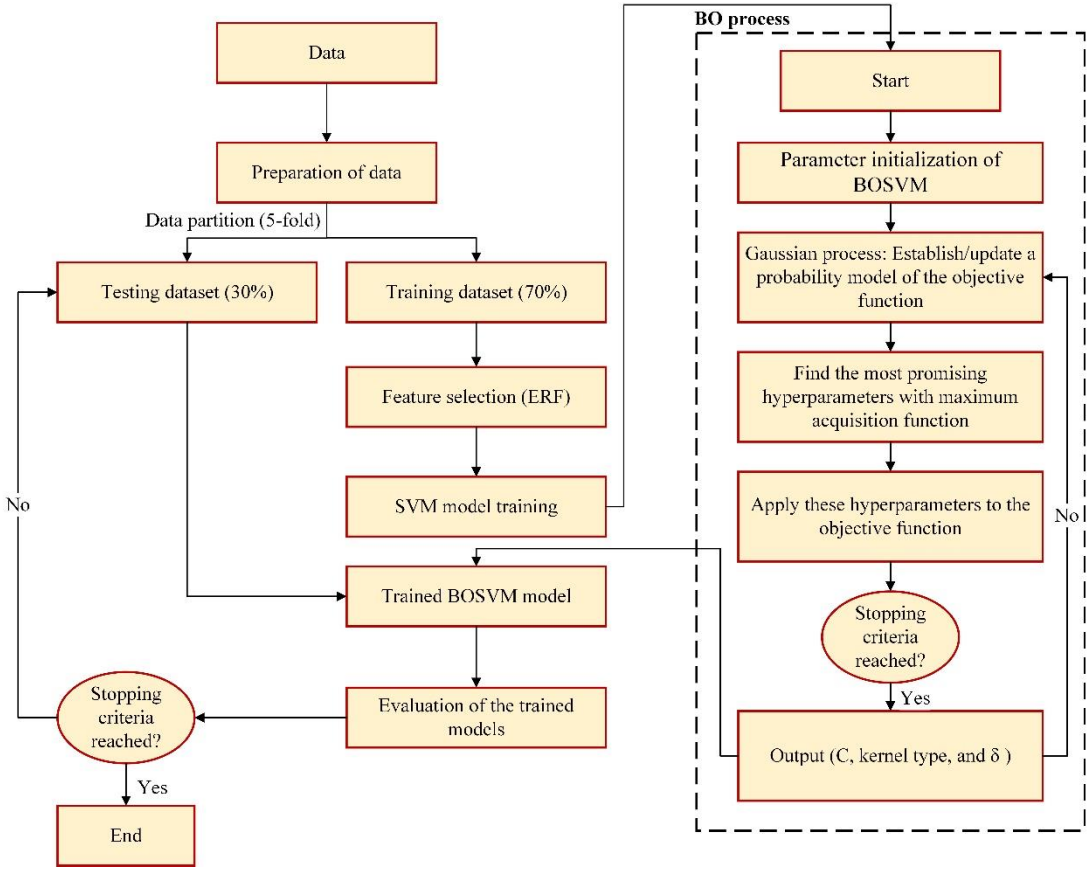

Figure 1. Flowchart of this study.

3.1. Evolutionary Random Forest (ERF)

Input selection is a critical step in the development of any ML model. Input selection refers to a process that identifies the most relevant inputs and removes irrelevant inputs from the dataset and modelling process. In this study, the evolutionary random forest (ERF) algorithm was employed. It is common practice to apply the random forest (RF) method and its ensemble theory when working with large datasets, selecting features for classification, and carrying out regression analyses. The RF method generates a variety of weak regressors based on decision trees (DTs) using randomly selected inputs or sample divisions from a training set. Each DT is created using data provided by the user, and generates a decision-making model. In other words, characteristics in the dataset are examined and disassembled in order to reach a satisfactory choice. Each model's forecasted decision outcomes are obtained by the algorithm throughout the regression procedure. The mean of all the forecasts is used to reach the final forecast. Regardless of whether

the overfitting issue is successfully mitigated, the RF's arbitrary rule may impair learning capacity. As a result, the evolutionary computation that improves the subset sampling process [56,57] is expected to play a critical role in complementing the RF by enhancing the searchability of the complex objective function.

As can be seen in Figure 2, randomly generated rules at the start of the experiment determine data partitions and assign these subsets to each and every poor classifier/regressor. The regressors anticipate the value of the training data and collect the average forecasts to make a consensus. Regression accuracy results are used to gauge an individual's fitness in the evolutionary process. To improve accuracy and genetic characteristics of the number of proposed individuals, repeated processes such as choosing, crossover, mutation, and evaluation are later applied. If the individuals converge, the algorithm stops the replicating phase and produces an optimum split of individuals as a model for regression. An ensemble regression based on a prior stage's optimum individual is offered in this subsequent round of use of the trained model.

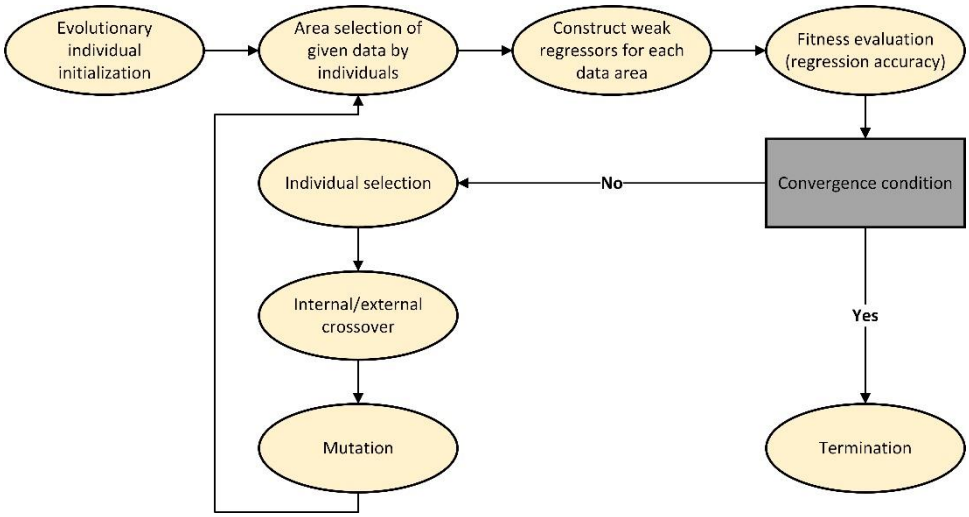

Figure 2. ERF flowchart.

3.2. Support Vector Machines

SVM is a ML approach that incorporates various methodologies such as maximum interval hyperplane, relaxation variables, and kernel function. Statistical principles are behind this ML model. The classification difficulties associate with few samples, nonlinearity, and complexity may be solved with this method [58]. SVM has been progressively used in civil engineering as interdisciplinary integration has become more widespread. A nonlinear transformation is used to translate the input space samples into a high-dimensional characteristic space, and then an optimum classification plane is found that divides the samples linearly within the characteristic space as the next step [59,60]. The incidence of soil liquefaction functions well with the features of the approach to overcome binary classification issues in the study of soil liquefaction and its risk assessment (e.g., [61]).

Figure 3 depicts a schematic representation of the SVM concept. When a hyperplane is compared to a sample point, it is known as a margin. The classifier's capacity to generalize improves with an increasing margin of error. As a result, finding the hyperplane that maximizes the margin (i.e., the ideal hyperplane) is the primary goal of the SVM. There are support vectors for every point on the hyperplane on either side of the margin, and the categorization border is decided only by the support vectors, not by additional data nor the quantity of data. Because of this, the optimization of the SVM's hyperparameters is essential. Among the several hyperparameters used in SVM, kernel type, C, and gamma are among the most important. As previously stated, the kernel transforms the observed data into a feature space. By imposing a penalty for every incorrectly classified data sample, hyperparameter C manages the exchange between the decision boundary and precision.

In various kernel types, gamma is a parameter linked to C. The influence of C is minimal when gamma is large. When gamma is modest, C has an effect on the model comparable to the effect it would have on a linear one.

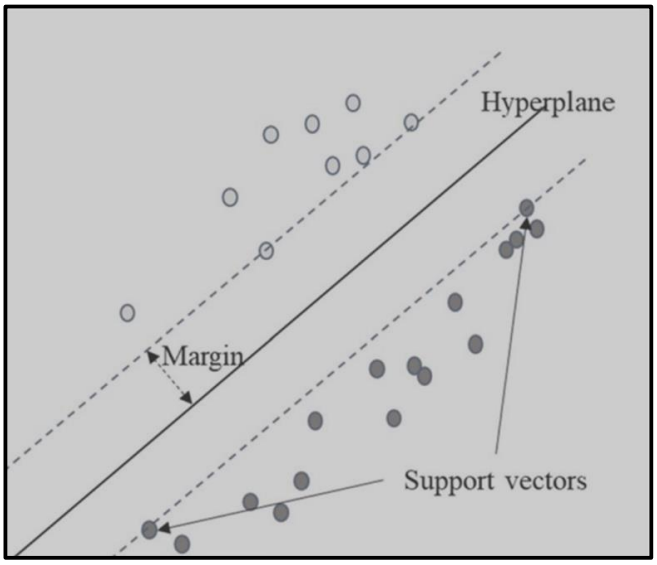

Figure 3. A schematic of SVM.

3.3. Bayesian Optimization Algorithm

The adjustment of learning parameters and model hyperparameters is an important part of the implementation of ML algorithms [62]. Model or training process qualities are defined by hyperparameters, which have a substantial impact on the model's ultimate outcome [63]. Conventional ML algorithms use BO as a hyperparameter optimization (picking) strategy, as part of their overall design. The BO algorithm is extensively used in pioneering AI because of its evident benefits when compared with the particle swarm optimization algorithm, genetic algorithm, or other algorithms [63,64]. The Gaussian process and the Bayesian theorem are used to optimize parameters in this technique. A Bayesian ML approach and Gaussian process regression are used to generate a surrogate for the objective, and to quantify the ambiguity in that surrogate. To determine the sample position, an acquiring function can be expressed from this substitute. In Appendix A, the typical circumstances in which the BO algorithm encounters difficulties are explained. In addition, Figure 4 depicts a generic pseudocode of the BO.

```
BEGIN
Set of hyperparameters of SVM model for kernel function and C
Set the objective function
Set i = 1
While i <= i_max
    Create a surrogate probability model of the objective function.
    Find the hyperparameters that perform best on the surrogate model.
    Use there hyperparameters to the true objective function.
    Update the surrogate model incorporating the new result.
    i=i+1
End of While
Extract optimized hyperparameters.
Build SVM model using these hyperparameters.
END
```

Figure 4. BO's generic pseudocode.

3.4. Performance Criteria

This study used several well-known performance criteria for classification. These criteria include the confusion matrix, accuracy (%), the receiver operating characteristic (ROC) curve, and the area under the ROC curve (AUC). The more accurate the model, the closer the curve is to the model's top-left corner. AUC values fall within a range of 0 to 1. The greater the AUC, the more accurate the model.

3.5. Data for Modeling

The Great Tangshan Earthquake, which occurred on 28 July 1976, was a major natural catastrophe in China. The number killed put the catastrophe at the top of the list of the most devastating earthquakes of the 20th century. Hebei's industrial metropolis of Tangshan, home to almost a million people, was the epicenter of the earthquake. Initial estimates put the death toll at 655,000, but this has since been revised to between 240,000 and 255,000, with 164,000 people suffering from serious injuries [1]. In order to build the models described in this research, a database from prior studies was used [1]. The Tangshan Earthquake was the subject of this database [65]. Several entries were omitted from the final analysis, owing to incomplete or inaccurate data. Liquefaction potential was the sole parameter included in the model output. Variables used in this study are listed in Table 1. A value of "1" indicates that liquefaction has occurred in each example, whereas "0" indicates that it has not. The overall cyclic shear stress caused by the earthquake is indicated by the term τ_{av}. Modeling included the utilization of 79 different sets of data. The data were split into training and test datasets, with a ratio of 70:30. To train the BOSVM model, this study used 5-fold cross-validation. The developed model was then tested using the test data.

Table 1. Variables used in this study.

Variable	Symbol	Unit	Min	Max
Earthquake magnitude	M	-	7.8	7.8
Effective vertical stress	σ'_{v0}	kPa	20.6	120.4
Total vertical stress	σ_v	kPa	16.7	244.2
Mean grain size	D_{50}	mm	0.06	0.48
Water table	d_w	m	0.21	3.6
Peak acceleration at the ground surface	a_{max}	g	0.1	1.1
Depth	d_s	m	0.9	13.1
Measured CPT tip resistance	q_c	MPa	0.98	18.57
CSR	$\frac{\tau_{av}}{\sigma'_{v0}}$	-	0.08	0.42
Liquefaction observed *	-	-	0	1

* Target variable.

4. Results and Discussion

4.1. Input Selection

Input selection is a critical phase in the machine learning modelling process [54–57,66–69], and is used to remove unnecessary variables while keeping those that are valuable. This study employed the evolutionary random forest (ERF) technique for input selection. The dataset used in this study consisted of nine candidate inputs, including M, d_w, d_s, σ_v, σ'_{v0}, a_{max}, q_c, CSR, and D_{50}. These nine parameters were selected because of their effects on the liquefaction from a geotechnical viewpoint; some of them were used in the previous related studies or suggested as the most influential factor in liquefaction occurrence [1,19,23,50,51]. Nonetheless, they have different levels of impact on liquefaction occurrence. It is necessary to keep intelligent models as simple as possible. This can be achieved by considering the most influential factors. To do this, the ERF selected six inputs, including d_w, σ'_{v0}, a_{max}, q_c, CSR, and D_{50}. Based on the ERF findings, a subset of these six inputs outperformed other input subsets on the dataset utilized in this research. These inputs were used to develop SVM and BOSVM models to predict soil liquefaction. It is important to mention that several parameters were used to develop the ERF model. The selection scheme was set as "tournament", p initialize

was set as 0.5, p mutation was set as -0.1, and p crossover was set as 0.5. The crossover type was uniform. The accuracy of this model was 92.50%.

4.2. BOSVM Model Development

The hyperparameter optimization of the prediction model based on SVM was carried out using the Bayesian optimization (BO) approach in this work. Hyperparameters such as box constraint level and kernel scale were optimized using the BO technique for SVM models based on the hybrid model. These settings were configured from 0.001 to 1000. An overview of how the BO optimization method is used to optimize SVM parameters is provided below:

1. Preparing the data: Using a suitable ratio, the data set is partitioned into training and testing sets (70:30). The distribution of inputs after the data split is shown in Figures 5 and 6.
2. Examination of fitness: The fitness function is computed and assessed before optimizing the target parameter value. The fitness function in this study is classification error.
3. Adjusting the settings: hyperparameter optimization criteria may be adjusted according to the outcomes of each iteration, if desired.
4. Stop checking for conditions: Optimization stops once the best parameters have been found.

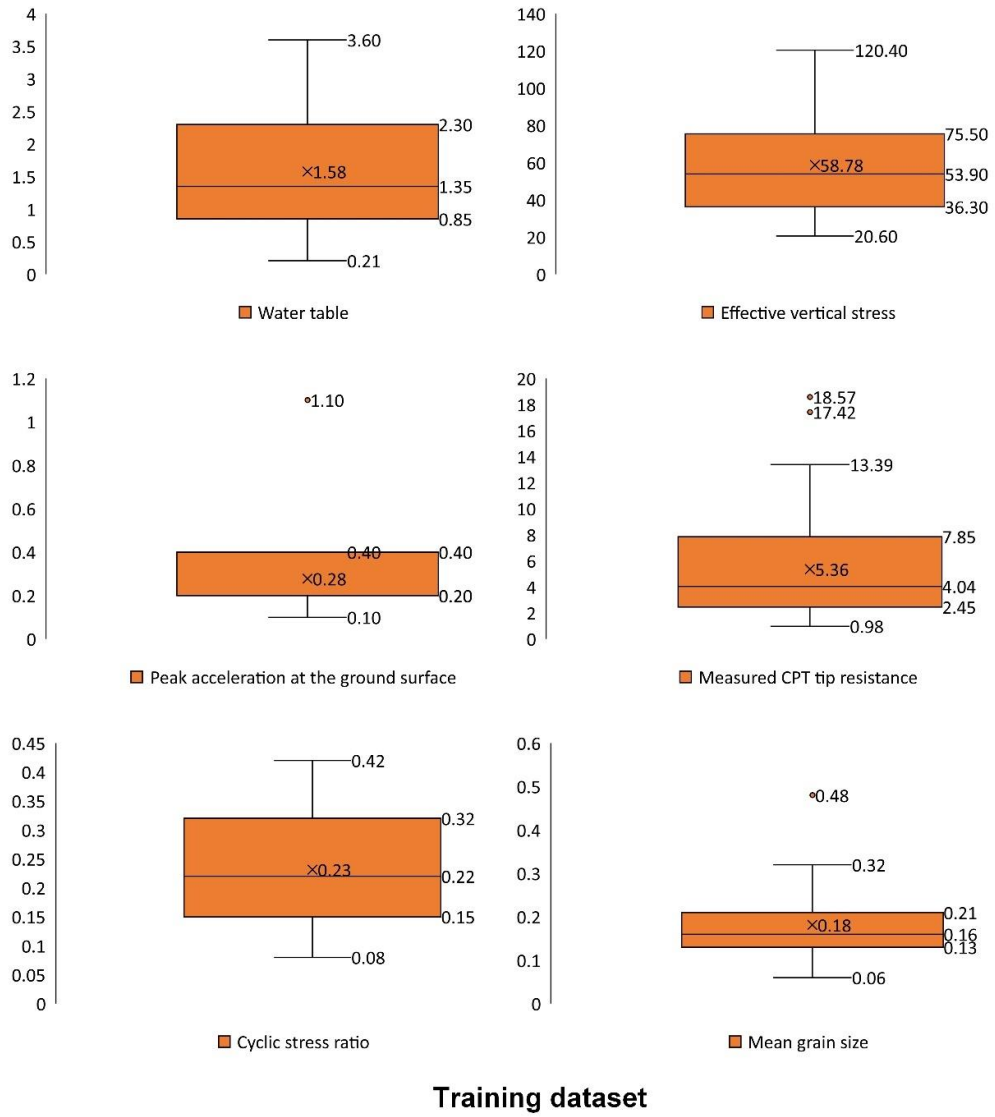

Figure 5. Distribution of inputs after data split (training set).

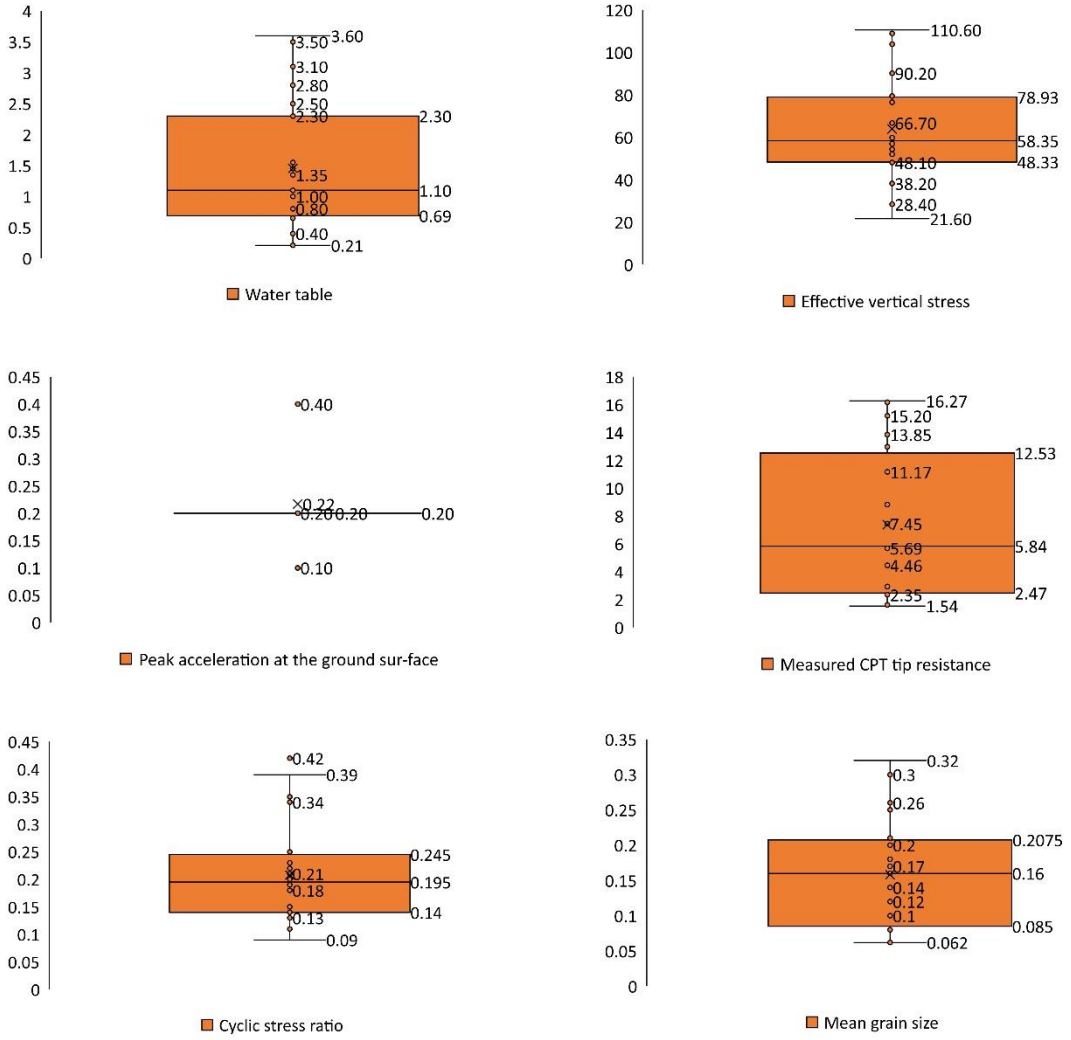

Figure 6. Distribution of inputs after data split (testing set).

SVM was used in conjunction with one optimization technique (i.e., BO) to create a hybrid intelligent model based on SVM that could better forecast soil liquefaction. As a result of the aforementioned optimization, several hyperparameter settings and model prediction results were produced.

One hundred iterations of the BOSVM model utilizing the fitness assessment of classification error were used to obtain the optimal SVM hyperparameters. As shown in Figure 7, convergence occurred in the BOSVM model before the maximum number of iterations had been completed. After 19 iterations using the BOSVM approach, the optimum SVM hyperparameters with the lowest classification error of 0.033 were found. This proves that the strategy is reasonably effective in identifying the optimum hyperparameters. The ability of BO to use all knowledge from prior runs in order to discover the next set of hyperparameters may explain this high rate of convergence [70,71].

As the kernel and regularization parameter (C) were optimized for BO, the linear kernel and a C value of 18.49 were the hyperparameters that best matched those values. Prior to modeling, these variables would be used as BOSVM hyperparameter values, whereas the standard SVM makes use of the default configuration. Both the SVM and BOSVM models were evaluated using the accuracy (%), confusion matrix, and ROC curve to verify and evaluate results. The ROC curve shows the predictive power of the models, while the confusion matrix shows the specifics of the model's prediction capacity.

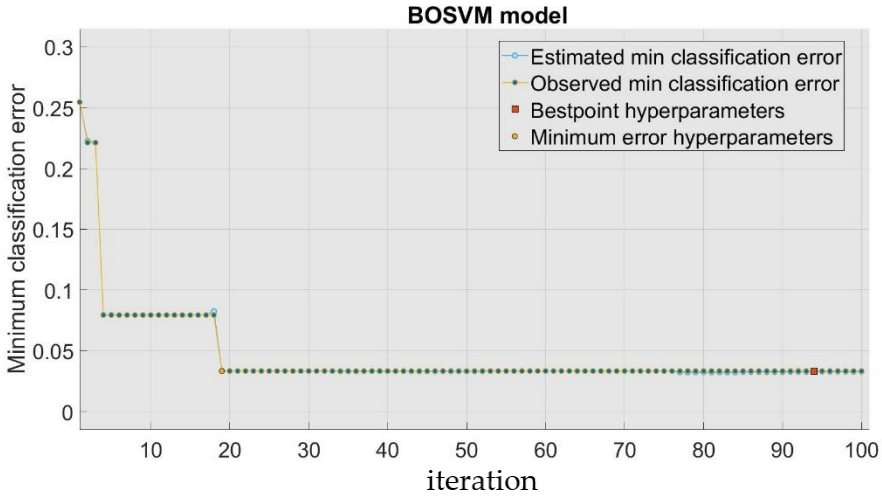

Figure 7. SVM model optimization process.

As stated in Table 2, the training accuracy of BOSVM is demonstrated to be 96.4%, which is almost 5.5% better than the SVM's 90.9% training accuracy. Moreover, the SVM model's test accuracy improved by 4.1% with the use of the BO algorithm. The BOSVM model's training and testing accuracy are fairly close together, indicating the model's stability in predicting soil liquefaction. Overall, soil liquefaction was better predicted with BOSVM than with SVM.

Table 2. The confusion matrix of the models developed in this study.

Model		Train			Test		
	Actual	Prediction			Prediction		
		0	1	Accuracy (%)	0	1	Accuracy (%)
SVM	0	9	5	90.9	9	1	91.7
	1	0	41		1	13	
BOSVM	0	12	2	96.4	10	0	95.8
	1	0	41		1	13	

Figure 8 shows the ROC curve for both the training (Figure 8a) and testing (Figure 8b) phases. The ROC curve is constructed by graphing the true positive rate versus the false positive rate at different threshold levels. In addition, values of the area under the ROC curve (AUC) are shown in this figure. AUC values higher than 0.9 are typically regarded as excellent, according to Merghadi et al. [72]. Both the training and testing phases of the BOSVM model have AUC values of above 0.9. There seems to be an adequate distribution of ROC values for the BOSVM, and the majority are clustered towards the top.

As can be seen in Figure 9, the BOSVM model's prediction performance was compared with that of other models, including those for logistic regression, single decision trees, boosted trees, and artificial neural networks (ANNs). The hybrid optimization model had better predictive performance than other models (see Figure 6). There can be no doubt that the BOSVM hybrid model can learn, evaluate, and forecast well from the given findings. Soil liquefaction can be predicted by applying the suggested BOSVM hybrid model.

In addition, it should be noted that the entire datasets reported in this research were utilized in the investigations carried out by Xue and Yang [1] and Cai et al. [53]. They used three more input parameters (i.e., M, d_s, and σ_v) together with the six inputs used in the current study, and developed an adaptive neuro fuzzy inference system (ANFIS), a least squares support vector machine (LSSVM) and a radial basis function neural network (RBFNN) in combination with the optimization algorithms (i.e., the grey wolf optimization (GWO), differential evolution (DE), and genetic algorithm (GA)) for predicting the soil

liquefaction values. The current study's results are comparable to those of the preceding investigations. This shows that the BOSVM model suggested in this work can make excellent forecasts.

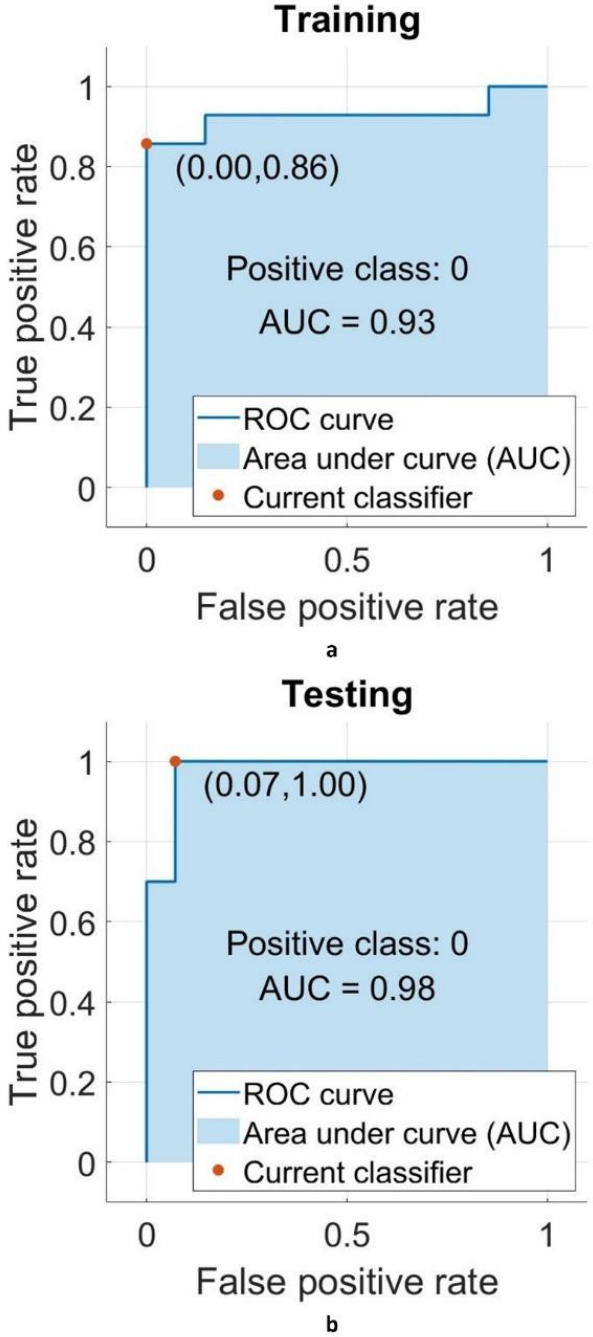

Figure 8. ROC curves of BOSVM model: (**a**) Training, (**b**) testing.

This study's findings compare favorably with those of many previous soil liquefaction studies that used different datasets. For example, accuracy values of 92.2% and 93.19% were obtained in the studies conducted by Zhang et al. [61] and Hoang and Bui [24], respectively, to predict soil liquefaction by introducing grey wolf optimization (GWO)-SVM and kernel Fisher discriminant analysis (KFDA) with least square support vector machine (LSSVM) techniques. In other words, the developed BOSVM prediction model outperformed the other models in terms of accuracy. Consequently, this study recommends that the BOSVM model be used and developed to anticipate soil liquefaction in the future.

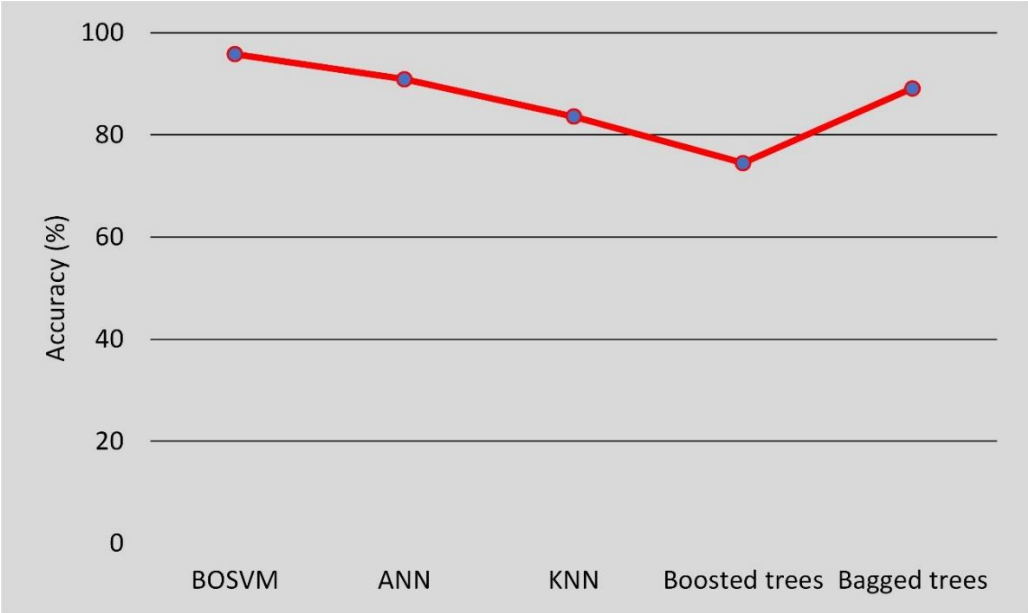

Figure 9. Comparison of accuracy with other models.

5. Limitations and Future Works

Future studies might use the model created in this research to predict soil liquefaction. Soil liquefaction under more severe situations requires further data and research, and this should be emphasized. Only under identical circumstances and with a suitable range of database information should the hybrid model described here be used. It is recommended that in the future more data samples and characteristics should be included in the experimental database in order to improve model accuracy.

6. Conclusions

Soil liquefaction was the subject of this research, which used the hybridization of SVM models. A renowned optimization strategy (i.e., BO) that has been effectively studied by other scholars was chosen and integrated with SVM, and a BOSVM hybrid model was constructed for prediction purposes. This model was constructed using six model inputs and an output (i.e., soil liquefaction). For input selection, an ERF approach was used prior to the development of this model. The nine possible inputs were narrowed down to the six that were ultimately used. The performance of the SVM-based model was assessed using accuracy (%), ROC curve, AUC, and confusion matrix. In addition, for comparison purposes we predicted soil liquefaction using other proposed models (i.e., SVM, ANN, KNN, boosted trees, and bagged trees). The BOSVM model outperformed all other applied predictive approaches, with an accuracy of 96.4% and 95.8% and an AUC of 0.93 and 0.98 for training and testing, respectively, after being evaluated against all other created and applied models. Therefore, the model developed in this work may be applied in future studies to forecast soil liquefaction.

Author Contributions: Conceptualization, X.Z., B.H., M.M.S.S. and D.V.U.; methodology, X.Z., B.H., M.M.S.S. and D.V.U.; software, X.Z., B.H., M.M.S.S. and D.V.U.; formal analysis, X.Z., B.H., M.M.S.S. and D.V.U.; writing—original draft preparation, X.Z., B.H., M.M.S.S. and D.V.U.; writing—review and editing, X.Z., B.H., M.M.S.S., M.A.-B. and D.V.U.; visualization, X.Z., B.H., M.M.S.S. and D.V.U.; supervision, M.M.S.S., M.A.-B. and D.V.U.; funding acquisition, M.M.S.S. All authors have read and agreed to the published version of the manuscript.

Funding: The research is partially funded by the Ministry of Science and Higher Education of the Russian Federation under the strategic academic leadership program 'Priority 2030' (Agreement 075-15-2021-1333 dated 30 September 2021).

Institutional Review Board Statement: Not applicable.

Informed Consent Statement: Not applicable.

Data Availability Statement: The data is available from the corresponding author upon reasonable request.

Conflicts of Interest: The authors declare no conflict of interest.

Abbreviations

Acronym	Term
AUC	Area Under the ROC Curve
ANN	Artificial Neural Network
BO	Bayesian Optimization
CPT	Cone Penetration Test
CSR	Cyclic Stress Ratio
DT	Decision Tree
DE	Differential Evolution
EGMDH	Ensemble Group Method of Data Handling
ERF	Evolutionary Random Forest
DMT	Flat Dilatometer Test
FSVM	Fuzzy Support Vector Machine
GA	Genetic Algorithm
GWO	Grey Wolf Optimization
KELM	Kernel Extreme Learning Machine
KFDA	Kernel Fisher Discriminant Analysis
LSSVM	Least Squares Support Vector Machine
ML	Machine Learning
MGGP	Multi-Gene Genetic Programming
ANFIS	Neuro Fuzzy Inference System
PSO	Particle Swarm Optimization
RBFNN	Radial Basis Function Neural Network
RF	Random Forest
ROC	Receiver Operating Characteristic Curve
Vs	Shear Wave Velocity
SPT	Standard Penetration Test
SVM	Support Vector Machine

Appendix A

The following are common situations in which the BO algorithm finds difficulties:

$$A^* = arg_{a \in Q} max f(a) \tag{A1}$$

where Q is the set of possible a. The objective is to select a from Q such that the value of $f(a)$ is the smallest or largest.

At every iteration of the series optimization problem, BO is required to choose the most advantageous observation value. The above-mentioned Gaussian method fully solves this critical issue. The following formula expresses this:

$$f(a) \sim GP(\mu(a), k(a, a^*)) \tag{A2}$$

where the mean function denotes $\mu(a)$, and the kernel function stands for $k(a, a^*)$. The following is the formula for the Gaussian kernel:

$$k(a, a^*) = \exp\left(-\frac{1}{2}\|a - a^*\|^2\right) \tag{A3}$$

The original value of the hyperparameter is replaced with the value determined by the BO technique. A new hybrid model (BOSVM) is then developed.

References

1. Xue, X.; Yang, X. Application of the adaptive neuro-fuzzy inference system for prediction of soil liquefaction. *Nat. Hazards* **2013**, *67*, 901–917. [CrossRef]
2. Xue, X.; Yang, X. Seismic liquefaction potential assessed by support vector machines approaches. *Bull. Eng. Geol. Environ.* **2016**, *75*, 153–162. [CrossRef]
3. Sami, M.; de Patrick, B. Minimum principle and related numerical scheme for simulating initial flow and subsequent propagation of liquefied ground. *Int. J. Numer. Anal. Methods Geomech.* **2005**, *29*, 1065–1086.
4. Huang, Y.; Yu, M. Review of soil liquefaction characteristics during major earthquakes of the twenty-first century. *Nat. Hazards* **2013**, *65*, 2375–2384. [CrossRef]
5. Zhang, W.; Goh, A.T.; Zhang, Y.; Chen, Y.; Xiao, Y. Assessment of soil liquefaction based on capacity energy concept and multivariate adaptive regression splines. *Eng. Geol.* **2015**, *188*, 29–37. [CrossRef]
6. Chen, G.; Xu, L.; Kong, M.; Li, X. Calibration of a CRR model based on an expanded SPT-based database for assessing soil liquefaction potential. *Eng. Geol.* **2015**, *196*, 305–312. [CrossRef]
7. Yang, Y.; Chen, L.; Sun, R.; Chen, Y.; Wang, W. A depth-consistent SPT-based empirical equation for evaluating sand liquefaction. *Eng. Geol.* **2017**, *221*, 41–49. [CrossRef]
8. Pei, X.; Zhang, X.; Guo, B.; Wang, G.; Zhang, F. Experimental case study of seismically induced loess liquefaction and landslide. *Eng. Geol.* **2017**, *223*, 23–30. [CrossRef]
9. Kayabasi, A.; Gokceoglu, C. Liquefaction potential assessment of a region using different techniques (Tepebasi, Eskişehir, Turkey). *Eng. Geol.* **2018**, *246*, 139–161. [CrossRef]
10. Chen, J.; Hideyuki, O.; Takeyama, T.; Oishi, S.; Hori, M. Toward a numerical-simulation-based liquefaction hazard assessment for urban regions using high-performance computing. *Eng. Geol.* **2019**, *258*, 105153. [CrossRef]
11. Huang, Y.; Jiang, X. Field-observed phenomena of seismic liquefaction and subsidence during the 2008 Wenchuan earthquake in China. *Nat. Hazards* **2010**, *54*, 839–850. [CrossRef]
12. Juang, C.H.; Yuan, H.; Lee, D.-H.; Lin, P.-S. Simplified cone penetration test-based method for evaluating liquefaction resistance of soils. *J. Geotech. Geoenviron. Eng.* **2003**, *129*, 66–80. [CrossRef]
13. Duan, W.; Zhao, Z.; Cai, G.; Pu, S.; Liu, S.; Dong, X. Evaluating model uncertainty of an in situ state parameter-based simplified method for reliability analysis of liquefaction potential. *Comput. Geotech.* **2022**, *151*, 104957. [CrossRef]
14. Pal, M. Support vector machines-based modelling of seismic liquefaction potential. *Int. J. Numer. Anal. Methods Geomech.* **2006**, *30*, 983–996. [CrossRef]
15. Sulewska, M.J. Applying artificial neural networks for analysis of geotechnical problems. *Comput. Assist. Methods Eng. Sci.* **2017**, *18*, 231–241.
16. Samui, P.; Sitharam, T. Machine learning modelling for predicting soil liquefaction susceptibility. *Nat. Hazards Earth Syst. Sci.* **2011**, *11*, 1–9. [CrossRef]
17. Tolon, M. A comparative study on computer aided liquefaction analysis methods. *Int. J. Hous. Sci.* **2013**, *37*, 121–135.
18. Erzin, Y.; Ecemis, N. The use of neural networks for CPT-based liquefaction screening. *Bull. Eng. Geol. Environ.* **2015**, *74*, 103–116. [CrossRef]
19. Duan, W.; Congress, S.S.C.; Cai, G.; Liu, S.; Dong, X.; Chen, R.; Liu, X. A hybrid GMDH neural network and logistic regression framework for state parameter–based liquefaction evaluation. *Can. Geotech. J.* **2021**, *99*, 1801–1811. [CrossRef]
20. Muduli, P.K.; Das, S.K. CPT-based seismic liquefaction potential evaluation using multi-gene genetic programming approach. *Indian Geotech. J.* **2014**, *44*, 86–93. [CrossRef]
21. Muduli, P.K.; Das, S.K. Evaluation of liquefaction potential of soil based on standard penetration test using multi-gene genetic programming model. *Acta Geophys.* **2014**, *62*, 529–543. [CrossRef]
22. Javdanian, H.; Heidari, A.; Kamgar, R. Energy-based estimation of soil liquefaction potential using GMDH algorithm. *Iran. J. Sci. Technol. Trans. Civ. Eng.* **2017**, *41*, 283–295. [CrossRef]
23. Zhao, Z.; Duan, W.; Cai, G. A novel PSO-KELM based soil liquefaction potential evaluation system using CPT and vs. measurements. *Soil Dyn. Earthq. Eng.* **2021**, *150*, 106930. [CrossRef]
24. Hoang, N.-D.; Bui, D.T. Predicting earthquake-induced soil liquefaction based on a hybridization of kernel Fisher discriminant analysis and a least squares support vector machine: A multi-dataset study. *Bull. Eng. Geol. Environ.* **2018**, *77*, 191–204. [CrossRef]
25. Kurnaz, T.F.; Kaya, Y. A novel ensemble model based on GMDH-type neural network for the prediction of CPT-based soil liquefaction. *Environ. Earth Sci.* **2019**, *78*, 339. [CrossRef]
26. Rahbarzare, A.; Azadi, M. Improving prediction of soil liquefaction using hybrid optimization algorithms and a fuzzy support vector machine. *Bull. Eng. Geol. Environ.* **2019**, *78*, 4977–4987. [CrossRef]
27. Hasanipanah, M.; Monjezi, M.; Shahnazar, A.; Armaghani, D.J.; Farazmand, A. Feasibility of indirect determination of blast induced ground vibration based on support vector machine. *Measurement* **2015**, *75*, 289–297. [CrossRef]
28. Parsajoo, M.; Armaghani, D.J.; Mohammed, A.S.; Khari, M.; Jahandari, S. Tensile strength prediction of rock material using non-destructive tests: A comparative intelligent study. *Transp. Geotech.* **2021**, *31*, 100652. [CrossRef]
29. Asteris, P.G.; Mamou, A.; Hajihassani, M.; Hasanipanah, M.; Koopialipoor, M.; Le, T.-T.; Kardani, N.; Armaghani, D.J. Soft computing based closed form equations correlating L and N-type Schmidt hammer rebound numbers of rocks. *Transp. Geotech.* **2021**, *29*, 100588. [CrossRef]

30. Pham, B.T.; Nguyen, M.D.; Nguyen-Thoi, T.; Ho, L.S.; Koopialipoor, M.; Quoc, N.K.; Armaghani, D.J.; Van Le, H. A novel approach for classification of soils based on laboratory tests using Adaboost, Tree and ANN modeling. *Transp. Geotech.* **2021**, *27*, 100508. [CrossRef]
31. Zhou, J.; Qiu, Y.; Zhu, S.; Armaghani, D.J.; Khandelwal, M.; Mohamad, E.T. Estimation of the TBM advance rate under hard rock conditions using XGBoost and Bayesian optimization. *Undergr. Space* **2021**, *6*, 506–515. [CrossRef]
32. Harandizadeh, H.; Armaghani, D.J.; Hasanipanah, M.; Jahandari, S. A novel TS Fuzzy-GMDH model optimized by PSO to determine the deformation values of rock material. *Neural Comput. Appl.* **2022**, *34*, 15755–15779. [CrossRef]
33. Asteris, P.G.; Rizal, F.I.M.; Koopialipoor, M.; Roussis, P.C.; Ferentinou, M.; Armaghani, D.J.; Gordan, B. Slope stability classification under seismic conditions using several tree-based intelligent techniques. *Appl. Sci.* **2022**, *12*, 1753. [CrossRef]
34. Momeni, E.; Nazir, R.; Armaghani, D.J.; Maizir, H. Prediction of pile bearing capacity using a hybrid genetic algorithm-based ANN. *Measurement* **2014**, *57*, 122–131. [CrossRef]
35. Armaghani, D.J.; Mohamad, E.T.; Narayanasamy, M.S.; Narita, N.; Yagiz, S. Development of hybrid intelligent models for predicting TBM penetration rate in hard rock condition. *Tunn. Undergr. Space Technol.* **2017**, *63*, 29–43. [CrossRef]
36. Asteris, P.G.; Lourenço, P.B.; Roussis, P.C.; Adami, C.E.; Armaghani, D.J.; Cavaleri, L.; Chalioris, C.E.; Hajihassani, M.; Lemonis, M.E.; Mohammed, A.S. Revealing the nature of metakaolin-based concrete materials using artificial intelligence techniques. *Constr. Build. Mater.* **2022**, *322*, 126500. [CrossRef]
37. Zhou, J.; Huang, S.; Zhou, T.; Armaghani, D.J.; Qiu, Y. Employing a genetic algorithm and grey wolf optimizer for optimizing RF models to evaluate soil liquefaction potential. *Artif. Intell. Rev.* **2022**, *55*, 5673–5705.
38. Zeng, J.; Mohammed, A.S.; Mirzaei, F.; Moosavi, S.M.H.; Armaghani, D.J.; Samui, P. A parametric study of ground vibration induced by quarry blasting: An application of group method of data handling. *Environ. Earth Sci.* **2022**, *81*, 127. [CrossRef]
39. Barkhordari, M.S.; Armaghani, D.J.; Mohammed, A.S.; Ulrikh, D.V. Data-Driven Compressive Strength Prediction of Fly Ash Concrete Using Ensemble Learner Algorithms. *Buildings* **2022**, *12*, 132. [CrossRef]
40. Li, D.; Liu, Z.; Armaghani, D.J.; Xiao, P.; Zhou, J. Novel ensemble intelligence methodologies for rockburst assessment in complex and variable environments. *Sci. Rep.* **2022**, *12*, 1844.
41. He, B.; Armaghani, D.J.; Lai, S.H. A Short Overview of Soft Computing Techniques in Tunnel Construction. *Open Constr. Build. Technol. J.* **2022**, *16*. [CrossRef]
42. Koopialipoor, M.; Asteris, P.G.; Mohammed, A.S.; Alexakis, D.E.; Mamou, A.; Armaghani, D.J. Introducing stacking machine learning approaches for the prediction of rock deformation. *Transp. Geotech.* **2022**, *34*, 100756. [CrossRef]
43. Liu, Z.; Armaghani, D.-J.; Fakharian, P.; Li, D.; Ulrikh, D.-V.; Orekhova, N.-N.; Khedher, K.-M. Rock Strength Estimation Using Several Tree-Based ML Techniques. *Comput. Modeling Eng. Sci.* **2022**, *133*, 799–824. [CrossRef]
44. Barkhordari, M.S.; Armaghani, D.J.; Asteris, P.G. Structural Damage Identification Using Ensemble Deep Convolutional Neural Network Models. *Comput. Model. Eng. Sci.* **2022**, *134*, 835–855. [CrossRef]
45. Yang, H.; Li, Z.; Jie, T.; Zhang, Z. Effects of joints on the cutting behavior of disc cutter running on the jointed rock mass. *Tunn. Undergr. Space Technol.* **2018**, *81*, 112–120. [CrossRef]
46. Liu, B.; Yang, H.; Karekal, S. Effect of water content on argillization of mudstone during the tunnelling process. *Rock Mech. Rock Eng.* **2020**, *53*, 799–813. [CrossRef]
47. Yang, H.; Xing, S.; Wang, Q.; Li, Z. Model test on the entrainment phenomenon and energy conversion mechanism of flow-like landslides. *Eng. Geol.* **2018**, *239*, 119–125. [CrossRef]
48. Yang, H.; Zeng, Y.; Lan, Y.; Zhou, X. Analysis of the excavation damaged zone around a tunnel accounting for geostress and unloading. *Int. J. Rock Mech. Min. Sci.* **2014**, *69*, 59–66. [CrossRef]
49. Yang, H.; Wang, Z.; Song, K. A new hybrid grey wolf optimizer-feature weighted-multiple kernel-support vector regression technique to predict TBM performance. *Eng. Comput.* **2020**, *38*, 2469–2485. [CrossRef]
50. Schmidt, J.; Moss, R. Bayesian hierarchical and measurement uncertainty model building for liquefaction triggering assessment. *Comput. Geotech.* **2021**, *132*, 103963. [CrossRef]
51. Zhao, Z.; Congress, S.S.C.; Cai, G.; Duan, W. Bayesian probabilistic characterization of consolidation behavior of clays using CPTU data. *Acta Geotech.* **2022**, *17*, 931–948. [CrossRef]
52. Zhao, Z.; Duan, W.; Cai, G.; Wu, M.; Liu, S. CPT-based fully probabilistic seismic liquefaction potential assessment to reduce uncertainty: Integrating XGBoost algorithm with Bayesian theorem. *Comput. Geotech.* **2022**, *149*, 104868. [CrossRef]
53. Cai, M.; Hocine, O.; Mohammed, A.S.; Chen, X.; Amar, M.N.; Hasanipanah, M. Integrating the LSSVM and RBFNN models with three optimization algorithms to predict the soil liquefaction potential. *Eng. Comput.* **2022**, *38*, 3611–3623. [CrossRef]
54. Sladen, J.; D'hollander, R.; Krahn, J. The liquefaction of sands, a collapse surface approach. *Can. Geotech. J.* **1985**, *22*, 564–578. [CrossRef]
55. Castro, G. On the Behavior of Soils during Earthquakes–Liquefaction. In *Developments in Geotechnical Engineering*; Elsevier: Amsterdam, The Netherlands, 1987; Volume 42, pp. 169–204.
56. Fogel, D.B. *Evolutionary Computation: Toward a New Philosophy of Machine Intelligence*; John Wiley & Sons: Hoboken, NJ, USA, 2006; Volume 1.
57. Lee, J.-H.; Ahn, C.W. An Evolutionary Approach to Driving Tendency Recognition for Advanced Driver Assistance Systems. In Proceedings of the MATEC Web of Conferences, Amsterdam, The Netherlands, 23–25 March 2016; p. 02012.
58. Cortes, C.; Vapnik, V. Support-vector networks. *Mach. Learn.* **1995**, *20*, 273–297. [CrossRef]

59. Chang, C.-C.; Lin, C.-J. LIBSVM: A library for support vector machines. *ACM Trans. Intell. Syst. Technol. (TIST)* **2011**, *2*, 1–27. [CrossRef]
60. Smola, A.J.; Schölkopf, B. A tutorial on support vector regression. *Stat. Comput.* **2004**, *14*, 199–222. [CrossRef]
61. Zhang, Y.; Qiu, J.; Zhang, Y.; Xie, Y. The adoption of a support vector machine optimized by GWO to the prediction of soil liquefaction. *Environ. Earth Sci.* **2021**, *80*, 360. [CrossRef]
62. Snoek, J.; Larochelle, H.; Adams, R.P. Practical bayesian optimization of machine learning algorithms. *Adv. Neural Inf. Processing Syst.* **2012**, *25*. [CrossRef]
63. Greenhill, S.; Rana, S.; Gupta, S.; Vellanki, P.; Venkatesh, S. Bayesian optimization for adaptive experimental design: A review. *IEEE Access* **2020**, *8*, 13937–13948. [CrossRef]
64. Kobliha, M.; Schwarz, J.; Očenášek, J. Bayesian optimization algorithms for dynamic problems. In Proceedings of the Workshops on Applications of Evolutionary Computation, Budapest, Hungry, 10–12 April 2006; pp. 800–804.
65. Shibata, T.; Teparaksa, W. Evaluation of liquefaction potentials of soils using cone penetration tests. *Soils Found.* **1988**, *28*, 49–60. [CrossRef]
66. Zhou, J.; Shen, X.; Qiu, Y.; Li, E.; Rao, D.; Shi, X. Improving the efficiency of microseismic source locating using a heuristic algorithm-based virtual field optimization method. *Geomech. Geophys. Geo-Energy Geo-Resour.* **2021**, *7*, 89. [CrossRef]
67. Zhou, J.; Chen, C.; Wang, M.; Khandelwal, M. Proposing a novel comprehensive evaluation model for the coal burst liability in underground coal mines considering uncertainty factors. *Int. J. Min. Sci. Technol.* **2021**, *31*, 799–812. [CrossRef]
68. Zhou, J.; Qiu, Y.; Khandelwal, M.; Zhu, S.; Zhang, X. Developing a hybrid model of Jaya algorithm-based extreme gradient boosting machine to estimate blast-induced ground vibrations. *Int. J. Rock Mech. Min. Sci.* **2021**, *145*, 104856. [CrossRef]
69. Zhou, J.; Li, X.; Mitri, H.S. Classification of rockburst in underground projects: Comparison of ten supervised learning methods. *J. Comput. Civ. Eng.* **2016**, *30*, 04016003. [CrossRef]
70. Rashedi, E.; Nezamabadi-Pour, H.; Saryazdi, S. GSA: A gravitational search algorithm. *Inf. Sci.* **2009**, *179*, 2232–2248. [CrossRef]
71. Abdel-Basset, M.; Shawky, L.A. Flower pollination algorithm: A comprehensive review. *Artif. Intell. Rev.* **2019**, *52*, 2533–2557. [CrossRef]
72. Merghadi, A.; Yunus, A.P.; Dou, J.; Whiteley, J.; ThaiPham, B.; Bui, D.T.; Avtar, R.; Abderrahmane, B. Machine learning methods for landslide susceptibility studies: A comparative overview of algorithm performance. *Earth-Sci. Rev.* **2020**, *207*, 103225. [CrossRef]

sustainability

MDPI

Article

Mineral Texture Identification Using Local Binary Patterns Equipped with a Classification and Recognition Updating System (CARUS)

Saeed Aligholi [1,*], Reza Khajavi [2], Manoj Khandelwal [1] and Danial Jahed Armaghani [3]

[1] Institute of Innovation, Science and Sustainability, Federation University Australia, Ballarat, VIC 3350, Australia
[2] Earthquake Research Center, Ferdowsi University of Mashhad, Mashhad 9177948974, Iran
[3] Department of Urban Planning, Engineering Networks and Systems, Institute of Architecture and Construction, South Ural State University, 76 Lenin Prospect, 454080 Chelyabinsk, Russia
* Correspondence: s.aligholi@federation.edu.au

Abstract: In this paper, a rotation-invariant local binary pattern operator equipped with a local contrast measure (riLBPc) is employed to characterize the type of mineral twinning by inspecting the texture properties of crystals. The proposed method uses photomicrographs of minerals and produces LBP histograms, which might be compared with those included in a predefined database using the Kullback–Leibler divergence-based metric. The paper proposes a new LBP-based scheme for concurrent classification and recognition tasks, followed by a novel online updating routine to enhance the locally developed mineral LBP database. The discriminatory power of the proposed Classification and Recognition Updating System (CARUS) for texture identification scheme is verified for plagioclase, orthoclase, microcline, and quartz minerals with sensitivity (*TPR*) near 99.9%, 87%, 99.9%, and 96%, and accuracy (*ACC*) equal to about 99%, 97%, 99%, and 99%, respectively. According to the results, the introduced CARUS system is a promising approach that can be applied in a variety of different fields dealing with classification and feature recognition tasks.

Keywords: automated mineral identification; LBP; classification; texture feature

Citation: Aligholi, S.; Khajavi, R.; Khandelwal, M.; Armaghani, D.J. Mineral Texture Identification Using Local Binary Patterns Equipped with a Classification and Recognition Updating System (CARUS). *Sustainability* **2022**, *14*, 11291. https://doi.org/10.3390/su141811291

Academic Editor: Kaihui Li

Received: 27 July 2022
Accepted: 5 September 2022
Published: 8 September 2022

Publisher's Note: MDPI stays neutral with regard to jurisdictional claims in published maps and institutional affiliations.

Copyright: © 2022 by the authors. Licensee MDPI, Basel, Switzerland. This article is an open access article distributed under the terms and conditions of the Creative Commons Attribution (CC BY) license (https://creativecommons.org/licenses/by/4.0/).

1. Introduction

There has been growing interest among researchers to develop well-performing automated schemes in different areas of science and engineering, including rock analysis, in recent years [1–8]. Automated mineral identification (AMI) as well as geometry characterization of rock constituents, as two prerequisites of any petrography scheme, are demanded in different fields of geosciences including rock mechanics, engineering geology, volcanology, mining, and underground construction [9–15]. Accordingly, some pattern recognition and image processing methods including textural and color analyses as well as frequency domain analysis are applied for mineral identification and rock classification [16–21]. The proposed schemes are mostly designed as color-based, rather than texture-based, and might fail to successfully identify twinned minerals. Such problems may also frustrate segmentation algorithms, which are increasingly used for the shape-and-size analysis of rock constituents. Texture analysis, as a chief ingredient of the automated mineral identification (AMI) task, is thus potentially favorable, or necessary, to develop any unified automated rock analysis package [17]. This study aims at the automation of identifying plagioclase, orthoclase, microcline, and quartz minerals through texture analysis. For the purpose of rock classification, identification of these minerals is an essential task, however, they might rarely be distinguished from each other.

Texture analysis is useful and is essentially required for some image processing purposes. A human can easily distinguish different textures, but it is a complicated machine

learning task [22]. Texture analysis deals with the following problems: image classification according to textural features; image segmentation; designing textures; and shape analysis from texture contents [23]. Texture classification is employed in different scientific problems including medical image analysis [24], fabrics analysis [25], and remote sensing [26].

Different techniques have been employed for the texture description of images. Texture analysis procedures have been classified into the following categories: geometric, statistical, signal processing, and model-based approaches [23]. Different typical texture features are also introduced in the literature [27,28]. Pioneering methods for texture classification were based on the statistical quantification of texture information, ranging from co-occurrence matrices [27] and polarograms [29] to procedures such as Markov random fields [30], signal processing methods [31–33], and local binary pattern [34], which offer satisfactory results.

The local binary pattern (LBP) is a statistical-based texture analysis operator for local texture characterization. LBP-based texture feature extraction has become increasingly applied for texture analysis during the last decade. LBP features have achieved considerable success in many fields, e.g., face recognition, remote sensing, and several medical image analysis problems [35–45]. Different extensions of the method have been developed for further improvements in power discrimination [46], rotation invariance [47,48], and robust noise resistance [49]. The operator (riLBPc) has some unique characteristics including computational simplicity, tolerance to grayscale, high discriminatory power, and illumination variations [34].

Mineral texture identification has been the subject of several studies published in the past; in reality, the majority of researchers have focused their attention on rock texture analysis. Ross et al. [20] have partly considered some texture attributes for the task of mineral identification through genetic programming. They used the intensity component of hue–saturation–intensity (HSI) space to calculate standard parameters such as energy, contrast, homogeneity, and entropy by means of a gray-level co-occurrence matrix, calculated for each grain. Thompson et al. [21] trained their neural networks with the above four texture parameters to identify colorless minerals: quartz, K-feldspar, and plagioclase. While their designed net could distinguish quartz and plagioclase well from each other, its ability to identify K-feldspar deteriorated, which might be a consequence of minor alterations such as sericitization. Smith and Beermann [50] attempt to identify plagioclase from quartz by employing gray-level homogeneity recognition.

Although the texture is a significant characteristic of feldspars, there is no solid model that quantifies the complex nature of these image properties. Therefore, a texture analysis approach is developed that attempts to explain the textural features of some minerals. The main focus of this study is on the identification of textural features that yield the highest retrieval accuracy. Rotation-invariant local binary patterns (LBPs) equipped with a complementary contrast measure are employed, to develop a so-called CARUS software for the task of automatic mineral identification of mineral textures. The scheme is also provided by a mineral texture database, which is enhanced after each mineral texture identification task. The results are promising and the texture of the studied minerals is successfully identified by employing CARUS with very high accuracy.

The paper is presented as follows. In Section 2, distinctive texture features (twinning and undoluse extinction) of the minerals plagioclase, quartz, and alkali feldspars (orthoclase and microcline) are introduced. Some different typical versions of LBP texture operators are briefly overviewed in Section 3. Section 4 introduces the two main kernels of the CARUS, the classification/recognition algorithm, as well as the proposed database updating system. In Section 5, several experiments to verify the performance of the CARUS algorithm for mineral pattern analysis and identification are described. Finally, the main conclusions drawn from this study are presented in Section 6.

2. Typical Textures in Minerals

Texture analysis is an inevitable task for the automated identification of the minerals located in the first order of the Michel-Lévy interference color chart (a chart that indi-

cates the interference color of minerals against the sample (thin section) thickness under cross-polarized light microscopy). Among these minerals, plagioclase, quartz, and alkali feldspars (orthoclase and microcline) are typically important for the development of any rock classification, e.g., [51,52]. These minerals usually have distinctive texture features (twinning and undoluse extinction). Twinning is a symmetrical intergrowth of two or more crystals of the same substance [53].

Quartz (Qtz). In thin sections, quartz can be distinguished from twinned feldspars by its lack of twinning. Quartz in some igneous as well as metamorphic rocks indicates undulatory extinction because of strain. Therefore, patterns similar to fine lamellae may occur that are related to translation gliding [54]. Figure 1 (Q1,Q2) shows undoluse extinction in quartz grains.

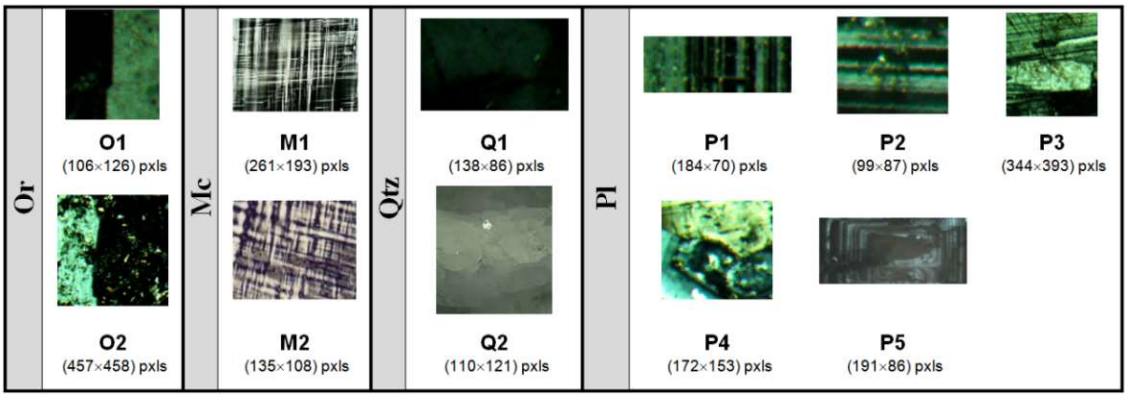

Figure 1. Examples of typical twinnings in real mineral images under XPL. (**O1**,**O2**) Orthoclase (Or); (**M1**,**M2**) microcline (Mc); (**Q1**,**Q2**) quartz (Qtz); and (**P1**–**P5**) plagioclase (Pl).

Twinning in feldspars varies according to the composition and the crystal system. Twinning in these minerals is the result of various mechanisms [54]: (a) it can occur during crystal growth, (b) it can be induced by deformation, and (c) it can be based on thermal transformation. There are different feldspathic twin laws. Feldspars commonly indicate three twin laws: normal, parallel, and complex. The feldspars best illustrate the twinning in the triclinic system. They are almost always twinned according to the albite law with the {010} twin plane and the pericline law with [010] as the twin axis. In the monoclinic system, twinning on {100} and {001} is most common. Carlsbad twinning was observed in the thin section as a pair of individual crystals, separated by a single line. Carlsbad twins may be either the interpenetrant or contact type. Carlsbad twinning is seen in monoclinic (such as sanidine and orthoclase) and triclinic feldspars (plagioclase and microcline).

Orthoclase (Or) can be distinguished from plagioclase feldspars by the absence of albite twinning and the frequent occurrence of simple Carlsbad twins. Orthoclase commonly shows simple twins. Figure 1 (O1,O2) shows simple twins in orthoclase grains.

Microcline (Mc) is characterized by a combination of albite and pericline twinning (tartan pattern) which is different from that found in albite. The combination produces a distinctive grid pattern and is particularly common in microclines because microclines are often formed by transformation. Sometimes, tartan twins are observed in plagioclase. However, in contrast to microcline, twin planes are well defined in plagioclase. Figure 1 (M1,M2) shows tartan twinning in microcline grains.

Plagioclase (Pl). Multiple twinning is a distinguishing feature of all plagioclase feldspars. Carlsbad–albite, Carlsbad or simple, and pericline or repeated are also other typical twinning laws in Pl. Some plagioclase feldspars indicate zoning as a consequence of interior-to-outer variations in the composition of the crystal. Figure 1 shows multiple twins (P1–P3) and zoning (P4–P5) in plagioclase grains.

A modification, especially for the Or and Pl cases, may change typical texture features. Or usually changes to clay minerals; these minerals occur as discrete particles on the feldspar crystal. The amount and magnitude of the clay particles increase with alteration;

thus, they are usually termed sericite. Late-stage hydrothermal activity during solidification of the rock mass and chemical weathering is the main cause of Pl alteration. Zoisite minerals are also formed by feldspars during late-stage hydrothermal activity by a process called saussuritization [55]. In Section 5.1, changes in the LBP histogram of the studied minerals due to alteration will be discussed.

3. Brief Review of LBP

The grayscale local binary pattern (LBP) was introduced by Ojala et al. [56] and modified later to account for the rotation invariance with uniform patterns [57] to characterize the spatial structure. For any central pixel (*i,j*) of the image with $n \times m$ pixels, the following LBP number is obtained through a simple comparison of the central pixel value with those of its P neighboring pixels, located at a radius R from it [47]:

$$LBP_{P,R}(i,j) = \sum_{p=0}^{P-1} H(g_p - g_c)2^p. \quad (1)$$

$H(x)$ is the discrete Heaviside step function, and g_p and g_c represent neighboring and central pixel grayscale values, respectively. In this study, P is examined for the typical values of 8 and 16, with 1 and 2 for the radius value R; thus, a total of 2^8 = 256 and 2^{16} = 65,536 different labels might be obtained depending on the gray levels of the center and the pixels in its neighborhood.

As proposed by the literature, the texture might be distinguished by both texture patterns and the strength of the patterns (contrast). Contrast is regarded as an important texture property for human vision, which entails useful grayscale-dependent information for the task of texture classification. However, the previous LBP operators totally ignore the magnitude of contrasts. A contrast measure (C) might be considered for each pixel by subtracting the average of the gray levels below the center pixel from those above (or equal to) it. For equal values of thresholded neighbors, the value of contrast is set to zero. It is proposed that *LBP* values divided by corresponding contrast (or variance) values will give better results as presented by Ojala et al. [57] and Pietikäinen et al. [58]:

$$LBPC_{P,R}(i,j) = LBP_{P,R}(i,j)/C(i,j). \quad (2)$$

The obtained *LBP* image of the sample mineral is represented as the following histogram:

$$h = \sum_{i=1}^{n} \sum_{j=1}^{m} f(LBP_{P,R}(i,j), k), \quad (3)$$

with the integer, $k \in [0, K]$, where K is the maximum *LBP* value (e.g., K = 17 for P = 16), and the function f is defined as:

$$f(x,y) = \begin{cases} 1 & x = y \\ 0 & otherwise \end{cases}. \quad (4)$$

The obtained histogram h can easily be compared with a model histogram h_0 for possible similarity, using the following Kullback–Leibler divergence-based metric to evaluate their goodness-of-fit (*gof*) [28]:

$$gof_{h,h_0} = \sum_{i=1}^{N} h(i)logh(i) + \sum_{i=1}^{N} h_0(i)logh_0(i) - \sum_{i=1}^{N} (h(i) + h_0(i))(logh(i) + logh_0(i)) + 2log2. \quad (5)$$

In this study, uniform *LBP* operator ($U2$), as introduced by Mäenpää et al. [59], is used, in which the number of bitwise 0/1 transitions $U \leq 2$, where:

$$U = |H(g_{P-1} - g_c) - H(g_0 - g_c)| + \sum_{p=1}^{P-1} |H(g_P - g_c) - H(g_{p-1} - g_c)|. \quad (6)$$

In the uniform *LBP* operator, different output labels are assigned for uniform patterns, and a single label is assigned for the rest of the non-uniform patterns. This will return the output label number for patterns of P bits as $P(P-1) + 3$; e.g., for P = 8, the uniform *LBP* will produce 59 labels.

Since the rotation of any sample mineral image causes the *LBPs* to be shifted to different locations, the following rotationally invariant uniform *LBP* operator, rather than the one in Equation (1), might be employed:

$$LBP_{P,R}^{ri,\,U2}(i,j) = \begin{cases} \sum_{p=0}^{P-1} H(g_p - g_c), & U \leq 2 \\ P+1, & otherwise \end{cases} \quad (7)$$

4. CARUS Algorithm for MI

Precise rock characterization and classification require correct identification of quartz and feldspars, that might be recognized from each other based on typical texture feature observation through optical microscopy of rock thin sections in cross-polarized light (XPL); so, texture analysis is an inevitable task for automation of rock photomicrograph analysis. As noted in Section 2, mineral texture patterns are sometimes polluted by chemical (or instrumental) factors and may thus show atypical texture features; true classification/recognition of such minerals might fail unless a reasonable degree of algorithm flexibility is considered. The proposed algorithm is designed with this problem in mind, with an adaptive sense to incorporate algorithm flexibility and robustness. Details of the proposed CARUS algorithm are presented as follows.

4.1. Classification and Recognition

In manual MI through optical microscopy, the experienced operator attempts to identify texture features of minerals by examining the nature of the changes observed in the appearance of the unknown mineral, as the sample (rock/mineral thin section) is rotated with respect to the polarizers under XPL illumination. In automated MI for modeling rotation of a sample with respect to the polarizers, some photomicrographs of the sample in different rotations can be taken, e.g., [16,20]. This study aims at the automation of such mineral texture classification/recognition through texture analysis with the use of an appropriate LBP operator. For this purpose, the texture-based mineral identification (TMI) Algorithm 1 and Figure 2 is designated. The procedure of the algorithm is as follows:

(a) For an unknown mineral, an appropriate XPL image (usually the one with the maximum standard deviation (maxSD_Img)) from a set of rotated images is selected. This image is commonly expected to show typical textural features of a mineral.
(b) The histogram (***h***) of its LBP image (LBP_Img) with *nb* bins is obtained (Equation (7)). Usually, *nb* is considered to be 100 × (P + 1), where P is the number of LBP samples as introduced in Section 3.
(c) The *h* histogram of the LBP_Img is compared with those included in the ***h-db*** (a database of LBP image histograms of *nt* (*i*) typical samples for any mineral class i ≤ *nc*) through a distance metric gof, as introduced in Equation (5). Steps 1 through 5 of the TMI algorithm will provide a ***GOF*** matrix which incorporates the *gof* values corresponding to the ***h*** of the unknown mineral and those included in the ***h-db***.
(d) In steps 6 through 8, a mean function might be used, as shown in Figure 3, to develop a ***gof*** vector which specifies the *gof* values of the unknown mineral with any mineral classes included in ***h_db***. The averaging scheme, as will be verified in Section 5, does have enough accuracy, increases robustness (in comparison with methods such as k-nearest neighbor (kNN)), and reduces the computational cost.
(e) In steps 9 and 10, the minimum entry of ***gof*** is found, and its corresponding mineral class *c* is introduced as the one to which the unknown mineral belongs.

Algorithm 1. Pseudo code for texture-based mineral identification algorithm (TMI).

Input: unknown mineral XPL image with standard deviation (maxSD_Img)
Output: mineral class of the unknown mineral (c)
Initialization: find $\boldsymbol{h} \equiv \{h_i\}^{nb}_{i=1}$ from LBP image of unknown mineral image

1 : **for** $i \leftarrow 1 : nc$ **do**
2 : **for** $j \leftarrow 1 : \boldsymbol{nt}(i)$ **do**
3 : $\boldsymbol{GOF}(i,j) \leftarrow \text{gof}\left[\boldsymbol{h}, \boldsymbol{h}^i_j \, \epsilon \, \boldsymbol{h_db}\right]$
4 : **end for**
5 : **end for**
6 : **for** $i \leftarrow 1 : nc$ **do**
7 : $\boldsymbol{gof}(i) \leftarrow \text{mean}\left[\{\boldsymbol{GOF}(i,j)\}^{nt(i)}_{j=1}\right]$
8 : **end for**
9 : $gof \leftarrow \min\left[\{\boldsymbol{gof}(i)\}^{nc}_{i=1}\right] = \boldsymbol{gof}(c)$
10 : return⟨mineral class⟩c

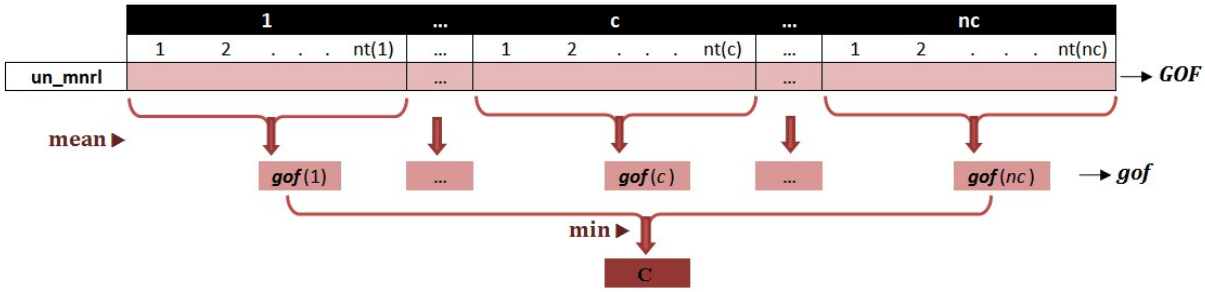

Figure 2. Schematic view of TMI algorithm.

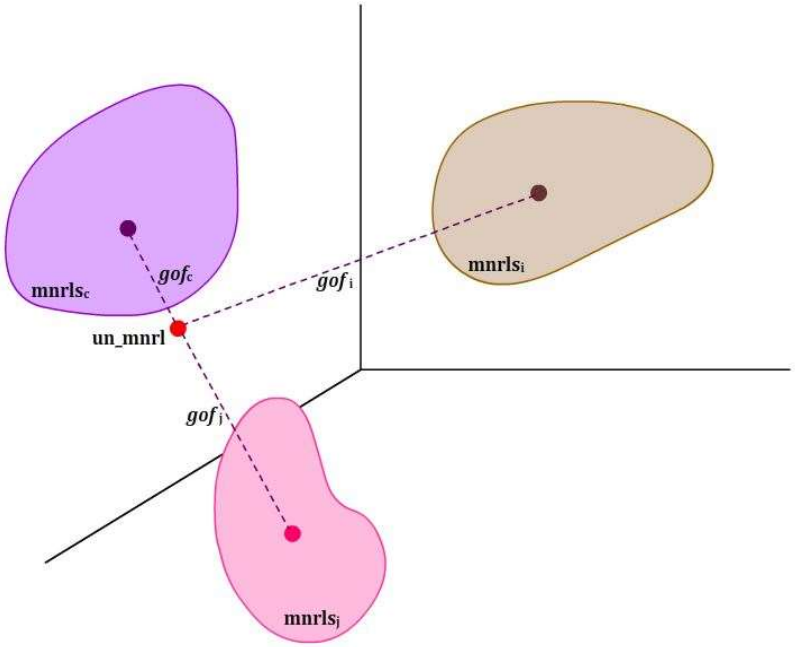

Figure 3. Schematic view of mean *gof*s between the unknown histogram and those of mineral classes (points represent histograms).

4.2. Updating System

An important prerequisite of the above texture-based mineral identification scheme is a database of LBP histograms obtained for some typical samples of the mineral classes, ***h_db***. In contrast to some pattern recognition applications such as face recognition, for which

several standard databases have been developed, no unified standard mineral database has been developed yet in the mineralogy community, and research studies for MI are inevitably based upon local databases. This means that any research group starts with a limited number of available mineral instances, which can be developed as more instances are inspected.

In this study, a second algorithm for database updating (HDU), illustrated in Algorithm 2 and Figure 4, is proposed to successively update an initial ***h_db*** after each run of the TMI scheme. The ***h_db*** updating algorithm is as follows:

(a) An initial database of LBP histograms, ***h_db***, obtained from an initial collection of some typical mineral samples, is established. In developing such a dataset, mineral images must be selected such that they can well represent different types of structural and non-structural conditions. While structural conditions (S factors) pertain to both the genesis of the mineral (S-I factors) and the environmental conditions such as temperature, pressure, and hydrothermal solution (S-II factors) that cause different degrees of alteration, the non-structural ones (NS factors) are mostly related to laboratory and equipment conditions (e.g., microscopes and digital cameras with different qualities, lighting changes, different magnification in microscopy, different orientations, etc.). It will be shown that a poor initial database may deteriorate the performance of the developed database.

(b) A ***GOFc*** matrix, incorporating all gof values obtained for the sample minerals of the ***h_db*** belonging to the *c*th mineral class, is established (steps 1 through 5).

(c) Mean gof values for each sample of the mineral class *c* are calculated, which gives the vector ***gofc*** (steps 6 through 8); a ***gofc_s*** vector is obtained by sorting ***gofc*** in descending order (step 9).

(d) In steps 10 through 14, the HDU algorithm decides whether to add the LBP histogram of the identified mineral sample (in the previous TMI run) to ***h_db*** or not. For this purpose, the two following conditions are investigated:

(1) gof value of the identified sample must be less than ***gofc_s***(1) which is the maximum entry of the ***gofc*** vector. The condition is schematically illustrated in Figure 5a. LBP histograms of mineral instances in class *c*, $\mathbf{mnrls_c}$, are within an acceptance circle $\mathbf{C}^1{}_{max}$ with the radius of ***gofc_s***(1) (the center of the circle is a virtual point and is depicted for geometric interpretation). As the first condition, the identified mineral, **un_mnrl**, must be located within the acceptance circle of $\mathbf{mnrls_c}$.

(2) ***gofc_s***(1) is checked for being less than all gof values of the ***gof*** vector (other than *gof* =***gof***(*c*)); it is reminded that ***gof*** is obtained in steps 6–8 of the TMI algorithm (refer to Algorithm 1 (and Figure 3)). The geometric interpretation of this criterion is illustrated in Figure 5a, where the mean virtual points of all mineral classes (except c) are located out of the dashed circle $\mathbf{C'}_{max}$ (a circle with the center point of un-mnrl, and the same radius as $\mathbf{C}^1{}_{max}$). If this condition is satisfied, an LBP histogram of the identified sample ***h*** is added to ***h_db***. Otherwise, the next entry of ***gofc_s***, i.e., the next maximum value of ***gofc***, is examined for this criterion. This loop is continued until both conditions are satisfied. Figure 5b illustrates a situation where the second criterion is not satisfied (i.e., both virtual centers of $\mathbf{mnrls_c}$ and $\mathbf{mnrls_j}$ classes are within the light dashed circle), but by selecting the *k*th maximum entry of ***gofc_s***, a circle $\mathbf{C'}_{max}$ (with the same radius as $\mathbf{C}^k{}_{max}$) is introduced for which centers of $\mathbf{mnrls_c}$ and $\mathbf{mnrls_j}$ are, respectively, within and out of it. There might be cases for which such reduction in the acceptance circle may fail the first condition (i.e., the identified mineral, **un_mnrl**, located out of the acceptance circle ($\mathbf{C'}_{max}$) of $\mathbf{mnrls_c}$); thus, the mineral will not be added to the database.

Algorithm 2. Pseudo code for ***h-db*** update algorithm (HDU).

Input: c, gof, h_db
Output: update h_db

for $i \leftarrow 1 : nt(c)$ **do**
  for $j \leftarrow 1 : nt(c)$ **do**
    $GOFc(i,j) \leftarrow \text{gof}\left[h_i^c \,\epsilon\, h_db, h_j^c \,\epsilon\, h_db\right]$
  end for
end for
for $i \leftarrow 1 : nt(c)$ **do**
  $gofc(\text{i}) \leftarrow \text{mean}\left[\{GOFc(i,j)\}_{j=1}^{nt(i)}\right]$
end for
$gofc_s \leftarrow \text{sort}[gofc, \text{descending}]$
for $i \leftarrow 1 : nt(c)$ **do**
  if $\left(gof = gof(c) < gofc_s(i) < \{gof(i)\}_{i=1, i\neq c}^{nc}\right)$ **then**
    add h to h_db
  exit
end for

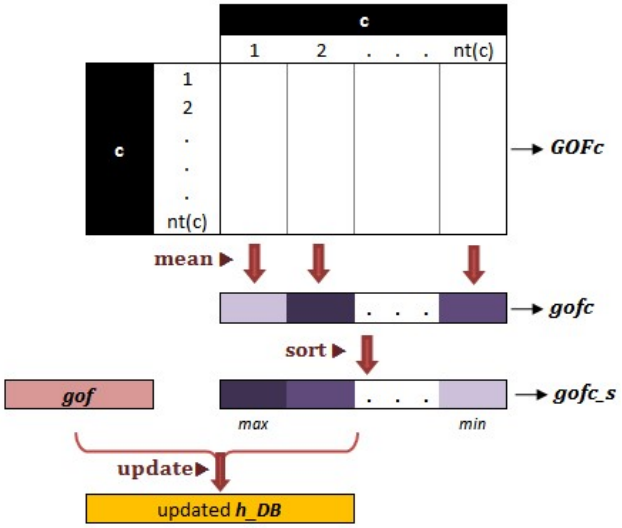

Figure 4. Schematic view of HDU algorithm.

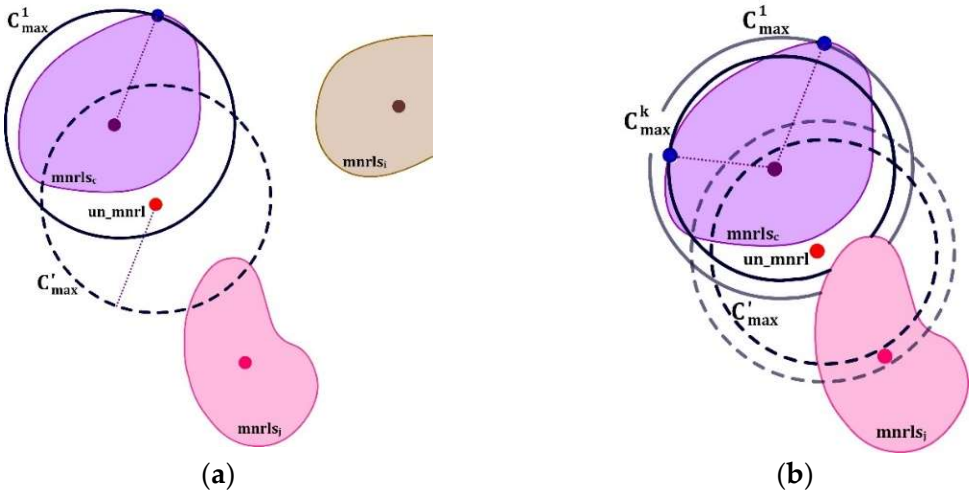

Figure 5. Geometric interpretation of updating step of the CARUS: (**a**) un_mnrl is added to the database, and (**b**) un_mnrl is added to the database after reducing the acceptance circle.

5. Experiments and Results

Different experiments are carried out to indicate the performance of different aspects of the CARUS algorithm for mineral pattern analysis and identification. In Section 5.1, different local binary patterns are examined and investigated, through a simple example, to give an essence of their performance in dealing with mineral images. It will be shown that the rotation-invariant LBP equipped with contrast (riLBPc) is the most well-performing compared to the others, and is employed as the representative LBP variant for the task of mineral pattern identification. In Section 5.2, the proposed TMI scheme is tested and compared with the routine of Haralick's gray-level co-occurrence matrices (GLCMs). The performance of the CARUS algorithm (with the updating part included) will then be verified in Section 5.3. In Section 5.4, the CARUS classification scheme and the well-known k-nearest neighbor method are compared in terms of how well they work.

5.1. Comparison of LBPs for TMI

In this section, the accuracy and performance of four different LBP schemes: basic LBP (bLBP), uniform LBP (uLBP), rotation-invariant LBP (riLBP), and rotation-invariant LBP equipped with contrast (riLBPc), are examined for the task of texture identification of the four minerals under consideration, i.e., orthoclase, plagioclase, microcline, and quartz. For comparing the four schemes, 11 sample minerals from Figure 1 are employed. Figure 6 illustrates the LBP (8,1) images and their corresponding histograms of each sample mineral, obtained by the four schemes. In Figure 7, the ***gof*** values obtained for any pair of the sample minerals in Figure 1 are reported. For the sake of simplicity, the limit value of 0.2 is considered for the discrimination of the minerals; i.e., $gof > 0.2$ implies dissimilarity between the twinning patterns. It is, however, mentioned that using 0.2 as a fixed threshold for feature discrimination is not robust, and just gives an essence of the performance of different methods. In Figure 7, the *gof* values larger than 0.2 are highlighted for better comparison.

The bLBP section in Figure 7a shows the results of the conventional basic local binary patterns, as proposed by Ojala et al. [56]. While *gof* values for most similar minerals are less than 0.2, dissimilar minerals are not well discriminated. The scheme, as is expected, is not reliable and robust for the task of texture classification of minerals.

Using some uniform patterns rather than all patterns enhances recognition results for most applications. uLBP seems to be more statistically robust and stable (i.e., less prone to noise), while it requires fewer LBP labels [58]. Texture noise is an inevitable part of thin-section mineral images. Usually, due to the distributed (or even point-wise) regions of alteration in orthoclase or plagioclase, some non-uniform patterns might appear; such image contamination can be alleviated by the use of uBLP. However, if alteration, as a typical feature of Pl or Or, spreads over a large region of the sample, it should be considered as a texture feature of the mineral. High gof values that may appear for the samples of the same mineral could be associated with this. Microscope magnification, as well as the resolution of the camera, might intensify such errors. For example, if a thin section with point-wise alteration is observed with high magnification, the alteration spreads over the image, giving a different gof. The same situation appears when an improved camera resolution is applied. Thus, the alteration area is dependent on the magnification of the microscope, as well as the camera resolution. Though uLBP performs nearly as well in alleviating noise effects and dealing with parameters such as alteration, exsolution, fractures, and veins, it fails to effectively categorize minerals, mostly due to its sensitivity to orientation.

The abovementioned deficiencies of the previous two LBP schemes must partly be associated with their inability to deal with the orientation. Different orientations of the input image cause the LBPs to translate into different locations while rotating about their origin. Translation can be normalized by computing the histogram of LBP codes, and rotation can be normalized by using a simple rotation invariant scheme [58]. A comparison of the results of the riLBP method with those of the two previous ones in Figure 7 clearly shows that errors due to dissimilar texture orientations have been efficiently reduced. For example,

the gof values for P1 and P2 (which are well characterized for their nearly perpendicular orientations) are 0.25 and 0.22 in bLBP and uLBP schemes, respectively; however, the value has decreased to 0.09 by riLBP. From Figure 7, it can easily be verified that except for the pair of Pl–Mc, the gof values for dissimilar minerals have generally increased. It must be pointed out that both Pl and Mc are crystallized in a triclinic system, with albite and plagioclase twinnings; however, Pl usually exhibits one of such twinnings perfectly, while Mc, which is often formed by transformation from Or as a consequence of temperature decrease, shows both twinnings in a pinch and swell manner. Thus, the textural features of the two minerals are similar. This might easily be examined by comparing the LBP images of the two minerals illustrated in Figure 6. Thus, their LBP codes are similar, especially when normalized to 1.

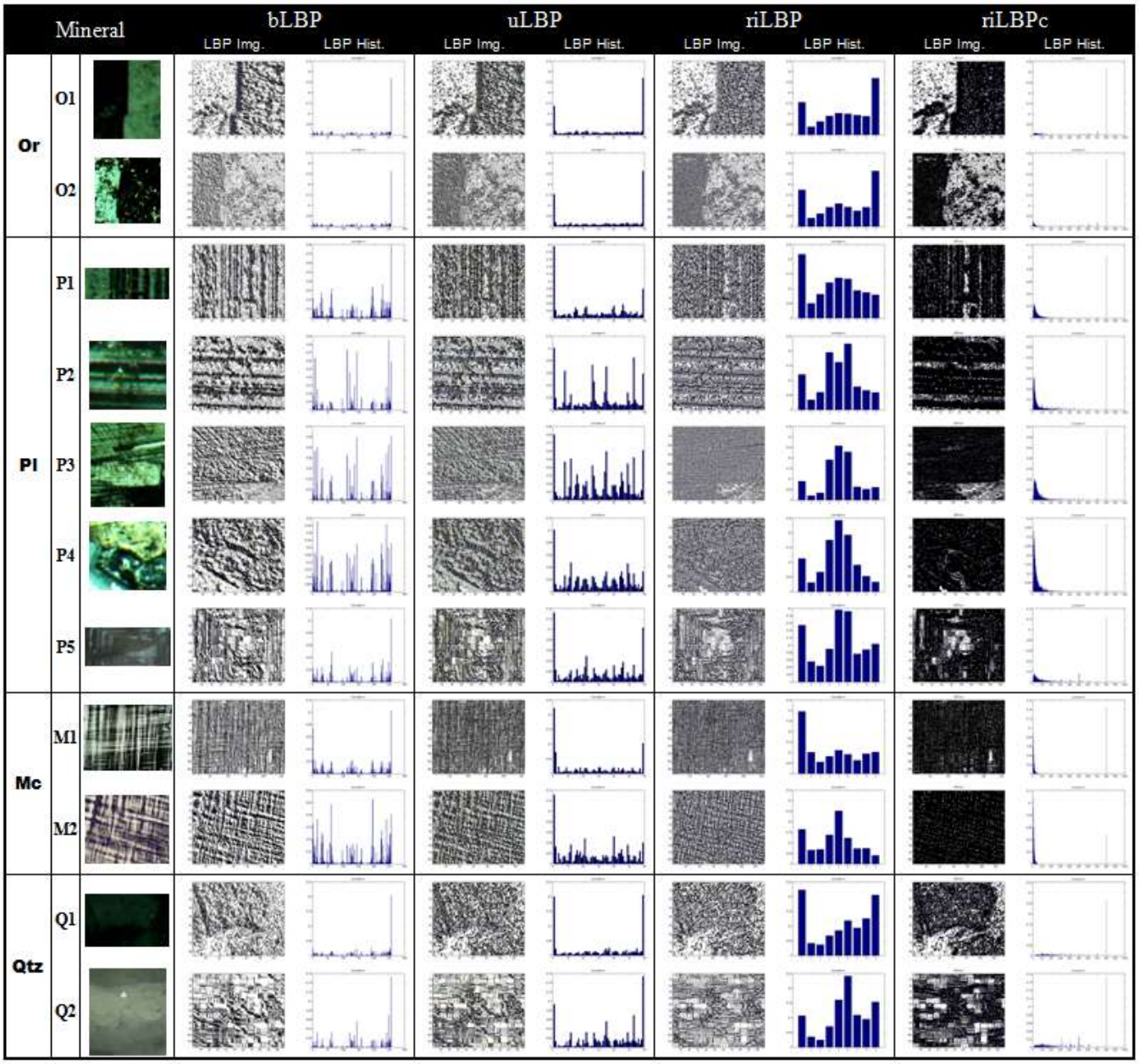

Figure 6. LBP (8,1) images and their corresponding histograms for sample minerals of Figure 1, obtained for different LBP schemes: basic LBP (bLBP), uniform LBP (uLBP), rotation-invariant LBP (riLBP), and rotation-invariant LBP equipped with contrast (riLBPc).

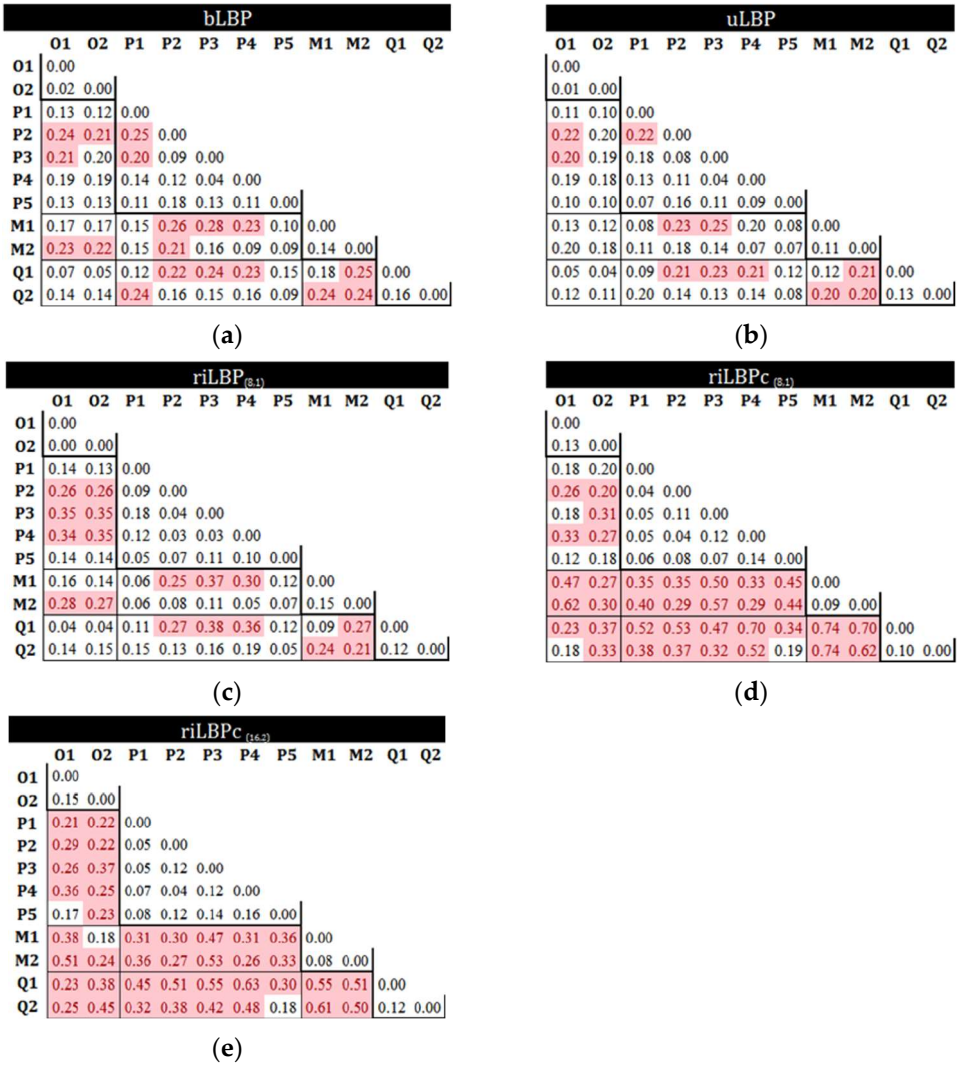

Figure 7. gofs obtained for any pair of the sample minerals of Figure 1, obtained for different LBP schemes: (**a**) bLBP, (**b**) uLBP, (**c**) riLBP, (**d**) riLBPc (8,1), and (**e**) riLBPc (16,2).

For better mineral texture classification of similar minerals such as Pl–Mc, the contrast feature is employed, which is usually more in Mc samples compared with the Pl ones, mostly due to their chemical composition and different birefringence. An alteration may also produce some different colors in Pl which helps in recognizing the mineral if contrast is used.

From Figure 7, it can be clearly seen that consideration of the contrast (using LBPc scheme according to Equation (2)) has efficiently improved the results. The *gof* values for the samples belonging to the same minerals have generally decreased, while those associated with dissimilar ones have mostly increased, especially for minerals such as Mc and Qtz. However, for some minerals such as Pl and Or which usually have the same contrast and alteration, the results have slightly deteriorated in some cases. O1 and O2 have small *gof*s before using contrast because O2 is affected by alteration and has changed to secondary minerals with high birefringence (light colors), which are characteristically in contrast with unaltered parts.

After that, the riLBPc version of the local binary pattern is selected as the texture descriptor of the minerals. Two options of (8,1) and (16,2) are examined for the P–R pair introduced in Equation (1). Figure 7 verifies that riLBPc (16,2) has well discriminated Or from Pl, and Or from Qtz, and performs much better than riLBPc (8,1). However, the scheme is a bit less efficient than riLBPc (8,1) in the discrimination of Or from Mc, since

the gof values given by riLBPc (8,1) are greater than those of riLBPc (16,2). As presented in Figure 7, the *gof* magnitudes obtained for mineral samples of the same class have not changed much. As a final conclusion of this section, the riLBPc (16,2) is employed for the task of texture recognition in the process of mineral identification.

5.2. Comparison of LBP with GLCM

Haralick et al. [27] proposed the gray-level co-occurrence matrix (GLCM) analysis based on the idea that texture data are contained in the spatial arrangement of gray level values. The GLCM is measuring how often various combinations of neighboring pixel values occur. GLCMs can be used to obtain statistical features that characterize the texture. To capture texture properties, we chose a subset of four features: energy, contrast, correlation, and homogeneity. In this study, level B is set to 8, following studies focused on texture analysis by means of GLCM [32].

The immediate neighboring pixels are considered along the four directions of 0°, 45°, 90°, and 135° [60], with the distance between the center and neighboring pixels, δ, set to 1 or 2. Therefore, for a considered δ, a GLCM composed of 16 descriptors (four statistical features for four different orientations) is obtained for characterizing mineral textures. A multi-scale feature pattern of dimension 32 (GLCM) is then defined by integrating the descriptors obtained from the two considered values of δ. Figure 8a shows the mutual distances of the feature vectors for the 11 sample templates of Figure 1. It is notable that amongst these 4 features, homogeneity shows the best performance. Figure 8b demonstrates the results of the *gof*s obtained from the riLBPc (16,2) scheme. A simple comparison between the two figures shows that the latter is more efficient for the task of mineral texture classification.

Mineral	Mineral	Or		Pl					Mc		Qtz	
Mineral	Temp.	O1	O2	P1	P2	P3	P4	P5	Mc1	Mc2	Q1	Q2
Or	O1	0.00	0.18	0.47	0.49	0.40	0.44	0.47	1.00	0.88	0.24	0.30
	O2	0.18	0.00	0.34	0.34	0.29	0.27	0.33	0.82	0.70	0.17	0.22
Pl	P1	0.47	0.34	0.00	0.06	0.09	0.10	0.05	0.53	0.41	0.39	0.22
	P2	0.49	0.34	0.06	0.00	0.10	0.09	0.08	0.51	0.39	0.41	0.24
	P3	0.40	0.29	0.09	0.10	0.00	0.07	0.13	0.60	0.48	0.39	0.18
	P4	0.44	0.27	0.10	0.09	0.07	0.00	0.14	0.56	0.44	0.38	0.19
	P5	0.47	0.33	0.05	0.08	0.13	0.14	0.00	0.53	0.41	0.38	0.22
Mc	Mc1	1.00	0.82	0.53	0.51	0.60	0.56	0.53	0.00	0.21	0.91	0.75
	Mc2	0.88	0.70	0.41	0.39	0.48	0.44	0.41	0.21	0.00	0.80	0.63
Qtz	Q1	0.24	0.17	0.39	0.41	0.39	0.38	0.38	0.91	0.80	0.00	0.22
	Q2	0.30	0.22	0.22	0.24	0.18	0.19	0.22	0.75	0.63	0.22	0.00

min

max

(a)

Mineral	Mineral	Or		Pl					Mc		Qtz	
Mineral	Temp.	O1	O2	P1	P2	P3	P4	P5	Mc1	Mc2	Q1	Q2
Or	O1	0.00	0.24	0.33	0.47	0.42	0.57	0.27	0.61	0.81	0.37	0.40
	O2	0.24	0.00	0.35	0.34	0.60	0.40	0.37	0.29	0.38	0.61	0.72
Pl	P1	0.33	0.35	0.00	0.08	0.08	0.11	0.12	0.49	0.57	0.72	0.51
	P2	0.47	0.34	0.08	0.00	0.19	0.06	0.19	0.48	0.43	0.81	0.61
	P3	0.42	0.60	0.08	0.19	0.00	0.20	0.23	0.76	0.84	0.87	0.67
	P4	0.57	0.40	0.11	0.06	0.20	0.00	0.26	0.49	0.42	1.00	0.76
	P5	0.27	0.37	0.12	0.19	0.23	0.26	0.00	0.58	0.52	0.48	0.29
Mc	Mc1	0.61	0.29	0.49	0.48	0.76	0.49	0.58	0.00	0.12	0.88	0.97
	Mc2	0.81	0.38	0.57	0.43	0.84	0.42	0.52	0.12	0.00	0.82	0.79
Qtz	Q1	0.37	0.61	0.72	0.81	0.87	1.00	0.48	0.88	0.82	0.00	0.19
	Q2	0.40	0.72	0.51	0.61	0.67	0.76	0.29	0.97	0.79	0.19	0.00

(b)

Figure 8. Results of: (**a**) combined Haralick multi-scale feature, and (**b**) rotation-invariant LBP (16,2) with a complementary contrast measure. (Numbers are normalized to 1 for the sake of comparison).

To compare the performance of different variants of LBP with the method of GLCM, a set of 200 RGB images of 50 microcline, 33 orthoclase, 57 plagioclase, and 60 quartz mineral samples are provided in the PNG format. The mineral dataset is split into 10 folds, each containing 20 sample images with roughly five images per class. The system uses each fold as an initial dataset, and the other nine folds (the remaining 180 images) as a test set. The

obtained classification results based on different texture operators and features are illustrated in Table 1. kNN is used as the classifier with Euclidean distance for all operator variants. The discriminatory power values reported are obtained as the mean magnitudes of results of the above 10 test sets. According to Table 1, both riLBPc (8,1) and (16,2) are clearly more efficient than the others. It is also interesting to note the effect of contrast, which has efficiently improved the discriminatory power in comparison with the riLBP operator.

Table 1. Discriminatory power results in different texture operators.

Method	Discriminatory Power
bLBP	0.61
uLBP	0.645
$riLBP_{(8,1)}$	0.745
$riLBPc_{(8,1)}$	0.82
$riLBPc_{(16,2)}$	0.825
$GLCM_1$	0.75
$GLCM_2$	0.77

5.3. CARUS Algorithm Validation

In this section, the proposed algorithm is examined to verify its performance for the task of texture identification of the minerals based on database updating. For this purpose, the 10-fold dataset, introduced in the previous section, is used. Again, each fold is considered as the initial database and the other folds as test ones. The CARUS algorithm is run 10 times successively, which means that each image is included once in the initial database and there is no bias between the initial database and test samples.

For each unknown mineral, the TMI scheme is employed to determine the type of twinning class (c). After the mineral identification step, the algorithm is performed to check whether the identified mineral might be included in the database or not. Initial databases, wrongly added minerals (minerals that are falsely included in other classes), and the minerals which are not appended to the database are shown in Figure 9, while in Figure 10, convergence diagrams obtained by 10 successive runs of the above procedure for each fold are illustrated. The convergence diagrams for any mineral classes of Or, Pl, Mc, and Qtz, as well as the one for the whole ***h_db***, are included. The three sets of convergence diagrams are associated with the ***h_db*** size and the two following values of discriminatory power including sensitivity or true positive rate (TPR) and accuracy (ACC):

$$TPR = \frac{TP}{TP + FN} \tag{8}$$

$$ACC = \frac{TP + TN}{TP + FN + FP + TN} \tag{9}$$

where TP is the number of correct predictions and FN is the number of incorrect predictions that an instance is positive, while FP is the number of correct predictions and TN is the number of incorrect predictions that an instance is negative. As will be shown later, the performance and efficiency of the method can be evaluated well based on both ACC and TPR measures.

It is seen that for most folds, after nearly six runs, the mineral database ***h_db*** becomes stable, with most mineral samples being included in the database. It is interesting to note that some specific samples in most folds, as shown in Figure 8, are wrongly included or are not appended to the database. For example, in all folds except fold 4, the same quartz mineral sample is wrongly included in the orthoclase class of the database (because in fold 4, the sample is introduced in the quartz class of the initial database).

As shown by the diagrams, almost all Pl, Or, and Mc samples are appended to the ***h_db***. Additionally, in some cases, a few samples are falsely added to the database in the initial runs of the updating procedure; e.g., Pl in fold 6, or Mc in fold 9; however, subsequent runs of the updating algorithm have improved the results, since, after each update, the

acceptance circles change, which accordingly modifies the new database; i.e., some samples might be included in or removed from the database.

As a further experiment, we introduced all 200 samples as the initial database to investigate the response of the CARUS updating system. The wrongly located samples as well as those which are not included (i.e., removed or substituted) in the initial database are shown in Figure 11. It is interesting that these mineral samples are mostly observed in the results of the ten folds introduced in Figure 8. The wrongly located minerals are clearly different from typical templates of their associated mineral classes and their confusion is thus naturally expected.

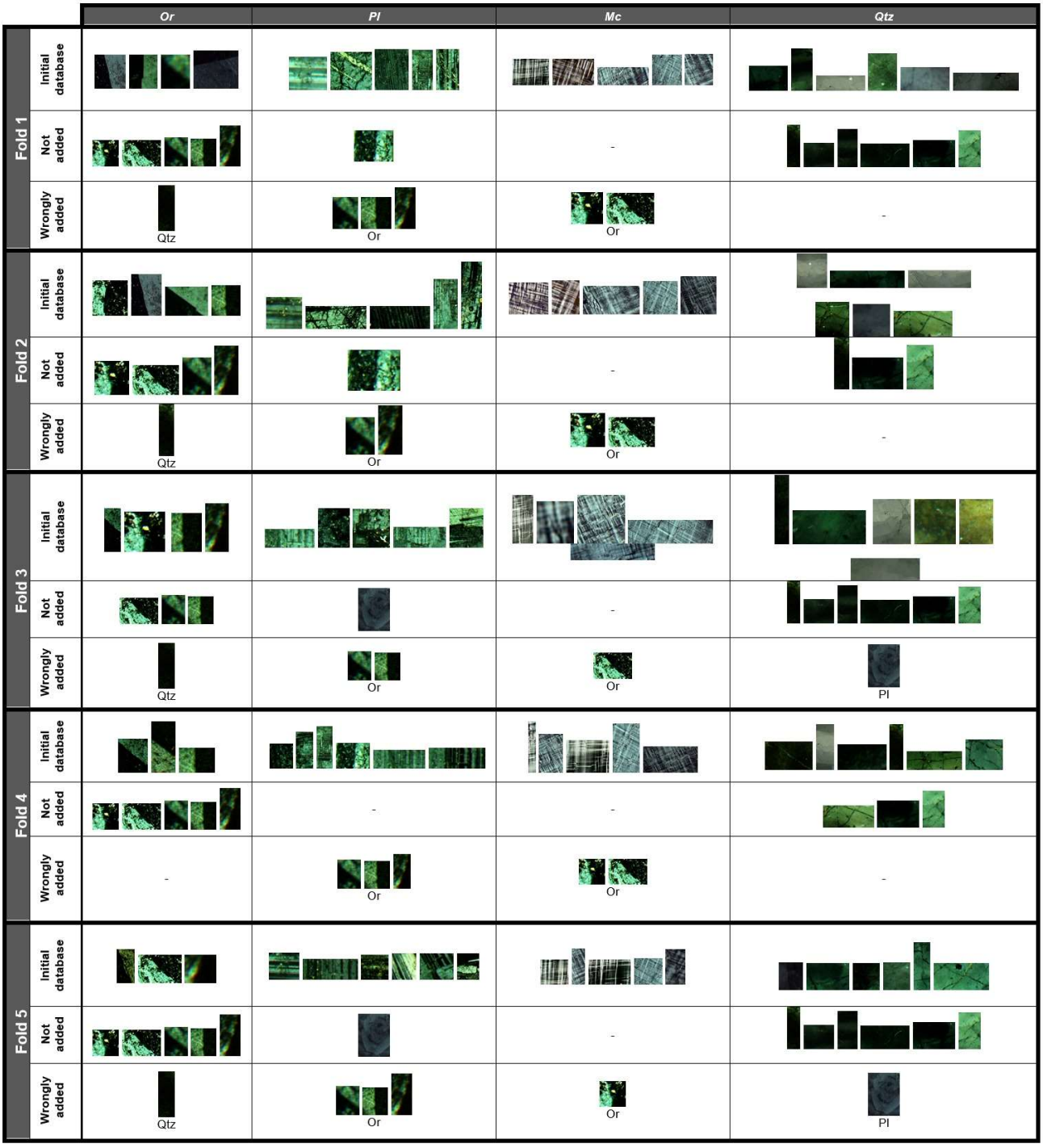

Figure 9. *Cont.*

Figure 9. Initial database, wrongly added minerals, and minerals which are not included in their associated classes, obtained for all 10 folds.

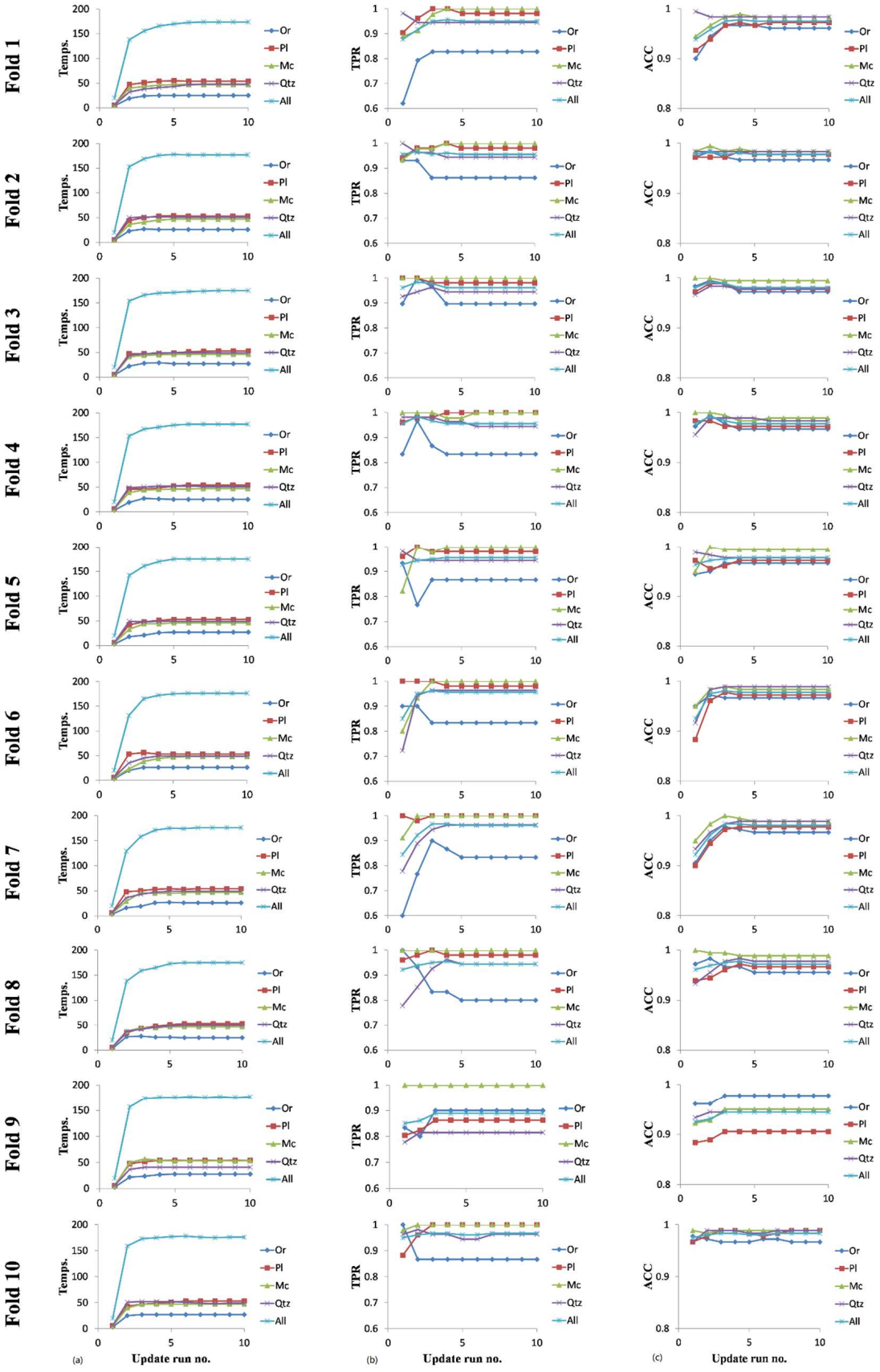

Figure 10. Convergence diagrams for 10 CARUS algorithm runs obtained for each fold; (**a**) ***h_db*** size; (**b**) *TPR*; (**c**) *ACC*.

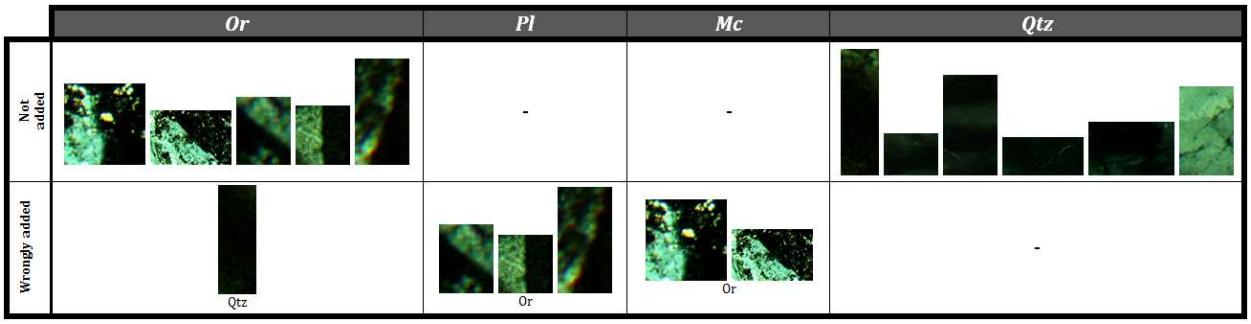

Figure 11. Wrongly added minerals, and minerals which are not included in their associated classes, for the case of all 200 samples as initial database.

5.4. Comparison of CARUS Classification Method with kNN

Different schemes have been used for the classification task, among which the k-nearest neighbors algorithm has obtained much reputation and application. In kNN classification, the class membership of an object is reported as the output, on the basis of a majority vote of its neighbors in the feature space; i.e., the object is assigned to the class most common among its k nearest neighbors, where k is a positive, typically small integer. However, the mineral classification method used in this research is based on a comparison of mean distances of the object (unknown mineral) in the feature space (LBP histogram), as introduced in Section 4. In this experiment, the two classification methods are compared. Again, the 10 mineral dataset folds, each with 20 sample images, are used, from which one fold is considered as the training set and the other fold as the testing set. kNN with Euclidean distance and three neighboring samples (which has been proved to be the most efficient option) is employed. The results, along with those of the proposed method, are introduced in Table 2. The reported discriminatory power values are the mean values of the 10 folds. It is clearly seen that the proposed method has efficiently performed better than kNN.

Table 2. The discriminatory power results for the CARUS classification method and kNN riLBP (16,2) is used as the texture operator.

Method	Discriminatory Power
kNN	0.825
CARUS (before updating) TPR	0.91
CARUS (before updating) ACC	0.955
CARUS (after updating) TPR	0.95
CARUS (after updating) ACC	0.975

6. Limitations and Future Work

The focus of this study is on the classification and identification of four main rock-forming minerals showing typical textural features. For the task of rock classification, however, identification of all rock-forming minerals is essential. For the identification of other minerals by means of automated digital microscopy, color features are proven to be efficient [17]. In future studies, combining color-based mineral identification with CARUS might be applied for the task of rock classification. Moreover, it might be useful to apply CARUS for identifying other minerals based on their textural features as well. Lastly, an online database might be developed for enriching the mineral data and empowering CARUS introduced here by adding images taken by different microscopes.

7. Conclusions

In this study, texture identification and classification of minerals according to the images taken under crossed polarized light (XPL) is considered. Texture features are effective for automated identification of minerals with low birefringence, including quartz, plagioclase, and K-feldspar. It would be a difficult task to recognize these minerals unless texture features such as twinning or undulose extinction are considered. For the purpose of automated rock classification, the identification of these minerals is of significant importance. It is also notable that other minerals also show significant texture characterization and texture analysis is an important task for any MI scheme.

The three following steps were conducted to develop an efficient well-performing automatic mineral texture identification algorithm, CARUS:

1. **Texture feature selection:** For mineral texture identification, noise and rotation are two main problems, and contrast has a key role in better recognition; thus, an LBP operator benefits from contrast and reduces the negative effects of noise and rotation is of much interest. The rotation-invariant local binary patterns, equipped with a complementary contrast measure, are proved to be a well-performing option for this purpose. It was shown that the selected rotation-invariant LBP can effectively outperform other texture features, such as GLCM, in the MI problem.
2. **Classification algorithm:** Mineral textures might be affected by structural and non-structural conditions; so, for reliable and robust TMI automation, a reasonable flexible classification algorithm is required. Here, in this study, a new classification scheme was designed based on mean distances between the LBP histogram of the unknown mineral with those belonging to a mineral class. The TMI results showed accuracies above 95% and proved to be better than the well-known kNN classification scheme, especially when an initial well-adjusted mineral database is provided.
3. **Database updating procedure:** Since no standard mineral texture database is available in the mineralogy community, an updating procedure was designed to improve any local initial database. The updating procedure incorporates newly identified minerals in the database if they satisfy certain criteria. Since during the TMI procedure, some minerals might falsely be recognized and located in the database, iterative runs of the updating algorithm will stabilize the LBP histogram database. Thus, the proposed updating procedure can automatically extend initial databases and produce efficient and rich mineral texture databases. It is notable that the update algorithm automatically removed samples that have high differences from samples in a certain class.

The CARUS LBP-based texture identification algorithm can efficiently be integrated with color-based MI schemes for the task of rock classification in subsequent research.

Author Contributions: Conceptualization, S.A. and R.K.; methodology, S.A. and R.K.; software, S.A.; validation, S.A. and R.K.; formal analysis, S.A. and R.K.; investigation, S.A. and R.K.; data curation, S.A. and R.K.; writing—original draft preparation, S.A., R.K., M.K. and D.J.A.; writing—review and editing, M.K. and D.J.A.; visualization, S.A. and R.K.; supervision, R.K., M.K. and D.J.A. All authors have read and agreed to the published version of the manuscript.

Funding: This study received no external funding.

Institutional Review Board Statement: Not applicable.

Informed Consent Statement: Not applicable.

Data Availability Statement: Data can be accessed by contacting the corresponding author.

Conflicts of Interest: The authors declare no conflict of interest.

References

1. Autio, J.; Lepisto, L.; Visa, A. Image analysis and data mining in rock material research. *Materia* **2004**, *4*, 36–40.
2. Asmussen, P.; Conrad, O.; Günther, A.; Kirsch, M.; Riller, U. Semi-automatic segmentation of petrographic thin section images using a "seeded-region growing algorithm" with an application to characterize wheathered subarkose sandstone. *Comput. Geosci.* **2015**, *83*, 89–99. [CrossRef]
3. Filho, I.M.; Spina, T.V.; Falcao, A.X.; Vidal, A.C. Segmentation of sandstone thin section images with separation of touching grains using optimum path fores operators. *Comput. Geosci.* **2013**, *57*, 146–157. [CrossRef]
4. Marschallinger, R.; Hofmann, P. The application of object based image analysis to petrographic micrographs. *Microsc. Sci. Technol. Appl. Educ.* **2010**, *4*, 1526–1532.
5. Mlynarczuk, M.; Gorszczyk, A.; Slipek, B. The application of pattern recognition in the automatic classification of microscopic rock images. *Comput. Geosci.* **2013**, *60*, 126–133. [CrossRef]
6. Lawal, M.O. Tomato detection based on modified YOLOv3 framework. *Sci. Rep.* **2021**, *11*, 1447. [CrossRef] [PubMed]
7. Huizhen, H.; Zhiwei, J.; Shipping, G.; Cong, W.; Qing, G. Siamese Adversarial Network for image classification of heavy mineral grains. *Comput. Geosci.* **2022**, *159*, 105016.
8. Fueten, F.; Mason, J. An artificial neural net assisted approach to editing edges in petrographic images collected with the rotation polarizer stage. *Comput. Geosci.* **2007**, *33*, 1176–1188. [CrossRef]
9. Changyu, J.; Kai, W.; Tao, H.; Yu, L.; Aixin, L.; Dong, L. Segmentation of ore and waste rocks in borehole images using the multi-module densely connected U-net. *Comput. Geosci.* **2022**, *159*, 105018.
10. Ge, S.; Wang, C.; Jiang, Z.W.; Hao, H.Z.; Gu, Q. Dual-input attention network for automatic identification of detritus from river sands. *Comput. Geosci.* **2021**, *151*, 104735. [CrossRef]
11. Prikryl, R. Assessment of rock geomechanical quality by quantitative rock fabric coefficients: Limitations and possible source of misinterpretations. *Eng. Geol.* **2006**, *87*, 149–162. [CrossRef]
12. Tandon, S.R.; Gupta, V. The control of mineral constituents and textural characteristics on the petrophysical & mechanical (PM) properties of different rocks of the Himalaya. *Eng. Geol.* **2013**, *153*, 125–143.
13. Yilmaz, N.G.; Goktan, R.M.; Kibici, Y. Relation between some quantitative petrographic characteristics and mechanical strength properties of granitic building stones. *Int. J. Rock Mech. Min. Sci.* **2011**, *48*, 506–513. [CrossRef]
14. Aligholi, S.; Lashkaripour, G.R.; Ghafoori, M.; TrighAzali, S. Evaluating the relationships between NTNU/SINTEF drillability indices with index properties and petrographic data of hard igneous rocks. *Rock Mech. Rock Eng.* **2017**, *50*, 2929–2953. [CrossRef]
15. Aligholi, S.; Lashkaripour, G.R.; Ghafoori, M. Estimating engineering properties of igneous rocks using semi-automatic petrographic analysis. *Bull. Eng. Geol. Environ.* **2019**, *78*, 2299–2314. [CrossRef]
16. Aligholi, S.; Khajavi, R.; Razmara, M. Automated mineral identification algorithm using optical properties of crystals. *Comput. Geosci.* **2015**, *85*, 175–183. [CrossRef]
17. Aligholi, S.; Lashkaripour, G.R.; Khajavi, R.; Razmara, M. Automatic mineral identification using color tracking. *Pattern Recognit.* **2017**, *65*, 164–174. [CrossRef]
18. Naseri, A.; Rezaei Nasab, A. Automatic identification of minerals in thin sections using image processing. *J. Ambient Intell. Humaniz. Comput.* **2021**, 1–13. [CrossRef]
19. Zeng, X.; Xiao, Y.; Ji, X.; Wang, G. Mineral Identification Based on Deep Learning That Combines Image and Mohs Hardness. *Minerals* **2021**, *11*, 506. [CrossRef]
20. Ross, B.J.; Fueten, F.; Yashkir, D.Y. Automatic mineral identification using genetic programming. *Mach. Vis. Appl.* **2001**, *13*, 61–69. [CrossRef]
21. Thompson, S.; Fueten, F.; Bockus, D. Mineral identification using artificial neural networks and the rotating polarizer stage. *Comput. Geosci.* **2001**, *27*, 1081–1089. [CrossRef]
22. Backes, A.R.; Casanova, D.; Bruno, O.M. Color texture analysis based on fractal descriptors. *Pattern Recognit.* **2012**, *45*, 1984–1992. [CrossRef]
23. Tuceryan, M.; Jain, A.K. *Texture Analysis in Handbook of Pattern Recognition and Image Processing*; World Scientific: Singapore, 1993.
24. Ji, Q.; Engel, J.; Craine, E. Texture analysis for classification of cervix lesions. *IEEE Trans. Med. Imaging* **2000**, *19*, 1144–1149. [CrossRef] [PubMed]
25. Cohen, F.S.; Fan, Z.; Attali, S. Automated inspection of textile fabrics using textural models. *IEEE Trans. Pattern Anal. Mach. Intell.* **1991**, *13*, 803–808. [CrossRef]
26. Anys, H.; He, D.C. Evaluation of textural and multipolarization radar features for crop classification. *IEEE Trans. Geosci. Remote Sens.* **1995**, *33*, 1170–1181. [CrossRef]
27. Haralick, R.M.; Shanmugam, K.; Dinstein, I. Textural features for image classification. *IEEE Trans. Syst. Man Cy.* **1973**, *3*, 610–621. [CrossRef]
28. Petrou, M.; Sevilla, P.G. *Image Processing Dealing with Texture*; John Wiley & Sons: Hoboken, NJ, USA, 2006.
29. Davis, I.S. Polarograms: A new tool for Image Texture Analysis. *Pattern Recognit.* **1981**, *13*, 219–223. [CrossRef]
30. Chen, M.Y.; Kundu, A. A complemment to variable duration hidden Markov model in handwritten word recognition. In Proceedings of the IEEE International Conference on Image Processing, 1994 (ICIP-94), Austin, TX, USA, 13–16 November 1994; Volume 1, pp. 174–178.

31. Azencott, R.; Wang, J.P.; Younes, L. Texture classification using windowed fourier filters. *IEEE Trans. Pattern Anal. Mach. Intell.* **1997**, *19*, 148–153. [CrossRef]
32. Randen, T.; Husoy, J.H. Filtering for texture classification: A comparative study. *IEEE Trans. Pattern Anal. Mach. Intell.* **1999**, *21*, 291–310. [CrossRef]
33. Unser, M. Texture classification and segmentation using wavelet frames. *IEEE Trans. Image Process.* **1995**, *4*, 1549–1560. [CrossRef]
34. Ojala, T.; Pietikäinen, M.; Mäenpää, T. Multiresolution gray-scale and rotation invariant texture classification with local binary patterns. *IEEE Trans. Pattern Anal. Mach. Intell.* **2002**, *24*, 971–987. [CrossRef]
35. Ahonen, T.; Hadid, A.; Pietikainen, M. Face description with local binary patterns: Application to face recognition. *IEEE Trans. Pattern Anal. Mach. Intell.* **2006**, *28*, 2037–2041. [CrossRef] [PubMed]
36. Bereta, M.; Karczmarek, P.; Pedrycz, W.; Reformat, M. Local descriptors in application to the aging problem in face recognition. *Pattern Recognit.* **2013**, *46*, 2634–2646. [CrossRef]
37. Guo, Z.; Zhang, L.; Zhang, D. A completed modeling of local binary pattern operator for texture classification. *IEEE Trans. Image Process.* **2010**, *19*, 1657–1663.
38. Hadid, A.; Pietikäinen, M. Combining appearance and motion for face and gender recognition from videos. *Pattern Recognit.* **2009**, *42*, 2818–2827. [CrossRef]
39. Mehta, R.; Yuan, J.; Egiazarian, K. Face recognition using scale-adaptive directional and textural features. *Pattern Recognit.* **2014**, *47*, 1846–1858. [CrossRef]
40. Nanni, L.; Lumini, A.; Brahnam, S. Survey on LBP based texture descriptors for image classification. *Expert Syst. Appl.* **2012**, *39*, 3634–3641. [CrossRef]
41. Satpathy, A.; Jiang, X.; Eng, H.L. LBP based edge-texture features for object recognition. *IEEE Trans. Image Process.* **2014**, *23*, 1953–1964. [CrossRef]
42. Song, C.; Yang, F.; Li, P. Rotation invariant texture measured by local binary pattern for remote sensing image classification. In Proceedings of the Second International Workshop on Education Technology and Computer Science, Wuhan, China, 6–7 March 2010.
43. Vatsavai, R.R.; Cheriyadat, A.; Gleason, S. Unsupervised semantic labeling framework for identification of complex facilities in high-resolution remote sensing images. In Proceedings of the Data Mining Workshops (ICDMW), Sydney, Australia, 13 December 2010.
44. Wu, J.; Rehg, J. Centrist: A visual descriptor for scene categorization. *IEEE Trans. Pattern Anal. Mach. Intell.* **2011**, *33*, 1489–1501.
45. Zhao, G.; Pietikainen, M. Dynamic texture recognition using local binary patterns with an application to facial expressions. *IEEE Trans. Pattern Anal. Mach. Intell.* **2007**, *29*, 915–928. [CrossRef]
46. Liao, S.; Chung, A. Face recognition by using elongated local binary patterns with average maximum distance gradient magnitude. In Proceedings of the Computer Vision—ACCV 2007, Tokyo, Japan, 18–22 November 2007; pp. 672–679.
47. Guo, Z.; Zhang, L.; Zhang, D. Rotation invariant texture classification using lbp variance with global matching. *Pattern Recognit.* **2010**, *43*, 706–719. [CrossRef]
48. Qi, X.; Xiao, R.; Guo, J.; Zhang, L. Pairwise rotation invariant co-occurrence local binary pattern. In Proceedings of the Computer Vision–ECCV 2012, Florence, Italy, 7–13 October 2012; pp. 158–171.
49. Zhu, Z.; You, X.; Chen, C.L.P.; Tao, D.; Ou, W.; Zou, J. An adaptive hybrid pattern for noise-robust texture analysis. *Pattern Recognit.* **2015**, *48*, 2592–2608. [CrossRef]
50. Smith, J.V.; Beermann, E. Image analysis of plagioclase crystals in rock thin sections using grey level homogeneity recognition of discrete areas. *Comput. Geosci.* **2007**, *33*, 335–356. [CrossRef]
51. Pettijohn, F.J.; Potter, P.E.; Siever, R. *Sand and Sandstone*; Springer: Berlin/Heidelberg, Germany, 1987.
52. Streckeisen, A.L. To each plutonic rock its proper name. *Earth Sci. Rev.* **1976**, *12*, 12–33. [CrossRef]
53. Klein, C. *Manual of Mineralogy*, 22nd ed.; Wiley: Hoboken, NJ, USA, 2001.
54. Deer, W.A.; Howie, R.A.; Zusman, J. *Rock Forming Minerals*; Longman: New York, NY, USA, 1996.
55. Gribble, C.D.; Hall, A.J. *A Practical Introduction to Optical Mineralogy*; George Allen & Unwin: London, UK, 1985.
56. Ojala, T.; Pietikäinen, M.; Harwood, D. A comparative study of texture measures with classification based on feature distributions. *Pattern Recognit.* **1996**, *29*, 51–59. [CrossRef]
57. Ojala, T.; Pietikäinen, M.; Mäenpää, T. Gray scale and rotation invariant texture classification with local binary patterns. In Proceedings of the European Conference on Computer Vision. Lecture Notes in Computer Science, Dublin, Ireland, 26 June–1 July 2000; Springer: Berlin/Heidelberg, Germany, 2000; Volume 1842.
58. Pietikäinen, M.; Zhao, G.; Hadid, A.; Ahonen, T. *Computer Vision Using Local Binary Patterns*; Springer: Berlin/Heidelberg, Germany, 2011.
59. Mäenpää, T.; Ojala, T.; Pietikäinen, M.; Soriano, M. Robust texture classification by subsets of local binary patterns. In Proceedings of the 15th International Conference on Pattern Recognition, Barcelona, Spain, 3–7 September 2000.
60. Soh, L.K.; Tsatsoulis, C. Texture analysis of SAR sea ice imagery using gray level co-occurrence matrices. *IEEE Trans. Geosci. Remote Sens.* **1999**, *37*, 780–795. [CrossRef]

sustainability

MDPI

Article

Investigation of Some Property Changes of Light-Colored Turkish Natural Stones after High-Temperature Treatments

Engin Özdemir

Faculty of Engineering, Inonu University, Malatya 44280, Turkey; ozdemir.engin@inonu.edu.tr; Tel.: +90-422-377-47-32

Abstract: Natural stones are a widely used construction material for both structural and decorative purposes. It is a material used for many floors and cladding due to its special beauty and quite aesthetic appearance. However, natural stones are exposed to different temperatures due to natural, urban or industrial activities and they lose their physico-mechanical properties. It is known that high temperatures and fire cause degradation of construction and building stones. There are many studies investigating the effect of high temperatures on physical and mechanical properties of natural stones, while there are very limited studies on color and gloss. In this study, the changing physical and mechanical properties, color and gloss of different light-colored polished natural stones exposed to room temperature up to 1000 °C in the oven were investigated. For this purpose, natural stones were gradually exposed to 200, 400, 600, 800 and 1000 °C, starting from room temperature. After exposure to different temperatures, water absorption, porosity, Schmidt hammer hardness, point load strength, color and gloss were measured and compared to reference samples (at room temperature). However, all samples were decayed at 1000 °C, changes at this temperature value could not be determined. The results obtained at other temperature values were evaluated separately for each parameter. While the change in physico-mechanical properties of all samples up to 400 °C was limited, a dramatic change was observed with increasing temperature. In all samples, point load strength losses were observed due to an increase in porosity and water absorption. In addition, all samples darkened at 400 °C, while the whiteness value (L*) of samples increased at 800 °C. Gloss values gradually decreased due to the increase in temperature.

Keywords: natural stones; temperature; fire; thermal effect; point load strength; porosity; color; gloss

Citation: Özdemir, E. Investigation of Some Property Changes of Light-Colored Turkish Natural Stones after High-Temperature Treatments. *Sustainability* **2022**, *14*, 10298. https://doi.org/10.3390/su141610298

Academic Editors: Jian Zhou, Mahdi Hasanipanah and Danial Jahed Armaghan

Received: 26 June 2022
Accepted: 15 August 2022
Published: 18 August 2022

Publisher's Note: MDPI stays neutral with regard to jurisdictional claims in published maps and institutional affiliations.

Copyright: © 2022 by the author. Licensee MDPI, Basel, Switzerland. This article is an open access article distributed under the terms and conditions of the Creative Commons Attribution (CC BY) license (https://creativecommons.org/licenses/by/4.0/).

1. Introduction

Natural stones are one of the oldest building materials used by humans. Even when people resided in places made of clay and wood, they used natural stones in their various monumental structures. Until the 20th century, natural stones were used instead of bricks in Europe's important and large buildings. There are countless historical monuments made of natural stone in Anatolia, especially during the Ancient Greek, Roman, Byzantine, Seljuk and Ottoman periods. In Seljuk and Ottoman architecture, limestone and tuffs were handled with great skill and decorated the exterior and interior of buildings such as mosques and madrasas. Therefore, Turkey has an important position due to the use of natural stone as a construction and building material [1,2]

Natural stone products, such as marble, travertine, andesite, tuff and granite, are widely used construction materials for both structural and decorative purposes. In particular, they have been used in the construction industry for purposes such as interior–exterior coatings, flooring and landscaping. Natural stones are subject to physical and chemical changes due to different environmental conditions and lose their initial strength properties. While determining the usage areas of natural stones, not only their physico-mechanical properties, but also the environmental factors to which they are exposed, should be determined. Some researchers investigated the effects of environmental conditions, such

as temperature, freeze–thaw, salt crystallization, contact with acid-based solutions and wetting–drying of natural stones. Mutlutürk et al. (2004) developed a model to predict their changes depending on environmental cycles (freezing–thawing and heating–cooling) with an experimental study on 10 different rock types [3]. Yavuz (2011) determined that andesite caused decreases in P-wave velocity, Schmidt hammer hardness and compressive strength, and an increase in porosity and water absorption values, depending on the increase in the number of cycles of thermal shock and freeze–thaw [4]. Fener and Ince (2015) investigated changes in porosity, P-wave velocity, uniaxial compressive strength, point load strength, Bohme abrasion loss and Brazilian tensile strength of Konya–Sille andesite exposed to five F–T cycles [5]. They also evaluated the degree of degradation of structures built with Sille andesite. Ghobadi and Babazadeh (2015) examined changes in weight loss, Vp wave velocity, point load strength and uniaxial compressive strength values, by exposing nine different sandstones from Qazvin region (Western Iran) to accelerated tests (salt crystallization, freeze–thaw, warming–cooling, warming–cooling–wetting) [6]. Gökçe et al. (2016) investigated changes in physico-mechanical (porosity, P-wave velocity, point load strength, uniaxial compressive strength, Bohme abrasion loss and Brazilian tensile strength) properties of Konya–Gödene travertine due to freeze–thaw cycles. They obtained statistical relationships with experimental results obtained in F–T cycles [7]. Bozdag et al. (2016) determined the relationships between weathering and welding degree of pyroclastic rocks in the ancient city of Konya Kilistra by performing accelerated aging tests (freeze–thaw, salt crystallization and wetting–drying). The researchers stated that all three accelerated tests had negative effects on the physico-mechanical properties of rocks, but that F–T and SC were more destructive than WD [8]. Heidari et al. (2017) investigated changes in physico-mechanical properties of samples obtained from Chelmaran quarry after aging tests (freeze–thaw and salt crystallization). They stated that the mechanical strength of the rocks decreased considerably in both cycles [9]. Özşen et al. (2017) researched the effect of salt crystallization on physico-mechanical changes of pyroclastic rock samples collected from six different quarries in Cappadocia. Researchers found strong logarithmic relationships between dry weight loss values and mechanical strength properties [10]. Deng et al. (2018) experimentally investigated combined effects of acid and freeze–thaw cycles on sandstones. The combined effect of acid corrosion and freeze–thaw was found to be more destructive than acid corrosion [11]. Sun and Zhang (2019) researched the effect on the physico-mechanical properties of sandstones exposed to wetting–drying cycles with different saline solutions (0%, 4%, 6% and 8% magnesium sulfate). They stated that samples exposed to salt solution were more affected than pure water [12]. Amirkiyaei et al. (2020) conducted experimental investigations on 22 carbonate building stones (3 limestone, 12 travertine and 7 marble) extracted from different locations in Iran. Based on the data obtained, they developed an empirical equation to determine the Vp wave velocity of stones during freeze–thaw cycles [13]. Guler et al. (2021) investigated changes in physical, mechanical and index properties of six different carbonate rocks by exposing them to thermal cycles. They stated that as the number of T–S and F–T cycles increases, the internal structure of carbonate rocks increases and, as a result, their physico-mechanical properties change significantly [14]. Mardoukhi et al. (2021) determined the effect of test temperature and low temperature thermal cycles on the dynamic tensile strength of rocks in low temperature environments such as Mars. They emphasized that there is an increase in the mechanical strength of granitic rocks due to decreases in temperature, thus this increase should be taken into account in excavation operations [15].

High temperatures are one of main physical agents that cause durability problems of natural stones. Natural stones, which are used as building materials, are exposed to high temperature effects, generally due to fires. These stones deteriorate due to various fires that occur in the natural environment and internal structure of buildings. In the natural environment, fire emerges as a common tool effective in geomorphological and biological change. In such events, temperatures can exceed 1000 °C [16–19]. Fire causes physical and chemical degradation by affecting the material structure. Physical degradation is generally

observed as thermal deformations. Thermal deformations are physical magnitudes that occur within a material under different temperature effects and can generally be seen as thermal expansion or contraction. Many stone buildings have been destroyed as a result of fire damage throughout historical ages [20,21]. Hajpál (2002) stated that the potential impact of fires on buildings can be calculated during the construction of buildings; this data obtained from the buildings affected by fire can be used when constructing new stone buildings, and it is also possible to calculate the risk of such stone buildings. It has been stated that change in the physico-mechanical structure of rocks due to fire reduces the bearing capacity of the building [22]. Tian et al. (2014) experimentally investigated the changes in bulk density and the uniaxial and triaxial compressive strength of claystone exposed to high temperatures from room temperature (23 °C) to 1000 °C at laboratory scale [23]. Ozguven and Ozcelik (2014) investigated the changes in some physico-mechanical properties of eight different natural stones (limestones and marbles) exposed to high temperatures. They stated that there is a decrease in the mechanical strength of natural stones at every stage due to the increase in temperature values from room temperature (23 °C) to 1000 °C [24].

In this study, changes in physico-mechanical properties of five different light-colored natural stones were experimentally investigated by exposing them from room temperature to 800 °C. In particular, non-destructive test methods, such as hardness, porosity, water absorption, Schmidt hammer hardness, color and gloss, were chosen. Thus, the aim is to predict the changes in the physico-mechanical properties of natural stones exposed to fire or high temperatures. In addition, point load strength, which is the most common test method used in the estimation of both the uniaxial compressive and tensile strengths of rocks, was determined. For this purpose, the physico-mechanical changes of natural stones were investigated experimentally by exposing them to different temperatures (23, 200, 400, 600 and 800 °C). The importance of this study is that it contributes to the limited literature on color and gloss changes of natural stones after exposure to high temperatures. In particular, in the restoration of historical buildings after fires, in addition to physico-mechanical properties, changes in color and gloss should be taken into account.

2. Materials and Methods

2.1. Material

In this study, five different natural stone samples of sedimentary origin were used. A total of 150 samples, 30 of each rock type, were exposed to different temperatures. The location map of samples used in the experimental study is given in Figure 1. The codes, trade names and origins of the samples are given in Table 1. The 30 × 40 × 40 mm-sized samples were prepared to determine the physico-mechanical properties of natural stones. Test samples and devices are given in Figure 2a–f.

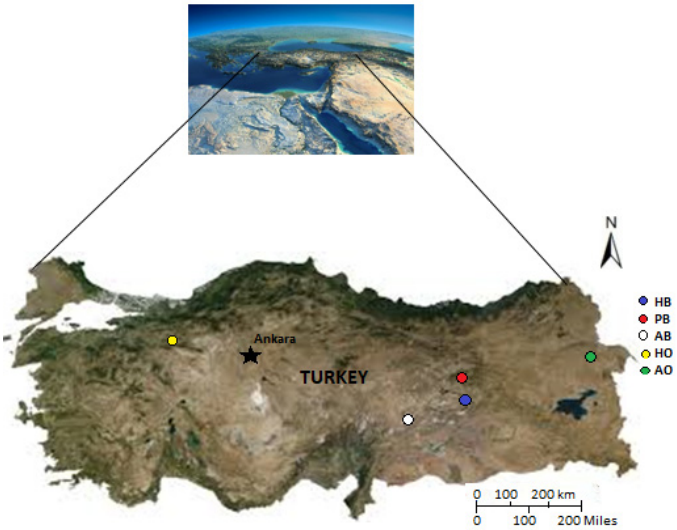

Figure 1. Location map of samples.

Table 1. Codes, trade names and origins of natural stones.

Code	Commercial Name	Stone Type	Location
HB	Hazar Beige	Limestone	Hazar-Elazig
PB	Pertek Beige	Limestone	Pertek-Tunceli
AB	Akçadağ Beige	Limestone	Akçadağ-Malatya
HO	Honey Onyx	Limestone	Sögüt-Bilecik
AO	Ağrı Onyx	Dolomite	Diyadin-Ağri

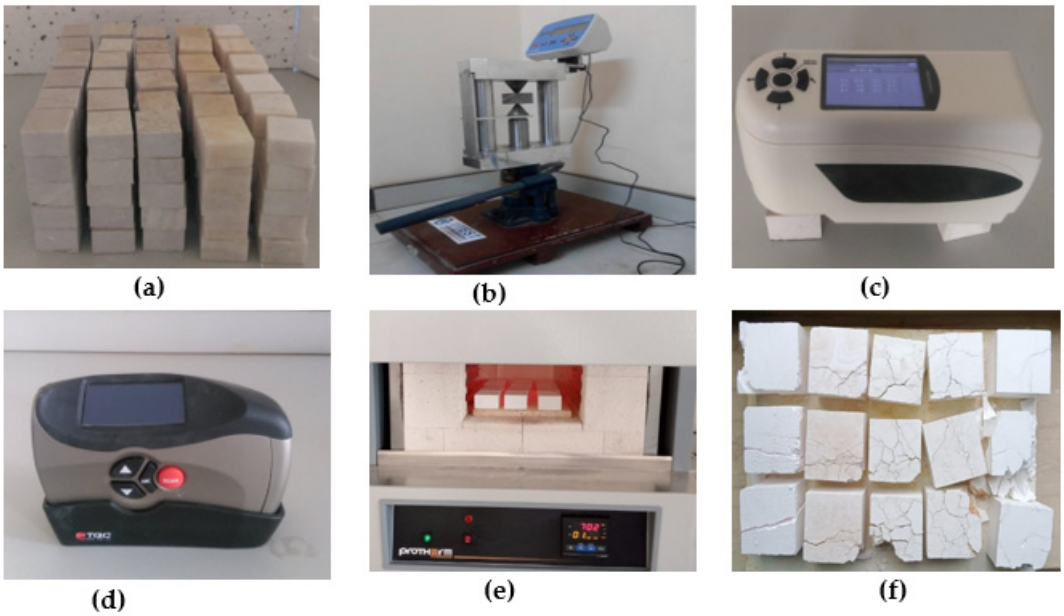

Figure 2. (**a**) Test samples, (**b**) Point load test device, (**c**) Colorimeter, (**d**) Gloss meter, (**e**) Samples being exposed to temperature and (**f**) Samples exposed to 1000 °C.

2.2. Methods

2.2.1. High Temperature Test

Samples at room temperature (i.e., not exposed to any temperature) were accepted as reference samples. Then, other samples were compared with the reference samples after exposure to each temperature. In the current literature, laboratory ovens are most commonly used to determine the effect of fire on natural stones. In order to explain the effect of temperature, temperature values were preferred in different ranges. The purpose of choosing different temperature values is to clearly see changes occurring in each temperature range. The highest temperature value used in the study was selected as 1000 °C. However, measurements could not be taken due to the natural stones being broken at this temperature (see Figure 2f). The experimental study was conducted by exposing samples to five different temperature values (23, 200, 400, 600 and 800 °C). Using a Protherm PLF model oven, each temperature value was adjusted by considering the heating rate of the oven. Thus, the natural stones were exposed to required high temperatures. After reaching the specified temperature, the natural stones remained at that temperature in the oven for 120 min. Natural stones exposed to high temperatures were kept in the oven until they were at room temperature in order to avoid sudden thermal shock. After the samples reached room temperature, non-destructive tests (water absorption, porosity, color, gloss, Schmidt hammer hardness) were performed, and then point load strength was determined.

2.2.2. Non-Destructive Tests

Non-destructive tests are highly preferred due to being fast, easy and practical in studies related to earth sciences. In this study, non-destructive tests (water absorption, porosity, color, gloss, Schmidt hammer hardness) were applied before determining the

point load strength of the samples. For the water absorption and porosity of the rocks, 5 samples with dimensions of 70 × 70 × 70 mm were used. Water absorption by weight and apparent porosity were determined according to TS EN 13755 and TS EN 1936, respectively [25,26]. For this purpose, the dry, saturated weights and volumes of the samples were determined. The water absorption and porosity values of the rocks were determined by using Equations (1) and (2).

$$Aw = \frac{Ws - Wd}{Wd} \quad (1)$$

$$P = \frac{Ws - Wd}{V}\% \quad (2)$$

where Aw: Water absorption by weight (%), Ws: Saturated sample (gr), Wd: Dry sample (gr), P: Porosity (%) and V: Volume (cm^3).

The Schmidt hammer is a fast and inexpensive test that is widely used to predict material properties of rocks such as uniaxial compressive strength and Young's modulus. The Schmidt hammer is divided into L and N types with different impact energies. The L-type hammer is most commonly used to estimate uniaxial compressive strength and Young's modulus [27]. An L-type Schmidt hammer with an impact energy of 0.74 Nm was used to determine Schmidt hammer hardness values. Measurements were taken 20 times from different points of each cubic sample and evaluated according to the method suggested by Aydin [28]. Accordingly, the arithmetic mean of the highest 10 values was accepted as the Schmidt hammer hardness of rock.

A subjective assessment of color measurement by eye can sometimes be misleading. For this reason, objective measurements made with various devices are required. It has become common to evaluate color and color differences instrumentally according to the method developed by the International Lighting Commission. This method is known as the CIELAB (L*, a*, b*) three-point measurement [29]. The coordinate system of colors is given in Figure 3. In this system, L* is the degree of darkness and lightness of color on a scale ranging from white (L* = 100) to black (L* = 0), a* is the scale on the axis ranging from green (−a*) to red (+a*) and b* is the scale on the axis ranging from blue (−b*) to yellow (+b*). Color changes occurring at different temperatures were determined by the Hunter CIELAB colorimeter. In this study, the NR200 colorimeter, introduced by 3nh, which has passed tens of thousands of tests and applied many innovative technologies, was used. The arithmetic averages were obtained by measuring from four different points around the midpoint of each sample.

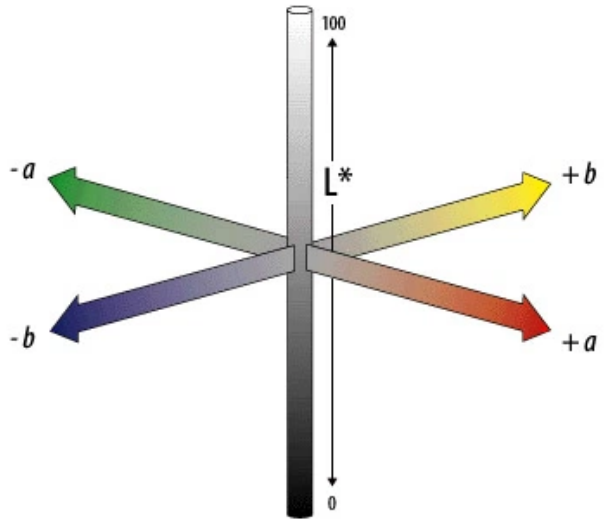

Figure 3. Coordinate system for CIELAB.

A beam of light shining onto a bright surface is theoretically refracted at the angle it came from. Thus, gloss is the reflected amount of beam coming to the surface at a certain angle, expressed as a percentage (%) relative to the gloss of glass with a refractive index of 1.57. Gloss measurements are made by sending the light at angles of 20, 45, 60 and 85 degrees [30]. This study is based on measurements made at an angle of 60°. Changes of gloss occurring at different temperatures were determined using the Q TQC GL0010 digital gloss meter (Range: 0–2000 GU; Repeatability r*: 0.2 GU; Reproducibility R*: 1.6 GU and Bias: 0.6 GU). The arithmetic averages were obtained by measuring from four different points around the midpoint of each sample. Measured values were obtained in GU (gloss units).

2.2.3. Point Load Strength Test

The uniaxial compressive strength of rocks is the most preferred mechanical test in earth science projects such as mining and civil engineering. This test requires time-consuming, expensive equipment, uniformly geometrically shaped specimens and skilled personnel [31–33]. However, in some situations where time is limited and sufficient samples cannot be obtained, it is easier to use the point load strength suggested by ISRM 1985 [34]. Point load strength is a simple, fast and inexpensive index test method that can be applied both in the field and in the laboratory. To determine this strength, core samples (for diametric and axial tests), cut block samples or irregular-sized samples can be used [35,36]. In this study, cut block samples were preferred. The experimental study was conducted according to the method recommended by ISRM 1985 [34]. The tests were conducted using a Digital Point Load Tester (UTEST-UTR-0580 model) that has a 60 kN capacity test body and a digital readout unit loaded with a hydraulic hand pump. For this purpose, 30 × 40 × 40 mm-sized samples were prepared. To determine the point load strength of the natural stones, firstly the uncorrected point loading strength is calculated by Equation (3).

$$Is = \frac{P}{De^2} \tag{3}$$

where *Is* is uncorrected point load strength (MPa), *P* is failure load (kN, kgf, etc.) and *De* is equivalent core diameter (mm).

Equivalent core diameter is calculated by Equation (4) for cut block samples.

$$De^2 = \frac{4A}{\pi} \tag{4}$$

where *A* is the smallest cross-sectional area of the sample passing through contact points of conical heads. Corrected point loading strength is calculated by Equations (5) and (6).

$$F = \left(\frac{De}{50}\right)^{0.45} \tag{5}$$

$$Is_{(50)} = F \times Is \tag{6}$$

where $Is_{(50)}$ is corrected point load strength (MPa) and *F* is correction factor.

3. Results and Discussion

The XRF results of the samples used in the experimental study are given in Table 2, and the XRD results are given in Figure 4. While the main minerals of the AO sample are limestone and dolomite, other samples contain limestone. Since all samples are resistant to 800 °C, measurements could not be taken at higher temperatures. As a result of each temperature, water absorption, porosity, Schmidt hammer hardness and point load strength were recorded for each natural stone. These values of the samples obtained at different temperatures are given in Table 3. The percentage change in temperature-related physico-mechanical properties is given in Table 4. As can be clearly seen in Table 4, as the temperature value increased, it led to an increase in the water absorption and porosity

and also a decrease in the Schmidt hammer hardness and point load strength of all natural stones. These changes vary among natural stones; for this reason, each experimental parameter was considered separately.

Table 2. Results of XRF analysis of samples.

Sample	HB (%)	PB (%)	AB (%)	HO (%)	AO (%)
Fe_2O_3	0.06	0.06	0.15	2.45	1.66
MgO	0.45	0.42	0.30	0.69	14.48
Al_2O_3	0.04	0.04	0.08	<0.01	<0.01
SiO_2	<0.01	<0.01	<0.01	<0.01	<0.01
P_2O_5	<0.01	<0.01	0.01	0.06	0.07
K_2O	<0.01	<0.01	<0.01	0.01	0.01
CaO	54.14	53.15	53.70	52.16	38.82
TiO_2	<0.01	<0.01	0.01	<0.01	<0.01
MnO	<0.01	<0.01	<0.01	0.29	0.35
ZnO	<0.01	<0.01	<0.01	<0.01	<0.01
SrO	0.02	0.02	0.01	<0.01	<0.01
PbO	<0.01	<0.01	<0.01	<0.01	<0.01
Na_2O	2.20	2.18	2.01	0.08	0.12
LOI	43.08	44.12	43.73	44.25	44.48

(LOI: Loss on ignition).

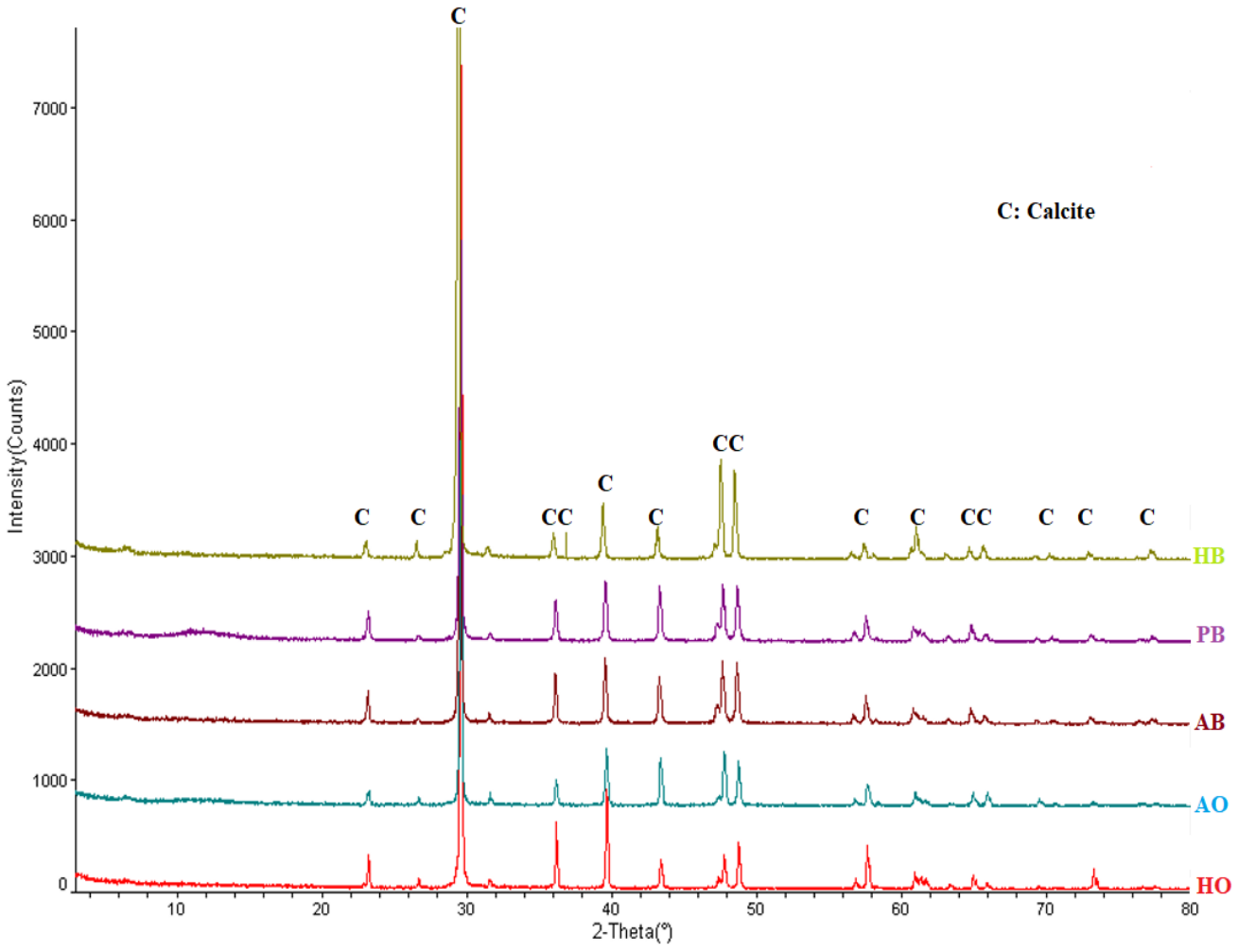

Figure 4. XRD chart of natural stones.

Table 3. Average results of physico-mechanical properties at different temperatures.

Test	Code	23 °C	200 °C	400 °C	600 °C	800 °C
Water Absorption (%)	HB	0.162 ± 0.031	0.164 ± 0.034	0.587 ± 0.053	1.008 ± 0.088	4.862 ± 0.245
	PM	0.158 ± 0.030	0.161 ± 0.037	0.787 ± 0.062	1.321 ± 0.101	5.142 ± 0.271
	AB	0.151 ± 0.032	0.155 ± 0.040	0.889 ± 0.069	1.719 ± 0.124	6.541 ± 0.432
	HO	0.202 ± 0.048	0.210 ± 0.044	0.907 ± 0.078	2.388 ± 0.142	9.643 ± 0.678
	AO	0.221 ± 0.042	0.229 ± 0.042	0.972 ± 0.101	2.524 ± 0.159	10.862 ± 0.702
Porosity (%)	HB	0.466 ± 0.058	0.472 ± 0.054	1.702 ± 0.122	2.993 ± 0.171	13.965 ± 0.897
	PM	0.422 ± 0.050	0.451 ± 0.051	2.423 ± 0.154	3.976 ± 0.192	15.785 ± 0.991
	AB	0.423 ± 0.048	0.433 ± 0.049	2.777 ± 0.158	5.570 ± 0.298	20.221 ± 1.131
	HO	0.589 ± 0.062	0.601 ± 0.060	2.884 ± 0.170	7.593 ± 0.542	24.294 ± 1.211
	AO	0.652 ± 0.060	0.672 ± 0.062	3.120 ± 0.181	8.134 ± 0.612	25.784 ± 1.227
Schmidt Hammer Hardness	HB	45.4 ± 0.6	45.3 ± 0.7	44.2 ± 0.7	40.4 ± 0.6	20.6 ± 0.4
	PM	44.8 ± 0.5	44.6 ± 0.6	43.0 ± 0.7	39.2 ± 0.7	19.2 ± 0.4
	AB	43.1 ± 0.5	43.0 ± 0.6	42.1 ± 0.6	36.2 ± 0.4	18.5 ± 0.3
	HO	38.4 ± 0.4	38.3 ± 0.4	37.4 ± 0.5	32.9 ± 0.5	13.8 ± 0.3
	AO	37.1 ± 0.5	37.0 ± 0.4	35.9 ± 0.6	29.8 ± 0.4	11.4 ± 0.2
Point Load Strength (MPa)	HB	7.67 ± 0.89	7.64 ± 0.63	7.01 ± 0.56	4.61 ± 0.37	2.24 ± 0.11
	PM	7.58 ± 0.33	7.53 ± 0.46	6.82 ± 0.48	4.02 ± 0.34	1.18 ± 0.12
	AB	5.89 ± 0.17	5.87 ± 0.47	4.91 ± 0.36	3.58 ± 0.29	1.42 ± 0.14
	HO	5.49 ± 0.32	5.44 ± 0.36	4.51 ± 0.32	3.18 ± 0.26	1.04 ± 0.19
	AO	5.21 ± 0.46	5.20 ± 0.41	5.06 ± 0.44	3.02 ± 0.14	0.82 ± 0.11

Table 4. The percentage change in temperature-related physico-mechanical properties.

Test	Heat (°C)	HB (%)	PB (%)	AB (%)	HO (%)	AO (%)
Water Absorption	200	+0.002	+0.003	+0.004	+0.008	+0.008
	400	+0.425	+0.629	+0.738	+0.705	+0.751
	600	+0.846	+1.163	+1.568	+2.186	+2.303
	800	+4.700	+4.984	+6.390	+9.441	+10.641
Porosity	200	+0.006	+0.029	+0.010	+0.012	+0.020
	400	+1.236	+2.001	+2.354	+2.295	+2.468
	600	+2.527	+3.554	+5.147	+7.004	+7.482
	800	+13.499	+15.363	+19.798	+23.705	+25.132
Schmidt Hammer Hardness	200	−0.220	−0.446	−0.232	−0.260	−0.270
	400	−2.643	−4.018	−2.320	−2.604	−3.235
	600	−11.013	−12.500	−16.009	−14.323	−19.677
	800	−54.626	−57.143	−57.077	−64.063	−69.272
Point Load Strength	200	−0.391	−0.660	−0.340	−0.911	−0.192
	400	−8.605	−10.026	−16.638	−17.851	−2.879
	600	−39.896	−46.966	−39.219	−42.077	−42.035
	800	−70.795	−84.433	−75.891	−81.056	−84.261

(+: Increase; −: Decrease).

Many researchers have determined that there is a strong relationship between water absorption and porosity [37,38]. This strong relationship is clearly seen in this study as well. Changes in porosity and water absorption values of natural stones due to high temperatures are parallel to each other. The result of water absorption values measured from samples exposed gradually to high temperatures from room temperature up to 800 °C is given in Figure 5. When Figure 5 is analyzed, it is seen that water absorption values of samples up to 400 °C do not change significantly with temperature. However, it is seen that all samples are highly affected when this temperature value increases gradually. A similar situation was discussed by Ferrero and Marini (2001) in their study on how high temperatures affect physical properties of rocks [39].

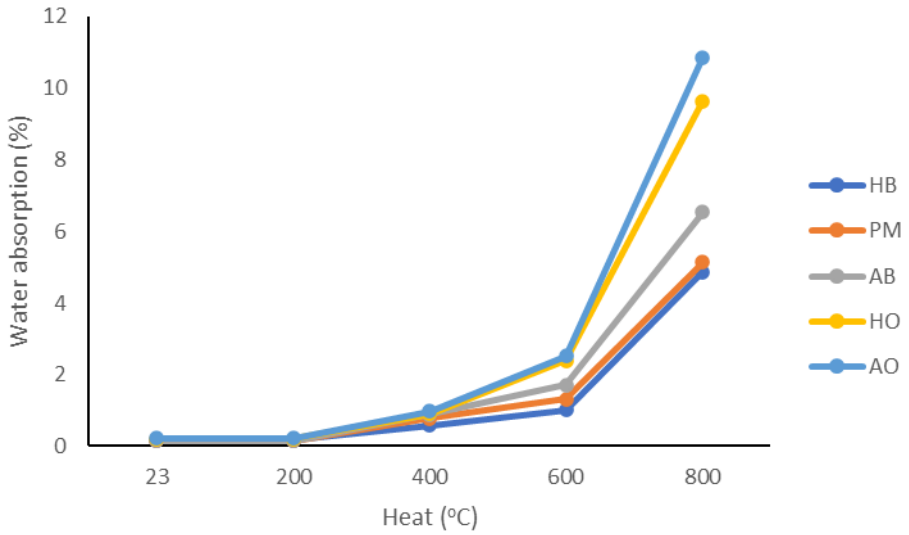

Figure 5. Water absorption change related to temperature.

There is generally an inverse relationship between the porosity and strength of natural stones. In other words, as the porosity of natural stones increases, its strength decreases. However, it is known that pore shape, pore size and spatial distribution are also important. Pores may occur at grain boundaries and within the grain of natural stones [40]. Therefore, a comprehensive pore study can be useful to determine how natural stones are affected by exposure to bad environmental conditions (freeze–thaw, high temperature, wetting–drying, salt crystallization, etc.). Porosity values of the samples subjected gradually to high temperatures, from room temperature (23 °C) to 800 °C, are given in Figure 6. As can be clearly seen in Figure 6, each gradual increase in temperature increased the porosity of the natural stones. It is seen that the porosity increase in onyx is higher than in limestone. As the temperature increases, the porosity of the HB sample is lower than other natural stones. In all natural stones, porosity increases suddenly at temperatures above 400 °C. Especially after this temperature, the porosity of the HO and AO samples increases dramatically. Many researchers state that there is a linear relationship between porosity and temperature, and the higher the temperature, the greater the porosity. The increase in porosity is more obvious at temperatures of 400 °C and above [41–43]. Gomez-Heras et al. (2006) reveal that the porosity of certain rocks increases due to an increase in temperature. Similar results were obtained in this study [44].

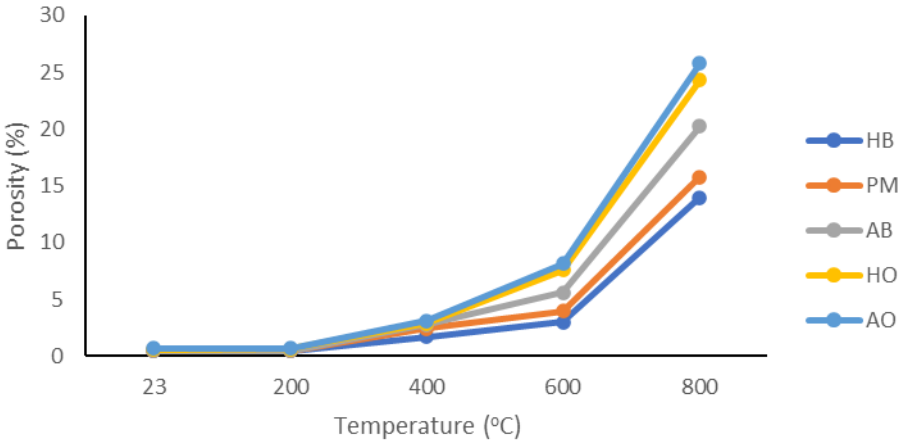

Figure 6. Porosity changes related to temperature.

Schmidt hammer hardness is a very important parameter in the investigation of high temperature effects on natural stones, since it is a non-destructive test and is used to predict

the mechanical strength of rocks. In this study, it contributes to the evaluation of the mechanical strength of natural stone as a result of a possible fire (high temperature) using a non-destructive testing method of Schmidt hardness hammer. Schmidt hammer hardness values of samples subjected to high temperatures, from room temperature (23 °C) to 800 °C, are given in Figure 7. It is clear that, as the temperature value increases, the Schmidt hammer hardness results are negatively affected. In particular, at the critical temperature of 600 °C, there were significant decreases in the Schmidt hammer hardness of all samples. At 800 °C, the biggest Schmidt hardness loss is in the HO and AO samples, with 64.1% and 69.3%, respectively, and the smallest loss is in HB sample, with 54.6%. The formation of new micro–macro cracks, fracture and distortion with the increase in temperature negatively affected the Schmidt hammer hardness values of rocks. Many researchers have obtained strong relationships between mechanical properties and Schmidt hammer hardness as a result of experimental and statistical studies [45–47]. In this case, when considering the strong relationship between Schmidt hammer hardness and mechanical properties (uniaxial compression, impact, bending strength, etc.), it is obvious that such a high loss cannot be ignored.

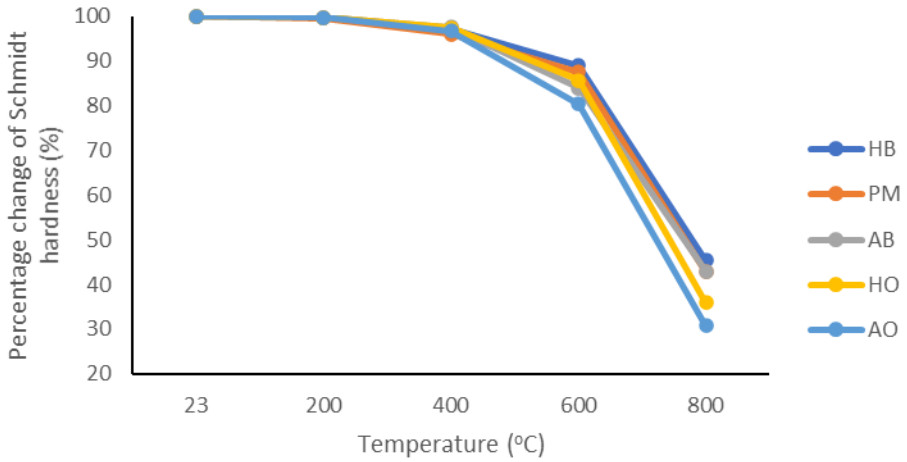

Figure 7. Schmidt hammer hardness change related to temperature.

The point load strength values of samples subjected to high temperatures, from room temperature (23 °C) to 800 °C, are given in Figure 8. As can be clearly seen in Figure 8, in limestone and onyx samples at temperatures above 400 °C, a remarkable decrease was observed in the strength of samples when compared with their initial point load strength at room temperature. This result is also related to the change in water absorption and porosity of the natural stones due to an increase in temperature. It is known that formation of new micro cracks and pores causes strength loss of natural stones. The increase in porosity makes natural stones less compact and consequently leads to loss of strength [48]. When Figure 8 is examined, it is seen that point load strength of all natural stones decreases due to an increase in porosity. In particular, it is clear that a high increase in the porosity of HO and AO samples significantly reduces their point load strength values. At 800 °C, the biggest point load strength loss is in PM and AO samples, with 84.4% and 84.2%, respectively, and the smallest loss is in the HB sample, with 70.8%. However, if it is necessary to make a general evaluation, it is seen that strength loss is over 70% in all samples. This shows that exposure of all natural stones used in this experimental study to such high temperatures may be inconvenient. The main reason for this is that elements and compounds in organic groups, such as C, H_2, N_2 and S_2, and inorganic groups, such as $CaCO_3$, $CaSO_4$ and Ca $(OH)_2$ undergo chemical changes during fires, causing the molecular structure of the material to deteriorate. In particular, this phenomenon can be encountered in some natural stone structures containing fossils. During the degradation of the molecular structure of the material, some harmful gases, such as CO_2, CO, SO_2 and SO_3, may occur; these gases

leave the body of the material and create chemical deformations. This change may differ according to the mineral components forming the natural stone [49–51]. Similar results were obtained in this study.

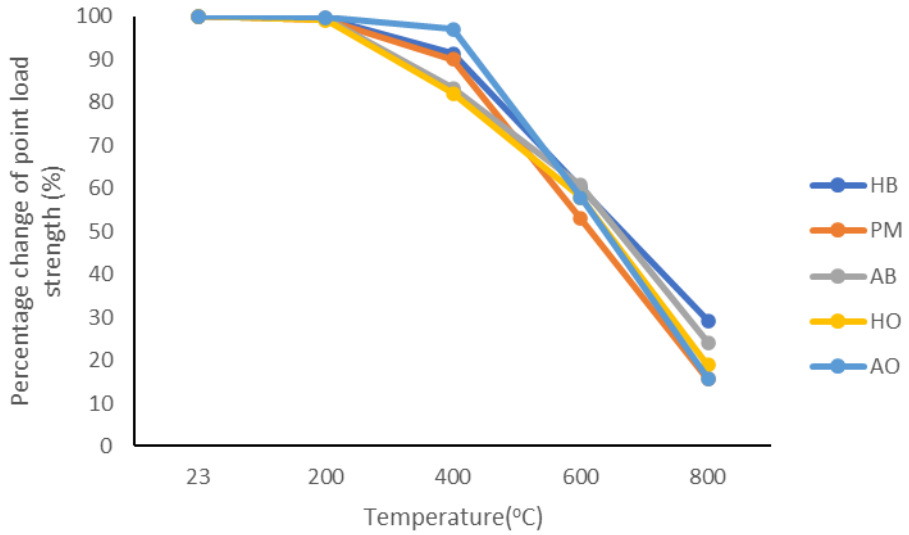

Figure 8. Point load strength values change related to temperature.

The average color and gloss values of the natural stones are given in Table 5. The color L*, a* and b* values on surfaces of the natural stone samples exposed to different temperatures are shown in Figure 9a–c. As can be seen in Figure 9a, while all samples darkened at 400 °C, the color of the samples became lighter with an increase in temperature. While the original surface whiteness value (L*) of the natural stones was 71.94–83.77, it was between 81.17–93.93 after the application of 800 °C. This situation may have increased the whiteness of the surface due to the decomposition of the sample at this temperature. Surface redness values (a*) of the samples after applying different temperatures are shown in Figure 9b. Except for HO and AO samples, other samples changed from red to green after 600 °C. The fact that the redness value (a*) approaches zero indicates that the surface of the sample is whitening. Although HO and AO samples do not change to green, their redness is reduced. It is thought that the fluctuation in the redness value of the HO sample may be due to Fe_2O_3 content. A similar situation is observed in the WO sample. However, the fluctuation is more in the HO sample with a high Fe_2O_3 content. As can be seen in Figure 9c, the surface yellowness value (b*) decreases significantly as a result of the high temperature applied to samples. The surface yellowness value of the HO sample was less affected than the others. The HM and PM samples changed from yellow to blue after the application of 800 °C. Gloss values of the samples subjected gradually to high temperatures, from room temperature (23 °C) to 800 °C, are given in Figure 9d. When gloss values were examined, it was observed that the gloss of the natural stone samples varied between 98.4–55.6 GU. While the highest brightness value was obtained from the HO sample (98.4 GU), this sample was followed by PM (74.6 GU), HB (74.1 GU), AO (56.4 GU) and AB (55.6 GU), respectively (Table 5). It was observed that gloss values changed slightly (6.5–23.9%) at temperatures up to 400 °C, and increased rapidly (55.4–84.5%) at 800 °C. The reason for this change is that the surfaces of natural stones are warmed up quickly and expand in volume due to the high temperature. As a result, the surface tension of the samples increases and creates micro or macro cracks on their surfaces. The visual appearance of color changes occurring on natural stone surfaces at different temperatures is given in Figure 10.

Table 5. Average of color and gloss values at different temperatures.

Code	L*, a*, b*, GU	23 °C	200 °C	400 °C	600 °C	800 °C
HB	L	74.09	72.87	69.67	70.15	88.11
	a	3.89	3.94	4.20	2.75	−2.01
	b	10.12	10.41	9.81	5.67	−4.15
	GU	74.1	73.2	68.2	60.3	26.3
PM	L	79.15	77.58	57.25	63.87	84.77
	a	3.77	4.07	3.13	3.10	−1.38
	b	12.32	12.28	8.08	6.07	−2.25
	GU	94.6	91.8	88.5	75.3	26.0
AB	L	72.54	71.22	55.42	61.72	81.17
	a	6.91	6.46	4.64	4.28	−0.75
	b	17.01	16.95	8.01	7.83	1.06
	GU	55.6	51.8	48.3	43.9	24.8
HO	L	71.94	73.51	69.86	79.77	92.98
	a	3.05	2.41	4.02	1.62	2.31
	b	8.02	11.8	11.8	4.66	5.38
	GU	98.4	95.8	91.1	52.4	15.3
AO	L	83.77	86.85	81.53	87.45	98.93
	a	1.28	1.15	1.59	1.33	0.69
	b	3.86	5.04	6.47	3.29	−0.48
	GU	56.4	45.9	42.9	22.3	12.1

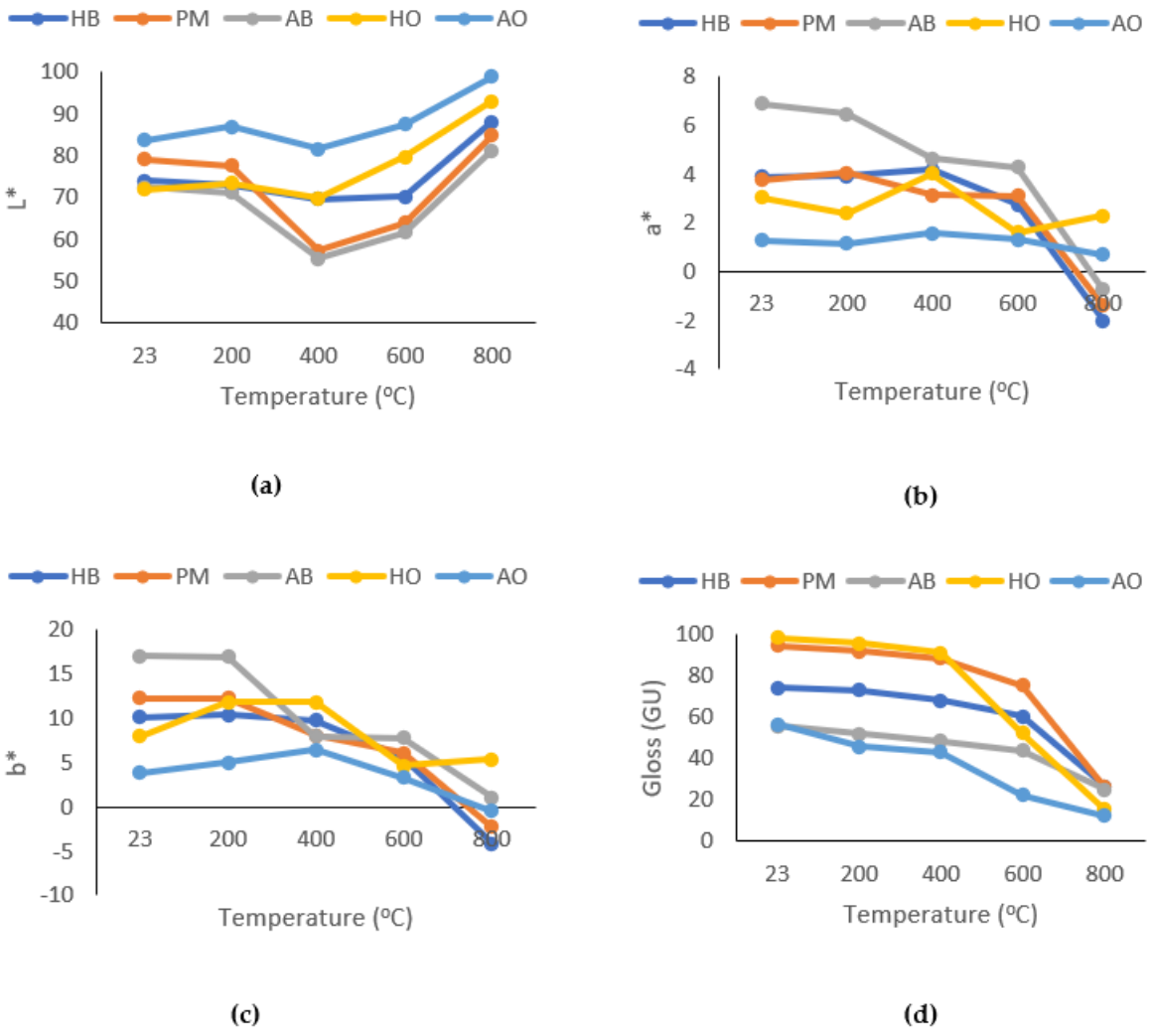

Figure 9. The color and gloss values of samples.

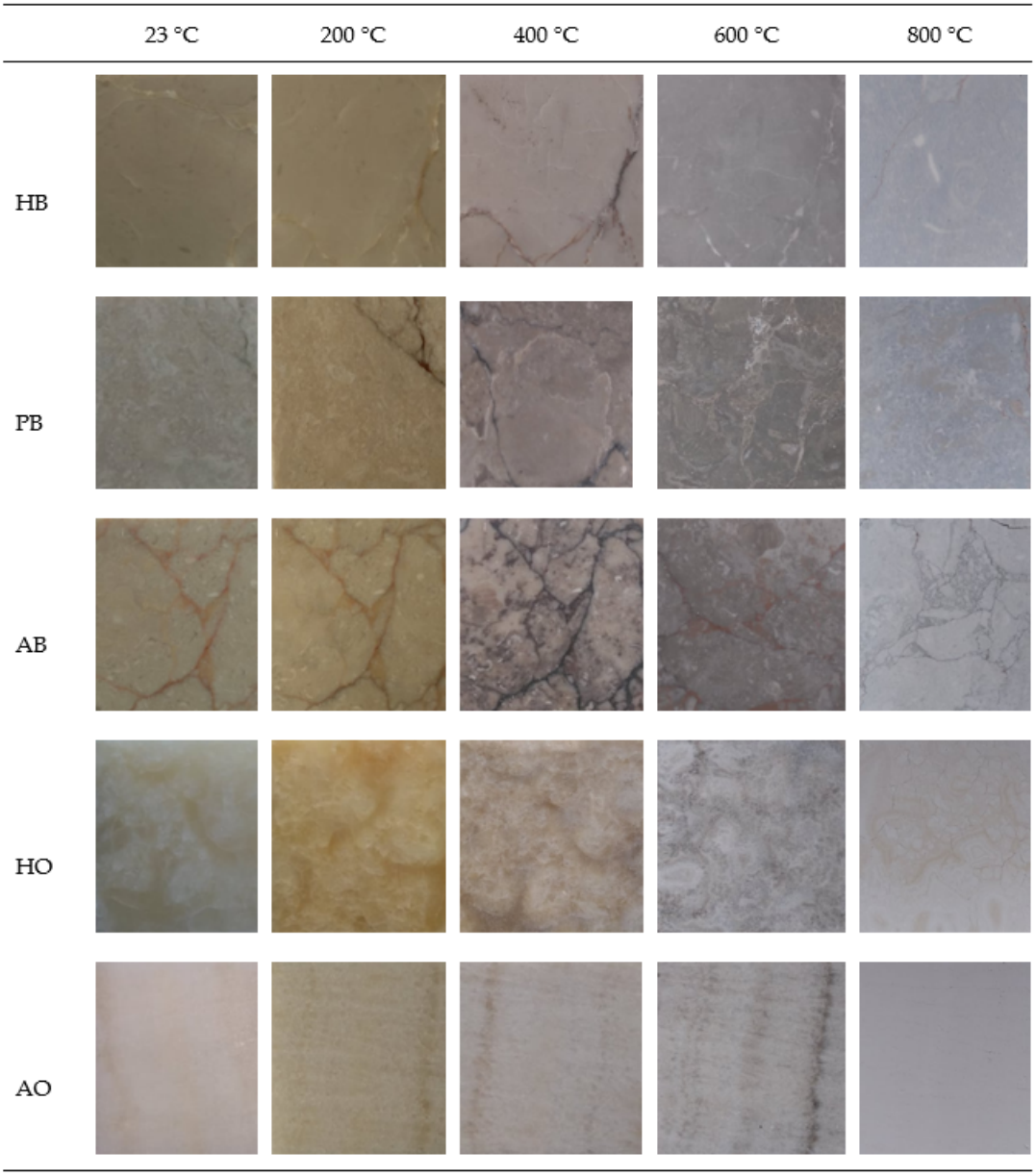

Figure 10. Visual appearance of color changes.

It is important for restoration studies to consider the color changes while examining the changes in properties of natural stones exposed to fire. In fact, color changes are a clue to determine what temperature building blocks are exposed to during fire. This study shows that there is a color change on the surfaces of natural stones at different temperatures. Color changes of natural stones exposed to different temperatures are given in Figure 10. When the sample surfaces are examined, it is seen that it darkens up to 400 °C, which is the turning point. However, it is seen that the white color dominates, depending on the temperature increase after 400 °C. The color change was mostly seen in the HO and AO samples.

4. Conclusions

In this study, five different light-colored natural stone samples (limestone and onyx) were exposed to different temperatures (from room temperature to 800 °C) and some physico-mechanical properties (water absorption, porosity, Schmidt hammer hardness and

point load strength) and color and gloss values were determined. The following results were obtained.

Although the highest temperature used in the study was chosen as 1000 ºC, all samples were broken down at this temperature. Therefore, measurements could not be taken at this temperature.

The physico-mechanical properties of samples exposed to temperatures up to 400 °C were not affected much. This temperature value can also be called the mutation point.

After 400 °C, sudden increases in water absorption and porosity values of all samples were determined. Especially after this temperature, water absorption and porosity of HO and AO samples increase dramatically. This situation is caused by newly formed capillary cracks due to the increasing temperature.

For Schmidt hammer hardness, the critical temperature was determined to be 600 °C. After this temperature, there is a dramatic decrease in hardness values of all samples. In particular, an almost 64–69% decrease was determined in the Schmidt hardness values of onyx samples.

As the temperature value increased, porosity and water absorption values of the samples increased. Therefore, the point load strength of the samples was affected negatively. In particular, point load strength values of samples at 600 °C and above dramatically decrease. In fact, the LOI from the XRF analysis supports these results.

In general, all samples darkened at 400 °C, while the whiteness value (L*) of samples increased at the 800 °C. The highest whiteness value was obtained at 1000 °C. However, measurements were not taken because other physico-mechanical properties could not be determined.

At exposure to 800 °C, the surface gloss of HO was greatly reduced (83 GU), while the BO sample was affected less (44 GU). However, when evaluated as a percentage, the surface gloss loss of the PM and HB samples is less than other samples.

As temperatures increased, the surface redness value (a*) of all samples decreased at varying rates, and this value of the HO sample decreased to a minimal level compared to the others. It is thought that fluctuation in the redness value of the HO sample may be due to Fe_2O_3 content. A similar situation is observed in the WO sample. However, the fluctuation is greater in the HO sample with a high Fe_2O_3 content.

The biggest advantage of color determination is that it gives information about the temperature the natural stone is exposed to during fires.

As a result, natural stones used in many areas are required to maintain their durability, gloss and color for long periods. For this, not only physico-mechanical properties of natural stones, but also the most suitable usage areas should be recognized. Considering the results of this study, temperatures of 600 °C and above caused destructive damage for all samples. Therefore, a large amount of loss in physico-mechanical strength of the samples can damage the building structure and also increase the cost of restoration. In addition, fire is generally effective on all types of materials. However, determining the burning time and maximum temperature to which rock is exposed during a fire is very important in the restoration of structures. It is seen that strength loss of natural stones is insignificant up to 400 °C, but there is a darkening in surface color. In the restoration of a structure exposed to such a fire, it is useful to focus on surface polishing rather than strength.

Funding: This research received no external funding.

Institutional Review Board Statement: Not applicable.

Informed Consent Statement: Not applicable.

Data Availability Statement: Data presented in this research paper can be obtained from the corresponding author upon request.

Acknowledgments: I appreciate helpful suggestions from this journal's reviewers.

Conflicts of Interest: The author declares that there is no conflict of interest.

References

1. Celik, M.Y. Types and usage areas of the decorative natural building stones. *Sci. Min. J.* **2003**, *42*, 3–15. (In Turkish)
2. Karakaş, A.; Morali, G.; Coruk, Ö.; Bozkurtoğlu, E. Geomechanical, durability–hygrothermal and thermal shock properties of Kocaeli Kandira stone used as building stone in historical structures. *Environ. Earth Sci.* **2021**, *80*, 130. [CrossRef]
3. Mutlutürk, M.; Altindag, R.; Türk, G. A decay function model for the integrity loss of rock when subjected to recurrent cycles of freezing-thawing and heating-cooling. *Int. J. Rock Mech. Min. Sci.* **2004**, *41*, 237–244. [CrossRef]
4. Yavuz, H. Effect of freeze–thaw and thermal shock weathering on the physical and mechanical properties of an andesite stone. *Bull. Eng. Geol. Environ.* **2011**, *70*, 187–192. [CrossRef]
5. Fener, M.; Ince, I. Effects of the freeze–thaw (F-T) cycle on the andesitic rocks (Sille-Konya/Turkey) used in construction building. *J. African Earth Sci.* **2015**, *109*, 96–106. [CrossRef]
6. Ghobadi, M.H.; Babazadeh, R. Experimental studies on the effects of cyclic freezing-thawing, salt crystallization, and thermal shock on the physical and mechanical characteristics of selected sandstones. *Rock Mech. Rock Eng.* **2015**, *48*, 1001–1016. [CrossRef]
7. Gökçe, M.V.; İnce, İ.; Fener, M.; Taşkıran, T.; Kayabali, K. The effects of freeze–thaw (F-T) cycles on the Gödene travertine used in historical structures in Konya (Turkey). *Cold Reg. Sci. Tech.* **2016**, *127*, 65–75. [CrossRef]
8. Bozdağ, A.; Bayram, A.F.; İnce, İ.; Asan, K. The relationship between weathering and welding degree of pyroclastic rocks in the Kilistra ancient city, Konya (Central Anatolia, Turkey). *J. African Earth Sci.* **2016**, *123*, 1–9. [CrossRef]
9. Heidari, M.; Torabi-Kaveh, M.; Mohseni, H. Assessment of the effects of freeze–thaw and salt crystallization ageing tests on Anahita Temple Stone, Kangavar, West of Iran. *Geotech. Geol. Eng.* **2017**, *35*, 121–136. [CrossRef]
10. Özşen, H.; Bozdağ, A.; İnce, İ. Effect of salt crystallization on weathering of pyroclastic rocks from Cappadocia, Turkey. *Arab. J. Geosci.* **2017**, *10*, 258. [CrossRef]
11. Deng, H.; Yu, S.; Deng, J. Damage characteristics of sandstone subjected to coupled effect of freezing-thawing cycles and acid environment. *Adv. Civ. Eng.* **2018**, *2018*, 3560780. [CrossRef]
12. Sun, Q.; Zhang, Y. Combined effects of salt, cyclic wetting and drying cycles on the physical and mechanical properties of sandstone. *Eng. Geol.* **2019**, *248*, 70–79. [CrossRef]
13. Amirkiyaei, V.; Ghasemi, E.; Faramarzi, L. Determination of P-wave velocity of carbonate building stones during freeze–thaw cycles. Geotech. *Geol. Eng.* **2020**, *38*, 5999–6009.
14. Guler, S.; Türkmenoğlu, Z.F.; Varol, O.O. Thermal shock and freeze–thaw resistance of different types of carbonate rocks. *Int. J. Rock Mech. Min. Sci.* **2021**, *137*, 104545. [CrossRef]
15. Mardoukhi, A.; Mardoukhi, Y.; Hokka, M.; Kuokkala, V.T. Effects of test temperature and low temperature thermal cycling on the dynamic tensile strength of granitic rocks. *Rock Mech. Rock Eng.* **2021**, *54*, 443–454. [CrossRef]
16. Goudie, A.S.; Allison, R.J.; McLaren, S.J. The relations between modulus of elasticity and temperature in the context of the experimental simulation of rock weathering by fire. *Earth Surf. Proc. Landf.* **1992**, *17*, 605–615. [CrossRef]
17. Allison, R.J.; Bristow, G.E. The effects of fire on rock weathering: Some further considerations of laboratory experimental simulation. *Earth Surf. Proc. Landf.* **1999**, *24*, 707–713. [CrossRef]
18. Chakrabarti, B.; Yates, T.; Lewry, A. Effect of fire damage on natural stonework in buildings. *Constr. Build. Mater.* **1996**, *10*, 539–544. [CrossRef]
19. Sippel, J.; Siegesmund, S.; Weiss, T.; Nitsch, K.H.; Korzen, M. Decay of natural stones caused by fire damage. *Geol. Soc. Lond. Spec. Publ.* **2007**, *271*, 139–151. [CrossRef]
20. Hajpál, M.; Török, Á. Mineralogical and colour changes of quartz sandstones by heat. *Environ. Geol.* **2004**, *46*, 311–322. [CrossRef]
21. Gillhuber, S.; Lehrberger, G.; Goske, J. Fire damage of trachyte: Investigations of the Tepla monastery building stones. *Geol. Soc. Lond. Spec. Publ.* **2010**, *333*, 73–79. [CrossRef]
22. Hajpál, M. Changes in sandstones of historical monuments exposed to fire or high temperature. *Fire Technol.* **2002**, *38*, 373–382. [CrossRef]
23. Tian, H.; Ziegler, M.; Kempka, T. Physical and mechanical behavior of claystone exposed to temperatures up to 1000 °C. *Int. J. Rock Mech. Min. Sci.* **2014**, *70*, 144–153. [CrossRef]
24. Ozguven, A.; Ozcelik, Y. Effects of high temperature on physico-mechanical properties of Turkish natural building stones. *Eng. Geol.* **2014**, *183*, 127–136. [CrossRef]
25. *TS EN 13755*; Natural Stone Test Methods—Determination of Water Absorption at Atmospheric Pressure. Turkish Standardization Institute: Ankara, Turkey, 2009. (In Turkish)
26. *TS EN 1936*; Natural Stone Test Methods—Determination of Real Density and Apparent Density and of Total and Open Porosity. Turkish Standardization Institute: Ankara, Turkey, 2010. (In Turkish)
27. Wang, M.; Wan, W. A new empirical formula for evaluating uniaxial compressive strength using the Schmidt hammer test. *Int. J. Rock Mech. Min. Sci.* **2019**, *123*, 104094. [CrossRef]
28. Aydin, A. ISRM Suggested Method for Determination of the Schmidt Hammer Rebound Hardness: Revised Version. In *The ISRM Suggested Methods for Rock Characterization, Testing and Monitoring: 2007–2014*; Ulusay, R., Ed.; Springer: Cham, Switzerland, 2008. [CrossRef]
29. Sousa, L.M.O.; Gonçalves, B.M.M. Differences in the quality of polishing between sound and weathered granites. *Environ. Earth. Sci.* **2013**, *69*, 1347–1359. [CrossRef]

30. Kompaníková, Z.; Gomez-Heras, M.; Michňová, J.; Durmeková, T.; Vlčko, J. Sandstone alterations triggered by fire-related temperatures. *Environ. Earth Sci.* **2014**, *72*, 2569–2581. [CrossRef]
31. Sharma, P.K.; Singh, T.N. A correlation between P-wave velocity, impact strength index, slake durability index and uniaxial compressive strength. *Bull. Eng. Geol. Env.* **2008**, *67*, 17–22. [CrossRef]
32. Khandelwal, M.; Ranjith, P.G. Correlating index properties of rocks with P-wave measurements. *J. Appl. Geophys.* **2010**, *71*, 1–5. [CrossRef]
33. Ozdemir, E. A New Predictive Model for Uniaxial Compressive Strength of Rock Using Machine Learning Method: Artificial Intelligence-Based Age-Layered Population Structure Genetic Programming (ALPS-GP). *Arab. J. Sci. Eng.* **2022**, *47*, 629–639. [CrossRef]
34. ISRM. Suggested method for determining point load strength. *Int. J. Rock Mech. Min. Sci. Geomech. Abstr.* **1985**, *22*, 51–60. [CrossRef]
35. Jamshidi, A.A. Comparative Study of Point Load Index Test Procedures in Predicting the Uniaxial Compressive Strength of Sandstones. *Rock Mech. Rock Eng.* **2022**, *55*, 4507–4516. [CrossRef]
36. Garrido, M.E.; Petnga, F.B.; Martínez-Ibáñez, V.; Serón, J.B.; Hidalgo-Signes, C.; Tomás, R. Predicting the Uniaxial Compressive Strength of a Limestone Exposed to High Temperatures by Point Load and Leeb Rebound Hardness Testing. *Rock Mech. Rock Eng.* **2022**, *55*, 1–17. [CrossRef]
37. Yavuz, H.; Demirdag, S.; Caran, S. Thermal effect on the physical properties of carbonate rocks. *Int. J. Rock Mech. Min. Sci. Geomech. Abstr.* **2010**, *47*, 94–103. [CrossRef]
38. Wang, S.R.; Hagan, P.; Li, Y.C.; Zhang, C.G.; Liu, X.L. Experimental study on deformation and strength characteristics of sandstone with different water contents. *J. Eng. Sci. Tech. Rev.* **2017**, *10*, 199–203. [CrossRef]
39. Ferrero, A.M.; Marini, P. Experimental studies on the mechanical behaviour of two thermal cracked marbles. *Rock Mech. Rock Eng.* **2001**, *34*, 57–66. [CrossRef]
40. Malaga-Starzec, K.; Åkesson, U.; Lindqvist, J.E.; Schouenborg, B. Microscopic and macroscopic characterization of the porosity of marble as a function of temperature and impregnation. *Constr. Build. Mater.* **2006**, *20*, 939–947. [CrossRef]
41. Zhang, L.; Mao, X.; Lu, A. Experimental study on the mechanical properties of rocks at high temperature. *Sci. China Ser. E Tech. Sci.* **2009**, *52*, 641–646. [CrossRef]
42. Zhang, W.; Qian, H.; Sun, Q.; Chen, Y. Experimental study of the effect of high temperature on primary wave velocity and microstructure of limestone. *Environ. Earth Sci.* **2015**, *74*, 5739–5748. [CrossRef]
43. Garrido, M.E.; Martínez-Ibáñez, V.; Hidalgo-Signes, C.; Company, J.; Tomás, R. Temperature threshold of sedimentary rocks: A comparative study. In Proceedings of the ISRM International Symposium Eurock 2020—Hard Rock Engineering Trondheim, Trondheim, Norway, 14–19 June 2020.
44. Gomez-Heras, M. *Procesos y Formas de Deterioro Térmico en Piedra Natural del Patrimonio Arquitectónico*; Editorial Complutense: Madrid, Spain, 2006.
45. Tondon, S.; Gupta, V. Estimation of strength from Schmidt hammer rebound, point load index and compressional wave velocity. *Bull. Eng. Geol. Environ.* **2014**, *74*, 521–533. [CrossRef]
46. Wang, M.; Wan, W.; Zhao, Y. Prediction of the uniaxial compressive strength of rocks from simple index tests using a random forest predictive model. *Comptes Rendus Mécanique* **2020**, *384*, 3–32. [CrossRef]
47. Sadeghi, E.; Nikudel, M.R.; Khamehchiyan, M.; Kavussi, A. Estimation of unconfined compressive strength (UCS) of carbonate rocks by index mechanical tests and specimen size properties: Central Alborz zone of Iran. *Rock Mech. Rock Eng.* **2022**, *55*, 125–145. [CrossRef]
48. Elhakim, A.F. The use of point load test for Dubai weak calcareous sandstones. *J Rock Mech. Geotech. Eng.* **2015**, *7*, 452–457. [CrossRef]
49. Gomez-Heras, M.; McCabe, S.; Smith, B.J.; Fort, R. Impacts of fire on stone-built heritage. *J. Archit. Conserv.* **2009**, *15*, 47–48. [CrossRef]
50. Ozguven, A.; Ozcelik, Y. Investigation of some property changes of natural building stones exposed to fire and high heat. *Constr. Build. Mater.* **2013**, *38*, 813–821. [CrossRef]
51. Vázquez, P.; Acuña, M.; Benavente, D.; Gibeaux, S.; Navarro, I.; Gomez-Heras, M. Evolution of surface properties of ornamental granitoids exposed to high temperatures. *Constr. Build. Mater.* **2016**, *104*, 263–275. [CrossRef]

sustainability

MDPI

Article

The Evaluation of Rock Mass Characteristics against Seepage for Sustainable Infrastructure Development

Muhammad Nasir Khurshid [1,*], Ammad Hassan Khan [1], Zia ur Rehman [1] and Tahir Sultan Chaudhary [2]

[1] Department of Transportation Engineering and Management (DTEM), University of Engineering and Technology (UET), G.T. Road, Lahore 54890, Pakistan
[2] Department of Civil Engineering, Bahauddin Zakariya University (BZU), Multan 60800, Pakistan
* Correspondence: 2019phdte03@student.uet.edu.pk

Abstract: The determination of rock seepage characteristics is a complex phenomenon due to the variability, discontinuities, and formation age of rocks. The available literature on rock mechanics covers empirical relationships and approaches for the estimation of seepage characteristics from the rock mass parameters. In this study, an area comprising of infrastructure such as a water reservoir, embankments, roads, etc., constructed on mix rock mass formations was selected. The field and laboratory tests' geo-mechanical data for the study area were evaluated. The data obtained from the field geo-mechanical engineering tests like Rock Quality Designation (RQD), Rock Core Recovery, Lugeon, etc., were analyzed. The data retrieved from the geological and geotechnical laboratory tests such as petrography, uniaxial compression, Hoek shear, elastic modulus, etc., were also evaluated. Rock mass was characterized based on petrographic and RQD, and was found in the hybrid formation of igneous, metamorphic, and sedimentary deposits. Seepage analysis in the study area was also carried out based on adit and piezometric data (installed in accordance with the mining technology guidelines), using Seep W Finite Element Method (FEM). The seepage observed in adits were compared with seepage calculated from Seep W. The trend of simulated flux was also presented against K ratio. Seepage quantities for different ranges of K ratio were plotted to evaluate interdependency between seepage and K ratio. Correlations of RQD were developed with hydraulic conductivity "k" for igneous, metamorphic, and sedimentary rocks for quick assessment of seepage characteristics of rock mass by RQD. These correlations and seepage related evaluations will be beneficial for the characterization of rock mass in relation to seepage for sustainable infrastructure development.

Keywords: rock mass; hydraulic conductivity; sustainability; rock mechanics; geotechnical engineering; geomechanical engineering; mining technology

Citation: Khurshid, M.N.; Khan, A.H.; Rehman, Z.u.; Chaudhary, T.S. The Evaluation of Rock Mass Characteristics against Seepage for Sustainable Infrastructure Development. *Sustainability* **2022**, *14*, 10109. https://doi.org/10.3390/su141610109

Academic Editors: Mahdi Hasanipanah, Danial Jahed Armaghani, Jian Zhou and Kaihui Li

Received: 28 April 2022
Accepted: 10 August 2022
Published: 15 August 2022

Publisher's Note: MDPI stays neutral with regard to jurisdictional claims in published maps and institutional affiliations.

Copyright: © 2022 by the authors. Licensee MDPI, Basel, Switzerland. This article is an open access article distributed under the terms and conditions of the Creative Commons Attribution (CC BY) license (https://creativecommons.org/licenses/by/4.0/).

1. Introduction

A large percentage of the earth surface is comprised of rocks. This makes rocks one of the significant areas of study for researchers. Rock is a basic unit of rock mass. Rock mass needs to be studied for resilient development leading to a sustainable environment, as the desired carbon emission is less during infrastructure developments [1]. Various researchers performed risk assessments for large infrastructure development projects using techniques ranging from conventional to hybrid nature to make them more sustainable [2]. The isotropic and anisotropy behavior of rock was studied by various researchers. The behavior of rock is different in an anisotropy condition as compared to normal isotropic conditions [3].

Rock mass is a collection of a rock body, which has distinct rock features like discontinuities, joints, and different planes of orientation. Types of rock mass are defined based on its classification systems. There are a number of rock mass classification systems with different relevant significance and uses. A few of them are Rock Quality Designation

(RQD), Barton Q system, and Rock Mass Rating (RMR). Among these, RQD is the most widely used rock classification system.

When a rock mass is in contact with water, the water tries to migrate into the pores of the rock mass and into the fractures. This penetration of water into the openings creates reduction in effective stress. This reduction in effective stress can reduce the strength and cause sliding of the water-affected mass. This water-affected mass, when holding material above it, leads to overall sliding of the inclined rock mass, causing slope failures. The cases of rock mass failures prone to seepage have been observed in different parts of the world in recent years. The ease with which fluid may travel through rock mass is termed seepage. The rock mass that allows a higher quantity of fluid to flow through it with more ease is more seepage prone compared to one that exhibits more resistance to the flow of fluid through it. The seepage of rock mass is governed by fractures. If the discontinuities are open and wide, the ease of the flow of fluid through rock mass will increase. The seepage can be estimated through the hydraulic conductivity of rock mass. The hydraulic conductivity is more often used in rock mass to represent the seepage. For determination of rock mass hydraulic conductivity in the field, the Lugeon test, also known as Water Pressure Test (WPT), can be used [4,5]. For determination of hydraulic conductivity in the field and in the laboratory, the Darcy (1856) relation can be used, as follows:

$$Q = AV = Aki \quad (1)$$

where "Q" is the rate of flow in m^3/sec, "A" is the cross-sectional area, "i" is the hydraulic gradient measured in the direction of flow, and k (m/sec) is the hydraulic conductivity.

Various researchers have determined patterns of hydraulic conductivity in rock mass fractures. They have proposed treatment methods for the rock mass fractures to make them more durable/sustainable against the effects of seepage. Hydraulic conductivity validation in rock mass fractures in mining technology has also been experimentally and numerically modeled by various researchers in the past [6–10]. Table 1 shows few noticeable correlations established between hydraulic conductivity and RQD.

Table 1. Summary of noticeable correlations available in literature between rock quality designation (RQD) and hydraulic conductivity.

Sr. No.	Equation	R^2	Rock Type	Data Type	Reference
1	$k = 177.45 \times e^{-0.0361 \times RQD}$	0.64	Sedimentary	Borehole data	[11]
2	$k = 890.9 \times e^{-0.0559 \times RQD}$	0.87		Field mapping data	
3	$k = 0.01382 - 0.0031 \ln RQD$	0.70		Borehole data	[12]

Where k is hydraulic conductivity and RQD is rock quality designation.

The rock mass internal and external factors deciding its mechanical behavior are key for its sustainable evaluation. Rock mass internal factors include pattern of discontinuities, strength/stiffness, fracture, behavior, friction factor, fracture distribution, etc. The effect of secondary constituents like clay filling and chemical changes causing variations in the rock mass discontinuities was studied by various researchers [5,13–22]. There are several external factors of rock mass such as location, geological formation, and type of infrastructure. Various infrastructures cause stress removal caused by excavation, fracture filing due to a water reservoir, fluid injection due to hydro-fracturing, and associated activities (oil and water), causing stress changes in rock fault, etc., which affect its behavior [8,10,23–28]. Literature reported the typical ranges of internal and external factors of rock mass. For evaluation of these factors, different destructive and nondestructive techniques can be employed [4,29–31]. Various simulation tools were also discussed in different studies for the prediction of rock mass internal and external factors. These simulation tools were employed to evaluate the response of external factors to interval properties of rock mass [6,7,9,32–41].

It is well established that for any infrastructure built on or in the rock mass, the seepage may affect its sustainability, including service life, working conditions, utility,

etc. [26–28,32,42]. The assessment of the hydraulic conductivity of rock mass allows the designers, constructors, and operators to forecast the response of rock mass against seepage behavior during sustainable evaluation of the infrastructure.

The effect of seepage can contribute, in a number of ways, to harming not only general ground conditions but also infrastructure facilities. Man-made activities such as blasting also affect the seepage in rock mass by causing destruction (opening of joints), affecting the steady state regime in comparison to pre-blast rock mass characteristics [25]. In addition to total failures, the problem of seepage poses threats to the stability of structures such that the cost of repairs becomes higher than original measures adopted at the time of design, as shown in Figure 1.

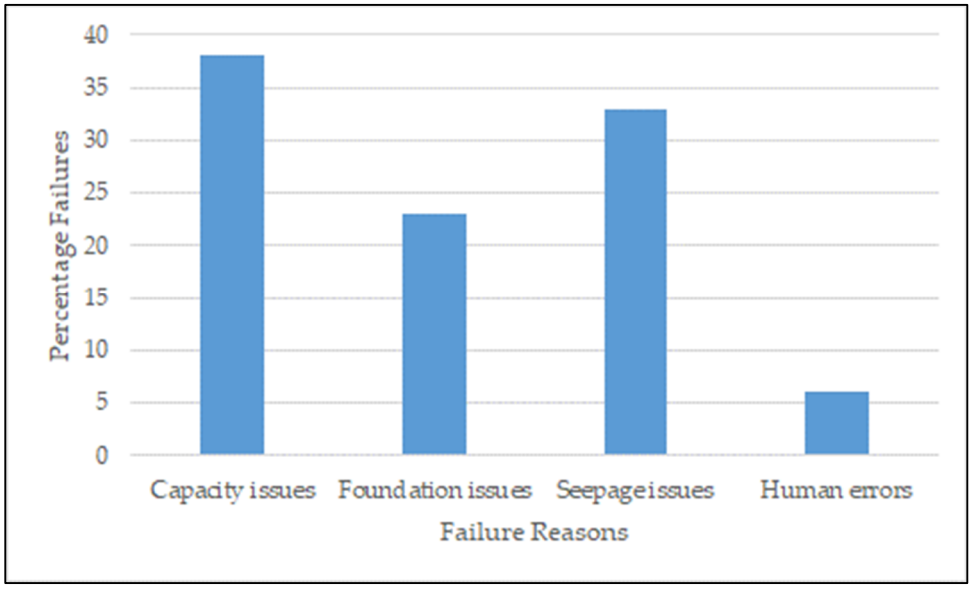

Figure 1. Summary of the seepage contribution in infrastructure failures constructed on rock mass.

Rock Quality Designation (RQD) is one the most quickly determinable rock mass parameters that can be evaluated with relative ease. Hence, in literature, an attempt was made by most of the researchers to correlate RQD with hydraulic conductivity. The correlations available for rock mass composite formations are quite limited in literature. This may be due to the rock mass' variations and its relatively non-homogenous behavior. The high cost of field and laboratory tests of rock mass is another significant factor.

An attempt was made in this study to identify rock mass formations surrounded by developed infrastructures and water front. Characterization of rock mass and its respective seepage response was planned to be determined from the geomechanical engineering database of the developed infrastructures by developing suitable correlations. The seepage and pressure head database from the adits and installed piezometers (in accordance with mining technologies) was also planned to be compared with actual seepage observed in the rock mass through Finite Element Model (FEM). The behavior of rock mass related to seepage was planned to be investigated by changing hydraulic conductivity, during preparation of model. The finite element methods (FEM) was used and both rock mass characteristics and hydraulic conductivity parameters, were varied in the FEM model. These variations in FEM models were carried out to observe the response of seepage due to change of rock mass characteristics. The FEM model results were validated with seepage results obtained from field instrumentations.

2. Materials and Methods

The following methodology was devised to achieve the objectives of the study:

- Extensive review of literature related to rock mass formation, distribution, and seepage characteristics in Pakistan and other countries. Different stakeholders involved in the infrastructure development projects on rock mass, such as the Geological Survey of Pakistan (GSP), Water and Power Development Authority of Pakistan [43], etc., were approached for guidance in study area selection and a collection of necessary geo-mechanical engineering data.
- Based on a review of literature and meetings with stakeholders, the study area was selected.
- A reconnaissance survey was carried out as per the guidelines of International Society of Rock Mechanics (ISRM) for study area profiling.
- Analysis of rock mass types, discontinuities/fault lines, etc., of the study area was carried out from the database of the Geological Survey of Pakistan.
- Field and laboratory tests (rock coring, Lugeon, uniaxial, triaxial, Hoek direct shear, point load index, etc.) and data (geological and geotechnical) obtained from WADPA were analyzed in accordance with relevant ASTM/ISRM standards.
- The rock types were classified based on the Rock Quality Designation (RQD) classification system and petrographic analysis. Determination of different rock mass properties including RQD, hydraulic conductivity, uniaxial compression strength, cohesion, friction angle, tensile strength, young's modulus, poison's ratio, specific gravity, void ratio, water absorption, seepage characteristics (hydraulic conductivity (K), anisotropy hydraulic conductivity (K ratio (Ky/Kx)), etc., were carried out.
- A seepage analysis model of the rock mass observed at the study area was also prepared using Seep W software. The input parameters, such as K, Ky/Kx, and boundary conditions were established for the model, keeping the nomenclature of the study area.
- In the study area, actual seepage data obtained from adits and piezometers were also compared with seepage characteristics (discharge and pressure head) obtained through Finite Element Model (FEM) Seep W model. Trends between seepage characteristics in rock mass were also plotted for assessment of the necessary seepage profile of the rock mass.
- Suitable correlations between RQD and hydraulic conductivity for observed rock mass were proposed.

The characterization of identified rock mass deposits in the study area and evaluation of their seepage behavior for utilization in possible future infrastructure developments of similar rock mass types was the most important objective of this study.

3. Results & Discussions

Various literature sources such as journals, books, conference proceedings, reports, etc., related to the topic under study were consulted. Nomenclature of rock mass formation was evaluated in detail. The information obtained from literature was discussed with the experts from the WAPDA and GSP. The stakeholders were briefed about the objectives of the study area selection; that the area should comprise rock mass formation along with existing infrastructures close to the waterfront.

The Himalayan mountain-system of South-Central Asia in the northwestern part of Pakistan was selected as the study area (Figure 2). The region is primarily comprised of composite rock mass types, i.e., igneous, sedimentary, and metamorphic. The geological distribution primarily observed was non-fossiliferous deposits and gabbroic (dolerite/diabase) intrusions (Precambrian to Permian age). The reconnaissance survey results also revealed that the rock mass formations were developed due to tectonic and extensive folding of the geological structure. The shearing and faulting patterns can be associated with Indian sub-continental crustal deformation that arose under thrust in the Indian sub-continental plate below the Eurasian plate.

Figure 2. Location plan of study area.

ISRM recommended to carry out rock mass profiling using visual inspection and photographic techniques. The same guidelines were adopted in this study. After selection of the study area, detailed site visits were carried out for necessary profiling of the study area through visual inspection, meetings with local stakeholders, and photographic records.

Figure 3 shows the distribution of existing infrastructures such as roads, embankments, waterfront, rock mass, etc., at the study area.

(**a**) (**b**)

Figure 3. Details of the study area during reconnaissance. (**a**) A view of rock mass with a road passing on the front. (**b**) Rock mass cut slopes facing the waterfront.

During reconnaissance, the stakeholders' representative at the study area jurisdiction were also contacted for historical database collection and seepage monitoring locations identification. Figure 4 shows location of a few of the existing instrumentation at the study area. The locations of field and laboratory tests points obtained from WAPDA database were also verified. The experiences of local stakeholders about the rock mass and its behavior in relation to the seepage was also brought on record.

(**a**) (**b**)

Figure 4. Study area details observed during reconnaissance. (**a**) View of an adit shown in cut slopes. (**b**) Piezometer installed.

Figure 5 shows that the study area comprises of composite rock mass types, i.e., igneous (quartzite), metamorphic (schist), and sedimentary (limestone, shale). The igneous rock observed was intrusive in nature and without bedding planes. These rocks usually were found less seepage-prone in response. The sedimentary and metamorphic rocks were found with more discontinuities and bedding planes resulting in more seepage-prone behavior. The orientation, location, and distribution of fault lines in rock mass may impact the critical seepage path to be used during FEM analysis. The seepage values determined from field instrumentation may also show inconsistency due to presence of faults in the rock mass. The seepage response against rock mass composite formation is a quite complex phenomenon. Very often during seepage analysis in such formations, the weakest rock type is modeled as a representative of the whole formation, which may not be the representative of actual field conditions. Correlations between rock formation and quantity of seepage are also not commonly available in literature.

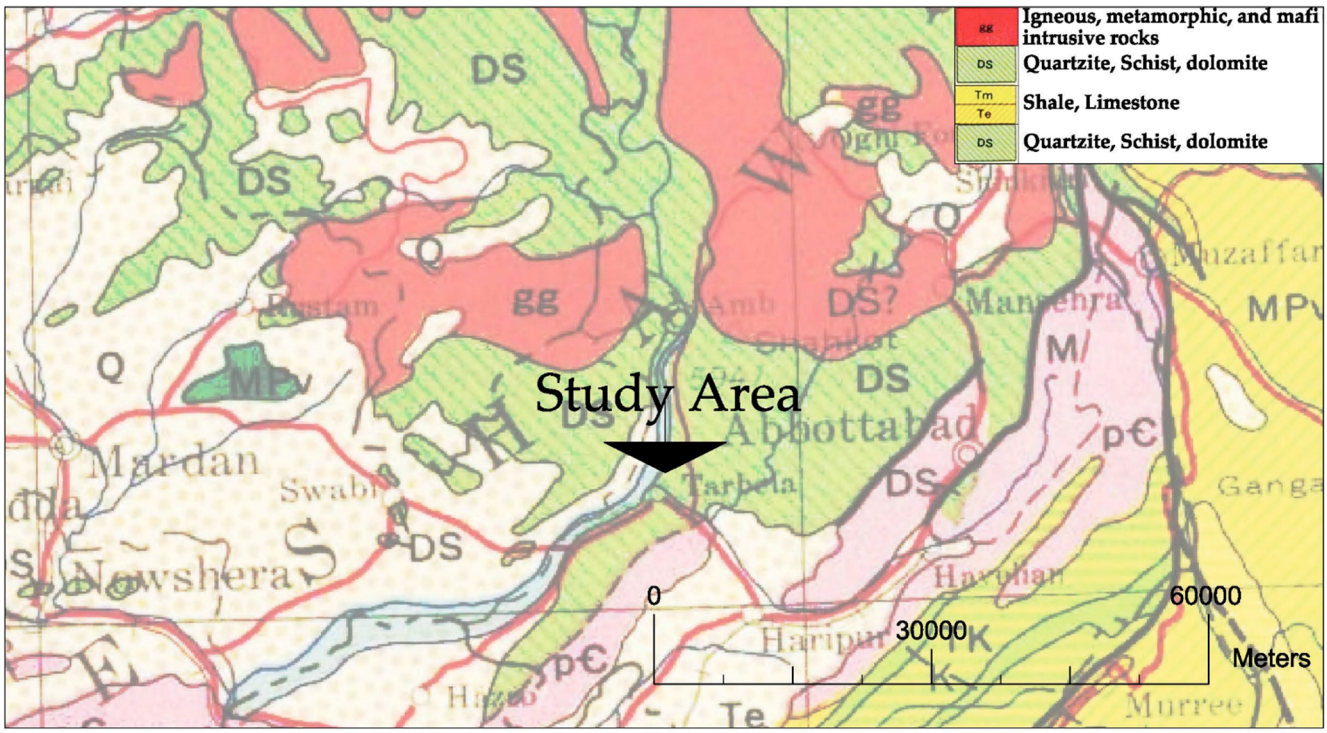

Figure 5. Geological map of the study area.

Details of field and laboratory explorations at the study area are summarized in Table 2, as received from WAPDA. The location of seventeen boreholes was also marked during reconnaissance, as shown in Figure 6. The data obtained from field and laboratory tests were analyzed and evaluated; the summary of which is presented afterwards. Boreholes were drilled in the rock mass formation by straight rotary drilling method using double tube core barrel of NQ/NX size. The maximum depth of a borehole was 120 m. The rock core samples were retrieved from the boreholes and preserved for laboratory testing at regular interval. Lugeon tests were performed in boreholes at regular intervals of 3 to 5 m depth. A total of 1234 RQD observations were made in the boreholes and a total of 161 Lugeon tests were performed in the boreholes. Thirteen boreholes were drilled vertically; two at an inclination of 30 degrees and two were drilled horizontally. The rock mass samples collected from each borehole were subjected to laboratory evaluation. The laboratory tests' matrix was planned in a way to record physical, strength, and elastic properties of the rock mass at different depths of borehole exploration. Some typical photographic records of the rock cores obtained from the boreholes are shown in Figure 7.

The summary of the typical range of core recovery (percentage), RQD, and Lugeon observed in different boreholes is presented in Table 3. The representative rock core samples obtained from the boreholes based on typical RQD range were subjected to petrographic analysis in the laboratory. Presented in Table 4 are the results of petrographic analysis. The results of petrographic analysis show that igneous formation with RQD 0–100 is comprised primarily of amphibole and plagioclase. Sedimentary formation with RQD 0–98 is comprised predominantly of calcite. Similarly, metamorphic formation with RQD 0–80 is comprised predominantly of quartz and muscovite/sericite. The results of RQD and petrographic analysis were used for primary and secondary rock classification, as shown in Table 3.

Figure 8 shows a typical subsurface profile of rock mass formation based on the analysis of boreholes and laboratory test data. The Natural Moisture Content (NMC) varies up to 0.4% for igneous, 3.34% for metamorphic, and 0.97% for sedimentary rocks. The unconfined compressive (UCS) strength values vary from 14 to 274 MPa for igneous, 14 to 153 MPa for metamorphic, and 43 to 105 MPa for sedimentary rocks. The UCS values observed in igneous, metamorphic, and sedimentary rock mass deposits are comparable with the UCS values reported in ISRM. The point load strength values changes from 1.84 to 15.58 MPa for igneous, 0.61 to 6.03 MPa for metamorphic, and 1.05 to 5.51 MPa for sedimentary rocks, respectively. The typical Brazilian tensile strength values range from 8.79 to 19.91 MPa for igneous, 7.58 to 11.06 MPa for metamorphic, and 7.29 to 22.02 MPa for sedimentary rock mass. The cohesion through Hoek direct shear test was found in a range of 0.01 to 0.53 MPa and 7.29 to 13.56 MPa; similarly, the friction angle from Hoek direct shear test ranges from 21.1 to 42.1 degree for igneous and 13.56 to 14.29 degree for sedimentary rocks. The values of Young's modulus vary from 17,400 to 301,000 MPa for igneous, 17,200 to 82,600 MPa for metamorphic, and 28,100 to 69,900 MPa for sedimentary rock mass. Table 5 shows the summary of typical range of geotechnical and geological engineering parameters in rock mass.

A seepage analysis model of the rock mass observed at the study area was also prepared using Seep W software. The input parameters such as K, Ky/Kx, and boundary conditions were established for the model, keeping the nomenclature of the laboratory and field test data of the study area.

To assess seepage characteristics of rock mass, a steady state seepage analysis was performed. A computer program, Seep W based on Finite Element Model (FEM), was used for analysis. The seepage analysis was carried out using a test cross section of the existing waterfront shown in Figure 9. The test cross-section was carefully prepared to include the existing instrumentation (adits and piezometers), with respect to their locations and elevations. The reservoir level at the upstream of this cross-section was at 472.5 m, while downstream it was at 341 m level.

Table 2. Details of geological and geotechnical exploration.

Borehole No.	Depth (m)	BH. Inclination Degree	RQD No.	Lugeon No.	Bulk Density	NMC * [44]	Water Absorption (%) [45]	Sp. Gravity [45]	UCS *** [46]	Point Load Strength [47]	Brazilian Tensile Strength [48]	Hoek Direct Shear [49]	Young's Modulus [46]	Poisson's ratio [46]
			Field Testing		Laboratory Testing									
BH-01	60	Vertical	61	5	✓	✓	✓	✓	✓	✓	✓	✓	✓	✓
BH-02	100	Vertical	20	3	✓	✓	✓	✓	✓	✓	✓	✓	✓	✓
BH-03	35	Vertical	77	14	✓	✓	✓	✓	✓	✓	✓	✓	✓	✓
BH-04	35	Vertical	116	18	✓	✓	✓	✓	✓	✓	✓	✓	✓	✓
BH-05	20	Vertical	62	12	✓	✓	✓	✓	✓	✓	✓	✓	✓	✓
BH-06	110	Vertical	49	6	✓	✓	✓	✓	✓	✓	✓	✓	✓	✓
BH-07	20	Vertical	29	3	✓	✓	✓	✓	✓	✓	✓	✓	✓	✓
BH-08	90	Vertical	82	12	✓	✓	✓	✓	✓	✓	✓	✓	✓	✓
BH-09	120	30°	117	15	✓	✓	✓	✓	✓	✓	✓	✓	✓	✓
BH-10	80	Vertical	156	9	✓	✓	✓	✓	✓	✓	✓	✓	✓	✓
BH-11	50	Hor. **	44	10	✓	✓	✓	✓	✓	✓	✓	✓	✓	✓
BH-12	50	Hor. **	62	3	✓	✓	✓	✓	✓	✓	✓	✓	✓	✓
BH-13	120	Vertical	14	1	✓	✓	✓	✓	✓	✓	✓	✓	✓	✓
BH-14	100	30°	0	1	✓	✓	✓	✓	✓	✓	✓	✓	✓	✓
BH-15	115	Vertical	90	13	✓	✓	✓	✓	✓	✓	✓	✓	✓	✓
BH-16	100	Vertical	106	18	✓	✓	✓	✓	✓	✓	✓	✓	✓	✓
BH-17	100	30°	149	18	✓	✓	✓	✓	✓	✓	✓	✓	✓	✓

* Natural Moisture Content, ** Horizontal, *** Uniaxial compressive strength.

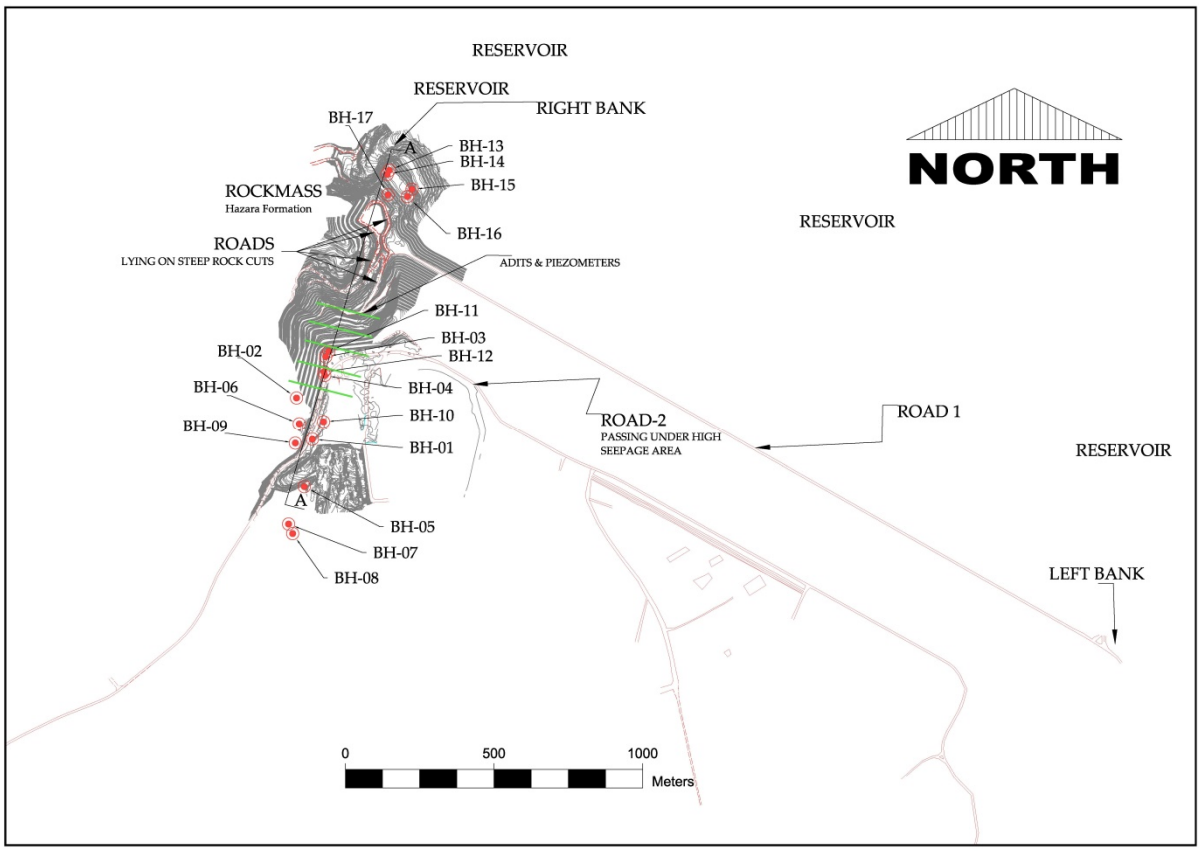

Figure 6. Details of the study area.

Seep W module uses the nodal mesh structure of elements, with defined material properties and boundary conditions, to evaluate the quantity of seepage through the rock mass. A 5 m mesh size was used in the model. Two-dimensional seepage flows through a rock mass in Seep W was calculated by following differential equation, which is a combination of Laplace and Darcy's law:

$$\frac{d}{dx}\left(Kx\frac{dH}{dx}\right) + \frac{d}{dy}\left(Ky\frac{dH}{dy}\right) + Q = \frac{d\theta}{dt} \quad (2)$$

where "H" is total head, "Kx" and "Ky" is the hydraulic conductivity in x and y direction, "Q" is the boundary flux defined, "θ" is the volumetric water content, and "t" is time.

The average values of the Lugeon test for sedimentary/metamorphic rock mass were evaluated and converted to respective hydraulic conductivity. The anisotropy property K Ratio (Ky/Kx) was varied in a range of 0.5 to 10 to see respective seepage and pressure head response in rock mass. The reason for K ratio variation was that the exact method to determine K ratio was not well established. The analysis was carried out keeping the rotation effect as zero, in steady state conditions with the function of pore water pressure inactive. The boundary conditions were modeled to simulate the field conditions of the study area (Figure 10). These field conditions include reservoir pressure head (water elevation) state conditions. These boundary conditions were modeled as pressure head in the form of total elevation head of water. The downstream boundary condition was kept as potential seepage face. The reason for keeping the downstream potential seepage face is to allow any flow of fluid, simulating actual field conditions. The instrumentation in the form of flow measuring adits and piezometers present at the study area was also modeled. The adits were modeled as circular region. The boundary condition for these regions for adits were defined as the elevation head, to simulate the fact that pressure will drop to the respective elevation level and any excess pressure will release in the form of seepage at

these locations. To measure the seepage quantity, flux sections were marked around these circular regions for adits. Similarly, the piezometers were modeled by adding points at the tip elevation of the mesh. These defined nodal points at the piezometer locations were used to get the results of total and pressure head.

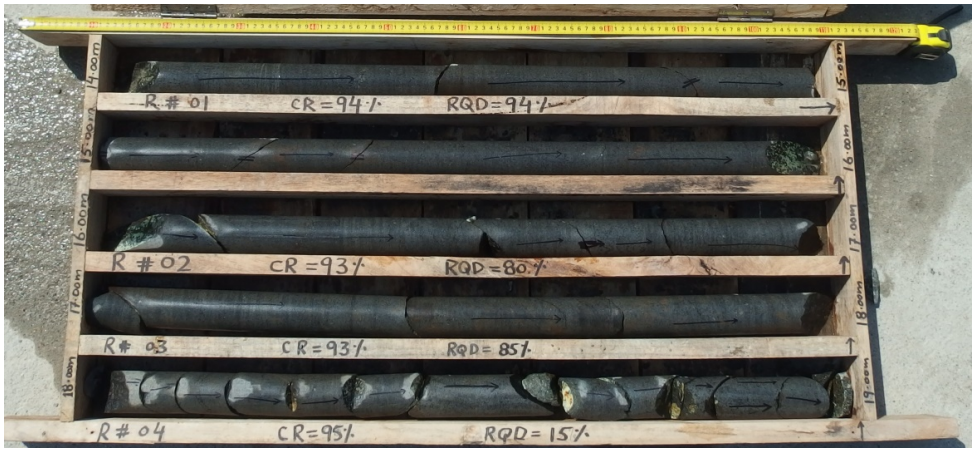

(**a**)

(**b**)

(**c**)

Figure 7. Typical rock core samples observed in (**a**) igneous rocks, (**b**) metamorphic rocks, (**c**) sedimentary rocks.

Table 3. Typical ranges of Core Recovery, RQD, and Lugeon values obtained in rock mass.

Bore Hole No.	Core Recovery (%)	RQD Values (%)	Lugeon Values	Primary Rock Type	Secondary Rock Type
BH-01	0–100	0–76	25–68	Metamorphic/Sedimentary	Schist/Limestone
BH-02	10–100	4–80	13–44	Metamorphic/Sedimentary	Schist/Limestone
BH-03	0–100	0–99	1–38	Metamorphic/Sedimentary	Schist/Limestone
BH-04	10–100	0–100	0.40–35	Metamorphic/Sedimentary	Schist/Limestone
BH-05	0–100	0–100	1–81	Metamorphic/Sedimentary	Schist/Limestone
BH-06	0–100	0–92	1–22	Metamorphic/Sedimentary	Schist/Limestone
BH-07	0–100	0–99	31–86	Metamorphic/Sedimentary	Schist/Limestone
BH-08	0–100	0–98	1–67	Metamorphic/Sedimentary	Schist/Limestone
BH-09	0–100	0–63	1–46	Metamorphic/Sedimentary	Schist/Limestone
BH-10	0–100	0–89	12–100	Metamorphic/Sedimentary	Schist/Limestone
BH-11	30–100	0–61.8	6–63	Metamorphic/Sedimentary	Schist/Limestone
BH-12	8–100	0–88	7–14	Metamorphic/Sedimentary	Schist/Limestone
BH-13	40–100	0–87	28–28	Igneous	Dolerite
BH-14	32–90	0–76	35–35	Igneous	Dolerite
BH-15	0–100	0–92	1–25	Igneous	Dolerite
BH-16	0–100	0–92	0.68–45	Igneous	Dolerite
BH-17	0–100	0–96	0.58–85	Igneous	Dolerite

Table 4. Petrographic test results.

Rock Type *	Typcial RQD %	Petrographic Results
Igneous	0–100	Amphibole 45.5%, Plagioclase 33.5%
Sedimentary	0–98	Predominantly Calcite Mineral
Metamorphic	0–80	Quartz 26.5%, Muscovite/Sericite 24%

* Visual observation.

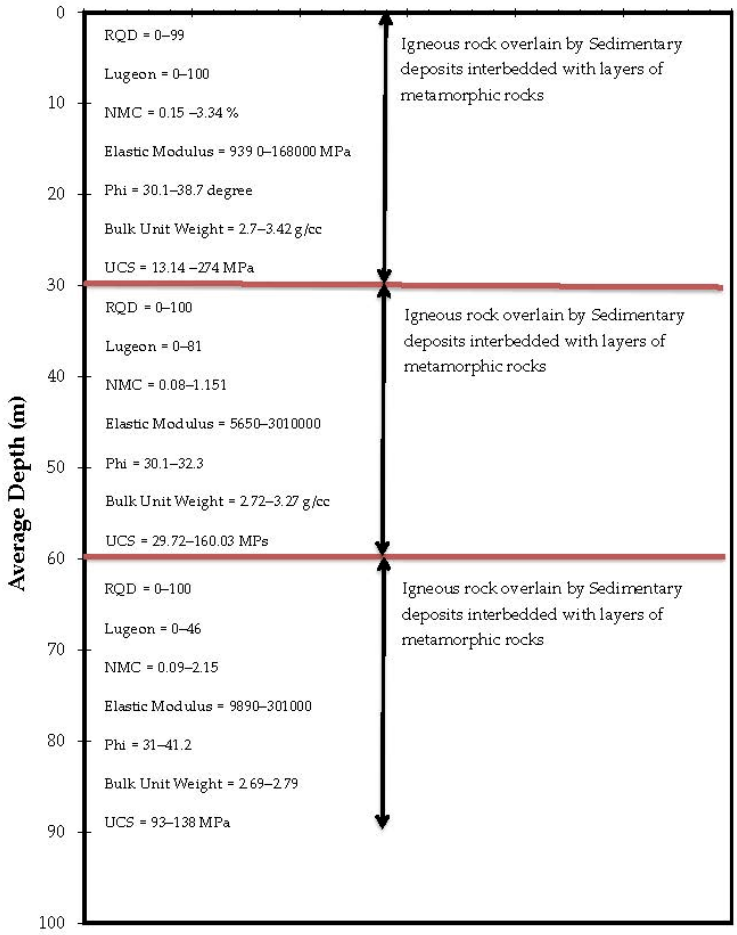

Figure 8. Typical subsurface profile of rock mass at the study area.

Table 5. Summary of geotechnical and geological engineering parameters' typical range obtained in rock mass.

Sr. No.	Test Parameters	Igneous	Metamorphic	Sedimentary
1	Bulk Density (gm/cm^3)	2.83–3.72	2.66–3.24	2.63–2.81
2	Natural Moisture Content (%)	0.08–0.40	0.15–3.34	0.22–0.97
3	Water Absorption (%)	0.06–0.60	0.52–1.19	0.29–1.45
4	Specific Gravity	2.86–3.78	2.69–3.30	2.71–2.85
5	Unconfined Compressive Strength (MPa)	14–274	14–153	43–105
6	Point Load Strength (MPa)	1.84–15.58	0.61–6.03	1.05–5.51
7	Brazilian Tensile Strength (MPa)	8.79–19.91	7.58–11.06	7.29–22.02
8	Hoek Direct Shear Test c (MPa)	0.01–0.53	-	7.29–13.56
9	Friction angle ϕ (deg)	21.1–42.1	-	14.29–13.56
10	Young's Modulus (MPa)	17,400–301,000	17,200–82,600	28,100–69,900
11	Poisson's Ratio	0.02–0.45	0.03–0.50	0.33–0.34
12	Hydraulic Conductivity (cm/sec)	0.4×10^{-4}–8.5×10^{-4}	0.8×10^{-4}	0.2×10^{-4}–10×10^{-4}

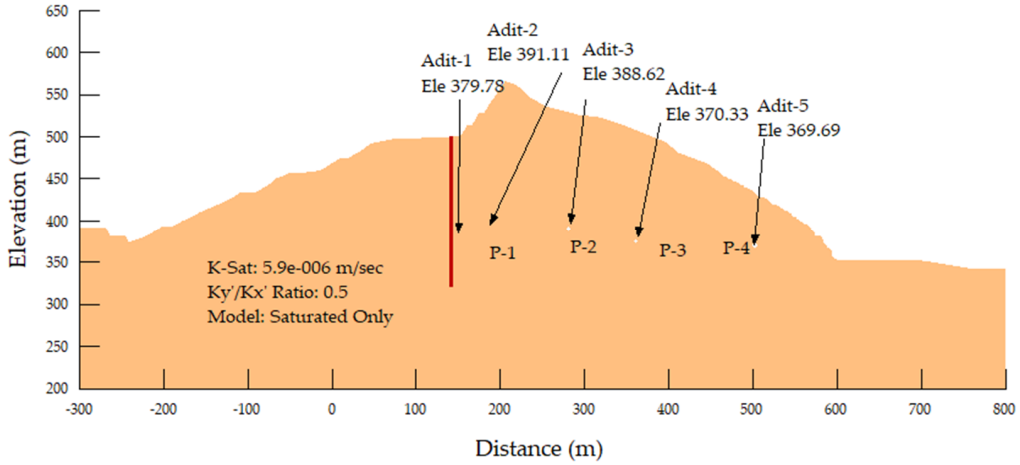

Figure 9. Cross-section showing topography and location of instrumentation point.

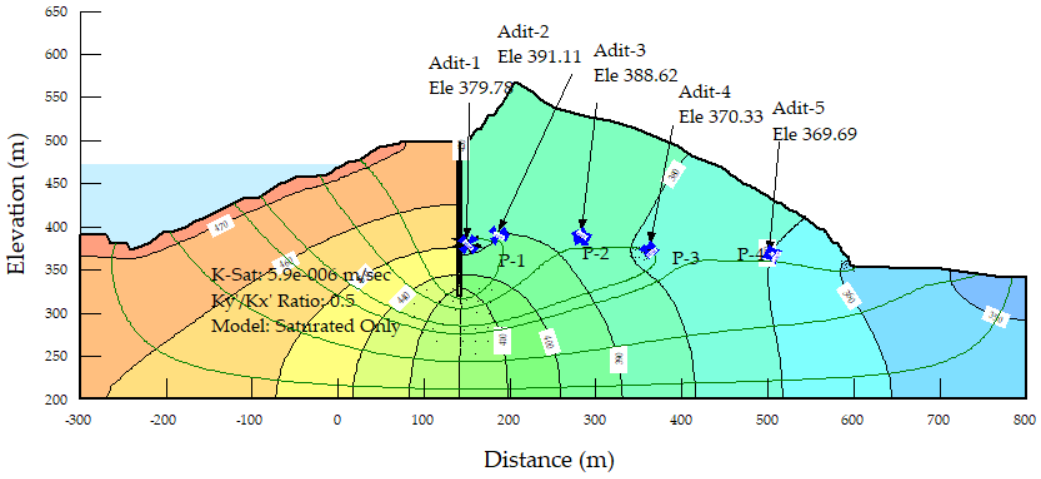

Figure 10. Results of seepage analysis.

The field database of seepage characteristics determined through adits and piezometers were used to validate the results of the Seep W model. A number of plots were developed comparing response of rock mass seepage against variation in rock mass hydraulic conductivity factors (Figures 11 and 12).

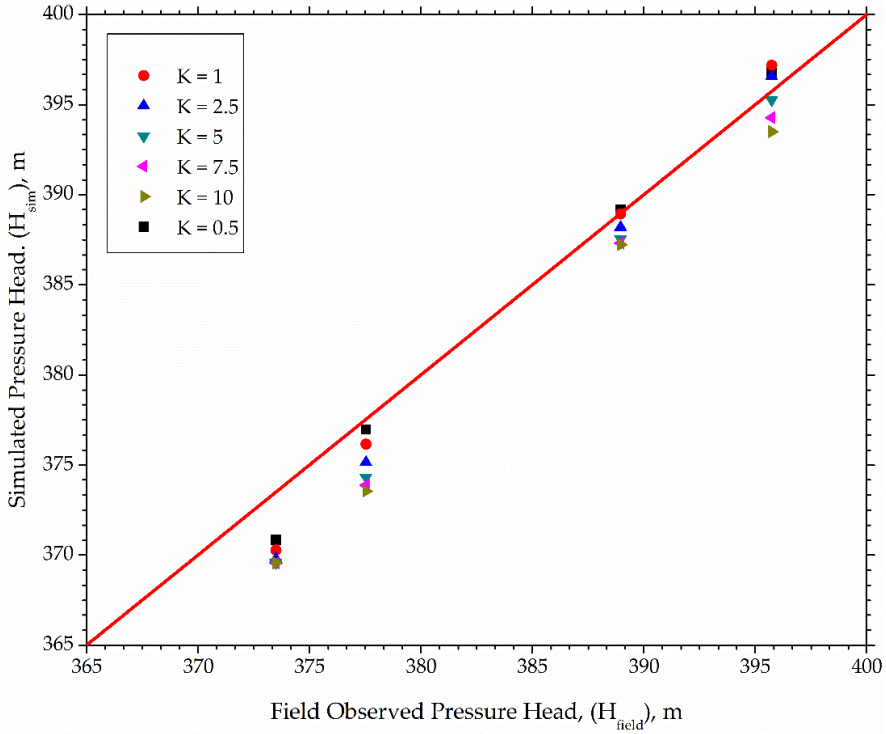

Figure 11. Pressure head observed vs. simulated pressure head from Seep W.

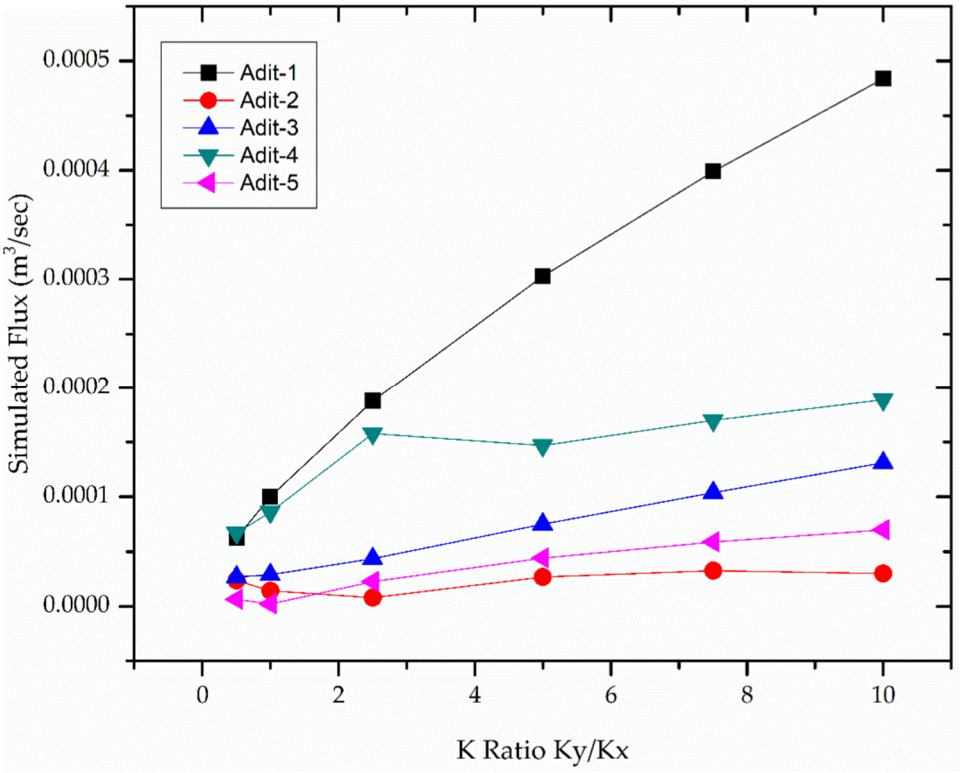

Figure 12. Trend between hydraulic conductivity K ratio (Ky/Kx) vs. Seep W flux.

Figure 11 shows comparison results of field observed pressure head (H_{field}) of four piezometers (P1–P4) and simulated pressure head (H_{sim}) measured from the Seep W model. The typical range of H_{field} observed was from 373 to 397 and H_{sim} from 369 to 398, respectively. The pressure head values were plotted for K ratio (Ky/Kx). A reference line of 45 degree was drawn to see the trend of values. The pressure head shows an

increasing trend with the increase in K Ratio (Ky/Kx) from 0.5 to 10. H_{sim} and H_{field} show good agreement.

Figure 12 represents the results of the Seep W flux values at the location of five selected adits (adit 1–adit 5). The flux values were plotted for K ratio (Ky/Kx). The flux values show overall an increasing trend in most of the data points with the increase in K Ratio (Ky/Kx).

Seep W has the capability to evaluate the anisotropy coefficient termed K ratio., i.e., K ratio = Ky/Kx. Kx is always specified, and Ky is always computed from the specified K ratio.

$$\text{Ky} = \text{K ratio} \times \text{Kx}$$

It can be seen in Figure 13, that with increase in K ratio from 0.1 to 10, the seepage increases, which reflects that with increase in Ky and or Kx values the seepage also increases. Figure 10 also shows the trend of K ratio with the total simulated seepage quantity of the rock mass determined from Seep W. It was observed from the instrumentation data (seepage from adits) that the actual seepage quantity as accumulative value of all the five adits was 5.90 cusec. The same is marked in Figure 13. It was noticed that the K ratio against 5.90 cusec value was 4.43. The lower and upper range of K ratio was taken as 0.1 to 10 with reference to the K ratio value of 4.43. The corresponding Ky for a K ratio of 4.43 was 2.6×10^{-5} m/sec. The variation of seepage quantity with hydraulic conductivity anisotropy parameter K ratio from 0.1 to 10 reveals that the rock discontinuities aligned with the vertical axis can contribute to higher seepage quantity and uplift pressure as compared to lying parallel to the horizontal axis.

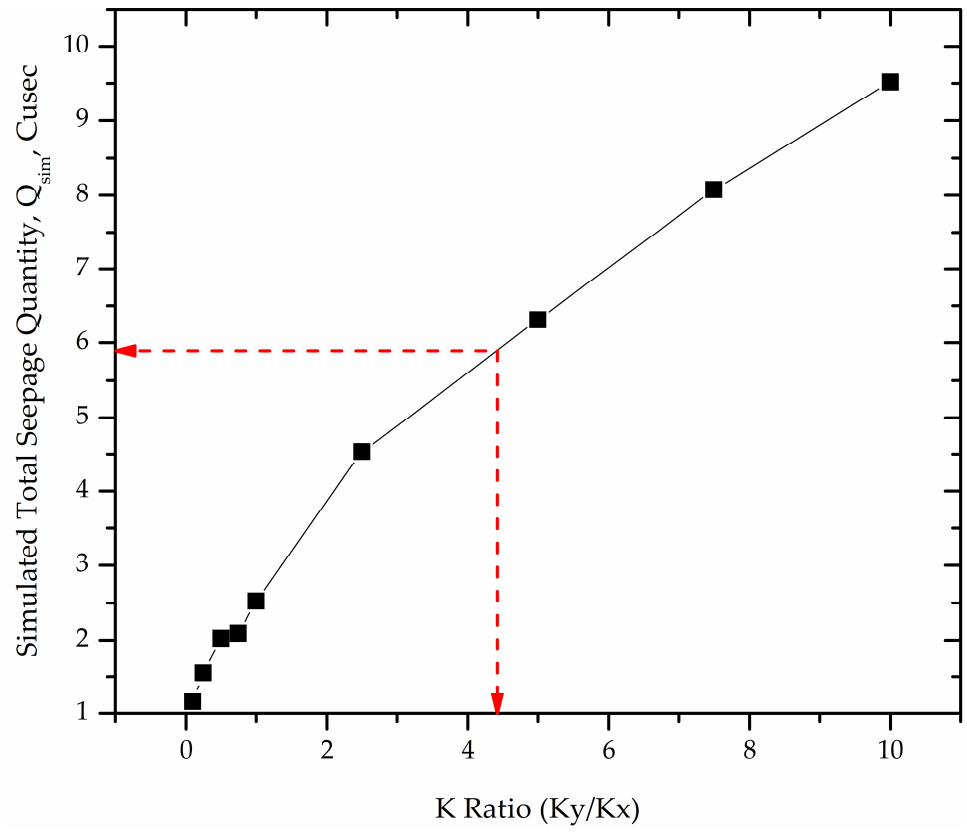

Figure 13. K ratio trend for seepage estimation.

A plot of all data points of hydraulic conductivity against respective RQD was prepared (Figure 14). The non-representative data points of wash out and failed Lugeon tests were omitted in the plots between RQD and hydraulic conductivity presented below. It was observed that at the junction of rock mass, the RQD values in the boreholes were relatively non-representative with depth. Further, during any abrupt variation in rock type,

the non-representative RQD values were observed. The hydraulic conductivity obtained against these non-representative values while potting was not giving the clear trend. A regression analysis was carried out between representative data points and a relationship was developed (Figure 14a) using best fitted logarithmic analysis, which is shown below.

$$Ka = 0.00129 - 2.90347 \times 10^{-4} \ln(\text{RQD} - 1.13595)(R^2 = 0.85) \quad (3)$$

where *Ka* is apparent hydraulic conductivity in cm/sec and RQD is in percentage.

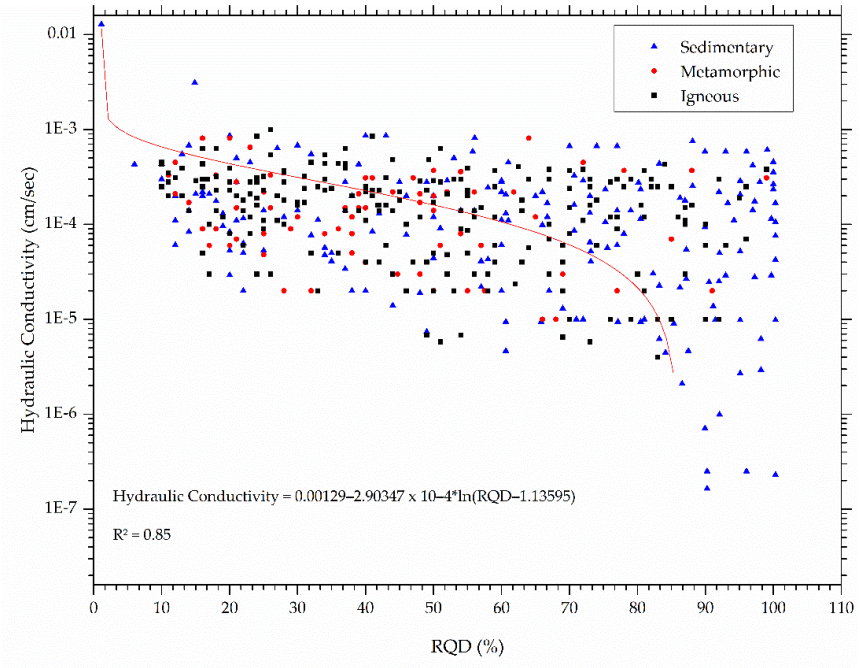

(**a**)

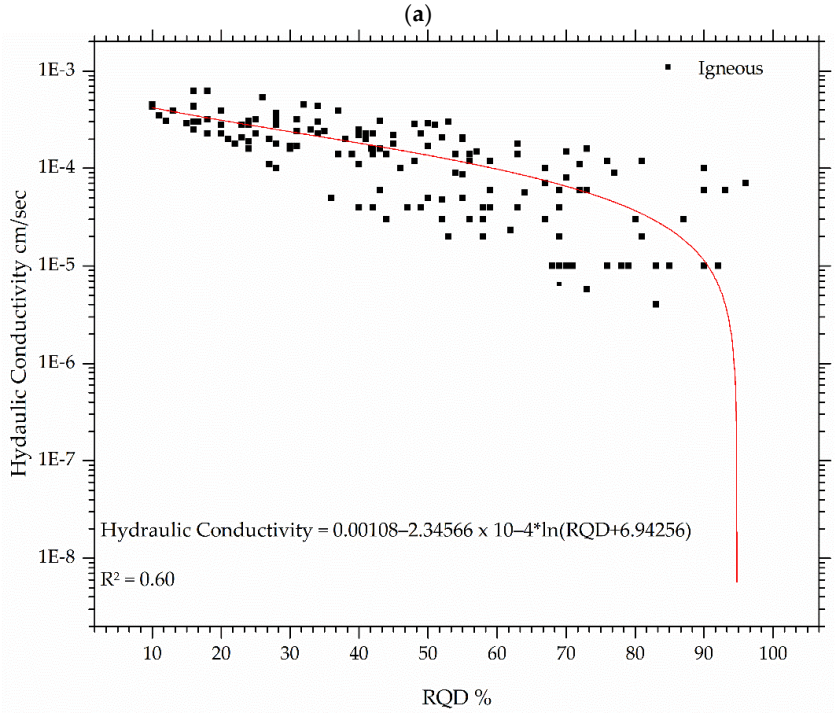

(**b**)

Figure 14. *Cont.*

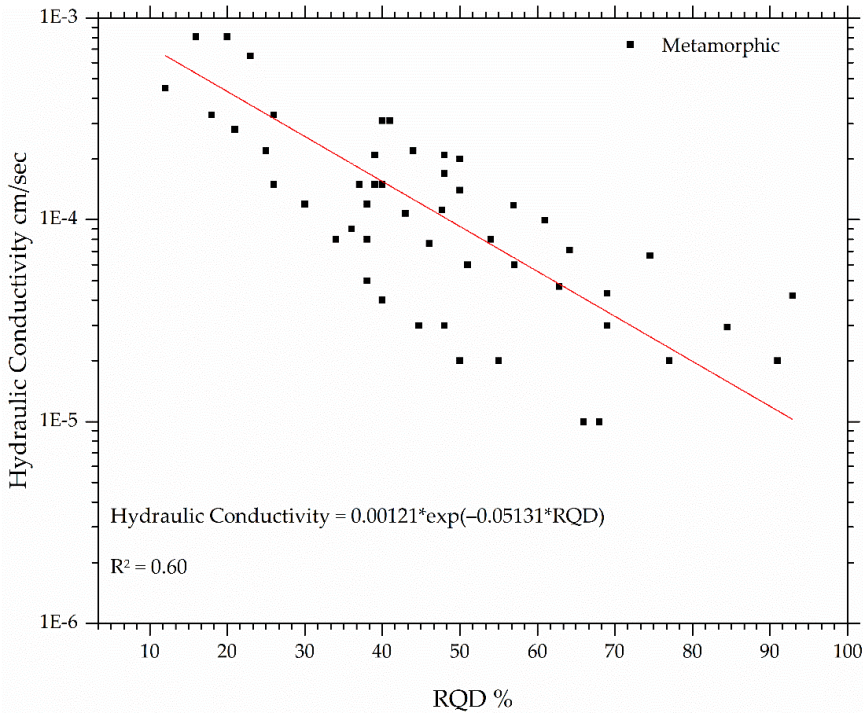

(**c**)

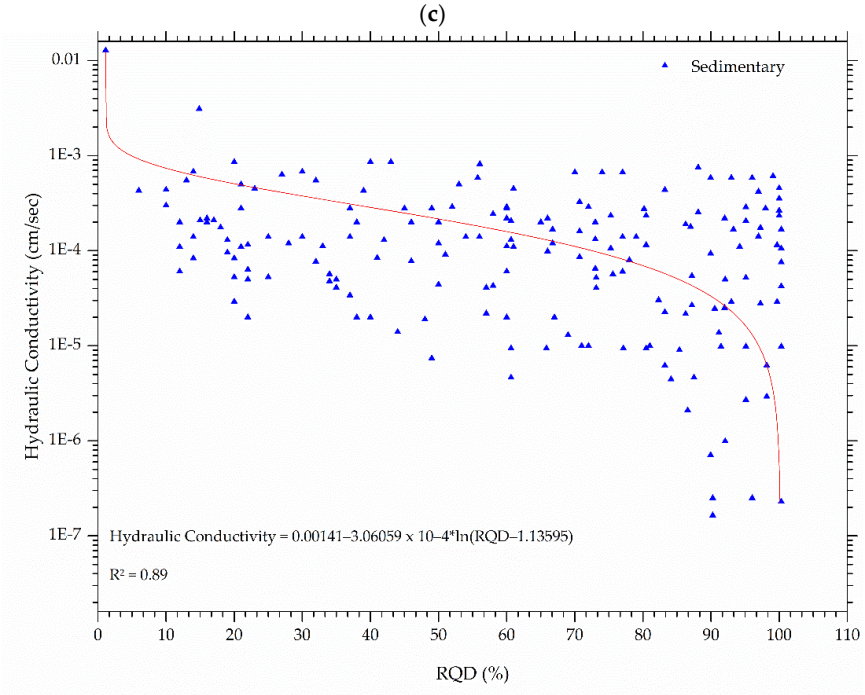

(**d**)

Figure 14. Correlations between hydraulic conductivity and RQD; (**a**) rock mass, (**b**) igneous rock, (**c**) metamorphic rock, (**d**) sedimentary rock.

Three different plots were also prepared, which were extracted from the data of Figure 14. The values of hydraulic conductivity against RQD were analyzed using logarithmic regression model (three parameter logarithmic function) for igneous and sedimentary rock mass while exponential regression model (two parameter exponential function) for metamorphic rock mass. The best fit result is presented in Figure 14b for igneous, in Figure 14c for metamorphic, and in Figure 14d for sedimentary rock mass. The correlation was developed and provided below:

For igneous rocks:

$$Ka = 0.00108 - 2.34566 \times 10^{-4} \ \ln(\text{RQD} + 6.94256)(R^2 = 0.60) \quad (4)$$

For metamorphic rock:

$$Ka = 0.00121^{(-0.05131\text{RQD})}(R^2 = 0.60) \quad (5)$$

For sedimentary rock:

$$Ka = 0.00141 - 3.06059 \times 10^{-4} \ \ln(\text{RQD} - 1.13595)(R^2 = 0.89) \quad (6)$$

While analyzing Figure 14, a strong correlation was observed between K and RQD for rock mass composite formation and sedimentary rock deposits. Reasonable correlation does exist between RQD and K for igneous and metamorphic rock deposits. These correlations can be used for evaluation of rock mass hydraulic conductivity using RQD data particularly during planning process of infrastructure development. These correlations proposed in this research can be used in relatively continuous rock mass formations. However, the applicability of these correlations in fractured rock mass needs to be further investigated. Sustainable infrastructure development requires realistic K determination, which is very often a costly and time-consuming undertaking. The determination of seepage characteristics of rock mass during preliminary design sometimes is also not affordable. These correlations help the engineers working in design to assess the rock mass seepage characteristics with confidence in similar rock mass formations.

4. Conclusions

A detailed literature/reconnaissance survey was carried out in the Hazara formation to finalize rock mass formation. The geological and geotechnical engineering data were analyzed for the evaluation of the RQD and hydraulic conductivity of rock mass. The seepage response of the rock mass was determined from the geo-mechanical engineering data of the developed infrastructures. The seepage and pressure head data from the adits and installed piezometers were analyzed using the Finite Element Model (FEM) and results were compared with actual seepage observed in the rock mass from instrumentation. The following conclusions can be drawn from the above findings:

- A strong correlation exists between RQD and hydraulic conductivity of the composite rock mass formation.

$$Ka = 0.00129 - 2.90347 \times 10^{-4} \ \ln(\text{RQD} - 1.13595) \ (R^2 = 0.85)$$

- Reasonable correlations do exist between RQD and hydraulic conductivity of the individual rock types.

$$Ka = 0.00108 - 2.34566 \times 10^{-4} \ \ln(\text{RQD} + 6.94256) \ (R^2 = 0.60)(\text{Igneous rocks})$$

$$Ka = 0.00121^{(-0.05131\text{RQD})} \ (R^2 = 0.60) \ (\text{Metamorphic rock})$$

$$Ka = 0.00141 - 3.06059 \times 10^{-4} \ \ln(\text{RQD} - 1.13595) \ (R^2 = 0.89)(\text{Sedimentary rock})$$

- The variation of seepage quantity with hydraulic conductivity anisotropy parameter K ratio reveals that the rock discontinuities contributing to a higher K ratio can contribute to higher seepage quantity and uplift pressure as compared to discontinuities resulting in a lower K ratio.

The instrumentation in the large infrastructures in such rock mass deposits is recommended from a sustainability perspective. These correlations help the engineers working in design to assess the rock mass seepage characteristics with confidence in similar rock mass formations.

Author Contributions: M.N.K.: conceptualization; data curation; formal analysis; methodology; writing—original draft. A.H.K.: supervision; resources; writing—review and editing. Z.u.R.: resources; writing—review and editing. T.S.C.: writing—review and editing. All authors have read and agreed to the published version of the manuscript.

Funding: This research received no external funding.

Institutional Review Board Statement: Not applicable.

Informed Consent Statement: Not applicable.

Data Availability Statement: Not applicable.

Acknowledgments: The authors are thankful to WAPDA for provision of data for present study and Tarbela 4th Consultants JV [43] for necessary coordination in this regard.

Conflicts of Interest: The authors declare no conflict of interest.

References

1. Jiang, T.; Shen, Z.; Liu, Y.; Hou, Y. Carbon Footprint Assessment of Four Normal Size Hydropower Stations in China. *Sustainability* **2018**, *10*, 2018. [CrossRef]
2. Tang, W.; Li, Z.; Tu, Y. Sustainability Risk Evaluation for Large-Scale Hydropower Projects with Hybrid Uncertainty. *Sustainability* **2018**, *10*, 138. [CrossRef]
3. Rasolofosaon, P.; Zinszner, B. Comparison between permeability anisotropy and elasticity anisotropy of reservoir rocks. *Geophysics* **2002**, *67*, 230. [CrossRef]
4. Quinones-Rozo, C. Lugeon Test Interpretation, Revisited. In Proceedings of the 30th Annual USSD Conference, Sacramento, CA, USA, 12–16 April 2010; pp. 405–414.
5. Öge, İ.F. Assessing Rock Mass Permeability Using Discontinuity Properties. *Procedia Eng.* **2017**, *191*, 638–645. [CrossRef]
6. Al-Yaarubi, A.H.B. *Numerical and Experimental Study of Fluid Flow in a Rough-Walled Rock Fracture*; Imperial College: London, UK, 2003.
7. Fan, Z.Q.; Jin, Z.-H.; Johnson, S.E. Modelling petroleum migration through microcrack propagation in transversely isotropic source rocks. *Geophys. J. Int.* **2012**, *190*, 179–187. [CrossRef]
8. Fan, Z.; Eichhubl, P.; Newell, P. Basement Fault Reactivation by Fluid Injection into Sedimentary Reservoirs: Poroelastic Effects. *J. Geophys. Res. Solid Earth* **2019**, *124*, 7354–7369. [CrossRef]
9. Gowida, A.; Moussa, T.; Elkatatny, S.; Ali, A. A Hybrid Artificial Intelligence Model to Predict the Elastic Behavior of Sandstone Rocks. *Sustainability* **2019**, *11*, 5283. [CrossRef]
10. Zhang, C.; Li, D.; Wu, S.; Chen, L.; Peng, J. Study on Evolution Mechanism of Structure-Type Rockburst: Insights from Discrete Element Modeling. *Sustainability* **2021**, *13*, 8036. [CrossRef]
11. El-Naqa, A. The hydraulic conductivity of the fractures intersecting Cambrian sandstone rock masses, central Jordan. *Environ. Geol.* **2001**, *40*, 973–982. [CrossRef]
12. Qureshi, M.; Khan, K.; Bessaih, N.; Al-Mawali, K.; Al-Sadrani, K. An empirical relationship between in-situ permeability and RQD of discontinuous sedimentary rocks. *Electron. J. Geotech. Eng.* **2014**, *19*, 4781–4790.
13. Ahmad, K.; Kristály, F.; Docs, R. Effects of clay mineral and physico-chemical variables on sandstone rock permeability. *J. Oil Gas Petrochem. Sci.* **2018**, *1*, 18–26. [CrossRef]
14. Hamm, S.-Y.; Kim, M.; Cheong, J.-Y.; Kim, J.-Y.; Son, M.; Kim, T.-W. Relationship between hydraulic conductivity and fracture properties estimated from packer tests and borehole data in a fractured granite. *Eng. Geol.* **2007**, *92*, 73–87. [CrossRef]
15. Lu, H.; Zhang, Y.; Zhang, G.; Zhang, M. A Thermal Effect Model for the Impact of Vertical Groundwater Migration on Temperature Distribution of Layered Rock Mass and Its Application. *Water* **2021**, *13*, 1285. [CrossRef]
16. Priest, S.D. *Discontinuity Analysis for Rock Engineering*; Springer: Berlin/Heidelberg, Germany, 1993.
17. Tsang, C.-F.; Neretnieks, I. Flow Channeling in Heterogeneous Fractured Rocks. *Rev. Geophys.* **1998**, *36*, 275–298. [CrossRef]
18. Youn, D.; Gutierrez, M. Effect of Fracture Distribution on Permeability of Fractured Rock Masses. In Proceedings of the 45th U.S. Rock Mechanics/Geomechanics Symposium, San Francisco, CA, USA, 1 January 2011; p. 7.
19. Zhang, Z. Hydro Mechanical Behaviour and Nonlinear Flow Characteristic of Rock Fractures. Ph.D. Thesis, University of Wollongong, Wollongong, Australia, 2013.
20. Zhang, Z.; Nemcik, J. Fluid flow regimes and nonlinear flow characteristics in deformable rock fractures. *J. Hydrol.* **2013**, *477*, 139–151. [CrossRef]

21. Zhang, Z.; Nemcik, J. Friction Factor of Water Flow Through Rough Rock Fractures. *Rock Mech. Rock Eng.* **2013**, *46*, 1125–1134. [CrossRef]
22. Zhu, Z.; Niu, Z.; Que, X.; Liu, C.; He, Y.; Xie, X. Study on Permeability Characteristics of Rocks with Filling Fractures Under Coupled Stress and Seepage Fields. *Water* **2020**, *12*, 2782. [CrossRef]
23. Baghbanan, A.; Jing, L. Stress effects on permeability in a fractured rock mass with correlated fracture length and aperture. *Int. J. Rock Mech. Min. Sci.* **2008**, *45*, 1320–1334. [CrossRef]
24. Li, Z.; Liu, H.; Dun, Z.; Ren, L.; Fang, J. Grouting effect on rock fracture using shear and seepage assessment. *Constr. Build. Mater.* **2020**, *242*, 118131. [CrossRef]
25. Donnelly, C.R. Icold 2015-Question 97, Spillways-Évacuateurs de Crues. In Proceedings of the 25th International Congress on Large Dams, Stavanger, Norway, 7 July 2015.
26. Donnelly, C.R.; Acharya, A. A Discussion on the Evolution and Application of Quantitative Risk Informed Dam Safety Decision Making. In Proceedings of the 1st International Conference on Dam Safety Management and Engineering, Penang, Malaysia, 21 November 2019.
27. Moeini, H.; Farhadian, H.; Nikvar-Hassani, A. Determination of the optimum sealing method for Azad pumped storage dam considering seepage analysis. *Arab. J. Geosci.* **2018**, *11*, 389. [CrossRef]
28. Zhang, Q.-H.; Liu, Q.-B.; Su, A.-J.; Li, Y.-J.; Zhang, Y.-H. Hydraulic Conductivity of Rock Masses Surrounding Water Curtain Boreholes for Underground Oil Storage Caverns. *Energies* **2021**, *14*, 4588. [CrossRef]
29. Kassab, M.A.; Abuseda, H.H.; El Sayed, N.A.; LaLa, A.M.; Elnaggar, O.M. Petrographical and petrophysical integrated studies, Jurassic rock samples, North Sinai, Egypt. *Arab. J. Geosci.* **2016**, *9*, 99. [CrossRef]
30. Wang, J.C.; Wang, C.Y.; Tang, X.J.; Hu, S.; Han, Z.; Wang, Y.T. A method for estimating rock mass joint size using borehole camera technique. *Yantu Lixue/Rock Soil Mech.* **2017**, *38*, 2701–2707. [CrossRef]
31. Xue, Y.; Liu, Y.; Dang, F.; Liu, J.; Ma, Z.; Zhu, L.; Yang, H. Assessment of the Nonlinear Flow Characteristic of Water Inrush Based on the Brinkman and Forchheimer Seepage Model. *Water* **2019**, *11*, 855. [CrossRef]
32. Arshad, I.; Muhammad Munir, B. Comparison of SEEP/W Simulations with Field Observations for Seepage Analysis through an Earthen Dam (Case Study: Hub Dam-Pakistan) Comparison of SEEP/W Simulations with Field Observations for Seepage Analysis through an Earthen Dam (Case Study: Hub Dam-Pakistan). *Int. J. Res.* **2014**, *1*, 57–70.
33. Bear, J. *Dynamics of Fluids in Porous Media*; Courier Corporation: Chelmsford, MA, USA, 2013.
34. Chouireb, M.; Djehiche, A. Simulation of seepage flow through an earthen dam with vertical drain and comparison of results with observations data (case study: Harreza dam-Algeria). *Arab. J. Geosci.* **2019**, *12*, 406. [CrossRef]
35. Khaleel, R. Scale dependence of continuum models for fractured basalts. *Water Resour. Res.* **1989**, *25*, 1847–1855. [CrossRef]
36. Li, H.; Tian, H.; Ma, K. Seepage Characteristics and Its Control Mechanism of Rock Mass in High-Steep Slopes. *Processes* **2019**, *7*, 71. [CrossRef]
37. Long, J.C.S.; Remer, J.S.; Wilson, C.R.; Witherspoon, P.A. Porous media equivalents for networks of discontinuous fractures. *Water Resour. Res.* **1982**, *18*, 645–658. [CrossRef]
38. Min, K.-B.; Jing, L.; Stephansson, O. Determining the equivalent permeability tensor for fractured rock masses using a stochastic REV approach: Method and application to the field data from Sellafield, UK. *Hydrogeol. J.* **2004**, *12*, 497–510. [CrossRef]
39. Niu, Z.; Zhu, Z.; Que, X. Constitutive Model of Stress-Dependent Seepage in Columnar Jointed Rock Mass. *Symmetry* **2020**, *12*, 160. [CrossRef]
40. Turturro, A.C.; Caputo, M.C.; Perkins, K.S.; Nimmo, J.R. Does the Darcy–Buckingham Law Apply to Flow through Unsaturated Porous Rock? *Water* **2020**, *12*, 2668. [CrossRef]
41. Xia, C.; Lu, G.; Bai, D.; Zhu, Z.; Luo, S.; Zhang, G. Sensitivity Analyses of the Seepage and Stability of Layered Rock Slope Based on the Anisotropy of Hydraulic Conductivity: A Case Study in the Pulang Region of Southwestern China. *Water* **2020**, *12*, 2314. [CrossRef]
42. Karakuş, H.; Erguler, Z.A.; Ediz, İ.G.; Beyhan, S. Assessment of hydraulic conductivity of disturbed and undisturbed rock masses in Tunçbilek lignite basin, Turkey. *Arab. J. Geosci.* **2021**, *14*, 1522. [CrossRef]
43. WAPDA. *Design Report for Tarbela 4th Extension Hydropower Project*; WB-P115893; World Bank: Washington, DC, USA, 2012.
44. *ASTM D2216*; Standard Test Methods for Laboratory Determination of Water (Moisture) Content of Soil and Rock by Mass. ASTM International: West Conshohocken, PA, USA, 2019.
45. *ASTM D6473*; Standard Test Method for Specific Gravity and Absorption of Rock For Erosion Control. ASTM International: West Conshohocken, PA, USA, 2015.
46. *ATM D7012*; Standard Test Methods for Compressive Strength and Elastic Moduli of Intact Rock Core Specimens under Varying States of Stress and Temperatures. ASTM International: West Conshohocken, PA, USA, 2014.
47. *ATM D5731*; Standard Test Method for Determination of the Point Load Strength Index of Rock and Application to Rock Strength Classifications. ASTM International: West Conshohocken, PA, USA, 2016.
48. *ASTM D3967*; Standard Test Method for Splitting Tensile Strength of Intact Rock Core Specimens. ASTM International: West Conshohocken, PA, USA, 2016.
49. *ASTM D5607*; Standard Test Method for Performing Laboratory Direct Shear Strength Tests of Rock Specimens Under Constant Normal Force. ASTM International: West Conshohocken, PA, USA, 2016.

sustainability

MDPI

Article

Application of Machine Learning and Multivariate Statistics to Predict Uniaxial Compressive Strength and Static Young's Modulus Using Physical Properties under Different Thermal Conditions

Naseer Muhammad Khan [1,2,3], Kewang Cao [2,4], Qiupeng Yuan [4,5,*], Mohd Hazizan Bin Mohd Hashim [6], Hafeezur Rehman [3,6,*], Sajjad Hussain [7], Muhammad Zaka Emad [8], Barkat Ullah [9], Kausar Sultan Shah [10] and Sajid Khan [7]

1 Department of Sustainable Advanced Geomechanical Engineering, Military College of Engineering, National University of Sciences and Technology, Risalpur 23200, Pakistan
2 Key Laboratory of Deep Coal Resource Mining (China University of Mining & Technology), Ministry of Education, Xuzhou 221116, China
3 Department of Mining Engineering, Balochistan University of Information Technology Engineering and Management Sciences, Quetta 87300, Pakistan
4 School of Management Science and Engineering, Anhui University of Finance and Economics, Bengbu 233030, China
5 State Key Laboratory of Mining Response and Disaster Prevention and Control in Deep Coal Mine, Anhui University of Science and Technology, Huainan 232001, China
6 School of Materials and Mineral Resources Engineering, University Sains Malaysia, Engineering Campus, Nibong Tebal 14300, Penang, Malaysia
7 Department of Mining Engineering, University of Engineering & Technology, Peshawar 25000, Pakistan
8 Department of Mining Engineering, University of Engineering and Technology, Lahore 54890, Pakistan
9 School of Resources and Safety Engineering, Central South University, Changsha 410083, China
10 Department of Mining Engineering, Karakoram International University, Gilgit 15100, Pakistan
* Correspondence: 2018100011@aust.edu.cn (Q.Y.); miner1239@yahoo.com (H.R.)

Citation: Khan, N.M.; Cao, K.; Yuan, Q.; Bin Mohd Hashim, M.H.; Rehman, H.; Hussain, S.; Emad, M.Z.; Ullah, B.; Shah, K.S.; Khan, S. Application of Machine Learning and Multivariate Statistics to Predict Uniaxial Compressive Strength and Static Young's Modulus Using Physical Properties under Different Thermal Conditions. *Sustainability* **2022**, *14*, 9901. https://doi.org/10.3390/su14169901

Academic Editors: Mahdi Hasanipanah, Danial Jahed Armaghani and Jian Zhou

Received: 26 May 2022
Accepted: 29 July 2022
Published: 10 August 2022

Publisher's Note: MDPI stays neutral with regard to jurisdictional claims in published maps and institutional affiliations.

Copyright: © 2022 by the authors. Licensee MDPI, Basel, Switzerland. This article is an open access article distributed under the terms and conditions of the Creative Commons Attribution (CC BY) license (https://creativecommons.org/licenses/by/4.0/).

Abstract: Uniaxial compressive strength (UCS) and the static Young's modulus (E_s) are fundamental parameters for the effective design of engineering structures in a rock mass environment. Determining these two parameters in the laboratory is time-consuming and costly, and the results may be inappropriate if the testing process is not properly executed. Therefore, most researchers prefer alternative methods to estimate these two parameters. This work evaluates the thermal effect on the physical, chemical, and mechanical properties of marble rock, and proposes a prediction model for UCS and E_S using multi-linear regression (MLR), artificial neural networks (ANNs), random forest (RF), and k-nearest neighbor. The temperature (T), P-wave velocity (P_V), porosity (η), density (ρ), and dynamic Young's modulus (E_d) were taken as input variables for the development of predictive models based on MLR, ANN, RF, and KNN. Moreover, the performance of the developed models was evaluated using the coefficient of determination (R^2) and mean square error (MSE). The thermal effect results unveiled that, with increasing temperature, the UCS, E_S, P_V, and density decrease while the porosity increases. Furthermore, ES and UCS prediction models have an R^2 of 0.81 and 0.90 for MLR, respectively, and 0.85 and 0.95 for ANNs, respectively, while KNN and RF have given the R^2 value of 0.94 and 0.97 for both E_S and UCS. It is observed from the statistical analysis that P-waves and temperature show a strong correlation under the thermal effect in the prediction model of UCS and E_S. Based on predictive performance, the RF model is proposed as the best model for predicting UCS and E_S under thermal conditions.

Keywords: thermal effect prediction model; uniaxial compressive strength; static Young's modulus; artificial neural network; multilinear regression

1. Introduction

In recent years, investigations into and understandings of reservoir rock behaviour under differing high temperatures (T) have become imperative for the safe implementation of engineering projects [1–8]. The behaviour of rock under high temperatures is a major concern in geological sciences, underground engineering, geothermal energy exploitation, deep mining, nuclear waste disposal, engineering structures, and coal gasification. The high temperatures alter and degrade the properties of the rock mass associated with these engineering structures [9]. Granite, in particular, contains heat-producing radioactive isotopes that raise the thermal gradient and stimulate the geothermal system (EGSs) up to 350 °C [10–13]. This thermal stress dramatically affects the mechanical properties of the reservoir rock. Furthermore, different heating conditions exhibit distinct mechanical properties compared to the intact rock's room temperature, affecting borehole stability. Therefore, it is essential to study the high thermal mechanics and their effects on the reservoir rock properties for the safe and efficient execution of the engineering project.

Previous research shows that rocks' physical and mechanical properties are significantly affected by increasing thermal conditions due to the alteration of mineral composition and intergrain bonding [14–16]. Furthermore, the high temperature can cause a thermal expansion in the rock-forming mineral, inducing thermal stress in the rock resulting in the development of micro-cracks and propagating the existing cracks and length [15,17–24]. For instance, Chen et al. [25] noted that the UCS and Young's modulus (E) of rock are decreased with the increases in temperature up to 1000 °C. Homand-Etienne and Houpert [14], and Chen, Ni, Shao, and Azzam [25], concluded from their research that the UCS of granite decreased slightly with an increase in temperature up to 400 °C, but a dramatic decline in UCS was observed when the temperature exceeded 400 °C. Peng, Rong, Cai, Yao, and Zhou [15] evaluated marble's physical and mechanical properties and found that the UCS and E both decrease with the increase in temperature. Considering the importance of UCS and E_S used as input parameters in the effective design and rock mass behaviour analysis, it is essential to evaluate these parameters under high-temperature mechanics.

It is possible determine UCS and E_S by both destructive and non-destructive methods [26]. The destructive testing for both parameters is time-consuming and expensive, and the core sampling needs high precision, while the obtained results can be ambiguous [27,28]. Therefore, researchers have focused their attentions on non-destructive techniques. Several studies have been conducted using various artificial intelligent (AI) techniques to predict rock's strength and stiffness properties [29]. In this regard, Manouchehrian et al. [26] predicted UCS using texture as input variables based on ANN and multivariate statistics. Likewise, [26,30] used porosity (η), P_V, and ρ as input variables and predicted UCS and E_S based on ANNs and ANFIS. Abdi, Garavand, and Sahamieh [28] proposed the ANN and MLR methods for predictive modeling of E using η in %, dry density (γd), P-wave velocity (P_V), and water absorption as input variables. It was found that the prediction performance of ANN is better than MLR. Dehghan et al. [31] predicted UCS and Es based on ANNs and MLR using P_V, the point load index, the Schmidt hammer rebound number, and η as input variables. Some cutting-edge machine learning models are also adopted to predict UCS and E_s. For example, Zhang et al. [32] proposed a beetle antennae search (BAS) algorithm-based RF model to accurately and effectively predict the UCS of lightweight self-compacting concrete (LWSCC). Matin et al. [33] used the RF model to select variables within several rock properties and indexes, namely porosity (η), water content, Is (50), p-wave velocity (P_V), and rebound numbers (Rn), along with an effective model for the prediction of UCS and E based on the RF preferred variables. Suthar [34] appraised the potential of five modeling approaches, namely M5 model tree, RF, ANN, SVM, and Gaussian processes (GPs) for predicting the UCS of stabilized pond ashes with lime and lime sludge. Wang et al. [35] proposed an RF model to accurately predict the UCS of rocks from simple index tests. Matin et al. [33] predicted E using RF, and multivariate regression (MVR) and a generalized regression neural network (GRNN) were used for comparison. The results revealed that RF performed well compared to MVR and GRNN. Ren et al. [36] developed

several ML algorithms, namely k-nearest neighbors (KNN), naive Bayes, RF, ANN, and SVM, to accurately predict rock's UCS using ANN and SVM. Ghasemi et al. [37] evaluated the UCS and E of carbonate rocks by developing a tree-based approach. According to their findings, the applied method revealed highly accurate results. Saedi et al. [38] studied the prediction of the UCS and E of migmatite rocks by ANN, ANFIS, and multivariate regression (MVR). Shahani et al. [39] developed an XGBoost model to predict the UCS and E of intact sedimentary rock. Armaghani et al. [40] developed a hybrid model based on ANN and imperialist competitive algorithm (ICA) to predict UCS and E of granite rocks. Although, the above-discussed literature has provided useful insights into predicting the UCS and E by utilizing different machine learning approaches, there has been, to date, no significant study documented which consider the thermal effect on the physical and mechanical behaviors of rock. The temperature has a great effect on these physical and mechanical properties. Therefore, it is imperative to increase the performance of the proposed model and to explore the use of a new input variable, i.e., temperature, in predicting the UCS and E_s.

This current research was carried out in the following three steps: (1) microscopic observation was performed on thin sections of various rock samples treated at different thermal conditions. (2) Secondly, the physical and mechanical properties of marble were investigated under the influence of temperature. (3) Finally, using physical and mechanical properties, such as T, $P_{V,}$ ρ, η, and E_d as input variables, the UCS and E_s were predicted using different statistical and computational intelligence methods, including MLR, ANN, RNN, and RF. The results of this study will serve to help researchers to better understand the thermal effect on the physical and mechanical properties of rocks in a sweltering environment.

2. Regional Geological Setting

Northward subduction of the Indian Plate under the Kohistan Island Arc results in upper amphibolite, blueschist, and eclogite facies under metamorphic conditions. These high-grade metamorphic rocks form exposures from west to east in the Kotah/Loe Sar domes. At the main mantle thrust (MMT), as well as in Indus syntaxis and Nanga Parbat, there is a rapid exhumation and crustal anatexis of the Indian affinity plutonic, oceanic, and metasedimentary rocks, as shown in Figure 1a. The grade of metamorphism and deformation decrease south of the main collisional front at the MMT. The Khairabad/Panjal thrust tectonically separates the more enormous Himalayan crystalline rocks from unmetamorphosed sedimentary rocks. For this reason, dimension stones including marble, granite, granodiorites, nephrite, gabbro, quartzite, and serpentine exist between the MMT and Khairabad/Panjal Thrust presented in Figure 1a. The current research focuses on the ~ Late to Middle Mesozoic Nikanai Ghar marble of the Nikanai Ghar Formation that crops at 24 to 27 Km south of the main convergent Indian plate margin at 34.501177″ N, 72.288059″ E in the southernmost limbs of the Kotah and Loe Sar domes in the Buner district, as shown in Figure 1b. The Nikanai Ghar marble, which is spread over 700 km^2 and belongs to the Alpurai Group metasediments, comprises marble, dolomite, and phyllites developed as a result of a high geothermal gradient associated with active crustal thickening and anatectic processes under the Barrovian metamorphic conditions between ca. 39 Ma and 28 Ma [41]. The total estimated marble in the district of Buner is 100 million tons. These marbles vary in color as well as in grain size [42]. The Nikani Ghar marble has a mainly fine to medium grain size. The marble individual bed thickness is 0.5–3.0 m, and the lateral extension (length) varies from 1.5–3.0 Km.

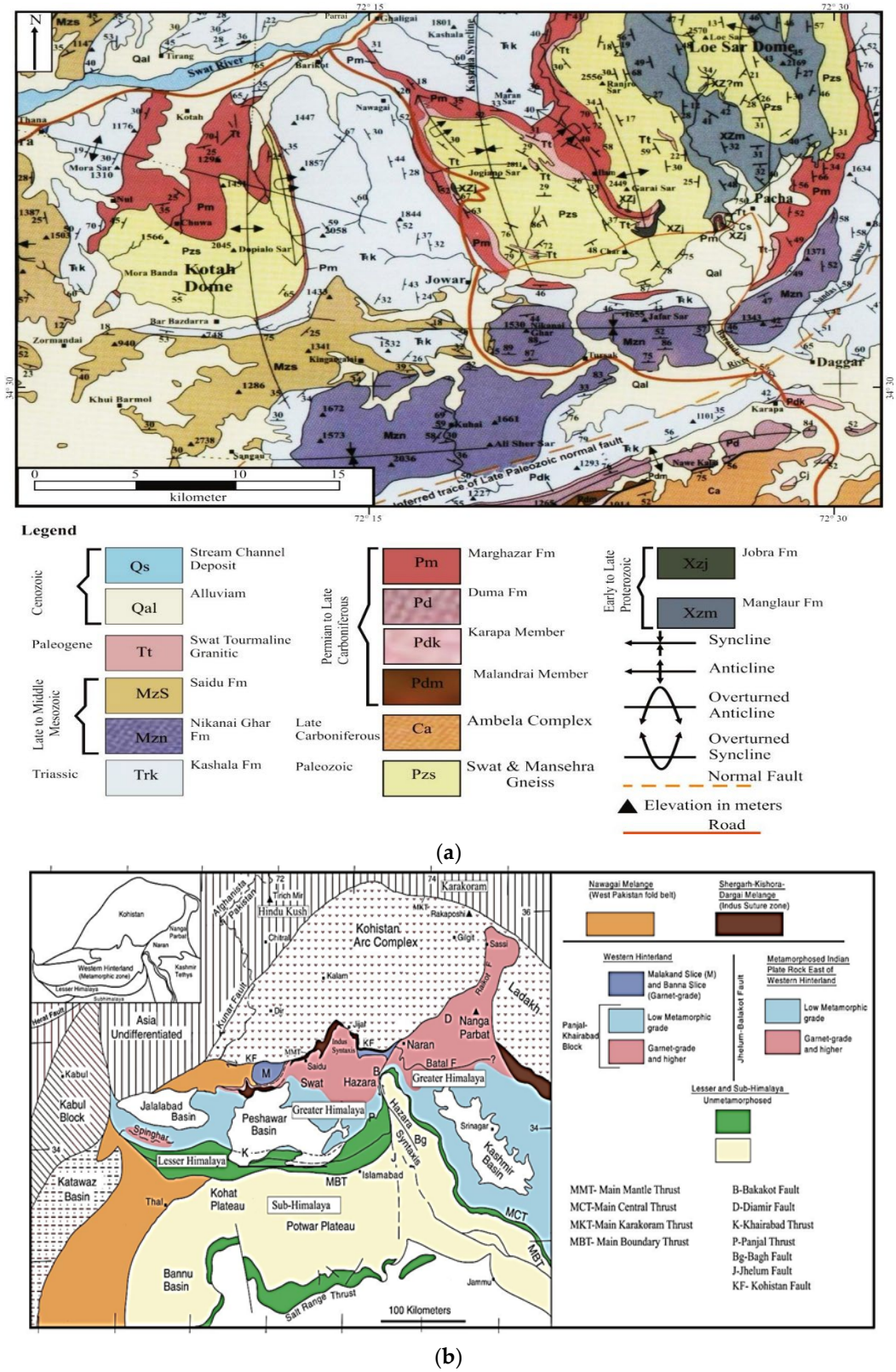

Figure 1. (**a**) Geological map of greater/higher and sub-Himalayan rocks [43]. (**b**) Detailed geological map of the Lower Swat after [44].

Regional geological map as presented in Figure 1a show the distribution of the greater/higher-, lesser-, and sub-Himalayan rocks. South of the convergent plate margin between the Indian plate and Kohistan Island Arc, high temperature and pressure con-

verted limestone stratigraphic units of the greater Himalaya into marble. Indian plate basement rocks are exposed in the cores of Indus syntaxis and Nanga Parbat. The MMT separates the Indian plate from the Kohistan Island Arc. The MKT is the convergent plate boundary between the Kohistan Island Arc and Karakoram microplate [44].

A detailed geological map is presented in Figure 1b of the Lower Swat, showing the main stratigraphic and structural components of the northernmost convergent plate margin of the Indian Plate. Crustal thickening, metamorphism, and partial melting of the middle crust resulted in the Barrovian metamorphic conditions during the prograde burial of the Indian affinity rocks beneath the Kohistan Island Arc. Marble, quartzite, schist, and gneisses developed from limestone, sandstone, shale, and granite protoliths, respectively (after Hussain et al. 2004 [44]).

3. Experimental Design

3.1. Rock Specimen

In this research, marble specimens were collected from Buner, Khyber Pakhtunkhwa, Pakistan, which has the coordinates 34.501177″ N, 72.288059″ E. The representative rock specimens were collected in boulder form from different points within the quarry. The cylindrical core samples (with dimensions of 54 × 108 mm) were prepared according to the International Standard of Rock Mechanics (ISRM) [45,46]. To avoid the nonparallelism between ends of the samples, the maximum allowable deviation of ±0.3 in length and ±0.5 were kept. The specimen's ends were carefully ground and polished within 0.03 mm. The rock processing and testing scheme are shown in Figure 2.

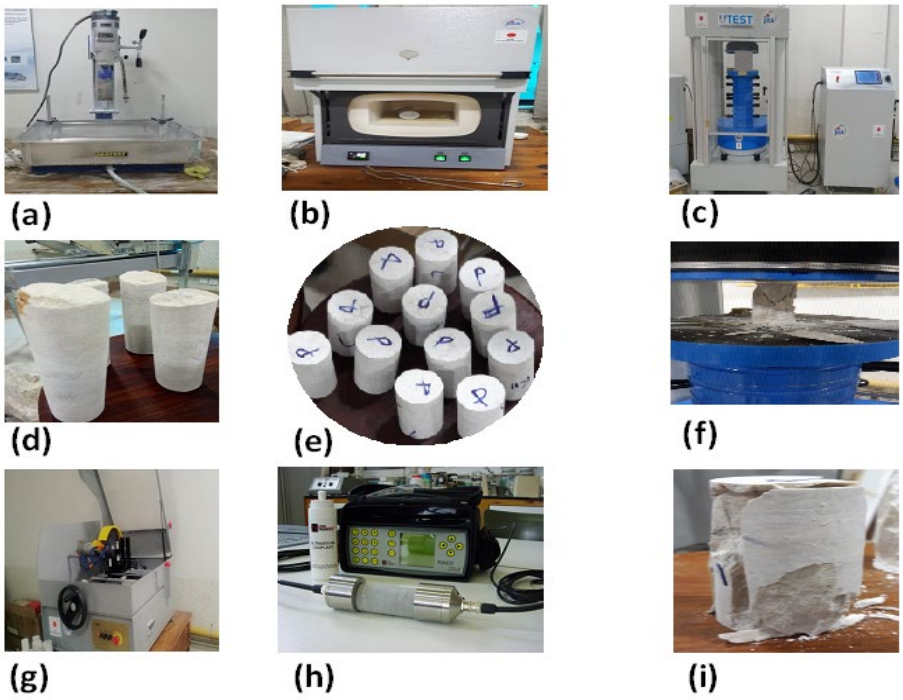

Figure 2. Schematic flowsheet of samples preparation and sample testing, as follows: (**a**) core bit machine for core extraction, (**b**) furnace for heating sample, (**c**) universal testing machine (UTM) for UCS, (**d**) cylindrical core before cutting and polishing, (**e**) cylindrical core after cutting and polishing, (**f**) core sample under compression in UTM, (**g**) core cutting & polishing instrument (**h**) the PUNDIT for P-waves, and (**i**) core samples after failure.

3.2. Heating Procedure

The samples were heated in a furnace with a maximum operating temperature of 1200 °C and a power of 10 kW, as shown in Figure 2b. A total of 64 samples were heated at different predetermined temperatures in a furnace for 24 h and then cooled down gradually

to room temperature. The predetermined temperatures were divided into ten groups, namely 25 °C, 200 °C, 250 °C, 300 °C, 350 °C, 400 °C, 450 °C, 500 °C, 550 °C, and 600 °C, and each group contained an average of 6 samples.

3.3. Samples Characterization

Representative samples were properly prepared, before being subjected to different types of analytical techniques for mineralogical evaluation. Thin-section study was carried out under an optical reflection microscope (Nikon Microphoto-FXA, Type 118) for mineral identification. The X'Pert PRO MPD instrument (with the specifications of Cu Kα, 40 mA current, and 40 kV voltage) was used for XRD analysis to determine the minerals; crystal size and mineral composition. A scanning electron microscope (SEM) with an energy dispersive X-ray spectrometer (SEM-EDX), with a specification of 6610LV+ OXFORD X-max, Japan, and an energy range 0–20 KV, was used for the determination of morphology and mineral microstructure element distribution in the specimen. Major oxides' element percentage was determined in the marble sample including SiO_2, Fe_2O_3, CaO, Al_2O_3, MgO, MnO, Na_2O, and K_2O and loss of ignition was assessed by X-ray fluorescence (XRF).

3.4. Ultrasonic Test

A portable ultrasonic nondestructive digital indicating tester (PUNDIT) was used to compute the ultrasonic parameters,0such as ultrasonic P-wave velocity. This is shown in Figure 2e. The E_d and P_V were determined by an empirical relation [24].

3.5. Universal Testing Machine (UTM)

The mechanical properties of marble were determined in the laboratory by UTM, as shown in Figure 2g. The maximum capacity of machine is 250 KN. The UCS, E_S, shear, and bulk modulus were determined for each predetermined temperature.

3.6. Intelligent Models

3.6.1. Multiple Linear Regression (MLR) Model

It is routine to use MLR to forecast the relationship between important parameters. It is understood that MLR is an expanded variant of basic linear regression, which is utilized in prediction modes with several predictive variables. In this study, MLR model design for UCS and E_S is based on five parameters, such as T, P_V, ρ, η, E_d, as shown in Table 1.

Table 1. Basic descriptive statistics for the original data set.

Parameter	Minimum	Maximum	Mean	Std. Deviation	Mean Std. Error
T	25	600	328.12	168.77	21.09
E_d	22	82	43.08	14.91	1.86
N	9	29	16.80	5.21	0.65
P	3	3	2.69	0.02	0.01
P_V	3	6	4.22	0.65	0.08
UCS	63	115	84.72	18.72	2.34
E_s	8	66	24.77	15.41	1.93

The multilinear regression result general equation is given as follows:

$$Y = c + b_1X_1 + b_2X_2 + b_3X_3 + \ldots\ldots\ldots b_nX_n \quad (1)$$

where, Y, c, X_1 to X_n, and b_1 to b_n are the dependent variable, constant, independent variable, and partial regression coefficient, respectively [47,48].

3.6.2. Artificial Neural Network (ANN) Model

An ANN plays a significant role and considered as an intelligent tool for solution of complex engineering-based problems in geotechnical engineering [49,50]. In this research, the multi-layered perception (MLP) is used. It is composed of three layers, as follows: (1) an input layer which is used to give data to the network; (2) a hidden layer which uses an algorithm and collection of features, the neurons, and the hidden layer selected on trial and error methods [51]; (3) an output layer which gives the output of the input data. Each layer contains many neurons depending on the specific application. Each layer neuron is in connection to the next successive layer and each link carries a weight [52]. Furthermore, several algorithms are used for the ANN model. Nevertheless, the most efficient is backpropagation (BP), which is used in many engineering problems due to its simple training function.

A supervised learning technique must be used throughout the training phase to ensure the accuracy and effectiveness of any classification and task in ANN. A group of examples are used in the training of the BP algorithm's networking to connect and link the nodes and to identify the parametric function, also referred to as weight inadequate methods. In order to minimize the discrepancy between the actual output and the anticipated output, the mean square error (MSE) is repeatedly lowered. Additionally, training aids in identifying each iteration weight [53]. When training various kinds of networks, the BP method is often used. Previous research has shown that the BP method takes into account and assumes a random value. This random value is then used by the NN operation to compute output. The weight value will be adjusted in order to cut down on the margin of error, and this procedure will be repeated as many times as necessary until the minimal result is reached [54]. The model must be trained, and a wide number of scholars have provided specifics of how this might be accomplished [55–57].

ANN Code Compilation in MATLAB

As shown in Figure 3a, our research constructed self-generated ANN code for n numbers of networks while preserving the same training and activation function for a single loop. This code includes a loop function that may run for as many networks as the user resembling. This code's activation function was fixed in general, but the data's nature could be altered. In this scenario, the code was run once for 100 networks. For each network in a loop, the number of neurons increased with each successor and, thus, network1 had one neuron, network2 had two, and so forth. Different algorithms are available for ANN, but the most efficient is BP with the Levenberg–Marquardt algorithm suggested by Ullah et al. [58]. He conducted a detailed study on types of learning algorithms available for ANN. Rao and Kumar [59] concluded that the Levenberg–Marquardt (LM) is more efficient and takes less of a time epoch, while giving better results as compared to other algorithms. Therefore, LM was used in the current model for both the hidden and output layers.

The fundamental structure in this study consists of five inputs (T, P_V, ρ, η, and E_d) and two outputs (UCS and E_S), as illustrated in Figure 3b. The dataset consisted of 60 data points in total. The data was separated into the following three sections: training (75%), testing (15%), and validation (15%).

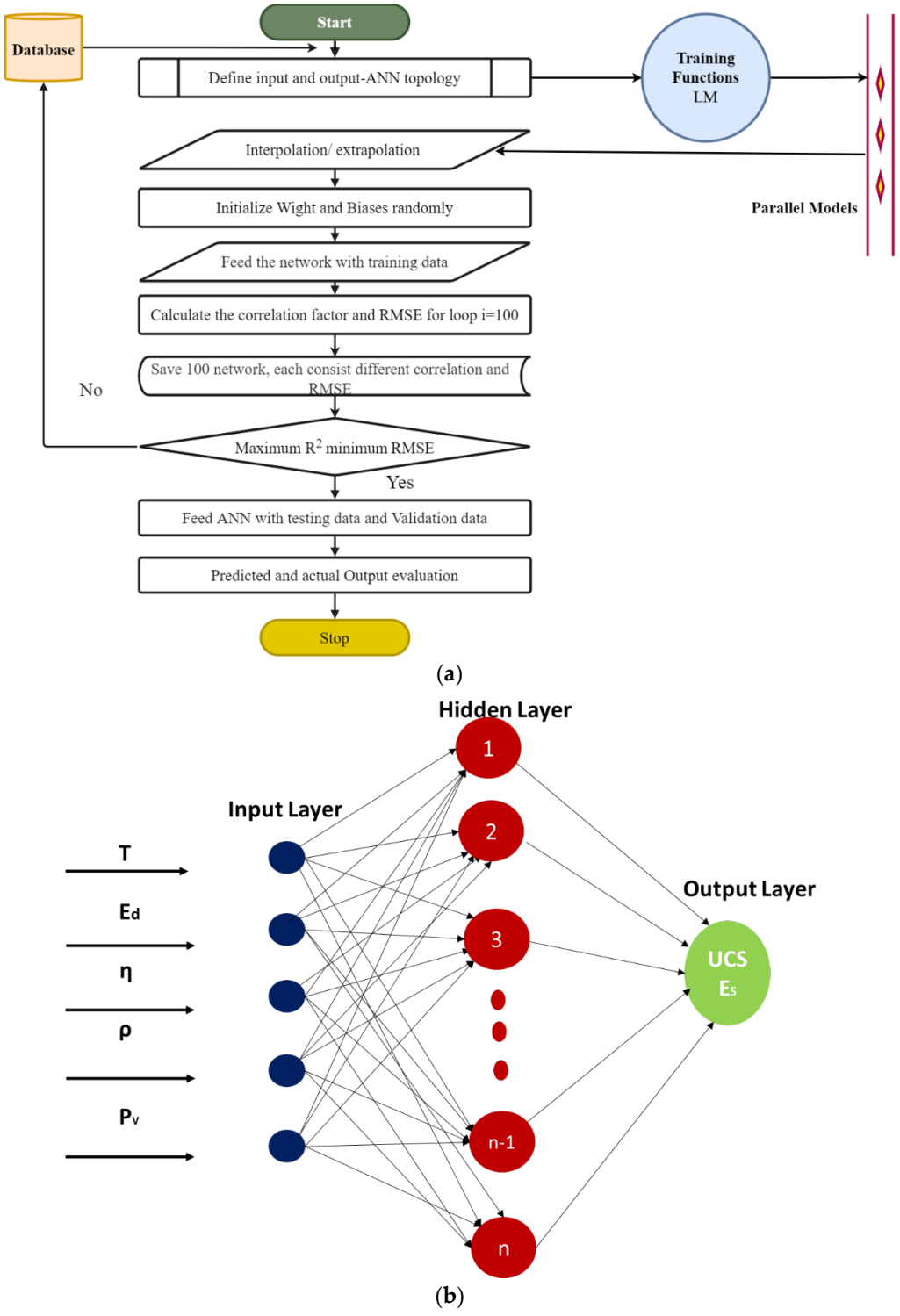

Figure 3. (**a**) Flowchart of ANN for the UCS and E_S prediction model. (**b**) The architecture topology of ANN for UCS and E_S.

3.6.3. Random Forest Regression

The random forest regression (RFR) method was created to aid in predicting hanging wall stability, because it can explain the non-linear relationship between inputs and outputs without relying on statistical assumptions. This made it possible to pinpoint the procedure. The RFR approach is used rather often in geotechnical engineering [60], but also used for the stability of rock pillars, landslide susceptibility assessment, soil liquefaction potential,

and for ground settlement prediction [58–62]. However, no research was documented that was associated with the use of the RFR algorithm on the prediction of the hanging wall's stability.

Two of the most important aspects of RFR are known as the decision tree (DT) approach and the bagging methodology. Depending on the datasets, the DT approach may be used to solve problems relating to classification as well as regression. When using the DT approach, the feature space will first be segmented into sub-regions. Iterative partitioning is carried out up to the point when the termination condition is met. During the construction of a DT, three different components are produced, namely branches, internal nodes, and exterior nodes. Nodes inside the network are always linked to decision functions, which are responsible for determining which node should be visited after the current one. In a DT, the nodes that are no longer divided are referred to as the output nodes. These nodes are also sometimes called terminals or leaf nodes. Because there are problems with classification, every external node will be assigned a class label. This label will be used to classify the data that is associated with that node. When building a DT, branches are used to connect the many nodes, both internally and externally.

In spite of the fact that the DT method may be beneficial in a variety of applications, including civil engineering, Breiman [61] claims that the RFR algorithm is a more effective strategy than the DT method. This is the case despite the fact that the DT method can be used to the study of a variety of different topics. It has been shown to be more reliable than the use of a single tree in a range of data mining applications [62–64]. The RFR technique is a sort of ensemble learning that makes predictions based on bagging the data. Bagging is the foundation of this strategy. In the process of RFR, many of the samples collected via the bagging method are joined with those gathered through other methods to form a collection of decorrelated DTs. The results of averaging all of the DTs are employed, and this is done so that the quality of the modelling may be improved without resorting to overfitting. Figure 4 presents an overview of RF's general architectural makeup. In this figure, the value n denotes the total number of trees, while the numbers k_1, k_2, etc., up to and including k_n, denote the results of each individual DT.

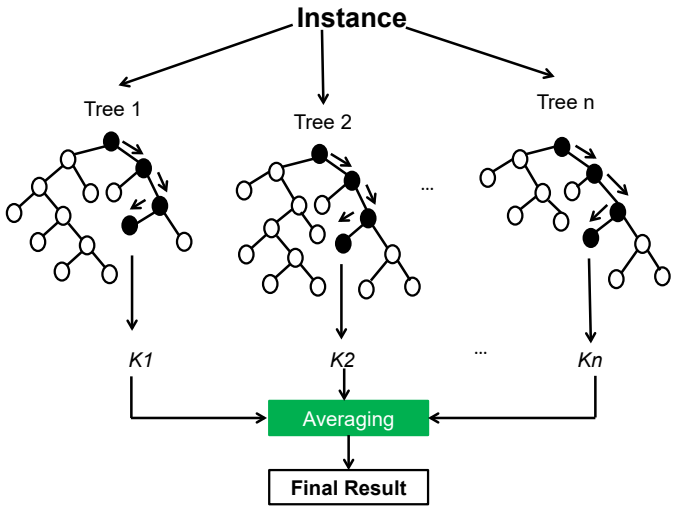

Figure 4. A simple sketch of a regression using a random forest.

3.6.4. k-Nearest Neighbor

The k-nearest neighbor (KNN) method is simple, powerful, and straightforward to implement [65]. In the same way that ANN and RF are used for classification and regression, so, too, is this technique. The following are some benefits associated with using this method:

1. It is straightforward to grasp and put into practice.

2. When it is employed for classification and regression, it can learn non-linear decision boundaries, and it can also invent a highly flexible choice limit by adjusting the value of K. Both of these capabilities are available when it is applied.
3. The KNN architecture does not have a step that is specifically dedicated to training.
4. Since there is only one hyperparameter, which is denoted by the letter K, adjusting the other hyperparameters is quite simple.

The essential concept behind KNN is to locate a group of "k" samples (for example, by applying distance functions) that are close in distance to unknown samples in the calibration dataset. This may be accomplished by searching for groups of samples that are similar to each other. In addition, KNN determines the class of unknown samples by calculating the average of response variables and then comparing those results to the "k" samples [66]. As a consequence of this, the value of k is critically important to the performance of the KNN [67]. For the purpose of the regression issue, the three distance function, which computes the distance between neighboring points and is presented in the following Equations (2)–(4), is utilized:

$$F(e) = \sqrt{\sum_{i=0}^{f} (x_i - y_i)^2} \quad (2)$$

$$F(ma) = \sum_{i=0}^{f} |x_i - y_i| \quad (3)$$

$$F(ma) = \left(\sum_{i=0}^{f} (|x_i - y_i|)^q \right)^{\frac{1}{q}} \quad (4)$$

where F(e) stands for the Euclidean function, F(ma) stands for the Manhattan function, F(mi) stands for the Minkowski function, xi and yi stand for the i^{th} dimension, and q stands for the order between the points x and y.

4. Experimental Results

4.1. Physical Properties

The temperature significantly affects the physical properties of a rock specimen, as shown by Peng et al. [15]. As the temperature increases, and at the maximum temperature of 600 °C, the color of the sample changes from milky white to gray. It is believed that, as the temperature increases, the composition and color of the samples changes accordingly. The percentages of mineral constitution of samples at room temperature and 600 °C temperature were noted to be different. These variations are confirmed through XRD and XRF, as shown in Table 2 and Figure 5a,b. The XRD and XRF results revealed that the samples are mainly composed of calcite, dolomite, and other minerals traces, as shown in Table 2. The increase in temperature has an inverse effect on the intensity of calcite, which is confirmed from the results of the XRD and XRF, as shown in Figure 5a,b. Moreover, it is clear from Table 2 that the temperature increase does not influence the composition of marble. For each mineral, some differences in mineral composition result from the heterogeneity of the marble as described in Table 2, which is in agreement with the previous studies [68,69].

Table 2. Average group XRF analysis of samples at different temperatures.

Temperature (°C)	SiO_2 (%)	TiO_2 (%)	Al_2O_3 (%)	Fe_2O_3 (%)	MnO (%)	MgO (%)	CaO (%)	Na_2O (%)	K_2O (%)	P_2O_5 (%)	LoI (%)
25	0.405	0	0.352	0.121	0.012	0.373	53.892	2.552	0.012	0.000	42.28
200	0.404	0	1.5	1	0.014	2.17	52.89	2.2	0.012	0.000	41.81
400	0.5	0	2.45	2.3	0.34	2.37	50	3.1	0.71	0.000	38.23
600	0.51	0	3.1	2.6	0.4	2.80	48.9	3.3	0.82	0.000	37.58

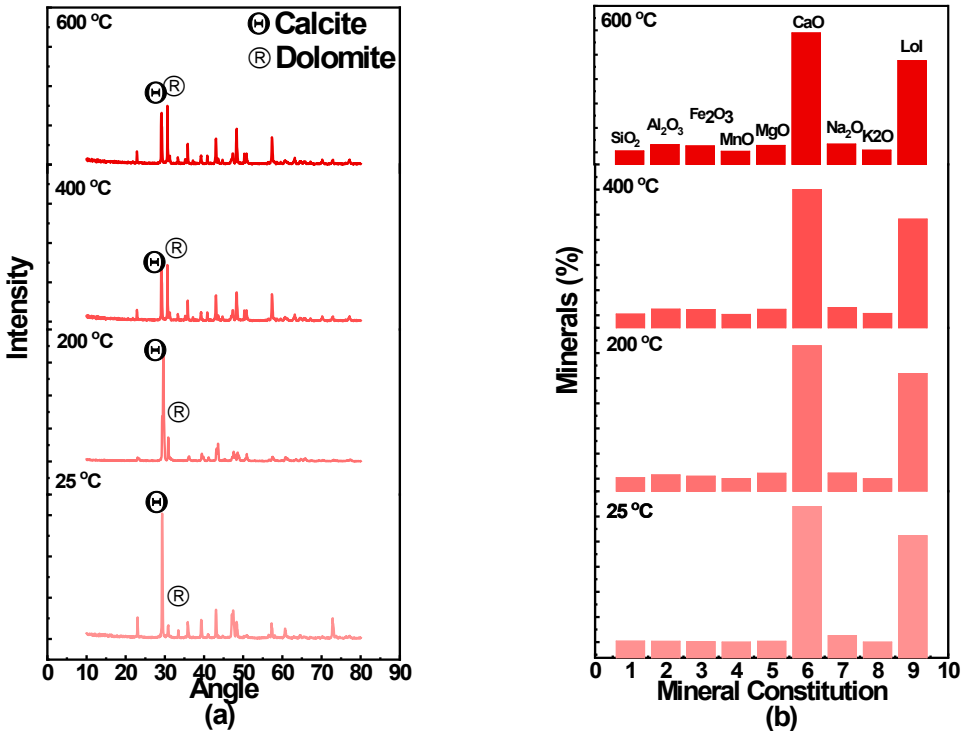

Figure 5. (**a**) The XRD peak at a different temperature and (**b**) the XRF analysis at different temperature ranges.

The XRD result shows that the rock is mainly composed of calcite and dolomite. The trends in Figure 5a,b show a decrease in the intensity of calcite as temperature increases. The increase in temperature also significantly increased the crystallite size that is determined using the Scherer formula. The result for different temperatures and crystallite size shows that the crystallite size increases with the increase in temperature, as presented graphically in Figure 6.

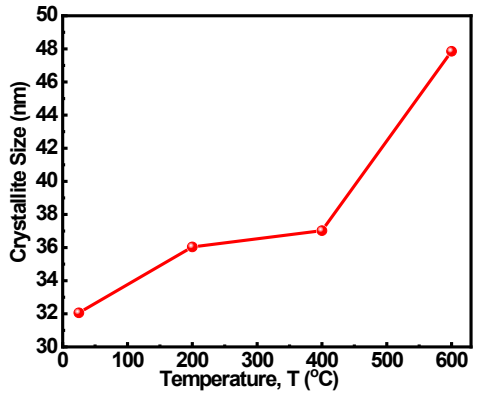

Figure 6. Crystallite size variation with temperature.

4.2. Micro Crack Analysis

The optical microscopy studies revealed that the grain of the marble is homogeneous. The samples are mainly composed of calcite and show the euhedral shape of crystals with perfect rhombohedral cleavages. Figure 5 depict that the calcite minerals and grain are considerably affected by thermal heat. The crack in the mineral and at the boundary of interlock increase with temperature as shown in Figure 7a, while minerals boundary and their interlock at high resolution were shown in Figure 7b. When temperature increases from 25 °C to 600 °C, more micro-cracks were produced, which also propagated along the

existing crack lengths. The samples at room temperature (25 °C), as shown in Figure 7a,b, contains no cracks and the grains are well cemented. While increasing the temperature from room temperature to 200 °C and 400 °C, the separation of some grains, more cracks, and, especially, micro-cracks at grain boundaries were observed in Figure 7a,b. Furthermore, when the temperature was increased to 600 °C, the trans-granular micro-cracks were detected, as shown in Figure 7a,b.

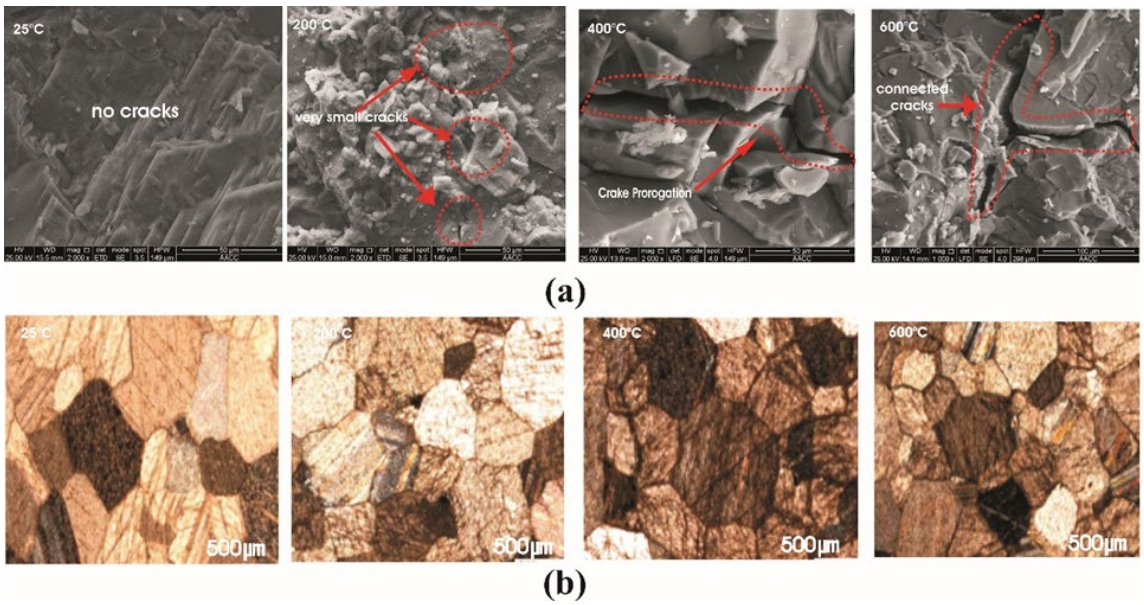

Figure 7. Optical microscopy at different temperatures. (**a**) SEM images for crack propagation; (**b**) Micrograph of the thin section.

4.3. P-Wave Analysis

The wave velocities traveled differently in the specimens at different temperatures, and this is shown in Figure 6. It can be seen from Figure 8 that the velocity of the wave travel decreases with the temperature increase. This decrease is due to the micro-crack generation, and to the existence of a crack and its extension in length, because wave velocity is sensitive to different mediums. When a crack occurred in rocks, the wave velocity spread slower in air than solid rocks, a pattern which is matched with the experimental results. The trend is presented in Figure 8.

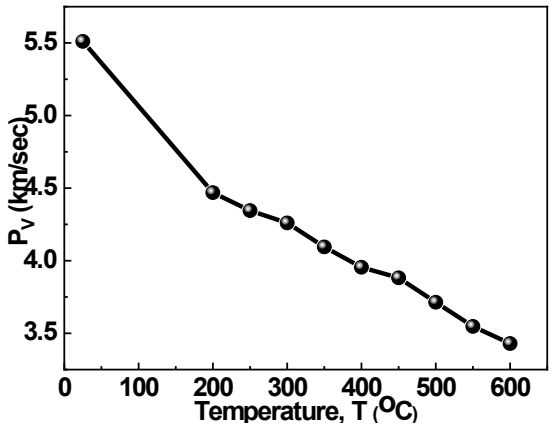

Figure 8. Longitudinal wave velocity variation with temperature.

4.4. Effect of Temperature on Stress–Strain Curve

The two parameters of rocks that play a significant role in engineering structure stability are UCS and E_S. The temperature effect on the stress–strain behaviors is shown in Figure 9a. A gradual increase in temperature has decreased both the UCS and E_S. Figure 9a shows the complete stress–strain curve at different temperatures. The pre-peak stress–strain is significantly influenced by temperature. Temperature variation illustrated a significant influence on stress–strain relations. The initial deformation of the non-linearity pattern increases in the stress–strain curve as the temperature increases. The stress–strain curves shape reveals that, as the temperature increases, the number of micro-cracks is increased and, as a result, the stress decreased. This is in agreement with the changes in material properties from brittle to ductile. The marble rock's overall ductility increases with the increase in thermal heat, showing a strong agreement with the results of [15].

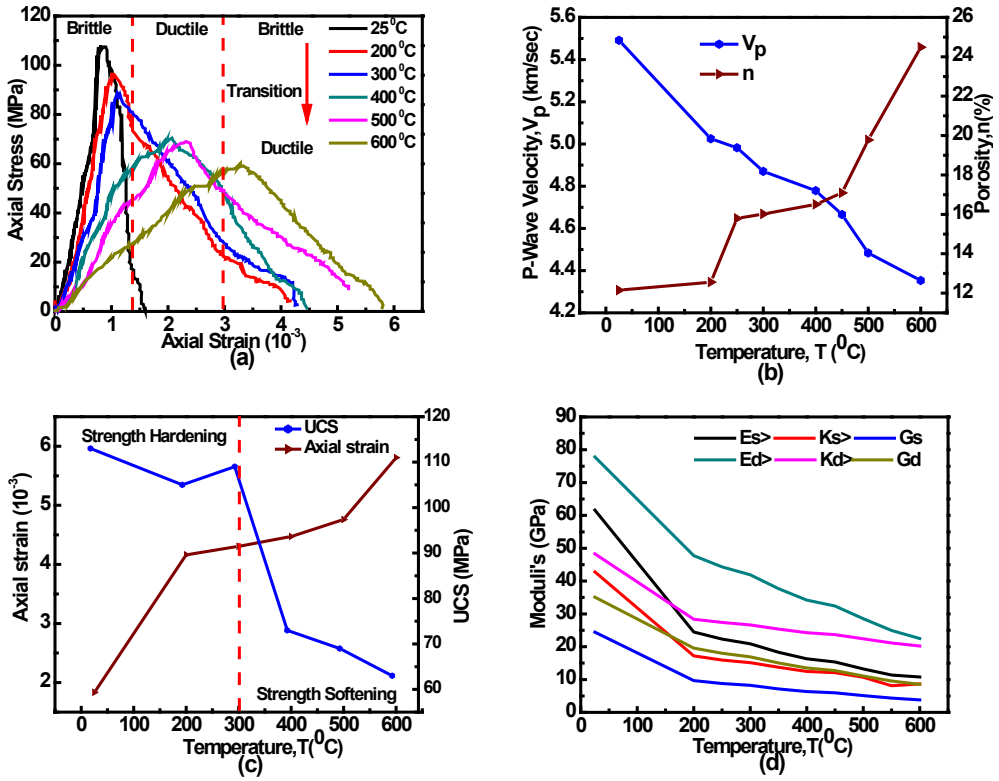

Figure 9. (**a**) Stress–strain curve, (**b**) porosity and PV curve, (**c**) UCS and strain curve and (**d**) all static and dynamic moduli at a different temperature.

The marble test results are summarized in Table 3. The result revealed the average UCS, E_S, P_V, and ρ inverse relation with the increase in temperature, while the strain, as well as η, shows a direct relationship, as indicated in Figure 9b,c. The value of UCS decreased at the temperature range of 25–200 °C, but showed an increase at 200–300 °C, which shows a resemblance to a previous study [70]. On the other hand, at temperatures above 300 °C, the UCS decreased again. The increase in η and decrease in P_V are in strong agreement with [71]. Overall, the E_S decreased with an increase in temperature, as shown in Figure 9d.

Table 3. Average physico-mechanical properties of marble rock.

S. No	T (°C)	P_V (km/s)	ρ (gr/cm^3)	n (%)	Dynamic Moduli			Static Moduli			Strain	UCS (MPa)
					E_d (GPa)	K_d (GPa)	G_d (GPa)	E_s (GPa)	K_s (GPa)	G_s (GPa)	ε_p (10^{-3})	
1	25	5.49	2.711	12.15	77.83	48.304	35.086	61.62	42.792	24.453	1.83	113
2	200	5.03	2.707	12.56	47.73	28.393	19.577	24.5	17.229	9.699	4.16	105
3	250	4.98	2.698	15.79	44.32	27.403	18.018	22.32	15.966	8.808	4.25	107
4	300	4.87	2.695	16.02	41.90	26.642	16.932	20.9	15.145	8.228	4.30	109
5	350	4.78	2.689	16.51	41.37	25.370	15.041	18.32	13.754	7.167	4.36	80
6	400	4.67	2.685	17.09	40.75	24.287	13.524	16.32	12.477	6.365	4.47	73
7	500	4.48	2.681	19.78	40.00	23.682	12.744	15.34	12.117	5.950	4.75	69
8	600	4.35	2.68	24.49	39.13	22.404	11.091	13.24	10.712	5.116	5.80	63

5. Prediction Models of UCS and ES

5.1. Preliminary Data Analysis

This study consists of the parameters T, $P_{V,}$ ρ, η, E_d, UCS, and E_s for machine learning and a statistical approach. The T, $P_{V,}$ ρ, η, E_d are used as input for the prediction of UCS and E_s. The statistical analysis of the inputs and outputs data is described in Table 4.

Table 4. Multiple linear regression model summaries for UCS and E_S.

Model	Variables	Coefficient	Std. Error	T	*p*-Value	R^2
UCS	C	186.017	95.212	1.954	0.056	0.905
	T(°C)	−0.116	0.013	−9.053	0.038	
	E_d (GPa)	−0.232	0.133	−1.747	0.086	
	η (%)	0.078	0.216	0.359	0.721	
	ρ (gr/cm^3)	−24.410	36.162	−0.675	0.502	
	P_V (km/sec)	2.694	2.898	0.930	0.356	
E_S	C	−164.932	108.981	−1.513	0.136	0.817
	T(°C)	0.003	0.015	0.235	0.036	
	E_d (GPa)	0.657	0.152	4.325	0.000	
	η (%)	−0.098	0.248	−0.397	0.693	
	ρ (gr/cm^3)	49.318	41.391	1.192	0.238	
	P_V (km/sec)	6.890	3.317	2.078	0.042	

A correlation matrix is a descriptive statistical tool that informs us about the variance and covariance of regressions that are included in the prediction model. It is often used in conjunction with other statistical matrices. Correlation, on the other hand, describes the regression variations with each other in predictive analysis. In general, the correlation matrix explains the variation of each variable. This can be shown in Figures 10 and 11 with correlation and pairwise correlation, respectively. This revealed that the inputs variables have negative relationship, positive relationship, and no relationship with outputs and each other. For example, temperature and density have a negative relationship, but this relationship is weak, P_V have a positive correlation, while other inputs and output have a negative correlation. Figures 10 and 11 enable a researcher to easily understand the effect of inputs on output results of the predicted model. The greater the negative or positive relationship, the greater will be the importance in model efficiency.

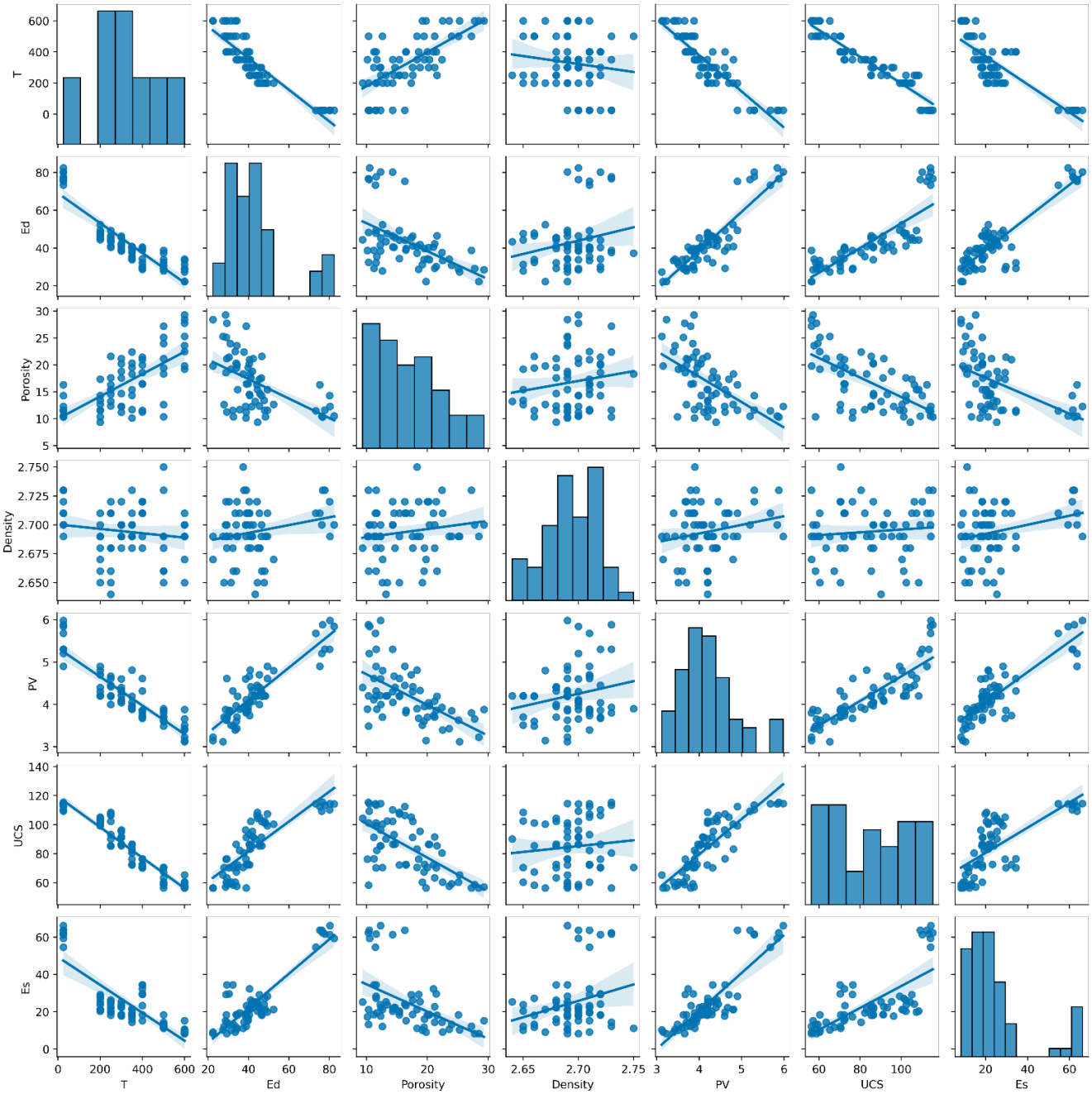

Figure 10. Pairwise correlation matrix and frequency distribution of inputs and outputs.

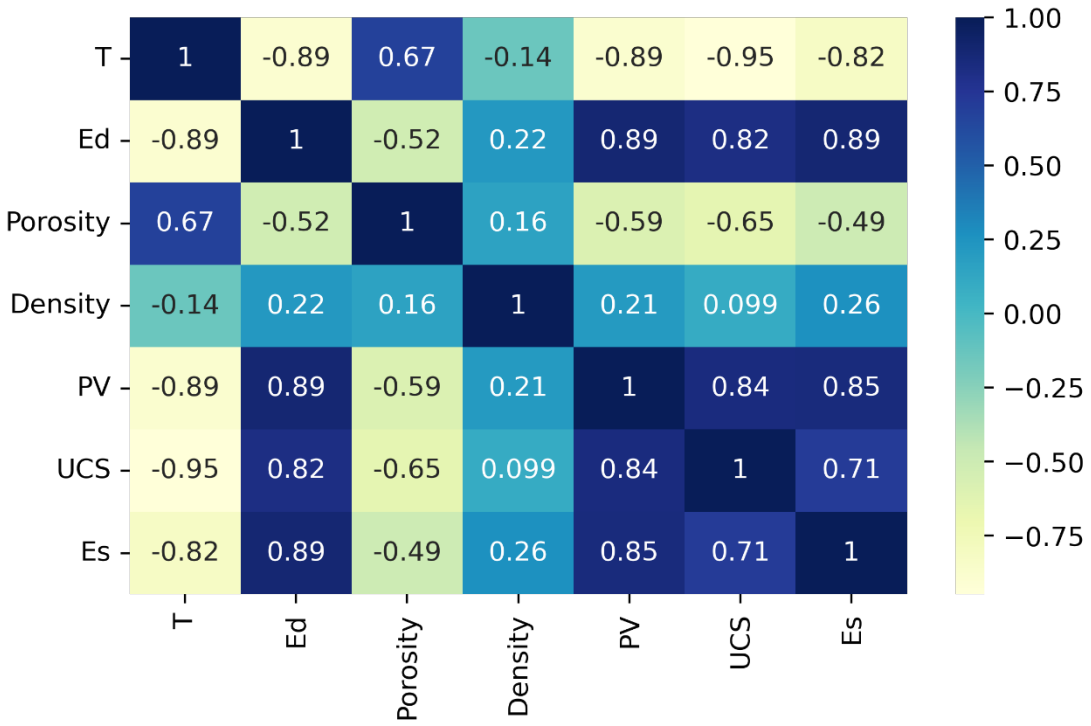

Figure 11. Correlation matrix of inputs and outputs.

5.2. MLR Prediction Models

Two different multilinear regression equations were developed for the prediction of UCS and E_s, respectively. These can be mathematically expressed using Equations (5) and (6), as follows:

$$UCS = 186.017 - 0.116T - 0.232E_d + 0.078\eta - 24.41\rho + 2.694P_v \quad (5)$$

$$E_s = -164.9 + 0.003T + 0.657E_d - 0.098\eta + 49.318\rho + 6.890P_v \quad (6)$$

where UCS is uniaxial compressive strength (Mpa) and E_s is the static Young's modulus (GPa), T is temperature (°C), E_d is the dynamic Young's modulus (GPa), η is porosity (%), ρ is density (gr/cm^3), and P_V is P-wave velocity (km/s).

The fundamental descriptive statistic of the original data is shown in Tables 3 and 4.

Importance of Variable in MLR Models

The MLR model for the UCS has a high coefficient of determination (R^2) between the actual and predicted UCS (R^2 = 0.90), as shown in Figure 12a. In the UCS model, out of five independent variables, two variables are highly correlated with UCS, namely T and P_V, and give a significant value less than (p = 0.05), while the other three parameters, namely ρ, η, and E_d, have less significance because of their P-value is greater than 0.05. The E_S model gives an effective coefficient of determination (R^2 = 0.817), as shown in Figure 12b. In this model, out of five parameters, the two parameters which are highly correlated with E_S are P_V with a significance value (p = 0.042), and T, with significance value (p = 0.036), while E_d is worthless. The other two variables, porosity and density, have a significance level more than 0.05, namely η (0.693) and ρ (0.238). These models revealed that the P_V and T have a dominant effect on both models of UCS and E_S, while the other three parameters have shown no obvious significance in both models.

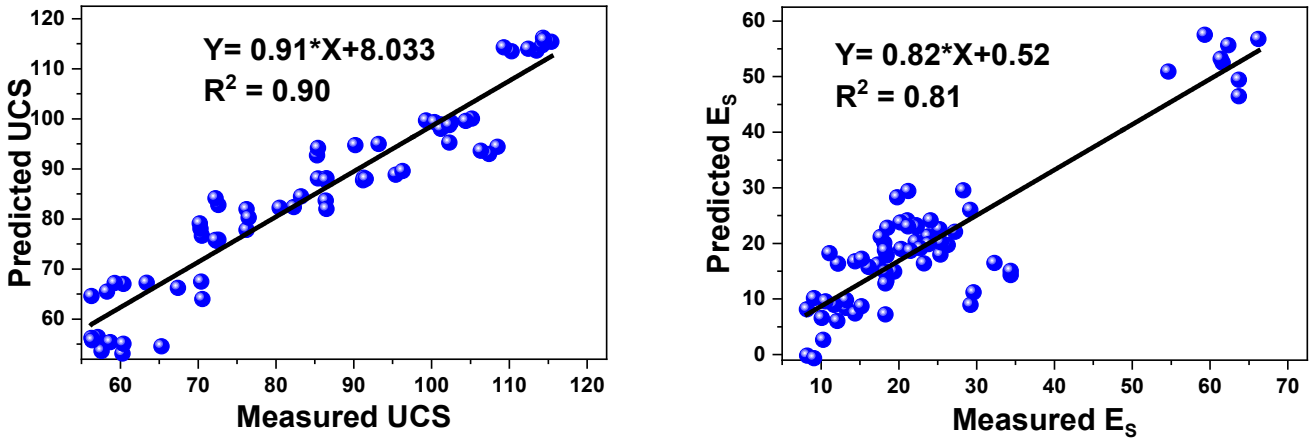

(**a**) UCS (**b**) Es

Figure 12. (**a**) Relationship between the predicted and actual UCS, (**b**) Relationship between the predicted and actual E_S.

5.3. Network Phases and Regression Model

Each phase of the ANN, i.e., training, validation, testing, and the regression values are shown in Figure 13a,b for the UCS and E_S models. The good regression is achieved in training and validation, and testing values between the predicted and measured values of UCS as shown in Figure 13b. In the case of E_S, the regression values of the predicted and measured show high validation regression values, as presented in Figure 13a. The plot draws from the ANN model are shown in Figure 14a,b. A good R^2 value (0.95) between the predicted and measured UCS is found as shown in Figure 14a. Figure 14b shows a relatively lesser coefficient of determination value (0.85) between predicted E_S and measured E_S, as compared to predicted and measured UCS.

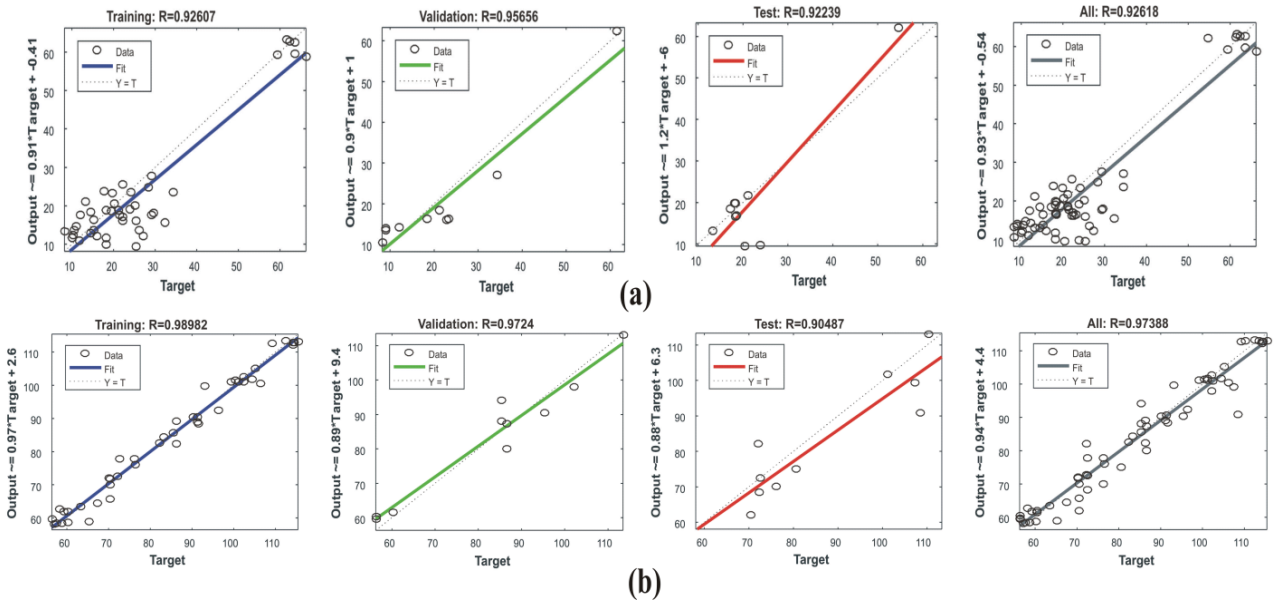

Figure 13. (**a**) The ANN phases of training, validation, and testing, and the regression coefficient for UCS, (**b**) The ANN phases of training, validation, and testing, and the regression coefficient for E_S.

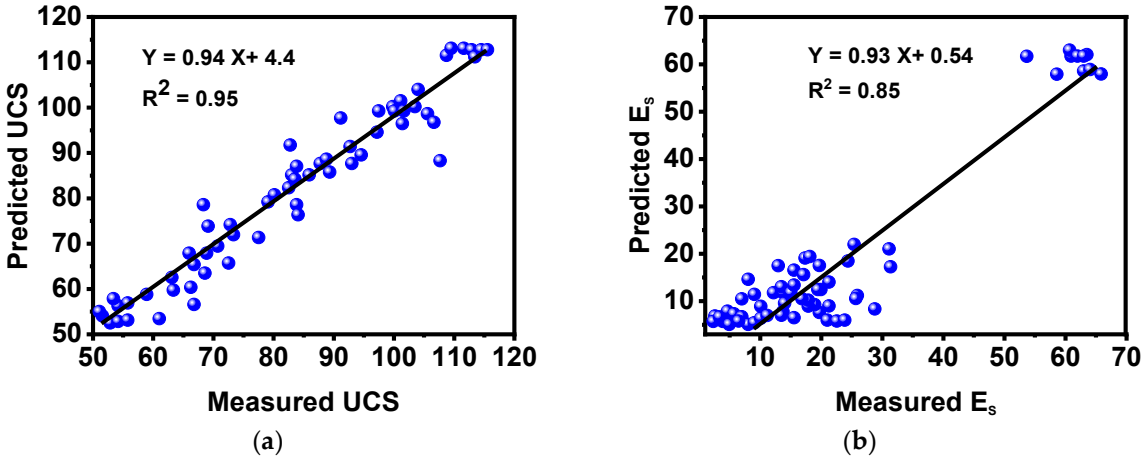

Figure 14. (**a**) The ANN scatter plot between the predicted and measured UCS and (**b**) scatter plot between the predicted and actual E_S.

5.3.1. Network Performance and Accuracy

The network performance and accuracy are evaluated by means of MSE (mean squared error) value. The MSE value decreases as the number iteration increased by increasing the neuron number of the hidden layer. For each model of UCS and E_S, the MSE is evaluated separately. The optimum regression model is achieved through a lesser MSE value at 250 and 300 epochs for UCS and E_S, respectively, as shown in Figures 15 and 16. This also revealed the number of iteration and number of neuron play key role in the accuracy achievement of the model. that The neuron convergence analysis shows that the optimum regression and least MSE for UCS and E_S are obtained on 5 and 7 neurons, respectively, as shown in Figure 17.

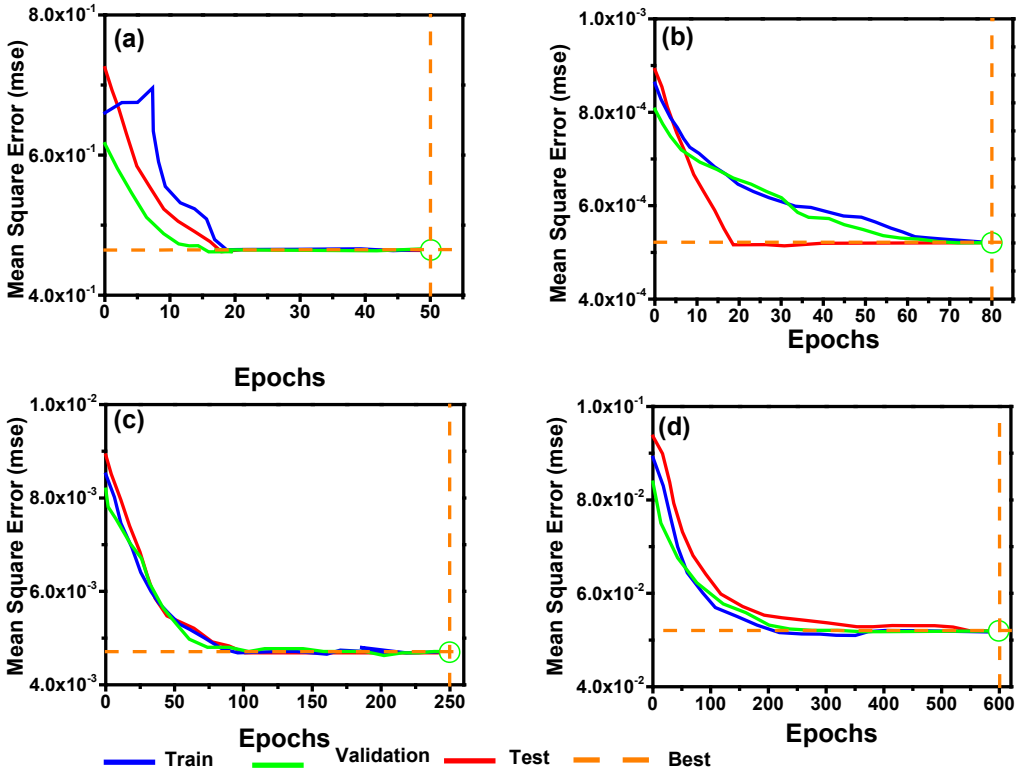

Figure 15. The UCS neural network performance for the selected network. (**a**) 50, (**b**) 80, (**c**) 250, and (**d**) 600.

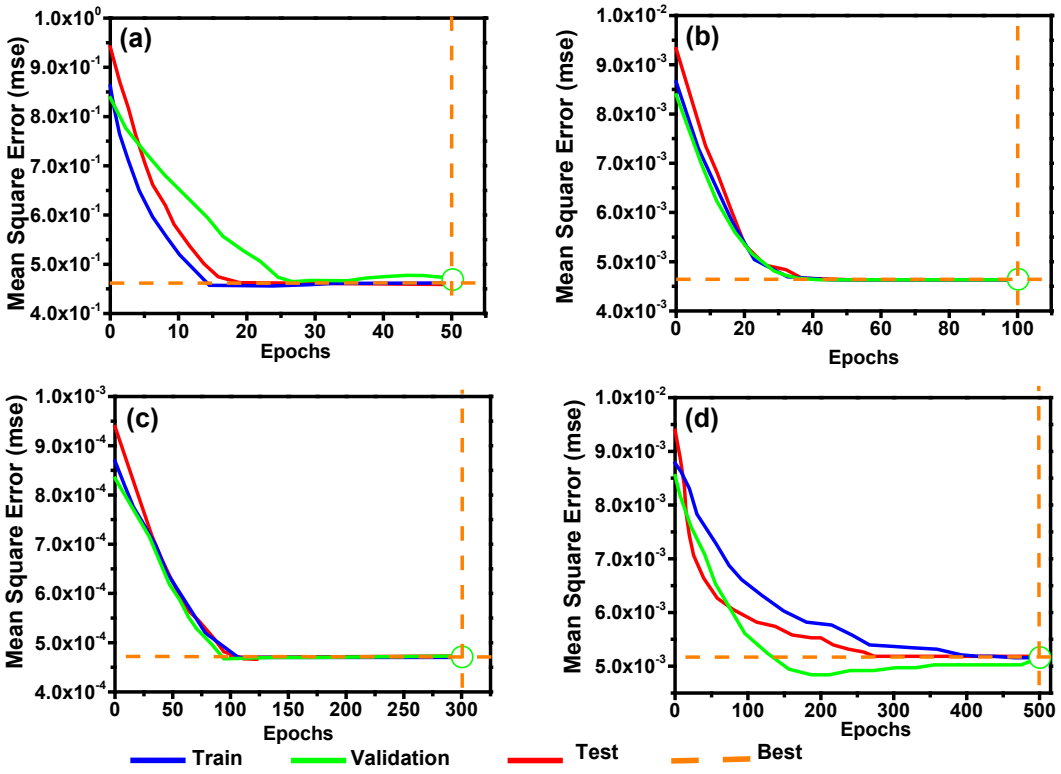

Figure 16. The E_S neural network performance for the selected network. (**a**) 50, (**b**) 100, (**c**) 300, and (**d**) 500.

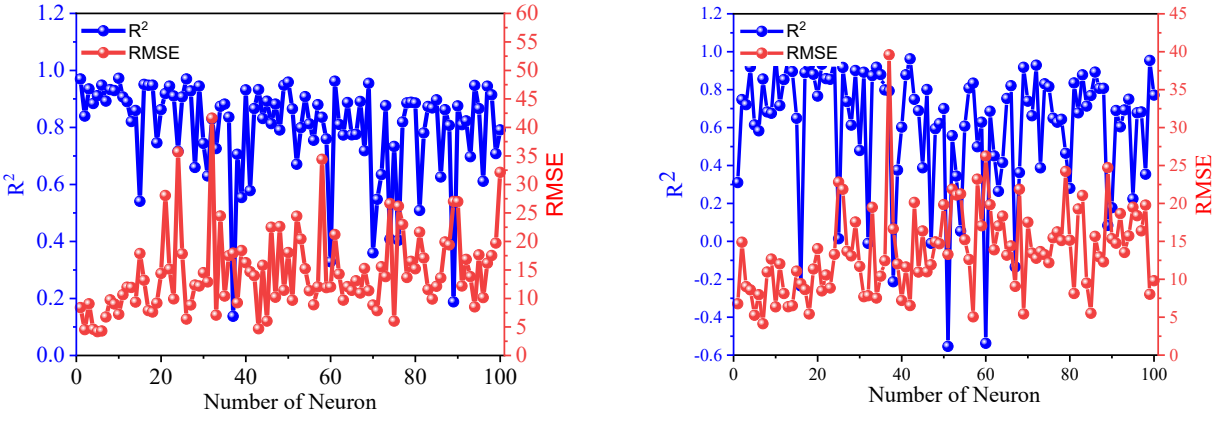

Figure 17. The optimum performance of network under different number of neurons; (**a**) UCS and (**b**) Es.

5.3.2. Importance of Variable in ANN Models

The importance of the ANN independent variable for UCS and E_S is shown in Figure 18a,b. In Figure 18a, it seems that the E_d, P_V, and T show a strong relation with E_S, while ρ and η show a weak relation to E_S. The independent variable, such as T, P_V, and E_d, have a strong relation with UCS, the most important of which is temperature, as shown in Figure 18b. Moreover, ρ and η have a very low relation to UCS.

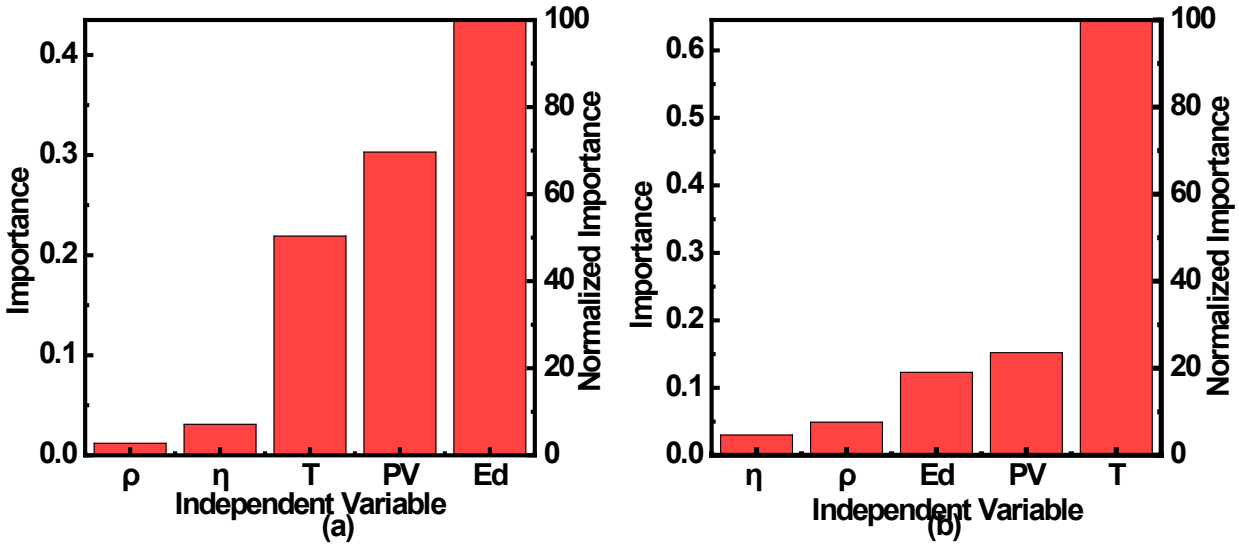

Figure 18. Independent variable importance chart from ANN model; (**a**) UCS, (**b**) E_S. Key is as follows: ρ density; η porosity; T: Temperature; Pv: p-wave velocity, and E_d: dynamic Young's modulus.

5.4. Random Forest

The Scikit-Learn package in Python was used to construct the random forest regression (RFR) and k-nearest neighbor's regression (KNN) models. It is a Python package that contains several different machine learning algorithms that are easily accessible for use in various applications. At the beginning of this research project, the data were normalized in order to adapt the values that were measured on various scales to a standard scale. After this, the models were trained on 70% of the data, and the remaining 30% of the data was split into two equal portions, namely the testing set (15%) and the validation set (15%). The hyperparameters were fine-tuned with the help of the testing set. In the RFR model, the hyperparameters, referred to as "n_estimators" and "max_depth", were subjected to a range of different values. Before calculating the maximum averages of predictions, the number of estimators refers to the number of decision trees that were constructed by the random forest regression model. The model becomes more computationally costly as the number of trees increases, but it also provides improved performance. The depth of each decision tree that makes up a random forest is represented by the maximum depth hyperparameters. The model is overfitted, since it was given a value for the maximum depth hyperparameter that was very high. The optimum value of n_estimators, max_depth, and random_state is described in Table 5. Furthermore, the predicted value at this optimum parameter's value has a high correlation coefficient (R^2 = 0.97) for USC and E_S, as shown in Figure 19.

Table 5. Optimized RFR hyperparameters.

Parameters	Values	Details
n_estimators	100	Number of trees in RFR
max_depth	12	Maximum depth of tree
random_state	32	Random state

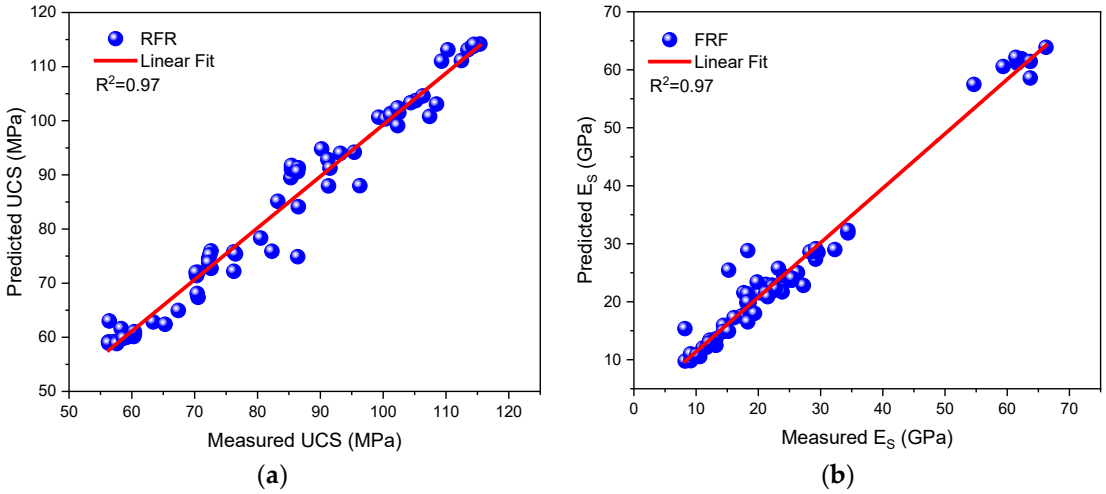

Figure 19. RFR Scatter plot between predicted and measured for UCS and E_S. (**a**) UCS; (**b**) E_S.

5.5. k-Nearest Neighbor

In the KNN model, the number of neighbors, denoted by the variable "n_neighbors," was subject to change. When making a forecast, the number of neighbors that should be included in the averaging process is specified by a hyperparameter referred to as the "number of neighbors." When the value of the n_neighbors hyperparameter is increased to a large number, the method becomes more accurate but also more computationally intensive. The grid search approach was used in order to arrive at the ideal values for the hyperparameters. The grid search approach determines the optimal combination by testing a broad variety of possible values for each hyperparameter that is being changed and then selecting one of those values. However, when working with huge datasets, it is computationally costly to pick the optimal combination of hyperparameters by selecting a broad range for each hyperparameter. This is done in order to maximize the accuracy of the results. In order to determine a workable range for each hyperparameter, the value was played about with on a number of different levels while the other hyperparameters remained the same. The range of values within which the "number of estimators" and "max depth" hyperparameters have an effect on the RFR model's performance. Table 6 has a description of the ideal combination of n neighbors and metric values. In addition, the projected value at this optimal value for the parameters has a good correlation coefficient (R^2 = 0.94), as can be shown in Figure 20. This is the case for both USC and E_S.

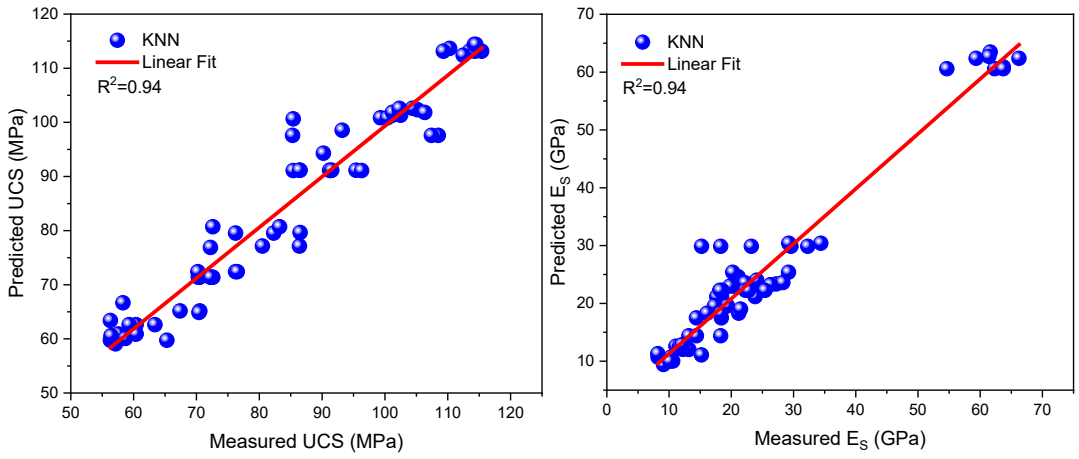

Figure 20. The KNN scatter plot between predicted and measured for UCS and E_S.

Table 6. Optimized KNN hyperparameters.

Parameters	Values	Descriptions
n_neighbors	5	Number neighbors
Metric	Minkowski	The distance metric to use

6. A Comparative Evaluation of Statistics and Intelligent Techniques

The comparison of correlation efficiencies of various developed models was used in this study to improve the performance of predicted models. Through this comparison, the subsequent performance indices, such as R^2, MAPE, RMSE, and VAF, were evaluated. An excellent model can be represented by performance indices as, R^2 = 1, MAPE = RMSE = 0, and VAF = 100%. The performance indices were calculated using Equations (7)–(10), as follows:

$$R^2 = \frac{\sum_{i=1}^{n} (y_i)^2 - \sum_{i=1}^{n} (y_i - k_i')^2}{\sum_{i=1}^{n} (y_i)^2} \quad (7)$$

$$MAPE = \frac{1}{2} \sum_{i=1}^{n} \left| \frac{y_i - k_i'}{y_i} \right| \times 100 \quad (8)$$

$$RMSE = \sqrt{\frac{\sum_{i=1}^{n} (y_i - k_i')}{n}} \quad (9)$$

$$VAF = \left[1 - \frac{var(y - k')}{var(y)} \right] x\ 100 \quad (10)$$

where, y is the actual value, and k' is the predicted value.

Table 7 describe the performance indices of all models. This shows that the MLR gives a lower coefficient of determination for both predicted parameters, while RFR gives a high coefficient of determination for UCS and E_S. On the basis of this performance indices, the RFR performed well.

Table 7. Performance indices of the developed models.

Predicted Paramter	Models	R^2	MSE	MAPE (%)	VAF (%)
UCS	MLR	0.90	23.15	31.53	90.23
	ANN	0.94	0.14	1.18	94.23
	RFR	0.97	2.04	0.25	97.22
	KNN	0.94	3.02	0.94	94.01
E_S	MLR	0.81	27.15	34.53	81.02
	ANN	0.86	0.54	2.18	86.03
	RFR	0.97	2.04	0.25	97.22
	KNN	0.94	3.02	0.94	94.23

7. Discussion

(1) Predictive models were developed for UCS and E_S based on statistical (MLR) and intelligent models (ANNs, RFR, and KNN). The accuracy and performance of models are satisfactory on the basis of MSE, MAPE, VAF, and R^2. The MSE, MAPE, VAF of the MLR is greater than that of the intelligent models. The intelligent models have shown a better prediction performance than the statistical model due to its MSE, MAPE, VAF values and high R^2 value. The MSE, MAPE, VAF, R^2 values of the MLR are fixed, while the MSE, MAPE, VAF and R^2 of the intelligent model are varied. It depends on the neuron optimization in the hidden layer for ANN and the hyperparameters. The MSE, MAPE, and VAF of a prediction model can improve through trial and error methods using an intelligent model. The intelligent model's optimization needs an expert person who can know the

tuning the of hyperparameters number, and how to fine-tune hyperparameters to obtain more reliable results.

(2) The intelligent models with high correlation for UCS and E_S respectively are better, as shown in Figure 14a,b, Figure 19a,b, and Figure 20a,b, than MLR. In this research work, ANN gives 5% for UCS and 4% for E_S, RFR give 7% for UCS and 16% for E_S, and gives 4% for UCS and 13% for E_S, meaning that the intelligent model is more accurate than the MLR. Furthermore, RFR give 7% for UCS and 16% for E_S, which is more accurate than the statistical model and has 4-5% high accuracy than ANN and KNN. The models are based on limited data and only valid to a specific area. The models can extend to a generalized form in the future to take a large amount of data on different rocks. Temperature and P-wave velocity are strongly correlated in both models. The three other input parameters play a worthless role in the equation. This work result is strongly supported by existing research [35]. It suggested P_V, ρ, and η as input variables and, after prediction, revealed that only P-wave velocity has a strong correlation, and the other input variables have a worthless contribution. This study is based on thermal effect; therefore, the temperature is considered as an input parameter that has a strong influence on the mechanical and physical properties of rock. Furthermore, in these modes, the temperature and P-wave velocity both have a strong correlation with output, and the other three independent parameters are meaningless in the model. The performance of this model is better than in the model developed by Torabi-Kaveh, Naseri, Saneie, and Sarshari [26].

(3) After a comparative analysis of results obtained from MLR and the intelligent model, it is concluded that the intelligent model gives effective results as compared to MLR in predicting UCS and E_S. The variable performance in both MLR and the intelligent model shows that the T and P_V played an active role in the prediction models, while the ρ, η, and E_d have a less active predictive role.

(4) An important factor in marble's anisotropic behaviour is its temperature state, which may directly influence the material's characteristics and cause the cohesiveness along the grain boundary to weaken [15]. Although anisotropy has a significant impact on the physico-mechanical behaviour of intact and discontinuous geomaterials, it is often neglected in day-to-day geoengineering practice. This is despite the fact that it is an essential property. The presumption that anisotropic rocks have isotropic properties can primarily be explained by the following factors: (i) the complicated structure of anisotropic elasticity theory; (ii) the increased number of moduli required to describe the deformational behaviour of anisotropic materials; (iii) the significant challenges associated with the reliable sampling and testing of anisotropic geomaterials; (iv) the inherent difficulties of back analysis methodologies related to anisotropic rock. There are extremely few examples of completely isotropic rocks and soils in the natural world. Numerous rock properties, such as thermal conductivity, coefficient of thermal expansion, and other physical (electrical, magnetic, etc.) characteristics, as well as the deformational and strength characteristics of soils and rocks, may be directionally reliant on antecedent endogenetic (primary) or exogenetic (secondary) causes that occur at micro-, meso-, and macroscales. This may be the case for many rock properties, including thermal conductivity, coefficient of thermal expansion, and other physical properties (electrical, magnetic, etc). The former refers to the processes of sedimentation, compaction, and lithification that are responsible for the formation of sedimentary rock formations (such as limestones, sandstones, and other similar rocks), whereas the latter refers to environmental factors, such as pressure, temperature, chemical solutions, and other similar elements that are also responsible for the transformation of various rock types (i.e., diagenesis, metamorphosis, weathering, etc.). Crystallographic preferred orientations (textures) of the rock components, grain shape fabric, and microcrack fabric are principally responsible for influencing the anisotropic physical features of intact rocks at the microscopic and mesoscopic scales, respectively. At the macroscopic level, the anisotropic character of discontinuous rocks is reflected in the foliation, cleavage, and fractures that make up these rocks [71]. The influence of anisotropic characteristics will be

taken into consideration in the prediction model that uses computer tomography in the near future.

8. Conclusions

The following conclusions are drawn from the research:

1. The physical and mechanical properties are greatly affected by the increase in temperature from 200–600 °C due to the generation and propagation of micro-cracks. The porosity is increased, while P_V is decreased with the increase in temperature. The strength properties i.e., UCS and E_S, of rock also decrease with the increasing temperature;
2. The behavior of the stress–strain curve is changed from brittle to ductile when the temperature is increased;
3. The MLR predictive models for UCS and E_S give a performance coefficient of 0.90% and 0.81%, respectively. The intelligent models i.e., ANN, RFR, and KNN for UCS and E_S give a performance coefficient, revealing that the model for UCS is (5–7%) and E_S is (4–16%) better than the statistical model (MRL models).
4. The model's important feature revealed that the temperature and P_V have a significant role in prediction models;
5. Based on comparative analysis of MLR, ANN, RFR, and KNN, it has been proposed that RFR model is suitable for use in the prediction of UCS and E_S under thermal treatment.

Author Contributions: N.M.K. and S.H. contributed to the research, designed experiments and wrote the paper. Q.Y. and M.Z.E. conceived this research and were responsible for the research. H.R. supervised this study. M.H.B.M.H. and K.C. contributed in the original as well as in the revised version of the manuscript. H.R., S.K., K.S.S. and B.U. reviewed and revised the paper. All authors have read and agreed to the published version of the manuscript.

Funding: This research received no external funding.

Informed Consent Statement: Not applicable.

Data Availability Statement: All the data and models employed and/or generated during the study appear in the submitted article.

Conflicts of Interest: The authors declare no conflict of interest.

References

1. Qin, Y.; Tian, H.; Xu, N.-X.; Chen, Y. Physical and mechanical properties of granite after high-temperature treatment. *Rock Mech. Rock Eng.* **2020**, *53*, 305–322. [CrossRef]
2. Vagnon, F.; Colombero, C.; Colombo, F.; Comina, C.; Ferrero, A.M.; Mandrone, G.; Vinciguerra, S.C. Effects of thermal treatment on physical and mechanical properties of Valdieri Marble-NW Italy. *Int. J. Rock Mech. Min. Sci.* **2019**, *116*, 75–86. [CrossRef]
3. Gautam, P.; Verma, A.; Jha, M.; Sharma, P.; Singh, T.N. Effect of high temperature on physical and mechanical properties of Jalore granite. *J. Appl. Geophys.* **2018**, *159*, 460–474. [CrossRef]
4. Lin, K.; Huang, W.; Finkelman, R.B.; Chen, J.; Yi, S.; Cui, X.; Wang, Y.J. Distribution, modes of occurrence, and main factors influencing lead enrichment in Chinese coals. *Int. J. Coal Sci. Technol.* **2020**, *7*, 1–18. [CrossRef]
5. Liu, S.; Tan, F.; Huo, T.; Tang, S.; Zhao, W.; Chao, H.J. Origin of the hydrate bound gases in the Juhugeng Sag, Muli Basin, Tibetan Plateau. *Int. J. Coal Sci. Technol.* **2020**, *7*, 43–57. [CrossRef]
6. Chen, L.; Mao, X.; Wu, P. Effect of High Temperature and Inclination Angle on Mechanical Properties and Fracture Behavior of Granite at Low Strain Rate. *Sustainability* **2020**, *12*, 1255. [CrossRef]
7. Zhang, W.; Wang, T.; Zhang, D.; Tang, J.; Xu, P.; Duan, X. A Comprehensive Set of Cooling Measures for the Overall Control and Reduction of High Temperature-Induced Thermal Damage in Oversize Deep Mines: A Case Study. *Sustainability* **2020**, *12*, 2489. [CrossRef]
8. Gomah, M.E.; Li, G.; Sun, C.; Xu, J.; Yang, S.; Li, J. On the Physical and Mechanical Responses of Egyptian Granodiorite after High-Temperature Treatments. *Sustainability* **2022**, *14*, 4632. [CrossRef]
9. Meng, Q.-B.; Wang, C.-K.; Liu, J.-F.; Zhang, M.-W.; Lu, M.-M.; Wu, Y. Physical and micro-structural characteristics of limestone after high temperature exposure. *Bull. Eng. Geol. Environ.* **2020**, *79*, 1259–1274. [CrossRef]
10. Lian, X.; Hu, H.; Li, T.; Hu, D. Main geological and mining factors affecting ground cracks induced by underground coal mining in Shanxi Province, China. *Int. J. Coal Sci. Technol.* **2020**, *7*, 362–370. [CrossRef]

11. Zuo, J.; Wang, J.; Jiang, Y. Macro/meso failure behavior of surrounding rock in deep roadway and its control technology. *Int. J. Coal Sci. Technol.* **2019**, *6*, 301–319. [CrossRef]
12. Barla, G. Comprehensive study including testing, monitoring and thermo-hydro modelling for design and implementation of a geothermal system in Torino (Italy). *Geomech. Geophys. Geo-Energy Geo-Resour.* **2017**, *3*, 175–188. [CrossRef]
13. Breede, K.; Dzebisashvili, K.; Liu, X.; Falcone, G. A systematic review of enhanced (or engineered) geothermal systems: Past, present and future. *Geotherm. Energy* **2013**, *1*, 4. [CrossRef]
14. Homand-Etienne, F.; Houpert, R. Thermally induced microcracking in granites: Characterization and analysis. *Int. J. Rock Mech. Min. Sci. Geomech. Abstr.* **1989**, *26*, 125–134. [CrossRef]
15. Peng, J.; Rong, G.; Cai, M.; Yao, M.-D.; Zhou, C.-B. Physical and mechanical behaviors of a thermal-damaged coarse marble under uniaxial compression. *Eng. Geol.* **2016**, *200*, 88–93. [CrossRef]
16. Ferreira, A.P.G.; Farage, M.C.; Barbosa, F.S.; Noumowé, A.; Renault, N. Thermo-hydric analysis of concrete–rock bilayers under fire conditions. *Eng. Struct.* **2014**, *59*, 765–775. [CrossRef]
17. Tang, Z.C.; Sun, M.; Peng, J. Influence of high temperature duration on physical, thermal and mechanical properties of a fine-grained marble. *Appl. Therm. Eng.* **2019**, *156*, 34–50. [CrossRef]
18. Jansen, D.P.; Carlson, S.R.; Young, R.P.; Hutchins, D.A. Ultrasonic imaging and acoustic emission monitoring of thermally induced microcracks in Lac du Bonnet granite. *J. Geophys. Res. Solid Earth* **1993**, *98*, 22231–22243. [CrossRef]
19. Dwivedi, R.D.; Goel, R.K.; Prasad, V.V.R.; Sinha, A. Thermo-mechanical properties of Indian and other granites. *Int. J. Rock Mech. Min. Sci.* **2008**, *45*, 303–315. [CrossRef]
20. Zhao, Y.; Wan, Z.; Feng, Z.; Yang, D.; Zhang, Y.; Qu, F. Triaxial compression system for rock testing under high temperature and high pressure. *Int. J. Rock Mech. Min. Sci.* **2012**, *52*, 132–138. [CrossRef]
21. Wong, T.-F. Effects of temperature and pressure on failure and post-failure behavior of Westerly granite. *Mech. Mater.* **1982**, *1*, 3–17. [CrossRef]
22. Chaki, S.; Takarli, M.; Agbodjan, W.P. Influence of thermal damage on physical properties of a granite rock: Porosity, permeability and ultrasonic wave evolutions. *Constr. Build. Mater.* **2008**, *22*, 1456–1461. [CrossRef]
23. Lion, M.; Skoczylas, F.; Ledésert, B. Effects of heating on the hydraulic and poroelastic properties of bourgogne limestone. *Int. J. Rock Mech. Min. Sci.* **2005**, *42*, 508–520. [CrossRef]
24. Malaga-Starzec, K.; Åkesson, U.; Lindqvist, J.E.; Schouenborg, B. Microscopic and macroscopic characterization of the porosity of marble as a function of temperature and impregnation. *Constr. Build. Mater.* **2006**, *20*, 939–947. [CrossRef]
25. Chen, Y.-L.; Ni, J.; Shao, W.; Azzam, R. Experimental study on the influence of temperature on the mechanical properties of granite under uni-axial compression and fatigue loading. *Int. J. Rock Mech. Min. Sci.* **2012**, *56*, 62–66. [CrossRef]
26. Torabi-Kaveh, M.; Naseri, F.; Saneie, S.; Sarshari, B. Application of artificial neural networks and multivariate statistics to predict UCS and E using physical properties of Asmari limestones. *Arab. J. Geosci.* **2015**, *8*, 2889–2897. [CrossRef]
27. Heidari, M.; Khanlari, G.; Momeni, A. Prediction of Elastic Modulus of Intact Rocks Using Artificial Neural Networks and non-Linear Regression Methods. *Aust. J. Basic Appl. Sci.* **2010**, *4*, 5869–5879.
28. Abdi, Y.; Garavand, A.T.; Sahamieh, R.Z. Prediction of strength parameters of sedimentary rocks using artificial neural networks and regression analysis. *Arab. J. Geosci.* **2018**, *11*, 587. [CrossRef]
29. Tariq, Z.; Elkatatny, S.; Mahmoud, M.; Ali, A.Z.; Abdulraheem, A. A new approach to predict failure parameters of carbonate rocks using artificial intelligence tools. In Proceedings of the SPE Kingdom of Saudi Arabia Annual Technical Symposium and Exhibition, Dammam, Saudi Arabia, 24–27 April 2017.
30. Manouchehrian, A.; Sharifzadeh, M.; Moghadam, R. Application of artificial neural networks and multivariate statistics to estimate UCS using textural characteristics. *Int. J. Min. Sci. Technol.* **2012**, *22*, 229–236. [CrossRef]
31. Dehghan, S.; Sattari, G.; Chehreh Chelgani, S.; Aliabadi, M.A. Prediction of uniaxial compressive strength and modulus of elasticity for Travertine samples using regression and artificial neural networks. *Min. Sci. Technol.* **2010**, *20*, 41–46. [CrossRef]
32. Zhang, J.; Ma, G.; Huang, Y.; Aslani, F.; Nener, B.J. Modelling uniaxial compressive strength of lightweight self-compacting concrete using random forest regression. *Constr. Build. Mater.* **2019**, *210*, 713–719. [CrossRef]
33. Matin, S.; Farahzadi, L.; Makaremi, S.; Chelgani, S.C.; Sattari, G. Variable selection and prediction of uniaxial compressive strength and modulus of elasticity by random forest. *Appl. Soft Comput.* **2018**, *70*, 980–987. [CrossRef]
34. Suthar, M. Applying several machine learning approaches for prediction of unconfined compressive strength of stabilized pond ashes. *Neural Comput. Appl.* **2020**, *32*, 9019–9028. [CrossRef]
35. Wang, M.; Wan, W.; Zhao, Y. Prediction of the uniaxial compressive strength of rocks from simple index tests using a random forest predictive model. *Comptes Rendus Mec.* **2020**, *348*, 3–32. [CrossRef]
36. Ren, Q.; Wang, G.; Li, M.; Han, S. Prediction of rock compressive strength using machine learning algorithms based on spectrum analysis of geological hammer. *Geotech. Geol. Eng.* **2019**, *37*, 475–489. [CrossRef]
37. Ghasemi, E.; Kalhori, H.; Bagherpour, R.; Yagiz, S. Model tree approach for predicting uniaxial compressive strength and Young's modulus of carbonate rocks. *Bull. Eng. Geol. Environ.* **2018**, *77*, 331–343. [CrossRef]
38. Saedi, B.; Mohammadi, S.D.; Shahbazi, H. Prediction of uniaxial compressive strength and elastic modulus of migmatites using various modeling techniques. *Arab. J. Geosci.* **2018**, *11*, 574. [CrossRef]
39. Shahani, N.M.; Zheng, X.; Liu, C.; Hassan, F.U.; Li, P. Developing an XGBoost Regression Model for Predicting Young's Modulus of Intact Sedimentary Rocks for the Stability of Surface and Subsurface Structures. *Front. Earth Sci.* **2021**, *9*, 761990. [CrossRef]

40. Armaghani, D.J.; Tonnizam Mohamad, E.; Momeni, E.; Monjezi, M.; Sundaram Narayanasamy, M. Prediction of the strength and elasticity modulus of granite through an expert artificial neural network. *Arab. J. Geosci.* **2016**, *9*, 48. [CrossRef]
41. Larson, K.P.; Ali, A.; Shrestha, S.; Soret, M.; Cottle, J.M.; Ahmad, R. Timing of metamorphism and deformation in the Swat valley, northern Pakistan: Insight into garnet-monazite HREE partitioning. *Geosci. Front.* **2019**, *10*, 849–861. [CrossRef]
42. Fahad, M.; Iqbal, Y.; Riaz, M.; Ubic, R.; Abrar, M. Geo-mechanical properties of marble deposits from the Nikani Ghar and Nowshera formations of the Lesser Himalayas, Northern Pakistan—A review Himal. *Himal. Geol.* **2016**, *37*, 17–27.
43. DiPietro, J.A.; Ahmad, I.; Hussain, A. Cenozoic kinematic history of the Kohistan fault in the Pakistan Himalaya. *Geol. Soc. Am. Bull.* **2008**, *120*, 1428–1440. [CrossRef]
44. Hussain, A.; Dipietro, J.; Pogue, K.; Ahmed, I. *Geologic Map of 43-B Degree Sheet of NWFP, Pakistan*; Geological Map Series; Geological Survey of Pakistan: Peshawar, Pakistan, 2004.
45. Hatheway, A.W. The complete ISRM suggested methods for rock characterization, testing and monitoring; 1974–2006. *Environ. Eng. Geosci.* **2009**, *15*, 47–48. [CrossRef]
46. Fairhurst, C.; Hudson, J. Draft ISRM suggested method for the complete stress-strain curve for intact rock in uniaxial compression. *Int. J. Rock Mech. Min. Sci.* **1999**, *36*, 279–289.
47. Garson, G.D. *Multiple Regression*; Statistical Associates Publishers: Fargo, ND, USA, 2014.
48. Cohen, J.; Cohen, P.; West, S.S.; Aiken, L. *Applied Multiple Regression/Correlation Analysis for the Behavioral Sciences*; Routledge: New York, NY, USA, 2002.
49. Roy, M.; Singh, P. Application of artificial neural network in mining industry. *Indian Min. Eng. J.* **2004**, *43*, 19–23.
50. Lawal, A.I.; Aladejare, A.E.; Onifade, M.; Bada, S.; Idris, M.A. Predictions of elemental composition of coal and biomass from their proximate analyses using ANFIS, ANN and MLR. *Int. J. Coal Sci. Technol.* **2021**, *8*, 124–140. [CrossRef]
51. Aboutaleb, S.; Behnia, M.; Bagherpour, R.; Bluekian, B. Using non-destructive tests for estimating uniaxial compressive strength and static Young's modulus of carbonate rocks via some modeling techniques. *Bull. Eng. Geol. Environ.* **2018**, *77*, 1717–1728. [CrossRef]
52. Atkinson, P.M.; Tatnall, A. Introduction neural networks in remote sensing. *Int. J. Remote Sens.* **1997**, *18*, 699–709. [CrossRef]
53. Lee, S.; Ha, J.; Zokhirova, M.; Moon, H.; Lee, J. Background Information of Deep Learning for Structural Engineering. *Arch. Comput. Methods Eng.* **2018**, *25*, 121–129. [CrossRef]
54. Facchini, L.; Betti, M.; Biagini, P. Neural network based modal identification of structural systems through output-only measurement. *Comput. Struct.* **2014**, *138*, 183–194. [CrossRef]
55. Ham, F.K.I. *Principles of Neurocomputing for Science and Engineering*; McGraw-Hill Education Europe: London, UK, 2001; p. 642.
56. Sonmez, H.; Gokceoglu, C.; Nefeslioglu, H.A.; Kayabasi, A. Estimation of rock modulus: For intact rocks with an artificial neural network and for rock masses with a new empirical equation. *Int. J. Rock Mech. Min. Sci.* **2006**, *43*, 224–235. [CrossRef]
57. Ceryan, N.; Okkan, U.; Kesimal, A. Prediction of unconfined compressive strength of carbonate rocks using artificial neural networks. *Environ. Earth Sci.* **2013**, *68*, 807–819. [CrossRef]
58. Ullah, H.; Khan, I.; AlSalman, H.; Islam, S.; Asif Zahoor Raja, M.; Shoaib, M.; Gumaei, A.; Fiza, M.; Ullah, K.; Mizanur Rahman, S.M.; et al. Levenberg–Marquardt Backpropagation for Numerical Treatment of Micropolar Flow in a Porous Channel with Mass Injection. *Complexity* **2021**, *2021*, 5337589. [CrossRef]
59. Rao, A.R.; Kumar, B. Neural Modeling of Square Surface Aerators. *J. Environ. Eng.* **2007**, *133*, 411–418. [CrossRef]
60. Qi, C.; Fourie, A.; Du, X.; Tang, X. Prediction of open stope hangingwall stability using random forests. *Nat. Hazards* **2018**, *92*, 1179–1197. [CrossRef]
61. Breiman, L. Random forests. *Mach. Learn.* **2001**, *45*, 5–32. [CrossRef]
62. Qi, C.; Tang, X. Slope stability prediction using integrated metaheuristic and machine learning approaches: A comparative study. *Comput. Ind. Eng.* **2018**, *118*, 112–122. [CrossRef]
63. Qi, C.; Fourie, A.; Ma, G.; Tang, X.; Du, X. Comparative study of hybrid artificial intelligence approaches for predicting hangingwall stability. *J. Comput. Civ. Eng.* **2018**, *32*, 04017086. [CrossRef]
64. Kuhn, M.; Johnson, K. *Applied Predictive Modeling*; Springer: Berlin/Heidelberg, Germany, 2013; Volume 26.
65. Wu, X.; Kumar, V.; Ross Quinlan, J.; Ghosh, J.; Yang, Q.; Motoda, H.; McLachlan, G.J.; Ng, A.; Liu, B.; Yu, P.S.; et al. Top 10 algorithms in data mining. *Knowl. Inf. Syst.* **2008**, *14*, 1–37. [CrossRef]
66. Akbulut, Y.; Sengur, A.; Guo, Y.; Smarandache, F. NS-k-NN: Neutrosophic Set-Based k-Nearest Neighbors Classifier. *Symmetry* **2017**, *9*, 179. [CrossRef]
67. Qian, Y.; Zhou, W.; Yan, J.; Li, W.; Han, L. Comparing Machine Learning Classifiers for Object-Based Land Cover Classification Using Very High Resolution Imagery. *Remote Sens.* **2015**, *7*, 153–168. [CrossRef]
68. Yang, S.-Q.; Ranjith, P.; Jing, H.-W.; Tian, W.-L.; Ju, Y. An experimental investigation on thermal damage and failure mechanical behavior of granite after exposure to different high temperature treatments. *Geothermics* **2017**, *65*, 180–197. [CrossRef]
69. Heap, M.; Lavallée, Y.; Laumann, A.; Hess, K.-U.; Meredith, P.; Dingwell, D. How tough is tuff in the event of fire? *Geology* **2012**, *40*, 311–314. [CrossRef]

70. Brotons, V.; Tomás, R.; Ivorra, S.; Alarcón, J. Temperature influence on the physical and mechanical properties of a porous rock: San Julian's calcarenite. *Eng. Geol.* **2013**, *167*, 117–127. [CrossRef]
71. Entwisle, D.; Hobbs, P.; Jones, L.; Gunn, D.; Raines, M. The relationships between effective porosity, uniaxial compressive strength and sonic velocity of intact Borrowdale Volcanic Group core samples from Sellafield. *Geotech. Geol. Eng.* **2005**, *23*, 793–809. [CrossRef]

sustainability

MDPI

Article

Study on Damage Characteristics of Water-Bearing Coal Samples under Cyclic Loading–Unloading

Hongxin Xie, Qiangling Yao *, Liqiang Yu and Changhao Shan

School of Mines, China University of Mining and Technology, No. 1 University Rd., Xuzhou 221116, China; xhx1998xhx@163.com (H.X.); yuliqiangcumt@163.com (L.Y.); shanchanghao_cumt@163.com (C.S.)
* Correspondence: yaoqiangling@cumt.edu.cn

Abstract: For underground water reservoirs in coal mines, the complex water-rich environment and changing overburden stress can damage coal pillar dams. In this paper, the coal samples from coal seam 2^2 of Shangwan coal mine were taken as research objects and the damage mechanism and characteristics of coal samples with different moisture content and wetting-drying cycles under cyclic loading were investigated. The results show that as the moisture content and wetting-drying cycles increase, the post-peak stage of the coal samples under cyclic stress becomes obvious, and the hysteresis loop changes from dense to sparse. Compared to the uniaxial compression experiment, when w = 5.28% (the critical water content), mechanical parameters such as peak strength and modulus of elasticity decrease the most. Under cyclic loading, the damage mode of both sets of coal samples was tensile damage, but the increase in wetting-drying cycles promotes the development of shear fractures. For evaluating fracture types, the RA-AF density map is more applicable to wetting-drying cycle coal samples, whereas for the coal samples with different moisture contents this should be carried out with caution. This study can provide some theoretical basis for the stability evaluation of coal pillar dams in underground water reservoirs.

Keywords: moisture content; dry–wet cycles; cyclic loading; injury mechanism; acoustic emission RA-AF

Citation: Xie, H.; Yao, Q.; Yu, L.; Shan, C. Study on Damage Characteristics of Water-Bearing Coal Samples under Cyclic Loading–Unloading. *Sustainability* **2022**, *14*, 8457. https://doi.org/10.3390/su14148457

Academic Editors: Mahdi Hasanipanah, Danial Jahed Armaghani and Jian Zhou

Received: 15 June 2022
Accepted: 6 July 2022
Published: 11 July 2022

Publisher's Note: MDPI stays neutral with regard to jurisdictional claims in published maps and institutional affiliations.

Copyright: © 2022 by the authors. Licensee MDPI, Basel, Switzerland. This article is an open access article distributed under the terms and conditions of the Creative Commons Attribution (CC BY) license (https://creativecommons.org/licenses/by/4.0/).

1. Introduction

Western China is rich in coal resources but short of water resources. The uncoordinated distribution of coal and water has become an important factor restricting the realization of green mining in Western China [1,2]. To solve the contradiction of coal and water co-mining, the construction of underground reservoirs in coal mines has been put forward to solve the water shortage in arid and semi-arid mining areas in Western China [3,4]. However, the coal pillar dam of the reservoir will be damaged or made unstable under the joint action of water immersion and periodic pressure of overburden [5]. Therefore, it is important to study the deformation, failure characteristics, and instability precursor information of coal samples with different moisture content under cyclic compression loads.

In recent years, research on water–rock interactions has been widely performed. By studying the micro-structure and adsorption behavior of clay minerals, Cherblanc et al. concluded that the weakening of the mechanical strength of water-bearing limestone is related to the adsorption capacity and that the clay delays the weakening of the rock [6]. Moreover, Chen et al. found that the weakening of mechanical factors such as the compressive strength of rock materials after water damage was related to changes in the micro-structure by SEM [7].The results have shown that with the increase in moisture content, rock samples present more significant plastic characteristics, whereas its uniaxial compressive strength and elastic modulus decreased to varying degrees [8,9]. Through the analysis of the mineral composition of "Macigno" sandstone, the water absorption and water saturation are increased with the increase in montmorillonite content, which may play an important role in the decay process of sandstone [10]. Bensallam et al. studied the mechanical behavior of

clay under the alternation of dry and wet, and found that the deformation of expansion and shrinkage decreased by the alternation of dry and wet, and the change of soil behavior was affected by load-deformation [11]. Yao et al. first studied the weakening mechanism of moisture content and different soaking times on the mechanical properties of coal rock [12]. Huang et al. studied the effects of dry–wet cycles on the mechanical properties of sandstone and mudstone and found both the elastic modulus and uniaxial compressive strength of sandstone and mudstone were reduced by dry–wet cycles, and the degradation rate of the two mechanical parameters of mudstone was always larger than sandstone [13]. At the same time, water and temperature have multiple weakening effects on the mechanical properties of coal measures mudstone. Through creep experiments, it is found that high temperatures will aggravate the weakening effect of water [14].

Moreover, research on the mechanical properties of coal rock under cyclic loading has been also carried out [15,16]. For porous sandstone, the two damage mechanisms of compaction and micro-cracking under cyclic loading are affected by the dip angle of isotropic plane load, which decreases gradually with increasing confining pressure [17]. In addition, the residual strain method and the axial secant modulus method could describe the initial fatigue damage and degradation process of sandstone samples [18]. Through scanning an electron microscope, Erarslan et al. found that the failure of the Brisbane tuff is inter-granular fracturing and trans-granular fracturing, which may be due to frictional sliding within the weak matrix [19]. Combined with the experimental study of deformation and damage of fine sandstone under cyclic loading, Jia et al. found the change rate of a transverse and longitudinal strain first increases and then remains unchanged. With the increase in cyclic stress levels, the failure mode changes from compaction to expansion [20]. Zhang et al. applied the Single-link cluster (SLC) method to the spatial and temporal evolution of acoustic emission and the damage evolution process of coal samples, confirming the effectiveness of the SLC method [21]. A large number of studies on the damage to coal under cyclic loading show that the elastic modulus increased at first and then decreased with the number of cycles, the peak stress increased step by step, and the damage to coal was related to the level of cyclic stress [22,23].

The above studies mainly focus on the damage characteristics of coal rock with different water-bearing conditions under the uniaxial compression, as well as the mechanical properties and AE characteristics of coal rock under cyclic loading–unloading tests. However, research on the mechanical properties and fracture damage of water-bearing coal samples under cyclic compression load has been rarely carried out.

In this study, the self-designed, non-destructive water immersion equipment [24] was used to conduct non-destructive water immersion and dry–wet cycle treatment on coal samples [25]. Coal samples with a moisture content of 0%, 3.95%, 7.46%, and 15.25% were marked as Experimental group A, and those treated by dry–wet cycles of 1, 2, and 3 were marked as Experimental group B. The MTS universal servo testing machine was used for the mechanical experiment, and real-time photography and an acoustic emission system were used for monitoring during the experiment. In this study, the mechanical properties and damage mechanism of coal samples with different moisture contents under the cyclic compression load were mainly studied. The research results are important for understanding the failure mechanism and precursory information of coal pillar dams under the action of moisture content and cyclic compression load.

2. Materials and Methods

2.1. Test Materials and Specimen Preparation

Shang-wan Coal Mine is in EjinHoro Banner, Ordos City, Inner Mongolia Autonomous Region. It belongs to the western mining area and is short of water resources. If the mine water is not stored, a large amount of water resources will be drained and lost on the surface, which will aggravate the ecological damage on the surface and cause a water shortage in the mine and surrounding areas. Therefore, Shang-wan Coal Mine has implemented the underground reservoir technology in the 2^2 coal gob, that is, through the connection

between the artificial dam and the protective coal pillar, the mine water is sealed in the gob to form a storage dam to protect the mine water resources.

As shown in Figure 1, the underground reservoir diagram shows that the coal pillar dam is not only in the complex stress field affected by mining stress, the lateral stress of caving gangue, and stagnant water pressure in the gob, but also affected by the long-term erosion of stagnant water in the gob, resulting in dynamic changes in the water content of the coal pillar. In addition, the repeated scouring effect of water makes the coal pillar in a dry-saturated water-bearing state. Considering the stress redistribution under the influence of mining and the long-term erosion of water to the coal pillar dam, an experiment is designed to study the long-term stability of the coal pillar dam.

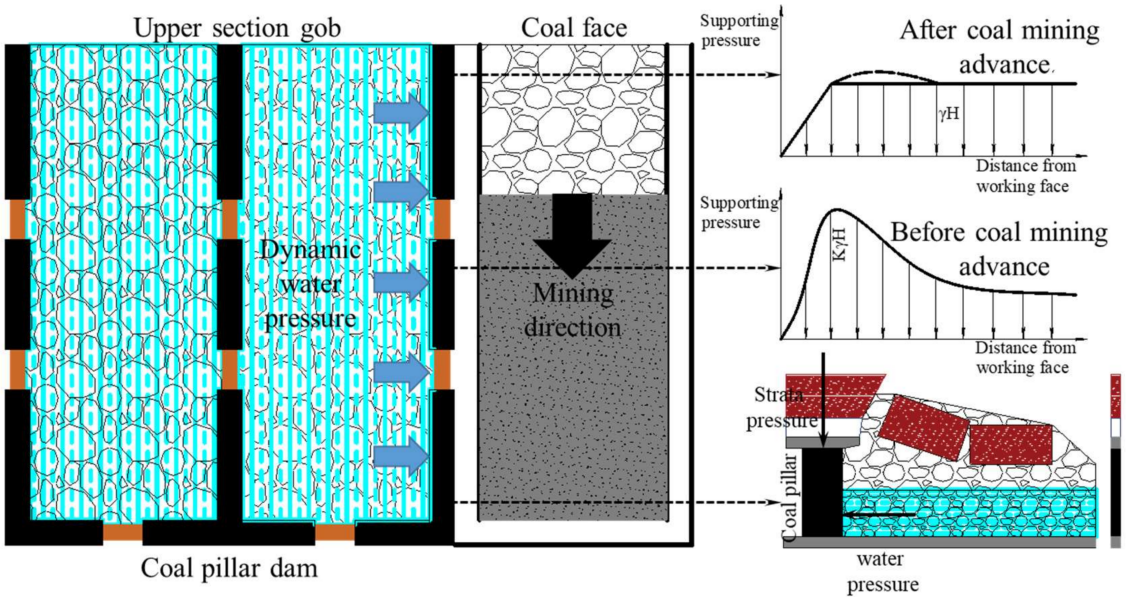

Figure 1. Schematic diagram of underground reservoir.

In this test, coal samples were taken from the coal seam 2^2, as shown in Figure 2. The moisture content of coal samples in the natural state was 7.59%. According to the requirements of the Test Code of the *International Society of Rock Mechanics* [26], the raw coal was processed into 30 standard cylindrical samples of 50 mm × 100 mm. The presence of bedding in the coal samples has an effect on deformation damage and permeability evolution [27,28]. In order to eliminate the influence of the bedding layer on this cyclic loading and unloading experiment, we carried out a wave velocity test before preparing the specimen to ensure the homogeneity of the specimen as much as possible [24].

The samples were divided into 7 groups: there are 4 groups of samples with different moisture contents (Experimental group A: 0%, 3.95%, 7.46%, and 15.25%) and 3 groups of samples treated by different dry–wet cycles (Experimental group B: 1, 2 and 3 cycles). These samples were numbered in the form of Experimental group No.—Moisture content/dry–wet cycles—Number. For example, A-1-1 represents the first coal sample with the moisture content of 0% in Experimental group A, and B-1-2 represents the second coal sample with one dry–wet cycle in Experimental group B. The uniaxial compression experiments and cyclic loading–unloading uniaxial compression experiments were carried out. Table 1 shows detailed information about the samples. Refer to Equation (1) for calculating moisture content.

$$w = \frac{M' - M_{dry}}{M_{dry}} \times 100\% \quad (1)$$

where, M' is the mass of the characteristic water-bearing coal samples, and M_{dry} is the mass of the drying samples.

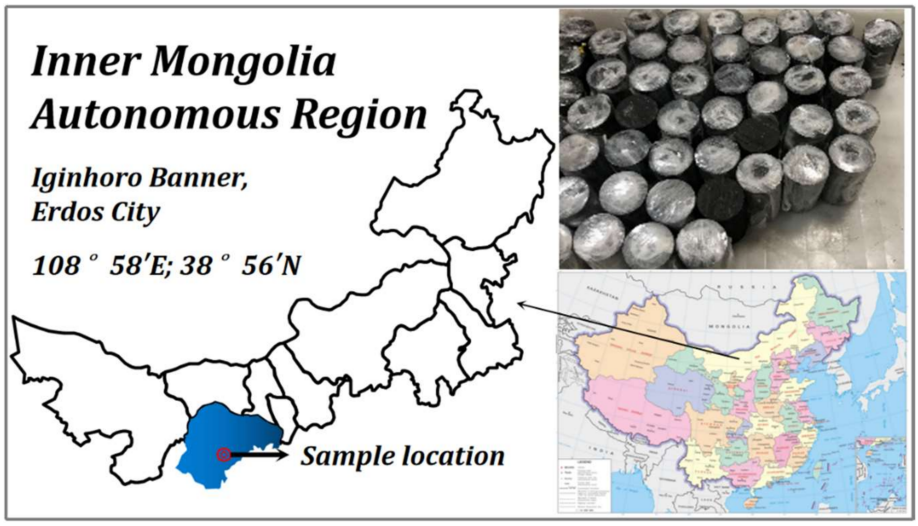

Figure 2. Sampling location.

Table 1. Sample number.

Sample No.	A-1	A-2	A-3	A-4
Moisture content	0.00%	3.95%	7.46%	15.25%
Table	A-1-1~A-1-3	A-2-1~A-2-3	A-3-1~A-3-3	A-4-1~A-4-3
Table	B-1	B-2	B-3	
Immersion times	1	2	3	
Table	B-1-1~B-1-3	B-2-1~B-2-3	B-3-1~B-3-3	

2.2. Experimental Scheme and Equipment

The experiment was divided into two parts: (1) uniaxial compression experiment and AE experiment of coal samples with different moisture contents. The variation laws of mechanical parameters (such as stress, strain, and AE characteristics) of coal samples with different moisture contents and different dry–wet cycles at a constant loading rate were measured. Based on this, the initial loading strength value of cyclic loading–unloading was set. (2) In the second part, the uniaxial cyclic loading–unloading experiment and AE experiments of coal samples with different moisture contents were carried out, and the variation laws of mechanical properties and AE characteristics of coal samples with different moisture contents under cyclic loading–unloading were obtained and compared with those under the ordinary uniaxial loading mode.

As shown in Figure 3a, the wave velocity of the specimen was tested using an ultrasonic velocimeter (Model RSM-SY6, Wuhan Zhong Yan Technology Co., Ltd., Wuhan, China). As can be seen in Figure 3b, the wave velocity of the coal sample was distributed in the interval of 1425–1520 $m \cdot s^{-1}$, with an average wave velocity of 1477 $m \cdot s^{-1}$, and the variance and skewness were 0.6 and −0.2, respectively, with a small dispersion. This indicates that the internal structure and defect distribution of the specimens are consistent, which can reduce experimental errors.

The 101-2 electric constant temperature drying oven was selected as the drying equipment, as shown in Figure 4a. According to the requirements of the Test Code of the *International Society of Rock Mechanics* [26], the drying temperature was set at 110° and the drying duration was set at 12 h. After drying, the coal sample was taken out and wrapped tightly with plastic wrap in time to prevent its water absorption in the natural environment from affecting the accuracy of the experiment. The self-designed HL-8-1WS rock moisture content continuous weighing detector [29] was used to immerse coal samples, as shown in Figure 4b. The coal samples were in full contact with the saturated humidity water vapor in the constant temperature and humidity box to absorb water freely. In this way, the damage

to the coal sample caused by excessive direct immersion water pressure was avoided, and the integrity of the coal sample was protected to a great extent.

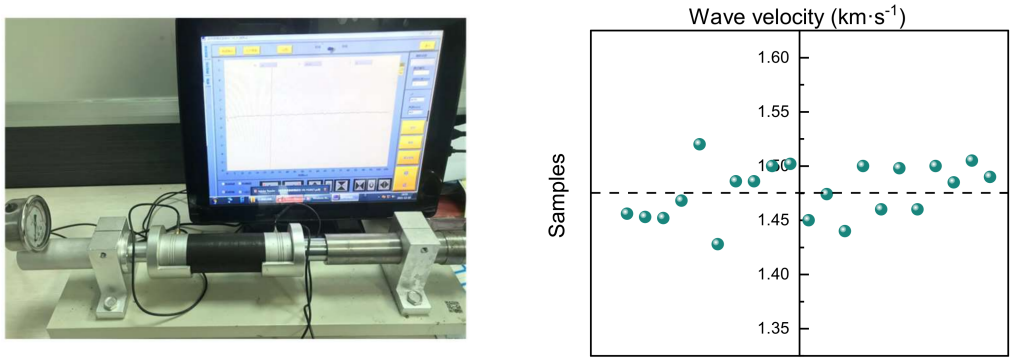

(**a**) Ultrasonic Velocimetry (**b**) Specimen wave velocity

Figure 3. Specimen wave velocity testing.

(**a**) (**b**)

Figure 4. (**a**) Electro-thermal constant temperature drying oven; (**b**) Continuous weighing detector for rock water content.

The MTS electro-hydraulic servo universal testing machine in the State Key Laboratory of Coal Resources and Safe Mining, China University of Mining and Technology was selected as the loading system. The displacement loading at a rate of 0.3 mm/min was employed in the uniaxial compression and cyclic loading–unloading uniaxial compression experiments. The difference was that in the latter experiment, 50–70% of the expected peak strength (which was obtained from the uniaxial compression test) was first loaded and unloaded to 1% of the expected peak strength and added with a gradient loading (taking 10% of the expected peak strength as a gradient), and then repeated until the coal sample was damaged. At the same time, the PCI-II acoustic emission system produced by the American Acoustic Physics Company (PAC) was used to monitor the acoustic emission signals during the experiment. Referring to the previous study conducted by Xia et al. [30], a total of 4 probes were arranged at the upper and lower 1/3 points of the 4 surfaces of the coal sample cylinder (2 probes on the upper and lower horizontal planes, respectively), with a distribution of 90°, to ensure the accuracy of acoustic emission monitoring. During the test, the Nikon Z6II high-definition SLR camera was used to monitor the loading process and record the fracture failure mode of coal samples during compression. Figure 5 shows the test system and the load loading path.

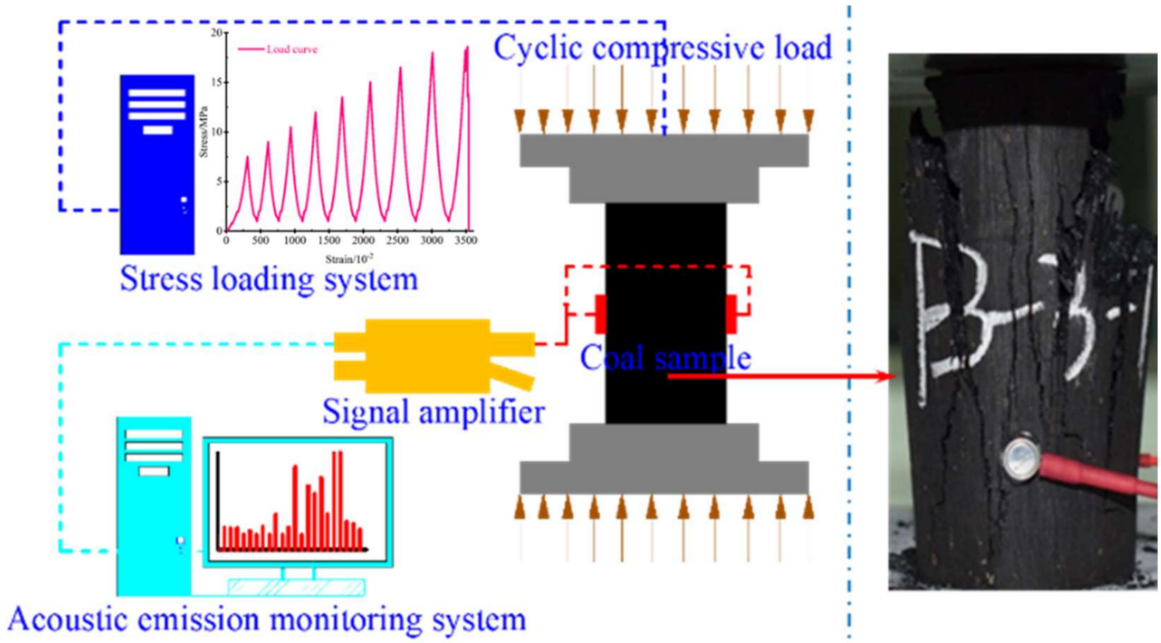

Figure 5. Schematic diagram of rock mechanics and acoustic emission test system.

2.3. Acoustic Emission RA-AF Relational Density Method

Acoustic emission *RA* value (Rise time/Amplitude) can be used to characterize the failure mechanism of coal rock, as well as the precursor information to predict the fracture development and failure of coal rock [31,32].

Reference *RA* value definition [33]:

$$RA = \frac{RiseTime(RT)}{Ampltitude(Amp)} \tag{2}$$

where *RT* is the rise time of the AE waveform, in us, *Amp* is the amplitude, in dB. If the amplitude is given on a logarithmic scale (for example, dB), it should be converted to the original voltage. The AE pair *V* is solved as follows, with the result expressed in volts.

$$A(dB) = 20 \times \lg\left(\frac{V}{V_{ref}}\right) - G \tag{3}$$

where *G* is the AE amplification gain (threshold value), in this experiment *G* = 40 dB, V_{ref} is the reference value used in AE software is 1 μv.

The Equation (4) for calculating the *RA* value expressed by the original voltage *V* can be obtained by the deformation of Equation (3).

$$V = V_{ref} \times 10^{\frac{V}{V_{ref}}} - G \tag{4}$$

The *AF* value is defined as:

$$AF = \frac{Ringcount(\mathrm{AE})}{Duration(\mu s)} \tag{5}$$

In order to reflect the RA-AF distribution characteristics more intuitively, the RA-AF probability density distribution maps of coal samples with different moisture content were made by using MATLAB R2022a. The color evolution of the AE data density allows a clearer qualitative analysis of the loss evolution of the experimental specimen. The red area

represents the maximum data density, the blue area represents the minimum data density, and the white dashed line is the line dividing the pulling shear cleavage.

3. Results and Discussion

3.1. Mechanical Properties of Water-Bearing Coal Samples under Uniaxial and Cyclic Loading–Unloading Experiments

Figure 6 shows the stress curve and mechanical parameter characteristics under the uniaxial compression tests and cyclic loading–unloading uniaxial compression tests.

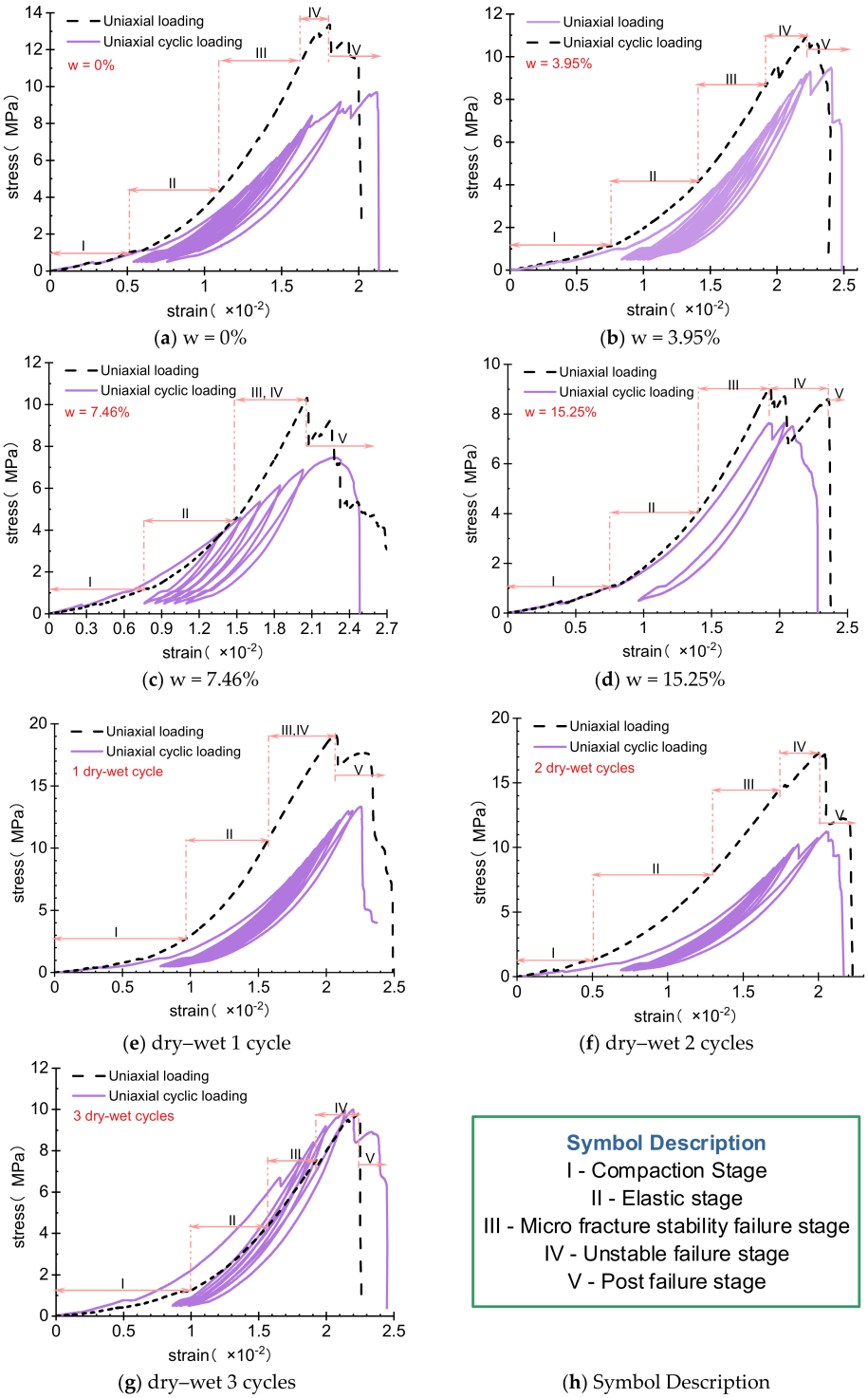

Figure 6. Different moisture state coal sample stress-strain curve.

As shown from Figure 6a–d, the stress-strain characteristics of the uniaxial compression conditions of coal samples with different moisture contents can be divided into five stages, as follows: compaction stage, elastic stage, micro-fracture stability failure stage, unstable failure stage, and post-failure stage. The peak stress and peak strain of dry coal samples (i.e., coal samples with the moisture content of 0%) under uniaxial compression load is 13.36 MPa and 1.71×10^{-2}, whereas that under cyclic compression load is 9.69 Mpa a is 2.11×10^{-2}. The peak stress under the cyclic compression load is 72.53% of that under the uniaxial compression load, but the peak strain under the cyclic compression load is higher than that under the uniaxial compression load. As presented in Figure 6a–d, the strain peak on the stress-strain curves in the cyclic loading–unloading test lags that in the uniaxial compression test. These curves are concave and have a high coincidence in the compaction stage and elastic stage.

It indicates that at the initial stage of stress loading, initial pores and fractures in dry coal samples are gradually compacted and closed, and the stress increases rapidly with the increase in loading displacement. In the stage of micro-fracture stable failure, with the increase in loading cycles, the stress-strain curve during the cyclic loading–unloading test gradually deviates downward from that in the uniaxial compression test, and the hysteresis loop area gradually increases. In the unstable failure stage, the coal sample in the uniaxial compression test loses stability and fails rapidly after reaching the peak stress, whereas the coal sample in the cyclic loading–unloading test has a long-term instability process with the increase in cyclic loading–unloading. After the 9^{th} cyclic loading–unloading, the coal sample is destroyed.

When the moisture content is 7.46%, most of the stress-strain curves of the cyclic loading–unloading test are still below those of the uniaxial compression test. After the sixth cyclic loading–unloading, the coal sample is destroyed. Different from the uniaxial compression test, the stress-strain curve of the coal sample in the cyclic loading–unloading test has no obvious post-peak stage.

As shown from Figure 6e–g, the peak stress and peak strain of the coal sample after 1 dry–wet cycle in the uniaxial compression test are 19.08 Mpa and 2.07×10^{-2}, whereas those in the cyclic loading–unloading test are 13.34 Mpa and 2.25×10^{-2}. It shows that in the cyclic loading–unloading test, the compressive strength of coal samples decreases, the peak stress is 70.04% of that in the uniaxial compression test, and the peak strain is slightly higher than that in the uniaxial compression test. Under cyclic compression load, the coal sample loses stability immediately after crack propagation and penetration; whereas under uniaxial compression load, it has an obvious post-peak stage.

The peak stress of coal samples after 3 dry–wet cycles under cyclic compression load is like that under uniaxial compression load, but the peak strain of coal samples under cyclic compression load is relatively small. In addition, there is no obvious post-peak stage of coal samples under uniaxial compression load, and the stress–strain curve under cyclic compression load has an obvious post-peak stage.

3.2. Mechanical Parameter of Water-Bearing Coal under Cyclic Loading

The compressive strength, peak strain, and elastic modulus of coal samples are important parameters for studying the mechanical properties of coal [34]. In order to reduce the experimental error, the average values of compressive strength and peak strain under cyclic loading–unloading are used, and the elastic modulus in the unloading curve in each cycle is used. Tables 2–4 show the detailed parameters of coal samples.

Table 2. Mechanical parameters of coal samples with different moisture contents under cyclic loading–unloading.

W (%)	σ_{max} (Mpa)	$\sigma_{max}{}'$ (Mpa)	ε_{max} ($\times 10^{-2}$)	$\varepsilon_{max}{}'$ ($\times 10^{-2}$)	E (Gpa)	E' (Gpa)
0	13.36	9.69	1.71	2.11	1.22	1.05
3.95	10.99	9.46	2.22	2.39	0.74	0.97
7.46	10.30	7.44	2.29	2.31	0.63	0.95
15.25	9.11	7.64	1.94	2.04	0.56	0.88

Table 3. Mechanical properties of coal samples after different dry–wet cycles under cyclic loading–unloading.

Dry–Wet Cycles	σ_{max} (Mpa)	$\sigma_{max}{}'$ (Mpa)	ε_{max} ($\times 10^{-2}$)	$\varepsilon_{max}{}'$ ($\times 10^{-2}$)	E (Gpa)	E′ (Gpa)
1	19.08	13.34	2.07	2.25	1.51	1.37
2	17.34	11.23	2.00	2.05	0.98	1.40
3	9.79	10.00	2.50	2.20	0.56	1.24

Table 4. Statistical table of elastic modulus of coal samples in different water-bearing states under cyclic loading and unloading.

Water-Bearing State	Elastic Modulus of Each Cycle Loading (Mpa)							
	1	2	3	4	5	6	7	8
w = 0%	1192.75	1100.90	1051.66	1043.79	1032.91	1023.10	997.63	996.62
w = 3.95%	1067.15	1016.32	999.10	987.95	967.31	960.13	903.19	880.56
w = 7.64%	1030.57	1020.54	1017.25	844.17	825.00			
w = 15.25%	925.54	821.72						
1 dry–wet cycle	1186.26	1197.42	1273.36	1291.79	1285.47	1596.83	1620.82	1748.02
2 dry–wet cycles	1270.55	1254.42	1370.17	1469.69	1499.80			
3 dry–wet cycles	1109.43	1216.62	1300.85	1315.02				

As shown in Figure 7, the determination of elastic modulus E' in each cycle refers to the determination method proposed by Pourhosseini and Shabanimashcool [35], that is, the area enclosed by the elastic modulus E' straight line and the strain axis is equal to the area enclosed by the unloading curve and the strain axis of each cycle. The elastic modulus of each cycle can be obtained by making a straight line representing the elastic modulus of the same area.

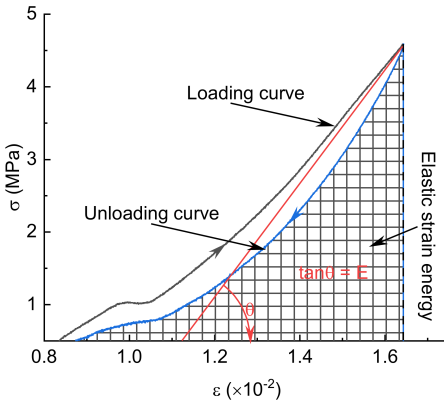

Figure 7. Calculation method of elastic modulus under cyclic loading–unloading.

As shown in Figure 8a,c,e, the peak stress of the dry coal sample is the highest, which is 9.69 Mpa. With the increase in moisture content, the peak stress and peak strain decreased

to varying degrees. From the microscopic point of view, water molecules enter the microcracks and pores in the coal body and adhere to the inner surface of the coal to form bound water. Under the action of external load, part of the bound water expands, promotes the expansion of the cracks in the coal, reduces the bearing capacity of the coal, and accelerates its damage.

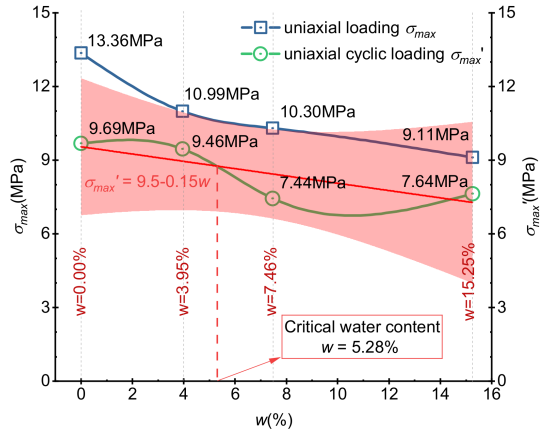

(**a**) uniaxial compressive strength—moisture content

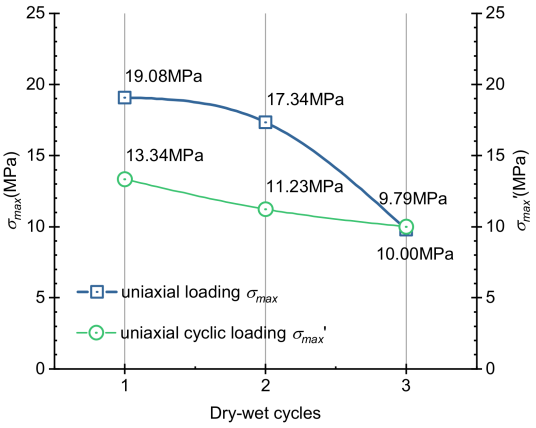

(**b**) uniaxial compressive strength—dry–wet cycles

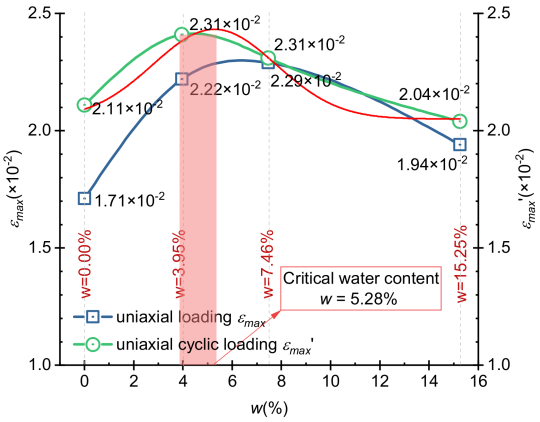

(**c**) strain—moisture content

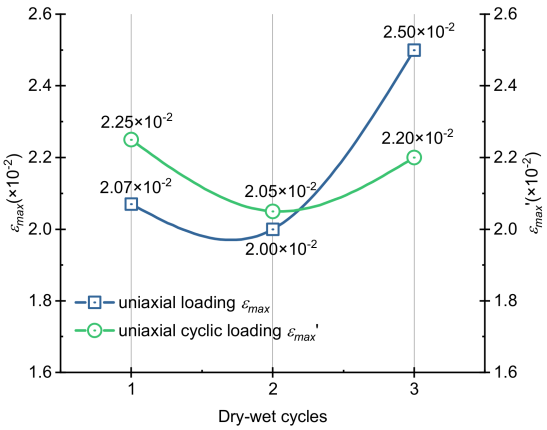

(**d**) strain—dry–wet cycles

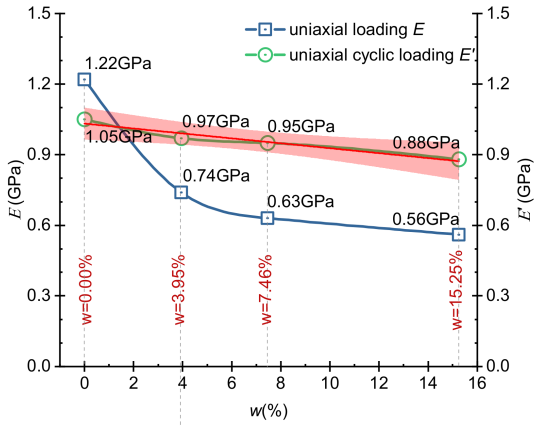

(**e**) Elastic Modulus—moisture content

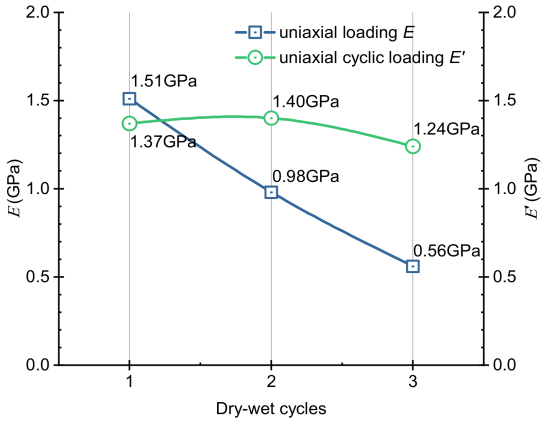

(**f**) Elastic Modulus—dry–wet cycles

Figure 8. Evolution of uniaxial loading and cyclic loading mechanical parameters of coal samples with different water content states, (the red area represents the confidence interval of the fitted straight line).

It is worth noting that when the moisture content increases from 3.95% to 7.46%, the changing range of compressive strength and peak strain is the largest. Specifically, the compressive strength decreases from 9.46 MPa to 7.44 Mpa, which decreases by 21.20%; the peak strain decreases from 2.39 × 10^{-2} to 2.31 × 10^{-2}, which decreases by 3.33%. This is because when the moisture content reaches a certain value, most of the water molecules have been filled into the natural fractures; under the external pressure of cyclic loading, the fracture expansion effect is the strongest, and the macroscopic performance is that the compressive strength of coal body decreases sharply. Therefore, there is an inflection point in the strength attenuation of coal samples under cyclic loading, that is, the critical moisture content. It is speculated that when w = 5.28% as indicated in the figure, the strength attenuation of coal samples is the largest.

As shown in Figure 8b,d,f, with the increasing number of dry–wet cycles, the peak stress and peak strain of the coal sample after dry–wet cycles treatment decrease under the action of cyclic compression load. After three dry–wet cycles, the peak stress of the coal sample decreases from 13.34 Mpa to 10.00 Mpa, decreased by 24.72%, and the peak strain decreases from 2.25 × 10^{-2} to 2.20 × 10^{-2}, reduced by 0.5%. Therefore, the dry–wet cycle treatment of coal samples has a great impact on the weakening of coal strength.

Figure 9a depicts the changing trend of elastic modulus of coal samples with different moisture contents under different numbers of cyclic loading–unloading. The change of elastic modulus in the first three cyclic loading–unloading of dry coal samples is the largest. The elastic modulus decreases from 1192.75 Mpa to 1051.66 Mpa in the first cyclic loading–unloading, and then slowly decreases to 996.62 Mpa in the second cyclic loading–unloading and then tends to be stable. The change of elastic modulus of coal samples with the moisture content of 3.95% is the largest in the first and sixth cyclic loading–unloading, decreasing 50.83 Mpa and 56.94 Mpa respectively. The coal sample with the moisture content of 7.46% will be unstable and damaged after 5 loading–unloading cycles. The change of elastic modulus is the largest in the third cyclic loading–unloading, which is reduced by 173.08 Mpa. Therefore, the higher the moisture content, the smaller the elastic modulus at the sample failure, and the elastic modulus decrease gradually with the increasing number of cyclic loading–unloading.

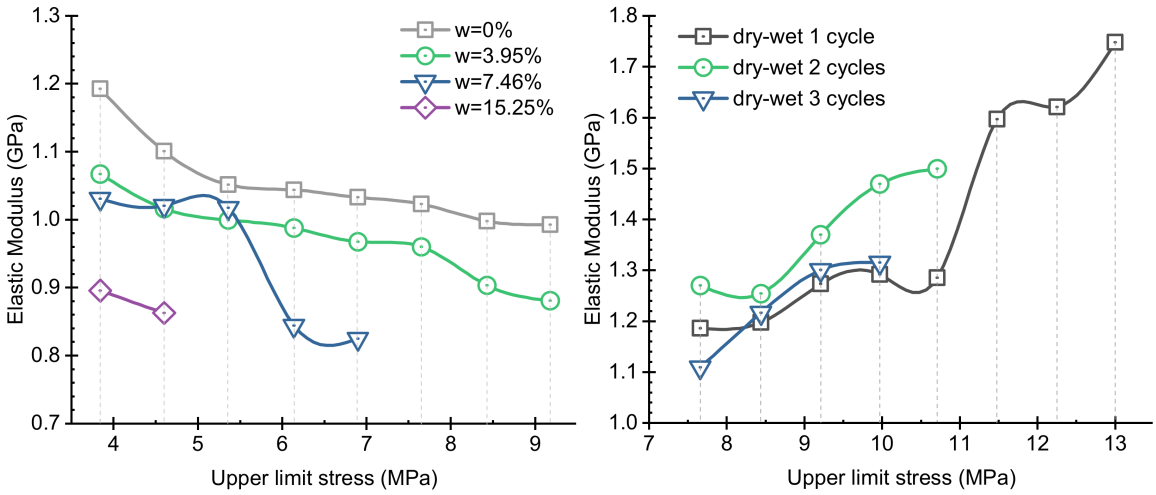

(**a**) Moisture Content—Elastic Modulus (**b**) Dry and wet Cycling—Elastic Modulus

Figure 9. Relationship between upper limit stress and elastic modulus of coal samples with different water content.

Figure 9b shows the variation law of elastic modulus of coal samples after different dry–wet cycles. The elastic modulus of coal samples after dry–wet cycles is positively correlated with the number of dry–wet cycles, that is, the elastic modulus increases with the increasing number of dry–wet cycles. This shows that under the action of cyclic

compression load, the plasticity of coal samples is gradually enhanced by repeated soaking and drying treatment. In addition, the coal samples treated by one dry–wet cycle are unstable and damaged after the eighth cyclic loading–unloading, and its elastic modulus is 1748.02 MPa at this time. The coal samples treated by 2 and 3 dry–wet cycles failed at the fifth and fourth cyclic loading–unloading, and the elastic modulus of these samples are 1499.80 Mpa and 1315.02 Mpa, respectively. The more dry–wet cycles on the coal samples, the lower the elastic modulus of coal samples.

3.3. Failure Characteristics of Water-Bearing Coal Samples under Cyclic Loading–Unloading

As shown in Figure 10a–d, under the action of cyclic load, with the increase in moisture content, the position of fracture development shifts from the edge to the interior., the number of secondary fractures around the main fracture decreases gradually, and the failure mode changes from shear failure to shear-tensile failure. This is because water gradually invades the coal sample from outside to inside. When the moisture content is low, water hardly penetrates the coal sample and is mainly located at the edge, that is, the strength at the edge is clearly weakened and longitudinal cracks are mostly generated. With the increase in moisture content, the cracks begin to expand, and gradually stabilize when the crack failure limit is exceeded. When the crack density reaches the level when the cracks condense into shear bands or stretch and peel off the coal sample [36].

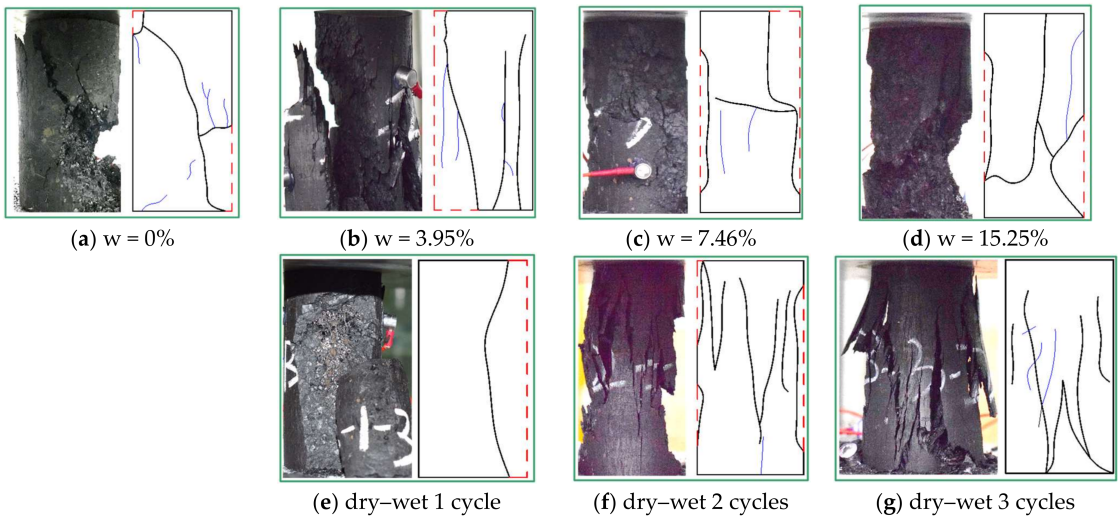

Figure 10. Failure characteristics of coal samples after different dry–wet cycles under cyclic loading–unloading.

As shown in Figure 10e–g, a main longitudinal crack is generated in the coal sample after one dry–wet cycle under cyclic loading–unloading conditions. This longitudinal crack runs through the entire coal sample. The stripped coal body is massive and has high integrity. With the increasing number of dry–wet cycles, the length of the fracture decreases, but the number of fractures increases. These fractures are approximately V-shaped, and evenly and symmetrically distributed about the axis of the coal sample. The stripped coal body gradually decreases, changing from block to debris; the integrity of the coal sample is enhanced. The fracture morphology of coal samples is consistent with the various characteristics of mechanical parameters under cyclic loading–unloading. The more dry–wet cycles on coal samples, the more significant the plastic failure.

3.4. Acoustic Emission Characteristics of Water-Bearing Coal under Cyclic Loading

As shown in Figure 11, where (a), (b), (c) and (d) represent water content of 0, 3.95%, 7.46% and 15.25% of coal samples. The transformation from blue area to red area represents the distribution density from small to large. From the probability density diagram, the core areas of the three kinds of water-bearing coal samples are all located at the upper

left of the tension-shear boundary, indicating that the penetration of tension cracks under cyclic loading finally leads to the macroscopic failure of coal samples. According to the observation of the failure characteristic diagram of coal samples, with the increase in water content, the shear crack decreases gradually, and the dominant role of tension crack increases gradually. So, the RA-AF density map has limitations in evaluating fracture types in coal samples of different moisture contents subjected to cyclic loading conditions.

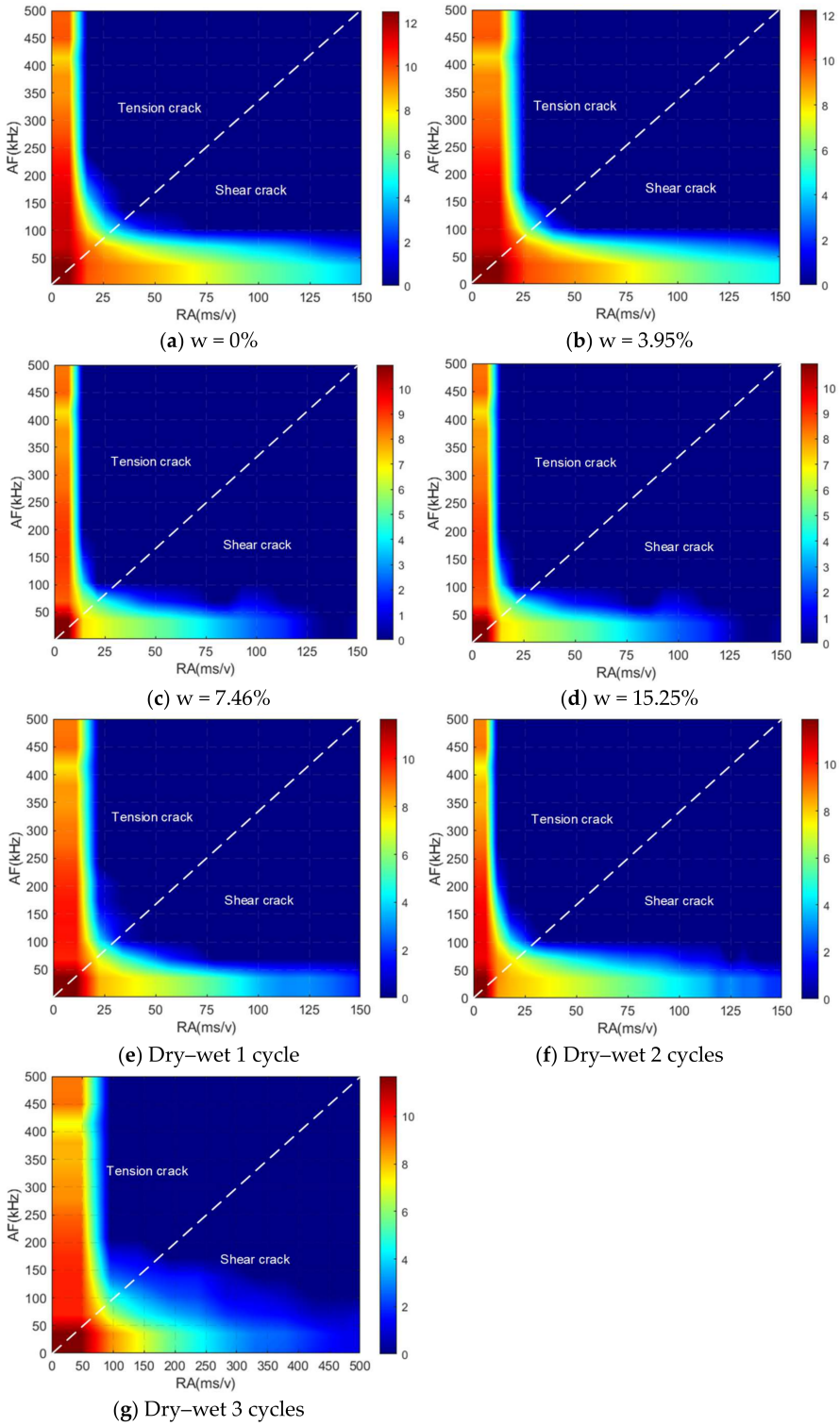

(**a**) w = 0% (**b**) w = 3.95%

(**c**) w = 7.46% (**d**) w = 15.25%

(**e**) Dry–wet 1 cycle (**f**) Dry–wet 2 cycles

(**g**) Dry–wet 3 cycles

Figure 11. RA-AF probability density distribution map.

From Figure 11e–g, the core area of the damaged fissures of coal samples treated with different numbers of wet and dry cycles are all located at the upper left of the tension-shear dividing line, indicating that the penetration of tension fissures under the cyclic loading eventually leads to the macroscopic damage of coal samples. With the increase in the number of dry and wet cycle treatments, both tension fractures and shear fractures gradually increase, and the dominant role of tension fractures gradually increases.

The fracture evolution and failure characteristics of water-bearing coal samples can be explained in combination with the water weakening mechanism and pore mechanics. Firstly, water enters the internal lattice, weakening the bonds of the original structure inside coal samples, which changes the coal microstructure and reduces its cohesion. It leads to the decrease of pore connectivity, and the increase in pore pressure in pores with poor connectivity will cause the rotation of stress direction and lead to tensile failure under cyclic loading [37].

4. Conclusions

In this study, the uniaxial cyclic loading–unloading experiments of coal samples with different moisture contents and dry–wet cycles were performed under acoustic emission and photographic monitoring, and the variation law and failure characteristics of mechanical properties of coal samples were studied. The main conclusions are as follows:

(1) The loading mode has a significant influence on the strength and deformation characteristics of water-bearing coal samples. The peak stress of coal samples under cyclic loading–unloading is about 80% of that under the uniaxial loading, and the peak stress gradually decreases with the increase in moisture content and dry–wet cycles. With the increase in moisture content and dry–wet cycles, the hysteresis loop of coal samples changes from a dense state to a sparse state. With the increasing number of dry–wet cycles, the resistance to fatigue damage increases and is inversely proportional to the moisture content, and the stress-strain curve of coal samples appears post-peak stage, and the plasticity of coal samples is enhanced.

(2) Water has a significant effect on mechanical parameters such as elastic modulus. Under cyclic load, when the moisture content is 5.28%, the mechanical parameters (such as strength and elastic modulus) of the coal sample decrease the most. Under the condition of moisture content, the elastic modulus of the coal sample is inversely proportional to the number of the cyclic loading–unloading. The higher the moisture content, the greater the decreasing rate of elastic modulus. After the dry–wet cycle treatment, the elastic modulus of the coal sample is directly proportional to the number of wet–dry cycles, and the more dry–wet cycles, the smaller the increasing rate of elastic modulus.

(3) The fracture development characteristics are controlled by the moisture content of coal samples. With the increase in moisture content, the position of fracture development shifts from the edge to the interior, the number of secondary fractures around the main fracture decreases gradually, and the failure mode changes from shear failure to shear-tensile failure. After one dry–wet cycle treatment, the coal sample produces a main longitudinal crack, which runs through the sample. The stripped coal body is massive and has high integrity. With the increase in dry–wet cycles, the length of fracture decreases, but the number of fractures increases. These fractures are approximately V-shaped, evenly, and symmetrically distributed about the axis of the coal sample. The stripped coal body gradually decreases, changing from block to debris, and the integrity of the coal sample is enhanced.

(4) From the probability density diagram, the penetration of tension cracks under cyclic loading finally leads to the macroscopic failure of coal samples. For evaluating fracture types, the RA-AF density map is more applicable to wetting–drying cycle coal samples, whereas for the coal samples with different moisture contents should be carried out with caution. With the increase in water content, the shear crack decreases gradually, and the dominant role of tension crack increases gradually. With the increase in the number of dry and wet cycle treatments, both tension fractures and shear fractures gradually increase, and the dominant role of tension fractures gradually increases.

Author Contributions: C.S.: investigation. H.X.: methodology. L.Y.: data curation. H.X.: writing and original draft preparation. Q.Y.: writing, review and editing. All authors have read and agreed to the published version of the manuscript.

Funding: The authors gratefully acknowledge financial support from the National Natural Science Foundation of China (No. 51874283).

Institutional Review Board Statement: Not applicable.

Informed Consent Statement: Not applicable.

Data Availability Statement: Not applicable.

Acknowledgments: The authors gratefully thank the anonymous reviewers for their constructive comments on improving the presentation. All authors have agreed to the listing of authors.

Conflicts of Interest: The authors declare they have no financial interests.

References

1. Liu, S.; Li, W.; Wang, Q.; He, J.; Xue, S. Water Inrush Risk zoning and Water Conservation Mining Technology in the Shennan Mining Area, Shaanxi, China. *Arab. J. Sci. Eng.* **2018**, *43*, 321–333. [CrossRef]
2. Sun, Q.; Zhang, J.X.; Zhou, N.; Qi, W.Y. Roadway Backfill Coal Mining to Preserve Surface Water in Western China. *Mine Water Environ.* **2018**, *37*, 366–375. [CrossRef]
3. Deng, X.P.; Shan, L.; Zhang, H.P.; Turner, N.C. Improving agricultural water use efficiency in arid and semiarid areas of China. *Agric. Water Manag.* **2006**, *80*, 23–40. [CrossRef]
4. Zhang, L.; Wong, M.H. Environmental mercury contamination in China: Sources and impacts. *Environ. Int.* **2007**, *33*, 108–121. [CrossRef]
5. Qiao, X.J.; Li, G.M.; Li, M.; Zhou, J.L.; Du, J.; Du, C.Y.; Sun, Z.H. Influence of coal mining on regional karst groundwater system: A case study in West Mountain area of Taiyuan City, northern China. *Environ. Earth Sci.* **2011**, *64*, 1525–1535. [CrossRef]
6. Cherblanc, F.; Berthonneau, J.; Bromblet, P.; Huon, V. Influence of Water Content on the Mechanical Behaviour of Limestone: Role of the Clay Minerals Content. *Rock Mech. Rock Eng.* **2016**, *49*, 2033–2042. [CrossRef]
7. Chen, S.J.; Jiang, T.Q.; Wang, H.Y.; Feng, F.; Yin, D.W.; Li, X.S. Influence of cyclic wetting-drying on the mechanical strength characteristics of coal samples: A laboratory-scale study. *Energy Sci. Eng.* **2019**, *7*, 3020–3037. [CrossRef]
8. Hashiba, K.; Fukui, K. Effect of Water on the Deformation and Failure of Rock in Uniaxial Tension. *Rock Mech. Rock Eng.* **2015**, *48*, 1751–1761. [CrossRef]
9. Hua, W.; Dong, S.M.; Li, Y.F.; Xu, J.G.; Wang, Q.Y. The influence of cyclic wetting and drying on the fracture toughness of sandstone. *Int. J. Rock Mech. Min.* **2015**, *78*, 331–335. [CrossRef]
10. Franzini, M.; Leoni, L.; Lezzerini, M.; Cardelli, R. Relationships between mineralogical composition, water absorption and hydric dilatation in the "Macigno" sandstones from Lunigiana (Massa, Tuscany). *Eur. J. Miner.* **2007**, *19*, 113–123. [CrossRef]
11. Bensallam, S.; Bahi, L.; Alaoui, M.; Ejjaaouani, H.; Shakhirev, V. The effect of surcharge pressure on the cyclic vertical deformations for expansive clayey soils in Morocco. *Geosci. J.* **2014**, *18*, 81–87. [CrossRef]
12. Yao, Q.L.; Li, X.H.; Zhou, J.; Ju, M.H.; Chong, Z.H.; Zhao, B. Experimental study of strength characteristics of coal specimens after water intrusion. *Arab. J. Geosci.* **2015**, *8*, 6779–6789. [CrossRef]
13. Huang, S.Y.; Wang, J.J.; Qiu, Z.F.; Kang, K. Effects of Cyclic Wetting-Drying Conditions on Elastic Modulus and Compressive Strength of Sandstone and Mudstone. *Processes* **2018**, *6*, 234. [CrossRef]
14. Lu, Y.L.; Wang, L.G. Effect of water and temperature on short-term and creep mechanical behaviors of coal measures mudstone. *Environ. Earth Sci.* **2017**, *76*, 597. [CrossRef]
15. Du, K.; Tao, M.; Li, X.B.; Zhou, J. Experimental Study of Slabbing and Rockburst Induced by True-Triaxial Unloading and Local Dynamic Disturbance. *Rock Mech. Rock Eng.* **2016**, *49*, 3437–3453. [CrossRef]
16. Xiao, F.; Jiang, D.Y.; Wu, F.; Zou, Q.L.; Chen, J.; Chen, B.; Sun, Z.G. Effects of prior cyclic loading damage on failure characteristics of sandstone under true-triaxial unloading conditions. *Int. J. Rock Mech. Min.* **2020**, *132*, 104379. [CrossRef]
17. Gatelier, N.; Pellet, F.; Loret, B. Mechanical damage of an anisotropic porous rock in cyclic triaxial tests. *Int. J. Rock Mech. Min.* **2002**, *39*, 335–354. [CrossRef]
18. Liu, E.L.; He, S.M. Effects of cyclic dynamic loading on the mechanical properties of intact rock samples under confining pressure conditions. *Eng. Geol.* **2012**, *125*, 81–91. [CrossRef]
19. Erarslan, N.; Alehossein, H.; Williams, D.J. Tensile Fracture Strength of Brisbane Tuff by Static and Cyclic Loading Tests. *Rock Mech. Rock Eng.* **2014**, *47*, 1135–1151. [CrossRef]
20. Jia, C.J.; Xu, W.Y.; Wang, R.B.; Wang, W.; Zhang, J.C.; Yu, J. Characterization of the deformation behavior of fine-grained sandstone by triaxial cyclic loading. *Constr. Build. Mater.* **2018**, *162*, 113–123. [CrossRef]
21. Zhang, Z.B.; Wang, E.Y.; Li, N.; Li, X.L.; Wang, X.R.; Li, Z.H. Damage evolution analysis of coal samples under cyclic loading based on single-link cluster method. *J. Appl. Geophys.* **2018**, *152*, 56–64. [CrossRef]

22. Duan, M.K.; Jiang, C.B.; Xing, H.L.; Zhang, D.M.; Peng, K.; Zhang, W.Z. Study on damage of coal based on permeability and load-unload response ratio under tiered cyclic loading. *Arab. J. Geosci.* **2020**, *13*, 250. [CrossRef]
23. Wang, H.J.; Li, J. Mechanical Behavior Evolution and Damage Characterization of Coal under Different Cyclic Engineering Loading. *Geofluids* **2020**, *2020*, 8812188. [CrossRef]
24. Yu, L.Q.; Yao, Q.L.; Li, X.H.; Wang, W.N.; Han, H.; Zhang, M.T. Experimental study of failure characteristics and fissure propagation in hydrous siltstone. *Arab. J. Geosci.* **2020**, *13*, 527. [CrossRef]
25. Wong, L.; Maruvanchery, V.; Liu, G. Water effects on rock strength and stiffness degradation. *Acta Geotech.* **2016**, *11*, 713–737. [CrossRef]
26. Muralha, J.; Grasselli, G.; Tatone, B.; Blumel, M.; Chryssanthakis, P.; Jiang, Y.J. ISRM Suggested Method for Laboratory Determination of the Shear Strength of Rock Joints: Revised Version. *Rock Mech. Rock Eng.* **2014**, *47*, 291–302. [CrossRef]
27. De Silva, G.; Ranjith, P.G.; Perera, M.; Chen, B. Effect of bedding planes, their orientation and clay depositions on effective re-injection of produced brine into clay rich deep sandstone formations: Implications for deep earth energy extraction. *Appl. Energy* **2016**, *161*, 24–40. [CrossRef]
28. Liu, C.; Yin, G.Z.; Li, M.H.; Shang, D.L.; Deng, B.Z.; Song, Z.L. Deformation and permeability evolution of coals considering the effect of beddings. *Int. J. Rock Mech. Min.* **2019**, *117*, 49–62. [CrossRef]
29. Yao, Q.L.; Tang, C.J.; Xia, Z.; Liu, X.L.; Zhu, L.; Chong, Z.H.; Hui, X.D. Mechanisms of failure in coal samples from underground water reservoir. *Eng. Geol.* **2020**, *267*, 105494. [CrossRef]
30. Xia, Z.; Yao, Q.L.; Li, X.H.; Yu, L.L.; Shan, C.H.; Li, Y.; Hao, Y.S. Acoustic emission characteristics and energy mechanism of CFRP-jacketed coal specimens under uniaxial compression. *Constr. Build. Mater.* **2022**, *342*, 1883–1889. [CrossRef]
31. Wang, P.T.; Yang, T.H.; Xu, T.; Cai, M.F.; Li, C.H. Numerical analysis on scale effect of elasticity, strength and failure patterns of jointed rock masses. *Geosci. J.* **2016**, *20*, 539–549. [CrossRef]
32. Cao, A.Y.; Wang, C.B.; Jing, G.C.; Cai, W.; Zhu, G.A.; Li, J. Passive velocity tomography for mudstone under uniaxial compression using acoustic emission. *Geosci. J.* **2017**, *21*, 93–109. [CrossRef]
33. Li, J.S.; Lian, S.L.; Huang, Y.S.; Wang, C.L. Study on Crack Classification Criterion and Failure Evaluation Index of Red Sandstone Based on Acoustic Emission Parameter Analysis. *Sustainability* **2022**, *14*, 5143. [CrossRef]
34. Wang, H.; Wang, Y.Y.; Yu, Z.Q.; Li, J.G. Experimental Study on the Effects of Stress-Induced Damage on the Microstructure and Mechanical Properties of Soft Rock. *Adv. Civ. Eng.* **2021**, *2021*, 6696614. [CrossRef]
35. Pourhosseini, O.; Shabanimashcool, M. Development of an elasto-plastic constitutive model for intact rocks. *Int. J. Rock Mech. Min.* **2014**, *66*, 1–12. [CrossRef]
36. Shang, D.L.; Chen, Y.D.; Zhao, Z.H.; Shangguan, S.; Qi, X.F. Mechanical behavior and acoustic emission characteristics of intact granite undergoing direct shear. *Eng. Fract. Mech.* **2021**, *245*, 107581. [CrossRef]
37. Zhong, C.L.; Zhang, Z.Y.; Ranjith, P.G.; Lu, Y.Y.; Choi, X. The role of pore water plays in coal under uniaxial cyclic loading. *Eng. Geol.* **2019**, *257*, 105125. [CrossRef]

sustainability

MDPI

Article

A Safe and Efficient Mining Method with Reasonable Stress Release and Surface Ecological Protection

Zhenghu Li [1,2], Junhui Zhang [1], Hui Chen [1], Xiuzhi Shi [1,*], Yanyang Zhang [1] and Yanjun Zhang [2]

[1] School of Geology and Mining Engineering, Xinjiang University, Urumqi 830046, China; lzh622822@126.com (Z.L.); zhangjunhui@xju.edu.cn (J.Z.); chenhui@xju.edu.cn (H.C.); zyy@xju.edu.cn (Y.Z.)
[2] Shenmu Zhangjiamao Mining Co., Ltd., Shaanxi Coal Chemical Industry Group, Xi'an 710000, China; ca506116342@163.com
* Correspondence: baopo@csu.edu.cn

Abstract: Coal is an important basic energy source, widely distributed throughout the world, but resource abundance is uneven. Despite the need to develop and form new energy sources, coal energy maintains its dominant position. However, due to the uneven distribution and non-renewable nature of coal resources, the relationship between the supply and demand of coal resources is tight. The rational exploitation of coal and reducing resource mining wastes are particularly important at the present stage. The original mining method of the Zhangjiamao coal mine resulted in a large waste of coal resources. After replacing the "110 construction method", the original advanced end-support was canceled, which saved a lot of process time and engineering costs and greatly improved the mine production efficiency. With an average mining depth of +300 m, the working face is in a safe and stable state, and the 110-mining process has little impact on surface subsidence. Its successful application provides a reference experience for other mines to promote resource-saving and efficient mining.

Keywords: non-renewable; clean coal technology; waste of resources; "110 construction method"; collapse settlement control

Citation: Li, Z.; Zhang, J.; Chen, H.; Shi, X.; Zhang, Y.; Zhang, Y. A Safe and Efficient Mining Method with Reasonable Stress Release and Surface Ecological Protection. *Sustainability* **2022**, *14*, 5348. https://doi.org/10.3390/su14095348

Academic Editors: Jian Zhou, Danial Jahed Armaghani and Mahdi Hasanipanah

Received: 17 March 2022
Accepted: 26 April 2022
Published: 28 April 2022

Publisher's Note: MDPI stays neutral with regard to jurisdictional claims in published maps and institutional affiliations.

Copyright: © 2022 by the authors. Licensee MDPI, Basel, Switzerland. This article is an open access article distributed under the terms and conditions of the Creative Commons Attribution (CC BY) license (https://creativecommons.org/licenses/by/4.0/).

1. Introduction

Coal is a solid combustible mineral. It is formed by ancient plants buried underground through complex biochemical and physicochemical changes (Figure 1). Coal is also known as black gold or industrial blood. Coal is an important basic energy source and the raw material foundation of the steel, cement, chemical industry, and other industries. In 2012, coal accounted for a record 29.9% of the global disposable energy consumption [1]. In China, coal accounted for about 70% of the disposable energy consumption structure (Table 1). According to the data of relevant departments, coal will account for more than 50% of China's energy structure by 2050 [2]. China's coal pollution is also very serious. Eighty-five percent of coal is directly used for combustion, which once made China a typical soot-polluted environment. Coal burning emits a large amount of SO_2, and 30% of China's land has been affected by acid rain [3]. Many studies show that in the next 10~20 years, with the development of clean coal technology (Figure 2), coal will surpass oil and become the largest energy consumption in the world. At the executive meeting of the State Council held in 2021, the Chinese government set RMB 200 billion ($3.14 billion) of special refinancing to support the clean and efficient utilization of coal based on the early establishment of financial support tools for carbon emission reduction to form a policy and promote green and low carbon developments. In recent years, with the acceleration of coal energy consumption, the mining depth of coal mines has also grown rapidly. Based on the analysis of the current situation and the existing problems of deep surrounding rock control and intelligent mining technology, Kang et al. [4] discussed key scientific problems and technical ideas. These scientific problems mainly focused on safe and efficient mining and the interaction between the roadway and stope. The technical ideas mainly focus

on reasonably increasing the length of the working face, realizing intensive production, reducing the tunneling rate, and improving the coal recovery rate [5,6].

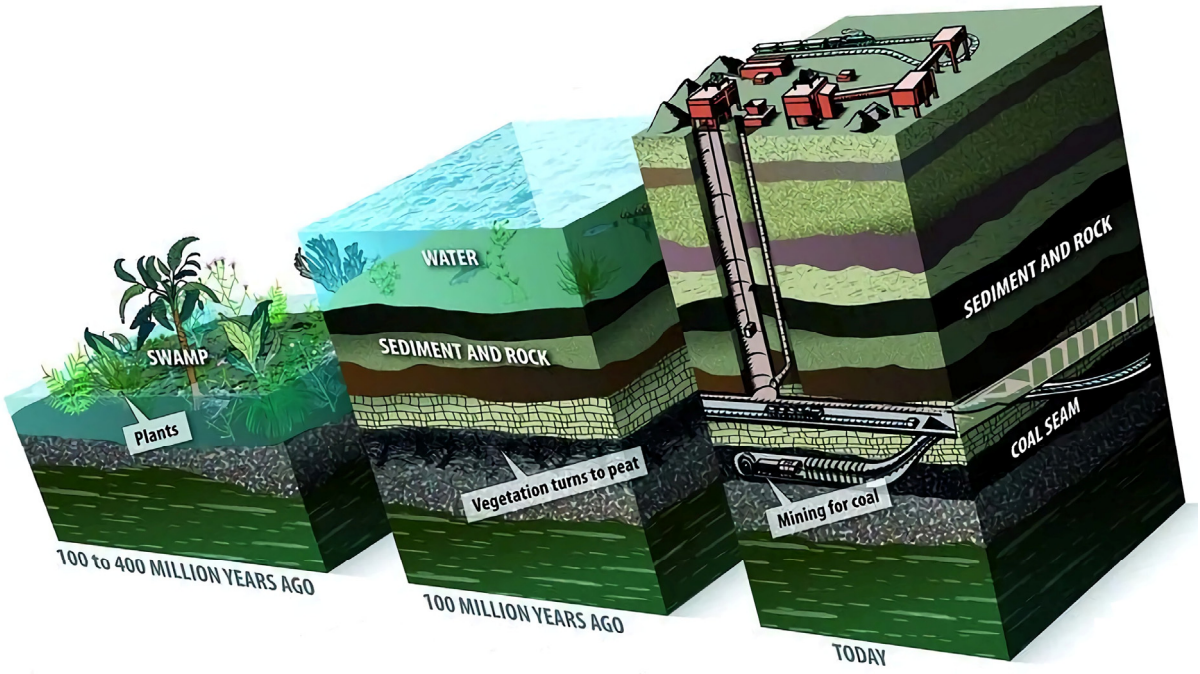

Figure 1. Formation process of coal resources.

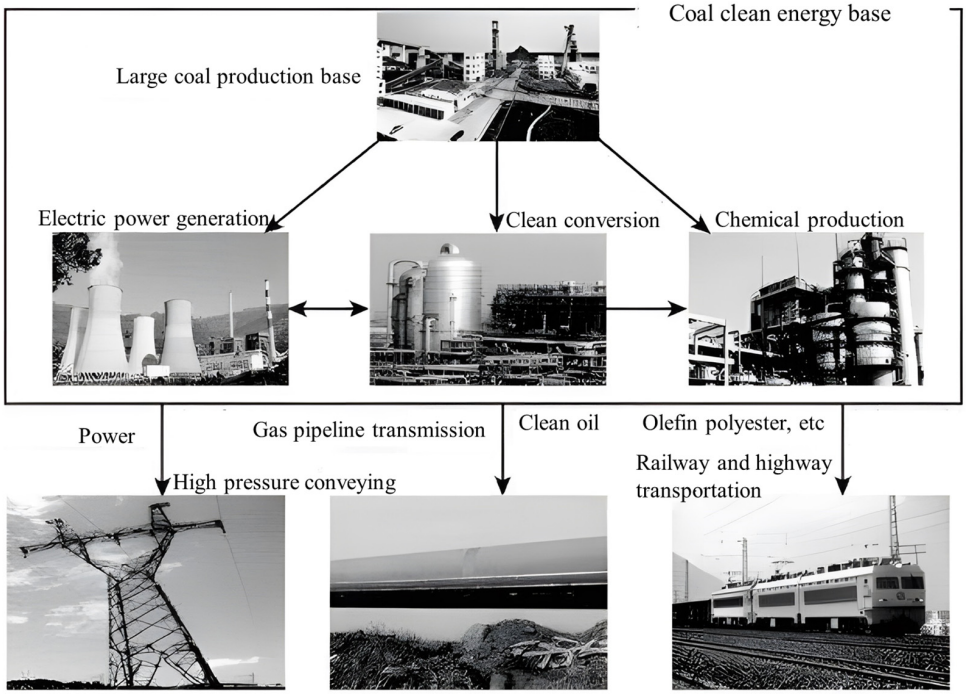

Figure 2. Application of clean coal technology.

The traditional utilization of coal in China is inefficient, and the power industry has become the main emission source of CO_2. It is urgent to build a low-carbon power industry system. At the same time, there is serious waste in China's coal mining due to technical or human factors. In the environment of promoting comprehensive energy utilization, this problem must be improved. From the evolution and development trend of coal science and technology, the integration of coal, mine construction, and underground

space development and utilization are inseparable. Some scholars have put forward a roadmap for coal technology revolution in the whole industrial chain based on four aspects: scientific mining, near-zero ecological damage, clean and low-carbon utilization, mine construction, and comprehensive utilization of underground space [7–9].

Coal resources will still occupy the status of the basic national energy source for a long time in the future. To solve the inequality between coal resource distribution areas and consumption areas, the Chinese government should vigorously develop the transportation industry and improve the transportation capacity of the central and western regions. China's major coal-producing areas have been concentrated in east and south China for a long time. Due to the distribution of railway transportation capacity, coal supply, especially power coal supply, is relatively tight in most provinces and cities in central Hunan, Hubei, Jiangxi, and some western regions. The Chinese government should adjust the structure of railway transport capacity, increase investment in railway construction, and rationally allocate the country's coal resources [10].

Because of the strategic position of coal resources, the globalization of the coal trade has become an inevitable trend. Coal resources are widely distributed all over the world. In the northern hemisphere, two huge world-class coal accumulation belts are the most prominent. One stretches across Eurasia, starting from Britain in the west, passing through Germany, Poland, and the former Soviet Union in the east, extending eastward to the east of North China and Russia's far east. The other extends in the east–west direction in north-central North America, including the coal fields of the USA and Canada. Coal resources in the southern hemisphere are mainly distributed in temperate regions, and coal resources in Australia, South Africa, Botswana, and Mozambique are affluent. The recoverable reserves of the world's major coal resource countries are shown in Figure 3. The proportion of coal resources in a country's disposable energy structure reflects the position of the coal industry in the country's energy consumption, which is also the basic factor determining the development of the country's coal industry. The composition of disposable energy structure and the proportion of coal in the world's major countries are shown in Table 1. China's coal resources account for 69.3% of the country's energy. Coal will continue to be China's primary energy source for a long time. Therefore, it is of great practical significance to reduce the waste of coal resources and realize the efficient and economic mining of coal resources. The COVID-19 pandemic had a great impact on the global energy market. The reduction in disposable energy and carbon emissions reached a new high since World War II. However, the important position of coal in traditional energy will continue for a long time.

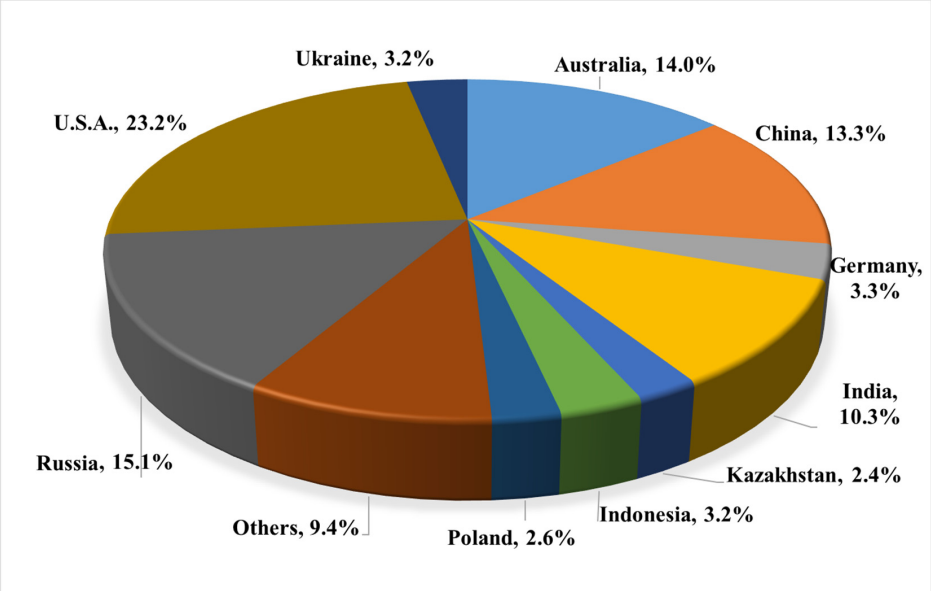

Figure 3. Proportion of proved recoverable reserves in major coal resource countries [11].

Table 1. Composition of disposable energy structure and proportion of coal in major countries in the world/million tons of oil equivalent [12].

	Petroleum	Natural Gas	Coal	Nuclear Energy	Hydropower	Total	Proportion of Coal
South Africa	26.9	3.4	89.8	3.2	0.4	123.7	72.59%
China	483.7	129.5	1873.3	22	194.8	2703.3	69.30%
Kazakhstan	12.8	8.5	35	—	1.8	58.1	60.24%
Poland	25.1	14.9	54	—	0.5	94.5	57.14%
India	171.6	49.1	289.3	7.5	6.2	543.7	53.21%
Australia	46.7	22.9	49.3	—	4.1	123	40.08%
Indonesia	71.6	32.2	50.4	—	2.9	157.1	32.08%
Republic of Korea	108.8	45	81.8	34	0.7	270.3	30.26%
Germany	111.5	67.7	79.2	22.5	4.8	285.7	27.72%
Japan	218.2	105.1	124.4	4.1	18.3	470.1	26.46%
U.S.A.	819.9	654	437.8	183.2	63.2	2158.1	20.29%
Russia	147.5	374.6	93.3	40.3	37.8	693.5	13.45%
Columbia	12.7	8.9	4	—	10.8	36.4	10.99%

Data Source: BP world energy statistics yearbook, 2013.

2. Need for Research

China's coal resource reserve is very important and related to the development of the national economy and society. Due to the non-renewable nature of coal, the rational utilization of coal resources is very important for China to achieve sustainable development. In the process of mining coal resources, enterprises generally have the behavior of "mining fertilizer and losing thin". When the coal price rises, enterprises generally have the phenomenon of blindly expanding production. To promote coal production enterprises to save resources and reasonably develop resources, the state should establish and improve relevant systems as soon as possible to curb the waste of coal resources in all aspects. The long-standing common problems in the process of coal mining are resource waste and ecological damage. With the global energy shortage and the increasing importance of the ecological environment, the rational exploitation and utilization of coal resources have become more important than ever. Starting from the important position and role of the coal industry in China's economic and social development, Dr. Ouyang studied the contradictory relationship between the development of the coal industry and the development of the national economy and the cost of resources and environment, and proposed that the intensive development of China's coal industry under the constraints of resources and environment is feasible and beneficial [13]. Zhang comprehensively and objectively analyzed the current situation of China's coal resources, pointed out many problems existing in the process of coal resource exploration and coal mining, and put forward ideas and countermeasures to improve the guarantee degree of coal resources and rational development and utilization. These opinions are of great significance for promoting the comprehensive, coordinated, and sustainable development of China's coal industry [14]. Liao and Qian first put forward the concept of realizing the green mining of coal resources, along with scientific research a and technical framework, and then put forward the academic viewpoint of realizing scientific mining, comprehensively describing the important progress made in breaking through the concept of traditional coal mining technology [15].

3. Problems and Countermeasures for a Working Face

The 14,211-mining face is the 11th fully mechanized mining face of the 4^{-2} coal in panel 1 of the Zhangjiamao company (Northern Shaanxi mining); the average buried depth of the working face is +300 m. The working face is a double lane layout with one entry and one return. The designed advancing mining dip length is 2370.3 m, the strike length is 305.7 m, and the mining area is 724,600.7 m^2. The geological reserves of coal in the mining area are 6.83 million tons. The one-time inclined longwall mining method and comprehensive mechanized mining technology were adopted in the 14,211 fully mechanized mining face.

The natural caving method was adopted for the goaf roof, and the advanced pre-splitting roof cutting method was adopted for the reserved roadway side. The ventilation mode was two inlets and one return.

There is no false roof in the coal seam of the 14,211 fully mechanized mining face. The direct roof of the coal seam is gray siltstone with a thickness of 3.1 m. The key layer of the basic roof is the interbedding of medium sandstone and medium-grained sandstone, with a thickness of 42.06 m. The average saturated compressive strength of the roof rock stratum is 23.7 Mpa, belonging to the unstable~relatively stable type (I~II). The mechanical parameters of the coal and rock mass are shown in Table 2, and the lithologic column within the upper and lower range of the coal seam is shown in Figure 4. In recent years, the model operation based on batch data verification has become popular. Some studies have used it to estimate the shear strength of rock joints, evaluate the stability of underground entrance excavation, and predict the mine safety evaluation system under the encouraged pillar strength, which has positive significance for mine safety mining and management [16–18].

Table 2. Mechanical parameters of the strata.

Position	Rock Stratum	Thickness/ m	Bulk Modulus/ GPa	Shear Modulus/ GPa	Cohesion/ MPa	Tensile Strength/ MPa	Friction Angle/ (°)	Density/ (kg·m^{-3})
Main roof	Medium sandstone	42.06	10.8	6.5	3.90	5.8	37	2755
Direct Roof	Siltstone	3.1	8.5	4.3	2.75	1.84	34	2460
Coal seam	No. 4	3.88	0.99	0.35	1.0	0.5	28	1855
Immediate bottom	Mudstone	1.85	2.1	1.2	5.3	0.5–1.2	31	2150

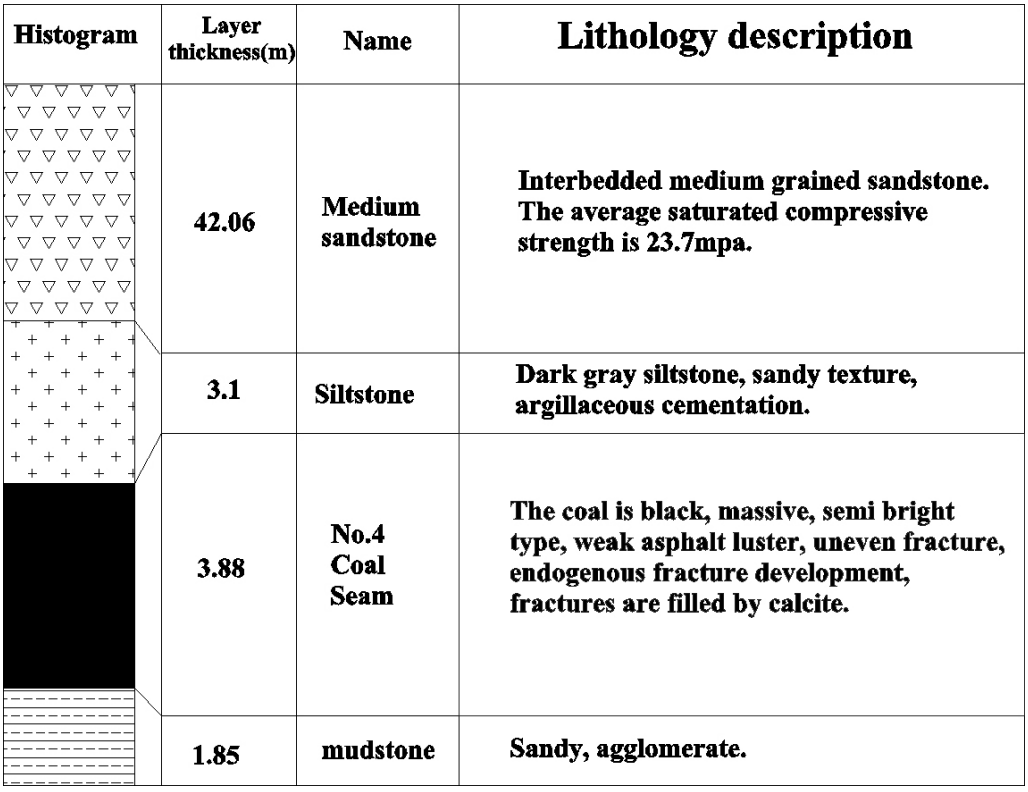

Figure 4. Lithology histogram of roof and floor of 4# coal seam.

The fixed attribute of traditional coal mining methods (retaining protective coal pillars) leads to the waste of a large amount of coal resources during coal resource mining. This part of the lost resources may become permanent due to the characteristics of the goaf. The roof control of the 14,211 working face adopted shield support. In the original support process,

the roof adopted advanced support, and both the return air chute and transportation chute were 20 m ahead of the working face. In the mining process, the repeated movement of the advance support and the occupation of roadway space greatly affect the production efficiency of the mine, which also increases the construction technology and operation cost at the end of the roadway. The 110-roof cutting roadway protection method proposed by academician He Manchao is used to solve or reduce the impact of this problem on the Zhangjiamao coal mine. From the perspective of economic benefits and resource recovery rate, the 110 method greatly reduces the excavation cost of the fully mechanized mining face. The pillar-free mining technology adopted by the 110 method greatly improves the recovery rate of coal resources. Compared with the original mining method, the 110 method can reduce coal waste by 173,600 tons, which accounts for 4.9% of the coal reserves of the working face.

4. Principle, Advantages, and Process Design of the "110 Construction Method"

The so-called "110 construction method" refers to "1 working face, 1 roadway, and 0 coal pillars" [19–21]. The "110 construction method" is developed based on the "roof cutting short-arm beam theory" proposed by academician He Manchao; that is, directional roof cutting is carried out on one side of the goaf, and the roof is cut off by the mine pressure. The combination of high preload, constant resistance, and a large deformation anchor cable is used to control the stability of the roadway roof and ensure the stability and safety of the roadway surrounding rock on the goaf side. The local surrounding rock technology is adopted to realize the automatic cyclic roof cutting of the large-area roof. The pillar-free mining technology in this environment eliminates or reduces the occurrence of accidents and disasters. The mining technology of the bottomless coal pillar with roof directional presplitting and roadway automatic pressure relief has been successfully formed [22–24]. Some scholars have studied the external container composed of polyvinyl chloride (PVC) with large fracture strain and fiber-reinforced polymer (FRP) with a high strength to weight ratio. The addition of cement-based grouting material to the container can improve the axial deformation capacity, which can be used as a reference for similar working face support [25]. The field support form and principle diagram of the "110 construction method" are shown in Figure 5.

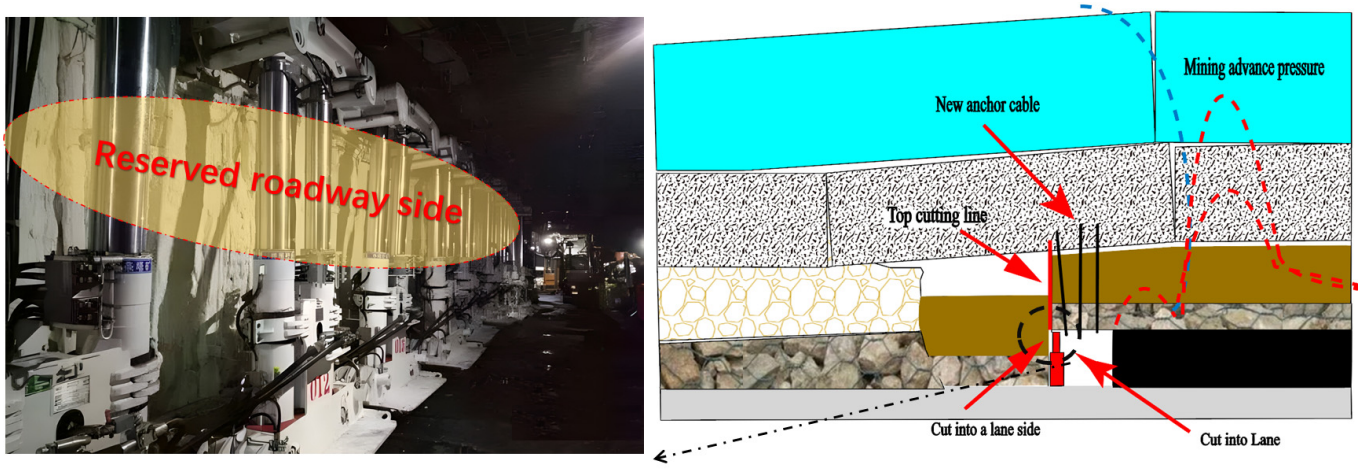

Figure 5. Schematic diagram and site picture of the "110 construction method".

Before the "110 construction method" is adopted, a ventilation system with two roadway air inlets and one roadway air return should be formed. The Zhangjiamao coal mine belongs to a coal seam with low gas and low spontaneous combustion. If two tunnels are used for air intake on the working face, it is better to adopt the Y-type ventilation in the next working face. The fresh air becomes dirty after flowing through the working face, and the dirty air flows out of the working face through the reserved roadway section. The

Y-type ventilation mode is shown in Figure 6. With the rapid development of the economy and the intensification of energy consumption, the mining depth of coal mines worldwide has increased yearly. Gas emission and accumulation have become a great obstacle to mine safety and efficiency; the use of Y-type ventilation is an effective way to ameliorate this problem [26,27]. Due to the stable safety protection and positive economic benefits of the "110 construction method", this technical measure has been successfully popularized and implemented in the mine.

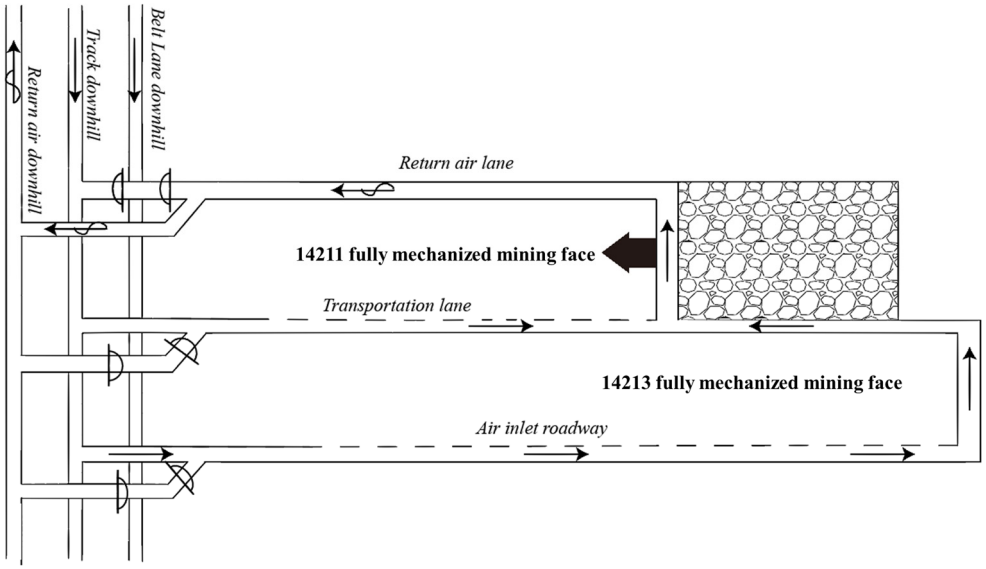

Figure 6. Schematic diagram of Y-type ventilation mode of the working face (top view).

5. Engineering Application and Effect Analysis

According to the design support parameters, the roadway support is strengthened. The transportation chute and the top plate of the chute shunting room were designed, and the "anchor cable + W steel belt support" was added, based on the anchor mesh beam support. All these measures prevent roof instability or roof fall of the reserved roadway section when the goaf roof is cut or periodic roof pressure occurs. Prestressed steel strands with a nominal diameter of φ 21.8 mm and lengths of 10 m and 9 m were used as the anchor cables; the roadway section support parameters are shown in Figure 7 and Table 3. Some studies have used discontinuous deformation to simulate surface settlement and achieved good results. The research verified that the joint inclination and excavation position were two important factors in the excavation design of underground space, because they affect the surface settlement and the stress concentration around the excavation area [28,29]; this research is helpful for us to carry out numerical simulation in the future.

Table 3. Support parameters of the working face transportation chute.

Support Location	Support Mode	Support Material Parameters	Spacing × Row Spacing
Roof	Anchor cable, and W steel strip	Φ21.8 mm × 9000 mm. Φ21.8 mm × 10,000 mm (goaf side)	1500 mm × 2400 mm 1500 mm × 1200 mm (goaf side)
Left side (Goaf side)	Bolt support Wire (reinforcing) mesh	Φ22.0 mm × 2200 mm. 50 mm× 50 mm (100 mm× 100 mm)	900 mm × 1200 mm
Right side	Bolt support	Φ22.0 mm × 2200 mm.	900 mm × 1200 mm

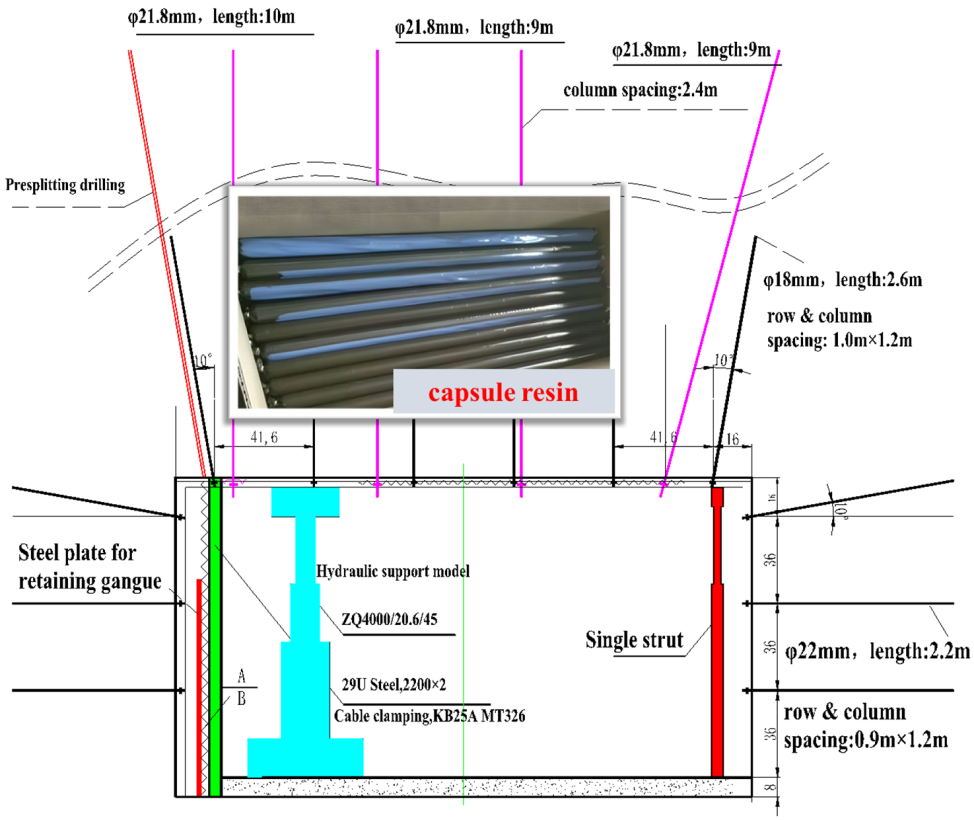

Figure 7. Schematic diagram of roadway support. A: φ 4 mm lead wire mesh, mesh size 50 mm × 50 mm. B: φ 6.5 mm reinforcing mesh, mesh size 100 mm × 100 mm. Cable row spacing and column spacing: 1500 mm × 1200 mm.

Each cable was anchored with one k2360 capsule resin and two z2360 capsule resins. The preload was no less than 280 kN, the ultimate tensile breaking force was not less than 583 kN, and the elongation was not less than 3.5%. The transportation chute was close to the primary mining side, the anchor cable spacing was 1200 mm, and the anchor point was 300 mm from the cutting top line and 600 mm from the main mining side. Three adjacent anchor cables were connected by a 2700 mm long W steel belt along the roadway. The row spacing between the other anchor cables was 1500 × 2400 mm, and the length of the supporting W steel strip was 3300 mm, which was arranged perpendicular to the roadway trend. The row spacing between anchor cables in the transport shunting chamber was 1250 × 2400 mm, the supporting W steel strip length was 2800 mm, and the anchor cable tray adopted an arched iron tray with a specific size of 300 × 300 × 16 (mm). In roadway excavation, the bolt support density was increased to ensure the surrounding rock stability of the roadway secondary mining side and the shunting room. The bolts used were glass fiber reinforced plastic bolts with a diameter of 22 mm and a length of 2200 mm. The support spacing and row spacing were 900 × 1200 mm; the top view of the roadway roof support is shown in Figure 8.

In this project, the bi-directional shaped charge blasting presplitting technology was adopted, and specific explosives were installed in the shaped charge device, which had the energy accumulation effect in two set directions. After the explosive was detonated, the surrounding rock pressure was uniformly compressed in the non-set direction but concentrated in the set direction. A microseismic (MS) system was used to monitor vibration signals and collect and analyze vibration signals in the process of drilling string construction. The purpose of "one hole for multiple purposes" can be achieved in drilling depth monitoring, bearing pressure distribution, and pressure relief effect evaluation, which can evaluate the mine pressure more accurately and effectively [30,31]. The GS-GMDH model proposed by some researchers has verified its ability to predict the ground vibra-

tion caused by blasting, which has guiding significance for the feasibility of predicting a blasting operation in advance [32]. According to the characteristic that rock is easily damaged by tension, the tensile fracture forming of rock mass in the set direction was realized. The calculated depth of the pre-crack hole was 8.25 m, the designed depth of the crack hole was 8.5 m, and the hole diameter was 50 mm. The slit hole was arranged 0.3 m away from the main mining side of the roadway, and the included angle between the top slit hole and the plumb line direction was 10° (towards the goaf). As the roof of the working face was mainly siltstone and fine-grained sandstone, the slit hole spacing of the roof was designed to be 600 mm, with one pre-split hole in each row. The pre-crack of advance blasting was ~70 m away from the working face. The W steel strip made the roof connection structure an interrelated whole, which played a better bearing role [33]. As an effective blasting method, pressure relief blasting is widely used. Some scholars use the mixed model of information entropy and unascertained measure with different membership functions to evaluate explosive areas. The results showed that the combined model can eliminate the interference of subjective factors and ensure the reliability of the evaluation results [34].

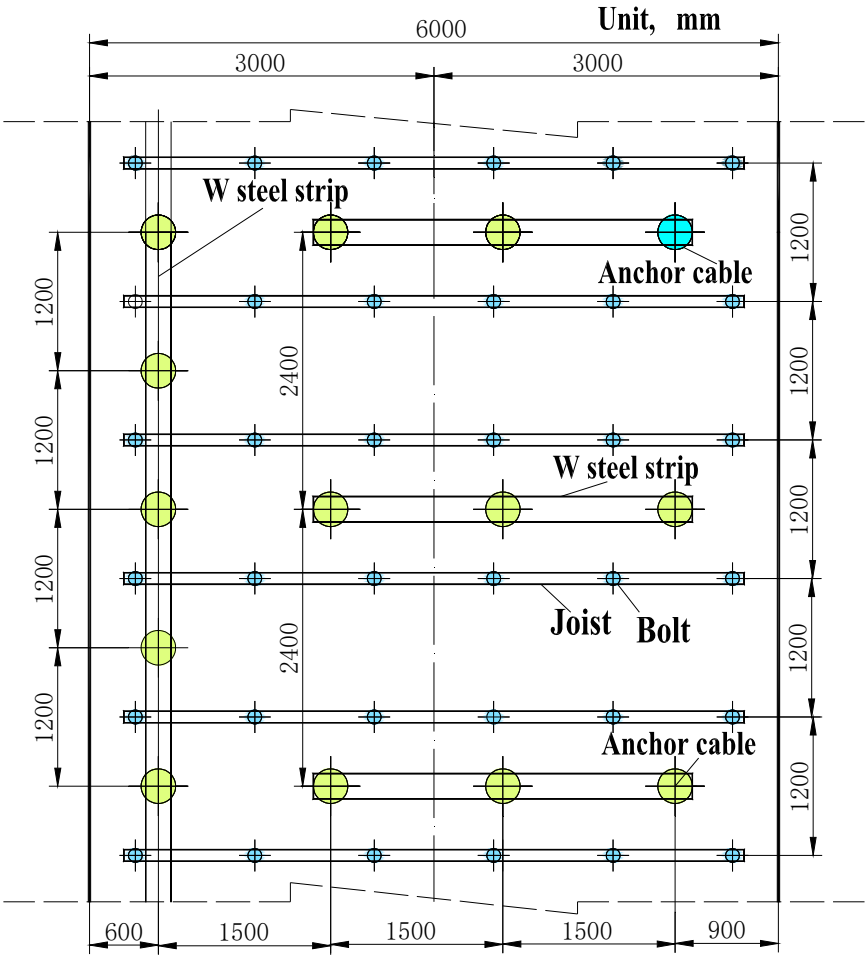

Figure 8. Top support plan of 14,211 and 14,212 transport chute (unit, mm).

The ground above the working face is an area without personnel activities. After implementing the design scheme, the surface settlement was small, and the impact of mining activities on the ground was not obvious. The relative position between the development trend of ground fissures and the working face is shown in Figure 9.

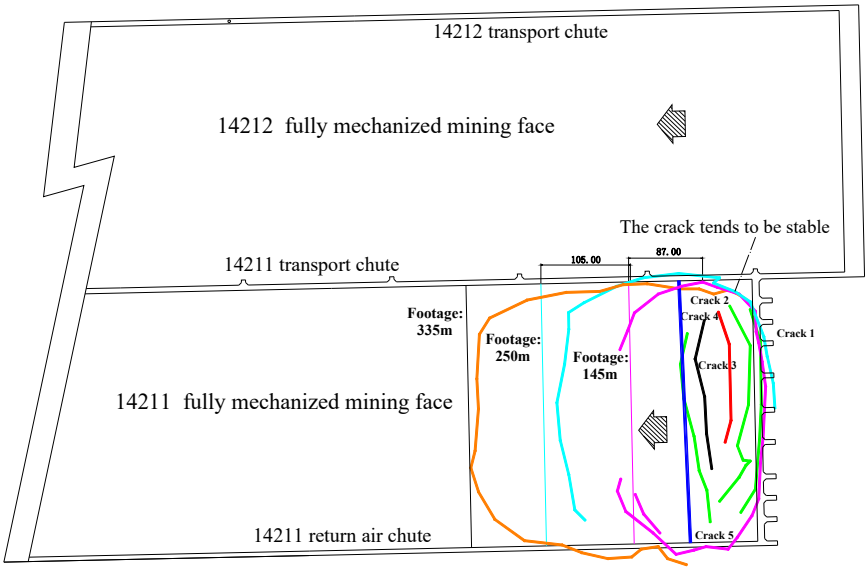

Figure 9. Working face layout and ground crack position.

The fracture distribution area photographed and depicted by the UAV was consistent with the roof activity law during the advancement of the underground working face. The initial collapse of the roof led to large surface subsidence at the cut hole position. When the working face entered the stage of cyclic top caving, the surface cracks gradually decreased. The farther away from the cut hole, the smaller the cracks became; the later roof collapse had a very slight impact on the surface. This is consistent with the gradual reduction and thinning of cracks photographed and drawn by UAV in Figure 9. Figure 10 shows the impact of the collapse and extension of the goaf to the ground during mining activity. The surface subsidence of the cut hole part was apparent, but the area was limited. The fracture area was only limited to the cut hole position. As the working face entered the normal cycle, the surface subsidence was weakened, and the surface fissures tended to be stable. The slight fissures and subsidence of the ground did not threaten the surface vegetation and ecology.

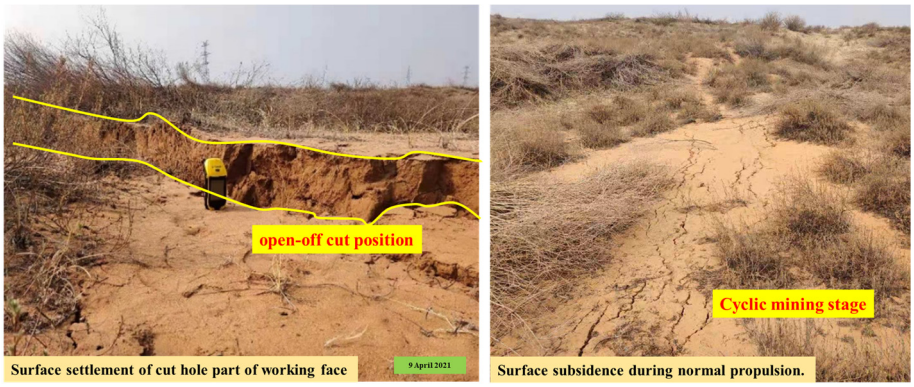

Figure 10. Comparison of surface subsidence between cut hole position and normal mining.

6. Conclusions

By implementing the 110-construction method, the coal recovery rate was improved, and the waste of resources was reduced. Field engineering verified the feasibility of the design scheme; and the main conclusions are as follows:

(1) The distribution of global coal resources is uneven, and the contradiction between social development and the intensified energy consumption is irreconcilable. In the

process of resource development, it is imperative to improve the resource recovery rate and reduce the waste of coal resources.

(2) The successful application of the 110-construction method in the Zhangjiamao coal mine avoided the waste of 173,600 tons of coal, with a value of RMB 152.814 million ($23.33 million), which provides a direct and beneficial experience for other coal mines.

(3) During the implementation of the 110-construction method, the maximum subsidence of the roof was 8.39 cm, and the average subsidence was ~4.5 cm; the roof was complete and reliable. There were no major safety accidents or casualties in the mining process.

(4) After the working face entered the normal mining process, the surface settlement was significantly reduced. Only small cracks extended to the surface, which did not threaten the ground vegetation and organisms. On the premise of safe production, the technology saved excavation quantities, reduced coal loss rate, improved production efficiency, and protected the surface ecology, so as to form a positive cycle of the technology.

Author Contributions: Z.L. and J.Z. designed and wrote the paper; X.S. supervised the paper writing; H.C., Y.Z. (Yanyang Zhang) and Y.Z. (Yanjun Zhang) collected and collated materials and field data collection. All authors have read and agreed to the published version of the manuscript.

Funding: This research was funded by the "Accurate delay rock breaking mechanism and key technology innovation team", grant No. 2020D14043.

Institutional Review Board Statement: Not applicable.

Informed Consent Statement: Not applicable.

Data Availability Statement: The data used to support the findings of this study are available from the corresponding author upon request.

Conflicts of Interest: We declare that we do not have any commercial or associative interest that represents a conflict of interest in connection with the work submitted.

References

1. Wang, W.; Li, S.; Han, J. Analysis of coal supply and demand situation and industry development prospect of major coal resources in the world. *China Min. Mag.* **2015**, *24*, 5–9.
2. Cui, C. Coal resources and distribution characteristics in China. *Sci. Technol. Inf. Dev. Econ.* **2011**, *21*, 181–182.
3. Wei, Z.; Jing, Q.; Zhu, C. From the sustainable development strategy to formulate China's coal resources policy. *Res. Coal Econ.* **2003**, *7*, 19–22.
4. Kang, H.; Wang, G.; Jinag, P.; Wang, J.; Zhang, N.; Jing, H.; Huang, B.; Yang, B.; Guan, X.; Wang, Z. Concept of surrounding rock control and intelligent mining technology for 1000-meter deep Coal Mine. *J. China Coal Soc.* **2018**, *43*, 1789–1800. [CrossRef]
5. Li, W. Status quo and development direction of intelligent mining technology for deep coal resources. *Coal Sci. Technol.* **2021**, *49*, 139–145. [CrossRef]
6. Wang, G.; Pang, Y.; Ren, H. Key technology and prospect of intelligent mining of three soft coal seams in kilometer deep well. *Coal Eng.* **2019**, *51*, 1–6.
7. Zhao, J. Analysis and policy suggestions on clean utilization of coal industry from the perspective of low-carbon economy. *J. China Coal Soc.* **2011**, *36*, 514–518. [CrossRef]
8. Xie, H.; Wang, Y.; Ren, H.; Liu, J.; Ge, S.; Zhou, H.; Wu, G.; Ren, S. New idea of Coal Revolution and development of coal science and technology. *J. China Coal Soc.* **2018**, *43*, 1187–1197. [CrossRef]
9. Lu, X. Present situation and development suggestions of coal clean exploitation and utilization in China. *Coal Eng.* **2016**, *48*, 8–10.
10. China Industry Research Report—Panoramic Survey and Investment Strategy Report of China's Coal Industry from 2019 to 2025. Available online: https://www.huaon.com/channel/coal/602026.html#abstract (accessed on 15 March 2022).
11. BP. *BP Statistical Review of World Energy 2021*; BP: London, UK, 2021.
12. BP. *BP Statistical Review of World Energy 2013*; BP: London, UK, 2013.
13. Ouyang, X. Research on the Intensive Development of China's Coal Industry under the Constraints of Resources and Environment. Ph.D. Thesis, China University of Geosciences, Beijing, China, 2007.
14. Zhang, S. Guarantee degree and rational development and utilization of coal resources in China. *China Coalf. Geol.* **2004**, *1*, 4–6.
15. Miao, X.; Qian, M. Research on Green Mining of Coal Resources in China: Current and Status a Future Prospects. *J. Min. Saf. Eng.* **2009**, *26*, 1–14.

16. Hasanipanah, M.; Meng, D.; Keshtegar, B.; Trung, N.T.; Thai, D.K. Nonlinear models based on enhanced Kriging interpolation for prediction of rock joint shear strength. *Neural Comput. Appl.* **2021**, *33*, 4205–4215. [CrossRef]
17. Zhou, J.; Huang, S.; Qiu, Y. Optimization of random forest through the use of MVO, GWO and MFO in evaluating the stability of underground entry-type excavations. *Tunn. Undergr. Space Technol.* **2022**, *124*, 104494. [CrossRef]
18. Du, K.; Li, X.; Su, R.; Tao, M.; Lv, S.; Luo, J.; Zhou, J. Shape ratio effects on the mechanical characteristics of rectangular prism rocks and isolated pillars under uniaxial compression. *Int. J. Min. Sci. Technol.* **2022**, *32*, 347–362. [CrossRef]
19. China Coal Construction Association; China National Energy Administration. *Code for No-Pillar Mining with Gob-Entry Retaining of the 110 Method*; China Coal Construction Association: Beijing, China; China National Energy Administration: Beijing, China, 2019.
20. He, M.; Guo, Z. Anti-Collapse Structure beside Roadway Based on 110 Construction Method for Breaking Roof. Available online: https://patentscope2.wipo.int/search/en/detail.jsf?docId=WO2016206617 (accessed on 29 December 2016).
21. Kang, H.; Niu, D.; Zhang, Z.; Lin, J.; Li, Z.; Fan, M. Deformation characteristics and supporting technology of surrounding rock of deep goaf retaining roadway. *Chin. J. Rock Mech. Eng.* **2010**, *29*, 1977–1987.
22. Zhang, X.; Pak, R.Y.S.; Gao, Y.; Liu, C.; Zhang, C.; Yang, J.; He, M. Field experiment on directional roof presplitting for pressure relief of retained roadways. *Int. J. Rock Mech. Min. Sci.* **2020**, *134*, 104436. [CrossRef]
23. Yang, X.; Sun, Y.; Wang, E.; Mao, W. Study and Application of Gob-Side Entry Retaining Formed by Roof Cutting and Pressure Relief in Medium-Thickness Coal Seam with Hard Roof. *Geotech. Geol. Eng.* **2020**, *38*, 3709–3723. [CrossRef]
24. Zhang, X.; Chen, L.; Gao, Y.; Hu, J.; Yang, J.; He, M. Study of an Innovative Approach of Roof Presplitting for Gob-Side Entry Retaining in Longwall Coal Mining. *Energies* **2019**, *12*, 3316. [CrossRef]
25. Zhao, H.; Ren, T.; Remennikov, A. A hybrid tubular standing support for underground mines: Compressive behaviour. *Int. J. Min. Sci. Technol.* **2021**, *31*, 215–224. [CrossRef]
26. Yuan, L. Theory and practice of coal pillar—Free co-mining in low permeability coal seam group. *Chin. Eng. Sci.* **2009**, *11*, 72–80.
27. Yuan, L. Distribution characteristics and extraction technology of gas in mined-out side during pressure relief mining of key strata in the first mining of low permeability coal seam group. *J. China Coal Soc.* **2008**, *33*, 1362–1367.
28. Do, T.-N. Verifying discontinuous deformation analysis simulations of the jointed rock mass behavior of shallow twin mountain tunnels. *Int. J. Rock Mech. Min. Sci.* **2020**, *130*, 104322. [CrossRef]
29. Do, T.N.; Wu, J.-H. Simulation of the inclined jointed rock mass behaviors in a mountain tunnel excavation using DDA. *Comput. Geotech.* **2020**, *117*, 103249. [CrossRef]
30. Zhang, W.; Li, C.; Jin, J.; Qu, X.; Fan, S.; Xin, C. A new monitoring-while-drilling method of large diameter drilling in underground coal mine and their application. *Measurement* **2021**, *173*, 108840. [CrossRef]
31. Zhang, W.; Li, C.; Ren, J.; Wu, Z. Measurement and application of vibration signals during pressure relief hole construction using microseismic system. *Measurement* **2020**, *158*, 107696. [CrossRef]
32. Jahed Armaghani, D.; Hasanipanah, M.; Bakhshandeh Amnieh, H.; Tien Bui, D.; Mehrabi, P.; Khorami, M. Development of a novel hybrid intelligent model for solving engineering problems using GS-GMDH algorithm. *Eng. Comput.* **2020**, *36*, 1379–1391. [CrossRef]
33. Zhang, J.; Chen, H.; Shi, X.; Guan, W.; Sun, X. Research on Stress Distribution Characteristics for Uniquely Shaped Roadway with Hard Roof in Steeply Inclined Coal Seam and Support Technology of Reducing Vibration Impact. *Shock. Vib.* **2021**, *2021*, 2785479. [CrossRef]
34. Zhou, J.; Chen, C.; Du, K.; Jahed Armaghani, D.; Li, C. A new hybrid model of information entropy and unascertained measurement with different membership functions for evaluating destressability in burst-prone underground mines. *Eng. Comput.* **2020**, *38*, 381–399. [CrossRef]

sustainability

MDPI

Article

On the Physical and Mechanical Responses of Egyptian Granodiorite after High-Temperature Treatments

Mohamed Elgharib Gomah [1,2], Guichen Li [1,*], Changlun Sun [3], Jiahui Xu [1], Sen Yang [1] and Jinghua Li [1]

[1] Key Laboratory of Deep Coal Resource Mining, School of Mines, China University of Mining and Technology, Ministry of Education of China, Xuzhou 221116, China; mohammedel-ghareeb.12@azhar.edu.eg (M.E.G.); tb20020033b3ld@cumt.edu.cn (J.X.); ts20020064a31tm@cumt.edu.cn (S.Y.); ljhcumt@cumt.edu.cn (J.L.)
[2] Mining and Petroleum Engineering Department, Faculty of Engineering, Al-Azhar University, Cairo 11884, Egypt
[3] Department of Future and Smart Construction Research, Korea Institute of Civil Engineering and Building Technology, Gyeonggi 10223, Korea; sunchanglun@kict.re.kr
* Correspondence: liguichen@cumt.edu.cn; Tel.: +86-158-0521-5566

Abstract: In the design and stability of thermal engineering applications, a thorough understanding of the evolution of damage in the rock following high-temperature treatments is crucial. Hence, this study investigates the influence of high temperatures on Egyptian granodiorite rock properties, given its widespread use as ornamental stones and aggregate material for roadways. Temperature effects up to 800 °C on its physical and mechanical responses were examined in conjunction with microstructure alterations. The results show that the density of granodiorite decreases after heat exposure due to a gain in volume and a loss in mass, with volume expansion being the most important component. In addition, the uniaxial compressive strength increases up to 400 °C before reducing linearly as the temperature increases, while the elastic modulus and P-wave velocity show a reducing trend with the temperature. This study suggests that granodiorite has a thermal damage threshold of 400 °C, beyond which its microstructure and physical and mechanical characteristics deteriorate, and granodiorite becomes less brittle and more ductile. Hence, at the mutation range (between 400 and 600 °C), the physical and mechanical responses shift from a stable to an unstable state. As a result, the microstructure of the granodiorite samples was destroyed at 800 °C, resulting in a significant drop in compressive strength and dilemmas in measuring the P-wave and elastic modulus. Accordingly, the findings of this study can be used to aid in the safe handling of this rock in high-temperature conditions.

Keywords: physical and mechanical responses; Egyptian granodiorite; thermal damage threshold; microstructure; thermal constructions

Citation: Gomah, M.E.; Li, G.; Sun, C.; Xu, J.; Yang, S.; Li, J. On the Physical and Mechanical Responses of Egyptian Granodiorite after High-Temperature Treatments. *Sustainability* **2022**, *14*, 4632. https://doi.org/10.3390/su14084632

Academic Editor: Giovanna Pappalardo

Received: 25 February 2022
Accepted: 8 April 2022
Published: 13 April 2022

Publisher's Note: MDPI stays neutral with regard to jurisdictional claims in published maps and institutional affiliations.

Copyright: © 2022 by the authors. Licensee MDPI, Basel, Switzerland. This article is an open access article distributed under the terms and conditions of the Creative Commons Attribution (CC BY) license (https://creativecommons.org/licenses/by/4.0/).

1. Introduction

In recent decades, high-temperature rock mechanics have garnered considerable attention, particularly in geological engineering fields such as deep mining, geothermal energy extraction, nuclear engineering construction, coal mining, and hydrothermal systems [1–5]. The temperature in these thermal applications varies based on the type of environment. The temperature of a coal fire, for example, is usually between 700 and 900 °C [6,7]. Moreover, temperatures can extend to 1000 °C during coal gasification procedures [8]. Fire damage to rocks is also relevant to various sectors, including geomorphology, cultural heritage, civil works, and engineering geology. For example, in the case of a building fire, construction materials can be exposed to temperatures exceeding 700 °C [9]. Hence, the temperature has numerous effects on rocks' physical and mechanical properties [10], which leads to several inevitable problems to be solved in rock mechanics [11].

Recognizing the consequences of temperature on various rocks' physical and mechanical responses is of extraordinary significance for reducing the potential jeopardies generated by thermal damage and safety evaluation in rock engineering [12–16]. At high temperatures, all rocks are susceptible to deterioration. On the other hand, porous sedimentary stones tend to show less visible mechanical damage than dense, low-porosity rocks, specifically multi-mineral rocks like granites [17]. Furthermore, due to intrinsic mineralogical and textural varieties, the impact of the temperature on the alteration of the rock properties may differ among rocks of similar origins [18,19]. For example, high-porosity weathered granites may withstand higher temperatures than low-porosity fresh granites [20]. Therefore, the physical and mechanical behaviors of different kinds of stones after heat treatment have been investigated in some of the former literature, among them being granite [21–26], marble [27–29], sandstone [30,31], shale [32], salt rock [33], limestone [34,35], and mudstone [36–38]. Commonly, it has been observed that in all rocks that have been examined below their melting point, the physical and mechanical properties for them altered following heat treatment.

The physical responses [39] showed, for example, that the rates of mass loss, volume expansion, and density reduction increase as the temperature rises. Quartz's thermal expansion is very nonlinear, while the rest of the granodiorite-forming minerals, on the other hand, have linear temperature dependencies in their thermal expansion [40]. The mismatch of thermal expansion and the associated thermal stress within mineral grains subjected to high temperatures induce microcracks between and inside mineral particles [41], leading to rock structural damage. Hence, the ultrasonic wave velocity falls dramatically [42,43]. Some studies were primarily concerned with evaluating thermal damage from the microscopic approach. They detailed the internal mechanisms that modify rocks following a temperature rise that induces macroscopic property changes. For example, the authors of [44] investigated the P-wave velocity and microstructure modification of granite under open fire, concluding that microcrack creation is mostly responsible for reducing the P_v of granite as the temperature increases. In addition, the authors of [18] proposed that the chemical reactions in minerals during heating alter these physical properties of rock at high temperatures.

The uniaxial compressive strength (UCS) and elastic modulus (E) tests are most commonly used to evaluate mechanical rock properties in mining and civil engineering projects. However, the UCS and E tests have difficulties with direct measurements, including the necessity for accurate sample preparation and a large testing apparatus and the reality that these are destructive and time-consuming examinations [45,46]. On the other side, the mechanical responses of rocks may vary after thermal treatment [47–49]. Heat treatment can enhance or weaken rock strength within a specified temperature range [50–52]. Many researchers have examined the strength, deformation characteristics, and failure modes of rock that has been exposed to high temperatures [53–55]. For instance, depending on the rock type, structure, and mineral content, the peak strength of many rocks decreased by 40–60% with increasing temperatures (from 400 to 800 °C) [10,56]. According to [4], the stress–strain curves of Strathbogie granite showed plastic behavior at temperatures above 800 °C, and the brittle-plastic transformation has been observed under uniaxial compression between 600 and 800 °C. The authors of [24] performed uniaxial compression tests on granite to assess the impact of high temperatures on the crack damage and strength. They revealed that the crack damage threshold, strength, and static elastic modulus of granite increased at 300 °C before decreasing up to the max temperature of 800 °C.

Although the thermal damage of some rocks has been thoroughly explored, such as granite, marble, mudstone, and sandstone, systematic exploration of a new rock is crucial, and this research attempts to fill that gap. Hence, due to its rare experimental studies, the thermal damage impact on Egyptian granodiorite's physical and mechanical responses has been investigated. Granodiorite specimens were thermally treated at high temperatures up to 800 °C before being slowly cooled to ambient temperature. The experimental schemes started with estimating the initial physical properties of the

granodiorite specimens (e.g., density, size, mass measurement, and longitudinal wave). The next step was to subject each rock specimen to thermal processing by placing them in a high-temperature furnace with a temperature controller at the target temperatures. Afterward, the samples were gradually cooled to room temperature in the open air. Each rock specimen's physical parameters were then calculated once more. X-ray diffraction (XRD) and scanning electron microscopy (SEM) were used to illustrate the temperature-induced mineralogical changes and related microstructure degradation. Finally, the rock specimens were subjected to uniaxial compression examinations to examine the effect of thermal damage on the treated granodiorite's mechanical properties and failure patterns. These results will contribute as reference data for developing the knowledge of granodiorite rock thermal damage to predict and assess the stability and safety risks in thermal construction environments. As a result, a more realistic assessment of natural building stone thermal deterioration can be obtained.

2. Egyptian Granodiorite Rock

Granodiorites are coarse-grained igneous rocks with a grayish-white granularity and an intermediate composition between granite and diorite, with more plagioclase feldspar than orthoclase feldspar. Egyptian granite is divided into two types: young granite, which is pinkish to red in appearance and varies in kind from granitic to alkali granite, and old granite, which is dark gray and ranges from tonalite to granodiorite [57]. Due to settling in abundance in Egypt's eastern desert, the granodiorite stones were assembled from Egypt's Abo Marw region 130 km east of Aswan (Figure 1).

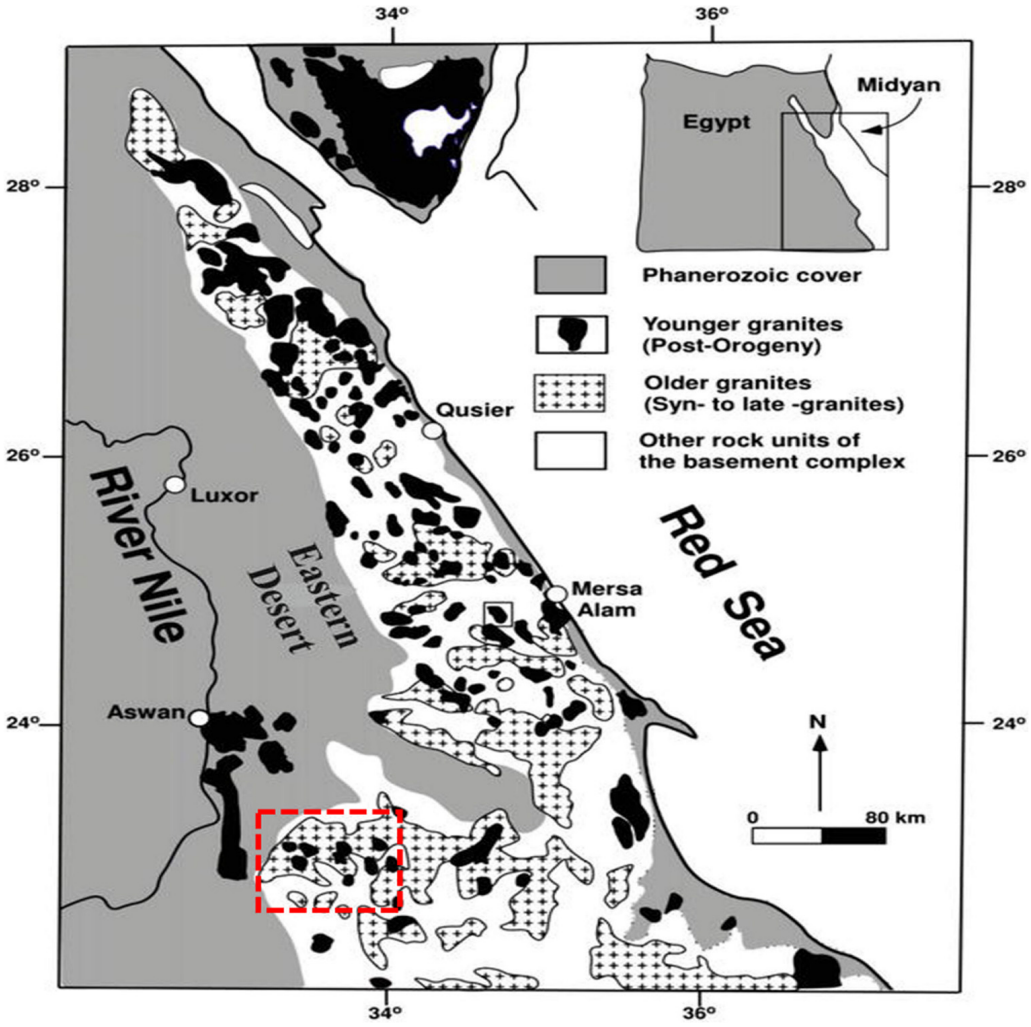

Figure 1. Map displaying the collection location of the granodiorite samples.

As a typical igneous rock widely used in modern constructions such as stairwells, hydro-engineering and bridges, road paving stones, architecture, and monuments, granodiorite's physical and mechanical properties when exposed to high temperatures were examined. Twenty-five cylindrical samples 55.5 mm in diameter and approximately 130 mm in length were drilled, following the standard the American Standard Test Method (ASTM) D7012–14 [58]. Granodiorite samples were prepared from cut blocks by the core-drilling machine. The granodiorite under study were fresh specimens distinguished by a gray color, with an average dry density of 2.69 g/cm^3, and the main components included quartz, P-feldspar, K-feldspar, and biotite. Before testing, the samples were dried at 105 °C in the oven for at least 24 h to remove all moisture content.

3. Methods

3.1. Heat Treatment Process

Thermal treatments were performed on the granodiorite samples in a Nabertherm B410 electric furnace, with a maximum heating temperature of 1300 °C and a temperature control precision of ±3 °C (Figure 2b). A modest heating rate of 5 °C/min was applied to minimize any potential thermal shock inside the specimens caused by the rapid temperature gradient [22,31,34]. Furthermore, the samples were maintained in the oven for 2 h after reaching the desired temperature to preserve the temperature uniformity within the specimens. The thermal effects on granodiorite were examined at five discrete spot temperatures: 200 °C, 400 °C, 500 °C, 600 °C, and 800 °C. Finally, the specimens were then gently cooled to room temperature in "the open air". To determine the thermal loss rate of granodiorite throughout the cooling process following the thermal treatments at the target temperatures, the cooling rate and time required to reach room temperature for the air-cooled samples were monitored by a stopwatch and a contact thermometer (Figure 2c).

Figure 2. The principal used devices in this study: (**a**) P-wave velocity measurement tool, (**b**) Nabertherm electric furnace, (**c**) a contact thermometer, (**d**) uniaxial compression test machine, (**e**) the SEM apparatus, and (**f**) the XRD unit.

3.2. Mass, Volume, and Density Determination

Physical parameters such as the mass losses, volume expansion, and density reduction can quantify the extent of thermal damage induced in rock specimens after thermal treatment [50]. Hence, before and after heat treatment, the physical features of the studied granodiorite specimens were calculated. The samples were divided into 5 groups of "4 each". Any test performed at least three times before the average value could be declared acceptable.

In this study, the mass loss rate η_m, volume growth rate η_V, and density decrease rate η_ρ were described as follows and as indicated in Equation (1):

$$\eta_m = (m_1 - m_2)/m_1 * 100\%, \eta_V = (V_2 - V_1)/V_1 * 100\%, \eta_\rho = (\rho_1 - \rho_1)/\rho_1 * 100\% \quad (1)$$

where m_1, V_1, and ρ_1 are the primary rock specimen's mass, volume, and density, respectively, and m_2, V_2, and ρ_2 are the treated rock specimen's mass, volume, and density, respectively.

3.3. UPV Measurements

The microstructural degradation of granodiorite caused by temperature was investigated using P-wave velocity calculations before and after thermal treatment. The elastic characteristics of rocks influence the dispersion of seismic waves by their mineralogy, texture, porosity, and cementation. As a result, knowing the size of the seismic waves in thermally treated rocks is crucial for their description [16]. Therefore, thermally induced microcrack degradation may be evaluated by equating the P-wave velocities before and after heat treatment. Hence, to measure the P-wave velocity along the specimen's long axis, an ultrasonic pulse generation and acquisition system was employed in this study (Pundit PL-2 device (Figure 2a) with 2 54-kHz point-source transmitter-receivers). Vaseline was used to keep the transducers and specimen contacts together to ensure optimal energy transfer. Only samples with P-wave velocities that were comparable were selected. The measurements were performed five times for each specimen while following ASTM test designations (D2845), with the average P-wave velocity value chosen as the P-wave velocity value.

3.4. Mechanical Tests

Using a compression machine (CONTROLS) with a loading capacity of 200 T, a set of uniaxial compressive strength tests was executed on the thermally treated samples under uniaxial circumstances following ASTM D7012–14 specifications. The loading rate of the machine was reduced to a constant displacement rate of 0.05 mm per minute (Figure 2d). The stress–strain curve during axial compression was computed using the software ADVANTEST9, and the load was steadily grown at a constant pace until the sample failed in minutes. Two strain gauges and Linear Variable Differential Transducers (LVDTs) were used to measure the specimen's axial and lateral deformation by strain meters during loading using a data collection system.

3.5. XRD and SEM Investigations

A scanning electron microscopy (SEM) examination evaluated the microcracks generated during the heating and cooling treatments. Thin sections of granodiorite specimens subjected to various treatments were employed to examine the growth of inter-granular and intra-granular cracks in the rock matrix. An FEI Quanta INSPECT-S device (Figure 2e) was employed in the SEM investigation to observe the granodiorite microstructure following thermal treatments, with magnifications ranging from 400 to 6000×. Using a Bruker D8 Advance X-ray diffractometer (Figure 2f), the mineral compositions of the powdered granodiorite samples were investigated from a starting position (2θ) of 5° to an end position (2θ) of 89.9° with a step size of 0.06°. The primary granodiorite content was determined by the diffraction data as follows: quartz (31%), plagioclase (39%), and K-feldspar (28%).

4. Results and Analysis

4.1. Thermal Loss of Granodiorite

In agreement with [59,60], the cooling rate for the specimens that cooled in the air was rapid at first due to the significant thermal loss, as seen in Figure 3, and the reduction had an exponential trend until the specimen approached room temperature. The cooling rates were 2.3, 3.1, 4, and 5.35 °C/min for 200, 400, 600, and 800 °C, respectively. The interesting point is that the air-cooled samples at 600 °C took a longer time to cool than those cooled at 800 °C, owing to surface microcracks that formed within and on the surface of the granodiorite specimens at 800 °C.

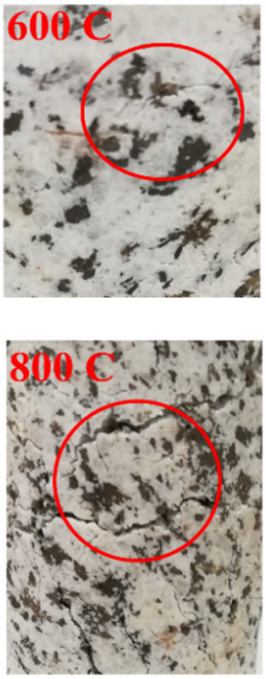

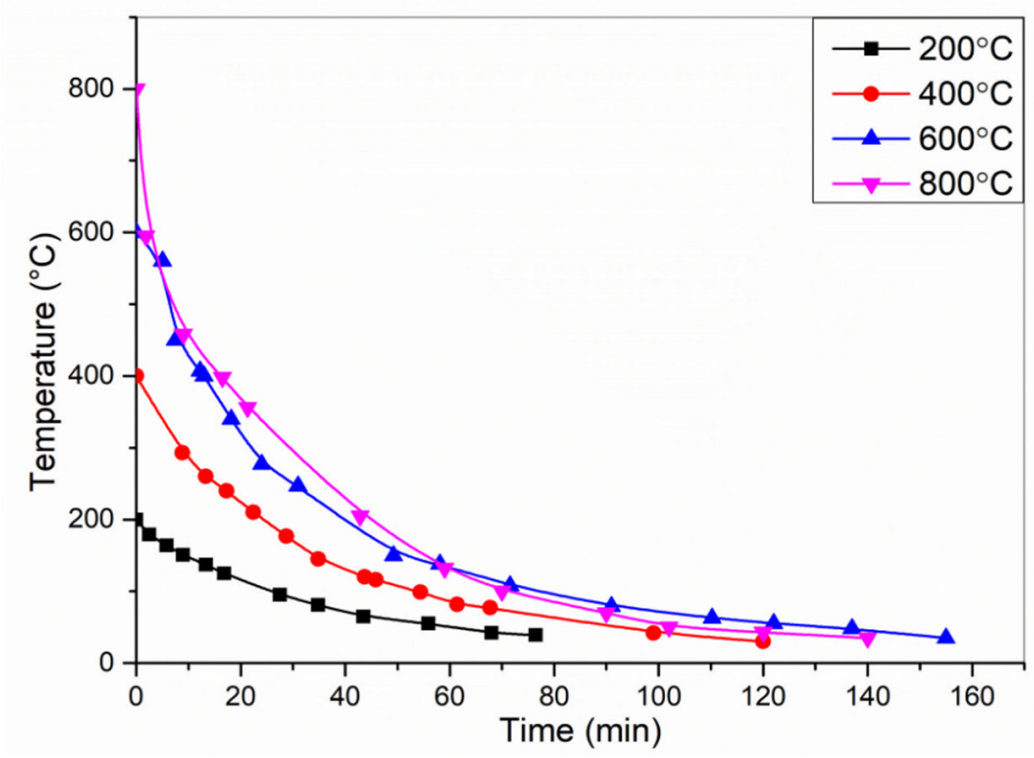

Figure 3. Cooling curves of the air-cooled samples at the target temperatures: 200, 400, 600, and 800 °C.

4.2. Temperature Effects on Mass, Volume, and Density

Figure 4 represents the variations in the mass loss ratio, volume growth rate, and density reduction ratio of the rock specimens exposed to thermal treatment. There are clear trends: the granodiorite's mass loss, volume expansion, and density decrease rates steadily increased as the temperatures rose. The mass loss of the granodiorite is predominantly due to the evaporation of various types of water [61]. Therefore, because of the low water content, the amount at which the granodiorite mass diminished with a temperature up to 400 °C was modest, as seen in Figure 4. For example, it extended to 0.09% and 0.14% at 200 and 400 °C, respectively (Table 1). In contrast, the volume expansion of the granodiorite had a meaningful value at this range of temperatures, reaching 1.6% at 400 °C.

Furthermore, there were similar values between the volume growth and density reduction rates, confirming its effectiveness in reducing the density. The mass loss, volume growth, and density reduction rates increased significantly over 400 °C, and the mass loss readings nearly doubled (0.31%), while the volume and density rates nearly tripled (5%) at 600 °C. As a result, this phase represents a mutation range for the deterioration of the parameters under investigation. At 800 ° C, granodiorite's significant thermal degradation resulted in large reductions in the mass, volume, and density rates of 0.64%, 18.4%, and 16%, respectively.

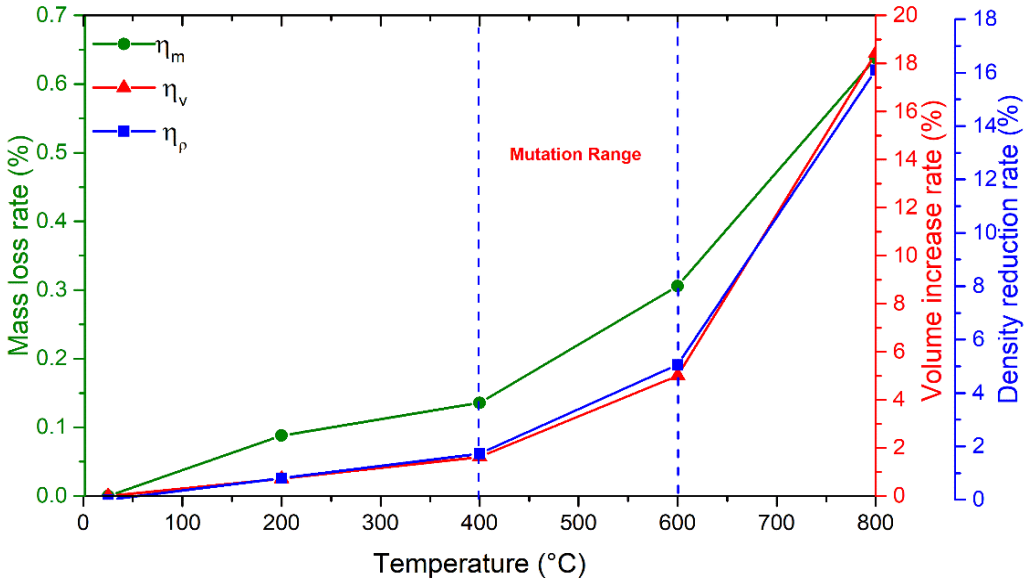

Figure 4. Relationships between average values of the mass loss rate (η_m), volume growth rate (η_V), and density decrease rate (η_ρ) for the target temperatures.

Table 1. Measured values of granodiorite physical parameters at various temperatures, where ηm is the mass loss rate, η_V is the volume growth rate, ηρ is the density decrease rate, V_p is the P-wave velocity, V_p% is the P-wave loss ratio, and D. F (V_p) is the damage factor for the P-wave velocity.

Temperature (°C)	η_m (%)	η_V (%)	η_p (%)	V_p (m/s)	V_p (%)	D. F (V_p) (%)
25	0	0	0	5620	0	0
				5645		
				5518		
				5634		
				5593		
200	0.10	0.69	0.75	4415	22.55	0.40
	0.10	1.23	1.30	4420	20.73	0.37
	0.06	0.37	0.46	4461	19.33	0.35
	0.09	0.61	0.69	4519	20.74	0.37
400	0.13	1.58	1.68	3404	38.59	0.62
	0.13	1.57	1.67	3480	38.51	0.62
	0.15	1.61	1.72	3231	42.74	0.67
	0.14	1.73	1.85	3243	41.35	0.66
600	0.25	4.64	4.79	840	85.24	0.98
	0.31	6.12	6.01	888	84.60	0.98
	0.38	4.76	4.84	783	86.44	0.98
	0.28	4.51	4.58	795	86.26	0.98
800	0.50	18.49	16.03	...	...	1.00
	0.77	17.81	15.77	...	...	1.00
	0.64	18.97	16.49	...	...	1.00

4.3. Ultrasonic Velocity

Figure 5 demonstrates that as the temperature rose, the P-wave velocity of the granodiorite exhibited a thoroughly negative trend [62], diminishing when the temperature increased. There are three phases to the longitudinal velocity vs. temperature curve: up to 400 °C, 400–600 °C, and above 600 °C (Figure 5a,b). The V_p decreased markedly between the ambient temperature and 400 °C. For example, V_p diminished from 5606 m/s at room temperature to 4454 (with a 21% loss ratio) and 3340 (40% loss ratio (Table 1)) at 200 and 400 °C, respectively. The number of microcracks generated increased as the thermal treatment temperatures went up. As a response, the P-wave velocity dropped, since sonic waves travel slower in the air than in rock. Hence, 400 °C was considered the threshold point of the P-wave velocity measurements. It is noticeable that the P-wave reduced significantly after 400 °C, mainly between 400 to 600 °C, where the reduction rate was the sharpest (Figure 5b). Therefore, the average P-wave measurements at 600 °C were 826 m/s, with an 86% decrease ratio. Furthermore, the severity of the thermal cracks made measuring the longitudinal wave velocities impossible beyond 600 °C (predicted 0 m/s at 800 °C).

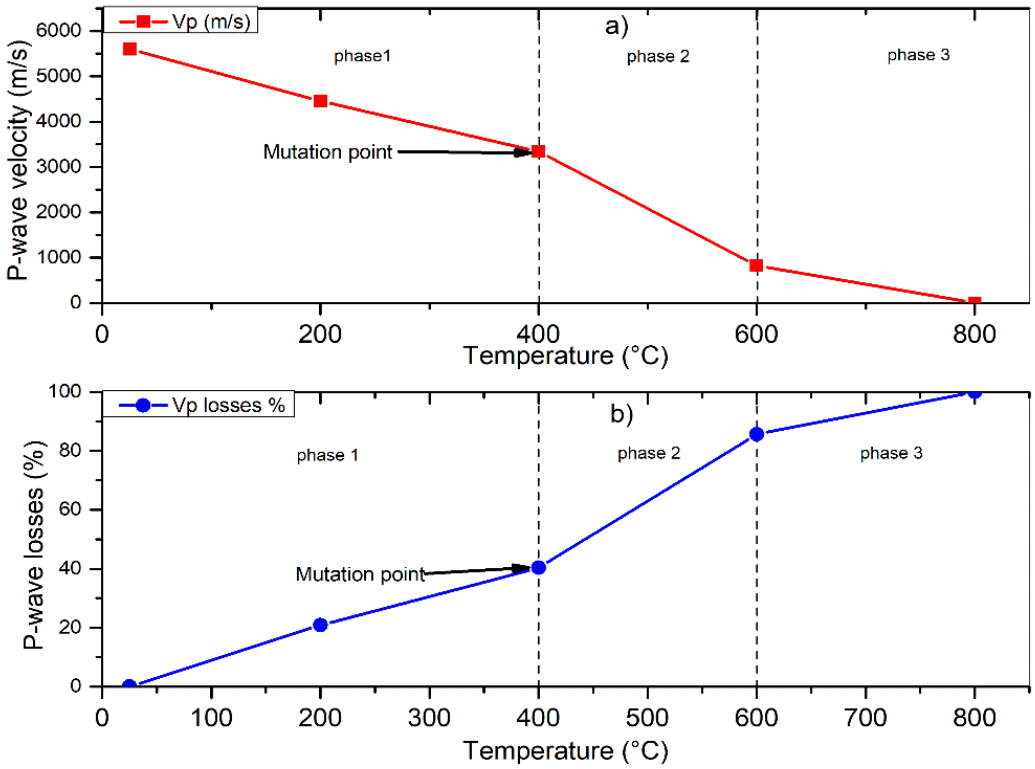

Figure 5. Relation between temperatures: (**a**) P-wave velocity and (**b**) P-wave loss ratio.

4.4. Temperature Effects on Mechanical Properties

4.4.1. Uniaxial Compressive Strength (UCS)

The compressive strength of granodiorite was investigated from the ambient temperature to 800 °C (Figure 6). Heat treatment can enhance rock strength by causing plastic expansions of minerals and strengthening friction among the mineral particles within a specified temperature range [50,51]. As a result, up to 400 °C, the granodiorite demonstrated a slowly rising trend, with the temperature and peak stress increasing by 5.74 MPa from 62.7 MPa to 68.44 MPa at 200 °C and 7.8 MPa at 400 °C, respectively. The principal motivation is that the granodiorite's granules slide less, owing to water evaporation and thus the presence of dry air within it. Furthermore, due to the thermal expansion of the interior mineral components, the initial cracks were also filled. Accordingly, microcracks were less frequent, and densification was better [63]. Therefore, the temperatures significantly impacted the granodiorite peak strength, which increased as the temperature was

less than 400 °C. When the temperature exceeded 400 °C, the related impact of thermal stress and applied uniaxial compression caused a significant creation of new microcracks to form, leading the granodiorite specimen to disintegrate. Consequently, the granodiorite compressive strength dropped dramatically from 70.2 MPa to 20.12 MPa at temperatures between 400 °C and 600 °C, a loss of 71%.

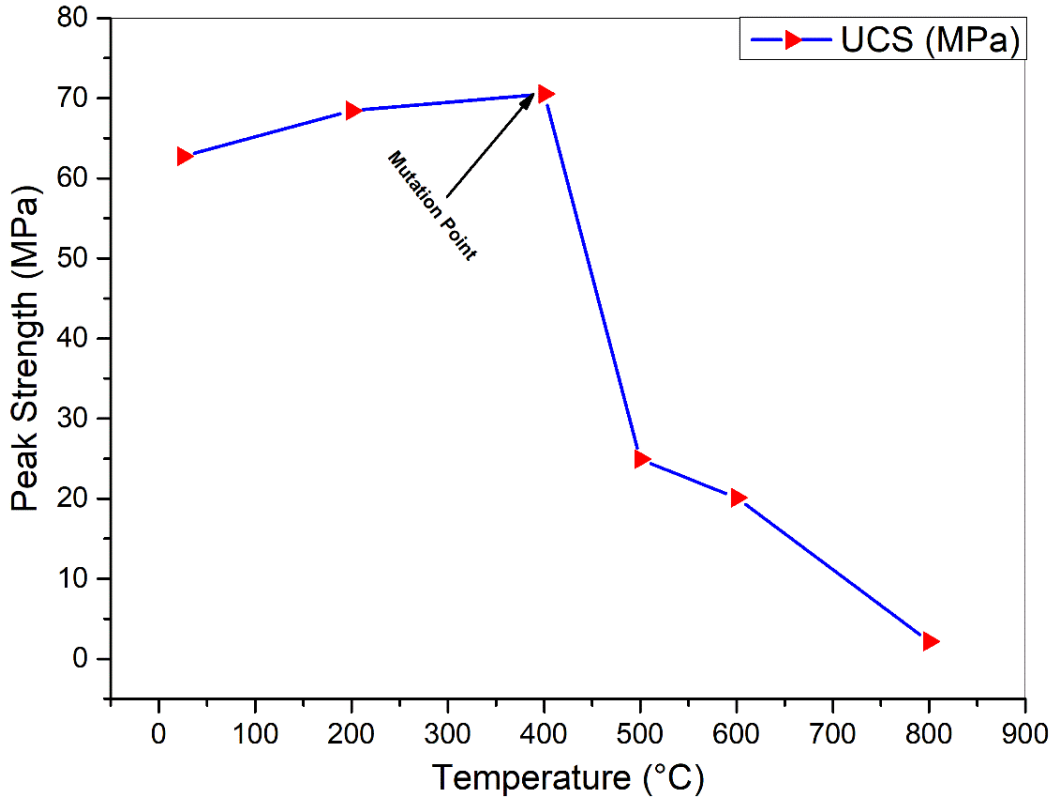

Figure 6. The variation of granodiorite's uniaxial compressive strength (UCS) following thermal treatment.

Moreover, between 400 °C and 600 °C, the quartz alpha-beta transition occurred at about 573 °C, resulting in a further steep drop. This suggests that 400 °C is the critical temperature for granodiorite microstructural and UCS modification. The peak stress distinctly reduced to 2.5 MPa at 800 °C (Table 2) due to various minerals starting to disintegrate and forming new microcracks, resulting in extensive macro-structural damage in the granodiorite.

4.4.2. Elastic Modulus (E)

Based on the empirical data for the granodiorite samples after thermal treatment, as illustrated in Figure 7, the elastic modulus reached its peak of 48.2 GPa at ambient temperature. From 25 °C to 400 °C, the elastic modulus of the granodiorite dropped by 41%. Thus, the governing causes in this stage were crystal and structural water evaporation, crack formation, and compressive deformation. Between 400 and 600 °C, the elastic modulus declined by 88% from 28.5 GPa to 5.6 GPa. These higher temperature ranges impaired the cohesiveness of the mineral grains, leading to thermal softening and causing microstructural degradation across the rock, ending in a notable decline in the elastic modulus. The E measurements were impossible after 600 °C because of severe degradation in the granodiorite specimens, as evidenced by the lower values of its UCS at this temperature range (Table 2).

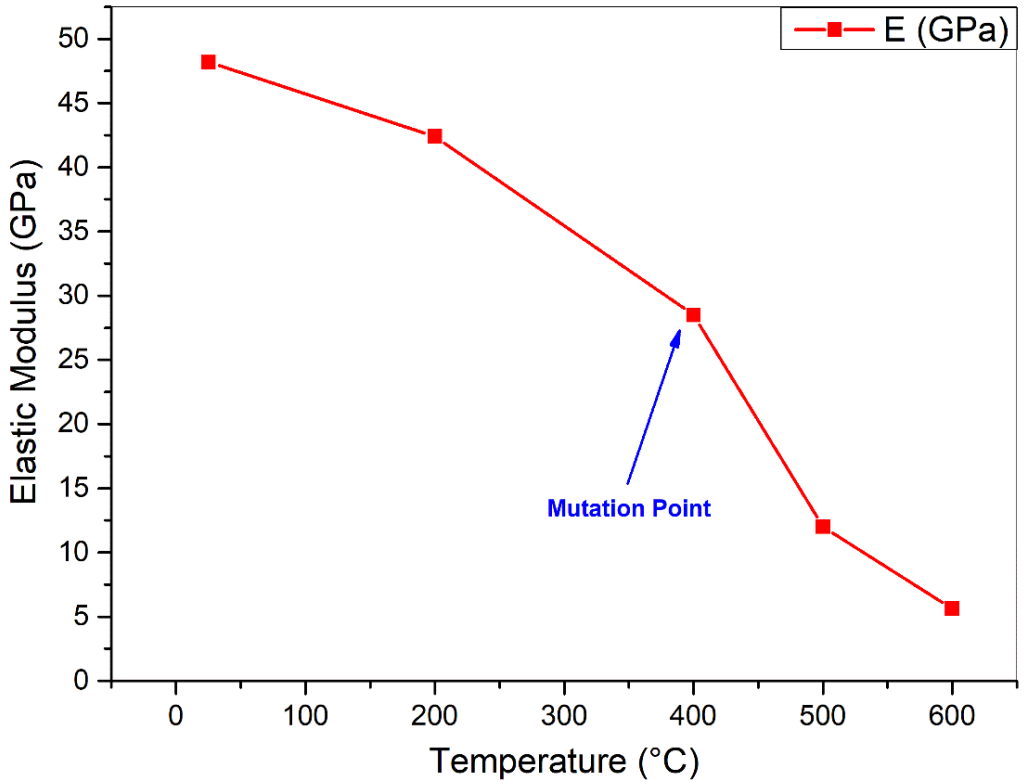

Figure 7. The variation of granodiorite's elastic modulus (E) with the temperature.

Table 2. Calculated values of granodiorite's mechanical parameters at different temperatures.

Temperature (°C)	Peak Strength (MPa)	Av. (USC) (MPa)	Elastic Modulus (GPa)	Av. (E) (GPa)	Thermal Damage (E) (%)
25	66.9	62.7	50.7	48.2	0.00
	65.9		47.8		
	59.2		48.0		
	59.0		46.2		
200	66.8	68.4	42.3	42.4	0.12
	63.5		39.7		
	75.0		45.2		
400	71.6	72.2	25.5	28.5	0.41
	74.2		24.7		
	70.8		35.3		
500	21.48	24.9	13.70	12	0.75
	28.39		10.30		
600	18.4	20.1	4.10	5.63	0.88
	23.0		9.60		
	18.9		3.20		
800	2.5	2.5	...	...	1.00
	Failed		...		
	2.6		...		

4.4.3. Stress–Strain Curves

Figure 8 shows the axial stress–strain curves by the LVDTs for the granodiorite specimens following various thermal treatments. As verified, the temperatures had a significant effect on the strength and deformation attributes of the granodiorite. Hence, the granodiorite's axial stress–strain curves revealed a nonlinear deformation at first, which was induced by the closing of pre-existing microcracks. Furthermore, the temperature treatments impacted this phase (i.e., when the temperature rose, the stage of the first nonlinear deformation became more apparent). The increased number of thermal cracks caused by higher temperatures was most likely responsible. The linear regions dominated the stress–strain curves following the microcrack closure stage during the elastic deformation phase. With increasing axial stress, the stress–strain curves of the granodiorite began to deviate from the linear characteristics, indicating specimen yielding. The specimens then attained peak strength and started the post-peak deformation period.

As demonstrated in Figure 8, as the temperature rose, the brittleness diminished, and the ductility increased. The axial stress–axial strain curves of the granodiorite at lower temperatures (25–400 °C) exhibit apparent brittleness following the peak strength. The stress–strain curves were comparable under compression loading until the elastic deformation. In this zone, the stress–strain response was linear, with a rise in axial stiffness. In contrast, at higher temperatures (500 and 600 °C), the post-peak response of the granodiorite was more ductile, which was connected to the concentration of thermal cracks inside the specimens. Hence, after the elastic stage, visible plastic deformation occurred, during which the plastic characteristics of the granodiorite increased and the brittle properties diminished with the increasing temperature. Consequently, it has been revealed that as the temperature went up, the failure behavior shifted from a brittle to ductile shear zone. Additionally, on the granodiorite stress–strain curves, there are several stress mutations points due to the interconnection and nucleation of microcracks during the loading process, which is commonly described as an indicator for local failures [64].

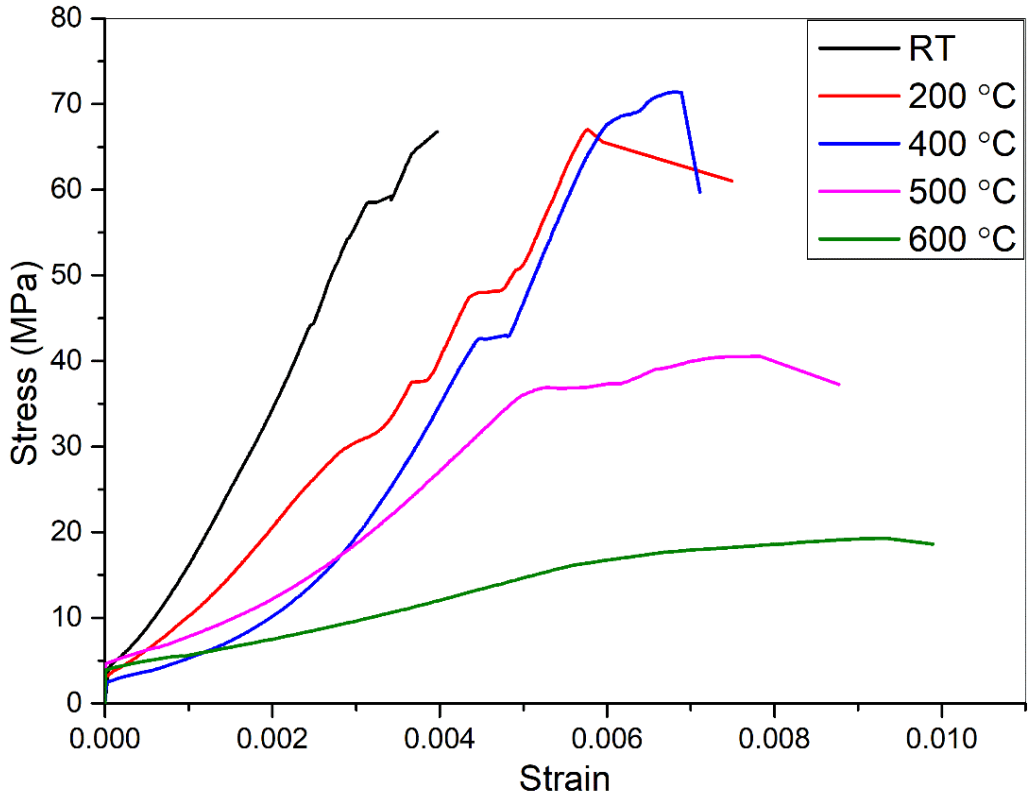

Figure 8. Stress–strain curves for granodiorite following different thermal treatments.

4.4.4. Failure Modes

Visual assessment for the post-failure samples revealed valuable information regarding the behavior of the tested rock samples at various temperatures. Various failure mechanisms involve inherent mechanical features such as the quantity of energy liberated throughout the failure and microstructural modifications during deformation. As a result, knowing the rock failure mechanisms at various temperatures is critical in anticipating failure mechanisms at different temperatures [4]. The failure modes after the compression stress of the thermally heated granodiorite specimens at various temperatures were compared and investigated. The failure mechanisms of the preheated granodiorite samples at 200, 400, 600, and 800 °C are shown in Figure 9a–d, respectively. It appears that as the temperature increased, the axial splitting failure mode at 200, 400 °C (Figure 9a,b) transformed to a shear failure mode at 600 °C (Figure 9c) due to the concentration of thermal cracks in the samples, in agreement with the stress–strain curves (Figure 8). The failure mode of the granodiorite was very complex at 800 °C, and many samples failed before the UCS tests, as shown in Figure 9d, due to the sharp degradation in the specimens.

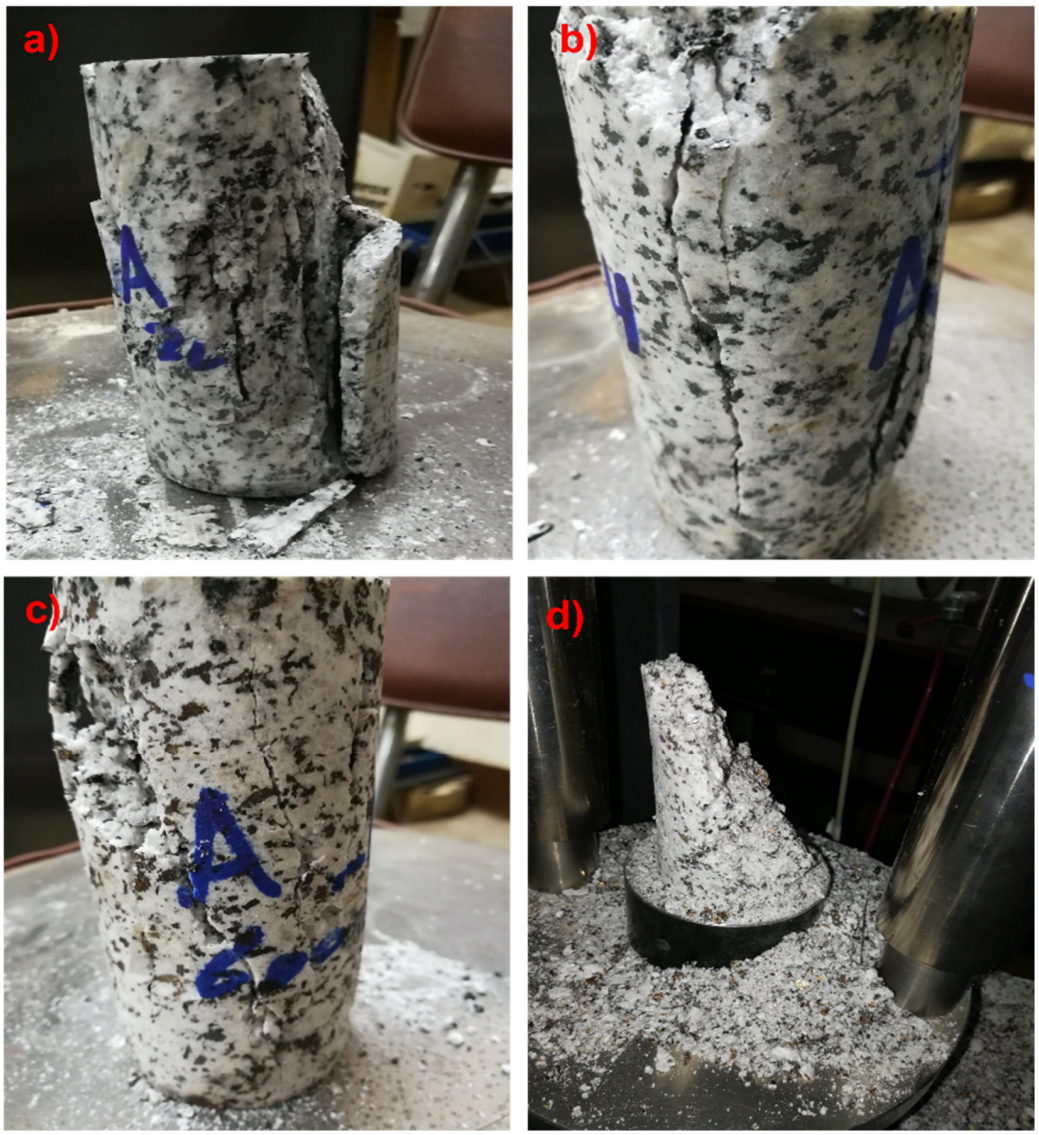

Figure 9. Failure modes of granodiorite samples at various thermal treatments: (**a**) 200 °C, (**b**) 400 °C, (**c**) 600 °C, and (**d**) 800 °C.

4.5. Microstructural Evaluation

After being exposed to different temperatures (200, 400, 600, and 800 °C), SEM investigations were performed on the granodiorite specimens to assess any microstructural alterations, as shown in Figure 10. At 200 °C, the granodiorite specimens maintained their integrity (Figure 10a), with the mineral grains tightly linked and hairline cracks visible. When the temperature approached 400 °C, the granodiorite structure was subjected to significant thermal stresses due to different thermal expansions and water escaping. Therefore, the granodiorite's microstructure deteriorated as the temperature increased, and pores and intergranular cracks appeared, along with the emergence of intragranular cracks (Figure 10b). Due to the significant destruction of the microstructure, the cracks expanded considerably in width and length at 600 ° C, and their frequency increased dramatically, as illustrated in Figure 10c. For the 800 °C specimens, the sample integrity crashed, and many thermal microcracks joined and coalesced, leading to substantially larger macroscopic crack densities and lengths compared with the specimens at 600 °C (Figure 10d).

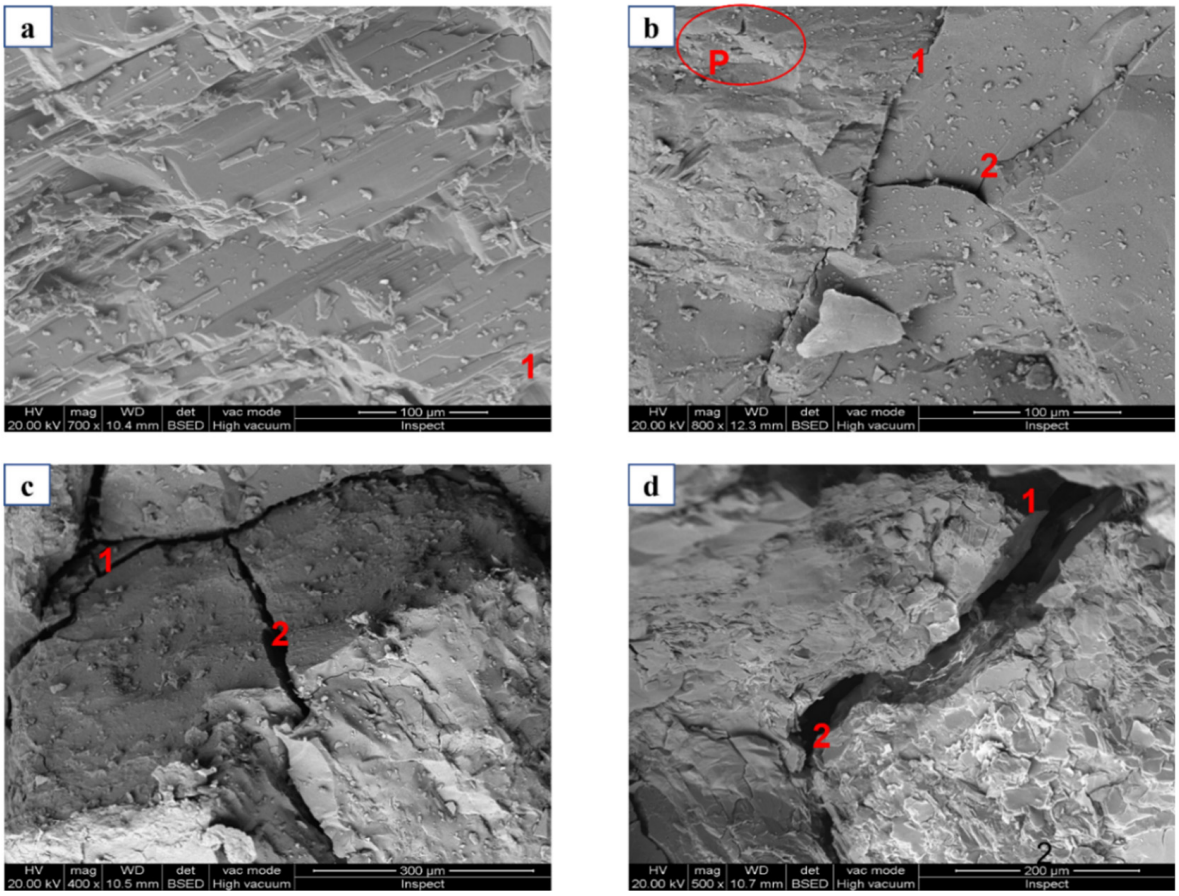

Figure 10. SEM images of granodiorite samples at various thermal treatments: (**a**) 200 °C, (**b**) 400 °C, (**c**) 600 °C, and (**d**) 800 °C. The abbreviations used are as follows: 1 = intergranular microcracks, 2 = intragranular microcracks, and P = pores.

5. Discussion

In this article, the thermal damage of several physical and mechanical characteristics following thermal treatments of Egyptian granodiorite were investigated, assessed, and compared with some previously published research, and all parameters that were measured mirrored this impact. Furthermore, regarding the responses at temperatures above 400 °C, the thermochemical processes dramatically promoted fracture damage creation and propagation, suggesting a potential trend.

5.1. Physical Responses as a Function of Temperature

Physical characteristics like the density, for example, are a reliable indicator for measuring the degree of damage produced in rock samples following thermal treatment [50]. When rock is heated, it undergoes several modifications; the size, shape, and mass of the sample change, leading to a shift in the volume and bulk density of the specimen. Hence, the density can be evaluated by comparing the volume and mass of the granodiorite samples before and after thermal treatment. The weight loss of granodiorite is mostly motivated by the evaporation of various kinds of water during heat treatment. Because granodiorite has a low water level in this temperature range, changes in the rate of mass decline were negligible at temperatures up to 400 °C. Hence, the losses in weight were restricted to the vaporization of interlayer water and bound water [61]. Beyond 400 °C, the mass loss rate rose considerably, suggesting that the granodiorite specimens' interior minerals suffered severe physical and chemical changes (Figure 4). In this mutation range, the crystalline water quantities decreased due to mineral dehydration, and the structural water contents declined due to dehydroxylation. Furthermore, decomposition of the opaque minerals and quartz, as well as feldspar phase shifts and recrystallization of the minerals distinguished these zones. At 600–800 °C, the mass loss rates were the greatest (Table 1), reflecting those chemical reactions which were the most pronounced [19].

On the other hand, the quartz transition is a common attribute in the volume expansion curve. It affects the granodiorite's thermal expansion slope, since it is a quartz-feldspar rock rich in silica. Consequently, between 25 and 400 °C, there was no substantial volumetric growth in the granodiorite samples, and the volume expansion was lineal and primarily attributable to the mineral extension [65]. Nevertheless, with the continuous development of minerals for temperatures above 400 °C, the volume expansion ratio of the rock samples accelerated dramatically, and the minerals' boundaries cracked. Therefore, there was a nonlinear volumetric increase (Figure 4). As a result, the volume expansion rate rose sharply at 600 °C due to the quartz suffering a transition of an α-quartz to β-quartz phase at around 570 °C, and transgranular cracks evolved quickly at this stage and extended in volume; hence, the volumes expanded considerably. Consequently, between 400 and 600 °C, the physical parameters shifted from a stable to an unstable state in this mutation range. Because of the severe thermal damage to the granodiorite, the peak that reflected the volumetric expansion occurred between 600 and 800 °C. Correspondingly, the combined impact of the mass and volume shifts influenced the density levels. Accordingly, the density levels were altered by the combined impact of the mass and volume variations. However, the observed density drop rate corresponded to the increase in the volume growth rates, implying that the volume expansion had a greater effect on the density than the mass losses, as shown in Figure 4. Thus, up to 600 °C, the volume growth rate and density decline ratio had approximately similar values. When over 600 °C, the density reduction ratio was influenced by high rates for the mass losses and volume rise ratios, resulting in a significant increase in the density drop rate.

V_p was affected by the type of rock, grain size and shape, density, porosity, water content, clay concentration, and temperature, among other factors [66]. Hence, the longitudinal wave velocity dropped as the temperature rose, implying that the sonic wave energy values were progressively reflected and absorbed into the granodiorite specimens, as seen in Table 1. Up to 400 °C, the water loss and volume expansion were accelerated by the thermal treatment, which grew the porosity of the granodiorite. Hence, the longitudinal wave's energy levels were consumed, resulting in a gradual reduction in the wave velocity. Between 400 and 600 °C, more water escaped, boundary cracks developed, and the minerals underwent significant chemical and physical changes. Furthermore, the crystals suffered transgranular cracks, severely forcing the wave velocity to fall. The longitudinal wave's loss ratio was extremely high in this phase, and V_p was very low, suggesting that the cracks absorbed the bulk of the longitudinal wave's energy (Figure 5). Thus, the mutation point of longitudinal wave absorption began after the 400 °C limits. The impacts of high temperatures were more pronounced at 800 °C, and the transgranular cracks widened quickly.

In addition, the inner structures of the granodiorite specimens were destroyed, leading to the absorption of the whole longitudinal wave and barring them from penetrating the rock specimens.

Microscopically, thermal fractures in crystalline rocks are usually caused by two main mechanisms: (1) a mismatch in the thermal expansion coefficients between different mineral granules (causing intergranular cracks) and (2) anisotropy of thermal expansion within single minerals (causing intragranular cracks) [67,68]. The heat treatment alters the microstructures of the rocks, allowing microcracks to emerge and propagate. As seen in Figure 10, the quantity and breadth of microcracks inside the granodiorite specimens increased dramatically as the temperature rose. Accordingly, the matrix's compaction and integrity were significantly thermally damaged. Due to the various minerals with different thermal properties in granodiorite, thermal expansion mismatches form between particles, causing unequal thermal stresses, which exacerbate and expand the microcracks. The more substantial thermal expansion occurs as the temperature rises. As a result, intragranular and transgranular microcracks emerge one after the other, and the initial microcracks tend to extend along the weak areas to become larger [69]. Thus, granodiorite underwent relatively minimal chemical and structural changes at lower temperatures, which created small expansion of the pre-existing microcracks and new cracks (Figure 10a). The intergranular cracks grew, and the transgranular cracks formed when the temperature rose to 400 °C (Figure 10b) due to bound water loss, dihydroxylation in the absence of constitutional water, and solid mineral growth. Hence, thermally generated cracks resulted from significant thermal stresses by differential elongation of the minerals along the crystal axes as the temperature rose, which formed when the thermal stress surpassed the maximum strength among or inside the minerals, resulting in damage to the microstructures. For example, under atmospheric pressure, the transition of α-quartz to β-quartz at 573 °C produced a linear expansion of 0.45% of the quartz [40]. Therefore, the intragranular cracks extended because of the intense volumetric growth of grains at 600 and 800 °C, and a microcrack network was generated in the specimen as the intergranular and transgranular microcracks coalesced (Figure 10c,d).

5.2. Mechanical Properties as a Function of Temperature

High temperatures altered the physico-chemical characteristics of the water and minerals in the rocks, causing changes in the density, content, structural properties and start and spread of microcracks as well as a change in the mechanical response [70]. Hence, rock strength, or failure stress in uniaxial compression tests, is a fundamental indicator of thermal rock mechanical deterioration. The granodiorite strength was enhanced between 25 and 400 °C because of heat treatment (Figure 6), generating an axial splitting failure mode (Figure 9). This was mainly due to plastic expansions of the minerals and strengthening friction among the mineral particles within a specified temperature range [50]. Evaporation of moisture lowered the sliding between grains, leading to an increase in the friction between them. This friction creates a minor resistance to deformation or mobility between the grains, resulting in a higher UCS [10]. However, the elastic modulus decreased dramatically (41%) in this phase (Figure 7). This was due to the dissimilar thermal expansion coefficients of the granodiorite mineral grains, creating new microcracks in the specimens and forcing the microcracks to close under the applied uniaxial compression [71]. As a result, the cracks' closure, new cracks' formation, and irreversible microcrack growth, which were responsible for the difference in the microstructure, produced a low elastic modulus. Furthermore, the crystal and structural water of the minerals would evaporate, resulting in expansion of the grains because of heat treatment. Hence, the dominant factors in this phase were crystal and structural water evaporation, crack closure, new crack creation, and compressive deformation.

Granodiorite is composed of several minerals, each having a unique coefficient of thermal expansion and thermo-elastic features. Hence, due to the asymmetric thermal expansion of the mineral grains' boundaries, the internal stresses were encouraged to build in or between them. Moreover, dehydration, thermal decomposition, and thermal expansion of the rocks and minerals occur at high temperatures. That leads to an increase in cracks and pores, a reduction in density, and mineral alteration [63]. Accordingly, when the temperature of the granodiorite samples was above 400 °C, the mechanical strength and elastic modulus noticeably reduced. Thermal stress and the formation of new inter- and transgranular microcracks generated by high-temperature treatments were attributed to the significant decrease in the UCS (Figure 10b,c). Hence, at a temperature higher than 400 °C, the critical temperature of granodiorite, the mechanical characteristics deteriorated remarkably. Biotite's ability to react with oxygen and change the microstructure of granodiorite may be the reason for this [72]. That aside, variations in the average compressive strength and average elastic modulus of granodiorite rose significantly, which was connected to the α-to-β transition of the quartz [12]. Correspondingly, this stage reflects the onset of phase-change behaviors and mineral alterations in the lattice crystals through the transformation from brittle to plastic. Thus, the failure mode shifted from axial splitting to shear failure (Figure 9).

Furthermore, the stress–strain curve of granodiorite became smoother, and the compaction phase stretched as the temperatures rose, as seen in Figure 8, whereas the elastic modulus declined and the brittleness of granodiorite decreased, which was consistent with earlier research. At 800 °C, the effects of high temperatures were more prominent, and inter- and transgranular cracks were created quickly, building a microcrack network. Furthermore, the granodiorite specimens' interior structures were shattered (Figure 10d), resulting in a significant loss of rock strength values and problematic measurements of E (Table 2).

5.3. Thermal Damage Evolution

Damage mechanics has lately been adopted as a novel technique for studying rock thermodynamics in geotechnical engineering [53]. The anisotropic expansion of granodiorite is connected to thermal damage as a thermal stress concentration emerges between mineral grains, causing microcracking. Once subjected to high temperatures, thermal cracks develop inside the rock and are destroyed when the thermal stress exceeds the bonding energy between the mineral grains [41]. The physical and mechanical characteristics of granodiorite following exposure to high temperatures were investigated in this study. The results indicate that the physical and mechanical features of the samples were modified as the temperature rose. Different criteria can predict the thermal damage characteristic of rock for the thermal damage severity. In this investigation, the thermal damage of granodiorite was estimated by the elastic modulus and the P-wave velocity. A thermal damage index D (T) was specified as the ratio of the parameter at the target temperature to the parameter at room temperature, as indicated in Equations (2) and (3):

$$D(T) = 1 - E_T/E_o \quad (2)$$

$$D(T) = 1 - (Vp_T/Vp_o)^2 \quad (3)$$

The rock damage after heating and cooling is almost identical to the thermal cracking mechanism [62]. Hence, changes in the rock microstructure following thermal treatment (Figure 10) can be reflected by the rock thermal damage differences. Figure 11 depicts the relations between temperature, D (V_p), and D (E). Both D (V_p) and D (E) of the granodiorite subjected to thermal treatment rose with the ultimate heating temperature and followed a similar trend. As illustrated in Figure 11, because the P-wave velocities were more sensitive to the temperature than the elastic modulus, the D (V_p) of the granodiorite specimens was higher than D (E) [73]. The thermal damage factor for the studied parameters reached its maximum at 600 °C due to substantial heat damage in the granodiorite microstructure

caused by the higher temperature. Hence, after 600 °C, because of the extreme thermal deterioration in the granodiorite specimens, the measurements of V_p and E were impossible at 800 °C.

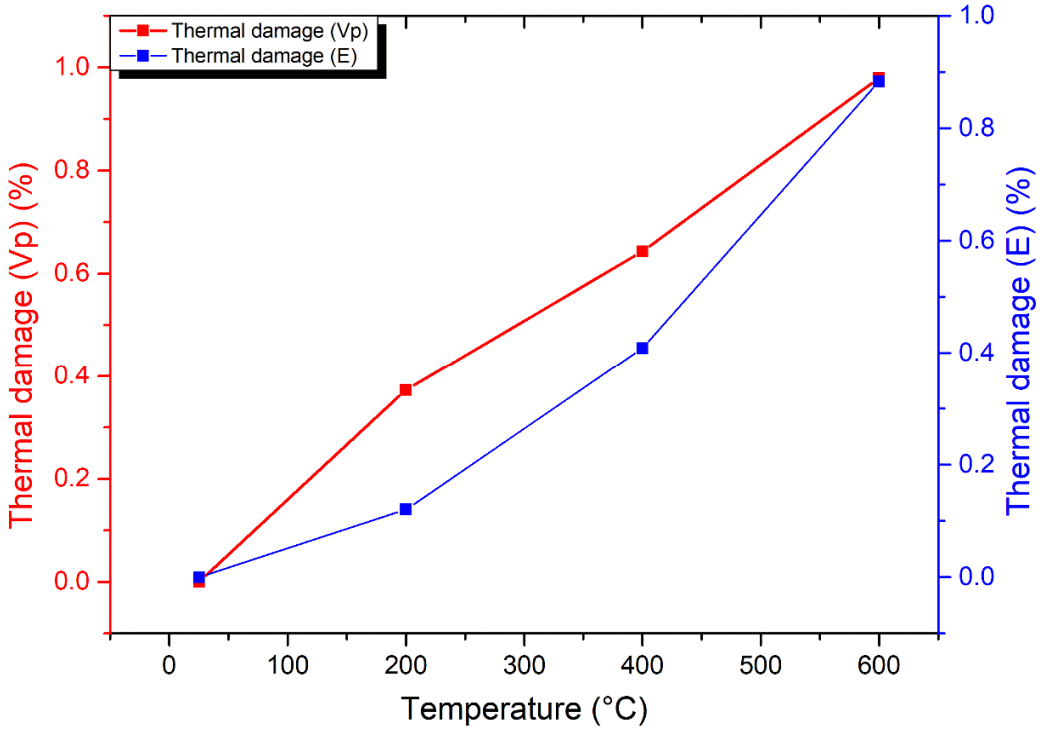

Figure 11. Relations between temperature and thermal damage of granodiorite, described through V_p and E.

5.4. In Comparison to Earlier Investigations

In this part, we assessed the mechanical response of granodiorite to that of other formerly examined granites. However, due to the wide variety of rocks and their compositions, origins, and so on, this research used the normalized value, reflecting the relationships between the UCS and E at the target temperature and those at room temperature (UCS_T/UCS_0 and E_T/E_0). Hence, it was possible to compare the thermal damage's effects on the granodiorite characteristics with other granites. The relationships between the temperatures and the normalized uniaxial compressive strength were obtained, as shown in Figure 12. Aside from that, the relations between the temperatures and normalized elastic modulus are presented in Figure 13.

Based on these findings, it is possible to deduce that the UCS_T/UCS_0 and E_T/E_0 trends with the thermal treatments of granites and granodiorite may rise, fall, or stay constant (Figures 12 and 13) under 400 °C. However, these values "fell only" after this temperature, indicating that 400 °C was the mutation temperature for the rocks investigated. The mechanical features of granodiorite are substantially equivalent to granite when subjected to temperatures up to 400 °C. The characteristics of granodiorite, however, were drastically damaged after this temperature. Consequently, at the mutation range "between 400 and 600 °C", there was a considerable decrease in the normalized UCS from 1.12% to 0.32% and the normalized E from 0.59% to 0.12% (Figures 12 and 13). Accordingly, due to the ignored value of the UCS at 800 °C, measurements for the elastic modulus were difficult to perform (Table 2).

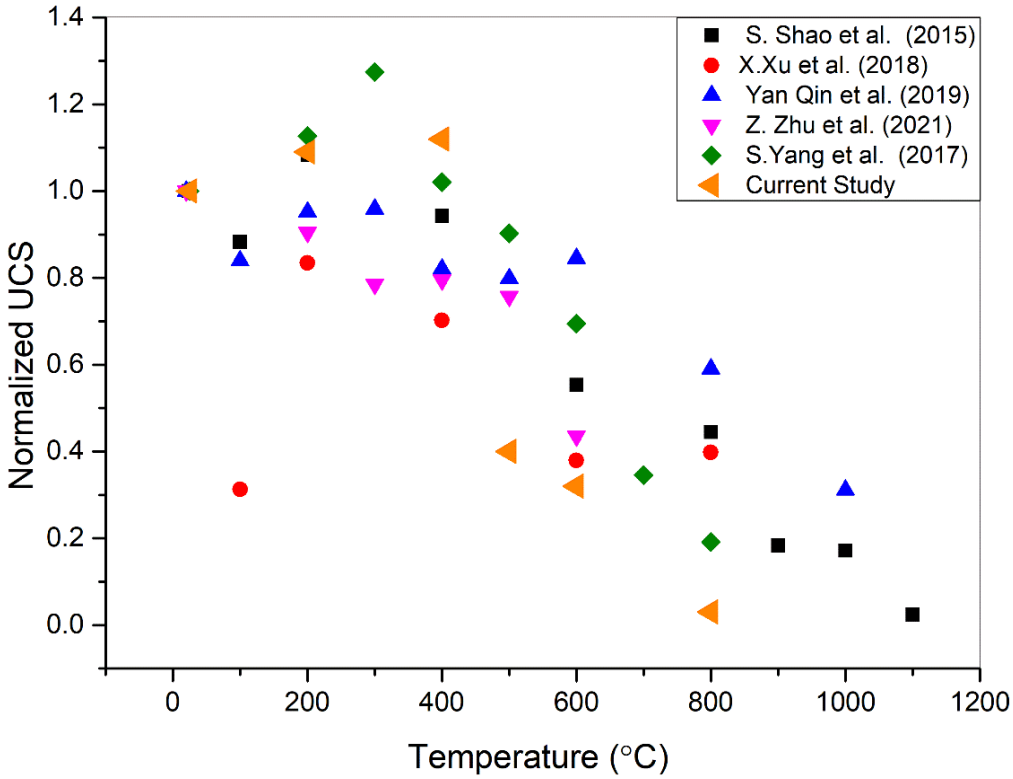

Figure 12. A comparison of the normalized value of UCS of granodiorite with some previous studies on granite heat-treated rock.

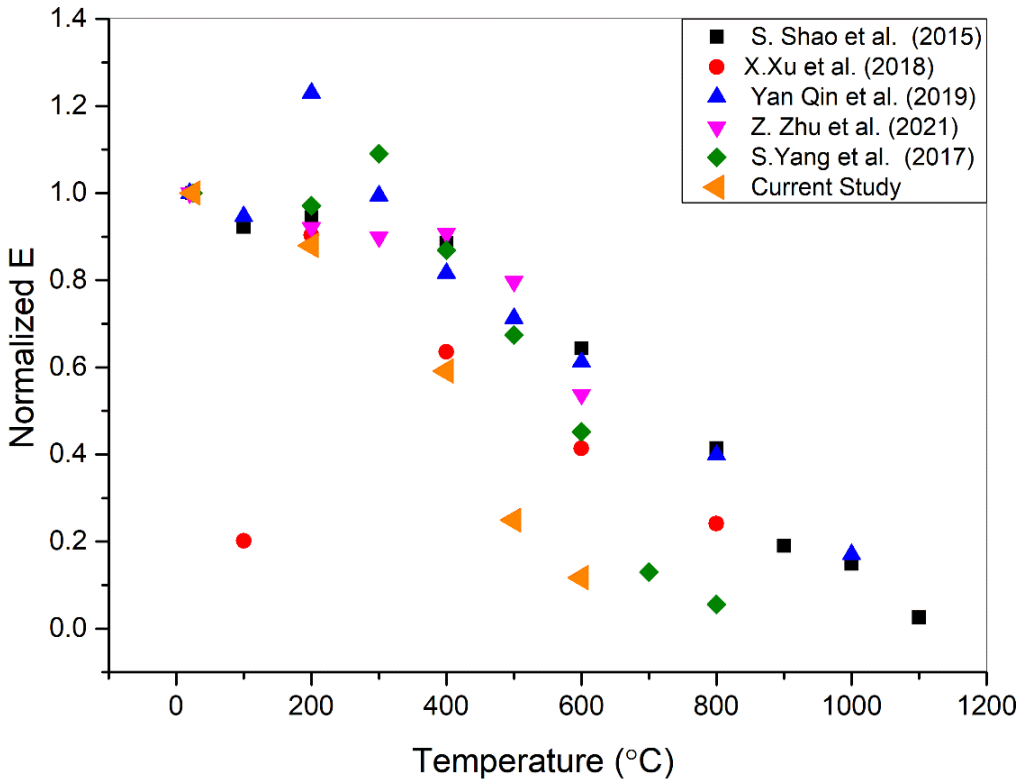

Figure 13. A comparison of the normalized value of E of granodiorite with some early studies on granite heat-treated rock.

One limitation of this work is that sensitivity analysis for model calibration must demonstrate the impact on the results and identify the most important factors [74]. In contrast, the findings of this study provide insights into the physical and mechanical responses and thermal damage of pre-heated granodiorite, which has rarely been investigated, although it is widespread in modern constructions.

6. Conclusions

In this study, thermal treatments of Egyptian granodiorite samples were conducted at temperatures of 200, 400, 500, 600, and 800 °C followed by air cooling to examine its thermo-physical and mechanical responses. A scanning electron microscope was also employed to correlate alterations in the microstructural qualities to changes in the physical and mechanical properties. The following are the main observations:

(1) The density of the Egyptian granodiorite fell after high-temperature exposure because of a loss in mass and a rise in volume, with the latter being the more governing factor up to 600 °C. After 600 °C, the mass loss and volume growth rates both rose considerably, resulting in massive density losses. Furthermore, the average P-wave velocity of the granodiorite dropped approximately linearly with the temperature from 5606 m/s at ambient temperature to 826 m/s at 600 °C.

(2) The UCS of the granodiorite specimens rose at first for the samples heat-treated up to 400 °C due to thermal hardening but then fell linearly between 400 °C and 800 °C. On the other hand, the Young's modulus had a declining trend when the heat treatment temperature rose. Furthermore, due to the interactions and coalescences of the boundary and transgranular cracks, the UCS dropped extensively at 800 °C, explaining the impossible measurement of E.

(3) The temperature affected the failure modes of granodiorite, and two main failure modes may be summarized: the axial splitting mode, which happened at temperatures below 400 °C, and the shear mode, which occurred at temperatures over 400 °C. Furthermore, the granodiorite sample failed more severely, the brittle-ductile transition phase occurred, and the fracture surface became rougher after 400 °C.

(4) When subjected to high temperatures up to 400 °C, the thermal damage for the physical and mechanical responses of granodiorite were nearly identical to granite, according to an exhaustive analysis of granite behavior in some of the former literature and a comparison with granodiorite. However, after this temperature range, the properties of granodiorite were severely degraded.

(5) The temperature threshold of Egyptian granodiorite is 400 °C. This was connected to a substantial drop in density and a P-wave velocity as well as the evolution of the trans-granular cracks detected via SEM, which led to a significant loss in the UCS and E. Consequently, the physical and mechanical responses transitioned from a stable to an unstable state in the mutation range (between 400 and 600 °C). As a result, this temperature must be considered when using granodiorite in thermal applications.

7. Recommendation

Future research may incorporate the sensitivity analysis technique to demonstrate uncertainties in variable inputs like the density, P-wave velocity, UCS, and so on, and their impact on the expected output to identify the most influential factors. Hence, this technique can be involved in the high-complexity modeling process and then overcome.

Author Contributions: Conceptualization, M.E.G.; methodology, M.E.G.; validation, M.E.G. and G.L.; analysis, M.E.G.; writing—original draft, M.E.G.; writing—review and editing, M.E.G., G.L., C.S., J.X., S.Y. and J.L.; supervision, M.E.G. and G.L.; funding acquisition, G.L. All authors have read and agreed to the published version of the manuscript.

Funding: This research was funded by Fundamental Research Funds for the Central Universities (2020ZDPY0221), Project "52174089", supported by the National Natural Science Foundation of China.

Data Availability Statement: Not applicable.

Acknowledgments: The first author greatly appreciates Mohamed Elkarmoty and Mohamed Ismael for their support in carrying out the experiments at the Rock Engineering Laboratory (REL), Faculty of Engineering, Cairo University (FECU), Egypt.

Conflicts of Interest: The authors declare no conflict of interest.

References

1. Allison, R.J.; Bristow, G.E. The effects of fire on rock weathering: Some further considerations of laboratory experimental simulation. *Earth Surf. Process. Landf. J. Br. Geomorphol. Res. Gr.* **1999**, *24*, 707–713. [CrossRef]
2. Zhu, C.; Arson, C. A thermo-mechanical damage model for rock stiffness during anisotropic crack opening and closure. *Acta Geotech.* **2014**, *9*, 847–867. [CrossRef]
3. Zhao, Y.S.; Wan, Z.J.; Feng, Z.J.; Xu, Z.H.; Liang, W.G. Evolution of mechanical properties of granite at high temperature and high pressure. *Geomech. Geophys. Geo-Energy Geo-Resour.* **2017**, *3*, 199–210. [CrossRef]
4. Shao, S.; Ranjith, P.G.; Wasantha, P.L.P.; Chen, B.K. Experimental and numerical studies on the mechanical behaviour of Australian Strathbogie granite at high temperatures: An application to geothermal energy. *Geothermics* **2015**, *54*, 96–108. [CrossRef]
5. Kumari, W.G.P.; Ranjith, P.G.; Perera, M.S.A.; Chen, B.K.; Abdulagatov, I.M. Temperature-dependent mechanical behaviour of Australian Strathbogie granite with different cooling treatments. *Eng. Geol.* **2017**, *229*, 31–44. [CrossRef]
6. Ding, Q.L.; Ju, F.; Mao, X.B.; Ma, D.; Yu, B.Y.; Song, S.B. Experimental Investigation of the Mechanical Behavior in Unloading Conditions of Sandstone after High-Temperature Treatment. *Rock Mech. Rock Eng.* **2016**, *49*, 2641–2653. [CrossRef]
7. Burton, E.A.; Upadhye, R.; Friedmann, S.J. *Best Practices in Underground Coal Gasification*; Lawrence Livermore National Lab. (LLNL): Livermore, CA, USA, 2017.
8. Verma, A.K.; Gautam, P.; Singh, T.N.; Bajpai, R.K. Discrete element modelling of conceptual deep geological repository for high-level nuclear waste disposal. *Arab. J. Geosci.* **2015**, *8*, 8027–8038. [CrossRef]
9. Kourkoulis, S.K. *Fracture and Failure of Natural Building Stones: Applications in the Restoration of Ancient Monuments*; Springer Science & Business Media: Berlin/Heidelberg, Germany, 2007; ISBN 1402050771.
10. Zhang, L.; Mao, X.; Lu, A. Experimental study on the mechanical properties of rocks at high temperature. *Sci. China Ser. E Technol. Sci.* **2009**, *52*, 641–646. [CrossRef]
11. Jansen, D.P.; Carlson, S.R.; Young, R.P.; Hutchins, D.A. Ultrasonic imaging and acoustic emission monitoring of thermally induced microcracks in Lac du Bonnet granite. *J. Geophys. Res. Solid Earth* **1993**, *98*, 22231–22243. [CrossRef]
12. Somerton, W.H. *Thermal Properties and Temperature-Related Behavior of Rock/Fluid Systems*; Elsevier: Amsterdam, The Netherlands, 1992; ISBN 0444890017.
13. Li, Q.; Yin, T.; Li, X.; Shu, R. Experimental and Numerical Investigation on Thermal Damage of Granite Subjected to Heating and Cooling. *Mathematics* **2021**, *9*, 3027. [CrossRef]
14. Vazquez, P.; Benavente, D.; Montiel, D.; Gomez-Heras, M. Mineralogical Transformations in Granitoids during Heating at Fire-Related Temperatures. *Appl. Sci.* **2021**, *12*, 188. [CrossRef]
15. Saksala, T. 3D Numerical Prediction of Thermal Weakening of Granite under Tension. *Geosciences* **2021**, *12*, 10. [CrossRef]
16. Tripathi, A.; Gupta, N.; Singh, A.K.; Mohanty, S.P.; Rai, N.; Pain, A. Effects of Elevated Temperatures on the Microstructural, Physico-Mechanical and Elastic Properties of Barakar Sandstone: A Study from One of the World's Largest Underground Coalmine Fire Region, Jharia, India. *Rock Mech. Rock Eng.* **2021**, *54*, 1293–1314. [CrossRef]
17. Chakrabarti, B.; Yates, T.; Lewry, A. Effect of fire damage on natural stonework in buildings. *Constr. Build. Mater.* **1996**, *10*, 539–544. [CrossRef]
18. Hajpál, M. Changes in sandstones of historical monuments exposed to fire or high temperature. *Fire Technol.* **2002**, *38*, 373–382. [CrossRef]
19. Tian, H.; Kempka, T.; Yu, S.; Ziegler, M. Mechanical properties of sandstones exposed to high temperature. *Rock Mech. Rock Eng.* **2016**, *49*, 321–327. [CrossRef]
20. Vazquez, P.; Acuña, M.; Benavente, D.; Gibeaux, S.; Navarro, I.; Gomez-Heras, M. Evolution of surface properties of ornamental granitoids exposed to high temperatures. *Constr. Build. Mater.* **2016**, *104*, 263–275. [CrossRef]
21. Wong, T.-F. Effects of temperature and pressure on failure and post-failure behavior of Westerly granite. *Mech. Mater.* **1982**, *1*, 3–17. [CrossRef]
22. Chaki, S.; Takarli, M.; Agbodjan, W.P. Influence of thermal damage on physical properties of a granite rock: Porosity, permeability and ultrasonic wave evolutions. *Constr. Build. Mater.* **2008**, *22*, 1456–1461. [CrossRef]
23. Liu, S.; Xu, J. Mechanical properties of Qinling biotite granite after high temperature treatment. *Int. J. Rock Mech. Min. Sci.* **2014**, *71*, 188–193. [CrossRef]
24. Yang, S.-Q.; Ranjith, P.G.; Jing, H.-W.; Tian, W.-L.; Ju, Y. An experimental investigation on thermal damage and failure mechanical behavior of granite after exposure to different high temperature treatments. *Geothermics* **2017**, *65*, 180–197. [CrossRef]
25. Chandrasekharam, D.; Pabasara Kumari, W.G.; Avanthi Isaka, B.L.; Gamage, R.P.; Rathnaweera, T.D.; Anne Perera, M.S. An influence of thermally-induced micro-cracking under cooling treatments: Mechanical characteristics of Australian granite. *Energies* **2018**, *11*, 1338. [CrossRef]

26. Kant, M.A.; Ammann, J.; Rossi, E.; Madonna, C.; Höser, D.; Rudolf von Rohr, P. Thermal properties of Central Aare granite for temperatures up to 500 C: Irreversible changes due to thermal crack formation. *Geophys. Res. Lett.* **2017**, *44*, 771–776. [CrossRef]
27. Liu, S.; Xu, J. Study on dynamic characteristics of marble under impact loading and high temperature. *Int. J. Rock Mech. Min. Sci.* **2013**, *62*, 51–58. [CrossRef]
28. Peng, J.; Rong, G.; Cai, M.; Yao, M.-D.; Zhou, C.-B. Physical and mechanical behaviors of a thermal-damaged coarse marble under uniaxial compression. *Eng. Geol.* **2016**, *200*, 88–93. [CrossRef]
29. Vagnon, F.; Colombero, C.; Colombo, F.; Comina, C.; Ferrero, A.M.; Mandrone, G.; Vinciguerra, S.C. Effects of thermal treatment on physical and mechanical properties of Valdieri Marble—NW Italy. *Int. J. Rock Mech. Min. Sci.* **2019**, *116*, 75–86. [CrossRef]
30. Sirdesai, N.N.; Mahanta, B.; Ranjith, P.G.; Singh, T.N. Effects of thermal treatment on physico-morphological properties of Indian fine-grained sandstone. *Bull. Eng. Geol. Environ.* **2019**, *78*, 883–897. [CrossRef]
31. Zhang, W.; Sun, Q.; Zhu, Y.; Guo, W. Experimental study on response characteristics of micro–macroscopic performance of red sandstone after high-temperature treatment. *J. Therm. Anal. Calorim.* **2019**, *136*, 1935–1945. [CrossRef]
32. Mohamadi, M.; Wan, R.G. Strength and post-peak response of Colorado shale at high pressure and temperature. *Int. J. Rock Mech. Min. Sci.* **2016**, *84*, 34–46. [CrossRef]
33. Liang, W.G.; Xu, S.G.; Zhao, Y.S. Experimental study of temperature effects on physical and mechanical characteristics of salt rock. *Rock Mech. Rock Eng.* **2006**, *39*, 469–482. [CrossRef]
34. Killc, Ö. The influence of high temperatures on limestone P-wave velocity and Schmidt hammer strength. *Int. J. Rock Mech. Min. Sci.* **2006**, *43*, 980–986. [CrossRef]
35. Zhang, W.; Sun, Q.; Zhu, S.; Wang, B. Experimental study on mechanical and porous characteristics of limestone affected by high temperature. *Appl. Therm. Eng.* **2017**, *110*, 356–362. [CrossRef]
36. Luo, J.; Wang, L. High-temperature mechanical properties of mudstone in the process of underground coal gasification. *Rock Mech. Rock Eng.* **2011**, *44*, 749–754. [CrossRef]
37. Zhang, L.; Mao, X.; Liu, R.; Li, Y.; Yin, H. Meso-structure and fracture mechanism of mudstone at high temperature. *Int. J. Min. Sci. Technol.* **2014**, *24*, 433–439. [CrossRef]
38. Liu, X.; Zhang, C.; Yuan, S.; Fityus, S.; Sloan, S.W.; Buzzi, O. Effect of High Temperature on Mineralogy, Microstructure, Shear Stiffness and Tensile Strength of Two Australian Mudstones. *Rock Mech. Rock Eng.* **2016**, *49*, 3513–3524. [CrossRef]
39. Huang, Y.-H.; Yang, S.-Q.; Tian, W.-L.; Zhao, J.; Ma, D.; Zhang, C.-S. Physical and mechanical behavior of granite containing pre-existing holes after high temperature treatment. *Arch. Civ. Mech. Eng.* **2017**, *17*, 912–925. [CrossRef]
40. Ohno, I.; Harada, K.; Yoshitomi, C. Temperature variation of elastic constants of quartz across the α-β transition. *Phys. Chem. Miner.* **2006**, *33*, 1–9. [CrossRef]
41. Sippel, J.; Siegesmund, S.; Weiss, T.; Nitsch, K.-H.; Korzen, M. Decay of natural stones caused by fire damage. *Geol. Soc. Lond. Spec. Publ.* **2007**, *271*, 139–151. [CrossRef]
42. Keshavarz, M.; Pellet, F.L.; Loret, B. Damage and changes in mechanical properties of a gabbro thermally loaded up to 1000 °C. *Pure Appl. Geophys.* **2010**, *167*, 1511–1523. [CrossRef]
43. Inserra, C.; Biwa, S.; Chen, Y. Influence of thermal damage on linear and nonlinear acoustic properties of granite. *Int. J. Rock Mech. Min. Sci.* **2013**, *62*, 96–104. [CrossRef]
44. Sha, S.; Rong, G.; Peng, J.; Li, B.; Wu, Z. Effect of open-fire-induced damage on Brazilian tensile strength and microstructure of granite. *Rock Mech. Rock Eng.* **2019**, *52*, 4189–4202. [CrossRef]
45. Abbaszadeh Shahri, A.; Asheghi, R.; Khorsand Zak, M. A hybridized intelligence model to improve the predictability level of strength index parameters of rocks. *Neural Comput. Appl.* **2021**, *33*, 3841–3854. [CrossRef]
46. Teymen, A. Statistical models for estimating the uniaxial compressive strength and elastic modulus of rocks from different hardness test methods. *Heliyon* **2021**, *7*, e06891. [CrossRef] [PubMed]
47. Zhang, Y.; Zhang, X.; Zhao, Y. Process of sandstone thermal cracking. *Chin. J. Geophys.* **2005**, *48*, 722–726. [CrossRef]
48. Freire-Lista, D.M.; Fort, R.; Varas-Muriel, M. Thermal stress-induced microcracking in building granite. *Eng. Geol.* **2016**, *206*, 83–93. [CrossRef]
49. Zhu, Z.; Tian, H.; Mei, G.; Jiang, G.; Dou, B.; Xiao, P. Experimental investigation on mechanical behaviors of Nanan granite after thermal treatment under conventional triaxial compression. *Environ. Earth Sci.* **2021**, *80*, 46. [CrossRef]
50. Ferrero, A.M.; Marini, P. Experimental studies on the mechanical behaviour of two thermal cracked marbles. *Rock Mech. Rock Eng.* **2001**, *34*, 57–66. [CrossRef]
51. Wu, X.; Huang, Z.; Zhang, S.; Cheng, Z.; Li, R.; Song, H.; Wen, H.; Huang, P. Damage Analysis of High-Temperature Rocks Subjected to LN2 Thermal Shock. *Rock Mech. Rock Eng.* **2019**, *52*, 2585–2603. [CrossRef]
52. Zhao, Y.; Wan, Z.; Feng, Z.; Yang, D.; Zhang, Y.; Qu, F. Triaxial compression system for rock testing under high temperature and high pressure. *Int. J. Rock Mech. Min. Sci.* **2012**, *52*, 132–138. [CrossRef]
53. Liu, S.; Xu, J. An experimental study on the physico-mechanical properties of two post-high-temperature rocks. *Eng. Geol.* **2015**, *185*, 63–70. [CrossRef]
54. Tian, H.; Ziegler, M.; Kempka, T. Physical and mechanical behavior of claystone exposed to temperatures up to 1000 °C. *Int. J. Rock Mech. Min. Sci.* **2014**, *70*, 144–153. [CrossRef]

55. Kumari, W.G.P.; Beaumont, D.M.; Ranjith, P.G.; Perera, M.S.A.; Avanthi Isaka, B.L.; Khandelwal, M. An experimental study on tensile characteristics of granite rocks exposed to different high-temperature treatments. *Geomech. Geophys. Geo-Energy Geo-Resour.* **2019**, *5*, 47–64. [CrossRef]
56. Chen, Y.L.; Ni, J.; Shao, W.; Azzam, R. Experimental study on the influence of temperature on the mechanical properties of granite under uni-axial compression and fatigue loading. *Int. J. Rock Mech. Min. Sci.* **2012**, *56*, 62–66. [CrossRef]
57. El-Taher, A.; Uosif, M.A.M.; Orabi, A.A. Natural radioactivity levels and radiation hazard indices in granite from Aswan to Wadi El-Allaqi southeastern desert, Egypt. *Radiat. Prot. Dosim.* **2007**, *124*, 148–154. [CrossRef] [PubMed]
58. Rock, A.C.D. *Standard Test Method for Compressive Strength and Elastic Moduli of Intact Rock Core Specimens under Varying States of Stress and Temperatures*; ASTM International: West Conshohocken, PA, USA, 2010.
59. Kim, K.M.; Kemeny, J. Effect of thermal shock and rapid unloading on mechanical rock properties. In Proceedings of the 43rd US Rock Mechanics Symposium & 4th US, Canada Rock Mechanics Symposium, Asheville, NC, USA, 28 June–1 July 2009.
60. Gomah, M.E.; Li, G.; Bader, S.; Elkarmoty, M.; Ismael, M. Damage Evolution of Granodiorite after Heating and Cooling Treatments. *Minerals* **2021**, *11*, 779. [CrossRef]
61. Zhang, W.; Sun, Q.; Hao, S.; Geng, J.; Lv, C. Experimental study on the variation of physical and mechanical properties of rock after high temperature treatment. *Appl. Therm. Eng.* **2016**, *98*, 1297–1304. [CrossRef]
62. Zhang, J.; Shen, Y.; Yang, G.; Zhang, H.; Wang, Y.; Hou, X.; Sun, Q.; Li, G. Inconsistency of changes in uniaxial compressive strength and P-wave velocity of sandstone after temperature treatments. *J. Rock Mech. Geotech. Eng.* **2021**, *13*, 143–153. [CrossRef]
63. Gautam, P.K.; Verma, A.K.; Jha, M.K.; Sharma, P.; Singh, T.N. Effect of high temperature on physical and mechanical properties of Jalore granite. *J. Appl. Geophys.* **2018**, *159*, 460–474. [CrossRef]
64. Cai, C.; Li, G.; Huang, Z.; Tian, S.; Shen, Z.; Fu, X. Experiment of coal damage due to super-cooling with liquid nitrogen. *J. Nat. Gas Sci. Eng.* **2015**, *22*, 42–48. [CrossRef]
65. Homand-Etienne, F.; Houpert, R. Thermally induced microcracking in granites: Characterization and analysis. In *International Journal of Rock Mechanics and Mining Sciences & Geomechanics Abstracts*; Elsevier: Amsterdam, The Netherlands, 1989; Volume 26, pp. 125–134.
66. Abbaszadeh Shahri, A.; Larsson, S.; Johansson, F. Updated relations for the uniaxial compressive strength of marlstones based on P-wave velocity and point load index test. *Innov. Infrastruct. Solut.* **2016**, *1*, 17. [CrossRef]
67. Hale, P.A.; Shakoor, A. A laboratory investigation of the effects of cyclic heating and cooling, wetting and drying, and freezing and thawing on the compressive strength of selected sandstones. *Environ. Eng. Geosci.* **2003**, *9*, 117–130. [CrossRef]
68. Vázquez, P.; Shushakova, V.; Gómez-Heras, M. Influence of mineralogy on granite decay induced by temperature increase: Experimental observations and stress simulation. *Eng. Geol.* **2015**, *189*, 58–67. [CrossRef]
69. Zhang, B.; Tian, H.; Dou, B.; Zheng, J.; Chen, J.; Zhu, Z.; Liu, H. Macroscopic and microscopic experimental research on granite properties after high-temperature and water-cooling cycles. *Geothermics* **2021**, *93*, 102079. [CrossRef]
70. Hajpál, M.; Török, Á. Mineralogical and colour changes of quartz sandstones by heat. *Environ. Geol.* **2004**, *46*, 311–322. [CrossRef]
71. Singh, B.; Ranjith, P.G.; Chandrasekharam, D.; Viete, D.; Singh, H.K.; Lashin, A.; Al Arifi, N. Thermo-mechanical properties of Bundelkhand granite near Jhansi, India. *Geomech. Geophys. Geo-Energy Geo-Resour.* **2015**, *1*, 35–53. [CrossRef]
72. Pavese, A.; Curetti, N.; Diella, V.; Levy, D.; Dapiaggi, M.; Russo, U. P-V and T-V Equations of State of natural biotite: An in-situ high-pressure and high-temperature powder diffraction study, combined with Mössbauer spectroscopy. *Am. Mineral.* **2007**, *92*, 1158–1164. [CrossRef]
73. Zhu, Z.; Kempka, T.; Ranjith, P.G.; Tian, H.; Jiang, G.; Dou, B.; Mei, G. Changes in thermomechanical properties due to air and water cooling of hot dry granite rocks under unconfined compression. *Renew. Energy* **2021**, *170*, 562–573. [CrossRef]
74. Asheghi, R.; Hosseini, S.A.; Saneie, M.; Shahri, A.A. Updating the neural network sediment load models using different sensitivity analysis methods: A regional application. *J. Hydroinform.* **2020**, *22*, 562–577. [CrossRef]

sustainability

MDPI

Article

Accuracy of Two-Dimensional Limit Equilibrium Methods in Predicting Stability of Homogenous Road-Cut Slopes

Fhatuwani Sengani [1,2,*] and Dhiren Allopi [1]

[1] Department of Civil Engineering and Geomatics, Faculty of Engineering and the Built Environment, Durban University of Technology, P.O. Box 1334, Durban 4000, South Africa; allopid@dut.ac.za
[2] Department of Geology and Mining, Faculty of Science and Agriculture, University of Limpopo, Private Bag X1106, Sovenga 0727, South Africa
* Correspondence: fhatugeorge@gmail.com

Abstract: Although limit equilibrium methods are widely used by engineers and scientists in predicting the stability of homogenous slopes, their use has been demonstrated to present significant errors due to the violation of kinematic and static admissibility. The concern is often voiced regarding the accuracy of limit equilibrium methods (LEMs) solutions in predicting the stability of homogenous slopes. There are no exact limit equilibrium solutions or charts available that could be used to check the LEMs solutions. The present study has used the rigorous upper and lower bounds solutions of limit analysis based on finite element formulations of the bound theorems to benchmark and develop an accuracy classification chart of limit equilibrium methods in predicting the stability of the homogenous slope. Six case studies of homogenous road-cut slopes that vary with material properties were used and the effect of the increase in material strength with depth was considered. The results of LEMs and limit analysis solutions have shown that Janbu simplified limit equilibrium solutions are closely related to those of rigorous upper bound solutions with an accuracy error ranging from 1 to 7% in various slope materials. Meanwhile, the Corp of Engineer 2 limit equilibrium solutions were found to overestimate among other methods, with an accuracy error ranging from 12 to 17% in various cases. Based on the results of the study an accuracy error classification chart of LEMs is developed.

Keywords: limit equilibrium method (LEM); limit analysis; accuracy; slope stability; homogenous slopes; error accuracy classification chart

Citation: Sengani, F.; Allopi, D. Accuracy of Two-Dimensional Limit Equilibrium Methods in Predicting Stability of Homogenous Road-Cut Slopes. *Sustainability* **2022**, *14*, 3872. https://doi.org/10.3390/su14073872

Academic Editors: Mahdi Hasanipanah, Danial Jahed Armaghani and Jian Zhou

Received: 29 January 2022
Accepted: 4 March 2022
Published: 25 March 2022

Publisher's Note: MDPI stays neutral with regard to jurisdictional claims in published maps and institutional affiliations.

Copyright: © 2022 by the authors. Licensee MDPI, Basel, Switzerland. This article is an open access article distributed under the terms and conditions of the Creative Commons Attribution (CC BY) license (https://creativecommons.org/licenses/by/4.0/).

1. Introduction

The stability of road-slope embankments is one of the common subjects of study in geotechnical engineering with its application in both civil and mining engineering projects [1]. The stability of these slopes has been based on two common techniques, which include Factor of Safety (FOS) and the Strength Reduction Factor (SRF). Hoek and Bray [2] among other scholars (e.g., [1,3–5]) defined FoS as "the value by which the shear strength of the slope material must be divided in order to bring the slope to the point of failure". Nevertheless, the so-called limit equilibrium methods (LEMs) are widely used by engineers and scientists when establishing the stability of the slope based on the FOS method. Indeed, it has been evidenced that LEMs are preferred to other techniques when evaluating the FOS of the slope due to their simplicity; such evidence can be dated back to studies such as those of Fredlund and Krahn [4], Duncan and Wright [6] as well as Nash [7].

However, the 2D LEM simplifies the problem based on plane strain conditions that do not consider the true 3D properties of the given slope (soil or rock slope) [8]; in other words, the displacements are not incorporated in the analysis and it is also assumed that the driving and resisting forces are independent of deformation. There is no doubt that several scholars [5,8–12] have strived to improve shortcoming of the 2D LEMs by introducing 3D

LEMs for slope stability analysis that was based on extensions of the 2D LEMs. However, the improved 3D LEMs are very relevant to complex failure surfaces, though most slope stability problems do not involve such complicity. Owing to the previous statements, 2D and 3D LEMs still present some critical limitations when performing slope stability analysis; some of the limitations have been documented in several studies such as those of Lu et al. [13], Renani and Martin [1], and those limitations include firstly, the exclusion of stress and deformation of rock slope, and, secondly, the failure surface of the slope are predefined by engineers. Thirdly, there are many assumptions on the internal force distributions used to simplify the governing equations in order to solve the FOS, and lastly, the evolution process of the failure surface may not be simulated using LEMs [13].

Based on the previous discussion, the concern is often voiced on how accurate the LEMs 2D solutions are, indeed, the strength reduction method (SRM)/strength reduction factor (SRF) is normally used to avoid the concern. The SRM/SRF is based on the finite element method (FEM) or finite difference method (FED) to encounter the limitations presented by the LEMs in analyzing slope stability. The concern mentioned above is very critical, especially in those situations wherein the only method or technique available (in terms of resources) are LEMs to deal with the problem of slope stability. Therefore, the present paper strives to address the following objectives: firstly, to identify the most appropriate LEM, in terms of predicting the stability of the slope with a solution that is close to those of SRM/SRF, and secondly, to identify which of the bound solutions (lower and upper) is closely related to LEMs solutions in homogenous soil and rock slope. Several practical examples are used to establish a reliable LEM method by comparing the slope stability analysis solutions of the SRF method with eight LEMs.

The practical examples are implemented in homogenous slopes material with the Mohr–Coulomb model implemented based on the case study. The limit analysis computer software so-called Optimum 2G is used in conjunction with limit equilibrium computer software called SLIDEs 2D in order to answer the above-mentioned objectives. The optimum 2G is based on finite element formulations of the bound theorems of limit analysis, such as the best lower and upper bound solutions are obtained through the optimization of the admissible stress fields and kinematically admissible velocity field using linear programming techniques. On the other hand, the SLIDEs numerical model uses limit equilibrium formulations by locating the critical surface failure, and many methods have been developed; however, this study uses the Bishop Simplified [14], Lowe Karafiath, Gle/Morgenstern–Price [3], Janbu Simplified, and Janbu Corrected [15], Spencer [16], and Corp of Engineer number one, and Corp of Engineer number two [17] formulations.

Following the introductory section, a brief literature review is documented, which is intended to outline the gap knowledge regarding the LEMs, and the Finite Element Limit Analysis as a complementary method is outlined. The previous sections led to the discussion of methodology in terms of the numerical formulations of both LEMs and lower and upper bound of limit analysis using finite elements. The results of the study are thereafter documented with six case studies and concluding remarks are also given.

1.1. Brief Literature Review on Limit Equilibrium Methods

The limit equilibrium methods have been used in assessing the stability of the slope for the past many years with an assumption that the soil material obeys the perfectly plastic Mohr–Coulomb criteria (an example of a study documenting this is Fellenius, [18]). The improvement on these methods has been demonstrated for decades with well-known contributions by Bishop [14], Janbu [15], Morgenstern–Price [3], and Spencer [16] among others. Though critical improvement has been demonstrated in the literature, the methods turn to apply a global equilibrium condition, and as such, the approach is purely static since it neglects the plastic flow rule of soil. Owing to that the static admissibility of the stress field is also not satisfied due to arbitrary assumptions made to remove the static indeterminacy. In summary, the methods only satisfied the global equilibrium conditions. To overcome the limitations of LEMs, the finite element limit analysis is used in slope

stability problems. The finite element limit analysis uses the lower and upper bound rigorous solutions in simulating the stability of the slope. The lower bound limit analysis was firstly introduced by Lysmer [18]. Nevertheless, the lower bound method has been improved by several scholars [19–24] in order to meet all requirements for the stability analysis, and the method uses three types of the elements under the conditions of plane strain as shown in Figure 1. It has been documented that the stress field for each of these elements is assumed to vary linearly.

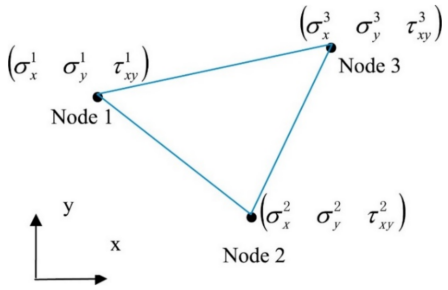

Figure 1. Elements used for lower bound limit analysis [24].

On the other hand, the literature [19] reveals that the first formulation for the upper bound theorem was developed in 1972, with the purpose of analyzing the plate problems, further modifications were then introduced thereafter by scholars such as Bottero et al. [20], Sloan [22], and Yu et al. [25], to incorporate velocity discontinuities in a plane strain of limit analysis. Although there has been some improvement, the upper bound formulations did not have a large number of discontinuities in the velocity field, therefore, Sloan and Kleeman [26] strived to address the problem in the formulation of the upper bounds, which is the recent bound used in the current study. An example of the constant-strain triangular element used in the upper bound analysis is shown in Figure 2.

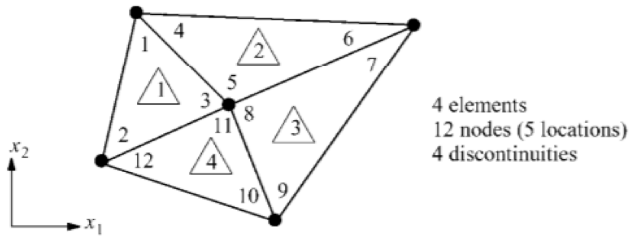

Figure 2. Elements used for upper bound limit analysis [18].

1.2. Brief Discussion on Literature

Although there have been several improvements on the LEMs in predicting the stability of the slope, the method still presents some limitations as stated within the introduction section. Furthermore, the use of LEMs has gained momentum despite their accuracy error. One may say their simplicity increases their use in the industry, yet there is no accurate predicting chart to benchmark the LEMs solutions, though the SRF method is preferred by few engineers due to its complexity. The recent study is intended to identify the error accuracy of LEMs benchmarked with lower and upper bound limit analysis methods. It is anticipated that the error accuracy chart will give freedom to those engineers who still prefer LEMs over any other method; the authors will be able to benchmark their solutions. Indeed, six common types of soil slope material were chosen to identify the accuracy per material of the slope; however, several case studies also increase the confidence of the outcome of the study.

2. Materials and Methods

The material and methods section of the paper is divided into two sections. The first section documents the limit equilibrium method applied in this study, and the mathematical formulation of each method is documented followed by the description of the procedures followed when simulating LEM solution using a computer code called SLIDEs 2D. In the second section of governed by limit equilibrium method, a brief description of the strength reduction factor method of limit analysis is documented followed by its mathematical formulations in terms of governing equations, lower and upper bounds principles, bounds and duality formulations, and lastly the procedure for a computer code called Optum G2 is briefly documented.

2.1. Limit Equilibrium

The limit equilibrium approach assumes that a slope is stable when any free-body inside the soil medium is at rest; this implies that the static equilibrium conditions are satisfied. Based on this assumption, LEMs cannot yield a direct measure of system reliability; instead, they analyze multiple paths within the soil profile to determine the critical slip surface. For the given soil slopes surfaces, the stability level was quantified using a constant name called Factor of Safety (FOS), which is the ratio between the available soil shear strength and the equilibrium shear stress at the slip surface. In this regard, the FOS of the soil slopes is expressed by Equations (1) and (2). Equations (1) and (2) were formulated considering the generic slip surface as shown in Figure 3, the mobilized shear strength was determined based on the inertial forces and external loads as well as base reactions. Depending on the type of problem and the accuracy of results required, this approach uses different analysis methods such as Ordinary method, Bishop Simplified, Gle/Morgenstern–Price, Janbu Simplified, and Janbu Corrected, Spencer and Corp of Engineer number one, and Corp of Engineer number two. A detailed description of the formulation of the methods is documented below since all these methods were used in this study.

$$F_S = \frac{\tau}{S} = \frac{C + \sigma_n \tan \varnothing}{C_m + \sigma_n \tan \varnothing_m} \tag{1}$$

$$F_S = \frac{c}{c_m} = \frac{\varnothing}{\varnothing_m} \tag{2}$$

where τ: peak shear stress, S: equilibrium shear stress, σ_n: normal stress, C and $\varnothing$: soil cohesion and friction angle (i.e., subscript "m" denotes the mobilized parameters).

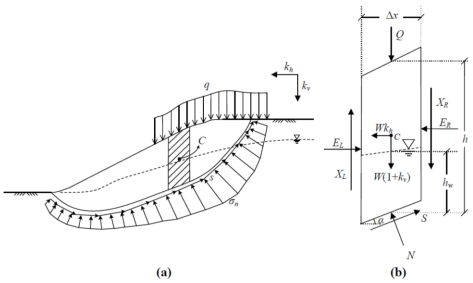

Figure 3. Free-body diagram of a generic slip surface (**a**) overall diagram; (**b**) vertical slice diagram [25].

2.1.1. Ordinary Method

The Ordinary method (OM) has been well known to satisfy the moment equilibrium for a circular slip surface [27], while neglecting both the interslice normal (E) and the shear forces (T). The common advantage of this method is its simplicity in solving the safety factor (FOS), because its equation does not require interaction processes. Furthermore, the method is considered inaccurate for a flat slope with high pore pressure. As already indicated,

the FoS of the method is based on moment equilibrium, therefore, the FoS equations are computed as follows [7,27]:

$$F_m = \frac{\sum(C'l + N' \tan \varnothing')}{\sum W \sin \alpha} \tag{3}$$

$$N' = (W \cos \alpha - ul) \tag{4}$$

where: α, c', φ', u, l and F are the inclination of slip surface at the middle of slice, cohesion, friction angle, pore pressure, and slice base length, respectively.

2.1.2. Bishop's Simplified

The Bishop's Simplified method (BSM) is very popular in geotechnical engineering, the method is considered accurate for only circular slip surfaces [27,28]. Nonetheless, the method also satisfies vertical equilibrium and the overall moment equilibrium. Furthermore, the method assumes that side forces on slices are horizontal. The method is given by the following equation;

$$N' = \frac{1}{m_\alpha} \sum \left(W - \frac{C'l \sin \alpha}{F} - ul \cos \alpha \right) \tag{5}$$

where $m_\alpha = \cos \alpha \left(1 + \tan \alpha \frac{\tan \varnothing'}{F} \right)$.

Lastly, the FOS is determined through the iteration processes [28].

2.1.3. Janbu's Simplified

Janbu's Simplified method (JSM) is considered to be a force equilibrium method and it is applicable to any shape of the slip surface. The method assumes that side forces are horizontal (same for all slices) and safety factors are usually lower as compared to another method that calculated safety factors by satisfying all conditions of equilibrium. The safety factor equation that governs this method is shown below [28].

$$F_O = \frac{\sum \left\{ \frac{b(C' + (p-u) \tan \varnothing')}{n_\alpha} \right\}}{\sum p.b \tan \alpha} \tag{6}$$

where $n_\alpha = \cos^2 \alpha \left(1 + \tan \alpha \frac{\tan \varnothing'}{F} \right)$.

2.1.4. Janbu's Generalised

Janbu's Generalised method (JGM) satisfies all the conditions of equilibrium, it is also applicable to any shape of the slip surface. The method assumes the heights of side forces above the base of the slice (usually varied from slice to slice). It is also considered to be the accurate method and the one that is applied most frequently in numerical convergence problems. The FOS equation that governs this method is shown below [28].

$$F_f = \frac{\sum [\{C'l + (N - ul) \tan \varnothing'\} \sec \alpha]}{\sum \{W - (T_2 - T_1)\} \tan \alpha + \sum (E_2 - E_1)} \tag{7}$$

where, F_f is FoS E, T, W re forces.

2.1.5. Corps of Engineers

Corps of Engineers method (CEM) is an accurate method of force equilibrium, and it is also applicable to any shape of the slip surface. The method assumes that the side force inclination is equal to the inclination of the shape (same from slice to slice). The Factor of Safety is often considered higher than when calculated using another method that satisfies all equilibrium conditions. The FOS equation that governs this method is shown below [28].

$$T = E \tan \theta \tag{8}$$

where, λ is scale factor of the assumed function, E is the interslice forces, T is the FOS.

2.1.6. Morgenstern-Price

Morgenstern–Price method (MPM) is an accurate method of force equilibrium, and it is also applicable to any shape of the slip surface. The method assumes that the inclination of the side force follows a prescribed pattern, so-called $f(x)$; the side force inclination can be the same or vary for every slice and the side force inclination is calculated in the process of the solution to ensure that the equilibrium conditions are satisfied. The FOS equation that governs this method is shown below [28].

$$T = f(x).\lambda.E \tag{9}$$

where, $f(x)$ is the interslice force function that varies continuously along the slip surface, λ is the scale factor of the assumed function, E is the interslice forces, T is the FOS.

2.1.7. Spencer's Method

Spencer's method (SM) is an accurate method of force equilibrium, and it is also applicable to any shape of the slip surface. The method assumes that the inclination of the side force is the same for every slice and the side force inclination is calculated in the process of the solution to ensure that the equilibrium conditions and satisfied. The FOS equation that governs this method is shown below [28].

$$T = E \tan \theta \tag{10}$$

All mentioned above governing equations of the limit equilibrium methods were applied in a Rocscience code called SLIDEs 2D to simulate the stability number of the slope. The procedure for the computer code is documented below.

2.1.8. SLIDES Computer Code Procedures

The computational procedures for SLIDEs are well explained in several studies such as those of Sengani and Mulenga [29,30]. The SLIDEs were utilized to estimate the FOS of the slopes in six scenarios; however, the code has the ability to use various LEMs at a time. In terms of model building, it starts with the creation of a new project. Similar to other modeling platforms, the new project required the delimitation of the model limitation in XY coordinates. For that, various X and Y coordinates defining the region were entered. The ultimate goal of this step was to draw the model of the region. Upon generating the boundaries of the model, the actual initial conditions of the simulation are defined next for the project. Inputs such as the statistics associated with groundwater conditions, the computational methods, and the failure directions are captured.

2.2. Limit Analysis

The limit analysis of this study is performed using the so-called strength reduction factor (SRF) or strength reduction method (SRM). The SRM is mostly based on the finite element method (FEM) or finite difference method (FDM) to overcome the limitations presented by limit equilibrium methods. The SRM method was firstly proposed by Zienkiewicz et al. (1975) with the purpose of analyzing slope stability; however, the method has gained more interest with many scholars [31–35] striving to improve the method. It has been observed that several scholars [36,37] have confirmed that SRM solutions are more accurate and can be closely related to the LEM solutions; this allows us to use the SRM as a benchmark method in evaluating the accuracy of the LEM method.

In the strength reduction method, the Factor of Safety (FOS) is defined as the ratio between the actual shear strength and the reduced shear strength for the fault, joints, and intact rock when the slope arrives at a critical state. When implementing the strength

reduction procedure, the reduced shear strength parameters, cohesive force C_r and the fiction angle φ_r are obtained by the following (see Equation (11)):

$$C_r = \frac{C}{SRF} \tag{11}$$

$$\varphi_r = \tan^{-1}\left(\frac{\tan\varphi}{SRF}\right)$$

As already stated that the SRMs are based on FEM, therefore, these methods have governing equations followed by their mathematical formulations in terms of the bound solutions (lower and upper) as well as the duality and bounds equations of the model. A detailed description of the mathematical formulation of the used SRM is documented below.

2.2.1. Governing Equations

Governing equations defining the mathematical implementation of the FEM model of a solid system are encapsulated in Equations (12)–(17). Assuming an infinitesimal deformation is to be simulated, the equations can be expressed as follows [38]

Equilibrium and static boundary conditions of the model:

$$\nabla^T\sigma + b = 0, \text{ in V} \tag{12}$$

where $\sigma = \begin{bmatrix} \sigma_x & \sigma_y & \sigma_z & \sigma_{xy} & \sigma_{yz} & \sigma_{zx} \end{bmatrix}^T$ are the stresses, $b = \begin{bmatrix} b_x & b_y & b_z \end{bmatrix}^T$ are the body forces stemming for example from self-weight, and V is the domain under consideration.

$$\mathrm{P}^T\sigma = \alpha t \quad on \quad S_\sigma \tag{13}$$

Meanwhile, the yield conditions of the model are as follows:

$$F^T\sigma - k + s = 0 \tag{14}$$

Since the current situation is dealing with strain problems, therefore, associate flow rules or strain-displacement compatibility has to be incorporated as follows;

$$\nabla\dot{u} = F\dot{\lambda} \tag{15}$$

where $\dot{\lambda}$ is the plastic multiplier that satisfies the complementarity conditions.

Therefore, the scaling applied with respect to the rate of work done by the reference tractions t as indicated above, in short, the scaling equation is denoted as follows;

$$\int_{S_\sigma} t^T\dot{u}dS = 1 \tag{16}$$

where $\dot{u}$ is taken as the exact velocity, t is traction vector

Lastly, the complementarity conditions of the model are, therefore, incorporated as follows:

$$S^T\dot{\lambda} = 0,\ S \geq 0,\ \dot{\lambda} \geq 0 \tag{17}$$

Nevertheless, a detailed description of the model in terms of lower bound principle, upper bound principles, bounds are documented below.

2.2.2. Lower Bound Principle

In terms of the lower bound principles, the principle ensures that the strain-softening aligns with the governing equation of the limit analysis of the finite element. However, the kinematic quantities, which are absent from the governing equations, appear as Lagrange multipliers when solving the problem. The main strength of the lower bound principle is that it allows for a lower bound on the exact collapse multiplier to be computed,

through constructing a stress field that satisfies the constraints without necessarily being optimal [39].

$$\begin{array}{c} \text{Maximize} \alpha \\ \text{Subjected to } \nabla^T \sigma + b = 0, \text{ in V} \\ \mathrm{P}^T \sigma = \alpha t \text{ on } S_\sigma \\ F^T \sigma - k + s = 0 \end{array} \tag{18}$$

2.2.3. Upper Bound Principle

As already stated, the problem at hand incorporates the kinematic quantities that the LEMs do not have the ability to handle; therefore, the upper bound is intended to incorporate the compatible velocity field that satisfies the flow rule. A similar flow rule cannot be activated using the LEMs, therefore, this upper bound is indeed critical. In order to achieve that, the rate of work done by the reference tractions is scaled to unity and the objective function, which comprises the internal rate of work minus the contribution from the constant body forces, is then the collapse multiplier sought. The upper bound principles are denoted in Equation (19).

$$\begin{array}{l} \text{Minimize} \quad \int_V^{\cdot} k^T \lambda \cdot dV - \int_V^{\cdot} b^T u \cdot dV \\ \text{Subjected to } \nabla \dot{u} = F\dot{\lambda}, \lambda \geq 0 \\ \int_{S_\sigma} t^T \dot{u} dS = 1 \end{array} \tag{19}$$

2.2.4. Bounds

The bounds are a critical part of the numerical simulation because this stage is used to verify the lower and upper bound principles to ensure that the bounds furnish with a collapse multiplier. Therefore, the stress field is considered first, to ensure that they satisfy the yield condition and the equilibrium conditions as well as the boundary conditions. Such expression on how the bound is performed is documented by Equation (20).

$$\begin{aligned} {}_a b &= \int_V^{\cdot} k \lambda_b dV - \int_V^{\cdot} b^T u \cdot dV \\ &= \int_V^{\cdot} \left(F^T \sigma_b \right)^T \dot{\lambda_b} dV - \int_V^{\cdot} b^T u \cdot dV \\ &= \int_V^{\cdot} \sigma_b^T F \lambda_b - \int_V^{\cdot} b^T u \cdot dV \end{aligned} \tag{20}$$

2.2.5. Optum G2 Computer Code Procedures

The model procedure followed in Optum G2 is readily available on the Optum Computational Engineering website under Optum G2 analysis and examples. In summary, the procedure followed includes the project definition (project file dialog, slope parameters dialog, model layout), building the model in terms of model layers, input properties of the material, and model setting. After processing the provided information in the model, the results of the model are then presented in terms of SRF, gravity multiplier, though the current study is interested in SRF analysis only. Furthermore, the model can also provide results on displacement, stress, the strain among other aspects such as yielding function and dissipation. As already stated, the model build was varied based on the material properties the case is interested in and the material properties of each case are given in Table 1 below.

Table 1. Material properties used for case studies.

	Material Type	Loose Sand	Medium Sand	Dense Sand	Soft Clay	Firm Clay	Stiff Clay	Dimensions of the Model	
Stiffness	E (MPa)	30	30	30	30	30	30	Rise (m)	10
	ν (-)	0.25	0.25	0.25	0.25	0.25	0.25	Depth (m)	4
Strength	c (kPa)	03	04	06	09	12	20	Left (m)	10
	ϕ (°)	13	15	17	18	20	22	Run (m)	20
Tension cut-off	kt (kPa)	0	0	0	0	0	0	Right (m)	15
	ϕt (°)	90	90	90	90	90	90	Slope degree	27°
Unit Weights	γdry (kN/m^3)	14	16	18	19	20	21		
	γsat (kN/m^3)	19	20	21	19	20	21		
Initial Conditions	$K0$ (-)	0.5	0.43	0.36	0.69	0.66	0.63		
	$\sigma 0$ (kPa)	0	0	0	0	0	0		
Hydraulic Model	Kx (m/day)	1×10^{-5}	1×10^{-5}	1×10^{-5}	1×10^{-5}	1×10^{-5}	1×10^{-5}		
	Ky (m/day)	1×10^{-5}	1×10^{-5}	1×10^{-5}	1×10^{-5}	1×10^{-5}	1×10^{-5}		
	h (m)	0.5	0.5	0.5	0.5	0.5	0.5		

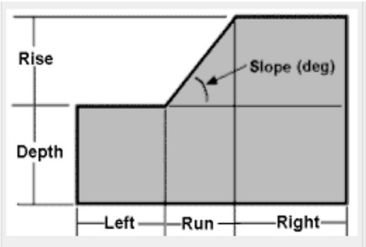

3. Results

The results of this paper are divided into two sections, the first section presents numerical simulation results in a homogenous road slope using the Mohr–Coulomb model. In this section, several examples on the prediction of Factor of Safety or Strength Reduction Factor using both limit equilibrium (SLIDEs) and limit analysis (Optum G2) are presented. Indeed, a detail comparing the accuracy of the LEMs in predicting the stability of the slope is well presented, the presentation of these results also incorporates the overestimation of FOS by several LEMs compared with the SRF stability number predicted. As already stated, several examples were used to quantify the accuracy prediction of slope stability using LEMs benchmarking with a limit analysis approach, a homogenous road slope with loose sand, medium sand, dense sand, soft clay, firm clay, and stiff clay mechanical properties are used to conduct the investigations. However, the slope solid material properties differ in terms of stiffness, strength, flow rule, unit weight, and hydraulic conditions. As such, a clear distinction of the accurate prediction of slope stability of the road slope in strain-softening has been documented.

The second section of the results document a classification chart in terms of accurate prediction of slope stability among the LEMs. The chart classifies LEMs accuracy in terms of their rate of overestimating the stability of the slope, with the most accurate methods considered to be those with less percentage of overestimating the stability of the slope. The chart was based on the previous section and benchmarked with the limit analysis results.

3.1. Stability Analysis of a Homogenous Road Embankment Slope

The results of homogenous slope stability calculations using the rigorous upper and lower bound methods of limit analysis and the limit equilibrium method (Ordinary, Bishop, Gle/Morgenstern–Price, Janbu Simplified, and Janbu Corrected, Spencer, and Corp of Engineer number one, and Corp of Engineer number two) are presented in Figure 4, for slope with homogenous loose sand, medium sand, dense sand, soft clay, firm clay, and stiff clay, respectively. The limit analysis results are plotted in terms of Strength Reduction Factor for both lower and the upper bounds; however, the simulation also included the slope total displacement though it is not of interest. The solutions from limit equilibrium computer code SLIDEs 2D are presented in terms of Factor of Safety for all stated methods. In both computer codes, it is assumed that the material gain strength with depth. Similar to other studies such as Yu et al. [40], to account for the effect of increasing strength with depth, the results are always presented in terms of stability number (SRF or FOS) against the dimensionless parameters. For each homogenous slope, the stiffness, strength (cohesion, friction angles) unit weight (dry and saturated soil), and hydraulic conditions differ greatly. Furthermore, the geometry of the slope was kept constant throughout different case studies given, details of each case study are outlined below.

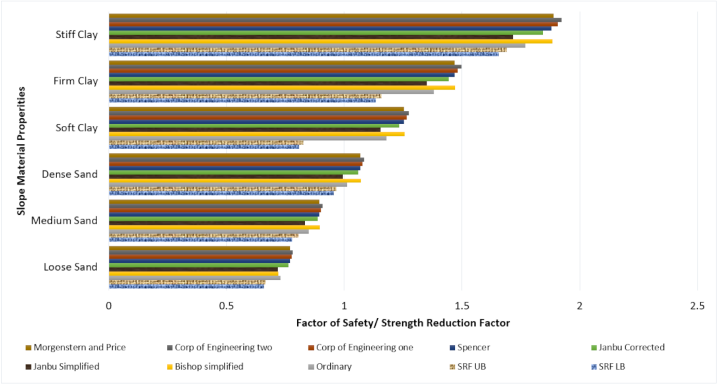

Figure 4. Distribution of Stability number (SRF and FOS) in various homogenous slope materials with limit equilibrium benchmarked with limit analysis.

3.1.1. Road Embankment Slope with Loose Sand

A soil slope with a slope angle of 45° is selected as a case study shown in Figures 5–7. In the slope, loose sand with a friction angle of 13°, the cohesion of 3 kPa, and unit weight of 14 kN/m^3, and other input parameters as shown in Table 1, were taken into consideration. Both rigorous lower and upper bounds limit analysis and limit equilibrium methods were used to perform the analysis through separate numerical codes and were implemented as stated by the methodology section. The results of the limit analysis have shown that the slope is expected to be unstable considering the effect of an increase in strength of material with a depth of slope. Furthermore, the lower bound solution estimated the SRF of 0.6588 while the upper bound solution was about 0.666 SRF. On the other hand, the limit equilibrium method solutions were ranging from 0.718 FOS to 0.776 FOS. For all the cases considered (see Figures 6 and 7), it has been denoted that the exact solutions are bracketed within 8 to 17% of error accuracy. This implies that among the limit equilibrium methods, none of them were able to provide the exact solutions as compared to the rigorous lower or upper bound solutions; however, the LEMs solutions were denoted to be closely related to those of the upper bound solutions. Indeed, this type of result has been demonstrated by previous scholars such as those of Yu et al. [40]. Meanwhile, the Corp of Engineer number two was found to produce the highest accuracy error in predicting the stability number. Though several scholars assumed that the LEMs produce similar results with the limit analysis based on the predicted SRF and FOS number without considering the calculation of error accuracy or benchmarking the two methods, the outcome of this analysis demonstrated different views within those studies, such as Renani and Martin [1]. One may denote that, previous studies such as those of Renani and Martin did not consider exact solutions but closely related solutions and by so doing the author came to the conclusion that the solutions of LEMs and rigorous upper bound solutions are similar.

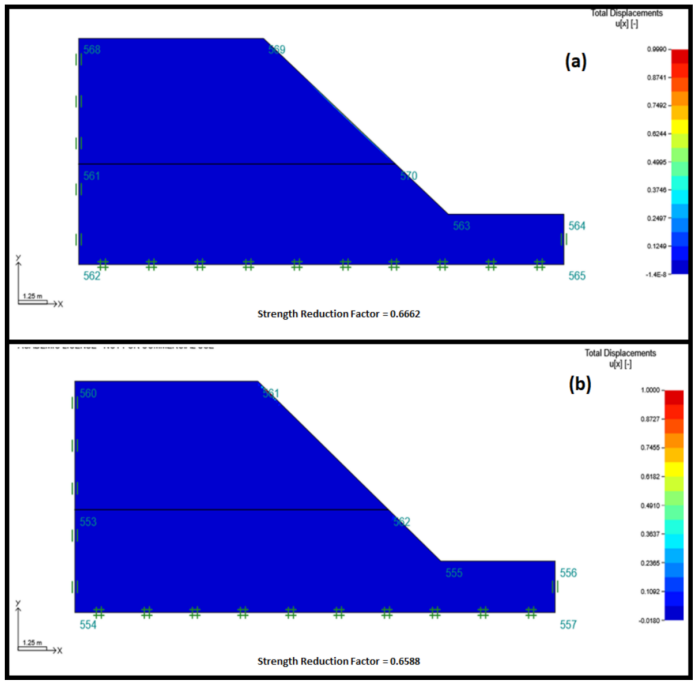

Figure 5. Predicted stability number using limit analysis method of strength reduction factor in loose sand (**a**) the SRF of the upper bound solutions of limit analysis; (**b**) the SRF of the lower bound solutions of the limit analysis.

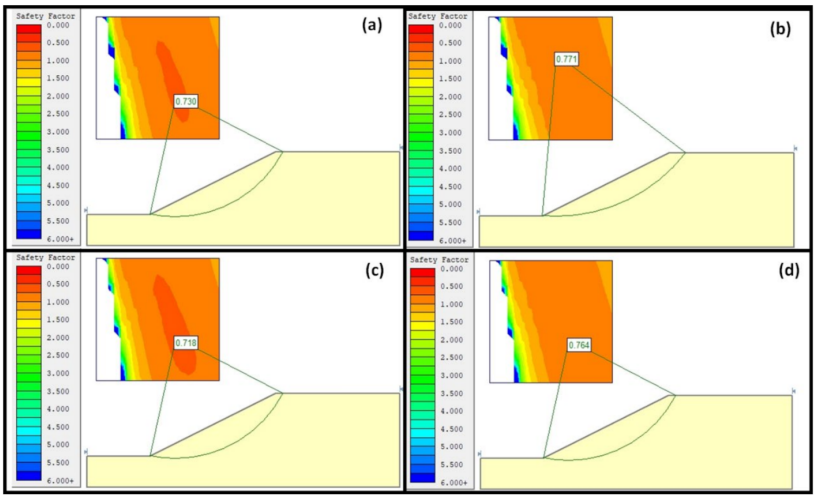

Figure 6. Limit equilibrium stability number of loose sand slope produced using (**a**) Ordinary method; (**b**) Bishop Simplified method; (**c**) Janbu Simplified method; (**d**) Janbu Corrected method.

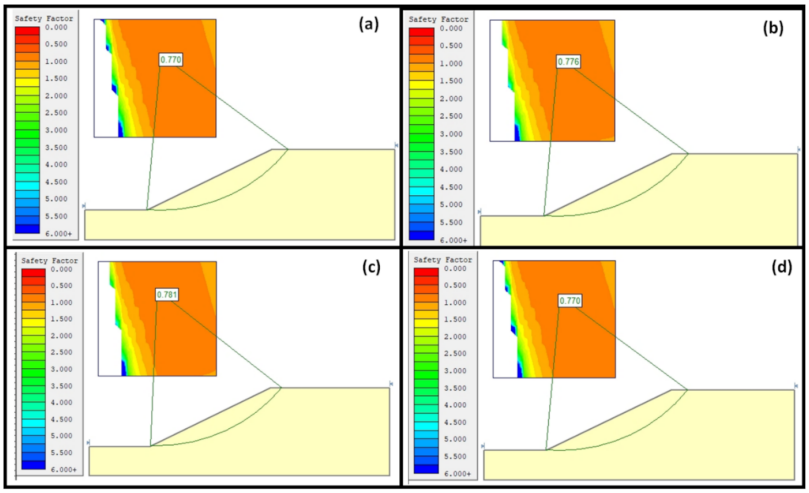

Figure 7. Limit equilibrium stability number of loose sand slope produced using (**a**) Spencer method; (**b**) Corp of Engineering one; (**c**) Corp of Engineering two; (**d**) Morgenstern–Price method.

It was also observed that the Bishop Simplified method of limit equilibrium also produces a stability number that has a good agreement with the upper bound solutions of the limit analysis. The method has produced a stability number with an accuracy error of about 9%, which is acceptable in the industry. That being said, the Bishop Simplified method accuracy error solution was closely related to that of the Janbu Simplified method with just a 1% difference. Furthermore, another method including Spencer, Morgenstern–Price, and Corp of Engineering produced an accuracy error above 10% but less than 20%. In summary, all the LEMs produce the stability number that is closely related to that of the upper bound solutions but the stability numbers are not the same. Further case studies are discussed below to solidify the outcome.

3.1.2. Road Embankment Slope with Medium Sand

Similar soil slope profiles were considered in this case as well, as shown in Figures 7–9. In the slope, medium sand with a friction angle of 15°, the cohesion of 4 kPa, and unit weight of 16 kN/m^3, and other input parameters as shown in Table 1, were taken into consideration. Both rigorous lower and upper bounds limit analysis and limit equilibrium methods were used to perform the analysis. The results of the limit analysis have shown that the slope is expected to be unstable. The lower bound solution estimated the SRF of

0.7782 while the upper bound solution was about O.8068 SRF. On the other hand, the limit equilibrium method solutions (FOS) ranged from 0.834 to 0.908. For all the cases considered (see Figures 8 and 10), it was denoted that the exact solutions are bracketed within 3 to 13% of error accuracy. This implies the limit equilibrium method is still considered to produce reasonable solutions in medium sand; however, the Janbu and Ordinary methods were found to produce very small accuracy errors ranging between 3 and 5%, which is still within the acceptable error accuracy.

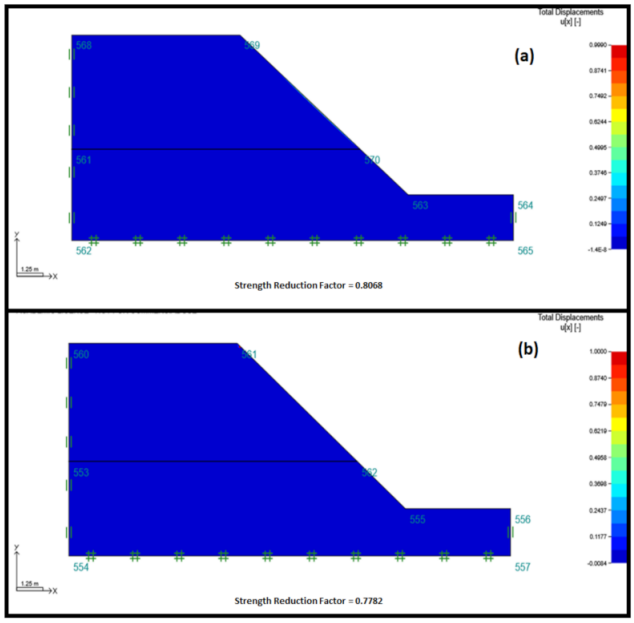

Figure 8. Predicted stability number using limit analysis method of strength reduction factor in medium sand (**a**) the SRF of the upper bound solutions of limit analysis (**b**) the SRF of the lower bound solutions of the limit analysis.

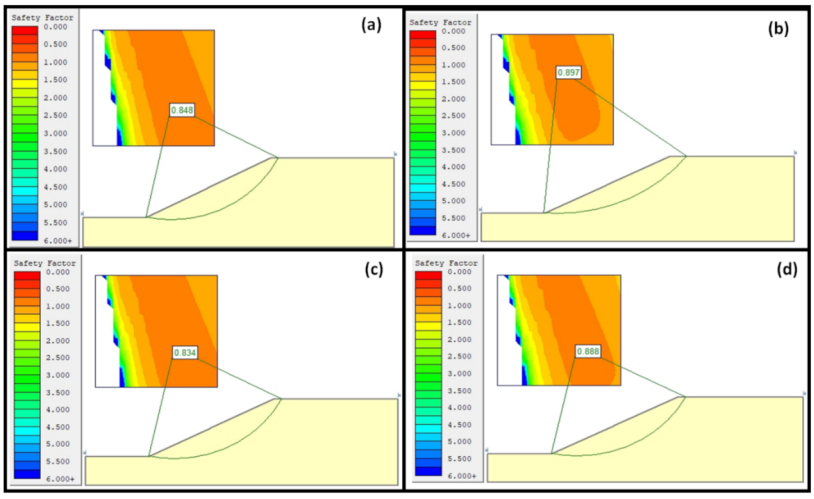

Figure 9. Limit equilibrium stability number of medium sand slope produced using (**a**) Ordinary method; (**b**) Bishop Simplified method; (**c**) Janbu Simplified method; (**d**) Janbu Corrected method.

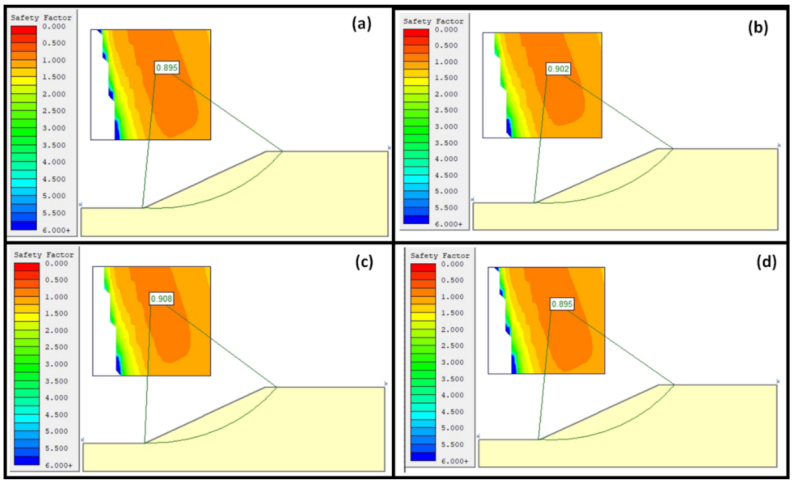

Figure 10. Limit equilibrium stability number of medium sand slope produced using (**a**) Spencer method, (**b**) Corp of Engineering one (**c**) Corp of Engineering two (**d**) Morgenstern–Price method.

On the other hand, Corp Engineering two was also observed to produce the highest error of accuracy but in this case, the error was just about 10%. This gives an impression that almost all limit equilibrium methods can produce solutions that are in good agreement with the upper solutions in medium sand. Similar observation as the previous case the spencer and Morgenstern–Price methods produced similar stability.

3.1.3. Road Embankment Slope with Dense Sand

A soil slope with a slope angle of 45° is selected as a case study shown in Figures 5–7. In the slope, dense sand with a friction angle of 17°, the cohesion of 4 kPa, and unit weight of 16 kN/m^3, and other input parameters as shown in Table 1, were taken into consideration. Both rigorous lower and upper bounds limit analysis and limit equilibrium methods were used to perform the analysis through separate numerical codes were implemented as stated by the methodology section. The results of the limit analysis have shown that the slope is expected to be unstable considering the effect of the increase in strength of material with a depth of slope.

Furthermore, the lower bound solution estimated the SRF of 0.9559 while the upper bound solution was about 0.9672 SRF. On the other hand, the limit equilibrium method solutions were ranging from 0.994 FOS to 1.085 FOS. For all the cases considered (see Figures 11–13), it has been denoted that the exact solutions are bracketed within 8 to 17% of error accuracy. In this case, the limit equilibrium method produces two scenarios wherein Janbu Simplified classifies the slope as unstable and the solutions are closely related to those of the upper solutions. On the other scenario the rest of the method classified the slope as stable, this implies that most of the LEMs have overestimated the stability of the slope.

3.1.4. Road Embankment Slope with Soft Clay

A soil slope with a slope angle of 45^0 was selected as a case study shown in Figures 14–16. In the slope, a soft clay with a friction angle of 18^0, the cohesion of 9 kPa, and unit weight of 19 kN/m^3, and other input parameters as shown in Table 1, were taken into consideration. Both rigorous lower and upper bounds limit analysis and limit equilibrium methods were used to perform the analysis. The results of the limit analysis have shown that the slope is expected to be unstable using the rigorous lower and upper bound solutions with the SRF of 0.8257 and 0.8079 for upper and lower, respectively. Meanwhile, the limit equilibrium method solutions estimated a stable slope with FOS ranging from 1.155 to 1.274 (see the simulation results in Figures 14–16).

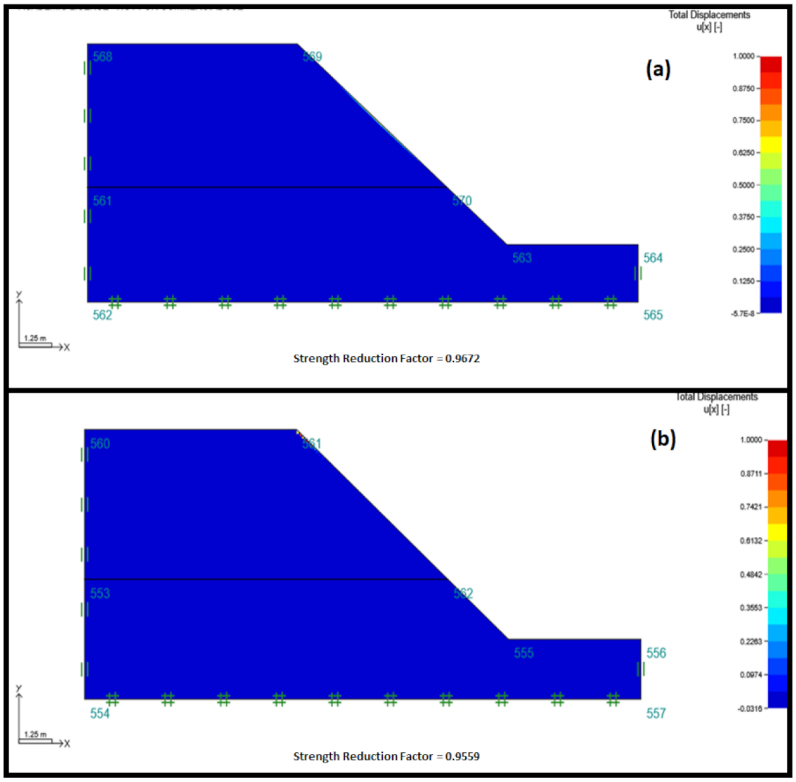

Figure 11. Predicted stability number using limit analysis method of strength reduction factor in dense sand (**a**) the SRF of the upper bound solutions of limit analysis; (**b**) the SRF of the lower bound solutions of the limit analysis.

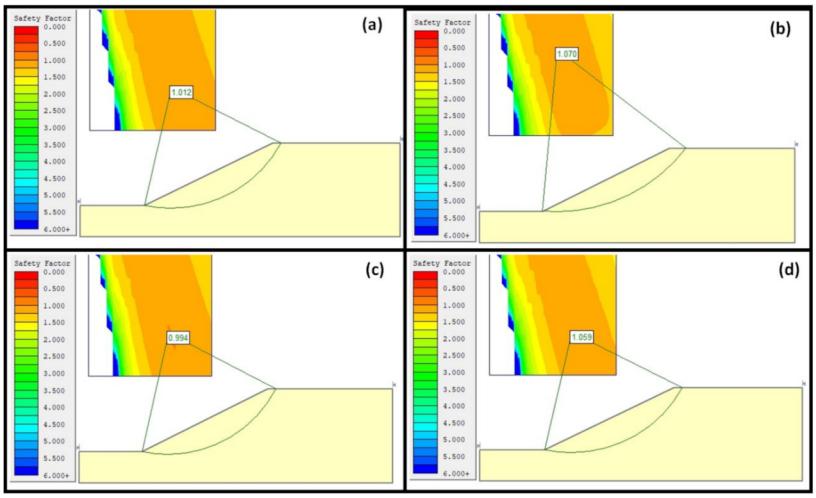

Figure 12. Limit Equilibrium stability number of dense sand slope produced using (**a**) Ordinary method; (**b**) Bishop Simplified method; (**c**) Janbu Simplified method; (**d**) Janbu Corrected method.

For all the cases considered (see Figures 14 and 16), it has been denoted that the exact solutions are bracketed within 40 to 54% of error accuracy. This implies among the limit equilibrium method, none of them were able to provide the exact solutions as compared to the rigorous lower or upper bound solutions. In this regard, all methods were found to overestimate the stability number of the slope. This implies that LEMs are not best to use in soft clay soil slope due to the high accuracy error produced by the methods.

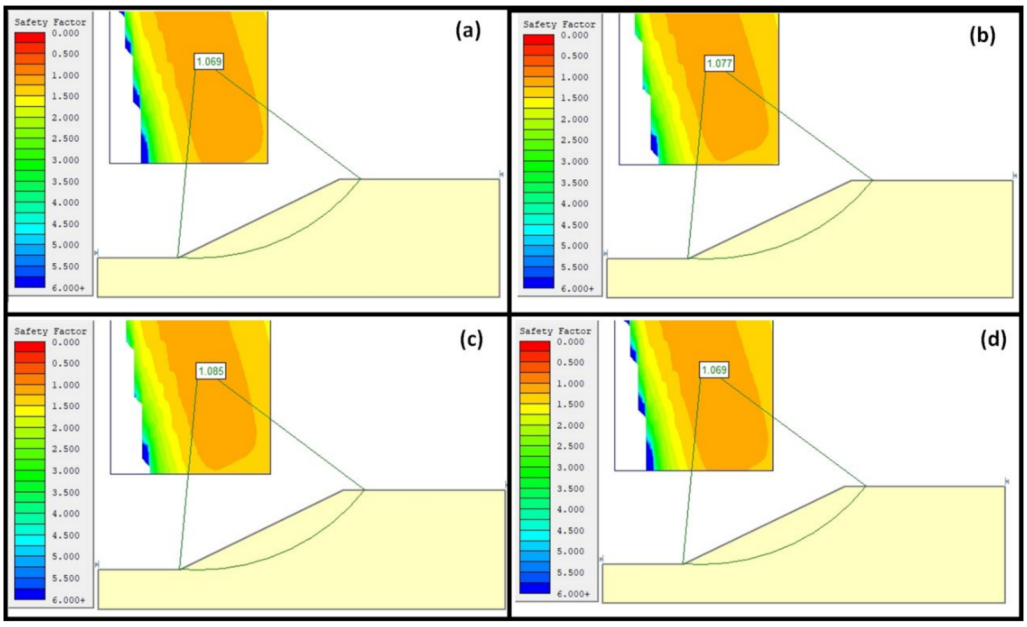

Figure 13. Limit Equilibrium stability number of dense sand slope produced using (**a**) Spencer method; (**b**) Corp of Engineering one (**c**) Corp of Engineering two; (**d**) Morgenstern–Price method.

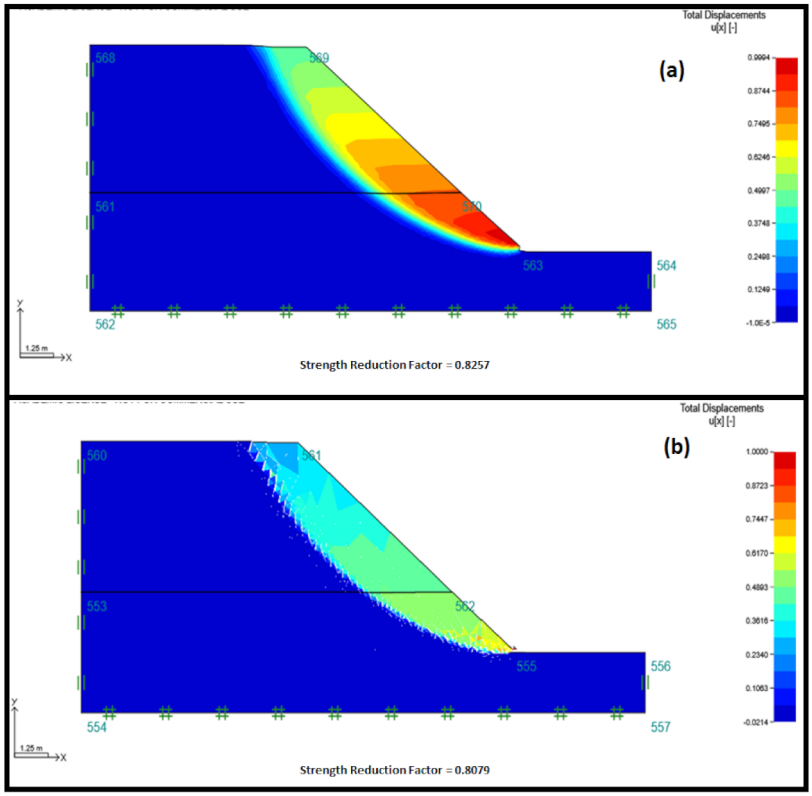

Figure 14. Predicted stability number using limit analysis method of strength reduction factor in soft clay (**a**) the SRF of the upper bound solutions of limit analysis; (**b**) the SRF of the lower bound solutions of the limit analysis.

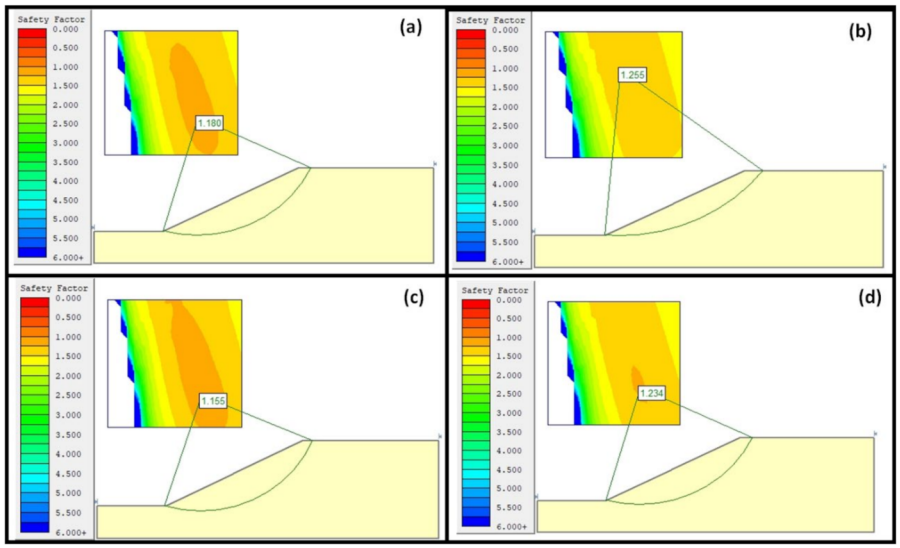

Figure 15. Limit Equilibrium stability number of soft clay slope produced using (**a**) Ordinary method; (**b**) Bishop Simplified method; (**c**) Janbu Simplified method; (**d**) Janbu Corrected method.

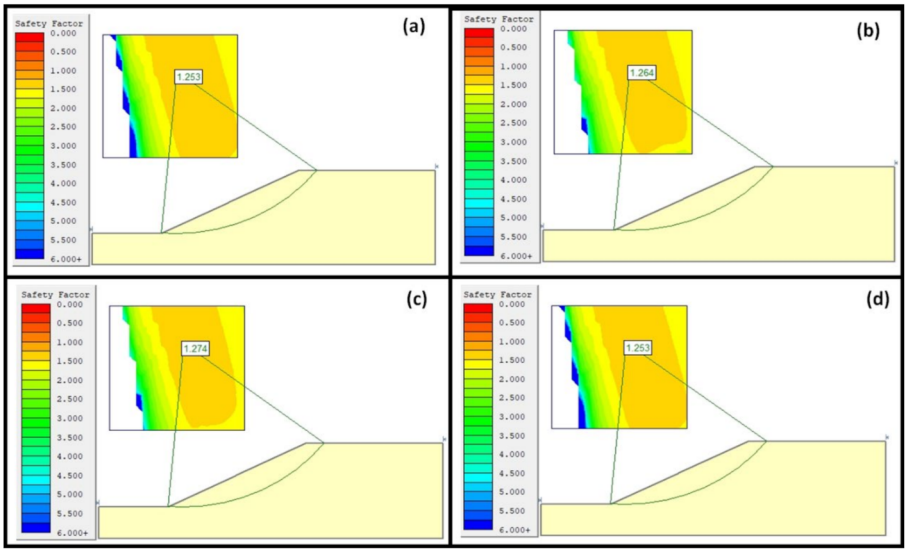

Figure 16. Limit Equilibrium stability number of soft clay slope produced using (**a**) Spencer method; (**b**) Corp of Engineering one; (**c**) Corp of Engineering two; (**d**) Morgenstern–Price method.

It was also observed that this material behaves differently among others, which demonstrates that though the slope maybe consists of soil, the properties of the soil matter in order to estimate the stability number accurately. One may argue that such abnormality observed could be due to the fact that the limit equilibrium formulations suffer from including stress and deformation of the material [1], meanwhile, the failure surface is predefined by engineers, which results in predicting such high stability number.

3.1.5. Road Embankment Slope with Firm Clay

A soil slope with a slope angle of 45° is selected as a case study shown in Figures 17–19. In the slope, firm clay and with friction angle of 13°, the cohesion of 3 kPa, and unit weight of 14 kN/m^3, and other input parameters as shown in Table 1, were taken into consideration. Both rigorous lower and upper bounds limit analysis and limit equilibrium methods were used to perform the analysis through separate numerical codes and were implemented as stated by the methodology section. The results of the limit analysis have shown that the slope is expected to be unstable considering the effect of the increase in strength of

material with a depth of slope. Furthermore, the lower bound solution estimated the SRF of 0.6588 while the upper bound solution was about 0.666 SRF. On the other hand, the limit equilibrium method solutions ranged from 1.350 to 1.497. For all the cases considered (see Figures 17 and 19), it has been denoted that the exact solutions are bracketed within 17 to 29% of error accuracy. This implies among the limit equilibrium method, none of them were able to provide the exact solutions as compared to the rigorous lower or upper bound solutions.

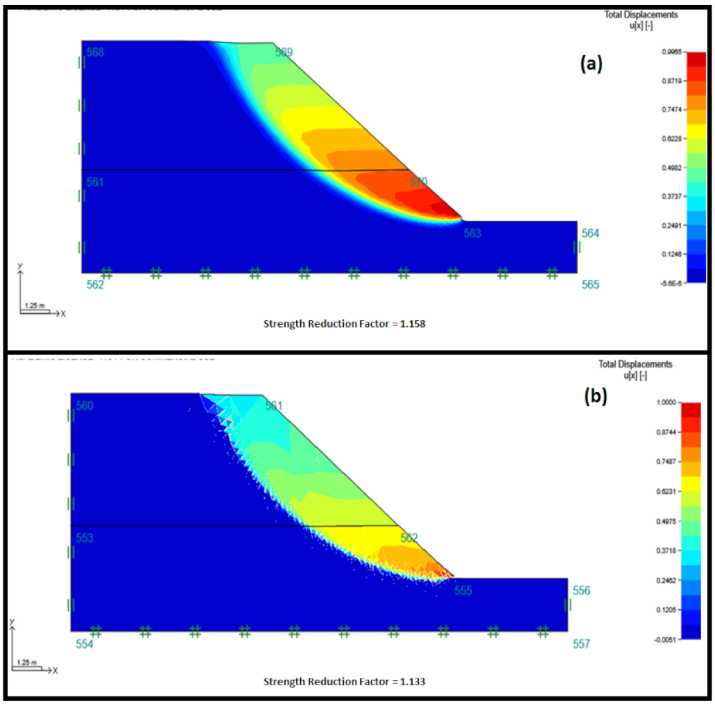

Figure 17. Predicted stability number using limit analysis method of strength reduction factor in firm clay; (**a**) the SRF of the upper bound solutions of limit analysis; (**b**) the SRF of the lower bound solutions of the limit analysis.

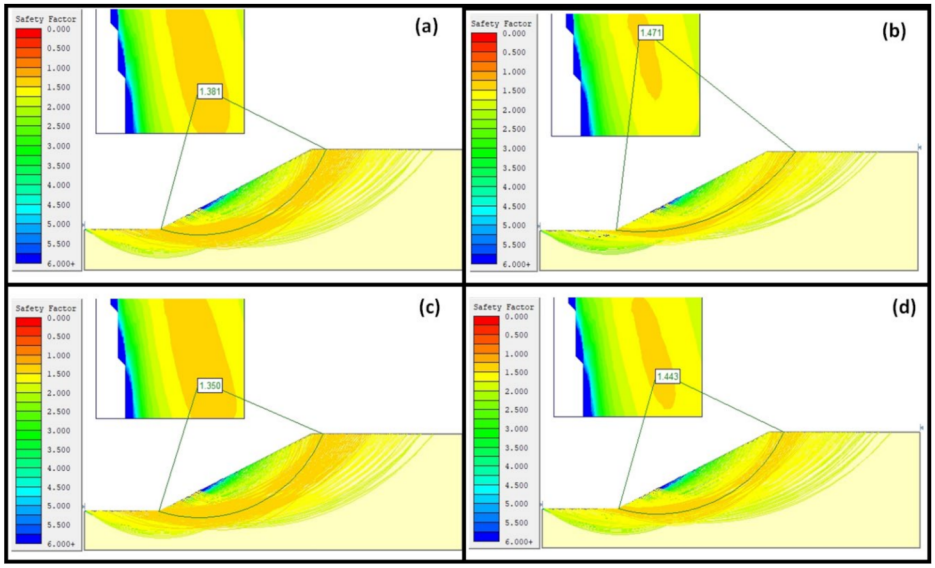

Figure 18. Limit equilibrium stability number of firm clay slope produced using (**a**) Ordinary method; (**b**) Bishop simplified method; (**c**) Janbu Simplified method; (**d**) Janbu Corrected method.

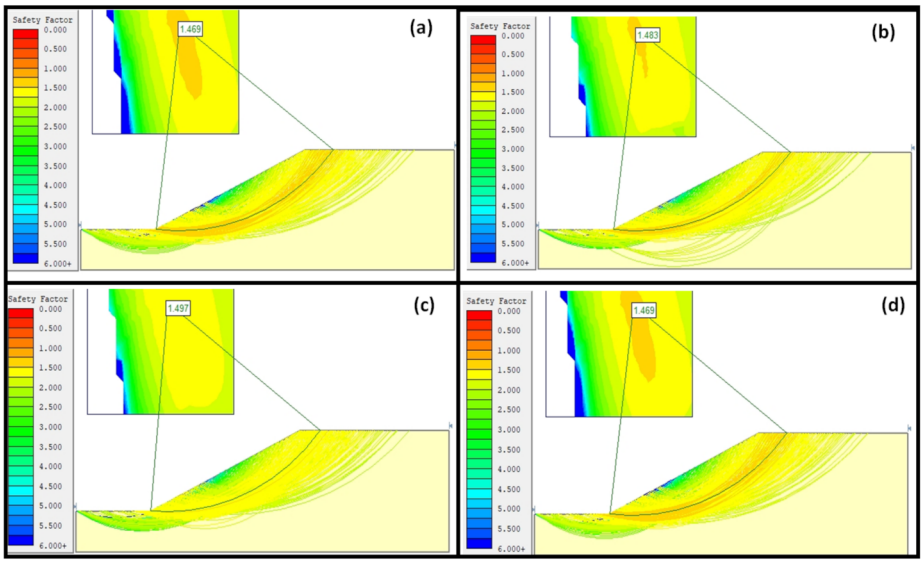

Figure 19. Limit equilibrium stability number of firm clay slope produced using (**a**) Spencer method; (**b**) Corp of Engineering one; (**c**) Corp of Engineering two; (**d**) Morgenstern–Price method.

It was also observed that the result also shows that the Janbu Simplified limit equilibrium method had much closely related solution to those of the upper bound solutions as compared to other LEMs; however, the method produces about 17% error accuracy as compared to the benchmarking rigorous upper bound solutions of limit analysis. This implies that none of the limit equilibrium methods have an accuracy error below the acceptable industry, therefore, LEMs are not recommended in analyzing soil slope with firm clay.

3.1.6. Road Embankment Slope with Stiff Clay

A soil slope with a slope angle of 45° is selected as well as demonstrated in Figures 20–22. In the slope, a stiff clay with a friction angle of 22°, the cohesion of 20 kPa, and unit weight of 21 kN/m^3, and other input parameters as shown in Table 1, were taken into consideration. Both rigorous lower and upper bounds limit analysis and limit equilibrium methods were used to perform the analysis through separate numerical codes and (SLIDEs and Optum G2) were implemented. The results of the Limit Analysis have shown that the slope is expected to be stable. Furthermore, the lower bound solutions estimated the SRF of 1.655 while the upper bound solutions were about 1.689 SRF, while the limit equilibrium method solutions ranged from 1.717 FOS to 1.932 FOS. For all the cases considered (see Figures 20 and 22), it has been denoted that the exact solutions are bracketed within 5 to 14% of error accuracy. This implies among the limit equilibrium method, none of them were able to provide the exact solutions as compared to the rigorous lower or upper bound solutions; however, the LEMs solutions were denoted to be closely related to those of the upper bound solutions.

It was observed that among other cases considered, limit equilibrium methods perform much better in stiff clay, in summary, the error accuracy produced by Janbu Simplified was about 2%, which is almost the same as the exact solutions of the upper bound solutions. This implies that though the LEMs are known to produce less accurate solutions, the method produces different accuracy errors based on the material dealt with. In this study, it may be deduced that almost all LEMs used for the study were within the required acceptable accuracy error of the industry. Furthermore, the Ordinary method was also found to be the second-best method in terms of producing low error accuracy, and results show that Ordinary and Janbu Simplified can be recommended as reasonable methods to use in order to acquire close related solutions to those of upper bound solutions of limit analysis. On the other hand, the Corp Engineering Two method was still found to be the last method to

produce closely related solutions to those of upper bounds, but their solutions were still less than 15%.

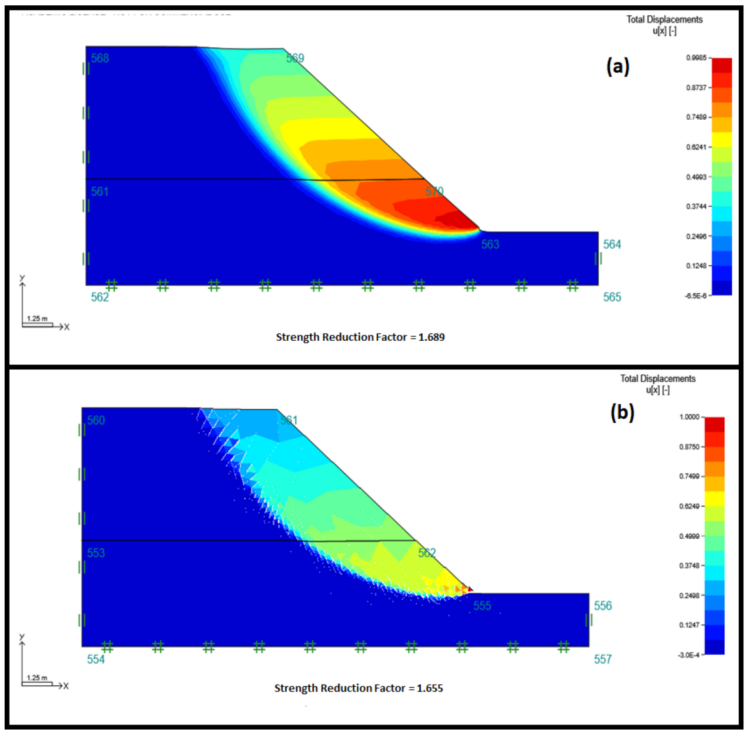

Figure 20. Predicted stability number using limit analysis method of strength reduction factor in stiff clay; (**a**) the SRF of the upper bound solutions of limit analysis; (**b**) the SRF of the lower bound solutions of the limit analysis.

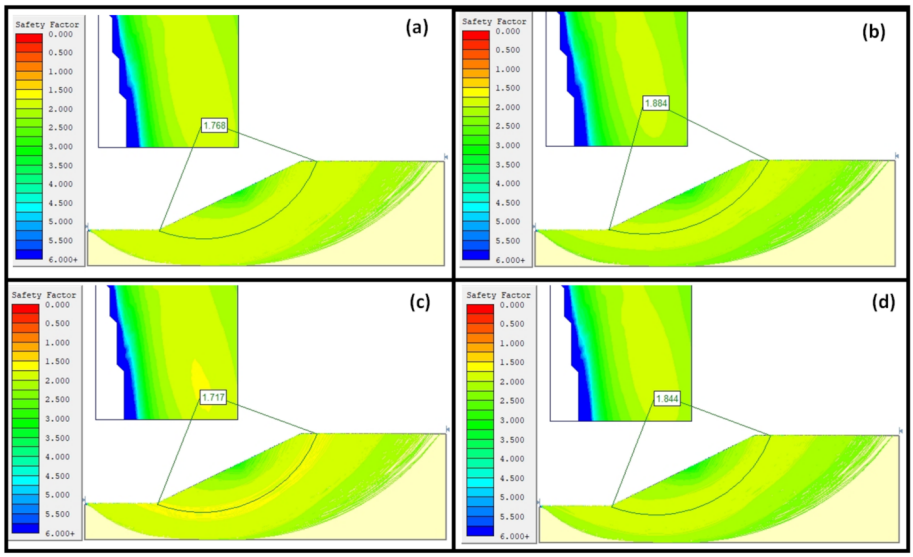

Figure 21. Limit equilibrium stability number of stiff clay slope produced using (**a**) Ordinary method; (**b**) Bishop Simplified method; (**c**) Janbu Simplified method; (**d**) Janbu Corrected method.

These results bring a similar argument that it cannot be assumed that LEMs produce similar results though the solutions produced by two methods are not exact. In simple terms, the results of this paper demonstrate some disagreement with previous studies such as Cheng et al. [36], Renani and Martin [1]; however, the disagreement lies along the lines of assuming that no exact solutions are similar without considering the error accuracy generated by very small differences in solutions. Indeed, the behavior of the material in

terms of how they respond to each method may have been partial captured, some of the studies that strive to capture the response of different soil material behavior on the slope are those of Bjerrum [41], Skemton [42], Hettler and Vardoulakis [43], but still there is no specification of error accuracy of the LEMs. A section below is, therefore, intended to develop an accuracy classification chart of LEMs in predicting stability numbers based on the benchmarking discussed in this paper.

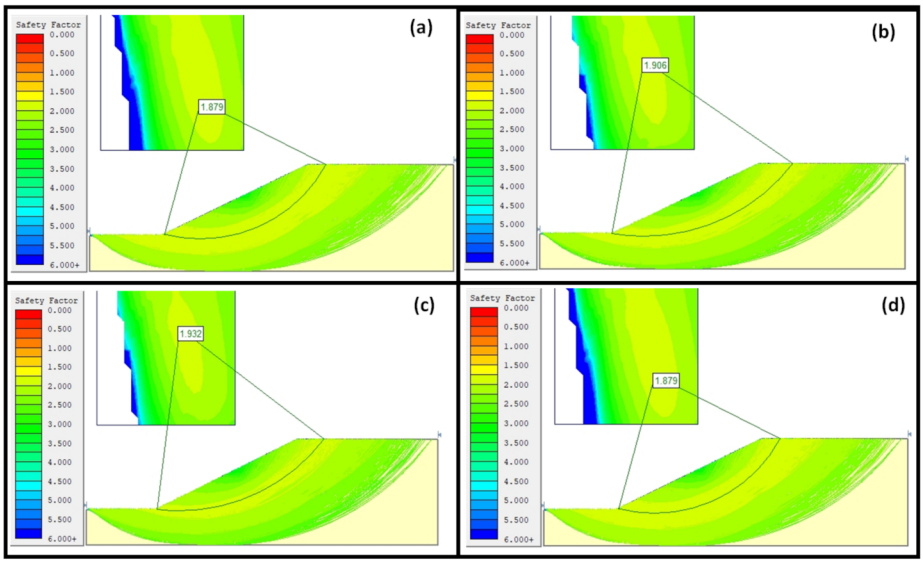

Figure 22. Limit equilibrium stability number of stiff clay slope produced using (**a**) Spencer method; (**b**) Corp of Engineering one; (**c**) Corp of Engineering two; (**d**) Morgenstern–Price Method.

3.2. Accuracy Classification Chart of Limit Equilibrium Method in Predicting the Stability of the Homogenous Slope

For all the cases considered in the sections above (Figure 21), it has been observed that in almost all cases, the Janbu Simplified limit equilibrium solutions are found to be in good agreement with the rigorous upper and lower bounds, but close to the limit analysis rigorous solutions of the upper bounds. In all cases, the limit equilibrium results were generally close to those of the upper bound solutions, while the lower bound solutions appeared to be underestimated compared to all the limit equilibrium solutions presented.

In summary, the Janbu Simplified limit equilibrium method produces the most reasonable accurate solutions for the stability of homogenous soil slope whose strength increases with depth. Nevertheless, the Janbu Simplified limit equilibrium method was very accurate (1–7% of overestimated as compared to the rigorous upper bound solutions) in homogenous slope consisting of stiff clay, dense sand, and medium sand. In fact, the method (Janbu Simplified) presented an accuracy error of about 1% when estimating the stability of the slope in stiff clay, these results imply that the method has the ability to produce similar or closely related results to those of the upper rigorous bound solutions of limit analysis. Furthermore, the reliability of the method (Janbu Simplified) was also demonstrated when estimating about 2% accuracy error of the slope stability in dense sand slope, indeed further demonstration was shown when estimating the stability of slope with medium sand, which results in 3% of accuracy error. It was also demonstrated when estimating the stability of the slope with loose sand that the method produces 7% error accuracy, which is still below the acceptable error accuracy of 10%.

In other cases, the method was still denoted to be the most accurate as compared to other limit equilibrium methods; however, in firm clay, loose sand, and soft clay, the predicted stability number was over the acceptable accuracy error percentage, in fact, it was more than 10%. Though the study was focusing on benchmarking the Limit Equilibrium solutions with the limit analysis solution since limit solutions are usually used to overcome

the accuracy predicting problem associated with the limit equilibrium solution, one may deduce that the Janbu Simplified solution is in good agreement with the upper bound solution; although in soft clay, the method overestimates by about 40%. In the case of firm clay, the method is just after the acceptable accuracy error (10%) but less than 20%. These results can still be used in cases where rigorous upper and lower bound solutions are not available.

Fair enough, the Janbu Simplified method was not the only method found to produce stability numbers with very low error accuracy, the so-called Ordinary limit equilibrium method was observed to produce very fair solutions or closely related to the rigorous upper bound solution but the solution produces were always greater than those of Janbu Simplified limit equilibrium solutions by about 2–3%. Similar to the Janbu Simplified, the Ordinary limit equilibrium method has produced stability numbers with acceptable error accuracy in almost all cases with the exception of the soft and firm clay. This implies that this method is not in good agreement with the upper bound solutions of limit analysis when predicting the stability of the homogenous slopes subjected to either soft clay or firm clay. Nevertheless, the method has shown its constant prediction throughout the case study given and it was always found to be the second-best in terms of stability number in relationship with the benchmark solutions produced by upper bound solutions.

On the other hand, the Corp of Engineer (2) limit equilibrium solutions was found to overestimate the stability of the homogenous slopes in all given case studies. The overestimation was found to be greater than the acceptable error accuracy in all cases. The accuracy error of this method was also found to be 10 to 13% more than those of Janbu Simplified Limit Equilibrium solutions. Similarly, the method was also denoted to overestimate the stability of the slope in soft clay though the overestimation was about 54%; this result provided a trend in all limit equilibrium solutions that soft clay cannot be accurately predicted despite the method to be used in limit equilibrium.

Another interesting observation was to note that both the Spencer limit equilibrium solutions and the Gle/Morgenstern–Price limit equilibrium solutions were similar throughout. The similarity was observed in each case study given though the method provided reasonable accuracy in other cases and unreasonable accuracy in the other case.

As far as the limit equilibrium method is widely used by engineers and scientists in predicting the stability number of the slope, the concern will always be voiced about the accuracy of these types of solutions. Therefore, a classification chart on accuracy predicting of the limit equilibrium method in a homogenous slope is proposed (see Figure 23). The chart is based on the results and discussion pointed out above; however, the chart is more concerned with the error accuracy of the limit equilibrium methods in different soil materials, considering the effect of the increase in material strength with depth. Furthermore, the chart can suggest the best limit equilibrium method in estimating the stability of the slope based on material properties. However, the chart is more applicable to those who prefer to use limit equilibrium solutions due to their simplicity.

The chart demonstrates that in the case of loose sand soil slope, the Janbu Simplified and Ordinary methods are preferred to be used due to an acceptable error accuracy ranging between 6 and 10% as compared to the upper bound solutions of limit analysis. Owing to that the chart also denotes that the other six methods may be used but the accuracy error will be ranging from 11 to 20%, in which such error accuracy is not recommended for industry use. In terms of medium sand soil slope, both the Janbu Simplified and the Ordinary are recommended to be used due to their highly acceptable error accuracy, which ranges from 1 to 5%. Meanwhile, others can still be used with caution because of the present accuracy error above the acceptable stand. A similar situation has been observed in dense sand though Janbu is the most accurate method followed by the Ordinary with an error accuracy ranging from 6 to 10%. However, in the case of soft clay, none of the LEMs are recommended due to large error accuracy numbers ranging from 40 to 54%. In firm clay, there are no LEMs that can be used within the acceptable accuracy error, while in stiff clay, the Janbu and the Ordinary are within the acceptable zone.

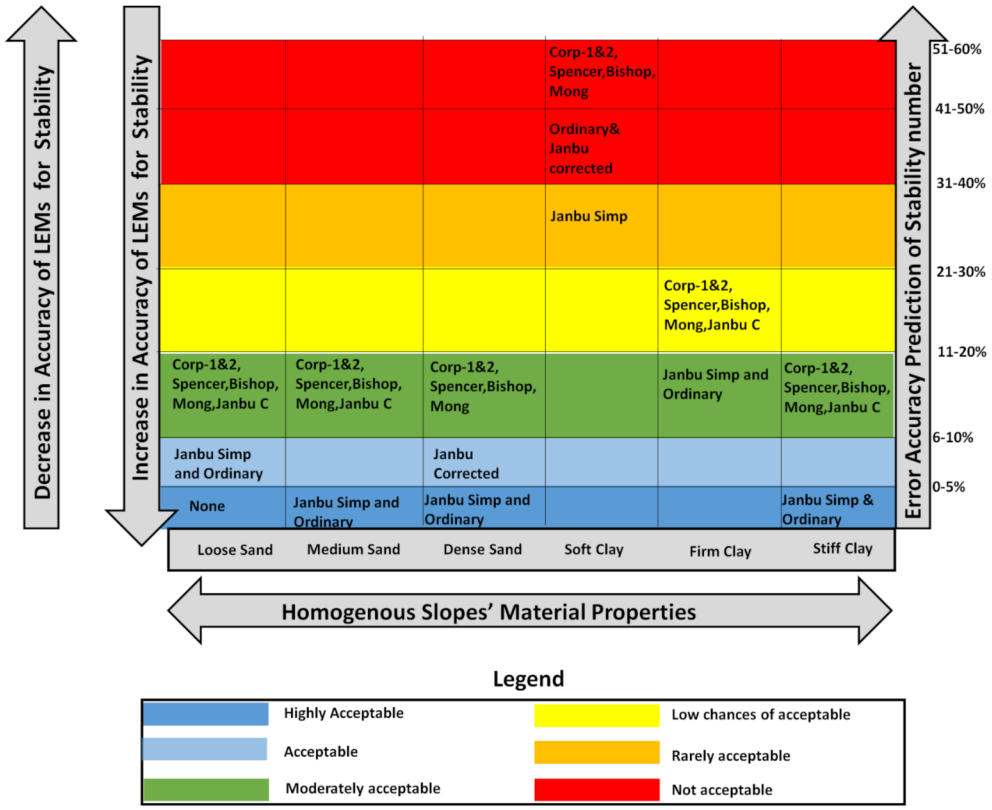

Figure 23. Classification chart of accurate prediction of LEMs on stability number.

4. Concluding Remarks

The accuracy of the limit equilibrium methods in terms of estimating the stability number of soil or rock slope has been questioned or called out, yet alternative methods are used rather than addressing the problem at hand. On the other hand, the limit equilibrium methods are preferred over other methods such as limit analysis due to their simplicity. The concern that is often voiced by many engineers and scientists has motivated the present study. Therefore, the present paper strives to address the following objectives: firstly, to identify the most appropriate LEM, in terms of predicting the stability of the slope with a solution that is close to those of SRM/SRF; secondly, to identify which of the bound solutions (lower and upper) is closely related to LEMs solutions in a homogenous soil and rock slope. Several practical examples are used to establish the reliable LEM by comparing the slope stability analysis solutions and the bounding solutions with limit equilibrium methods (eight methods). Six case studies were utilized to establish the above-mentioned objectives and two computer codes (SLIDES-used for LEMs solutions and Optum G2 used for bounding solutions of limit analysis) using finite element formulations were used.

Based on the six case studies considered in this study, it was found that the exact stability solutions produced by the Janbu Simplified and Ordinary methods of limit equilibrium in most cases are bracketed within 2–10% accuracy error as compared to the rigorous upper bound solutions of the limit analysis. However, these conditions of lower accuracy error were noted in loose sand, medium sand, dense sand, and stiff clay soil slope, with the consideration of the effect of the increase in strength of material with depth. It is, therefore, concluded that in cases of the above-mentioned soil slope material, the Janbu Simplified and Ordinary methods of limit equilibrium are the best to implement.

Furthermore, the detailed comparison of the bounding solutions with limit equilibrium methods has also demonstrated that the prediction of stability numbers by Spencer and Morgenstern–Price method are similar throughout, though the methods were not producing

closely related solutions to those of upper bound solutions. This implies that the use of these two methods simultaneously is not required since they give similar solutions.

It was also observed that the Corp Engineering number two method of limit equilibrium produced the highest accuracy error percentages throughout the case studies provided; however, its error accuracy was also found to differ from those of the Janbu Simplified bracketed within 10–12%. In simple terms, the method has been found to overestimate the stability number in all cases.

Though the focus was to benchmark the limit equilibrium solutions with the upper and lower bound solutions of limit analysis, all the lower bound solutions were found to be a bit smaller than those of limit equilibrium solutions in all cases. It is, therefore, concluded that the lower bound solutions can be used for designing stable excavation; in other words, the lower bound solutions are closely related to the realistic stability number of the slope as stated by previous scholars such as Yu et al. [40].

Indeed, a simple accuracy classification chart was developed based on the results of the study. The chart shows various methods of LEMs and their accuracy error percentage per material or soil slope material. It is believed that the chart is useful to engineers who prefer to apply LEMs in classifying the stability of soil slope. Furthermore, the chart also provides room to explore other sophisticated methods that can improve the prediction of error accuracy of the LEMs instability analysis.

Author Contributions: Conceptualization, F.S.; methodology, F.S.; software, F.S. and D.A. validation, F.S. and D.A. formal analysis, F.S. and D.A. investigation, F.S. resources, F.S. and D.A. data curation, F.S. and D.A.; writing—original draft preparation, F.S. writing—review and editing, D.A.; visualization, F.S. and D.A. supervision, D.A.; project administration, F.S.; funding acquisition, F.S., and D.A. All authors have read and agreed to the published version of the manuscript.

Funding: This research was funded by Durban University of Technology and University of Limpopo, grant number 2022-01 and The APC was funded by University of Limpopo.

Institutional Review Board Statement: Not applicable.

Informed Consent Statement: Not applicable.

Data Availability Statement: Not applicable.

Acknowledgments: The authors would like to appreciate the support provided by the Durban University of Technology, Department of Civil Engineering Geomatics.

Conflicts of Interest: The authors declare no conflict of interest.

Abbreviations

FOS	Factor of Safety
SRF	Strength Reduction Factor
LEM	Limit Equilibrium Methods
FEM	Finite Element Method
FED	Finite Difference Method
OM	Ordinary Method
BSM	Bishop's Simplified Method
JSM	Janbu's Simplified Method
JGM	Janbu's Generalized Method
CEM	Corps of Engineers Method
MPM	Morgenstern–Price Method
SM	Spencer's Method

References

1. Renani, H.R.; Martin, C.D. Factor of safety of strain-softening slopes. *J. Rock Mech. Geotech. Eng.* **2020**, *12*, 473–483. [CrossRef]
2. Hoek, E.; Bray, J.W. *Rock Slope Engineering*; Institution of Mining and Metallurgy: London, UK, 1981.
3. Morgenstern, N.R.; Price, V.E. The analysis of the stability of general slip surfaces. *Geotechnique* **1965**, *15*, 79–93. [CrossRef]

4. Fredlund, D.G.; Krahn, J. Comparison of slope stability methods of analysis. *Can. Geotech. J.* **1977**, *14*, 429–439. [CrossRef]
5. Zhou, X.P.; Cheng, H. Analysis of stability of three-dimensional slopes using the rigorous limit equilibrium method. *Eng. Geol.* **2013**, *160*, 21–33. [CrossRef]
6. Duncan, J.M.; Wright, S.G. The accuracy of equilibrium methods of slope stability analysis. *Eng. Geol.* **1980**, *16*, 5–17. [CrossRef]
7. Nash, D. Chapter 2: A Comparative Review of Limit Equilibrium Methods of Stability Analysis. In *Slope Stability*; Anderson, M.G., Richards, K.S., Eds.; John Wiley & Sons, Inc.: New York, NY, USA, 1987.
8. Jiang, Q.; Zhou, C. A rigorous method for three-dimensional asymmetrical slope stability analysis. *Can. Geotech. J.* **2018**, *55*, 495–513. [CrossRef]
9. Chen, R.H.; Chameau, J.L. Three-dimensional limit equilibrium analysis of slopes. *Geotechnique* **1982**, *33*, 31–40. [CrossRef]
10. Lam, L.; Fredlund, D.G. A general limit equilibrium model for three-dimensional slope stability analysis. *Can. Geotech. J.* **1993**, *30*, 905–919. [CrossRef]
11. Yin, H. A three-dimensional rigorous method for stability analysis of landslides. *Eng. Geol.* **2012**, *145–146*, 30–40.
12. Jiang, Q.; Zhou, C. A rigorous solution for the stability of polyhedral rock blocks. *Comput. Geotech.* **2017**, *90*, 190–201. [CrossRef]
13. Lu, R.; Wei, W.; Shang, K.; Jing, X. Stability Analysis of Jointed Rock Slope by Strength Reduction Technique considering Ubiquitous Joint Model. *Adv. Civ. Eng.* **2020**, *2020*, 1–13. [CrossRef]
14. Bishop, A.W. The use of the Slip Circle in the Stability Analysis of Slopes. *Geotechnique* **1955**, *5*, 7–17. [CrossRef]
15. Janbu, N. *Slope Stability Computations. Soil Mechanics and Foundation Engineering Report*; Technical University of Norway: Trondheim, Norway, 1968.
16. Spencer, E. A method of analysis of the stability of embankments assuming parallel interslice forces. *Geotechnique* **1967**, *17*, 11–26. [CrossRef]
17. U.S. Army Corps of Engineers. *Engineering and Design—Stability of Earth and Rockfill Dams. Engineer Manual EM 1110-2-1902*; Department of the Army, Corps of Engineers: Washington, DC, USA, 1970.
18. Lysmer, J. Limit analysis of plane problems in soil mechanics. *J. Soil Mech. Found. Div.* **1970**, *96*, 1131–1334. [CrossRef]
19. Anderheggen, E.; Knopfel, H. Finite element limit analysis using linear programming. *Int. J. Solids Struct.* **1972**, *8*, 1413–1431. [CrossRef]
20. Bottero, A.; Negre, R.; Pastor, J.; Turgeman, S. Finite element method and limit analysis theory for soil mechanics problems. *Comput. Methods Appl. Mech. Eng.* **1980**, *22*, 131–149. [CrossRef]
21. Sloan, S.W. Lower bound limit analysis using finite elements and linear programming. *Int. J. Numer. Anal. Methods Geomech.* **1988**, *12*, 61–77. [CrossRef]
22. Sloan, S.W. Upper bound limit analysis using finite elements and linear programming. *Int. J. Numer. Anal. Methods Geomech.* **1989**, *13*, 263–282. [CrossRef]
23. Sloan, S.W. *Limit analysis in geotechnical engineering. Modem Developments in Geomechanics*; Haberfield, C.M., Ed.; Monash University: Melbourne, Australia, 1995; pp. 167–199.
24. Li, C.; Sun, C.; Li, C.; Zheng, H. Lower bound limit analysis by quadrilateral elements. *J. Comput. Appl. Math.* **2017**, *315*, 319–326. [CrossRef]
25. Sloan, S.W.; Kleeman, P.W. Upper bound limit analysis using discontinuous velocity fields. *Comput. Methods Appl. Mech. Eng.* **1995**, *127*, 293–314. [CrossRef]
26. Yalçin, Y. Integrated Limit Equilibrium Method for Slope Stability Analysis. Master's Thesis, The Graduate School of Natural and Applied Sciences of Middle East Technical University, Ankara, Turkey, 2018; p. 8.
27. Abramson, L.W.; Lee, T.S.; Sharma, S.; Boyce, G.M. *Slope Stability and Stabilization Methods*; John Wiley & Sons Inc.: Hoboken, NJ, USA, 2002; p. 712.
28. Duncan, J.M. State of the art: Limit equilibrium and finite-element analysis of slopes. *J. Geotech. Eng.* **1996**, *122*, 577–596. [CrossRef]
29. Sengani, F.; Mulenga, F. Application of Limit Equilibrium Analysis and Numerical Modeling in a Case of Slope Instability. *Sustainability* **2020**, *12*, 8870. [CrossRef]
30. Sengani, F.; Mulenga, F. Influence of rainfall intensity on the stability of unsaturated soil slope: Case Study of R523 road in Thulamela Municipality, Limpopo Province, South Africa. *Appl. Sci.* **2020**, *10*, 8824. [CrossRef]
31. Matsui, T.; San, K.-C. Finite element slope stability analysis by shear strength reduction technique. *Soils Found.* **1992**, *32*, 59–70. [CrossRef]
32. Griffiths, D.V.; Lane, P.A. Slope stability analysis by finite elements. *Geotechnique* **1999**, *49*, 387–403. [CrossRef]
33. Dawson, E.M.; Roth, W.H.; Drescher, A. Slope stability analysis by strength reduction. *Geotechnique* **1999**, *49*, 835–840. [CrossRef]
34. Zheng, H.; Liu, D.F.; Li, C.G. Slope stability analysis based on elasto-plastic finite element method. *Int. J. Numer. Methods Eng.* **2005**, *64*, 1871–1888. [CrossRef]
35. Griffiths, D.V.; Marquez, R.M. Three-dimensional slope stability analysis by elasto-plastic finite elements. *Geotechnique* **2007**, *57*, 537–546. [CrossRef]
36. Cheng, Y.M.; Lansivaara, T.; Wei, W.B. Two-dimensional slope stability analysis by limit equilibrium and strength reduction methods. *Comput. Geotech.* **2007**, *34*, 137–150. [CrossRef]
37. Schneider-Muntau, B.; Medicus, W.G.; Fellin, W. Strength reduction method in Barodesy. *Comput. Geotech.* **2018**, *95*, 57–67. [CrossRef]

38. Zienkiewicz, O.C.; Humpheson, C.; Lewis, R.W. Associated and non-associated visco-plasticity and plasticity in soil mechanics. *Geotechnique* **1975**, *25*, 671–689. [CrossRef]
39. Optum, G.; Theory of the Model. Optum Computational Engineering; Denmark. 2019. Available online: https://optumce.com/wp-content/uploads/2016/05/Theory.pdf (accessed on 28 January 2022).
40. Yu, H.S.; Salgado, R.; Sloan, S.W.; Kim, J.M. Limit analysis versus limit equilibrium for slope stability. *J. Geotech. Geoenvironmental Eng.* **1998**, *124*, 1–11. [CrossRef]
41. Bjerrum, L. Theoretical and Experimental Investigations on the Shear Strength of Soils. PhD Thesis, ETH Zurich, Zurich, Switzerland, 1954.
42. Skempton, A.W. Long-term stability of clay slopes. *Geotechnique* **1964**, *14*, 77–102. [CrossRef]
43. Hettler, A.; Vardoulakis, I. Behaviour of dry sand tested in a large triaxial apparatus. *Geotechnique* **1984**, *34*, 183–197. [CrossRef]

sustainability

MDPI

Article

Machine Learning-Based Intelligent Prediction of Elastic Modulus of Rocks at Thar Coalfield

Niaz Muhammad Shahani [1,2], Xigui Zheng [1,2,3,4,*], Xiaowei Guo [1,2] and Xin Wei [1,2]

[1] School of Mines, China University of Mining and Technology, Xuzhou 221116, China; shahani.niaz@cumt.edu.cn (N.M.S.); ckgwx@cumt.edu.cn (X.G.); ts21020059a31@cumt.edu.cn (X.W.)
[2] The State Key Laboratory for Geo Mechanics and Deep Underground Engineering, China University of Mining & Technology, Xuzhou 221116, China
[3] School of Mines and Civil Engineering, Liupanshui Normal University, Liupanshui 553004, China
[4] Guizhou Guineng Investment Co., Ltd., Liupanshui 553600, China
* Correspondence: 3774@cumt.edu.cn; Tel.: +86-139-1204-1768

Abstract: Elastic modulus (E) is a key parameter in predicting the ability of a material to withstand pressure and plays a critical role in the design of rock engineering projects. E has broad applications in the stability of structures in mining, petroleum, geotechnical engineering, etc. E can be determined directly by conducting laboratory tests, which are time consuming, and require high-quality core samples and costly modern instruments. Thus, devising an indirect estimation method of E has promising prospects. In this study, six novel machine learning (ML)-based intelligent regression models, namely, light gradient boosting machine (LightGBM), support vector machine (SVM), Catboost, gradient boosted tree regressor (GBRT), random forest (RF), and extreme gradient boosting (XGBoost), were developed to predict the impacts of four input parameters, namely, wet density (ρ_{wet}) in gm/cm^3, moisture (%), dry density (ρ_d) in gm/cm^3, and Brazilian tensile strength (BTS) in MPa on output E (GPa). The associated strengths of every input and output were systematically measured employing a series of fundamental statistical investigation tools to categorize the most dominant and important input parameters. The actual dataset of E was split as 70% for the training and 30% for the testing for each model. In order to enhance the performance of each developed model, an iterative 5-fold cross-validation method was used. Therefore, based on the results of the study, the XGBoost model outperformed the other developed models with a higher accuracy, coefficient of determination (R^2 = 0.999), mean absolute error (MAE = 0.0015), mean square error (MSE = 0.0008), root mean square error (RMSE = 0.0089), and a20-index = 0.996 of the test data. In addition, GBRT and RF have also shown high accuracy in predicting E with R^2 values of 0.988 and 0.989, respectively, but they can be used conditionally. Based on sensitivity analysis, all parameters were positively correlated, while BTS was the most influential parameter in predicting E. Using an ML-based intelligent approach, this study was able to provide alternative elucidations for predicting E with appropriate accuracy and run time at Thar coalfield, Pakistan.

Keywords: elastic modulus; K-fold cross-validation; mining; rock engineering; sensitivity analysis; XGBoost

Citation: Shahani, N.M.; Zheng, X.; Guo, X.; Wei, X. Machine Learning-Based Intelligent Prediction of Elastic Modulus of Rocks at Thar Coalfield. *Sustainability* **2022**, *14*, 3689. https://doi.org/10.3390/su14063689

Academic Editors: Mahdi Hasanipanah, Danial Jahed Armaghani and Jian Zhou

Received: 11 February 2022
Accepted: 13 March 2022
Published: 21 March 2022

Publisher's Note: MDPI stays neutral with regard to jurisdictional claims in published maps and institutional affiliations.

Copyright: © 2022 by the authors. Licensee MDPI, Basel, Switzerland. This article is an open access article distributed under the terms and conditions of the Creative Commons Attribution (CC BY) license (https://creativecommons.org/licenses/by/4.0/).

1. Introduction

Elastic modulus (E) is a key parameter in predicting the ability of a material to withstand pressure and plays a critical role in the design process of rock-related projects. E has broad applications in the stability of structures in mining, petroleum, geotechnical engineering, etc. Accurate estimation of deformation properties of rocks, such as E, is very important for the design process of any underground rock excavation project. Intelligent indirect techniques for designing and excavating underground structures make use of a limited amount of data for design, saving time and money while ensuring the stability of the structures. This study has economic and even social implications, which

are integral elements of sustainability. Moreover, this paper aims to determine the stability of underground mine excavation, which may otherwise result in a disturbed overlying aquifer and earth surface profile, adversely affecting the environment. E provides insight into the magnitude and characteristics of the rock mass deformation due to changes in the stress field. Deformation and behavior of different types of rocks have been examined by different scholars [1–4]. Usually, there are two common methods, namely, direct (destructive) and indirect (non-destructive), to calculate the strength and deformation of rocks. Based on the principles suggested by ISRM (International Society for Rock Mechanics) and the ASTM (American Society for Testing Materials), direct evaluation of E in the laboratory is a complex, laborious, and costly process. Simultaneously, in the case of fragile, internally broken, thin, and highly foliated rocks, the preparation of a sample is very challenging [5]. Therefore, attention should be given to evaluate E indirectly by the use of rock index tests.

Several authors have developed prediction frameworks to overcome these limitations by using machine learning (ML)-based intelligent approaches such as multiple regression analysis (MRA), artificial neural network (ANN), and other ML methods [6–21]. Advances in ML have so far been driven by the development of new learning algorithms and theories, as well as by the continued explosion of online data and inexpensive computing [22]. Similarly, Waqas et al. used linear and nonlinear regression, regularization and ANFIS (using a neuro-fuzzy inference system) to predict the dynamic E of thermally treated sedimentary rocks [23]. Abdi et al. developed ANN and MRA (linear) models, including porosity (%), dry density (γd) (g/cm^3), P-wave velocity (Vp) (km/s), and water absorption (Ab) (%) as input features to predict the rock E. According to their results, the ANN model showed high accuracy in predicting E compared to the MRA [10]. Ghasemi et al. evaluated the UCS and E of carbonate rocks by developing a model tree-based approach. According to their findings, the applied method revealed highly accurate results [24]. Shahani et al. developed a first-time XGBoost regression model in combination with MLR and ANN for predicting E of intact sedimentary rock and achieved high accuracy in their results [25]. Ceryan applied the minimax probability machine regression (MPMR), relevance vector machine (RVM), and generalized regression neural network (GRNN) models to predict the E of weathered igneous rocks [26]. Umrao et al. determined strength and E of heterogeneous sedimentary rocks using ANFIS based on porosity, Vp, and density. Thus, the proposed ANFIS models showed superb predictability [27]. Davarpanah et al. established robust correlations between static and dynamic deformation properties of different rock types by proposing linear and nonlinear relationships [28]. Aboutaleb et al. conducted non-destructive experiments with SRA (simple regression analysis), MRA, ANN, and SVR (support vector regression) and found that ANN and SVR models were more accurate in predicting dynamic E [29]. Mahmoud et al. employed an ANN model for predicting sandstone E. In that study, 409 datasets were used for training and 183 datasets were used for model testing. The established ANN model exposed highly accurate results (coefficient of determination (R^2) = 0.999) and the lowest mean absolute percentage error ((AAPE) = 0.98) in predicting E [30]. Roy et al. used ANN, ANFIS, and multiple regression (MR) to predict the E of CO_2 saturated coals. Thus, ANN and ANFIS outperformed the MR models [31]. Armaghani et al. predicted E of 45 main range granite samples by applying the ANFIS model in comparison with MRA and ANN. Based on their results, ANFIS proved to be an ideal model against MRA and ANN [32]. Singh et al. proposed an ANFIS framework for predicting E of rocks [33]. Köken predicted the deformation properties of rocks, i.e., tangential E (E_{ti}) and tangential Poisson's ratio (v_{ti}) of coal-bedded sandstones located in the Zonguldak Hard Coal Basin (ZHB), northwestern Turkey, using various statistical and soft computing methods such as different regression and ANN evaluations including the physicomechanical, mineralogical, and textural properties of the rocks. According to this analysis, the remarkable results were that the mineralogical characteristics of the rock have a significant influence on the deformation properties. In addition to comparative analysis, ANN was considered as a more effective tool than regression analysis in predicting E_{ti}

and v_{ti} of coal-bed sandstones [34]. Yesiloglu-Gultekin et al. used the different ML-based regression models such as NLMR, ANN, and ANFIS, and 137 datasets using unit weight, porosity, and sonic velocity to indirectly determine E of basalt. Based on the results and comparisons of various performance matrices such as R^2, RMSE, VAF, and a20-index, ANN was successful in predicting E over NLMR and ANFIS [35]. Rashid et al. used non-destructive tests, i.e., MLR and ANN, to estimate the Q-factor and E for intact sandstone samples collected from the Salt Range region of Pakistan. The ANN model predicted Q-factor (R^2 = 0.86) and E (R^2 = 0.91) more accurately than MLR regression for Q-factor (R^2 = 0.30) and E (R^2 = 0.36) [36]. E was predicted using RF by Matin et al. For comparison, multivariate regression (MVR) and generalized regression neural network (GRNN) were used for the prediction of E. The input V_p-R_n was used for E. According to their results, RF yielded more satisfactory conclusions than MVR and GRNN [37]. Cao et al. used an extreme gradient boosting (XGBoost) integrated with the firefly algorithm (FA) model for predicting E. consequently, the proposed model was appropriate for predicting E [17]. Yang et al. developed the Bayesian model to predict the E of intact granite rocks; thus, the model performed with satisfactory predicted results [38]. Ren et al. developed several ML algorithms, namely, k-nearest neighbors (KNN), naive Bayes, RF, ANN, and SVM, to predict rock compressive strength by ANN and SVM with high accuracy [39]. Ge et al. determined rock joint shear failures using scanning and AI techniques. Thus, the developed SVM and BPNN were considered as sound determination methods [40]. Xu et al. developed several ML algorithms, namely, SVR, nearest neighbor regression (NNR), Bayesian ridge regression (BRR), RF, and gradient tree boosting regression (GTBR), to predict microparameters of rocks by RF with high accuracy [41].

Based on the above literature and the limitations of the conventional predictive methods, a single model has low robustness, cannot achieve ideal solutions for all complex situations, and its performance varies with the input features. Therefore, authors have endeavored to use ML-based intelligent models that integrate multiple models to overcome the drawbacks of individual models and play a key role in determining the accuracy of the corresponding data for tests performed in the laboratory. However, there are few studies in predicting E. In addition, there are no comprehensive studies on the selection and application of such models in E prediction. To address this gap, this study developed six models based on an intelligent prediction approach, namely, light gradient boosting machine (LightGBM), support vector machine (SVM), Catboost, gradient boosted tree regressor (GBRT), random forest (RF), and extreme gradient boosting (XGBoost) to predict E, including wet density (ρ_{wet}) in gm/cm^3, moisture in %, dry density (ρ_d) in gm/cm^3, and Brazilian tensile strength (BTS) in MPa as input features under intricate and unsteady engineering situations. Next, 70% of the actual dataset of 106 is used for training and 30% for testing each model. To enhance the performance of the developed models, a repetitive 5-fold cross-validation approach is used. Intelligent prediction of E of sedimentary rocks from Block-IX of Thar coalfield has been applied for the first time. To the best of the author's knowledge, application of intelligent prediction techniques in this scenario is lacking. Figure 1 depicts a systematic ML-based intelligent approach for predicting E.

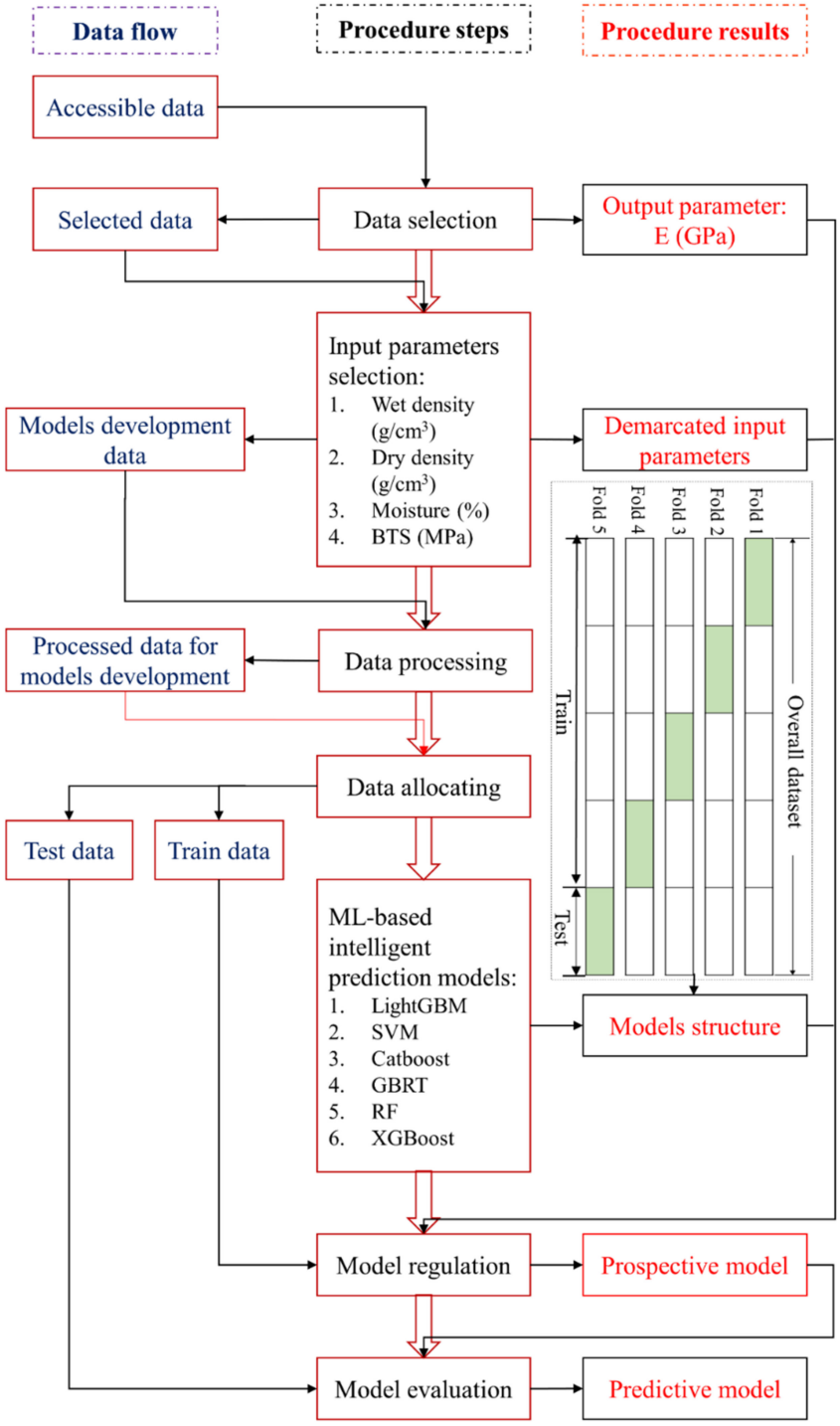

Figure 1. Systematic ML-based intelligent approach for predicting E.

2. A Brief Summary of the Study Area

The Thar coalfield is located in Sindh Province of Pakistan and is the seventh largest coal mine around the world in terms of coal potential [42]. Thar coal is classified as 175.5 billion tons of lignite, which can be used for fuel and power generation. The Thar coalfield is distributed in twelve different blocks as shown in Figure 2. The Thar coalfield is enclosed by dune sand that spreads to a normal distance of 80 m and rests upon an essential stand in the eastern portion of the desert. The general stratigraphic arrangement in the Thar coalfield encompasses the Basement Compound, coal posture Bara Formation, alluvial deposits, and dune sand. For coal mining in the region, both open-pit and

underground mining methods can be preferred. Particularly, Sindh Engro Coal Mining Company (SECMC) has fully developed Block-II of the twelve blocks using an open-pit mining method, whereas Block-1 is under a development stage by Sino-Sindh Resources Ltd. (SSRL) in partnership with China and the Sindh government of Pakistan. Block-IX has been recommended for the underground mining method. The thickness of the coal seam of Block-IX of the Thar coalfield is approximately 12 m, the dip angle is 0° to 7°, and the top-bottom plate is siltstone–claystone to claystone. Shahani et al. proposed the use of the mechanized longwall caving (LTCC) method at Block-IX of the Thar coalfield in Pakistan for the first time [42,43]. In addition, Shahani et al. developed various gradient boosting machine learning algorithms to predict UCS of sedimentary rocks of Block-IX of the Thar coalfield [44]. Similarly, correct determination of the mechanical properties of Block-IX of the Thar coalfield, particularly E, plays an important role in fully understanding the behavior of the roof and ground prior to mining operations.

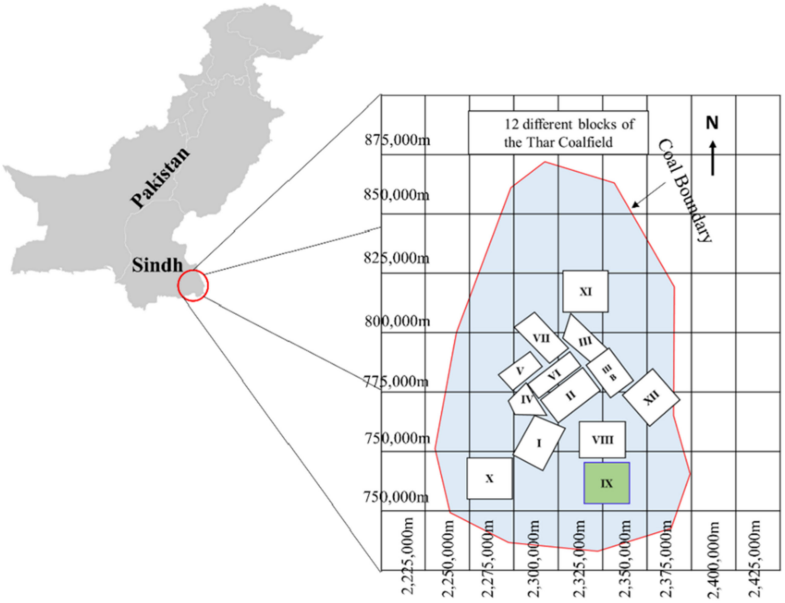

Figure 2. Location map of the study area.

3. Data Curation

In this research, 106 samples of soft sedimentary rocks, i.e., siltstone, claystone, and sandstone were collected from Block-IX of the Thar coalfield, as shown Figure 2, with the location map in the green. Then, the rock samples were prepared and partitioned according to the principles suggested by ISRM [45] and the ASTM [46] to maintain the same core size, and geological and geometric characteristics. In the laboratory of the Mining Engineering Department of Mehran University of Engineering and Technology (MUET), the experimental work was conducted on the studied rock samples to determine the physical and mechanical properties such as wet density (ρ_{wet}) in g/cm^3, moisture (%), dry density (ρ_d) in g/cm^3, Brazilian tensile strength (BTS) in (MPa), and elastic modulus (E) in (GPa). Figure 3 shows (a) collected core samples, (b) universal testing machine (UTM), (c) deformed core sample under compression for E test, and (d) deformed core sample for BTS test. The purpose of the UCS test was conducted on the standard core samples of NX size 54 mm in diameter with an applied load of 0.5 MPa/s using UTM according to the recommended ISRM standard to find the E of the rocks. Similarly, in order to find the tensile strength of the rock samples indirectly, we performed the Brazilian test using UTM. Figure 4 illustrates the statistical distribution of the input features and output in the original dataset used in this study. In Figure 4, the legend of boxplots can be explained as: ▭ 25~75%, ⊥ Range within 1.5 IQR, – Median line, and ○ Outliers.

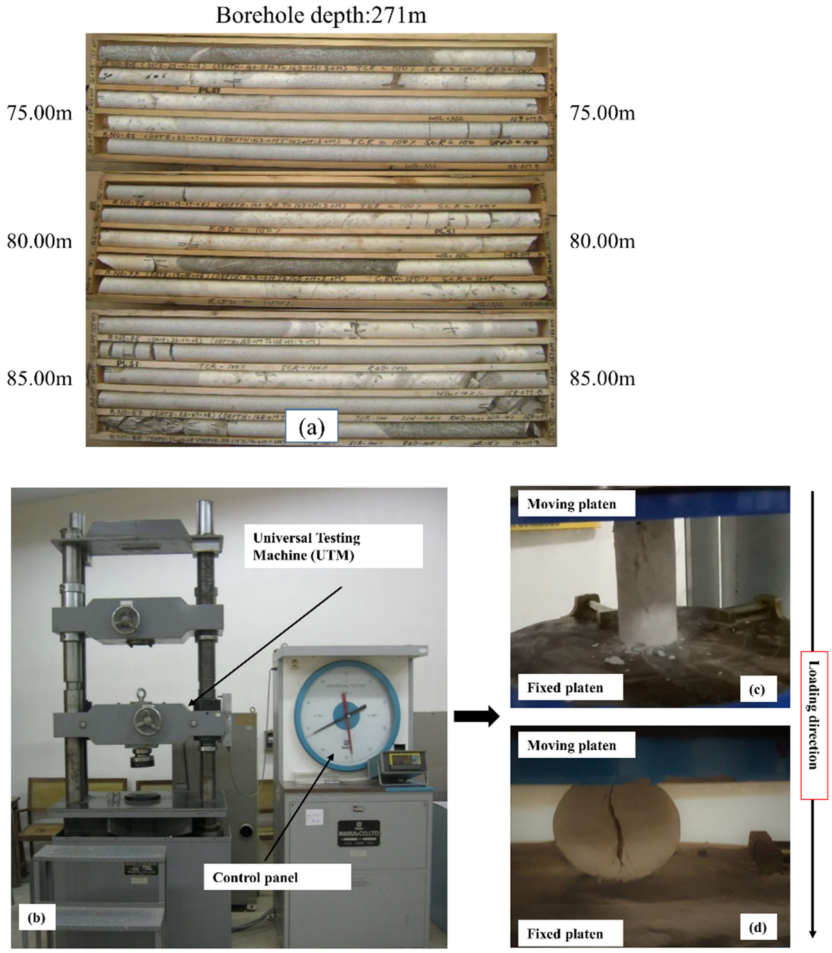

Figure 3. (**a**) Rock core samples for test, (**b**) uniaxial testing machine, (**c**) deformed rock core specimen under compression, and (**d**) deformed core sample for BTS test.

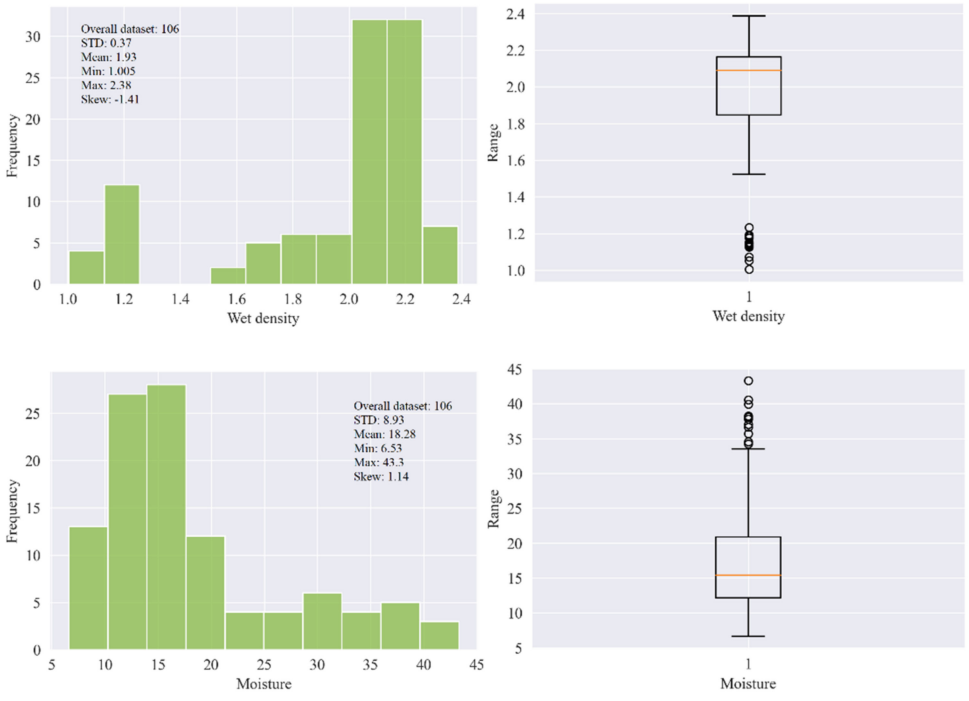

Figure 4. *Cont.*

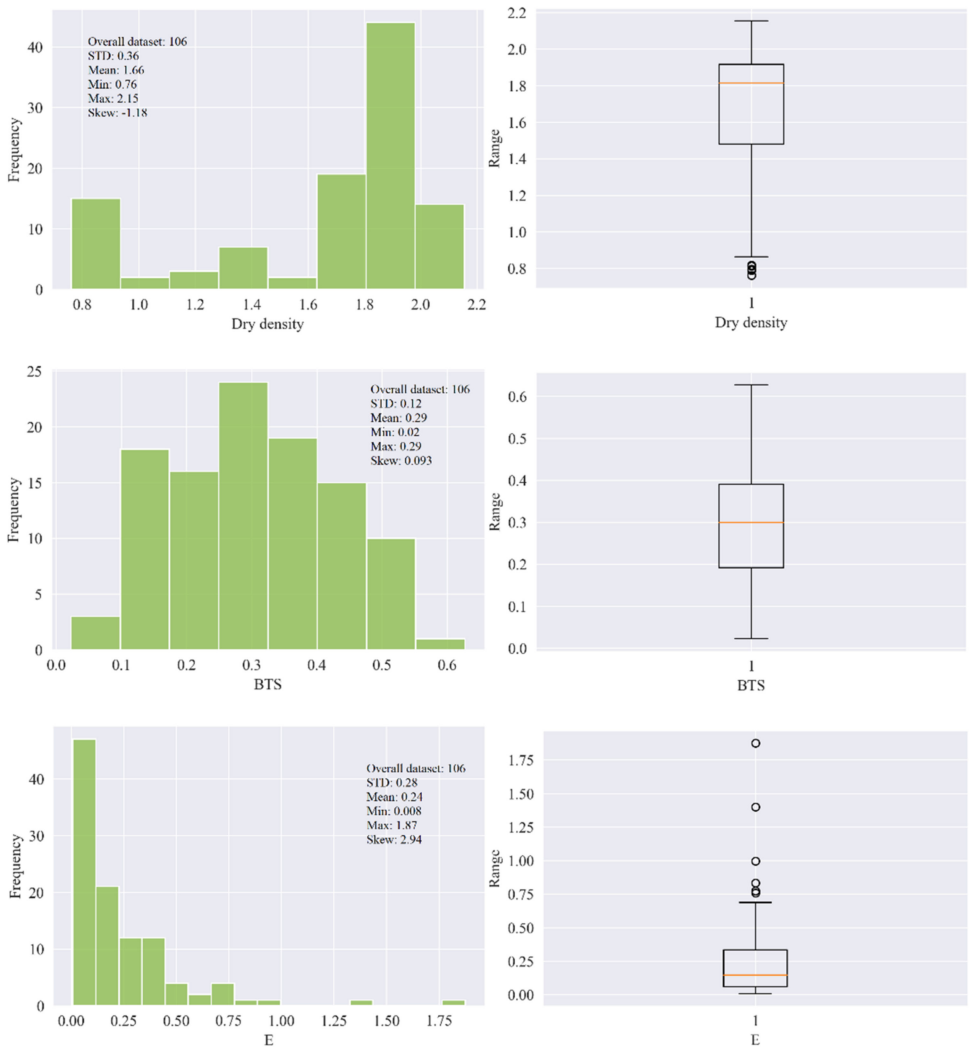

Figure 4. The statistical distribution of the input features and output in the original dataset.

In order to visualize the original dataset of E, the seaborn module in Python was employed in this study, and Figure 5 demonstrates the pairwise correlation matrix and distribution of different input features and output E. It can be seen that BTS is moderately correlated to the E, whereas ρ_{wet} and ρ_d are negatively correlated to the E. Moisture representation does not correlate with E. It is worth mentioning that each feature cannot be well correlated with E independently, so all features are evaluated together to predict E.

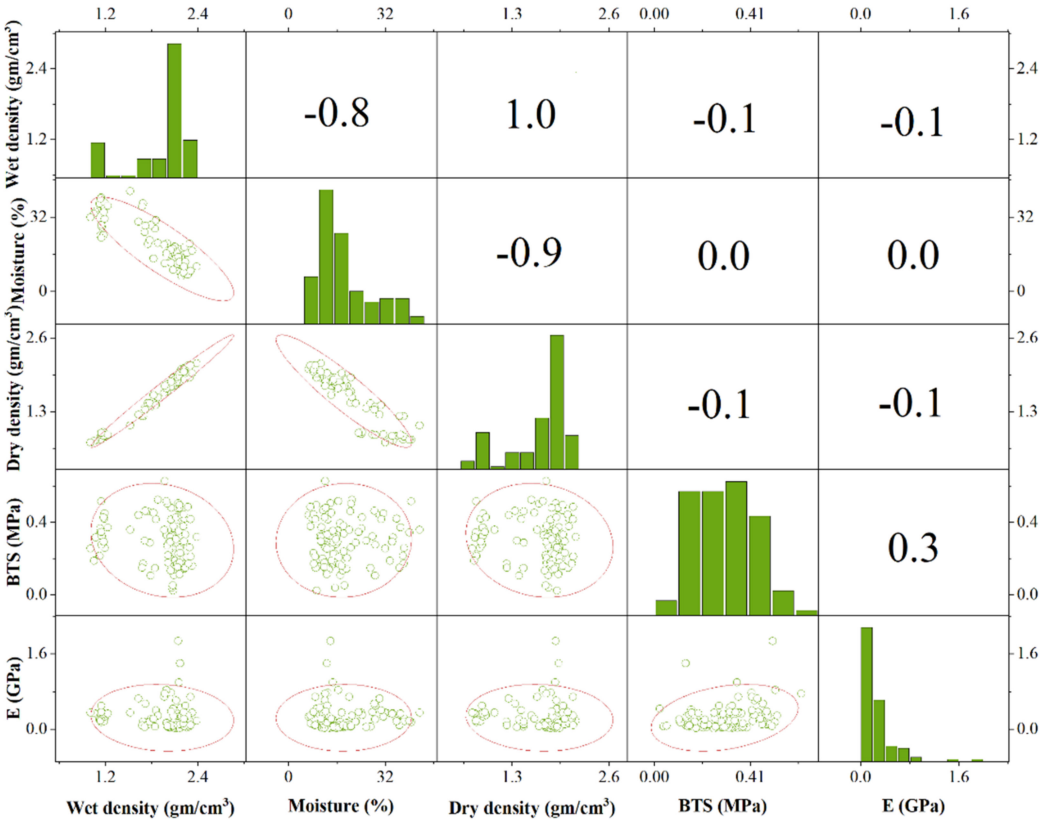

Figure 5. Pairwise correlation matrix and distribution of different input features and output E.

4. Developing ML-Based Intelligent Prediction Models

4.1. Light Gradient Boosting Machine

Light gradient boosting machine abbreviated as LightGBM, an open-source gradient boosting ML model from Microsoft, uses decision trees as the base training algorithm [47]. LightGBM puts continuous buckets of elemental values into separate bins with greater adeptness and a fast speed of training. It uses a histogram-based algorithm [48,49] to improve the learning phase, reduce consumption of memory, and integrate updated communication networks to enhance the regularity of training and is known as a parallel voting decision tree ML algorithm. The data for learning were partitioned into several trees, and local voting techniques were executed in each iteration to select top-k elements and gain globing voting techniques. As shown in Figure 6, LightGBM operates the leaf-wise approach to identify the leaf with the maximum splitter gain. LightGBM is best adopted for regression, classification, sorting, and several ML schemes. It builds a more complex tree than the level-wise distribution method through the leaf-wise distribution method, which can be considered as the main component of the execution algorithm with greater effectiveness. For all that, it can cause overfitting; however, by using the maximum depth element in LightGBM, it can be disabled.

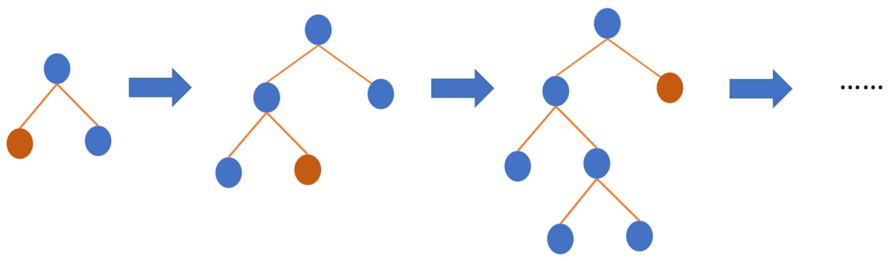

Figure 6. The general structure of LightGBM.

LightGBM [47] is a widespread library for performing gradient boosting, with some modifications intended. The implementation of gradient boosting is mainly focused on algorithms for building a computational system. The library includes tenfold training hyperparameters to validate the implementation of the framework in different scenarios. The implementation of LightGBM also demonstrates advanced capabilities on CPUs and GPUs, which can work like gradient boosting with multifold integrations, comprising column randomization, bootstrap subsampling, and so on. The main features of LightGBM are gradient-based one-sided sampling and unique attribute bundling. Gradient-based one-sided sampling is a sub-sampling technique used to construct the base tree of learning data as an ensemble. In the AdaBoost ML algorithm, the purpose of this technique is to increase the significance of samples with greater likelihood that are connected with samples with higher gradients. When gradient-based one-sided sampling is executed, the base learner's learning data are articulated based on the top portion of samples with greater gradients (a) plus the portion of arbitrary orders (b) recouped from samples with lower gradients. To compensate for changes in measurement propagation, samples from the lesser gradient class are organized together and weighted by $(1 - x)/y$, and at the same time, computing the data gain. In contrast, the unique attribute bundling technique accrues meager elements into an individual element. This can be ended in the absence of impeding any information when these elements do not contain a non-zero number of coincidences. Both mechanisms predict a gain in the complementary learning rate.

4.2. Support Vector Machine

In 1997, Vapnik et al. originally proposed support vector machines (SVMs), which are a type of supervised learning [50]. SVMs can be widely used for regression analysis and for classification using hyperplane classifiers. The ideal hyperplane enhances the boundary between the two classes in which the support vector is positioned [51]. The SVM utilizes a high-extent feature space to develop the forecast function by proposing kernel functions and Vapnik's ε-insensitive loss function [52].

For a dataset P = {(x_1, y_1), (x_2, y_2) … (x_n, y_n)}, where $x_i \in R^n$ is the input and $y_i \in R^n$ is the output, the SVM employs a kernel function to plot the nonlinear input data in a high-extent feature space, and attempts to discover the best hyperplane to disperse them. This permits the narration of the original input to the output by a linear regression function [53–55] characterized as follows in Equation (1).

$$f(x) = M_v \cdot \varphi(x) + l_b \tag{1}$$

where $\varphi(x)$ shows the kernel function, M_v and l_b show the weight vector and bias term, respectively. In order to obtain M_v and l_b, the cost function proposed by Cortes and Vapnik [56] is required to be reduced as follows in Equation (2).

$$cost\ function = \frac{1}{2} M_v^2 + C \sum_{i=1}^{k} \left(\xi_i^- + \xi_i^+\right) \tag{2}$$

$$\text{Subject to :} \begin{cases} y_i - (M_v \cdot \varphi(x_1) + l_b) \ \leq \ \varepsilon_0 + \xi_i^+ \\ (M_v \cdot \varphi(x_1) + l_b) - y_i \ \leq \ \varepsilon_0 + \xi_i^- \\ \xi_i^-, \xi_i^+ \geq 0, \ i = 1, \ 2, \ \ldots, n \end{cases}$$

When converted to the dual space using the Lagrange multiplier method, Equation (2) can be reduced to obtain the following solution in Equation (3).

$$f(x) = \sum_{i=1}^{n} \left(\infty_i - \infty_i'\right) \varphi\left(x_i, x_j\right) + l_b \tag{3}$$

where ∞_i and ∞_i' are Lagrange multipliers with $0 \leq \infty_i$ and $\infty_i' \leq$ C, though $\varphi\ \left(x_i, x_j\right)$ is the kernel function. The choice of the latter is important to the accomplishment of SVR. A

large number of kernel functions have been studied in SVM, such as linear, polynomial, sigmoid, gaussian, radial basis, and exponential radial basis [54]. Figure 7 illustrates the basic structure of the SVM model.

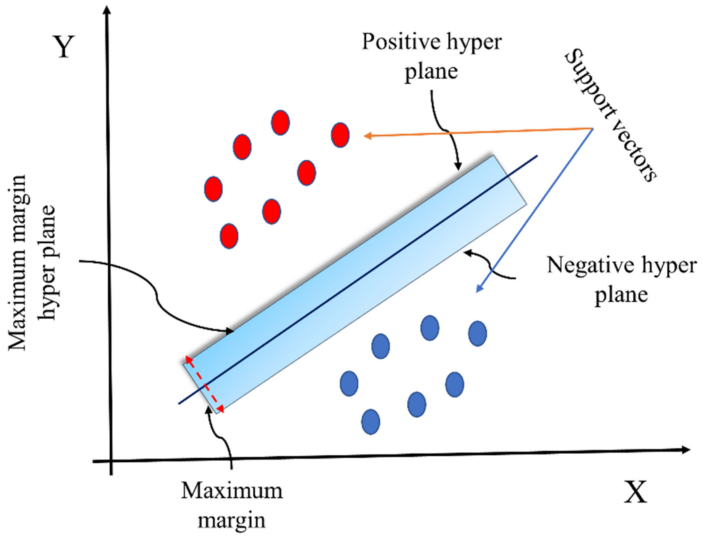

Figure 7. The basic structure of the SVM model.

4.3. Catboost

Catboost is a gradient boosting algorithm recently inherited by Dorogush et al. [57]. Catboost solves the complex problem of regression and classification simultaneously and is publicly available in an open-source multi-platform gradient boosting library [57,58]. In the Catboost algorithm, the decision tree is used as the underlying weak learner and the gradient boosting is successively fitted to the decision tree. To improve the implementation of the Catboost algorithm and to avoid overfitting, an inconsistent arrangement of gradient learning information is used [57].

The purpose of the Catboost algorithm is to reduce the predictive movement that occurs in the learning phase. Propagation movement is the deletion of **F(y) | (yi)** in the case that **yi** is the learning sample, related to **F(y) | (yi)** of the test sample y. In the learning phase, gradient boosting uses the same samples to compute the gradient and the model for lowering that gradient. The Catboost's concept is to initiate *j*... *n*, the framework underlying the repetition of separate P enhancing. The mth recurrence's ith framework is learned from the permutation of the initial ith sample and is suitable for computing the *j* + 1 sample's gradient of the p + 1 recurrence. Subsequently, in order not to be limited by the starting arbitrary permutation, the technique employs an arbitrary permutation of s reciprocals. Each repetition constructs a distinguished framework that achieves all combinations and frameworks. Symmetric trees are used as the basis of the framework. These trees are prolonged by using the same partitioning criterion so that all leaf nodes grow level-wise.

In the Catboost algorithm, the mechanism proposed is to compute the identical up-to-date characters as the ones imitated when the network was built. Thus, for any specified samples' permutation, data samples <i are utilized to computing the character values for each sample i. Then, different combinations are implemented, and the character values obtained for each sample are averaged. Catboost is a large-scale comprehensive library consisting of several elements such as GPU learning, standard boosting, and including fivefold hyperparameter optimization to amend to various practical examination situations. Standard gradient boosting is to be considered as part of the Catboost algorithm also. Figure 8 shows an explanation of the Catboost algorithm.

It is very important to note that the Catboost algorithm's training ability is managed by its framework hyperparameters, i.e., iterations number, rate of learning, maximum depth,

etc. Determining the optimal hyperparameters of a model is a challenging, laborious, and tedious task that depends on the user's skills and expertise.

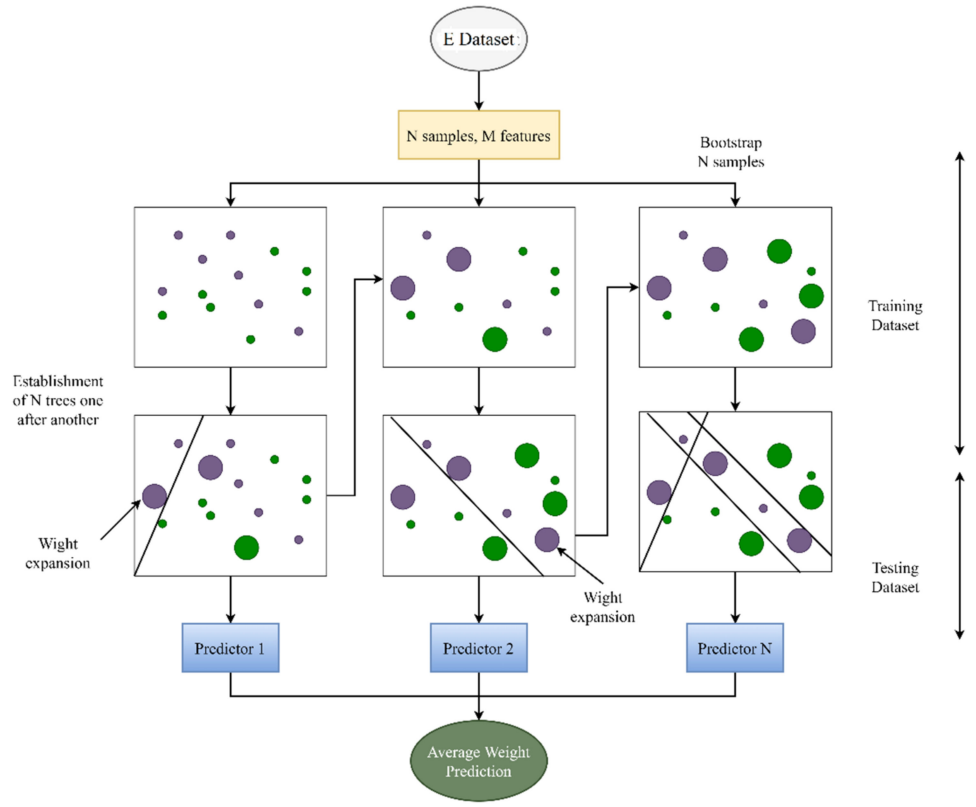

Figure 8. Explanation of the Catboost.

4.4. Gradient Boosted Regressor Tree

The gradient boosted regressor tree (GBRT) regression integrates the weak learner, i.e., the learner algorithms with average performance compared to random algorithms into a robust learner with an iterative method [59]. Contradictory of the bagging method, the boosted algorithm continuously generates the underlying framework. The soundness of the predictive framework is improved by prioritizing this hard-to-evaluate learning information to generate several frameworks in a series. In the boosting algorithm, underlying frameworks that were previously not suitable for estimation are frequently established in the training dataset compared to those frameworks that have been accurately evaluated. Each complementary underlying framework is designed to correct inaccuracies arising from its prior underlying framework. The occurrence of the boosting mechanism comes from reaction of Schapire's feedback to Kearns' investigation [60,61] (Kearns): Is the aggregation of weak learners a substitute for distinguishing strong learners? Weak learners are explained as the algorithms that work well compared to random approximation; strong underlying frameworks are a more realistic classification or regression algorithms that are incoherent with their effective counterparts to the problem. The reaction to such inquiry is extremely noteworthy. Assessments of weak frameworks tend to be less challenging than strong frameworks, and Schapire's establishment of a "yes" response to Kearns' inquiry, as evidenced by the combination of several weak frameworks into an upgraded and independent sound framework. The key dissimilarity between the boosting and bagging mechanism is that in the boosting approach, the training dataset is analytically investigated in order to predict the most appropriate instructions for each subsequent framework. In every phase of training, the modified propagation is dependent on the inaccuracies raised by the previous frameworks. On the contrary, in the bagging mechanism, every trial is constantly specified to produce a training dataset, and for the boosting mechanism, the vagueness of specifying

an independent trial is conflicting. Trials which were erroneously assessed were more likely to set higher weights. Accordingly, each newly evolved framework underscores trials that are inaccurately assessed by subsequent frameworks.

Boosting assembles the auxiliary frameworks that decrease a specific loss function averaged over the learning dataset, i.e., the MAE or the MSE. The loss function computes the total number of predicted values that differ from the investigated values. The advanced staged modeling method is one of the assessed elucidations to the problem. This modeling method continuously attaches the new underlying framework without substituting the coefficients and specifications of the previously connected model. Referring to the regression model, the boosting mechanism is a "function gradient descent" configuration. Functional gradient descent is an optimization mechanism that minimizes the loss function by connecting the underlying framework to each stage to reduce the loss function by a certain amount. Figure 9 demonstrates the schematic diagram of GBTR (after [62,63]).

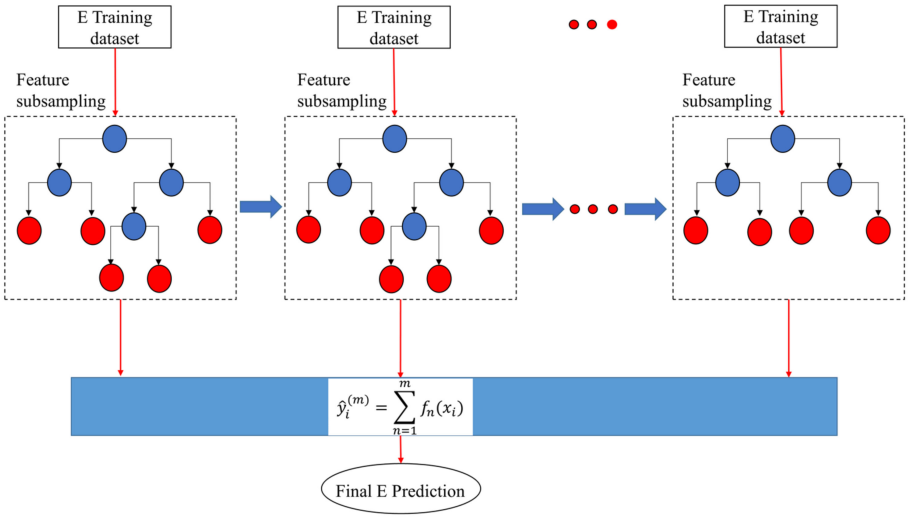

Figure 9. The schematic diagram of the GBRT model.

Friedman recommended improving the gradient boosting regression model by using pre-established regression trees for the underlying framework. The improved framework amplifies the performance of Friedman's model [64]. For predicting E, the improved version of gradient boosted regression was used. Considering that the number of leaves is l, each tree divides the input space into l independent territory T_{1p}, T_{2p} … … … T_{lp} and a perpetual value k_{lp} is predicted for territory T_{lp}. Equation (4) represents the gradient boosting regression tree as follows:

$$f_p(a) = \sum_{l=1}^{L} k_{lp} F\ (a\ \in\ T_{lp}) \tag{4}$$

where $F\left(a\ \in\ T_{lp}\right) = \begin{cases} 1,\ if\ a\ \in\ T_p \\ 0,\ otherwise \end{cases}$.

By using a regression tree to recover $f_p\ (a)$ in the generic gradient boosting mechanism, the framework gradient descent stage size and updating equation are given by Equations (5) and (6), respectively.

$$f_p(a) = f_{p-1}(a) + \rho_p g_p\ (a) \tag{5}$$

$$\rho_p = argmin_\rho\ \sum_{l=1}^{L} M(b_i, f_{p-1}(a_i) + \rho g_p(a_i)) \tag{6}$$

Hence, Equations (5) and (6) fit as Equations (7) and (8).

$$f_p\ (a) = f_{p-1}(a) + \sum_{l=1}^{L} \rho_p k_{lp} F(\ a\ \in\ T_{lp}) \tag{7}$$

$$\rho_p = argmin_\rho \sum_{l=1}^{L} M(b_i, f_{p-1}(a_i) + \sum_{l=1}^{L} \rho_p k_{lp} F(a \in T_{lp})) \quad (8)$$

By applying a discrete ideal ρ_{lp} for each territory T_{lp} k_{lp} should be separated. The simplified framework Equations (9) and (10) are given by

$$f_p(a) = f_{p-1}(a) + \sum_{l=1}^{L} \rho_p F(a \in T_{lp}) \quad (9)$$

$$\rho_p = argmin_\rho \sum_{l=1}^{L} M(b_i, f_{p-1}(a_i) + \sum_{l=1}^{L} \rho_p F(a \in T_{lp})) \quad (10)$$

The overfitting of the framework can be limited by managing the number of iterations of gradient boosting or more competently by evaluating the degree of benefit of each tree by J ∈ (0, 1). Thus, the simplified model is given by Equation (11).

$$f_p(a) = f_{p-1}(a) + L \sum_{l=1}^{L} \rho_p F(a \in T_{lp}) \quad (11)$$

4.5. Random Forest

In 2001, Breiman originally proposed random forest (RF), a type of ensemble machine learning algorithm [65]. RF can be widely used for regression analysis and classification. RF is a state-of-the-art approach to bootstrap aggregating or bagging. RF perceives a one-of-a-kind relationship of model embodiment and predictive accuracy among alternative recognized AI computing [66].

To calculate the performance of the model, RF of 100 trees with a range of default settings was chosen for the study. Figure 10 shows the basic structure of the RF model.

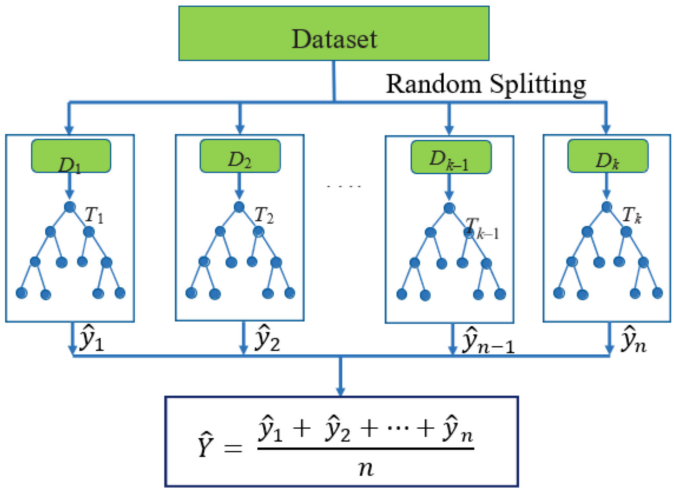

Figure 10. The basic structures of RF model.

4.6. Extreme Gradient Boosting

Extreme gradient boosting (XGBoost) is an important type of ensemble learning algorithm in ML approaches [67]. XGBoost consists of usual regression and classification trees with the addition of analytical boosting methods. The boosting method improves the accurate framework assessment by constructing different trees as alternatives to develop an addressed tree and then connecting them to estimate a systematic predictive algorithm [68]. It instigates the tree by consecutively holding the residuals of the historical trees as the effect of the resultant tree. Because of this, the resultant tree builds a full prediction by generating errors in the past tree. In the loss function reduction stage, the consecutive framework structural relationship can be subdivided into gradient descent types, which advances the forecast by connecting a supplementary tree at every stage to lessen the depletion [69]. Tree development stops at the time of the most unprecedented tree's predetermined number is obtained, or at the time of the training stage error when it cannot be amplified to the predicted number of sequential trees. By attaching an arbitrary survey, the performance

timeliness and estimation accuracy of gradient boosting can be greatly improved. In particular, for all symmetric trees, a random subsample of training information from the whole training dataset is considered, without substitutions. This arbitrarily described subsample replaces the whole sample, which is later used to adapt the tree and is identified as an improved framework. XGBoost is a state-of-the-art rearranged gradient boosting ML algorithm that manages and implements the latest prediction demonstrations [49]. The loss function's subsequent assessment is used in the XGBoost and is fast and rapidly matched to the usual gradient boosting algorithms. XGBoost has widely been used to mine the features of gene coupling. Figure 11 shows the general structure of XGBoost models.

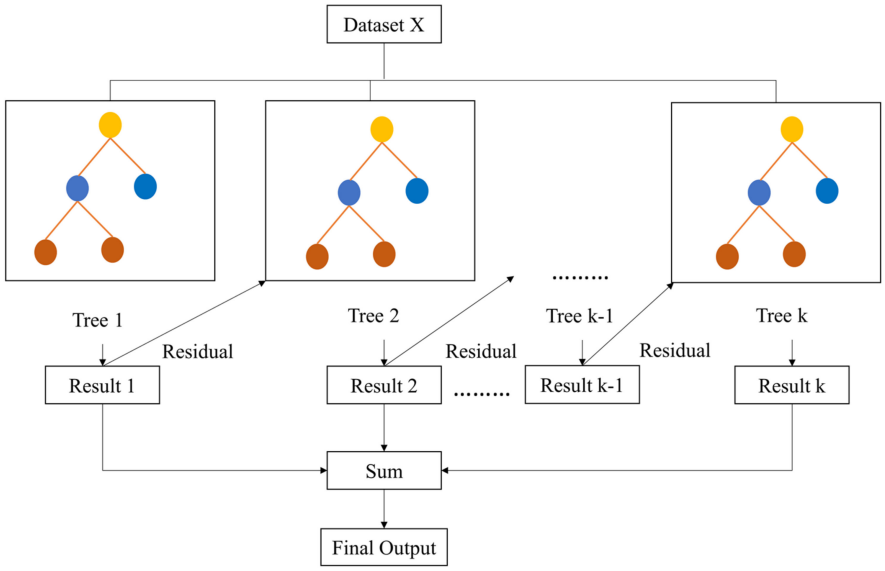

Figure 11. The general structure of XGBoost model.

Consider $\overline{u_i}$ is the predicted outcome of the ith data, where the feature vector is V_i; E denotes the number of estimators and for every estimator f_k (with k from 1 to E) analogous to the analysis of a single tree. u_i^0 describes the initial hypothesis and is the mean of the examined features in the data for learning. Equation (12) executes different extension functions to predict the results.

$$\overline{u_i} = u_i^0 + \eta \sum_{K=1}^{E} f_k(V_i) \tag{12}$$

Additionally, the η parameter is the learning rate, which is contiguous to the implementation of the improved model to enhance the model, perform rhythmically when connecting the latest trees, and combat overfitting.

With respect to Equation (12), the kth character is attached to the model in the kth state, the kth prediction u_i^{-k} is realized by the prediction $u_i^{-(k-1)}$ of the previous state, and the additional kth character augmentation f_k is described as in Equation (13).

$$u_i^{-k} = u_i^{-(k-1)} + \eta\, f_k \tag{13}$$

where f_k denotes the weight of the leaves established by decreasing the kth tree's objective function signified by Equation (14).

$$obj = \gamma N + \sum_{a=1}^{N} [\, U_a \omega_a + \frac{1}{2}\,(V_a + \lambda)\,\omega_a^2 \tag{14}$$

where N represents the kth tree's leaves, ω_a denotes the leaves' weights from 1 to N. γ and λ are the regularity attributes to achieve anatomical consistency to avoid the model's

overfitting. The V_a and U_a parameters are the sets of whole data connected with the prior data's leaf and the gradient of the posterior loss function, respectively.

In the process of building the kth tree, individual leaves are partitioned into a different number of leaves. Equation (15) represents the dissection using the gain parameter. Consider that U_R and V_R describe inter-reliant right leaves and U_L and V_L are inter-reliant left leaves for divergence. At this point, the gain parameter is near to zero, which is traditionally considered as the benchmark for divergence. γ and λ are uniform features that affect the gain features, such as the gain parameter being reduced by a higher regularization parameter and thus avoiding leaf convolution. However, it reduces the adaptability of the framework to the training dataset.

$$gain = \frac{1}{2}\left[\frac{U_L^2}{V_L+\lambda} + \frac{U_R^2}{V_R+\lambda} + \frac{(U_L+U_R)^2}{V_L+V_R+\lambda}\right] \tag{15}$$

XGBoost is a broadly adopted ML algorithm that brings together articulation and logical achievements of gradient boosting ML algorithms. A numerical value causes the problem with the prediction regression model. XGBoost can be accomplished in a timely manner in a probabilistic regression framework. The ensemble is built from a decision tree model. Ensembles are continuously connected trees that can be adjusted to predict imprecise models. These ensemble-type ML methods are called boosting. These frameworks are built by executing any random gradient descent optimization method with a unique loss function. When the model is executed, the gradient loss function is reduced, and so this technique is known as "gradient boosting". Compared with LightGBM, SVM, Catboost, GBRT, and RF, the XGBoost model performed well on the E dataset with the identical parameters n_splits = 5, n_repeats = 3, and random_state = 1 (all remaining parameters were used as default parameters in Python). Although in this study, gbm_param_grid was further implemented in order to further improve the XGBoost model's performance.

4.7. K-Fold Cross-Validation

The K-fold cross-validation is a technique employed to regulate the hyperparameters [70]. The technique accepts a search within a demarcated hyperparameters' range and describes the predictable outcomes leading to the best outcome for calculation criteria such as R^2, MAE, MSE and RMSE. In the scikit-learn Python programing language, K-fold Cross-Validation has been implemented to handle this approach. This method simply calculates the score of CV for all hyperparameters integrated with a specific range. In this study, a 5-fold iterated arbitrary arrangement practice was integrated into the CV command as illustrated in Figure 12. GridSearchCV() permits not only the calculation of the anticipated hyperparameters, but also the evaluation of the metric values to their anticipated results.

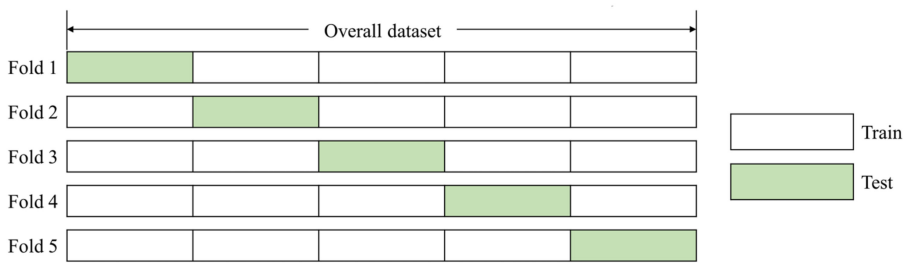

Figure 12. The diagram of 5-fold cross-validation used in this study.

4.8. Models Performance Evaluation

To accurately and approximately evaluate the performance of ML-based intelligent models, different authors have used different estimation criteria, namely, coefficient of determination (R^2) [71], mean absolute error (MAE), mean square error (MSE), root mean

square error (RMSE) [72], and a20-index [71]. Performance criteria are the main metrics used to assist in the highly accurate model evaluation, with the highest R^2, minimum MAE, MSE, RMSE, and appropriate a20-index. The following performance indices are employed to evaluate the performance of each model in E prediction.

$$R^2 = 1 - \frac{\sum_{i=1}^{n}(\mathrm{E}_i - \hat{\mathrm{E}}_i)}{\mathrm{E}_i - \overline{\mathrm{E}}_i} \tag{16}$$

$$\mathrm{MAE} = \frac{1}{N}\sum_{i=1}^{n}\left|\mathrm{E}_i - \hat{\mathrm{E}}_i\right| \tag{17}$$

$$\mathrm{MSE} = \frac{\sum_{i=1}^{n}(\mathrm{E}_i - \hat{\mathrm{E}}_i)^2}{N} \tag{18}$$

$$\mathrm{RMSE} = \sqrt{\frac{\sum_{i=1}^{n}(\mathrm{E}_i - \hat{\mathrm{E}}_i)^2}{N}} \tag{19}$$

$$a20 - index = \frac{m20}{N} \tag{20}$$

where $\overline{\mathrm{E}}_i$ and $\hat{\mathrm{E}}_i$ are the mean values of the measured and predicted values of E, and E_i are measured values of E, respectively. m20 represents the datasets with a value of rate original/estimated values between 0.80 and 1.20 and N denotes the number of datasets.

5. Analysis of Results and Discussion

This study aims to examine the capability of various ML-based intelligent prediction models, namely, LightGBM, SVM, Catboost, GBRT, RF, and XGBoost, for predicting a substantial E using Python programming. In order to propose the most suitable prediction model to predict E, the selection of appropriate input features can be considered as one of the most important tasks. In this study, wet density (ρ_{wet}) in gm/cm^3, moisture (%), dry density (ρ_{d}) in gm/cm^3, and Brazilian tensile strength (BTS) in (MPa) were taken as the input features for all developed models.

Later, the measured and predicted output values were organized and plotted to facilitate the performance analysis and correlation of the developed models. The final output was examined using various analytical indices such as R^2, MAE, MSE, RMSE, and a20-index as performance criteria to analyze and compare the anticipated models and to evaluate the ideal model in terms of data prediction. The106 data points of the overall dataset were allocated as 70% (74 data points) for training and 30% (32 data points) for testing the model.

Figure 13 illustrates the scatter plots of predicted E of the test data by LightGBM, SVM, Catboost, GBRT, RF, and XGBoost models. The R^2 value of each model is determined according to the test prediction. The R^2 value of LightGBM, SVM, Catboost, GBRT, RF, and XGBoost models is 0.281, 0.32, 0.577, 0.988, 0.989, and 0.999, respectively.

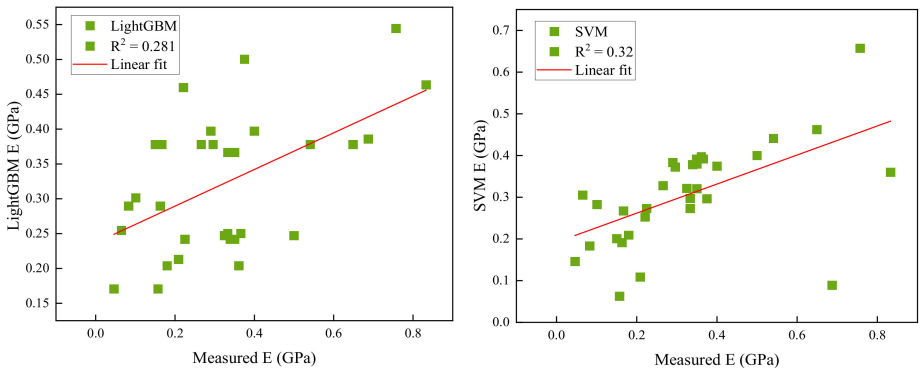

Figure 13. *Cont.*

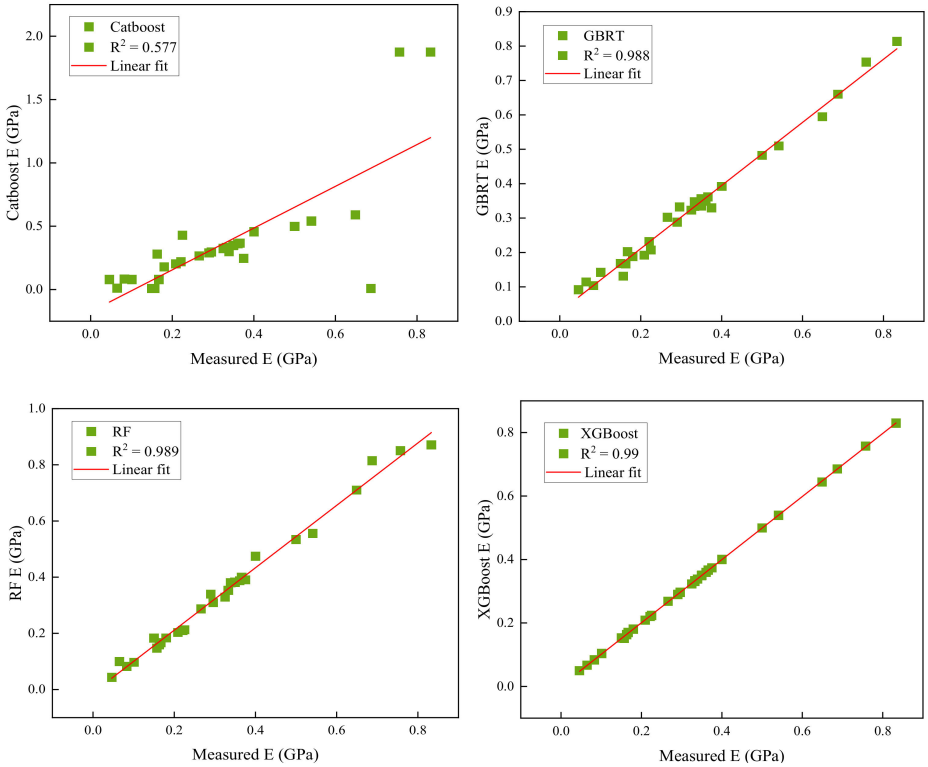

Figure 13. Scatter plots of E prediction by LightGBM, SVM, Catboost, GBRT, RF, and XGBoost models at the test data.

Furthermore, to further understand the performance of the predicted E, it will be interesting to study the prediction rules of six developed ML-based intelligent models due to the wide dispersion of the range of values of E in the established dataset of the test data. The residuals (GPa) and percentage errors (%) of six models were utilized to view the predicting results. The residuals allow for the observation of the contrast between the predicted E and the measured E for each data point, and the percentage error shows the percentage by which the predicted E surpasses the measured E. They are expressed as Equations (21) and (22).

$$r = \mathrm{E}_m - \mathrm{E}_p \tag{21}$$

$$p_{error} = \frac{r}{\mathrm{E}_m} * 100 \tag{22}$$

where r = residual in GPa; E_m and E_p are the measured and predicted E, respectively; and p_{error} is the percentage error in %.

In Figure 14, the residuals indicate a direct relationship with the E, since the corresponding residuals can increase as the E increases. In contrast, in Figure 15, the percentage error shows an inverse relationship with the E, because it decreases as the E increases. Some models show negative residuals and percentage errors for smaller E measures and positive values for larger E measures. It revealed that these ML-based intelligent models seem to tend to have a predicted E higher than the measured E when the measured E was small, and tend to have a predicted E smaller than the measured E when the measured E is higher.

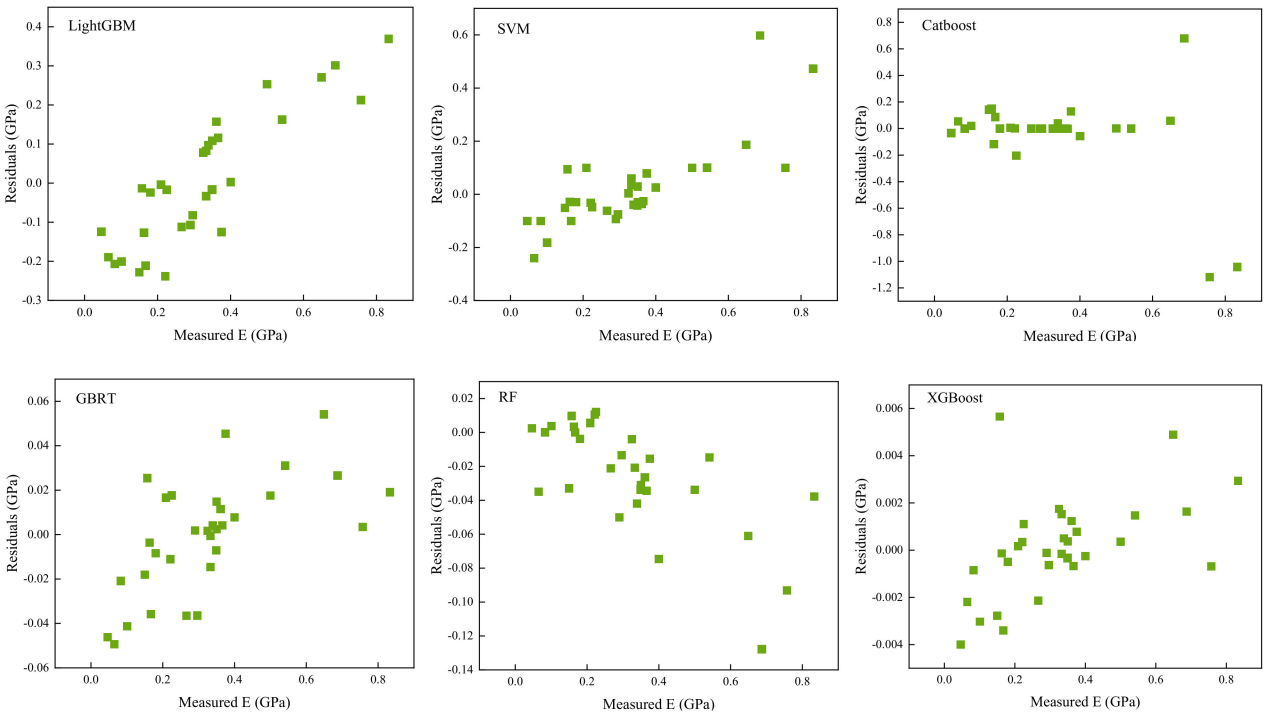

Figure 14. Residual plots of E prediction by LightGBM, SVM, Catboost, GBRT, RF, and XGBoost models of the test data.

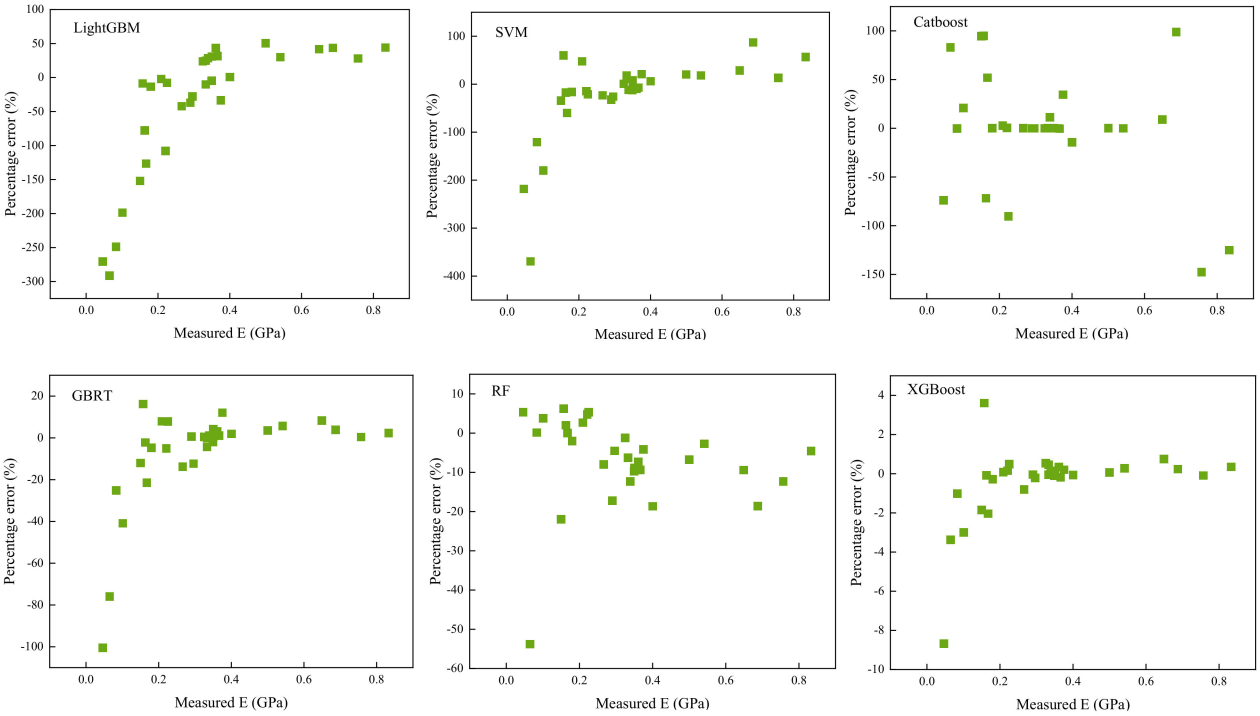

Figure 15. Percentage error plots of E prediction by LightGBM, SVM, Catboost, GBRT, RF, and XGBoost models of the test data.

Table 1 exhibits the performance indices of the developed LightGBM, SVM, Catboost, GBRT, RF, and XGBoost models computed by Equation (16) to Equation (20). In this study, according to the proposed LightGBM, SVM, Catboost, GBRT, RF, and XGBoost models, the XGBoost outperformed when at the test data with R^2 of 0.999, MAE of 0.0015, MSE of 0.0008,

RMSE of 0.0089, and a20-index of 0.996, for E prediction. In addition, GBRT and RF have also shown high accuracy and achieved second place next to XGBoost in predicting E, but they can be used conditionally. Therefore, XGBoost is an applicable ML-based intelligent approach that can be applied to accurately predict E, as shown in Figure 16.

Table 1. Performance indices of the developed ML-based intelligent models in this study.

Model	Training					Testing				
	R^2	MAE	MSE	RMSE	a20-Index	R^2	MAE	MSE	RMSE	a20-Index
LightGBM	0.496	0.1272	0.0470	0.2168	0.836	0.281	0.1340	0.0269	0.1640	1.012
SVM	0.324	0.1461	0.0805	0.2837	1.07	0.32	0.1031	0.0259	0.1609	1.22
Catboost	0.891	0.1091	0.0113	0.1069	1.04	0.577	0.218	0.0948	0.3101	0.86
GBRT	0.995	0.0162	0.0004	0.0200	0.96	0.988	0.0147	0.0003	0.0173	0.962
RF	0.991	0.0102	0.0018	0.0424	0.99	0.989	0.0284	0.0016	0.0400	0.943
XGBoost	0.999	0.0008	0.0004	0.0089	0.914	0.999	0.0015	0.0008	0.0089	0.996

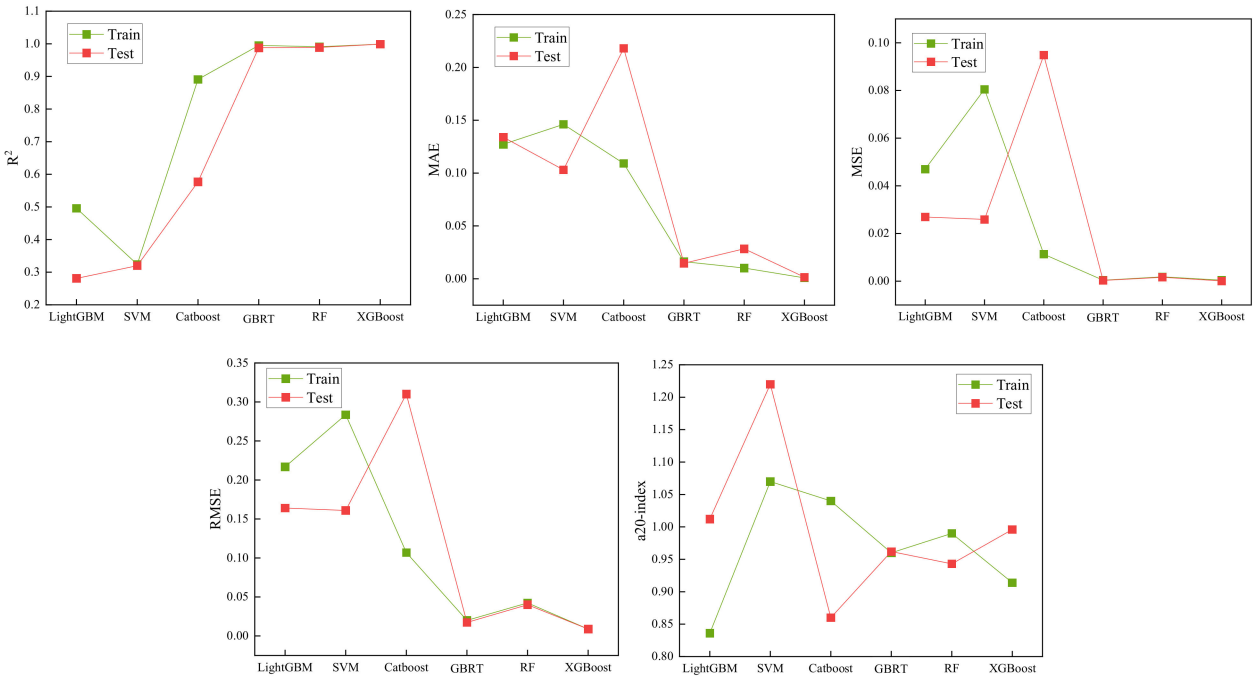

Figure 16. Performance indices of the developed LightGBM, SVM, Catboost, GBRT, RF, and XGBoost models of the test data.

The Taylor diagram explains a brief qualitative depiction of the best fit of the model to standard deviations and correlations. The expression for the Taylor diagram is given in Equation (23) [73].

$$R = \frac{\frac{1}{P}\sum_{p}^{P}(r_n - \overline{r})\left(f_n - \overline{f}\right)}{\sigma_r \sigma_f} \quad (23)$$

where R denotes a correlation, P shows the discrete point number, r_n and f_n show two vectors, σ_r and σ_f show r and f standard deviation, and r_n and f_n illustrate the mean value of vectors r_n and f_n, respectively.

Figure 17 represents the correlation between the predicted E and the measured E for the LightGBM, SVM, Catboost, GBRT, RF, and XGBoost models from Figure 16 in terms of standard deviation (STD), RMSE, and R^2. Based on the consequences, the XGBoost model was highly correlated with measured E than the other models developed in this study in predicting E.

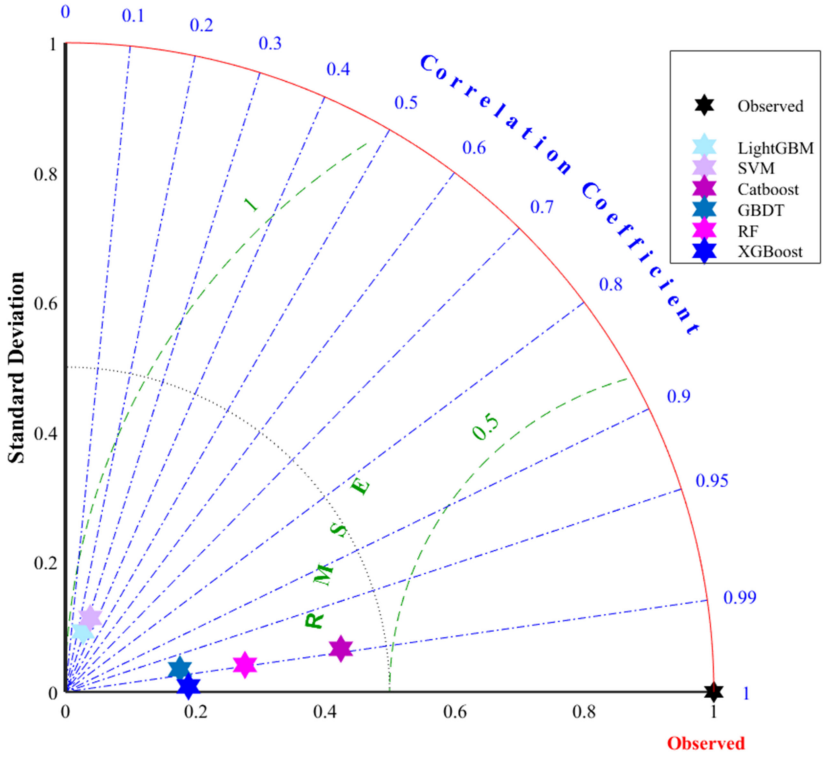

Figure 17. Taylor diagram of the developed LightGBM, SVM, Catboost, GBDT, RF, and XGBoost models of the test data.

Furthermore, the standard deviation (STD) of XGBoost was closest to the measured STD. Thus, compared to the existing published literature [8,74–76], XGBoost exhibits high accuracy and proved to be a highly accurate model for predicting E. The STD of GBTR and RF was also close to the measured STD but indicates the lowest R^2 values. Meanwhile, LightGBM, SVM, and Catboost showed the least correlation and were far from the measured STD.

6. Sensitivity Analysis

It is very important to correctly evaluate the essential parameters that have a large impact on the E of rock, which is undoubtedly a challenge in the design of rock structures. Thus, in this study, the cosine amplitude method [77,78] was adopted to investigate the relative impact of the inputs over the output. The general formulation of the adopted method is shown in Equation (24).

$$XGBoost_{ij} = \frac{\sum_{k=1}^{n}(E_{ik}E_{jk})}{\sqrt{\sum_{k=1}^{n}E_{ik}^2 \sum_{k=1}^{n}E_{jk}^2}} \quad (24)$$

where E_i and E_j are the input and output values, respectively, and n is the number of datasets in the test phase. Finally, the range of $XGBoost_{ij}$ is between 0 and 1, additionally proving the precision between each variable and the target. According to Equation (24), if $XGBoost_{ij}$ of any parameter has a value of 0, it shows that there is no significant relationship between that parameter and the target. On the contrary, when $XGBoost_{ij}$ is equal to 1 or nearly 1, it can be considered a significant relationship that has a large effect on the E of the rock.

Because of the high accuracy of the XGBoost model in predicting E, only a sensitivity analysis was performed on it at the testing level. Figure 18 shows the relationship between each input parameter of the developed model and output. Therefore, it can be seen from the figure that all parameters are positively correlated, while BTS is the most influential

parameter in predicting E. The feature importance of each input parameter is given as ρ_{wet} = 0.0321, moisture = 0.0293, ρ_d = 0.0326, and BTS = 0.0334.

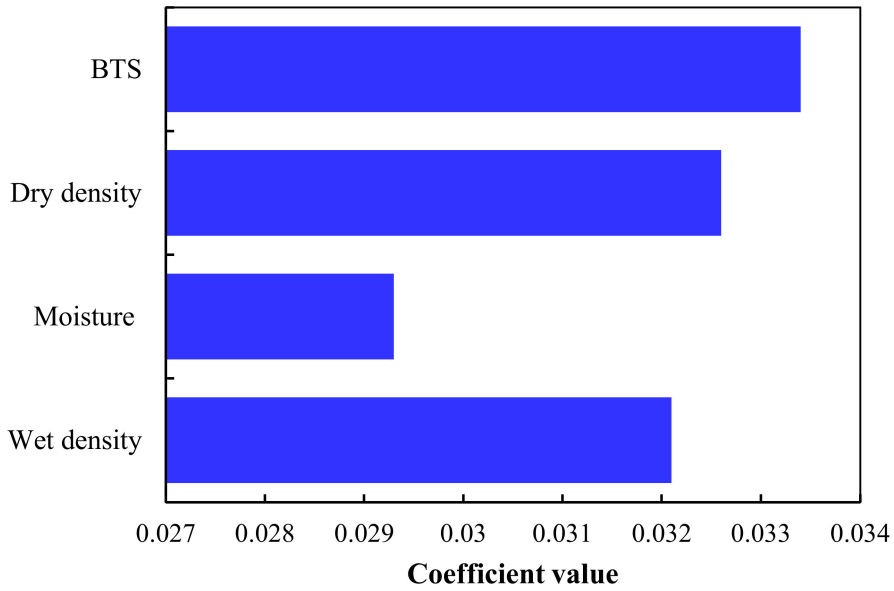

Figure 18. The effect of input variables on the result of the established XGBoost model.

7. Conclusions

Elastic modulus (E) plays a key role in the designing of any rock engineering project. Therefore, an accurate determination of E is a prerequisite. In this study, six novel ML-based intelligent models, namely, LightGBM, SVM, Catboost, GBRT, RF, and XGBoost, were developed to predict E, including four input features, namely, ρ_{wet}, moisture, ρ_d, and BTS. To avoid overfitting of these models, the original dataset was distributed into 70% for the training and 30% for the testing of 106 data points. The study concludes that the XGBoost model performed more accurately than the other developed models, such as LightGBM, SVM, Catboost, GBRT, and RF, in predicting E with R^2, MAE, MSE, RMSE, and a20-index values of 0.999, 0.0015, 0.0008, 0.0089, and 0.996 of the test data, respectively. By employing the ML-based intelligent approach, this study was able to provide alternative elucidations for predicting E with appropriate accuracy and run time.

In future rock engineering projects, it is highly recommended to undertake proper field investigations prior to decision making. The XGBoost ML-based intelligent model performed well to predict the E. The conclusions of GBRT and RF are also applicable for the prediction of E; however, these methods can be used conditionally. Thus, for a large-scale study, this study recommends an adequate dataset to overcome the above limitation. In order to undertake other projects, the model proposed in this study should be considered as a foundation and the result should be reanalyzed, reevaluated, and even re-addressed.

Author Contributions: Conceptualization, N.M.S.; methodology, N.M.S.; software, X.G.; validation, X.W.; formal analysis, X.G.; investigation, N.M.S., X.Z.; resources, X.Z.; data curation, N.M.S., X.G.; writing—original draft preparation, N.M.S.; writing—review and editing, N.M.S., X.Z.; visualization, N.M.S., X.G.; supervision, X.Z.; project administration, X.Z.; funding acquisition, X.Z. All authors have read and agreed to the published version of the manuscript.

Funding: This research was supported by the Science and Technology Innovation Project of Guizhou Province (Qiankehe Platform Talent (2019) 5620 to X.Z.). No additional external funding was received for this study.

Institutional Review Board Statement: Not applicable.

Informed Consent Statement: Not applicable.

Data Availability Statement: The data will be available on request by the corresponding author.

Conflicts of Interest: The authors declare no potential conflict of interest.

References

1. Davarpanah, M.; Somodi, G.; Kovács, L.; Vásárhelyi, B. Complex analysis of uniaxial compressive tests of the Mórágy granitic rock formation (Hungary). *Stud. Geotech. Mech.* **2019**, *41*, 21–32. [CrossRef]
2. Xiong, L.X.; Xu, Z.Y.; Li, T.B.; Zhang, Y. Bonded-particle discrete element modeling of mechanical behaviors of interlayered rock mass under loading and unloading conditions. *Geomech. Geophys. Geo-Energy Geo-Resour.* **2019**, *5*, 1–16. [CrossRef]
3. Rahimi, R.; Nygaard, R. Effect of rock strength variation on the estimated borehole breakout using shear failure criteria. *Geomech. Geophys. Geo-Energy Geo-Resour.* **2008**, *4*, 369–382. [CrossRef]
4. Zhao, Y.S.; Wan, Z.J.; Feng, Z.J.; Xu, Z.H.; Liang, W.G. Evolution of mechanical properties of granite at high temperature and high pressure. *Geomech. Geophys. Geo-Energy Geo-Resour.* **2017**, *3*, 199–210. [CrossRef]
5. Jing, H.; Rad, H.N.; Hasanipanah, M.; Armaghani, D.J.; Qasem, S.N. Design and implementation of a new tuned hybrid intelligent model to predict the uniaxial compressive strength of the rock using SFS-ANFIS. *Eng. Comput.* **2021**, *37*, 2717–2734. [CrossRef]
6. Lindquist, E.S.; Goodman, R.E. Strength and deformation properties of a physical model melange. In Proceedings of the 1st North American Rock Mechanics Symposium, Austin, TX, USA, 1–3 June 1994; Nelson, P.P., Laubach, S.E., Eds.; Balkema: Rotterdam, The Netherlands, 1994.
7. Singh, T.N.; Dubey, R.K. A study of transmission velocity of primary wave (P-Wave) in Coal Measures sandstone. *J. Sci. Ind. Res.* **2000**, *59*, 482–486.
8. Tiryaki, B. Predicting intact rock strength for mechanical excavation using multivariate statistics, artificial neural networks and regression trees. *Eng. Geol.* **2008**, *99*, 51–60. [CrossRef]
9. Ozcelik, Y.; Bayram, F.; Yasitli, N.E. Prediction of engineering properties of rocks from microscopic data. *Arab. J. Geosci.* **2013**, *6*, 3651–3668. [CrossRef]
10. Abdi, Y.; Garavand, A.T.; Sahamieh, R.Z. Prediction of strength parameters of sedimentary rocks using artificial neural networks and regression analysis. *Arab. J. Geosci.* **2018**, *11*, 587. [CrossRef]
11. Teymen, A.; Mengüç, E.C. Comparative evaluation of different statistical tools for the prediction of uniaxial compressive strength of rocks. *Int. J. Min. Sci. Technol.* **2020**, *30*, 785–797. [CrossRef]
12. Li, C.; Zhou, J.; Armaghani, D.J.; Li, X. Stability analysis of underground mine hard rock pillars via combination of finite difference methods, neural networks, and Monte Carlo simulation techniques. *Undergr. Space* **2021**, *6*, 379–395. [CrossRef]
13. Momeni, E.; Yarivand, A.; Dowlatshahi, M.B.; Armaghani, D.J. An efficient optimal neural network based on gravitational search algorithm in predicting the deformation of geogrid-reinforced soil structures. *Transp. Geotech.* **2021**, *26*, 100446. [CrossRef]
14. Parsajoo, M.; Armaghani, D.J.; Mohammed, A.S.; Khari, M.; Jahandari, S. Tensile strength prediction of rock material using non-destructive tests: A comparative intelligent study. *Transp. Geotech.* **2021**, *31*, 100652. [CrossRef]
15. Armaghani, D.J.; Harandizadeh, H.; Momeni, E.; Maizir, H.; Zhou, J. An optimized system of GMDH-ANFIS predictive model by ICA for estimating pile bearing capacity. *Artif. Intell. Rev.* **2021**, *55*, 2313–2350. [CrossRef]
16. Harandizadeh, H.; Armaghani, D.J. Prediction of air-overpressure induced by blasting using an ANFIS-PNN model optimized by GA. *Appl. Soft Comput.* **2021**, *99*, 106904. [CrossRef]
17. Cao, J.; Gao, J.; Rad, H.N.; Mohammed, A.S.; Hasanipanah, M.; Zhou, J. A novel systematic and evolved approach based on XGBoost-firefly algorithm to predict Young's modulus and unconfined compressive strength of rock. *Eng. Comput.* **2021**, 1–17. [CrossRef]
18. Yang, F.; Li, Z.; Wang, Q.; Jiang, B.; Yan, B.; Zhang, P.; Xu, W.; Dong, C.; Liaw, P.K. Cluster-formula-embedded machine learning for design of multicomponent β-Ti alloys with low Young's modulus. *npj Comput. Mater.* **2020**, *6*, 1–11. [CrossRef]
19. Duan, J.; Asteris, P.G.; Nguyen, H.; Bui, X.N.; Moayedi, H. A novel artificial intelligence technique to predict compressive strength of recycled aggregate concrete using ICA-XGBoost model. *Eng. Comput.* **2020**, *37*, 3329–3346. [CrossRef]
20. Pham, B.T.; Nguyen, M.D.; Nguyen-Thoi, T.; Ho, L.S.; Koopialipoor, M.; Quoc, N.K.; Armaghani, D.J.; Van Le, H. A novel approach for classification of soils based on laboratory tests using Adaboost, Tree and ANN modeling. *Transp. Geotech.* **2021**, *27*, 100508. [CrossRef]
21. Asteris, P.G.; Mamou, A.; Hajihassani, M.; Hasanipanah, M.; Koopialipoor, M.; Le, T.T.; Kardani, N.; Armaghani, D.J. Soft computing based closed form equations correlating L and N-type Schmidt hammer rebound numbers of rocks. *Transp. Geotech.* **2021**, *29*, 100588. [CrossRef]
22. Jordan, M.I.; Mitchell, T.M. Machine learning: Trends, perspectives, and prospects. *Science* **2015**, *349*, 255–260. [CrossRef] [PubMed]
23. Waqas, U.; Ahmed, M.F. Prediction Modeling for the Estimation of Dynamic Elastic Young's Modulus of Thermally Treated Sedimentary Rocks Using Linear–Nonlinear Regression Analysis, Regularization, and ANFIS. *Rock Mech. Rock Eng.* **2020**, *53*, 5411–5428. [CrossRef]
24. Ghasemi, E.; Kalhori, H.; Bagherpour, R.; Yagiz, S. Model tree approach for predicting uniaxial compressive strength and Young's modulus of carbonate rocks. *Bull. Eng. Geol. Environ.* **2018**, *77*, 331–343. [CrossRef]

25. Shahani, N.M.; Zheng, X.; Liu, C.; Hassan, F.U.; Li, P. Developing an XGBoost Regression Model for Predicting Young's Modulus of Intact Sedimentary Rocks for the Stability of Surface and Subsurface Structures. *Front. Earth Sci.* **2021**, *9*, 761990. [CrossRef]
26. Ceryan, N. Prediction of Young's modulus of weathered igneous rocks using GRNN, RVM, and MPMR models with a new index. *J. Mt. Sci.* **2021**, *18*, 233–251. [CrossRef]
27. Umrao, R.K.; Sharma, L.K.; Singh, R.; Singh, T.N. Determination of strength and modulus of elasticity of heterogenous sedimentary rocks: An ANFIS predictive technique. *Measurement* **2018**, *126*, 194–201. [CrossRef]
28. Davarpanah, S.M.; Ván, P.; Vásárhelyi, B. Investigation of the relationship between dynamic and static deformation moduli of rocks. *Geomech. Geophys. Geo-Energy Geo-Resour.* **2020**, *6*, 29. [CrossRef]
29. Aboutaleb, S.; Behnia, M.; Bagherpour, R.; Bluekian, B. Using non-destructive tests for estimating uniaxial compressive strength and static Young's modulus of carbonate rocks via some modeling techniques. *Bull. Eng. Geol. Environ.* **2018**, *77*, 1717–1728. [CrossRef]
30. Mahmoud, A.A.; Elkatatny, S.; Ali, A.; Moussa, T. Estimation of static young's modulus for sandstone formation using artificial neural networks. *Energies* **2019**, *12*, 2125. [CrossRef]
31. Roy, D.G.; Singh, T.N. Regression and soft computing models to estimate young's modulus of CO_2 saturated coals. *Measurement* **2018**, *129*, 91–101.
32. Armaghani, D.J.; Mohamad, E.T.; Momeni, E.; Narayanasamy, M.S. An adaptive neuro-fuzzy inference system for predicting unconfined compressive strength and Young's modulus: A study on Main Range granite. *Bull. Eng. Geol. Environ.* **2015**, *74*, 1301–1319. [CrossRef]
33. Singh, R.; Kainthola, A.; Singh, T.N. Estimation of elastic constant of rocks using an ANFIS approach. *Appl. Soft Comput.* **2012**, *12*, 40–45. [CrossRef]
34. Köken, E. Assessment of Deformation Properties of Coal Measure Sandstones through Regression Analyses and Artificial Neural Networks. *Arch. Min. Sci.* **2021**, *66*, 523–542.
35. Yesiloglu-Gultekin, N.; Gokceoglu, C. A Comparison Among Some Non-linear Prediction Tools on Indirect Determination of Uniaxial Compressive Strength and Modulus of Elasticity of Basalt. *J. Nondestruct. Eval.* **2022**, *41*, 10. [CrossRef]
36. Awais Rashid, H.M.; Ghazzali, M.; Waqas, U.; Malik, A.A.; Abubakar, M.Z. Artificial Intelligence-Based Modeling for the Estimation of Q-Factor and Elastic Young's Modulus of Sandstones Deteriorated by a Wetting-Drying Cyclic Process. *Arch. Min. Sci.* **2021**, *66*, 635–658.
37. Matin, S.S.; Farahzadi, L.; Makaremi, S.; Chelgani, S.C.; Sattari, G. Variable selection and prediction of uniaxial compressive strength and modulus of elasticity by random forest. *Appl. Soft Comput.* **2018**, *70*, 980–987. [CrossRef]
38. Yang, L.; Feng, X.; Sun, Y. Predicting the Young's Modulus of granites using the Bayesian model selection approach. *Bull. Eng. Geol. Environ.* **2019**, *78*, 3413–3423. [CrossRef]
39. Ren, Q.; Wang, G.; Li, M.; Han, S. Prediction of rock compressive strength using machine learning algorithms based on spectrum analysis of geological hammer. *Geotech. Geol. Eng.* **2019**, *37*, 475–489. [CrossRef]
40. Ge, Y.; Xie, Z.; Tang, H.; Du, B.; Cao, B. Determination of the shear failure areas of rock joints using a laser scanning technique and artificial intelligence algorithms. *Eng. Geol.* **2021**, *293*, 106320. [CrossRef]
41. Xu, C.; Liu, X.; Wang, E.; Wang, S. Calibration of the microparameters of rock specimens by using various machine learning algorithms. *Int. J. Geomech.* **2021**, *21*, 04021060. [CrossRef]
42. Shahani, N.M.; Wan, Z.; Guichen, L.; Siddiqui, F.I.; Pathan, A.G.; Yang, P.; Liu, S. Numerical analysis of top coal recovery ratio by using discrete element method. *Pak. J. Eng. Appl. Sci.* **2019**, *24*, 26–35.
43. Shahani, N.M.; Wan, Z.; Zheng, X.; Guichen, L.; Liu, C.; Siddiqui, F.I.; Bin, G. Numerical modeling of longwall top coal caving method at thar coalfield. *J. Met. Mater. Miner.* **2020**, *30*, 57–72.
44. Shahani, N.M.; Kamran, M.; Zheng, X.; Liu, C.; Guo, X. Application of Gradient Boosting Machine Learning Algorithms to Predict Uniaxial Compressive Strength of Soft Sedimentary Rocks at Thar Coalfield. *Adv. Civ. Eng.* **2021**, *2021*, 2565488. [CrossRef]
45. Brown, E.T. *Rock Characterization Testing & Monitoring—ISRM Suggested Methods, ISRM—International Society for Rock Mechanics*; Pergamon Press: London, UK, 2007; Volume 211.
46. *D4543-85*; Standard Practices for Preparing Rock Core as Cylindrical Test Specimens and Verifying Conformance to Dimensional and Shape Tolerances. ASTM—American Society for Tenting and Materials: West Conshohocken, PA, USA, 2013.
47. Ke, G.; Meng, Q.; Finley, T.; Wang, T.; Chen, W.; Ma, W.; Ye, Q.; Liu, T.Y. Lightgbm: A highly efficient gradient boosting decision tree. *Adv. Neural Inf. Process. Syst.* **2017**, *30*, 3146–3154.
48. Zeng, H.; Yang, C.; Zhang, H.; Wu, Z.H.; Zhang, M.; Dai, G.J.; Babiloni, F.; Kong, W.Z. A lightGBM-based EEG analysis method for driver mental states classification. *Comput. Intell. Neurosci.* **2019**, *2019*, 3761203. [CrossRef]
49. Liang, W.; Luo, S.; Zhao, G.; Wu, H. Predicting hard rock pillar stability using GBDT, XGBoost, and LightGBM algorithms. *Mathematics* **2020**, *8*, 765. [CrossRef]
50. Vapnik, V.; Golowich, S.E.; Smola, A. Support vector method for function approximation, regression estimation, and signal processing. *Adv. Neural Inf. Process. Syst.* **1997**, *9*, 281–287.
51. Sun, J.; Zhang, J.; Gu, Y.; Huang, Y.; Sun, Y.; Ma, G. Prediction of permeability and unconfined compressive strength of pervious concrete using evolved support vector regression. *Constr. Build. Mater.* **2019**, *207*, 440–449. [CrossRef]

52. Negara, A.; Ali, S.; AlDhamen, A.; Kesserwan, H.; Jin, G. Unconfined compressive strength prediction from petrophysical properties and elemental spectroscopy using support-vector regression. In Proceedings of the SPE Kingdom of Saudi Arabia Annual Technical Symposium and Exhibition, Dammam, Saudi Arabia, 24–27 April 2017.
53. Xu, C.; Amar, M.N.; Ghriga, M.A.; Ouaer, H.; Zhang, X.; Hasanipanah, M. Evolving support vector regression using Grey Wolf optimization; forecasting the geomechanical properties of rock. *Eng. Comput.* **2020**, 1–15. [CrossRef]
54. Barzegar, R.; Sattarpour, M.; Nikudel, M.R.; Moghaddam, A.A. Comparative evaluation of artificial intelligence models for prediction of uniaxial compressive strength of travertine rocks, case study: Azarshahr area, NW Iran. *Model. Earth Syst. Environ.* **2016**, *2*, 76. [CrossRef]
55. Dong, L.; Li, X.; Xu, M.; Li, Q. Comparisons of random forest and support vector machine for predicting blasting vibration characteristic parameters. *Procedia Eng.* **2011**, *26*, 1772–1781.
56. Cortes, C.; Vapnik, V. Support-vector networks. *Mach. Learn.* **1995**, *20*, 273–297. [CrossRef]
57. Dorogush, A.V.; Ershov, V.; Gulin, A. CatBoost: Gradient boosting with categorical features support. *arXiv* **2018**, arXiv:1810.11363.
58. Prokhorenkova, L.; Gusev, G.; Vorobev, A.; Dorogush, A.V.; Gulin, A. CatBoost: Unbiased boosting with categorical features. *Adv. Neural Inf. Process. Syst.* **2018**, *31*, 6638–6648.
59. Freund, Y.; Schapire, R.; Abe, N. A short introduction to boosting. *J. Jpn. Soc. Artif. Intell.* **1999**, *14*, 771–780.
60. Schapire, R.E. The strength of weak learnability. *Mach. Learn.* **1990**, *5*, 197–227. [CrossRef]
61. Kearns, M. Thoughts on Hypothesis Boosting. Mach. Learn. Class Proj.. 1988, pp. 1–9. Available online: https://www.cis.upenn.edu/~{}mkearns/papers/boostnote.pdf (accessed on 10 February 2022).
62. Friedman, J.H. Greedy function approximation: A gradient boosting machine. *Ann. Stat.* **2001**, *29*, 1189–1232. [CrossRef]
63. Friedman, J.; Hastie, T.; Robert, T. The elements of statistical learning. In *Statistics*; Springer: New York, NY, USA, 2001; Volume 1.
64. Friedman, J.H. Stochastic gradient boosting. *Comput. Stat. Data Anal.* **2002**, *38*, 367–378. [CrossRef]
65. Breiman, L. Random forests. *Mach. Learn.* **2001**, *45*, 5–32. [CrossRef]
66. Yang, P.; Hwa, Y.; Zhou, B.; Zomaya, A.Y. A review of ensemble methods in bioinformatics. *Curr. Bioinform.* **2010**, *5*, 296–308. [CrossRef]
67. Meng, Q.; Ke, G.; Wang, T.; Chen, W.; Ye, Q.; Ma, Z.M.; Liu, T.Y. A communication-efficient parallel algorithm for decision tree. *Adv. Neural Inf. Process. Syst.* **2016**, *29*, 1271–1279.
68. Ranka, S.; Singh, V. Clouds: A decision tree classifier for large datasets. In Proceedings of the 4th Knowledge Discovery and Data Mining Conference, New York, NY, USA, 27–31 August 1998; pp. 2–8.
69. Jin, R.; Agrawal, G. Communication and memory efficient parallel decision tree construction. In Proceedings of the 2003 SIAM International Conference on Data Mining, San Francisco, CA, USA, 1–3 May 2003; pp. 119–129.
70. Bergstra, J.; Bengio, Y. Random search for hyper-parameter optimization. *J. Mach. Learn. Res.* **2012**, *13*, 281–305.
71. Shahani, N.M.; Kamran, M.; Zheng, X.; Liu, C. Predictive modeling of drilling rate index using machine learning approaches: LSTM, simple RNN, and RFA. *Pet. Sci. Technol.* **2022**, *40*, 534–555. [CrossRef]
72. Willmott, C.J. Some comments on the evaluation of model performance. *Bull. Am. Meteorol. Soc.* **1982**, *63*, 1309–1313. [CrossRef]
73. Taylor, K.E. Summarizing multiple aspects of model performance in a single diagram. *J. Geophys. Res.* **2001**, *106*, 7183–7192. [CrossRef]
74. Zhong, R.; Tsang, M.; Makusha, G.; Yang, B.; Chen, Z. Improving rock mechanical properties estimation using machine learning. In *Proceedings of the 2021 Resource Operators Conference, Wollongong, Australia, 10–12 February 2021*; University of Wollongong-Mining Engineering: Wollongong, Australia, 2021.
75. Ghose, A.K.; Chakraborti, S. Empirical strength indices of Indian coals. In Proceedings of the 27th U.S. Symposium on Rock Mechanics, Tuscaloosa, AL, USA, 23–25 June 1986.
76. Katz, O.; Reches, Z.; Roegiers, J.C. Evaluation of mechanical rock properties using a Schmidt Hammer. *Int. J. Rock Mech. Min. Sci.* **2000**, *37*, 723–728. [CrossRef]
77. Momeni, E.; Nazir, R.; Armaghani, D.J.; Maizir, H. Prediction of pile bearing capacity using a hybrid genetic algorithm-based ANN. *Measurement* **2014**, *57*, 122–131. [CrossRef]
78. Ji, X.; Liang, S.Y. Model-based sensitivity analysis of machining-induced residual stress under minimum quantity lubrication. *Proc. Inst. Mech. Eng. Part B J. Eng. Manuf.* **2007**, *231*, 1528–1541. [CrossRef]

sustainability

MDPI

Article

The Recent Progress China Has Made in High-Concentration Backfill

Shuai Li, Zheng Yu, Haoxuan Yu * and Xinmin Wang

School of Resources and Safety Engineering, Central South University, Changsha 410083, China; shuaige@csu.edu.cn (S.L.); 215511038@csu.edu.cn (Z.Y.); 8210183016@csu.edu.cn (X.W.)
* Correspondence: yuhaoxuan@csu.edu.cn

Abstract: With the development of science and technology, backfill technology has made continuous progress, and the traditional backfill method is no longer suitable for various complicated practical engineering situations. Therefore, researchers in the field of backfill mining have gradually shifted their research focus to the study of high-concentration backfill, and Chinese researchers are no exception. In order to solve the problems caused by the traditional backfill method, China began to vigorously develop high-concentration backfill in recent years, and achieved a lot of results. In this paper, some important achievements made by Chinese researchers on high-concentration backfill in recent years are reviewed; it also presents a summary report of the latest research results from several key laboratories across China. Therefore, this paper reviews the development progress of high-concentration backfill China has made, of which the main contents include: (1) research progress of the high-concentration backfill theory in China; and (2) research progress of high-concentration backfill equipment in China. Finally, we claim that this paper serves just as a guide to start a conversation, and we hope many more experts and scholars will be interested and engage in the research of this field.

Keywords: mining engineering; backfill mining; high-concentration backfill

Citation: Li, S.; Yu, Z.; Yu, H.; Wang, X. The Recent Progress China Has Made in High-Concentration Backfill. *Sustainability* **2022**, *14*, 2758. https://doi.org/10.3390/su14052758

Academic Editors: Mahdi Hasanipanah, Danial Jahed Armaghani and Jian Zhou

Received: 12 January 2022
Accepted: 24 February 2022
Published: 26 February 2022

Publisher's Note: MDPI stays neutral with regard to jurisdictional claims in published maps and institutional affiliations.

Copyright: © 2022 by the authors. Licensee MDPI, Basel, Switzerland. This article is an open access article distributed under the terms and conditions of the Creative Commons Attribution (CC BY) license (https://creativecommons.org/licenses/by/4.0/).

1. Introduction

The development process of backfill mining and backfill technology in the world can be roughly divided into the following three stages:

1. The first stage (before 1900): Water and sand backfill.

In 1864, a coal mining area in Pennsylvania in the United States carried out the world's first water-sand backfill experiment to protect a church from subsidence and collapse. Subsequently, South Africa, Germany, Australia and other countries have also tested and successfully used the sand backfill process. At this stage, water-sand backfill takes water as the main transport carrier, and the mass concentration of backfill slurry is only 30~40%. After entering the stope, a large amount of dehydration and a long time are needed, resulting in extremely low backfill strength, so it is difficult to produce rigid support and effective ground pressure control effect [1,2].

2. The second stage (1900 to 1980): Graded tailings backfill.

After entering the 20th century, thanks to the continuous improvement and development of tailings classification dehydration devices such as hydrocyclones, the United States, Canada and other countries took the lead in carrying out experimental research on tailings backfill. The whole tailings produced by the concentrator are cycloned and classified, the coarse tailings are used as the backfill aggregate to fill the goaf and the fine particle overflow is directly discharged into the tailings reservoir, thus realizing the pumping or self-flow backfill of graded tailings. However, when only using hierarchical backfilling materials filling the backfilling materials with a coarse particle size, surplus accounts for about 50% of the still, requiring the row of the tailings backfilling materials to be a fine particle size.

3. The third stage (1980 to present): Full tailings backfill.

In view of the problems existing in grading tailings, in the 1980s, the former Soviet Union, Australia, South Africa and other countries carried out experimental research on full tailings backfill, and successfully carried out the field application in some mines; for example, the concentration of full tailings backfill slurry reached 70~78% in the West Dryfenden gold mine in South Africa. Since the full tailings backfill can effectively solve the problem that the fine-particle-size tailings in the grading tailings backfill cannot be damped naturally, it has been rapidly popularized and applied in the mines in the world. In the 21st century, on the basis of the full tailings high-concentration backfill, paste backfill and paste backfill are further subdivided. At the same time, a new high-water quick-setting backfill process has emerged and been popularized in some coal mines [3].

Compared with other countries, China also experienced the three development stages of backfill technology. However, for China, the slow industrial development before 1960 led to the development of backfill technology that was unable to keep up with the progress of other countries. Therefore, the backfill mining method in China started late, but developed rapidly. Similar to the development conditions of China's mining industry, China's backfill (filling) technology started late, so the theory and equipment level of the foundation is weak, but the development has been particularly rapid [4]. Especially after entering the 21st century, with the national high attention to safety and environmental protection and the continuous implementation of the development concept of "clear water and green mountains are gold and silver mountains", China's backfill theory system has become increasingly perfect, and the level of backfill technology and equipment has gradually reached the world's advanced level. The development process of China's backfill technology can be roughly divided into the following three stages:

1. The first stage (1960 to 1980): Water and sand backfill [5].

In 1960, Xiang-tan Manganese Mine in Hunan province took the lead in using the hydraulic backfill process of crushed stone to prevent pit fire and achieved good results. In 1965, in order to control the large area of ground pressure, Shannan Mine of Leng-shui-jiang Tin Mine, Hunan Province, adopted the tailings hydraulic backfill goaf technology for the first time, which effectively slowed down the surface subsidence. Subsequently, Tong-lu-shan Copper Mine, Zhao-yuan Gold Mine, Fan-kou Lead-Zinc Mine and other mines began to use sand backfill process to treat goaf [6,7].

2. The second stage (1980 to 2000): Graded tailings backfill.

Since the 1980s, the process and technology of graded tailing backfill has been rapidly popularized and applied in China. More than 60 non-ferrous, black and gold mines, such as An-qing Copper Mine, Zhang-ma-tun Iron Mine and San-shan-dao Gold Mine, have built graded tailing backfill systems. During this period, the cemented backfill process and technology with natural sand and rod grinding materials as aggregate has become mature, and has been popularized and applied in more than 20 mines such as Fan-kou Lead-Zinc Mine, Xiao-tie-shan Lead-Zinc Mine, Feng-huang-shan Copper Mine and Mu-ping Gold Mine [8,9].

3. The third stage (2000 to present): Full tailings backfill.

In the early years, China carried out key experimental studies on the high concentration (weight concentration of 78%) full tailings cemented backfill technology in Jin-chuan Company and Fan-kou Lead-Zinc Mine, respectively, and both have achieved success. However, it was not until 2000 that full tailings backfill really replaced graded tailings backfill and was widely used in mines. In the long-term backfill practice, people gradually realized that in the case of a given cement-sand ratio, the strength of backfill body is positively correlated with the slurry concentration within a certain range, that is, the higher the backfill concentration is, the more favorable the strength of the backfill body. Under the same strength requirement, increasing the backfill slurry concentration can greatly reduce the cement consumption, reduce the backfill cost and solve a series of problems such as stope dehydration. Therefore, the high-concentration backfill technology to reduce the backfill water began to be widely accepted by people quickly, and was put into use in

Fan-kou Lead-Zinc Mine, Jinan Zhang-ma-tun Iron Mine, Xiang-xi Gold Mine, Da-chang Tong-keng Tin Mine, Feng-shan Copper Mine and Tong-lu-shan Copper Mine. On this basis, more refined and higher concentration paste backfill, paste backfill and high-water quick-setting backfill technology have also been introduced into China, and have become the preferred process of new mine backfill system [10–12]. Figure 1 shows the development process of backfill technology in China.

Figure 1. The development process of backfill technology in China: (**a**) schematic diagram of sand backfill; (**b**) waste rock dry backfill; (**c**) graded tailings backfill system; (**d**) full tailings backfill system; (**e**) paste backfill system; (**f**) high-water quick-setting backfill. Image source (**a**–**e**): taken by authors; image source (**f**): https://www.sohu.com/a/438644662_358956 (accessed on 18 February 2022).

Therefore, this paper (also an information article), as a medium to lead readers to China's mining industry, mainly introduces two aspects to readers:

(1) Research progress of the high-concentration backfill theory in China;
(2) Research progress of high-concentration backfill equipment in China.

2. Research Progress of High-Concentration Backfill Theory in China

2.1. Paste-Like and Paste Backfill Technology

High-concentration backfill (filling) is a relative concept. Compared with traditional low-concentration backfill, high-concentration backfill has higher concentration, lower bleeding rate, shorter solidification time, higher early strength and better overall bearing and support effect after dehydration. At the same time, high-concentration backfill is also a very broad concept, and the backfill slurry with a mass concentration of more than 60% and s bleeding rate of less than 10% belongs to the category of high concentration. In order to facilitate the actual production management, improve the backfill effect and guarantee the backfill quality, paste and paste-like backfill technology with more accurate concentration ranges and clearer rheological states have emerged one after another. In any case, paste and paste-like are in the category of high-concentration backfill [13,14].

Paste backfill technology was first developed successfully in the Grund Lead-Zinc Mine in Germany in 1979. Due to its advantages, such as no bleeding, no precipitation and no segregation in the natural static state, it has quickly become a hot spot in the global mining green revolution technology. The team of Professor A.B. Fourie of the Australian Center for Rock Mechanics concluded that the content of -20 μm particles exceeded 15%, there was no segregation or bleeding in the natural static state, no stratification or settlement in pipeline transportation, the collapse degree was less than 230 mm and the rheological properties were non-Newtonian flow plastic bodies. Since it was successfully tested in Jin-chuan No.2 Mining Area for the first time in 1994, paste backfill technology has developed rapidly in China; however, it usually falls for the mistake of paying too much attention to "high concentration, no bleeding water" and ignoring liquidity, resulting in complex paste preparation process, poor liquidity of pipe transportation, high energy consumption of pumping and low stope backfill rate [13,15].

As a new type of the tailing backfill mode, paste-like technology has the advantages of good fluidity and easy transportation of cemented backfill slurry, high paste mass concentration, less underground dehydration and high strength of backfill consolidation, and has been paid more and more attention by scholars all over the world. Xinmin Wang from Central South University summarized the advantages of paste-like backfill: the higher the tailing mass concentration is, the lower the bleeding rate, and the higher the strength of backfill consolidation body is, the better the backfill effect. However, the higher the preparation cost is, the worse the fluidity and the higher the energy consumption for pipeline transportation. Therefore, the paste-like technology is the most economical and reasonable tailings backfill method at present under the condition of considering the backfill effect and the flow of pipe transportation, as shown in Figure 2.

2.2. New Backfill Materials

Backfill materials generally composed of backfill aggregate, cementitious materials and admixtures. The selection of backfill materials not only affects the quality of backfill body, but also directly affects the investment and cost of backfill system in mine. According to the actual conditions of the mine, materials or industrial wastes with wide sources, low costs, stable physical and chemical properties, non-toxicity and harmlessness and the skeleton function is generally selected as the backfill aggregate. At present commonly used include: tailings, waste rock, sand and river sand mountain, gobi aggregate, coal gangue, phosphogypsum and red mud. The recycling of solid waste as backfill aggregate not only solves the problem of the source of backfill aggregate, but also protects the surface environment and creates better economic and social and environmental benefits [16]. As shown in Figure 3, these are commonly used backfill aggregate sources in China.

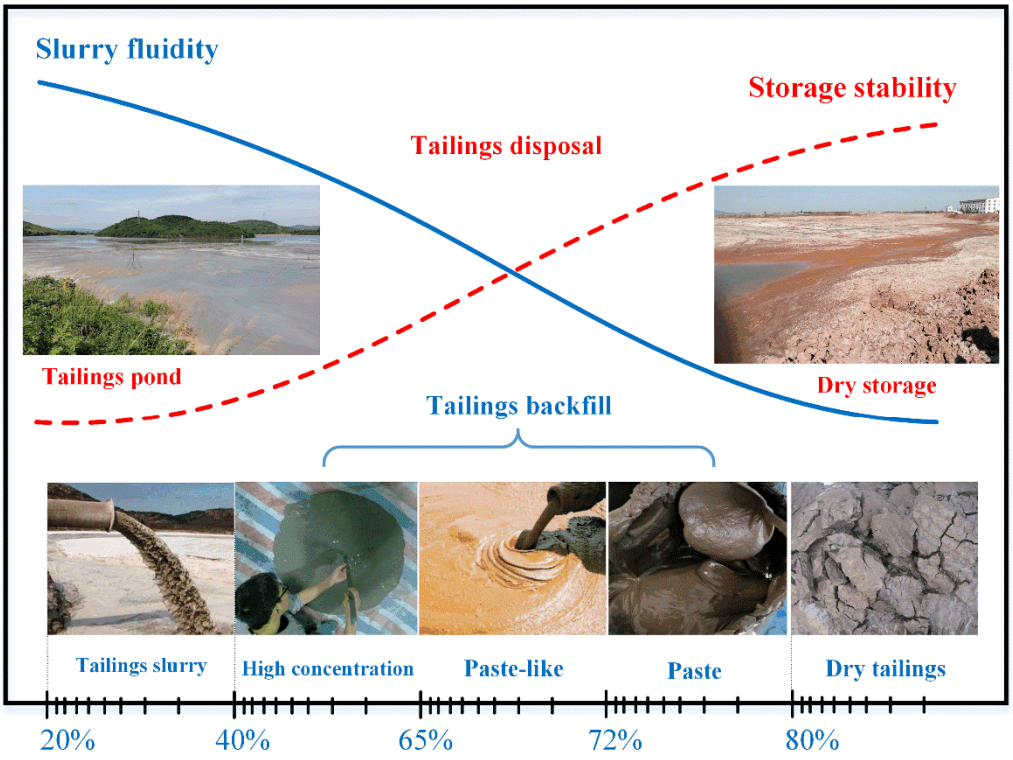

Figure 2. The mass concentration of tailings slurry and flow pattern division. Image source: taken by authors.

Portland cement is the most widely used backfill cementing materials in China. In recent years, with the rising price of cement and the continuous high operation, many mines in China began to test the use of industrial wastes with certain cementing capacity as cement substitute materials to reduce the cost of cementing backfill, such as water quenching slag, fly ash, high water quick-setting materials, etc. [17,18] In addition, the emergence of new concrete materials has also brought some enlightenment to the development of backfill materials [19].

Slag and fly ash are volcanic ash materials, which are characterized by more active SiO_2 and Al_2O_3 components. Under certain conditions, stable cementing calcium silicate hydrate and calcium aluminate hydrate double salt can be formed. During the hardening process, the strength increases with the age and has good late strength. At present, most of the new cementified materials sold on the market are powder materials formed by a variety of inorganic materials calcined at high temperature, and then an appropriate amount of natural minerals and chemical activator ingredients are added after grinding and homogenization. Most of the physical form is white and white fine powder, and the specific surface area is generally more than 4000 cm^2/g. The main chemical components are SiO_2, Al_2O_3, Fe_2O_3, CaO, MgO and so on [20]. Table 1 shows the main chemical composition of the volcanic ash materials commonly used in China, and Figure 4 shows the microstructure of the new cement substitute materials used in China.

Figure 3. Commonly used backfill aggregate sources: (**a**) river sand; (**b**) Gobi sand; (**c**) mine excavation of waste rock; (**d**) coal gangue; (**e**) strong acid phosphogypsum; (**f**) strongly alkaline red mud. Image source (**a**): https://www.sohu.com/a/435113802_800178 (accessed on 18 February 2022); image source (**b**): https://bbs.hlgnet.com/info/u1_18103903 (accessed on 18 February 2022); image source (**c**–**f**): taken by authors.

Table 1. Main chemical composition of volcanic ash material (%).

Volcanic Ash Material	SiO_2	Al_2O_3	Fe_2O_3	CaO	MgO	$Na_2O + K_2O$	SO_3	Ignition Loss
Tuff	4~73	11~19	2.6~6.4	2~1.4	0.4~2	2.4~10	-	7~16
Power plant fly ash	43~56	20~32	4~10	1.5~5	0.6~2	1~2.5	3~1.5	3~20
Coal gangue	40~15	15~35	2~9	1~7	1~4	1~2.5	-	12~17
Iron blast furnace slag	26~42	6~17	0.15~2	38~49	1~13	-	-	-
Bessemer slag	8~20	0.6~6	6.5~30	42~50	-	-	-	-
Reflecting slag of steelmaking furnace	35.5	3.6	Fe 36	7.9	1.9	-	S 0.9	-
Water quenched slag of lead smelting	17.6	4.0	Fe 27.4	20	1.37	-	S 1.3	-
Sintered red mud	20~23	5~8	8~12	43~46	1~2	-	6~10	-

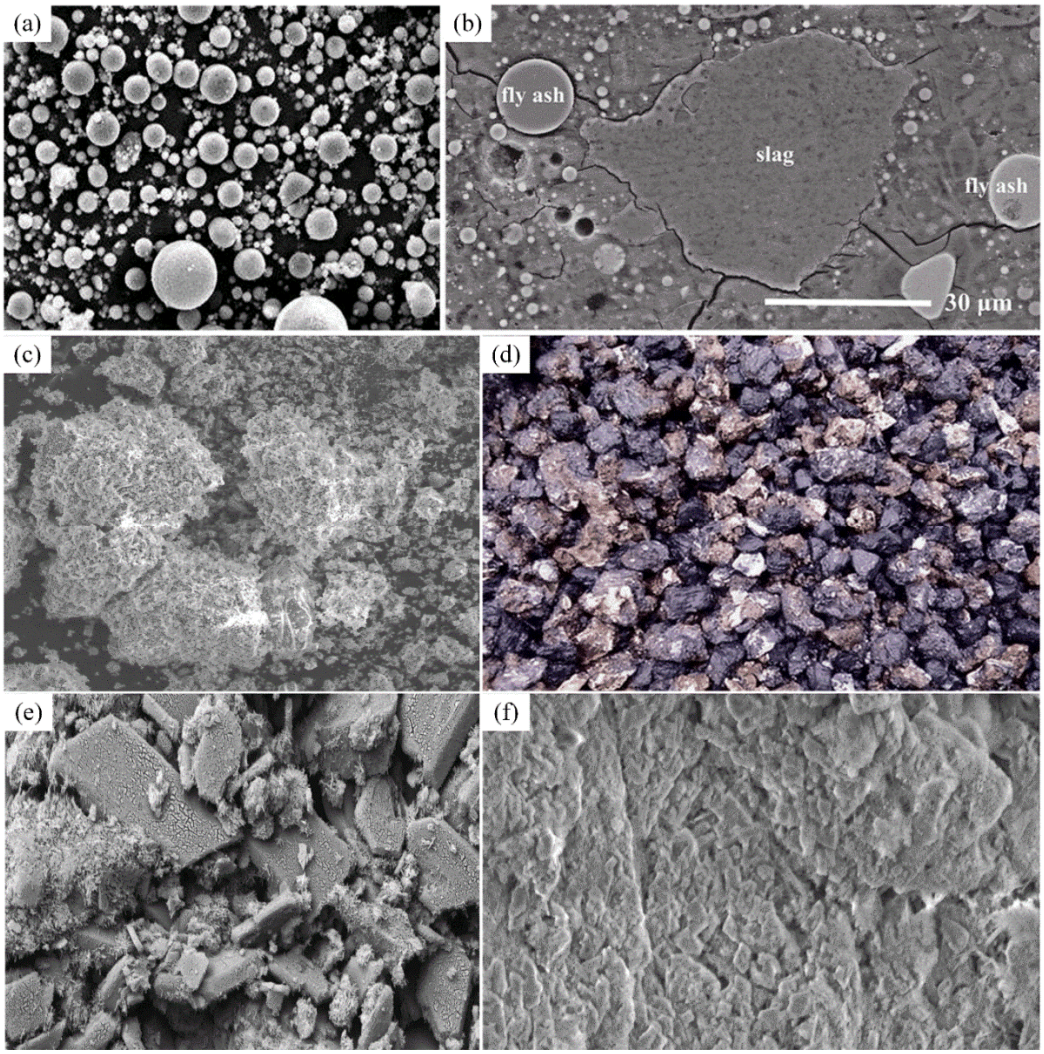

Figure 4. Microstructure of new cement substitute materials: (**a**) SEM figure of fly ash; (**b**) SEM of fly ash slag; (**c**) SEM map of coal gangue; (**d**) morphology of smelting slag; (**e**) SEM of phosphorus slag; (**f**) SEM of steel slag. Image source (**a**,**b**): http://www.mianfeiwendang.com/doc/34be220bb2bcd174055fcf33 (accessed on 18 February 2022); image source (**c**,**e**,**f**): taken by authors; image source (**d**): https://baike.baidu.com/item/%E6%B8%85%E7%82%89%E6%B8%A3/14477035 (accessed on 18 February 2022).

2.3. Bearing Mechanism of Backfill Body

After nearly half a century of the continuous improvement and development of backfill mining technology in China, its application practice in engineering has become

increasingly perfect. In view of different mining technical conditions, in-depth research on the bearing mechanism of backfill body, especially based on the special mining technical conditions of deep wells, systematic and in-depth research on deep well backfill theory and rockburst prevention and control technology, has become a new research hotspot and the development direction [21].

Particle size composition, particle size distribution, physical and chemical properties of tailings, the cement-sand ratio, mass concentration, permeability and dehydration performance, curing environment and other factors will affect the damage and failure characteristics of backfill. After entering the goaf, the backfill slurry interacts with surrounding rock through flow settlement, osmotic dehydration and consolidation hardening, including providing lateral pressure to the sliding trend of unloading rock blocks, supporting broken rock mass and primary cataclastic rock mass, and resisting the closure of surrounding rock in the stope [22]. From the perspective of energy, rockburst is a process of sudden and violent release of elastic deformation potential energy accumulated in rock mass, and the release rate of energy in rock mass directly affects the action intensity and damage effect of rockburst. At present, many researchers in China, such as Xibing Li and Shaofeng Wang from Central South University, are researching the stability of rockburst, surrounding rock and the bearing mechanism of backfill. Figure 5 shows the schematic diagram of coupling action between surrounding rock and backfill body [23].

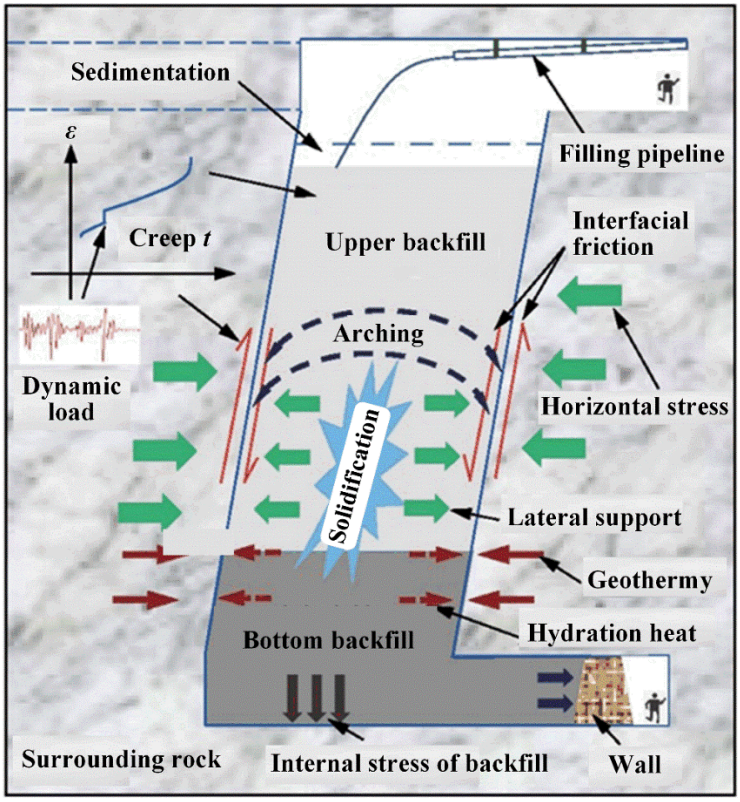

Figure 5. The schematic diagram of coupling action between surrounding rock and backfill body (image source from [23]).

2.4. Rheological Study on High Concentration Filled Slurry

Backfill slurry is generally transported into the goaf by pipeline. It is of great significance to fully analyze and master the rheological properties of backfill slurry for calculating the pipeline resistance of backfill slurry, preventing the settlement of coarse particles from blocking the pipe, and ensuring the stability and reliability of the whole pipeline transportation system. A large number of experimental studies have been carried out at home

and abroad on the rheological properties of filled slurry and its influencing factors, and important progress has been made [4].

However, Wang Xinmin from Central South University found an obvious thixotropic phenomenon in the rheological test of the backfill slurry of Jinchuan tailings paste. At the same time, other Chinese researchers found that for high-concentration backfill slurry, mass concentration, water-cement ratio, shear rate and rest time all have a great impact on the backfill process. Figure 6 shows the shear thixotropic characteristics of the filled slurry [24].

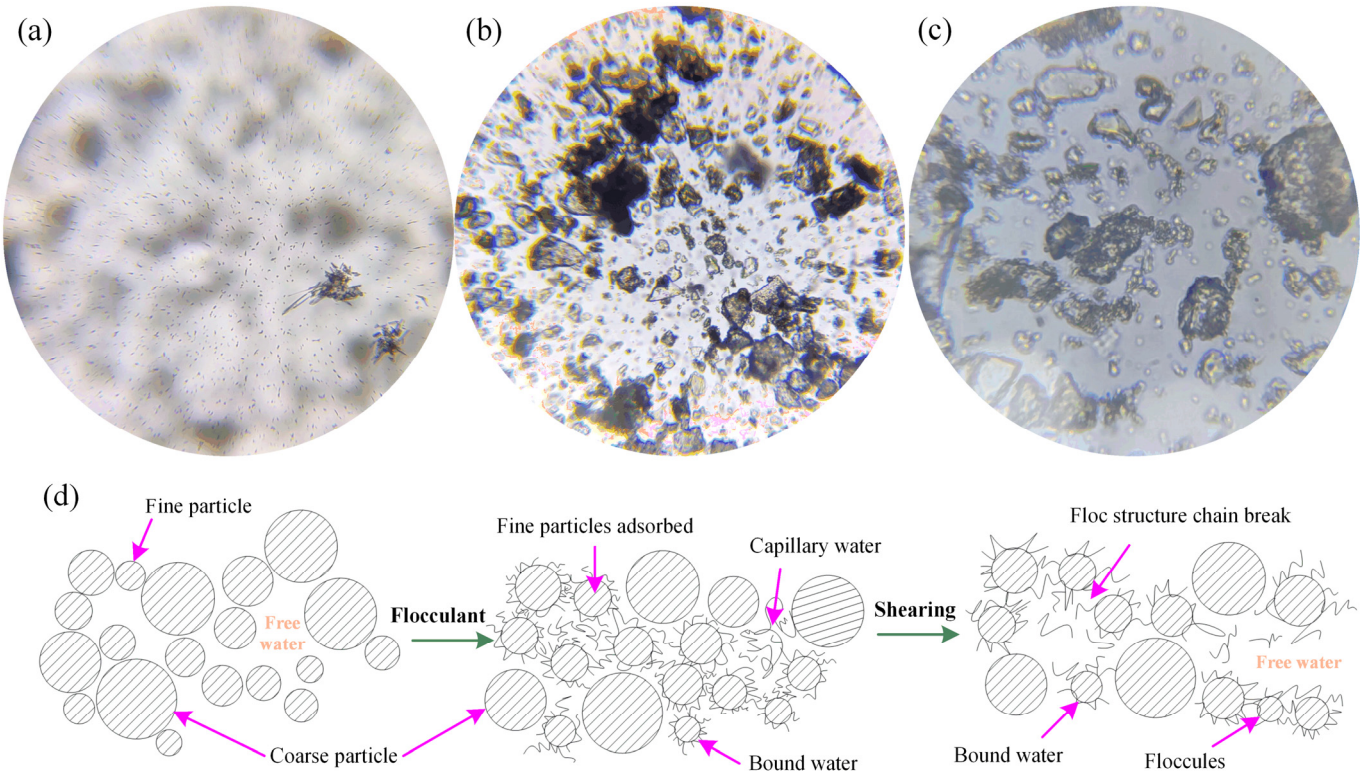

Figure 6. The shear thixotropic characteristics of the filled slurry: (**a**) the microstructure of the filled slurry in the static state; (**b**) microstructure of the slurry after shear mixing; (**c**) microstructure of the slurry after shear mixing; (**d**) schematic diagram of shear rheological mechanism of backfill slurry. Image source (**a**–**c**): taken by authors; image source (**d**) from [24].

2.5. Study on Creep Damage and Plastic Failure Characteristics of Backfill

After nearly half a century of continuous improvement and development of backfill mining technology, its application in engineering practice has become increasingly perfect. It has become a new research hotspot and the development direction to carry out in-depth research on the bearing mechanism of backfill and research on deep well backfill theory and rockburst prevention and control technology according to different mining technical conditions.

Wang Xinmin [4,21] from Central South University found that for high-concentration backfill, particle size composition, particle size distribution, physical and chemical properties of tailings, cement-sand ratio, mass concentration, permeability and dehydration performance, curing environment and other factors would affect the damage and failure characteristics of backfill. Therefore, they simplified the compression failure process of backfill into initial deformation stage, elastic deformation stage, plastic yield stage and failure stage.

3. Research Progress of High-Concentration Backfill Equipment in China

Due to the increase in direct mining cost, the backfill method is the first kind of method used in non-ferrous metal mines and precious metal mines. However, in recent years, with

the rapid progress of backfill technology and equipment, the cost of backfill has been constantly reduced, and backfill method has been widely used in coal mines, iron mines, chemical mines and other mines. According to the backfill process, the special equipment for backfill includes: tailings concentration and the dehydration device, mixing device and pumping equipment. For high-concentration backfill, these pieces of equipment are very important. With the continuous development of China's industry, great progress has been made in the research of high-concentration backfill equipment.

Figure 7 shows the relevant equipment.

Figure 7. Tailings thickener dehydration equipment: (**a**) hydrocyclone; (**b**) high frequency vibration dehydration sieve; (**c**) inclined plate thickener; (**d**) deep cone thickener; (**e**) plate and frame filter press;

(**f**) belt vacuum filter; (**g**) ceramic filter. Image source (**a**): https://b2b.hc360.com/supplyself/571519270.html?confr=B12 (accessed on 18 February 2022); image source (**b**): http://www.chinafa.org/enterprise/u21091557669848.html (accessed on 18 February 2022); image source (**c**): http://www.nzrhb.com/aspcms/news/2019-3-19/685.html (accessed on 18 February 2022); image source (**e**): http://groups.tianya.cn/post-yzt-h696710296.shtml (accessed on 18 February 2022); image source (**f**): http://www.zkdsglj.cn/item/3095.html (accessed on 18 February 2022); image source (**g**): http://byksjx.machineryinfo.net/product/65940028.htm (accessed on 18 February 2022).

3.1. Development Progress of Tailings Concentration and Dehydration Device

3.1.1. Hydrocyclone (Hydrocyclone Group)

Hydrocyclone is a kind of classification equipment that uses centrifugal force to accelerate tailings settlement. It is one of the commonly used classification equipment for tailings backfill. It has the advantages of simple structure, low equipment cost and small occupation area [25,26]. In recent years, with the continuous maturity and development of the application of hydrocyclone in tailing backfill field, a hydrocyclone group, which is formed by several or dozens of hydrocyclones, began to appear and be applied in the backfill system of mines (see Figure 7a).

3.1.2. Vibrating Screen

A vibrating screen is a new type of tailings dehydration equipment for solid-liquid separation by controlling the yield of coarse and fine particle size of vibrating screen network (see Figure 7b). The high frequency vibration of the screen driven by the motor helps the water to rapidly infiltrate from the filter layer of the screen surface, and pushes the filter cake to move forward continuously. Therefore, it has high dehydration efficiency for coarse particles in the tailings. High frequency vibration dehydration screen is often used with hydrocyclone, thickener and filter press for tailings classification and dehydration. The processing capacity and dehydration effect of the vibrating screen is not only related to the size of the screen, but also has a great relationship with the vibration frequency and dehydration area. At present, the new high frequency vibrating screen is in effective control of the amplitude at the same time; the operation frequency has been increased to 1500–7200 r/min, gradually forming a single layer, a double layer until the declamination of high efficiency and a large capacity overlapping high frequency vibration dehydration screen series of products [27].

3.1.3. Vertical Sand Bin

As a typical aggregate concentration and storage equipment, a vertical sand bin is generally composed of bin top, overflow tank, bin bottom and pulping pipe fittings in the bin [28].

Bin roof structure includes a bin roof room, sand inlet pipe, hydrocyclone (tailings classification), material level gauge and pedestrian trestle, etc. The overflow groove is located in the inner or outer wall of the bin mouth, and the bottom of the groove has a slope toward the overflow pipe interface. The function of the overflow groove is to reduce the overflow speed and improve the utilization rate of tailings. The bin body is the main component of sand storage, generally built with reinforced concrete or directly welded steel plate, due to the past use of spherical silo bottom structure sand concentration is low and easy to harden, so the modern vertical sand bin has generally been changed to conical sand structure. A vertical sand bin is widely used in metal backfill mines, and the technology is relatively mature, but there are also many problems, such as small processing capacity, low sand discharge concentration and instability and the bin wall caving suddenly blocking sand discharge mouth, resulting in flow interruption, overflow water running muddy. In recent years, Chinese scholars have mostly improved the sand discharge concentration and reduced the solid content of overflow water by optimizing the types, addition methods and dosage of flocculant or coagulant aid, and have improved the sand discharge effect

and reduced the blockage of flow by improving the design of the nozzle at the bottom of sand bin or using feng shui combined slurry [29].

3.1.4. Thickener

Thickener is based on the traditional rake thickener with flocculant adding device. The principle of flocculation sedimentation is used to condense fine particles into groups, which can reduce the diameter of thickener by more than 50%, reduce the area of occupation by about 20% and improve the processing capacity per unit area by several times. High-efficiency thickener has mature technology and wide application range, but there are also problems such as large footprint, small processing capacity and low concentration efficiency [30]. Figure 7c shows the inclined plate thickener, and Figure 7d shows the deep cone thickener.

At the same time, since the mass concentration of bottom flow of the high-efficiency thickener can only reach 40~50%, the high-efficiency thickener is often used as the equipment for thickening tailings of one stage, and a second-stage dehydration device is needed to obtain the high-concentration bottom flow that meets the requirements of mine backfill.

At present, the thickener is developing towards large-scale, high efficiency and automatic control. For example, on the basis of adding flocculant to the high efficiency thickener, the deep-cone thickener further increases the wall height and diameter to increase the tailings treatment efficiency, improve the bottom flow concentration and reduce the solid content of overflow water [31].

3.1.5. Filter and Filter Press

A filter and filter press are the most commonly used pieces of equipment in the second stage of tailings dehydration. According to the different principles of dehydration, the filter can be divided into vacuum filter and ceramic filter, as shown in Figure 7e–g.

The core of the disc vacuum filter is a disc composed of a number of separate fans. The disc rotates in a tank full of pulp. When passing through the filtration and adsorption area, the pressure difference is formed on both sides of the filter medium under the action of the vacuum pump, and solid particles can form filter cake on the surface of the filter cloth. A disc vacuum filter has the advantages of small occupation area, large processing capacity, easy to large-scale and a good application prospect. At present, the largest tailings filtration and dehydration equipment in China is the xPG-200 vacuum filter produced by Shenyang Mining Machinery Co., Ltd. which is located at Shenyang Province, China. The actual processing capacity of Skavarakino Gold Mine in Russia is 85p, and the water content of filter cake is controlled within 19%.

A filter press is a kind of tailings dehydration equipment to achieve solid-liquid separation by applying mechanical pressure on one side of the filter medium. Through mechanical extrusion and dehydration of pulp drying, dewatering product water content of filter press is very low. At present, the filter presses widely used in tailings dry heap dehydration are belt-type filter press, box-type filter press, vertical filter press and plate-frame filter press. Compared with the ceramic filter, the filter press has higher energy consumption and needs to change the filter cloth frequently, so the application of filter press in the field of mine backfill is less [32].

In addition, we have summarized a set of principle for the thickening and dehydration equipment selection for different tailings, which is intuitively presented in Figure 8.

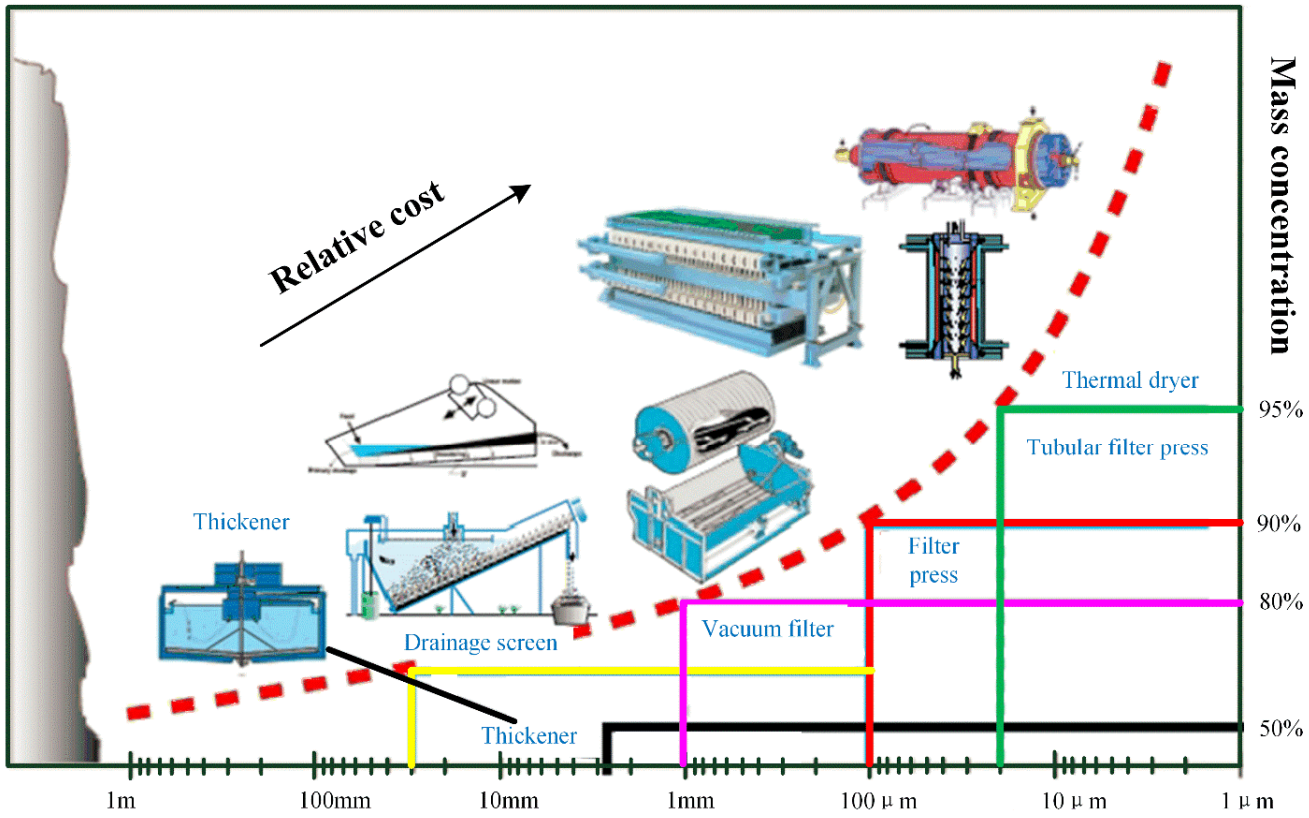

Figure 8. Principle of selection of tailings thickening and dewatering equipment (the corresponding author will explain the source of this figure upon request).

3.2. Development Progress of Agitator

The preparation of high quality and high concentration slurry for backfill is the key of backfill technology, and the high efficiency and high-speed mixer is the most important equipment for the preparation of high concentration slurry.

3.2.1. Mixing Barrel (Mixing Tank or Agitation Vat)

The mixing barrel is the most commonly used stirring equipment for mine backfill, which is driven by the motor triangle belt to rotate the impeller to fully mix and evenly different aggregates. It has the advantages of small investment, low cost and good applicability to aggregates with different particle sizes, as shown in Figure 9a [33].

Considering that in practical use, due to the interaction between solid particles and water in the prepared backfill material, it is easy to form agglomeration effect (agglomeration effect), which makes the core fragile agglomeration group adhere to a layer of cement slurry outside and is not easy to be pounded. Under the premise of not significantly increasing the stirring barrel power, continuously increasing the rotational speed of propeller blades is an effective means to solve such problems. At present, the mixing barrel with the power of 55 kW is commonly used in mines (the rotational speed is up to 240 r/min). Therefore, large capacity, high rotational speed and low energy consumption will be the development direction of the new type of mixing drum for mining backfill.

3.2.2. Horizontal Double Shaft Mixer

The mixing barrel has a good stirring effect for one or two kinds of mixed materials, but the stirring effect for a variety of materials is general.

However, a horizontal double-shaft mixer (See Figure 9b) has better mixing as well as mixing and conveying effect for more than two kinds of mixed materials. Its main parts include: stirring rotor rod, spindle, outer shell, motor, coupling, equipment frame and so on. When the double-shaft mixer is working, the backfill material enters the mixing tank

through the feed port, and the two mixing shafts rotate in reverse under the motor drive. The mixing blades are installed on the mixing shaft, and the mixing blades are distributed in a spiral line on the mixing shaft. The backfill material is driven by the rotation of the mixing blades and then moves in the same direction, mixing each other to complete the mixing. In the overlapping area between the two mixing shafts of the two-axis mixer, the backfill materials with different rotation directions are extruded and rubbed together to improve the mixing effect of backfill materials.

Due to the horizontal double shaft mixer speed is generally not high, for viscous or agglomerate material stirring effect is general, agglomerate phenomenon is more obvious. Therefore, large capacity, high speed and low energy consumption are also the development directions of new horizontal double-shaft mixers for mining [34].

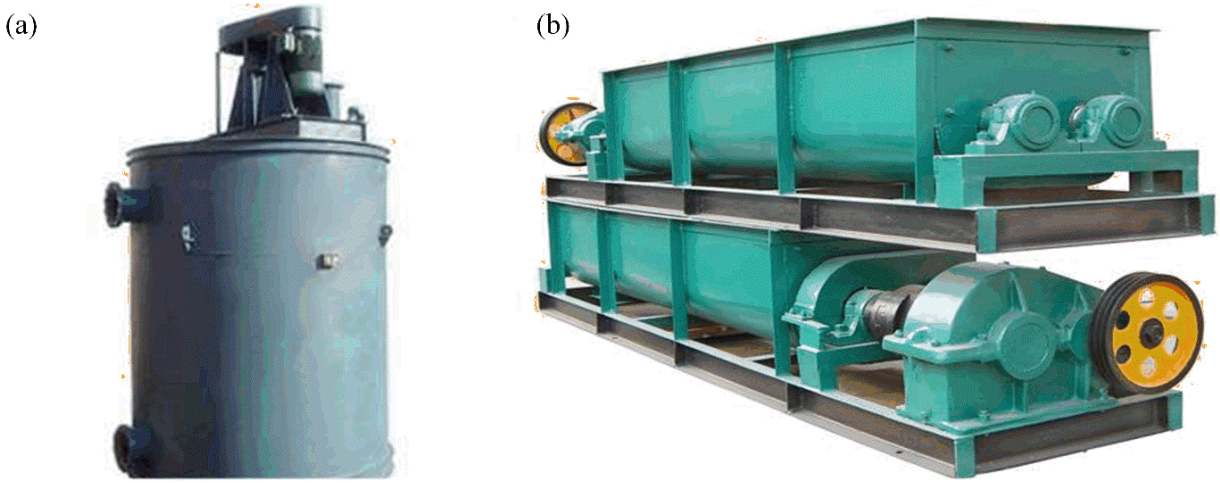

Figure 9. Agitator equipment: (**a**) mixing barrel; (**b**) horizontal double shaft mixer. Image source (**a**): http://byksjx.machineryinfo.net/product/65940028.htm (accessed on 18 February 2022); image source (**b**): http://www.kuyibu.com/c_ddc2836950/p22589921.html (accessed on 18 February 2022).

3.3. Development Progress of Backfill Industrial Pump

With the continuous development of backfill technology, the mass concentration of backfill slurry is increasing and the pipeline transportation distance is getting farther and farther. However, the long-distance pipeline transportation technology and equipment of high-concentration backfill slurry has always been a bottleneck restricting the development of backfill technology in China. In recent years, high pressure, large displacement, high reliability of backfill the emergence and rapid development of industrial pump have effectively solved the bottleneck problem; quick backfill mining in coal mines and metal mines has caused non-metallic mineral tailings backfill, high concentration of emissions, metallurgy, petrochemical industry wastewater treatment and solid waste treatment and other fields to be widely applied. It provides an effective guarantee for safe and reliable long-distance transportation of high solid and viscous materials, as shown in Figure 10 [35].

Figure 10. Backfill industrial pump: (**a**) pumping part; (**b**) dynamic component. Image source: https://hnrealtop.en.made-in-china.com/product/GKFEDqRVhfcW/China-Mining-Concrete-Pump-HGBS-200-15-800-.html (accessed on 18 February 2022).

4. Discussion: The Development Direction of High-Concentration Backfill

Compared with the traditional backfill mining method, there are many innovations in high-concentration backfill mining. However, there is no doubt that the current high-concentration backfill technology in China is not developed, and the current high-concentration backfill in China mainly has the following two problems:

(1) The overall cost of the high-concentration backfill method is high;

(2) High-concentration backfill requires high-level backfill and production equipment.

Therefore, in order to continue to develop high-concentration backfill technology, China needs to solve these two problems.

4.1. Research and Development of New Low Cost Cementing Materials

As raw material prices and the national attention to environmental protection are rising, cement as mine backfill is the most commonly used gelling material, as its prices stay high for a long time and there is still a larger rise space: some remote mining areas of bulk cement to ore prices have risen to RMB 500/t, therefore, development of a new mine backfill gelled material to replace cement has become a new research hotspot. A lot of research and application practice show that water quenching slag of smelter, fly ash of thermal power plant, yellow phosphorus slag of phosphorous chemical industry, red mud of sintering process and other materials are good cement substitutes [36,37].

For China, many mines in recent years have also begun to study the improvement of backfill materials:

(1) By adding fly ash into gangue backfill slurry in Shandong Sun-cun Coal Mine, not only the single consumption of cement is effectively reduced, but also the flow performance of backfill slurry and suspension performance of aggregate are greatly improved;

(2) Guizhou Kai-yang Phosphate Mine has developed the first international cemented backfill technology of total phosphorus waste with phosphogypsum as backfill aggregate and yellow phosphorus slag as cementing material.

4.2. Large-Capacity, High-Efficiency and Low-Cost Backfill Equipment

After nearly a century of development, the theory of backfill has formed a complete theoretical system and perfect application technology. However, in the actual backfill application process, backfill equipment is still an important prerequisite to restrict the successful application of backfill technology. For example, before the emergence of vertical sand silo, due to the lack of large capacity and high efficiency tailings concentration device, the traditional horizontal sand silo covers a large area, low water filtration efficiency, and serious overflow water running and mixing, resulting in a very small and discontinuous backfill capacity. After the emergence of the vertical sand silo, the horizontal sand silo was quickly eliminated, but the vertical sand silo in the application process also produced low sand concentration and instability, high energy consumption of high-pressure wind and

high-pressure water combined slurry, so overflow water is easy to run and mix, plus there are many other problems [38].

Therefore, when the deep cone thickener with larger processing capacity, higher sand discharging concentration and more stability appeared, so the vertical sand silo was quickly eliminated. At present, the new backfill systems of large- and medium-sized mines at home and abroad almost all take the deep cone thickener as the core equipment. In addition, the large investment and high operating cost of backfill system are also the main reasons that limit the popularization and application of backfill in mines. At present, the paste backfill system with deep cone thickener as the core generally has an investment of RMB 25~50 million/set, and the backfill cost is generally as high as RMB 150~200/m^3.

Therefore, the development of large capacity, high efficiency and low cost backfill equipment, and the continuous reduction of backfill system investment and backfill operation cost will be an important development direction of backfill technology.

5. Conclusions

In recent years, China has made great progress in mining engineering [39–42], especially high-concentration backfill. The main reasons for this are the development of new materials and technologies, such as the use of high-performance cementitious materials with higher content of CaO and MgO, as well as a more efficient utilization of existing resources. In addition to these improvements in technology, there is also an improvement in the understanding and application of basic science principles [43,44]. This paper reviews some important achievements that have been made recently by Chinese researchers on various aspects related to high-concentration backfill including its design principles, construction methods and performance characteristics; it also introduces a summary report on the latest research findings from several key laboratories across China [45,46].

Therefore, this paper, as a medium to lead readers to China's mining industry, can be roughly divided into three sections:

(1) An introduction of the research progress of the high-concentration backfill theory in China;

In the first section: this paper primarily introduces paste-like and paste backfill technology, new backfill materials and the bearing mechanism of the backfill body in the high-concentration backfill progress.

(2) A description of the research progress of high-concentration backfill equipment in China.

In the first section: this paper primarily introduces the backfill equipment for the high-concentration backfill method, such as the backfill industrial pump.

(3) Discussion part.

In the discussion part, this paper mainly discusses the development direction of the backfill mining method.

As a medium to guide the readers to understand the development of mining industry in China, this paper systematically reviews the research progress of high-concentration backfill, which plays an important role in the future development of backfill mining. At the same time, we also call on relevant researchers to actively invest in backfill mining research to promote the rapid development of backfill mining methods, which will undoubtedly bring benefits to people around the world.

Finally, we claim that this information article only serves as a guide to start the dialogue, and we hope that more experts and scholars will be interested in and participate in research in this area.

Author Contributions: Conceptualization, S.L.; validation, H.Y. and Z.Y.; investigation, H.Y.; resources, S.L.; writing–original draft preparation, S.L.; writing–review and editing, H.Y. and S.L.; visualization, H.Y.; supervision, H.Y.; project administration, X.W.; funding acquisition, S.L. All authors have read and agreed to the published version of the manuscript.

Funding: This research was funded by the Natural Science Foundation of Hunan Province (Grant No. 2021JJ40745) and the National Natural Science Foundation of China (Grant No. 51804337).

Institutional Review Board Statement: Not applicable.

Informed Consent Statement: Not applicable.

Data Availability Statement: Not applicable.

Acknowledgments: First of all, the authors appreciate the financial support from the Natural Science Foundation of Hunan Province (Grant No. 2021JJ40745) and the Natural Science Foundation of China (Grant No. 51804337); secondly, the authors express gratitude to the Chinese experts in the research field of the backfill mining method for their effort in the development of China's mining industry; finally, the authors express sincere thanks to Central South University.

Conflicts of Interest: The authors declare no conflict of interest.

References

1. Li, S.; Zhao, Z.; Yu, H.; Wang, X. The recent progress China has made in the backfill mining method, part II: The composition and typical examples of backfill systems. *Minerals* **2021**, *11*, 1362. [CrossRef]
2. Yu, H.; Li, S.; Wang, X. The recent progress China has made in the backfill mining method, part III: Practical engineering problems in stope and goaf backfill. *Minerals* **2022**, *12*, 88. [CrossRef]
3. Hu, B.; Zhang, Q.; Li, S.; Yu, H.; Wang, X.; Wang, H. Application of numerical simulation methods in solving complex mining engineering problems in dingxi mine, China. *Minerals* **2022**, *12*, 123. [CrossRef]
4. Yu, H.; Li, S.; Wang, X. The recent progress China has made in the backfill mining method, part I: The theory and equipment of backfill pipeline transportation. *Minerals* **2021**, *11*, 1274. [CrossRef]
5. Liu, Y.; Liu, J.; Yang, B.; Yuan, S. Assessing water and sand inrushes hazard reductions due to backfill mining by combining gis and entropy methods. *Mine Water Environ.* **2021**, *40*, 956–969. [CrossRef]
6. Sui, W.; Zhang, D.; Cui, Z.C.; Wu, Z.; Zhao, Q. Environmental implications of mitigating overburden failure and subsidences using paste-like backfill mining: A case study. *Int. J. Min. Reclam. Environ.* **2015**, *29*, 521–543. [CrossRef]
7. Liu, J.; Sui, W.; Zhang, D.; Zhao, Q. Durability of water-affected paste backfill material and its clean use in coal mining. *J. Clean. Prod.* **2020**, *250*, 119576. [CrossRef]
8. Yao, Y.; Cui, Z.; Wu, R. Development and challenges on mining backfill technology. *J. Mater. Sci. Res.* **2012**, *1*, 73. [CrossRef]
9. Qi, C.; Fourie, A. Cemented paste backfill for mineral tailings management: Review and future perspectives. *Miner. Eng.* **2019**, *144*, 106025. [CrossRef]
10. Qiu, J.; Yang, L.; Sun, X.; Xing, J.; Li, S. Strength characteristics and failure mechanism of cemented super-fine unclassified tailings backfill. *Minerals* **2017**, *7*, 58. [CrossRef]
11. Cao, S.; Song, W.; Yilmaz, E. Influence of structural factors on uniaxial compressive strength of cemented tailings backfill. *Constr. Build. Mater.* **2018**, *174*, 190–201. [CrossRef]
12. Chen, Q.; Zhang, Q.; Wang, X.; Xiao, C.; Hu, Q. A hydraulic gradient model of paste-like crude tailings backfill slurry transported by a pipeline system. *Environ. Earth Sci.* **2016**, *75*, 1–9. [CrossRef]
13. Guo, Y.; Ran, H.; Feng, G.; Du, X.; Zhao, Y.; Xie, W. Deformation and instability properties of cemented gangue backfill column under step-by-step load in constructional backfill mining. *Environ. Sci. Pollut. Res.* **2022**, *29*, 2325–2341. [CrossRef] [PubMed]
14. Chen, Q.S.; Zhang, Q.L.; Fourie, A.; Chen, X.; Qi, C.C. Experimental investigation on the strength characteristics of cement paste backfill in a similar stope model and its mechanism. *Constr. Build. Mater.* **2017**, *154*, 34–43. [CrossRef]
15. Liu, L.; Xin, J.; Feng, Y.; Zhang, B.; Song, K.I. Effect of the cement—Tailing ratio on the hydration products and microstructure characteristics of cemented paste backfill. *Arab. J. Sci. Eng.* **2019**, *44*, 6547–6556. [CrossRef]
16. Zhang, J.; Li, M.; Taheri, A.; Zhang, W.; Wu, Z.; Song, W. Properties and application of backfill materials in coal mines in China. *Minerals* **2019**, *9*, 53. [CrossRef]
17. Zhu, X.; Guo, G.; Liu, H.; Peng, X.; Yang, X. Stability analysis of the composite support pillar in backfill-strip mining using particle flow simulation method. *Environ. Earth Sci.* **2022**, *81*, 1–19. [CrossRef]
18. Zhou, N.; Zhang, J.; Ouyang, S.; Deng, X.; Dong, C.; Du, E. Feasibility study and performance optimization of sand-based cemented paste backfill materials. *J. Clean. Prod.* **2020**, *259*, 120798. [CrossRef]
19. Ma, C.; Liu, Y.T.; Song, D.Q.; Cao, L.; He, F.Q.; Liu, X.L.; Zhou, H.J. Characterizing the influencing factors in a novel repairing material for concrete structures by AC impedance spectroscopy. *J. Build. Eng.* **2021**, *47*, 103858. [CrossRef]
20. Luan, H.; Jiang, Y.; Lin, H.; Wang, Y. A new thin seam backfill mining technology and its application. *Energies* **2017**, *10*, 2023. [CrossRef]
21. Shao, X.; Li, X.; Wang, L.; Fang, Z.; Zhao, B.; Liu, E.; Liu, L. Study on the pressure-bearing law of backfilling material based on three-stage strip backfilling mining. *Energies* **2020**, *13*, 211. [CrossRef]
22. Zhang, J.W.; Wang, H.L.; Chen, S.J. Bearing capacity of backfill body and roof stability during strip coal pillar extracted with paste backfill. *Geotech. Geol. Eng.* **2018**, *36*, 235–245. [CrossRef]

23. Yilmaz, E.; Belem, T.; Benzaazoua, M. Specimen size effect on strength behavior of cemented paste backfills subjected to different placement conditions. *Eng. Geol.* **2015**, *185*, 52–62. [CrossRef]
24. Wang, S.; Li, S.; Qin, J.C.; Xiao, G.Z.; Yang, G.C.; Feng, X. Effect of anionic polyacrylamide on the structural stability of thickened tailings slurry in pipeline transportation. *Adv. Mater. Sci. Eng.* **2018**, *2018*, 7131487. [CrossRef]
25. Cilliers, J.J.; Hinde, A.L. An improved hydrocyclone model for backfill preparation. *Miner. Eng.* **1991**, *4*, 683–693. [CrossRef]
26. Toprak, N.A.; Altun, O. Considering hydrocyclone operation for tailings dewatering purpose and its effects on product specifications of paste backfill operations. *Miner. Eng.* **2021**, *173*, 107176. [CrossRef]
27. Chang, Q.; Chen, J.; Zhou, H.; Bai, J. Implementation of paste backfill mining technology in Chinese coal mines. *Sci. World J.* **2014**, *2014*, 821025. [CrossRef]
28. Shi, X.Z.; Hu, H.Y.; Du, X.H.; Li, M.L.; Wang, H.Y. Experimental study on flocculating sedimentation of tailings slurry in a vertical sand tank. *Min. Metall. Eng.* **2010**, *30*, 1–3.
29. Wang, X.M.; Zhao, B.; Zhang, Q.L.; Xu, D.S. Cemented backfilling technology with unclassified tailings based on vertical sand silo. *J. Cent. South Univ. Technol.* **2008**, *15*, 801–807. [CrossRef]
30. Ruan, Z.; Wang, Y.; Wu, A.; Yin, S.; Jin, F. A theoretical model for the rake blockage mitigation in deep cone thickener: A case study of lead-zinc mine in China. *Math. Probl. Eng.* **2019**, *2019*, 2130617. [CrossRef]
31. Jiao, H.; Wu, A.; Wang, H.; Zhong, S.; Ruan, R.; Yin, S. The solids concentration distribution in the deep cone thickener: A pilot scale test. *Korean J. Chem. Eng.* **2013**, *30*, 262–268. [CrossRef]
32. Yan, J.; Wang, Y.; Tu, Y.; Han, P.; Liu, X.; Ye, S. Green treatment of cyanide tailings using a "Filter press backwash–Chemical precipitation–Gaseous membrane absorption" method. *Appl. Sci.* **2021**, *11*, 2091. [CrossRef]
33. Li, B.; Yan, H.; Zhang, J.; Zhou, N. Compaction property prediction of mixed gangue backfill materials using hybrid intelligence models: A new approach. *Constr. Build. Mater.* **2020**, *247*, 118633. [CrossRef]
34. Zhang, H.; Feng, P.; Ying, W. Abrasive wear and optimal installation angle of concrete double-horizontal shaft mixer stirring blades. *SN Appl. Sci.* **2020**, *2*, 1–10. [CrossRef]
35. Yang, K.; Zhao, X.; Wei, Z.; Zhang, J. Development overview of paste backfill technology in China's coal mines: A review. *Environ. Sci. Pollut. Res.* **2021**, *28*, 67957–67969. [CrossRef] [PubMed]
36. Li, S.; Zhang, R.; Feng, R.; Hu, B.; Wang, G.; Yu, H. Feasibility of recycling bayer process red mud for the safety backfill mining of layered soft bauxite under coal seams. *Minerals* **2021**, *11*, 722. [CrossRef]
37. Li, S.; Zhang, Y.; Feng, R.; Yu, H.; Pan, J.; Bian, J. Environmental safety analysis of red mud-based cemented backfill on groundwater. *Int. J. Environ. Res. Public Health* **2021**, *18*, 8094. [CrossRef]
38. Yin, S.; Shao, Y.; Wu, A.; Wang, H.; Liu, X.; Wang, Y. A systematic review of paste technology in metal mines for cleaner production in China. *J. Clean. Prod.* **2020**, *247*, 119590. [CrossRef]
39. Di Nardo, M.; Yu, H. Special issue "Industry 5.0: The prelude to the sixth industrial revolution". *Appl. Syst. Innov.* **2021**, *4*, 45. [CrossRef]
40. Yu, H.; Li, S. The function design for the communication-based train control (CBTC) system: How to solve the problems in the underground mine rail transportation? *Appl. Syst. Innov.* **2021**, *4*, 31. [CrossRef]
41. Nardo, M.D.; Yu, H. Intelligent ventilation systems in mining engineering: Is zigbee wsn technology the best choice? *Appl. Syst. Innov.* **2021**, *4*, 42. [CrossRef]
42. Li, S.; Wang, G.; Yu, H.; Wang, X. Engineering project: The method to solve practical problems for the monitoring and control of driver-less electric transport vehicles in the underground mines. *World Electr. Veh. J.* **2021**, *12*, 64. [CrossRef]
43. Zhang, B.; Xin, J.; Liu, L.; Guo, L.; Song, K.I. An experimental study on the microstructures of cemented paste backfill during its developing process. *Adv. Civ. Eng.* **2018**, *2018*, 9783046. [CrossRef]
44. Xu, W.; Chen, W.; Tian, M.; Guo, L. Effect of temperature on time-dependent rheological and compressive strength of fresh cemented paste backfill containing flocculants. *Constr. Build. Mater.* **2021**, *267*, 121038. [CrossRef]
45. Zheng, J.; Guo, L.; Sun, X.; Li, W.; Jia, Q. Study on the strength development of cemented backfill body from lead-zinc mine tailings with sulphide. *Adv. Mater. Sci. Eng.* **2018**, *2018*, 7278014. [CrossRef]
46. Li, W.; Guo, L.; Liu, G.; Pan, A.; Zhang, T. Analytical and experimental investigation of the relationship between spread and yield stress in the mini-cone test for cemented tailings backfill. *Constr. Build. Mater.* **2020**, *260*, 119770. [CrossRef]

sustainability

MDPI

Article

Hybrid Finite-Discrete Element Modelling of Various Rock Fracture Modes during Three Conventional Bending Tests

Huaming An [1,*], Shunchuan Wu [2], Hongyuan Liu [3] and Xuguang Wang [4]

[1] Faculty of Public Security and Emergency Management, Kunming University of Science and Technology, Kunming 650093, China
[2] Faculty of Land Resource Engineering, Kunming University of Science and Technology, Kunming 650093, China; wushunchuan@kust.edu.cn
[3] College of Science and Engineering, University of Tasmania, Hobart, TAS 7001, Australia; hong.liu@utas.edu.au
[4] School of Civil and Resources Engineering, University of Science and Technology Beijing, Beijing 100083, China; Xuguang.wang@hotmail.com
* Correspondence: huaming.an@kust.edu.cn

Abstract: The numerical techniques for modelling the rock fracture have been briefly reviewed. A hybrid finite-discrete element method (HFDEM) is proposed to simulate various fracture types of rock. A fracture model is implemented in the HFDEM for simulation of the three main fracture types. In addition, the influence of the strain rate is considered during the HFDEM modelling rock behavior. Then, two typical rock mechanism tests are employed to calibrate the HFDEM. The proposed method has well modelled the rock fracture processes and can obtain reasonable stress distribution and force–displacement curves. After that, the HFDEM is used to model three convention bending tests. The obtained rock fracture processes indicates that the HFDEM can simulate various fracture types. The obtained rock strengths and fracture toughness indicate that the HFDEM can reflect the influence of the strain rate. It is concluded that the HFDEM can model the entire and complete rock fracture process during the three convention bending tests, and it also can capture the rock's behavior on the strain rate.

Keywords: HFDEM; numerical method; rock fracture; strain rate

Citation: An, H.; Wu, S.; Liu, H.; Wang, X. Hybrid Finite-Discrete Element Modelling of Various Rock Fracture Modes during Three Conventional Bending Tests. *Sustainability* **2022**, *14*, 592. https://doi.org/10.3390/su14020592

Academic Editors: Mahdi Hasanipanah, Danial Jahed Armaghani and Jian Zhou

Received: 20 October 2021
Accepted: 29 December 2021
Published: 6 January 2022

Publisher's Note: MDPI stays neutral with regard to jurisdictional claims in published maps and institutional affiliations.

Copyright: © 2022 by the authors. Licensee MDPI, Basel, Switzerland. This article is an open access article distributed under the terms and conditions of the Creative Commons Attribution (CC BY) license (https://creativecommons.org/licenses/by/4.0/).

1. Introduction

Rock fracture behavior has been widely studied, especially under a variety of loading conditions. The numerical method is now a popular technique for studying rock behaviors. In numerical method, the rock materials can be considered as continuum, such as finite element method, while it can also be regarded as a discontinuum, such as the discrete element method. For the continuum method, the model is treated as continuous body, and it is discretized into elements. The continuous-based method has been successfully applied in rock fracture modelling, in which the discontinuity of the rock mass can be ignored due to that the modelled scale is much larger than the existing or produced cracks in the rock mass. However, when the discontinuity of the geo-materials cannot be neglected due to the original existing original produced fractures are comparable to the interest area, the discontinuity should be taken into account.

Discontinuum-based methods are also popular tools employed in the study of rock mechanics. In the discontinuum-based methods, the rock mass is assumed to be an assembly of discrete elements [1]. Thus, the discontinuity of the rock mass has been fully considered. Since Cundall [2] proposed the distinct element method (DEM) and implemented it widely into the investigate rock fracture and resultant fragmentation process [3], discontinuum-based methods have been extensively used in various rock failure problems [4,5]. For example, the Gutiérrez-Ch et al. (2018 and 2021) used the DEM models to successfully

simulate the rock response during direct shear tests and all stages of rock creep behaviour in the laboratory tests [6,7]. The representative discontinuum-based methods are the distinct element method, the bounded particle method (BPM), and the discontinuous deformation analysis (DDA) [8,9]. Compared with the continuum method, the distinct element method allows the displacement and rotation of discrete bodies. The UDEC and 3DEC might be the most common used DEM code [10] for modelling the rock fracture and result fragmentation process. The domain is divided into rigid discrete bodies in the UDEC or 3DEC, which can move, rotate, or slip during the contact interaction of the discrete bodies [10]. The fractures in DEM are modelled along the boundary of discrete bodies when the stress reaches its maximum. The bounded particle method (BPM) is a particle-based discontinuum method. The domain in this method is divides into circular and spherical rigid elements [11]. Shi and Godman (1985) proposed discontinuous deformation analysis (DDA), which is an implicit formulation of DEM [12]. The DDA employs sub-block techniques to modelling the continuous–discontinuous transition [13]. Thus, the fracture and fragmentation of rocks can be modelled along the block boundaries.

To realistically model the rock fracture process, numerical methods should be able to model the fracture initiation and propagation [14]. For this purpose, the continuum–discontinuum methods are proposed [9,15]. It should be noted that the combined or hybrid continuum–discontinuum methods are different from the coupled combined or hybrid continuum–discontinuum methods. The former can freely model the continuum and discontinuum behaviours of rocks and their transitions, while the latter adopts a physical boundary to couple the two methods.

The ELFEN might be the most widely used commercial software of the combined FEM/DEM. The Y-code is open source for the implementation of the combined FEM/DEM, originally developed by Munjiza [15]. Then, the Y-Geo was developed for the convenient use of the Y-code. The Y-code has its difficulties in modelling mixed mode fractures and lacks consideration of the loading rate and material heterogeneity [16]. To address these limitations, many extensions of the Y-code have been developed. An et al. (2017) developed Y2D/3D IDE to model the blast-induced frock fracture and resultant fragmentation processes [16]. The open source Y-code accelerates the development of the combined/hybrid FEM/DEM method, and many extensions of the Y-code have been well implemented in rock fracture and fragmentation modelling [17].

In this study, the authors developed the HFDEM, which is proposed to simulate the various rock fracture types. The fracture model and the curve are specially implemented in the HFDEM for modelling the complete rock fracture process and taking the influence of the loading rate into account, respectively. The HFDEM is verified by the simulation of typical rock mechanism test. Then, the HFDEM is used to simulate three convention point bending tests to obtain various fracture modes.

2. HFDEM for Modelling Dynamic Rock Fracture

To completely model the rock fracture process, the HFDEM needs to be able to model the rock initiation, propagation, and interaction of fractured rock and resultant fragmentation. In addition, the influence due to different loading rates should also be taken into account. Thus, in this section, the above two key components are explained in detail.

2.1. Transition from Continuum to Discontinuum

In HFDEM, the transition from continuum to discontinuum is modelled through the fracture of the discrete bodies. As illustrated in Figure 1, the stress–strain curve is divided into two parts, the stress hardening and stress softening parts, separated by the peak stress. Constitutive law is employed to model the stress hardening parts, while the opening or sliding displacement of the finite elements can describe the stress softening part.

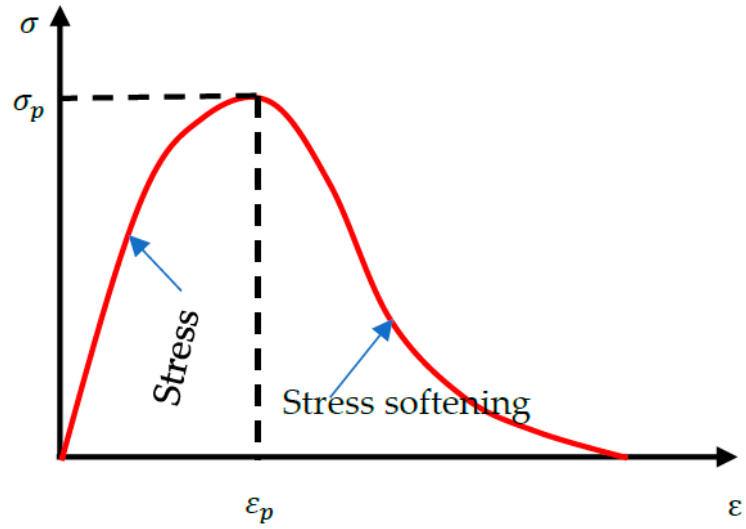

Figure 1. Typical brittle material stress–strain curve. σ, σ_p, ε, ε_p represent the stress loading, peak stress, strain, and peak strain, respectively.

Figure 2 illustrates the HFDEM models, which are comprised of three-node finite elements describing the deformability of the rock material and four-node crack elements describing the fracture propagation. In addition, the four-node crack elements can be distorted in the normal direction, causing tensile failure (mode-I fracture), and the tangential direction, causing shear failure (mode-II fracture). Figure 2b–d demonstrate the model under tension, shear, and combined tension and shear condition, respectively, while the corresponding stress opening/sliding curves are illustrated in Figure 3.

In HFDEM, the fractures occur at finite element edges, and the separation of the finite elements induce a bonding stress. The value of the bonding stress is related to the distortion of the four-node elements. Equation (1) illustrates the four-node elements distortion:

$$\delta = \delta_n \boldsymbol{n} + \delta_s \boldsymbol{t} \tag{1}$$

where $\boldsymbol{n}$ indicates the unit vector's normal direction, while $\boldsymbol{t}$ is that in the tangential direction. δ_n and δ_s are the magnitudes of the the components of δ in the two directions.

Figure 3a indicates the stress-opening relationship for pure mode I fracture, i.e., tensile failure. It should be noted that the opening or sliding of finite elements from the element edges means the distortion of the four nodes crack elements in normal or tangential directions in the following text. As illustrated in Figure 3a, as δ_n increases in the normal direction, the stress increases. Before the opening reaches δ_{np}, i.e., $0 \le \delta_n < \delta_{np}$, the stress is increasing but no crack occurs. When the opening reaches a critical value δ_{np}, i.e., $\delta_n = \delta_{np}$, the stress reaches the tensile strength σ_t and crack occurs. With the separation of the finite element edges continues, the opening is δ_{nu}, i.e., $\delta_n > \delta_{nu}$, the finite elements are completely separated from the element edges, i.e., and the four-node crack element among the finite elements is removed. Thus, the tensile fracture has completed.

During the tensile rock fracture process, the normal direction bonding stress can be calculated using Equation (2):

$$\sigma_n = \begin{cases} \left[2 \cdot \frac{\delta_n}{\delta_{np}} - \left(\frac{\delta_n}{\delta_{np}}\right)^2\right] \cdot \sigma_t & if \quad 0 \le \delta_n \le \delta_{np} \\ f(D) \cdot \sigma_t & if \quad \delta_{np} \le \delta_n \le \delta_{nu} \\ 0 & if \quad \delta_n \ge \delta_{nu} \end{cases} \tag{2}$$

In Equation (2), D indicates the damage variable, and the value is between 0 and 1. $f(D)$ is the function from the damage model [18].

G_{f_I} is the fracture energy release rate for governing mode-I fracture and can be calculated using Equation (3):

$$G_{fI} = \int_{\delta_{np}}^{\delta_{nu}} \sigma_n(\delta_n) d\delta_n \tag{3}$$

Figure 3b illustrates the pure mode II fracture process. As Figure 3b illustrates, the shear stress τ increases while the adjacent finite element slides, i.e., $\delta_s < \delta_{sp}$. When the shear stress τ reaches shear strength δ_{sp}, it decreases while the adjacent finite element slides $\delta_s \geq \delta_{sr}$. Eventually, the shear stress τ deceases to a value equal to the pure frictional resistance. Thus, the shear fracture has completed.

Equation (4) shows how to calculate the tangential bonding stress during the mode-II fracture process:

$$x\tau = \begin{cases} 2 \cdot \frac{\delta_s}{\delta_{sp}} \cdot \sigma_c & if \quad 0 \leq \delta_s \leq \delta_{sp} \\ g(D) & if \quad \delta_{sp} \leq \delta_s \leq \delta_{sr} \\ \sigma_n \cdot tan(\varnothing_f) & if \quad \delta_s \geq \delta_{sr} \end{cases} \tag{4}$$

In Equation (4), the damage function $g(D)$ can be found from literature [18], and $\varnothing_f$ is the angle of the joint fraction.

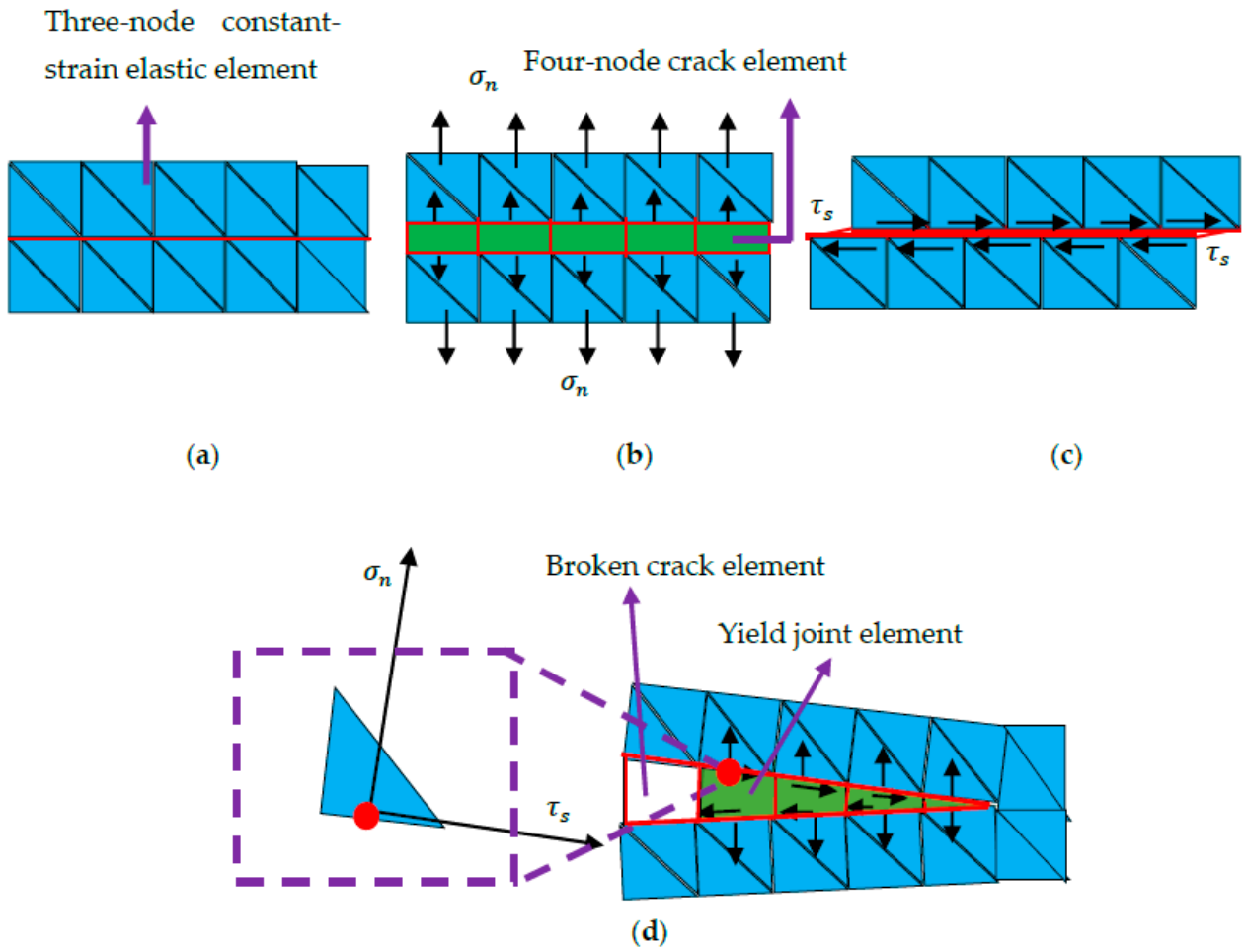

Figure 2. Hybrid Finite–discrete fracture model (red line represents edges of joint elements while the black line represents the edge of the finite elements): (**a**) Without stress; (**b**) Under tension condition; (**c**) Under shear condition; (**d**) Under both tension and shear condition.

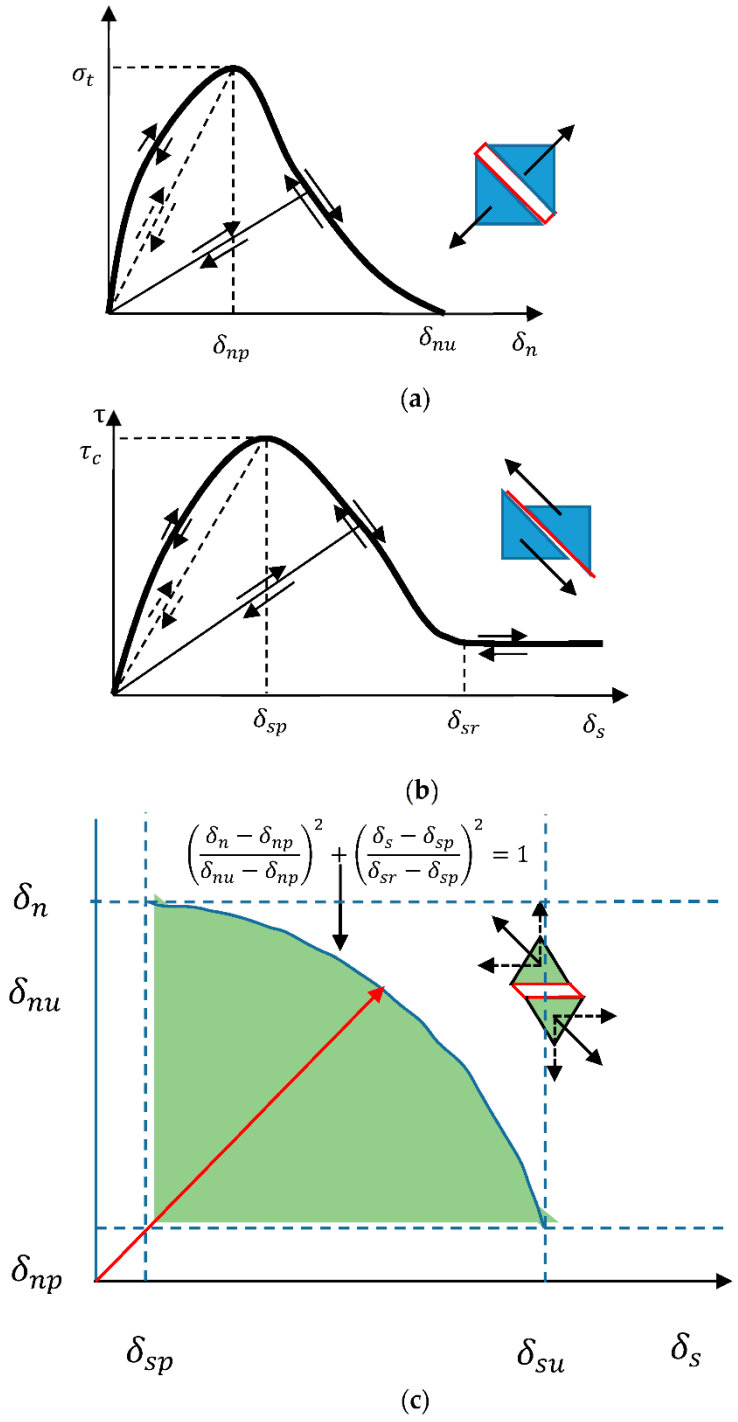

Figure 3. Bonding stress and opening or sliding displacement: (**a**) Mode-I; (**b**) Mode-II; (**c**) Mixed mode I–II.

The residual sliding displacement δ_{sr} is determined by the fracture energy release rate $G_{f_{II}}$ and can be expressed by Equation (5):

$$G_{fII} = \int_{\delta_{sp}}^{\delta_{sr}} [\tau(\delta_s) - \tau_r] d\delta_s \quad (5)$$

In most cases, the rock mass is not subjected to a pure tensile or shear stress. Thus, the rock fractures induced by both tensile and shear stress should be considered in the HFDEM. Equation (6) is the criterion. When the criterion is satisfied, mixed mode I–II occurs:

$$\left(\frac{\delta_n - \delta_{np}}{\delta_{nu} - \delta_{np}}\right)^2 + \left(\frac{\delta_s - \delta_{sp}}{\delta_{sr} - \delta_{sp}}\right)^2 \geq 1 \quad (6)$$

2.2. The Straite Rate Effect

As the strain rate varies in a wide rage and significantly influences the rock properties and final results, the strain rate or loading rate should be taken into account. In this research, Equation (7) is employed to regulate the fracture process under various strain rates. The equation is obtained from the experimental research conducted by Zhao(2000) [19]:

$$\sigma_{cd} = A \cdot log\left(\frac{\dot{\sigma}_{cd}}{\dot{\sigma}_c}\right) + \sigma_c \quad (7)$$

where σ_{cd} is the dynamic uniaxial compressive strength (MPa), $\dot{\sigma}_{cd}$ is the dynamic loading rate (MPa/s), σ_c is the uniaxial compressive strength at the quasi-static loading rate (MPa), $\dot{\sigma}_c$ is the quasi-static loading rate (MPa/s) and A is the parameter related to different materials.

In the HFDEM, the fracture behaviour of rock under dynamic loading can be modelled according to the fracture model mention above and the increase in rock strengths can be obtained according to Equation (7).

3. Calibration of HFDEM

In this section, two typical rock mechanism tests are employed to calibrate the HFDEM in modelling dynamic rock behaviours.

3.1. Numerical Modelling UCS Test78

On the basis of the ISRM (1979) [20] suggested method, the geometry of the UCS test is illustrated in Figure 4a. The width of the UCS sample is 54 mm while the length is 135 mm. Figure 4b show the numerical model, which is discretized using three-mode finite elements. Table 1 gives the rock parameters. The loading plate properties are tensile strength 100×10^{16} Mpa, compressive strength 100×10^{16} Mpa, Young's modulus 200 Gpa, surface friction coefficient 0.1, and Mode-I and Mode-II fracture energy release 3×10^{12} Nm^{-1}. During the test, the loading rates of 1 m/s is applied on the two loading plates on the vertical direction while the plates are fixed in the horizontal direction. The loading rate, i.e., 1 m/s, is much higher than those in the laboratory test, which is about 0.05 mm/s. The reason to use a high loading rate is to significantly decrease computational time, as the increase in the loading rate can dramatically decrease the computational time. The processor used for the simulation is inter(R) Core (TM) i7-4500U with CPU from 1.80 GHz to 2.40 GHz, while the installed memory (RAM) is 16.0 GB. The system installed in the computer is Windows 8.1 with system type 64-bit Operating System. The current loading rate, i.e., 1 m/s, can reduce at least one order of magnitude in terms of the calculation time compared with loading rate for static tests in laboratory, i.e., around 0.05 m/s.

Figure 5 illustrates the fracture process. The red colour indicates the tensile fractures while the blue colour indicates shear fractures.

As the loading plates contact the rock sample, stress concentrations can be observed immediately, as shown in Figure 5a(A). The stresses induced from two sides of the specimen continue to propagate (Figure 5a(B)) when the plate moves. Then, the stresses from the two sides interact (Figure 5a(C)) to form a uniform stress distribution (Figure 5a(D)). The force-loadings increase dramatically and reach their peaks when the plates have moved 44 μm (Figure 6a,b(A–E)). Meanwhile, a small shear crack can be seen in Figure 5b(E).

Then, more shear cracks initiate and propagate in the specimen (Figure 5b(F,G)). While the force-loadings drop dramatically (Figure 6a,b(F,I)), two almost parallel shear cracks are produced (Figure 5b(I)). Finally, the force-loadings drop to the bottom (Figure 6a,b(J)). Thus, the rock specimen losses its ability to carry loads, and more cracks are generated, including both shear failure (in blue colour) and tensile failure (Figure 5b(J)).

The uniaxial compressive strength can be calculated as:

$$\sigma_c = \frac{P_{Max}}{A} = \frac{21.5 \times 10^6}{54 \times 10^{-3} \times 1} = 398 \text{ MPa} \quad (8)$$

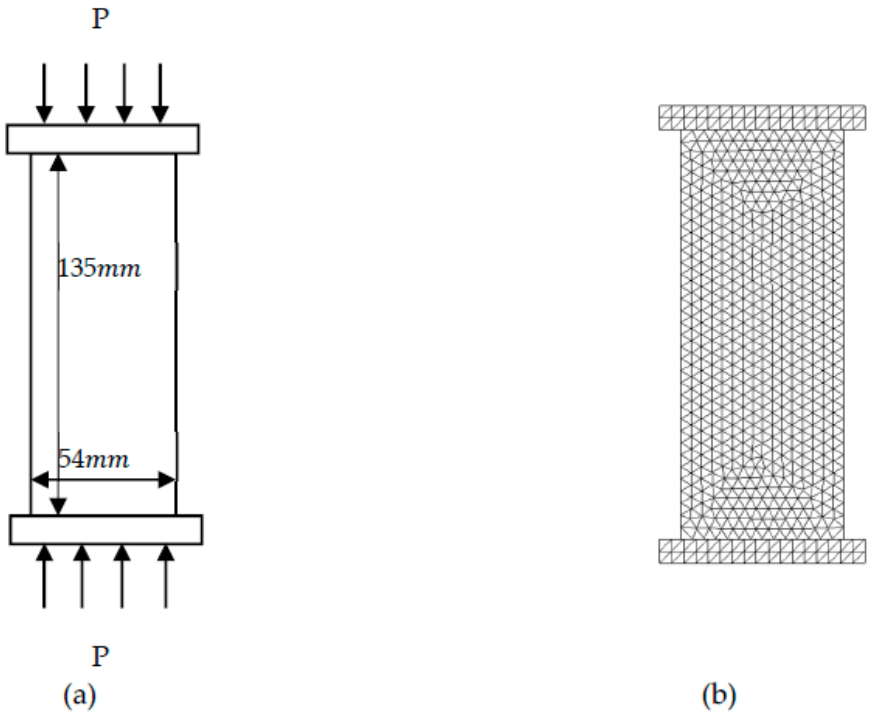

Figure 4. Geometrical and numerical model of uniaxial compression test: (**a**) Geometrical model; (**b**) Numerical model.

Table 1. Rock properties for the hybrid Finite–discrete models.

Symbols	Properties	Values	Units
E	Young's modulus	60	GPa
ν	Poisson's ration	0.26	N/A
ρ	Density	2600	Kgm^{-3}
σ_t	Tensile strength	20	MPa
σ_c	Compressive Strength	200	MPa
$\varnothing$	Internal friction coefficient	30	°C
u	Surface friction coefficient	0.1	N/A
G_{fI}	Mode-I Fracture energy release	50	Nm^{-1}
G_{fI}	Mode-II Fracture energy release	250	Nm^{-1}

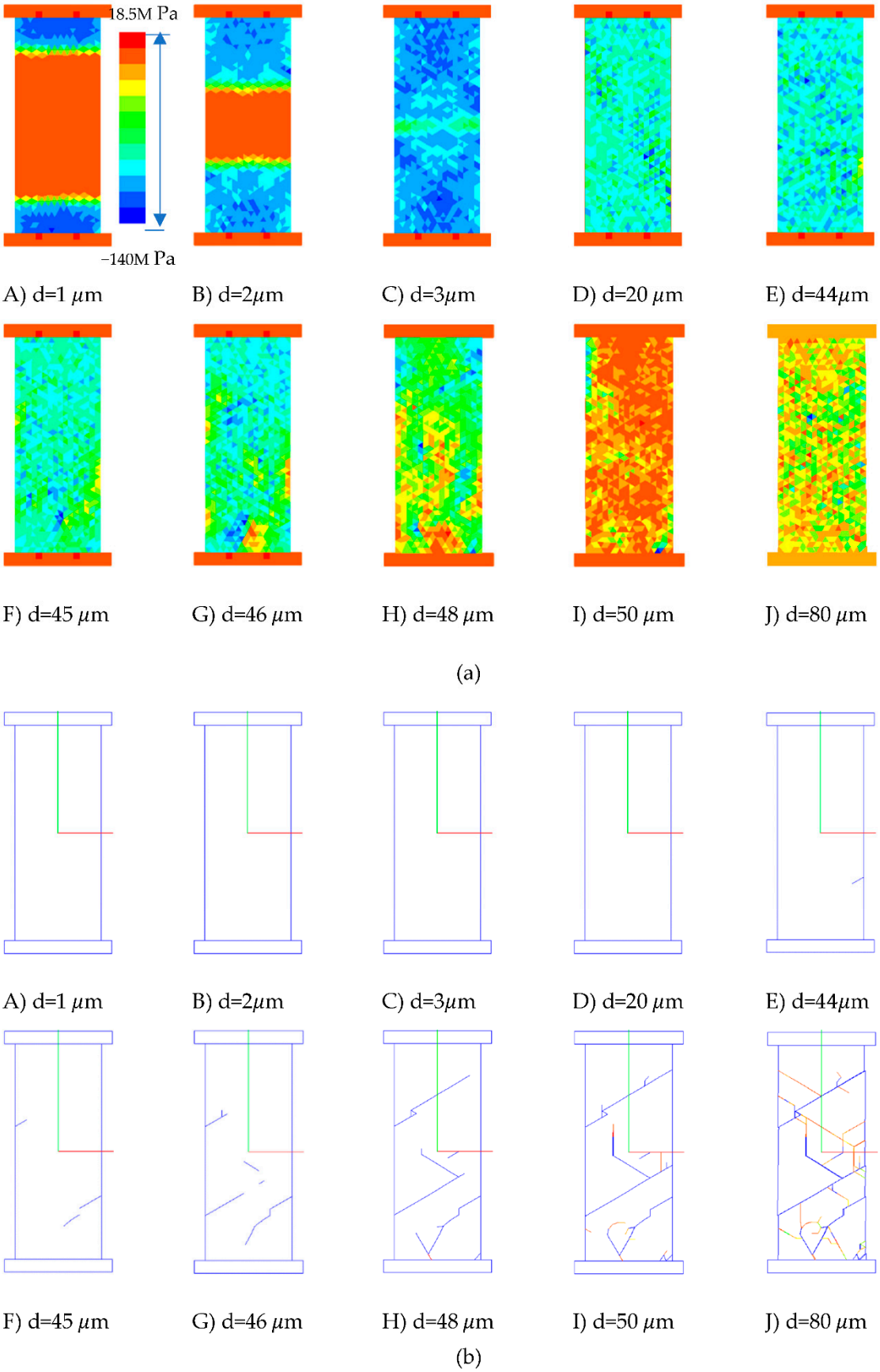

Figure 5. HFDEM modelling UCS test: (**a**) Minor principal stress; (**b**) fracture process.

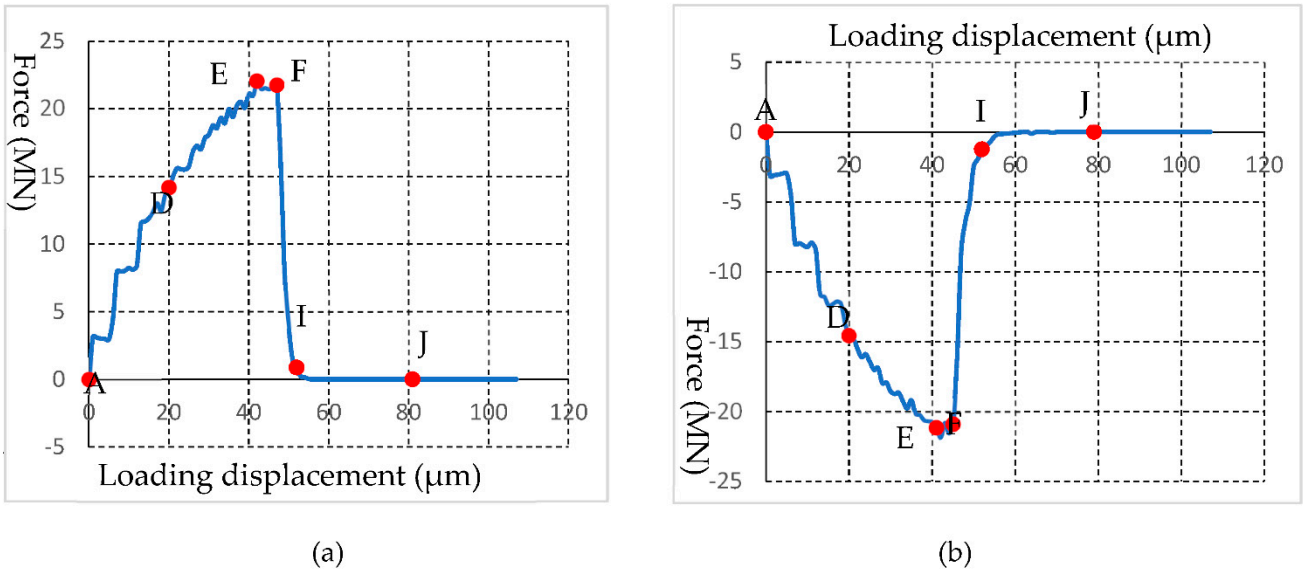

Figure 6. HFDEM obtained curves during the UCS test: (**a**) Top plate force; (**b**) Bottom plate force.

3.2. Numerical Modelling Rock Fracture during BTS Tests

Figure 7a shows the geometrical model for the BTS test, while Figure 7b illustrated the numerical model. For the BTS geometrical model, the diameter is 54 mm. The loading plate moves at the speed of 1 m/s, while the stress is radially applied on the strip with a radian of 2α. In the numerical model, the disc is meshed using the three-node finite element. The sample and loading plate parameter are the same as that used for the UCS test. The tensile strength can be obtained according to Equation (9) [21]:

$$\sigma_t = \frac{2P}{\pi D t} \tag{9}$$

where P is the applied load, D is the diameter, t is specimen thickness.

The analytical solutions for the stress on the vertical diameter can be calculated according to Equations (10) and (11), which are given by Hondros (1959) [22]:

$$\sigma_{xx} = \frac{P}{\pi R t \alpha}\left\{\frac{\left[1-\left(\frac{r}{R}\right)^2\right]Sin2\alpha}{1-2\left(\frac{r}{R}\right)^2 Cos2\alpha+\left(\frac{r}{R}\right)^4} - tan^{-1}\left[\frac{1+\left(\frac{r}{R}\right)^2}{1-\left(\frac{r}{R}\right)^2}tan(\alpha)\right]\right\} \tag{10}$$

$$\sigma_{yy} = -\frac{P}{\pi R t \alpha}\left\{\frac{\left[1-\left(\frac{r}{R}\right)^2\right]Sin2\alpha}{1-2\left(\frac{r}{R}\right)^2 Co2\alpha+\left(\frac{r}{R}\right)^4} + tan^{-1}\left[\frac{1+\left(\frac{r}{R}\right)^2}{1-\left(\frac{r}{R}\right)^2}tan\alpha\right]\right\} \tag{11}$$

where r, 2α, σ_{xx} and σ_{yy} indicate the means in Figure 7a, i.e., the distance from the disc center, radian, horizontal stress, and vertical stress on the vertical diameter, respectively.

Figure 8a shows the stress propagation process during the BTS test with plates move at 1 m/s. Figure 8b shows the stress fracture evolution process. During the test, high stress is firstly produced from the contact areas (Figure 8a(A)). Then, the two stresses propagate towards the centre of the disc (Figure 8a(B,C)). As shown in the Figure, the forces from the top and bottom plates increases sharply (Figure 9a,b(A–C)). A fracture firstly initiates from the disc's centre (Figure 8b(C)) and propagates to the disc's top and bottom (Figure 8b(C)). With the plates moving, the stress is mainly distributed in the centre line of the disc (Figure 8a(D–F)). As the fracture from the centre of the disc reaches the disc top and bottom, shear cracks are observed due to the stress concentrations. After the stress

research their peaks, it drops dramatically to the bottom (Figure 9a,b(D–G)), and the disc is separated to two halves (Figure 8b(G)).

$$\sigma_{t1} = \frac{2P_{Max}}{\pi Dt} = \frac{2 \times 2.8698}{3.14 \times 0.054 \times 1} = 34 \text{ MPa} \quad (12)$$

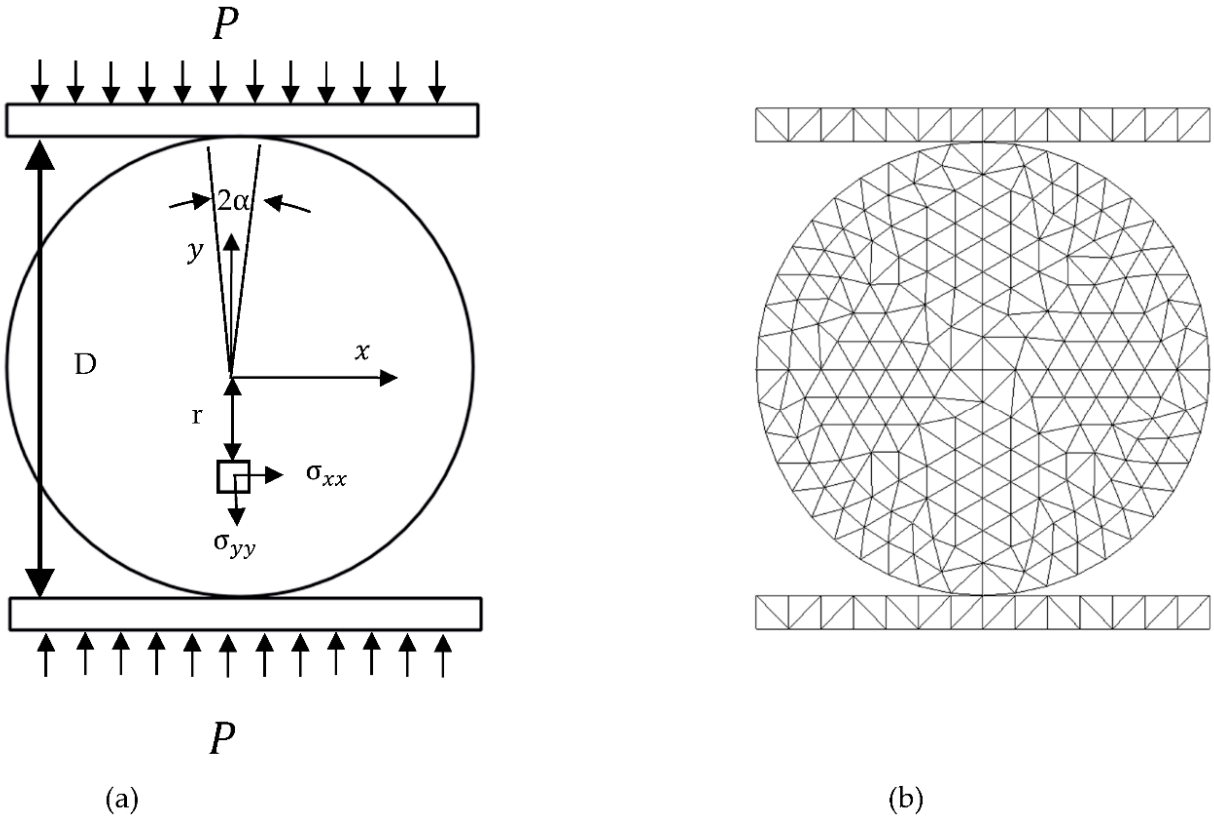

Figure 7. HFDEM model for BTS test: (**a**) Geometrical model; (**b**) Numerical model.

The tensile strength obtained by HFDEM is 34 MPa, while the input value of static tensile strength is 20 MPa. Thus, the HFDEM can well model the strain rate influence on the dynamic strength of rock.

Figure 10 illustrates the stress distribution obtained both by the analytical method and the HFDEM modelling. In addition, the $2P/\pi Dt$ is used to normalize the stress distribution for better comparison. It can be found from Figure 10 that the HFDEM results agree with the theoretical solution except that the theoretical solution at the loading points is much higher than the modelled result. The reason for having a relatively lower force at the loading points for numerical results maybe because of the tensile and shear failure, which makes the specimen gradually lose its bearing capability.

Figure 11 compares the HFDEM modelled and experimental fracture pattern [23,24]. The two fracture patterns are similar, and they both fracture in the in the vertical direction.

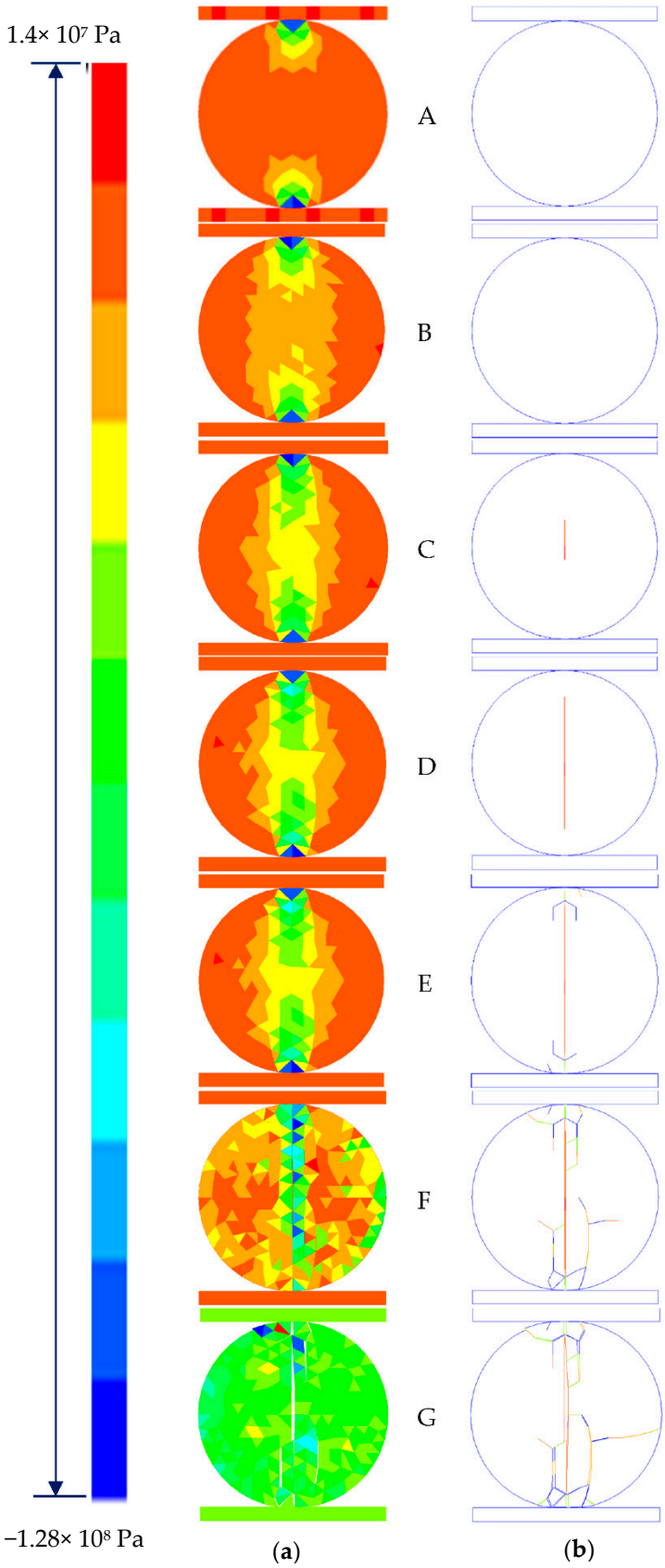

Figure 8. HFDEM modelling of Brazilian tensile strength tests: (**a**) Minor principal stress; (**b**) fracture propagation; (**A**) d = 1 μm; (**B**) d = 20 μm; (**C**) d = 33.5 μm; (**D**) d = 39 μm; (**E**) d = 41 μm; (**F**) d = 58 μm; (**G**) d = 166 μm.

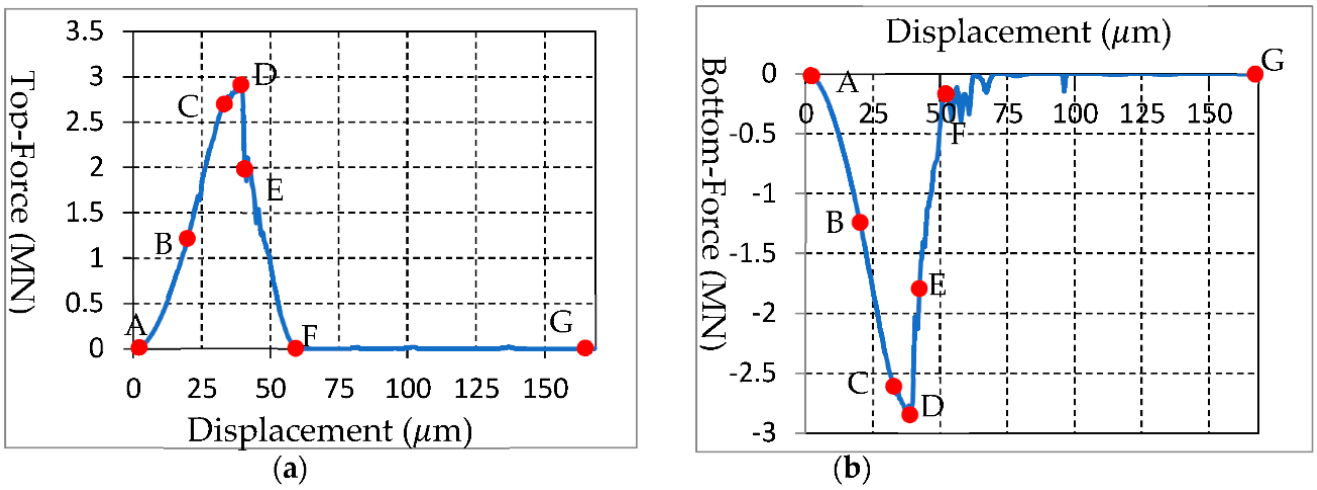

Figure 9. HFDEM obtained curves during BTS test: (**a**) force from the top plate; (**b**) force from the bottom plate.

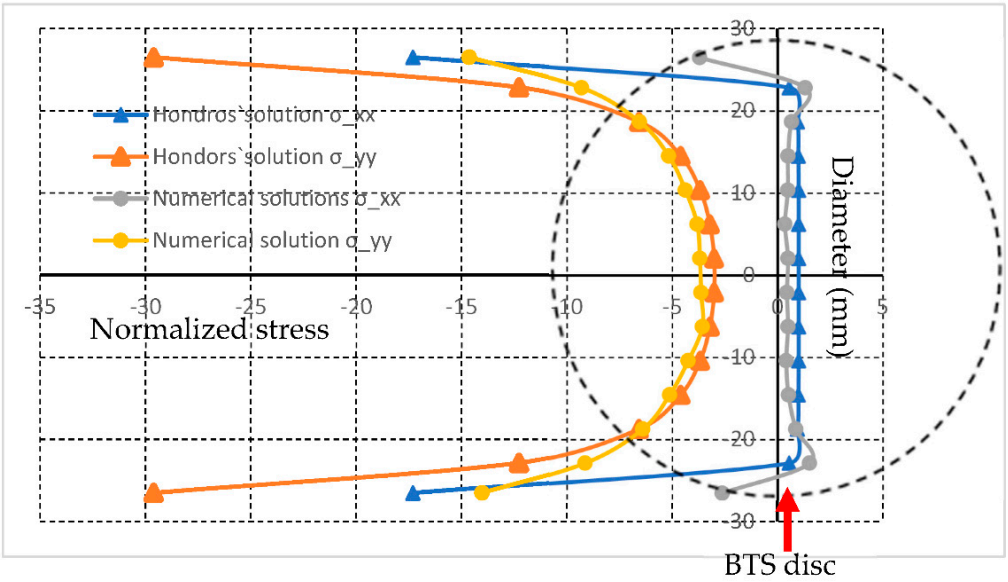

Figure 10. Comparison of the HFDEM obtained results with analytical solutions in terms of stress distribution.

Figure 11c indicates a typical failure pattern for the BTS under loading. It can be seen that the tensile fracture occurs in the vertical diameter, and it separates the sample into two halves, while shear fractures occur at the top and bottom loading contacts due to the compressive stresses concentrating at the contact areas.

To sum up, HFDEM has well modelled the crack process during the BTS test. The main characteristics are captured and show good agreements with typical brittle material under compression. The obtained tensile strength indicates that the HFDEM can capture the effects of the loading rate on rock behaviour.

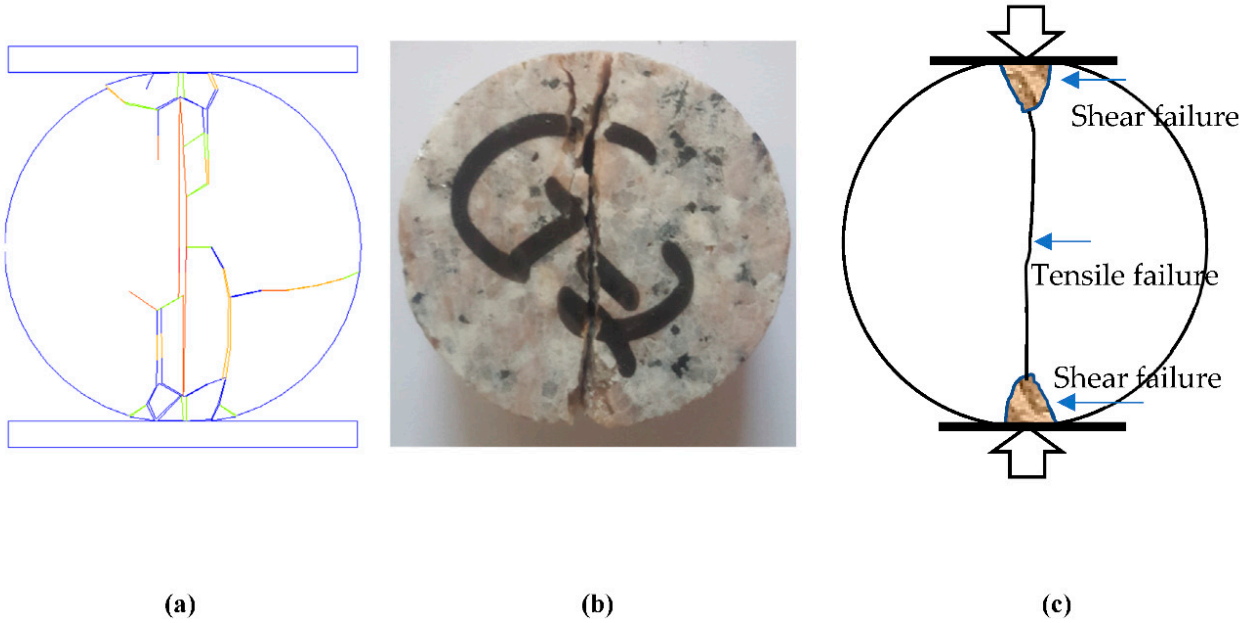

Figure 11. Comparison of HFDEM result with results from the literature: (**a**) HFDEM result; (**b**) experimental result [25]; (**c**) Typical rock failure pattern [23,24].

4. HFDEM Modelling Three Conventional Bending Tests

The HFDEM is used to model the three conventional bending tests in this section to obtain the three fracture models. Figure 12 depicts the geometrical modes for the symmetrical three-point bending (3PB) test, the four-point bending (4PB) test, and the asymmetrical three-point bending (A3PB) test.

The 3PB test, as shown in Figure 12a, is used to obtain the mode-I fracture toughness, and Equation (13) [26] can be used to calculate the values:

$$K_{IC} = \frac{P_{Max} L\sqrt{a}}{BD^2}\left[2.9 - 4.6\left(\frac{a}{D}\right) + 21.8\left(\frac{a}{D}\right)^2 - 37.6\left(\frac{a}{D}\right)^3 + 38.7\left(\frac{a}{D}\right)^4\right] \quad (13)$$

In the above equation, K_{IC} indicates the fracture toughness for mode-I fracture, and P_{Max} indicates the peak load. L, a, B, and D are the distances between the supporting points, notch length, thickness, and width of the beam, respectively.

The 4PB test, as shown in Figure 12b, is used to simulate the shear fracture process and obtain the fracture toughness for mode-II fracture. During the test, two rigid rolls on the top of the beam will move at the same speed for applying loads on the beam. Equation (14) is the analytical solution for mode II fracture toughness [27].

$$K_{IIC} = \frac{P_{Max}}{B\sqrt{D}}\left[\frac{L_2 - L_1}{L_2 + L_1}\right]\left[1.44 - 5.08\left(\frac{a}{D} - 0.507\right)^2\right]\sec\left[\frac{\pi a}{2D}\right]\sqrt{sin\left[\frac{\pi a}{2D}\right]} \quad (14)$$

In Equation (14), K_{IIC} and P_{Max} indicate the mode-II fracture toughness and Peak load, respectively. B and D are the thickness and width of the beam, respectively. L_1 and L_2 are the distances as illustrated in Figure 12. a is the height of the notches as shown in Figure 12.

The A3PB test (Figure 12c) is used to model the fracture process for mixed mode I–II. The fracture toughness for this mixed model can be calculated as follows [28]:

$$K_I = \frac{P_{max}}{B\sqrt{D}} f_1(a/D, 2L_1/L) \quad (15)$$

$$K_{II} = \frac{P_{max}}{B\sqrt{D}} f_2(a/D, 2L_1/L) \quad (16)$$

In Equations (15) and (16), K_I means the mode-I stress intensity factor, and K_{II} indicates the mode-II stress intensity factor. $f_1(a/D, 2L_1/L)$ and $f_2(a/D, 2L_1/L)$ are the coefficients, and in this research, the values are 4.180 and 0.675, respectively.

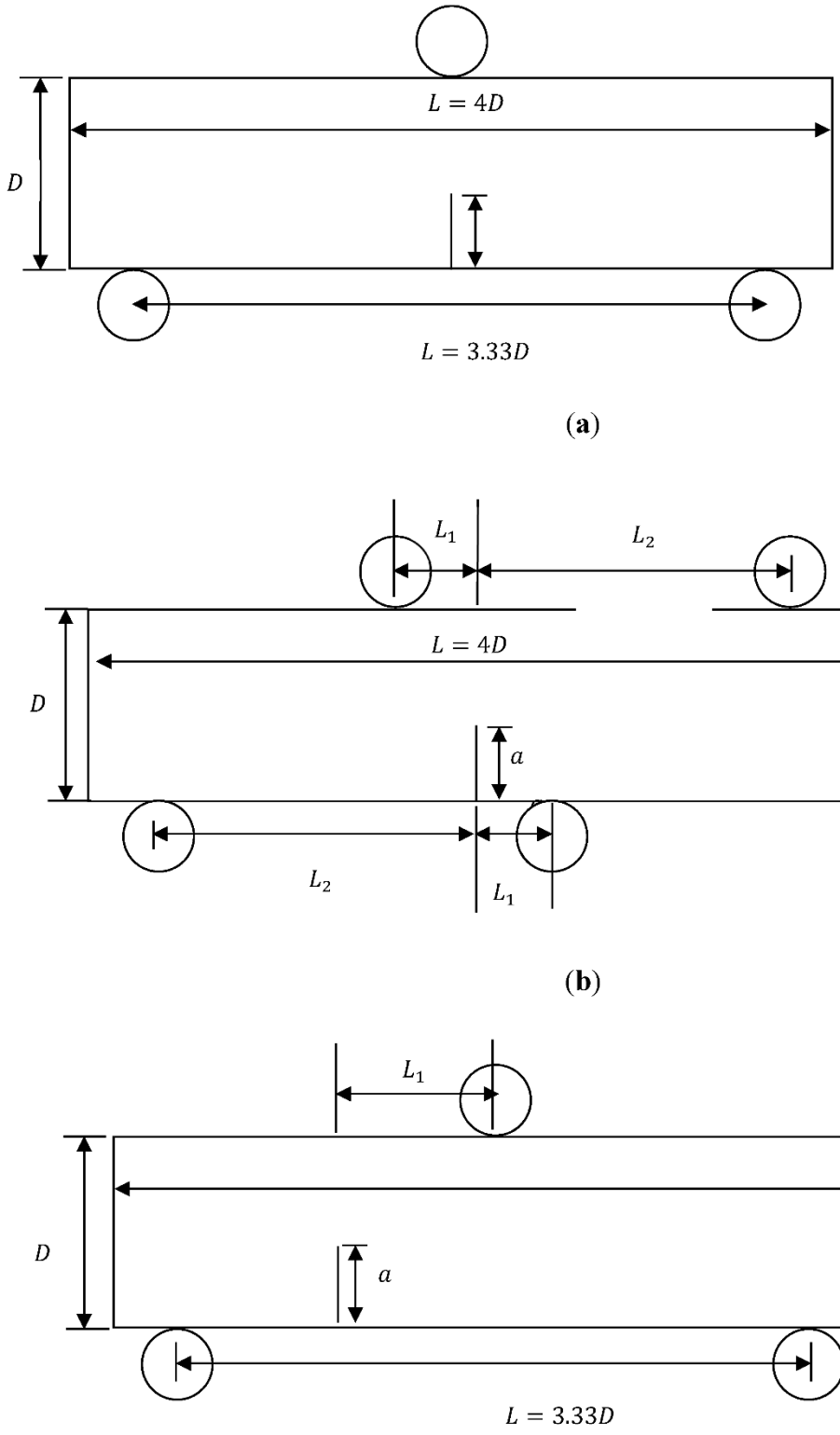

Figure 12. Geometrical mode for 3PB and 4PB tests: (**a**) 3PB test; (**b**) 4PB test; (**c**) Asymmetrical A3PB test.

Figure 13 depicts the numerical modes for the 3PB test, 4PB test, and A3PB test. In Figure 13, triangle elements are employed to discretize the models.

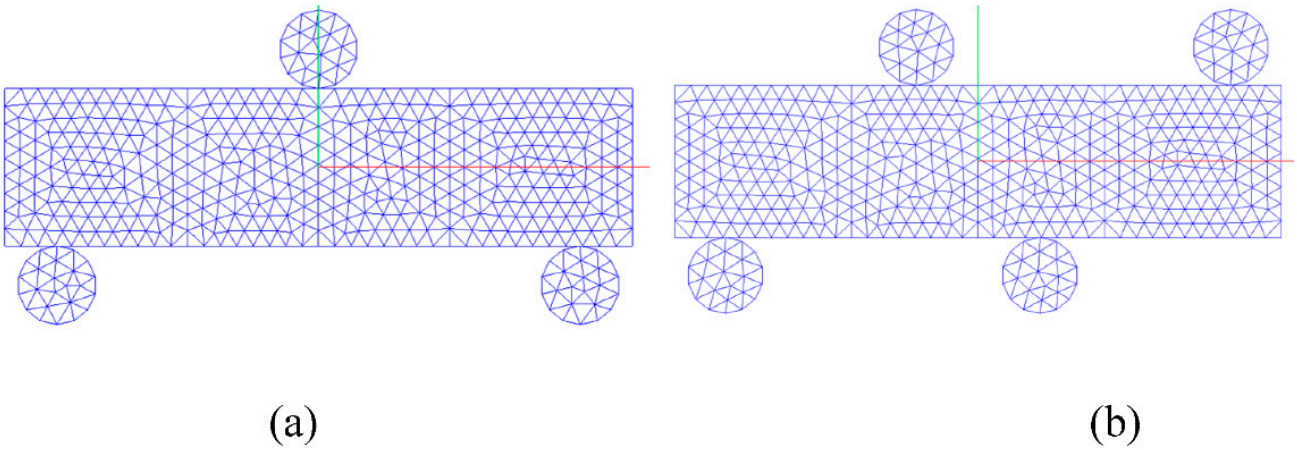

Figure 13. Numerical model for 3PB and 4PB tests: (**a**) 3PB or A3PB tests models; (**b**) 4PB test.

4.1. 3PB Test

Figure 14 visually tests the 3PB modelling under the loading rates of 1 m/s. Figure 15a illustrates the force-loading displacement curves. Figure 15b shows the force-loading crack mount opening displacement (CMOD) curve, while Figure 15b(C) depicts the CMOD time curve. The letters marked on Figure 15 are from Figure 14.

During the tests, the loading rate on the top of the beam moves at 1m/s for the models of the three types of fracture, i.e., tensile, shear, and mixed fractures.

The stress is produced immediately (Figure 15a(A,B)) as the top roll moves. Meanwhile, a crack starts to propagate from the original notch in the beam (Figure 14B). With the moving of the rigid roll, the force continues to increase and finally reaches Point B (Figure 15a(B)). Then, the force begins to drop quickly while the crack from the tip of notch continue to propagate. The Figure 15c(B,C) illustrates that the CMOD continues to increase while the force continues to drop (Figure 15a(B,C)). In the end, the beam is separated into two halves (Figure 14E).

The FDEM modelled 3PB test agree with the literature [29,30] in terms of the fracture propagation process and fracture patterns. The force-loading CMOD curve obtained by FDEM (Figure 15b) show the same characteristic as recorded in the literature [29].

The fracture toughness for mode-I obtained using HFDEM modelling 3PB test can be calculated using Equation (17):

$$K_{IC1} = \frac{697.71 \times 3.33 \times 54\sqrt{0.4 \times 54 \times 10^{-3}}}{1 \times 54^2}\left[2.9 - 4.6 \times 0.4 + 21.8 \times 0.4^2 - 37.6 \times 0.4^3 + 38.7 \times 0.4^4\right] = 19.48\ \text{MPa}\sqrt{m} \quad (17)$$

4.2. Four-Point Bending Test (Pure Mode-II Fracture)

Figure 16 visually shows the HFDEM modelling 4PB test. The loading rate of 1m/s for the two rigid roll is applied on top of the beam. The curve illustrating the relationship between loading force and the displacement is recorded in Figure 17a, while the relationships between the force-loading and the crack mouth opening/sliding displacements are shown in Figure 17b,c. In Figure 17, the curves are marked using alphabets, which referee to those in Figure 16.

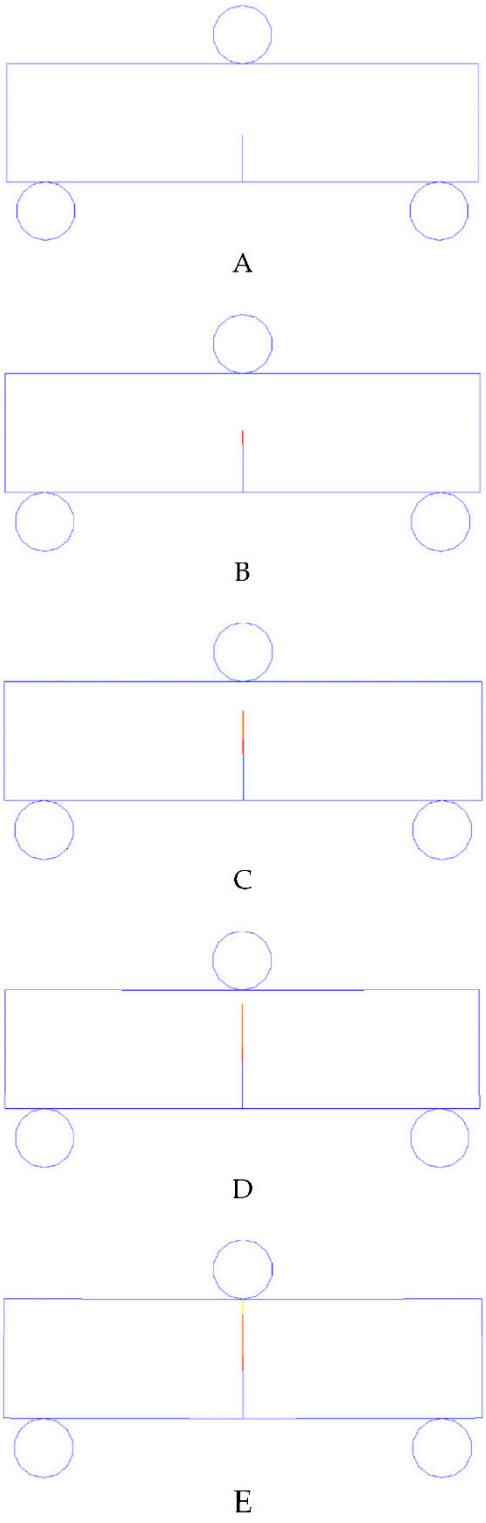

Figure 14. HFDEM modelling rock failure processes in 3PB test. (**A**) Initial state; (**B**) Crack initation; (**C**) Crack propagation; (**D**) Crack continual propagation; (**E**) Crack completion.

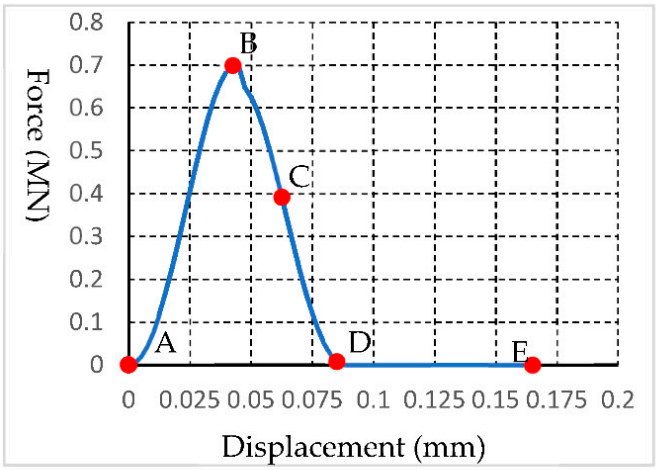

(**a**)

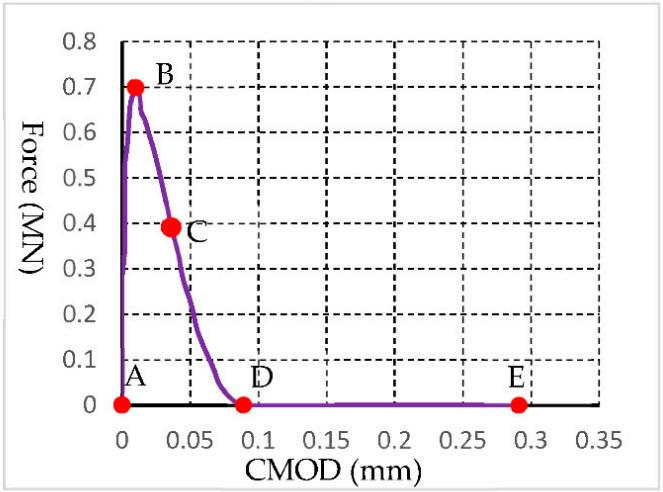

(**b**)

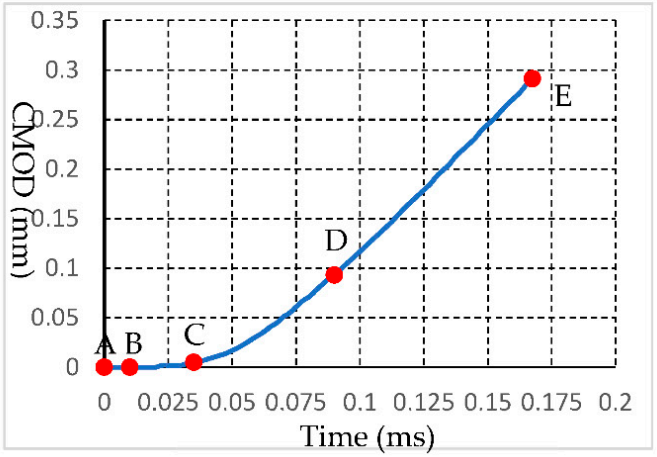

(**c**)

Figure 15. Curves for force-loading with displacement, CMOD, and Time during 3PB test: (**a**) Force-loading displacement curve; (**b**) Force-loading CMOD curve; (**c**) Force-loading CMOD curve.

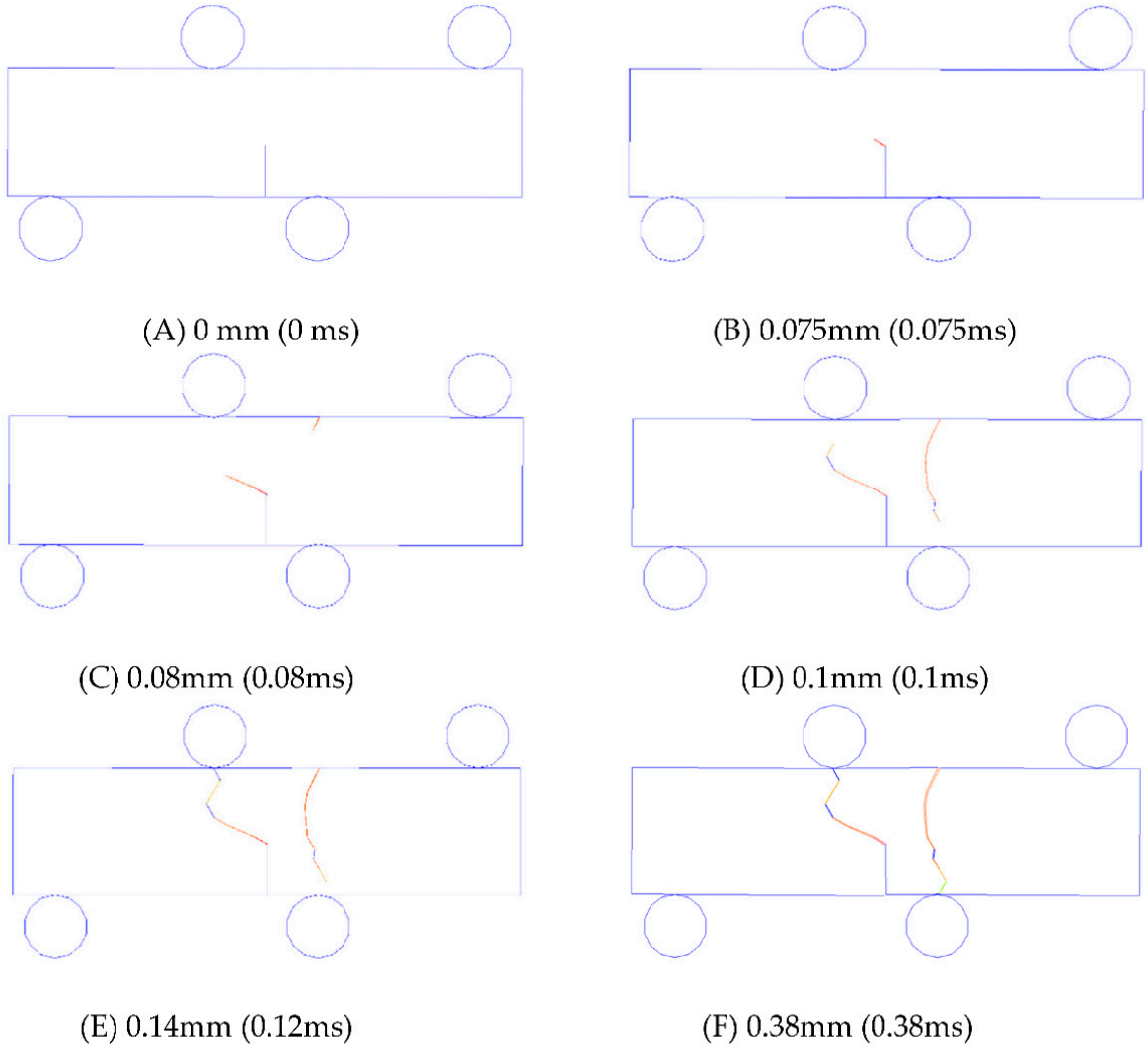

Figure 16. Crack initiation and propagation of 4PB test.

Initially, a notch is placed in the middle of the bottom beam (Figure 16A). As the top roll moves downwards and contact the beam, a force is induced immediately and increases rapidly, although there is a fluctuation (Figure 17a(A,B)). The pre-fabricated notch is slightly opened (Figure 17b(A,B)) while almost no sliding occurs (Figure 17c(A,B)). Then, a crack firstly occurs at the tip of the notch, and it propagates towards the left loading point (Figure 16B). Due to the crack initiated from the prefabricated notch, the force suddenly drops (Figure 17a(A,B)). However, the beam does not completely lose its ability to carry loads. As the top roll moves, the force continually increases (Figure 17a(B,C)). While the crack continues to propagate, a new crack at the top of the beam between the two loading points is induced (Figure 16C). As the two cracks propagate (Figure 16D), the force rapidly increases to its peak (Figure 17a(D)). Meanwhile, the CMOD and CMSD are both increased (Figure 17b,c(B–D)). Then, the force-loading begins to drop quickly (Figure 17a(D,E)) as the crack induced from the tip of notch reaches the left loading point (Figure 16E). Finally, the opening and sliding distances of the crack mouth reach their maximums (Figure 17a(E,F)).

There are two peaks on the force loading–displacement curves. When the crack starts to occur from the tip of the notch, the stress reaches its first peak. Thus, the first peak stress is used to obtain the fracture toughness for mode-II fracture according to Equation (18):

$$K_{IIC1} = \frac{1.21MN}{B\sqrt{D}}\left[\frac{L_2 - L_1}{L_2 + L_1}\right]\left[1.44 - 5.08\left(\frac{a}{D} - 0.507\right)^2\right]\sec\left[\frac{\pi a}{2D}\right]\sqrt{sin\left[\frac{\pi a}{2D}\right]} = 4.979\text{Mpa}\sqrt{m} \quad (18)$$

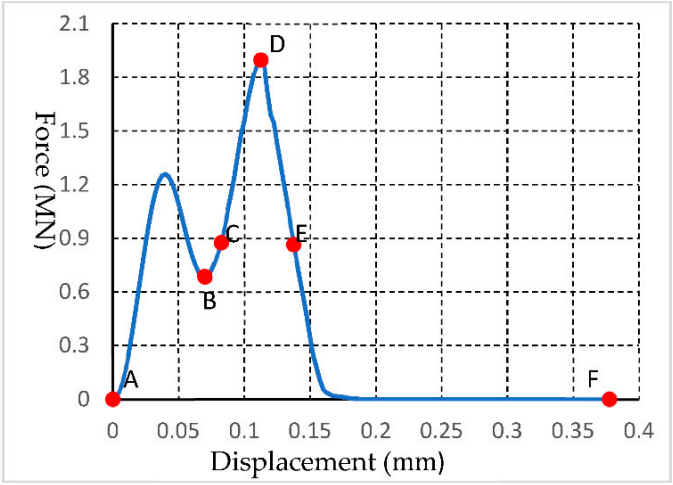

(a)

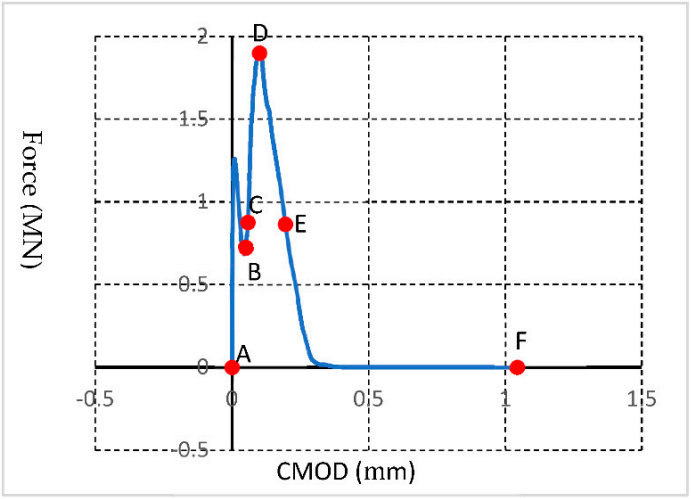

(b)

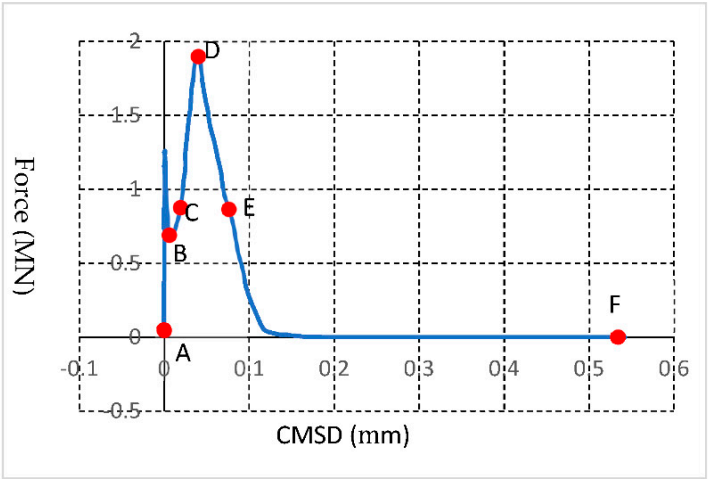

(c)

Figure 17. Force loading related curves for 4PB test: (**a**) Force-loading displacement curve; (**b**) Force-loading CMOD curve; (**c**) Force-loading CMSD curve.

4.3. Asymmetrical Three-Point Bending Test (Mixed-Mode I–II Fracture)

Figure 18 depicts the fracture initiation and propagation process for A3PB, while Figure 19 shows the relationship between the force loading and the displacement. When the loading rolls contact the beam, compressive stresses are produced immediately and increase quickly to their peaks (Figure 19A,B). During this period, no cracks occur in the beam (Figure 18A,B). Then, a crack is produced at the tip of the notch (Figure 18B). As the force loading continues to decrease (Figure 18B–D), a tensile crack is observed at the bottom.

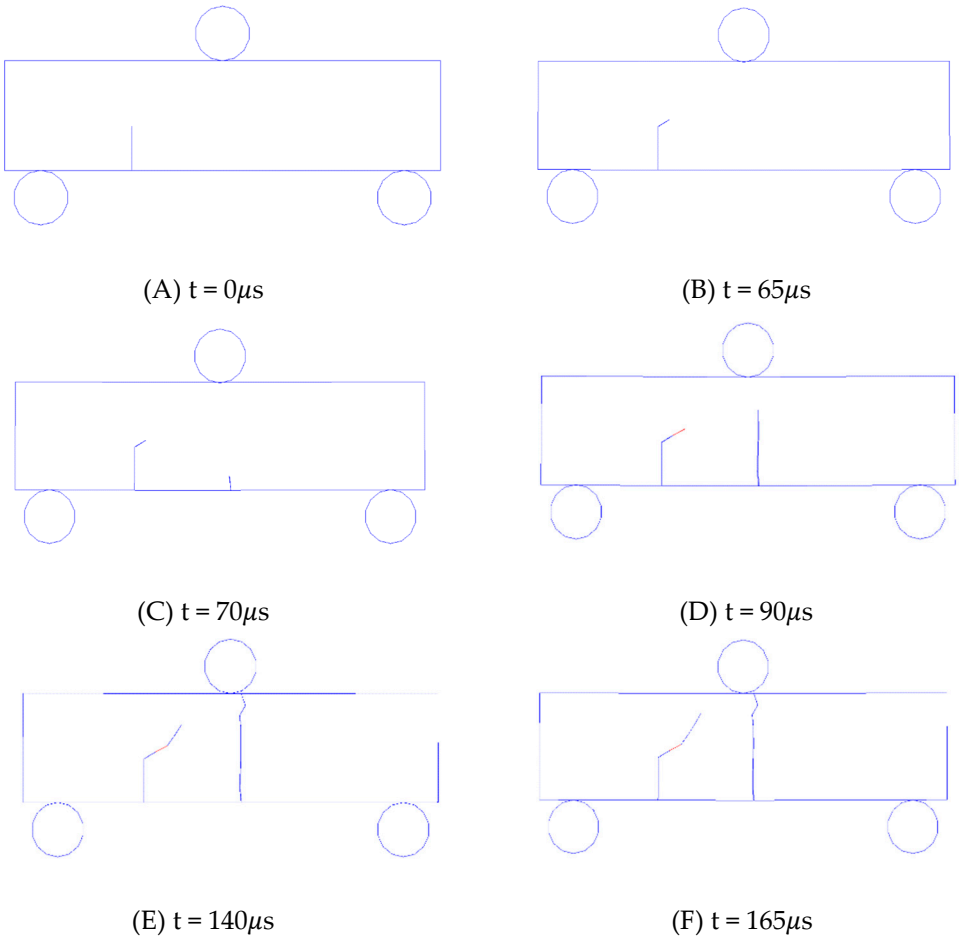

Figure 18. Fracture initiation and propagation for A3PB test.

At the end, the crack from the middle of the bottom beam first reaches the top loading point while the crack from the notch reaches the top beam boundary. According to the colour indication, the crack from the bottom of beam is mainly tensile failure while the crack from the prefabricated notch is mixed by tensile and shear failures. Finally, the beam is divided into two parts by the tensile failure at the middle of the beam (Figure 18F) and the force disappears (Figure 18E,F).

According to the peak force (Figure 19), the fracture toughness for pure mode-I and mode-II can be calculated using Equations (19) and (20), respectively:

$$K_I = \frac{P_{max}}{B\sqrt{D}} f_1(a/D, 2L_1/L) = 15.29 \text{ MPa}\sqrt{m} \quad (19)$$

$$K_{II} = \frac{P_{max}}{B\sqrt{D}} f_2(a/D, 2L_1/L) \quad (20)$$

Figure 20 illustrates the force-loading CMOD/CMSD curves for the A3PB test. The alphabet in Figure 20 corresponds to those in Figure 18. Before 0.022 ms, there is no displacement or sliding at the notch tip according to Figure 20. After that, the CMOD and CMSD begins to increase. According to Figure 19, at point B, the force loading reaches its peak, and the crack occurs. Then, the CMOD and CMSD continue to propagate (Figure 20C–E) while the force loading drops dramatically (Figure 20C–E). Finally, as the crack reaches top boundary (Figure 18F), the CMOD and CMSD reach their maximum (Figure 20F).

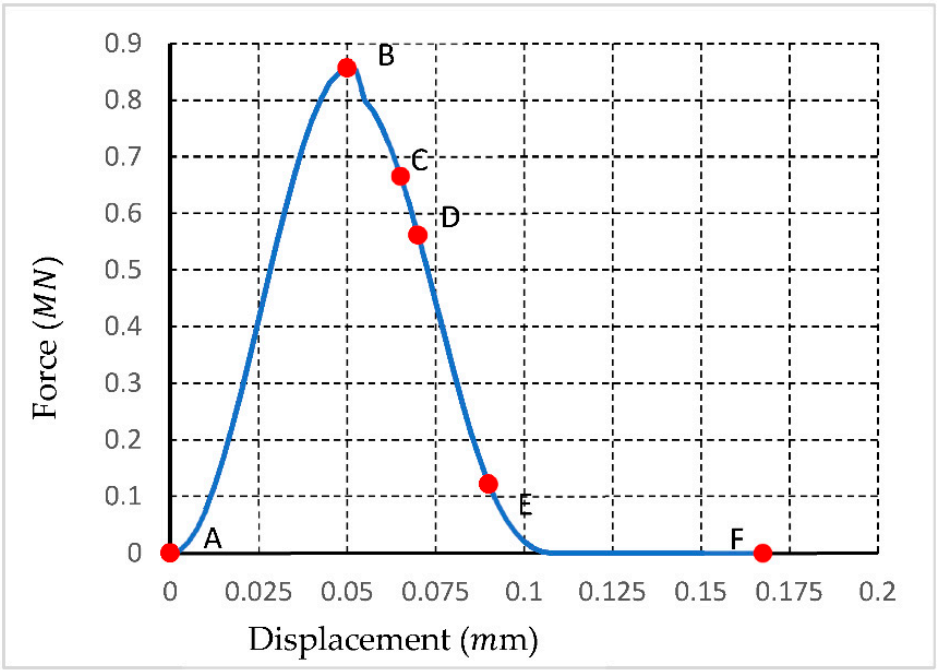

Figure 19. Force-loading displacement for A3PB test.

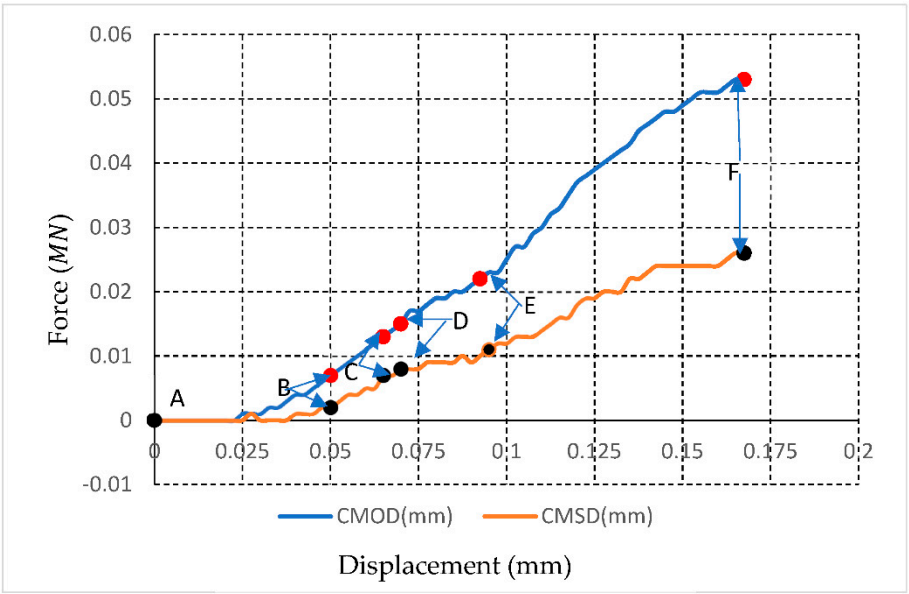

Figure 20. Force-loading CMOD/CMSD curves for A3PB test under the loading rate of 1 m/s.

5. Discussion

5.1. Effect of the Strain Rate Rock Strength

To compare the influence of the loading rate, the increasing factor of dynamic strength (DIF) is employed herein. The DIFs obtained from the HFDEM modelling of the of BTS tests. Figure 21 shows the comparison between the HFDEM obtained DIF with those obtained from literatures.

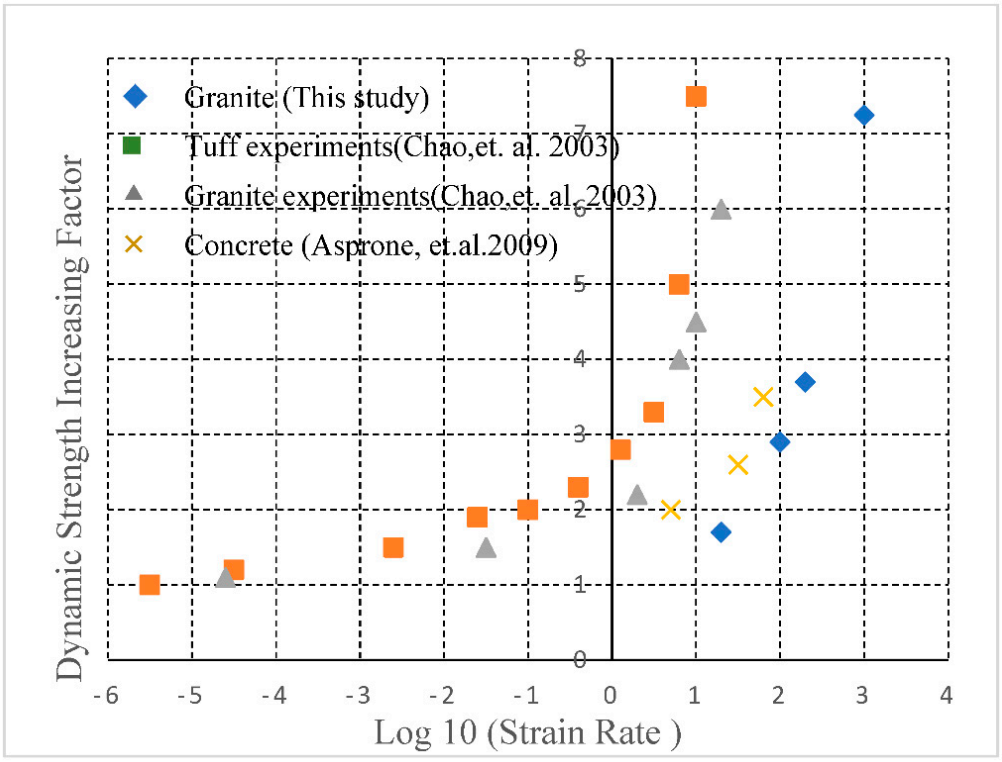

Figure 21. DIFs obtained from HFDEM modelling and literature [31,32].

As shown in Figure 21, the DIFs increase with the strain rate increasing before the strain rate increases to a certain threshold, i.e., 10/s. After the threshold, the rock strengths increase with the strain rate increasing dramatically. As can be seen for the rock strength obtained from the BTS test by the hybrid method, the increasing trends are the same with those obtained from literature. Thus, the HFDEM can reflect the influence of the strain on the dynamic rock strength.

5.2. Loaidng Rate Influence on Rock Toughness

In this section, the loading rate influences on the fracture toughness are studied. Figure 22 illustrates the relationship between the loading rate and the fracture toughness.

One group of the results is from the experimental study [33], while the group of the research is from this study. The fracture toughness is not influenced by the loading rate while the loading rate is smaller than a certain threshold, i.e., 10^5 MPa$\sqrt{m}$/s. After that, the dynamic fracture toughness is obviously related to the the loading rate, and the dynamic fracture dramatically increases with the loading rate. The obtained fracture toughness shows the same characters as shoes in literature as shown in Figure 22. Thus, the HFDEM can capture the rock fracture characters.

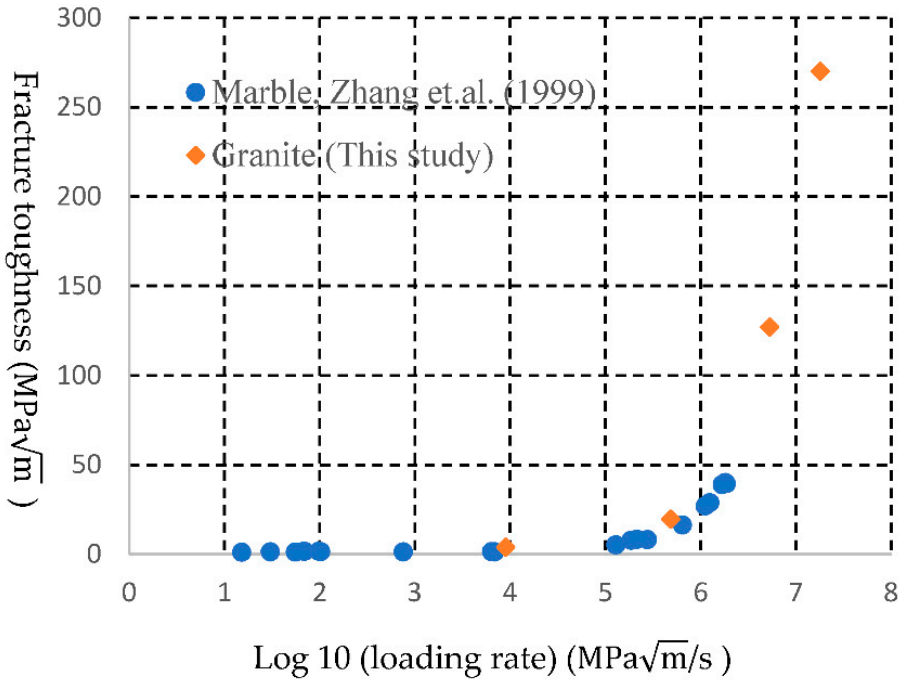

Figure 22. The modelled result and the experimental results [33] comparison t in terms of relationship between the fracture toughness (mode-I) and loading rate.

5.3. Effect of the Mesh Orientation

In the HFDEM, the fracturing of the rock is modelled through the separation of the adjunct finite element in the form of opening or sliding. Thus, the orientation and size of the discretized meshes will definitely affect the fracture pattern.

To illustrate the effect the mesh size, the UCS test model is meshed using structural meshes and modelled by the hybrid method to compare with the modelled result with free meshes. Figure 23 shows the UCS test mode with structural mesh, while Figure 24 indicates the modelled results

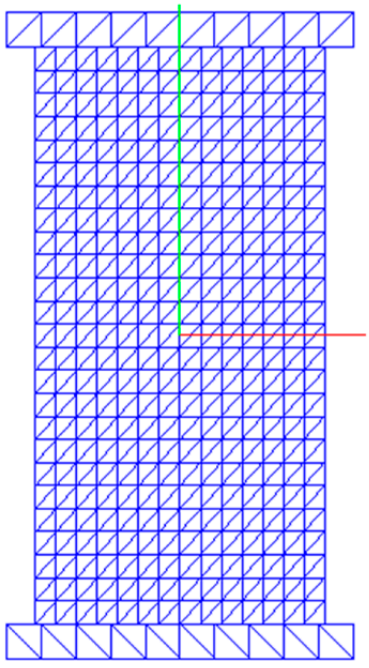

Figure 23. Structural meshed UCS test model.

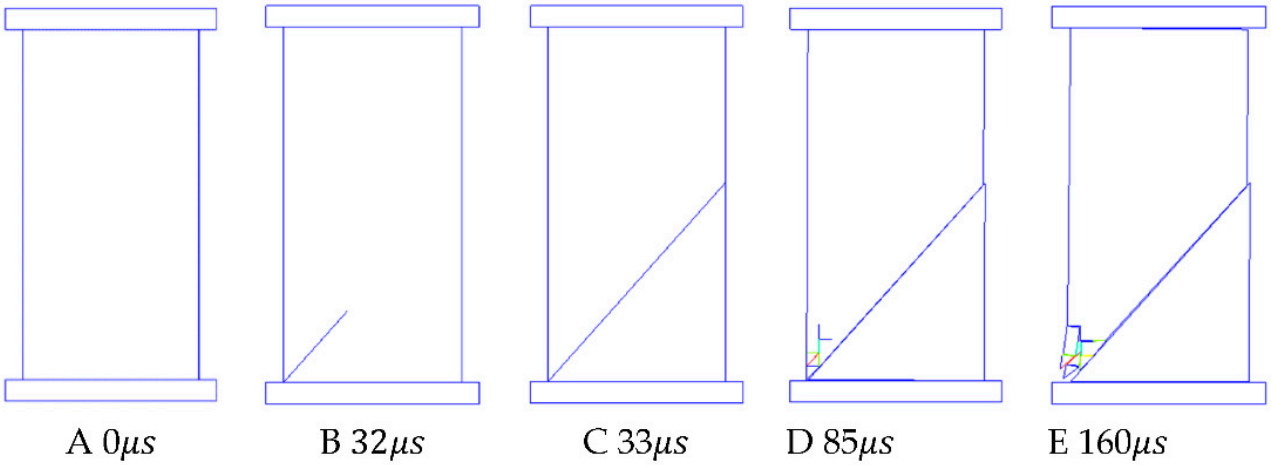

Figure 24. HFDEM modelling fracture process of UCS test.

Initially, a shear fracture occurs at the bottom of the sample as shown in Figure 24B. Then, the crack propagates linearly to the right side of the model as illustrated in Figure 24C. Thus, the specimen is separated into two parts. After that, the two parts of the specimen slide along the new formed shear cracks (Figure 24E). Compared with the modelled result using free mesh in Figure 5, both modelled results have the same characteristics in general, i.e., inclined cracks separating the specimen. However, the fracture patterns are not exactly the same. The size and orientation of the mesh can obviously affect the fracture patterns.

6. Conclusions

This research briefly reviews the numerical method based on their material hypothesis. Among all types of numerical method, the HFDEM is proposed to model the different fracture modes using three conventional point bending tests. Three fracture modes and strain rate effects are taken into account in the HFDEM. Then, the HFDEM is calibrated by modelling UCS and BTS tests. The modelled fracture patterns are similar to experimental results, and the obtained rock strength indicates that the HFDEM can reflect the influence of strain rate. Then, the HFDEM is used to model three conventional bending tests. The various fracture types are modelled, and the corresponding fracture toughness are obtained. It is found that:

The HFDEM is able to simulate various fracture types by the implementation of three fracture modes.

The HFDEM can capture the influence of the strain rate on rock behaviours such as the static and dynamic strength relationships implemented in the HFDEM.

The FDEM is a useful numerical technique for rock engineering since it can simulate the complete rock fracture process and take the influence of the strain rate into account.

Author Contributions: Conceptualization, H.A. and H.L.; methodology, H.A. and H.L.; software, H.A. and H.L.; validation, H.A. and H.L.; writing—original draft preparation, H.A.; writing—review and editing, H.A.; supervision, H.L., S.W. and X.W.; funding acquisition, H.A. All authors have read and agreed to the published version of the manuscript.

Funding: This research was partly funded by the Research Start-up Found for Talent of Kunming University of Science and Technology, grant number KKSY201867017, Fund from the Science and Technology Department of Yunnan Province (202003AC10002), Fund from the Research Centre for Analysis and Measurement KUST (Analytic and Testing Research Centre of Yunnan), grant number 2020T20180040.

Institutional Review Board Statement: Not applicable.

Informed Consent Statement: Not applicable.

Data Availability Statement: The data used to support the findings of this study are available from the corresponding author upon request.

Acknowledgments: The research is partly supported by a two-year visiting PhD scholarship for the first author provided by the China Scholarship Council (CSC). The CSC's support is greatly appreciated. Moreover, the authors would like to thank the anonymous reviewers for their valuable comments and constructive suggestions.

Conflicts of Interest: The authors declare no conflict of interest.

References

1. Donzé, F.V.; Richefeu, V.; Magnier, S.-A. Advances in discrete element method applied to soil, rock and concrete mechanics. State of the art of geotechnical engineering. *Electron. J. Geotech. Eng.* **2009**, *44*, 31.
2. Cundall, P.A. A computer model for simulating progressive, large-scale movement in blocky rock systems. *Proc. Symp. Int. Soc. Rock Mech.* **1971**. Available online: https://www.scienceopen.com/document?vid=838c3a34-fe64-4dc6-8d2b-e9aee0c5b466 (accessed on 19 October 2021).
3. Lisjak, A.; Grasselli, G. A review of discrete modeling techniques for fracturing processes in discontinuous rock masses. *J. Rock Mech. Geotech. Eng.* **2014**, *6*, 301–314. [CrossRef]
4. Mayer, J.M.; Stead, D. Exploration into the causes of uncertainty in UDEC Grain Boundary Models. *Comput. Geotech.* **2017**, *82*, 110–123. [CrossRef]
5. Aliabadian, Z.; Sharafisafa, M.; Nazemi, M.; Khameneh, A.R.; Kazerani, T. Discrete element modeling of wave and fracture propagation in delay time breakage. *Rock Dyn. Appl. State Art* **2013**, *7*, 401–407.
6. Gutiérrez-Ch, J.G.; Senent, S.; Melentijevic, S.; Jimenez, R. Distinct element method simulations of rock-concrete interfaces under different boundary conditions. *Eng. Geol.* **2018**, *240*, 123–139. [CrossRef]
7. Gutiérrez-Ch, J.G.; Senent, S.; Estebanez, E.; Jimenez, R. Discrete element modelling of rock creep behaviour using rate process theory. *Can. Geotech. J.* **2021**, *58*, 1231–1246. [CrossRef]
8. Jing, L. A review of techniques, advances and outstanding issues in numerical modelling for rock mechanics and rock engi-neering. *Int. J. Rock Mech. Min. Sci.* **2003**, *40*, 283–353. [CrossRef]
9. Jing, L.; Hudson, J.A. Numerical methods in rock mechanics. *Int. J. Rock Mech. Min. Sci.* **2002**, *39*, 409–427. [CrossRef]
10. Board, M. *UDEC (Universal Distinct Element Code) Version ICG1. 5*; NUREG/CR-5429-Vol.2; Itasca Consulting Group, Inc.: Minneapolis, MN, USA, September 1989.
11. Cundall, P.A.; Strack, O.D.L. *The Distinct Element Method as a Tool for Research in Granular Material*; University of Minnesota: Minneapolis, MN, USA, 1978.
12. Shi, G.H.; Goodman, R.E. Two dimensional discontinuous deformation analysis. *Int. J. Numer. Anal. Methods Geomech.* **1985**, *9*, 541–556. [CrossRef]
13. Lin, C.T.; Amadei, B.; Jung, J.; Dwyer, J. Extensions of discontinuous deformation analysis for jointed rock masses. *Int. J. Rock Mech. Min. Sci. Geomech. Abstr.* **1996**, *33*, 671–694. [CrossRef]
14. Fukuda, D.; Mohammadnejad, M.; Liu, H.; Dehkhoda, S.; Chan, A.; Cho, S.; Min, G.; Han, H.; Kodama, J.; Fujii, Y. Development of a GPGPU-parallelized hybrid finite-discrete element method for modeling rock fracture. *Int. J. Numer. Anal. Methods Geomech.* **2019**, *43*, 1797–1824. [CrossRef]
15. Munjiza, A.A. *The Combined Finite-Discrete Element Method*; John Wiley & Sons Ltd.: Chichester, UK, 2004.
16. An, H.; Liu, H.; Han, H.; Zheng, X.; Wang, X. Hybrid finite-discrete element modelling of dynamic fracture and resultant fragment casting and muck-piling by rock blast. *Comput. Geotech.* **2017**, *81*, 322–345. [CrossRef]
17. Mahabadi, O.K.; Grasselli, G.; Munjiza, A. Y-GUI: A graphical user interface and pre-processor for the combined finite-discrete element code, Y2D, incorporating material heterogeneity. *Comput. Geosci.* **2010**, *36*, 241–252. [CrossRef]
18. Liu, H.; Kou, S.; Lindqvist, P.-A.; Tang, C. Numerical studies on the failure process and associated microseismicity in rock under triaxial compression. *Tectonophysics* **2004**, *384*, 149–174. [CrossRef]
19. Zhao, J. Applicability of Mohr–Coulomb and Hoek–Brown strength criteria to the dynamic strength of brittle rock. *Int. J. Rock Mech. Min. Sci.* **2000**, *37*, 1115–1121. [CrossRef]
20. Bieniawski, Z.T.; Bernede, M.J. Suggested methods for determining the uniaxial compressive strength and deformability of rock materials: Part 1. Suggested method for determination of the uniaxial compressive strength of rock materials. *Int. J. Rock Mech. Min. Sci. Geomech. Abstr.* **1979**, *16*, 137. [CrossRef]
21. Timoshenko, S.P.; Goodier, J.N. *Theory of Elasticity*; McGraw-Hill: New York, NY, USA, 1970.
22. Hondros, G. The evaluation of Poisson's ratio and the modulus of materials of a low tensile resistance by the Brazilian (indirect tensile) test with particular reference to concrete. *Aust. J. Appl. Sci.* **1959**, *10*, 243–268.
23. Li, D.; Wong, L.N.Y. The Brazilian disc test for rock mechanics applications: Review and new insights. *Rock Mech. Rock Eng.* **2013**, *46*, 269–287. [CrossRef]
24. Hobbs, D.W. The tensile strength of rocks. *Int. J. Rock Mech. Min. Sci. Geomech. Abstracts.* **1964**, *1*, 385–396. [CrossRef]
25. An, H.; Liu, H.; Wang, X.; Shi, J.; Han, H. Hybrid continuum-discontinuum modelling of rock fracutre process in Brazilian tensile strength test. *Civ. Eng. J.* **2017**, *26*, 237–249. [CrossRef]

26. Brown, W.F.; Srawley, J.E. *Plain Strain Fracture Toughness Testing of High Strength Metallic Materials*; ASTM International: West Conshohocken, PA, USA, 1966.
27. Rao, Q. Pure Shear Fracture of Brittle Rock-A Theoretical and Laboratory Study. Ph.D. Thesis, Luleå University of Technology, Luleå, Sweden, 1999.
28. Whittaker, B.N.; Singh, R.N.; Sun, G. *Rock Fracture Mechanics: Principles, Design, and Applications*; Elsevier: Amsterdam, The Netherlands, 1992.
29. Zhou, X.-P.; Qian, Q.-H.; Yang, H.-Q. Effect of loading rate on fracture characteristics of rock. *J. Cent. South Univ. Technol.* **2010**, *17*, 150–155. [CrossRef]
30. Liu, H.Y.; Kou, S.Q.; Lindqvist, P.-A.; Tang, C.A. Numerical Modelling of the Heterogeneous Rock Fracture Process Using Various Test Techniques. *Rock Mech. Rock Eng.* **2006**, *40*, 107–144. [CrossRef]
31. Asprone, D.; Cadoni, E.; Prota, A. Experimental analysis on tensile dynamic behavior of existing concrete under high strain rates. *ACI Struct. J.* **2009**, *106*, 106–113.
32. Cho, S.H.; Ogata, Y.; Kaneko, K. Strain-rate dependency of the dynamic tensile strength of rock. *Int. J. Rock Mech. Min. Sci.* **2003**, *40*, 763–777. [CrossRef]
33. Zhang, Z.X.; Kou, S.Q.; Yu, J.; Yu, Y.; Jiang, L.G.; Lindqvist, P.-A. Effects of loading rate on rock fracture. *Int. J. Rock Mech. Min. Sci.* **1999**, *36*, 597–611. [CrossRef]

sustainability

MDPI

Article

Experimental Test on Nonuniform Deformation in the Tilted Strata of a Deep Coal Mine

Hai Wu [1,2,*], Qian Jia [2], Weijun Wang [2], Nong Zhang [3,4] and Yiming Zhao [4]

[1] Work Safety Key Lab on Prevention and Control of Gas and Roof Disasters for Southern Goal Mines, Hunan University of Science and Technology, Xiangtan 411201, China
[2] School of Resources, Environment and Safety Engineering, Hunan University of Science and Technology, Xiangtan 411201, China; gj_wkjq@163.com (Q.J.); wjwang@hnust.edu.cn (W.W.)
[3] School of Resources, Academy of Interdisciplinarity & Application, Jiangsu Normal University, Xuzhou 221116, China; zhangnong@126.com
[4] School of Mines, Key Laboratory of Deep Coal Resource Mining, Ministry of Education, China University of Mining and Technology, Xuzhou 221008, China; zhaoyiming001@163.com
* Correspondence: wuhai@hnust.edu.cn

Abstract: Taking a deep-mine horizontal roadway in inclined strata as our research object, the true triaxial simulation technique was used to establish a model of the inclined strata and carry out high-stress triaxial loading experiments. The experimental results show that the deformation of surrounding rock in the roadway presents heterogeneous deformation characteristics in time and space: the deformation of the surrounding rock at different positions of the roadway occurs at different times. In the process of deformation of the surrounding rock, deformation and failure occur at the floor of the roadway first, followed by the lower shoulder-angle of the roadway, and finally the rest of the roadway. The deformation amount in the various areas is different. The floor heave deformation of the roadway floor is the greatest and shows obvious left-right asymmetry. The deformation of the higher side is greater than that of the lower side. The model disassembly shows that the development of cracks in the surrounding rock is characterized by more cracks on the higher side and fewer cracks on the lower side but shows larger cracks across the width. The experimental results of high-stress deformation of the surrounding rock are helpful in the design of supports, the reinforcement scheme, and the parameter optimization of roadways in high-stress-inclined rock, and to improve the stability control of deep high-stress roadways.

Keywords: tilted strata; roadway; nonuniform deformation; physical simulation

Citation: Wu, H.; Jia, Q.; Wang, W.; Zhong, N.; Zhao, Y. Experimental Test on Nonuniform Deformation in the Tilted Strata of a Deep Coal Mine. *Sustainability* **2021**, *13*, 13280. https://doi.org/10.3390/su132313280

Academic Editors: Mahdi Hasanipanah, Danial Jahed Armaghani and Jian Zhou

Received: 24 October 2021
Accepted: 27 November 2021
Published: 30 November 2021

Publisher's Note: MDPI stays neutral with regard to jurisdictional claims in published maps and institutional affiliations.

Copyright: © 2021 by the authors. Licensee MDPI, Basel, Switzerland. This article is an open access article distributed under the terms and conditions of the Creative Commons Attribution (CC BY) license (https://creativecommons.org/licenses/by/4.0/).

1. Introduction

More than 50% of the development and mining roadways in China's coal mines pass through inclined rock strata, making the surrounding rock of the roadway prone to asymmetric deformation. With any increase in the buried depth of roadway, the deformation of roadway-surrounding rock of inclined rock strata increases, and stability control becomes very challenging. Therefore, it is imperative to investigate the deformation characteristics of roadway-surrounding rock in the case of deep inclined rock strata. Many factors are known to influence the stability of roadways; in general, they include: overburden, coal seam thickness, geological conditions, the presence of unfavorable structures, clay minerals, mining methods, and, most importantly, the dip angle of the coal seams. Due to the importance of this topic, there has been a great deal of research on the deformation laws of roadways with steep dip angles. For example, Yu et al. [1] established a mechanical model of a coal body on two sides of a mining roadway under abutment pressure and analyzed the basic distribution law of interface stress between the coal body and the roof and floor, as well as the axial force of the coal body. Zhang et al. [2] researched asymmetric deformation and the failure mechanisms of roadway-surrounding rock in a large dip coal seam; they

proposed asymmetric coupling support countermeasures for key parts of the surrounding rock of the roadway in a large dip coal seam. Li et al. [3] established a mechanical model for the plastic zone of a coal seam and believed that with the increase in width of the supporting structure, the width of the plastic zone of the coal seam decreases linearly. The friction angle in the supporting structure increases and the plastic zone width of the coal seam decreases. Zhang et al. [4] proposed the technical principle of constructing an integral closed support with an anchor bolt, anchor cable, grouting, and other active support as the main body, supplemented by structural reinforcement. Zhang et al. [5] analyzed the deformation characteristics of inclined rock drift using different support methods and grasped the distribution characteristics of cracks in roadway-surrounding rock when under plane strain conditions. Zhang et al. [6] used the new, combined three-dimensional geomechanical model testbed in their research and showed that the range of the partition fracture of the cavern is related to the shape and size of the cavern; the larger the size of the cavern, the larger the partition fracture range. Guo et al. [7] used a numerical simulation to analyze the influence of the lateral pressure coefficient of the surrounding rock pressure on roadway deformation and its influence on the stress distribution around it. Xue [8] conducted similar simulation research on the deformation characteristics of horizontal roadways that are without support. The results show that the roof force comes from the dislocation of the old roof, and the floor force comes from the weight of the overlying rock and stress from mining operations. The force of the coal beside the roadway comes from energy release and the dilatancy deformation stress undermining conditions. Liu et al. [9] analyzed the size effect on tunnels surrounding rock deformation. The relationship between bending deformation and a section of the laminated roof is pointed out from the point of view of the simply supported beam. Sun et al. [10] numerically simulated the asymmetric deformation of a roadway in inclined strata and proposed the control countermeasures of asymmetric coupling support. Zhang et al. [11] adopted a reinforcement control strategy for the deep roadway in the Qishan mining area, which greatly improved the stability of the surrounding rock of the roadway. Bao et al. [12] established the model of a layered roadway in a layered rock mass using finite element software, ANSYS, and analyzed the deformation characteristics of a layered roadway. Wang et al. [13] proposed the idea of reinforcing two sides of a deep roadway to control floor heave and verified that reinforcing two sides can control the floor heave of a deep roadway to a certain extent. Fan et al. [14] used acoustic emission to research the large-scale three-dimensional physical similarity simulation experimental model of roadway shield excavation and established the law of acoustic emission regarding surrounding rock failure during excavation. Chen et al. [15] found that under the conditions of shallow-buried hydrostatic pressure, the surrounding rock of the roadway showed the characteristics of "shallow tensile strain and deep zero strain". Gao et al. [16] researched the mechanical deformation behavior characteristics of an in-situ rock mass under high stress. Zhang et al. [17] researched the mechanical behavior of the progressive failure of sandstone under true triaxial conditions. Yin et al. [18,19] researched the stability and plastic zone characteristics of borehole-surrounding rock under true triaxial stress. Wang et al. [20] conducted an experimental study of the deformation and failure of a fractured rock mass around the roadway, under true triaxial loading and unloading. Through Flac3D numerical simulation, H. Zhang et al. [21] found that under seepage, especially with an increase in water head and porosity, the mechanical properties of the surrounding rock were weak, and the deformation was large, which was consistent with the field observation. X.J. Yang et al. [22] researched the support problem of deep soft rock roadway with large deformation. The deformation, stress and crack propagation characteristics of the roadway are revealed by simulating the failure modes of the unsupported roadway and the initially supported roadway. M. Li et al. [23] researched an innovative mining method for a thick separated seam. The coal seam is divided into different zones, according to the thickness of the rock separation, and three mining schemes comprising full coal-seam mining, combined backfill caving mining (CMBC), and lowering-height mining are used to mine the three zones. D.D. Qin et al. [24] researched the surrounding

rock structure distribution characteristics of this kind of roadway by combining theoretical analysis and numerical simulation. Based on the control effect of different supporting modes on the surrounding rock structure, a reinforcement scheme for a deep dynamic soft rock roadway is proposed and applied. The problem of deformation of a rock mass with a layered structure has already been analyzed by many researchers, but so far, no models have been studied in the macro scale under three-axial conditions. In these studies, there is a lack of research on the internal failure of roadway-surrounding rock, so the research cannot fully explain the essential mechanism of the occurrence of the inhomogeneous deformation law of inclined layers in the rock surrounding a roadway. The purpose of this paper is to research the characteristics and deformation mechanism of the inhomogeneous deformation of a horizontal roadway in deep inclined strata via true triaxial experiment and explain the deformation and aging characteristics of the surrounding rock and the failure mechanism within the surrounding rock.

2. Similar Simulation Engineering Background

Introduction of Experimental Equipment

The experimental study used the Jiangxi Qujiang Mining Company -850 East Roadway Extension as the engineering background of a similar simulation. The -850 East Roadway is arranged along a strike in the floor strata of a coal seam; the strata are generally monocline, with an inclination of 15°. The roadway of the East Roadway Extension is cut through whole rock, and the lithology is grayish-black siltstone with thin to medium-thick bedding. It is interbedded with thin-layered mudstone and a fine sandstone belt containing a small number of siderite nodules, fossilized plant rhizome, joint development, and calcium clay cementation of medium and low hardness. The cross-section of the roadway is a straight-walled semicircular arch with a width of 4.4 m and a height of 3.5 m. The supporting method is of a combined support with an anchor rod, anchor net, ladder beam, shotcrete, and anchor cable, and the row distance between the bolts is 700 × 700 mm. For spraying, 425 ordinary Portland cement and pure river sand are used, and the thickness of the spraying layer is 100 mm. Three single anchor cables of 6.3 m at intervals of 1.6 m were arranged in the middle of the two shoulders and the arch of the roadway. The field investigation showed that the deformation of the surrounding rock in the east roadway exhibits the following characteristics. (1) The roof of the roadway was asymmetrically deformed, and continuous failure cracks along the axial direction appeared at the right shoulder angle of the roadway roof, while the left shoulder angle was relatively complete, as shown in Figure 1a. (2) The asymmetric deformation from floor heave is manifested thus: the floor heave is greater on the left side of the roadway than on the right side, and the maximum floor heave is 0.8 m to the left of the line of the roadway, as shown in Figure 1b. (3) The results of observation via boreholes on both sides of the roadway show that the development of internal fractures in both sides of the roadway is asymmetrical, and that there are more fractures in the rock mass to the left side of the roadway than to the right side of the roadway (for more details, see [25]).

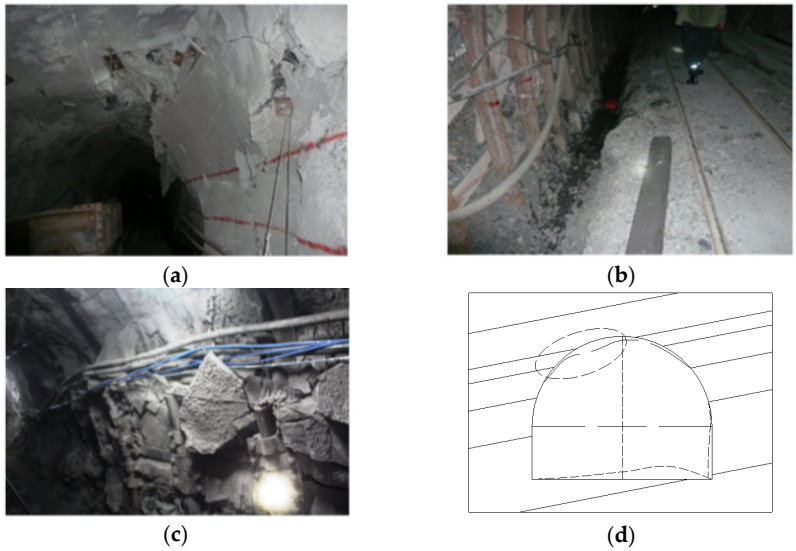

Figure 1. Asymmetrical deformation of the roadway and its schematic diagram. (**a**) Failures in part of the right roof-side wall of the roadway. (**b**) Floor upheaval is severe. (**c**) Roadway failure at the lower side. (**d**) Sketch of the non-uniform deformation of the roadway.

3. Experimental Model Making and Experimental Scheme

3.1. Introduction of Experimental Equipment

The 20 MPa "three directions and on five sides" vertical main loading experimental system is composed of four parts: the host system, the electro-hydraulic servo system, the measurement and control system, and the sample preparation system, realizing independent active loading in "3 directions and on 5 surfaces" for a large sample (1000 × 1000 × 400 mm) (Figure 2). The loading size, speed, and load-holding time of each surface can be adjusted independently, and the maximum loading stress of each surface is 20 MPa. The system adopts a separate design for test block fabrication and the experimental loading processes are independent of each other. Multiple test blocks with different parameters can be prefabricated in advance and multiple loading experiments can be carried out continuously. The equipment can be used to complete the uniaxial, biaxial, and triaxial compression test, simulating the high-stress excavation of a roadway and of a roadway affected by mining. The characteristics of timeliness under high stress were observed by simulating the high-stress loading of a rock mass. The time-effectiveness characteristics of simulated rock mass alter under high stress and simulate the dynamic characteristics of rock mass after multiple loading and unloading in a complex stress environment. The model test space's length × width × height = 1000 × 1000 × 400 mm. In the vertical direction, the loading surface's length × width = 1000 × 1000 mm; in the horizontal direction, the four surfaces' length × width = 1000 × 400 mm. The force frame diagram of the test block is shown in Figure 3. The displacement resolution of the equipment is 0.007 mm. The relative error of displacement indication and the relative error of the test pressure indication is $\leq \pm$ 0.5%.

Figure 2. The true triaxial simulation experiment system.

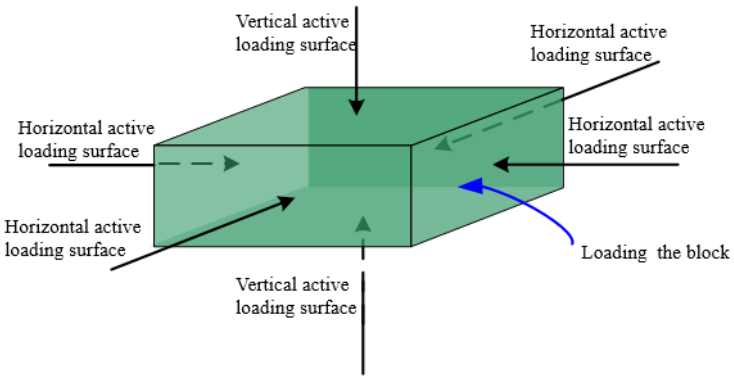

Figure 3. Force frame diagram of the test block.

3.2. Experimental Model-Making Process

(1) Equivalent material selection—similar equivalent materials to the rock in question are made of cement, gypsum, and river sand. To master the mechanical properties of similar materials, different overproportioning samples are made and uniaxial compression tests are carried out. To improve the ductility of similar materials, a set amount of the mortar fiber used in construction is added. The fiber is made of polypropylene material, the fiber length is 12 mm, and the addition amount is 5 kg per cubic meter. We added a certain amount of borax as retarder; the amount of borax is 5% of the water used. Ten groups of test blocks were made using the mold for standard mortar test blocks, with three in each group. The sample size of the small test block is 70.7 mm × 70.7 mm × 70.7 mm. The mold was removed 3 days after the completion of production, and the compressive strength of the test blocks was tested 10 days after drying. Figure 4 shows the No.3 test block (473 is the ratio number of sand cement gypsum, and the dosage ratio is sand: cement: gypsum is 40:7:3) in the uniaxial compressive test, and Figure 5 shows the compressive strength curve of the test block.

Figure 4. Uniaxial compressive test of the block. ("3": 3 shows the No.3 test block; "序号": the serial number; "473": 473 is the ratio number of sand cement gypsum; "配比号": Material dosage ratio).

Figure 5 shows that the uniaxial compressive strength of the material reaches 3.8 MPa. Considering that the strength of the test block will be improved to a certain extent under the conditions of triaxial compression, a physically similar material with a ratio number of 473 was selected for similarity simulation. There is a small fluctuation in the rising stage of the curve, which is a stage of stress adjustment (see Table 1 for the specific parameters of the material).

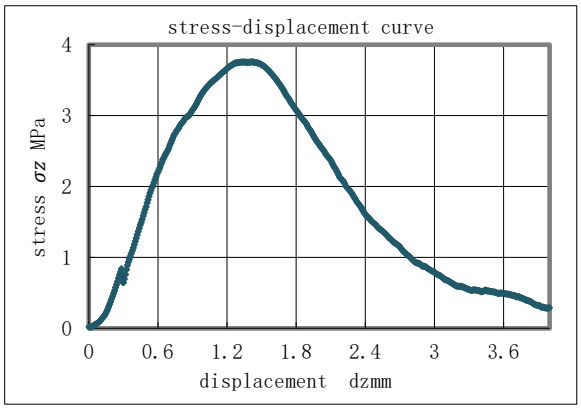

Figure 5. Typical stress σz—displacement dz characteristics of the sample under uniaxial compression.

Table 1. Physical modeling material parameter.

Material Number	Density, g/cm^3	Compressive Strength, MPa
473	2.20	2.77

(2) Determination of model scale and roadway size—correlation studies of similar simulations and numerical models show that when the ratio of model excavation radius to boundary distance is 1:5, the experimental error is about 6%. The maximum size of the similar simulation test block is width × height = 1000 mm × 1000 mm, so the ratio of roadway excavation radius and boundary distance is 90:500 = 0.9:5, and the roadway excavation radius is set at 90 mm.

(3) Preparation of a similar simulation test block—(i) According to the roadway position, rock stratum histogram, and model scale, the physical structure diagram of a similar simulation test block was made. (ii) Fix the physical structure drawing on the base of the test block to make the model and cover it with a thin film. Install the test block to make the mold. (iii) According to the physical structure diagram, using the selected similarity ratio, calculate the number of similar materials required by each layer of rock mass, mix and stir these similar materials, and layer the model. Special attention should be paid to the uniformity of the model density during model layering. (iv) The manufactured test block and the mold are sent together to the pressing platform for prepress to ensure that each surface is flat and parallel. (v) After the preloading is completed, the test block would be dried for 2–3 days, and the roadway excavation and surface leveling would be carried out according to the design requirements, as shown in Figure 6.

Figure 6. Production of a similar simulation sample block model.

3.3. Experimental Data Acquisition

Photogrammetry was used to measure the deformation and displacement of the surrounding rock. The layout of the monitoring points for the photogrammetric displacement

of the surrounding rock is shown in Figure 7. To further understand the mechanism of the deformation and failure of the surrounding rock, the crack development in the surrounding rock of the roadway was statistically analyzed when the model was disassembled.

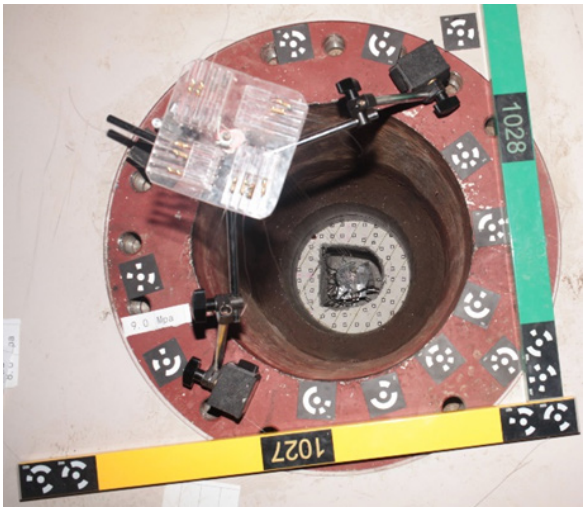

Figure 7. Displacement monitoring point layout.

3.4. Experimental Stress-Loading Scheme

Stress loading is carried out in two steps: (1) The vertical, front and rear, and left and right stress in synchronized loading increased from 0 MPa to 3 MPa. This comprises the stress adjustment stage of the experimental equipment and test block. (2) When the stress of the surrounding rock is greater than 3 MPa, the stress increases by 0.2 MPa each time, then the stress remains unchanged for 3 min, and then the stress continues to increase by 0.2 MPa. The real stress loading curve is shown in Figure 8.

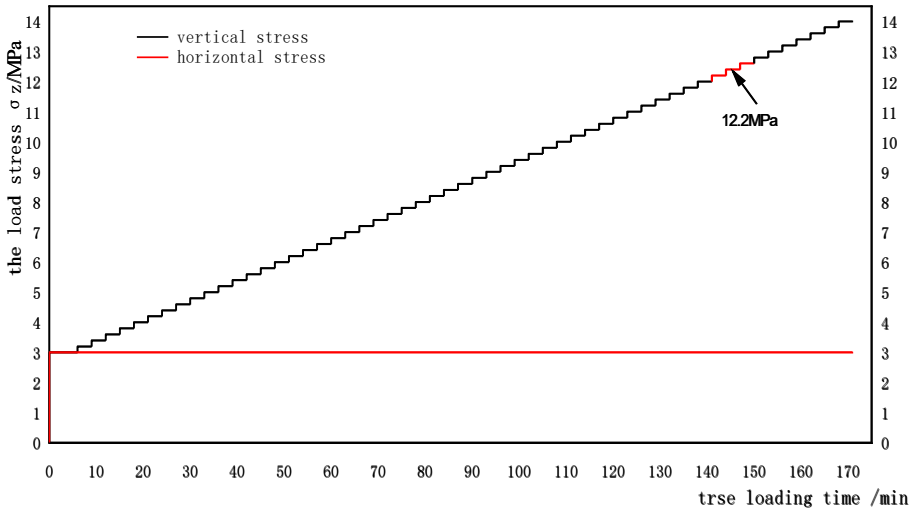

Figure 8. Stress curve of experimental loading time.

4. Analysis of Asymmetric Deformation Characteristics of Roadway-Surrounding Rock

4.1. Characteristics of Roadway Surrounding Rock Deformation

With an increase in stress, the surrounding rock of the roadway gradually deforms and becomes unstable until it is destroyed. Photographic monitoring was carried out to obtain a comparative analysis diagram of roadway surface deformation at different stress stages (Figure 3), which shows that: (1) when stress on the surrounding rock is low (the surrounding rock stress is less than 6 MPa), the surrounding rock does not demonstrate

obvious deformation, as shown in Figure 9a,b. (2) When the surrounding rock stress increased to 6 MPa (Figure 9c), relatively obvious transverse cracks first appeared at the bottom corner of the roadway, on the lower side. With the increase in stress in the surrounding rock, new cracks were constantly being generated in the surrounding rock at the bottom corner of the lower side (Figure 9d). (3) Figure 9e,f shows that when the stress of the surrounding rock increases to 9 MPa below the higher side of the roadway, an interlayer dislocation deformation of the different rock strata occurs along the direction of bedding, and the floor of the roadway shows the phenomenon known as bed separation. At the same time, there are cracks on both sides of the roadway arc at the lower shoulder angle and at the tangent of the rock layer. As the stress level of the surrounding rock continues to increase, the floor heave of the roadway increases continuously. Layered slip and bending fracture occurred in the in-floor strata; the surface of the roadway showed asymmetrical floor heave on both sides, and the cracks on both sides of the low shoulder angle increased continuously. (4) Figure 9g shows that when the surrounding rock stress is 11.6 MPa, substantial deformation and failure occur in the surrounding rock and floor heave occurs in the floor of the roadway. Both sides of the low shoulder angle were damaged along the rock boundary. When the stress loading reaches 12.2 MPa, the roadway suddenly fails. The deformation of the surrounding rock of the roadway in a similar model and the in-field measurements all show that the floor heave of the roadway-surrounding rock is asymmetric and deformation on both sides of the low shoulder angle shows that it is easy to damage the relative integrity of the high surface.

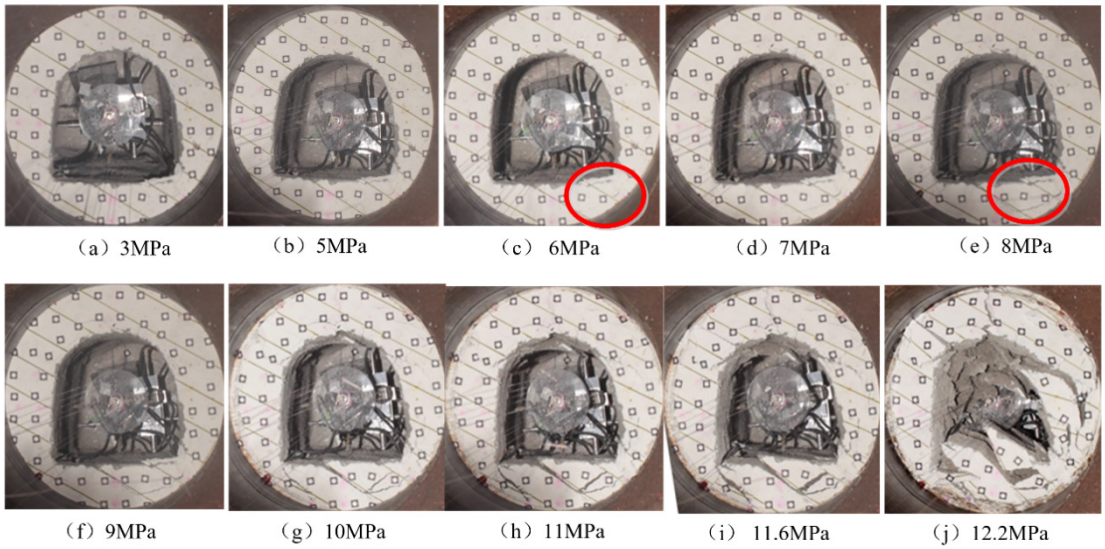

Figure 9. Surface deformation of the roadway.

4.2. Spacial Deformation Displacement Distribution Characteristics of a Roadway

The coordinate data from monitoring points before and after the large deformation and failure of the roadway-surrounding rock were extracted by photogrammetry. The mapping software was used to obtain the position changes of monitoring points on the surrounding rock surface before and after the deformation and failure of the model roadway (see Figure 10).

Analysis of the positions before and after the monitoring points shows that the deformation characteristics of the surrounding rock can be analyzed in four regions, namely, the higher side of the roadway, the lower side of the roadway, the floor, and the roof. (1) The surrounding rock monitoring points within the higher side of the roadway move towards the center and floor of the roadway. With the increase in the distance between the monitoring point and the floor, the horizontal and vertical displacements of the monitoring point decrease gradually. (2) The monitoring points on the lower side of the roadway move

towards the center and floor of the roadway. The horizontal displacement increases with the increase in the distance from the monitoring point to the floor height and reaches its maximum value at the shoulder angle. The vertical displacement at the bottom angle of the lower side is upward and gradually decreases with the increase in the distance from the monitoring point to the floor height. The vertical displacement at the shoulder angle is downward, and there is zero displacement of the point at the low shoulder angle. (3) The vertical displacement of the monitoring points on the floor of the roadway all point to the center direction of the roadway, and the displacement on the higher side is large, while the displacement on the lower side is relatively small. On the other hand, the horizontal displacements are in opposite directions, with the center of the roadway floor as the boundary, all pointing to the center of the roadway floor; the displacement on the higher side is greater than that on the lower side. The floor deformation is the same as in the field reality, which is the area with the largest roadway deformation and the area where deformation and failure occur first. (4) The horizontal displacement of the monitoring points on the roof of the roadway all point to the higher side, and the horizontal displacement on the higher side is greater than that on the lower side. The vertical displacement showed the minimum value at the higher side shoulder-angle and the maximum at the lower side shoulder angle.

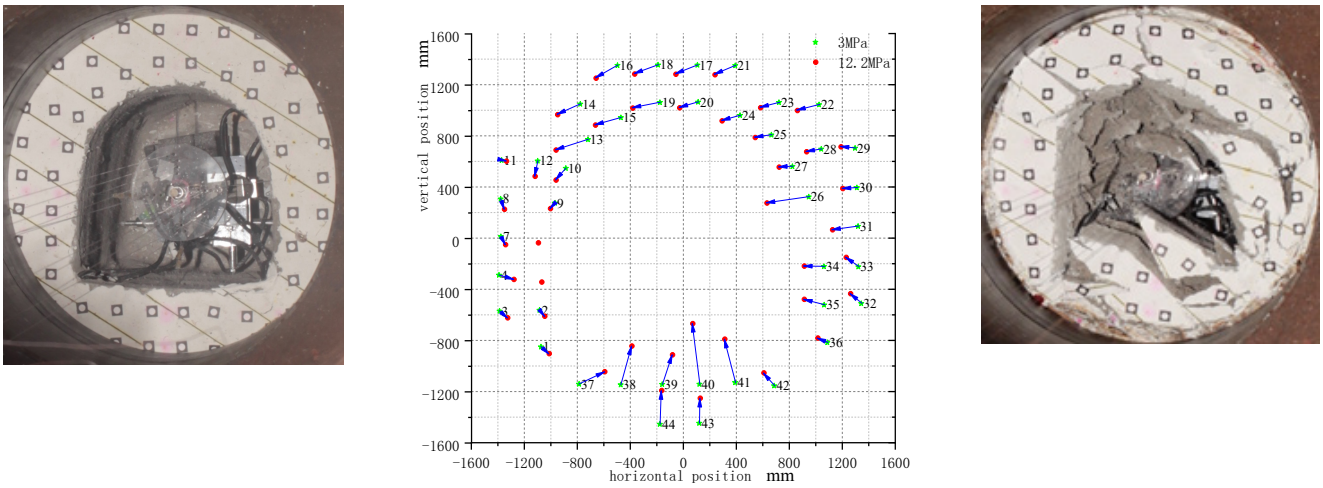

Figure 10. Comparison diagram of monitoring points before and after roadway failure.

The displacement data of monitoring points on the roadway surface are compared and analyzed in order to further research the heterogeneity of the displacement of surrounding rock deformation in the inclined roadway. The positions of specific monitoring points and the magnitude of displacement are shown in Table 2. After summing up the displacement of the monitoring points on the roadway surface, the average value is obtained, namely:

$$d_{average} = \frac{\sum_1^n d_i}{n} \quad (1)$$

where d_i is the displacement of the "i" monitoring point; "n" is the number of monitoring points. In terms of the situation of $d_{average} < d_i$ in each partition, the statistical results show that: (1) The deformation at the monitoring point of the roadway floor surface deformation is the largest. The number of monitoring sites exceeding the average deformation was the largest here, at 4. (2) There are two monitoring points where the deformation of the roadway roof exceeds the average value. (3) There was one monitoring point where the deformation of the lower side of the roadway exceeded the average value. (4) The deformation of no monitoring point in the higher-level wall of the roadway exceeds the average value. Therefore, the deformation of the surrounding rock of the roadway shows heterogeneous characteristics: floor > roof > lower side > higher side.

Table 2. Comparative analysis of the displacement of monitoring points on the roadway surface.

No.	Location	Displacement (cm)	Number	Location	Displacement (cm)	Number	Location	Displacement (cm)
1	high-level wall	1.69	19	roof	4.53	36	low-level wall	1.80
2	high-level wall	1.30	20	roof	3.19	37	floor	4.46
5	high-level wall	1.24	24	roof	3.12	38	floor	6.54
6	high-level wall	1.13	25	roof	2.75	39	floor	5.04
9	high-level wall	1.24	26	low-level wall	6.88	40	floor	10.02
10	high-level wall	2.54	27	low-level wall	2.26	41	floor	7.31
13	roof	5.46	34	low-level wall	3.30	42	floor	2.71
15	roof	4.32	35	low-level wall	3.45			

Note: boxes with a color background highlight areas where the displacement is greater than the mean value.

4.3. Analysis of Internal Crack Development Characteristics of Roadway-Surrounding Rock

After the experiment, the observation results showed that some joint opening and slippage occurred along the bedding plane of the model, and the specific distribution is shown in the Figure 11.

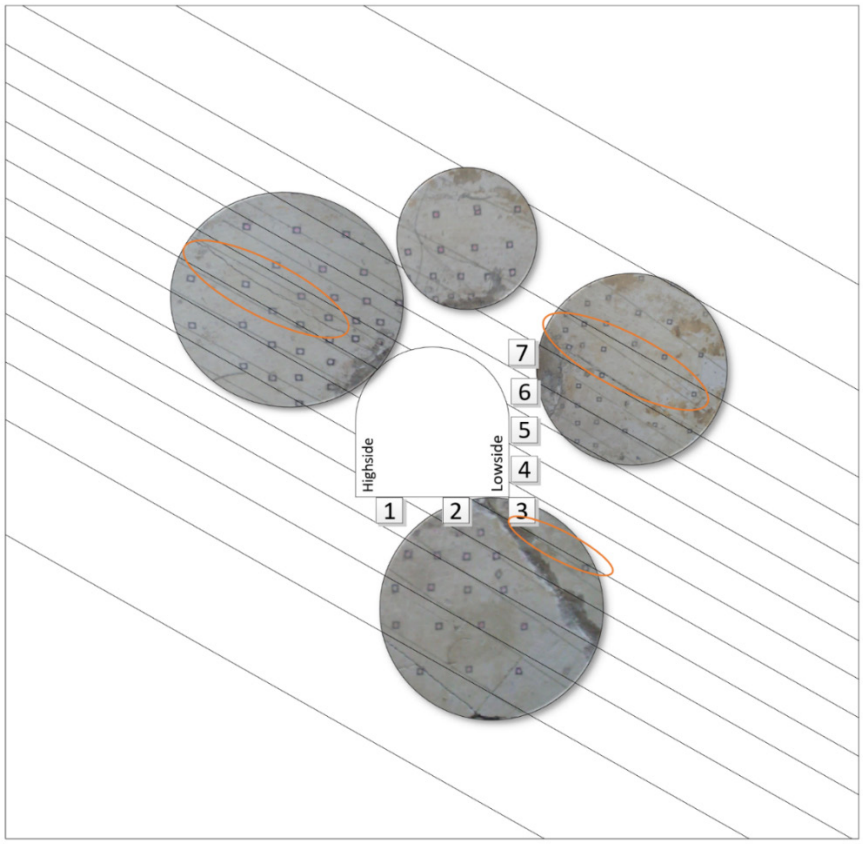

Figure 11. Surface fractures—position on the model.

The model was further disassembled along the inner layer to examine the internal damage conditions of the surrounding rock of the roadway at different layers, as shown in Figures 11–13. The development characteristics of internal cracks after model failure can thus be obtained. The proportions of the pictures and photos are the same, with the numbers 1–7 representing the different rock layers. These pictures were taken from the outside of the model and cracks appeared, so they were shown in the model for comparison.

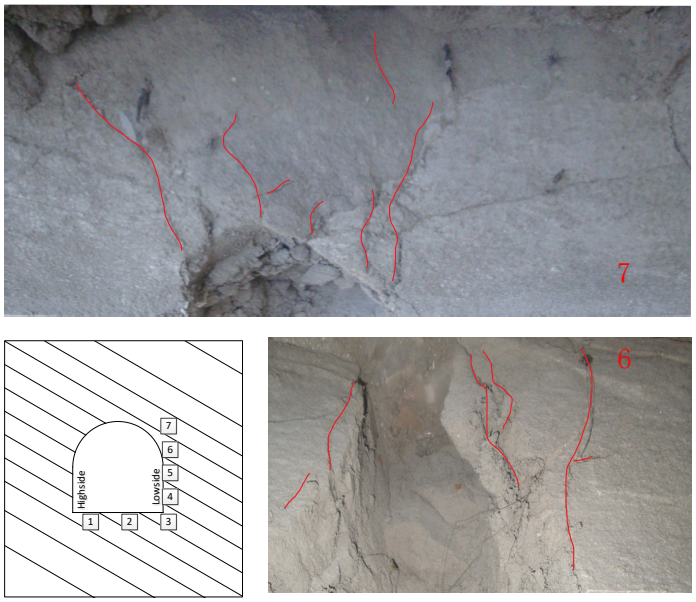

Figure 12. Inner failure of the surrounding rock of the roadway.

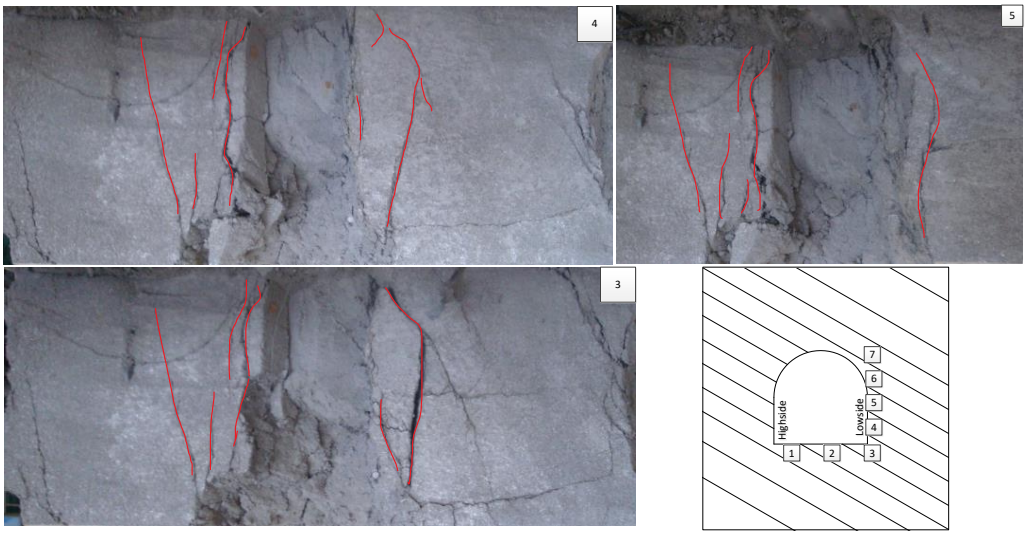

Figure 13. Failure structure of the surrounding rocks of two sides of the roadway.

(1) Failure characteristics of the surrounding rock in the roadway roof (see Figure 11)—Under the scenario of a 30° inclination, the failure of the surrounding rock in the roadway roof is mainly concentrated in a position near the shoulder angle of the roadway roof, and the tangent point between the rock layer and roadway surface is at the center. From the direction of crack development, most of the crack directions run parallel to the direction of the roadway. From the point of view of the number of cracks, the number of cracks on the higher side is less than that on the lower side.

(2) Characteristics of crack development on two sides of the roadway—Figure 12 shows that the cracks in the higher and lower sides of the roadway show obvious asymmetry, which is mainly manifested in the fact that the cracks in the higher and lower sides are mainly parallel to the direction of the roadway. The number of internal cracks in the higher-wall rock is more than that in the lower-side rock, but the width of the cracks in the higher-side rock is smaller than that in the lower-side rock. As for the crack location, the crack at the lower-side shoulder angle of the roadway was close to the surface of the roadway, and the depth of the crack location increased with the decrease in height. Higher-side cracks are mainly concentrated on the surface of the roadway. In terms of crack

width, the crack width near the lower-side surface is smaller, and the crack width at the deeper side is larger. The width of the internal crack on the higher side decreases gradually from the outside to the inside.

(3) Characteristics of crack development in roadway floor—Figure 13 shows that the floor of the roadway is the area with the largest deformation of surrounding rock, and the rock strata in the middle of the floor of the roadway are fractured and rotated. There is an obvious relative sliding and opening phenomenon between the different strata on the floor. The surrounding rock at the bottom corner of the higher side is broken in pieces, and the broken zone extends along the direction of the roadway. A large number of cracks appeared in the deeper rock mass in the floor plate of the lower side. From the perspective of crack distribution, the number of cracks on the lower side was greater than that on the higher side, as shown in Figure 13.

(4) Overall development characteristics of internal cracks in roadway surrounding rock—According to Figures 11–14, obtained from the model disassembly, a sketch of the crack development in the surrounding rock of the roadway was drawn, as shown in Figure 15. The crack development showed asymmetry, with more cracks on the higher side and fewer cracks on the lower side.

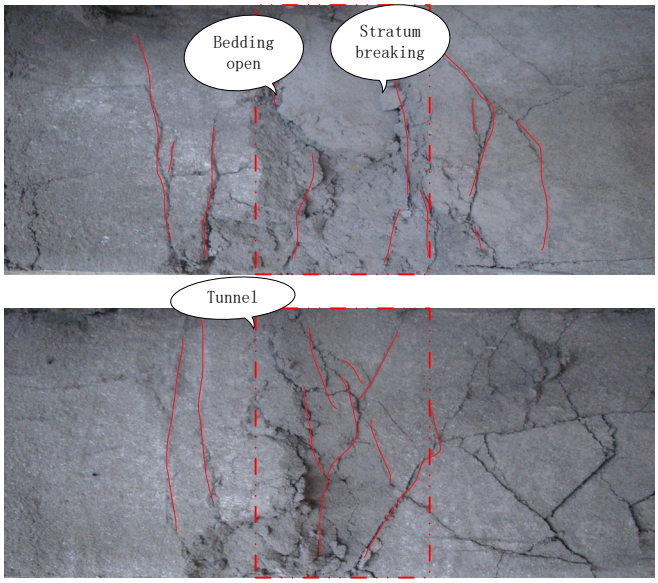

Figure 14. Floor crack development of the roadway.

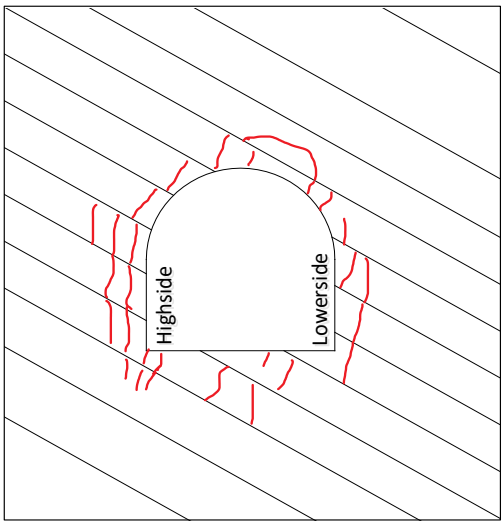

Figure 15. Crack development of the roadway-surrounding rock.

5. Conclusions

The experimental results show that the experimental platform can simulate the surrounding rock stress of a deep high-stress roadway, and the obtained deformation of an inclined rock strata roadway is consistent with findings in the field.

The simulation experiment shows that the deformation of roadway-surrounding rock in deep high-stress-inclined rock strata shows obvious aging characteristics: the first is floor heave deformation, the second is roof and lower side shoulder-angle deformation, and the third is higher side shoulder-angle and lower-side deformation.

The simulation results show that the deformation of roadway-surrounding rock in deep high-stress-inclined rock strata is non-homogeneous. Deformation at the higher side below the center line and on the lower side at the shoulder angle is great. The deformation of the roof, the higher-side shoulder angle, and the lower-side center line is small. The floor heave deformation of the roadway floor is the greatest and shows obvious left-right asymmetry. The deformation of the higher side is greater than that of the lower side.

The simulation experiment shows that crack development in the surrounding rock of the roadway is non-homogeneous. The number of cracks in the higher side and bottom plate is larger, while the number of cracks in the lower side is smaller and the crack width is larger.

Author Contributions: Data curation, Q.J. and Y.Z.; Investigation, W.W.; Project administration, H.W.; Resources, N.Z. All authors have read and agreed to the published version of the manuscript.

Funding: This work was supported by the National Natural Science Foundation of China (No. 51774133, No. 52074117).

Conflicts of Interest: The authors declare no conflict of interest.

References

1. Yu, Y.; Hong, X.; Chen, F. Study on load transmission mechanism and limit equilibrium zone of coal-wall in extraction opening. *J. China Coal Soc.* **2012**, *37*, 1630–1636.
2. Zhang, B.; Cao, S.; Wang, L. Deformation Failure Mechanism and Support Measurements in Roadway of Steeply Inclined Coal Seam. *J. Min. Saf. Eng.* **2011**, *28*, 214–219.
3. Li, S.; Pan, Z.; Wang, W. Analysis of Plastic Region of Sidewalls in Coal Drifts Reinforced by Association of Rock Bolt and Grouting. *J. Hunan Univ. Sci. Technol. Nat. Sci. Ed.* **2007**, *2*, 5–8.
4. Zhang, N.; Li, B.; Li, G. Inhomogeneous damage and sealing support of roadways through thin-bedded coal-rock crossovers. *J. Min. Saf. Eng.* **2013**, *30*, 1–6.
5. Zhang, M.; Gao, J.; Wei, S. Similarity Simulation Study of Failure Characteristics ofSurrounding Rocks of Titled Strata Roadway. *J. Rock Mech. Eng.* **2010**, *29*, 3259–3264.
6. Zhang, Q.; Zhang, X.; Xiang, W. Model Test Study of Zonal Disintegration in Deep Rock mass Under Different Cavern Shapes and Loading Conditions. *Chin. J. Rock Mech. Eng.* **2013**, *32*, 1564–1571.
7. Guo, J.; Yang, Z.; Tang, H. The Effect of Lateral Pressure Coefficient on Deformation and Stress Distribution Rules AroundRoadway. *J. Min. Saf. Eng.* **2011**, *28*, 566–570.
8. Xue, D. Research on similarity simulation of soft rock entry deformation and destruction. *China Coal* **2010**, *36*, 58–61.
9. Liu, J.; Zhao, Y.; Li, P. Study of size effect of deformation of rock mass surrounding tunnel. *Rock Soil Mech.* **2013**, *34*, 2165–2173.
10. Sun, X.; Zhang, G.; Cai, F. Asymmetric Deformation Mechanical within Inclined Rock Strata Induced by Excavation in Deep Roadway and its Controlling Countermeasures. *J. Rock Mech. Eng.* **2009**, *28*, 1137–1143.
11. Zhang, G.; He, M.; Jin, L. Deformation and Stability Lost Mechanism and Support Technology of Inclined Layer Roof in Seam Gateway. *Coal Sci. Technol.* **2011**, *39*, 1–5.
12. Bao, H.; Meng, Y.; Wu, X. Numerical Simulation of Deformation Mechanism of Deep Inclined Roadway. *J. Hefei Univ. Technol. Nat. Sci. Ed.* **2012**, *35*, 673–677.
13. Wang, W.; Feng, T. Study on Mechanism of Reinforcing Sides to Control Floor Heave of Extraction Opening. *J. Rock Mech. Eng.* **2005**, *5*, 808–811.
14. Fan, G.; Cheng, K.; Lai, X. Acoustic Emission Characteristics of Surrounding Deformation of Shield Tunnel Based on 3D Physical Similar Simulation Experiment. *Saf. Coal Mines* **2018**, *49*, 50–54.
15. Zhang, N.; Wang, X.; Kan, J. Extrusion Displacement Model and Displacement Quantization Method of Roadway Surrounding Rock. *J. China Univ. Min. Technol.* **2013**, *42*, 899–904.
16. Gao, M.; Wang, M.; Xie, J. In-situ disturbed mechanical behavior of deep coal rock. *J. China Coal Soc.* **2020**, *45*, 2691–2703.

17. Zhang, J.; Song, Z.; Fan, W. Experimental investigation on progressive damage mechanical behavior of sandstone under true triaxial condition. *J. China Coal Soc.* **2019**, *44*, 2700–2709.
18. Yin, G.; Lu, J.; Li, X. Stability and plastic zone characteristics of surrounding rock under true triaxial stress conditions. *J. China Coal Soc.* **2018**, *43*, 2709–2717.
19. Yin, G.; Lu, J.; Li, X. Influence of intermediate principal stress on dilation and strength characteristics of sandstone. *J. China Coal Soc.* **2017**, *42*, 879–885.
20. Wang, M.; Zhu, Z.; Feng, R. Experimental study on THE failure behavior of cracked rocks around tunnels under true triaxial unloading. *J. China Coal Soc.* **2015**, *40*, 278–285.
21. Zhang, H.; Adoko, A.C.; Meng, Z. Mechanism of the Mudstone Tunnel Failures Induced by Expansive Clay Minerals. *Geotech. Geol. Eng.* **2017**, *35*, 263–275. [CrossRef]
22. Yang, X.; Wang, E.; Wang, Y. A Study of the Large Deformation Mechanism and Control Techniques for Deep Soft Rock Roadways. *Sustainability* **2018**, *10*, 1100. [CrossRef]
23. Li, M.; Zhang, J.; Quan, K. Innovative Extraction Method for a Coal Seam with a Thick Rock-Parting for Supporting Coal Mine Sustainability. *Sustainability* **2017**, *9*, 1982. [CrossRef]
24. Qin, D.; Wang, X.; Zhang, D. Study on Surrounding Rock-Bearing Structure and Associated Control Mechanism of Deep Soft Rock Roadway Under Dynamic Pressurey. *Sustainability* **2019**, *11*, 1892. [CrossRef]
25. Wu, H. *Research on Asymmetrical Deformation Laws and Stability Control of Deep Inclined Rock Strata Roadway*; China University of Mining and Technology: Xuzhou, China, 2014.

sustainability

MDPI

Article

Optimized Support Vector Machines Combined with Evolutionary Random Forest for Prediction of Back-Break Caused by Blasting Operation

Qun Yu [1], Masoud Monjezi [2], Ahmed Salih Mohammed [3], Hesam Dehghani [4], Danial Jahed Armaghani [5,*] and Dmitrii Vladimirovich Ulrikh [5]

1 School of Architecture and Civil Engineering, Shenyang University of Technology, Shenyang 110870, China; snoopy.351@hotmail.com
2 Department of Mining, Faculty of Engineering, Tarbiat Modares University, Tehran 14115-143, Iran; monjezi@modares.ac.ir
3 Civil Engineering Department, College of Engineering, University of Sulaimani, Sulaymaniyah 46001, Iraq; ahmed.mohammed@univsul.edu.iq
4 Department of Mining Engineering, Hamedan University of Technology, Hamedan 6516913733, Iran; dehghani@hut.ac.ir
5 Department of Urban Planning, Engineering Networks and Systems, Institute of Architecture and Construction, South Ural State University, 76, Lenin Prospect, 454080 Chelyabinsk, Russia; ulrikhdv@susu.ru
* Correspondence: danialarmaghani@susu.ru

Abstract: Back-break is an adverse event in blasting works that causes the instability of mine walls, equipment collapsing, and reduction in effectiveness of drilling. Therefore, it boosts the total cost of mining operations. This investigation intends to develop optimized support vector machine models to forecast back-break caused by blasting. The Support Vector Machine (SVM) model was optimized using two advanced metaheuristic algorithms, including whale optimization algorithm (WOA) and moth–flame optimization (MFO). Before the models' development, an evolutionary random forest (ERF) technique was used for input selection. This model selected five inputs out of 10 candidate inputs to be used to predict the back break. These two optimized SVM models were evaluated using various performance criteria. The performance of these two models was also compared with other hybridized SVM models. In addition, a sensitivity evaluation was made to find how the selected inputs influence the back-break magnitude. The outcomes of this study demonstrated that both the SVM–MFO and SVM–WOA improved the performance of the standard SVM. Additionally, the SVM–MFO showed a better performance than the SVM–WOA and other hybridized SVM models. The outcomes of this research recommend that the SVM–MFO can be considered as a powerful model to forecast the back-break induced by blasting.

Keywords: blasting; back-break; SVM; metaheuristic algorithms; moth–flame optimization; whale optimization algorithm

Citation: Yu, Q.; Monjezi, M.; Mohammed, A.S.; Dehghani, H.; Armaghani, D.J.; Ulrikh, D.V. Optimized Support Vector Machines Combined with Evolutionary Random Forest for Prediction of Back-Break Caused by Blasting Operation. *Sustainability* **2021**, *13*, 12797. https://doi.org/10.3390/su132212797

Academic Editor: Guang-Liang Feng

Received: 9 October 2021
Accepted: 16 November 2021
Published: 19 November 2021

Publisher's Note: MDPI stays neutral with regard to jurisdictional claims in published maps and institutional affiliations.

Copyright: © 2021 by the authors. Licensee MDPI, Basel, Switzerland. This article is an open access article distributed under the terms and conditions of the Creative Commons Attribution (CC BY) license (https://creativecommons.org/licenses/by/4.0/).

1. Introduction

Back-break (*BB*) is an undesired outcome of blasting in mining operations. This phenomenon refers to the breaking into pieces of rocks exceeding the thresholds of the rear row of holes in a blast design [1]. Some undesirable impacts of the *BB* include instability of rock mine wall, fallings, and increment of the overall cost of blasting [2,3]. There are three main categories of parameters which affect the *BB*; these categories include (1) parameters related to blast design, (2) explosive material characteristics, and (3) the rock mass traits and breaks. While the first and second types of variables are regarded as manageable, the third group is viewed as uncontrollable blasting variables [4–8]. The factors that may affect the *BB* include low stiffness ratio, extreme burden, over stemming of the hole, and geological structure [1,9,10]. As many parameters affect *BB*, suitable appraisal and prediction of this

environmental consequence are extremely challenging. The mentioned challenge can be solved using different, well-designed models for blasting pattern parameters. In addition, geological conditions should be observed and considered before blasting operations [11]. Many previous studies endeavored to forecast *BB* through numerous machine learning (ML) techniques such as support vector machines (SVM), artificial neural networks (ANN), and so on [3,12–16]. Monjezi, Rezaei and Yazdian [14] developed two multiple-based techniques, namely multiple regression (MR) and fuzzy inference system (FIS) to forecast *BB* induced by blasting. They used burden, the charge per delay, hole depth, specific drilling, stemming spacing, powder factor, and rock density as input variables. They also discovered the FIS model outperforms the MR model. The ANN, neuro-fuzzy and MR models were used by Esmaeili, Osanloo, Rashidinejad, Bazzazi and Taji [3] to forecast the *BB* employing data of Sangan iron mine, Iran. Compared to other models, they demonstrated that the neuro-fuzzy model receives a superior performance. Using 10 input parameters, for the same problem, Monjezi, Ahmadi, Varjani and Khandelwal [13] developed an ANN model using a database comprising of 97 data samples. In addition to the ANN model, they suggested an MR equation for the *BB* prediction. They successfully showed that the ANN model outperforms the MR model. Another study, which was conducted by Mohammadnejad, Gholami, Sereshki and Jamshidi [2], showed the applicability and practicability of the SVM for prediction of *BB* and concluded that the SVM technique is a reliable and precise tool for the *BB* prediction. Some other ML techniques, such as random forest and its optimized approaches, optimized fuzzy-rule techniques with rock engineering systems, and genetic-based models have been suggested in literature for forecasting *BB* resulting from blasting [17–19]. The details of some recent studies on *BB* prediction using ML and artificial intelligence (AI) techniques are described in Table 1. In this table, input variables of *BB* predictive models together with the size of the database used by various researchers are presented. It is worth stating that these models have been used by other investigators in fields of blasting, rock mechanics, geotechnics, and civil and mining engineering [20–41].

The victorious utilizations of SVM and its associated combination variants in determining different geotechnical difficulties were informed by many scholars [49–52]. In the domain of blasting and its environmental effects, many scholars established SVM models to forecast ground vibration, fly-rock distance, rock fragmentation, and blast-caused rock movement [24,53–55]. The SVM is regarded as a robust method that can confidently determine geotechnical-related difficulties. Thus, this research concluded to utilize various hybrid SVM models to explain the *BB* issue. It is necessary to remark that to the best of the authors' knowledge, the SVM models were implemented and offered in the domain of *BB* forecast. Nevertheless, the application of innovative combined predictive models based on the idea of an SVM model optimized by any robust optimization methods are neglected in this domain. Therefore, the central role of this study is to utilize and propose the novel combination of SVM models in forecasting *BB* extent. To accomplish this, the authors selected to use two renowned, robust, and fit optimization methods, including moth–flame optimization (MFO) and whale optimization algorithm (WOA), in integrated SVM models of this research. Consequently, two SVM-centered models, such as SVM–MFO and SVM–WOA, are developed in this study for *BB* magnitude forecasts. The objective of the MFO and WOA systems is to optimize the SVM parameters, including 'C' and 'ε', to observe more eminent performance capabilities for forecast views. Tuning and optimizing SVM parameters by optimization algorithms has been used by researchers for improving the performance of the base model (SVM).

The following explains the remainder of this paper. First, the case study of this research and the methods of the data collection are presented. Second, the structure of the SVM model and its optimizers (MFO and WOA) is presented. Third, the results of this study are presented, evaluated, and discussed. Finally, a summary of this paper is presented in the Section 7.

Table 1. Some recent ML and AI studies on the *BB* prediction.

Method	Study	Input	Dataset Size
FIS	Monjezi, Rezaei and Yazdian [14]	Burden, charge per delay, hole depth, powder factor, rock density, spacing, specific drilling, stemming	-
ANN–GA	Monjezi et al. [42]	Burden, charge per delay, hole diameter, hole length, powder factor, rock mass rating, spacing, specific drilling	195
ANN	Monjezi, Ahmadi, Varjani and Khandelwal [13]	Burden, charge per delay, hole depth, hole diameter, powder factor, spacing, specific drilling, stemming, uniaxial compressive strength water content	97
ANN	Sayadi et al. [43]	Burden, hole depth, spacing, specific charge, specific drilling	103
SVM	Mohammadnejad, Gholami, Sereshki and Jamshidi [2]	Burden, hole depth, powder factor, spacing, specific drilling, stemming	193
SVM	Khandelwal and Monjezi [12]	Burden, hole length, powder factor, spacing, specific drilling, stemming	234
ANN	Monjezi et al. [44]	Burden, delay per burden, number of rows, powder factor rock factor, spacing, specific drilling, stemming	-
ANN, neuro-fuzzy	Esmaeili, Osanloo, Rashidinejad, Bazzazi and Taji [3]	Charge last row, number of rows, specific charge, stemming	42
ANN, ABC	Ebrahimi et al. [45]	Burden, hole depth, powder factor, spacing, stemming length	34
GP	Faradonbeh et al. [46]	Burden, powder factor, spacing, stemming, stiffness ratio	175
fuzzy RES–GA, fuzzy RES–ICA	Hasanipanah and Bakhshandeh Amnieh [17]	Burden, blast-hole inclination, burden to hole diameter ratio, charge per delay, hole diameter, spacing to burden ratio, stemming to burden ratio, velocity of detonation	62
RF	Kumar et al. [47].	Spacing to burden ratio, P-wave, hole length to stemming ratio, density of explosive	140
SCA–RF, HHO–RF	Zhou, Dai, Khandelwal, Monjezi, Yu and Qiu [18]	Burden, hole length, powder factor, spacing, specific drilling, stemming	234
ANN, ACO	Saghatforoush et al. [48]	Burden, hole length, powder factor, spacing, stemming length	97

GP: genetic programing, ACO: ant colony optimization, GA: genetic algorithm, ICA: imperialism competitive algorithm, RES: rock engineering system, RF: random forest, HHO: Harris hawks optimizer, SCA: sine cosine algorithm.

2. Field Observation and Measurement

The data of this present research were gathered from a blasting operation in Gol-E-Gohar Iron mine. This mine is situated in Kerman province, Iran (Figure 1). During the blasting operation, the height of the blast holes and diameter were 17 m and 203 mm, respectively. The lag time between the first and second row was 80 ms. The lag time for the other rows was set as 50 ms. The stemming material used was drilling cuttings. In this mine, the *BB* phenomenon has worsened and reached up to 20 m because of its inappropriate blasting patterns. The problem of the *BB* (with 20 m) induced by the blasting operation in the investigated mine is shown in Figure 2.

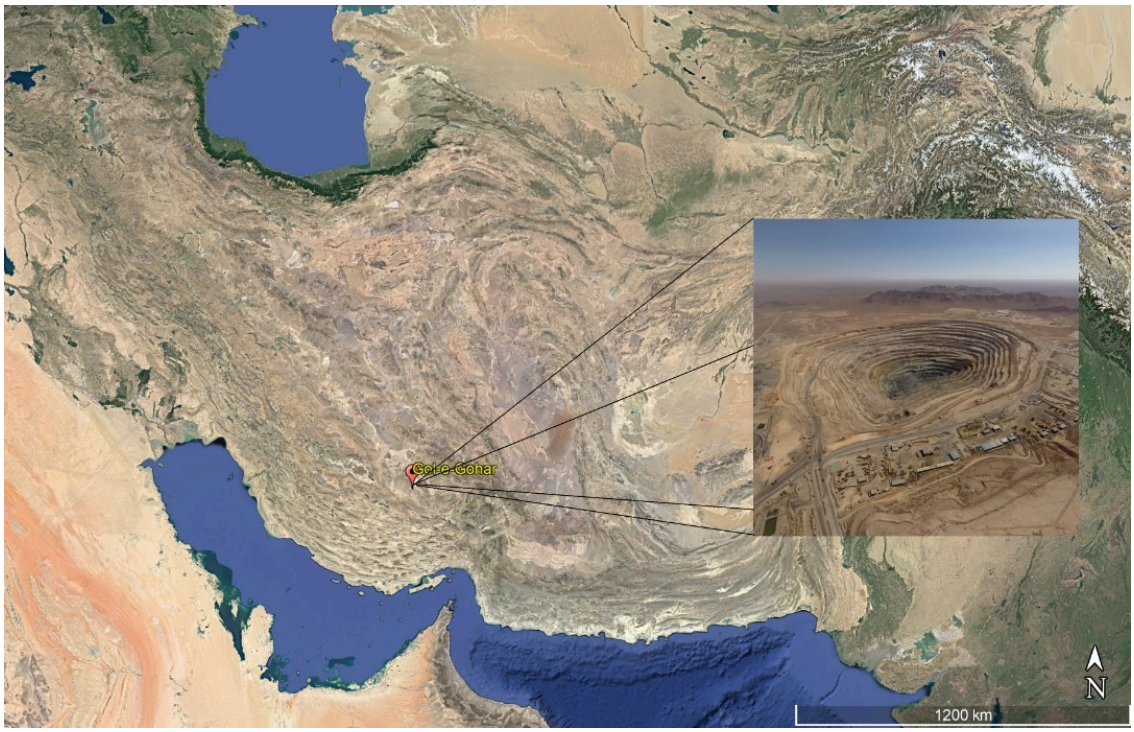

Figure 1. Position of the research area in Iran.

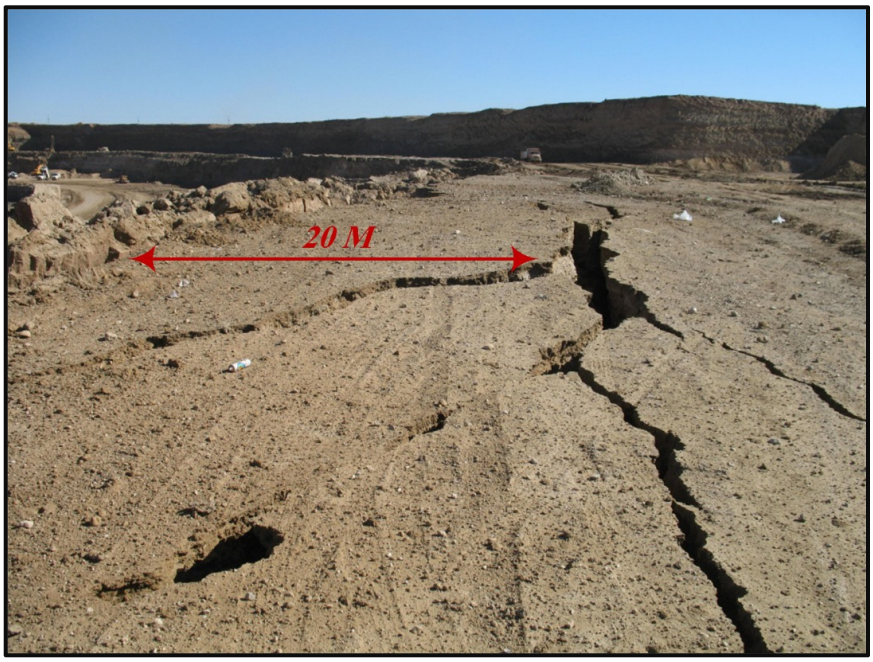

Figure 2. *BB* problem induced by blasting in the studied mine.

Table 2 demonstrates the scale, unit and symbol of the assessed parameters in the study site together with more information of the *BB* parameter. In total, 85 blasting events were considered and their data were used in this research for the *BB* forecast. In the following, the process of selecting the most important parameters among these 10 measured parameters on the *BB* will be discussed and then the modeling procedure using tree-based models will be described in detail.

Table 2. Summary of gathered data with their symbol, unit and range.

Parameter	Class	Unit	Acronym	Min	Max
Powder factor	Input	kg/ton	PF	1.90	0.30
Burden	Input	m	B	5.00	6.50
Spacing to burden ratio	Input	—	S/B	1.18	1.30
Number of rows	Input	—	No. row	2.00	5.00
Charge per delay	Input	Kg	CPD	72.00	455.96
Last row charge to total charge ratio	Input	—	LRC/TC	0.04	0.55
Stemming to burden ratio	Input	—	St/B	0.80	1.60
Joint condition	Input	—	JC	1.00	4.00
Uniaxial compressive strength	Input	MPa	UCS	55.00	90.00
Water height to burden ratio	Input	—	W/B	0.00	2.00
Back-break	Target	m	*BB*	3.00	20.00

3. Methods

3.1. SVM

The SVM is considered as a supervised ML technique that is successfully implemented in the domain of geotechnical and tunnelling engineering [56]. The linear function of SVM can be explained as follow:

$$f(a) = w.a + d \tag{1}$$

where a denotes the input variable, w denotes the weight vector, and d points to model error values. SVM strives to decrease the disparity between the real and predicted values. Therefore, SVM predicts according to reducing the objective function, which is an error indicator. Below is the optimization procedure [57]:

$$min\frac{1}{2}\|w\|^2 + c\sum_{i=1}^{k}(\xi_i^- - \xi_i^+) \tag{2}$$

$$Subject(to)(wx_i + d) - b_i < \varepsilon + \xi_i^+ \tag{3}$$

$$b_i - (w_i a_i + d) \leq (\varepsilon + \varepsilon_i^-) \tag{4}$$

where C denotes the coefficient of penalty, k means the number of training data, ξ_i^- and ξ_i^+ signify the data violations whose various values are higher than ξ the allowed range with observable values, and w_i, a_i, and b_i refer to the variables' weight, the input variable, and the target observation. Equations (2) and (3) are used to estimate the values of w and d and are then replaced into Equation (1). In SVM, to represent the input data points to a high-dimensional feature space, the kernel function can be employed. The kernels are able to resolve the issues with numerous dimensions. A total of four well-known SVM kernels are used, including sigmoid, linear, polynomial, and radial basis function (RBF). In this study, the RBF kernel was used since this kernel was proved to possess a desirable generalization capability for various types of datasets. Thus, Equation (1) is regarded as follows:

$$f(a) = w.H(a, a_i) + d \tag{5}$$

$$H(a, a_i) = \exp\left(-\frac{a - a_i}{2\gamma^2}\right) \tag{6}$$

where $H(a, a_i)$ stands for the kernel function, and γ signifies the kernel function's parameter. SVM parameters such as C and ε have unknown values and are assumed as decision variables. Thus, they should enter the optimization process. The aim of hybrid SVM, MFO, and WOA is to determine the precise value of the parameters mentioned above and predict *BB* by SVM. Figure 3 indicates the optimization process employed by each optimization method, including WOA and MFO, as well as their functions in two combined models of SVM–MFO and SVM–WOA to forecast *BB* values.

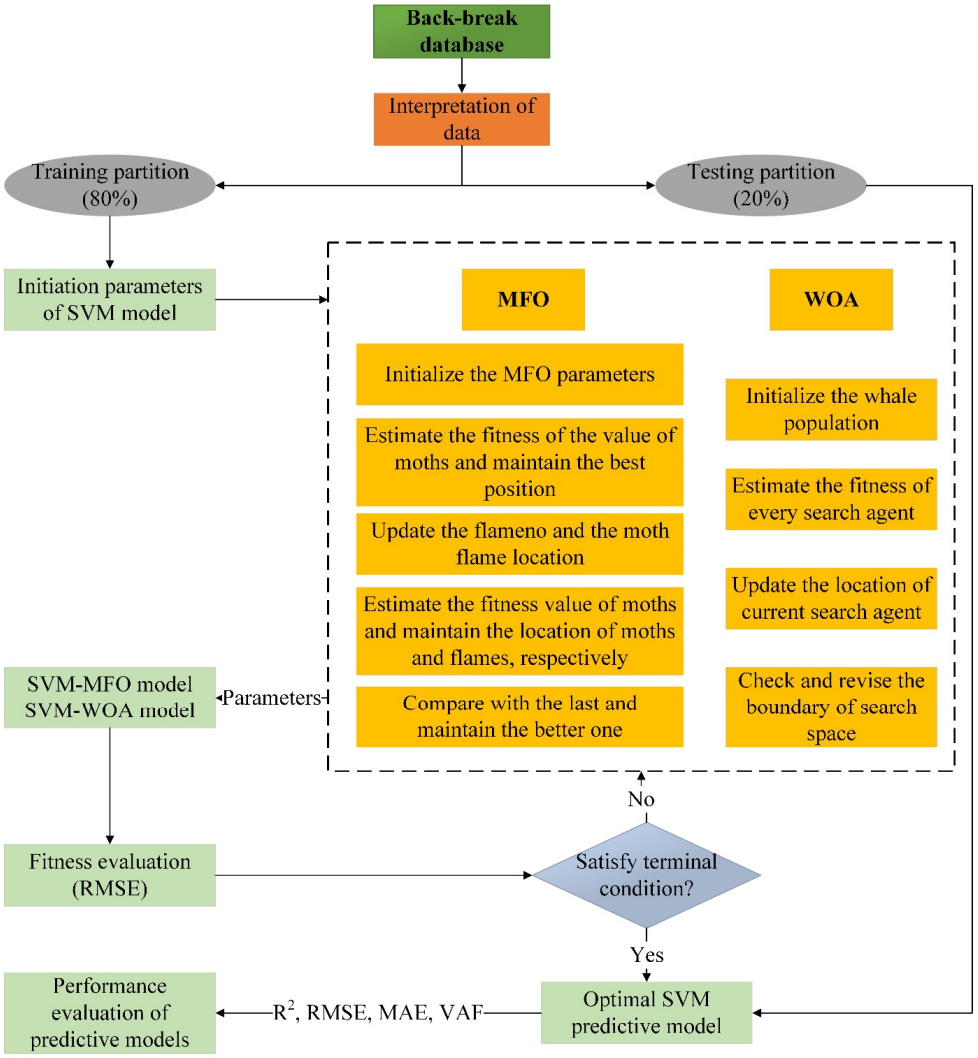

Figure 3. Flowchart of this investigation.

3.2. MFO

MFO is one of the most effective optimization algorithms that mimics the fly styles of moths in the darkness. Typically, moths try to keep a fixed position to the moon for shuttling at nighttime [58]. They engage a method defined as a transverse orientation to navigate. Nevertheless, sometimes this method is useless, and especially so for straight movement if the light origin is extremely far away. If moths find irregular lighting, they endeavor to preserve an analogous form with the brightness to pass it in a straight way. Notwithstanding that this bright origin is closer to the moths than the moon, holding a comparable angle to the origin of light creates an incompetent or killing spiral fly-path for moths. This sort of killing flow, while the origin of light is close, is used to determine the optimization problems in the actual practice. In this method, the probable answers are moths, and variables are moths' coordinate vectors in the exploration space. The MFO equation used for optimizing SVM is presented in Equation (7).

$$Flame\ number = round(N - m * \frac{N-1}{Q}) \tag{7}$$

where m indicates the current number of repetitions, the highest quantity of flames is represented by N, and Q implies the largest number of repetitions.

3.3. WOA

The WOA is an optimization approach that imitates the humpback whale's social practice in following their hunt in seas [59]. This algorithm utilizes a different method following the particular bubble net and the feeding habits of the whale. The WOA method comprises three principal activities, including encircling prey, bubble-net attacking (Equation (8)) and prey exploring (Equation (9)). Here is the mathematical presentation of these activities.

$$X^{s+1} = \begin{cases} X^s_{gbest} - F.\left|M.X^s_{gbest} - X^s\right|, p < 0.5 \\ X^s_{gbest} + Q.e^{bl}.\cos(2\pi l),\ p \geq 0.5 \end{cases} \quad (8)$$

$$X^{s+1} = X^s_{rand} - F.|M.X^s_{rand} - X^s| \quad (9)$$

where s refers to the present repetition, X^s is the existing position vector, X^{s+1} is the new position, X^s_{gbest} represents the existing position of the best solution achieved, F and M are the coefficient vectors, l stands for an arbitrary number within [−1,1], b signifies a constant for limiting the form of the logarithmic spiral, p signifies an arbitrary number within [0,1], X^s_{rand} denotes a position vector of a whale individual at random selected from the existing inhabitants, and $Q = \left|X^s_{gbest} - X_s\right|$ stands for the space between the whale and the target.

Every humpback whale signifies an individual, and the location of every individual in the search space describes a solution. The whale can know the position of the prey and circle the prey within the echolocation (encircling prey). The whale strikes the target by spiraling up and constantly narrowing the circling (bubble-net attacking). If the coefficient vector $|F| > 1$, it indicates that the whale moves beyond the lessening encircling circle. At this point in time, the humpback whale explores arbitrarily based on every other's position.

4. SVM Optimized Models

For developing the optimized SVM models, the aim of employing WOA and MFO algorithms is to optimize the SVM hyperparameters 'ε' and 'C'. The values of these parameters were set within the following ranges:

- C: 0.01–100;
- ε: 0.01–50.

The key procedure of optimizing SVM parameters utilizing WOA and MFO optimization methods is indicated in Figure 4. The first step involved is preparing the data and dividing it into training and testing sets. The second step involved is assigning appropriate values to the WOA and MFO parameters. In the third step, *RMSE* was used as an indicator for assessing the models' fitness. The parameters were revised based on the outcomes of each repetition in the fourth step. In the final step, the most suitable values for the parameters were achieved, and the stopping conditions were met.

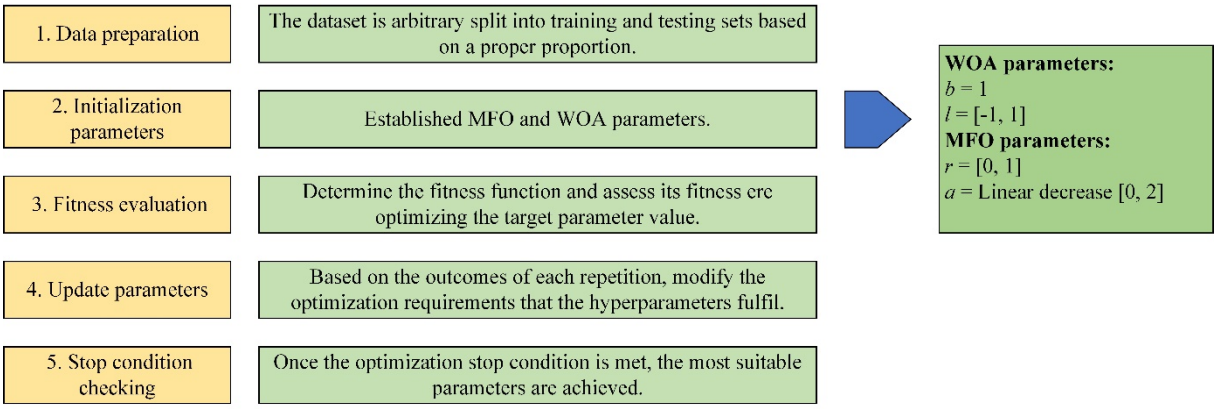

Figure 4. The primary procedure of optimizing parameters of SVM.

5. Results and Discussions

5.1. Feature Selection

An evolutionary random forest (ERF) technique was employed to select the most significant factors for *BB* prediction. This model was applied to ten candidate inputs, including PF, B, S/B, No. row, CPD, LRC/TC, St/B, JC, and UCS. The ERF selected five important inputs, including PF, No. row, CPD, LRC/TC, and St/B. These inputs were used to develop the SVM model and its optimized variants. This model was ran using the parameters shown in Figure 5. Figure 6 demonstrates the frequency distribution of each selected input and *BB*. The coefficient of determination (R^2)-linear regression of this model was obtained as 0.909.

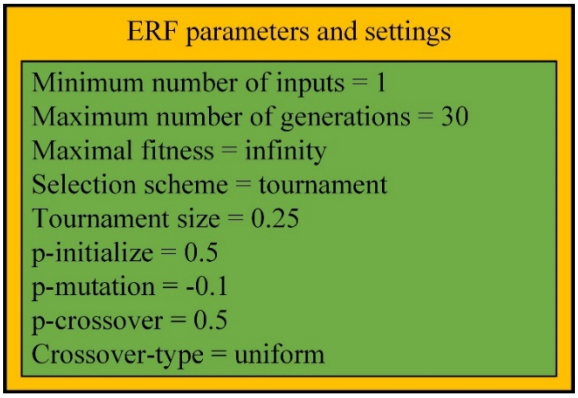

Figure 5. ERF parameters and their associated values.

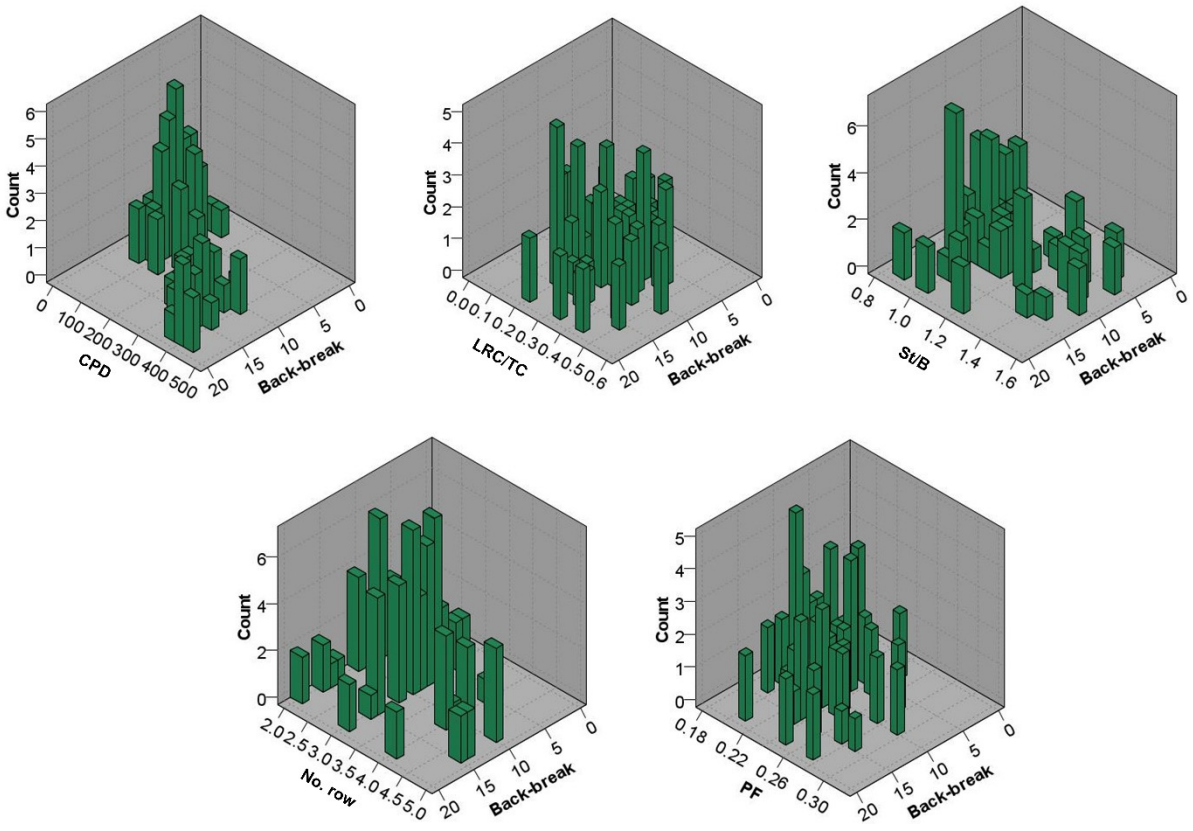

Figure 6. A 3D histogram of each selected input and *BB*.

5.2. Models' Development and Evaluation

Once the models are developed, it is vital to assess the performance of them. To this end, four performance criteria, including R^2, the mean absolute error (*MAE*), the root mean squared error (*RMSE*), and the variance accounted for (*VAF*), were employed. The formulas for estimating these criteria are shown in Equations (10)–(13). In these equations, BB_i is the real value, $\widehat{BB}_i$ stands for the forecasted value, $\overline{BB_i}$ implies the mean of the real values, and N signifies the number of samples in the training or testing phases. It is important to mention that these performance criteria have been used in many published works (e.g., [60–65]).

$$RMSE = \sqrt{\frac{1}{N}\sum_{i=1}^{N}\left(\widehat{BB_i} - BB_i\right)^2} \tag{10}$$

$$R^2 = 1 - \frac{\sum_{i=1}^{N}\left(BB_i - \widehat{BB_i}\right)^2}{\sum_{i=1}^{N}\left(BB_i - \overline{BB_i}\right)^2} \tag{11}$$

$$MAE = \frac{1}{N}\sum_{i=1}^{N}\left|\widehat{BB_i} - BB_i\right| \tag{12}$$

$$VAF = \left[1 - \frac{var(BB_i - \widehat{BB_i})}{var(BB_i)}\right] \times 100 \tag{13}$$

Figure 7 shows the association between the predicted and real values of *BB*. The outcomes indicate that the testing and training outcomes of these algorithms are great. The training and test values are scattered adjacent to the best fitting line. Concerning the performance indicators, the forecast performance of the SVM–MFO is somewhat greater than the other model. For the training phase, the R^2 (linear regression), *RMSE*, *MAE*, and *VAF* values were 0.992, 0.364, 0.044, and 99.150, correspondingly. For the testing phase, the R^2, *RMSE*, *MAE*, and *VAF* values were 0.985, 0.629, 0.332, and 98.371, respectively. It is worth noticing that the SVM–MFO is a more reliable model than the other optimized model for both the training and testing phases. Expectedly, these two hybrid models are capable of considerably improving the performance capability of a single SVM model in predicting *BB*, as displayed in Table 3. For example, the *RMSE* value can be lessened from 1.714 to below 0.6 (in the training phase) by optimizing the SVM models.

Table 3. Performance of the models developed.

Model	Training				Testing			
	R^2 (rank)	RMSE (rank)	VAF (rank)	MAE (rank)	R^2 (rank)	RMSE (rank)	VAF (rank)	MAE (rank)
SVM	0.885 (1)	1.714 (1)	88.404 (1)	1.135 (1)	0.844 (1)	1.949 (1)	82.391 (1)	1.553 (1)
SVM–MFO	0.992 (3)	0.364 (3)	99.150 (3)	0.044 (3)	0.985 (3)	0.629 (3)	98.371 (3)	0.332 (3)
SVM–WOA	0.981 (2)	0.559 (2)	98.064 (2)	0.125 (2)	0.974 (2)	0.805 (2)	97.168 (2)	0.391 (2)

Tables 3 and 4 review the performance indicator outcomes (R^2, *RMSE*, *MAE*, and *VAF*) and overall ranking outcomes of the standard SVM and two hybrid models in forecasting *BB*. The joining outcomes of the training and testing sets are that the total ranking of SVM–MFO is superior. This explains that the SVM–MFO gives greater precision and robustness in forecasting *BB* compared to the SVM–WOA.

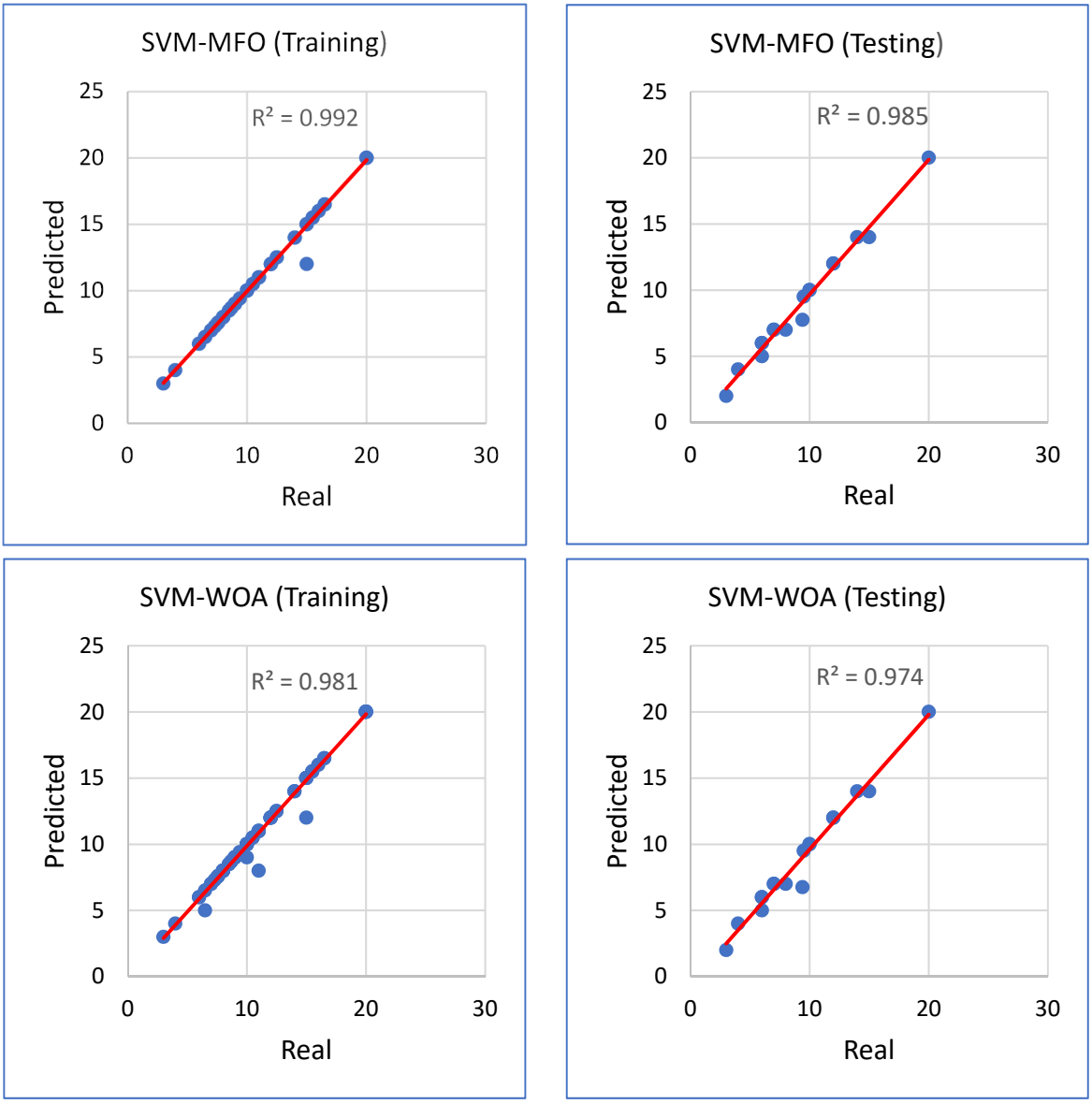

Figure 7. Real and predicted values of *BB* using different SVM-based models.

Table 4. Total ranking of the models developed.

	Training Rank	Testing Rank	Total Rank
SVM	4	4	8
SVM–MFO	12	12	24
SVM–WOA	8	8	16

The performance of the two models established in this research was also compared with two more well-known SVM optimized models, including SVM–particle swarm optimization (PSO) and SVM–cuckoo optimization algorithm (COA). The outcomes of this comparison are displayed in Figure 8. The parallel graph outcomes explain that the forecast performance of the SVM models established in this research is more precise than the other algorithms. Amongst all the models, the SVM–MFO is more reliable. According to the findings of this study, it is evident that the SVM–MFO has excellent learning and forecast capacities. Hence, this present study suggests employing the developed SVM–MFO model for *BB* prediction.

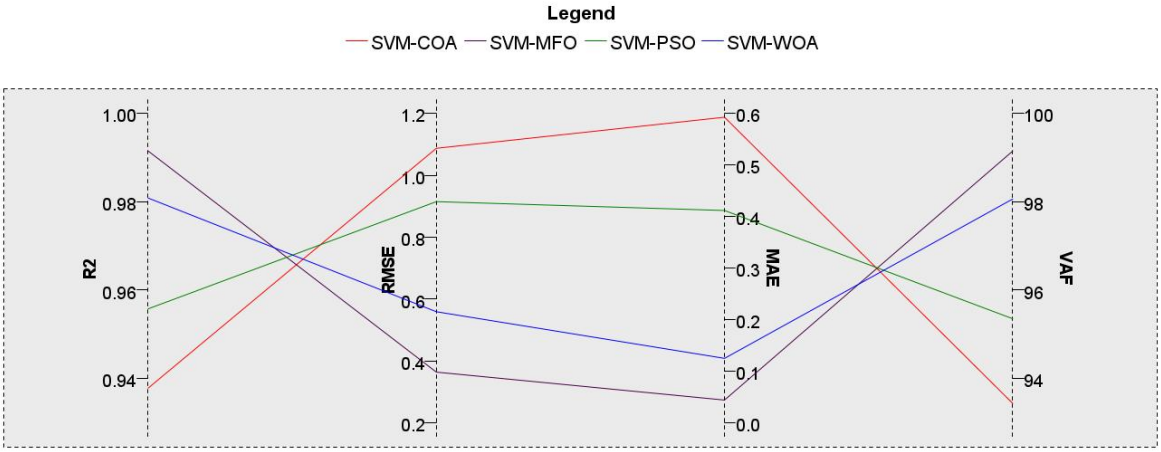

Figure 8. Performance of models developed in this investigation (training phase).

The data used in this study were also used by Monjezi and Dehghani [66]. They did not employ a feature selection technique and used seven inputs for developing neural network models. The best values of R^2 and *RMSE* that they achieved were 0.972 and 0.643, respectively. For both training and testing, the R^2 of SVM–MFO is better than those presented by Monjezi and Dehghani [60]. In addition, these data were used by Monjezi, Rezaei and Yazdian [14], and they applied fuzzy set theory and MR models to eight inputs. Their best R^2 value was 0.954. This comparison shows that despite the usage of fewer inputs for developing the SVM–MFO, this model showed better performance than the models developed in the above studies. It is important to mention that one of the shortcomings and disadvantages of ML and AI models is their limited practical application. We as engineers should always try to make them as simple as possible in practice for other researchers and designers. In this way, one of the possible options is related to the number of inputs that we need to give to the system. The level of complexity can be decreased by reducing the number of input parameters. Another point is related to the fact that if a lower number of inputs are needed to be collected, the process of data collection would be easier and faster compared with the situation in which we need to collect and have all inputs.

6. Analysis of Sensitivity

In mechanical tunnel engineering, the forecast of a *BB* is the solution under specific rock circumstances. Different determinants of *BB* should be systematically examined to forecast the *BB* precisely and decrease the great cost and danger of tunnel building. It can be identified that whole inputs, namely PF, No. row, CPD, LRC/TC, and St/B, contribute to the *BB* forecast. Nevertheless, the sensitivity of every input is ambiguous and requires further investigation.

In this part, the mutual information (MI) test method [67] is employed for examining the significance of *BB* factors and their sensitivity. MI is a filtering technique that obtains the arbitrary connection between inputs and the target. MI tests the dependence among variables and shows the intensity of the association among them. The MI magnitude among variables is estimated by means of the information gain:

$$Gain(A,\ B) = Ent(A) - \sum_{s-1}^{S} \frac{|A^s|}{|A|} Ent(A^s) \tag{14}$$

where s denotes the number of all probable values of B, As is the set of A when B takes the value Bs, and $Ent(A)$ signifies the information entropy. The larger the value of gain (A, B), the better the relationship between B and A.

Finally, based on the variable score in the MI examination, the significance intensity of the input that forecasts *BB* was ascertained. The results of this analysis are indicated in Figure 9. The most crucial variables for forecasting *BB* were CPD, PF, and St/B. Their

significance scores were 59.52, 15.09, and 11.92, respectively. The lowest score belonged to LRC/TC (significance score = 2.94). Nevertheless, it should be mentioned that inputs, such as LRC/TC and No. row, still have a deep influence on *BB*.

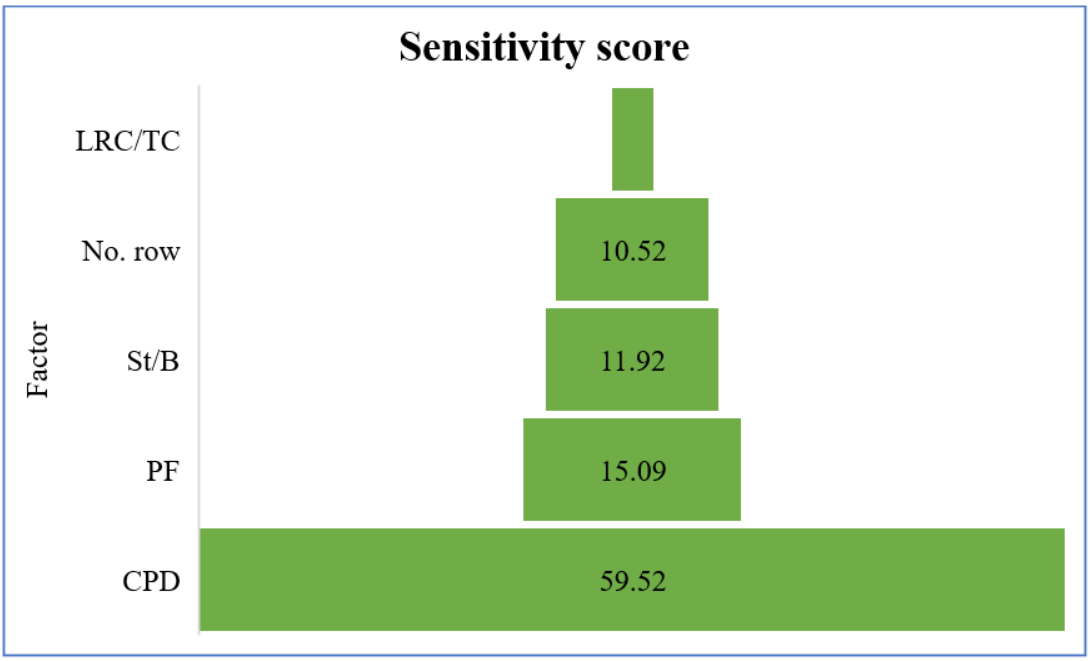

Figure 9. Analysis of sensitivity of five factors on *BB*.

7. Conclusions

This study attempts to hybridize the SVM algorithm with well-known and efficient optimization algorithms in the domain of *BB* prediction. To achieve this goal, two renowned optimization algorithms, including WOA and MFO, which were effectively investigated by previous scientists, were chosen and integrated with SVM, and later, SVM–MFO and SVM–WOA were built for forecasting intentions. The models were built employing ten inputs and one target, which was *BB*. Before the models' development, an ERF was used as the feature selection method to lessen the data dimensionality and identify the most relevant inputs for *BB* prediction. The inputs selected by this technique were PF, No. row, CPD, LRC/TC, and St/B. To appraise the performance of the developed models, several measures were employed, including R^2, *RMSE*, *VAF*, and *MAE*. Additionally, for the purpose of comparison, the authors have forecasted *BB* developing different models, including standard SVM, SVM-PSO, and SVM-COA. Finally, following the evaluation of the performance of the entire implemented and built models, it was discovered that the SVM–MFO had an R^2 of (0.992 and 0.985), *RMSE* of (0.364 and 0.629), *VAF* of (99.150 and 98.371), and *MAE* of (0.044 and 0.332), correspondingly, for training and test phases, which are better results than those of other employed projecting methods. Consequently, the model offered in this research can be employed in different schemes relating *BB*s for forecasting their accomplishments. By administering the sensitivity investigation, the relevance score of all inputs was achieved utilizing the MI method. This method was executed among those five variables that were identified by the ERF technique. The importance scores of LRC/TC, No. row, St/B, PF, and CPD were 2.94, 10.52, 11.92, 15.09, and 59.52. These results proved that CPD, PF, and St/B variables are regarded as greatly sensitive determinants on *BB*. Nevertheless, it should be mentioned that additional data and examination are required to analyze the *BB* under different, severe circumstances. Hence, the employment of the integrated model offered in this article is solely advised under comparable circumstances and in a consistent range of data. Future studies should employ datasets with more data and inputs to enhance the predictive capability of the model. Furthermore, AI-based systems cannot entirely substitute conventional practical techniques.

Regarding geotechnical engineering, the potential advancement path of AI technology is a mixed method, which simply evolves in the direction of decision support instruments. Prominently, the smart systems employed are just suggested to be implemented under comparable circumstances in this research. The principal weakness of such methods in the geotechnical domain can be regarded as site-specific data employed in developing AI models. The geotechnical data and measurements can vary from location to location, and because of this issue, the generalization of the developed AI models is a challenging task.

Author Contributions: Conceptualization, D.J.A., M.M. and H.D.; methodology, Q.Y., D.J.A. and A.S.M.; software, Q.Y., D.J.A. and A.S.M.; formal analysis, Q.Y., D.J.A. and A.S.M.; writing—original draft preparation, Q.Y., D.J.A., A.S.M., M.M., H.D. and D.V.U.; writing—review and editing, H.D., A.S.M., D.J.A., M.M. and D.V.U.; supervision, D.J.A., M.M., A.S.M. and H.D.; data curation, M.M. and H.D. All authors have read and agreed to the published version of the manuscript.

Funding: The research was funded by Act 211 Government of the Russian Federation, contract No. 02.A03.21.0011.

Institutional Review Board Statement: Not applicable.

Informed Consent Statement: Not applicable.

Data Availability Statement: The data are available upon request.

Conflicts of Interest: The authors declare no conflict of interest.

References

1. Jimeno, C.L.; Jimeno, E.L.; Carcedo, F.J.A. *Drilling and Blasting of Rocks*; Balkema: Rotterdam, The Netherlands, 1995; pp. 183–184. [CrossRef]
2. Mohammadnejad, M.; Gholami, R.; Sereshki, F.; Jamshidi, A. A new methodology to predict backbreak in blasting operation. *Int. J. Rock Mech. Min. Sci.* **2013**, *60*, 75–81. [CrossRef]
3. Esmaeili, M.; Osanloo, M.; Rashidinejad, F.; Bazzazi, A.A.; Taji, M. Multiple regression, ANN and ANFIS models for prediction of backbreak in the open pit blasting. *Eng. Comput.* **2014**, *30*, 549–558. [CrossRef]
4. Konya, C.J.; Walter, E.J. *Surface Blast Design*; Prentice Hall: Englewood Cliffs, NJ, USA, 1990.
5. Bhandari, S. *Engineering Rock Blasting Operations*; A.A. Balkema: Rotterdam, The Netherlands, 1997.
6. Agrawal, H.; Mishra, A. Modified scaled distance regression analysis approach for prediction of blast-induced ground vibration in multi-hole blasting. *J. Rock Mech. Geotech. Eng.* **2019**, *11*, 202–207. [CrossRef]
7. Jayasinghe, B.; Zhao, Z.; Chee, A.G.T.; Zhou, H.; Gui, Y. Attenuation of rock blasting induced ground vibration in rock-soil interface. *J. Rock Mech. Geotech. Eng.* **2019**, *11*, 770–778. [CrossRef]
8. Armaghani, D.J.; Koopialipoor, M.; Bahri, M.; Hasanipanah, M.; Tahir, M.M. A SVR-GWO technique to minimize flyrock distance resulting from blasting. *Bull. Int. Assoc. Eng. Geol. Environ.* **2020**, *79*, 4369–4385. [CrossRef]
9. Gates, W.C.; Ortiz, L.T.; Florez, R.M. Analysis of rockfall and blasting backbreak problems, US 550, Molas Pass, CO. In Proceedings of the Alaska Rocks 2005 the 40th US Symposium on Rock Mechanics (USRMS), Anchorage, AK, USA, 25–29 June 2005.
10. Kumar, R.; Choudhury, D.; Bhargava, K. Determination of blast-induced ground vibration equations for rocks using mechanical and geological properties. *J. Rock Mech. Geotech. Eng.* **2016**, *8*, 341–349. [CrossRef]
11. Bhagade, N.V.; Murthy, V.M.S.R. Controlling backbreak and enhancing fragmentation in dragline bench blasting—A geo-engineering approach. *Arab. J. Geosci.* **2020**, *13*, 304. [CrossRef]
12. Khandelwal, M.; Monjezi, M. Prediction of Backbreak in Open-Pit Blasting Operations Using the Machine Learning Method. *Rock Mech. Rock Eng.* **2012**, *46*, 389–396. [CrossRef]
13. Monjezi, M.; Ahmadi, Z.; Varjani, A.Y.; Khandelwal, M. Backbreak prediction in the Chadormalu iron mine using artificial neural network. *Neural Comput. Appl.* **2013**, *23*, 1101–1107. [CrossRef]
14. Monjezi, M.; Rezaei, M.; Yazdian, A. Prediction of backbreak in open-pit blasting using fuzzy set theory. *Expert Syst. Appl.* **2010**, *37*, 2637–2643. [CrossRef]
15. Faramarzi, F.; Farsangi, M.A.E.; Mansouri, H. An RES-Based Model for Risk Assessment and Prediction of Backbreak in Bench Blasting. *Rock Mech. Rock Eng.* **2013**, *46*, 877–887. [CrossRef]
16. Sari, M.; Ghasemi, E.; Ataei, M. Stochastic Modeling Approach for the Evaluation of Backbreak due to Blasting Operations in Open Pit Mines. *Rock Mech. Rock Eng.* **2014**, *47*, 771–783. [CrossRef]
17. Hasanipanah, M.; Amnieh, H.B. Developing a new uncertain rule-based fuzzy approach for evaluating the blast-induced backbreak. *Eng. Comput.* **2021**, *37*, 1879–1893. [CrossRef]
18. Zhou, J.; Dai, Y.; Khandelwal, M.; Monjezi, M.; Yu, Z.; Qiu, Y. Performance of Hybrid SCA-RF and HHO-RF Models for Predicting Backbreak in Open-Pit Mine Blasting Operations. *Nat. Resour. Res.* **2021**, *30*, 4753–4771. [CrossRef]
19. Sharma, M.; Agrawal, H.; Choudhary, B.S. Multivariate regression and genetic programming for prediction of backbreak in open-pit blasting. *Neural Comput. Appl.* **2021**. [CrossRef]

20. Khandelwal, M.; Singh, T.N. Prediction of Blast Induced Air Overpressure in Opencast Mine. *Noise Vib. Worldw.* **2005**, *36*, 7–16. [CrossRef]
21. Armaghani, D.J.; Momeni, E.; Abad, S.V.A.N.K.; Khandelwal, M. Feasibility of ANFIS model for prediction of ground vibrations resulting from quarry blasting. *Environ. Earth Sci.* **2015**, *74*, 2845–2860. [CrossRef]
22. Qiu, Y.; Zhou, J.; Khandelwal, M.; Yang, H.; Yang, P.; Li, C. Performance evaluation of hybrid WOA-XGBoost, GWO-XGBoost and BO-XGBoost models to predict blast-induced ground vibration. *Eng. Comput.* **2021**. [CrossRef]
23. Rezaeineshat, A.; Monjezi, M.; Mehrdanesh, A.; Khandelwal, M. Optimization of blasting design in open pit limestone mines with the aim of reducing ground vibration using robust techniques. *Géoméch. Geophys. Geo-Energy Geo-Resour.* **2020**, *6*, 40. [CrossRef]
24. Yu, Z.; Shi, X.; Miao, X.; Zhou, J.; Khandelwal, M.; Chen, X.; Qiu, Y. Intelligent modeling of blast-induced rock movement prediction using dimensional analysis and optimized artificial neural network technique. *Int. J. Rock Mech. Min. Sci.* **2021**, *143*, 104794. [CrossRef]
25. Yang, H.; Zeng, Y.; Lan, Y.; Zhou, X. Analysis of the excavation damaged zone around a tunnel accounting for geostress and unloading. *Int. J. Rock Mech. Min. Sci.* **2014**, *69*, 59–66. [CrossRef]
26. Yang, H.; Li, Z.; Jie, T.; Zhang, Z. Effects of joints on the cutting behavior of disc cutter running on the jointed rock mass. *Tunn. Undergr. Space Technol.* **2018**, *81*, 112–120. [CrossRef]
27. Yang, H.; Xing, S.; Wang, Q.; Li, Z. Model test on the entrainment phenomenon and energy conversion mechanism of flow-like landslides. *Eng. Geol.* **2018**, *239*, 119–125. [CrossRef]
28. Yang, H.; Wang, Z.; Song, K. A new hybrid grey wolf optimizer-feature weighted-multiple kernel-support vector regression technique to predict TBM performance. *Eng. Comput.* **2020**. [CrossRef]
29. Liu, B.; Yang, H.; Karekal, S. Effect of Water Content on Argillization of Mudstone During the Tunnelling process. *Rock Mech. Rock Eng.* **2020**, *53*, 799–813. [CrossRef]
30. Zhou, J.; Shen, X.; Qiu, Y.; Li, E.; Rao, D.; Shi, X. Improving the efficiency of microseismic source locating using a heuristic algorithm-based virtual field optimization method. *Géoméch. Geophys. Geo-Energy Geo-Resour.* **2021**, *7*, 89. [CrossRef]
31. Zhou, J.; Qiu, Y.; Khandelwal, M.; Zhu, S.; Zhang, X. Developing a hybrid model of Jaya algorithm-based extreme gradient boosting machine to estimate blast-induced ground vibrations. *Int. J. Rock Mech. Min. Sci.* **2021**, *145*, 104856. [CrossRef]
32. Zhou, J.; Li, X.; Mitri, H.S. Classification of Rockburst in Underground Projects: Comparison of Ten Supervised Learning Methods. *J. Comput. Civ. Eng.* **2016**, *30*, 04016003. [CrossRef]
33. Zhou, J.; Chen, C.; Wang, M.; Khandelwal, M. Proposing a novel comprehensive evaluation model for the coal burst liability in underground coal mines considering uncertainty factors. *Int. J. Min. Sci. Technol.* **2021**, *31*, 799–812. [CrossRef]
34. Li, Y.; Hishamuddin, F.N.S.; Mohammed, A.S.; Armaghani, D.J.; Ulrikh, D.V.; Dehghanbanadaki, A.; Azizi, A. The Effects of Rock Index Tests on Prediction of Tensile Strength of Granitic Samples: A Neuro-Fuzzy Intelligent System. *Sustainability* **2021**, *13*, 10541. [CrossRef]
35. Parsajoo, M.; Armaghani, D.J.; Mohammed, A.S.; Khari, M.; Jahandari, S. Tensile strength prediction of rock material using non-destructive tests: A comparative intelligent study. *Transp. Geotech.* **2021**, *31*, 100652. [CrossRef]
36. Armaghani, D.J.; Harandizadeh, H.; Momeni, E.; Maizir, H.; Zhou, J. An optimized system of GMDH-ANFIS predictive model by ICA for estimating pile bearing capacity. *Artif. Intell. Rev.* **2021**. [CrossRef]
37. Al-Bared, M.A.M.; Mustaffa, Z.; Armaghani, D.J.; Marto, A.; Yunus, N.Z.M.; Hasanipanah, M. Application of hybrid intelligent systems in predicting the unconfined compressive strength of clay material mixed with recycled additive. *Transp. Geotech.* **2021**, *30*, 100627. [CrossRef]
38. Mohammed, A.; Asteris, P.; Koopialipoor, M.; Alexakis, D.; Lemonis, M.; Armaghani, D. Stacking Ensemble Tree Models to Predict Energy Performance in Residential Buildings. *Sustainability* **2021**, *13*, 8298. [CrossRef]
39. Briševac, Z.; Hrženjak, P.; Buljan, R. Models for estimating uniaxial compressive strength and elastic modulus. *Građevinar* **2016**, *68*, 19–28. [CrossRef]
40. Briševac, Z.; Pollak, D.; Maričić, A.; Vlahek, A. Modulus of Elasticity for Grain-Supported Carbonates—Determination and Estimation for Preliminary Engineering Purposes. *Appl. Sci.* **2021**, *11*, 6148. [CrossRef]
41. Briševac, Z.; Hrženjak, P.; Cotman, I. Estimate of Uniaxial Compressive Strength and Young's Modulus of the Elasticity of Natural Stone Giallo d'Istria. *Procedia Eng.* **2017**, *191*, 434–441. [CrossRef]
42. Monjezi, M.; Khoshalan, H.A.; Varjani, A.Y. Prediction of flyrock and backbreak in open pit blasting operation: A neuro-genetic approach. *Arab. J. Geosci.* **2012**, *5*, 441–448. [CrossRef]
43. Sayadi, A.; Monjezi, M.; Talebi, N.; Khandelwal, M. A comparative study on the application of various artificial neural networks to simultaneous prediction of rock fragmentation and backbreak. *J. Rock Mech. Geotech. Eng.* **2013**, *5*, 318–324. [CrossRef]
44. Monjezi, M.; Rizi, S.M.H.; Majd, V.J.; Khandelwal, M. Artificial Neural Network as a Tool for Backbreak Prediction. *Geotech. Geol. Eng.* **2014**, *32*, 21–30. [CrossRef]
45. Ebrahimi, E.; Monjezi, M.; Khalesi, M.R.; Armaghani, D.J. Prediction and optimization of back-break and rock fragmentation using an artificial neural network and a bee colony algorithm. *Bull. Int. Assoc. Eng. Geol.* **2016**, *75*, 27–36. [CrossRef]
46. Faradonbeh, R.S.; Monjezi, M.; Armaghani, D.J. Genetic programing and non-linear multiple regression techniques to predict backbreak in blasting operation. *Eng. Comput.* **2016**, *32*, 123–133. [CrossRef]
47. Kumar, S.; Mishra, A.K.; Choudhary, B.S. Prediction of back break in blasting using random decision trees. *Eng. Comput.* **2021**. [CrossRef]
48. Saghatforoush, A.; Monjezi, M.; Faradonbeh, R.S.; Armaghani, D.J. Combination of neural network and ant colony optimization algorithms for prediction and optimization of flyrock and back-break induced by blasting. *Eng. Comput.* **2015**, *32*, 255–266. [CrossRef]

49. Nguyen, H.; Bui, X.-N.; Choi, Y.; Lee, C.W.; Armaghani, D.J. A Novel Combination of Whale Optimization Algorithm and Support Vector Machine with Different Kernel Functions for Prediction of Blasting-Induced Fly-Rock in Quarry Mines. *Nat. Resour. Res.* **2021**, *30*, 191–207. [CrossRef]
50. Guo, H.; Nguyen, H.; Bui, X.-N.; Armaghani, D.J. A new technique to predict fly-rock in bench blasting based on an ensemble of support vector regression and GLMNET. *Eng. Comput.* **2021**, *37*, 421–435. [CrossRef]
51. Hasanipanah, M.; Monjezi, M.; Shahnazar, A.; Armaghani, D.J.; Farazmand, A. Feasibility of indirect determination of blast induced ground vibration based on support vector machine. *Measurement* **2015**, *75*, 289–297. [CrossRef]
52. Armaghani, D.J.; Asteris, P.G.; Askarian, B.; Hasanipanah, M.; Tarinejad, R.; Van Huynh, V. Examining Hybrid and Single SVM Models with Different Kernels to Predict Rock Brittleness. *Sustainability* **2020**, *12*, 2229. [CrossRef]
53. Khandelwal, M. Blast-induced ground vibration prediction using support vector machine. *Eng. Comput.* **2011**, *27*, 193–200. [CrossRef]
54. Shi, X.-Z.; Zhou, J.; Wu, B.; Huang, D.; Wei, W. Support vector machines approach to mean particle size of rock fragmentation due to bench blasting prediction. *Trans. Nonferrous Met. Soc. China* **2012**, *22*, 432–441. [CrossRef]
55. Rad, H.N.; Hasanipanah, M.; Rezaei, M.; Eghlim, A.L. Developing a least squares support vector machine for estimating the blast-induced flyrock. *Eng. Comput.* **2018**, *34*, 709–717. [CrossRef]
56. Vapnik, V. *The Nature of Statistical Learning Theory*; Springer Science & Business Media: New York, NY, USA, 2013.
57. Feng, Y.; Peng, Y.; Cui, N.; Gong, D.; Zhang, K. Modeling reference evapotranspiration using extreme learning machine and generalized regression neural network only with temperature data. *Comput. Electron. Agric.* **2017**, *136*, 71–78. [CrossRef]
58. Mirjalili, S. Moth-flame optimization algorithm: A novel nature-inspired heuristic paradigm. *Knowl.-Based Syst.* **2015**, *89*, 228–249. [CrossRef]
59. Mirjalili, S.; Lewis, A. The Whale Optimization Algorithm. *Adv. Eng. Softw.* **2016**, *95*, 51–67. [CrossRef]
60. Armaghani, D.J.; Hajihassani, M.; Mohamad, E.T.; Marto, A.; Noorani, S.A. Blasting-induced flyrock and ground vibration prediction through an expert artificial neural network based on particle swarm optimization. *Arab. J. Geosci.* **2014**, *7*, 5383–5396. [CrossRef]
61. Armaghani, D.J.; Mohamad, E.T.; Narayanasamy, M.S.; Narita, N.; Yagiz, S. Development of hybrid intelligent models for predicting TBM penetration rate in hard rock condition. *Tunn. Undergr. Space Technol.* **2017**, *63*, 29–43. [CrossRef]
62. Armaghani, D.J.; Yagiz, S.; Mohamad, E.T.; Zhou, J. Prediction of TBM performance in fresh through weathered granite using empirical and statistical approaches. *Tunn. Undergr. Space Technol.* **2021**, *118*, 104183. [CrossRef]
63. Parsajoo, M.; Armaghani, D.J.; Asteris, P.G. A precise neuro-fuzzy model enhanced by artificial bee colony techniques for assessment of rock brittleness index. *Neural Comput. Appl.* **2021**. [CrossRef]
64. Harandizadeh, H.; Armaghani, D.J.; Asteris, P.G.; Gandomi, A.H. TBM performance prediction developing a hybrid ANFIS-PNN predictive model optimized by imperialism competitive algorithm. *Neural Comput. Appl.* **2021**, *33*, 16149–16179. [CrossRef]
65. Armaghani, D.J.; Mohamad, E.T.; Momeni, E.; Narayanasamy, M.S. An adaptive neuro-fuzzy inference system for predicting unconfined compressive strength and Young's modulus: A study on Main Range granite. *Bull. Int. Assoc. Eng. Geol. Environ.* **2015**, *74*, 1301–1319. [CrossRef]
66. Monjezi, M.; Dehghani, H. Evaluation of effect of blasting pattern parameters on back break using neural networks. *Int. J. Rock Mech. Min. Sci.* **2008**, *45*, 1446–1453. [CrossRef]
67. Verron, S.; Tiplica, T.; Kobi, A. Fault detection and identification with a new feature selection based on mutual information. *J. Process. Control* **2008**, *18*, 479–490. [CrossRef]

sustainability

MDPI

Article

Mining Method Optimization of Gently Inclined and Soft Broken Complex Ore Body Based on AHP and TOPSIS: Taking Miao-Ling Gold Mine of China as an Example

Qinqiang Guo [1,2], Haoxuan Yu [3,†], Zhenyu Dan [1,*] and Shuai Li [3,*]

[1] School of Energy Science and Engineering, Henan Polytechnic University, Jiaozuo 454000, China; 111902010006@home.hpu.edu.cn
[2] The First Institute of Geological & Mineral Resources Survey of Henan, Luoyang 471000, China
[3] School of Resources and Safety Engineering, Central South University, Changsha 410083, China; yuhaoxuan@csu.edu.cn
* Correspondence: 382002020222@home.hpu.edu.cn (Z.D.); shuaige@csu.edu.cn (S.L.)
† Equal contribution as first author.

Abstract: The gently inclined thin to medium thickness ore body under a weak rock stratum is one of the typical difficult bodies to mine. In order to solve the fuzziness, randomness, and uncertainty in the process of mining method optimization for such ore bodies, a multi-level, multi-factor, multi-objective, and multi-index comprehensive evaluation system involving technology, economy, construction, and safety was constructed by combining the analytic hierarchy process (AHP) and technique for order preference by similarity to ideal solution (TOPSIS). Taking the Miao-ling gold mine in China as an example, the AHP-TOPSIS comprehensive decision model of mining method optimization is established, the comprehensive superiority degrees of the four mining schemes are 67.57%, 45.07%, 56.07%, and 31.63%, and the upward horizontal drift backfill mining method is determined as the optimal scheme. The method is verified in the actual production of the mine, which not only ensures the safe production of the mine, but also achieves better technical and economic effects. The research results provide a reference for the optimization of mining methods for gently inclined and soft broken complex ore bodies at home and abroad.

Keywords: mining method; soft broken complex ore body; improved AHP; comprehensive evaluation index

Citation: Guo, Q.; Yu, H.; Dan, Z.; Li, S. Mining Method Optimization of Gently Inclined and Soft Broken Complex Ore Body Based on AHP and TOPSIS: Taking Miao-Ling Gold Mine of China as an Example. *Sustainability* **2021**, *13*, 12503. https://doi.org/10.3390/su132212503

Academic Editors: Mahdi Hasanipanah, Danial Jahed Armaghani and Jian Zhou

Received: 27 October 2021
Accepted: 9 November 2021
Published: 12 November 2021

Publisher's Note: MDPI stays neutral with regard to jurisdictional claims in published maps and institutional affiliations.

Copyright: © 2021 by the authors. Licensee MDPI, Basel, Switzerland. This article is an open access article distributed under the terms and conditions of the Creative Commons Attribution (CC BY) license (https://creativecommons.org/licenses/by/4.0/).

1. Introduction and Background

1.1. Retrospective: The Progress of Mining Method Optimization and Evaluation in China

Beginning in the 2000s, Chinese mining engineers and researchers began to try to apply mathematical methods or systems engineering methods to the optimization of mining operation and production.

Around 2007, a growing number of Chinese researchers began publishing their research in international journals: In 2008, Z. Li et al. [1] adopted the analytic hierarchy process (AHP) in order to develop a framework of sustainability assessment indicators and methods for mining communities. Their research was published in the journal *International Journal of Sustainable Development and World Ecology* and provided a useful tool for monitoring key policy outcomes, measuring progress toward targets, comparing the development characteristics of different mining communities, and informing decision making. In 2010, H. Si et al. [2] established an environmental evaluation system for environmental conditions, resource protection, and economic benefits based on the analysis of environmental pollution from coal mining and the increasing demand for raw coal in order to promote the sustainable development of coal mining. Combined with the analytic hierarchy process (AHP), they put forward a method to calculate the weight of each index and environmental sustainability, used the index system to evaluate the environmental sustainability of

coal mining in the Qi-jiang area in Western China, and verified the effectiveness of the index system. The significance of this study is that the environmental assessment system established by the researchers can be used as a tool to assess the environmental impact of mining areas and measures to promote the sustainable development of coal mining: also in 2010, S. Su, J. Yu, and J. Zhang [3] paid attention to the development of urban mining. They established a scientific and applicable method to accurately measure the degree of sustainable development of mineral resources (DSDMR). Their research will accelerate the adaptive genetic algorithm (AGA), analytic hierarchy process (AHP), and fuzzy comprehensive judgment to measure the sustainability of mineral resources, which is of great inspiration to the future development of China's mining industry.

Since 2010, mining technology in China has developed rapidly, and more and more researchers have applied mathematical models, physical models, and even machine learning to the optimization of mining methods. For example, in 2012, Y. H. Teng and W. Zhu [4] developed a method to predict the height of the fracture zone in coal mining through on-site measurement and numerical and physical simulation. In 2013, H. Jang and E. Topal [5] focused on the transcendental control of the drilling and blasting method in mining. They used multiple regression analysis and an artificial neural network to develop an over-mining prediction model as an over-mining warning and prevention system, which can effectively predict potential over-mining.

Around 2020, as China advocated for the construction of green mines, more and more researchers began focusing on the sustainable development of mining. For example, in 2018, Yu et al. [6] focused on the impact of mining on the safety of surface structures and the environmental health status of surrounding mining areas, and developed an evaluation method for the surface settlement mechanism and surrounding rock stability by using mathematical and physical models, and in 2020, Bao et al. [7] evaluated the impact of mining activities on the city.

To put it simply, in recent years in China, more and more mining researchers have applied mathematical models, physical models, systems engineering methods, and artificial intelligence, such as deep neural networks, to the optimization of mining methods and the assessment of the impact caused by mining. However, the systems engineering method has had good application effects on mining optimization in China in the past 20 years. Even in 2021, Li et al. [8] used the fractal-AHP-vulnerability index method to optimize the mining methods.

1.2. Background: Status Quo of Miao-Ling Gold Mine in Henan Province, China

The western part of Henan Province is the second largest gold-producing base in China, and the altered rock type gold deposit in the fractured zone is the main gold mineralization type in this area [9]. Due to the multi-stage tectonic superposition in the fracture zone, ductile and brittle rocks such as mylonite, cataclastic rock, fault breccia, and fault greccia are mostly developed in the fracture zone, while ore bodies occur in and around the fracture zone [10]. Under the influence of fault tectonic activity, the joints of the roof and floor of the surrounding rock of the ore body are relatively developed, forming weak rock layers of several meters to tens of meters. The phenomenon of splints and floor heave often occurs in the mining engineering, threatening the safety of the operation [11]. At the same time, most ore bodies are gently inclined thin to medium thick vein ore bodies, the caved ore is difficult to release, and the stope operation conditions are poor [12]. Therefore, it is of great practical significance to carry out optimization research on mining methods [13] in combination with the engineering and technical conditions of such ore bodies to promote the progress of mining technology for complex and difficult mining bodies.

As mining method selection is a multi-level, multi-factor, multi-objective, and multi-index decision-making process involving technology, economy, construction, and safety, traditional mining method determination based on experience and analogy is often characterized by great fuzziness, randomness, and uncertainty [14]. According to Liang [15],

based on fuzzy theory and the Tomada de Deciso Interativa Multicriterio method, the index system of seabed mining method selection is established from the aspects of technical feasibility, safety status, economic benefit, and management complexity. G. Tian, Z. Guo, and S. Li [16] optimized the treatment of landslides and side slopes, especially Tarva landslides, by using the AHP-fuzzy comprehensive evaluation model. M. Javanshirgiv and M. Safari [17] carried out a mining method optimization study based on the fuzzy TOPSIS method. On the basis of the above research, considering the inconsistency of decision measures in the construction of a judgment matrix in the traditional analytic hierarchy process (AHP), this paper proposes constructing a consistency judgment matrix through a transfer matrix, and using the improved AHP-TOPSIS evaluation model to obtain the weight vector value at one time, so as to obtain the weight value without a consistency test. It was applied to the mining method optimization process of Miao-ling gold mine in China in order to provide a reference for the safe and efficient mining of gently inclined and soft broken complex ore bodies at home and abroad.

2. Materials and Methods

2.1. The Weight Vector Determined Based on the Improved AHP

The AHP is a multi-criteria, multi-objective, and multi-scheme decision analysis method that combines qualitative and quantitative methods [18]. In the decision making of the actual mining scheme, it is difficult to construct a judgment matrix meeting the requirement of consistency at one time because of the subjectivity of experts in the decision-making measure, especially when there are many factor indexes. If the inconsistent judgment matrix examined is the result of comprehensive and serious thinking by experts, even if the judgment matrix is reconstructed through an additional expert survey, it will not have much practical significance, because the shift in expert judgment quasi-measurement focus is non-conscious [19]. Therefore, this paper adopts an improved AHP that can reconstruct the judgment matrix and calculate the weight vector without adjusting the initial data of experts. It can not only avoid the expenditure waste caused by multiple expert investigations, but also reduce the repeated calculations caused by adjusting the judgment matrix [20,21].

2.1.1. Constructing the Comparison Matrix

The comparison matrix A is constructed as Equation (1), and the value of element a_{ij} in A is the relative importance of element x_i in the index layer to element x_j.

$$A = \begin{pmatrix} a_{11} & a_{12} & \cdots & a_{1n} \\ a_{21} & a_{22} & \cdots & a_{2n} \\ \vdots & \vdots & \ddots & \vdots \\ a_{n1} & a_{n2} & \cdots & a_{nn} \end{pmatrix} = \begin{pmatrix} \frac{x_1}{x_1} & \frac{x_1}{x_2} & \cdots & \frac{x_1}{x_n} \\ \frac{x_2}{x_1} & \frac{x_2}{x_2} & \cdots & \frac{x_2}{x_n} \\ \vdots & \vdots & \ddots & \vdots \\ \frac{x_n}{x_1} & \frac{x_n}{x_2} & \cdots & \frac{x_n}{x_n} \end{pmatrix} \quad (1)$$

2.1.2. Constructing the Consistency Judgment Matrix

In order to avoid the measurement inconsistency of the initial comparison matrix, this paper introduces an improved AHP [22] and used the concept of the optimal transfer matrix to obtain the index weight value at one time. The theorems and methods introduced are as follows:

Theorem 1. Matrix $A =)_{n\times n}$, $U = 1, 2, \ldots, n$. If $a_{ij} = \frac{1}{a_{ji}}$, while $a_{ij} = a_{ik} \cdot a_{kj}$, $i, j, k \in U$. Then, matrix A is the consistency matrix.

Theorem 2. Matrix $A =)_{n\times n}$, $B =)_{n\times n}$, $b_{ij} = lg^{a_{ij}}$, $i, j, k \in U$, $U = 1, 2, \ldots, n$. If matrix A is the consistency matrix, then $b_{ij} = -b_{ji}$, while $b_{ij} = b_{ik} + b_{kj}$, B is called the transfer matrix of A; conversely, if B is the transfer matrix of A, then A is the consistency matrix.

Theorem 3. Matrix $B =)_{n\times n}$, $C =)_{n\times n}$. If $b_{ij} = -b_{ji}$, the optimal transfer matrix C of B satisfies $c_{ij} = \frac{1}{n}\sum_{k=1}^{n}\left(b_{ik} - b_{jk}\right)$, $i, j, k \in U$, $U = 1, 2, \ldots$, n.

The process of solving the weight vector by the improved AHP is shown in Figure 1.

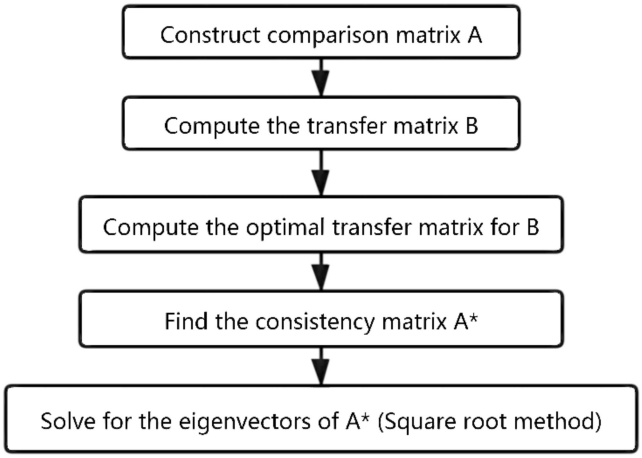

Figure 1. Flow chart of the improved AHP method to solve the weight vector.

2.2. Construction of the AHP-TOPSIS Comprehensive Evaluation Model

The technique for order preference by similarity to ideal solution (TOPSIS) is used to define positive and negative ideal solutions, and evaluate the superiority of the proposed scheme according to its proximity to the ideal solution. The general goal is to approach the positive ideal solution, but move away from the negative ideal solution [23].

2.2.1. The Initial Evaluation Matrix Is Established

There are $P_1, P_2, \ldots, P_m$, m alternatives.

All schemes are combined to form $P = \{P_1, P_2, \ldots, P_m\}$; the evaluation index of each scheme is set as the standard set $X = \{X_1, X_2, \ldots, X_n\}$ jointly composed of $X_1, X_2, \ldots, X_n$; and the corresponding evaluation index can be expressed as $X_{ij}(i = 1, 2, \ldots, m; j = 1, 2, \ldots, n)$, that is, X_{ij} is the J evaluation index of the ith scheme [24].

Then, the initial evaluation matrix P can be described as Equation (2).

$$P = \left(X_{ij}\right)_{m\times n} = \begin{pmatrix} X_{11} & X_{12} & \cdots & X_{1n} \\ X_{21} & X_{22} & \cdots & X_{2n} \\ \vdots & \vdots & \ddots & \vdots \\ X_{m1} & X_{m2} & \cdots & X_{mn} \end{pmatrix} \quad (2)$$

2.2.2. Establishment of the Standardized Decision Matrix

Considering the complexity of all evaluation objects and the incompatibility of all evaluation indicators, dimensionless processing of all evaluation indicators is required [25]. The elements of the standardized decision matrix $Q = \left(q_{ij}\right)_{m\times n}$ are calculated as follows:

The indicator where bigger is better can be described as Equation (3):

$$q_{ij} = \frac{x_{ij} - \min\limits_{j}(x_{ij})}{\max\limits_{j}(x_{ij}) - \min\limits_{j}(x_{ij})} \quad (3)$$

The smaller the better indicator can be described as Equation (4):

$$q_{ij}{}' = \frac{\max\limits_{j}(x_{ij}) - x_{ij}}{\max\limits_{j}(x_{ij}) - \min\limits_{j}(x_{ij})} \tag{4}$$

where $\max\limits_{j}(x_{ij})$ represents the maximum data in the J column of matrix P; $min\limits_{j}(x_{ij})$ represents the minimum data in the J column of matrix P.

2.2.3. Construction of the Weighted Standardized Decision Matrix

By multiplying the above standardized decision matrix Q and the corresponding weight w_i of each indicator [26], the weighted standardized matrix R can be obtained as Equation (5).

$$R = (r_{ij})_{m\times n} = \begin{pmatrix} w_1q_{11} & w_2q_{12} & \cdots & w_nq_{1n} \\ w_1q_{21} & w_2q_{22} & \cdots & w_nq_{2n} \\ \vdots & \vdots & \ddots & \vdots \\ w_1q_{m1} & w_2q_{m2} & \cdots & w_nq_{mn} \end{pmatrix} \tag{5}$$

2.2.4. Calculation of Closeness of the Evaluation Object

The ideal solution of the weighted standardized decision matrix can be described as Equation (6),

$$\begin{cases} R^+ = \left\{ \left(\max\limits_{j}(q_{ij})|X_j \in J_1\right), \left(\min\limits_{j}(q_{ij})|X_j \in J_2\right) \right\} \\ R^- = \left\{ \left(\min\limits_{j}(q_{ij})|X_j \in J_1\right), \left(\max\limits_{j}(q_{ij})|X_j \in J_2\right) \right\} \end{cases} \tag{6}$$

where R^+ and R^- are the positive and negative ideal solutions, respectively; J_1 and J_2 are the benefit and cost indicator sets, respectively.

Then the distance between the evaluation object and the ideal solution can be described as Equation (7):

$$\begin{cases} f_i^+ = \sqrt{\sum\limits_{j=1}^{n}(r_{ij} - r_j^+)^2} \\ f_i^- = \sqrt{\sum\limits_{j=1}^{n}(r_{ij} - r_j^-)^2} \end{cases} \tag{7}$$

where f_i^+ and f_i^- are, respectively, the distance between the evaluation object and the positive and negative ideal solution; r_i^+ and r_i^- are elements of R^+ and R^-, respectively.

The closeness vector E^+ between each evaluation object and the positive ideal solution can be described as Equation (8).

$$E_i{}^+ = \frac{f_i^-}{f_i^+ + f_i^-}, \quad e^+ \in [0,1] \tag{8}$$

The matrix E composed of E^+ is called the comprehensive evaluation matrix. Under the same first-level index, the advantages and disadvantages of the evaluation object can be preliminarily judged by the descending arrangement of progress values (close to one is superior, and close to zero is inferior).

3. Results: Examples of Application

3.1. Engineering Background and Comprehensive Evaluation Index System of Mining Method Optimization

The Miao-ling gold deposit is a structural altered rock type gold deposit (see Figure 2); the ore body occurrence is strictly controlled by the faults striking nearly north to south, mainly distributed along the fault structural belt and its hanging wall altered surrounding rock, which is mostly vein-like, lenticular, etc., with the characteristics of expansion and narrowing, branching compounds. At present, the ore body is mainly mined, with the grade of 2.86 g/t. Ore body dip is 250°~290°, the dip angle is 16°~57°, and the thickness of the ore body is 0.60~23.46 m. The ore is of cataclastic type and alteration type. The surrounding rock is rhyolite, and the joints and fissures are well-developed. There is local kaolin mineral development, which is argillaceous, as well as water softening and poor stability. The contact relationship between the surrounding rock and the ore body floor is obvious, but the gradual metasomatic alteration relationship with the roof is not obvious. With the increase in mining intensity, the ore resources continue to move down, and the occurrence of ore also changes, mainly manifested as the dip angle becoming slow (20°~30°) and ore transport becoming difficult (see Figure 3). The complex phenomenon of ore-body branching occurs frequently, and the occurrence changes are complicated. The stability of the surrounding rock becomes worse, the phenomenon of roof collapse occurs frequently, the ore dilution becomes serious, and the safety problem becomes prominent. The geological grade of ore becomes low, and the cost per ton of ore increases.

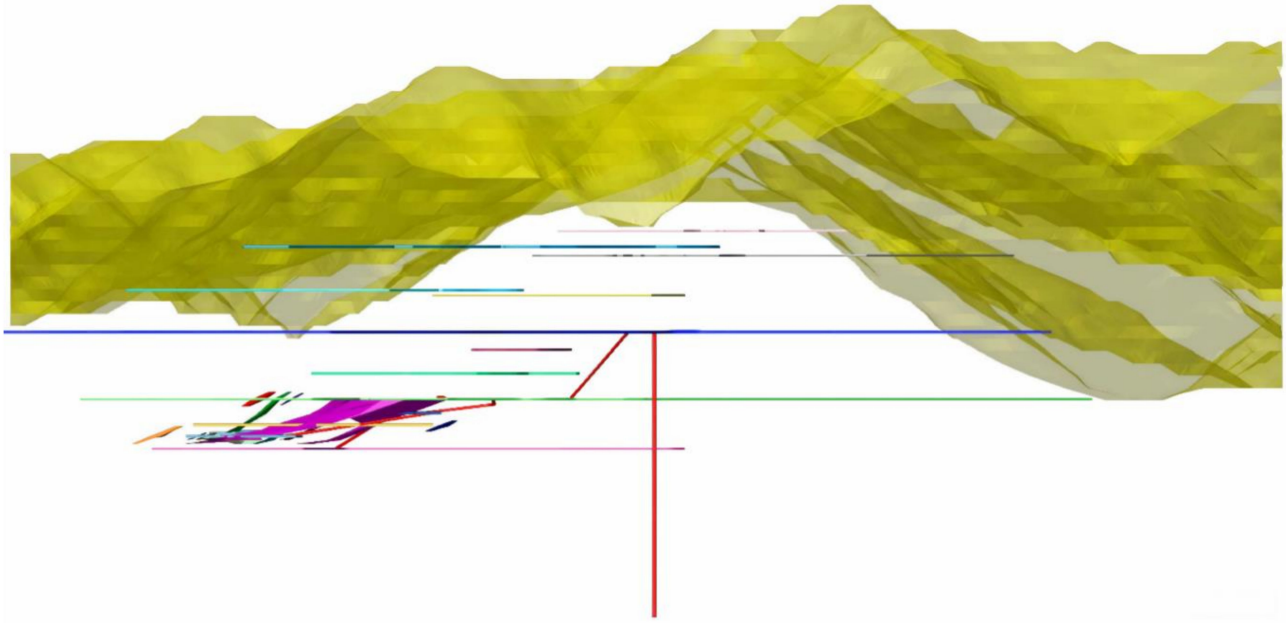

Figure 2. Three-dimensional model of Miao-ling gold mine.

According to the occurrence status of the ore body and mining technical conditions, especially the stability of the ore rock and the thickness, grade, and dip angle of the ore body, the following four filling mining comparison schemes are proposed: upward horizontal drift filling mining method (Plan I), upward horizontal slicing and filling mining method (Plan II) (see Figure 4), pre-control roof sublevel stopping filling mining method (Plan III), and medium-deep hole room pillar subsequent filling mining method (Plan IV) (see Figure 5), as shown in Table 1.

Figure 3. Picture of occurrence of ore body in Miao-ling gold mine.

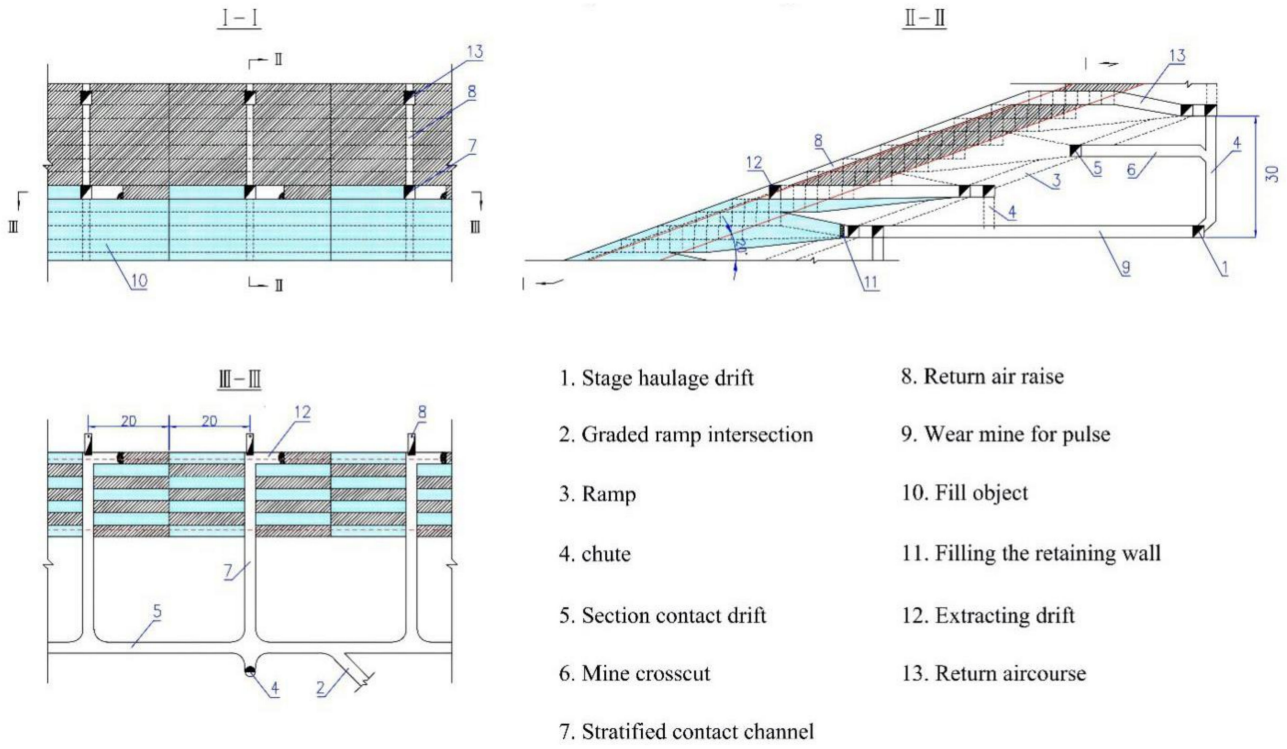

Figure 4. Plan II: upward horizontal slicing and filling mining method in Miao-ling gold mine. I-I: front view; II-II: side view; III-III: top view.

Since only Plans II and IV have practical applications in Miao-ling gold Mine, mining method maps for only Plan II and Plan IV are attached below in Figures 4 and 5, respectively.

According to the basic principle of the AHP, the comprehensive evaluation (O) index system of mining method optimization for a moderately inclined, medium-thick ore body (i.e., target layer) was established [22], as shown in Figure 6.

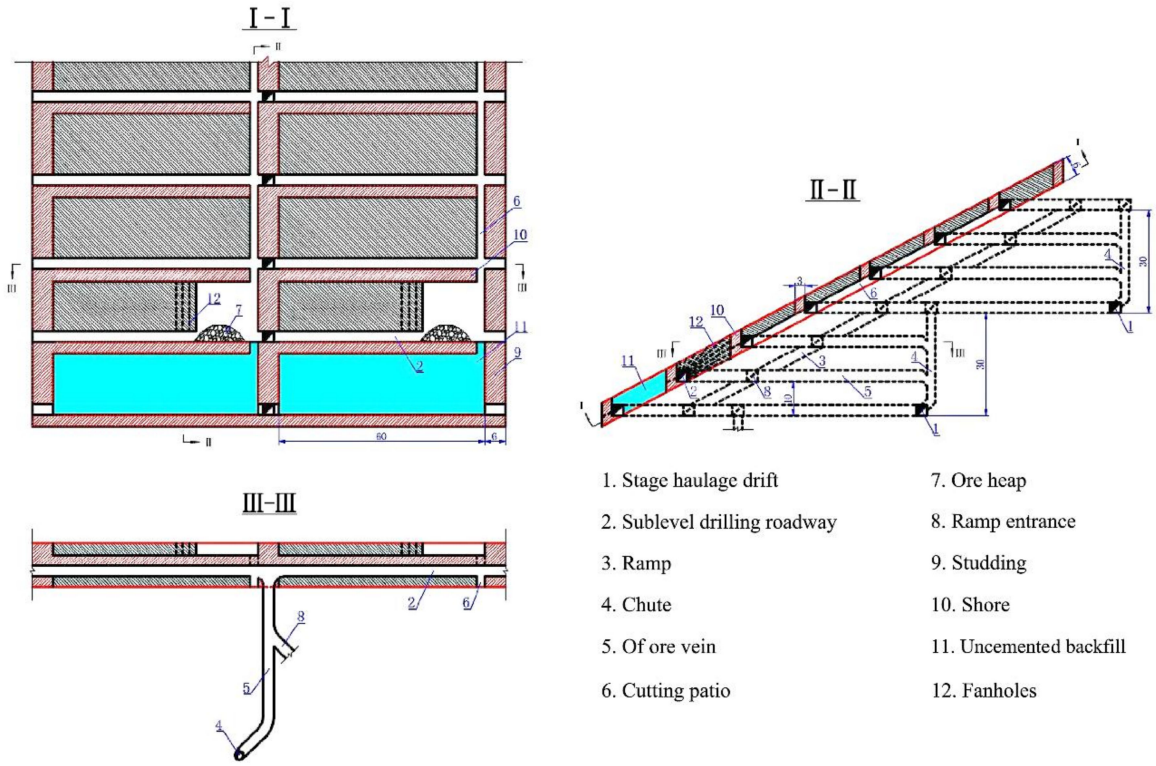

Figure 5. Plan IV: medium-deep hole room pillar subsequent filling mining method in Miao-ling gold mine. I-I: front view; II-II: side view; III-III: top view.

Table 1. Comparison of evaluation indexes of each backfill mining method.

Project		Plan I	Plan II	Plan III	Plan IV
Criterion Layer	**Index Layer**				
Economic indicators S_1	X_1/(Chinese yuan/t)	94.2	84.7	88.6	78.5
	X_2/(%)	95	90	92	85
	X_3/(%)	6	8	8	25
Technical indicators S_2	X_4/(t/d)	100	150	140	180
	X_5/(m^3/kt)	79.6	79.6	71.5	62.8
	X_6	8	4	6	4
	X_7	6	4	8	4
	X_8/(%)	5	6	8	10
Safety indicators S_3	X_9	140	180	200	320
	X_{10}	8	8	8	6

The evaluation system chart contains criterion layers: namely, economic index (S1), including the total cost of mining and filling (X1), ore recovery rate (X2), and ore dilution rate (X3); second, technical index (S2), including stope production capacity (X4), 1000 t cutting ratio (X5), flexibility and adaptability of the scheme (X6), construction difficulty (X7), ore bulk rate (X8); third, safety index (S3), mining roof exposed area (X9), and ventilation conditions (X10). X1, X2, X3, X4, X5, X8, and X9 in the evaluation system are quantitative indicators, which can be comprehensively estimated by analogy with similar mines at home and abroad and based on obtained expert opinions. X6, X7, and X10 in the evaluation system are qualitative indicators. Given five grades, they are very good, good, general, poor, and very poor, respectively, corresponding to 10, 8, 6, 4, and 2 in sequence.

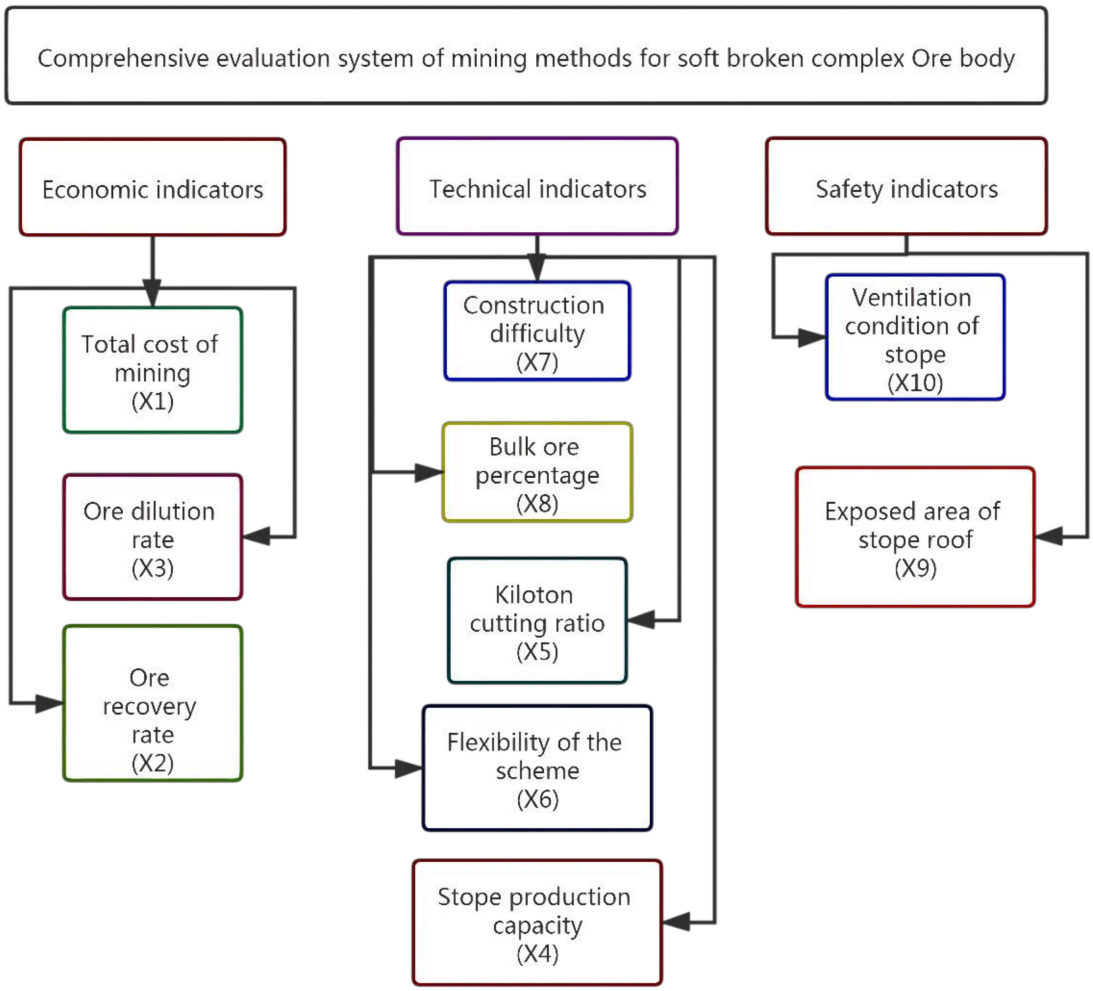

Figure 6. Evaluation system chart of mining methods for soft fracture complex ore body.

3.2. Index Weight Determination

The total cost depends on the mining technical condition, mineral filling mining method, mechanization level, management level, and the cost of a local quantity machine for a mine. After determining the mining method, the index shows little change in a short time, and the ore recovery rate and impoverishment rate index are important to the mine's economic benefit. This paper assumes that if the surrounding rock is excluding gold (gold grade is zero), then every one ton of ore lost in the process of mining, the enterprise economic losses on the numerical equivalent of selecting one profitable ton of ore, mixed with the processing fee for one ton of ore, is equal to one of the selecting ore comprehensive cost; obviously, the two rates index is based on the total cost index, which is filled in the mining work on mining efficiency indicators. For most precious metal mines with low ore grade, the index of dilution rate is more important than the index of recovery rate [27].

According to the basic principle of the AHP and comparison scale table, combined with the situation of Miao-ling gold mine in China and discussed with relevant experts and scholars, the initial comparison matrix of the criterion layer index (S_0), economic index (S_1), technical index (S_2), and safety index (S_3) is determined as Equation (9).

$$S_0 = \begin{pmatrix} 1 & 1 & 4 \\ 1 & 1 & 2 \\ \frac{1}{4} & \frac{1}{2} & 1 \end{pmatrix} S_1 = \begin{pmatrix} 1 & 3 & 2 \\ \frac{1}{3} & 1 & \frac{2}{3} \\ \frac{1}{2} & \frac{3}{2} & 1 \end{pmatrix} S_2 = \begin{pmatrix} 1 & \frac{3}{8} & \frac{1}{2} & \frac{3}{4} & \frac{3}{2} \\ \frac{8}{3} & 1 & \frac{4}{3} & 2 & 4 \\ 2 & \frac{3}{4} & 1 & \frac{3}{2} & 2 \\ \frac{4}{3} & \frac{1}{2} & \frac{2}{3} & 1 & 2 \\ \frac{2}{3} & \frac{1}{4} & \frac{1}{3} & \frac{1}{2} & 1 \end{pmatrix} S_3 = \begin{pmatrix} 1 & \frac{5}{7} \\ \frac{7}{5} & 1 \end{pmatrix} \quad (9)$$

According to the improved AHP algorithm, the consistency judgment matrix and the total ranking weight of hierarchy can be obtained without tests, as shown in Table 2.

Table 2. Final administrative levels compositor.

X	S			Weight (W)
	S_1 (0.472)	S_2 (0.377)	S_3 (0.151)	
x_1	0.545			0.258
x_2	0.182			0.086
x_3	0.273			0.129
x_4		0.13		0.049
x_5		0.348		0.131
x_6		0.261		0.098
x_7		0.174		0.066
x_8		0.087		0.033
x_9			0.417	0.063
x_{10}			0.583	0.087

3.3. Comprehensive Evaluation of Factors and Indicators

Construct the initial judgment matrix P according to Equation (10).

$$P = \begin{pmatrix} 94.2 & 95 & 6 & 100 & 79.6 & 8 & 6 & 5 & 140 & 8 \\ 84.7 & 90 & 8 & 150 & 79.6 & 4 & 4 & 6 & 180 & 8 \\ 88.6 & 92 & 8 & 140 & 71.5 & 6 & 8 & 8 & 200 & 8 \\ 78.5 & 85 & 25 & 180 & 62.8 & 4 & 4 & 10 & 320 & 6 \end{pmatrix} \quad (10)$$

According to Equations (3)–(5), the standardized decision matrix R can be described as Equation (11).

$$R = \begin{pmatrix} 0 & 0.086 & 0.129 & 0 & 0 & 0.098 & 0.033 & 0.033 & 0 & 0.087 \\ 0.156 & 0.043 & 0.115 & 0.031 & 0 & 0 & 0.066 & 0.026 & 0.014 & 0.087 \\ 0.092 & 0.06 & 0.115 & 0.025 & 0.063 & 0.049 & 0 & 0.02 & 0.021 & 0.087 \\ 0.258 & 0 & 0 & 0.049 & 0.131 & 0 & 0.066 & 0 & 0.063 & 0 \end{pmatrix} \quad (11)$$

According to Equation (6), the ideal solution of the weighted normalized matrix is calculated. In the comprehensive evaluation index system of each scheme, X1, X3, X5, X7, and X8 belong to the cost indicator, and X2, X4, X6, X9, and X10 belong to the benefit indicator, so the positive ideal solution and negative ideal solution of the weighted standardized matrix can be described as Equation (12).

$$\begin{cases} R^+ = (\ 0,\ 0.086,\ 0,\ 0.049,\ 0,\ 0.098,\ 0,\ 0,\ 0.063,\ 0.087\ ) \\ R^- = (\ 0.258,\ 0,\ 0.129,\ 0,\ 0.131,\ 0,\ 0.066,\ 0.033,\ 0,\ 0\ ) \end{cases} \quad (12)$$

According to Equation (7), calculate the distance between each scheme and the positive ideal solution and the negative ideal solution as Equation (13).

$$\begin{cases} f_1^+ = 0.159 \\ f_1^- = 0.331 \end{cases}, \begin{cases} f_2^+ = 0.239 \\ f_2^- = 0.196 \end{cases}, \begin{cases} f_3^+ = 0.178 \\ f_3^- = 0.227 \end{cases}, \begin{cases} f_4^+ = 0.336 \\ f_4^- = 0.155 \end{cases} \quad (13)$$

3.4. Final Evaluation of Mining Methods

According to Equation (8), the closeness degree E^+ of each scheme to the positive ideal solution is calculated as Equation (14):

$$E^+ = \begin{pmatrix} 0.6757, & 0.4507, & 0.5607, & 0.3163 \end{pmatrix} \quad (14)$$

This method was tested in the mine. The ore block is arranged along the direction of the ore body; the length of the ore block is 40 m, the width is the thickness of the ore body, and the middle section is 30 m high. The middle section is divided into three sections with a height of 10 m, and each section is further divided into three layers with a height of 3.3 m and a path width of 3.5 m.

According to the statistical data of the mining path, the main technical and economic indicators were as follows: the production capacity of the mining path was 105 t/d, the recovery rate was 95.7%, the dilution rate was 5.34%, the cutting ratio was 69.8 m^3/kt, and the total cost of mining and filling was 89 yuan/t, which achieved the expected effect.

4. Discussion

We developed this mining method optimization based on the AHP and TOPSIS by referring to and borrowing from the literature [18–26,28–30], which was helpful. Through this study, we can judge that the upward horizontal drift filling mining method is the most suitable mining method for Miao-ling gold mine in Henan Province in China by using the AHP and TOPSIS. However, it led to the following questions:

(1) Are the AHP and TOPSIS the most suitable evaluation methods for mining method optimization?

Although many research experts use the AHP or TOPSIS in the optimization process of mining methods or mining production [31,32], there are other methods that are also applicable.

Different methods should be selected according to specific situations. For example, in 2021, J. Sheng et al. [33] proposed four deep mining schemes for large deep ore bodies, which were optimized by the vague set model.

There are even some researchers who are trying to use artificial intelligence techniques, such as machine learning, for mining method optimization, and that is what we are working on. In conclusion, the optimization of mining methods depends on different circumstances to decide what assessment method to use.

(2) Is the upward horizontal drift filling mining method the most suitable mining method in China or in the world?

For this matter, obviously not. Each mine has its suitable mining method; however, intelligent mining is undoubtedly the development trend of all mines, both in China and around the world.

With the continuous progress and development of science and technology, artificial intelligence has begun to show a global development trend, and intelligent mining is no exception. In China, the concept of intelligent mining was put forward around 2017 [34], and many Chinese universities have gradually taken intelligent mining as the basic discipline construction. C. Qi, once an outstanding research expert in Australia, now one of the top intelligent mining research experts in China, has long been engaged in intelligent mining research: As early as 2018, he began to apply artificial intelligence methods to slope stability analysis, backfill mining methods, and the optimization of backfill materials [35,36]; he is also pursuing research into intelligent mining [37,38].

In the world, there are also many outstanding researchers studying intelligent mining. Choi [39,40], a mining research expert from South Korea, has been devoted to the research of transportation robots in mining; Yu H. [41–44] is also committed to the study of intelligent rail transportation in underground mines; Danial J.A. [44,45], a mining and rock mechanics expert from Iran, used artificial bee colony techniques to evaluate the brittleness coefficient of rock during mining; and A. Jha [46,47], a mining researcher from the United States, has

also been conducting research on the application of artificial intelligence technology in mining blasting and mine ventilation.

Due to the progress of science and technology, mining technology is in continuous development; therefore, we think that, one day, intelligent mining can be realized, improving the efficiency of mining while ensuring the safety of workers, which is good news for people all over the world.

5. Conclusions

(1) Taking Miao-ling gold mine in China as an example, the AHP-TOPSIS comprehensive decision model of mining method optimization was established. According to Section 3.4., the comprehensive superiority degrees of mining Plans I–IV are 67.57%, 45.07%, 56.07%, and 31.63%, respectively, so Plan I (the upward horizontal drift backfill mining method) is the best. The upward horizontal drift filling mining method was determined as the optimal scheme, and the mining effect was verified through a field industrial test, which provides a reference for the optimization of mining methods for gently inclined and soft broken complex ore bodies at home and abroad.

(2) Based on the selection of technical and economic mining methods, we constructed a multi-level, multi-factor, multi-objective, and multi-index mining method for a slowly inclined soft broken ore body to improve the comprehensive evaluation system determined by experience and that is limited by fuzziness, randomness, and unpredictability.

(3) To introduce an improved AHP, using the concept of the optimal transfer matrix, which eliminates the need to test the index weight of vector-valued for a one-time gain, overcomes the barycenter offset caused by the decision-making measure and the inconsistency of the judgment matrix, and simplifies the weight vector of the calculation process, reduced by adjusting the weight vector of repeated calculations.

Finally, we claim that this paper serves just as a guide to starting the conversation. In our future research, we will continue to study mining method optimization, especially the application of machine learning, and we hope many more experts and researchers will be interested and engage in the research in this field.

Author Contributions: Conceptualization, S.L.; methodology, Q.G.; software, Q.G.; validation, S.L.; formal analysis, Z.D.; investigation, Z.D.; resources, S.L.; data curation, Z.D.; writing—original draft preparation, Q.G.; writing—review and editing, H.Y. and S.L.; visualization, H.Y.; supervision, H.Y.; project administration, Q.G.; funding acquisition, S.L. All authors have read and agreed to the published version of the manuscript.

Funding: This research was funded by the National Natural Science Foundation of China (grant No. 51804337) and the Natural Science Foundation of Hunan Province (grant No. 2021JJ40745).

Institutional Review Board Statement: Institutional approval was obtained from the Henan Polytechnic University and the Central South University prior to the study.

Informed Consent Statement: Not applicable.

Data Availability Statement: Raw data from the study are available on request.

Acknowledgments: The authors are thankful for the financial support from the National Natural Science Foundation of China (grant No. 51804337) and the Natural Science Foundation of Hunan Province (grant No. 2021JJ40745).

Conflicts of Interest: The authors declare no conflict of interest.

References

1. Li, Z.; Zhao, Y.; Zhao, H. Assessment indicators and methods for developing the sustainability of mining communities. *Int. J. Sustain. Develop. World Ecol.* **2008**, *15*, 35S–43S. [CrossRef]
2. Si, H.; Bi, H.; Li, X.; Yang, C. Environmental evaluation for sustainable development of coal mining in Qijiang, Western China. *Int. J. Coal Geol.* **2010**, *81*, 163–168. [CrossRef]
3. Su, S.; Yu, J.; Zhang, J. Measurements study on sustainability of China's mining cities. *Expert Syst. Appl.* **2010**, *37*, 6028–6035. [CrossRef]

4. Zhu, W.; Teng, Y.H. Characteristic of Development of the Fractured Zone in Mining under Medium Hard Overburden Using Fully-Mechanized Top-Coal Caving Method. *Appl. Mech. Mater.* **2012**, *226–228*, 1312–1317. [CrossRef]
5. Jang, H.; Topal, E. Optimizing overbreak prediction based on geological parameters comparing multiple regression analysis and artificial neural network. *Tunn. Undergr. Space Technol.* **2013**, *38*, 161–169. [CrossRef]
6. Yu, Y.; Chen, S.-E.; Deng, K.-Z.; Wang, P.; Fan, H.-D. Subsidence Mechanism and Stability Assessment Methods for Partial Extraction Mines for Sustainable Development of Mining Cities—A Review. *Sustainability* **2018**, *10*, 113. [CrossRef]
7. Bao, K.; He, G.; Jin, L.; Yang, J.; Zhou, Q. Study on Sustainable Development of Mining Cities by the Method of Relative Resources Carrying Capacity and GM (1, 1) Model. *Pol. J. Environ. Stud.* **2020**, *29*, 3983–3995. [CrossRef]
8. Li, J.-L.; Wang, S.-W.; Wang, Y.; Wang, X.-Y.; Wang, X.-X. Water Inrush Risk Assessment of Coal Floor After CBM Development Based on the Fractal-AHP-Vulnerlability Index Method. *Geotech. Geol. Eng.* **2021**, *39*, 3487–3497. [CrossRef]
9. Lin, C.; He, Y.; Chen, X.; Shi, L.; Zhang, X.; Qi, X.; Hao, R.; Gong, R.; Zhang, J. Relationship between ductile shear zone and gold mineralization—Taking Jinchangyu gold mine, eastern Hebei Province, China. *Int. J. Rock Mech. Min. Sci. Geomech. Abstr.* **1996**, *33*, A104. [CrossRef]
10. Wu, J. Research on sublevel open stoping recovery processes of inclined medium-thick orebody on the basis of physical simulation experiments. *PLoS ONE* **2020**, *15*, e0232640. [CrossRef]
11. Chen, D.; Wu, X.; Xie, S.; Sun, Y.; Zhang, Q.; Wang, E.; Sun, Y.; Wang, L.; Li, H.; Jiang, Z.; et al. Study on the Thin Plate Model with Elastic Foundation Boundary of Overlying Strata for Backfill Mining. *Math. Probl. Eng.* **2020**, *2020*, 8906091. [CrossRef]
12. Lin, Y. Research on Mining Technology of Steeply Inclined Thin Ore Body in High-grade Content Mine. *IOP Conf. Ser. Earth Environ. Sci.* **2021**, *632*, 022038. [CrossRef]
13. Ligen, Y.; Xiumin, X. Research on the Comprehensive Evaluation Model of Knowledge Capital of Mining Enterprise Based on AHP and Fuzzy Mathematics. In Proceedings of the 2009 Second International Conference on Intelligent Computation Technology and Automation, Changsha, China, 10–11 October 2009; Volume 2, pp. 784–787.
14. Yavuz, M. The application of the analytic hierarchy process (AHP) and Yager's method in underground mining method selection problem. *Int. J. Min. Reclam. Environ.* **2013**, *29*, 1–23. [CrossRef]
15. Liang, W.-Z.; Zhao, G.Y.; Hao, W.U.; Chen, Y. Optimization of mining method in subsea deep gold mines: A case study. *J. Transac. Nonferrous Metals Soc. China* **2019**, *29*, 2160–2169. [CrossRef]
16. Tian, G.; Guo, Z.; Li, S. Optimization of Tawa Landslide Treatment Scheme Based on the AHP-Fuzzy Comprehensive Evaluation Method. *IOP Conf. Ser. Earth Environ. Sci.* **2020**, *598*, 012032. [CrossRef]
17. Javanshirgiv, M.; Safari, M. The selection of an underground mining method using the fuzzy topsis method: A case study in the kamar mahdi ii fluorine mine. *Min. Sci.* **2017**, *24*, 161.
18. Sensuse, D.I.; Sari, F.R. penerapan metode analytic hierarchy process dalam sistem penunjang keputusan untuk pemilihan asuransi. *J. Sist. Inf.* **2008**, *4*, 100. [CrossRef]
19. Yu, H.; Wang, N.; Pan, J. Application of Fuzzy Extension Analytic Hierarchy Process in Location Selection of Logistics Center. *J. Phys. Conf. Ser.* **2021**, *1995*, 012035. [CrossRef]
20. Dogan, O. Process mining technology selection with spherical fuzzy AHP and sensitivity analysis. *Expert Syst. Appl.* **2021**, *178*, 114999. [CrossRef]
21. Ke, X.; Feng, M.; Xiang, M. The application of analytic hierarchy process and fuzzy comprehensive evaluation in the evaluation of ecological security in coal mine areas. *Int. J. Netw. Virtual Organ.* **2018**, *18*, 80. [CrossRef]
22. Asghari, M.; Nassiri, P.; Monazzam, M.R.; Golbabaei, F.; Arabalibeik, H.; Shamsipour, A.; Allahverdy, A. Weighting Criteria and Prioritizing of Heat stress indices in surface mining using a Delphi Technique and Fuzzy AHP-TOPSIS Method. *J. Environ. Heal. Sci. Eng.* **2017**, *15*, 1. [CrossRef]
23. Hwang, C.-L.; Lai, Y.-J.; Liu, T.-Y. A new approach for multiple objective decision making. *J. Comput. Oper. Res.* **1993**, *20*, 889–899. [CrossRef]
24. Rezaiee-Pajand, M.; Ghalishooyan, M.; Salehi-Ahmadabad, M. Comprehensive evaluation of structural geometrical nonlinear solution techniques Part I: Formulation and characteristics of the methods. *Struct. Eng. Mech.* **2013**, *48*, 849–878. [CrossRef]
25. Masum, A.K.M.; Karim, A.R.; Bin Al Abid, F.; Islam, S.; Anas, M. A New Hybrid AHP-TOPSIS Method for Ranking Human Capital Indicators by Normalized Decision Matrix. *J. Comput. Sci.* **2019**, *15*, 1746–1751. [CrossRef]
26. Ibrahim, M.R.; Suseno, J.E.; Surarso, B. Emergency Service Search using Ant Colony Optimization Algorithm and AHP-TOPSIS Method. *J. Phys. Conf. Ser.* **2021**, *1943*, 012104. [CrossRef]
27. Zhao, L.; Li, H.; Wang, Z.; Peng, D.; Xue, Y.; Ai, X. Comprehensive Evaluation of Power Grid Security and Benefit Based on BWM Entropy Weight TOPSIS Method. *IOP Conf. Ser. Earth Environ. Sci.* **2020**, *619*, 12053. [CrossRef]
28. Zhou, J.; Chen, C.; Armaghani, D.J.; Ma, S. Developing a hybrid model of information entropy and unascertained measurement theory for evaluation of the excavatability in rock mass. *Eng. Comput.* **2020**, *1*, 24. [CrossRef]
29. Zhou, J.; Chen, C.; Wang, M.; Khandelwal, M. Proposing a novel comprehensive evaluation model for the coal burst liability in underground coal mines considering uncertainty factors. *Int. J. Min. Sci. Technol.* **2021**, *31*, 799–812. [CrossRef]
30. Zhou, J.; Chen, C.; Khandelwal, M.; Tao, M.; Li, C. Novel approach to evaluate rock mass fragmentation in block caving using unascertained measurement model and information entropy with flexible credible identification criterion. *Eng. Comput.* **2021**. [CrossRef]

31. Shen, L.; Muduli, K.; Barve, A. Developing a sustainable development framework in the context of mining industries: AHP approach. *Resour. Policy* **2015**, *46*, 15–26. [CrossRef]
32. Karan, S.K.; Samadder, S.R.; Singh, V. Groundwater vulnerability assessment in degraded coal mining areas using the AHP-Modified DRASTIC model. *Land Degrad. Dev.* **2018**, *29*, 2351–2365. [CrossRef]
33. Sheng, J.; Wan, W.; Liu, D.; Jiang, F.; Li, X.; Zhang, H. Investigation of the Optimization of Unloading Mining Scheme in Large Deep Deposit Based on Vague Set Theory and Its Application. *Adv. Civ. Eng.* **2021**, *2021*, 1–13. [CrossRef]
34. Wang, J.; Huang, Z. The recent technological development of intelligent mining in China. *J. Eng.* **2017**, *3*, 439–444. [CrossRef]
35. Qi, C.; Fourie, A.; Chen, Q. Neural network and particle swarm optimization for predicting the unconfined compressive strength of cemented paste backfill. *Constr. Build. Mater.* **2018**, *159*, 473–478. [CrossRef]
36. Qi, C.; Fourie, A.; Chen, Q.; Zhang, Q. A strength prediction model using artificial intelligence for recycling waste tailings as cemented paste backfill. *J. Clean. Prod.* **2018**, *183*, 566–578. [CrossRef]
37. Qi, C.; Fourie, A.; Chen, Q.; Zhang, Q. Improved strength prediction of cemented paste backfill using a novel model based on adaptive neuro fuzzy inference system and artificial bee colony. *Constr. Build. Mater.* **2021**, *284*, 122857. [CrossRef]
38. Li, G.; Sun, Y.; Qi, C. Machine learning-based constitutive models for cement-grouted coal specimens under shearing. *Int. J. Min. Sci. Technol.* **2021**, *31*, 813–823. [CrossRef]
39. Kim, S.-M.; Choi, Y.; Suh, J. Applications of the Open-Source Hardware Arduino Platform in the Mining Industry: A Review. *Appl. Sci.* **2020**, *10*, 5018. [CrossRef]
40. Kim, Y.; Baek, J.; Choi, Y. Smart Helmet-Based Personnel Proximity Warning System for Improving Underground Mine Safety. *Appl. Sci.* **2021**, *11*, 4342. [CrossRef]
41. Li, S.; Wang, G.; Yu, H.; Wang, X. Engineering Project: The Method to Solve Practical Problems for the Monitoring and Control of Driver-Less Electric Transport Vehicles in the Underground Mines. *World Electr. Veh. J.* **2021**, *12*, 64. [CrossRef]
42. Yu, H.; Li, S. The Function Design for the Communication-Based Train Control (CBTC) System: How to Solve the Problems in the Underground Mine Rail Transportation? *Appl. Syst. Innov.* **2021**, *4*, 31. [CrossRef]
43. Nardo, M.; Yu, H. Intelligent Ventilation Systems in Mining Engineering: Is ZigBee WSN Technology the Best Choice? *Appl. Syst. Innov.* **2021**, *4*, 42. [CrossRef]
44. Di Nardo, M.; Yu, H. Special Issue "Industry 5.0: The Prelude to the Sixth Industrial Revolution". *Appl. Syst. Innov.* **2021**, *4*, 45. [CrossRef]
45. Parsajoo, M.; Armaghani, D.J.; Asteris, P.G. A precise neuro-fuzzy model enhanced by artificial bee colony techniques for assessment of rock brittleness index. *Neural Comput. Appl.* **2021**. [CrossRef]
46. Dumakor-Dupey, N.; Arya, S.; Jha, A. Advances in Blast-Induced Impact Prediction—A Review of Machine Learning Applications. *Minerals* **2021**, *11*, 601. [CrossRef]
47. Jha, A.; Tukkaraja, P. Monitoring and assessment of underground climatic conditions using sensors and GIS tools. *Int. J. Min. Sci. Technol.* **2020**, *30*, 495–499. [CrossRef]

sustainability

MDPI

Article

Study on the Geological Condition Analysis and Grade Division of High Altitude and Cold Stope Slope

Ruichong Zhang [1], Shiwei Wu [1], Chenyu Xie [2,*] and Qingfa Chen [1,*]

[1] School of Resources, Environment and Materials, Guangxi University, Nanning 530004, China; zhangruichong2002@163.com (R.Z.); gxumining@163.com (S.W.)
[2] School of Environment and Resources, Xiangtan University, Xiangtan 411105, China
* Correspondence: xiechengyu42@xtu.edu.cn (C.X.); chqf98121@163.com (Q.C.); Tel.: +86-182-2948-4803 (C.X.); +86-159-7816-9802 (Q.C.)

Abstract: Analysis of the geological conditions of high-altitude and low-temperature stope slopes and the study of grade division are the basis for the evaluation of slope stability. Based on the engineering background of the eastern slope of the Preparatory iron mine in Hejing County, Xinjiang, we comprehensively analyse and summarize the factors that affect the geological conditions of high-altitude and cold slopes and finally determine nine geological conditions that affect the index parameters. Based on a back-propagation (BP) neural network algorithm, we establish an applicable network model to analyse the geological conditions of slopes in cold areas. The model is applied to the eastern slope to analyse and classify the geological conditions of the high-altitude and low-temperature slopes. The research results show that the skarn rock layer in the eastern slope is in a stable state and not prone to landslides, and its corresponding geological condition is Grade I; meanwhile, the monzonite porphyry rock layer is in a relatively stable state, with a potential for landslides and a corresponding geological condition Grade II. The marble rock layer is in a generally stable state, there is the possibility of landslide accidents, and the corresponding geological condition level is Grade III. The limestone rock layer is in an unstable state and prone to landslide accidents, it has a corresponding geology condition Grade IV. Therefore, the eastern slope can be divided into different geological condition regions: Zone I, Zone II, Zone III, and Zone IV, and the corresponding geological condition levels for these are Grade I, Grade II, Grade III, and Grade IV. These results may provide a basis for the stability evaluation of high altitudes and cold slopes.

Keywords: high-altitude slope; BP neural network; freeze-thaw cycle; geological conditions

Citation: Zhang, R.; Wu, S.; Xie, C.; Chen, Q. Study on the Geological Condition Analysis and Grade Division of High Altitude and Cold Stope Slope. *Sustainability* **2021**, *13*, 12464. https://doi.org/10.3390/su132212464

Academic Editors: Mahdi Hasanipanah, Danial Jahed Armaghani and Jian Zhou

Received: 2 October 2021
Accepted: 7 November 2021
Published: 11 November 2021

Publisher's Note: MDPI stays neutral with regard to jurisdictional claims in published maps and institutional affiliations.

Copyright: © 2021 by the authors. Licensee MDPI, Basel, Switzerland. This article is an open access article distributed under the terms and conditions of the Creative Commons Attribution (CC BY) license (https://creativecommons.org/licenses/by/4.0/).

1. Introduction

Slope instability is one of the world's geological disasters [1–4]. Every year, the economic losses of various countries in the world caused by geological disasters due to slope instability reach immeasurable levels [5–7]. Currently, there are no accurate statistics on the loss, but the loss is still huge. Under the action of freezing and thawing cycles, blasting mining, weathering and other factors, slopes in cold areas can easily cause damage to the mechanical properties of rock slopes and lead to their instability in mines in cold areas [8–11]. Therefore, open pit mine slope landslides are a potential hazard in harsh environments with high altitudes and cold areas. For example, the "329" landslide disaster. On 29 March 2013, a landslide occurred on Zeri Mountain in the Jiama (in Tibet Province) mining area of the China National Gold Group, causing more than 2 million cubic metres of slope landslides. Eighty-three field workers were buried, and the landslide was investigated afterwards. The reason was found to be factors such as the freezing and thawing of ice and snow.

With the implementation of Western development and progress of engineering technology, difficult-to-mine mineral resources and hidden dangers left over by exploited mineral resources in the harsh environments of Tibet, Xinjiang and other cold regions have

begun to receive national attention. The stability of the geological conditions of stope slopes directly affect the smooth development of the mine. Therefore, it is very important to effectively analyse the geological conditions of stope slopes.

The analysis and classification of slope geological conditions can provide an important basis to formulate disaster prevention and mitigation measures and have guiding significance for landslide disaster mitigation planning [12]. Based on the engineering background of the eastern slope of the Preparatory iron mine in Hejing County, Xinjiang, this paper comprehensively analyses and summarizes the factors that affect the geological conditions of high-altitude and cold slopes and finally determines nine geological conditions that affect the index parameters [5,7,13–16]. Based on a back-propagation (BP) neural network algorithm, a network mode is established that is suitable for the analysis of the geological conditions of slopes in cold areas. This model is applied to the east slope to analyse and classify the geological conditions of high-altitude and low-temperature slopes.

2. BP Neural Network

2.1. BP Neural Network Operation Mechanism

In the early 1980s, the theory and research of artificial neural networks (ANNs) made considerable progress under the influence of the sound and continuous development of computers and the continuous breaking of new technical barriers. The theory of artificial neural networks sprouted during this golden period [17] and flourished as a new research paradigm.

Many studies [18,19] have shown that the efficiency of traditional system theory analysis methods is low, and the scientific nature is slightly lacking. Compared with the traditional system theory analysis method, the analysis method of the BP neural network (back-propagation neural network) is more scientific and efficient, the result is more accurate and can convince most researchers in the process of practical application. Compared with the traditional system theory analysis method, it obviously shows stronger competitiveness.

In addition, many studies [20] have found that the adaptive and self-learning capabilities of a BP neural network are outstanding, and the linear function mapping and nonlinear function mapping problems based on a BP neural network are easier to identify for mining systems.

These reasons have made many researchers in the current scientific research field strongly affirm BP neural networks. A BP neural network is a multi-layer feedforward neural network that must reduce the error between the network output and the actual value to a certain range through repeated training and learning so that the network output can reach the required accuracy. A BP neural network method to reduce the error between the network output result and the actual value trains the propagation algorithm according to the forwards multi-layer network structure and reverse feedback. The flow chart of the learning process of a BP neural network is shown in Figure 1.

2.2. Data Processing

This article uses a BP neural network-supervised algorithm to classify the data. The specific method is as follows: by continuously selecting certain characteristic parameters from the sample data that have been collected, trained, checked, filtered, and subsequently set according to the classifier in advance we can determine the criteria and summarize and sort the samples that have been further screened out and have been identified.

Before the data classification process begins, a certain amount of training data must be mastered because the continuous and stable operation of the BP neural network strictly requires the input of relevant training data. Only in this way can it be extracted through the feature extraction of the input training data in the subsequent classification process to establish a scientific and rigorous classification model. Then, the existing training data are analysed by comparing the classification model with the verification model. Finally, the classification of the data is completed.

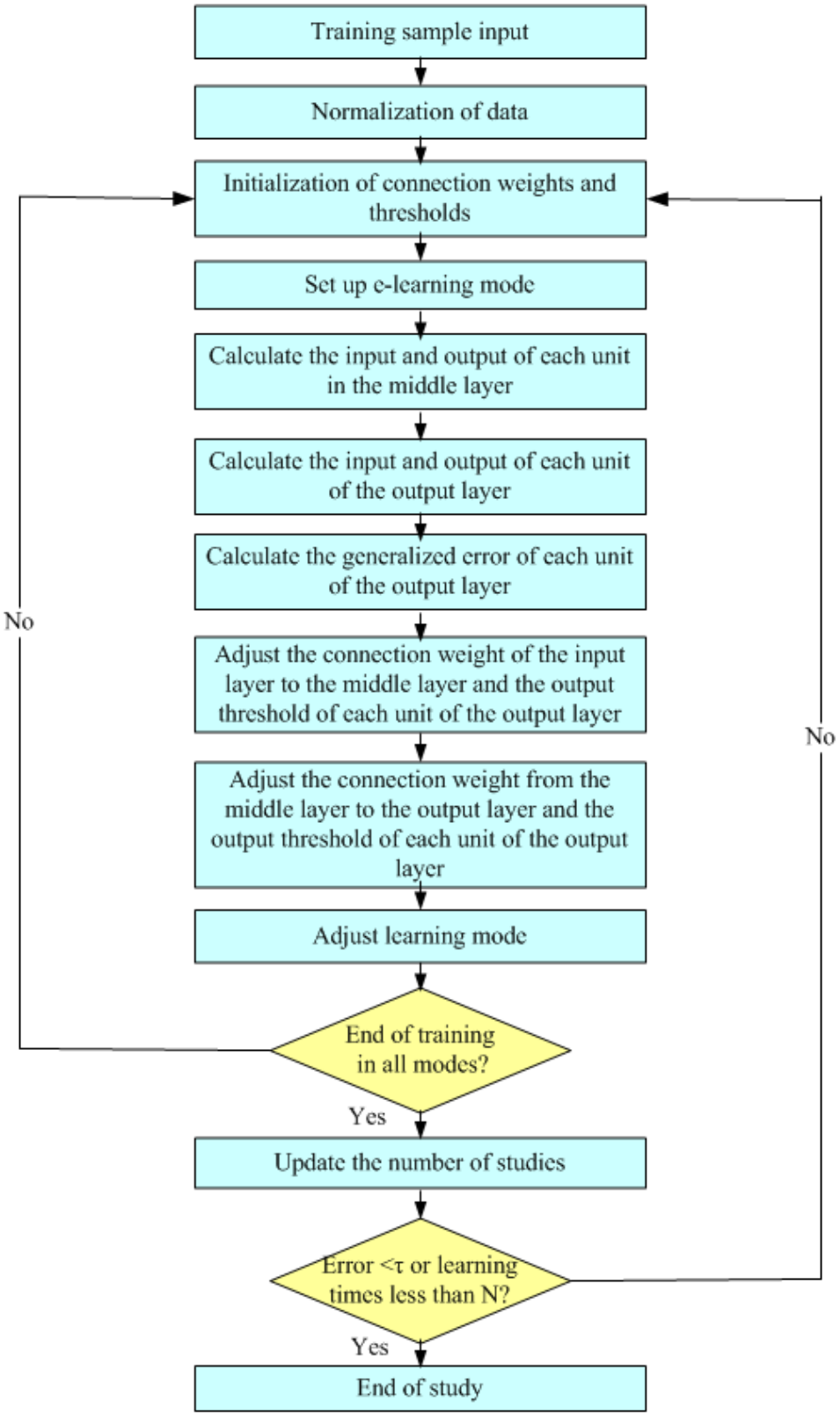

Figure 1. BP neural network operation flow chart.

To eliminate the influence of other transformation functions on the transformed image as much as possible, it is necessary to normalize the collected data. Normalization processing refers to the use of the principle of invariant moments to convert the unquantifiable expression form into a value in the range of 0–1 for processing so that the expression form becomes a scalar.

The formula for data normalization is:

$$y = \frac{x - Min_{value}}{Max_{value} - Min_{value}} \quad (1)$$

where x is the value before conversion, y is the converted value, Min_{value} is the sample minimum and Max_{value} is the sample maximum.

The BP neural network actually achieves the accuracy requirements through repeated training of multiple samples to find the minimum value of the error function. The most common method to determine whether the error satisfies the error accuracy requirement is logistic regression. This article uses a binary logistic regression method to determine the two results (True/False) of the input data and the corresponding probability (PTrue/PFalse) of the results to determine whether the accuracy of the network system satisfies the requirements. The formula is as follows:

$$t = wx + b \quad (2)$$

In the formula:
x—input sample parameters;
t—temporary variable;
w, b—model parameters.

The sigmoid function is usually used as the use condition of the conversion function: in the logical judgment, when $h(t) > 0.5$, $y = 1$. The formula is as follows:

$$h(t) = \frac{1}{1 - e^{-t}} \quad (3)$$

From formula (3), we can see: its parameter curve is shown in Figure 2.

2.3. BP Neural Network Forward Transmission and Reverse Feedback

(1) Forward transmission

The input parameters of the neural network reach the output end through the input end and each node of the intermediate layer (hidden layer). This method is forward transmission. The intermediate layer can be adjusted by changing the weight relationship between the intermediate layer and the output layer, output threshold updating of the intermediate layer, and other adjustment methods to reduce the generalization error between each node and the actual value, and to therefore achieve the desired result.

The multi-layer perceptron is composed of one or more single-layer perceptrons, which can calculate nonlinear data. The input and output ends of the multi-layer perceptron contain multiple hidden layers [18]. However, thus far, there are different opinions on the number of hidden layers.

The decision-making area of a single-layer perceptron is divided by an extended two-dimensional data plane. In addition, when the multi-layer perceptron contains only one hidden layer, the decision-making area can be an open convex area or a closed concave area. When the multilayer perceptron contains more than one hidden layer, its decision-making area can show diversified shapes and area divisions. Figure 3 shows the change in the weight relationship during the forward transmission.

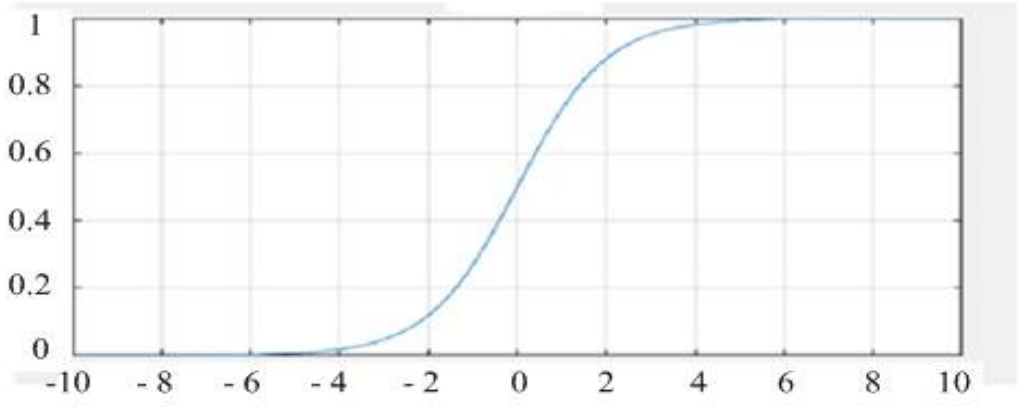

Figure 2. The Sigmoid curve.

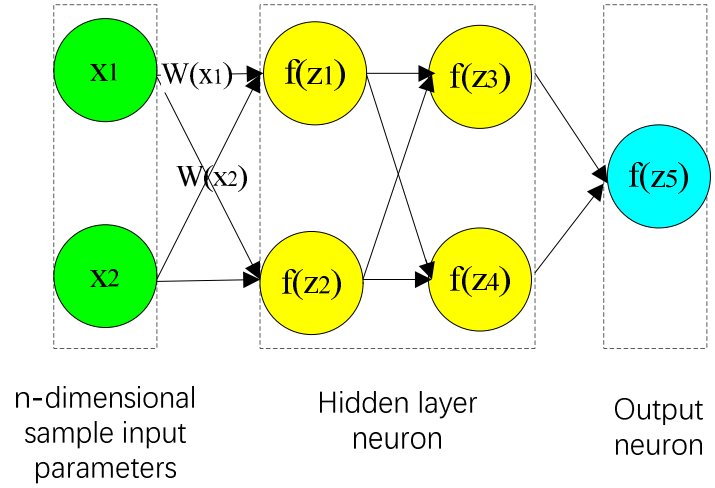

Figure 3. Graph of the weight relation changes.

Neural network training samples must introduce randomly assigned weights and biases. Simultaneously, the randomly assigned weights and random assigned biases introduced are not randomly selected but must satisfy the weights. The condition of interval real number is (–1, 1), and the offset is (0, 1) interval real number. Only after the abovementioned conditions are satisfied can the network model be forward propagated again. In this process, X_1 and X_2 are calculated by formulas (4)–(8).

For the neuron $f(z_1)$, the following calculations are performed when only the weight assignment is considered:

$$y_1 = f(z_1) = f(w_{(x_1)1} \times x_1 + w_{(x_2)1} \times x_2) \tag{4}$$

In the formula,$w_{(x_1)1}$ represents the weight of x_1 to y_1, as shown in Figure 3. Similarly, we can calculate:

$$y_2 = f(z_2) = f(w_{(x_2)2} \times x_1 + w_{(x_2)2} \times x_2) \tag{5}$$

$$y_3 = f(z_3) = f(w_{(y_1)1} \times y_1 + w_{(y_2)1} \times y_2) \tag{6}$$

$$y_4 = f(z_4) = f(w_{(y_1)2} \times y_1 + w_{(y_2)2} \times y_2) \tag{7}$$

$$y_5 = f(z_4) = f(w_{(y_3)1} \times y_3 + w_{(y_4)1} \times y_4) \tag{8}$$

In summary, the output value of each node can be calculated by the formula of forward transmission. Accordingly, the actual output result of the forward transmission model

can also be obtained by calculation, and the final output result y_5 obtained by the above formula is exactly the actual output result of the forward transmission mode.

(2) Back feedback

To facilitate the error to participate in subsequent calculations, this article assumes that t is the expected output value of the training data. Because y_5 is the actual output value of the forward propagation model, it is assumed that the difference between the actual output value and the expected output value is $\delta = t - y_5$. In addition, the difference between the actual output value and the expected output value must be based on actual conditions during the definition process. It is assumed that there is an error between the actual output value and the expected output value of each node, and this error is defined as δi. By training the error between the actual value and the expected value, the adjustment of the weight is a crucial step for the feedback adjustment of the BP neural network. The specific process is shown in Figure 4.

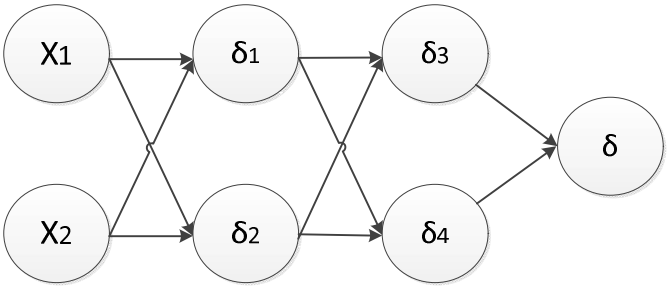

Figure 4. Variation diagram of the error feedback relationship.

For the error, $\delta_3 = w_{(y_3)}\delta$, and similarly,. $\delta_4 = w_{(y_4)}\delta$ The calculation method for δ_1 and δ_2 is as follows:

$$\delta_1 = w_{(y_1)1}\delta_3 + w_{(y_1)2}\delta_4 \tag{9}$$

$$\delta_2 = w_{(y_2)1}\delta_3 + w_{(y_2)2}\delta_4 \tag{10}$$

Using formula (9) and calculating according to the principle of this formula, the value of $\delta_1, \delta_2, \delta_3, \delta_4$ can be finally obtained. In addition, the theoretical basis of back propagation is the change in relationship between the error and the weight. The variation Δw_i obtained by adjusting the weight is calculated by error. The calculation formula of the weight variation is as follows:

$$\Delta w_i = \eta\delta_i \frac{df(z_i)}{dz_i} x_i \tag{11}$$

where: η is the learning rate.

The weight of $w_{(x_1)1}$ can be adjusted as follows:

$$w'_{(x_1)1} = w_{(x_1)1} + \eta\delta_i \frac{df(z_i)}{dz_i} x_1 \tag{12}$$

Similarly, the weight of $w_{(x_2)1}$ is adjusted as:

$$w'_{(x_2)1} = w_{(x_2)1} + \eta\delta_i \frac{df(z_i)}{dz_i} x_1 \tag{13}$$

The weight is calculated and adjusted according to Formula (12), and the final result is an update of the weight. A single back propagation includes the calculation, adjustment and updating of the weights of all nodes. Only after these tasks are completed is back propagation considered completed once. The essence of the realization of the reverse transmission algorithm is to complete the parameter adjustment of the sample model. In this process, forward transmission and reverse feedback are continuously performed. Finally, the error, weight and accuracy of the model reach the desired value.

In summary, the training process of the neural network can be completed through forward transmission and reverse feedback. However, this type of training will not continue indefinitely. Under certain conditions, the training will stop. The BP network training model stops in two situations; after setting and reaching the maximum number of iterations and after reaching a certain threshold.

3. Construction of a BP Neural Network Suitable for Preparing Iron Ore Slopes

3.1. Geological Condition Analysis and Network Output Parameter Setting

(1) Determine the geological conditions index

In the process of using the BP neural network to classify and predict the geological conditions of the stope slope, it is necessary to establish the corresponding BP neural network model. The first step in establishing a BP neural network model is to evaluate the reliability of its input parameters and filter the parameters to exclude unreliable input parameters so that the final output parameters are as accurate and reliable as possible and can show the influence of different geological factors on the geological conditions of the slope.

Generally, the geological influencing factors of slopes are the slope, slope height, lithology, unit weight, internal friction angle, porosity, cohesion, freeze-thaw cycles, etc. The slope and slope height determine the geometry of the slope and are indispensable factors for its existence. Furthermore, the lithology, gravity, internal friction angle, porosity, cohesion, etc. are important characteristics of the rock mass of the slope as they characterize the quality of the rock mass that composes it. As a unique feature of a slope in a cold region, the freeze-thaw cycle plays a huge role in the classification of geological conditions there. Various geological factors have a certain connection, while some other factors do not. Despite this, all of these factors play a vital role in the division of the slope geological conditions and therefore all will be divided. This is an important factor in the grade of slope geological conditions.

Generally, the number of parameters has little effect on neurons, and the number of parameters only represents the number of input neurons. In addition, the increase in number of parameters increases the simulation recognition time, and the actual engineering volume greatly increases. Therefore, to reduce the actual workload, this paper simplifies the input parameters of the model, and according to the modelling data and simulation results, the slope geological condition indicators are the freeze-thaw coefficient, hydrogeology, rock gravity, cohesion, internal friction angle, slope, slope height, porosity, and other factors.

(2) Set model output parameters

The output parameters are the grades of the geological conditions of the slopes in preparation for the iron ore mine, and the output parameters are divided into 4 grades according to the four expected output values of Grade I, Grade II, Grade III, and Grade IV. The specific content is shown in Table 1.

Table 1. Classification table of slope geological conditions.

Geological Condition Level	Grade Description	Represents the Value
Grade I	Good, not easy to damage	(0, 0, 0, 1)
Grade II	Better, with potential destructive factors	(0, 0, 1, 0)
Grade III	Poor, damage may occur	(0, 1, 0, 0)
Grade IV	Poor, easy to cause damage	(1, 0, 0, 0)

3.2. Determination of the Grid Structure

(1) Determination of the number of perceptrons

The input layer, hidden layer and output layer constitute the basic structure of the BP neural network. The number of hidden layers depends on the complexity of parameter selection. For a more complex problem to be solved, there are more hidden layers, and the difficulty of the corresponding model convergence increases.

(2) Determination of the number of network nodes

The method of dividing the network nodes of the input layer and output layer is unified and clear: generally, once the number of research projects is determined, the input layer and output layer are determined, but there is no scientific and consistent method of dividing the hidden layer of network nodes.

However, the neural network model constructed based on the slope parameters contains only a single hidden layer, so simply calculating the number of nodes in this layer can reveal the number of hidden layer nodes in the entire neural network model, which greatly simplifies the calculation process.

Because the number of rows of the input vector is equal to the number of nodes of the input layer, by knowing that the number of rows of the input vector is 8, it can be directly obtained that the input layer has 8 nodes. In addition, the number of nodes in the output layer is equal to the amount of output data points. Because the number of output data points is 4, it can be concluded that the number of nodes in the output layer is also 4. In addition to the above information and because the number of nodes in the hidden layer is 12, it is finally determined that the structure of the BP neural network is 8-12-4, as shown in Figure 5.

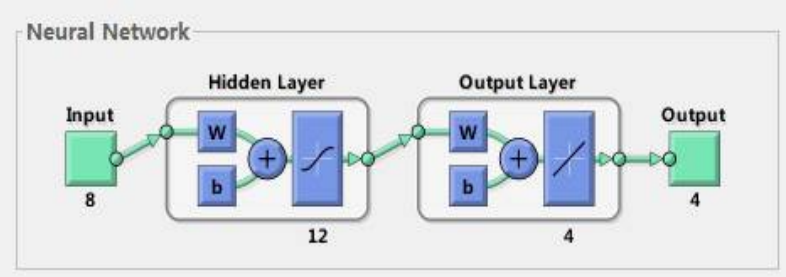

Figure 5. BP neural network structure diagram.

3.3. Selection and Processing of Training Samples

Two key factors of the network model training sample selection are mainly related to the complexity of the training sample. Firstly, the accuracy of the training sample. For training samples, the accuracy is positively correlated with the complexity of the samples. If the accuracy of the training samples increases, the complexity of the samples also increases, which will eventually increase the demand for the number of samples. Secondly, noise in the data. The noise in the sample data is also positively correlated with the complexity of the sample. If the noise in the data increases, the complexity of the training sample will also significantly increase, which affects the selection of the final training sample. Therefore, when training a neural network, it is necessary to control the relationship between the complexity of the sample and the accuracy of the training data and to provide as much key and useful information as possible to reduce the interference of redundant and useless information.

After consulting a large quantity of mine slope data, 54 neural network training samples were selected from them, with the literature [21,22] has mentioning the necessity of checking the dependency of each parameter before the ANN. However, the dependency of the parameters does not need to be discussed in this study. Because all the parameters are randomly selected, there is no dependence between the parameters in the nine main slope-influencing factors (according to the actual situation of Beizhan iron ore). All parameters are shown in Table 2, and the normalized data processing is shown in Table 3.

Table 2. Training sample parameter table.

Serial Number	Freeze-Thaw Coefficient	Hydrology Geology	Unit Weight (KN/m^3)	Cohesion (KPa)	Internal Friction Angle φ (°)	Slope (°)	Slope Height (m)	Porosity (%)	Geology Grade
1	0.42	2	12	0	30	45	8	1.62	IV
2	0.61	1	12	0	30	35	4	1.38	II
3	0.77	1	18	5	30	20	8	0.56	I
4	0.77	1	18	36	11	65	50	1.64	I
5	0.2	1	18.5	25	0	30	6	0.8	IV
7	0.42	2	20	20	36	45	50	1.38	IV
7	0.43	2	20	17	14	65	36	1.4	III
8	0.64	1	20	20	36	45	500	1.21	IV
9	0.76	1	21.4	10	30.34	30	20	0.65	I
10	0.62	1	21.4	8	28	45	31	0.73	I
11	0.68	2	21.4	10	30	30	20	0.75	I
12	0.54	1	22	10	36	45	50	1.1	IV
13	0.48	1	22	20	36	45	50	1.22	IV
14	0.33	2	22.4	10	35	45	10	1.62	IV
15	0.38	2	22.4	15	15	70	66	0.36	I
16	0.82	1	22.4	10	35	30	10	0.7	I
17	0.8	1	25	48	40	49	330	1.23	I
18	0.7	1	25	46	35	50	284	0.8	II
19	0.91	1	25	55	36	44.5	299	0.68	I
20	0.78	1	25	46	35	46	393	1.52	I
21	0.8	1	25	60	20	65	48	0.8	IV
22	0.7	1	25	20	16	45	123	1.3	I
23	0.91	1	25	50	35	50	84	0.66	IV
24	0.78	1	25	25	22	35	68	1.46	IV
25	0.4	2	26	150	45	30	200	1.46	IV
26	0.4	2	26	10	8	40	164	0.58	I
27	0.56	2	27	40	35	43	420	1.64	IV
28	0.88	1	27	50	40	42	407	0.8	I
29	0.93	1	27	35	35	42	359	0.68	I
30	0.35	2	27	32	33	42.4	289	1.4	IV
31	0.44	2	27	40	35	47.1	292	0.21	IV
32	0.84	1	27	37.5	35	37.8	320	0.65	II
33	0.36	2	27	17	20	50	98	0.56	I
34	0.55	1	27	16	13	60	164	0.68	I
35	0.88	2	27	18	45	70	212	0.82	IV
36	0.76	2	27	16	13	35	30	1.2	IV
37	0.37	1	27	17	20	80	15	0.96	IV
38	0.92	1	27.3	14	31	41	110	0.73	II
39	0.79	1	27.3	31.5	29.7	41	135	0.75	I
40	0.86	1	27.3	16.8	28	50	90.5	1.1	III
41	0.82	1	27.3	10	39	40	480	1.22	I
42	0.78	1	27.3	26	31	50	92	0.48	I
43	0.61	1	27.3	36	11	35	55	1.24	I
44	0.86	1	27.3	17	20	70.1	135	0.88	IV
45	0.54	1	27.3	60	23	45	95	0.92	I
46	0.46	1	27.3	14	17	45	22	0.66	III
47	0.56	2	31	68	37	49	200	0.68	IV
48	0.22	2	31.3	68	37	46	366	0.68	IV
49	0.47	2	31.3	68.6	37	47	305	1.52	IV
50	0.6	2	31.3	68	37	47	213	1.3	IV
51	0.22	2	31.3	20	15	30	35	1.4	I
52	0.47	2	31.3	14	17	60	22	0.86	II
53	0.33	2	31.3	5	34	55	10.5	1.23	I
54	0.74	2	31.3	60	25	52	143	0.76	IV

Table 3. Sample normalization.

Serial Number	Freeze-Thaw Coefficient	Hydrology Geology	Unit Weight (KN/m^3)	Cohesion (KPa)	Internal Friction Angle φ (°)	Slope (°)	Slope Height (m)	Porosity (%)
1	0.971	0.911	0.467	1.000	0.333	1.000	0.644	0.928
2	0.965	0.943	0.314	1.000	0.714	1.000	0.771	0.921
3	0.986	0.970	0.185	0.698	1.000	0.321	0.495	1.000
4	1.000	0.993	0.463	0.097	0.681	1.000	0.533	0.973
5	0.987	0.933	0.233	0.667	1.000	1.000	0.600	0.947
7	1.000	0.941	0.213	0.213	0.433	0.799	1.000	0.967
7	1.000	0.957	0.396	0.489	0.584	1.000	0.100	0.975
8	1.000	0.999	0.922	0.922	0.858	0.822	1.000	0.998
9	0.993	0.976	0.398	0.370	1.000	0.977	0.303	1.000
10	1.000	0.983	0.064	0.667	0.234	1.000	0.369	0.995
11	1.000	0.910	0.413	0.364	1.000	1.000	0.318	0.995
12	1.000	0.981	0.132	0.617	0.434	0.798	1.000	0.977
13	1.000	0.979	0.131	0.212	0.435	0.798	1.000	0.970
14	1.000	0.925	0.012	0.567	0.552	1.000	0.567	0.942
15	0.999	0.953	0.367	0.580	0.580	1.000	0.885	1.000
16	0.993	0.983	0.265	0.458	1.000	0.708	0.458	1.000
17	1.000	0.999	0.853	0.713	0.762	0.707	1.000	0.997
18	1.000	0.998	0.828	0.680	0.758	0.652	1.000	0.999
19	0.998	0.998	0.837	0.636	0.763	0.706	1.000	1.000
20	1.000	0.999	0.876	0.769	0.826	0.769	1.000	0.996
21	1.000	0.994	0.246	0.844	0.402	1.000	0.470	1.000
22	1.000	0.995	0.603	0.684	0.750	0.276	1.000	0.990
23	0.994	0.992	0.416	0.184	0.175	0.183	1.000	1.000
24	1.000	0.994	0.280	0.280	0.370	0.017	1.000	0.9790
25	1.000	0.934	0.743	0.499	0.553	0.703	1.000	0.989
26	1.000	0.980	0.687	0.883	0.907	0.516	1.000	0.998
27	1.000	0.993	0.874	0.812	0.836	0.798	1.000	0.995
28	1.000	0.999	0.871	0.758	0.807	0.797	1.000	1.000
29	0.999	0.998	0.853	0.808	0.808	0.769	1.000	1.000
30	1.000	0.989	0.815	0.781	0.774	0.709	1.000	0.993
31	0.998	0.988	0.816	0.727	0.762	0.679	1.000	1.000
32	0.999	0.998	0.835	0.769	0.785	0.767	1.000	1.000
33	1.000	0.967	0.455	0.660	0.597	0.018	1.000	0.997
34	1.000	0.993	0.675	0.810	0.848	0.273	1.000	0.998
35	0.999	0.989	0.752	0.837	0.582	0.345	1.000	1.000
36	1.000	0.928	0.533	0.110	0.285	1.000	0.708	0.974
37	1.000	0.984	0.331	0.582	0.507	1.000	0.633	0.985
38	0.997	0.995	0.514	0.757	0.446	0.263	1.000	1.000
39	0.999	0.996	0.604	0.542	0.569	0.400	1.000	1.000
40	1.000	0.997	0.410	0.644	0.394	0.096	1.000	0.995
41	1.000	0.999	0.889	0.962	0.841	0.836	1.000	0.998
42	0.993	0.989	0.414	0.442	0.333	0.082	1.000	1.000
43	1.000	0.986	0.019	0.301	0.618	0.265	1.000	0.977
45	1.000	1.000	0.924	0.954	0.945	1.000	0.617	1.000
45	1.000	0.990	0.433	0.259	0.524	0.059	1.000	0.992
46	1.000	0.976	0.205	0.392	0.257	1.000	0.033	0.991
47	1.000	0.986	0.695	0.324	0.635	0.514	1.000	0.999
48	1.000	0.990	0.830	0.629	0.799	0.750	1.000	0.997
49	1.000	0.990	0.798	0.553	0.760	0.694	1.000	0.993
51	1.000	0.987	0.711	0.365	0.657	0.563	1.000	0.993
51	1.000	0.898	0.787	0.137	0.150	0.712	1.000	0.932
52	1.000	0.949	0.036	0.545	0.445	1.000	0.277	0.987
53	1.000	0.939	0.133	0.829	0.232	1.000	0.628	0.967
54	1.000	0.982	0.570	0.167	0.659	0.279	1.000	1.000

3.4. Sample Training and Result Analysis

The training steps are shown in Figure 6.

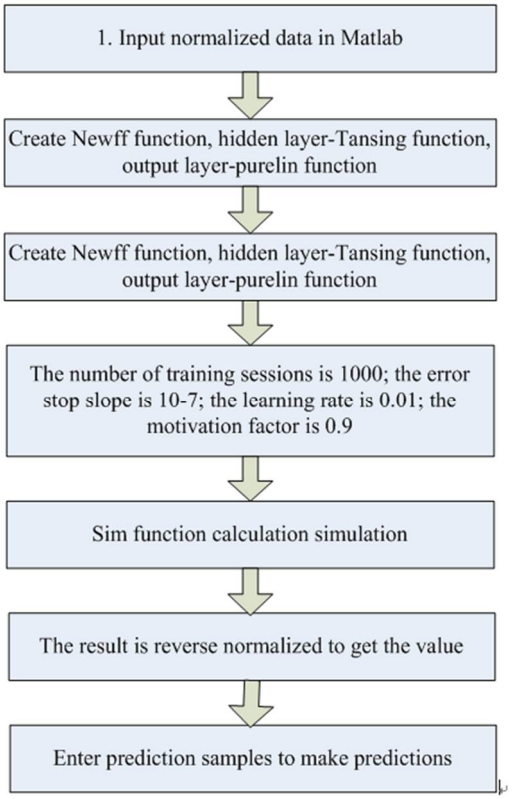

Figure 6. Training step diagram.

(1) Convergence graph

According to the data, the convergence curve is shown in Figure 7, which shows that the minimum momentum is added to the training so that the probability that the convergence curve has a local minimum is reduced after 1000 iterations of learning.

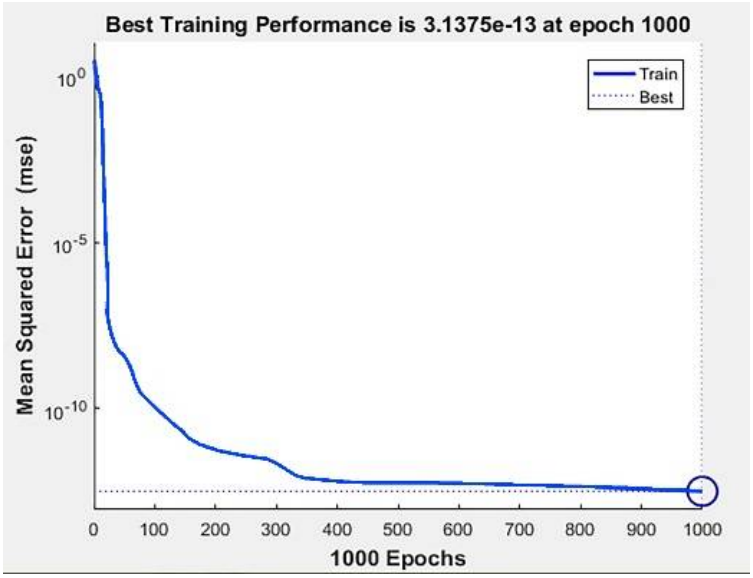

Figure 7. Convergent plot.

(2) Error distribution diagram

According to the data, the error distribution histogram is shown in Figure 8. The distribution histogram shows that the predicted sample is compared with the actual sample, and the error value is mostly distributed between –6% and 6%, which indicates that the result after training is reliable.

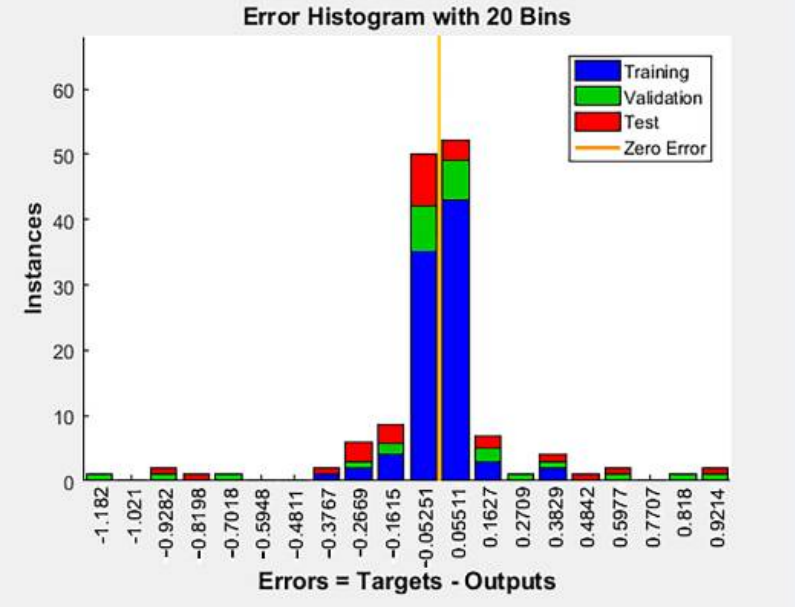

Figure 8. Error distribution histogram.

(3) Regression analysis graph

Regression diagrams are made according to the data: Figure 9 shows the regression diagram of 70% training samples; Figure 10 shows the regression diagram of 15% verification samples; Figure 11 shows the regression diagram of 15% test samples; Figure 12 shows the regression diagram of the overall sample. Among them, the abscissas 0 and 1 represent the target value, and the ordinate represents the sample value after debugging. If the slope of the curve approaches 1, it means that the target value is very close to the theoretical value, which implies that the regression analysis is very accurate.

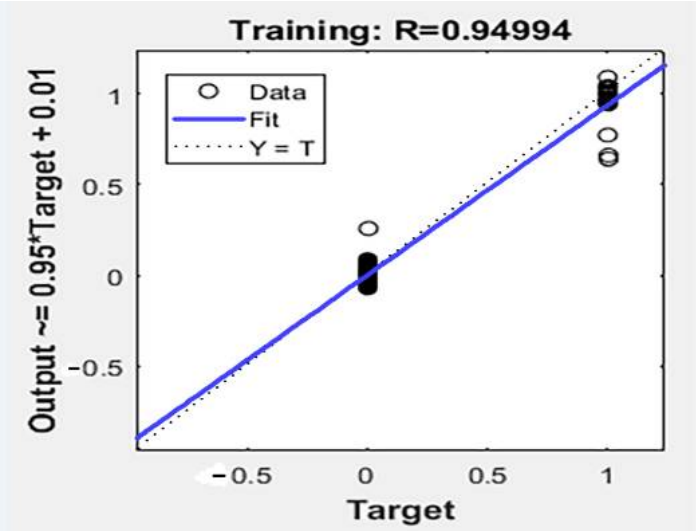

Figure 9. Regression diagram of training samples.

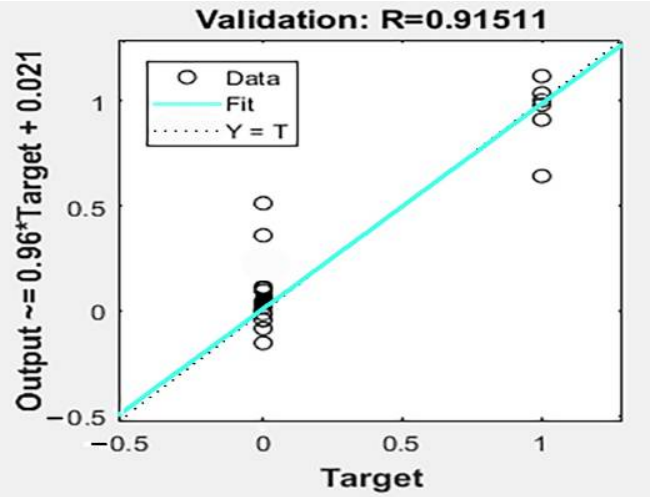

Figure 10. Regression graph of verify samples.

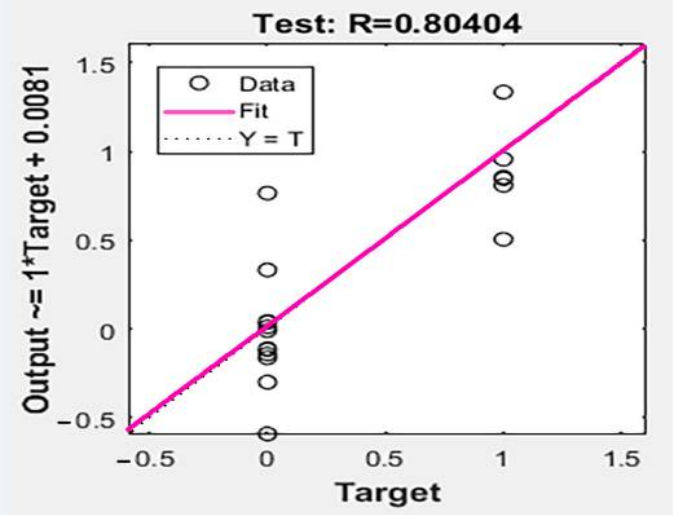

Figure 11. Regression diagram of test samples.

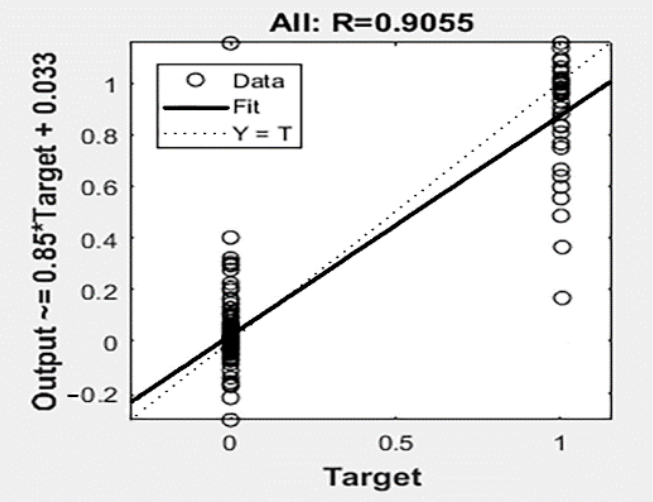

Figure 12. Regression diagram of overall samples.

The sample data in Table 4 represent the true value and predicted value of the sample and the error between them. In the table, the error is small (the maximum is 6.1%), which shows that the accuracy of network training is high.

Table 4. Comparison table of the actual situation and forecast results.

Sample Number	Actual Value				Predictive Value				Error
1	1	0	0	0	1.0323	0.0366	0.0356	0.0030	0.5%
2	0	0	1	0	0.0524	0.1953	0.9481	0.0667	0.2%
3	0	0	0	1	0.0081	0.2105	0.0158	0.9531	0.6%
4	0	0	0	1	0.0758	0.2103	0.0406	0.9659	2.5%
5	1	0	0	0	1.0478	0.2342	0.0339	0.2317	0.8%
6	1	0	0	0	1.0489	0.0696	0.1896	0.0642	0.7%
7	0	1	0	0	0.1145	1.0945	0.0374	0.0337	0.6%
8	1	0	0	0	0.9673	0.3092	0.0422	0.0443	2.2%
9	0	0	0	1	0.0918	0.0512	0.1962	1.0266	0.6%
10	0	0	0	1	0.0752	0.0833	0.0209	1.0914	1.8%
11	0	0	0	1	0.0293	0.2429	0.0194	0.9601	1.3%
12	1	0	0	0	1.0302	0.2388	0.0558	0.0764	0.3%
13	1	0	0	0	0.9711	0.2089	0.0480	0.3424	0.3%
14	1	0	0	0	0.9865	0.0538	0.0670	0.1878	1.2%
15	0	0	0	1	0.0209	0.2636	0.0014	0.9606	1.0%
16	0	0	0	1	0.0847	0.0299	0.0434	0.9824	2.0%
17	0	0	0	1	0.3618	0.2470	0.1938	0.9189	1.5%
18	0	0	1	0	0.0325	0.0948	1.1287	0.0322	3.1%
19	0	0	0	1	0.0057	0.0249	0.1771	0.9764	2.5%
20	0	0	0	1	0.3223	0.2309	0.0500	1.0462	1.7%
21	1	0	0	0	1.1517	0.1701	0.0186	0.4066	0.9%
22	0	0	0	1	0.0044	0.0317	0.2256	1.1242	0.5%
23	1	0	0	0	1.1481	0.2136	0.0531	0.0356	0.3%
24	1	0	0	0	0.9817	0.0341	0.0399	0.0888	1.2%
25	1	0	0	0	0.9511	0.2632	0.0954	0.3807	1.5%
26	0	0	0	1	0.3125	0.0374	0.2708	1.0236	0.5%
27	1	0	0	0	1.0945	0.1763	0.0556	0.1471	0.4%
28	0	0	0	1	0.1113	0.2537	0.0143	0.9117	0.6%
29	0	0	0	1	0.1085	0.2106	0.0484	0.2079	3.2%
30	1	0	0	0	0.9495	0.1847	0.1203	0.3937	0.4%
31	1	0	0	0	1.1025	0.2556	0.0029	0.2041	1.3%
32	0	0	1	0	0.1315	0.0895	1.0778	0.1361	0.5%
33	0	0	0	1	0.3289	0.3344	0.0241	0.2299	2.2%
34	0	0	0	1	0.1908	0.0543	0.1349	0.9842	1.2%
35	1	0	0	0	1.0539	0.0071	0.2508	0.3960	0.8%
36	1	0	0	0	1.1564	0.0238	0.2560	0.3913	6.1%
37	1	0	0	0	0.2317	0.0826	0.1567	0.0636	0.6%
38	0	0	1	0	0.3396	0.0003	1.0133	0.0363	0.4%
39	0	0	0	1	0.0323	0.0366	0.1356	1.0230	2.1%
40	0	1	0	0	0.0524	0.9953	0.0481	0.0667	0.1%
41	0	0	0	1	0.0081	0.0105	0.0158	0.9531	0.5%
42	0	0	0	1	0.0758	0.2103	0.3406	0.9659	0.4%
43	0	0	0	1	0.0511	0.0632	0.0954	0.9807	0.6%
44	1	0	0	0	0.9825	0.0374	0.2708	0.0236	3.2%
45	0	0	0	1	0.0945	0.1763	0.0556	0.9471	0.4%
46	0	1	0	0	0.1113	1.0537	0.0143	0.2117	1.3%
47	1	0	0	0	1.1085	0.2106	0.0484	0.2079	0.5%
48	1	0	0	0	0.9495	0.1847	0.1203	0.3937	2.2%
49	1	0	0	0	1.1025	0.2556	0.0029	0.2041	1.2%
50	1	0	0	0	1.1315	0.0895	0.0778	0.1361	0.8%
51	0	0	0	1	0.0289	0.3344	0.0241	0.9299	0.6%
52	0	0	1	0	0.0308	0.0543	0.9349	0.0842	0.8%
53	0	0	0	1	0.0539	0.0071	0.2508	0.9960	1.6%
54	1	0	0	0	0.9564	0.0238	0.0560	0.3913	2.3%

4. Grade Division of Slope Geological Conditions in Preparation for Iron Mines

4.1. Determination of Parameter Samples of Geological Condition Indicators

There are two main mining areas in the current mining area of the preparation for iron ore: open-pit mining and side-hanging mining. The slope area of this study is mainly the side slope between the pit and the side-hanging mine, which forms after the open-pit mining, i.e., the east side slope area of the mine. Referring to the geological report of the area and the index data of the test items, a set of parameter samples containing geological conditions index can be obtained, as shown in Table 5.

Table 5. Indicators and parameters of slope geological conditions.

Sample	Freeze-Thaw Coefficient	Hydrogeology	Unit Weight (kN/m^3)	Cohesion C (MPa)	Internal Friction Angle φ (°)	Slope Gradient (°)	Slope Height (m)	Porosity (%)
1	0.88	2	25	8.2	28.8	65	122	1.96
2	0.83	2	23.7	7.3	31	27	185	1.25
3	0.76	2	28.4	18.2	28.3	28	137	0.7
4	0.92	2	24.1	11.1	29.6	37	240	1.23
5	0.9	2	24.8	3.2	37.9	36	185	0.8
6	0.94	2	29.2	17.7	33.3	38	180	0.68
7	0.36	1	25.3	6.8	30.6	55	80	1.94
8	0.28	1	24.2	4.5	35.1	60	85	0.8
9	0.7	1	23.8	4.3	32.4	52	40	1.65
10	0.72	1	27.2	11.1	30.4	31	73	0.73
11	0.75	1	26.4	9	31	35	30	0.75
12	0.8	1	27	12.3	33	41	55	1.1
13	0.79	1	29.6	8.5	32.2	43	35	1

4.2. Calculation Results and Analysis

According to the training results of the BP neural network model based on the training samples in the previous section, the accuracy of the network is high, so it can be used to prepare for the calculation of the iron ore geological index parameter samples. After normalizing the data in the geological condition parameter table (Table 5), it is input into the neural network model for calculation, and the result is shown in Table 6. Table 7 is obtained after summarizing the samples of the same geological condition level among 13 groups of samples.

Table 6. Classification table of slope geological conditions.

Sample Number	MATLAB Algorithm Prediction Results				Slope Grade
1	0.0759	0.0378	0.0457	1.0286	I
2	0.1556	0.9543	0.1673	0.1744	III
3	1.0885	0.0844	0.2401	0.9332	I
4	0.1281	0.3648	0.3191	0.1930	IV
5	0.3929	0.4178	0.1265	0.7675	II
6	0.4028	0.3458	0.1476	0.9204	I
7	0.5088	0.0963	0.8371	0.2608	II
8	0.3147	0.4021	0.3597	0.3112	I
9	0.5993	0.1380	0.8891	0.2342	IV
10	0.1224	0.0445	0.9446	0.1536	I
11	0.2659	0.0408	0.6098	0.1285	III
12	0.5896	0.2179	0.7807	0.1128	III
13	0.5292	0.1991	0.7404	0.1057	II

Table 7. Summary of the grades of the slope geological conditions.

	Grade and Status of Slope Geological Conditions
1, 3, 6, 8, 10	Grade I: good geological conditions, not easy to damage
5, 7, 13	Grade II: Good geological conditions, with potential damage factors
2, 11, 12	Grade III: The geological conditions are poor, which may cause damage
4, 9	Grade IV: Poor geological conditions, easy to cause damage

Based on Table 7, the BP neural network analysis shows that among the 13 samples of the eastern slope in this cold area, 5 have geological conditions of Grade I, and 3 have geological conditions of Grade II. There are 3 with condition Grade III and 2 with Grade IV conditions. The 13 sample numbers are distributed in different locations on the eastern slope. After their positions have been marked on the eastern slope, the distribution area map of the eastern slope samples, as shown in Figure 13, is obtained.

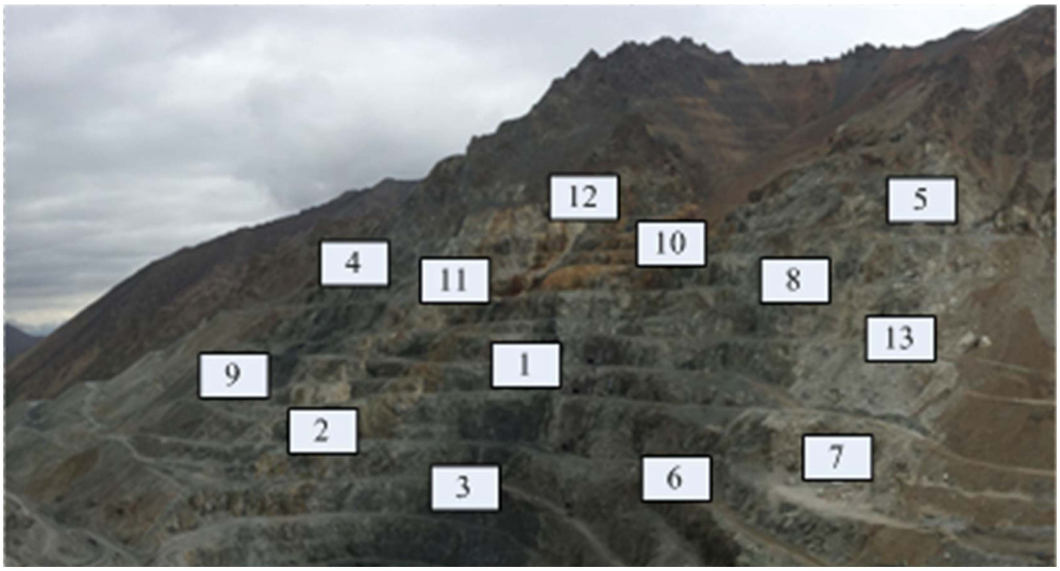

Figure 13. Sample distribution map of the east slope.

The numbers 1 to 13 in the diagram are the sampling points, and 13 samples are taken from different areas of the east slope of Beizhan Iron Mine.Figure 13 shows that although the distribution positions of the 13 samples on the eastern slope are random; there is a certain distribution law, i.e., the distribution among the samples at identical or similar geological condition levels is relatively dense, and samples of different geological conditions are far apart and sparsely distributed. As a result, the regions where samples with identical or similar geological condition levels are located can be statistically divided, so that the eastern slope can be divided into geological conditions. The specific divisions are shown in Figure 14.

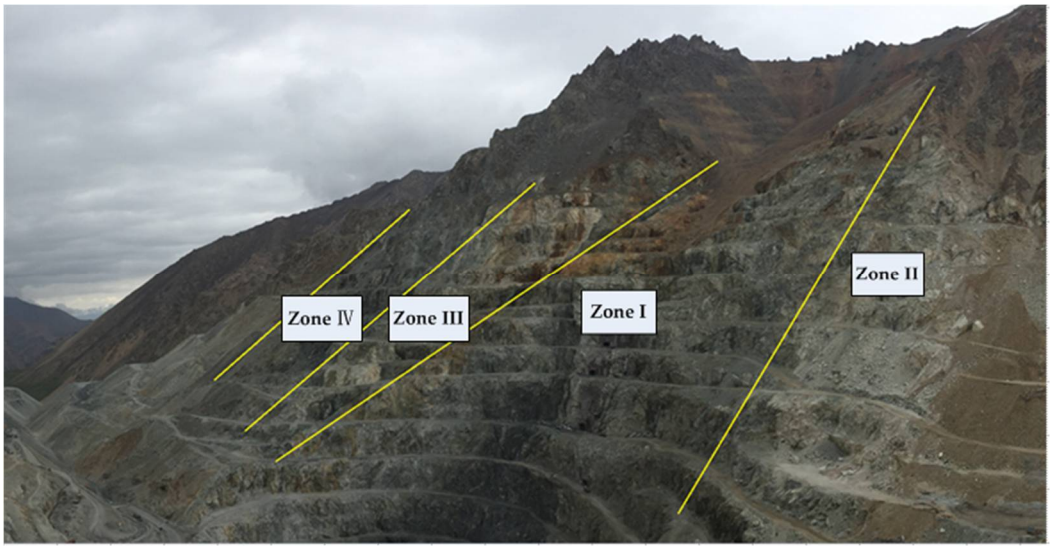

Figure 14. Zoning map of geological conditions of the east slope.

5. Concluding Remarks

A BP neural network is used to classify the geological conditions of the eastern slope of the preparatory iron mine and the overall division. The eastern slope of the iron mine preparation is divided into four areas: Zone I, Zone II, Zone III, and Zone IV. The corresponding geological condition grades for zones I to IV are grade I, grade II, grade III, and grade IV, respectively. Among them, the rock formation in Zone I is mainly skarn rock formation, which is also the main occurrence area of ore bodies. It has high unit weight, high hardness, undeveloped rock joints, high integrity, and good physical and mechanical properties, so its geological conditions are good. Damage does not easily occur, and the corresponding geological condition is grade I. The rock formation in Zone II is mainly monzonite porphyry. Compared with skarn its weight and hardness are slightly lower, however, the rock layer is thick and the joints are less developed. Therefore, it has better physical and mechanical properties. The conditions are good, there are only potential destructive factors, and the corresponding geological conditions are grade II. The rock formations in Zone III are mainly marble formations. Compared with skarn and monzonite porphyries, marble is relatively poor in lithology, has low gravity and hardness, and has more joints in the formations. The physical and mechanical properties are poor, but its thickness is large, and the layered distribution slightly compensates for the lack of lithology. Therefore, its geological conditions are general, and there is a possibility of damage. The corresponding geological conditions are grade III. The rock formation in Zone IV is mainly limestone rock. It has the worst lithology among the four rock formations, with low unit weight, low hardness, well-developed joints, and large porosity. After long-term weathering, erosion, and freezing and thawing cycles, its physical properties are destroyed. Therefore, the geological conditions in this area are poor and easily destroyed. The corresponding geological conditions are grade IV.

Author Contributions: The research articles with four authors, the Conceptualization R.Z. and S.W.; methodology, Q.C.; software, S.W; validation, R.Z., S.W and Q.C.; formal analysis, C.X.; investigation, C.X.; resources, Q.C.; data curation, S.W.; writing—original draft preparation, S.W.; writing—review and editing, R.Z.; visualization, C.X.; supervision, Q.C.; project administration, Q.C. All authors have read and agreed to the published version of the manuscript.

Funding: The research was funded by the national key research and development project "Slope instability mechanism and early warning technology of open pit in high altitude and cold area" (No. 2018YFC0808402) and the Hunan Province Science Foundation, grant number 2021JJ30679.

Institutional Review Board Statement: This paper does not involve human or animal studies.

Informed Consent Statement: This paper does not involve human research.

Data Availability Statement: All the data included in this study are available upon request by contact with the corresponding author.

Conflicts of Interest: The authors declare no conflict of interest.

References

1. Fang, R.K.; Liu, Y.H. Review of regional landslide risk assessment methods based on machine learning. *Chin. J. Geol. Hazard Control* **2021**, *32*, 1–5.
2. Feng, T.J. Assessment of the Loss of Ecological Carrying Capacity Caused by Landslide Disasters in the Southeastern Mountainous Area of Jilin Province. Master's Thesis, Northeast Normal University, Changchun, China, 2016.
3. Shang, G.A. Analysis of dump slope deformation monitoring data based on the re-scaled range analysis method. *Opencast Min. Technol.* **2018**, *33*, 64–67.
4. Li, C.H.; Xiao, Y.G. Research status and trend of deformation and failure mechanisms of rock slopes in high altitude and cold areas. *Chin. J. Eng. Sci.* **2019**, *41*, 1374–1386.
5. Han, G. Research on the Key Technique of Stability and Safety Control of High Bedding Rock Slope in Open-Pit Mine. Ph.D. Thesis, University of Science and Technology Beijing, Beijing, China, 2017; pp. 57–63.
6. Liu, J. Stability Evaluation of Open-Pit Mine Slope Based on Fuzzy-Random Reliability. Master's Thesis, Central South University, Changsha, China, 2013; pp. 56–58, 70–72.
7. Luo, X.D. *Stability Analysis and Engineering Application of High Slope in Open-Pit Mine in Cold Area*, 1st ed.; China Meteorological Press: Beijing, China, 2015; pp. 38–39, 46–48.
8. Chen, Y.C. Preliminary Study on Rock and Soil Slope Stability under the Freez-ing-Thawing Condition. Master's Thesis, Xi'an Technological University, Xi'an, China, 2006; pp. 7–10, 14–15.
9. Luo, X.D.; Huang, C.L.; Rong, Z.X.; Lv, Q.S. Study of physico-mechanical characteristics of rocks in slope of Mengku iron mine under freezing-thawing cyclic effect. *Rock Soil Mech.* **2011**, *32* (Suppl. S1), 155–159.
10. Deng, H.W.; Tian, W.G.; Zhou, K.P.; Li, J.L. Progress in freezing-thawing rock mechanics from 2001 to 2012. *Tech. Rev.* **2013**, *31*, 74–79.
11. Meng, L.L.; Chen, Q.F. Stability analysis of high-altitude and high-cold slopes in preparation for iron mine. *Non-Ferr. Met. Min. Part* **2020**, *72*, 5–9.
12. Li, Z.; Nadim, F.; Huang, H.; Uzielli, M.; Lacasse, S. Quantitative vulnerability estimation for scenario-based landslide hazards. *Landslides* **2010**, *7*, 125–134. [CrossRef]
13. Zhang, B. Geological Characteristics and Genesis of the Preparatory Iron Deposit in Hejing County, Xinjiang. Master's Thesis, Chang'an University, Xi'an, China, 2016; pp. 14–15, 64–66.
14. Jordá-Bordehore, L. Application of Q slope to Assess the Stability of Rock Slopes in Madrid Province, Spain. *Rock Mech. Rock Eng.* **2017**, *50*, 1947–1957. [CrossRef]
15. Bar, N.; Barton, N. The Q-Slope Method for Rock Slope Engineering. *Rock Mech. Rock Eng.* **2017**, *50*, 3307–3322. [CrossRef]
16. Bar, N.; Barton, N. Rock Slope Design using Q-slope and Geophysical Survey Data. *Period. Polytech. Civ. Eng.* **2018**, *62*, 893–900. [CrossRef]
17. Niu, P.F.; Zhou, A.H. Stability prediction of rock slopes of Central South Highway based on PCA and BP neural network. *J. Inst. Disaster Prev. Sci. Technol.* **2020**, *22*, 10–16.
18. Jiang, J. BP neural Networks for Prediction of Factor of safety of Slope Stability. In Proceedings of the 2011 IEEE 2nd International Conference on Computing, Control and Industrial Engineering, Wuhan, China, 20–21 August 2011; Institute of Electrical and Electronics Engineers Inc.: Piscataway, NJ, USA, 2011; Volume 115, pp. 347–350.
19. Zhao, Y.J.; Zhang, E.L.; Gong, Z.Z. The application of BP neural network in slope stability prediction. *West. Explor. Eng.* **2014**, *26*, 23–25.
20. Feng, X.T.; Wang, Y.J. Neural network estimation of slope stability. *J. Eng. Geol.* **1995**, *3*, 54–61.
21. Chang, S.K.; Lee, D.H.; Wu, J.H.; Juang, C.H. Rainfall-based criteria for assessing slump rate of mountainous highway slopes: A case study of slopes along Highway 18 in Alishan, Tai-wan. *Eng. Geol.* **2011**, *118*, 63–74. [CrossRef]
22. Lin, H.M.; Chang, S.K.; Wu, J.H.; Juang, C.H. Neural network-based model for assessing failure potential of highway slopes in the Alishan, Taiwan Area: Pre- and post-earthquake investigation. *Eng. Geol.* **2009**, *104*, 280–289. [CrossRef]

sustainability

MDPI

Article

Nonlinear Elasto-Visco-Plastic Creep Behavior and New Creep Damage Model of Dolomitic Limestone Subjected to Cyclic Incremental Loading and Unloading

Xingkai Wang [1,2,3], Leibo Song [1,*], Caichu Xia [1,*], Guansheng Han [1] and Zheming Zhu [3]

[1] School of Civil Engineering, Shaoxing University, Shaoxing 312000, China; xkwang@cumt.edu.cn (X.W.); han_gs@cumt.edu.cn (G.H.)
[2] Key Laboratory of Rock Mechanics and Geohazards of Zhejiang Province, Shaoxing University, Shaoxing 312000, China
[3] College of Architecture & Environment, Sichuan University, Chengdu 610065, China; zhuzm1965@163.com
* Correspondence: song_leibo@163.com (L.S.); caichuxia@163.com (C.X.)

Abstract: For many rock engineering projects, the stress of surrounding rocks is constantly increasing and decreasing during excavating progress and the long-term operation stage. Herein, the triaxial creep behavior of dolomitic limestone subjected to cyclic incremental loading and unloading was probed using an advanced rock mechanics testing system (i.e., MTS815.04). Then, the instantaneous elastic strain, instantaneous plastic strain, visco-elastic strain, and visco-plastic strain components were separated from the total strain curve, and evolutions of these different types of strain with deviatoric stress increment were analyzed. Furthermore, a damage variable considering the proportion of irrecoverable plastic strain to the total strain was introduced, and a new nonlinear multi-element creep model was established by connecting the newly proposed damage viscous body in series with the Hookean substance, St. Venant body, and Kelvin element. The parameters of this new model were analyzed. The findings are listed as follows: (1) When the deviatoric stress is not more than 75% of the compressive strength, only instantaneous deformation, transient creep, and steady-state creep deformation occur, rock deformation is mainly characterized by the instantaneous strain, whereas the irrecoverable instantaneous plastic strain accounts for 38.02–60.27% of the total instantaneous strain; (2) Greater deviatoric stress corresponds to more obvious creep deformation. The visco-elastic strain increases linearly with the increase of deviatoric stress, especially the irrecoverable visco-plastic strain increases exponentially with deviatoric stress increment, and finally leads to accelerated creep and delayed failure of the sample; (3) Based on the experimental data, the proposed nonlinear creep model is verified to describe the full creep stage perfectly, particularly the tertiary creep stage. These results could deepen our understanding of the elasto-visco-plastic deformation behavior of dolomitic limestone and have theoretical and practical significance for the safe excavation and long-term stability of underground rock engineering.

Keywords: triaxial creep experiment; cyclic loading and unloading; elasto-visco-plastic strain; irrecoverable strain; tertiary creep stage; nonlinear creep damage model

Citation: Wang, X.; Song, L.; Xia, C.; Han, G.; Zhu, Z. Nonlinear Elasto-Visco-Plastic Creep Behavior and New Creep Damage Model of Dolomitic Limestone Subjected to Cyclic Incremental Loading and Unloading. *Sustainability* **2021**, *13*, 12376. https://doi.org/10.3390/su132212376

Academic Editors: Mahdi Hasanipanah, Danial Jahed Armaghani and Jian Zhou

Received: 22 September 2021
Accepted: 5 November 2021
Published: 9 November 2021

Publisher's Note: MDPI stays neutral with regard to jurisdictional claims in published maps and institutional affiliations.

Copyright: © 2021 by the authors. Licensee MDPI, Basel, Switzerland. This article is an open access article distributed under the terms and conditions of the Creative Commons Attribution (CC BY) license (https://creativecommons.org/licenses/by/4.0/).

1. Introduction

The time-dependent deformation characteristics of rock, especially the creep behaviors, are related to the long-term stability of underground rock engineering, such as tunnels and roadways [1–11]. Many scholars have carried out extensive research on creep mechanical behaviors of different types of rocks. Maranini and Brignoli [12], Yang et al. [11], Fujii et al. [13], and Wang et al. [14] have obtained a lot of research achievements in uniaxial and triaxial compression creep characteristics of soft rocks such as limestone, salt, clastic-rock, weathered sandstone, and coal rock. The creep mechanical properties of hard rocks, such as greenschist [15], diabase [16], marble [17], and red sandstone [18] under stepwise

loading, have been systematically studied. Furthermore, the constitutive model theory has been developed and applied to describe rock creep behavior. There are two main expression types for rheological models: One is the empirical model, the curtain function, exponential function, and logarithmic function are commonly used to fit the creep test data. Generally, the fitting effect is perfect, but the physical meaning of the model is not clear [14]. The other is the component combined model. The classical multi-component models include the Maxwell model, Kelvin model, Bingham model, and Burgers model [9]. However, since these models are composed of linear elements, they cannot describe the nonlinear accelerated rheological behavior [9,14]. Thus, more and more nonlinear rheological models have been established to describe the whole creep process reasonably. There are mainly two modeling methods: one is to propose a new nonlinear rheological element, and then connect it with the original linear model to build a nonlinear creep model that can describe the three creep stages [16,17]; The other is to establish a nonlinear creep damage model based on fracture or damage mechanics, which could reasonably describe the damage evolution during three creep stages of rocks [18,19].

However, the triaxial compression creep tests are still limited due to the limitation of test apparatus and strict requirements for creep test conditions; Previous studies have paid much attention to the creep behavior of rock under a constant load or multi-stage load, with little being paid to the time-dependent deformation behavior of rock during unloading. Previous creep experiments seldom have been carried out to separate the instantaneous elastic, instantaneous plastic strain, visco-elastic strain, and visco-plastic strain components from creep strain curves [20]. Furthermore, the previous constitutive models have not sufficiently considered the difference between visco-elastic and visco-plastic strains. For a lot of rock engineering, the stress of surrounding rocks is constantly changing and adjusting between increasing and decreasing during the excavating progress and long-term operation stage [20–22]. Therefore, the time-dependent deformation behavior of surrounding rocks subjected to cyclic loading and unloading is a scientific problem that needs to be focused on, which has important theoretical and practical significance for the safe construction and long-term operation of rock engineering.

In this work, the chosen dolomitic limestone specimens were drilled from Yangzong Tunnel in Yunnan Province, southwest China. The triaxial compression creep experiments were performed to capture the visco-elastic-plastic deformation behaviors of the dolomitic limestone under cyclic incremental loading and unloading. Creep data was analyzed, and the total creep strain was separated into the instantaneous elastic strain, instantaneous plastic strain, visco-elastic strain, and visco-plastic strain components. Then, a new nonlinear visco-elasto-plastic creep model was proposed to describe the full creep stages, especially the tertiary stage. Finally, the creep parameters were identified by employing the Levenberg-Marquardt optimization algorithm and the accuracy of the creep model was verified based on the experimental data.

2. Experimental Method

The creep experiment was carried out using a servo-controlled high rigidity rock mechanics testing system (MTS815.04) at Shaoxing University in China. The specific parameters of this apparatus: maximum axial pressure is 4600 kN; maximum confining pressure is 140 MPa; adjustable temperature is in the range of 0–200 °C The duration, axial pressure, confining pressure, axial and lateral strain can be displayed on the computer monitor during the testing progress. The size of cylindrical samples used in both the conventional compression experiment and the creep experiment are Φ50 mm × 100 mm. The test apparatus and the deformation monitoring sensor system are shown in Figure 1.

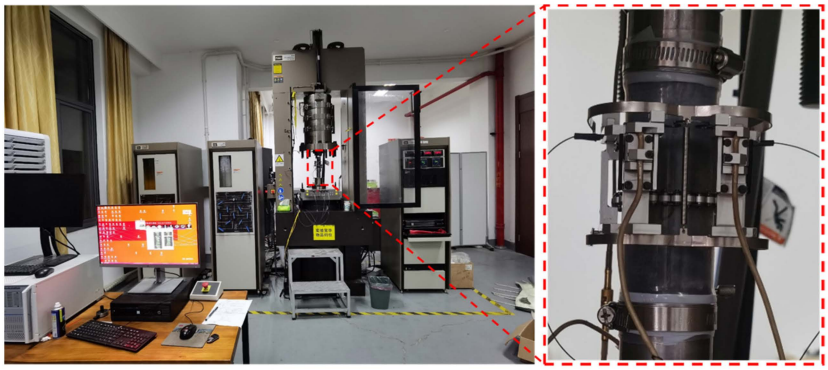

Figure 1. (**a**) Test apparatus and (**b**) installation of samples and deformation monitoring sensors.

A conventional triaxial compression test was carried out first to reveal the short-term mechanical properties of the studied rock and provide a basis for determining the stress level in the creep test. According to in-situ stress measurement, the horizontal stress is about 9 MPa, which is designed as the confining stress in conventional test and creep tests. An axial displacement rate of 0.001 mm/s and a confining stress loading rate of 0.1 MPa/s were used for conventional compression experiments. Based on testing results, the short-term mechanical parameters could be calculated, as shown in Table 1.

Table 1. Results of conventional triaxial compression experiment and loading stress data of creep experiment.

Conventional Triaxial Compression Experiment				Triaxial Creep Experiment						
Confining Pressure (MPa)	Compressive Strength (MPa)	Elastic Modulus (GPa)	Poisson Ratio	Confining Pressure (MPa)	Axial Loading Stress Levels (MPa)					
					1st	2nd	3rd	4th	5th	6th
9	68.08	14.41	0.184	9	27	37	42	50	60	65

The confining pressure was applied first at a rate of 0.1 MPa/s to achieve 9 MPa, which then was maintained unchanged throughout creep testing until the specimen failed. Six levels of axial stress were set in the creep test, as listed in Table 1, and the first axial loading stress was 35% of the axial compressive strength, i.e., the first stress level was 27 MPa. The loading and unloading process is shown in Figure 2, an axial loading rate of 0.5 kN/s was adopted to reach the target stress and then remained constant for 48 h, after which, the deviatoric stress (i.e., the difference between axial stress and confining stress) was unloaded to 0 at a rate of 0.5 kN/s and then maintained for 20–30 h until the visco-elastic strain was recovered. After this unloading period, the loading and unloading of the next axial stress level were performed, until the specimen was damaged, the experiment was completed. The axial and radial strain data of the specimen were acquired in real-time by the testing machine and stored in the computer during the whole experiment.

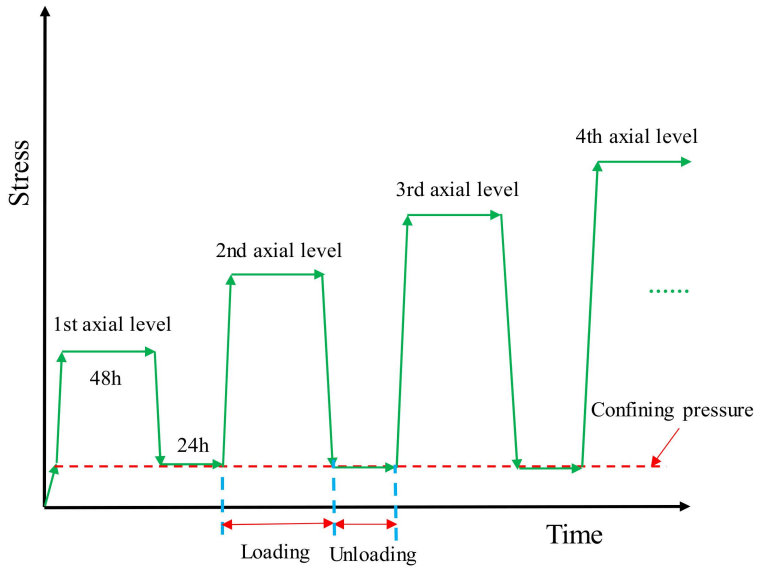

Figure 2. Loading and unloading process during the creep test.

3. Experimental Results and Creep Model Construction

3.1. Data Processing

Three samples were tested in the creep experiment, and the results show little scattering due to the natural heterogeneities and discreteness of the rock samples. In this paper, only the most representative test results are selected and analyzed. Figure 3 shows the total axial and radial creep curves of dolomitic limestone subjected to cyclic incremental loading and unloading. Taking the axial strain-time curve (as shown in Figure 4) under loading and unloading of a certain deviatoric stress level (i.e., cycle *i*) for example, the elasto-visco-plastic strain separation is analyzed as follows.

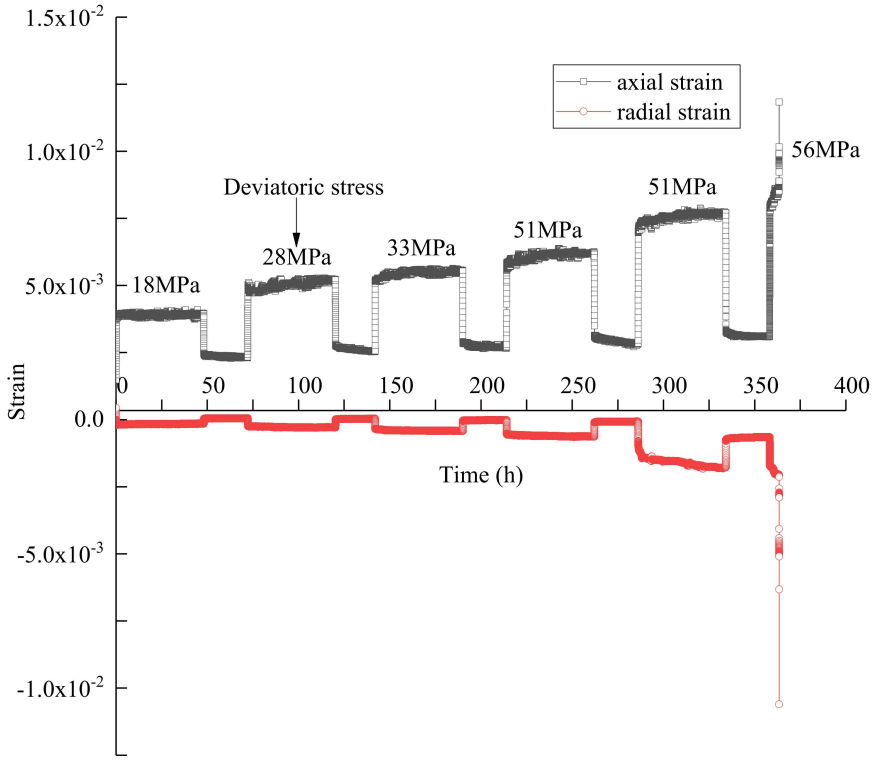

Figure 3. Total axial and radial strain-time curves of dolomitic limestone subjected to cyclic incremental loading and unloading.

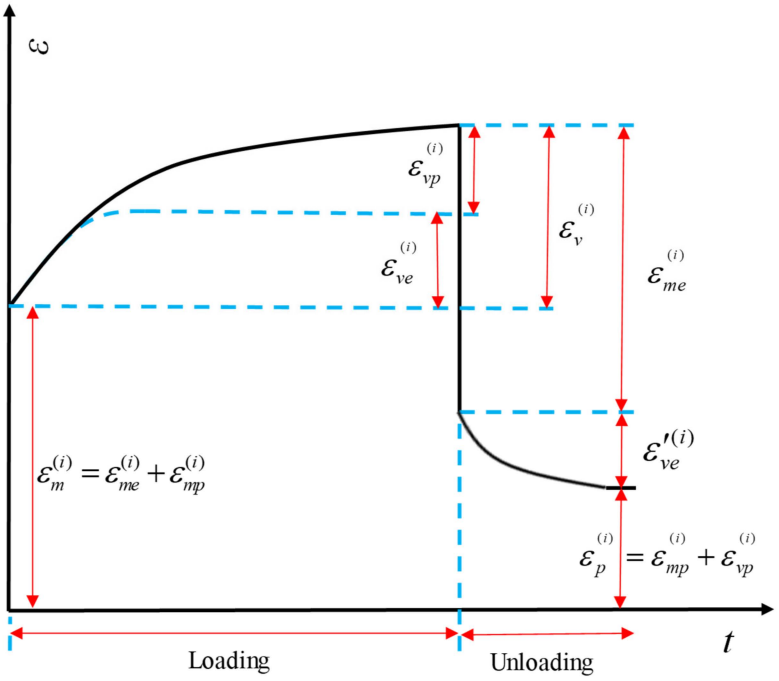

Figure 4. Representative axial strain-time curve and separation method of different types of strain under a certain deviatoric stress level loading and unloading.

The total strain could be separated into the instantaneous elastic, instantaneous plastic strain, visco-elastic strain, and visco-plastic strain components.

$$\varepsilon^{(i)} = \varepsilon_m^{(i)} + \varepsilon_v^{(i)} = \varepsilon_{me}^{(i)} + \varepsilon_{mp}^{(i)} + \varepsilon_{ve}^{(i)} + \varepsilon_{vp}^{(i)} \tag{1}$$

where $\varepsilon_m^{(i)}$ and $\varepsilon_v^{(i)}$ are the instantaneous strain and creep strain, respectively. The former consists of instantaneous elastic strain $\varepsilon_{me}^{(i)}$ and instantaneous plastic strain $\varepsilon_{mp}^{(i)}$, the latter includes visco-elastic strain $\varepsilon_{ve}^{(i)}$ and visco-plastic strain $\varepsilon_{vp}^{(i)}$.

It should be noted that $\varepsilon_{me}^{(i)}$ and $\varepsilon_{ve}^{(i)}$ could be identified directly from the unloading curve. Especially, $\varepsilon_{ve}^{(i)}$ during the loading progress is equal to the recovery viscoelastic strain $\varepsilon_{ve}^{\prime(i)}$ during the unloading stage, according to the principles of elastic and plastic mechanics [23]. However, the plastic strain can only be obtained by considering the history of loading [24], i.e., $\varepsilon_{mp}^{(i)}$ and $\varepsilon_{vp}^{(i)}$ can be expressed as:

$$\varepsilon_{mp}^{(i)} = \sum_{n=1}^{i} \Delta\varepsilon_{mp}^{(n)} \tag{2}$$

$$\varepsilon_{vp}^{(i)} = \sum_{n=1}^{i} \Delta\varepsilon_{vp}^{(n)} \tag{3}$$

where $\Delta\varepsilon_{mp}^{(n)}$ and $\Delta\varepsilon_{vp}^{(n)}$ are the instantaneous plastic strain increment and visco-plastic strain increment caused by deviatoric stress increment $\Delta\sigma^{(n)} = (\sigma_1 - \sigma_3)^n - (\sigma_1 - \sigma_3)^{n-1}$, respectively.

It should be pointed out that the evolution law of radial creep strain is similar to that of axial creep strain, the elasto-visco-plastic strain characteristics of radial creep behavior would not be analyzed here.

3.2. Elasto-Visco-Plastic Strain Analysis

The strain curves (in Figure 3), during different deviatoric stress levels, indicate that instantaneous deformation occurred firstly, after which creep deformation occurred. When the loading deviatoric stress was not more than 51 MPa (i.e., the fifth deviatoric stress level), only transient creep stage and steady-state creep stage occurred. However, the rock underwent accelerated creep deformation as the deviatoric stress reached 56 MPa, which accounts for 82.35% of the conventional compressive strength.

According to the strain separation method shown in Figure 4, the axial elasto-visco-plastic strain data of the specimen subjected to cyclic incremental loading and unloading could be obtained, as listed in Table 2. Additionally, the variation curves of instantaneous elastic strain, instantaneous plastic strain, visco-elastic strain, and visco-plastic strain with deviatoric stress are illustrated in Figure 5.

Table 2. Axial elasto-visco-plastic strain data of dolomitic limestone under cyclic incremental loading and unloading.

Confining Pressure (MPa)	Axial Stress (MPa)	ε_m (10^{-3})	ε_v (10^{-3})	ε_{me} (10^{-3})	ε_{mp} (10^{-3})	ε_{ve} (10^{-3})	ε_{vp} (10^{-3})	$\blacktriangle\varepsilon_{mp}$ (10^{-3})	$\blacktriangle\varepsilon_{vp}$ (10^{-3})
9	27	3.75	0.20	1.49	2.26	0.13	0.07	2.26	0.07
	37	4.84	0.36	2.41	2.43	0.24	0.12	0.17	0.05
	42	5.16	0.38	2.63	2.53	0.22	0.16	0.09	0.04
	50	5.64	0.57	3.06	2.58	0.30	0.26	0.05	0.10
	60	6.98	0.72	4.32	2.65	0.26	0.46	0.08	0.20
	65	7.86	3.97	-	-	-	3.97	-	3.51

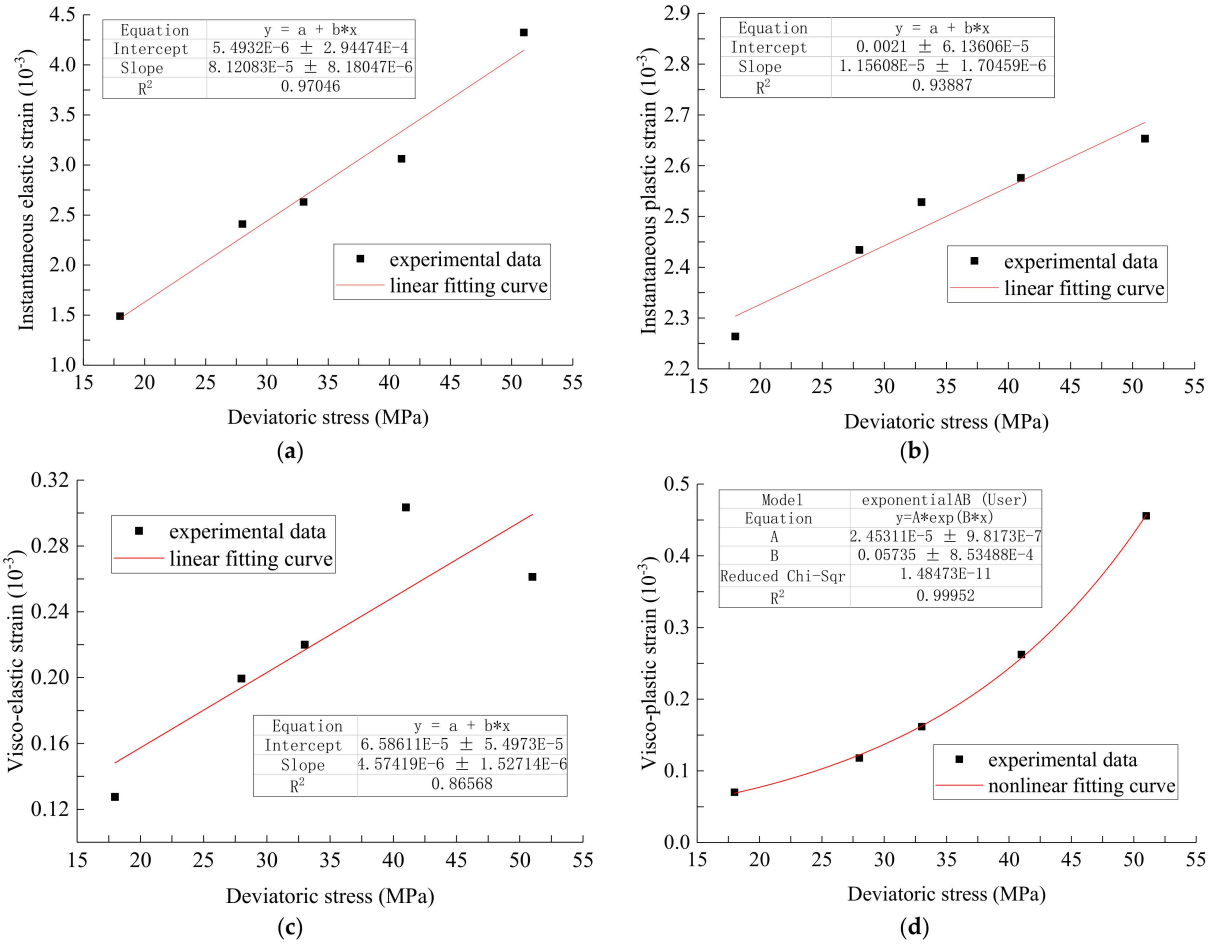

Figure 5. Curves of variation of (**a**) instantaneous elastic strain, (**b**) instantaneous plastic strain, (**c**) visco-elastic strain, and (**d**) visco-plastic strain with deviatoric stress.

It is observed from Figure 5a,b that both instantaneous elastic and instantaneous plastic strain increase linearly with deviatoric stress. The irrecoverable instantaneous plastic strain accounts for 37.97–60.27% of instantaneous strain (using the axial elasto-visco-plastic strain data listed in Table 2), yet it would often belong to recoverable instantaneous elastic deformation in the creep tests without unloading process [14,16], which may cause errors in engineering design. Besides, the creep strain, which consists of visco-elastic strain and visco-plastic strain, increases with deviatoric stress increment. Specifically, as the deviatoric stress increases from 18 MPa to 56 MPa, the proportion of creep strain in total strain increases from 5.06% to 33.56%, which means creep deformation is more and more obvious as the deviatoric stress increases. In addition, it should be noted that the visco-plastic strain increases nonlinearly and exponentially with the increase of deviatoric stress, as shown in Figure 5d. Moreover, the proportion of irrecoverable visco-plastic strain in total creep strain increases from 35.00% to 63.89% with the deviatoric stress increasing from 18 MPa to 51 MPa. It suggests that the recoverable visco-elastic strain accounts for the main part of the total creep strain when the deviatoric stress is not more than 51 MPa. However, the creep deformation is mainly characterized by visco-plastic strain as the deviatoric stress is greater than 51 MPa, especially during the accelerated creep stage, the total creep deformation could be considered as the development of irrecoverable visco-plastic strain, which leads to delayed failure of the specimen. As illustrated in Figure 6, the specimen shows shear failure, an inclined failure surface runs through the whole specimen, which is similar to the creep failure mode of hard rock found by Zhao et al. [20].

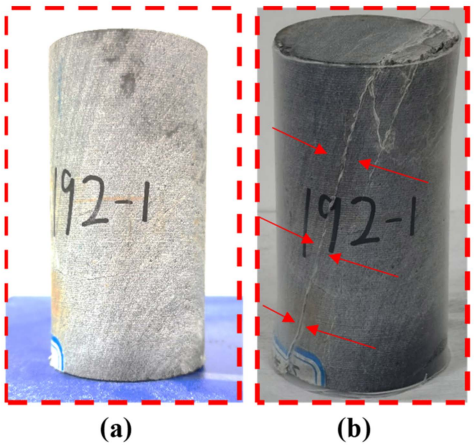

Figure 6. Rock sample (**a**) before the test and (**b**) after creep failure.

3.3. Development of Nonlinear Creep Damage Model

In Figure 7, a new multi-element rheological model is developed to describe the nonlinear visco-elasto-plastic creep behavior of dolomitic limestone under cyclic incremental loading and unloading. This multi-element model consists of the Hookean substance, St. Venant substance, Kelvin body, and a newly proposed damage viscous body, which are used to exhibit instantaneous elastic strain, instantaneous plastic strain, visco-elastic strain, and nonlinear visco-plastic strain, respectively. Their constitutive relations and creep equations are derived as follows.

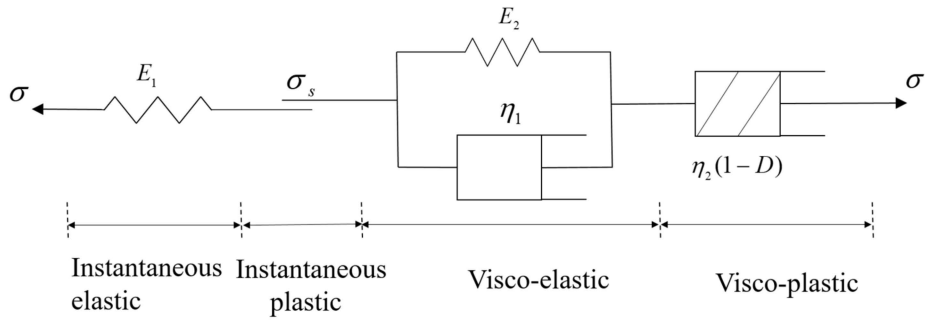

Figure 7. Multi-element diagram of a new nonlinear visco-elasto-plastic creep moel.

3.3.1. Instantaneous Strain Model

According to the constitutive relation of Hooke body [25], axial instantaneous elastic strain ε_{me} is given by

$$\varepsilon_{me} = \frac{\sigma_1 - \sigma_3}{E_1} \tag{4}$$

where E_1 is the elastic modulus of the single Hooke body 1.

Similarly, the axial instantaneous plastic strain could be expressed by [26]

$$\varepsilon_{mp} = \frac{\sigma_1 - \sigma_3 - \sigma_s}{P} I(\sigma_1 - \sigma_3 - \sigma_s) \tag{5}$$

where P is the plastic deformation modulus of the St. Venant substance, and $I(\sigma_1 - \sigma_3 - \sigma_s)$ is a unit jump function, namely,

$$I(\sigma_1 - \sigma_3 - \sigma_s) = \begin{cases} 0, \sigma_1 - \sigma_3 < \sigma_s \\ 1, \sigma_1 - \sigma_3 \geq \sigma_s \end{cases} \tag{6}$$

3.3.2. Visco-Elastic Strain Model

Based on the constitutive relationship of Kevin body [25,27], the axial visco-elastic strain of the specimen during the loading stage could be presented as

$$\varepsilon_{ve} = \frac{\sigma_1 - \sigma_3}{E_2} \left[1 - \exp\left(-\frac{E_2}{\eta_1} t \right) \right] \tag{7}$$

where E_2 and η_1 are elastic modulus and viscous coefficient of Kelvin substance, respectively, and t is creep time.

At the time point $t = t_1$, the deviator stress $\sigma_1 - \sigma_3$ is unloaded to zero, the unloading creep equation of visco-elastic strain ε'_{ve} is given by Equation (8) [28].

$$\varepsilon'_{ve} = \frac{\sigma_1 - \sigma_3}{E_2} \left[1 - \exp\left(-\frac{E_2}{\eta_1} t_1 \right) \right] \exp\left(\frac{E_2}{\eta_1} (t_1 - t) \right) \tag{8}$$

3.3.3. Visco-Plastic Strain Model

In terms of damage mechanics, rock failure is the joint action result of external load and evolution of internal defects of rock materials, which is a gradual creep accumulation process [9,18,29]. Under the long-term influence of large deviatoric stress, the damage of rock materials will continue to accumulate, resulting in fissures increase in the amount and crack expansion and penetration. In this process, the damage degree of rock will develop rapidly, the viscous coefficient will continue to decrease. Macroscopically, it shows the accumulation and nonlinear increase of unrecoverable visco-plastic strain (as shown in Figures 3 and 5d). Finally, the rock deformation increases sharply, and the specimen is

destroyed. Therefore, similar to the elastic-plastic theory, a new damage variable could be defined by considering the development of the plastic strain of the rock material, i.e.,

$$D = 1 - \frac{\varepsilon_e}{\varepsilon_e + \varepsilon_p} \tag{9}$$

where ε_e and ε_p are the elastic and plastic strain of rock material, respectively. The former is a summation of instantaneous elastic strain and visco-elastic strain, the latter consists of instantaneous plastic strain and visco-plastic strain. At the initial loading time point $t = 0$, instantaneous plastic deformation occurs, and the damage variable, $D \neq 0$, indicates that the damage variable can also reflect the initial damage, which is an essential feature of rock due to the existence of joints and micro-fractures. Then, based on the constitutive relationship of dashpot element [27], the constitutive equation of this newly proposed damaged viscous body could be given as

$$\dot{\varepsilon}_{vp} = \frac{\sigma}{\eta} = \frac{\sigma_1 - \sigma_3}{\eta_2(1 - D)} = \frac{(\sigma_1 - \sigma_3)(\varepsilon_e + \varepsilon_p)}{\eta_2 \varepsilon_e} \tag{10}$$

where η_2 is the initial viscosity coefficient of visco-plastic element, $\dot{\varepsilon}_{vp}$ is the creep rate of visco-plastic strain.

Then, the following Equation (10) could be obtained.

$$\dot{\varepsilon}_{vp} = \frac{q(\varepsilon_{me} + \varepsilon_{ve} + \varepsilon_{mp} + \varepsilon_{vp})}{\eta_2(\varepsilon_{me} + \varepsilon_{ve})} \tag{11}$$

where $q = (\sigma_1 - \sigma_3)$. Besides, the visco-elastic strain could be omitted due to the fact that the visco-elastic strain of rock is more than one order of magnitude smaller than the instantaneous elastic strain during the triaxial compression creep process (as proven in Table 2), then, Equation (11) can be simplified to Equation (12).

$$\dot{\varepsilon}_{vp} = \frac{q(\varepsilon_{me} + \varepsilon_{mp} + \varepsilon_{vp})}{\eta_2 \varepsilon_{me}} \tag{12}$$

Equation (12) is a first-order linear non-homogeneous differential equation concerning time. The creep equation of visco-plastic strain can be obtained by solving this differential equation, as shown in Equation (13). During creep testing, when the loading stress is constant, the instantaneous elastic strain and instantaneous plastic strain of the sample are constant, so Equation (13) can be expressed as Equation (14).

$$\varepsilon_{vp}(t) = C \exp\left(\frac{q}{\eta_2 \varepsilon_{me}} t\right) - \varepsilon_{me} - \varepsilon_{mp} \tag{13}$$

$$\varepsilon_{vp} = A + C \exp\left(\frac{\sigma_1 - \sigma_3}{\eta_2 B} t\right) \tag{14}$$

where A is a variable related to instantaneous strain, B is a variable related to instantaneous elastic strain, C is the primary integration constant. Based on the above contents, the axial creep equation of the new nonlinear creep model can be obtained as follows.

$$\varepsilon(t) = \frac{\sigma_1 - \sigma_3}{E_1} + \frac{\sigma_1 - \sigma_3 - \sigma_s}{P} I(\sigma_1 - \sigma_3 - \sigma_s) + \frac{\sigma_1 - \sigma_3}{E_2}\left[1 - \exp\left(-\frac{E_2}{\eta_1} t\right)\right] + A + C \exp\left(\frac{\sigma_1 - \sigma_3}{B\eta_2} t\right) \tag{15}$$

3.3.4. Model Parameters Identification

In general, there are two methods for model parameter identification [14], i.e., the curve analysis method and the numerical iteration method. This work uses the direct curve analysis method to identify the instantaneous parameters, and then uses the numerical iteration method (also named numerical fitting) to determine the creep parameters. The

parameters of E_1, P, and σ_s could be identified using the instantaneous strain data in Table 2. Then, E_2 and η_1 could be obtained by fitting the unloading creep curves using Equation (8). Finally, η_2, A, B, and C can be solved by fitting the visco-plastic creep curve with Equation (14) based on the Levenberg-Marquardt optimization algorithm. All the model parameters of the specimen under six deviatoric stress levels are listed in Table 3. Figure 8 presents the experimental curves and theoretical curves of the proposed model at every stress level. Additionally, the evolution curves of the damage variable with time under two typical deviatoric stress levels are plotted in Figure 9.

Table 3. Model parameters of the testing specimen under six deviatoric stress levels.

$\sigma_1-\sigma_3$ (MPa)	E_1 (GPa)	P (GPa)	σ_s (MPa)	E_2 (GPa)	η_1 (10^3·GPa·h)	A (10^{-4})	B (10^{-3})	C (10^{-4})	η_2 (GPa·h)	R^2
18	12.08	6.86	2.50	196.72	1.28	0.75	−1.49	0.61	86.29	0.72
28	11.62	10.49		139.98	1.12	0.14	−2.41	0.69	2.67	0.93
33	12.55	12.06		185.48	1.23	1.67	−2.63	−1.81	96.52	0.78
41	13.40	14.92		154.52	1.61	3.41	−3.06	−2.55	273.44	0.85
51	11.81	18.30		295.99	1.08	5.93	−4.32	−3.66	251.18	0.92
56	-	-		-	-	-2.41×10^4	−4.32	2.41×10^4	1.98×10^5	0.90

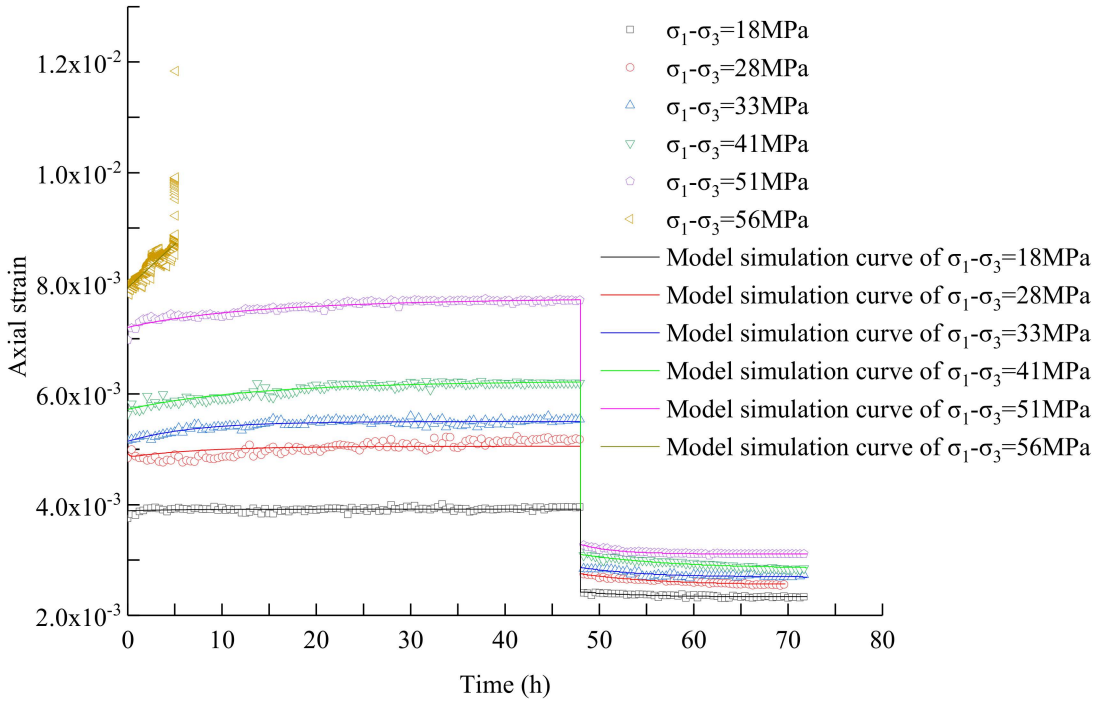

Figure 8. Comparison between the simulation curves of the proposed model and the testing results at different axial stresses with confining stress being 9 MPa.

It could be found that the theoretical curves fit well with the experimental curves, correlation coefficients are between 0.72–0.93. The damage variables are in good agreement with the increasing trend of strain. These suggest that the proposed nonlinear creep damage model could legitimately describe the elasto-visco-plastic strain characteristics of dolomitic limestone under cyclic incremental loading and unloading.

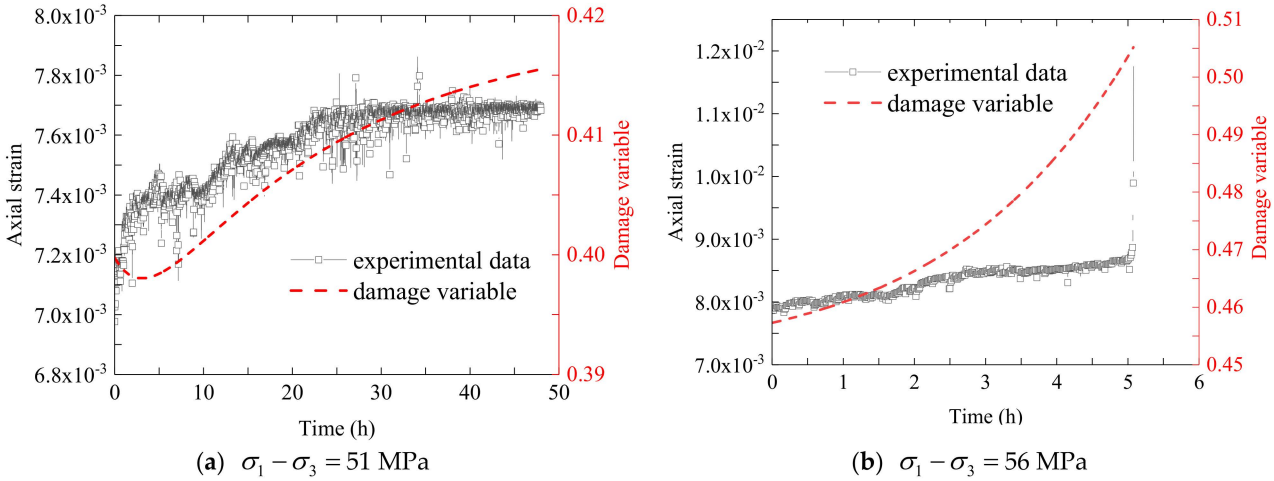

Figure 9. Evolutions of damage variable and strain versus time under two typical deviatoric stress levels.

3.3.5. Model Parameters Analysis

In order to expand the application scope of the new model and deepen the understanding of this model, a parameter analysis is required. As the Hookean substance, St. Venant substance, and Kelvin body are well-known models, herein, only the analysis of the parameter A, B, and C within the newly proposed viscous body is carried out, the variation curves of visco-plastic strain with time under different model parameters are drawn in Figure 10. Here, η_2 and $\sigma_1 - \sigma_3$ are taken as 300 GPa·h and 50 MPa, respectively.

It could be found that the value of parameter A only affects the initial value of visco-plastic strain (see Figure 10a,b), while parameters B and C have an important impact on the evolution law of visco-plastic creep curve. Specifically: (1) When the value of parameter C is among $1-4 \times 10^{-4}$, the model curve is characterized by an accelerated creep process, and the creep rate decreases with the increase of parameter B, as presented in Figure 10c. While parameter B is constant, the accelerated creep rate increases with the increase of parameter C (see Figure 10e). (2) When the value of C is among $-4-(-1) \times 10^{-4}$, the model curves are featured by attenuation creep or steady-state creep. As the value of parameter C is relatively large, the model curve mainly shows an attenuation creep process, and the creep rate increases with the increase of parameter B, i.e., the duration of the attenuation creep stage decreases, as revealed in Figure 10d. While the value of parameter C is small and the value of parameter B is large, the visco-plastic model curves mainly show a steady-state creep process, and the rate decreases with the increase of parameter C, as presented in Figure 10f.

Moreover, the theoretical model in this paper is suitable for the creep law description of many rocks under the condition of loading and unloading in engineering practice. The creep parameters of different rocks could be obtained by using the creep testing results combined with one of the model parameter identification methods. Then, a more accurate creep theoretical model with definite creep parameters of the studied rocks could be applied to the long-term stability analysis and engineering design.

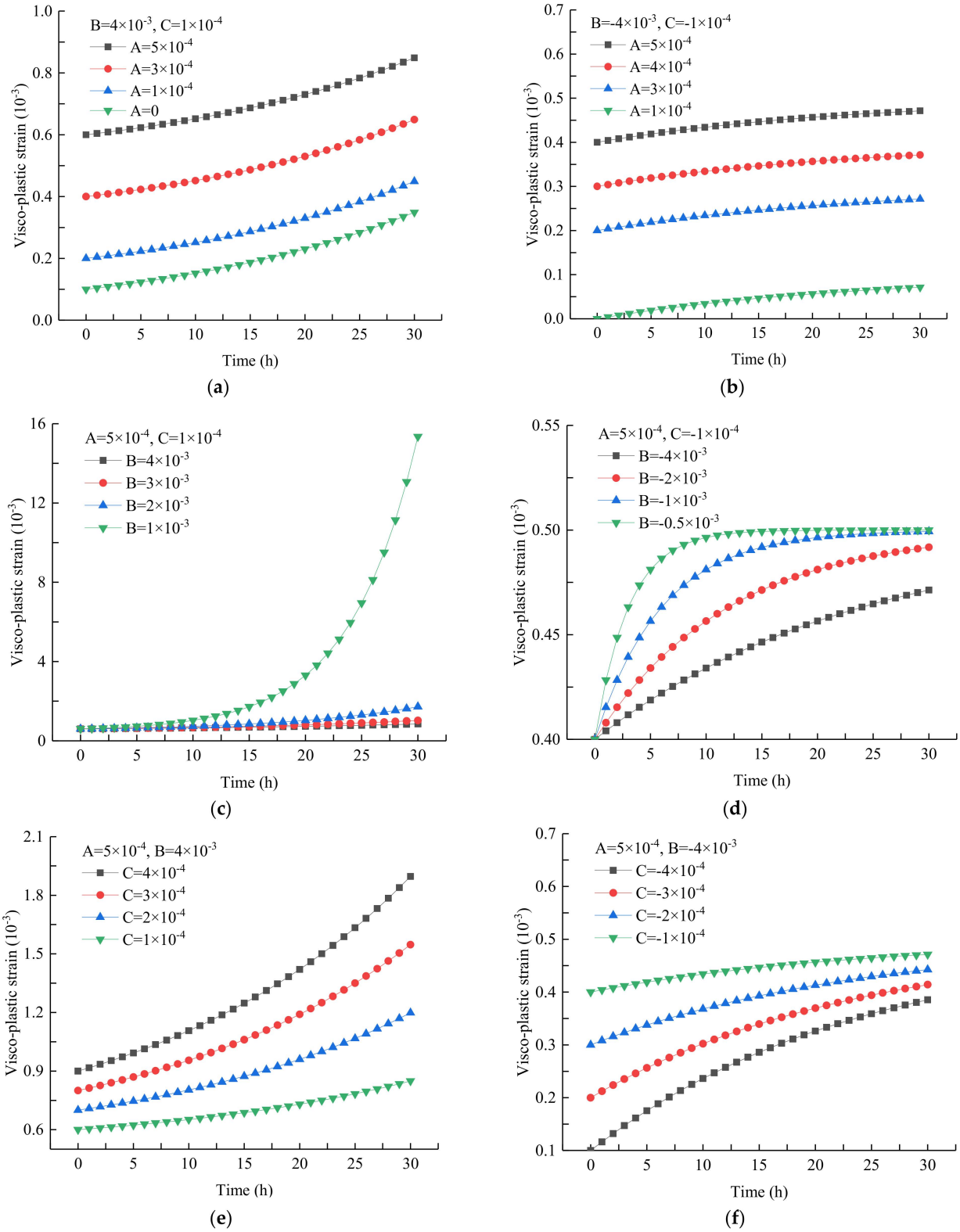

Figure 10. Variation curves of visco-plastic strain with time under different model parameters.

3.3.6. Advantages and Disadvantages of the Developed Model

The classical multi-component models, such as the Maxwell model, Kelvin model, Bingham model, Burgers model, as well as Xiyuan model, cannot describe the nonlinear accelerated rheological behavior [9,14]. Moreover, they cannot reveal the progressive

damage properties of rock during the creep process, especially the accelerated creep stage. The developed model includes a newly proposed damage viscous body, which could describe the evolution of nonlinear visco-plastic strain in the accelerated creep stage.

Besides, the damage variable is usually defined as an equation concerning the elastic modulus in previous studies [21,29]. However, the elastic modulus changes with time, and the initial elastic modulus is difficult to define during the creep process [21]. Here, during compressive creep test of rock subjected to cyclic loading and unloading, elastic strain and plastic strain could be measured and calculated, which is consistent with the important principle of the definition of damage variable: the parameters should be easy to measure and easy to establish contact with macro mechanical properties [29].

In addition, it can be seen from Figure 10 that the new visco-plastic model would reflect different evolutionary trends of creep strain under different testing conditions and has wide applicability. Thus, the multi-element creep model can be used universally for describing the creep behaviors of rock subjected to cyclic incremental loading and unloading.

However, the disadvantage of this model is that, as shown in Figure 10a, there was a short-lived fluctuation (i.e., the value of the damage variable decreased) in the initial stage of the damage variable curve. This is mainly because that the visco-elastic strain curve is always attenuated creep process, while the visco-plastic strain curve shows steady-state creep (i.e., red curve Figure 10f) under the condition of deviatoric stress being 51 MPa, the initial creep rate of the former is relatively large, whereas the initial creep rate of the latter is relatively small, causing the growth rate of visco-elastic strain will be greater than that of visco-plastic stain in a short time during the beginning stage of creep process. In fact, as shown in Figure 10d, this phenomenon would not occur when the visco-plastic strain curve also belongs to the type of attenuation creep. Subsequent studies should pay more attention to and explore the definition of more satisfactory damage variables.

4. Conclusions

(1) The triaxial compression creep behaviors of dolomitic limestone subjected to cyclic incremental loading and unloading manifest that the instantaneous deformation occurs firstly during every deviatoric stress level and then creep deformation occurs. When the loading deviatoric stress is not more than 75% of the conventional triaxial compression strength, only transient creep stage and steady-state creep stage occur successively. However, the rock undergoes accelerated creep deformation while the loading stress reaches 82.35% of the instantaneous compressive strength.

(2) The separation of elasto-visco-plastic strain component shows that rock deformation is mainly characterized by instantaneous strain while the deviatoric stress is not more than 75% of the conventional compressive strength, especially the irrecoverable instantaneous plastic strain accounts for 37.97–60.27% of total instantaneous strain and should not be ignored during rock engineering design. Greater deviatoric stress contributes to more obvious creep deformation, the visco-elastic strain increases linearly with deviatoric stress, More importantly, the irrecoverable visco-plastic strain increases exponentially with the deviatoric stress increasing from 26.47% to 82.35% of the compressive strength, and finally leads to the occurrence of accelerated creep and rock failure.

(3) A damage variable considering the proportion of irrecoverable plastic strain to the total strain is put forward, and then the creep equation of a new damaged viscous body is deduced, based on which, a new nonlinear multi-element creep model is established by connecting the new damaged viscous body in series with the Hookean substance, St. Venant body, and Kelvin element. The theoretical curves of the proposed model fit accurately with the experimental curves, indicating the nonlinear multi-element creep model could describe the elasto-visco-plastic deformation characteristics precisely, especially the nonlinear accelerated creep behavior.

The obtained findings can help our understanding of the elasto-visco-plastic deformation behavior of dolomitic limestone and provide a more accurate creep theoretical model for long-term stability analysis and engineering design.

Author Contributions: Conceptualization, X.W. prepared the manuscript and conducted the investigation, L.S. and C.X. were responsible for the methodology, G.H. carried out the data processing, L.S. acquired the funding, C.X. and Z.Z. reviewed and edited the manuscript. All authors have read and agreed to the published version of the manuscript.

Funding: This work was financially supported by the National Natural Science Foundation of China (Grant No. 42002275), the Open Fund of Key Laboratory of Rock Mechanics and the Geohazards of Zhejiang Province for Shaoxing University (ZJRMG-2020-01), and the Natural Science Foundation of Zhejiang Province (Grant No. LQ21D020001, LQ21E040003).

Data Availability Statement: The data presented in this study are available on request from the corresponding author.

Acknowledgments: We wish to thank Linxiang Wang for supporting this experiment.

Conflicts of Interest: The authors declare no conflict of interest.

References

1. Singh, T.N.; Verma, A.K. Prediction of creep characteristic of rock under varying environment. *Environ. Geol.* **2005**, *48*, 559–568. [CrossRef]
2. Verma, A.K.; Singh, T.N. Modeling of a jointed rock mass under triaxial conditions. *Arab. J. Geosci.* **2010**, *3*, 91–103. [CrossRef]
3. Singh, T.N.; Kanchan, R.; Verma, A.; Singh, S. An intelligent approach for prediction of triaxial properties using unconfined uniaxial strength. *Min. Eng. J.* **2003**, *5*, 12–16.
4. Li, D.; Cai, M.; Masoumi, H. A constitutive model for modified cable bolts exhibiting cone shaped failure mode. *Int. J. Rock Mech. Min.* **2021**, *145*, 104855. [CrossRef]
5. Li, D.; Li, Y.; Zhu, W. Analytical modelling of load-displacement performance of cable bolts incorporating cracking propagation. *Rock Mech. Rock Eng.* **2020**, *53*, 3471–3483. [CrossRef]
6. Sun, Y.; Li, G.; Zhang, J.; Qian, D. Stability control for the rheological roadway by a novel high-efficiency jet grouting technique in deep underground coal mines. *Sustainability* **2019**, *11*, 6494. [CrossRef]
7. Li, Z.; Yan, S.; Liu, L.; Yang, J. Investigation into creep characteristics and model of recycled construction and demolition waste used in Embankment Filler. *Sustainability* **2020**, *12*, 1924. [CrossRef]
8. Bérest, P.; Gharbi, H.; Brouard, B.; Brückner, D.; DeVries, K.; Hévin, G.; Hofer, G.; Spiers, C.; Urai, J. Very slow creep tests on salt samples. *Rock Mech. Rock Eng.* **2019**, *52*, 2917–2934. [CrossRef]
9. Hou, R.; Zhang, K.; Tao, J.; Xue, X.; Chen, Y. A nonlinear creep damage coupled model for rock considering the effect of initial damage. *Rock Mech. Rock Eng.* **2019**, *52*, 1275–1285. [CrossRef]
10. Mansouri, H.; Ajalloeian, R. Mechanical behavior of salt rock under uniaxial compression and creep tests. *Int. J. Rock Mech. Min.* **2018**, *110*, 19–27. [CrossRef]
11. Yang, C.; Daemen, J.J.K.; Yin, J. Experimental investigation of creep behavior of salt rock. *Int. J. Rock Mech. Min.* **1999**, *36*, 233–242. [CrossRef]
12. Maranini, E.; Brignoli, M. Creep behaviour of a weak rock: Experimental characterization. *Int. J. Rock Mech. Min.* **1999**, *36*, 127–138. [CrossRef]
13. Fujii, Y.; Ishijima, Y.; Ichihara, Y.; Kiyama, T.; Kumakura, S.; Takada, M.; Sugawara, T.; Narita, T.; Kodama, J.; Sawada, M.; et al. Mechanical properties of abandoned and closed roadways in the Kushiro Coal Mine, Japan. *Int. J. Rock Mech. Min.* **2011**, *48*, 585–596. [CrossRef]
14. Wang, X.; Xia, C.; Zhu, Z.; Xie, W.; Song, L.; Han, G. Long-term creep law and constitutive model of extremely soft coal rock subjected to single-stage load. *Rock Soil Mech.* **2021**, *42*, 2078–2088. [CrossRef]
15. Xu, W.; Yang, S.; Yang, S.; Xie, S.; Shao, J.; Wang, Y. Investigation on triaxial rheological mechanical properties of greenschist specimen (I): Experimental results. *Rock Soil Mech.* **2005**, *26*, 531–537. [CrossRef]
16. Yang, W.; Zhang, Q.; Li, S.; Wang, S. Time-dependent behavior of diabase and a nonlinear creep model. *Rock Mech. Rock Eng.* **2014**, *47*, 1211–1224. [CrossRef]
17. Jiang, Y.; Zhang, M.; Li, L. Study on nolinear viscoelasto-plastic creep model of rock and its parameter identification. *Chin. J. Rock Mech. Eng.* **2008**, *27*, 832–839. [CrossRef]
18. Hu, B.; Yang, S.; Xu, P. A nonlinear rheological damage model of hard rock. *J. Cent. South Univ.* **2018**, *25*, 1665–1677. [CrossRef]
19. Ma, L.J.; Liu, X.Y.; Fang, Q.; Xu, H. A new elasto-viscoplastic damage model combined with the generalized Hoek-Brown failure criterion for bedded rock salt and its application. *Rock Mech. Rock Eng.* **2013**, *46*, 53–66. [CrossRef]
20. Zhao, Y.; Wang, Y.; Wang, W.; Wan, W.; Tang, J. Modeling of non-linear rheological behavior of hard rock using triaxial rheological experiment. *Int. J. Rock Mech. Min.* **2017**, *93*, 66–75. [CrossRef]

21. Xu, P.; Yang, S. Study of visco-elasto-plastic constitutive model of coal under cyclic loading. *Chin. J. Rock Mech. Eng.* **2015**, 537–545. [CrossRef]
22. Fan, J.; Jiang, D.; Liu, W.; Wu, F.; Chen, J.; Daemen, J.J.K. Discontinuous fatigue of salt rock with low-stress intervals. *Int. J. Rock Mech. Min.* **2019**, *115*, 77–86. [CrossRef]
23. Yu, T.Q.; Wang, X.W.; Liu, Z.H. *Elasticity and Plasticity*; China Architecture and Building Press: Beijing, China, 2004; pp. 170–173.
24. Xia, C.C.; Zhong, S.Y. Experimental data processing method in consideration of influence of loading history on rock specimen deformation. *J. Cent. South Univ. Sci. Technol.* **1989**, *20*, 18–24.
25. Nomikos, P.; Rahmannejad, R.; Sofianos, A. Supported axisymmetric tunnels within linear viscoelastic Burgers rocks. *Rock Mech. Rock Eng.* **2011**, *44*, 553–564. [CrossRef]
26. Sterpi, D.; Gioda, G. Visco-plastic behaviour around advancing tunnels in squeezing rock. *Rock Mech. Rock Eng.* **2009**, *42*, 319–339. [CrossRef]
27. Aydan, O.; Ito, T.; Oezbay, U.; Kwasniewski, M.; Shariar, K.; Okuno, T.; Ozgenoglu, A.; Malan, D.F.; Okada, T. ISRM suggested methods for determining the creep characteristics of rock. *Rock Mech. Rock Eng.* **2014**, *47*, 275–290. [CrossRef]
28. Cai, M.; He, M.; Liu, D. *Rock Mechanics and Engineering*; Science Press: Beijing, China, 2012; 121p.
29. Xie, H.; Ju, Y.; Li, L.; Peng, R. Energy mechanism of deformation and failure of rock mass. *Chin. J. Rock Mech. Eng.* **2008**, *27*, 1729–1740. [CrossRef]

sustainability

MDPI

Article

The Stability of Roadway Groups under Rheology Coupling Mining Disturbance

Sen Yang [1,2], Guichen Li [1,2,*], Ruiyang Bi [3], Bicheng Yao [1,2], Ruiguang Feng [1,2] and Yuantian Sun [1,2]

[1] School of Mines, China University of Mining and Technology, Xuzhou 221116, China; ts20020064a31tm@cumt.edu.cn (S.Y.); ts20020178p21@cumt.edu.cn (B.Y.); ts20020100p21@cumt.edu.cn (R.F.); yuantiansun@cumt.edu.cn (Y.S.)
[2] Key Laboratory of Deep Coal Resource Mining of the Ministry of Education, University of Mining and Technology, Xuzhou 221116, China
[3] School of Resources and Safety Engineering, Central South University, Changsha 410083, China; biruiyang@csu.edu.cn
* Correspondence: liguichen@cumt.edu.cn; Tel.: +86-1580-521-5566

Abstract: The deep roadway groups play an important role in transportation and ventilation in coal mine production. Therefore, it is very important to comprehensively analyze the coupling effect of rheological deformation and coal mining on the stability of the roadway groups. In this paper, the disturbance effects of different stop-mining lines on roadway groups under long-term rheology were investigated by numerical simulation, and the failure mechanism of roadway groups with large sections and multiple disturbances in a deep well was revealed. The results show that the long working face will lead to the collapse of key strata, and the influence range will spread to the adjacent roadway groups. When the distance between the working face and the stop-mining line is 100 m, the roadway groups cannot be affected by the working face mining, and the reserved width of the coal pillar can be determined to be 100 m, which increases the stability of the roadway's surrounding rock and maintains the mine safety production. This paper aims to provide a reference for groups design and control under similar conditions.

Keywords: rheological deformation; key stratum; roadway groups; roadway deformation; surrounding rock control

Citation: Yang, S.; Li, G.; Bi, R.; Yao, B.; Feng, R.; Sun, Y. The Stability of Roadway Groups under Rheology Coupling Mining Disturbance. *Sustainability* **2021**, *13*, 12300. https://doi.org/10.3390/su132112300

Academic Editor: Giovanna Pappalardo

Received: 2 October 2021
Accepted: 3 November 2021
Published: 8 November 2021

Publisher's Note: MDPI stays neutral with regard to jurisdictional claims in published maps and institutional affiliations.

Copyright: © 2021 by the authors. Licensee MDPI, Basel, Switzerland. This article is an open access article distributed under the terms and conditions of the Creative Commons Attribution (CC BY) license (https://creativecommons.org/licenses/by/4.0/).

1. Introduction

In recent years, with the continuous increase in mining intensity and depth, a large number of difficult-to-support roadways have appeared, such as roadways with high stress, strong mining-affected roadways, roadways with extremely broken surrounding rocks, and roadways with extra-large cross-sections. Under the influence of factors such as tectonic stress, strong mining, faults, etc., roadway section shrinkage is serious, surrounding rock fragmentation is high, the floor experiences heave, and supporting components fail frequently, which increases the intensity and frequency of roadway repair [1]. Therefore, the stability of the deep roadway groups is essential for safe and efficient production.

For deep roadways, the ground stress of the environment in which the roadway is located increases. Under the action of high ground stress, rheological deformation occurs in the deep roadway [2,3]. The deformation of the deep soft rock roadway includes the deformation during the roadway excavation, the rheological deformation of the roadway during the service production period, and the deformation caused by other factors such as support failure and stress disturbance. The theory and technology of group control, originally applicable to shallow parts, cannot meet the requirements of the control effect in the deep part [4]. For the control of coal roadways with rheological properties, the theory and technology of soft rock support can be used for reference [5–9]. For soft rock roadways, many deep soft rock roadway control technologies have been produced on the basis of

clarifying the damage influence range of surrounding rock, such as the combined support technology of high prestressed bolt primary support and cable reinforcement, bolt-grouting combined support technology, and high-efficiency jet grouting (JG) techniques, etc. [10–18]. In the middle and late 20th century, Austrian engineers put forward the basic theory of deep roadway surrounding rock control; a new Austrian tunnelling method based on predecessors. Previous researchers [19–21] have conducted exploratory research on the advanced support technology of rheological roadways, and have achieved fruitful results. The shape of the underground roadway is irregular, and the positional relationship of the roadway group is complicated, coupled with deep in-situ stress, which results in greater complexity. A large number of researchers chose to use numerical simulation combined with field cases to conduct research, and summarized the rheological deformation laws of different positions of the roadway, including the side part, roof and floor, and the obtained data from the roadway's surrounding rock deformation are closer to the actual field [22–25].

During deep mining, the appearance of rock pressure caused by rock movement has become increasingly serious. When mining coal seams, it will cause the redistribution of coal and rock mass stress and form a new mining stress field [26–28], which will affect roadway support and other projects. In the deep mine roadway, the main roadway with a long service life forms the roadway groups. These roadways are relatively close to each other, and the disturbance effect is large, which causes serious fragmentation and instability of the rock surrounding the roadway [29–31]. A number of researchers [32–35] have conducted exploratory research on the new technology of roadway deformation control and support, and made great progress. Aiming at the disturbance of mining to roadways, researchers have conducted a lot of work, analyzed the damage and movement law of the overburden structure of coal roadway under the influence of mining, and mastered the influence range after mining [36–39].

The deep mine roadway groups are continuously affected by the superposition of rheological deformation and coal and rock mining. At present, there are few research results of a comprehensive analysis of mining and rheology on roadway stability. Because of this situation, this paper intends to comprehensively explore its impact on roadway stability from the two dimensions of mining and rheology, to increase the stability of roadway surrounding rock and maintain mine safety production.

2. Project Overview

Jining No. 2 Coal Mine is located in Jining City, China. The coal seam mined belongs to Jining Coal Field, with an area of approximately 87.1 square kilometers. Its geographic location is shown in Figure 1.

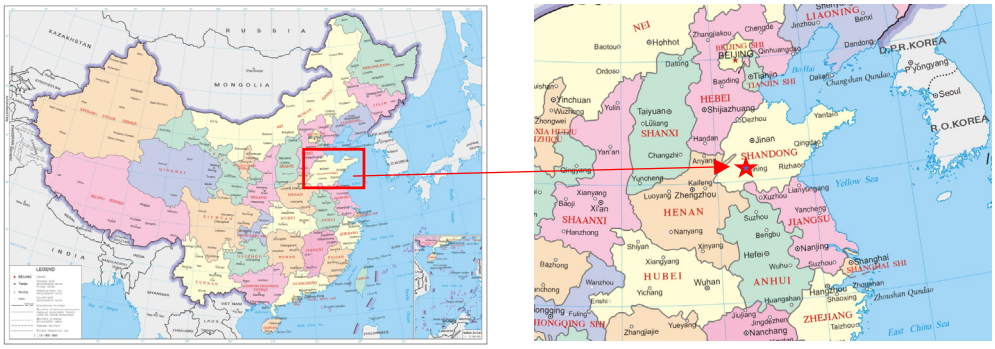

Figure 1. Geographical location map of Jining No. 2 Coal Mine.

The three lower coal seams were mined at the 11th district of the No. 2 Mine of Yankuang Groups, with a coal thickness of 3.6 to 4.8 m, with an average of 4.13 m. The direct roof is medium sandstone with a thickness of 7.6~9.95 m and an average thickness of 8.78 m. The main roof is siltstone with a thickness of 6.1~9.2 m and an average thickness of 7.65 m. The floor is mudstone with a thickness of 1.5–3.0 m and an average thickness of

2.2 m. The generalized stratigraphic column and the character description of Jining No. 2 Coal Mine is shown in Figure 2.

Thickness /m	Columnar	Lithology	Buried depth /m	Description
3.24~5.3 / 4.27		Fine-grained sandstone	742.69	Grayish white, mainly composed of quartz and feldspar, with horizontal bedding.
6.3~7.2 / 6.75		Medium sandstone	749.44	Grayish white, mainly composed of quartz and feldspar, with hard lithology.
6.1~9.2 / 7.65		Siltstone	757.09	Dark gray, massive, with well-developed fissures.
7.6~9.95 / 8.78		Medium sandstone	765.87	Grayish white, mainly composed of quartz and feldspar, with hard lithology.
3.6~4.8 / 4.13		Coal	770.0	Black, mainly bright coal, partially containing 0.2m gangue.
1.5~3.0 / 2.2		Mudstone	772.2	Gray-black, with plant root fossils, with swelling properties.
4.1~6.3 / 5.5		Siltstone	777.7	Grayish white, mainly composed of quartz and feldspar, with horizontal bedding.
3.3~9.0 / 6.2		Fine-grained sandstone	783.9	Grayish white, mainly composed of quartz and feldspar, with horizontal bedding.
9.7~15.2 / 13.1		Fine siltstone	797.0	Gray-black, with a small amount of pyrite particles, with slightly developed cracks.

Figure 2. Generalized stratigraphic column.

2.1. Position Relationship between Working Face and Roadway

Figure 3 shows the distribution of four main roadways and working faces at −740 levels in the south wing of Jining No. 2 Coal Mine of Yankuang Groups. The elevation of the track roadway is −740 m, the elevation of the ventilation roadway is −732 m, the elevation of the belt conveyor roadway is −738 m, and the elevation of the auxiliary transport roadway is −738 m. The horizontal distance between the track roadway and the ventilation roadway is 30 m, the horizontal distance between the ventilation roadway and the belt conveyor roadway is 30 m, and the horizontal distance between the belt conveyor roadway and the auxiliary transport roadway is 50 m. The track roadway, belt conveyor roadway, and auxiliary transport roadway are all excavated in the rock, and the ventilation roadway is in the coal seam.

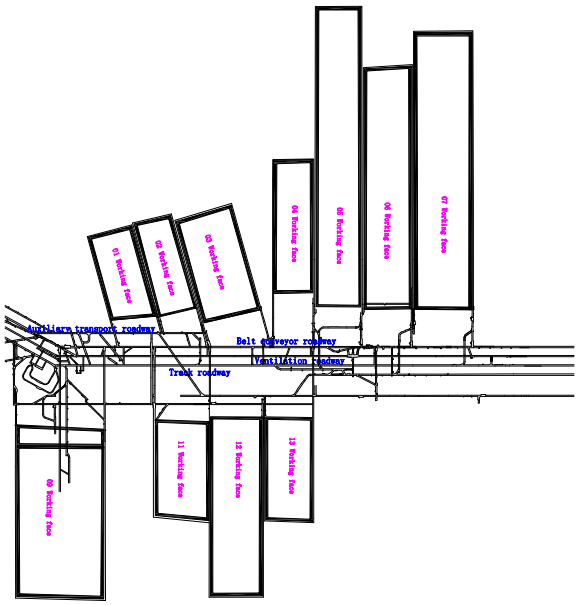

Figure 3. Roadway location distribution map.

2.2. The Influence of Working Face Rheological Coupling Mining on Roadway Stability

The mining level where the roadway is located has a large buried depth and high stress The vertical ground stress of the −740 m roadway reaches 19.45 MPa (the ground elevation is +38 m), which is a deep-well high-stress roadway. After the excavation of the roadway is completed, under the action of high ground stress, the surrounding rock stress is continuously adjusted over time, and the roadway undergoes rheological deformation, which causes the roadway to gain instable characteristics, such as bolt failure, roof subsidence, and floor heave.

The thickness of the coal seam in the mining area is as high as 5~6 m. When the working face is close to the main roadway, the stress area is large. The average horizontal distance between the four main roadways at the −740 m level is 30 m, and the stopping line is only about 40 m away from the nearest roadway. Therefore, the main roadway is affected by multiple strong mining operations, which makes it difficult to control the surrounding rock of the roadway.

There are four main roadways with large deformations and a large roadway span, averaging more than 4.5 m. The length of the supporting bolt adopted is only 2.4 m, and the effective length is 2.3 m. Theoretically, it cannot form an effective supporting structure, and it is difficult to reflect the effect of active support. The roof spray strata cracked severely, floor heave was serious, there was a roof fall phenomenon, the falling height was 3 m, and the length was 6.7 m. Recently, roadway's surrounding rock deformation is serious, roadway maintenance workload is large, and safety guarantee is low. The partial destruction of the roadway is shown in Figure 4.

(**a**) (**b**) (**c**)

Figure 4. Damage of roadway. (**a**) Anchor failure, (**b**) Roof subsidence, (**c**) Floor heave.

Several drill boreholes were drilled in the belt conveyor roadway, the track roadway, the ventilation roadway, and the auxiliary transportation roadway, respectively, for monitoring. The roadway groups facing the 01 and 10 working faces are used as test sections. In specific steps, three boreholes are set up in each of the four main roadways, each with an interval of 50 m, and the drilling positions are located in the middle of the roof of the roadway and on both shoulders. The hole diameter is 32 mm and the depth is 10 m. Among them, the monitoring drill view of the track roadway is shown in Figure 5. The mudstone is severely broken in the deep part of the borehole, is moderately broken in the coal seam, and the surrounding rock is intact in the middle sandstone part.

(**a**)

(**b**) (**c**)

Figure 5. Peeking observation results of the roadway boreholes.(**a**) Mudstone, badly fractured, (**b**) Coal seam, medium crushing, (**c**) Medium sandstone, complete surrounding rock.

3. Establishment of a Numerical Simulation Model for Disturbance Effect of Roadway Groups in a Deep Well

Through on-site measurements and theoretical analysis, the cause of the instability of the surrounding rock in the −740 m horizontal roadway groups in Jining No. 2 Mine is obtained. Further, through the combination of theoretical analysis and numerical simulation, the instability mechanism of the roadway groups is revealed. Using Flac3D finite element numerical simulation software, by simulating the distance from different stop-mining lines to the roadway groups, the optimal stop-mining line position is determined. The supporting system of the surrounding rock under the influence of deep roadway groups disturbance is obtained.

3.1. Numerical Simulation Modeling Process

Taking the −740 m horizontal roadway groups in the south wing of Jining No. 2 Mine as the research object, the 100–200 m roadway is taken as the test section within the roadway range of the 01 and 10 working faces. The CVISC rheological model is adopted for the roadway [40,41]. The model works by simulating the mutual influence law of the full excavation of the roadway, and the influence of the two wings' working faces on the test section roadway during the mining process. It then analyzes the damage of the roadway and provides a theoretical basis for later determining the roadway support parameters. Moreover, it guides the determination of the stop-mining line at the working face. The model has a length of 529.4 m, a height of 140 m, and a width of 30 m. It contains a total of 9 rock strata. A load of 17.5 MPa is applied to the top of the model to simulate the pressure of the overburden. Boundary conditions are imposed on the model, and the left and right horizontal displacement of the model is limited to within ±0.1 m, and the bottom vertical displacement is limited to within ±0.1 m. The simplified boundary model is shown in Figure 6. The track roadway is arched with a width of 5.0 m and a clear height of 4.0 m. The belt conveyor roadway is arched with a width of 5.0 m and a clear height of 4.8 m. The ventilation roadway is rectangular, with a width of 4.6 m and a clear height of 3.3 m. The

auxiliary transportation roadway is rectangular, with a width of 4.8 m and a clear height of 3.2 m. Since the inclination angle of the coal seam is only 2°~10°, with an average of 5°, it is a nearly horizontal coal seam, and the test section roadway is only 100~200 m. Within this range, coal seams and rock strata can be regarded as horizontal rock strata. The rock mechanics parameters are shown in Table 1. Rheological parameters are shown in Table 2.

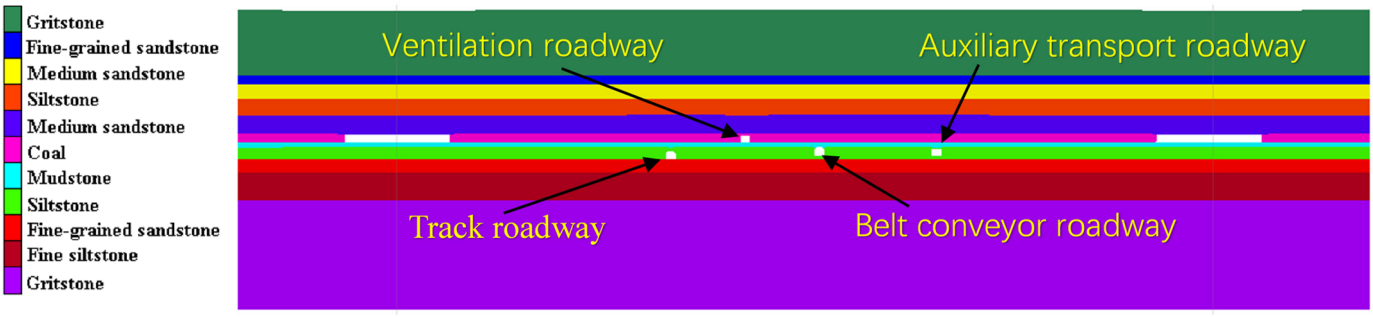

Figure 6. Model diagram.

Table 1. Physical and mechanical parameters of rock and coal in numerical simulations.

Lithology	Density kg/m^3	Bulk Modulus/GPa	Shear Modulus/GPa	Cohesion/MPa	Friction Angle/°	Tensile Strength/MPa
Gritstone	2450	34.37	24.71	9.81	45	10.51
Fine grained sandstone	2600	21.7	15.6	5.72	38	7.44
Medium sandstone	2550	30.14	21.67	7.30	41	8.21
Siltstone	2650	17.47	12.56	4.12	32	2.94
Coal	1450	0.55	0.33	2.45	22	0.24
Mudstone	2250	7.11	3.86	3.43	35	0.98
Fine siltstone	2620	19.00	14.08	4.92	34	5.19

Table 2. Parameters of the rheological model in numerical simulation.

G_K/Pa	G_M/Pa	N_K/Pa.s	N_M/Pa.s
1.38×10^8	2.2×10^8	2×10^{18}	15×10^{15}

3.2. Numerical Simulation Scheme

After the model stress is balanced, the four main roadways are first driven. In the process of excavating a group of roadways (distance 30~50 m), the stress redistributes after the roadway is excavated, and there is a mutual influence between the roadways. The mutual disturbance between the roadways increases the difficulty of controlling the surrounding rock of the roadways. By observing and analyzing the stress distribution, displacement distribution, and plastic zone distribution of the surrounding rock of the roadway after 2 years of rheological deformation, it can be judged whether there is a mutual disturbance in the roadway groups.

During the advancing process of the working face in the test section, it is affected by the disturbance of the 01 and 10 working faces, which belong to the multi-disturbed roadway. The study of the influence of the working face on the surrounding rock of the roadway during the mining process is of great significance to determine the stop line position. According to the actual situation, there should be a wait for the roadway rheology for two years before simulating the mining process of the working face. The simulation analyzes the distribution law of the stress field, displacement field, and plastic zone within the model range under the three scenarios of the stopping mining line of 50 m, 75 m, and 100 m, to obtain the best stopping line position through simulation.

4. Results and Discussion on Coupling Disturbance of Rheology and Mining in Deep Mine Roadway Groups

4.1. Influence of Rheological Disturbance during Roadway Excavation

In this section, by observing and analyzing the stress distribution, displacement distribution, and plastic zone distribution of the surrounding rock of the roadway after 2 years of rheological deformation, it can be judged whether there is a mutual disturbance in the roadway groups.

The vertical stress distribution of the surrounding rock in the roadway groups after 2 years of rheology is shown in Figure 7. It can be seen from the figure that for the four main roadways at the level of −740 m in the south wing, there is a slight difference between the track roadway, the ventilation roadway, and the belt conveyor roadway. There is no mutual disturbance between the belt conveyor roadway and the auxiliary transport roadway.

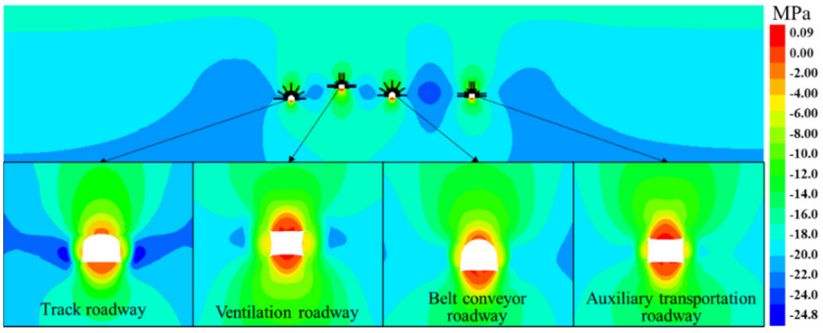

Figure 7. Vertical stress distribution of surrounding rock of roadway groups.

The surrounding rock displacement of the roadway groups after 2 years of rheological deformation is shown in Figure 8. It can be seen from the figure that after the roadway group is mined, the maximum deformation of the surrounding rock of the roadway is about 430 mm under the conditions of the design support parameters. Under this condition, the expansion of brush repair can realize the control of the deformation of the surrounding rock of the roadway.

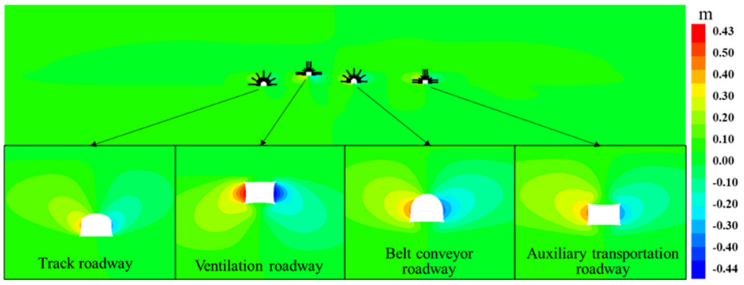

(**a**)

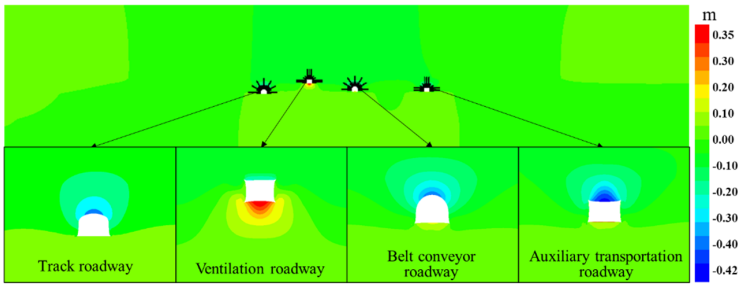

(**b**)

Figure 8. Displacement cloud map of surrounding rock behind the excavation roadway groups. (**a**) Deformation of the two sides of the roadway, (**b**) Deformation of roof and floor of roadway.

The plastic zone distribution of the surrounding rock of the roadway after 2 years of rheological deformation is shown in Figure 9. It can be seen from the figure that after 2 years of rheological deformation after roadway excavation, the surrounding rock of the roadway has plastic deformation under the condition of stress concentration. For the deep roadway groups, the surrounding rock of the roadway has a different distribution of plastic zone under different rock strata conditions. Among them, the plastic zone of the roof and floor of the auxiliary transportation roadway is larger. Among them, the roof and floor of the ventilation roadway have a larger plastic zone. The depth of the floor plastic zone is about 4.2 m, and the plastic failure range is large, which is difficult for roadway control. In the subsequent roadway treatment process, it is necessary to ensure the quality of the roadway roof support and ensure the stability of the surrounding rock's roof. For the four roadways studied, the failure range of the roof and floor plastic zone is about 2–4.2 m.

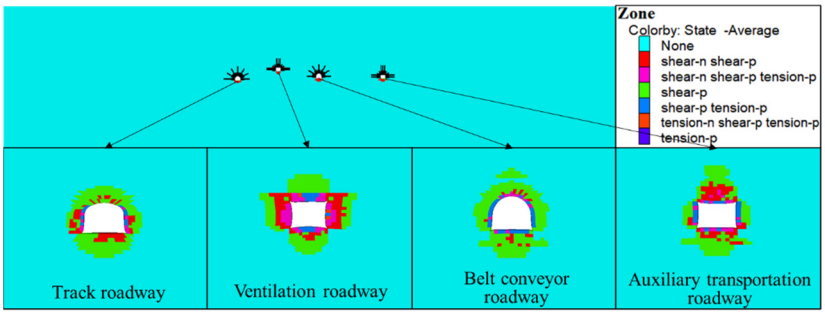

Figure 9. Distribution of plastic zone after roadway groups excavation.

4.2. The Influence of Rheological Coupling Mining of Working Face on Stress Disturbance of Roadway Groups

A total of two years after the roadway was rheologically deformed, coal mining began at the working face. The vertical stress distribution of the surrounding rock of the model is shown in Figure 10. It can be seen from the figure that mining has disturbance effects on the four main roadways. When the distance between the working face and the roadway is 50 m, the disturbance effect of the track roadway and auxiliary transport roadway is the most severe. When the distance between the working face and the roadway is 75 m, the impact of the mining on the disturbance of the track roadway and auxiliary transport roadway is reduced. When the distance between the working face and the roadway is 100 m, the impact of the mining on the roadway groups disturbance is minimal.

When the distance between the working face and the roadway is 50 m, 75 m, and 100 m, the maximum vertical stress of the surrounding rock of the roadway is shown in Figure 11. After the excavation of the roadway groups, the maximum vertical stress on the left and right sides of the track roadway is 24.2 MPa, and the maximum vertical stress on the two sides of the auxiliary transport roadway is 20.6 MPa and 22.1 MPa, respectively. After the coal seam is mined, the maximum vertical stress on both sides of the roadway is increased. When the distance of the stopping line increases from 50 m to 100 m, the maximum vertical stress of the two sides of the track roadway and auxiliary transport roadway decreases gradually. When the distance between the stopping line and the roadway is 100 m, the change rate of the maximum vertical stress is the smallest.

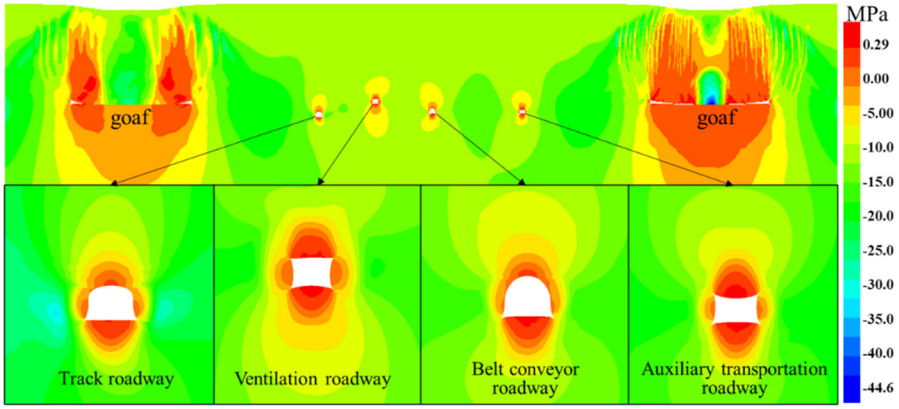

(**a**)

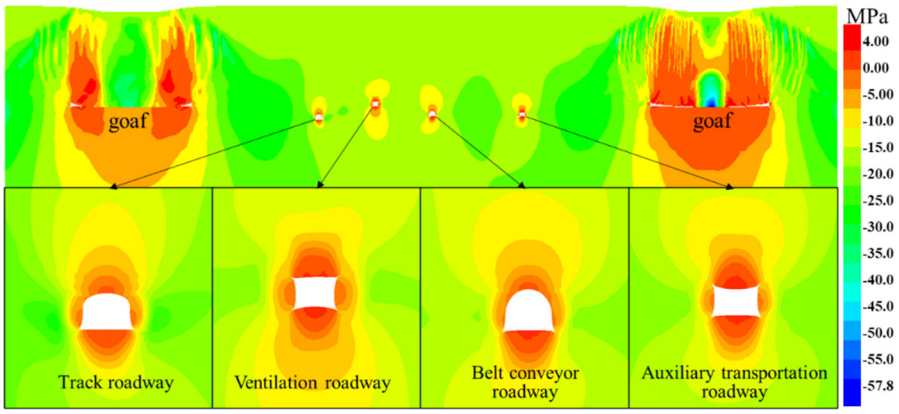

(**b**)

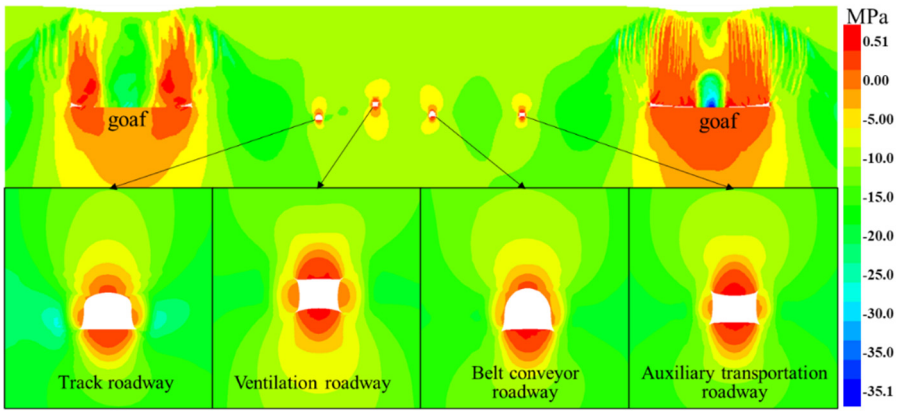

(**c**)

Figure 10. Vertical stress distribution of the different distances between working face and roadway. (**a**) The stop line is 50 m away from the roadway. (**b**) The stop line is 75 m away from the roadway. (**c**) The stop line is 100 m away from the roadway.

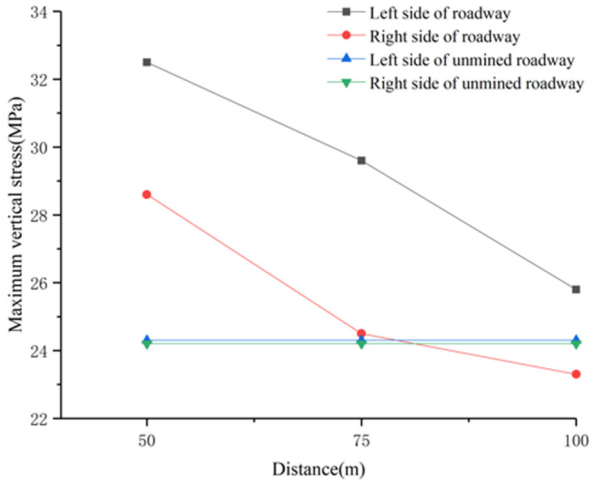

(**a**)

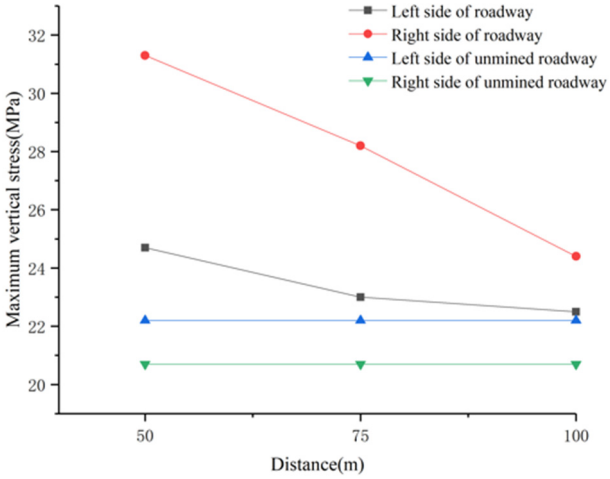

(**b**)

Figure 11. Maximum vertical stress at different distances between working face and roadway. (**a**) Maximum vertical stress at different locations from the track roadway. (**b**) Maximum vertical stress at different locations from the auxiliary transport roadway.

4.3. The Influence of Working Face Rheological Coupling Mining on Deformation Disturbance of Roadway Groups

The horizontal displacement distribution of the surrounding rock of the model roadway is shown in Figure 12, and the deformation of the two sides of the roadway changes with the rheological time, as shown in Figure 13. It can be seen from Figures 12 and 13 that the deformation of the two sides of the roadway groups increases with the increase in the rheological time. Within 0.2 years after the excavation of the roadway groups, the deformation first increased rapidly, and then tended to a stable rheological state. After the mining of the working face is completed, depending on the distance of the stop line, the roadway groups will be affected by different degrees of disturbance and rheology within a certain period, and they tend to a stable rheological state.

In the coal mining process of the working face, the track roadway and the auxiliary transport roadway are the closest to the working face, and they are also most affected by disturbance and rheology. When the mining stop line is 50 m and 75 m, respectively, within 0.6 years after the mining of the working face, the track roadway and the auxiliary transport roadway will have accelerated rheology. The horizontal displacement of the

roadway groups is rapidly increased by the impact of mining, and by when it reaches a stable rheological state.

When the stop line is 100 m, the mining face has almost no effect on the roadway groups, and the roadway is always in a stable rheological state. When the mining stop line is 50 m, the maximum deformation of the track main roadway is 1.22 m, and the maximum deformation of the auxiliary transportation main roadway is 1.49 m. When the mining stop line is 100 m, the maximum deformation of the track main roadway is 0.98 m, and the auxiliary transportation main roadway The maximum deformation is 1.26 m.

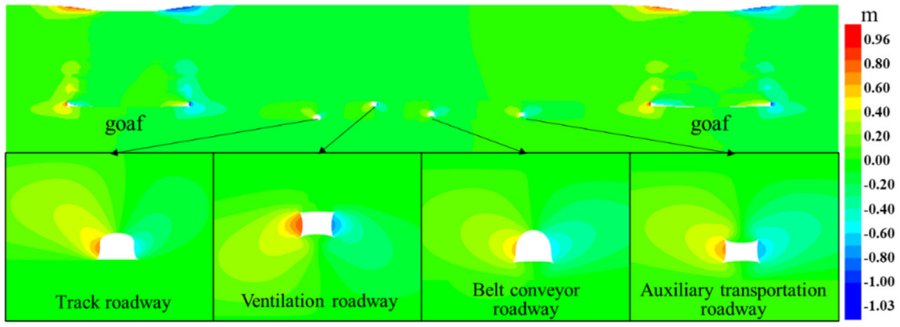

(**a**)

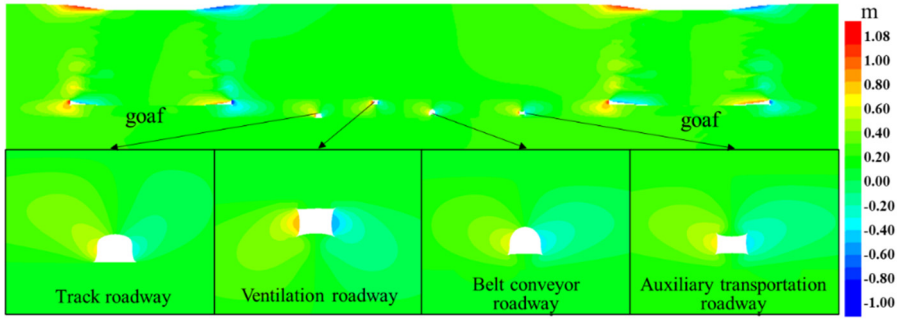

(**b**)

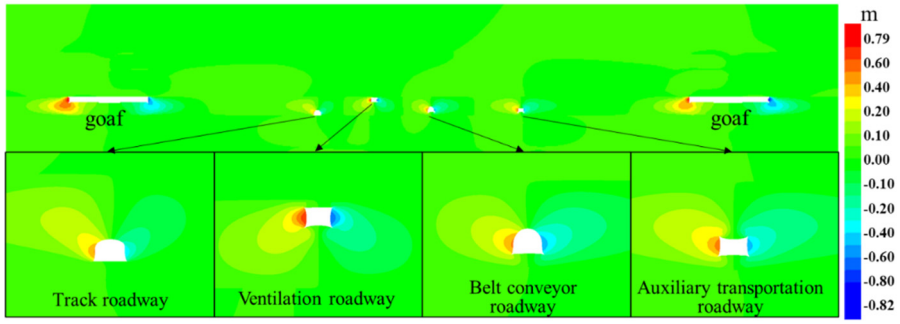

(**c**)

Figure 12. Cloud map of horizontal displacement distribution. (**a**) The stop line is 50 m away from the roadway. (**b**) The stop line is 75 m away from the roadway. (**c**) The stop line is 100 m away from the roadway.

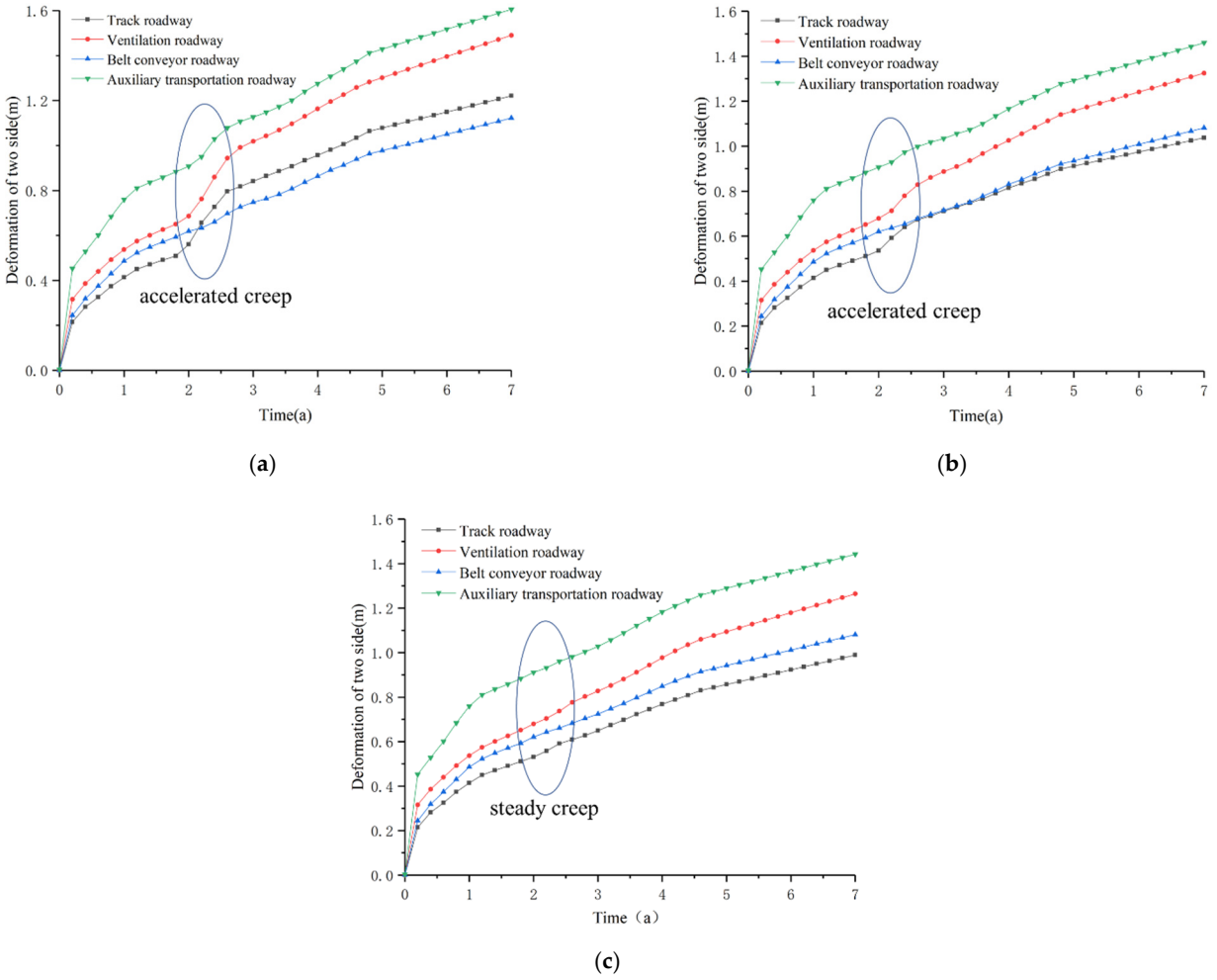

Figure 13. The deformation of the two sides of the roadway groups changed with the rheological time. (**a**) The stop line is 50 m away from the roadway. (**b**) The stop line is 75 m away from the roadway. (**c**) The stop line is 100 m away from the roadway.

The vertical displacement distribution of the surrounding rock of the model roadway is shown in Figure 14, and the deformation of the roof and floor of the roadway changes with the rheological time as shown in Figure 15. It can be seen from Figures 14 and 15 that the deformation trend of the roof and floor of the roadway is similar to that of the two gangs, and will not be repeated here.

When the mining stop line is 50 m and 75 m, the roadway groups have an obvious accelerated rheological phenomenon within 0.6 years after mining at the working face, and then it enters a stable rheological state; when the mining stop line is 100 m, the roadway is always stable rheological state. When the mining stop line is 50 m, the maximum deformation of the track roadway is 0.96 m, and the maximum deformation of the auxiliary transport roadway is 1.32 m. When the mining stop line is 100 m, the maximum deformation of the track roadway is 0.77 m, and the maximum deformation of the auxiliary transport roadway is 1.06 m.

From the above analysis, it can be seen that the stop line of 100 m is compared with the stop line of 50 m. When the stop line is 100 m, the maximum displacement of the two sides of the track roadway and the maximum displacement of the roof and floor are reduced by 20.0% and 18.8%, respectively. The maximum displacement of the two sides of the auxiliary transport roadway and the maximum displacement of the roof and floor decreased by 15.4% and 19.7%, respectively. Moreover, when the mining stop line is 100 m, the roadway deformation has been in a stable rheological state, which proves that the

roadway groups are not affected by mining. Therefore, the stop line of 100 m is beneficial to the long-term stability of the roadway.

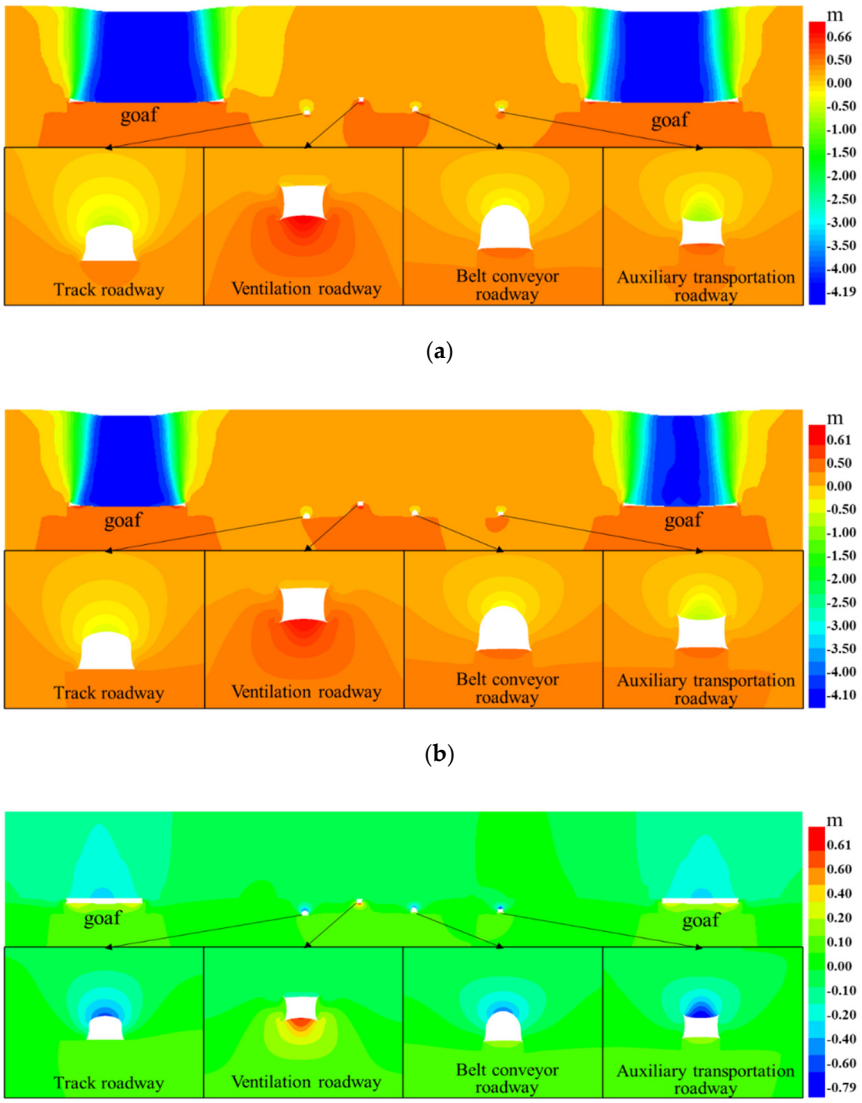

Figure 14. Cloud map of vertical displacement distribution. (**a**) The stop line is 50 m away from the roadway. (**b**) The stop line is 75 m away from the roadway. (**c**) The stop line is 100 m away from the roadway.

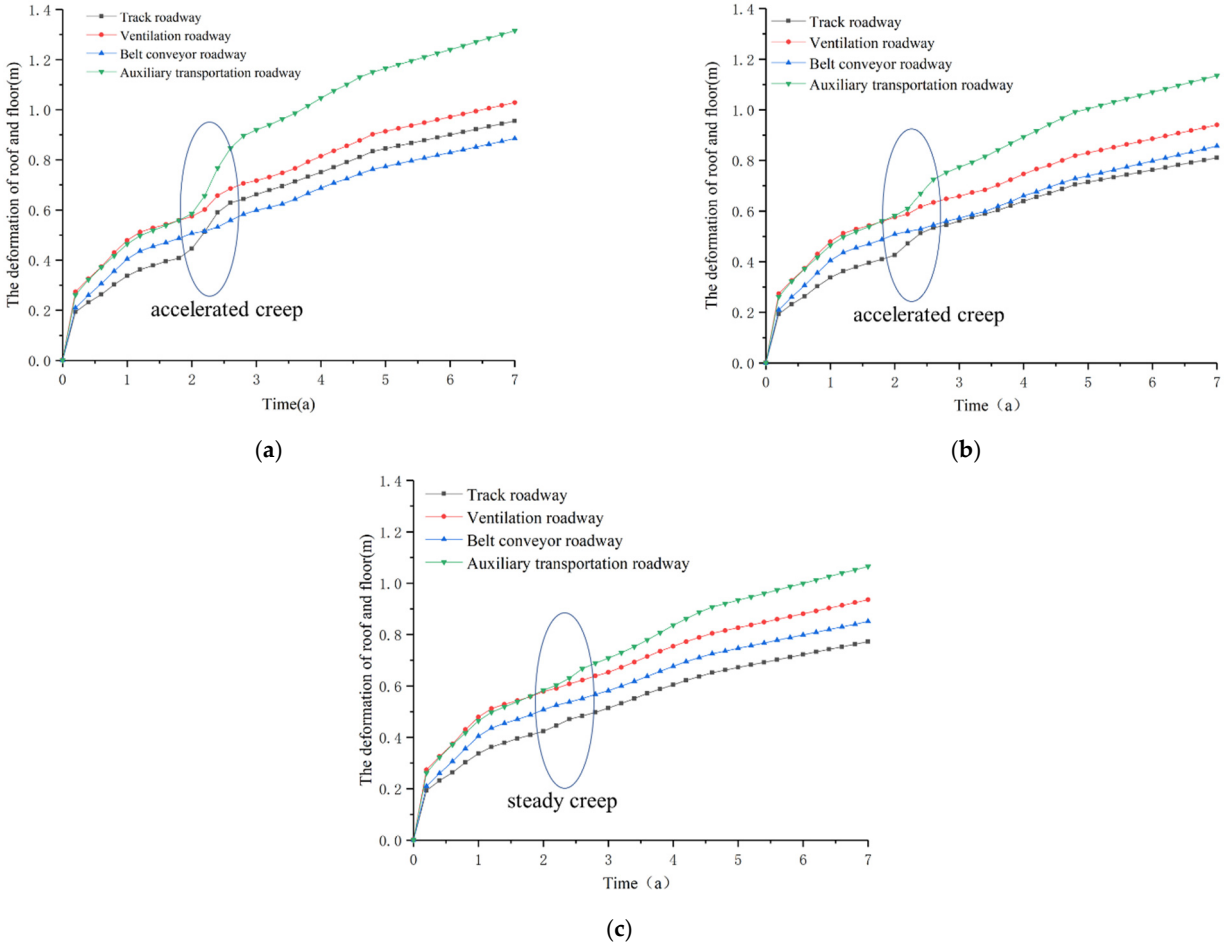

Figure 15. Variation of the roof and floor deformation of roadway groups with a rheological time. (**a**) The stop line is 50 m away from the roadway. (**b**) The stop line is 75 m away from the roadway. (**c**) The stop line is 100 m away from the roadway.

4.4. The Influence of Rheological Coupling Mining of Working Face on Disturbance of Plastic Zone of Roadway Groups

The plastic zone distribution of the surrounding rock of the model roadway is shown in Figure 16. Tables 3 and 4 show the expansion depth of the plastic zone of the roof and floor of the roadway and the two sides of the roadway under the conditions of different mining stop lines. It can be seen that after 5 years of rheological deformation of the roadway groups, the plastic areas of the four main roadways under different stop-line conditions have become larger than that when they were not mined. When the mining stop line is 50 m, the plastic zone change of the four main roadways is the largest. When the stop line is 75 m, the plastic area of the return airway and belt roadway will be less affected by the mining, while the plastic area of the track and auxiliary transportation roadway will change greatly.

When the mining stop line is 50 m, the depth of the plastic zone has been expanded under the influence of long-term rheological deformation and mining. Compared with the time when the working face is not mined, the total expansion depth of the plastic zone of the roadway groups at this time has increased by 8.6%. When the mining stop line is 100 m, the disturbance to the roadway groups is very small, and the total expansion depth of the plastic zone of the roadway groups only increases by 3.5% compared with the case of no mining, and the roadway groups are hardly affected by mining.

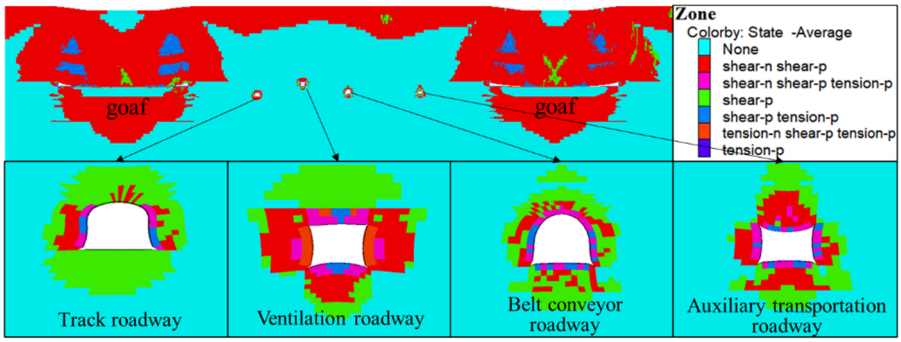

(**a**)

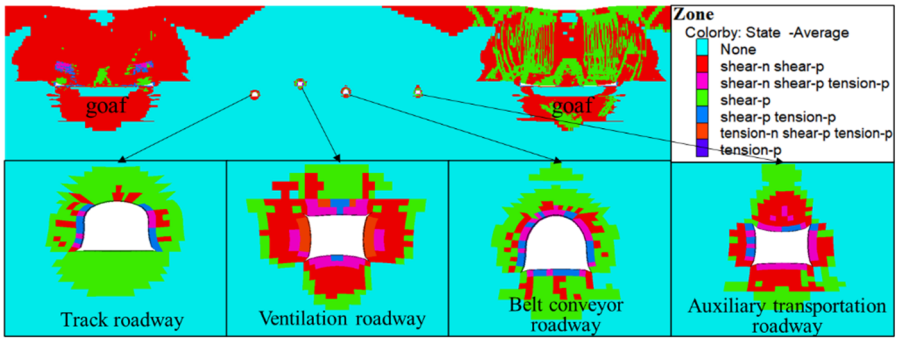

(**b**)

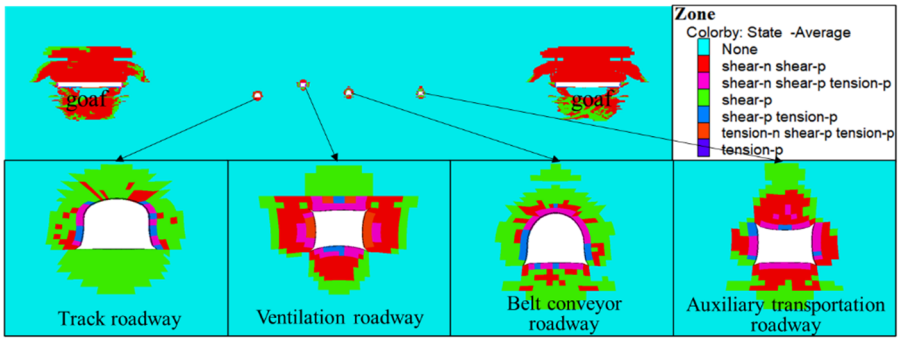

(**c**)

Figure 16. Distribution of plastic zone in the roadway. (**a**) The stop line is 50 m away from the roadway. (**b**) The stop line is 75 m away from the roadway. (**c**) The stop line is 100 m away from the roadway.

Table 3. The expansion depth of the roof and floor plastic zone.

	Expansion Depth			
Distance from Stoping Line /m	**Track Roadway**	**Ventilation Roadway**	**Belt Conveyor Roadway**	**Auxiliary Transportation Roadway**
Unmined	4524	6026	6149	7234
50	4718	6282	6391	7760
75	4670	6211	6366	7569
100	4655	6209	6373	7390

Table 4. The expansion depth of the plastic zone of both sides.

	Expansion Depth			
Distance from Stoping Line /m	**Track Roadway**	**Ventilation Roadway**	**Belt Conveyor Roadway**	**Auxiliary Transportation Roadway**
Unmined	3839	6294	4097	3239
50	4628	6345	4259	4578
75	4108	6337	4244	3410
100	4077	6336	4251	3392

In summary, when the stop line is 100 m, the mining face has little effect on the stress distribution, displacement distribution, and plastic zone of the surrounding rock of the roadway. The key layer theory and the theory of surface subsidence can be verified. When the width of the coal pillar exceeds the subsidence range of the rock layer, it will not affect the roadway. Therefore, it can be considered that leaving coal pillars of more than 100 m is beneficial to the stability control of the surrounding rock of the roadway.

5. Conclusions

In order to study the influence of rheological coupling mining disturbance on roadway stability, through numerical simulation, first the roadway has undergone two years of rheology, and secondly, the research on the influence of mining coupling rheology on the roadway is carried out. The rheological time is 5 years. The deformation and plastic zone conditions of the roadway when the working face is mined to the position of 50 m, 75 m and 100 m from the roadway group, respectively, are analyzed. The following conclusions can be drawn from the present study.

(1) After two years of rheological deformation of the excavation roadway groups, there is a slight mutual disturbance among the track roadway, ventilation roadway, and belt conveyor roadway; there is no mutual disturbance between the belt conveyor roadway and auxiliary transport roadway.

(2) After the coal seam is mined, the maximum vertical stress on both sides of the roadway is increased. In the process of increasing the stop line from 50 m to 100 m, the maximum vertical stress of the two sides of the track roadway and auxiliary transport roadway is gradually reduced. When the stop line is 100 m, the change rate of the maximum vertical stress is the smallest.

(3) Mining at the working face mainly has a disturbing effect on the track roadway and auxiliary transport roadway. As the distance from the mining stop line increases, the amount of surrounding rock deformation of the roadway groups gradually decreases. When the mining stop line is 100 m, mining has no obvious disturbing influence on the ventilation roadway and belt conveyor roadway, and the disturbance influence on the track roadway and auxiliary transport roadway is greatly reduced.

(4) The expansion depth of the plastic zone of the roadway groups decreases with the increase in the stop-mining line distance. When the stop-mining line distance is 100 m, the total expansion depth of the plastic zone of the roadway groups only increases by 3.5% compared with the case of no mining, and the roadway groups are hardly affected by mining.

Author Contributions: Conceptualization, S.Y., G.L. and R.B.; methodology, B.Y.; investigation, R.F.; writing—original draft preparation, S.Y. and G.L.; writing—review and editing, G.L., Y.S. and S.Y.; supervision, G.L.; funding acquisition, G.L. All authors have read and agreed to the published version of the manuscript.

Funding: This research was funded by the projects of "the Fundamental Research Funds for the Central Universities (2020ZDPY0221, 2021QN1003)", "National Natural Science Foundation of China (52104106, 52174089)", "Basic Research Program of Xuzhou (KC21017)".

Institutional Review Board Statement: Not applicable.

Informed Consent Statement: Not applicable.

Data Availability Statement: The Microsoft Excel Worksheet data used to support the findings of this study are available from the corresponding author upon request.

Acknowledgments: The authors are grateful to Jining No. 2 Coal Mine, Yanzhou Coal Minging Co. Ltd. Special thanks to the reviewers' comments and editor's work.

Conflicts of Interest: The authors declare no conflict of interest.

References

1. Wang, Q.; Gao, H.; Yu, H.; Jiang, B.; Liu, B. Method for Measuring Rock Mass Characteristics and Evaluating the Grouting-Reinforced Effect Based on Digital Drilling. *Rock Mech. Rock Eng.* **2018**, *52*, 841–851. [CrossRef]
2. Sun, Y.; Li, G.; Zhang, J.; Xu, J. Failure Mechanisms of Rheological Coal Roadway. *Sustainability* **2020**, *12*, 2885. [CrossRef]
3. Xiao, C.; Zheng, H.; Hou, X.; Zhang, X. A stability study of goaf based on mechanical properties degradation of rock caused by rheological and disturbing loads. *Int. J. Min. Sci. Technol.* **2015**, *25*, 741–747. [CrossRef]
4. Jia, J.; Yu, F.; Tan, Y.; Gao, X.; Zhang, H. Experimental Investigations on Rheological Properties of Mudstone in Kilometer-Deep Mine. *Adv. Civ. Eng.* **2021**, *2021*, 6615379. [CrossRef]
5. Qu, G.L.; Wang, J.; Liu, G.L. Research on Supporting Theory of Pressure-Bearing Ring and Yield Supporting Technology in Extremely Soft Rock Roadway. *Appl. Mech. Mater.* **2013**, *395*, 536–543. [CrossRef]
6. Lin, H. Study of Soft Rock Roadway Support Technique. *Procedia Eng.* **2011**, *26*, 321–326. [CrossRef]
7. Li, C.L.; Li, Z.Y. Geology Analysis and Support Scheme Design in Soft Rock Coal Mine. *Adv. Mater. Res.* **2012**, *446*, 1591–1595. [CrossRef]
8. Ma, N.J.; Zhao, Z.Q.; Zhao, H.; Jiang, L.S. High Strength Combined Support Technology in Deep High Stress Soft Rock Roadway. *Adv. Mater. Res.* **2012**, *524*, 598–603. [CrossRef]
9. Li, S.C.; Wang, H.T.; Wang, Q.; Jiang, B.; Wang, F.Q.; Guo, N.B.; Liu, W.J.; Ren, Y.X. Failure mechanism of bolting support and high-strength bolt-grouting technology for deep and soft surrounding rock with high stress. *J. Cent. South Univ.* **2016**, *23*, 440–448. [CrossRef]
10. Sun, Y.; Li, G.; Zhang, J.; Qian, D. Stability Control for the Rheological Roadway by a Novel High-Efficiency Jet Grouting Technique in Deep Underground Coal Mines. *Sustainability* **2019**, *11*, 6494. [CrossRef]
11. Chen, Y.; Meng, Q.; Xu, G.; Wu, H.; Zhang, G. Bolt-grouting combined support technology in deep soft rock roadway. *Int. J. Min. Sci. Technol.* **2016**, *26*, 777–785. [CrossRef]
12. He, M.C.; Yand, J.; Qi, G.; Wang, S.R. Optimized design and its application of coupling support for soft rock roadway at great depth. *J. Liaoning Tech. Univ.* **2007**, *1*, 40–42.
13. Li, J. The coal pillar design method for a deep mining roadway based on the shape of the plastic zone in surrounding rocks. *Arab. J. Geosci.* **2020**, *13*, 1–12. [CrossRef]
14. Yankai, R.C.L.K.Z. Study on Surrounding Rock Stability of Long-Span Coal Roadway under Influence of Mining and Support Technology Optimization. In Proceedings of the IOP Conference Series: Earth and Environmental Science, Hefei, China, 19–21 October 2018; p. 012016.
15. Zhai, C.; Xu, Y.; Xiang, X.; Yu, X.; Zou, Q.; Zhong, C. A novel active prevention technology for borehole instability under the influence of mining activities. *J. Nat. Gas Sci. Eng.* **2015**, *27*, 1585–1596. [CrossRef]
16. Zhan, Q.; Zheng, X.; Du, J.; Xiao, T. Coupling instability mechanism and joint control technology of soft-rock roadway with a buried depth of 1336 m. *Rock Mech. Rock Eng.* **2020**, *53*, 2233–2248. [CrossRef]
17. Li, G.; Sun, Y.; Zhang, J.; Zhang, Q.; Sun, C.; Zhang, S.; Bi, R. Experiment and application of coalcrete on roadway stability: A comparative analysis. *Adv. Mater. Sci. Eng.* **2020**, *2020*, 6813095. [CrossRef]
18. Sun, Y.; Li, G.; Zhang, J. Developing hybrid machine learning models for estimating the unconfined compressive strength of jet grouting composite: A comparative study. *Appl. Sci.* **2020**, *10*, 1612. [CrossRef]
19. Sun, Y.; Li, G.; Zhang, J. Investigation on jet grouting support strategy for controlling time-dependent deformation in the roadway. *Energy Sci. Eng.* **2020**, *8*, 2151–2158. [CrossRef]
20. Yu, W.; Pan, B.; Zhang, F.; Yao, S.; Liu, F. Deformation Characteristics and Determination of Optimum Supporting Time of Alteration Rock Mass in Deep Mine. *KSCE J. Civ. Eng.* **2019**, *23*, 4921–4932. [CrossRef]
21. Wu, K.; Shao, Z.; Qin, S.; Zhao, N.; Chu, Z. An improved non-linear creep model for rock applied to tunnel displacement prediction. *Int. J. Appl. Mech.* **2021**. [CrossRef]
22. Bondarenko, V.; Hardygora, M.; Symanovych, H.; Sotskov, V.; Snihur, V. Numerical methods of geomechanics tasks solution during coal deposits' development. *Min. Miner. Depos.* **2016**, *10*, 1–12. [CrossRef]
23. Pongpanya, P.; Sasaoka, T.; Shimada, H.; Hamanaka, A.; Wahyudi, S. Numerical study on effect of longwall mining on stability of main roadway under weak ground conditions in Indonesia. *J. Geol. Resour. Eng.* **2017**, *3*, 93–104.
24. Trigueros, E.; Cánovas, M.; Arzúa, J.; Alcaraz, M. Stability of an abandoned siderite mine: A case study in northern Spain. *Open Geosci.* **2021**, *13*, 359–376. [CrossRef]

25. Sun, Y.; Li, G.; Zhang, J.; Huang, J. Rockburst intensity evaluation by a novel systematic and evolved approach: Machine learning booster and application. *Bull. Eng. Geol. Environ.* **2021**, *80*, 8385–8395. [CrossRef]
26. Eremenko, V.A.; Galchenko, Y.P.; Kosyreva, M.A. Effect of Mining Geometry on Natural Stress Field in Underground Ore Mining with Conventional and Nature-Like Technologies. *J. Min. Sci.* **2020**, *56*, 416–425. [CrossRef]
27. Wen, Z.; Qu, G.; Wen, J.; Shi, Y.; Jia, C. Deformation failure characteristics of coal body and mining induced stress evolution law. *Sci. World J.* **2014**, *2014*, 714507. [CrossRef] [PubMed]
28. Wang, H.; Jiang, Y.; Xue, S.; Shen, B.; Wang, C.; Lv, J.; Yang, T. Assessment of excavation damaged zone around roadways under dynamic pressure induced by an active mining process. *Int. J. Rock Mech. Min. Sci.* **2015**, *77*, 265–277. [CrossRef]
29. Wang, H.; Shi, R.; Lu, C.; Jiang, Y.; Deng, D.; Zhang, D. Investigation of sudden faults instability induced by coal mining. *Saf. Sci.* **2019**, *115*, 256–264. [CrossRef]
30. Zhu, D.; Tu, S.; Tu, H.; Yang, Z. Mechanisms of support failure and prevention measures under double-layer room mining gobs—A case study: Shigetai coal mine. *Int. J. Min. Sci. Technol.* **2019**, *29*, 955–962. [CrossRef]
31. Wang, F.; Xu, J.; Xie, J.; Li, Z.; Guo, J. Mechanisms influencing the lateral roof roadway deformation by mining-induced fault population activation: A case study. *Int. J. Oil Gas Coal Technol.* **2016**, *11*, 411–428. [CrossRef]
32. Wang, Q.; He, M.; Li, S.; Jiang, Z.; Wang, Y.; Qin, Q.; Jiang, B. Comparative study of model tests on automatically formed roadway and gob-side entry driving in deep coal mines. *Int. J. Min. Sci. Technol.* **2021**, *31*, 591–601. [CrossRef]
33. Li, G.; Ma, F.; Guo, J.; Zhao, H.; Liu, G. Study on deformation failure mechanism and support technology of deep soft rock roadway. *Eng. Geol.* **2020**, *264*, 105262. [CrossRef]
34. Sun, Y.; Li, G.; Zhang, J.; Sun, J.; Huang, J.; Taherdangkoo, R. New Insights of Grouting in Coal Mass: From Small-Scale Experiments to Microstructures. *Sustainability* **2021**, *13*, 9315. [CrossRef]
35. Sun, Y.; Zhang, J.; Li, G.; Wang, Y.; Sun, J.; Jiang, C. Optimized neural network using beetle antennae search for predicting the unconfined compressive strength of jet grouting coalcretes. *Int. J. Numer. Anal. Methods Geomech.* **2019**, *43*, 801–813. [CrossRef]
36. Doan, D.V.; Zhao, H.C.; Cao, J.; Yong, C.; Meng, W. Control technology for soft rock roadway in inclined coal seam: A case study in Nui Beo mine, Quang Ninh, Vietnam. *Int. J.* **2018**, *14*, 175–182. [CrossRef]
37. Piotr, M.; Łukasz, O.; Piotr, B. Modelling the small throw fault effect on the stability of a mining roadway and its verification by in situ investigation. *Energies* **2017**, *10*, 2082. [CrossRef]
38. Shiliang, L.; Caigen, W. Strata pressure law for roadway in soft rocks and relationship between support and surrounding rock. In *Geotechnical Instrumentation and Monitoring in Open Pit and Underground Mining*; CRC Press: Boca Raton, FL, USA, 2020; pp. 339–344.
39. Xie, S.; Pan, H.; Zeng, J.; Wang, E.; Chen, D.; Zhang, T.; Peng, X.; Yang, J.; Chen, F.; Qiao, S. A case study on control technology of surrounding rock of a large section chamber under a 1200-m deep goaf in Xingdong coal mine, China. *Eng. Fail. Anal.* **2019**, *104*, 112–125. [CrossRef]
40. Wang, H.; Zheng, P.Q.; Zhao, W.J.; Tian, H.M. Application of a combined supporting technology with U-shaped steel support and anchor-grouting to surrounding soft rock reinforcement in roadway. *J. Cent. South Univ.* **2018**, *25*, 1240–1250. [CrossRef]
41. Chakravarthi, S.S.; Kassam, A.B.; Fukui, M.B.; Monroy-Sosa, A.; Rothong, N.; Cunningham, J.; Jennings, J.E.; Guenther, N.; Connelly, J.; Kaemmerer, T.; et al. Awake Surgical Management of Third Ventricular Tumors: A Preliminary Safety, Feasibility, and Clinical Applications Study. *Geofluids* **2019**, *17*, 208–226. [CrossRef]

sustainability

MDPI

Article

Experimental Study on Crack Propagation of Rock by Blasting under Bidirectional Equal Confining Pressure Load

Jinjin Ge [1,2], Ying Xu [1,2,*], Wei Huang [3], Haibo Wang [1], Rongzhou Yang [1] and Zhongyi Zhang [1]

[1] School of Civil Engineering and Architecture, Anhui University of Science and Technology, Huainan 232001, China; jge2@aust.edu.cn (J.G.); wanghb_aust@163.com (H.W.); rongzhouy@outlook.com (R.Y.); zzyyingaust@163.com (Z.Z.)
[2] Key Laboratory of Mining Response and Disaster Prevention and Control in Deep Coal Mine, Anhui University of Science and Technology, Huainan 232001, China
[3] School of Architecture and Art, Huainan United University, Huainan 232001, China; hwaust@163.com
* Correspondence: yxu@aust.edu.cn; Tel.: +86-159-5665-5885

Abstract: Rock blasting during tunneling has shown that the rock failure in high in situ stress environments is different from that in low in situ stress conditions or with a shallow rock mass. In particular, the propagation direction of the main crack induced by blasting is greatly affected by the in situ stresses. In order to study the law of crack propagation in rock during blasting under the conditions of an initial in situ stress, a transparent material that conformed to the mechanical properties of hard rock was used to carry out a similar model rock blasting test, under a unidirectional load. The results show that initial stress has a great influence on the propagation number, length, and direction of the main radial cracks. The specific performances were as follows: under the action of an equal confining pressure load, the longest main radial crack in the model specimen propagated along the diagonal direction, and the number and length of the main radial cracks propagated decreased with the gradual increase of confining pressure stress; in addition, the diameter of the circumferential cracks also decreased with the increase of stress, and there was a negative correlation between them. In view of the phenomenon where the longest main radial crack propagated along the diagonal direction in the model test, a mechanical model was established in this study to explain this process. This is of practical significance for understanding the mechanism of rock fracture when blasting with high in situ stresses.

Keywords: in situ stress; rock blasting; crack propagation; model test

Citation: Ge, J.; Xu, Y.; Huang, W.; Wang, H.; Yang, R.; Zhang, Z. Experimental Study on Crack Propagation of Rock by Blasting under Bidirectional Equal Confining Pressure Load. *Sustainability* **2021**, *13*, 12093. https://doi.org/10.3390/su132112093

Academic Editors: Mahdi Hasanipanah, Danial Jahed Armaghani and Jian Zhou

Received: 2 September 2021
Accepted: 26 October 2021
Published: 2 November 2021

Publisher's Note: MDPI stays neutral with regard to jurisdictional claims in published maps and institutional affiliations.

Copyright: © 2021 by the authors. Licensee MDPI, Basel, Switzerland. This article is an open access article distributed under the terms and conditions of the Creative Commons Attribution (CC BY) license (https://creativecommons.org/licenses/by/4.0/).

1. Introduction

With the increasing demand for natural resources, surface and subsurface mines are becoming depleted and underground mines continue to progress to deeper levels. The depths of many mines around the world are more than 1000 m below the surface, and the gold mine in Vaal Reefs, South Africa has reached the world's greatest mining depth, of 4800 m. This increasing mining depth leads to increasing in situ stress in the surrounding rock of roadways, which brings a series of new problems for roadway excavation and support [1,2].

Engineering evaluations of blasting operations carried out in a deep rock mass showed that the fracture failure in deep rock was different from that in a shallow rock mass. However, the influence of in situ stress was not taken into account in the design of the existing blasting parameters for roadway excavation, which resulted in low blasting efficiencies for the roadway, thus affecting the speed and efficiency of roadway construction [3]. In addition, in the process of the blasting construction of a cavern for a underground hydropower station, it was found that the in situ rock stress field in the stratum had an obvious influence on the design of the blasting parameters [4–6]. Under a condition of low in situ stress (horizontal in situ stress < 10 MPa), whether using smooth blasting or pre-splitting blasting,

an ideal blasting effect can be obtained. However, in areas of high in situ stress (horizontal in situ stress > 10 MPa), the appropriate blasting technology (pre-splitting blasting or smooth blasting) and sequence need to be considered comprehensively, according to the actual situation [7]. Thus, it can be seen that the effects of in situ stress on rock blasting cannot be ignored [8–14], and failures in deep rock mass are the result of the joint action of high in situ stress and as explosive impact load; that is, the superposition action of the initial static stress field and the explosive dynamic load.

Gao et al. [15] investigated the mechanism of controlled blasting under high in situ stress by using a dynamic photo-elastic experimental system with initial stress loading. It was concluded from their research results that (1) the direction without initial stress or with a small initial stress is the best direction for blasting deformation and compressive energy release; (2) the stress field superposed by the initial static stress field and the explosive dynamic load produces tensile stress, initially in the direction of the smaller static stress; (3) the stress boundary restrains the occurrence and development of reflected tensile waves to a certain extent, and the failure of the medium is mainly caused by extrusion and compression shear, which indicates that a blasting mechanism based on free surface reflection tension is not suitable for controlled blasting under high in situ conditions.

Existing studies have shown that the initial in situ stress has an obvious "suppression" effect on the development of blast-induced cracks and that the blast-induced cracks preferentially propagate in the direction of the maximum principal stress in a static stress field [16]. When the direction of cracks is perpendicular to the direction of the static compressive stress, the static compressive stress field hinders the propagation of cracks. However, when the cracks deflect towards or coincide with the direction of the static stress field, the hindrance of the static compressive stress field on the crack growth is greatly reduced [17]. According to research by Yang [18], this is because the initial compressive stress field reduces the stress concentration at the crack tip, hinders the crack growth, and thus shortens the propagation distance of the main blast-induced crack, which appears to have a 'suppression' effect on the crack.

In experiments and production practice, it is found that hole blasting in a medium with dynamic and static stress fields presents various phenomena of preferential crack initiation, good blasting effects, and low explosive consumption, which was described as a 'waveguide effect' by Zhang [19]. He suggested that the dynamic response of a rock mass must be changed due to the existence of complex in situ stress in the rock mass, and the superposition of a blasting stress wave and in situ stress conforms to the law of phase strength and phase weakness; that is, being strong in the same phase and weak in the contrary phase. In this regard, Xiao [20] proposed a principle, whereby the initial stress field has a 'guiding effect' on the propagation of cracks. According to this theory, the huge pressure generated by an explosion initially causes compressive stress waves in the rock. Then, the stress state in the hole wall propagates outward in the form of a cylindrical wave and at the same time produces tensile stress in the direction tangential to the hole wall. When the in situ stress is large enough, and the direction of principal stress is consistent with that of explosion stress wave, the explosion stress wave will collide with, and be superimposed on, the in situ stress, and tensile stress will be generated in the direction tangential to the collision. When the resultant tensile stress exceeds the tensile strength of the rock, the rock will crack along the direction of the principal stress.

In summary, existing studies only employed a qualitative analysis of the propagation direction of a blast-induced main crack in rock with an initial stress, which leads to their limited guidance value for actual blasting engineering in deep rock masses. In addition, there are few studies on the effect of in situ stress on the circumferential fractured zone in the central blasting area. To this end, blasting model tests of transparent rock under the action of confining pressure were carried out in this study, to study the mechanism of in situ stress in crack propagation by blasting and reveal the law of the effects of in situ stress on the direction and length of crack propagation when blasting, as well as the diameter of the circumferential fractured zone in the central blasting area.

2. Materials and Methods

2.1. Test Device

A self-developed test device with a plane stress loading system, data measurement system, and high-speed photography system was used to simulate the in situ stress constraint in a deep rock mass. The device includes a stress loading platform, oil pressure station, high-speed camera suspension, etc., as shown in Figure 1.

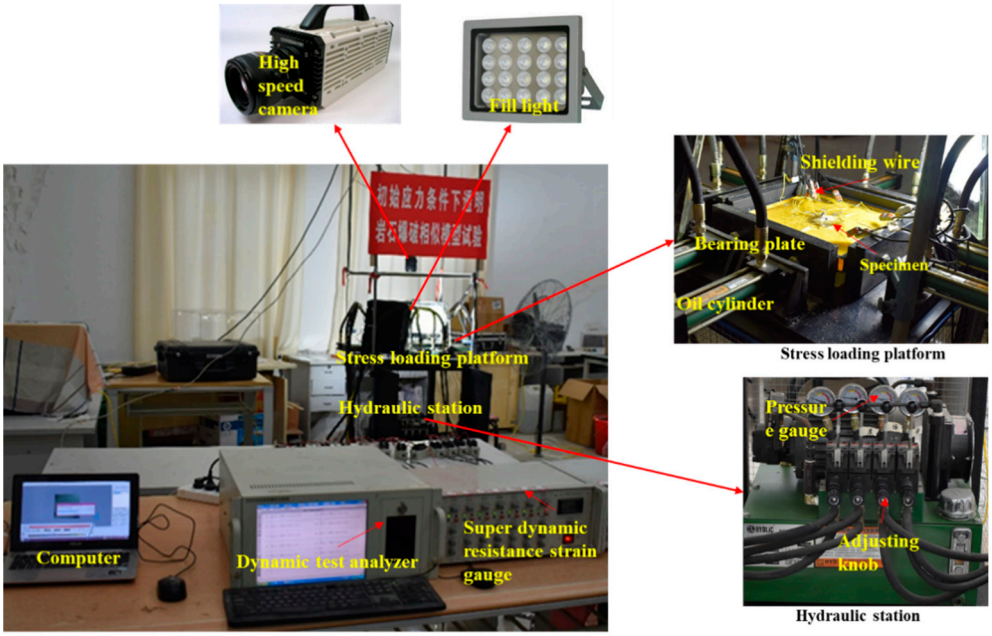

Figure 1. Device for plane stress loading of a model specimen.

The maximum size of model specimen applied to the stress loading platform was 500 ×500 × 100 mm (length × width × height). The rated power and extreme power of the oil pressure station used for the loading platform were 5 MPa and 7 MPa, respectively, and the piston area of a single oil cylinder was 7.065 cm^2. If the device is used to load a model specimen with a size of 300 × 300 × 20 mm, the rated load concentration and ultimate load concentration that can be reached inside the specimen are 1.18 Mpa and 1.65 Mpa, respectively, which basically satisfies the uniform conditions of the stress field in the model.

2.2. Similarity Coefficient

The deep roadway project of the Dingji Coal Mine, in the Huainan mining area, was used as the prototype for the model test. The in situ stress field in this mining area is mainly dominated by horizontal tectonic stress [21]. The cross-sectional shape of the roadway is a semicircular arch, and the cross-section size is 5000 × 3880 mm, while the depth of the roadway is 910 m. The roadway is mainly located in a stratum of medium sandstone and siltstone, and the physical and mechanical parameters of the protolith are shown in Table 1.

Table 1. Physicomechanical parameters of the prototype rock.

Material Type	$\frac{\gamma}{KN \cdot m^{-3}}$	$\frac{E}{GPa}$	$\frac{C}{MPa}$	$\frac{\varphi}{(^\circ)}$	ν	$\frac{\sigma_c}{MPa}$	$\frac{\sigma_t}{MPa}$
Sandstone	27	12.97	10.00	43	0.27	135	21.5

γ—Bulk density, E—Deformation modulus, C—Cohesion, φ—Internal friction angle/(°), ν—Poisson's ratio, σ_c—Compressive strength, σ_t—Tensile strength.

At present, the material most commonly used in similarity model experiments of rock blasting is cement mortar [22]. However, it is not transparent, which led to the problem that, after the test, the cracks in the model made of cement mortar could not be seen.

Therefore, a kind of transparent hard rock-like material, which could replace the existing model material to solve the above problem, was used in this study. This transparent hard rock-like material was made of a mixture of rosin-saturated solution (RSS), epoxy resin (ER), and curing agent (CA), and its physical and mechanical properties have been proven, through relevant tests, to be similar to those of hard rock [23]. The basic physical and mechanical parameters are shown in detail in Table 2.

Table 2. Basic mechanical parameters of the transparent rock-like material.

Physical Quantities	ρ	C	E/MPa	ν	σ_c/MPa	σ_t/MPa
Numerical value	1230	2423	360∼1802	0.26∼0.31	3.29∼96	0.26∼7.22

ρ—Density/kg·m^{-3}, C—Compressional wave velocity/(m/s).

In similar systems, the ratio of the similar physical quantities is called the similarity ratio (or called similarity constant and similarity coefficient); that is, 'prototype physical quantity (P)/model physical quantity (M) = similarity ratio (α)' [24,25]. According to the balance equation, geometry equation, physical equation, stress boundary condition, and displacement boundary condition of the prototype and model (process omitted), the similarity relation between the various physical quantities of the model test can be obtained as

$$\begin{cases} \alpha_\nu = 1,\ \alpha_\varepsilon = 1,\ \alpha_\varphi = 1 \\ \alpha_\delta = \alpha_L \\ \alpha_X = \alpha_Y = \alpha_Z = \alpha_\gamma \\ \alpha_\sigma = \alpha_L \cdot \alpha_\gamma \\ \alpha_{\sigma_c} = \alpha_{\sigma_t} = \alpha_E = \alpha_C = \alpha_\sigma \\ \alpha_T = \sqrt{\alpha_L} \end{cases} \quad (1)$$

According to the bulk density of the model material and prototype material, the similarity coefficient for the bulk density can be calculated as $\alpha_\gamma = 2.2$. The similarity scale of the model selected for the test was 1:16.7 in this study. Hence, it could be calculated using the above formula as: stress similarity coefficient $\alpha_\sigma = 36.7$, elastic modulus similarity coefficient $\alpha_E = 36.7$, cohesion similarity coefficient $\alpha_C = 36.7$, time similarity coefficient $\alpha_T = 4.15$, strain similarity coefficient $\alpha_\varepsilon = 1$, Poisson's ratio similarity coefficient $\alpha_\nu = 1$, and internal friction angle similarity coefficient $\alpha_\varphi = 1$.

2.3. Blasting Charge

Many engineering works on rock blasting show that the explosion shock wave acts directly on the hole wall of the blasthole when using a coupling charge, which forms into a large-scale crushed zone near the blasthole in the rock mass. In the crushing circle, the rock fragmentation absorbs most of the energy of the explosion shock wave, resulting in the rapid attenuation of energy. However, the impact pressure of the explosion shock wave on the hole wall is smaller when using an uncoupled charge, which makes the radius of the crushing circle shrink. Therefore, a stress wave with a smaller attenuation can act on the fracture circle of the rock mass for a longer time, and the effect on the production of cracks is good. It has been shown that using an uncoupled charge in rock blasting can enlarge the range of the fractured zone and make full use of the explosive energy [26].

The method of uncoupled charges is used in model tests of rock blasting. We designed the diameter of the blasthole, diameter for charging, and height for charging as 4 mm, 3 mm, and 20 mm, respectively. In view of the small amount of explosives used in the model test, a type of relatively safe and stable small detonator was selected as the explosive in the test, and its main component was DDNP (Table 3). According to the dynamic similarity criterion [27], it can be concluded that the relationship between the similarity explosive and the prototype explosive is satisfied with $C_\rho C_D = 1$ (C_ρ is the density ratio of the prototype explosive to the model explosive, and C_D is the detonation velocity ratio of the prototype explosive to the model explosive). The prototype explosive was a three-level permissible

water-gel explosive for coal mining, with a density of 1.1 g/cm^3 and a detonation speed of 3600 m/s. The model explosive was DDNP in bulk, with a density of about 0.7 g/cm^3 and a detonation speed of 5400 m/s. This was obtained through calculating that $C_\rho C_D$ = 1.047, which basically meets the principle of a 'similar blasting energy of explosives'.

Table 3. Explosive physical parameters of the special small detonator.

Geometric Dimension/$\times 10^{-3}$ m		Main Ingredients	Explosive Charge/g	Density /kg·m^{-3}	Detonation Velocity/m/s
Length	Diameter				
30	3	DDNP	0.043	700	5400

DDNP-dinitrodiazophenol, molecular formula -$C_6H_2N_4O_5$.

The blasthole for charging was located in the center of the specimen, and the two ends were bonded with 1 mm thick plastic discs, which were used for fixing the special small detonator. The detailed charging structure is shown in Figure 2.

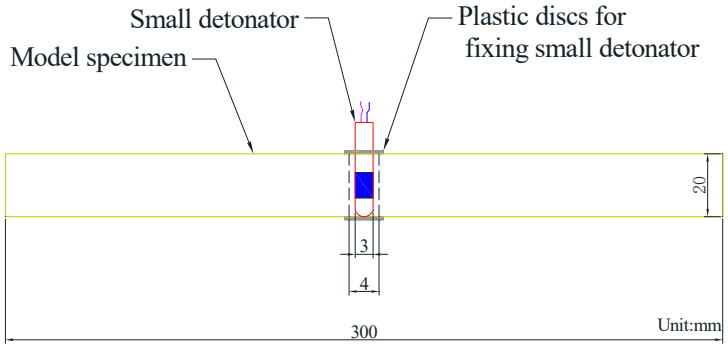

Figure 2. Schematic diagram of the charging structure.

2.4. Test Scheme

The uniaxial compressive strength (UCS) of the materials, value for the confining pressure, and usage of explosive required by the model test were calculated according to similarity theory. Before the formal model blasting test, a pre-blasting model test was carried out. The test results showed that the specimens were completely broken, due to the low UCS of the materials, which is unfavorable for studying the law of crack propagation of a specimen after blasting. Therefore, on the basis of theoretical calculation, and combined with the results of the pre-blasting test, the parameters of the blasting model were adjusted appropriately; and the parameters of the model specimens are shown in Table 4. The production method for the model specimens referred to the study by Ge [23].

Table 4. Basic physical and mechanical parameters of the model specimens.

Number	Mass Ratio	$\frac{\gamma}{\mathrm{KN\cdot m^{-3}}}$	$\frac{E}{\mathrm{MPa}}$	ν	$\frac{\sigma_c}{\mathrm{MPa}}$	$\frac{\sigma_t}{\mathrm{MPa}}$
TSG-0∼5	10:10:1	12.3	552	0.28	7.5	0.586

The mass ratio of 10:10:1 was, namely, epoxy resin: curing agent: saturated rosin solution.

It was known that C_σ = 36.7 (stress similarity coefficient), $\sigma_v = \gamma H$ (vertical stress), and we also assumed that $\sigma_{hav} = \sigma_v$ (average horizontal stress). Therefore, if the buried depth of the simulated rock mass designated in the test was from 0 m to 1300 m, the corresponding loading stress values of the simulated confining pressure of the vertical and horizontal would be from 0 MPa to 0.955 MPa. The six groups of loading schemes used in the actual model test are shown in Table 5.

Table 5. Test scheme for blasting of transparent model specimens.

Specimen Number	Buried Depth/m	$\sigma_v = \sigma_h$	
		C_P **Design /MPa**	C_P **Loading/MPa**
TSG-0	0	0	0
TSG-1	410	0.3	1.2
TSG-2	560	0.42	1.7
TSG-3	850	0.63	2.6
TSG-4	1000	0.74	3.1
TSG-5	1300	0.96	4.0

C_P—confining pressure.

2.5. Production Method

Taking the plate model specimen as an example [23], the detailed production steps were as follows:

(1) Pre-made solution. Unlike epoxy resins and curing agents, RSS cannot be purchased directly and needs to be made. First, the optimal rosin blocks were broken down into powders, which were screened through a 100-mesh screen. Then, a 100-mesh rosin powder was melted into an appropriate amount of anhydrous alcohol solution, until the solution reached a saturated state.

(2) Sticking film in the mold. From the exploratory test, it was found that pouring the mixed solution directly into the mold made it difficult to disassemble the mold, so it was necessary to pretreat the mold before pouring. First, a thin layer of Vaseline was applied to the surface of the mold, and then an anti-stick film was applied to the surface.

(3) Pouring specimen. First, the epoxy resin, curing agent, and RSS were weighed according to the designed experimental proportions and placed in a beaker. Then, the epoxy resin and curing agent were heated in an oven to 50 °C, and the RSS was heated in a water bath to 50 °C. When all the bubbles in the epoxy resin and curing agent were removed, they were mixed and stirred evenly. At this time, bubbles inevitably appeared again in the mixed solution, so they were heated in an oven at 50 °C until the bubbles were removed. Finally, the RSS was taken out from the water bath and poured into the epoxy resin system. After the mixture was stirred evenly, it was poured into the mold. It was concluded after many experiments that no bubbles will appear, as long as the mixture of three solutions is stirred slowly and uniformly when the preheated RSS is mixed with the non-bubbled thermal epoxy resin system.

(4) Maintenance and polishing of the specimen. The mold filled with the resin mixture solution was gently placed in a room at a constant temperature for maintenance. After the epoxy resin had cured completely, the mold was removed and the uneven areas of the specimen were polished with sandpaper or a small grinder.

3. Results and Analysis

3.1. Results of Blasting Model Test

The propagation of cracks in the specimens after blasting is shown in Figure 3. A relevant supplementary explanation is made for the cracks in Figure 3, before analyzing the law of crack propagation in the model specimen. It can be seen from Figure 3b–f that the cracks generated in the model specimens all reached the boundary of the specimens. This is because the cracks generated by the explosion load continued to propagate in different directions after the static confining pressure was unloaded. In Figure 3, the main radial cracks are marked by yellow lines, and the propagation range of circumferential cracks is marked by blue lines.

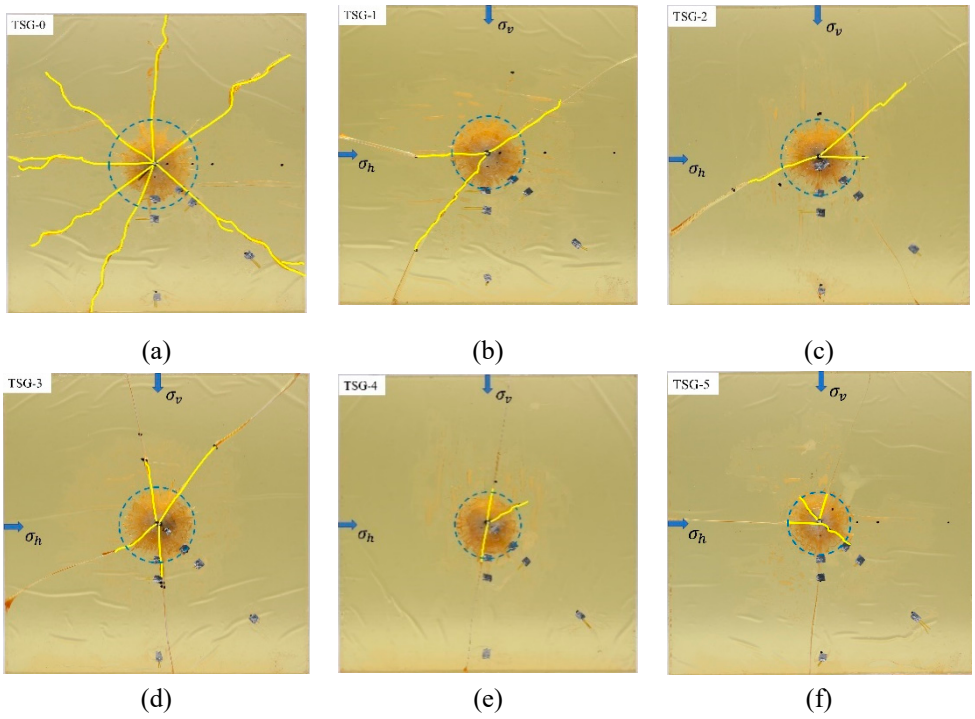

Figure 3. Transparent model specimens after explosion: (**a**) TSG-0 (**b**) TSG-1 (**c**) TSG-2 (**d**) TSG-3 (**e**) TSG-4 (**f**) TSG-5.

According to the fragmentation mechanism of rock blasting, for a certain amount of charge, if the minimum resistance line exceeds a certain threshold (called the critical resistance line, *Wc*), there will be no blasting signs on the free surface after the charge explosion. That is, the blasting only occurs inside the rock mass and fails to reach the free surface, which is equivalent to charge blasting in an infinite medium. This action is called internal action. When the charge only acts internally, the explosion action zone can be roughly divided into a crushed zone, fractured zone, and vibrated zone [28,29], as shown in Figure 4.

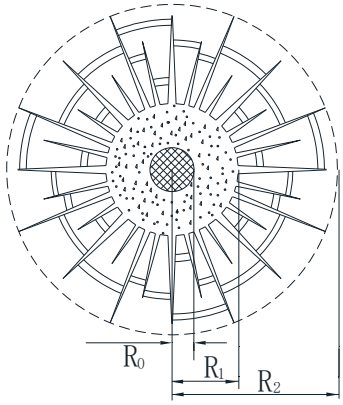

Figure 4. Internal action of blasting. R_0—charging radius, R_1—radius of crushed zone, and R_2—radius of fractured zone.

Under the action of an explosion shock wave and high temperature and pressure gas, rock near the blasthole will be crushed and produce a large plastic deformation, forming a crushed zone.

When the shock wave propagates to a certain distance, it becomes a compressive stress wave, due to its energy attenuation [30]. At this time, the peak value of the radial stress of the compressive stress wave is less than the value of the dynamic compressive

strength of the rock, and it cannot cause the crushing failure of the rock, but instead the radial displacement of rock. Compressive stress and compression deformation occur in the radial direction, while tensile stress and tensile deformation occur in the tangential direction. When the value of the tensile stress is more than that of the dynamic tensile strength, cracks are generated along the radial direction of the blasthole. The air wedge effect of explosive gas makes the crack expand and extend. When the stress wave and the pressure of the explosive gas are further attenuated, the energy accumulated by the radial compression of the rock will be released and transformed into an unloading wave towards the source of explosion, forming radial tensile stress. This causes the rock to be pulled apart by the radial tensile stress, forming tangential cracks. It can be concluded that the fractured zone is mainly formed by tensile failure.

In the vibrated zone [31], the original structure of the medium is not damaged, but only elastic deformation is produced. The vibration strength gradually weakens with the increase of distance through the medium from the explosion center, until it completely disappears.

Figure 3a shows the crack propagation of the post-explosion model specimen under the condition of no initial stress. It can be observed that a crushed zone, fractured zone, and vibrated zone were formed in the post-explosion specimen, which conforms to the fracture pattern of single-hole charge blasting in an infinite medium.

Figure 3b–f shows the crack propagation of a post-explosion model specimen under an equal confining pressure load. Compared with without a confining pressure, the crack propagation of the model specimens under a bi-directional equal confining pressure changed greatly, including in the number, length, and propagation direction of the main radial cracks in the cracked zone. If the post-explosion model specimen is divided into several areas (Figure 5), it can be clearly seen from the test results that the longest main radial cracks are distributed in four areas A, B, C, and D, and only a few radial cracks developed along the directions of σ_v or σ_h.

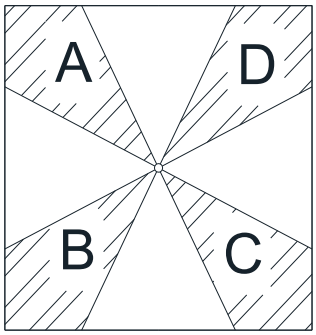

Figure 5. Crack distribution in transparent model specimens.

In the engineering of rock excavation by blasting, smooth blasting or presplitting blasting technology is often used for the boundary excavation, so as to reduce the damage from blasting to the surrounding rock and the reduction of its stability. Since the range of the fractured zone is an important reference basis for the design of controlled blasting parameters, this study focused on quantitatively describing the variation of crack propagation in the fractured zone of model specimens with the size of the applied load; and the main radial cracks of the post-explosion specimens are marked, as shown in Figure 6.

As shown in Figure 6, the post-explosion specimens were divided into a compression crushed zone (I), fractured zone (II and III), and vibrated zone (IV). With the increase of confining stress load on the model, the range of the fractured zone decreased greatly, the range of the vibrated zone increased, and only the range of the crushed zone did not change significantly. This study focuses on the propagation of the fractured zone, and Part II of the fractured zone was analyzed first.

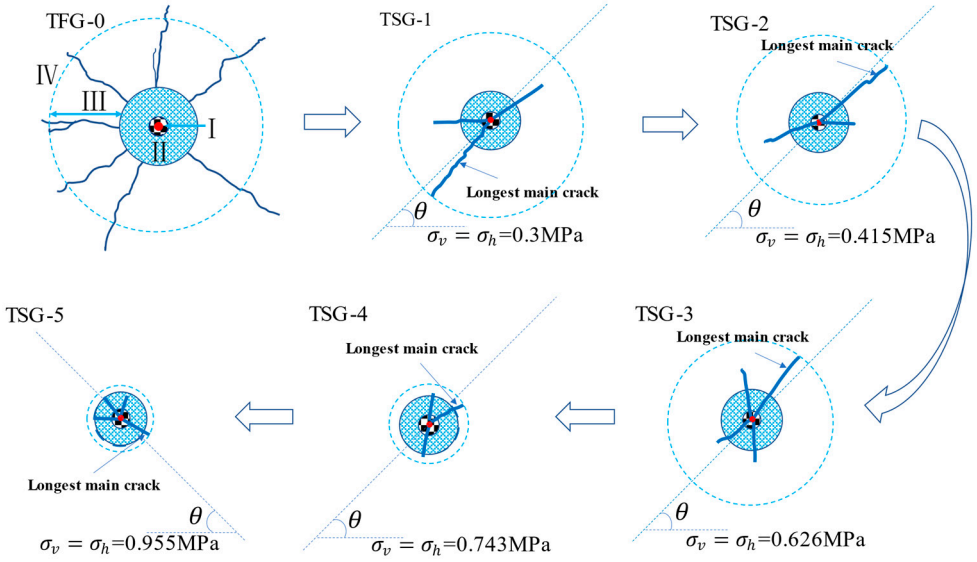

Figure 6. The variation of crack propagation with different stress loads in model specimens.

3.2. Crack Propagation Analysis

3.2.1. The Influence of Initial Stress on the Scope of the Circumferential Fractured Zone

As shown in Figure 3, the model specimens had the characteristics of geometric symmetry and mechanical symmetry. In theory, the diameter of the circumferential fracture along the direction σ_v is the same as that along the direction σ_h, and the diameters of the circumferential fractures along the two diagonals (the angle between diagonal and σ_v or σ_h is 45 °C) are also equal. The measurement results of the diameters of the circumferential cracks in the post-explosion specimens are shown in Table 6.

Table 6. The diameters of the circumferential cracks in the model specimens.

Number	Diameter/cm					
	Along σ_v	Along σ_h	Mean Value	Along Diagonal-1	Along Diagonal-2	Mean Value
TSG-1	7.4	8.2	7.8	7.2	7.0	7.1
TSG-2	7.6	7.8	7.7	6.0	6.2	6.1
TSG-3	7.0	7.2	7.1	5.8	5.8	5.8
TSG-4	6.2	6.4	6.3	5.5	5.3	5.4
TSG-5	6.0	5.8	5.9	5.3	5.3	5.3

It can be seen from Table 6 that the measured diameter of the circumferential fracture along the direction σ_v was not equal to that along the direction σ_h; whereas, these two values should be equal according to the symmetry principle. Similarly, the diameters of circumferential fracture along the diagonal direction were also not equal. Therefore, the average diameters were used to characterize the propagation range of the circumferential crack in the post-explosion specimen. The relationship between the average diameters of the circumferential crack and the stress of the confining pressure is shown in Figure 7.

As can be seen from Figure 7, the average diameters along the diagonal direction of the circumferential cracks were significantly smaller than those along the σ_v and σ_h directions, and both of them gradually decreased with the increase of initial stress, which was obviously 'constrained' by the confining pressure stress. As the model specimens were compressed by the initial stress, the dynamic compressive strength of medium inside the specimens increased, resulting in the weakening of the loading and unloading effect of compressive stress wave on the medium around the blasthole, and finally it resulted that the diameter of the circumferential crack decreased with the increase of stress.

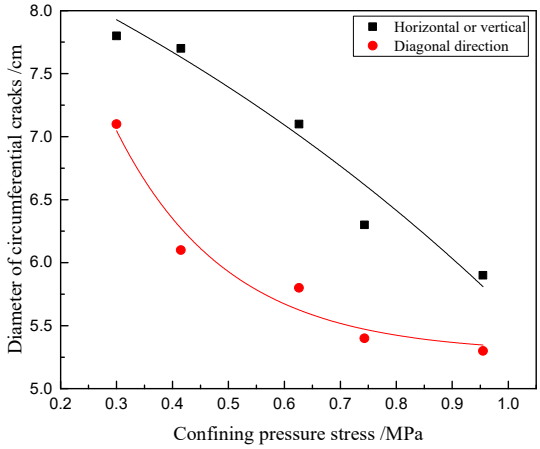

Figure 7. Relationship between the average diameter of the circumferential cracks and confining rstress.

Furthermore, by fitting the data points in Table 6, the relationship between the stress of the confining pressure and the diameter of the circumferential crack can be obtained, as follows:

$$D_1 = 11.037 - 2.451e^{\left(\frac{C_p}{1.261}\right)} \left(\mathrm{R}^2 = 0.942,\ C_p \in (0.3, 0.96)\mathrm{MPa}\right) \quad (2)$$

$$D_2 = 5.280 + 7.949e^{\left(\frac{-C_p}{0.1995}\right)} \left(\mathrm{R}^2 = 0.964,\ C_p \in (0.3, 0.96)\mathrm{MPa}\right) \quad (3)$$

where D_1 is the mean diameter of the circumferential crack along the horizontal and vertical direction; D_2 is the mean diameter of the circumferential crack along the direction of the two diagonals.

3.2.2. The Influence of Initial Stress on the Propagation Length and Direction of the Main Radial Crack

As shown in Figure 6, the number and length of the main radial cracks decreased with the change of load applied to specimen TSG-0~5. In addition, the propagation direction of the main radial crack also changed. In particular, the longest main radial crack propagated along the diagonal direction (namely, the angle between the propagation direction and horizontal or vertical direction is 45°), which made the confining stress have a 'guiding' effect on the propagation direction of the main radial cracks. This is consistent with the conclusion that many researchers have reached [32,33], but so far researchers have not provided a convincing explanation of the mechanism of this phenomenon. In this part of the discussion of this study, a mechanical model will be established with knowledge of the elasticity, explosion mechanics, and stress wave theory, in order to analyze the failure mechanism.

With a further increase of confining pressure stress applied to the model specimens, the propagation lengths of the main radial cracks tended to be the same, which were close to the diameters of the circumferential cracks. At the same time, the propagation direction presented diversification; that is, the propagation direction was evenly distributed along the vertical, horizontal, and diagonal lines, such as in the main cracks in post-specimens TSG-4 and TSG-5.

According to the mechanism of rock fragmentation by blasting, the fractured zone is mainly formed by tensile damage from the tensile stress wave. Then, with a further increase of confining pressure, the tensile strength of the specimens is further improved, resulting in it becoming difficult to produce rock tensile damage along all directions with the tensile stress wave. Even along the diagonal direction, it is difficult to produce tensile failure in rocks. Therefore, the 'guiding' effect of the confining pressure stress on the propagation of the longest main radial crack is weakened.

In order to study the variation law of the length of the main radial cracks with the initial stress, a ruler was used to measure the length of the radial cracks in the post-explosion model specimens, and the results are shown in Table 7.

Table 7. The length of the radial main cracks in the model specimens.

Number	Length of Radial Main Cracks/cm			Mean Value/cm
	1#	2#	3#	
TSG-0	18.7	16.8	16.5	17.33
TSG-1	8.2	10.9	8	9.03
TSG-2	10.3	8.8	4.9	8.0
TSG-3	6.8	8.6	5.8	7.06
TSG-4	5.1	4.4	4.4	4.63
TSG-5	3.6	3.4	3.1	3.37

Cracks 1#∼3# are the top three in length of the main radial cracks in the model specimens.

By taking the confining load as the X-axis and the crack length as the Y-axis, the relationship between crack propagation and initial stress was established, as shown in Figure 8.

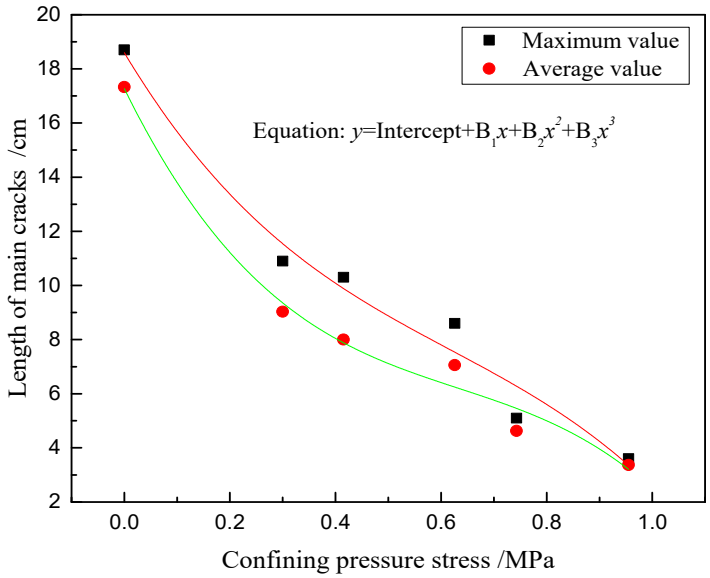

Figure 8. Variation of main crack length with loading stress.

It can be seen from Figure 8 that the length of the longest main radial crack and average length of the main radial cracks decreased gradually with the increase of initial stress. Furthermore, by fitting the data points in Figure 8, it can be shown that the relationship between the propagation length of the longest main radial crack and the initial stress conformed to the following formula.

$$L_{lg} = 18.598 - 32.54C_p + 35.893{C_p}^2 - 19.4{C_p}^3 \quad \left(R^2 = 0.978,\ C_p \in (0.0.96)\text{MPa}\right) \tag{4}$$

And the relationship between average propagation length of the main radial cracks and the stress of confining pressure is as follows.

$$L_{avg} = 17.27 - 39.66C_p + 52.55{C_p}^2 - 27.68{C_p}^3 \quad \left(R^2 = 0.988,\ C_p \in (0.0.96)\text{MPa}\right) \tag{5}$$

Equations (4) and (5) indicate that the length of the main radial cracks under a bidirectional confining pressure load depended on the initial stress, and there was a cubic function

relationship between the two. In this way, this can provide a reference for the design of controlled blasting parameters in a deep rock mass.

4. Discussion

A deep rock mass is mainly subjected to vertical and horizontal in situ stresses [34,35]. When a rock in a state of static in situ stresses is subjected to the dynamic loading of an explosion, it will start to be damaged at a certain time. In this process, the effect of in situ stress on the rock is usually regarded as quasi-static loading. Therefore, the stress state of deep rock mass engineering can be simulated using a combination of dynamic and static loading (shown in Figure 9). It is assumed that the initial stress of the rock mass in the vertical direction is σ_y, the initial stress in the horizontal direction is σ_x, the internal explosion load is P_d, and the compressive strength and tensile strength of the rock are σ_c, σ_t, respectively.

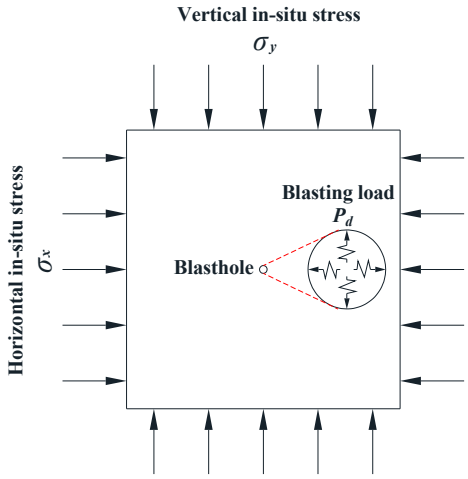

Figure 9. Force model of deep rock mass under blasting.

The fractured zone is the main area of rock failure in engineering blasting [36], and its failure range is much larger than that of the compression crushed zone. Moreover, the influence of the initial stress on the blast-induced compression crushed zone in rock is relatively small; therefore, this study discussed the influence of initial in situ stress on the crack propagation in the blast-induced fractured zone in rock. According to the stress mode of an engineering rock mass, the influence of initial stress on the crack propagation from rock blasting can be analyzed in different cases; that is, the rock mass is subjected to unequal confining pressure loads and equal confining pressure loads.

It is supposed that the in situ stress applied to the model is $\sigma_x = \sigma_y \neq 0$. In this case, the force model can be simplified, as shown in Figure 10a, and the explosion load is described by P_1, P_2, P_3, and P_4 ($P_1 = P_2 = P_3 = P_4$). Blasting theory indicates that the blast shock wave on the hole wall is attenuated into a stress wave when it propagates to the middle zone (fractured zone) of the blasting. The stress wave in the model, within the same radius of the fractured zone (the crack is still in propagation), at a certain moment is described by P_1', P_2', P_3', and P_4' ($P_1' = P_2' = P_3' = P_4'$), and a micro point taken from each of the eight different directions can be denoted as A, A_1, B, B_1, C, C_1, D, and D_1. The circumferential tensile stresses at the above eight points are described by P_t^1, P_t^2, P_t^3, and P_t^4. Meanwhile, it is assumed that $P_t^1 = P_t^2 = P_t^3 = P_t^4$. In this way, the dynamic load is also simplified to the static load (as shown in Figure 10b). In this case, stress analysis can be carried out according to the plane stress problem, in the theory of elastic mechanics.

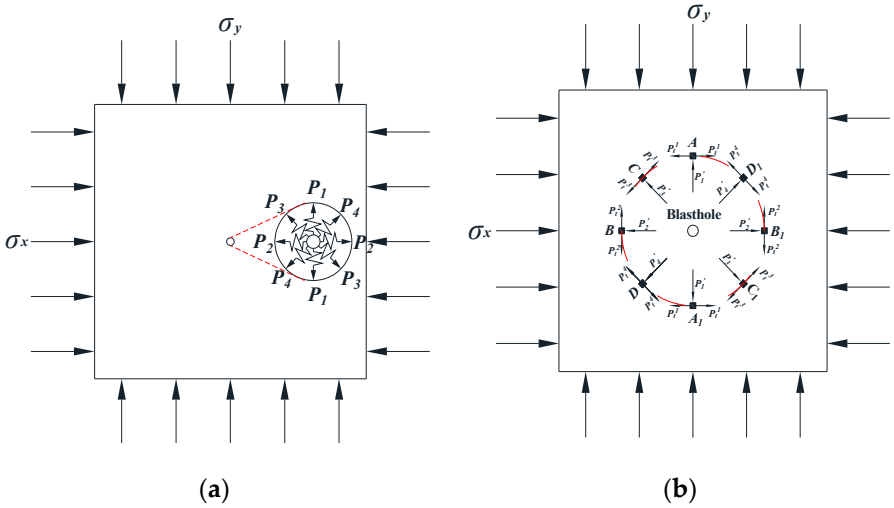

Figure 10. Force model of rock under bidirectional equal confining pressure and explosive load: (**a**) at the time of explosive detonating; (**b**) at the time of stress wave propagating to fractured zone.

Furthermore, the force model of a rock mass under bidirectional equal confining pressure and blasting is equivalent to the mechanical model in Figure 11 (external loading model + internal loading model).

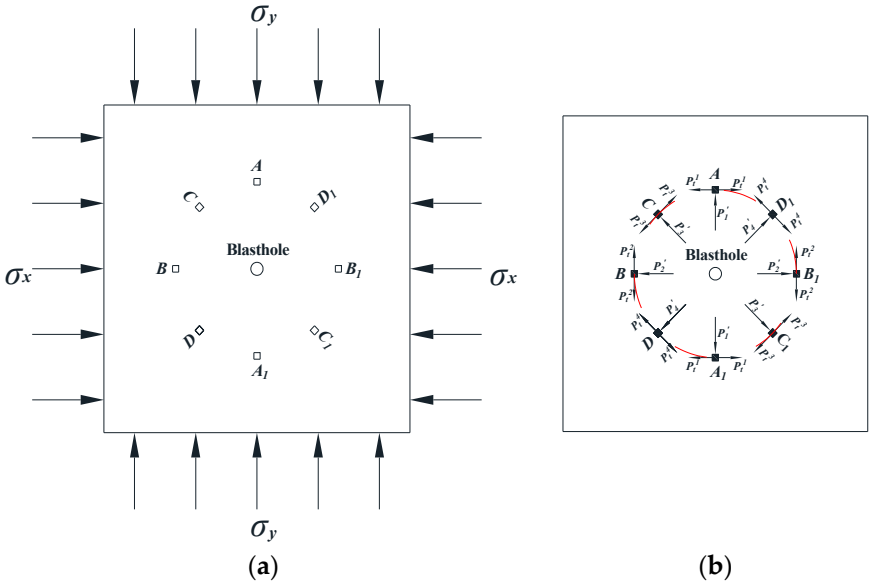

Figure 11. Equivalent force model of rock blasting under a bidirectional initial stress: (**a**) external loading model; (**b**) internal loading model.

Qian [37] suggested that the effect of an initial static load on a rock mass is to indirectly increase the dynamic compressive or tensile strength of the rock. Based on this view, the force of each micro element subjected to an external load in the model was calculated in this study; first, through static equilibrium analysis, so as to facilitate a comparison of the compressive and tensile strength of each micro element.

According to the symmetry of force model, half of the model was taken for analysis, as shown in Figure 12a. It was assumed that the side length of model was a, then the model can be simplified, as shown in Figure 12b, based on the relationship between stress and load.

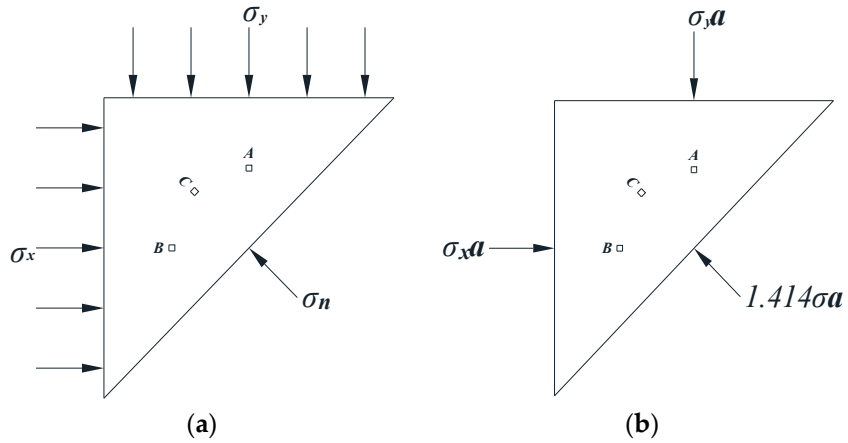

Figure 12. Force analysis of rock mass under an initial static load: (**a**) half of the model in Figure 11a; (**b**) the model simplified from Figure 12(a).

Suppose $\sigma_x = \sigma_y = \sigma$, then the concentrated load on each micro element point A, B, and C in the model can be calculated. As shown in Figure 13, $\sigma_y a$ is the concentrated load; M is the additional bending moment generated after the translation of concentrated load, and its magnitude is $\sigma_y ad$, where d is the translation distance.

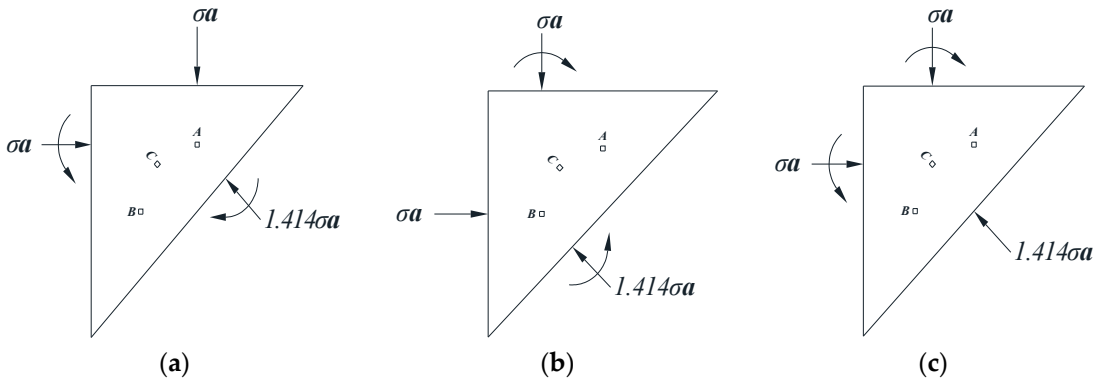

Figure 13. Force analysis of a micro element point in a rock mass under an initial static load: (**a**) force analysis on point A; (**b**) force analysis on point B; (**c**) force analysis on point C.

It should be noted that the stress applied on the model specimens in this study was far less than the compressive strength of rock. The translational concentrated load inevitably produces an additional bending moment, which means that it produces shear stress in the rock mass, but this is far from sufficient to cause damage to the rock mass. Therefore, the shear effect caused by the additional bending moment on the rock mass is not considered here.

As seen in Figure 13a, the micro element point A is subjected to external loads in both the horizontal and vertical directions, and its magnitude is σa; according to Figure 13b, the micro element point B is subjected to external loads in both the horizontal and vertical directions, and its magnitude is σa; from Figure 13c, it can be seen that the micro element C is subjected to external loads in both the horizontal and vertical directions, and its magnitude is σa. In addition, it can be calculated that the magnitude of the external load along the diagonal direction of micro element C is $\sqrt{2}/2$ (about 0.707) σa. It is assumed that the tensile strength of the micro element increases by 100% in the vertical direction under a vertical concentrated load (σa) compression, and then the tensile strength of the model specimen in this direction becomes $2\sigma_t$.

As the blasting stress wave located in the middle zone (fractured zone) of the blasting is no longer sufficient to crush the rock mass, it is impossible for the stress wave to produce compression failure in the vertical direction of point A. Hence, for point A, only the tensile

stress failure in the horizontal direction needs to be discussed. Similarly, it is impossible to produce compression failure in the horizontal direction of point B and perpendicular to the diagonal direction of point C (as shown in the Figure 11b). Therefore, it is only necessary to discuss the failure effect of tensile stresses on these. As seen in Figure 12b, the micro element points A, B, and C affected by the blasting stress wave are taken for stress analysis, as shown in Figure 14.

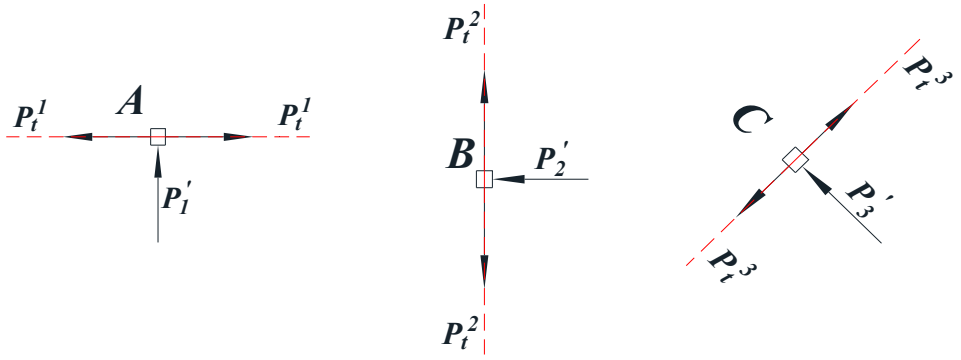

Figure 14. Force analysis of micro element points in rock mass under a dynamic blasting load: (**a**) force analysis on point A; (**b**) force analysis on point B; (**c**) force analysis on point C.

The above analysis showed that the damage in the middle zone (fractured zone) of blasting is mainly caused by tensile stress. Therefore, for micro element point A, the strength failure criterion is, when $P_t^1 > 2\sigma_t$, tensile failure of rock mass occurs. Similarly, for micro element points B and C, the tensile strength failure criteria are $P_t^1 > 2\sigma_t$ and $P_t^1 > (1+\sqrt{2}/2)\sigma_t$, respectively. It was stated in the hypothesis that all the taken points are from the fractured zone (radial cracks are propagating) and are at the same distance from the blast center. Therefore, with the further attenuation of the stress wave, there must be a situation where $2\sigma_t > P_t' > \left(1+\sqrt{2}/2\right)\sigma_t$, and where P_t' is attenuated from $P_t^1 = P_t^2 = P_t^3 = P_t^4$.

It can be concluded that the crack along CC_1/DD_1 direction will continue to propagate after the propagation has stopped for the crack along AA_1/BB_1 direction. In other words, the total length of the crack in the direction CC_1/DD_1 is greater than the total length of the crack in the direction AA_1/BB_1. Hence, the angle between the propagation direction of the longest radial crack and the direction of principal stress is 45°, which shows that the longest radial crack propagates along the direction at 45° of the macro level.

5. Conclusions

In this study, model specimens made of transparent rock-like materials were used to carry out an experiment of a blasting model under bidirectional equally confining pressure. Based on the analysis of the model test results, a law of blast-induced crack propagation, affected by bi-directional equal confining pressure, was obtained, and the conclusions are summarized as follows:

- The initial stress has the effect of 'suppression' of the propagation diameters of the circumferential cracks. With the increase of confining pressure, the average diameters of the circumferential cracks along the horizontal, vertical, and diagonal directions gradually decrease, and the diameters of the circumferential cracks along the diagonal directions are obviously smaller than those along the σ_v and σ_h directions;
- The initial stress also has the effect of 'suppression' of the number and length of propagated main radial cracks. The greater the load applied on the specimens, the fewer the number of main radial cracks; there is a negative correlation between the propagation length of the main radial cracks and the initial stress. However,

with a further increase of confining pressure stress, the propagation lengths of the main radial cracks tend to be the same, and their size is close to the diameter of the circumferential crack;

- The initial stress has a 'guiding' effect on the crack propagation direction of the longest main crack. Under the combined dynamic and static loads, the propagation direction of the main radial crack of a model specimen changes from radial without initial stress, to diagonal, and the longest main crack develops along the diagonal; with a further increase of confining pressure, the propagation directions are diversified; that is, the propagation directions are uniformly distributed along the diagonal, σ_v and σ_h, directions, where the confining stress loses its 'guiding' effect on the propagation of the longest main radial cracks.

Obviously, the confining pressure limits the opening of the crack surface, resulting in a greater driving force for crack propagation; that is, more energy is required for crack propagation per unit length. Therefore, under different initial stress conditions, there must be a critical value of energy for crack opening. If it is lower than the critical energy required for crack opening, the crack in the middle zone of blasting is not be able to propagate. Compared with a condition without initial stress (the charging parameters are the same), the ratio of energy used for crack propagation in the middle zone of blasting to the total explosive energy is reduced. According to the principle of energy conservation, it can be concluded that the energy loss in the far zone of blasting, the near zone of blasting, and other areas will inevitably increase. It can be seen that a confining pressure changes the distribution of the blasting energy.

If the energy in the far zone of blasting increases, the stress wave in the far zone of blasting increases; that is, the vibrational intensity increases, which brings great potential safety hazards for deep underground engineering. If the energy in the near zone of blasting increases, the fragmentation degree of the crushed zone is higher, which has no practical significance for blasting excavation. Therefore, it is necessary to study the distribution of blasting energy in a future study and obtain the critical energy value required for crack development under different confining stress conditions, so as to provide a reference for the design of blasting parameters in practical engineering.

Author Contributions: Conceptualization, J.G. and Y.X.; software, J.G.; formal analysis, J.G.; investigation, R.Y. and Z.Z.; writing—original draft preparation, J.G.; writing—review and editing, J.G., Y.X., W.H. and H.W.; visualization, J.G.; supervision, Y.X.; project administration, Y.X.; funding acquisition, J.G. and Y.X. All authors have read and agreed to the published version of the manuscript.

Funding: This research was funded by the university-level key projects of Anhui University of science and technology (No. xjzd2020–16); research grants project for bringing in talents of Anhui University of science and technology; National Natural Science Foundation of China (No. 52104116, No. 52074009).

Data Availability Statement: The datasets generated and analyzed during the current study are available from the corresponding author upon reasonable request.

Conflicts of Interest: The authors declare no conflict of interest.

Nomenclature

α	Similarity ratio	δ	Displacement
L	Length	E	Modulus of elasticity
ν	Poisson's ratio	σ	Stress
γ	Bulk density	σ_c	Compressive strength
σ_t	Tensile strength	X, Y, Z	Volume forces
ε	Strain	C	Cohesion
φ	Angle of internal friction	T	Time

References

1. Falls, S.D.; Young, R. Acoustic emission and ultrasonic-velocity methods used to characterise the excavation disturbance associated with deep tunnels in hard rock. *Tectonophysics* **1998**, *289*, 1–15. [CrossRef]
2. Egger, P. Design and construction aspects of deep tunnels (with particular emphasis on strain softening rocks). *Tunn. Undergr. Space Technol.* **2000**, *15*, 403–408. [CrossRef]
3. Dai, J.; Qian, Q.H. Break blasting parameters for driving a roadway in rock with high residual stress. *Explos. Shock Waves* **2007**, *27*, 272–277.
4. Xie, L.; Lu, W.; Zhang, Q.; Jiang, Q.; Chen, M.; Zhao, J. Analysis of damage mechanisms and optimization of cut blasting design under high in-situ stresses. *Tunn. Undergr. Space Technol.* **2017**, *66*, 19–33. [CrossRef]
5. Xie, L.; Lu, W.; Zhang, Q.; Jiang, Q.; Wang, G.; Zhao, J. Damage evolution mechanisms of rock in deep tunnels induced by cut blasting. *Tunn. Undergr. Space Technol.* **2016**, *58*, 257–270. [CrossRef]
6. Xie, L.X.; Lu, W.B.; Jiang, Q.H.; Zhang, Q.B.; Wang, G.H.; Chen, M.; Yan, P. Damage evolution mechanism of deep rock mass during cut blasting. Journal of Central South University. *Sci. Technol.* **2017**, *48*, 1252–1260.
7. Lu, W.B.; Chen, M.; Geng, X.; Shu, W.B.; Zhou, C.B. A study of excavation sequence and contour blasting method for under-ground powerhouses of hydropower stations. *Tunn. Undergr. Space Technol.* **2012**, *29*, 31–39. [CrossRef]
8. Fan, Y.; Lu, W.B.; Yan, P.; Chen, M.; Zhang, Y.Z. Transient characters of energy changes induced by blasting excavation of deep-buried tunnels. *Tunn. Undergr. Space Technol.* **2015**, *49*, 9–17. [CrossRef]
9. Yilmaz, O.; Unlu, T. Three dimensional numerical rock damage analysis under blasting load. *Tunn. Undergr. Space Technol.* **2013**, *38*, 266–278. [CrossRef]
10. Sainoki, A.; Emad, M.Z.; Mitri, H.S. Study on the efficiency of destress blasting in deep mine drift development. *Can. Geotech. J.* **2017**, *54*, 518–528. [CrossRef]
11. Guo, W.Y.; Zhao, T.B.; Tan, Y.L.; Yu, F.H.; Hu, S.C.; Yang, F.Q. Progressive mitigation method of rock bursts under complicated geological conditions. *Int. J. Rock Mech. Min. Sci.* **2017**, *96*, 11–22. [CrossRef]
12. Qiu, J.; Li, D.; Li, X.; Zhu, Q. Numerical investigation on the stress evolution and failure behavior for deep roadway under blasting disturbance. *Soil Dyn. Earthq. Eng.* **2020**, *137*, 106278. [CrossRef]
13. Jayasinghe, L.B.; Shang, J.L.; Zhao, Z.Y.; Goh, A.T.C. Numerical investigation into the blasting-induced damage characteristics of rocks considering the role of in-situ stresses and discontinuity persistence. *Comput. Geotech.* **2019**, *116*, 103207. [CrossRef]
14. Lak, M.; Marji, M.F.; Bafghi, A.Y.; Abdollahipour, A. A coupled finite difference-boundary element method for modeling the propagation of explosion-induced radial cracks around a wellbore. *J. Nat. Gas. Sci. Eng.* **2019**, *64*, 41–51. [CrossRef]
15. Gao, Q.C.; He, J.M.; Feng, G.W.; Zhao, H. Mechanism and technology of controlled blasting for high stress rock tunneling. *Blasting* **2003**, *20*, 52–55.
16. Kutter, H.; Fairhurst, C. On the fracture process in blasting. *Int. J. Rock Mech. Min. Sci. Geéomeéch. Abstr.* **1971**, *8*, 181–202. [CrossRef]
17. Rossmanith, H.P.; Knasmillner, R.E.; Daehnke, A.; Mishnaevsky, L. Wave propagation, damage evolution, and dynamic fracture extension. Part II. Blasting. *Mater. Sci.* **1996**, *32*, 403–410. [CrossRef]
18. Yang, L.Y.; Ma, J.H.; Wang, X.D.; Zhang, W.C.; Zhang, L. Experimental study on blasting crack initiation and propagation behavior in compression stress field. *Explos. Shock Waves* **2017**, *37*, 262–268.
19. Zhang, Z.C.; Xiao, Z.X.; Hu, J.; Li, C.X.; Zhang, Y.J. Experimental study on the wave transmission effect of the initial stress field as transmitting of quake wave from rock blasting. *Ind. Miner. Process.* **2005**, *34*, 21–24.
20. Xiao, Z.X.; Zhang, Z.C.; Li, D.M. The influence of initial stress field on blasting. *J. Chin. Coal Soc.* **1996**, *21*, 497–501.
21. Liu, Q.S.; Liu, K.D. Characteristics of in-situ stress field for deep levels in Huainan coal mine. *Rock Soil Mech.* **2012**, *33*, 2089–2096.
22. Wan, Y.L.; Wang, S.R. Experiment study on damage model of rock fragmentation by blasting. *Eng. Blasting* **1997**, *3*, 29–33.
23. Ge, J.; Xu, Y. A Method for Making Transparent Hard Rock-Like Material and Its Application. *Adv. Mater. Sci. Eng.* **2019**, *2019*, 1274171. [CrossRef]
24. Zhang, Q.Y.; Chen, X.G.; Lin, B.; Liu, D.J.; Zhang, N. Study of 3D geomechanical model test of zonal disintegration of sur-rounding rock of deep tunnel. *Chin. J. Rock Mech. Eng.* **2009**, *28*, 1757–1766.
25. Xu, Y.; Ge, J.; Huang, W. Energy Analysis on Dynamic Fragmentation Degree of Cemented Sand Specimens under Confining Pressure. *Shock. Vib.* **2019**, *2019*, 5893957. [CrossRef]
26. Xu, Y.; Meng, Y.P.; Cheng, Y.S. Study on control of blast crack by decoupling charge index. *Chin. J. Rock Mech. Eng.* **2002**, *21*, 1843–1847.
27. Yuan, W.H.; Ma, Q.Y.; Huang, W. Model experiment and analysis of wedge-shaped cutting millisecond blasting. *Chin. J. Rock Mech. Eng.* **2012**, *31*, 3352–3356.
28. Chi, L.Y.; Zhang, Z.X.; Arne, A.; Charlie, C.L. Experimental Investigation of Blast-Induced Fractures in Rock Cylinders. *Rock Mech. Rock Eng.* **2019**, *52*, 2569–2584. [CrossRef]
29. Hajibagherpour, A.; Mansouri, H.; Bahaaddini, M. Numerical modeling of the fractured zones around a blasthole. *Comput. Geotech.* **2020**, *123*, 103535. [CrossRef]
30. Lak, M.; Marji, M.F.; Bafghi, A.Y.; Abdollahipour, A. Analytical and numerical modeling of rock blasting operations using a two-dimensional elasto-dynamic Green's function. *Int. J. Rock Mech. Min. Sci.* **2019**, *114*, 208–217. [CrossRef]

31. Mohammadi, S.S.; Amnieh, H.B.; Bahadori, M. Predicting ground vibration caused by blasting operations in sarcheshmeh copper mine considering the charge type by adaptive neuro-fuzzy inference system (ANFIS). *Arch. Min. Sci.* **2011**, *56*, 701–710.
32. Yi, C.P.; Daniel, J.; Jenny, G. Effects of in-situ stresses on the fracturing of rock by blasting. *Comput. Geotech.* **2018**, *104*, 321–330. [CrossRef]
33. Tao, J.; Yang, X.-G.; Li, H.-T.; Zhou, J.-W.; Fan, G.; Lu, G.-D. Effects of in-situ stresses on dynamic rock responses under blast loading. *Mech. Mater.* **2020**, *145*, 103374. [CrossRef]
34. Qin, X.H.; Zhang, P.; Feng, C.J.; Sun, W.F.; Tan, C.X.; Chen, Q.C.; Peng, Y.R. In-Situ Stress Measurements and Slip Stability of Major Faults in Beijing Region. *Chin. J. Geophys.* **2014**, *57*, 415–430.
35. Brown, E.; Hoek, E. Trends in relationships between measured in-situ stresses and depth. *Int. J. Rock Mech. Min. Sci. Geéomeéch. Abstr.* **1978**, *15*, 211–215. [CrossRef]
36. Hu, Y.G.; Lu, W.B.; Chen, M.; Yan, P.; Yang, J.H. Comparison of Blast-Induced Damage Between Presplit and Smooth Blasting of High Rock Slope. *Rock Mech. Rock Eng.* **2014**, *47*, 1307–1320. [CrossRef]
37. Qin, Q.H. Some advances in rock blasting dynamics. *Chin. J. Rock Mech. Eng.* **2009**, *28*, 1945–1968.

sustainability

MDPI

Article

Factors Influencing Pile Friction Bearing Capacity: Proposing a Novel Procedure Based on Gradient Boosted Tree Technique

Chia Yu Huat [1], Seyed Mohammad Hossein Moosavi [1], Ahmed Salih Mohammed [2], Danial Jahed Armaghani [3,*], Dmitrii Vladimirovich Ulrikh [3], Masoud Monjezi [4] and Sai Hin Lai [1,*]

1 Department of Civil Engineering, Faculty of Engineering, Universiti Malaya, Kuala Lumpur 50603, Malaysia; 17107717@siswa.um.edu.my (C.Y.H.); mh.moosavi@um.edu.my (S.M.H.M.)
2 Civil Engineering Department, College of Engineering, University of Sulaimani, Sulaymaniyah 46001, Iraq; ahmed.mohammed@univsul.edu.iq
3 Department of Urban Planning, Engineering Networks and Systems, Institute of Architecture and Construction, South Ural State University, 454080 Chelyabinsk, Russia; ulrikhdv@susu.ru
4 Department of Mining, Faculty of Engineering, Tarbiat Modares University, Tehran 14115-143, Iran; monjezi@modares.ac.ir
* Correspondence: danialarmaghani@susu.ru (D.J.A.); laish@um.edu.my (S.H.L.)

Abstract: In geotechnical engineering, there is a need to propose a practical, reliable and accurate way for the estimation of pile bearing capacity. A direct measure of this parameter is difficult and expensive to achieve on-site, and needs a series of machine settings. This study aims to introduce a process for selecting the most important parameters in the area of pile capacity and to propose several tree-based techniques for forecasting the pile bearing capacity, all of which are fully intelligent. In terms of the first objective, pile length, hammer drop height, pile diameter, hammer weight, and N values of the standard penetration test were selected as the most important factors for estimating pile capacity. These were then used as model inputs in different tree-based techniques, i.e., decision tree (DT), random forest (RF), and gradient boosted tree (GBT) in order to predict pile friction bearing capacity. This was implemented with the help of 130 High Strain Dynamic Load tests which were conducted in the Kepong area, Malaysia. The developed tree-based models were assessed using various statistical indices and the best performance with the lowest system error was obtained by the GBT technique. The coefficient of determination (R^2) values of 0.901 and 0.816 for the train and test parts of the GBT model, respectively, showed the power and capability of this tree-based model in estimating pile friction bearing capacity. The GBT model and the input selection process proposed in this research can be introduced as a new, powerful, and practical methodology to predict pile capacity in real projects.

Keywords: tree-based techniques; feature selection; pile bearing capacity; gradient boosted tree; random forest

Citation: Huat, C.Y.; Moosavi, S.M.H.; Mohammed, A.S.; Armaghani, D.J.; Ulrikh, D.V.; Monjezi, M.; Hin Lai, S. Factors Influencing Pile Friction Bearing Capacity: Proposing a Novel Procedure Based on Gradient Boosted Tree Technique. *Sustainability* **2021**, *13*, 11862. https://doi.org/10.3390/su132111862

Academic Editor: Anjui Li

Received: 21 August 2021
Accepted: 25 October 2021
Published: 27 October 2021

Publisher's Note: MDPI stays neutral with regard to jurisdictional claims in published maps and institutional affiliations.

Copyright: © 2021 by the authors. Licensee MDPI, Basel, Switzerland. This article is an open access article distributed under the terms and conditions of the Creative Commons Attribution (CC BY) license (https://creativecommons.org/licenses/by/4.0/).

1. Introduction

There are several types of deep foundations, for instance, piles and caissons, which are required in situations where the soil is not able to support structural loads at a shallow depth. The main objective of the pile foundation is to transmit the structural load to deeper bearing strata in order to withstand the axial, lateral, and uplift load and to minimize the settlement. The load applied at the top of the pile head is transferred to the soil where the load is partially taken by normal stress at the pile base and the remaining load is taken by the lateral pile-soil interface via shear stress [1]. Thus, the piles can be classified into two types, which are end bearing pile and friction pile. The end bearing pile is a pile that transmits the structural load to a hard and incompressible stratum where the required bearing capacity is derived from end bearing at the pile base [2]. As for the friction pile, the pile-bearing capacity is derived from skin friction and cohesion between the pile surface and

the shaft that is encompassed by soil or rock along a pile [3]. Hence, the base and friction capacity of piles are crucial for carrying the axial loading. In the event of no stiff stratum at a reasonable depth, the loads are required to transfer by friction through the pile shafts [4].

The pile-bearing capacity can be governed by soil and pile properties [5,6]. The contribution of soil typically consists of cohesion and friction between the pile and the shaft of a pile at a depth. The pile friction capacity is calculated by a combination of the interface shear strength (τ_m) along the pile length and the pile surface area to compute the shaft resistance (Q_{su}) [7]. In addition, during the installation of driven piles, which are usually prefabricated, the loose deposit soil that encompasses the pile can be locally densified due to soil displacement and, thus, the pile capacity can be increased [7]. As such, it can be stated that the installation method of piles can be one of the factors that contributes to the pile capacity [8].

The pile-bearing capacity can be determined using several techniques, such as empirical, semi-empirical and finite element (FE). The extent of the FE model and computation time is limited with model boundaries in contexts where this can be done by redoing the model boundaries by taking the boundaries to be further away from the modeling object and comparing the results. This process can be more time consuming [9]. In industry practice, the Standard Penetration Test (SPT)-N is widely-used to determine the pile capacity [8,10–12]. There are many empirical formulas of pile friction bearing correlated with SPT-N in a general form of equation, as shown below:

$$q_s = n_s\, N \tag{1}$$

where, q_s is the limit skin friction stress at a given depth, which is proportional to the N value at the particular depth, and n_s is the skin friction factor proposed by researchers as presented in Table 1. However, according to previous studies, these empirical equations are not reliable in terms of accuracy [13,14]. This is because some of the pile's empirical analysis relationships are made by simplification in contexts where a large factor of safety is applied. This factor reduces the accuracy of the predictions and the deprivation of resources [15]. Other than this, there is a simple correlation between the pile bearing capacity and in-situ tests, for instance, the Cone Penetration Test (CPT) or SPT. However, this correlation method overestimates the pile bearing capacity [16].

Table 1. Some of empirical equations for determining the pile friction bearing capacity using n_s results.

No	References	Equation	n_s (kPa)	Type of Installation Pile
1	Bazaraa and Kurkur [17]	$q_s = 0.67\,N$ if $D \leq 0.5$ m. else $q_s = 1.34\,N$	0.67 if $D \leq 0.5$ m, 1.34 for the other D values (where D is pile diameter in m)	Bored
2	Decourt [18]	q_s =10 (N/3+1)	-	Bored
3	Lopes and Laprovitera [19]	$q_s = 1.62\,N$ $q_s = 1.94\,N$	1.62 in sand 1.94 in silty sand	Bored
4	Meyerhof [20]	$q_s = 1\,N$ $q_s = 2\,N$	1 2	Bored Driven
5	Shioi and Fukui [21]	$q_s = 1\,N$ $q_s = 2\,N$	1 2	Bored Driven
6	Aoki and Veloso [22]	$q_s = 2\,N$ $q_s = 2.28\,N$	2.00 in sand 2.28 in silty sand	Bored
7	Reese and O'Neill [23]	$q_s = 3.3\,N$	3.3	Bored
8	Robert [24]	$q_s = 1.9\,N$	1.90 1.90	Bored Driven

Pile tests are required during the construction process to reassure the design calculation, because the estimation of axial pile capacity at various soil types will never be more accurate than approximately 30% [25]. There are a few methods of pile tests used to calculate the axial capacity of the piles. The typical methods are Static Load Test (SLT) and High Strain Dynamic Testing (HSDT) [26]. SLT is considered as the most reliable predictor of long term pile performance. However, this testing is expensive and time consuming [27–29]. Other than the SLT test, HSDT is one of the methods used to determine the pile bearing capacity. In comparison with SLT, HSDT is quick and economical [26]. This test is carried out based on the theory of one-dimensional wave propagation and is given by a Pile Driving Analyzer (PDA). PDA has proven that the predicted bearing capacity values are closely related to SLT results [30]. Nevertheless, all pile tests are, basically, expensive and time consuming to set up at the site [31,32]. Due to the aforementioned situation, it is important to predict pile bearing capacity using new and effective calculation approaches, such as Machine Learning (ML) and Artificial Intelligence (AI).

AI, ML and data mining techniques have been used widely to solve many civil engineering and more specifically geotechnical problems [33–45]. In terms of piling related issues, such as pile bearing capacity, there are several studies that have applied and proposed AI and ML techniques [12,46–50]. One of the most-used models in this regard is the Artificial Neural Networks (ANN). These approaches demonstrated a number of successful predictions [29,50]. As discussed before, pile driving formulae were used to provide an approximate estimation of the driven pile capacity. This formula is derived from impulse-momentum principles. However, the accuracy of neural network predictions are significantly higher compared to the conventional pile driving formulae [51]. In another study, Pal [52] stated that the General Regression Neural Network (GRNN) model has shown higher accuracy of the pile load bearing capacity prediction in comparison to empirical approaches, but slightly lower accuracy than the ANN technique. In addition, the Gene Expression Programming (GEP) model was in good agreement with the results of the experiment, indicating that pile capacity has a good relationship with some inputs, such as pile geometry [53]. Alavi et al. [54] concluded that Linear Genetic Programming (LGP) model is the best behavior in modelling uplift capacity of suction caissons, followed by the GEP and tree-based genetic programming models in comparison with regression and FE models. A Gaussian Process Regression (GPR) approach was suggested by Momeni et al. [55] in the area of pile capacity after comparison with other ANN-based models. Another group of scholars applied and proposed a combination of at least two AI techniques for prediction of pile bearing capacity [26–28,31,47]. Actually, these combined techniques enjoyed the advantages of all the used AI models for prediction purposes and, due to that, they achieved higher performance compared to the single AI models. Table 2 presents the most important AI and ML studies for predicting the pile capacity, together with their soil types, number of data, model performance, and input parameters.

According to Table 2, many studies used ANN, ANN-based and genetic-based models for estimating pile capacity. In addition, several studies applied and proposed neuro-fuzzy and Support Vector Machine (SVM) models for the same purpose. However, there are very few approaches using tree-based techniques, like Random Forest (RF), to predict the pile capacity as far as the authors know. Due to this, this paper is aimed at applying and proposing the full applications of tree-based models only, i.e., Decision Tree (DT), RF and Gradient Boosted Tree (GBT) for the prediction of pile friction bearing capacity. To do this, a feature selection (i.e., input selection) will be conducted to select the most crucial input variables for pile friction bearing capacity. The mentioned models will then be constructed and the model with the highest accuracy will be selected and introduced for estimating the pile friction bearing capacity.

Table 2. Summary of important AI and ML studies to predict pile capacity.

No	Reference	Input	Model	Soil Type	Datasets	Performance
1	Goh [56] and Goh [51]	Pile length and diameter, effective overburden stress and undrained shear strength	ANN	Clay	65 driven piles (timber and steel)	R = 0.956
2	Lee and Lee [29]	Model pile load test: penetration depth ratio, mean normal stress of calibration chamber, number of hammer blows In-situ pile load test: penetration depth ratio, average SPT-N value with the pile shaft depth and close to the end of pile, pile set, final penetration depth/blow, hammer energy	ANN	Sand	Model pile load test: 28 steel tube In-situ pile load test: 24 piles	Maximum error of prediction < 25%
3	Goh [57]	Pile elastic modulus, pile length and cross sectional area, weight of pile, hammer drop height and weight, pile set and type of hammer	ANN	Sand	116 piles (timber precast concrete and steel)	R = 0.965
4	Kiefa [58]	Soil shear resistance encompassing the pile shaft, soil shear resistance at the tip of pile, effective overburden stress, pile length and pile area	GRNN	Sand	59 load tests on different type of driven pile	R^2 = 0.912
5	Das and Basudhar [59]	Pile diameter, pile length, eccentricity of load and undrained shear strength	MFPNN	Clay	38 short and rigid piles	R = 0.947
6	Pal and Deswal [60]	Force, velocity multiplied by impedance, hollow pipes piles diameter, wall thickness, and pile depth	SVM and GRNN	-	105 pre-stressed precast spun piles	R SVM = 0.964 GRNN = 0.977
7	Pal and Deswal [61]	Pile diameter, pile length, eccentricity of load and undrained shear strength	GPR	Non-cohesive soil	94 load tests piles (timber, precast concrete and steel piles)	R = 0.950
8	Alavi et al. [54]	Pile length/pile diameter, lateral force point of application distance/pile length, chain force angle with the horizontal, undrained shear strength at pile tip, and soil permeability	LGP	All soil types	62 suction caissons	R^2 = 0.994
9	Gandomi et al. [62]	Pile diameter and length, eccentricity of load, and pile tip undrained shear strength	Multi-Gene GP	Clay	38 short and rigid piles	R = 0.985
10	Alkroosh and Nikraz [53]	Pile diameter and length, CPT pile tip resistance, cone sleeve friction along pile length, CPT resistance along pile shaft, elastic modulus of pile and type of pile	GEP	Non-cohesive soil	25 driven piles (concrete and steel)	R = 0.94

Table 2. *Cont.*

No	Reference	Input	Model	Soil Type	Datasets	Performance
11	Kordjazi et al. [63]	Cross section area of the tip, perimeter of pile, embedded pile length, average cone tip resistance, average cone sleeve friction, and average cone tip resistance below the pile tip	Different SVM kernels	Sands, clays and silts	108 pile tests	R = range from 0.966–0.982
12	Momeni et al. [26]	Pile set, pile length and cross-sectional area, hammer drop height and weight	GA-ANN	-	50 pre-cast concrete piles	R^2 = 0.990
13	Ghorbani et al. [64]	Area of the pile at tip, unit shaft resistance of the soil, average of cone tip resistance for shaft and tip, and average of sleeve friction value along the pile embedded length	ANFIS	All soil types	108 concrete, steel and composite piles	R = 0.96
14	Harandizadeh et al. [27]	Pile length, cross-section shape and material, cone tip resistance and sleeve friction of cone	ANFIS-GMDH-PSO	Sand, silty sand, clay, sandy clay, and silty clay	41 Concrete and 31 Steel piles	R = 0.96
15	Dehghanbanadaki et al. [65]	Pile area, pile length, flap number, average soil cohesion and friction angle, average soil specific weight and average pile-soil friction angle	ANFIS-GWO	-	100 steel and concrete driven piles	R = 0.930
16	Momeni et al. [55]	Pile length and diameter, pile set, ram weight, and hammer drop height	GPR	-	296 precast driven piles	R^2 = 0.81
17	Pham et al. [66]	Pile diameter, pile tip segment length, second pile segment length, pile top segment length, natural ground elevation, pile top elevation, guide pile segment sop driving elevation, pile tip elevation, and average SPT	RF and ANN	-	2314 reinforced concrete piles	R^2 RF = 0.861 ANN = 0.811

Gray wolf optimization (GWO); Correlation coefficient (R); Determination coefficient (R^2); Genetic algorithm (GA); Adaptive neuro-fuzzy inference system (ANFIS); Group method of data handling (GMDH); Particle swarm optimization (PSO); Random forest (RF); Multilayer feedback propagation neural network (MFPNN); Support vector machine (SVM).

2. Methods and Material

2.1. Case Study and Established Database

In order to predict the pile friction bearing capacity values, there is a need to prepare a series of experiments on site. The case study in this research was located at Kepong, Malaysia and the area was about 4.4 acres in size. This site was located in the Limestone formation, as indicated in Figure 1. In Kuala Lumpur, there are many commercial centers that are built on heavily karstified limestone formations [67]. The study area was ex-mining land, a swampy area and a pond, as shown in Figure 2.

- Zone (1): Fresh water (Swamps)—The region is continuously or seasonally submerged by freshwater and commonly seen in the lower sections of rivers and near freshwater.
- Zone (2): Vegetation—The region is covered by plants.
- Zone (3): Mining Land—The region that used for the extraction of valuable minerals.
- Zone (4): Pond and Lake—The region that comprise of freshwater and living creatures.
- Zone (5): Building—The area covered by building.

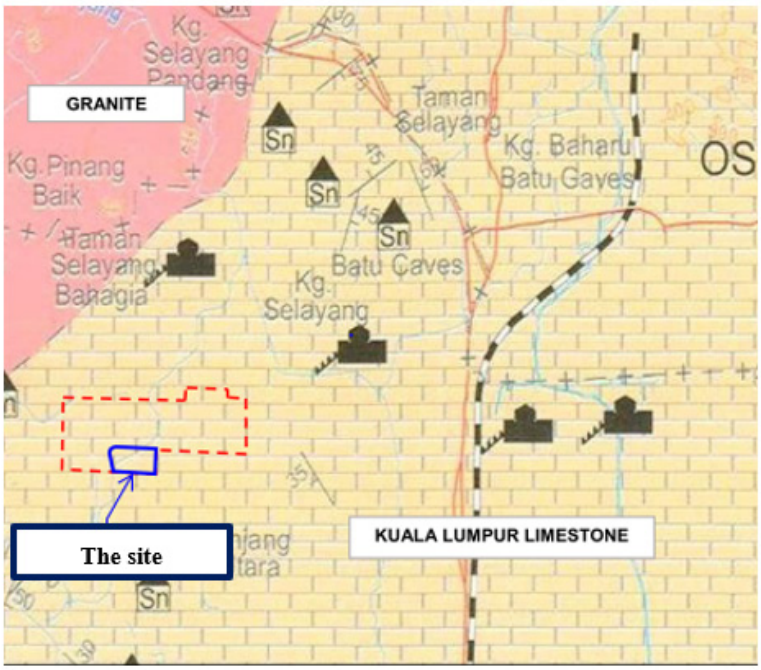

Figure 1. Geological map of the site.

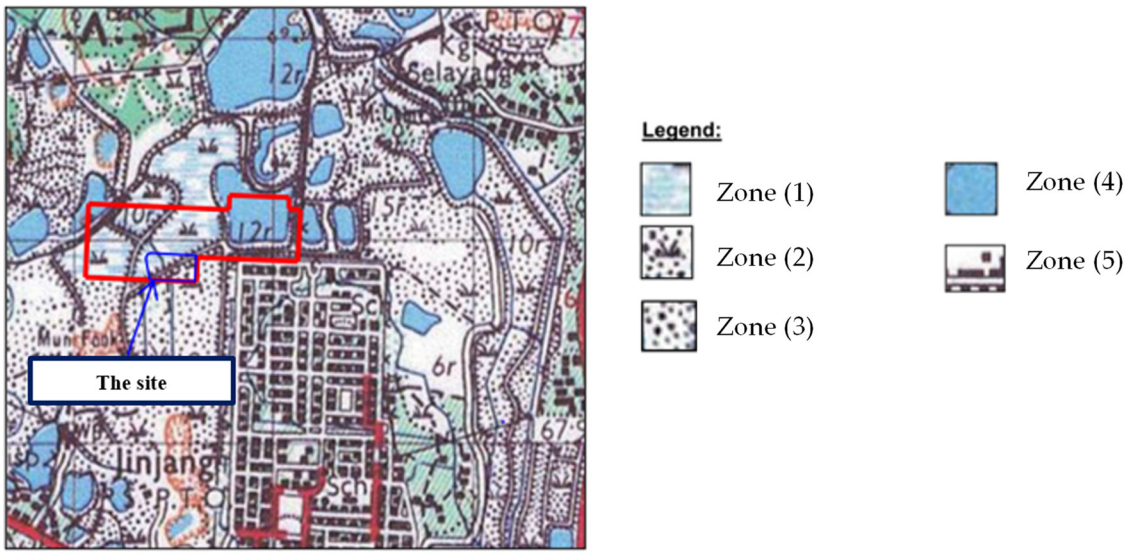

Figure 2. Topography map of Kuala Lumpur and the studied region.

The topography of the site is relatively flat ground, with the level of the ground ranging from about RL 55 m to RL 57.5 m. The site was proposed for the construction of high-rise buildings, with two towers of approximately 150 m in height and an eight-story car park. Therefore, deep foundations are necessary to withstand the structural load. The Jack-in installation method of pre-cast spun piles was the foundation of this development. Therefore, subsurface investigations have been carried out at the site to identify the ground condition. A total of 26 boreholes were investigated in order to determine the subsoil condition of the site. From the boreholes, the overburden of the site is mostly silt and clay material, with the SPT-N in the range of generally less than 10, as displayed in Figure 3.

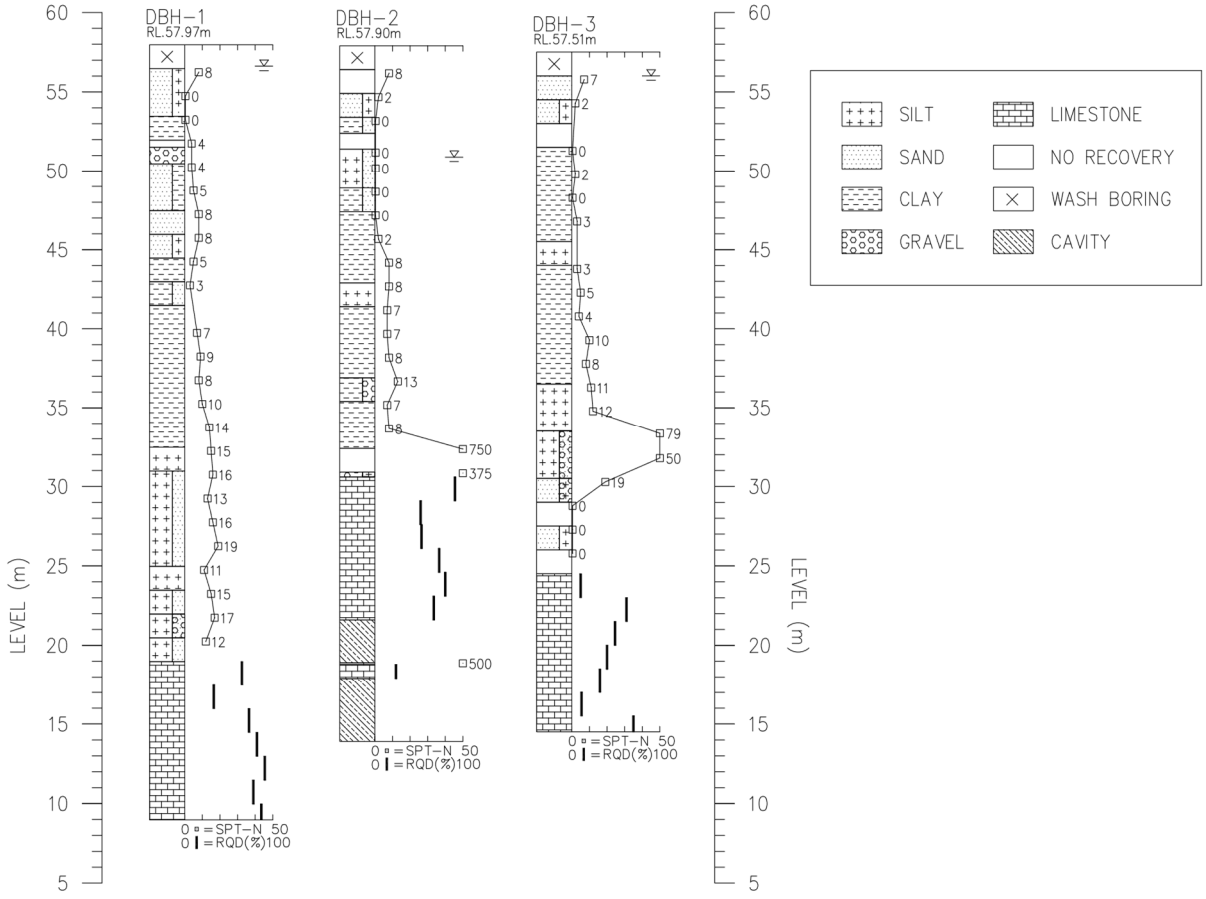

Figure 3. Example of three (3) boreholes soil profile of the ground with different geo-material and their SPT-N values.

SLT tests were carried out on the first installed piles to verify the pile design capacity. However, since SLT tests are expensive and time-consuming, the number of these tests is limited. Nevertheless, a total of 130 piles were selected to carry out HSDT. During the process of HSDT, a hydraulic hammer is dropped on the pile head with cushion and the force with velocity at the upper end of the pile are measured followed by a signal matching procedure. The HSDT is carried out on-site by testers who use a PDA system for data collection. Prior to the test, the soil around the test pile was excavated to ease the installation of transducers at about 1.5-3 times the pile's diameter from the pile head. A total of two strain and two accelerometer transducers were attached to opposite sides of each other close to the pile top, as shown in Figure 4. The applied load from the hammer drop was derived from the Strain transducers which act as strain measurements when the load is applied from a hammer drop on the pile head, whereas the movement of the pile head is measured by accelerometers during the impact.

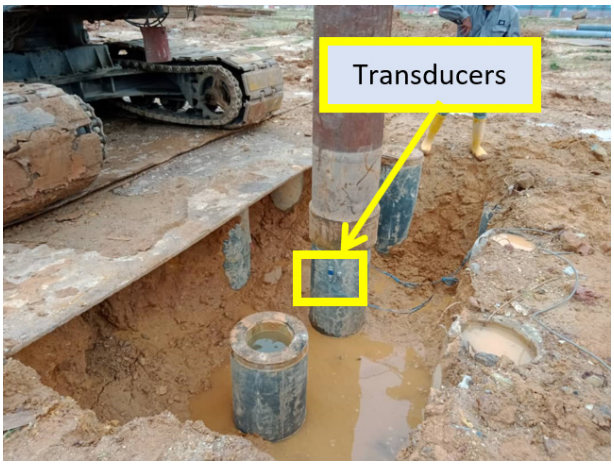

Figure 4. Indication of transducers on the piles.

When evaluating a model, the importance and contribution of parameters on the pile bearing capacity are significant. This can be extracted from the empirical equations or the statistical-based techniques. For example, as shown in Table 1, the SPT-N parameter is considered as an important factor in this regard. Apart from the empirical equations, several researchers have carried out sensitivity analyses on the influential parameters on the pile bearing capacity. Momeni et al. [26] stated that the weight of the hammer and pile geometrical properties, such as pile length and cross sectional area, have the highest impact on the pile bearing capacity. Ghorbani et al. [64] performed the sensitivity index of each parameter (pile shaft and tip area, the average cone tip resistance along the embedded length of the pile, the average cone tip resistance over the influence zone and the average sleeve friction along the embedded length of the pile which are obtained from CPT data) and found that pile soil surface area is the most contributing parameter. In another study, Pham et al. [66] found that average value of SPT-N number along the embedded pile length is the most crucial parameter in terms of pile capacity. Pile cross sectional area and length parameters were introduced as the most effective variables in another interesting study in the pile capacity estimation conducted by Momeni et al. [8].

According to the above discussion, and the available data for collection on the site, a total of six parameters, including pile diameter, hammer weight, pile length, hammer drop height, SPT-N average and pile friction bearing capacity (shaft friction) were measured on the site while conducting pile tests and from the borehole data. In order to calculate the SPT-N average for each pile, the zoning of the nearest SI to the pile test was considered. Subsequently, the SPT-N average of each pile was calculated based on the nearest SI work and varied according to the pile length. The mentioned parameters were collected for a total of 130 piles, which resulted in 130 data samples comprised of all six parameters. The next step is the identification and removal of outliers where outliers can be known as data that were significantly different from the observed data. This process is considered as a mandatory step when the data quantity is large, which is the case with the data in this study. With the presence of outliers, the database of variability will be increased, which can cause possible modeling errors. In this study, the statistical approach, which is based on the interquartile range rule, was used to identify outliers and these outliers were removed from the database. The interquartile range is the range between the first and third quartiles, namely Q1 and Q3. Any of the data that are smaller than Q1-1.5x interquartile range or higher than Q3 + 1.5 x interquartile range are considered outliers.

Eventually, five data samples were reduced from the whole 130 datasets and the used data samples reached 125 data samples. More information about these parameters can be found in Table 3. Among these factors, as highlighted in this study, the pile friction bearing capacity was considered as model output and the remaining factors were set as predictors.

However, the model predictors will be analyzed to select the most effective ones later in this paper.

Table 3. The parameters measured during conducting pile tests and from the boreholes data.

Parameter	Unit	Range
Pile Length	m	18.5–47
Hammer Drop Height	m	0.55–1.1
Pile Diameter	mm	400–450
Hammer Weight	Kg	7000
SPT-N Average	-	4–17
Pile Friction Bearing Capacity	kN	2028–4844

2.2. Decision Tree (DT)

ML involves algorithms that use historical data with independent and target variables to learn and produce decisions by referring to a certain objective. One of the advantages of ML techniques, in comparison with conventional statistical approaches, such as regression, is that they are applicable for more than two-dimensional data. Many researchers have used tree-based techniques for data-driven prediction analysis for various geotechnical problems [68,69]. Thus, in this study, tree-based ML algorithms, such as DT, were applied to construct models and identify the crucial predictors of pile soil friction. DT can be represented graphically, displaying certain decision conditions with the complex branching that happens in a constructed decision. This approach is one of the top and most widely used supervised learning algorithms for predicting the accuracy of a model.

DT is able to carry out all tasks related to recognition, classification and prediction issues. DT is a "tree" shaped model that comprises of a series questions, with each question being described by various variables. A real tree consists of roots, branches and leaves. Similarly, the graph for DT is comprised of nodes, which are leaves, and branches that represent connections between nodes [70]. During the process of DT, a variable is selected as a root, which is known as the first node. The first node is separated into multiple internal nodes by referring to the appointed features. DT is a top-down tree, with the roots is located at the top. The final product of the branches consists of roots, branches and nodes [71]. Every node can be separated into two branches and each node has a relation to a certain characteristic and branches that have been described by a specific range of input. A flowchart related to DT technique is shown in Figure 5.

2.3. Random Forest (RF)

RF is a method that based on several DTs with boostrap aggregation and is one of the supervised ensembles ML approaches. It is also a part of ensemble learning that is based on a bagging algorithm. RF comprises of three (3) main attributes, which are presented as follows [72,73].

1. Automatically provide estimation of missing value.
2. Weight data to balance the errors found in imbalanced data.
3. Determine the crucial variables by estimation for classification.

In comparison with bagging, during the process of constructing each tree, RF utilizes random sample prediction before each node segmentation in order to reduce bias. Every DT is generated in parallel by RF and these trees can be classification or regression trees. At each constructed DT, each note is separated using the best features that can generate the most optimal solution among all of the attributes. The RF algorithm is a well-known method used to extract useful but hidden information within huge amounts of data. Figure 6 shows the process of the RF algorithm in modeling an output parameter.

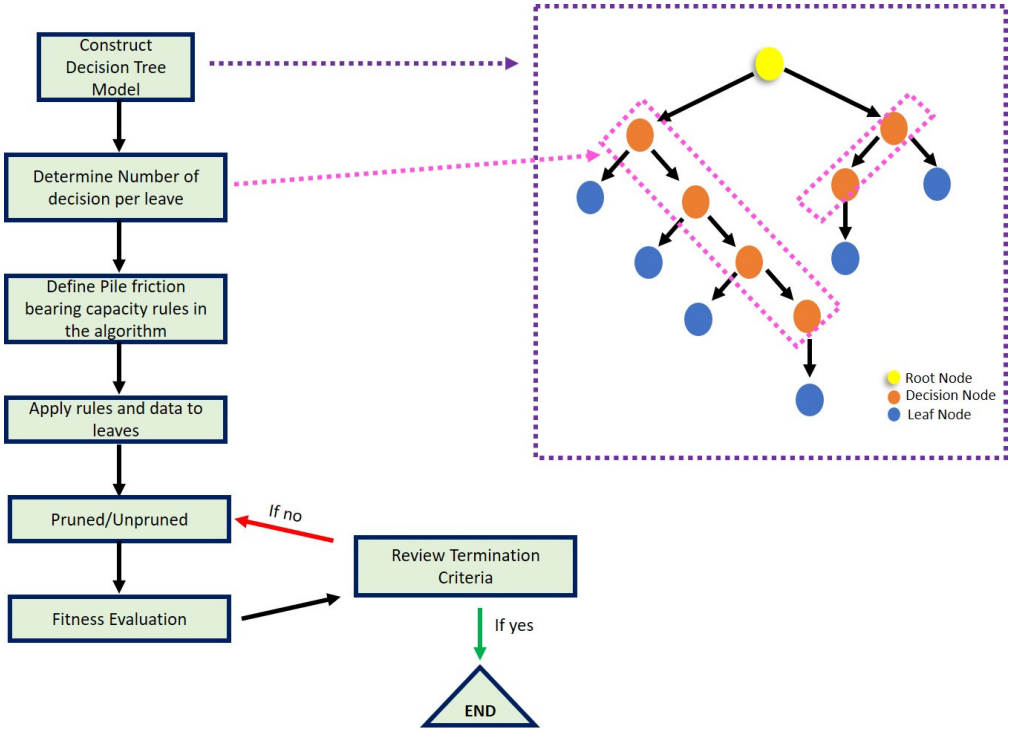

Figure 5. A Flowchart of DT technique for prediction purposes.

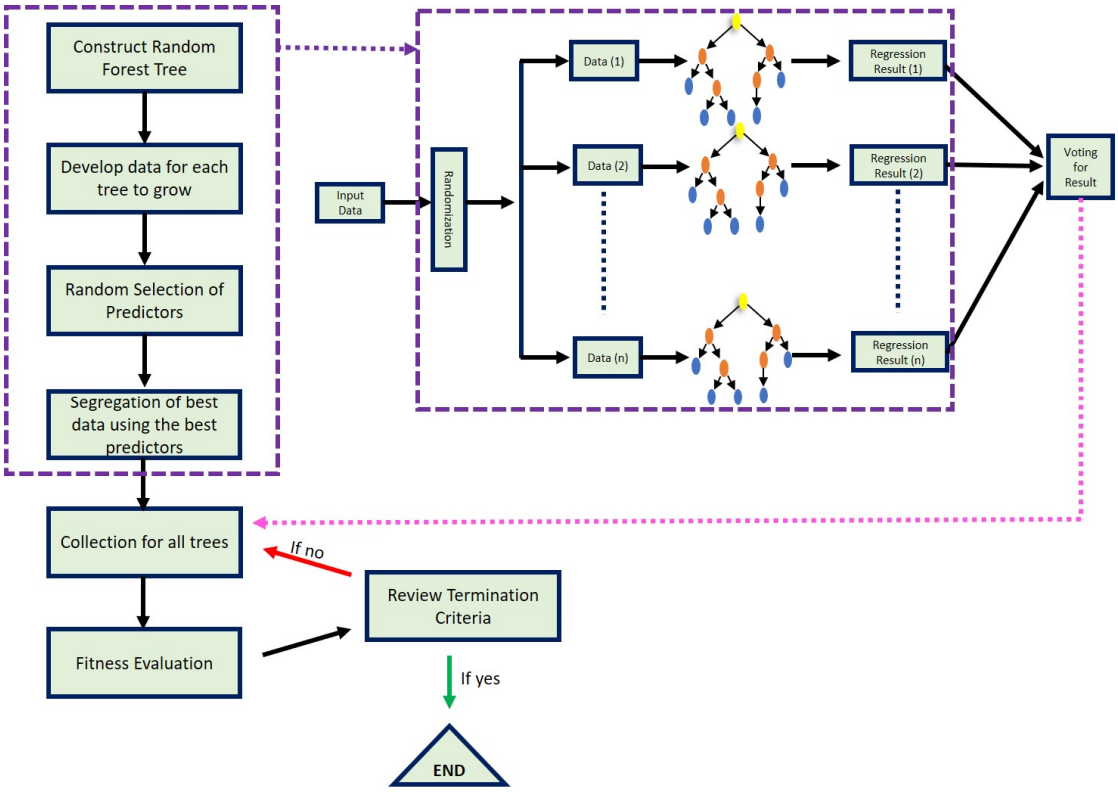

Figure 6. A Flowchart of RF technique for prediction purposes.

2.4. Gradient Boosted Tree (GBT)

A GBT is one of the tree-based methods that works on the principle of boosting. The models with low variance errors and high bias are combined with the purpose of lowering the bias and, at the same time, maintaining low variance [74]. Boosting is the process by

which it learns several classifiers by altering the sample weight for every process of training. All of the classifiers are combined linearly to enhance the classification performance. Unlike other tree-based methods, this approach uses similar training datasets in boosting. Similar datasets are trained and constructed as shallow trees in boosting trees but every tree has a different specific feature of the relationships between inputs and outputs. The objectives of the (n)th shallow tree are trained in series to reduce the prediction errors from the previous $(n-1)$th trees. The objective of GBT is to form a supplementary model that reduces the loss function. The process of the GBT method is described as follows:

1. A constant value is begun in the model to lower down the loss function.
2. During the iteration of training process, the residual value of the model is estimated from the negative gradient of the loss function.
3. The current residual value is fit by newly trained regression tree.
4. The combination of final regression with past models and residual is updated.
5. When the maximum number of iterations set by the user is achieved, the iteration in the algorithm is ceased.

Overall, the GBT model is able to improve the previous poorly executed data by continuously using a regression tree to fit the residual. The applications of this technique have been highlighted in several problems related to geotechnical engineering [74–77]. A GBT flowchart in modeling a predictive technique is displayed in Figure 7.

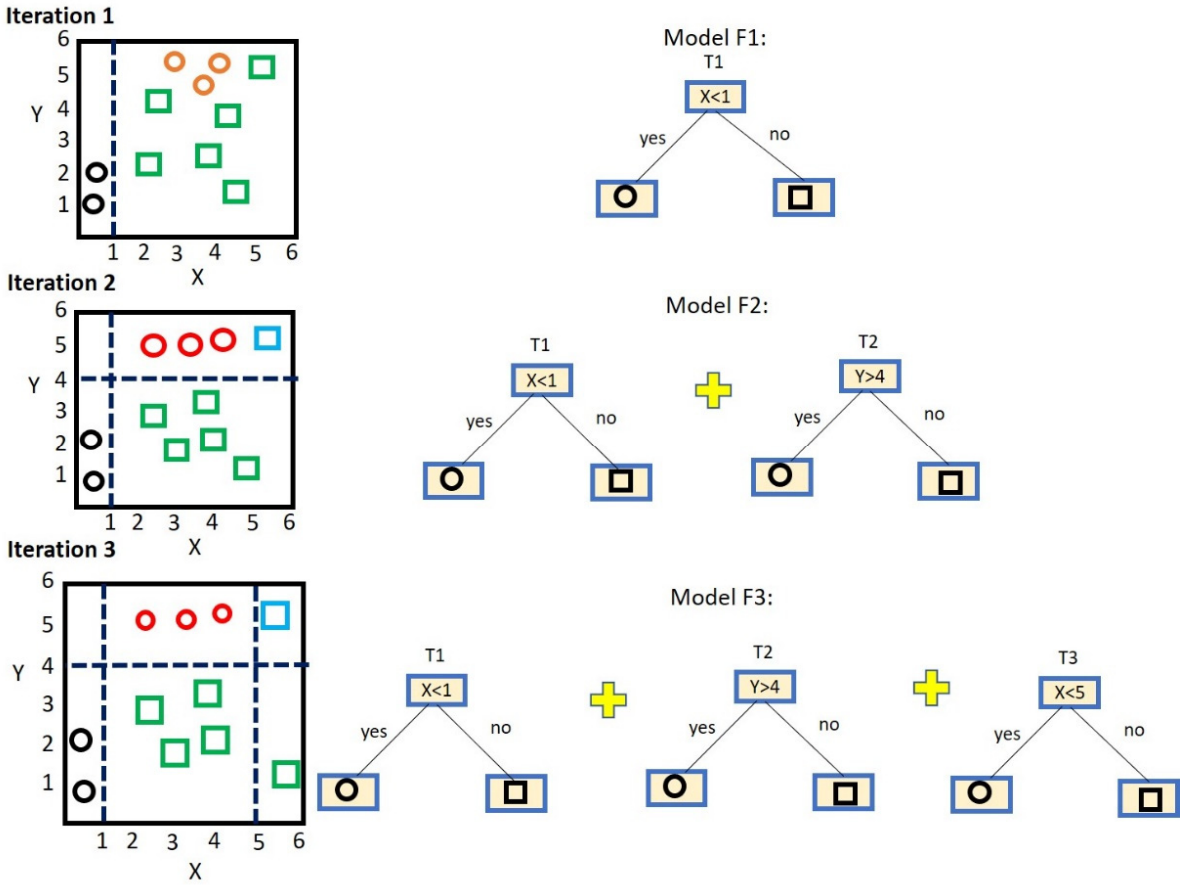

Figure 7. A GBT flowchart in modeling a predictive technique.

2.5. Performance Indices

Evaluation of the models in ML is a way of assessing the size effect in conventional statistics [78]. The ability of a model to predict for an unknown sample is a critical step in ML that increases trust in the model for use on other datasets. The accuracy, in terms of percentage, is the measurement for model evaluation. The authors of this study decided to

use several important performance indices, including root mean square error (RMSE), R^2, and absolute error. Willmott and Matsuura [79] stated that the total square error is affected by the larger error, rather than the minor error. When the variances associated with the frequency distribution of error magnitudes increase, the error values will be increased. The mentioned performance indices were utilized and computed in different studies and their formulas and process of calculation can be found in the literature [80–83]. In this study, the mentioned performance indices will be used to evaluate the model's prediction capacity.

2.6. Study Steps

This study was planned to introduce a process of modeling and a superior tree-based model for solving a problem related to piling technology. The prediction of the pile capacity is always important for geotechnical engineers right after pile installation, because the measurement of this parameter needs specific equipment and its setting in the site, which is not easy to do. In addition, conducting such tests are costly and sometimes includes human and machine errors [26]. The modeling process of this study was started by identifying and removing the outliers. The next step is related to feature selection or input selection so that the most effective parameters will be selected. In this way, the supervised and unsupervised feature selection methods will be utilized. After selecting the model predictors, three model trees, i.e., DT, RF and GBT, will be conducted to predict friction pile bearing capacity. These models' trees and their performance capacities will be assessed and discussed. The best tree model will be selected and introduced based on both model development and model assessment. A schematic diagram of the study steps is presented in Figure 8.

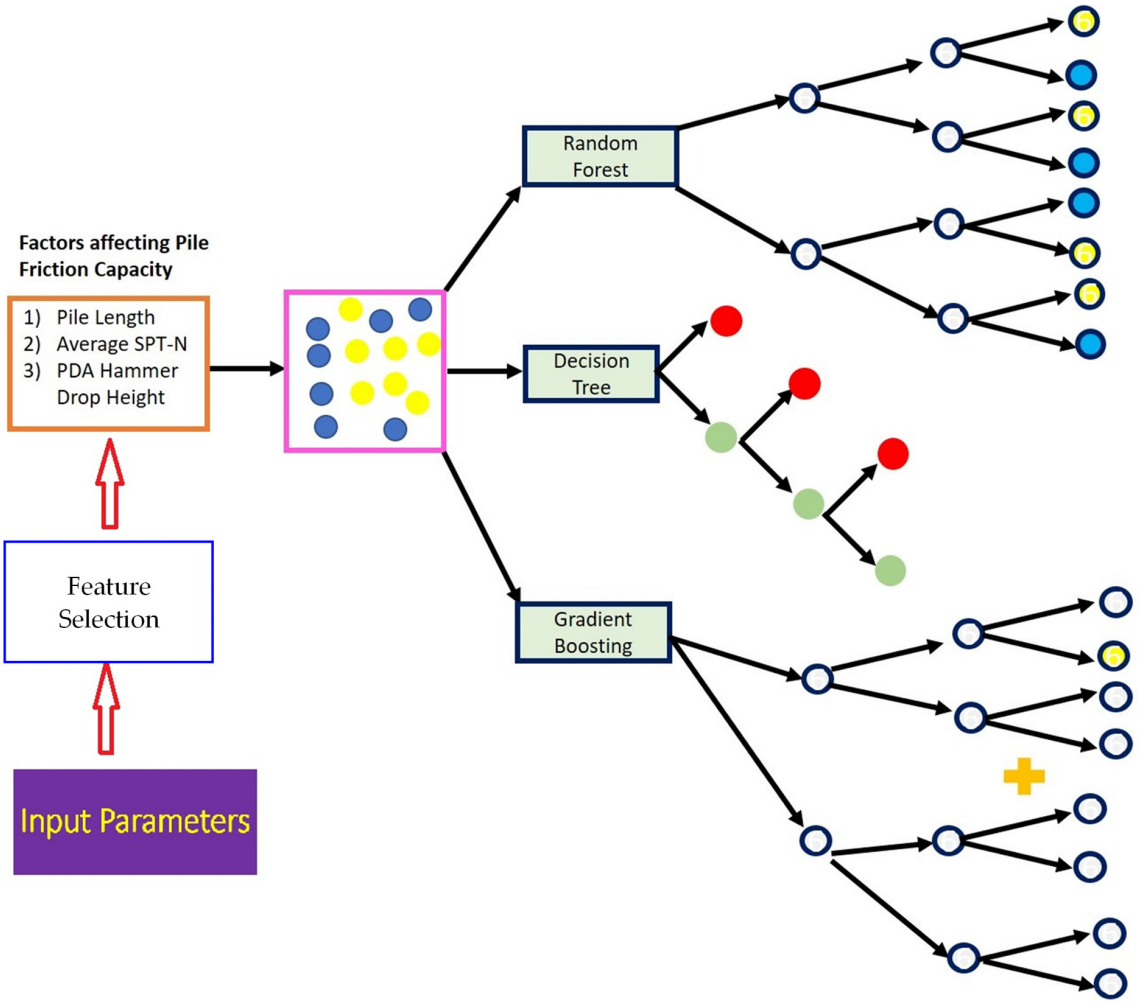

Figure 8. The process of this study to predict pile capacity.

3. Input Selection

Feature/input selection is an alternative to identifying significant factors in conventional statistics using measures of confidence interval and hypothesis testing. After performing model evaluation, the elements (independent variables) need to be explored further in terms of how they contribute to the accuracy measure. This technique removes variables that are insignificant or highly correlated with any other variable. The rank of variables based on importance score can be visualized to understand the prediction accuracy. The supervised and unsupervised feature selection methods differ in terms of the target variables. The supervised learning model needs a target variable to determine the important variables, while unsupervised learning ignores the target variable and selects important variables based on correlation. In the following sub-sections, supervised and unsupervised feature selection methods will be applied and their results will be discussed.

3.1. Correlation

Table 4 presents the correlations between the used input variables. Since the purpose of this study is to predict the shaft friction or pile friction bearing capacity, variables with strong positive correlation were considered for developing the final model. According to correlation analysis, pile capacity and pile length are highly positively correlated (0.794). The correlation of hammer weight with other variables is not reported in Table 4, which indicates no correlation between this variable and other variables. It should be noted that, in the database, there is only one value for the hammer weight and, because of this issue, this parameter was removed from the analysis of the correlation technique.

Table 4. Correlations between the independent variables.

Attributes	Hammer Drop Height Test	Pile Diameter	Pile Length	Shaft Friction	SPT-N Average
Hammer Drop Height Test	1	0.358	0.504	0.476	−0.025
Pile Diameter	0.358	1	0.103	0.436	0.207
Pile Length	0.504	0.103	1	0.794	−0.030
Shaft Friction	0.476	0.436	0.794	1	0.036
SPT-N Average	−0.025	0.207	−0.030	0.036	1

3.2. Supervised Feature Selection

This study adopts different feature selection methods to select only important variables and develop a prediction model based on the selected variables. The main reason behind reducing the number of variables (based on their level of importance and correlations) is to decrease the complexity and improve the applicability of the final model. Armaghani et al. [84] stated that a lower number of model inputs is considered as an advantage for the developed models, since the model complexity cannot be minimized. After conducting unsupervised clustering and understanding the correlation of the variables, it was compared the variables' importance based on three different tree-based supervised ML techniques. The importance of variables based on GBT, RF and DT results are shown and compared in Table 5. According to this table, pile length is indicated as the most important variable based on all three techniques. On the other hand, hammer weight does not have any impact on pile capacity. These results are in line with correlation analysis results, too. In addition, in order to make a better conclusion out of three feature selection methods, weight values of each variable were summed up and compared, as shown in Figure 9. The accumulated weight values were then sorted out from highest to lowest values. It can be concluded from Figure 9 that pile diameter and hammer weight is not significant enough to be considered as model inputs. Therefore, the authors decided to not consider these two attributes for developing the final predictive models in this research. However, it is

necessary to note that there are only two values of pile diameters in the provided database. Therefore, the impact of this parameter is not significant in our database (Figure 9). In general, pile geometry is considered as a significant predictor category for prediction of the pile capacity, as suggested in the literature [28,85] and it is suggested to use pile diameter as a model input with various values in future studies.

Table 5. Importance score (weight) of variables based on three supervised ML methods.

GB		RF		DT	
Attribute	**Weight**	**Attribute**	**Weight**	**Attribute**	**Weight**
Pile Length	0.75	Pile Length	0.80	Pile Length	0.35
SPT-N Average	0.125	SPT-N Average	0.17	Pile Dimeter	0.04
Hammer drop height test	0.031	Hammer drop height test	0.11	Hammer drop height test	0.037
Pile Dimeter	0.030	Pile Dimeter	0.025	SPT-N Average	0.018
Hammer Weight	0.00	Hammer Weight	0.00	Hammer Weight	0.00

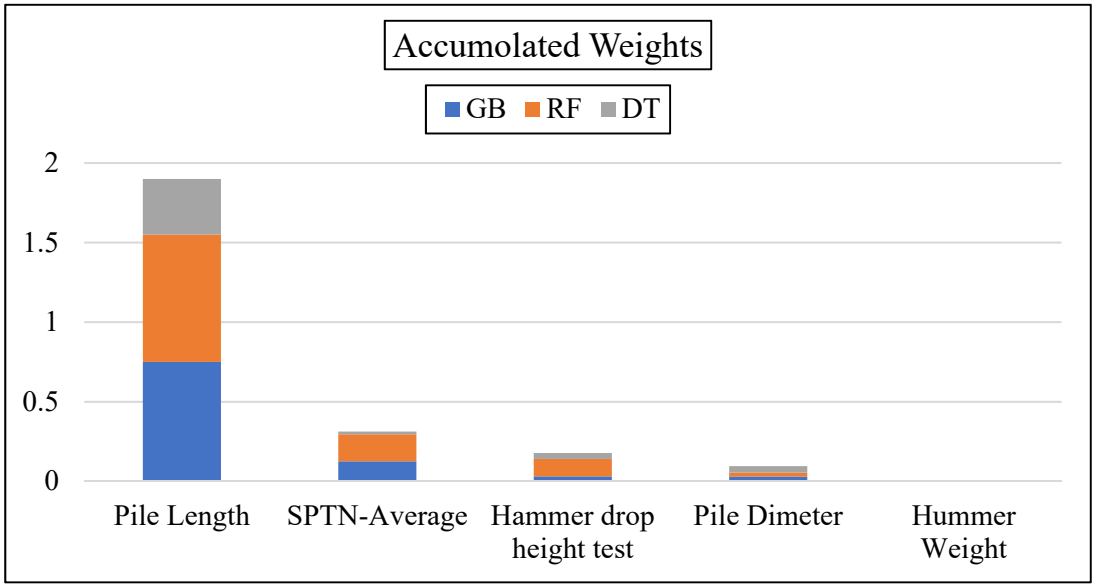

Figure 9. Accumulated weights of variables.

4. Modeling and Results

In order to have an accurate model proposal, both model development and model evaluation parts should be at an acceptable level. In the first stage of modeling all data samples were normalized using the following equation in the range of [0–1]:

$$Z = \frac{X - min(X)}{max(X) - min(X)} \quad (2)$$

where, X presents each parameter that needs to be normalized (i.e., each input and output), $min(X)$ and $max(X)$ are the minimum and maximum values of whole data of that specific parameter, respectively.

For this purpose, there is a need to divide the whole database into two groups: train and test. In this study, among all of the available suggestions in the literature, the authors decided to use a combination of 80–20% for train and test phases, respectively. Therefore, before starting the modeling, all 125 data samples were divided to 25 and 100 data samples for model evaluation and model development, respectively. As discussed

before, three tree-based ML techniques were employed to determine the most accurate model for predicting the pile friction bearing capacity. To do this, several parametric investigations were performed for different parameters of DT, RF and GBT techniques. In these analyses, three and five model inputs were utilized. Finally, the model performance results with three and five input variables are presented in Tables 6 and 7, respectively. In these tables, train and test results of R^2, RMSE and absolute error were presented. According to the results, GBT technique achieved the highest accuracy rate for both models with five and three variables, with R^2 equal to 0.911 and 0.901, respectively, for training datasets in predicting pile friction bearing capacity. In addition, the GBT model achieved the lowest RMSE and absolute error compared to the RF and DT models. The next best model after GBT is related to RF for three and five input variables, followed by the DT model. The R values of (0.813 and 0.761) and (0.773 and 0.712) were obtained for testing data samples of RF and DT techniques for three and five model inputs, respectively. It is obvious that the results obtained by the GBT technique are more accurate compared to the RF and DT models for both three and five input parameters.

Table 6. Models evaluation results using five input variables.

Technique	Train			Test		
	R^2	RMSE	Absolute Error	R^2	RMSE	Absolute Error
GBT	0.911	0.073	0.052	0.841	0.089	0.098
RF	0.892	0.082	0.073	0.813	0.071	0.100
DT	0.861	0.135	0.121	0.773	0.121	0.167

Table 7. Models evaluation results using three important input variables.

Technique	Train			Test		
	R^2	RMSE	Absolute Error	R^2	RMSE	Absolute Error
GBT	0.901	0.094	0.077	0.816	0.127	0.098
RF	0.881	0.095	0.081	0.761	0.081	0.100
DT	0.853	0.170	0.152	0.712	0.130	0.167

As was expected, the accuracy of the models decreased by decreasing the number of variables after feature selection. However, considering the train results of the GBT technique, the accuracy reduction is not significant (only 1%). For testing data, the GBT results based on R^2 are 0.841 and 0.816 for three and five models, respectively, which show a close model accuracy when three input parameters are used. Therefore, as discussed before, proposing a new predictive model with a lower number of model predictors is of importance in the area of piling and geotechnical engineering. The other researchers and designers can easily use a simpler model because they need a lower number of parameters to be measured. Therefore, in this study, the authors decided to propose and introduce a predictive model with lower model inputs, even though it has lower performance prediction results. Hence, the results presented in Table 7 will be considered in this study and, as such, the GBT model for three inputs will be discussed in more detail in the following paragraphs.

After reducing the number of variables through the feature selection process, the GBT model was conducted using three important selected variables. Table 8 presents the importance of input variables using the GBT technique with the final three variables. The importance values of 0.81, 0.21 and 0.075 were obtained, respectively, for pile length, SPT-N average, and hammer drop height. According to the results, pile length, with an importance of 0.81, plays the most important role in predicating pile friction bearing capacity using the GBT technique. On the other hand, hammer drop height has the lowest impact on the model output, which is the pile capacity.

Table 8. GBT importance of variables.

Attribute	Weight
Pile Length	0.81
SPT-N Average	0.21
Hammer drop height	0.075

In modelling GBT, there were many models constructed in order to see the difference between different parameters of GBT on the system performance. As presented in Table 9, 27 GBT models were built in this study with different properties in order to predict pile bearing capacity. In these 27 models, the authors considered different values for the number of trees, maximum depth and learning rate in the modeling. In addition, error results are presented in Table 9 for each GBT model. As a result, the optimal/best model is achieved when the number of trees is 90 with a maximum depth of two and 0.1 learning rate (i.e., GBT model number 20). The lowest error rate of 0.1889 and the highest accuracy (R values of 0.901 and 0.816 according to Table 7) were observed at the described point. Figure 10 shows the schematic tree generated by the proposed GBT model. More discussions regarding this technique will be given in the next section.

Table 9. Different GBT models to predict pile friction bearing capacity.

GBT Model No.	No. of Trees	Maximal Depth	Learning Rate	Error Rate
1	30	2.0	0.001	0.2891
2	90	2.0	0.001	0.2814
3	150	2.0	0.001	0.2745
4	30	4.0	0.001	0.2891
5	90	4.0	0.001	0.2814
6	150	4.0	0.001	0.2745
7	30	7.0	0.001	0.2891
8	90	7.0	0.001	0.2814
9	150	7.0	0.001	0.2745
10	30	2.0	0.01	0.2597
11	90	2.0	0.01	0.2366
12	150	2.0	0.01	0.2189
13	30	4.0	0.01	0.2597
14	90	4.0	0.01	0.2370
15	150	4.0	0.01	0.2209
16	30	7.0	0.01	0.2597
17	90	7.0	0.01	0.2370
18	150	7.0	0.01	0.2209
19	30	2.0	0.1	0.1986
20	90	2.0	0.1	0.1889
21	150	2.0	0.1	0.1953
22	30	4.0	0.1	0.1985
23	90	4.0	0.1	0.1912
24	150	4.0	0.1	0.1955
25	30	7.0	0.1	0.1985
26	90	7.0	0.1	0.1912
27	150	7.0	0.1	0.1955

Figure 10. GBT model tree using three variables.

5. Discussion

In this study, a series of experimental data were measured and recorded during SLT tests, and the capacity values of friction piles, together with some other important parameters on them, were collected. The idea was to propose a series of fully tree-based techniques, i.e., DT, RF and GBT, for estimation of the pile bearing capacity. Through feature selection, in order to propose a simpler model, the three most important parameters were identified as pile length, SPT-N average and hammer drop height. The mentioned tree-based models were then built to predict pile friction bearing capacity. In order to construct DT, RF and GBT models, many attempts have been made to achieve higher performance capacities based on the used statistical indices. These attempts were performed by setting different values for the most influential DT, RF and GBT parameters. As expected, the developed GBT model was able to provide a better performance capacity in estimating the actual results of pile friction bearing capacity. The training and testing results of the proposed GBT model are presented in Figures 11 and 12, respectively. It is important to note that the pile capacity values presented in these figures are normalized between [0–1], as described previously. The R^2 and other statistical indices are presented in these figures, which confirms that the GBT is a powerful tree-base technique in both phases of model development and model evaluation. RMSE results and absolute error results of (0.094, and 0.077) and (1.27, and 0.098) for train and test data samples, respectively, reveal that the GBT tree model is applicable in the field of piling and deep foundation. It is able to predict pile bearing capacity values with a low level of system error, which is of importance and advantage in the geotechnical engineering field.

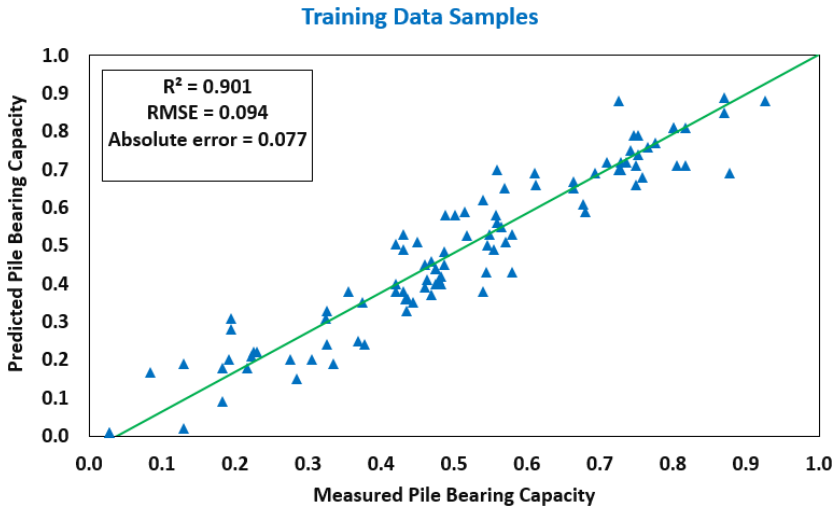

Figure 11. Statistical indices results of GBT for model development part.

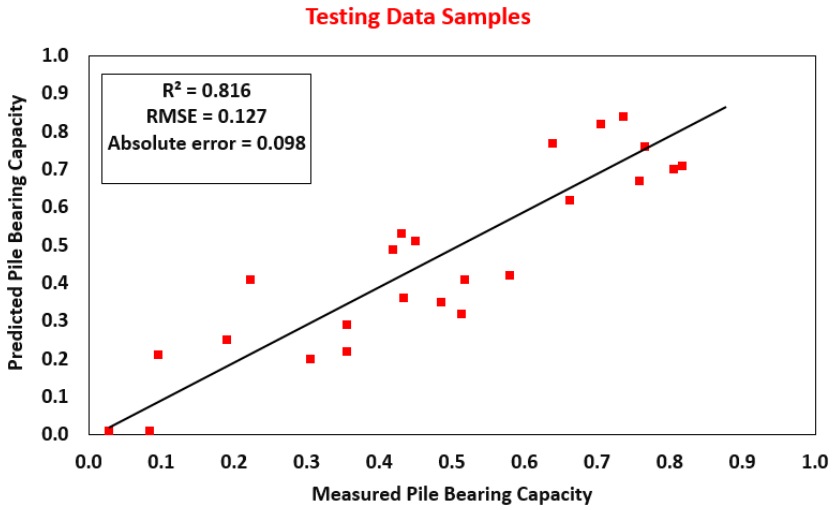

Figure 12. Statistical indices result of GBT for model evaluation part.

Compared to the previous ML related studies, this study focuses on only tree-based ML techniques. To date, only a few researchers have proposed similar techniques in this regard. The developed GBT model in this study was based on only three input parameters, and based on these three inputs, the GBT model provided R^2 values of 0.901 and 0.816 for the train and test phases, respectively. The results of the GBT model are not better than many of the relevant studies presented in Table 2. However, as presented in Table 2, most of the studies used five or more input parameters to predict the pile bearing capacity. This makes them complicated models for further use by other researchers. This is because they have to provide the related values for all inputs if they want to use the proposed models. Nevertheless, in this study, the presented results were constructed based on only three model inputs/predictors. In other words, the proposed GBT technique in this study is easier to implement by other researchers, designers, or engineers. Hence, the modelling process and the proposed GBT model in this study can be suggested as a reliable and applicable technique/process with a high level of accuracy in forecasting pile bearing capacity.

It is good to know that the GBT model can depict the promising accuracy of the prediction, provided that this study is carried out for different types of soils, piles, installation methods, and types of hammers. This study was carried out with limited data with one hammer weight, two types of pile dimension, an SPT-N value of generally about 10, and one installation method. Thus, it is highly recommended to further carry out this study with more variables in order to provide higher accuracy of the prediction.

6. Optimum Parameters Based on Simulation Model

In order to gain deeper insight into the factors affecting pile capacity, sensitivity analysis was conducted based on a desirable scenario: what is the optimal value of independent variables in order to gain the maximum pile friction bearing capacity? The simulation-based sensitivity analysis was conducted using RapidMiner Studio Educational Software version 9.8.001. The graphical results in this section are the outputs of the RapidMiner Software. The RapidMiner software conducts the tree-based models under the Python software environment. The optimization was run and determined the best input variables to meet our target under the specified constraints. In addition, the simulation-based sensitivity analysis is suitable for assessing and answering "what if" questions. Table 10 presents the optimal values of attributes based on the described scenario.

Table 10. Optimized value of attributes based on maximum scenario.

Attribute	Optimum Value (Normalized)	Optimum Value (Actual)	Maximum Pile Capacity
Pile Length	0.90	44	4844
Hammer Drop Height	0.419	1.1	
SPT-N Average	0.702	6	

According to the simulation-based optimization results, pile friction bearing capacity will be equal to 4844, when pile length, hammer drop height and SPT-N average are equal to 44, 1.1 and 6, respectively (Figure 13). These values are the optimum values (not maximum) of independent variables in order to achieve the maximum pile capacity values. For example, the optimum value for pile length is 44, which is almost equal to the maximum value (0.90 as normalized). Therefore, pile capacity will be decreased after this amount of pile length.

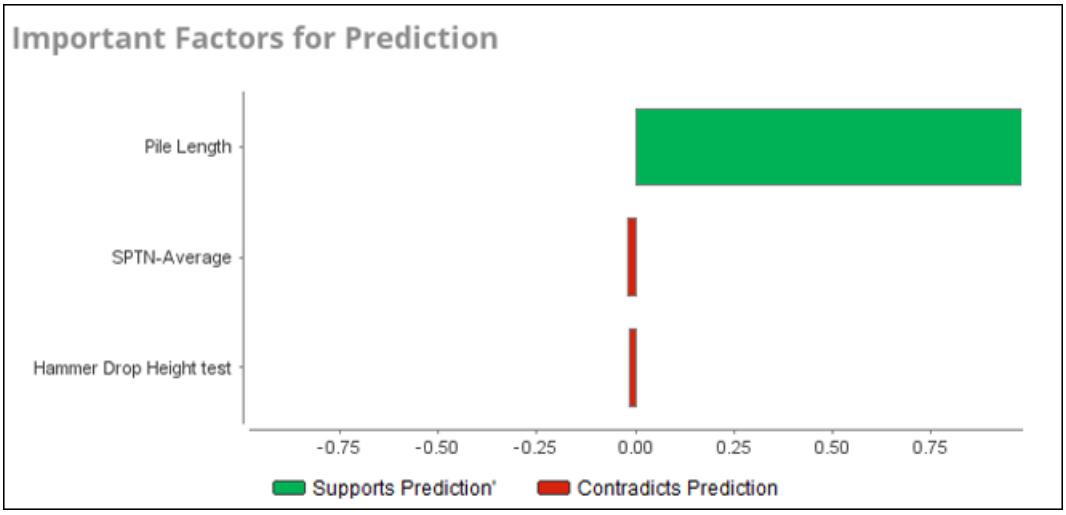

Figure 13. Optimization results and importance of variables.

7. Summary and Conclusions

The purpose of this research is to propose a more accurate and applicable model/approach for predicting pile friction bearing capacity, which is fully tree-based with a limited number of model inputs/predictors. To achieve this aim, first, among the initial five input variables, the three most effective ones, i.e., pile length, SPT-N average, and hammer drop height, were selected for the modelling part, based on a comprehensive feature selection process. Three tree-based techniques, i.e., DT, RF and GBT, were then built to estimate pile friction bearing capacity. In building these models, a series of parametric investigations based on their effective variables were planned and performed in order to obtain the best model in each category. In the next step, model assessment has been done using different performance prediction indices, and their results have been compared to each other. Overall, the findings demonstrated the successful application of tree-based techniques for the purpose of this paper. However, the best tree model was related to GBT with R^2 values of 0.901 and 0.816 for model development and model assessment parts, respectively. It should be noted that the other tree-based models received acceptable and applicable results for prediction of pile friction bearing capacity. The parametric study results showed that the optimum values of pile length, hammer drop height and SPT-N average are 44, 1.1, and 6, respectively, in order to get the maximal pile capacity values. The proposed tree-based techniques and their processes are easy to implement and can be

used by other researchers and designers to obtain very accurate pile capacity values for similar conditions. However, other researchers can prepare a larger database for the same problem and develop more comprehensive tree-based techniques, or even a combination of these techniques with new optimization techniques, such as the sparrow search algorithm, in order to achieve a higher accuracy level.

Author Contributions: Conceptualization, D.J.A., C.Y.H.; methodology, C.Y.H., D.J.A., S.M.H.M.; software, C.Y.H., D.J.A., S.M.H.M.; formal analysis, C.Y.H., D.J.A., S.M.H.M., S.H.L.; writing—original draft preparation, C.Y.H., D.J.A., S.M.H.M., S.H.L., A.S.M., M.M., D.V.U.; writing—review and editing, C.Y.H., D.J.A., S.M.H.M., S.H.L., A.S.M., M.M., D.V.U.; supervision, D.J.A., D.V.U., S.H.L., M.M., A.S.M.; Data curation, C.Y.H. All authors have read and agreed to the published version of the manuscript.

Funding: The research was funded by Act 211 Government of the Russian Federation, contract No. 02.A03.21.0011.

Institutional Review Board Statement: Not applicable.

Informed Consent Statement: Not applicable.

Data Availability Statement: The data are available upon request.

Acknowledgments: Authors of this study wish to express their appreciation to the University of Malaya for supporting this study and making it possible.

Conflicts of Interest: The authors declare no conflict of interest.

References

1. Viggiani, C.; Mandolini, A.; Russo, G. *Piles and Pile Foundations*; Spon Press: London, UK, 2012; p. 278, ISBN 1498725538.
2. Torshizi, M.F.; Saitoh, M.; Álamo, G.M.; Goit, C.S.; Padrón, L.A. Influence of pile radius on the pile head kinematic bending strains of end-bearing pile groups. *Soil Dyn. Earthq. Eng.* **2018**, *105*, 184–203. [CrossRef]
3. Ma, Y.; Deng, N. Deep foundations. *Substruct. Des.* **2014**, *239*, 18.
4. Vesic, A.S. *Design of Pile Foundations. National Cooperative Highway Research Program Synthesis of Practice no. 42*; Transportation Research Board: Washington, DC, USA, 1977; p. 3248.
5. Helwany, S. *Applied Soil Mechanics with ABAQUS Applications*; John Wiley & Sons: Hoboken, NJ, USA, 2007; ISBN 0471791075.
6. Liu, Y.J.; Liang, S.H.; Wu, J.W.; Fu, N. Prediction method of vertical ultimate bearing capacity of single pile based on support vector machine. *Adv. Mater. Res.* **2011**, *168–170*, 2278–2282. [CrossRef]
7. Shah, D.L.; Shroff, A.V. *Soil Mechanics and Geotechnical Engineering*; CRC Press: Boca Raton, FL, USA, 2003; ISBN 9058092356.
8. Momeni, E.; Nazir, R.; Armaghani, D.J.; Maizir, H. Application of artificial neural network for predicting shaft and tip resistances of concrete piles. *Earth Sci. Res. J.* **2015**, *19*, 85–93. [CrossRef]
9. Brinkgreve, R.B.J.; Engin, E. Validation of geotechnical finite element analysis. In Proceedings of the 18th International Conference on Soil Mechanics and Geotechnical Engineering, Paris, France, 2–6 September 2013; Volume 2, pp. 677–682.
10. Nawari, N.O.; Liang, R.; Nusairat, J. Artificial intelligence techniques for the design and analysis of deep foundations. *Electron. J. Geotech. Eng.* **1999**, *4*, 1–21.
11. Wardani, S.P.R.; Surjandari, N.S.; Jajaputra, A.A. Analysis of ultimate bearing capacity of single pile using the artificial neural networks approach: A case study. In Proceedings of the 18th International Conference on Soil Mechanics and Geotechnical Engineering, Paris, France, 2–6 September 2013; pp. 837–840.
12. Jianbin, Z.; Jiewen, T.; Yongqiang, S. An ANN model for predicting level ultimate bearing capacity of PHC pipe pile. In *Earth and Space 2010: Engineering, Science, Construction, and Operations in Challenging Environments*; ASCE: Reston VA, USA, 2010; pp. 3168–3176.
13. Suman, S. Prediction of Pile Capacity Parameters Using Functional Networks and Multivariate Adaptive Regression Splines. Doctoral Dissertation, Department of Civil Engineering National Institue of Technology Rourkela, Odisha, India, 2015.
14. Doherty, P.; Gavin, K. The shaft capacity of displacement piles in clay: A state of the art review. *Geotech. Geol. Eng.* **2011**, *29*, 389–410. [CrossRef]
15. Shahin, M.A. Artificial intelligence in geotechnical engineering: Applications, modeling aspects, and future directions. In *Metaheuristics in Water, Geotechnical and Transport Engineering*; Elsevier: Amsterdam, The Netherlands, 2013; p. 169204.
16. Momeni, E.; Maizir, H.; Gofar, N.; Nazir, R. Comparative study on prediction of axial bearing capacity of driven piles in granular materials. *J. Teknol.* **2013**, *61*, 15–20. [CrossRef]
17. Bazaraa, A.R.; Kurkur, M.M. N-values used to predict settlements of piles in Egypt. In Proceedings of the Use of In Situ Tests in Geotechnical Engineering, Virginia, VA, USA, 23–25 June 1986; pp. 462–474.

18. Décourt, L. Prediction of the bearing capacity of piles based exclusively on N values of the SPT. In *Penetration Testing*; Routledge: Oxfordshire, UK, 2021; pp. 29–34.
19. Lopes, F.R.; Laprovitera, H. On the prediction of the bearing capacity of bored piles from dynamic penetration tests. In Proceedings of the International Geotechnical Seminar on Deep Foundations on Bored and Auger Piles, Ghent, Belgium, 1–7 June 1988; pp. 537–540.
20. Meyerhof, G.G. Penetration tests and bearing capacity of cohesionless soils. *J. Soil Mech. Found. Div.* **1956**, *82*, 861–866. [CrossRef]
21. Shioi, Y.; Fukui, J. Application of N-value to design of foundations in Japan. In *Penetration Testing*; Routledge: Oxfordshire, UK, 2021; pp. 159–164.
22. Aoki, N.; Velloso, D.A. An approximate method to estimate the bearing capacity of piles. In Proceedings of the 5th Pan-American Conf. of Soil Mechanics and Foundation Engineering, Bueno Aires, Argentina, 17–22 November 1975; International Society of Soil Mechanics and Geotechnical Engineering Buenos. Volume 1, pp. 367–376.
23. Reese, L.C.; O'Neill, M.W. New design method for drilled shafts from common soil and rock tests. In *Foundation Engineering: Current Principles and Practices*; ASCE: Reston, VA, USA, 1989; pp. 1026–1039.
24. Robert, Y. A few comments on pile design. *Can. Geotech. J.* **1997**, *34*, 560–567. [CrossRef]
25. Randolph, M.F. Science and empiricism in pile foundation design. *Géotechnique* **2003**, *53*, 847–875. [CrossRef]
26. Momeni, E.; Nazir, R.; Armaghani, D.J.; Maizir, H. Prediction of pile bearing capacity using a hybrid genetic algorithm-based ANN. *Measurement* **2014**, *57*, 122–131. [CrossRef]
27. Harandizadeh, H.; Armaghani, D.J.; Khari, M. A new development of ANFIS–GMDH optimized by PSO to predict pile bearing capacity based on experimental datasets. *Eng. Comput.* **2021**, *37*, 685–700. [CrossRef]
28. Chen, W.; Sarir, P.; Bui, X.-N.; Nguyen, H.; Tahir, M.M.; Armaghani, D.J. Neuro-genetic, neuro-imperialism and genetic programing models in predicting ultimate bearing capacity of pile. *Eng. Comput.* **2020**, *36*, 1101–1115. [CrossRef]
29. Lee, I.-M.; Lee, J.-H. Prediction of pile bearing capacity using artificial neural networks. *Comput. Geotech.* **1996**, *18*, 189–200. [CrossRef]
30. Likins, G.E.; Rausche, F. Correlation of CAPWAP with static load tests. In Proceedings of the Seventh International Conference on the Application of Stresswave Theory to Piles, Petaling Jaya, Malaysia, August 2004; pp. 153–165.
31. Moayedi, H.; Armaghani, D.J. Optimizing an ANN model with ICA for estimating bearing capacity of driven pile in cohesionless soil. *Eng. Comput.* **2018**, *34*, 347–356. [CrossRef]
32. Jahed Armaghani, D.; Shoib, R.S.N.S.B.R.; Faizi, K.; Rashid, A.S.A. Developing a hybrid PSO–ANN model for estimating the ultimate bearing capacity of rock-socketed piles. *Neural Comput. Appl.* **2017**, *28*, 391–405. [CrossRef]
33. Huang, J.; Asteris, P.G.; Pasha, S.M.K.; Mohammed, A.S.; Hasanipanah, M. A new auto-tuning model for predicting the rock fragmentation: A cat swarm optimization algorithm. *Eng. Comput.* **2020**. Available online: https://link.springer.com/article/10.1007/s00366-020-01207-4 (accessed on 24 October 2021). [CrossRef]
34. Chen, H.; Asteris, P.G.; Jahed Armaghani, D.; Gordan, B.; Pham, B.T. Assessing Dynamic Conditions of the Retaining Wall: Developing Two Hybrid Intelligent Models. *Appl. Sci.* **2019**, *9*, 1042. [CrossRef]
35. Parsajoo, M.; Armaghani, D.J.; Mohammed, A.S.; Khari, M.; Jahandari, S. Tensile strength prediction of rock material using non-destructive tests: A comparative intelligent study. *Transp. Geotech.* **2021**, *31*, 100652. [CrossRef]
36. Armaghani, D.J.; Hajihassani, M.; Mohamad, E.T.; Marto, A.; Noorani, S.A. Blasting-induced flyrock and ground vibration prediction through an expert artificial neural network based on particle swarm optimization. *Arab. J. Geosci.* **2014**, *7*, 5383–5396. [CrossRef]
37. Xie, C.; Nguyen, H.; Choi, Y.; Armaghani, D.J. Optimized functional linked neural network for predicting diaphragm wall deflection induced by braced excavations in clays. *Geosci. Front.* **2021**, 101313. [CrossRef]
38. Apostolopoulou, M.; Asteris, P.G.; Armaghani, D.J.; Douvika, M.G.; Lourenço, P.B.; Cavaleri, L.; Bakolas, A.; Moropoulou, A. Mapping and holistic design of natural hydraulic lime mortars. *Cem. Concr. Res.* **2020**, *136*, 106167. [CrossRef]
39. Asteris, P.G.; Kolovos, K.G. Self-compacting concrete strength prediction using surrogate models. *Neural Comput. Appl.* **2019**, *31*, 409–424. [CrossRef]
40. Khandelwal, M.; Mahdiyar, A.; Armaghani, D.J.; Singh, T.N.; Fahimifar, A.; Faradonbeh, R.S. An expert system based on hybrid ICA-ANN technique to estimate macerals contents of Indian coals. *Environ. Earth Sci.* **2017**, *76*, 399. [CrossRef]
41. Khandelwal, M.; Singh, T.N. Prediction of blast induced air overpressure in opencast mine. *Noise Vib. Worldw.* **2005**, *36*, 7–16. [CrossRef]
42. Armaghani, D.J.; Harandizadeh, H.; Momeni, E. Load carrying capacity assessment of thin-walled foundations: An ANFIS–PNN model optimized by genetic algorithm. *Eng. Comput.* **2021**. Available online: https://link.springer.com/article/10.1007/s00366-021-01380-0 (accessed on 24 October 2021).
43. Gajurel, A.; Chittoori, B.; Mukherjee, P.S.; Sadegh, M. Machine learning methods to map stabilizer effectiveness based on common soil properties. *Transp. Geotech.* **2021**, *27*, 100506. [CrossRef]
44. Jahed Armaghani, D.; Asteris, P.G.; Askarian, B.; Hasanipanah, M.; Tarinejad, R.; Huynh, V. Van Examining Hybrid and Single SVM Models with Different Kernels to Predict Rock Brittleness. *Sustainability* **2020**, *12*, 2229. [CrossRef]
45. Mohammed, A.S.; Asteris, P.G.; Koopialipoor, M.; Alexakis, D.E.; Lemonis, M.E.; Armaghani, D.J. Stacking Ensemble Tree Models to Predict Energy Performance in Residential Buildings. *Sustainability* **2021**, *13*, 8298. [CrossRef]

46. Hajihassani, M.; Jahed Armaghani, D.; Kalatehjari, R. Applications of Particle Swarm Optimization in Geotechnical Engineering: A Comprehensive Review. *Geotech. Geol. Eng.* **2018**, *36*, 705–722. [CrossRef]
47. Harandizadeh, H.; Toufigh, M.M.; Toufigh, V. Application of improved ANFIS approaches to estimate bearing capacity of piles. *Soft Comput.* **2019**, *23*, 9537–9549. [CrossRef]
48. Mayerhof, G.G. Bearing capacity and settlemtn of pile foundations. *J. Geotech. Geoenviron. Eng.* **1976**, *102*, 196–228.
49. Armaghani, D.J.; Faradonbeh, R.S.; Rezaei, H.; Rashid, A.S.A.; Amnieh, H.B. Settlement prediction of the rock-socketed piles through a new technique based on gene expression programming. *Neural Comput. Appl.* **2016**, *29*, 1115–1125. [CrossRef]
50. Shahin, M.A. Intelligent computing for modeling axial capacity of pile foundations. *Can. Geotech. J.* **2010**, *47*, 230–243. [CrossRef]
51. Goh, A.T.C. Back-propagation neural networks for modeling complex systems. *Artif. Intell. Eng.* **1995**, *9*, 143–151. [CrossRef]
52. Pal, M. Modelling pile capacity using generalised regression neural network. In Proceedings of the Indian Geotechnical Conference, Kochi, India, 15–17 December 2011.
53. Alkroosh, I.; Nikraz, H. Predicting axial capacity of driven piles in cohesive soils using intelligent computing. *Eng. Appl. Artif. Intell.* **2012**, *25*, 618–627. [CrossRef]
54. Alavi, A.H.; Aminian, P.; Gandomi, A.H.; Esmaeili, M.A. Genetic-based modeling of uplift capacity of suction caissons. *Expert Syst. Appl.* **2011**, *38*, 12608–12618. [CrossRef]
55. Momeni, E.; Dowlatshahi, M.B.; Omidinasab, F.; Maizir, H.; Armaghani, D.J. Gaussian Process Regression Technique to Estimate the Pile Bearing Capacity. *Arab. J. Sci. Eng.* **2020**, *45*, 8255–8267. [CrossRef]
56. Goh, A.T.C. Nonlinear modelling in geotechnical engineering using neural networks. *Trans. Inst. Eng. Aust. Civ. Eng.* **1994**, *36*, 293–297.
57. Goh, A.T.C. Pile driving records reanalyzed using neural networks. *J. Geotech. Eng.* **1996**, *122*, 492–495. [CrossRef]
58. Kiefa, M.A.A. General regression neural networks for driven piles in cohesionless soils. *J. Geotech. Geoenvironmental Eng.* **1998**, *124*, 1177–1185. [CrossRef]
59. Das, S.K.; Basudhar, P.K. Undrained lateral load capacity of piles in clay using artificial neural network. *Comput. Geotech.* **2006**, *33*, 454–459. [CrossRef]
60. Pal, M.; Deswal, S. Modeling pile capacity using support vector machines and generalized regression neural network. *J. Geotech. Geoenvironmental Eng.* **2008**, *134*, 1021–1024. [CrossRef]
61. Pal, M.; Deswal, S. Modelling pile capacity using Gaussian process regression. *Comput. Geotech.* **2010**, *37*, 942–947. [CrossRef]
62. Gandomi, A.H.; Alavi, A.H. A new multi-gene genetic programming approach to nonlinear system modeling. Part I: Materials and structural engineering problems. *Neural Comput. Appl.* **2012**, *21*, 171–187. [CrossRef]
63. Kordjazi, A.; Nejad, F.P.; Jaksa, M.B. Prediction of ultimate axial load-carrying capacity of piles using a support vector machine based on CPT data. *Comput. Geotech.* **2014**, *55*, 91–102. [CrossRef]
64. Ghorbani, B.; Sadrossadat, E.; Bazaz, J.B.; Oskooei, P.R. Numerical ANFIS-based formulation for prediction of the ultimate axial load bearing capacity of piles through CPT data. *Geotech. Geol. Eng.* **2018**, *36*, 2057–2076. [CrossRef]
65. Dehghanbanadaki, A.; Khari, M.; Amiri, S.T.; Armaghani, D.J. Estimation of ultimate bearing capacity of driven piles in c-φ soil using MLP-GWO and ANFIS-GWO models: A comparative study. *Soft Comput.* **2020**, *25*, 4103–4119. [CrossRef]
66. Pham, T.A.; Ly, H.-B.; Tran, V.Q.; Van Giap, L.; Vu, H.-L.T.; Duong, H.-A.T. Prediction of pile axial bearing capacity using artificial neural network and random forest. *Appl. Sci.* **2020**, *10*, 1871. [CrossRef]
67. Zabidi, H.; De Freitas, M.H. Re-evaluation of rock core logging for the prediction of preferred orientations of karst in the Kuala Lumpur Limestone Formation. *Eng. Geol.* **2011**, *117*, 159–169. [CrossRef]
68. Gandomi, A.H.; Fridline, M.M.; Roke, D.A. Decision tree approach for soil liquefaction assessment. *Sci. World J.* **2013**, *2013*, 346285. [CrossRef]
69. Ramesh Murlidhar, B.; Yazdani Bejarbaneh, B.; Jahed Armaghani, D.; Mohammed, A.S.; Mohamad, E.T. Application of Tree-Based Predictive Models to Forecast Air Overpressure Induced by Mine Blasting. *Nat. Resour. Res.* **2021**, *30*, 1865–1887. [CrossRef]
70. Tiryaki, B. Predicting intact rock strength for mechanical excavation using multivariate statistics, artificial neural networks, and regression trees. *Eng. Geol.* **2008**, *99*, 51–60. [CrossRef]
71. Hasanipanah, M.; Faradonbeh, R.S.; Amnieh, H.B.; Armaghani, D.J.; Monjezi, M. Forecasting blast-induced ground vibration developing a CART model. *Eng. Comput.* **2017**, *33*, 307–316. [CrossRef]
72. Khalilia, M.; Chakraborty, S.; Popescu, M. *Predicting Disease Risks from Highly Imbalanced Data Using Random Forest*; Springer Link: New York, NY, USA, 2011.
73. Aghaabbasi, M.; Shekari, Z.A.; Shah, M.Z.; Olakunle, O.; Armaghani, D.J.; Moeinaddini, M. Predicting the use frequency of ride-sourcing by off-campus university students through random forest and Bayesian network techniques. *Transp. Res. Part A Policy Pract.* **2020**, *136*, 262–281. [CrossRef]
74. Kardani, N.; Zhou, A.; Nazem, M.; Shen, S.-L. Estimation of bearing capacity of piles in cohesionless soil using optimised machine learning approaches. *Geotech. Geol. Eng.* **2020**, *38*, 2271–2291. [CrossRef]
75. Zhou, J.; Qiu, Y.; Zhu, S.; Armaghani, D.J.; Khandelwal, M.; Mohamad, E.T. Estimation of the TBM advance rate under hard rock conditions using XGBoost and Bayesian optimization. *Undergr. Space* **2021**, *6*, 506–515. [CrossRef]
76. Nguyen, H.; Bui, X.N.; Choi, Y.; Lee, C.W.; Armaghani, D.J. A Novel Combination of Whale Optimization Algorithm and Support Vector Machine with Different Kernel Functions for Prediction of Blasting-Induced Fly-Rock in Quarry Mines. *Nat. Resour. Res.* **2021**, *30*, 191–207. [CrossRef]

77. Zhou, J.; Qiu, Y.; Armaghani, D.J.; Zhang, W.; Li, C.; Zhu, S.; Tarinejad, R. Predicting TBM penetration rate in hard rock condition: A comparative study among six XGB-based metaheuristic techniques. *Geosci. Front.* **2021**, *12*, 101091. [CrossRef]
78. Raschka, S. Model Evaluation, Model Selection, and Algorithm Selection in Machine Learning. *arXiv* **2018**, arXiv:1811.12808.
79. Willmott, C.J.; Matsuura, K. Advantages of the mean absolute error (MAE) over the root mean square error (RMSE) in assessing average model performance. *Clim. Res.* **2005**, *30*, 79–82. [CrossRef]
80. Xu, H.; Zhou, J.; Asteris, G.P.; Jahed Armaghani, D.; Tahir, M.M. Supervised Machine Learning Techniques to the Prediction of Tunnel Boring Machine Penetration Rate. *Appl. Sci.* **2019**, *9*, 3715. [CrossRef]
81. Harandizadeh, H.; Armaghani, D.J.; Mohamad, E.T. Development of fuzzy-GMDH model optimized by GSA to predict rock tensile strength based on experimental datasets. *Neural Comput. Appl.* **2020**, *32*, 14047–14067. [CrossRef]
82. Kardani, N.; Bardhan, A.; Samui, P.; Nazem, M.; Zhou, A.; Armaghani, D.J. A novel technique based on the improved firefly algorithm coupled with extreme learning machine (ELM-IFF) for predicting the thermal conductivity of soil. *Eng. Comput.* **2021**. Available online: https://link.springer.com/article/10.1007/s00366-021-01329-3 (accessed on 24 October 2021). [CrossRef]
83. Armaghani, D.J.; Yagiz, S.; Mohamad, E.T.; Zhou, J. Prediction of TBM performance in fresh through weathered granite using empirical and statistical approaches. *Tunn. Undergr. Space Technol.* **2021**, *118*, 104183. [CrossRef]
84. Armaghani, D.J.; Mohamad, E.T.; Momeni, E.; Narayanasamy, M.S. An adaptive neuro-fuzzy inference system for predicting unconfined compressive strength and Young's modulus: A study on Main Range granite. *Bull. Eng. Geol. Environ.* **2015**, *74*, 1301–1319. [CrossRef]
85. Armaghani, D.J.; Harandizadeh, H.; Momeni, E.; Maizir, H.; Zhou, J. An optimized system of GMDH-ANFIS predictive model by ICA for estimating pile bearing capacity. *Artif. Intell. Rev.* **2021**. Available online: https://link.springer.com/article/10.1007/s10462-021-10065-5 (accessed on 24 October 2021). [CrossRef]

sustainability

MDPI

Article

Stability Analysis of Paste Filling Roof by Cut and Fill Mining

Qingliang Chang [1], Yifeng Sun [1], Qiang Leng [1,*], Zexu Liu [2], Huaqiang Zhou [1] and Yuantian Sun [1,*]

[1] Key Laboratory of Deep Coal Resource Mining, Ministry of Education of China, School of Mines, China University of Mining and Technology, Xuzhou 221116, China; zkdcql@cumt.edu.cn (Q.C.); ts20020155p21@cumt.edu.cn (Y.S.); 2242@cumt.edu.cn (H.Z.)

[2] People's Government of Dongshan Town, Qilin District, Qujing City 655004, China; ts20020154p21@cumt.edu.cn

* Correspondence: ts20020030a31@cumt.edu.cn (Q.L.); yuantiansun@cumt.edu.cn (Y.S.); Tel.: +86-1318-234-9313 (Q.L.)

Abstract: Ensuring the stability of paste false rooves is an important issue in the study of the process of paste filling and slicing mining. Here, a mechanical model of a paste false roof is created to analyze its stability in the process of lower slicing mining in order to determine the minimum slicing thickness of the false roof. We use FLAC3D to simulate and analyze the influence of changes in paste false roof thickness on the stability of the roof. The quantitative functional relationship between the thickness and the subsidence of a false roof, and the optimal thickness of the artificial paste roof, is finally obtained by the development law of the plastic zone in the lower slicing face. The results show that when the thickness of the paste false roof is 3.2 m, the roof can maintain its self-stabilization state and ensure the normal mining of lower layers. Because the same thickness of the upper and lower layers is beneficial for mining replacement and equipment selection in different layered working faces, the optimal thickness of a paste false roof is determined to be 3.2 m.

Keywords: paste filling; slicing mining; false roof stability; optimal false roof thickness

Citation: Chang, Q.; Sun, Y.; Leng, Q.; Liu, Z.; Zhou, H.; Sun, Y. Stability Analysis of Paste Filling Roof by Cut and Fill Mining. *Sustainability* **2021**, *13*, 10899. https://doi.org/10.3390/su131910899

Academic Editors: Mahdi Hasanipanah, Danial Jahed Armaghani and Jian Zhou

Received: 24 July 2021
Accepted: 26 September 2021
Published: 30 September 2021

Publisher's Note: MDPI stays neutral with regard to jurisdictional claims in published maps and institutional affiliations.

Copyright: © 2021 by the authors. Licensee MDPI, Basel, Switzerland. This article is an open access article distributed under the terms and conditions of the Creative Commons Attribution (CC BY) license (https://creativecommons.org/licenses/by/4.0/).

1. Introduction

Paste filling mining can effectively control surface deformation and overlying rock movement and has become one of the most important technical means to recover coal resources under buildings (structures) [1]. Paste false roofs need to have sufficient strength and a stable bearing capacity. Mastering the instability law of paste filling and layered mining is a prerequisite for safe and efficient mining under pressure [2]. A series of studies have been carried out.

Some researchers established a mechanical model of the basic roof key blocks for paste filling mining and calculated the thickness of the cracked roof [3–5]. For example, the mechanical model of the roof rock beam for backfill mining and its differential equations were established. The thin plate theory was used to analyze the stress conditions of the false roof under the mine stope [6,7]. The "embedded beam" mechanical model for the overfilled roof of the roadway was established. The finite-length beam model was used to mechanically analyze the "filling body-direct roof" integral support structure [8–10].

At present, the existing research mainly analyzes the stability of the false roof as it relates to the backfill, regarding aspects such as the amount of underfilling, the compression rate of the filling, the filling rate, the mining method, and the overburden load [11,12]. There are few reports on the thickness, strength, and stability of the false roof layer during the layered filling and recovery operation under the paste filling and layered mining [13,14]. Because of the limited space, this study will focus on the influencing factor of the thickness of the paste top layer, and use the method of numerical simulation to study the effect of different thicknesses of the false top layer on its stability [15,16].

Under some mining geological conditions, to effectively control surface deformation, recover the "three-under" compressed coal resources, and digest gangue to protect the

ecological environment, paste filling mining is the best solution [17]. At present, the paste filling method has been used to implement paste filling in multiple mines, such as the Taiping Coal Mine of Jining Mining Group, the Daizhuang Coal Mine of Shandong Energy Zi Mining Group, the Xima Coal Mine (Shenyang Province, China)., and the Xiaotun Coal Mine of Jizhong Energy Fengfeng Group. Paste filling mining the full height at one time means extracting the full height of the coal seam at one time and then implementing the filling [18]. The paste filling layer mining method means filling the upper layer first, and the upper layer filling body is used as the false roof for the lower layer. The practice of backfill mining shows that layered mining with paste filling has a better ground deformation control effect than one-time mining with paste filling, and the early strength requirement of the filling is lower than that of the layered mining, so the former has stronger industrial applicability than the latter.

This study takes the paste filling mining project at the E1302 face of the Gaohe Coal Mine of Shanxi Lu'an Group as the background. According to the mining geological conditions of the Gaohe Coal Mine, the paste filling layered coal mining method is selected to recover coal resources. Theoretical analysis combined with numerical simulation is applied to study the relationship between the thickness of the paste false roof and the stability of the false roof.

2. Project Overview

The E1302 paste filling face is located in the East first panel of the Gaohe Mine, Lu'an, with a length of 230 m and an advanced length of 430 m. The main mining seam is the No. 3 coal seam, and the average coal thickness is 6.4 m. The paste filling is used for two-layer down mining. The coal hardness coefficient is 0.7, the average inclination angle of the coal seam is 8°, and the roof of the No. 3 coal seam is mudstone, sandy mudstone, siltstone, and partly sandstone. The floor is black mudstone, sandy mudstone, and dark-gray siltstone. The lithological characteristics of the roof and floor rocks are shown in Table 1.

Table 1. Lithological characteristics of the roof and floor of the No. 3 coal seam.

Top and Bottom Name	Rock Stone Name	Platts Hardness Coefficient	Thickness/m
Old top	Fine-grained sandstone—Siltstone	4.04	12.42~ 13.65
Direct top	Sandy mudstone—Fine siltstone	2.74	6.87~7.85
	Mudstone	1.22	1.82~2.13
Direct bottom	Mudstone—Siltstone	2.71	2.96~3.05
Old bottom	Sandy mudstone—Fine-grained sandstone	3.62	8.37~8.94

3. Analysis of the Mechanism of the Instability Thickness of the Paste False Roof

3.1. Calculation of False Roof Load

(1) Direct top load Q_1

$$Q_1 = h_1 L_1 \gamma_1 \quad (1)$$

Formula:

h_1—the thickness of the direct roof, m.

L_1—suspended ceiling distance, m.

γ_1—Volume force, MN/m^3.

If the suspended ceiling distance is equal to the controlled ceiling distance, then:

$$Q_1 = h_1 \gamma_1 = 0.216 \text{ MPa} \quad (2)$$

(2) Basic top load Q_2

According to the composite beam theory, the high-strength rock layer and the upper, softer rock layer form a composite beam structure, and the load formed by the upper, softer rock layer and the lower key layer can be solved using composite beam theory.

Considering the influence of n layers of overlying rock on the bottom layer, replace $(q_1)_x$ with $(q_n)_1$, and then:

$$(q_n)_1 = \frac{E_1 h_1^3(\gamma_1 h_1 + \gamma_2 h_2 + \cdots + \gamma_n h_n)}{E_1 h_1^3 + E_2 h_2^3 + \cdots + E_n h_n^3} \quad (3)$$

Using this formula to calculate the load formed on the bottom rock beam, it must be calculated gradually from bottom to top, that is, the sequence is $(q_1)_1$, $(q_2)_1$, ..., $(q_n)_1$; when the calculation is $(q_{i+1})_1 < (q_i)$, then the calculation stops at one o'clock. It shows that the i + 1 layer does not generate additional load on the bottom layer. At the time $(q_n)_1 = (q_i)_1$, it can be judged that the n + 1th layer does not affect the load of the first layer, that is, the strength of the nth layer on top of the rock. It is higher and can support the overburdened load without load on the basic roof. After calculating $(q_6)_1 < (q_5)_1$, the sixth layer of siltstone above the basic roof has the characteristics of large thickness and high strength, and the overlying load will not be transmitted downwards. Therefore, the load on the basic roof is $Q_2 = (q_5)_1 = 0.443$ MPa.

(3) Calculation of self-load of paste false top

The load of the paste false top is considered to be safe, and it is calculated according to the larger thickness of 5.2 m:

$$Q_3 = h_{max}\gamma_3 = 0.095 \text{ MPa} \quad (4)$$

In summary, the false roof bearing load q is calculated as:

$$q = Q_1 + Q_2 + Q_3 = 0.754 \text{ MPa} \quad (5)$$

3.2. Theoretical Analysis of False Roof Instability Thickness

There will be no collapse zone on the roof above the mining face with the paste filling, but only a fracture zone and curved subsidence zone [19]. The practice has shown that the roof control effect of paste filling mining is generally affected by factors such as the amount of roof and floor moving before filling, the amount of underfilling, the compression rate, and the filling rate of the filling body. With the continuous improvement of the filling process and the development of key filling equipment, paste filling technology has become more mature. The amount of top and bottom plate moving before filling, the amount of underfilling, and the compression rate of the filling body can be controlled within a small range, while still meeting the requirements [20,21]. The filling body fills the mined-out area and controls the roof in time, and therefore effectively controls the roof subsidence and the filling requirements of the surface collapse. At present, the commonly used mechanical models of the instability mechanism of the paste false top are the thin "plate" theoretical model and the simply supported "beam" theoretical model [22]. Both theoretical models assume that the paste false top is continuous and homogeneous, and that it was a linear elastic body before yield failure. Since the length of the filling working face in the inclined direction is much longer than the span in the strike direction, the roof in the middle of the working face can be regarded as a beam of countless unit widths inserted into the front and rear rock masses, so it will be filled. The artificial top is considered to be a simply supported beam for research purposes [22]. The load of the simply supported beam and above is transmitted from the beam to the front and rear of the stope before it breaks. At this time, the overburden load is regarded as the uniform load q, the false roof thickness h, and the rock beam length L, as shown in Figure 1. The mechanical model analyzes its force [23].

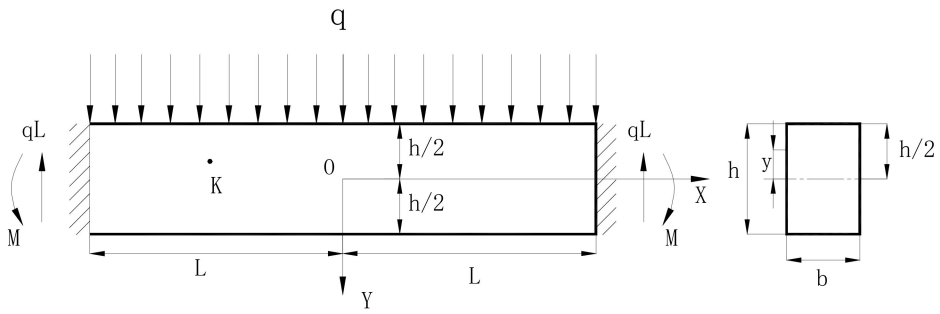

Figure 1. The mechanical model of the paste false top.

From elastic mechanics, we know that the bending stress in the beam σ_x is caused by the bending moment, the extrusion stress σ_y is caused by the overlying load q, and τ_{xy} is caused by the shear stress. Assuming that σ_y is only a function of y, we have:

$$\sigma_y = f(y) \tag{6}$$

The Airy stress function is:

$$\sigma_x = \frac{\partial^2 \Phi}{\partial y^2} - f_x x, \;\; \sigma_y = \frac{\partial^2 \Phi}{\partial x^2} - f_y y, \;\; \tau_{xy} = -\frac{\partial^2 \Phi}{\partial x \partial y} \tag{7}$$

Bringing the formula into the Airy stress function Formula (7), we obtain:

$$\Phi = \frac{x^2}{2} f(y) + x f_1(y) + f_2(y) \tag{8}$$

Solve the stress function from the compatibility equation, put the Equation (8) into the compatibility equation, and simplify it to obtain:

$$\frac{\partial^4 \Phi}{\partial x^4} + 2\frac{\partial^4 \Phi}{\partial x^2 \partial y^2} + \frac{\partial^4 \Phi}{\partial x^4} = 0 \tag{9}$$

Omit the primary term and constant term, and further simplify to obtain the stress function:

$$\begin{aligned} \Phi = \;\; & \tfrac{x^2}{2}\left(Ay^3 + By^2 + Cy + D\right) + x\left(Ey^3 + Fy^2 + Gy\right) \\ & - \tfrac{A}{10}y^5 - \tfrac{B}{6}y^4 + Hy^3 + Ky^2 \end{aligned} \tag{10}$$

Solve the stress component from the stress function, and put the Formula (10) into the Airy stress function (7) to obtain the stress component:

$$\sigma_x = \frac{x^2}{2}(6Ay + 2B) + x(6Ey + 2F) - 2Ay^3 - 2By^2 + 6Hy + 2K \tag{11}$$

$$\sigma_y = Ay^3 + By^2 + Cy + D \tag{12}$$

$$\sigma_{xy} = -x\left(3Ay^2 + 2By + C\right) - \left(3Ey^2 + 2Fy + G\right) \tag{13}$$

Considering that the span of the beam is much larger than the thickness of the beam, the stress boundary conditions on the main boundary can be satisfied, and the integral stress boundary of the Saint-Venant principle is used to replace the minor part of the boundary so that the boundary conditions are approximately satisfied:

$$\left(\sigma_y\right)_{y=\frac{h}{2}} = 0, \;\; \left(\sigma_y\right)_{y=-\frac{h}{2}} = -q, \;\; \left(\tau_{xy}\right)_{y=\pm\frac{h}{2}} = 0 \tag{14}$$

Therefore, first consider the main boundary conditions, combine the formula with the formula, and solve:

$$\sigma_x = -\frac{6q}{h^3}x^2y + \frac{4q}{h^3}y^3 + 6Hy + 2K \tag{15}$$

$$\sigma_y = -\frac{2q}{h^3}y^3 + \frac{3q}{2h}y - \frac{q}{2} \tag{16}$$

$$\tau_{xy} = \frac{6q}{h^3}xy^2 - \frac{3q}{2h}x \tag{17}$$

Next, consider the left and right boundary conditions. Since the model is arranged symmetrically, one side can be considered. On the right side of the beam, there is no horizontal plane force, that is, $\sigma_x = 0$, so:

$$\int_{-\frac{h}{2}}^{\frac{h}{2}} (\sigma_x)_{x=L} dy = 0 \tag{18}$$

$$\int_{-\frac{h}{2}}^{\frac{h}{2}} (\sigma_x)_{x=L} y dy = 0 \tag{19}$$

Combining Equations (15)–(17) with conditional Equations (18) and (19), the stress component is solved as:

$$\sigma_x = \frac{6q}{17h^3}(L^2 - x^2)y + q\frac{y}{h}\left(4\frac{y^2}{h^2} - \frac{3}{85}\right) \tag{20}$$

$$\sigma_y = -\frac{q}{2}\left(L + \frac{y}{h}\right) \times \left(L - \frac{2y}{h}\right)^2 \tag{21}$$

$$\tau_{xy} = -\frac{6q}{h^3}x\left(\frac{h^2}{4} - y^2\right) \tag{22}$$

It can be seen from the stress expressions (20)–(22) that in a long beam whose length is far greater than its thickness, the bending stress σ_x is of the same order as $q(L/h)^2$, which is the main stress; the shear stress τ_{xy} is the same as $q(L/h)^2$. The same order of $q(L/h)$ is the secondary stress; the extrusion stress σ_y is the same order of q, and this is secondary stress, which is not considered. Therefore, the failure of the false roof is mainly caused by the bending moment and shearing force.

Breaking of the false roof is caused by the bending moment:

The maximum bending stress on the beam reaches its maximum value at $y = h/2$, so:

$$\sigma_{max} = \frac{6q\left(L^2 - x^2\right)}{17h^2} + q\frac{1}{2h^6} - \frac{3q}{85h^2} \tag{23}$$

Omit the high-order infinitesimal terms, then:

$$\sigma_{max} = \frac{30q\left(L^2 - x^2\right) - 3q}{85h^2} \tag{24}$$

If the tensile strength of the false top is F_T, the critical conditions for the bending instability and breaking of the paste false top are considered as follows:

$$\sigma_{max} \le [\sigma] = F_T \tag{25}$$

Then there are:

$$\frac{30q\left(L^2 - x^2\right) - 3q}{85h^2} \le F_T \tag{26}$$

Breaking of the false roof is caused by shearing force:

If the maximum bending stress on the beam reaches its maximum value on the neutral axis at y = 0, omitting the high-order infinitesimal terms, then:

$$(\tau_{xy})_{max} = \frac{3q}{2h}x \tag{27}$$

If the tensile strength of the false roof is F_S, the critical condition of shear instability and fracture of the paste false roof is considered as follows:

$$(\tau_{xy})_{max} \leq [\tau_{xy}] = F_s \tag{28}$$

Then there are:

$$\frac{3q}{2h}x \leq F_s \tag{29}$$

According to the formula, the minimum thickness of false roof h_{min} is obtained because it also satisfies:

$$h_{min} \geq \sqrt{\frac{30q\left(L^2 - x^2\right) - 3q}{85F_T}} \tag{30}$$

$$h_{min} \geq \frac{3qx}{2F_s} \tag{31}$$

This is the case considering that x = 0.5 L is the dangerous section of the false roof's simply supported beam. According to the paste material mechanics experiment, the 28 d tensile strength of the paste false roof is 0.5 MPa, and the shear strength is 1.5 MPa. The false roof span L is 8 m, and the false roof bears the load of 0.754 MPa, and Formulas (30) and (31) are used to obtain:

$$h_{min} \geq \sqrt{\frac{30q\left(L^2 - x^2\right) - 3q}{85F_T}} = \sqrt{\frac{447q}{85F_T}} = 2.81m$$

Therefore, the comprehensive analysis shows that the thickness of the false roof layer should be greater than 3.01 m.

4. Numerical Simulation Analysis of the Instability Thickness of the Paste False Roof

4.1. Numerical Simulation Modeling of Layered Mining

The length of the E1302 working face is 230 m, the advance length is 430 m, the average thickness is 6.4 m, and the buried depth of the three coal seams is about 420 m. According to the actual filling and mining process of the working face, the geometric model of the stope structure of paste filling and layered mining is established as shown in Figure 2. By referring to the geometric model and combining the physical and mechanical parameters of the rock formation in Table 2, we can use FLAC^{3D} [24,25] to establish a numerical simulation model as shown in Figure 3. Horizontal displacement constraints are imposed on the north and south boundaries of the model, and the bottom boundary of the model is fixed in the vertical direction. The top rock layer is buried at about 310 m. Therefore, a vertical downward uniform load of 7.75 MPa is applied to the top to simulate the overburden load. To eliminate the influence of the boundary of the model, a boundary coal pillar of 60 m is left on both sides of the working face along the advancing direction. The size of the model is 550 m × 300 m × 160 m in the order of length × width × height. In the process of analysis and calculation, the weight of each rock layer is considered in the vertical direction of the model, and the Mohr–Coulomb strength criterion is used to solve the constitutive relationship [26,27].

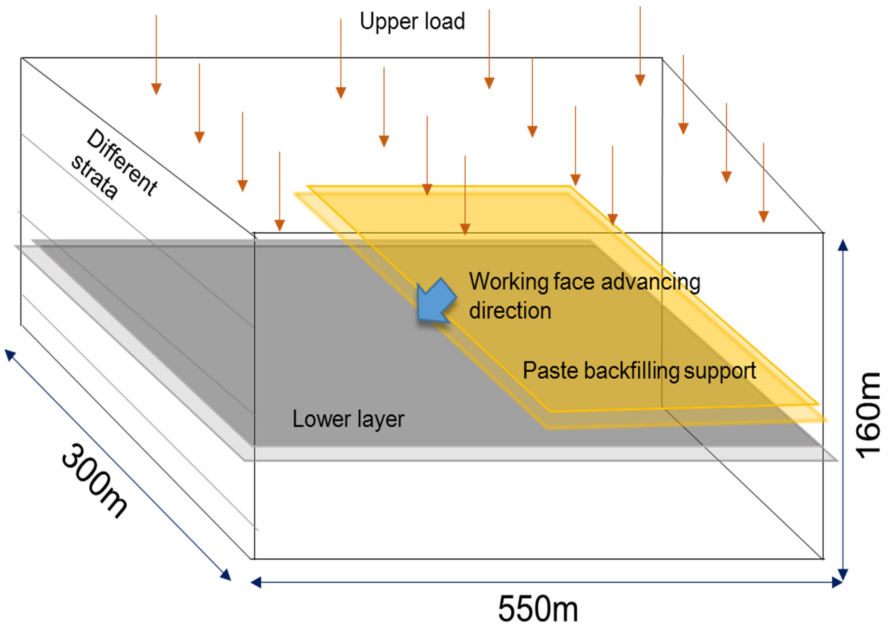

Figure 2. Schematic diagram of the geometric model of the stope structure of the paste filling and layered mining.

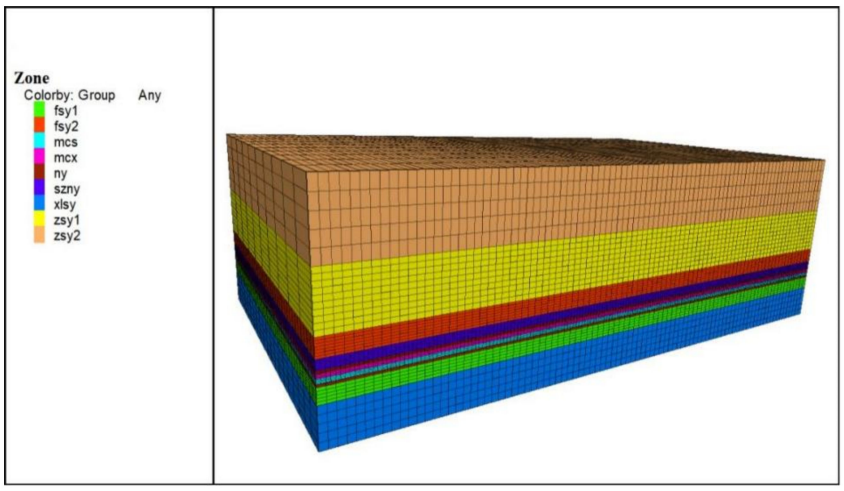

Figure 3. Numerical simulation model of paste filling and layered mining.

4.2. Numerical Simulation Schemes of Different False Roof Thicknesses

According to the actual mining and filling operation of the E1302 working face of Gaohe filling mining, the span of the roof control area of the working face is about 8 m. The upper stratified filling body is considered by the unidirectional force state, and the later strength requirement of the filling body is determined to be 5 MPa according to the Bieniawski paste late strength formula [28,29]. In the simulation, the controlled variable method is adopted to control the layer thickness as a single variable. According to the actual mining and filling operation, the compressive strength of the filling body false top is set to 5 MPa, and the collapse distance of the lower layer working face is 8 m. Other simulation variables are assumed to be consistent. The sum of the height of the false top layer and the lower layer working face of the model is the total thickness of the coal seam, which is 6.4 m. Based on the experience in the field, by changing the thickness of the false roof (2.2 m, 3.2 m, 4.2 m, 5.2 m), the distribution of the false roof plastic zone and the amount of roof subsidence have been analyzed. Previously, scholars have used the method of finite element numerical simulation to analyze the relationship between the

displacement of the middle part of the false roof section and the instability and fracture of the false roof under the action of the weight and the upper rock formation according to the simulation results of the displacement field [10]. Some scholars also use FLAC to establish a numerical simulation model and analyze the critical conditions for roof failure and the instability of the working face under different filling steps by observing the plastic zone.

In this paper, the FLAC3D 5.0 numerical simulation method is used to study the roof of the working face through the development of the plastic zone, and the influence of the false roof thickness on the stability of the false roof is studied [30]. In the 3D geometric model, the blue survey lines and pink survey points are arranged at the bottom of the upper paste filling roof, and 19 survey points are set at equal intervals with an interval of 1 m. The survey line layout section is shown in Figure 4.

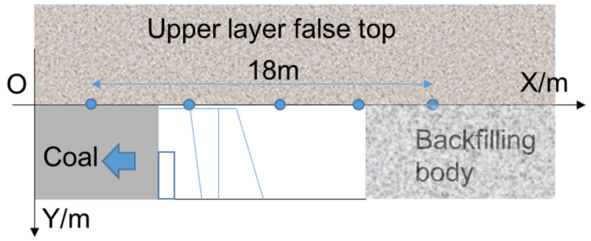

Figure 4. The sectional view of the model measuring the point layout.

Table 2. Part of the physical and mechanical parameters of the model rock.

Rock Formation Lithology Basic Parameters	Layered Thick Degree /m	Bulk Modulus the Amount/GPa	Shear Modulus/GPa	Elastic Modulus/GPa	Poisson's Ratio	Cohesion/MPa	Internal Friction Angle/°	Density/ kg·m^{-3}	Tensile Strength/MPa
Medium-grained sandstone	220	19.11	13.16	32.12	0.22	2.72	25.13	2650	2.7
Siltstone	13.1	13.06	8.60	21.16	0.23	2.02	26.10	2600	2
Sandy mudstone	7.2	10.48	6.29	15.73	0.25	1.19	30.67	2510	1.1
Mudstone	1.9	7.65	5.50	13.31	0.21	0.89	31.03	2320	0.8
3# coal seam	6.4	1.37	0.67	1.73	0.29	0.53	29.24	1450	0.5
Mudstone	1.1	7.65	5.50	13.31	0.21	0.89	31.03	2320	0.8
Siltstone	1.9	13.06	8.60	21.16	0.23	2.02	26.10	2600	2
Fine-grained sandstone	8.9	11.64	7.32	18.16	0.24	1.32	33.21	2410	2.3
5 MPa filling body	-	0.08	0.13	0.2	0.27	0.33	30.00	1900	0.24

4.3. Simulation Results and Analysis of the Displacement of the Paste False Top

4.3.1. Correlation Analysis of False Roof Thickness and False Roof Subsidence

According to the different thickness conditions in the scheme, a simulation is carried out, and the displacement cloud diagram of the lower layer working face is shown in Figure 5.

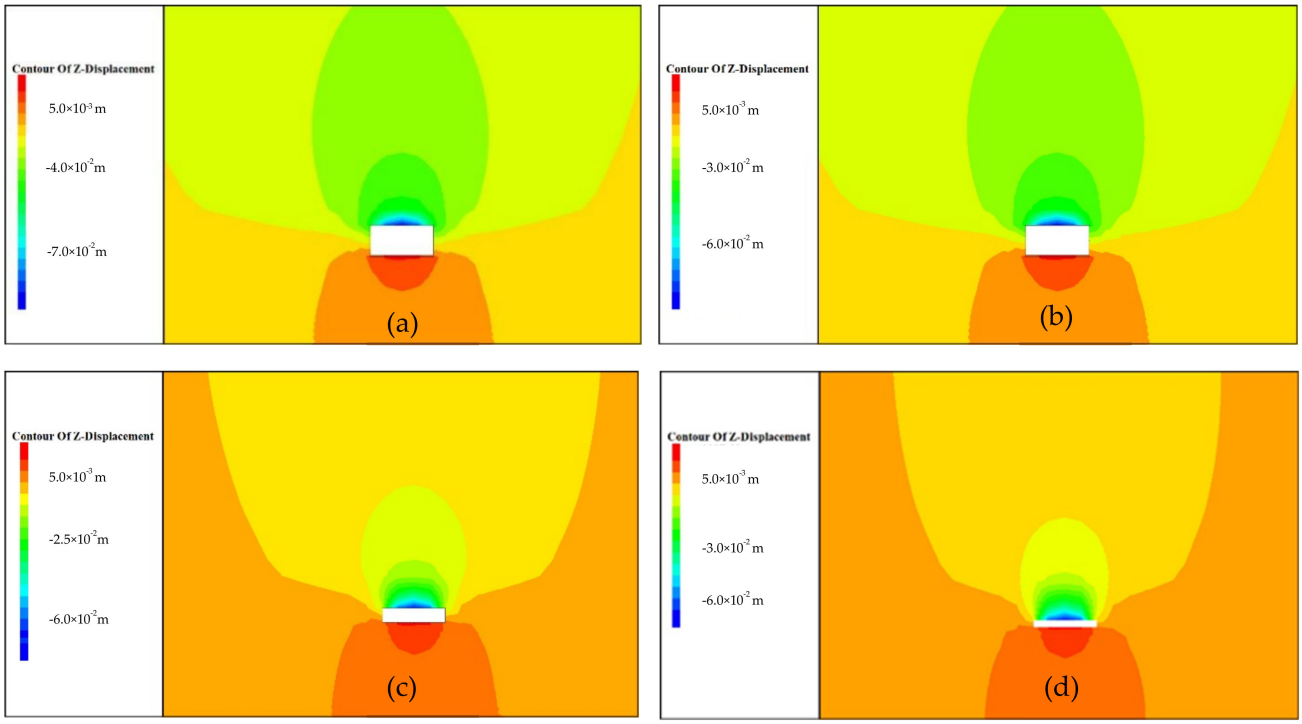

Figure 5. Displacement cloud diagrams of different false roof thicknesses. (**a**) Displacement cloud image of false roof thickness of 2.2 m, (**b**) Displacement cloud map of false roof thickness of 3.2 m, (**c**) Displacement cloud image of false roof thickness 4.2 m, (**d**) Displacement cloud image of false roof thickness of 5.2 m.

It can be seen from Figure 5 that: when the thickness of the false roof is 2.2 m, the maximum sinking amount of the roof is 81 mm; when the thickness of the false roof is 3.2 m, the maximum sinking amount of the roof is 75 mm; and when the thickness of the false roof is 4.2 m, the sinking amount of the roof is at its maximum. When the false roof is 72 mm and the thickness of the false roof is 5.2 m, the maximum subsidence of the roof is 58 mm. It can be roughly judged that the maximum subsidence of the false roof is negatively correlated with the thickness of the false roof.

One can draw the false roof subsidence curve of each measurement point according to the cloud map displacement. As shown in Figure 6, the false roof subsidence area can be divided into three areas, A, B, and C, according to the distribution law of the subsidence curve; that is, the false roof subsidence boundary zone (zone A), the false roof subsidence transition zone (zone B), and the false roof subsidence central zone (zone C). Select different sections in each area of A, B, and C in Figure 6, and one can draw the false roof in sections. The relationship between the amount of subsidence and the thickness of the false roof is shown in Figure 7.

$$y = 2.83x^3 - 27x^2 + 87.21x - 170 \quad (32)$$

To further quantitatively analyze the functional relationship between the false roof thickness and the false roof subsidence in the central area of false roof subsidence (zone C), the distance between the working face and the origin of the survey line is x, and when 52 m $\leq$ x $\leq$ 57 m, C is obtained the area function relationship is Formula (32), the degree of fit R2 = 0.989, and the fitted curve is shown in Figure 8.

From Figure 8 and Formula (32), it can be seen that in the central area of false roof subsidence (zone C), the thickness of the false roof is negatively correlated with the amount of false roof subsidence, and the amount of subsidence decreases with the increase of false roof thickness. The slope of the curve first gradually decreases and then increases, which means that when the false roof thickness is between 2.2 and 3.2 m, the subsidence speed of the false roof decreases with the increase in thickness. When the false roof thickness is

between 3.2 and 4.2 m, the subsidence value of the false roof changes little. The sinking speed of the false roof increases with the increase of thickness after 4.2 m.

Similarly, quantitatively analyze areas B and C, and one can obtain the piecewise function of the correlation between the false roof thickness and the false roof subsidence:

$$y = \left\{ \begin{array}{ll} -0.35x^2 + 0.51x - 1.11 & R^2 = 0.999, \quad x \in [30, 50] \cup [58, 78] \\ 2.33x^3 + 23x^2 - 67.66x + 20 & R^2 = 0.999, \quad x \in [50, 52] \cup [57, 58] \\ 2.83x^3 - 27x^2 + 87.21x - 170 & R^2 = 0.989, \quad x \in [52, 57] \end{array} \right\} \quad (33)$$

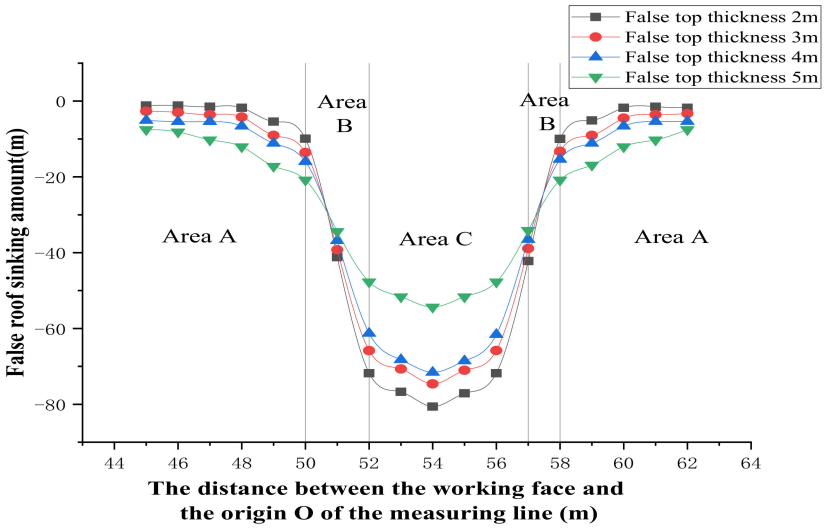

Figure 6. The amount of false roof subsidence at different positions of the working face.

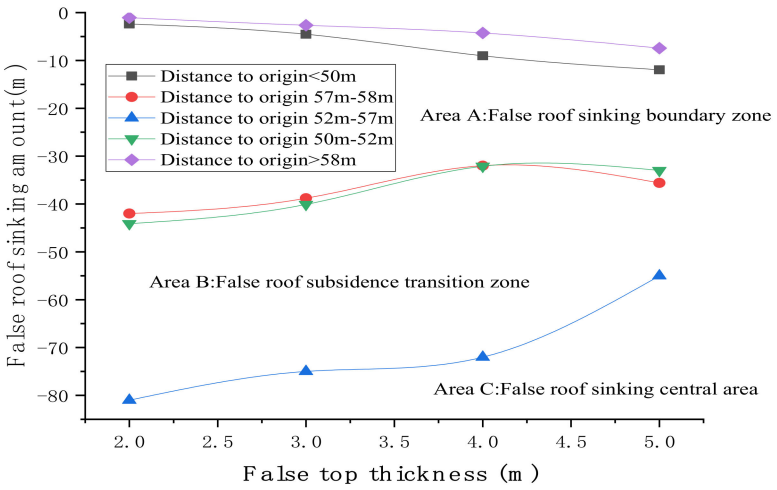

Figure 7. The relationship between false roof thickness and subsidence in different regions positions of the working face.

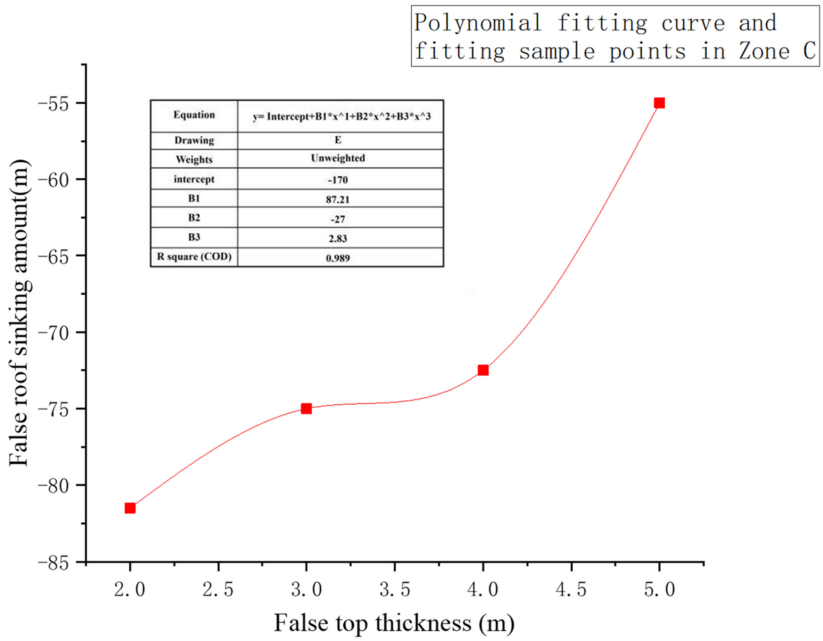

Figure 8. The fitting curve of false roof subsidence–thickness in area C.

4.3.2. Analysis of the Development Law of Plastic Zone under Different False Top Thickness

The plastic zone distribution of the lower layer working face with different filling body false roof thickness is shown in Figure 9.

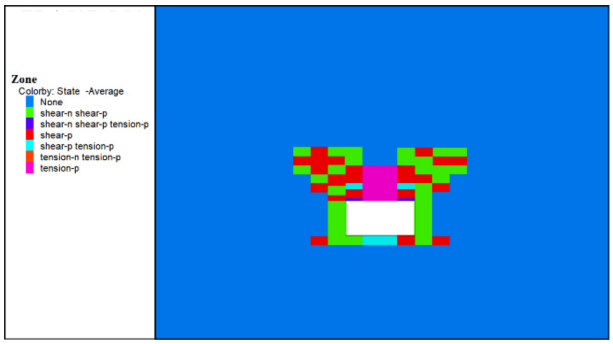

(**a**) Cloud map of the distribution of the plastic zone with a thickness of 2.2 m in the false roof

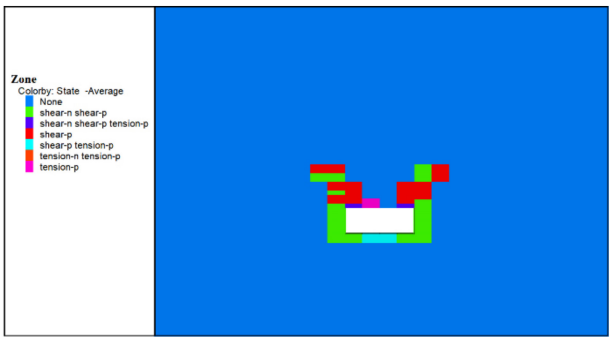

(**b**) Cloud map of plastic zone distribution with a thickness of 3.2 m in the false roof

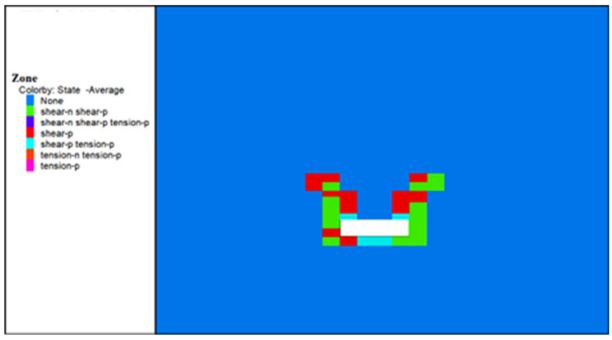

(**c**) The distribution cloud map of the plastic zone with the thickness of the false roof at 4.2 m

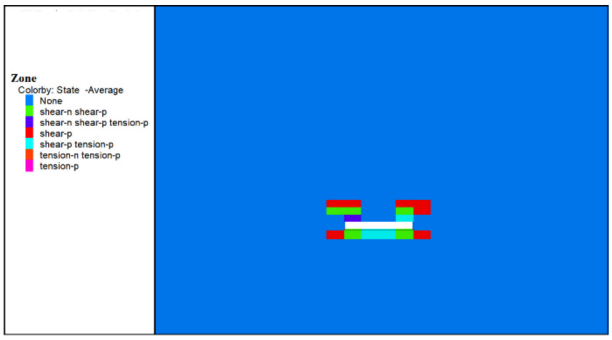

(**d**) Cloud map of plastic zone distribution with a thickness of 5.2 m for the false roof

Figure 9. Distribution of the plastic zone with different false roof thicknesses.

It can be seen from the figure that the failure rule of the plastic zone around the working face is the same. The false roof subsidence center area mainly has a tensile failure, and the subsidence boundary area has a shear failure. In the lower part of the subsidence transition area, the working face bottom plate is subjected to shear stress and tension at the same time. Plastic failure occurs under the influence of stress, and it is in a state of multi-directional stress failure.

When the thickness of the false roof is 2.2 m, tensile failure occurs mainly in the sinking center area of the false roof, while shear failure occurs in the sinking boundary area. When the false roof thickness is 3.2 m, there is a partial tensile failure within 1 m of the subsidence center area, and shear failure occurs in the subsidence boundary area. When the thickness of the false roof is 3.2~4.2 m, the deep part of the plastic zone does not increase significantly, but rather shear failure occurs in the sinking boundary area, and the plastic failure range does not increase significantly with the increase of the false roof thickness in the vertical and horizontal directions. When the thickness of the false roof is 4.2~5.2 m, the distribution area of the plastic zone around the working face is significantly reduced, and only less shear deformation occurs in the subsidence boundary area, and the false roof is in a stable state.

In summary, when the thickness of the false roof is less than 3.2 m, the extent of the plastic failure zone is significantly reduced as the thickness of the false roof increases; when the thickness of the false roof is 3.2–4.2 m, the thickness of the false roof increases, and in the plastic failure zone there is no significant expansion of the range; when the false roof thickness is greater than 4.2 m, the plastic failure zone will be further reduced with the increase of the false roof thickness. It should be pointed out that though the study is based on theoretical and numerical investigation, the results are relatively limited due to the selection of parameters. In the future, a field study will be conducted and then compared to the numerical study, which will be a guideline in this study.

5. Conclusions

(1) Based on the geological conditions of the Gaohe Mine, a mechanical model of the paste false top was established. By analyzing the two limit states of the paste false top in tensile failure and shear failure, it was concluded that the thickness of the upper layer should be at least 3.01 m for stability.

(2) The false roof subsidence area is divided into three areas: false roof subsidence boundary area, false roof subsidence transition area, and false roof subsidence central area, and the false roof thickness in the central area of false roof subsidence is obtained by the fitting curve. The cubic function relationship of the subsidence and the corresponding change trend of the false roof subsidence with the increase of thickness is analyzed through the slope of the curve.

(3) By analyzing the distribution of the plastic zone in the lower layered working face, it can be seen that when the false roof thickness is 2.2–3.2 m, the plastic failure range decreases with the increase of the false roof thickness; when the false roof thickness is 3.2–4.2 m, the plastic failure zone does not expand significantly with the increase of the false roof thickness; when the false roof thickness is 4.2–5.2 m, the plastic failure zone is further reduced with the increase of the false roof thickness. Since the total thickness of the top layer and the bottom layer is 6.4 m, the thickness of the top layer is too large or the thickness of the top layer is too small, which will increase the difficulty of mining, increase the requirements for support and equipment selection, and is not conducive to the work of upper and lower layers. Therefore, it is finally determined that the thickness of the false top layer of the paste filling is 3.2 m.

Author Contributions: Conceptualization by Q.C. and Y.S. (Yifeng Sun); methodology, Q.L.; investigation, Q.C.; writing—original draft preparation, Q.C. and Q.L.; writing—review and editing, Z.L., H.Z., and Y.S. (Yuantian Sun); supervision, Q.C.; funding acquisition, Q.C. and H.Z. All authors have read and agreed to the published version of the manuscript.

Funding: This research was supported by the projects of "the Fundamental Research Funds for the Central Universities (2020ZDPY0221, 2021QN1003)", and the "National Natural Science Foundation of China (52174130, 52104106, 52174089)".

Institutional Review Board Statement: Not applicable.

Informed Consent Statement: Not applicable.

Data Availability Statement: The data presented in this study are available on request from the corresponding author. The data are not publicly available due to privacy.

Acknowledgments: The authors are grateful to Gaohe coal mine.

Conflicts of Interest: The authors declare no conflict of interest.

References

1. Zhou, H.; Hou, C.; Sun, X.; Qu, Q.; Chen, D. Solid waste paste filling for none-village-relocation coal mining. *J. China Univ. Min. Technol.* **2004**, *33*, 154–158, 177.
2. Chang, Q.; Tang, W.; Xu, Y.; Zhou, H. Research on the width of filling body in gob-side entry retaining with high-water materials. *Int. J. Min. Sci. Technol.* **2018**, *28*, 519–524. [CrossRef]
3. Du, X.J.; Feng, G.R.; Qi, T.Y. Roof stability analyses of water-preserved and water-stored coal mining with construction backfill mining. *J. China Coal Soc.* **2019**, *44*, 821–830.
4. Xiuzhi, S.H.I.; Yonggang, G.O.U.; Xin, C.; Jia, L.U.O. Determination and application of the backfill thickness in the residual ore recovery of crown and sill pillar. *J. Min. Saf. Eng.* **2016**, *33*, 1080.
5. Wu, A.; Zhang, A.; Wang, H.; Gongcheng, L.; Rong, K. The mechanical model for the paste false roof and finite element analysis. *J. Min. Saf. Eng.* **2017**, *3*, 98–101.
6. Xikui, S.U.N.; Xiushan, L.I.; Xianyuan, S.H.I. Study on mine strata behavior with full backfill effect of paste backfill in coal mine. *Coal Sci. Technol.* **2017**, *45*, 48–53.
7. Tang, W.; Sun, X.; Wang, H.; Shi, X.Y.; Li, X.Y.; Li, Y. Study on effect of overlying strata stability during strip coal pillar excavation with paste backfilling. *Coal Sci. Technol.* **2017**, *45*, 109–115.
8. Sun, Y.; Li, G.; Zhang, J.; Xu, J. Failure Mechanisms of Rheological Coal Roadway. *Sustainability* **2020**, *12*, 2885. [CrossRef]
9. Basarir, H.; Sun, Y.; Li, G. Gateway stability analysis by global-local modeling approach. *Int. J. Rock Mech. Min. Sci.* **2019**, *113*, 31–40. [CrossRef]
10. Sun, Y.; Li, G.; Basarir, H.; Karrech, A.; Azadi, M.R. Laboratory evaluation of shear strength properties for cement-based grouted coal mass. *Arab. J. Geosci.* **2019**, *12*, 1–11. [CrossRef]
11. Ma, D.; Kong, S.; Li, Z.; Zhang, Q.; Wang, Z.; Zhou, Z. Effect of wetting-drying cycle on hydraulic and mechanical properties of cemented paste backfill of the recycled solid wastes. *Chemosphere* **2021**, *282*, 131163. [CrossRef]
12. Chen, J.; Liu, P.; Zhao, H.; Zhang, C.; Zhang, J. Analytical studying the axial performance of fully encapsulated rock bolts. *Eng. Fail. Anal.* **2021**, *128*, 105580. [CrossRef]
13. Sun, Y.; Li, G.; Zhang, J. Investigation on jet grouting support strategy for controlling time-dependent deformation in the roadway. *Energy Sci. Eng.* **2020**, *8*, 1–8. [CrossRef]
14. Sun, Y.; Li, G.; Zhang, J.; Qian, D. Experimental and numerical investigation on a novel support system for controlling roadway deformation in underground coal mines. *Energy Sci. Eng.* **2020**, *8*, 490–500. [CrossRef]
15. Ma, D.; Duan, H.; Liu, J.; Li, X.; Zhou, Z. The role of gangue on the mitigation of mining-induced hazards and environmental pollution: An experimental investigation. *Sci. Total Environ.* **2019**, *664*, 436–448. [CrossRef] [PubMed]
16. Chen, J.; Zhao, H.; He, F.; Zhang, J.; Tao, K. Studying the performance of fully encapsulated rock bolts with modified structural elements. *Int. J. Coal Sci. Technol.* **2021**, *8*, 64–76. [CrossRef]
17. Sun, Y.; Li, G.; Zhang, J.; Qian, D. Stability Control for the Rheological Roadway by a Novel High-Efficiency Jet Grouting Technique in Deep Underground Coal Mines. *Sustainability* **2019**, *11*, 6494. [CrossRef]
18. Ma, D.; Zhang, J.; Duan, H.; Huang, Y.; Li, M.; Sun, Q.; Zhou, N. Reutilization of gangue wastes in underground backfilling mining: Overburden aquifer protection. *Chemosphere* **2021**, *264*, 128400. [CrossRef]
19. Chang, Q.; Sun, X.; Dong, X.; Shao, S. Stability analysis of cemented paste backfill false roof in highwall mining: A case study. *Desalin. Water Treat.* **2021**, *219*, 96–102. [CrossRef]
20. Sun, Y.; Zhang, J.; Li, G.; Ma, G.; Huang, Y.; Sun, J.; Wang, Y.; Nener, B. Determination of Young's modulus of jet grouted coalcretes using an intelligent model. *Eng. Geol.* **2019**, *252*, 43–53. [CrossRef]
21. Sun, Y.; Li, G.; Zhang, N.; Chang, Q.; Xu, J.; Zhang, J. Development of ensemble learning models to evaluate the strength of coal-grout materials. *Int. J. Min. Sci. Technol.* **2021**, *31*, 153–162. [CrossRef]
22. Lv, W.; Wu, Y.; Ming, L.; Yin, J. Migration law of the roof of a composited backfilling longwall face in a steeply dipping coal seam. *Minerals* **2019**, *9*, 188. [CrossRef]
23. Fengshan, M.A.; Feng, L.I.U.; Jie, G.U.O.; Rong, L.U.; Huigao, G.U.O.; Yongyuan, K.O.U. Backfill stability analysis of steep dip mine using filling method. *J. Eng. Geol.* **2018**, *26*, 1351–1359.

24. Abbasi, B.; Russell, D.; Taghavi, R. FLAC3D mesh and zone quality. In Proceedings of the FLAC/DEM Symposium, Hangzhou, China, 22–24 October 2013; Itasca Consulting Group: Minneapolis, MN, USA, 2013.
25. Sears, M.M.; Slaker, B.; Rashed, G.; Winfield, J. Numerical model validation and analysis of a dipping limestone pillar using FLAC3D. In Proceedings of the 53rd US Rock Mechanics/Geomechanics Symposium, New York, NY, USA, 23 June 2019; OnePetro: New York, NY, USA, 2019.
26. Sun, Y.; Li, G.; Zhang, J.; Sun, J.; Huang, J.; Taherdangkoo, R. New Insights of Grouting in Coal Mass: From Small-Scale Experiments to Microstructures. *Sustainability* **2021**, *13*, 9315. [CrossRef]
27. Sun, Y.; Bi, R.; Chang, Q.; Taherdangkoo, R.; Zhang, J.; Sun, J.; Huang, J.; Li, G. Stability Analysis of Roadway Groups under Multi-Mining Disturbances. *Appl. Sci.* **2021**, *11*, 7953. [CrossRef]
28. Wu, K.; Shao, Z.; Qin, S.; Wei, W.; Chu, Z. A critical review on the performance of yielding supports in squeezing tunnels. *Tunn. Undergr. Sp. Technol.* **2021**, *115*, 103815. [CrossRef]
29. Wu, K.; Shao, Z.; Sharifzadeh, M.; Hong, S.; Qin, S. Analytical computation of support characteristic curve for circumferential yielding lining in tunnel design. *J. Rock Mech. Geotech. Eng.* **2021**, *13*, 1–13.
30. Zhu, D.; Yan, E.; Hu, G.; Lin, Y. Revival deformation mechanism of Hefeng Landslide in the Three Gorges Reservoir based on FLAC3D software. *Procedia Eng.* **2011**, *15*, 2847–2851. [CrossRef]

sustainability

MDPI

Article

The Effects of Rock Index Tests on Prediction of Tensile Strength of Granitic Samples: A Neuro-Fuzzy Intelligent System

Yan Li [1], Fathin Nur Syakirah Hishamuddin [2], Ahmed Salih Mohammed [3], Danial Jahed Armaghani [4,*], Dmitrii Vladimirovich Ulrikh [4], Ali Dehghanbanadaki [5] and Aydin Azizi [6]

1 Art College, Chongqing Technology and Business University, Xuefu Avenue, Nan'an District, Chongqing 4000678, China; 13272855916@163.com
2 Department of Civil Engineering, Faculty of Engineering, University of Malaya, Kuala Lumpur 50603, Malaysia; fathinnursyakirah@siswa.um.edu.my
3 Civil Engineering Department, College of Engineering, University of Sulaimani, Sulaymaniyah 46001, Iraq; ahmed.mohammed@univsul.edu.iq
4 Department of Urban Planning, Engineering Networks and Systems, Institute of Architecture and Construction, South Ural State University, 76, Lenin Prospect, 454080 Chelyabinsk, Russia; ulrikhdv@susu.ru
5 Department of Civil Engineering, Damavand Branch, Islamic Azad University, Damavand 39718-78911, Iran; A.dehghanbanadaki@damavandiau.ac.ir
6 School of Engineering, Computing and Mathematics, Wheatley Campus, Oxford Brookes University, Oxford OX33 1HX, UK; aydin.azizi@brookes.ac.uk
* Correspondence: danialarmaghani@susu.ru

Citation: Li, Y.; Hishamuddin, F.N.S.; Mohammed, A.S.; Armaghani, D.J.; Ulrikh, D.V.; Dehghanbanadaki, A.; Azizi, A. The Effects of Rock Index Tests on Prediction of Tensile Strength of Granitic Samples: A Neuro-Fuzzy Intelligent System. *Sustainability* **2021**, *13*, 10541. https://doi.org/10.3390/su131910541

Academic Editor: Anjui Li

Received: 18 August 2021
Accepted: 17 September 2021
Published: 23 September 2021

Publisher's Note: MDPI stays neutral with regard to jurisdictional claims in published maps and institutional affiliations.

Copyright: © 2021 by the authors. Licensee MDPI, Basel, Switzerland. This article is an open access article distributed under the terms and conditions of the Creative Commons Attribution (CC BY) license (https://creativecommons.org/licenses/by/4.0/).

Abstract: Rock tensile strength (TS) is an essential parameter for designing structures in rock-based projects such as tunnels, dams, and foundations. During the preliminary phase of geotechnical projects, rock TS can be determined through laboratory works, i.e., Brazilian tensile strength (BTS) test. However, this approach is often restricted by laborious and costly procedures. Hence, this study attempts to estimate the BTS values of rock by employing three non-destructive rock index tests. BTS predictive models were developed using 127 granitic rock samples. Since the simple regression analysis did not yield a meaningful result, the development of models that integrate multiple input parameters were considered to improve the prediction accuracy. The effects of non-destructive rock index tests were examined through the use of multiple linear regression (MLR) and adaptive neuro-fuzzy inference system (ANFIS) approaches. Different strategies and scenarios were implemented during modelling of MLR and ANFIS approaches, where the focus was to consider the most important parameters of these techniques. As a result, and according to background and behaviour of the ANFIS (or neuro-fuzzy) model, the predicted values obtained by this intelligent methodology are closer to the actual BTS compared to MLR which works based on linear statistical rules. For instance, in terms of system error and a-20 index, values of (0.84 and 1.20) and (0.96 and 0.80) were obtained for evaluation parts of ANFIS and MLR techniques, which revealed that the ANFIS model outperforms the MLR in forecasting BTS values. In addition, the same results were obtained through ranking systems by the authors. The neuro-fuzzy developed in this study is a strong technique in terms of prediction capacity and it can be used in the other rock-based projects for solving relevant problems.

Keywords: rock strength; tensile behaviour; neuro-fuzzy; regression; non-destructive tests

1. Introduction

In rock engineering, rock fracture mechanics are associated with the behaviours of rock deformation and failure patterns caused by crack initiation and propagation. The growth of cracks in rocks happens due to small micro-cracks, micro-defects, and failures of large pre-existing fractures in rock [1]. Rock has lower tensile resistance compared to compressive and shear resistance due to its brittleness properties. Therefore, understanding rock

behaviour such as tensile properties is essential for solving geotechnical problems during underground openings, surface excavation, and rock blasting and to ensure underground cavern stability. There are many methods for predicting rock tensile strength (TS). Direct test is considered the most effective method to derive the tensile capacity of rock specimen. Direct TS value can be determined accurately using a dumbbell-shaped specimen [2]. However, difficulties are often associated with the direct tensile test. Indirect approaches such as the Brazilian disc test are widely utilised by researchers due to their simplicity and efficiency during sample preparation and testing procedures [3]. Valid tensile pattern Brazilian disc of rock specimens can also be visualised through digital image correlation [4]. Several tests such as the half-ring and semi-circular bending tests are relevant to determine the TS of brittle rocks [5,6].

Aiming to obtain the most reliable method of TS value prediction, Xia et al. [7] examined the dynamic TS of Laurentian granite three ways, by the dynamic direct tension test (DTT), dynamic Brazilian test (BT), and dynamic semi-circular bend test (SCB). Their findings suggest that the overestimation of TS value for BT and DTT can be corrected using overload and internal friction impact mechanisms. The flat-joint model can reflect the peak tensile stress in Brazilian disc specimens [8]. Yuan and Shen [9] proposed improving the Brazilian tensile strength (BTS) method by increasing the number of disk specimens to twice the number of standard samples. Larger specimen size will underestimate the intrinsic rock TS as an indentation type of failure mechanism is anticipated [10]. The behaviour of rock in tension can be an effective indicator of the state of rock weathering. Aydin and Basu [11] stated that the Brazilian deformation index could differentiate rock weathering grade and demonstrate the distinct behavioural pattern of rock during the weathering process. Additionally, rock size contributes to underestimating TS value, while rock heterogeneity leads to an overestimation of TS [12]. Thus, extensive correction coefficient studies are needed to estimate rock tensile strength, ideally by using the Brazilian testing method [13].

Several experiments have been performed to estimate the rock TS reliably. To mention a few examples, Nazir et al. [14] and Kabilan [15] have presented the significant correlation between BTS and unconfined compressive strength in rocks statistically. Simple regression modelling revealed that input parameters such as point load index (Is_{50}), dry density (DD), and Schmidt hammer rebound number (R_n) gave an average level of accuracy to estimate the BTS values. Table 1 presents some of the important proposed empirical equations to estimate BTS values together with their regression types and performance predictions. Although performance capacities of these techniques are quite suitable, they are often unpredictable when some uncertainties are not addressed during the development process. However, numerous studies have highlighted the outstanding results of some new computational techniques, i.e., artificial intelligence in evaluating and predicting rock strength values [16,17].

Table 1. Some of the proposed empirically correlations between *BTS* and other rock tests.

References	Proposed Equations	Regression Type	R^2	Description
Heidari et al. [18]	$BTS = 0.88Is_{50} + 2.70$	L	0.9	40 Gypsum rocks
Altindag and Guney [19]	$BTS = 0.0423SH^{1.2799}$	NL	0.8	143 rock samples
Farah [20]	$UCS = 12.308BTS^{1.0725}$	NL	0.6	195 of limestone specimens
Kahraman et al. [21]	$UCS = 10.61BTS$	L	0.5	Igneous rocks
Nazir et al. [14]	$UCS = 9.25BTS^{0.947}$	NL	0.9	40 laboratory strength tests on dry limestone
Mohamad et al. [22]	$UCS = 15.361BTS - 10.303$	L	0.8	40 sets soft rock samples
Khandelwal et al. [23]	$BI = 0.59BTS^{0.769} - 5.085BTS^{0.531} + 0.009\gamma^{2.332}$	NL	0.9	13 types of rock from USA
Mahdiyar et al. [24]	$BTS = 1.993e^{0.027R_n}$	NL	0.7	100 granite block samples
Mahdiyar et al. [24]	$BTS = 0.022e^{2.182DD}$	NL	0.7	100 granite block samples

BTS = Brazilian tensile strength, Is_{50} = point load index, R_n = rebound number, γ = unit weight, DD = dry density, *UCS* = uniaxial compressive strength, *BI* = brittleness index, *SH* = surface hardness, L = linear, NL = non-linear, R^2 = coefficient of determination.

Artificial intelligence approaches perform the automatic creation of an analytical model that recognizes patterns and make decisions without human interventions. Many researchers have emphasised the capabilities of these techniques in the field of geotechnical engineering, and they have proven to aid various civil and mining engineering problems [25–40]. For forecasting BTS values, Singh et al. [41] performed artificial neural network (ANN) modelling analysis on schistose rock samples and they reported a good level of prediction performance. Çanakci et al. [42] evaluated the performance of the ANN and Gene Expression Programming model in predicting rock tensile and compressive strength. The mechanical properties of Yavuzeli basaltic rocks from a region in Turkey were used to construct the model algorithm. The neural network algorithm obtained better results in terms of coefficient of determination (R^2) with a value of 0.829. Ceryan et al. [43] did a thorough analysis of rock TS modelling using support vector machine (SVM) approaches, the least square SVM method, and ANN to weigh their computational advantage. Finally, they introduced LS-SVM as a robust model that can accurately and efficiently predict rock TS because the analysis process is much faster than the other two models. Table 2 shows some of the important studies in the areas of BTS prediction using different artificial intelligence approaches. As is obvious from this table, the artificial intelligence techniques are able to provide higher capability levels compared to empirical techniques in estimating BTS values.

Table 2. Artificial intelligence approaches presented to estimate rock BTS values.

References	Model	Input Parameters	Model Performance	Description
Singh et al. [41]	ANN	Petrographical characteristics	MAPE = 11%	Schistose rocks
Çanakci et al. [42]	ANN	V_p, DD, R_n, WA	R^2 = 0.99	86 samples of basalt from Turkey
Gurocak et al. [44]	MLPN	Is_{50}, R_n, γ	R^2 = 0.84	174 samples from Turkey
Ceryan et al. [43]	LS-SVM	POR, V_p, SDI, aggregate impact	R^2 = 0.86	55 carbonate rocks from Turkey
Mahdiyar et al. [24]	PSO-ANN	Is_{50}, DD, R_n	R^2 = 0.93	Granite rock samples
Huang et al. [45]	IWO-ANN	Is_{50}, DD, R_n	R^2 = 0.92	100 granite samples

V_p = p-wave velocity, Is_{50} = point load index, DD = dry density, R_n = rebound number, WA = water absorption, γ = unit weight, MAPE = mean absolute percentage error, MLPN = multilayer perceptron network, PSO = particle swarm optimization, IWO = invasive weed optimisation.

The problem related to the difficulty of conducting BTS tests, as mentioned before, can be solved using rock index tests, which are easier and faster to carry out. The focus of previous studies was to investigate the effects of both destructive and non-destructive rock index tests in estimating BTS values. However, sometimes there is a need to have non-destructive tests which will not fail during or after the test. Therefore, the objective of this study is to consider and use results of only non-destructive tests, i.e., ultrasonic velocity, Schmidt hammer, and density for prediction of BTS values. To do this, different basic and advanced statistical models, together with an adaptive neuro-fuzzy inference system (ANFIS) intelligent technique, are proposed for tensile strength prediction. The models, their backgrounds, design procedures, and the obtained results in evaluating behaviour of rock tensile strength will be discussed in detail. The more accurate and reliable model will be introduced for the same purpose.

2. Methods and Material

2.1. Laboratory Tests

One hundred fifty-four rock samples of blocks of granite were brought from a tunnel project located in Malaysia for assessment. In this project, there were three tunnel boring machines, namely Kamila, Selpah, and Tiara Midori. The tunnel is intended to help mitigate potential water shortages in the problematic region. The project utilized the available surface water runoffs from several important rivers, i.e., Kelau River, Bentong

River, and Telemong River. The tunnel starts in Pahang state with length of about 45 km and goes to Selangor state, with different overburden values in its route.

Rock index tests can be categorized into destructive and non-destructive tests. Destructive tests like point load are conducted to the specimen's failure to understand the sample behaviour under failure loading and stage, while non-destructive tests such as the Schmidt hammer are those without damage during and after tests conducted to evaluate a particular group behaviour, such as physical characteristics of the samples. This study focuses on the use of only non-destructive tests, i.e., ultrasonic velocity, Schmidt's hammer rebound, and density in assessment and evaluation of tensile response of the rock samples. Hardness of the rock surface was measured by performing non-destructive testing known as the Schmidt Hammer Rebound (SHR) test. Following the testing procedure found in the International Society for Rock Mechanics (ISRM) [46] guidelines, the average reading computed from 10 SHR tests was denoted as R_n rebound number. The L-type hammer was mounted vertically downwards against the rock samples. In addition, an ultrasonic velocity test was conducted to measure the degree of compactness of rock material. The core samples should be flat at both ends to transmit primary waves (p-wave) through the core samples. This test was conducted four times using Portable Ultrasonic Non-Destructive Digital Indicating Tester (PUNDIT) equipment following the ISRM [46] guidelines. The values recorded from the PUNDIT equipment are denoted as V_p. Specimens with higher density (lesser voids) display a higher V_p value. Apart from R_n and V_p, dry density (DD) tests were performed to measure the rock's physical properties.

Brazilian tests were performed to measure the TS of rock samples indirectly. Cylindrical disc-shaped specimens with flat end surfaces were prepared prior to the testing process. According to ISRM [46], the specimen's size should have an approximate thickness/diameter ratio of 2. In this article, a total of 127 data samples were established for the modelling and analyses, where DD, V_p, and R_n were set as predictors and BTS was assigned as the target value, which is very important to accurately predict.

The laboratory test results for this this study are summarized in Table 3.

Table 3. Laboratory test results summary.

Parameters Symbol	Group	Unit	Min	Max	Ave.	Sd.
R_n	Input	-	20	61	40.5	9.93
V_p	Input	m/s	2643	7702	5172.5	1331.60
DD	Input	g/cm^3	2.35	2.79	2.57	0.11
BTS	Output	MPa	3.2	12.9	8.05	2.58

Min = minimum value, Max = maximum value, Ave = average value, and Sd. = standard deviation.

2.2. ANFIS Background

ANFIS is a proper intelligent system that integrates fuzzy logic with the principle of neural networks [47]. Such a framework makes ANFIS modelling more systematic and less reliant on expert knowledge [48]. Hence, this section will describe ANFIS architecture and learning algorithms for the Takagi-Sugeno-Kang (TSK) fuzzy model. Generally, ANFIS efficiency is influenced by the selection of number and shape of membership function (MF), the number of rules, and their learning techniques. Seven fuzzy MFs are integrated in the ANFIS tools while four of them are the most widely applied. The four types of MF are Gaussian combination (gauss2mf), Gaussian curve (gaussmf), bell shape (gbellmf), and trapezoidal shape (trapmf). The output MFs for the TSK-model consist of two parameters which are constant and linear.

Five layers (i.e., fuzzy layer, product layer, normalised layer, defuzzy layer, and total output layer) are needed to construct this interference system. The ANFIS algorithm system can be simplified by assuming two inputs (x and y) and one output, f. The if-then rules for the first order of TSK fuzzy model may be conveyed as [48–50]:

$$Rule\ 1 : If\ (x\ is\ A_1)\ and\ (y\ is\ B_1),\ then\ z\ is\ f_1(x, y) \quad (1)$$

$$Rule\ 1: If\ (x\ is\ A_2)\ and\ (y\ is\ B_2),\ then\ z\ is\ f_2(x,y) \quad (2)$$

where x and y are the input of ANFIS, A and B are the nonlinear parameters, and $f_i(x,y)$ is the output of ANFIS expressed in terms of first-order polynomial. A five-layer ANFIS with three inputs and one output model structure will be used to estimate BTS. The nodes function for each layer will be further elaborated as follows:

- Layer 1 (fuzzy layer): Comprises adaptive nodes with functions expressed (Equations (3) and (4)) as:

$$O_{1,i} = \mu_{Ai}(x),\ i = 1,2 \quad (3)$$

$$O_{1,j} = \mu_{Bj}(y),\ j = 1,2 \quad (4)$$

  where x and y indicate the input nodes, A_i and B_i denotes the linguistic labels, $\mu(x,y)$ implies the MFs.
- Layer 2 (product layer): Includes the product layer of two fixed nodes labelled Π expressed as Equation (5).

$$O_{2,i} = \omega_i = \mu_{Ai}(x) \times \mu_{Bi}(y)\ ,\ i = 1,2 \quad (5)$$

- Layer 3 (normalised layer): Node function is to normalise the weight function of the following process and is labelled as N, Equation (6):

$$O_{3,1} = \overline{\omega}_i = \frac{\omega_i}{\omega_1 + \omega_1},\ (i = 1,2) \quad (6)$$

- Layer 4 (defuzzy layer): Contains adaptive nodes marked by a square, Equation (7):

$$O_{4,i} = \overline{\omega}_i f_i,\ (i = 1,2) \quad (7)$$

- Layer 5 (total output layer): Contains fixed node with function to compute overall output, Equation (8):

$$O_{5,i} = f_{out} = \sum \overline{\omega}_i f_i \quad (8)$$

  where $O_{1–5,i}$ denotes the output of each layer and ω_i represents the weight function of the next layer. Figure 1 illustrates the architecture of ANFIS. In addition, the overview of ANFIS flowchart is illustrated in Figure 2.

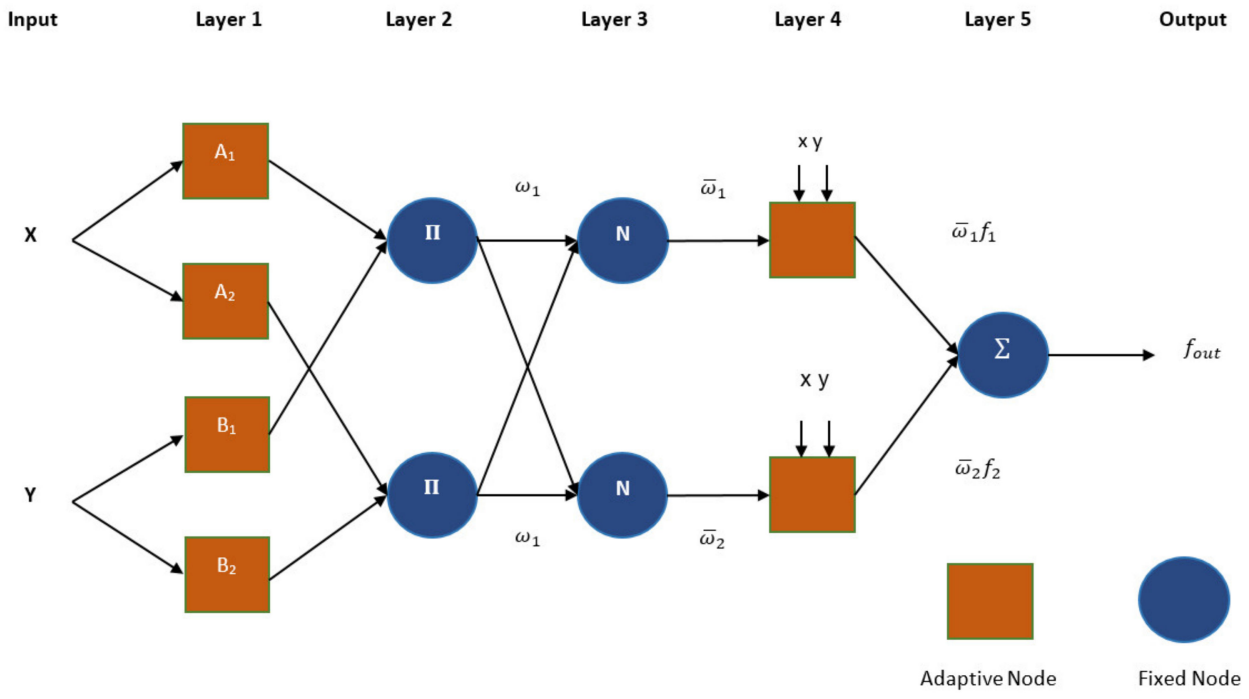

Figure 1. ANFIS architecture.

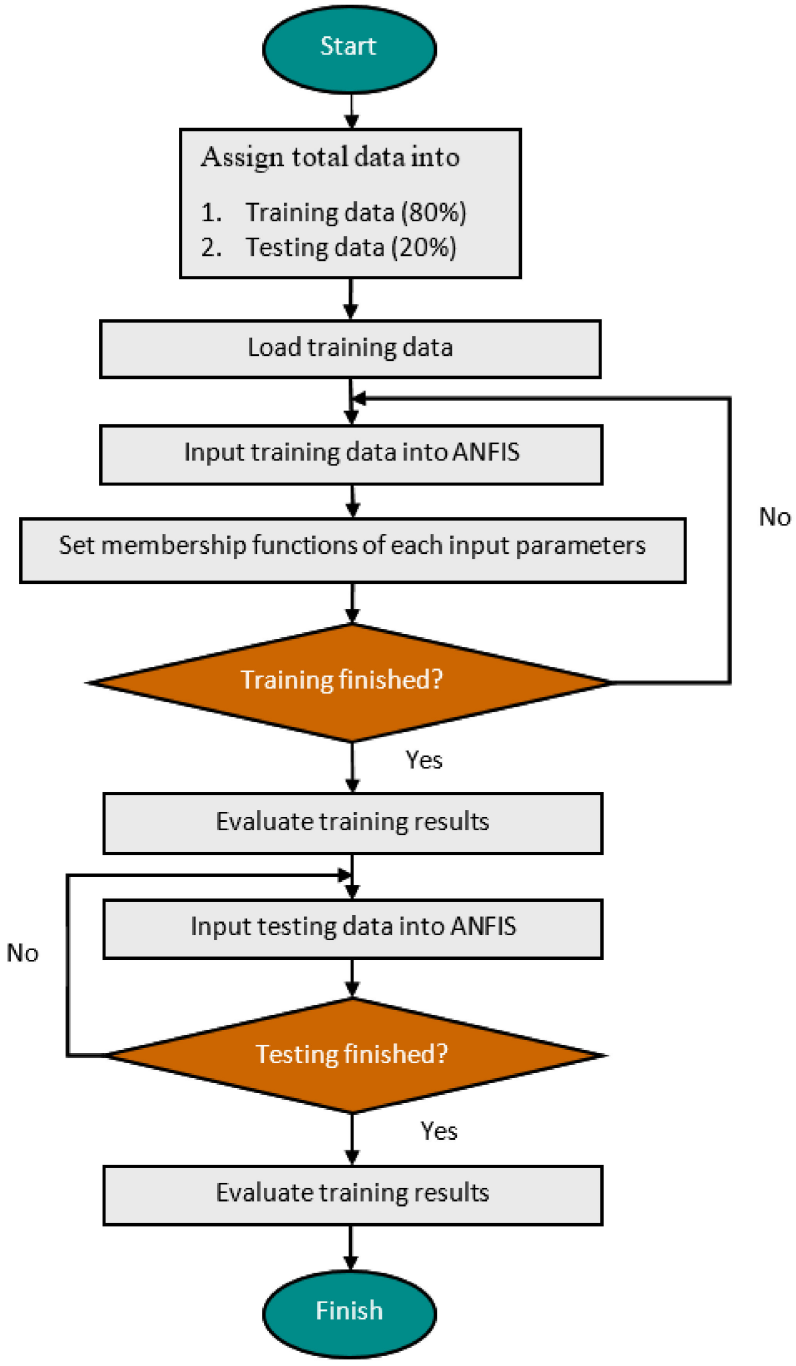

Figure 2. ANFIS flowchart for prediction purposes.

2.3. Step-by-Step Overview of Research

The general flowchart used for developing the rock TS model is shown in Figure 3. First, literature reviews of relevant research papers regarding indirect TS prediction were conducted. After identifying the research objective and problem statement, the Pahang-Selangor tunnel project was chosen to be studied. Obtaining adequate empirical data from related literature helped in the selection of the most influential parameters. In order to build the model, the database of non-destructive tests was prepared. In each model, the considered input parameters were R_n, V_p, and DD, while BTS was set as the target parameter. Then, both mathematical and soft-computing methods are used in this study to evaluate tensile behaviour of rock material. The empirical equations for TS estimation are proposed using simple regression (SR) and multiple linear regression (MLR).

Following that, ANFIS modelling is conducted to predict the rock TS values. Each model utilized the mentioned parameters and evaluated them based on their predictor intervals performance. For comparison purposes, performance indices are applied to the proposed model, respectively. Finally, the most reliable model is introduced as the suitable indirect approach for predicting TS rock.

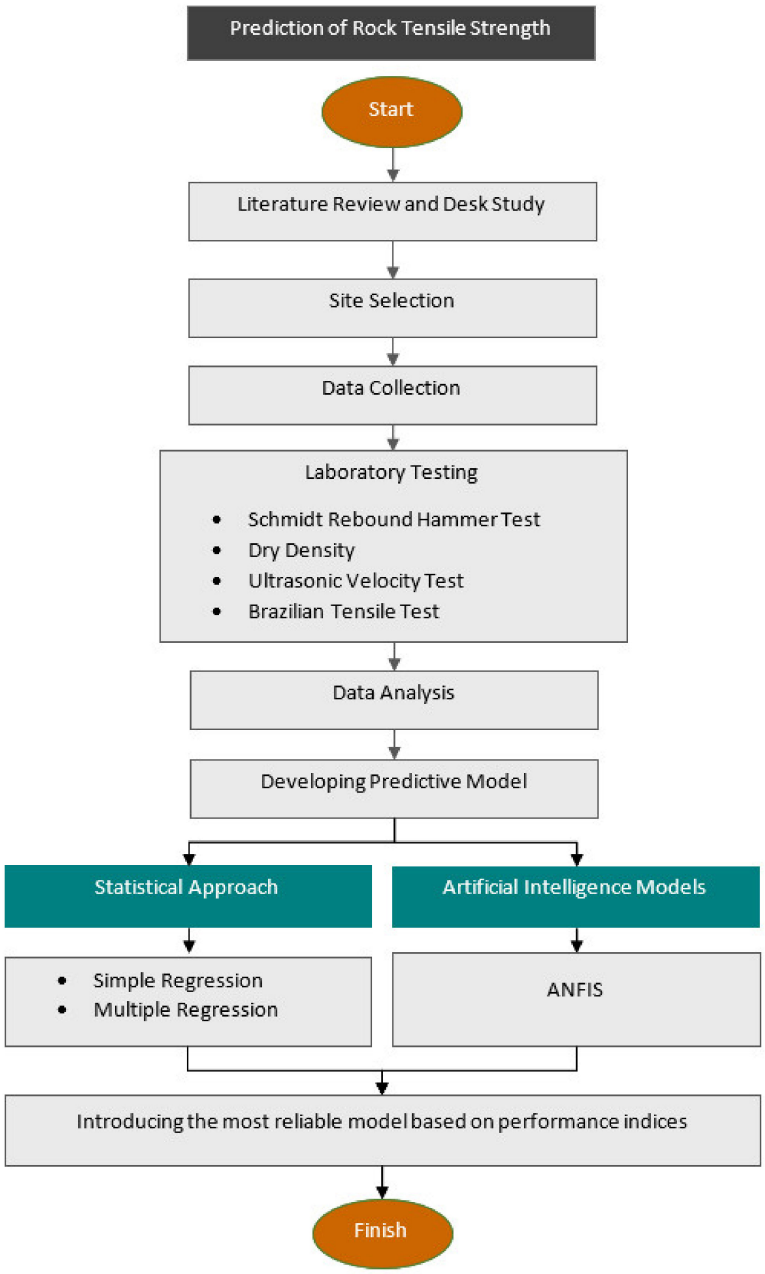

Figure 3. The sequence of research methodology.

It is important to note that we followed a typical flow of simulation and prediction studies in the area of rock mechanics [16,51]. They normally start with a SR technique, which is easy to conduct, but it is at the same time not accurate enough to solve the problems. Then, we move to a MLR model where more than one predictor can be used to increase prediction capacity. Finally, to increase the performance capacity, an intelligence technique (which is AFINS in this study) is used to predict the target values (which is BTS in this study).

2.4. Statistical Index

In this investigation, R^2, root mean square error (*RMSE*), variance account for (VAF%), and a-20 index were selected and used to assess the predictive models. Willmott and Matsuura [52] stated that large errors influenced the total square error rather than the smaller error. When the variances associated with the frequency distribution of error magnitudes increases, the *RMSE* increases. The fit accuracy of *RMSE* is numerically equivalent to zero. The *RMSE* formula is based on Equation (9).

$$RMSE = \sqrt{\frac{1}{n}\sum_{i=1}^{N}(y' - y)^2} \tag{9}$$

where y, y' and N conveys the measured, predicted, mean values, and the total numbers of data, respectively. R^2 is an indicator to determine the model fit for a set of quantitative dependent variables and their relation to the dependent variable. The determination of acceptable R^2 value is important to assess the adequacy and efficiency of the regression model. According to Menard [53], a "good" R^2 statistic should be dimensionless, have well defined values with endpoints that lead to a perfect fit to lack of fit range ($0 \leq R^2 \leq 1$), and be applicable to any models with random or non-random variables. The R^2 measurements in this study are based on Equation (10).

$$R^2 = 1 = \frac{\sum_i (y_i - \hat{y}_i)^2}{\sum_i (y_i - \overline{y})^2} \tag{10}$$

where y_i indicates the measured value of the dependent variable with a value between zero to one. $\hat{y}_i$ and $\overline{y}$ conveys the predicted and mean values of dependent variables, respectively. *VAF* is known as the proportion of the total population of the dependent variable that can be clarified by the factor of interest. Equation (11) can be used to describe the *VAF* formula:

$$VAF = \left[1 - \frac{var(y - y')}{var(y)}\right] \times 100\% \tag{11}$$

where observed, predicted, and mean values are represented by y and y', respectively. According to Xu et al. [54], a20-index is the newly proposed engineering index that is beneficial for evaluating artificial intelligence models by showing the number of samples that fit the prediction values with a deviation of $\pm$20% compared to experimental values, as presented in Equation (12).

$$a20 - index = \frac{m^{20}}{M} \tag{12}$$

where M represents the amount of dataset samples and m^{20} denotes the rate of experimental value/predicted value that lies between the range of 0.80 to 1.20.

3. Modelling, Analysis, and Results

3.1. SR Modelling

The SR technique can evaluate the correlation between two variables (predictors and targets parameters). SR assumes that the data followed a normal distribution pattern. In this study, SR analysis was performed for 127 data samples during the initial stage of the rock TS prediction. This part of the study was conducted to identify the relationship between each dependant variable (as mentioned in Table 3) and the BTS values as a target of the study. Various types of equations such as exponential ($y = mex^{cx}$), linear ($y = mx + c$), logarithmic ($y = m\ln(x) + c$), and power ($y = mx^c$) were used and the data samples were evaluated for each model to obtain the best empirical forecasting outcomes. Statistically, the best-fitted regression model results should project the value of R^2 = 1. Table 4 presents the results of each SR model analysis (according to the type of equations) and their ranking. Noted that for each SR model, rank 4 indicates the best correlation among all equations proposed.

Table 4. Results of SR model analysis in estimating rock strength values.

Model	Input	Equation Type	Equation	R^2	Rank
1	R_n	Exponential	$BTS = 2.5284e^{0.0279R_n}$	0.657	1
		Linear	$BTS = 0.2182R_n - 0.5659$	0.704	4
		Logarithmic	$BTS = 8.4797ln(R_n) - 22.854$	0.690	3
		Power	$BTS = 0.139R_n^{1.0984}$	0.659	2
2	Vp	Exponential	$BTS = 2.4945e^{0.0002V_p}$	0.646	4
		Linear	$BTS = 0.0015V_p - 0.3164$	0.638	2
		Logarithmic	$BTS = 7.518ln(V_p) - 56.298$	0.611	1
		Power	$BTS = 0.0013V_p^{1.0176}$	0.638	2
3	DD	Exponential	$BTS = 0.0101e^{2.5761DD}$	0.689	3
		Linear	$BTS = 19.171DD - 41.274$	0.670	1
		Logarithmic	$BTS = 49.169ln(DD) - 38.371$	0.671	2
		Power	$BTS = 0.0146DD^{6.6245}$	0.693	4

From Table 4, Model 1 shows a lack of fit approximation with a similar R^2 value of 0.658 ± 0.001 for exponential and power functions, respectively. In contrast, for Model 2, exponential function indicates a good correlation between V_p and BTS, with an R^2 of 0.646. It can be seen that both linear and power functions have the same ranking score (2) while logarithmic function ranks the lowest (1). Meanwhile, for Model 3, the power function has the second highest correlation coefficient (R^2 = 0.693) after Model 1. Therefore, the highest performance prediction equations were selected for each predictor (i.e., linear for R_n, exponential for V_p and power for DD). The graph of data plot for the best approximation equations for R_n, V_p and DD are shown in Figure 4. Overall, the scatter plot of all models has positive slopes, which corresponds to the positive correlation values. SR analyses indicate that Model 1 with R_n input has the strongest correlation value (R^2 = 0.70) among two other models. By referring to previous investigations [24], the results of R^2 for SR analyses fall within the range of 0.5 to 0.81. In this study, the average R^2 for SR analysis was 0.664, which is satisfactory. However, consideration of only one parameter for the prediction model is not enough to get the highest degree of accuracy. Hence, in the next prediction stage, the MLR modelling will be applied where more than one input is incorporated to predict BTS values.

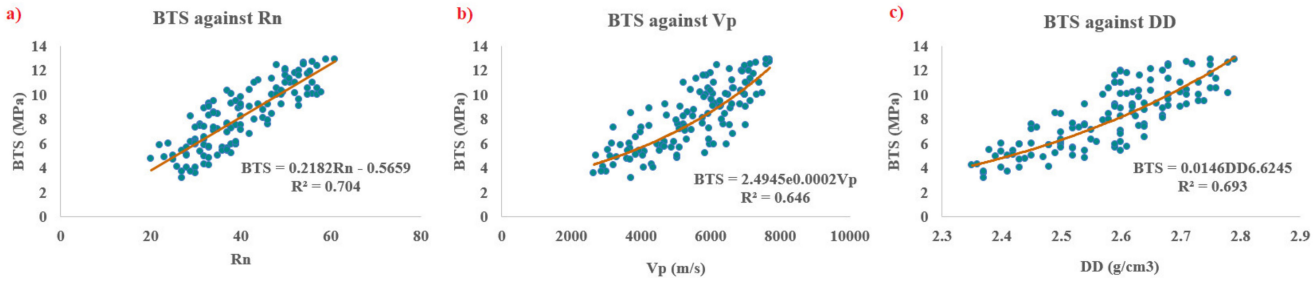

Figure 4. SR analysis results (**a**) BTS vs. R_n, (**b**) BTS vs. V_p, and (**c**) BTS vs. DD.

3.2. MLR Modelling

Generally, regression analysis requires a strong correlation between the variable to validate its credibility. In essence, MLR is the extension of ordinary least-squares regression that requires more than one independent variable. In the next stage of regression analysis, four models are introduced to predict *BTS*. Each model integrates different numbers of inputs but use the same output (i.e., *BTS*). Previous studies have mentioned that higher degree of accuracy can be achieved when more than one input is being considered [55,56]. A straightforward ranking approach can be used to evaluate each model [57]. The most fitting model for MLR analysis is the one that generates the highest-ranking score. By

referring to previous studies [58,59], 80% (102) of the whole data samples (127) were selected randomly for the model's training purposes. The remaining 20% (25) were used to test the models. Table 5 shows the MLR regression equations for different models with various combination types.

Table 5. MLR equations for BTS prediction.

Model No.	Input	Equation
MR1	V_p, DD	$BTS = 0.00089V_p + 11.5223DD - 26.4453$
MR2	R_n, DD	$BTS = 0.13804R_n + 10.5113DD - 24.5321$
MR3	R_n, V_p	$BTS = 0.143231R_n + 0.00076V_p - 1.76855$
MR4	R_n, V_p, DD	$BTS = 0.11068R_n + 0.00041V_p + 8.69973DD - 20.9934$

The series of MLR analyses for training and testing datasets together with prediction capacity indices results are presented in Tables 6 and 7, respectively. The testing R^2 values for MLR Model 1 (MLR1) which integrates two inputs appears to lie in satisfactory values of 0.68. Meanwhile, models MLR2 to MLR4 exhibit almost similar determination coefficient values (R^2 = 0.79, 0.71, and 0.78) that are acceptable. Considering the results of both train and test stages, it can be concluded that the MLR4 model reveals the highest total ranking score (15 + 13 = 28) for indices comparison with *RMSE*, *VAF*, R^2, and a20-index values of 1.051, 83.564%, 0.836, 0.843 for training datasets and 1.201, 77.869%, 0.780 and 0.80 for testing datasets. Hence, the recommended regression equation for MLR analysis is in fact the last equation presented in Table 5. Later, the performance of MLR models will be discussed in more detail.

Table 6. Training results of MLR analysis.

Model No.	Training Data				Training Ranking				Total Rank
	RMSE	VAF (%)	R^2	a20-Index	RMSE	VAF	R^2	a20-Index	
MR1	1.24	76.97	0.77	0.75	1	1	1	1	4
MR2	1.09	82.17	0.82	0.84	3	3	3	3	12
MR3	1.22	77.75	0.78	0.75	2	2	2	1	7
MR4	1.05	83.56	0.84	0.84	4	4	4	3	15

Table 7. Testing results of MLR analysis.

Model No.	Testing Data				Testing Ranking				Total Rank
	RMSE	VAF (%)	R^2	a20-Index	RMSE	VAF	R^2	a20-Index	
MR1	1.43	67.42	0.68	0.72	1	1	1	1	4
MR2	1.18	78.94	0.79	0.76	4	4	4	3	15
MR3	1.39	70.13	0.71	0.72	2	2	2	1	7
MR4	1.20	77.87	0.78	0.80	3	3	3	4	13

3.3. ANFIS Modelling

As mentioned in the last section, the modelling by ANFIS should be started using trained and test data that are already divided. In ANFIS modelling, the most important factors/values should be considered. The MFs in ANFIS modelling can be customised accordingly as one of the most important ANFIS parameters. According to MLR analyses, Model 4, which takes into account three inputs, outperforms the other MLR models. In this regard, the general characteristics of the ANFIS model consisted of three inputs data (including R_n, V_p, DD) and one output data (i.e., BTS). The size of 102 × 4 training and 25 × 4 testing data were imported in the workspace and loaded into the system. Initially, various fuzzy-interference system (FIS) properties were applied to define the acceptable ANFIS architecture basis. The FIS model structure set to "grid partition" was used to

classify the data and activate the neuro-fuzzy designer dialogue box. By utilising the same sequence of training and testing datasets as the MLR study, the constructed ANFIS models were educated with three types of MFs, namely Gaussian curve (gaussmf), Gaussian combination (gauss2mf), and generalized bell-shape (gbellmf). In addition, the model was constructed separately for each MF number (i.e., 2, 3, 4, and 5) and output type (i.e., constant and linear). Then, the fitness of each model with various ANFIS architectures were weighed against one another according to their statistical index results.

During the ANFIS modelling, a total number of 24 different models were developed to predict BTS values. However, to ensure that the prediction models are optimized and that the statistical data are not overfitted or underfitted, the chosen models should not have a substantial difference in training and testing performance. Hence, by following these benchmarks, the strength of remaining 8 ANFIS models were emphasized in this study and the models' specifications are presented in Table 8. Overfitting is a frequent issue in ANFIS modelling that appears when ANFIS overtrains the data [60]. The training of datasets using ANFIS has a maximum number of epochs before overfitting takes place which results in inaccurate prediction output. Multiple iteration guesses can be used to determine the optimal number of epochs. At first, to decide the minimum number of training epochs for each model, iteration was set up to 100 epochs, except for Model 1, which had its epoch increased up to 150. An optimal range of epochs value was created when the value of error tolerance became constant. The fitness of all ANFIS models was examined through evaluating their *RMSE*, *VAF*, R^2, and a20-index. A ranking system [61] was applied to each model to identify the model's performance in predicting BTS. The statistical indices computed and ranking scores for the ANFIS training and testing datasets are shown in Table 9. Based on this table, Model 4 was established as the most robust model in predicting BTS as it indicates the highest total ranking scores of (32 + 32 = 64 for train and test stages). Among all eight developed models, the statistical indices computed for Model 4 show significant improvement for training (*RMSE* = 0.69, *VAF* = 92.99%, R^2 = 0.93, a20-index = 0.96) and testing datasets (*RMSE* = 0.74, *VAF* = 91.62%, R^2 = 0.92, a20-index = 0.96) results. Figure 5 shows the base FIS and the proposed ANFIS structure for the selected model. Additionally, more information regarding the ANFIS parameters for Model 4 (i.e., the best model) is presented in Table 10. Gaussian MFs of the input parameters including R_n, V_p, DD are also displayed in Figure 6. These MFs and their range will give a better view to the readers or researchers when they wish to solve similar problems using ANFIS. More discussion regarding the best ANFIS model will be provided later.

Table 8. Eight ANFIS models and their specifications in predicting BTS values.

Model Name	Input		Output	Epoch
	MF No.	MF Type	MF Type	
Model 1	222	Bell Membership	Constant	117
Model 2	333	Bell Membership	Constant	10
Model 3	222	Gaussian	Constant	23
Model 4	333	Gaussian	Constant	88
Model 5	222	Gaussian 2	Constant	17
Model 6	333	Gaussian 2	Constant	6
Model 7	222	Bell Membership	Linear	9
Model 8	222	Gaussian 2	Linear	10

Table 9. Statistical indices for testing and training ANFIS models.

Model Name	Training Datasets									Testing Datasets								
	Statistical Index				Rank				Total	Statistical Index				Rank				Total
	RMSE	VAF (%)	R^2	a20-Index	RMSE	VAF	R^2	a20-Index		RMSE	VAF (%)	R^2	a20-Index	RMSE	VAF	R^2	a20-Index	
Model 1	0.98	85.69	0.86	0.89	3	3	5	5	16	1.10	81.19	0.81	0.84	7	7	6	7	27
Model 2	0.90	87.90	0.88	0.91	5	5	6	7	23	1.39	69.74	0.88	0.73	1	2	7	4	14
Model 3	1.01	84.80	0.85	0.87	2	2	4	3	11	1.15	79.37	0.79	0.80	5	5	4	6	20
Model 4	0.70	90.53	0.91	0.92	8	8	8	8	32	0.84	89.68	0.90	0.96	8	8	8	8	32
Model 5	1.01	84.73	0.85	0.88	2	1	4	4	11	1.14	79.50	0.80	0.84	6	6	5	7	22
Model 6	0.96	86.40	0.86	0.90	4	4	5	6	19	1.38	69.43	0.71	0.76	2	1	2	5	10
Model 7	0.85	89.20	0.89	0.88	7	7	7	4	25	1.32	71.82	0.73	0.84	3	3	3	7	16
Model 8	0.86	89.05	0.89	0.91	6	6	7	7	26	1.19	78.56	0.79	0.80	4	4	4	6	18

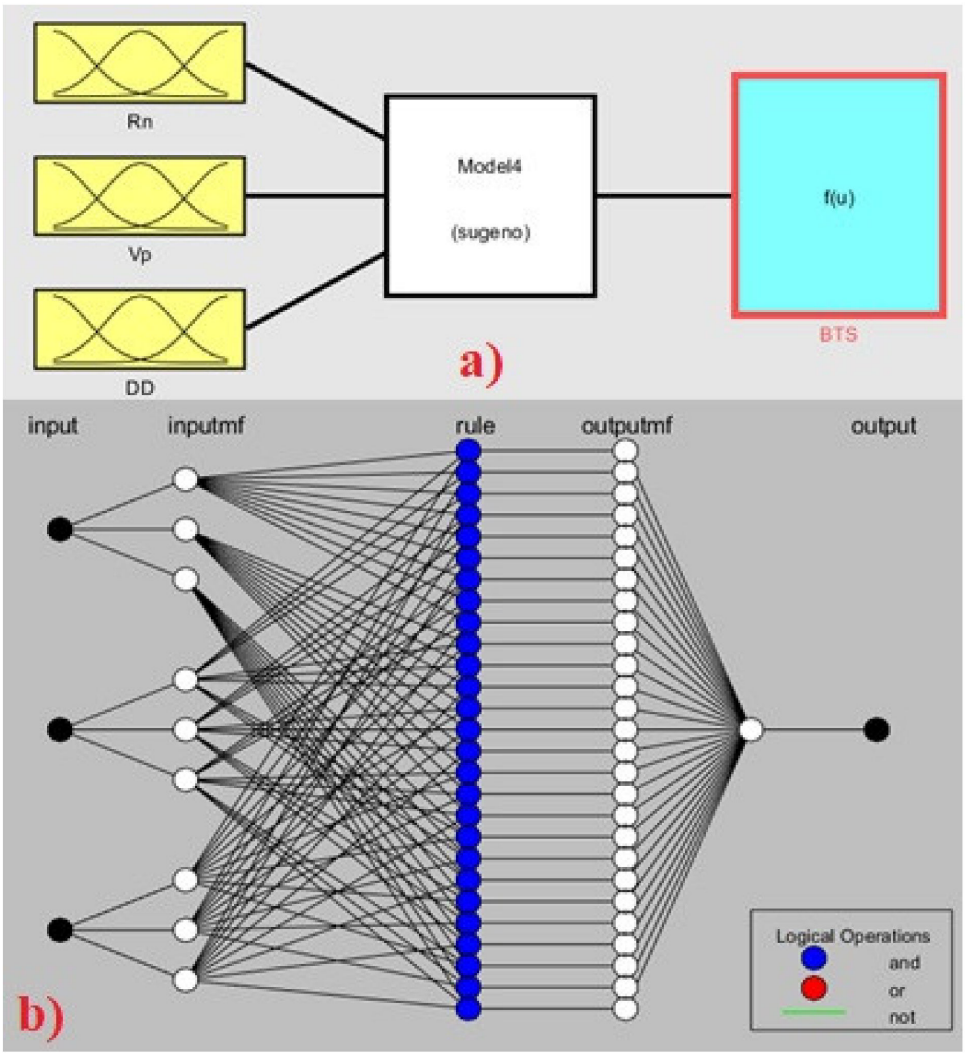

Figure 5. The proposed architecture used in this research: (**a**) base FIS model, (**b**) ANFIS structure.

Table 10. ANFIS Model 4 with its specifications.

Number of Layers	5
Training Data Size	102 × 4
Testing Data Size	25 × 4
FIS Properties	Grid Partition
Input FIS Structure	
MF Type	Gaussian
MF Number	333
Output FIS Structure	
MF Type	Constant
FIS Training	
Optimum Method	Hybrid
Error Tolerance	0
Epochs Number	88
FIS System	
Input	3
Output	1
Rules Number	27

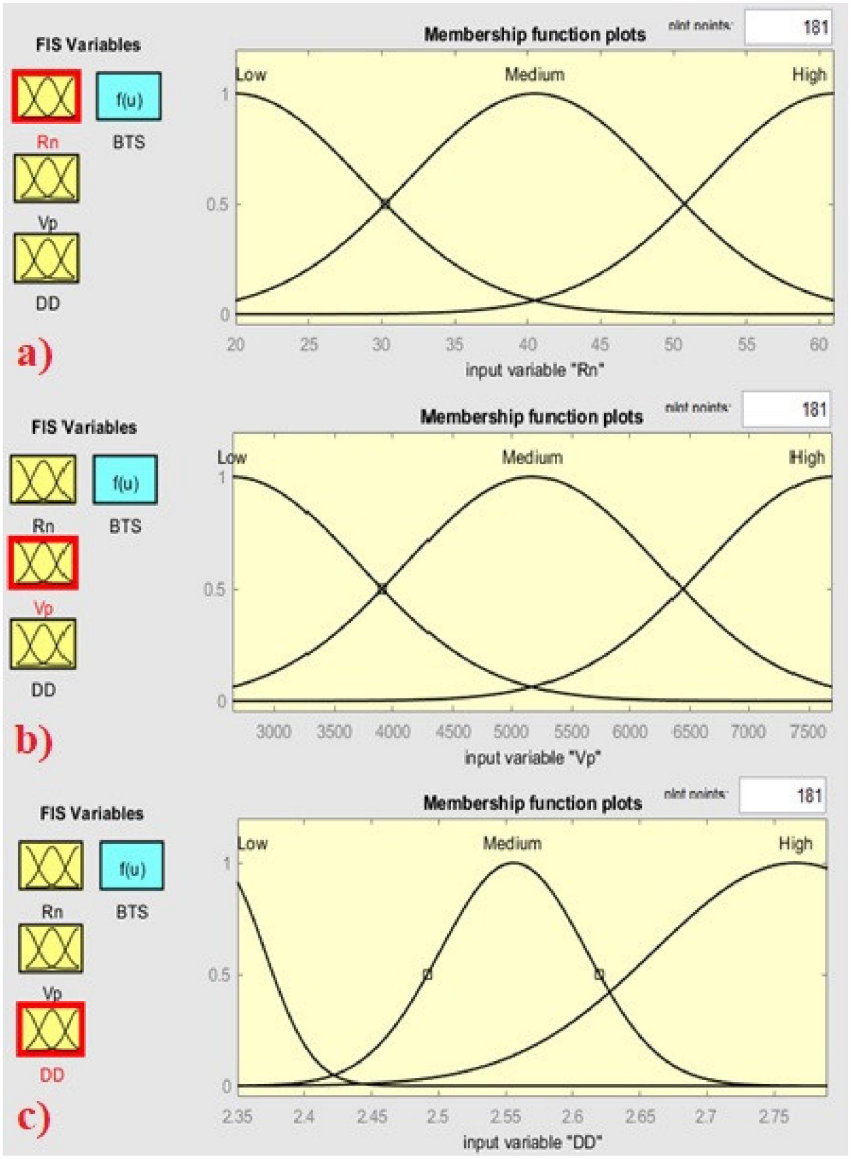

Figure 6. MFs plot of the selected ANFIS model: (**a**) R_n, (**b**) V_p, (**c**) DD.

4. Discussion

This section provides a quantitative assessment in terms of the performance of all established models during the testing and training phase. From the SR section, although the coefficient of determination results is within the acceptable range (based on previous studies), it did not yield a meaningful relationship with a strong level of accuracy. To improve prediction performance for BTS estimation, MLR and ANFIS modelling techniques were performed. As a result, four MLRs with multiple input parameters were proposed to enhance the BTS prediction significantly. Model MLR4 was able to generate a R^2 of 0.84 and 0.78 for the training and testing model, respectively. From this assessment, MLR R^2 (performance capacity) seems to be more reliable compared to the SR analysis with R^2 of 0.70 at most. It is important to mention that receiving a higher level of accuracy for predictive models is always of importance and interest in civil and mining engineering. Measured vs. predicted results of BTS for MLR4 are presented in Figure 7 for train and test stages. As shown, the prediction capacity was remarkably increased by the MLR model compared to SR models. However, higher R^2 or performance capacity values do not always imply that a model is superior. To evaluate the performance of the MLR model, the same dataset arrangement was employed using the ANFIS algorithm.

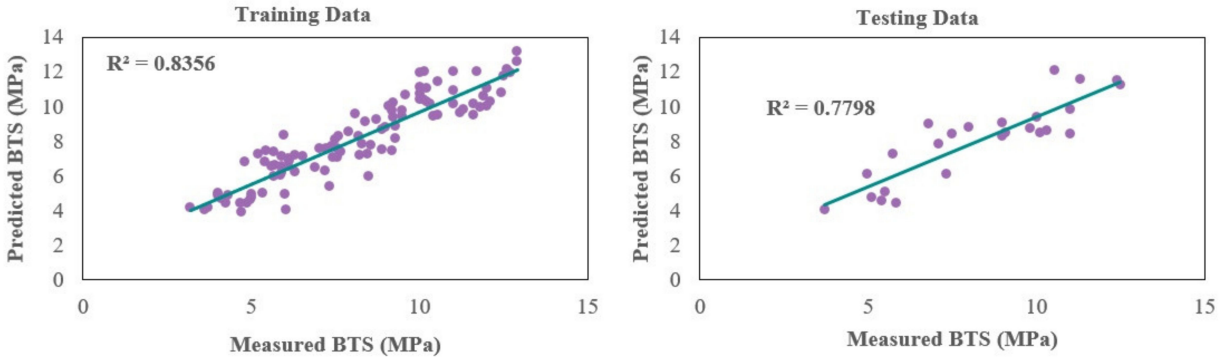

Figure 7. Measured vs. predicted BTS values by MLR Model 4.

The best predictive model will have the ideal best line of fit that minimizes the number of squares of divergence from the line of various data points [23]. Therefore, an outstanding predictive model will have the combination of lowest *RMSE* value and highest *VAF*, R^2, and a20-index values. Although the ANFIS model can run by using one training dataset, Al-Hmouz et al. [60] mentioned that the efficiency of the model can be improved when the testing datasets are combined with the training dataset to improve the accuracy of the model. The results of the ANFIS models showed that Model 4 was able to receive a high level of accuracy to predict tensile strength of rock material. The rule viewer of the proposed model displays a better visualization of the FIS structure (Figure 8). Based on the rule viewer, when the input parameter of R_n, V_p, and DD is 40.5, 5.17 × 10^3 m/s, and 2.57 g/cm^3, respectively, an output of BTS at 7.01 MPa is obtained. This figure also suggests that the ANFIS Model 4 has produced a total of 27 rules in which each rule has a single output MF, which is by default linear. The gradient vector was used to process the change in MF parameters, which shows how well the ANFIS is modelled by a given set of training data for a specific condition. FIS with many rules may generate a case-based reasoning model, in which each pair of training data have their own rules.

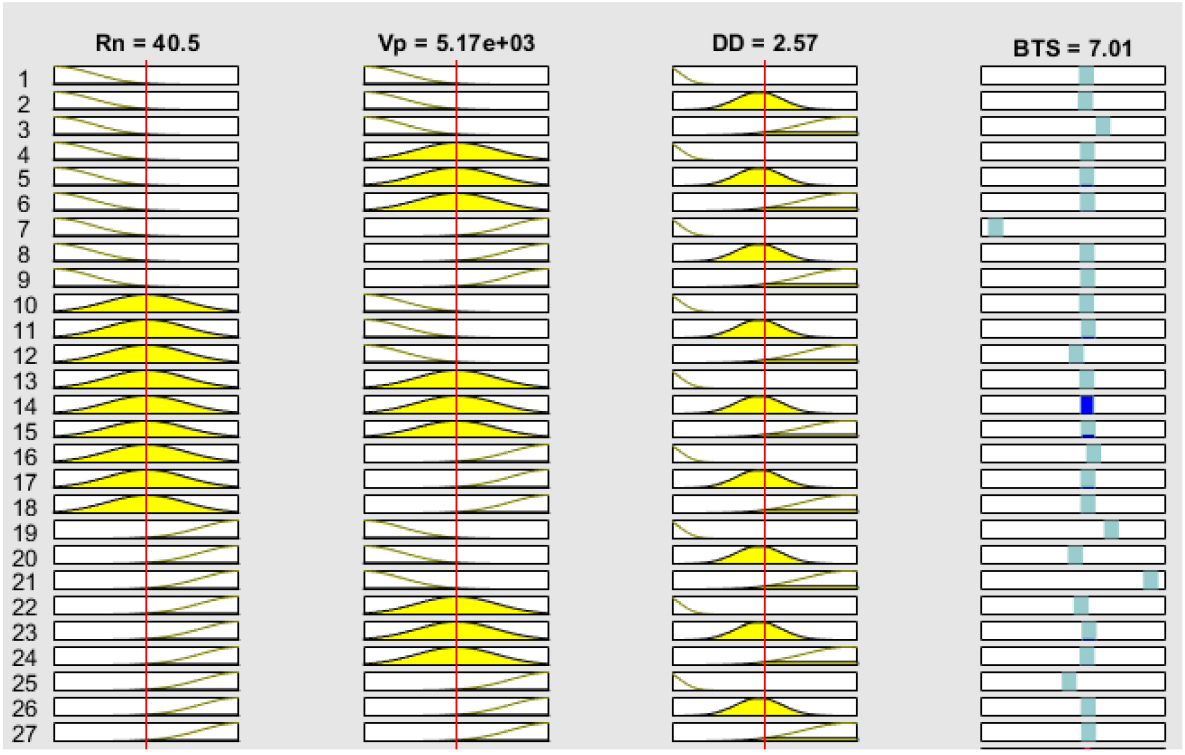

Figure 8. The integrated rules in the proposed ANFIS model.

The surface view tools generate and plot the output surface maps for the model which can be used to display the dependency of two inputs on the system output (Figure 9). For instance, high magnitude R_n and V_p will generate high BTS values (Figure 9a). Figure 9b shows that the model will generate a BTS approximation of 20 MPa when R_n and DD of 60 and 2.7 g/cm^3 are being presented. Meanwhile, the plot clustering in Figure 9c indicates that the model produces higher BTS output with the allocation of higher V_p and DD input values. Table 11 shows the results obtained by the selected MLR and ANFIS models to estimate BTS values. In addition, the graph of measured and predicted BTS values obtained by the best ANFIS model is displayed in Figure 10. According to Table 11 and Figure 10, it is obvious that the ANFIS model is able to increase prediction capacity of the MLR model in terms of all statistical indices. The clearer change is related to system error, which decreased from 1.05 to 0.69 in training and from 1.2 to 0.74 in testing. In addition, R^2 of the model improved from 0.84 to 0.93 and from 0.78 to 0.92 for training and testing stages, respectively. It is important to mention that full data used in the stage of testing are presented in Appendix A for better understanding.

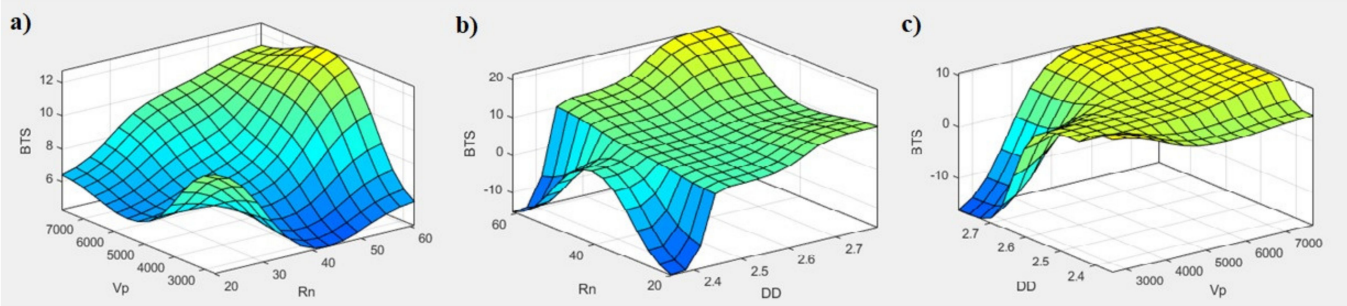

Figure 9. Surface visualization obtained from the selected ANFIS model. (**a**) BTS as a function of R_n and V_p, (**b**) BTS as a function of R_n and DD, and (**c**) BTS as a function of DD and V_p.

Table 11. The results obtained by the selected MLR and ANFIS models to estimate BTS values.

Model Name	Train				Test			
	RMSE	*VAF* (%)	R^2	a20-Index	*RMSE*	*VAF* (%)	R^2	a20-Index
ANFIS Model	0.70	90.53	0.91	0.96	0.84	89.68	0.90	0.96
MLR4	1.05	83.56	0.84	0.84	1.20	77.87	0.78	0.80

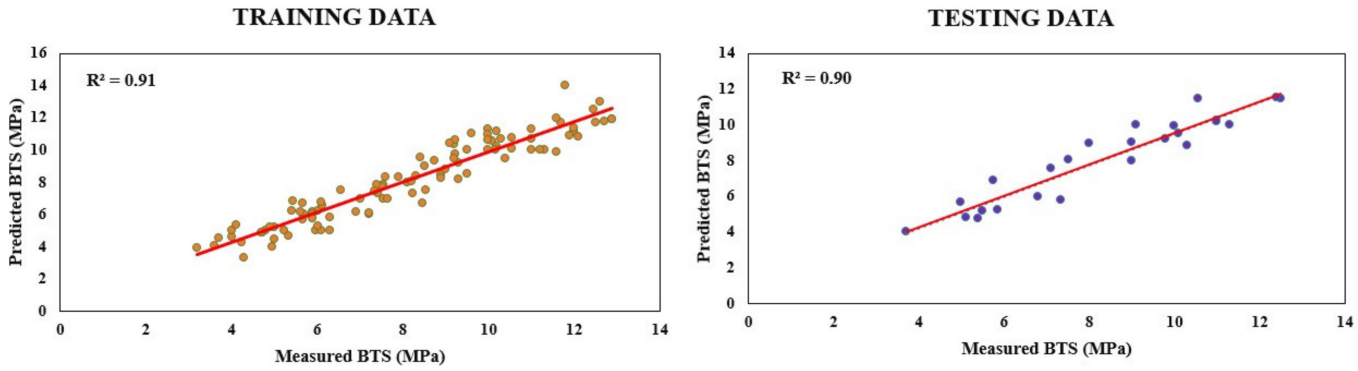

Figure 10. Measured vs. predicted BTS values by the proposed ANFIS model in this study.

A critical analysis of predictive modelling results by several researchers using soft computing techniques such as ANN was conducted to validate the outcomes of this research. For instance, the range of R^2 for an ANFIS predictive model proposed by Hasanipanah et al. [59] that integrates R_n, DD, and point-load index is between 0.857 to 0.897 for the testing stage of the model, which is lower than the performance prediction obtained in this

study. Ceryan et al. [43], who developed LS-SVM in predicting tensile strength of rock, obtained a R^2 of 0.86 which is lower than this study. In two other studies, Mahdiyar et al. [24] and Huang et al. [45] obtained similar results for their proposed models PSO-ANN and IWO-ANN, respectively. It is important to stress that most of the conducted studies in this field were focused on both non-destructive and destructive rock index tests. However, this study aimed to consider and use only non-destructive test results where the samples did not fail during or after these tests. By using these tests and the proposed structure of the ANFIS model in this study, similar results can be obtained by the other researchers and engineers.

5. Sensitivity Analysis

Sensitivity analysis (SA) which explores the relationship between a model's expectations and its model inputs, is useful for a computer-based framework. The multivariate nature of model inputs, as well as their uncertainty ranges, have a significant impact on systems. Conductive SA methodology can be beneficial for making more reliable prediction and allowing other researchers to make improvements in the future. Additionally, SA is able to identify the essential variable(s) that can give major influence on the predictive models. Hence, SA was carried out to recognize the relationship of each parameter with the ANFIS model. To apply this method, the following equation can be utilized to determine the relation strength (r_{ij}) between the model inputs (R_n, V_p, and DD) and output (BTS).

$$r_{ij} = \frac{\sum_{k=1}^{n} x_{ik} x_{jk}}{\sqrt{\sum_{k=1}^{n} x_{ik}^2 \sum_{k=1}^{n} x_{jk}^2}} \quad (13)$$

where x_{ik} is the model input, x_{jk} denotes the model output, and r_{ij} indicates the strength of relation. Figure 11 shows the r_{ij} values between each input and output parameter. The SA results demonstrate that R_n is the most important factor for BTS prediction, followed by V_p and DD. Similar results can be found in the SR and ANFIS techniques of the same study.

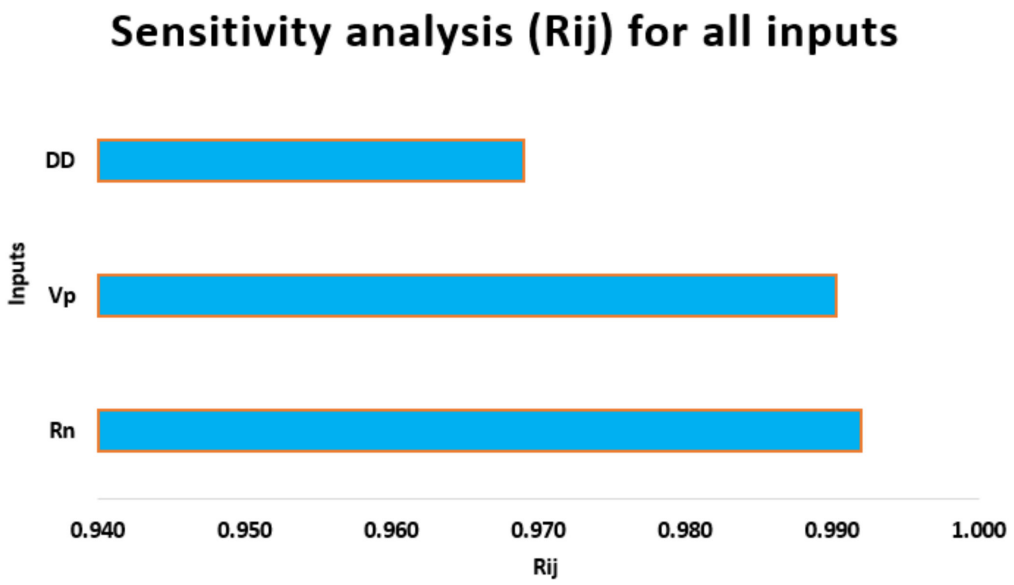

Figure 11. The importance of each input variable.

6. Limitations and Future Works

This research is subject to several limitations. Firstly, the database collected is predominantly made up of granite-type rock. According to Aydin and Basu [11], rock behaviours are site-specific, as they differ from one location to another. In this regard, the application of the recommended models to other types of rock that were not mentioned (such as basalts, marble, pumice, and so on) should be made with caution, as they might not yield the same

results as this study. It should also be noted that the model is appropriate to predict BTS when values of rock indices such as R_n and V_p are available in the same range as this research. It is suggested that future models should acquire data with larger sample sizes and variations to improve prediction accuracy. Among the various prediction techniques, this study focused on the capabilities of two conventional linear regression models (SR and MLR) and one form of artificial intelligence method (ANFIS). The implementation of optimization techniques such as IWO together with the ANFIS model can be considered in the future to examine their capability in predicting BTS values. In addition, a larger database comprising non-destructive rock index tests can be provided to propose a more comprehensive intelligence technique, since generalization of the proposed models is an important advantage in predictive models.

7. Conclusions

A comprehensive series of laboratory tests (i.e., non-destructive tests and Brazilian tests) were performed on more than 154 block samples brought from a water transfer tunnel project. Then, several SR-, MLR-, and ANFIS-based predictive models were designed and developed to assess the applicability of these methods in forecasting BTS. According to initial research, the need to develop BTS predictive models with higher degrees of accuracy was discovered through SR analyses. A range of 0.6–0.7 was recorded for the coefficient of determination of SR equations in predicting BTS values. Then, the authors decided to use another statistical-based technique which is able to consider the effects of all non-destructive tests as inputs in the analysis. From the regression statistic findings, the MLR4 model exhibited the best results with the highest-ranking scores of 28 among all other MLR models. The computed training RMSE, VAF, R^2 and a20-index values for this model were 1.05, 83.56, 0.84, and 0.84, respectively. The ANFIS model, on the other hand, significantly outperformed MLR analysis in terms of overall quality of the model. Model 4 of the ANFIS analysis achieved good model fit titles in which it ideally approximates the observed output. For this reason, the prediction using ANFIS Model 4 shall be introduced as the most robust approach in predicting BTS of granitic rock. In fact, the ANFIS structure proposed in this study, enjoying advantages of both ANN and fuzzy theory, can handle the BTS problem, which is complex and nonlinear. Proposing the ANFIS model, the accuracy of the MLR technique can be improved until 0.91 and 0.90 R^2 results are achieved. Additionally, based on sensitive analysis assessment, R_n indicates the most effective input parameters on BTS of the rock. Meanwhile, DD provides the lowest impact on BTS with R_{ij} value of 0.969.

Author Contributions: Conceptualization, D.J.A., A.A. and A.D.; methodology, F.N.S.H., D.J.A., Y.L.; software, F.N.S.H., D.J.A.; formal analysis, Y.L., F.N.S.H., D.J.A.; writing—original draft preparation, F.N.S.H., A.S.M., D.J.A.; writing—review and editing, Y.L., F.N.S.H., A.S.M., D.J.A., D.V.U., A.A., A.D.; supervision, D.J.A., D.V.U. All authors have read and agreed to the published version of the manuscript.

Funding: The research was funded by Act 211 Government of the Russian Federation, contract No. 02.A03.21.0011.

Institutional Review Board Statement: Not applicable.

Informed Consent Statement: Not applicable.

Data Availability Statement: The data are available upon request.

Acknowledgments: Authors of this study wish to express their appreciation to the University of Malaya for supporting this study and making it possible.

Conflicts of Interest: The authors declare no conflict of interest.

Appendix A

Table A1. The used data in testing phase.

Sample No.	R_n	V_p (m/s)	DD (g/cm^3)	BTS (MPa)
1	33	4670	2.61	5.75
2	34	3210	2.53	7.34
3	52	6102	2.59	11
4	54	7155	2.68	12.5
5	43	5217	2.59	11
6	42	6635	2.6	6.8
7	33	6080	2.68	9.1
8	57	6980	2.68	12.4
9	40	7003	2.54	7.5
10	27	3615	2.42	5.4
11	22	3430	2.48	5.85
12	37	6005	2.65	10.3
13	40	5832	2.63	9.8
14	50.8	7152	2.76	11.3
15	28	3866	2.42	5.1
16	48	6503	2.57	10
17	38	6430	2.6	10.1
18	37	3050	2.38	5.5
19	43	6320	2.58	7.99
20	57	6659	2.76	10.55
21	28	5040	2.52	4.99
22	29	2870	2.37	3.7
23	40	5463	2.55	7.1
24	42	7002	2.59	8.99
25	33	5125	2.7	9

References

1. Wu, H.; Kemeny, J.; Wu, S. Experimental and numerical investigation of the punch-through shear test for mode II fracture toughness determination in rock. *Eng. Fract. Mech.* **2017**, *184*, 59–74. [CrossRef]
2. Demirdag, S.; Tufekci, K.; Sengun, N.; Efe, T. Determination of the Direct Tensile Strength of Granite Rock by Using a New Dumbbell Shape and its Relationship with Brazilian Tensile Strength Determination of the Direct Tensile Strength of Granite Rock by Using a New Dumbbell Shape and its Relationship. In *IOP Conference Series: Earth and Environmental Science*; IOP Publishing: Bristol, UK, 2019.
3. Li, D.; Wong, L.N.Y. The brazilian disc test for rock mechanics applications: Review and new insights. *Rock Mech. Rock Eng.* **2013**, *46*, 269–287. [CrossRef]
4. He, W.; Chen, K.; Zhang, B.; Dong, K. Improving Measurement Accuracy of Brazilian Tensile Strength of Rock by Digital Image Correlation. *Rev. Sci. Instrum.* **2018**, *89*, 115107. [CrossRef] [PubMed]
5. Yao, W.; Xia, K.; Li, X. Non-Local Failure Theory and Two-Parameter Tensile Strength Model for Semi-Circular Bending Tests of Granitic Rocks. *Int. J. Rock Mech. Min. Sci.* **2018**, *110*, 9–18. [CrossRef]
6. Choi, B.H.; Lee, Y.K.; Park, C.; Ryu, C.H.; Park, C. Measurement of Tensile Strength of Brittle Rocks Using a Half Ring Shaped Specimen. *Geosci. J.* **2019**, *23*, 649–660. [CrossRef]
7. Xia, K.; Yao, W.; Wu, B. Dynamic Rock Tensile Strengths of Laurentian Granite: Experimental Observation and Micromechanical Model. *J. Rock Mech. Geotech. Eng.* **2017**, *9*, 116–124. [CrossRef]
8. Xu, X.; Wu, S.; Gao, Y.; Xu, M. Effects of Micro-structure and Micro-parameters on Brazilian Tensile Strength Using Flat-Joint Model. *Rock Mech. Rock Eng.* **2016**, *49*, 3575–3595. [CrossRef]

9. Yuan, R.; Shen, B. Numerical Modelling of the Contact Condition of a Brazilian Disk Test and Its Influence on the Tensile Strength of Rock. *Int. J. Rock Mech. Min. Sci.* **2017**, *93*, 54–65. [CrossRef]
10. Ma, Y.; Huang, H. DEM Analysis of Failure Mechanisms in The Intact Brazilian Test. *Int. J. Rock Mech. Min. Sci.* **2018**, *102*, 109–119. [CrossRef]
11. Aydin, A.; Basu, A. The Schmidt hammer in rock material characterization. *Eng. Geol.* **2005**, *81*, 1–14. [CrossRef]
12. Liao, Z.Y.; Zhu, J.B.; Tang, C.A. Numerical investigation of rock tensile strength determined by direct tension, Brazilian and three-point bending tests. *Int. J. Rock Mech. Min. Sci.* **2019**, *115*, 21–32. [CrossRef]
13. Briševac, Z.; Kujundžić, T.; Čajić, S. Sadašnje spoznaje o ispitivanju vlačne čvrstoće stijena uporabom Brazilskoga testa. *Rud.-Geol.-Naft. Zb.* **2015**, *30*, 101–114.
14. Nazir, R.; Momeni, E.; Armaghani, D.J.; Amin, M.F.M. Correlation between unconfined compressive strength and indirect tensile strength of limestone rock samples. *Electron. J. Geotech. Eng.* **2013**, *18*, 1737–1746.
15. Kabilan, N. Correlation between Unconfined Compressive Strength and Indirect Tensile Strength for Jointed Rocks. *Int. J. Res. Eng. Technol.* **2016**, *5*, 157–161.
16. Jahed Armaghani, D.; Mohd Amin, M.F.; Yagiz, S.; Faradonbeh, R.S.; Abdullah, R.A. Prediction of the uniaxial compressive strength of sandstone using various modeling techniques. *Int. J. Rock Mech. Min. Sci.* **2016**, *85*, 174–186. [CrossRef]
17. Jahed Armaghani, D.; Hajihassani, M.; Yazdani Bejarbaneh, B.; Marto, A.; Tonnizam Mohamad, E. Indirect measure of shale shear strength parameters by means of rock index tests through an optimized artificial neural network. *Meas. J. Int. Meas. Confed.* **2014**, *55*, 487–498. [CrossRef]
18. Heidari, M.; Khanlari, G.R.; Kaveh, M.T.; Kargarian, S. Predicting the Uniaxial Compressive and Tensile Strengths of Gypsum Rock by Point Load Testing. *Rock Mech. Rock Eng.* **2012**, *45*, 265–273. [CrossRef]
19. Altindag, R.; Guney, A. Predicting the relationships between brittleness and mechanical properties (UCS, TS and SH) of rocks. *Sci. Res. Essays* **2010**, *5*, 2107–2118.
20. Farah, R. Correlations between Index Properties and Unconfined Compressive Strength of Weathered Ocala Limestone. Master's Thesis, University North Florida, Jacksonville, FL, USA, 2011.
21. Kahraman, S.; Fener, M.; Kozman, E. Predicting the compressive and tensile strength of rocks from indentation hardness index. *J. South. Afr. Inst. Min. Metall.* **2012**, *112*, 331–339.
22. Mohamad, E.T.; Armaghani, D.J.; Momeni, E.; Abad, S.V.A.N.K. Prediction of the unconfined compressive strength of soft rocks: A PSO-based ANN approach. *Bull. Eng. Geol. Environ.* **2015**, *74*, 745–757. [CrossRef]
23. Khandelwal, M.; Faradonbeh, R.S.; Monjezi, M.; Armaghani, D.J.; Majid, M.Z.B.A.; Yagiz, S. Function development for appraising brittleness of intact rocks using genetic programming and non-linear multiple regression models. *Eng. Comput.* **2017**, *33*, 13–21. [CrossRef]
24. Mahdiyar, A.; Armaghani, D.J.; Marto, A.; Nilashi, M.; Ismail, S. Rock Tensile Strength Prediction Using Empirical and Soft Computing Approaches. *Bull. Eng. Geol. Environ.* **2019**, *78*, 4519–4531. [CrossRef]
25. Liu, B.; Yang, H.; Karekal, S. Effect of Water Content on Argillization of Mudstone during the Tunnelling process. *Rock Mech. Rock Eng.* **2019**, *53*, 799–813. [CrossRef]
26. Yang, H.; Wang, H.; Zhou, X. Analysis on the damage behavior of mixed ground during TBM cutting process. *Tunn. Undergr. Space Technol.* **2016**, *57*, 55–65. [CrossRef]
27. Zhou, J.; Qiu, Y.; Khandelwal, M.; Zhu, S.; Zhang, X. Developing a hybrid model of Jaya algorithm-based extreme gradient boosting machine to estimate blast-induced ground vibrations. *Int. J. Rock Mech. Min. Sci.* **2021**, *145*, 104856. [CrossRef]
28. Zhou, J.; Li, X.; Mitri, H.S. Classification of rockburst in underground projects: Comparison of ten supervised learning methods. *J. Comput. Civ. Eng.* **2016**, *30*, 4016003. [CrossRef]
29. Armaghani, D.J.; Hajihassani, M.; Mohamad, E.T.; Marto, A.; Noorani, S.A. Blasting-induced flyrock and ground vibration prediction through an expert artificial neural network based on particle swarm optimization. *Arab. J. Geosci.* **2014**, *7*, 5383–5396. [CrossRef]
30. Zhang, W.; Wu, C.; Zhong, H.; Li, Y.; Wang, L. Prediction of undrained shear strength using extreme gradient boosting and random forest based on Bayesian optimization. *Geosci. Front.* **2021**, *12*, 469–477. [CrossRef]
31. Zhang, W.G.; Li, H.R.; Wu, C.Z.; Li, Y.Q.; Liu, Z.Q.; Liu, H.L. Soft computing approach for prediction of surface settlement induced by earth pressure balance shield tunneling. *Undergr. Space* **2020**, *6*, 353–363. [CrossRef]
32. Zhang, W.; Li, H.; Li, Y.; Liu, H.; Chen, Y.; Ding, X. Application of deep learning algorithms in geotechnical engineering: A short critical review. *Artif. Intell. Rev.* **2021**, 1–41. [CrossRef]
33. Yang, H.; Wang, Z.; Song, K. A new hybrid grey wolf optimizer-feature weighted-multiple kernel-support vector regression technique to predict TBM performance. *Eng. Comput.* **2020**, 1–17. [CrossRef]
34. Armaghani, D.J.; Mohamad, E.T.; Narayanasamy, M.S.; Narita, N.; Yagiz, S. Development of hybrid intelligent models for predicting TBM penetration rate in hard rock condition. *Tunn. Undergr. Space Technol.* **2017**, *63*, 29–43. [CrossRef]
35. Park, S.-S.; Ogunjinmi, P.D.; Woo, S.-W.; Lee, D.-E. A Simple and Sustainable Prediction Method of Liquefaction-Induced Settlement at Pohang Using an Artificial Neural Network. *Sustainability* **2020**, *12*, 4001. [CrossRef]
36. Mohammed, A.S.; Asteris, P.G.; Koopialipoor, M.; Alexakis, D.E.; Lemonis, M.E.; Armaghani, D.J. Stacking Ensemble Tree Models to Predict Energy Performance in Residential Buildings. *Sustainability* **2021**, *13*, 8298. [CrossRef]

37. Gowida, A.; Moussa, T.; Elkatatny, S.; Ali, A. A hybrid artificial intelligence model to predict the elastic behavior of sandstone rocks. *Sustainability* **2019**, *11*, 5283. [CrossRef]
38. Yang, H.Q.; Lan, Y.F.; Lu, L.; Zhou, X.P. A quasi-three-dimensional spring-deformable-block model for runout analysis of rapid landslide motion. *Eng. Geol.* **2015**, *185*, 20–32. [CrossRef]
39. Zhou, J.; Shen, X.; Qiu, Y.; Li, E.; Rao, D.; Shi, X. Improving the efficiency of microseismic source locating using a heuristic algorithm-based virtual field optimization method. *Geomech. Geophys. Geo-Energy Geo-Resour.* **2021**, *7*, 89. [CrossRef]
40. Zhou, J.; Chen, C.; Wang, M.; Khandelwal, M. Proposing a novel comprehensive evaluation model for the coal burst liability in underground coal mines considering uncertainty factors. *Int. J. Min. Sci. Technol.* **2021**, *18*. [CrossRef]
41. Singh, V.K.; Singh, D.; Singh, T.N. Prediction of strength properties of some schistose rocks from petrographic properties using artificial neural networks. *Int. J. Rock Mech. Min. Sci.* **2001**, *38*, 269–284. [CrossRef]
42. Çanakci, H.; Baykasoğlu, A.; Güllü, H. Prediction of compressive and tensile strength of Gaziantep basalts via neural networks and gene expression programming. *Neural Comput. Appl.* **2009**, *18*, 1031–1041. [CrossRef]
43. Ceryan, N.; Okkan, U.; Samul, P.; Ceryan, S. Modeling of tensile strength of rocks based on support vector machines approaches. *Int. J. Numer. Anal. Methods Geomech.* **2012**, *37*, 2655–2670. [CrossRef]
44. Gurocak, Z.; Solanki, P.; Alemdag, S.; Zaman, M.M. New considerations for empirical estimation of tensile strength of rocks. *Eng. Geol.* **2012**, *144–145*, 1–8. [CrossRef]
45. Huang, L.; Asteris, P.G.; Koopialipoor, M.; Armaghani, D.J.; Tahir, M.M. Invasive Weed Optimization Technique-Based ANN to the Prediction of Rock Tensile Strength. *Appl. Sci.* **2019**, *9*, 5372. [CrossRef]
46. ISRM Turkish National Group. *The Complete ISRM Suggested Methods for Rock Characterization, Testing and Monitoring: 1974–2006*; ISRM Turkish National Group: Ankara, Turkey, 2009.
47. Armaghani, D.J.; Mohamad, E.T.; Momeni, E.; Narayanasamy, M.S. An adaptive neuro-fuzzy inference system for predicting unconfined compressive strength and Young's modulus: A study on Main Range granite. *Bull. Eng. Geol. Environ.* **2015**, *74*, 1301–1319. [CrossRef]
48. Çaydaş, U.; Hasçalik, A.; Ekici, S. An adaptive neuro-fuzzy inference system (ANFIS) model for wire-EDM. *Expert Syst. Appl.* **2009**, *36*, 6135–6139. [CrossRef]
49. Lo, S.P. The application of an ANFIS and grey system method in turning tool-failure detection. *Int. J. Adv. Manuf. Technol.* **2002**, *19*, 564–572. [CrossRef]
50. Armaghani, D.J.; Harandizadeh, H.; Momeni, E.; Maizir, H.; Zhou, J. An optimized system of GMDH-ANFIS predictive model by ICA for estimating pile bearing capacity. *Artif. Intell. Rev.* **2021**, 1–38. [CrossRef]
51. Armaghani, D.J.; Mohamad, E.T.; Hajihassani, M.; Yagiz, S.; Motaghedi, H. Application of several non-linear prediction tools for estimating uniaxial compressive strength of granitic rocks and comparison of their performances. *Eng. Comput.* **2016**, *32*, 189–206. [CrossRef]
52. Willmott, C.J.; Matsuura, K. Advantages of the mean absolute error (MAE) over the root mean square error (RMSE) in assessing average model performance. *Clim. Res.* **2005**, *30*, 79–82. [CrossRef]
53. Menard, S. Coefficients of determination for multiple logistic regression analysis. *Am. Stat.* **2000**, *54*, 17–24.
54. Xu, H.; Zhou, J.; Asteris, P.G.; Jahed Armaghani, D.; Tahir, M.M. Supervised Machine Learning Techniques to the Prediction of Tunnel Boring Machine Penetration Rate. *Appl. Sci.* **2019**, *9*, 3715. [CrossRef]
55. Bai, Q.S.; Tu, S.H.; Zhang, C. DEM investigation of the fracture mechanism of rock disc containing hole(s) and its influence on tensile strength. *Theor. Appl. Fract. Mech.* **2016**, *86*, 197–216. [CrossRef]
56. Kumar, B.R.; Vardhan, H.; Govindaraj, M. Prediction of Uniaxial Compressive Strength, Tensile Strength and Porosity of Sedimentary Rocks Using Sound Level Produced During Rotary Drilling. *Rock Mech. Rock Eng.* **2011**, *44*, 613–620. [CrossRef]
57. Gokceoglu, C.; Zorlu, K. A fuzzy model to predict the uniaxial compressive strength and the modulus of elasticity of a problematic rock. *Eng. Appl. Artif. Intell.* **2004**, *17*, 61–72. [CrossRef]
58. Liang, M.; Mohamad, E.T.; Faradonbeh, R.S.; Jahed Armaghani, D.; Ghoraba, S. Rock strength assessment based on regression tree technique. *Eng. Comput.* **2016**, *32*, 343–354. [CrossRef]
59. Hasanipanah, M.; Zhang, W.; Armaghani, D.J.; Rad, H.N. The potential application of a new intelligent based approach in predicting the tensile strength of rock. *IEEE Access* **2020**, *8*, 57148–57157. [CrossRef]
60. Al-Hmouz, A.; Shen, J.; Al-Hmouz, R.; Yan, J. Modeling and simulation of an Adaptive Neuro-Fuzzy Inference System (ANFIS) for mobile learning. *IEEE Trans. Learn. Technol.* **2012**, *5*, 226–237. [CrossRef]
61. Zorlu, K.; Gokceoglu, C.; Ocakoglu, F.; Nefeslioglu, H.A.; Acikalin, S. Prediction of uniaxial compressive strength of sandstones using petrography-based models. *Eng. Geol.* **2008**, *96*, 141–158. [CrossRef]

sustainability

MDPI

Article

New Insights of Grouting in Coal Mass: From Small-Scale Experiments to Microstructures

Yuantian Sun [1], Guichen Li [1,*], Junfei Zhang [2], Junbo Sun [3], Jiandong Huang [1,*] and Reza Taherdangkoo [4]

[1] Key Laboratory of Deep Coal Resource Mining, Ministry of Education of China, School of Mines, China University of Mining and Technology, Xuzhou 221116, China; yuantiansun@cumt.edu.cn
[2] School of Civil and Transportation Engineering, Hebei University of Technology, Tianjin 300401, China; junfeizhang@hebut.edu.cn
[3] School of Design and the Built Environment, Curtin University, Perth, WA 6102, Australia; junbo.sun@curtin.edu.au
[4] Institute of Geotechnics, TU Bergakademie Freiberg, Gustav-Zeuner-Str. 1, 09599 Freiberg, Germany; reza.taherdangkoo@ifgt.tu-freiberg.de
* Correspondence: liguichen@cumt.edu.cn (G.L.); huang@cumt.edu.cn (J.H.); Tel.: +86-1580-521-5566 (G.L.)

Abstract: Pre-grouting as an effective means for improving the stability of roadways can reduce maintenance costs and maintain safety in complex mining conditions. In the Guobei coal mine in China, a cement pre-grouting technique was adopted to enhance the overall strength of soft coal mass and provide sufficient support for the roadway. However, there are very limited studies about the effect of grouting on the overall strength of coal in the laboratory. In this paper, based on the field observation of a coal-grout structure after grouting, a series of direct shear tests were conducted on coal and grouted coal specimens to quantitatively evaluate the quality improvement of grouted coal mass. The results showed that the peak and residual shear strength, cohesion, friction angle and the shear stiffness of grouted coal were significantly improved with the increase of the diameter of grout column. Linear regression models were established for predicting these mechanical parameters. In addition, three failure models associated with coal and grouted coal specimens were revealed. According to microstructure and macroscopic failure performance of specimens, the application of the proposed models and some methods for further improving the stability of grouted coal mass were suggested. The research can provide the basic evaluation and guideline for the parametric design of cement pre-grouting applications in soft coal mass.

Keywords: pre-grouting; soft coal mass; coal-grout structure; shear behavior; quality improvement

Citation: Sun, Y.; Li, G.; Zhang, J.; Sun, J.; Huang, J.; Taherdangkoo, R. New Insights of Grouting in Coal Mass: From Small-Scale Experiments to Microstructures. *Sustainability* **2021**, *13*, 9315. https://doi.org/10.3390/su13169315

Academic Editor: Saeed Chehreh Chelgani

Received: 23 July 2021
Accepted: 14 August 2021
Published: 19 August 2021

Publisher's Note: MDPI stays neutral with regard to jurisdictional claims in published maps and institutional affiliations.

Copyright: © 2021 by the authors. Licensee MDPI, Basel, Switzerland. This article is an open access article distributed under the terms and conditions of the Creative Commons Attribution (CC BY) license (https://creativecommons.org/licenses/by/4.0/).

1. Introduction

The stability of tunnel projects is seriously affected by complex geological conditions such as water inflow, loose soil, fractured rock, etc. Grouting technique as an effective way to improve the integrity and continuity of geomaterials has been widely used in such poor conditions [1–3]. Among all grouting methods, the pre-grouting is commonly applied to ensure excavations safely and effectively, when tunneling in fractured rock mass or loose stratum [4]. The main function of pre-grouting is to increase the mechanical properties such as the overall strength (cohesion and friction angle) and stiffness of soft soil and rock mass before excavating tunnels [5]. The injected grout can fill the fractures in the rock and the voids in the soil, obstructing the penetration of water and enhancing the bearing capacity of surrounding strata [6]. Normally, cement-based grouts are used more often than any other materials in tunnel injection due to their characteristics of high strength, durability, ample source, and low costs [7].

Different from tunnels in rock or near-surface geotechnical level, roadways driven in coal seams for returning air and transporting coal out of the panel in deep underground coal mines are always exposed to worse surrounding conditions [8–12]. The structural and

mechanical properties of coal mass are dramatically degraded by the widely developed fractures, especially under deep burial and tectonic activities conditions [13]. In the Guobei coal mine in China, coal seams were subjected to complicated geological movements in the history yielding in substantial fractures and cracks in coal mass, which engendered extremely soft raw coal with low strength [14]. During the progress of the roadway excavation, the disturbance on soft coal mass results in collapse and localized failure at the driving face [15]. In the case of supporting such soft strata, the conventional supporting methods such as the bolting system, U-shaped steel with shotcrete could not control the large deformation effectively [16]. To address this problem, as per the experience of pre-grouting reinforcement in coal panels [17], and preventing groundwater inflow in the roadway [18] and jet grouting enhancement [19–21], a cement pre-grouting method was adopted to improve the overall strength of the soft coal mass and provide sufficient support for the roadway (shown in Figure 1). The strength improvement of soft coal mass after cement pre-grouting is a significant indicator to evaluate the grouting effect, which can be used for guiding the design of grouting parameters.

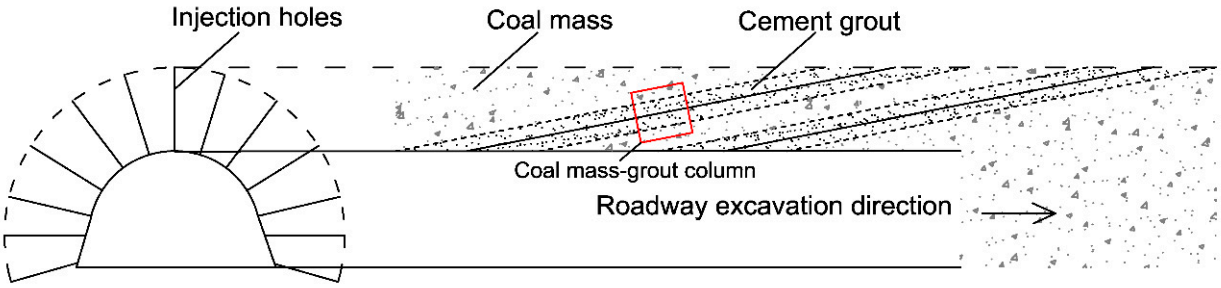

Figure 1. The pre-grouting technique used for soft coal seam in the Guobei coal mine and the formed coal mass-grout column in practice.

There are some studies on the evaluation of rock or soil improvement owing to cement grouting. Several researchers focused on conceptual consolidated models after cement injection [22]. Besides, other studies were interested in the quantitative evaluation of quality improvement of grouted rock and soil by field and laboratory tests [23–25]. For example, in situ dilatometer tests were conducted in rock before and after grouting to quantitatively examine the deformability of rock [26]. The shear strength of rock joint filled with injected cement was studied in the laboratory to assess the overall strength development [27]. The strength properties of soil after grouting treatment were investigated experimentally [28]. However, according to the diffusion of cement grout in soft coal mass in the field (Figure 1), to the authors' knowledge, quantitative research on the strength development of the formed coal mass-grout column is very limited. An effective way to estimate the strength of such a coal-grout structure is a shear test in the laboratory because it can comprehensively reflect the structures' stress conditions and easily obtain mechanical parameters such as cohesion and friction angle.

Therefore, according to the field observation of cement grouting to soft coal mass, this study focuses on investigating the grouting effect on the overall strength improvement of soft coal in a quantitative way. Different coal-grout models were designed and examined by laboratory shear tests. The shear properties (failure modes, deformation characteristics, shear strength, and shear stiffness) of coal and grouted coal specimens were examined. A set of linear regression formulas were proposed to predict the cohesion, friction angle and stiffness of grouted coal mass. Besides, the microscopic structure of the coal-grout interface and its effect on the failure characteristics were discussed. Based on the experimental results and microscopic observation, some methods for further improving the overall strength and stiffness of grouted coal mass were suggested.

2. Field Observation

The Guobei coal mine is located in the Huaibei Coalfield, in East China (Figure 2a) [29]. The extremely soft coal mass was observed in the No. 8 seam with the burial depth around 800 m, which is full of fractures and cracks (Figure 2b). The phenomenon of coal spalling and collapse was normally encountered at roadway working face because of the driving-induced stress and the poor quality of coal mass (Figure 2c) [30]. In addition, the present U-shaped shed support scheme cannot control the large displacement of roadway effectively, resulting in high maintenance costs. Accordingly, a pre-grouting technique was used to try to improve the strength of coal mass before driving the roadway in the field. The grouting material was P.O.325 with a water–cement ratio of 0.7 [31]. The grouting pressure was less than 4 MPa, normally around 2 MPa. After excavation, the typical consolidated structure of the coal-grout pile is shown in Figure 2d, indicating that the grout into such soft coal mass is compaction grouting instead of permeation grouting. The grouting diffusion radius was limited, but the coal around the grout was compacted. A schematic diagram of soft coal mass after grouting is shown in Figure 3. Hence, to qualitatively evaluate the effect of grouting for such coal mass, a reasonable model containing coal boundary and grout was presented, and its overall strength was assessed by direct shear tests.

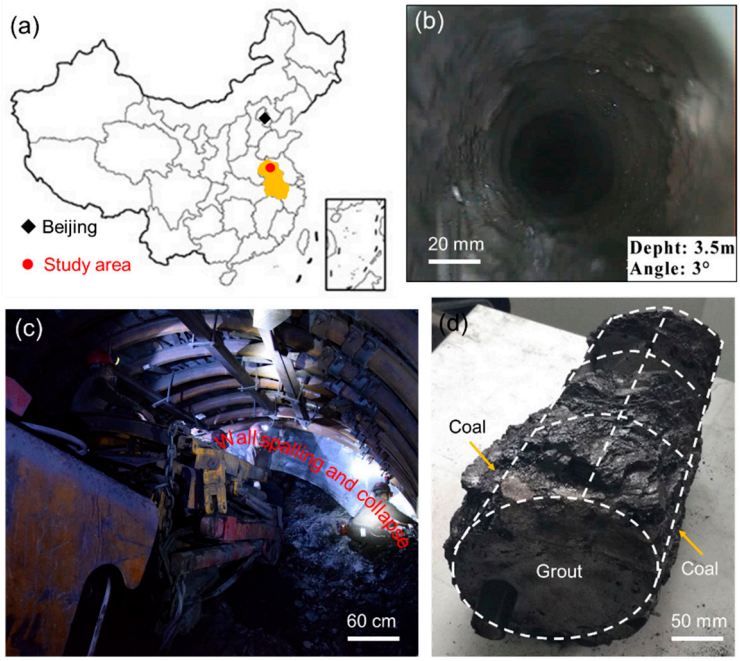

Figure 2. Field observation in the Guobei coal mine. (**a**) The location of the Guobei coal mine. (**b**) Cam view in the soft coal seam. (**c**) Wall spalling and collapse at driving working face. (**d**) Consolidated grouted coal after cement grouting.

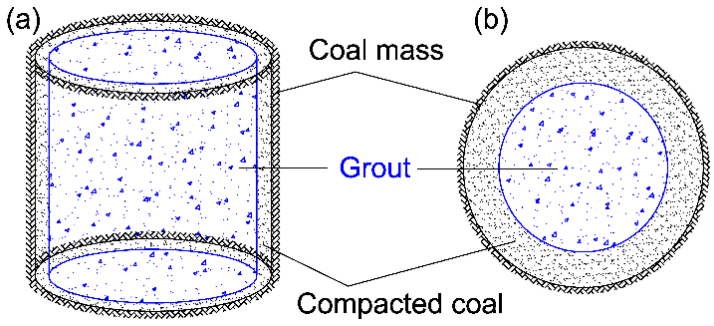

Figure 3. The schematic diagram of the coal-grout structure after compaction grouting. (**a**) the coal-grout structure. (**b**) cross section of coal-grout structure.

3. Experimental Methodology

3.1. Sample Preparation

Considering the field observation of cement grouting, a composite of the coal-grout specimen was designed and prepared to investigate the influence of grouting on soft coal mass. The specimen before grouting is shown in Figure 4. Both the outside diameter (D) and the height (H) of specimens are constant, 50 mm. The diameter of the inner grouting hole (d) is varied from 0 to 50 mm, in which it will be filled with cement grout (Figure 4a). To construct the external annulus of specimens (Figure 4b), a vertical load equivalent to in situ stress condition was applied to the fine-size coal collected from the driving roadway. Although the model we used may not perfectly represent the field conditions, it still provides a comparable way to investigate the reinforcement effect of compacting grouting on coal mass. To assess this, the grouting ratio (d/D) was defined, expressing the ratio of grout diameter (d) to the outside diameter (D) of the specimen.

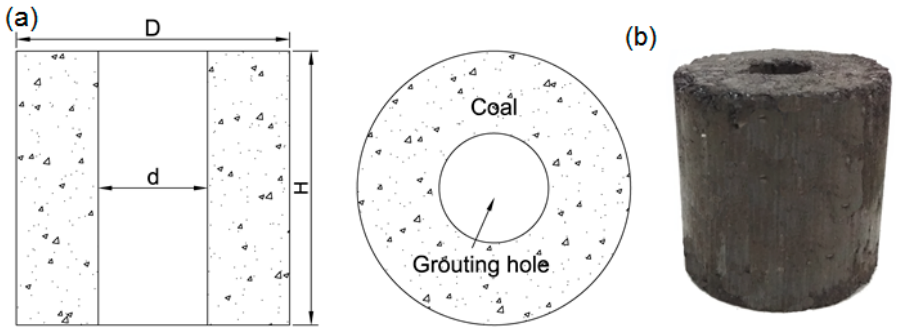

Figure 4. The geometry and size of the prepared specimen. (**a**) Diagrammatic sketch of coal specimen. (**b**) Real sample without grouting.

3.2. Grouting Procedure

To inject the cement grout into coal samples with pressure, an indoor grouting test system composed of a grouting chamber and pressure source was designed (Figure 5a). The grouting chamber was assembled by steel plates and bolts. Rubber seal was used for ensuring the airtightness between the steel plates. The pressure source was a nitrogen cylinder filled with compressed air to provide pressure for grouting. The cement used in this study was a locally available P.O. 325 with water reducer to improve the fluidity of the mix. The water–cement ratio (w:c) of the grout was 0.7. The coal sample was loaded into the grouting chamber, and then the prepared cement paste was poured into the inner hole until covering the top surface of the coal sample. After that, the grouting chamber was closed and sealed by bolts. The exhaust valve was opened, and the high-pressure gas entered the grouting chamber for further improving the consolidation of the grout. The pressure was kept at 1 MPa for 1 h. After grouting, the samples were cured for 28 days in a curing room at constant temperature and humidity (Figure 5b). The basic experiment of coal and grout such as compression tests was conducted. The compressive strength (UCS) of coal and cement paste (28 days' strength) is 2.5 MPa and 7.2 MPa, respectively.

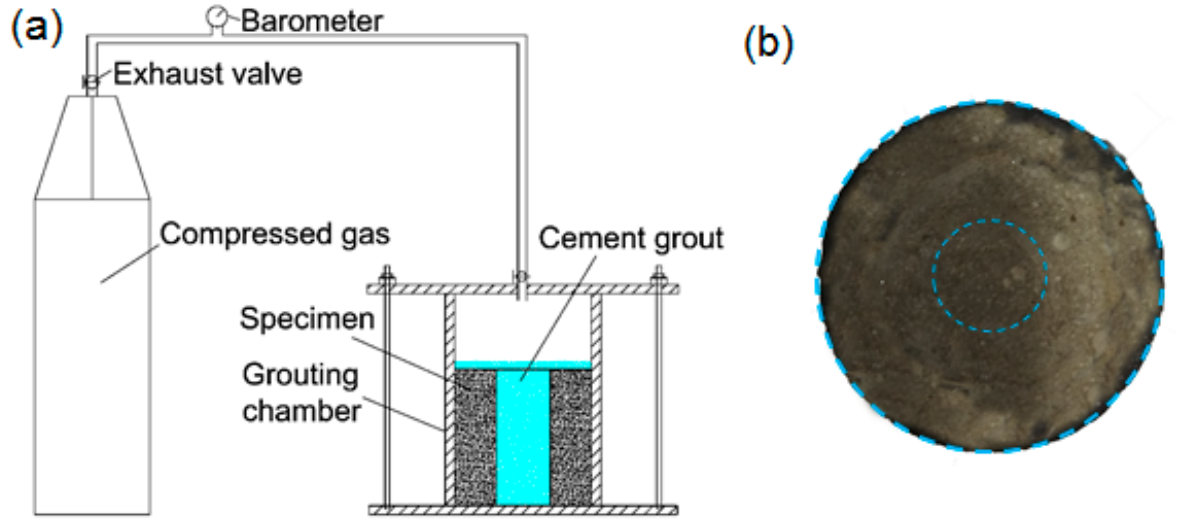

Figure 5. The grouting system and grouted samples. (**a**) Schematic diagram of the indoor grouting system. (**b**) Top view of samples after grouting.

3.3. Shear Tests Design

The shear tests of coal and grouted coal specimens were conducted using a servo-hydraulic direct shear apparatus (Figure 6a). The maximum horizontal shear displacement of the machine is 20 mm, gauged by a sensor with an accuracy of 0.001 mm. The normal/horizontal loading rate and their corresponding velocities can be chosen in the range of 0.01–2 kN/s, 0.001–2 mm/s, respectively. A special shear box was designed and manufactured to be used for shear test (Figure 6b,c). During the tests, the upper box is fixed and the lower box can be moved.

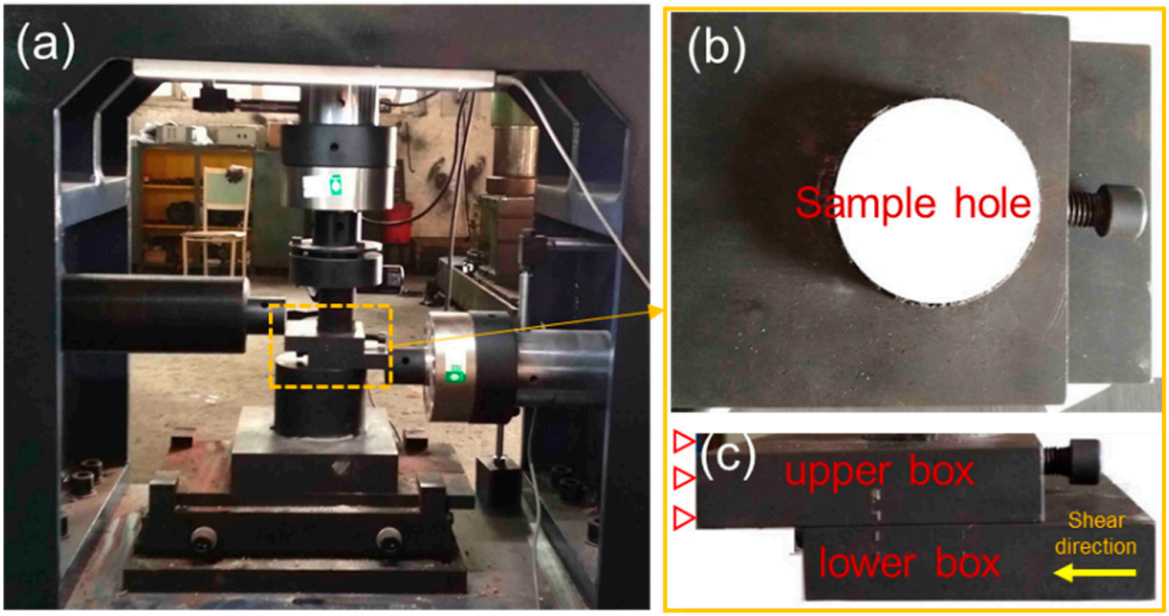

Figure 6. Servo-hydraulic shear test machine with a specially designed shear box. (**a**) Shear test apparatus with the loading control system. (**b**) Top view of the shear box. (**c**) Front view of the shear box.

The shear tests of pure coal and grouted coal specimens were examined according to Table 1. To reveal the effect of grouting ratio (d/D) on the shear behavior of reinforced samples, the different diameters of grouting holes were designed as 0, 10, 20, 30, 50 mm, corresponding to grouting ratio, d/D of 0, 20, 40, 60, 100%, respectively. During the shear

tests, normal loading was applied at 0.05 kN/s to a set value, then held constant. The magnitude of the normal load was divided into three catalogs, i.e., 1.0 kN, 1.5 kN, and 2.0 kN (given in Table 1). A shear load subsequently was applied with displacement control at a rate of 0.05 mm/s. All calculations have been done based on the standard test method for performing laboratory direct shear tests (ASTM D5607).

Table 1. Design of shear tests.

Grouting Ratio, d/D (%)	Diameter of Grouting Hole (mm)	Normal Load (kN)	Equivalent Normal Stress [b] (MPa)	Shear Velocity (mm/s)
0 [a]	0	1.0	0.51	0.05
20	10			
40	20			
60	30			
100	50			
0	0	1.5	0.77	
20	10			
40	20			
60	30			
100	50			
0	0	2.0	1.02	
20	10			
40	20			
60	30			
100	50			

[a] Without grout, pure coal samples. [b] Equivalent normal stress = Normal load/original area of test coal-grout cross-section (circular, diameter = 50 mm).

4. Experimental Results

4.1. Shear Behavior and Failure Modes

The shear stress versus shear displacement curves for different grouting ratios (d/D) under different normal stresses is illustrated in Figure 7. In general, both the peak and residual shear stress increased and the peak shear displacement decreased with increasing d/D and normal stress. Figure 7a depicts the shear stress-displacement curves under lower normal stress σn, 0.51 MPa. The shear stresses in the curves of d/D, 0%, 20%, 40% rose slowly until peak stress and then decreased gradually to a residual level. The peak shear stresses for pure coal samples and coal-grout samples signified the coal failure and composite failure, respectively. As the grouting ratio increased, even for lower normal stress, multi-stage failure can be observed. For the high d/D, 60%, there were two peak stress values, showing the non-simultaneous failure properties for grouted coal samples. The first and the second peak shear stress correspond to the failure of coal and failure of grout, respectively. Under the normal stress 0.51 MPa, the maximum peak shear stresses were 0.79, 0.88, 0.99, 1.61, 2.24 MPa for d/D, 0, 20, 40, 60, and 100%, respectively. Figure 7b (σn, 0.77 MPa) and Figure 7c (σn, 1.02 MPa) exhibited similar trends like that in Figure 7a. However, the number of curves of multi-stage failure modes increased with increasing normal stress. In Figure 7b, the maximum shear stresses of d/D, 0, 20, 40, 60, 100% were 0.99, 1.12, 1.29, 1.97, 3.18 MPa, respectively. Under the normal stress of 1.02 MPa, compared with shear stresses for grouting ratio d/D, 0%, the shear stress values of d/D, 20, 40, 60, 100% increased by 13.1, 27.1, 118, 241%, respectively. It should be pointed out that, though it is difficult to inject 100% cement grout into soft coal mass in real condition, testing the strength properties of pure grout samples (with grouting ratio of 100%) is helpful to understand the failure mechanism of coal-grout structure. It can be seen that, with the increase of the normal stress, the peak shear stress and residual stress increase.

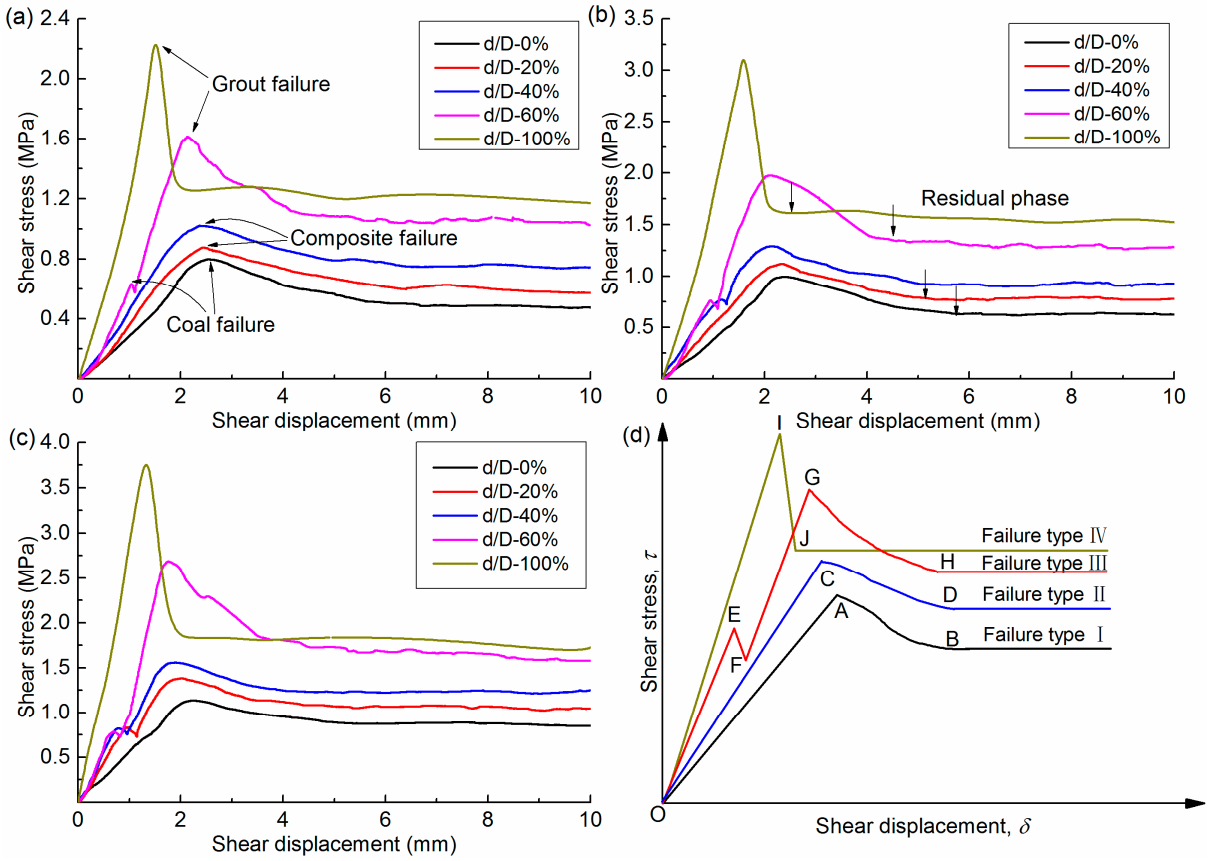

Figure 7. The measured shear stress versus shear displacement of specimens with grouting ratio (d/D, 0, 20, 40, 60, 100%) under different normal stresses. (**a**) Normal stress, σn = 0.51 MPa. (**b**) Normal stress, σn = 0.77 MPa. (**c**) Normal stress, σn = 1.02 MPa. (**d**) A simplified sketch of typical failure modes: type I, coal failure, type II, coal and grout composite failure, type III, coal failure before grout failure, multi-stage failure, type IV, pure grout failure.

A simplified sketch is depicted in Figure 7d to highlight key features in the shear stress-displacement curves. Three typical failure modes of coal and grouted coal were revealed. The failure type I represented the single-stage instability that can be observed in pure coal samples only. The shear stress increased to peak shear stress (A), then it declined to a residual value (B). During this process, coal was the only medium to resist the shear force. Type II had a trend similar to the first failure mode, but it had a higher peak shear stress (C) with lower displacement (D). It can be observed in the grouted coal specimen when normal stress and/or grouting ratio decreased. In this case, the coal and grout resisted the shear force and failed as a stable combination (composite failure). The failure type III was characterized by two peak shear stresses that can be observed, especially when normal stress and/or grout percentage increased. In the third type (multi-stage failure), the shear stress increased steeply to the first peak stress (E), wherein it represented the occurrence of the coal failure, and stress dropped suddenly (F). Then the sample continued to resist the shearing. Shear stress increased sharply again until the second peak stress value (G), owing to the grout failure, followed by a decreasing phase to the ultimate shear strength (H). As for failure type IV, it represents the pure grout failure during shear. The shear stress increases quickly within small shear displacement to the peak point (I) and then drops sharply to residual point (J).

To understand the rupture of the coal-grout structure clearly, a classical division of rupture mechanism (shown in Figure 8) was introduced according to the recommendation in the previous literature [32,33]. From Figure 8, the generalization rupture classification is dependent on the ratio of normal stress to compressive strength, i.e., σn/UCS. Normally, the rupture criteria of hard rock (UCS = 54 MPa) by the direct shear test are defined as

follows: at low ratios (σn/UCS < 0.16), specimens rupture in a predominantly tensile splitting mode as Class T; at medium ratios (0.17 < σn/UCS < 0.41), shear rupture via en echelon tensile fracture arrays as Class ET; at high ratios (0.41 < σn/UCS < 0.46), specimens rupture progressively in a mixed-mode or transition between Class T and ET, as Class M [34].

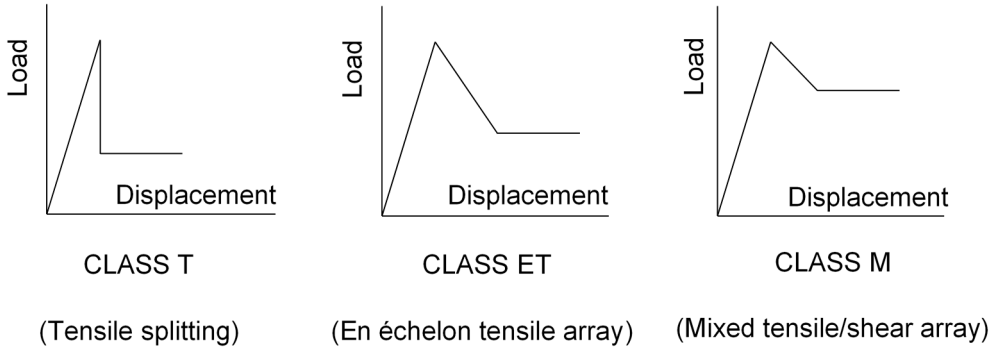

Figure 8. Division of rupture mechanism of rock materials suffering shear.

The coal-grout structure may exhibit distinctive rupture modes, because the UCS of the specimen (coal and cement grout) is much smaller than the rock. It is important to classify the rupture modes of coal and grout clearly in this study. According to the test results in Figure 7, the rupture of coal (0.19 < σn/UCS < 0.41) belongs to Class M. Its idealized load-displacement shows that the load transfers from slightly strain-weakening behavior to elastic-plastic behavior. For the grout in coal-grout structure, the σn/UCS is from 0.003 to 0.051, and its rupture modes belong to Class ET (shown in Figure 7). As we can see, the rupture of coal and grout is different from that of rock. The possible reason can be summarized as follows: the combination of the coal-grout structure is different from the rock materials. Based on the experiments, the coal normally fails firstly, and during its failure process, the microfractures in grout have developed, propagated and even coalesced. Then, after the coal rupture, more fractures would occur and be connected, but the grout rupture would not be sudden, as the fractures have already connected slightly during the process of coal failure. Hence, the rupture of grout in this study exhibits a strain-weakening with a less rapid stress drop post-peak. As for coal in coal-grout structure, due to the strength being too low, the residual strength could not drop obviously, leading to the idealized load-displacement behavior transitioning from slightly strain-weakening to elastic-plastic. Based on the shear test curves of pure grout (Figure 7), the rupture of pure grout (0.071 < σn/UCS < 0.142) belongs to Class T, its idealized load-displacement behavior shows a sudden drop when reaching peak shear stress, exhibiting a tensile splitting mode. The failure modes and rupture mechanism of the specimens observed from the direct shear tests are summarized in Table 2.

Besides, it should be pointed out that, in this study, the shear behavior and failure modes of the coal-grout structure were obtained under constant normal load (CNL) condition. As we can see from Figure 7, the normal stress was set as a constant during each test (i.e., 0.51 MPa, 0.77 MPa, and 1.02 MPa). However, the shear strength of the coal-grout structure could be also influenced by constant normal stiffness (CNS) boundary condition. When suffering shear stress, the surrounding coal mass in the underground may exhibit an obvious dilatant deformation, but the deformation of coal mass may be restrained by support structures, leading to an increase of normal (i.e., confining) stress. This phenomenon can be represented by the CNS boundary condition. In this case, the shear strength of the coal-grout structure measured in CNS direct shear would be much larger compared with that measured in CNL shear according to the results in the literature [35]. Besides, the stress-displacement curves in CNS shear may exhibit a clear yield behavior and elastic behavior dominated prior to the yield stage, while stress-displacement curves of CNL shear

exhibited none or small yield strength before peak shear strength based on the previous study [36].

Table 2. Classification of the failure modes of specimens.

Grouting Ratio, d/D (%)	Normal Stress (MPa)	σn/UCS (Coal)	σn/UCS (Grout)	Rupture Mechanism	Failure Modes
0	0.51	0.20	-	M [a]	Type I
0	0.77	0.31	-	M	Type I
0	1.02	0.41	-	M	Type I
20	0.51	0.19	0.003	M	Type II
20	0.77	0.30	0.004	M	Type II
20	1.02	0.39	0.006	ET [b]	Type III
40	0.51	0.17	0.011	M	Type II
40	0.77	0.26	0.017	ET	Type III
40	1.02	0.34	0.023	ET	Type III
60	0.51	0.13	0.026	ET	Type III
60	0.77	0.19	0.039	ET	Type III
60	1.02	0.26	0.051	ET	Type III
100	0.51	-	0.071	T [c]	Type IV
100	0.77	-	0.107	T	Type IV
100	1.02	-	0.142	T	Type IV

[a] Mixed shear and tensile array. [b] En echelon tensile fracture arrays. [c] Tensile splitting.

4.2. Shear Strength Characteristics

The effect of grout on peak and residual shear stress of specimen for different normal stresses is shown in Figure 9. It can be observed that both the maximum peak and residual shear stress increased with the increase in the grouting ratio under different normal stress levels (0.51 MPa, 0.77 MPa, and 1.02 MPa). A linear regression analysis was carried out to investigate the relation between shear stress and the grouting ratio. The coefficients R^2 of fitting lines were greater than 0.9, showing a strong relevance.

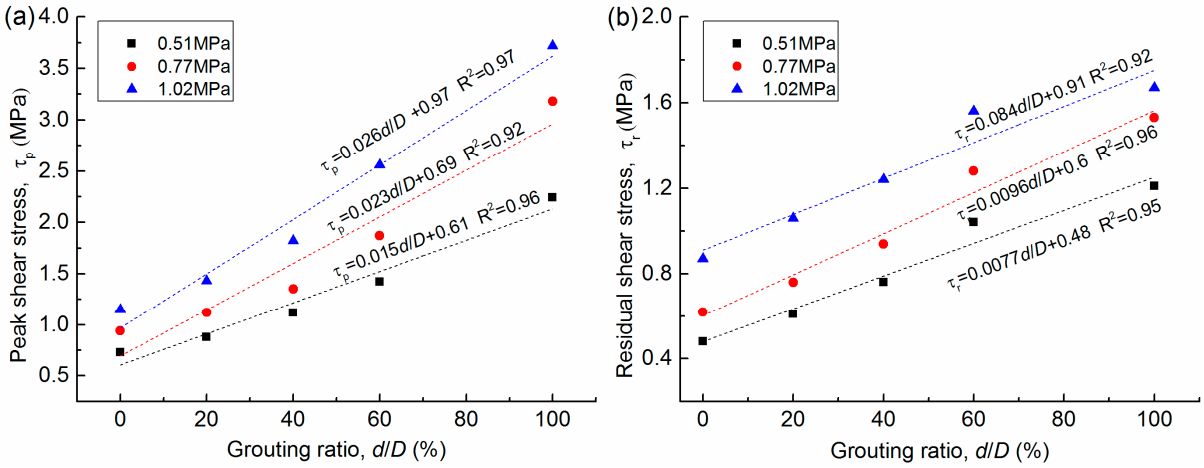

Figure 9. The relation between shear stress and grouting ratio (d/D) for different normal stresses, fitting lines shown in dotted lines. (**a**) Peak shear stress versus d/D under normal stress (0.51, 0.77, 1.02 MPa). (**b**) Residual shear stress versus d/D under normal stress (0.51, 0.77, 1.02 MPa).

Figure 10 shows the shear test results grouped by different grouting ratios in the shear stress-normal stress space. The relation between both peak/residual shear stresses and normal stresses was linearly fitted by the Mohr–Coulomb failure envelope. (Equations (1) and (2))

$$\tau_p = \sigma_n \cdot tan(\varphi_p) + c_p \quad (1)$$

$$\tau_r = \sigma_n \cdot tan(\varphi_r) + c_r \quad (2)$$

where τ_p, τ_r, φ_p, φ_r, c_p, c_r and σn are the peak shear stress, residual shear stress, peak friction angle, residual friction angle, peak cohesion, residual cohesion, and normal stress component, respectively.

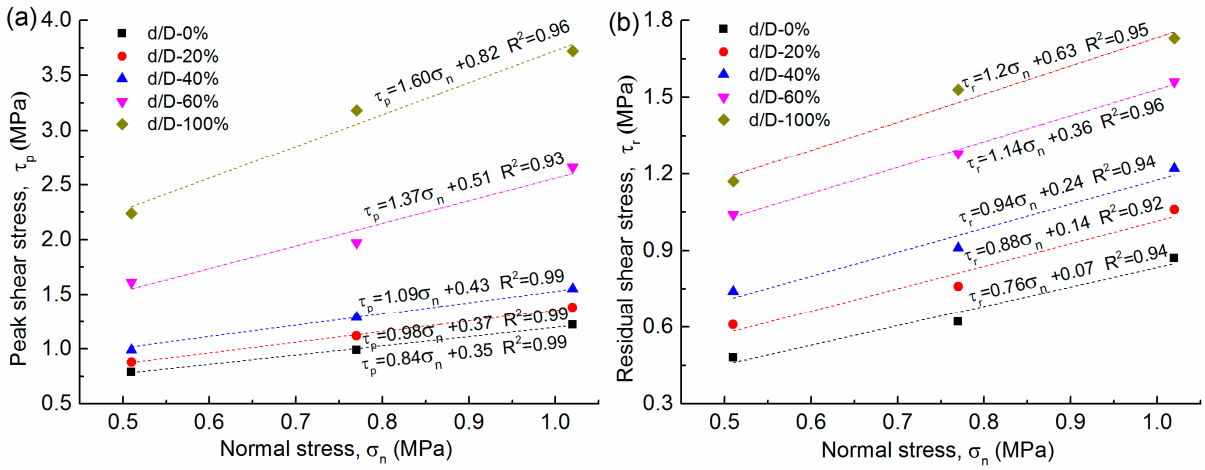

Figure 10. Peak and residual shear stress versus the normal stress for coal and grouted samples and the fitting relations using Mohr–Coulomb envelopes. (**a**) Peak shear stress versus normal stress for grouting ratios, 0, 20, 40, 60, 100%. (**b**) Residual shear stress versus normal stress for grouting ratios, 0, 20, 40, 60, 100%.

According to the linear fitting data in Figure 10a,b, the coefficients of determination were greater than 0.92, illustrating that the failure of coal, pure grout and grouted coal specimen followed the Mohr–Coulomb failure criterion well when they suffered the normal and shear stresses. The calculated peak and residual cohesion and friction angle are summarised in Table 3.

Table 3. Calculated cohesion and friction angle for coal and grouted samples.

Grouting Ratio, d/D (%)	Cohesion (MPa)		Friction Angle (°)	
	Peak	Residual	Peak	Residual
0	0.35	0.07	40.0	37.2
20	0.37	0.14	44.4	41.3
40	0.43	0.24	47.5	43.2
60	0.51	0.36	53.9	48.7
100	0.82	0.77	57.9	50.1

To quantify the relations between the amount of grout and shear strength for coal and grouted specimens, simple regression models were conducted (shown in Figure 11). The results indicated that there was a strong correlation between grout percent d/D and the peak/residual strength parameters (cohesion and friction angle). The established formulas for the prediction of peak/residual cohesion and friction angle are shown in Figure 11a,b, respectively. With the increase in the amount of grout, the cohesion and friction angle of composite samples increased evidently, quantitatively implying that grouting can significantly enhance the strength of coal mass. The relevance mechanism of strength improvement by grouting can be concluded as follows:

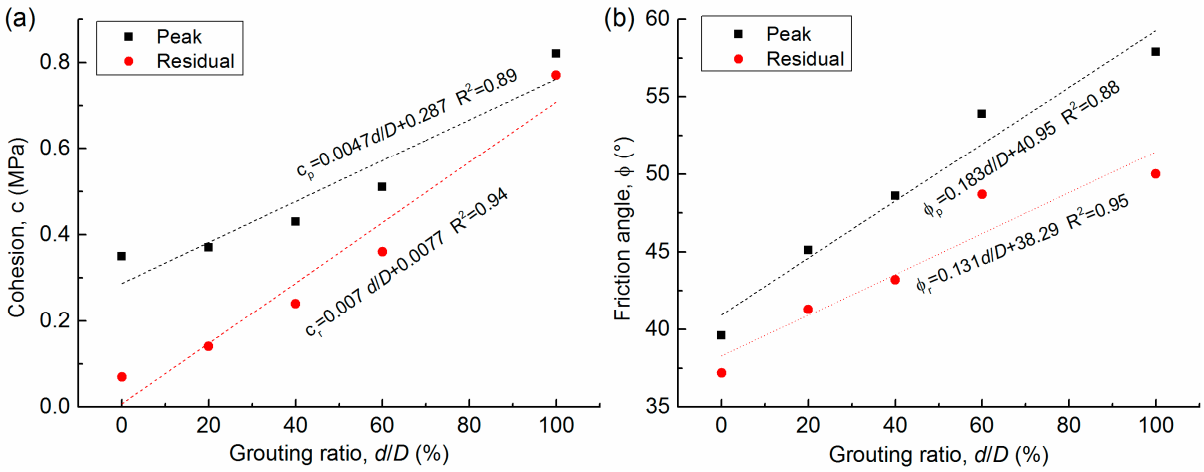

Figure 11. The relation between peak/residual shear strength parameters and grouting ratio (d/D). (**a**) Relation of peak and residual cohesion versus grouting ratio. (**b**) The relation between peak and residual friction angle and d/D.

For failure type II, the coal and grout suffer the shear strength together and the combined effect of the non-homogeneous coal and grouted column plays a key role in this process. As for failure type III, before the coal failure, the coal and grout bear the shear stress together and then with the increase of the shear displacement, the coal fails and the grout suffers the shear strength only. Due to the relative higher strength of the grout, the overall strength of the coal-grout exhibits higher shear stress.

4.3. Shear Stiffness Properties

The deformation behavior of coal and grout coal composite can be characterized by its shear stiffness. It represents the capacity of resistance in shearing. The average shear stiffness Ka is defined as follows: The maximum shear stress divides by the corresponding displacement. The relation between grouting ratio (d/D) and Ka for coal and grouted coal specimens is illustrated in Figure 12. A linear relation between Ka and d/D was illustrated by fitting lines. The coefficients of determination show that they were in strong relevance.

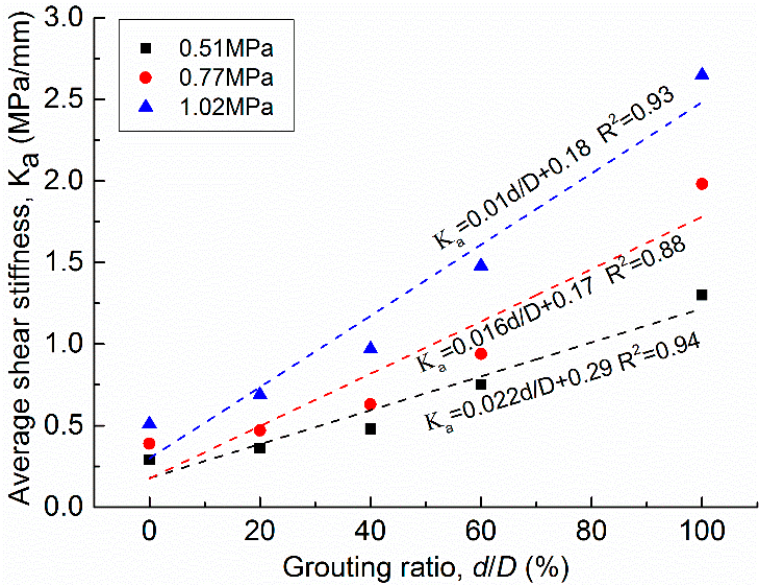

Figure 12. The relation between average shear stiffness (Ka) and grouting ratio (d/D) for different normal stresses (0.51, 0.77, 1.02 MPa), fitting lines shown in dotted lines.

Furthermore, the shear stiffness for each curve in multi-stage failure mode (type III) can be divided into coal failure stiffness (Kc) and grout failure stiffness (Kg), respectively. The stiffness results including Kc, Kg, and Ka for different d/D and normal stresses in failure type III are illustrated in Figure 13a. For the grouting ratio d/D (60%), it shows that Kg > Ka > Kc (mode I). As for the relatively low d/D (20%, 40%), it shows that Kc > Kg > Ka (mode II).

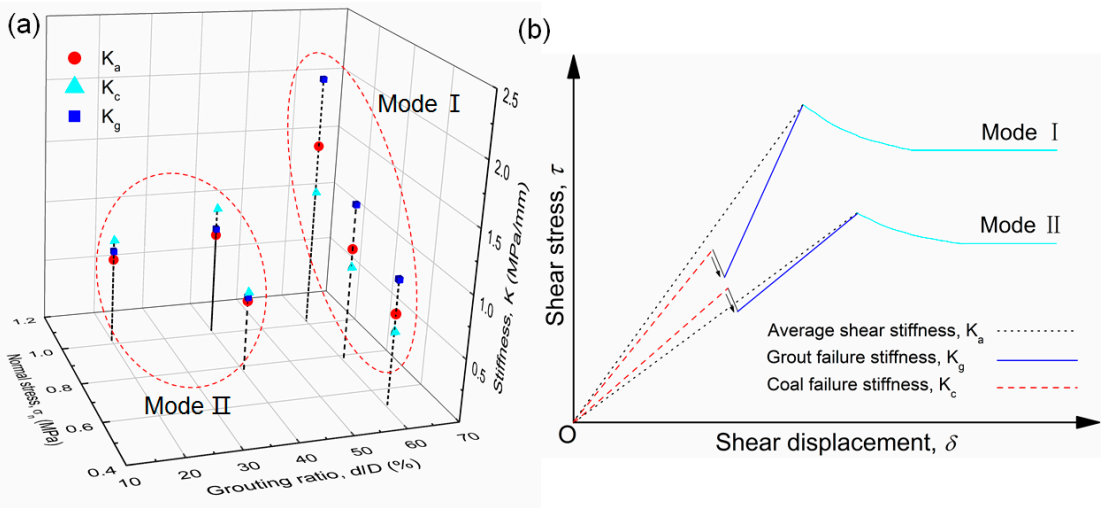

Figure 13. The results of shear stiffness in failure "type III" for the grouted specimen and schematic graph for stiffness failure modes. (**a**) The shear stiffness results (Ka, Kc, Kg) in failure type III. (**b**) Two failure modes of shear stiffness: mode I: Kg> Ka > Kc, mode II: Kc > Kg > Ka.

The two stiffness modes in failure type III are schematically shown in Figure 13b. The phase of sudden stress drop reduced the overall stiffness of samples evidently. Grout failure stiffness Kg determined the average failure stiffness Ka. This means that increasing the amount of grout in samples could obtain higher Ka, otherwise not. The stiffness mode I can be observed under high d/D. Although higher d/D resulted in the stress drop more easily (described in Section 4.1), the Ka is higher than Kc, which signifies that grouting improved the overall stiffness of coal. The failure stiffness model II can be found under low d/D, showing that the Ka is lower than Kc. It illustrates that less grout cannot take over the shear deformation of grouted coal completely. The stress drop is unfavorable for the overall stability of the coal-grout structure, especially under the low grouting ratio.

5. Discussion

5.1. Microstructure of the Coal–Grout Interface

The overall shear strength and stiffness of grouted coal is affected by the interface between coal and grout. Analyzing the microscopic interfacial structure is helpful to reveal the failure mechanism of the specimen. The scanning electron microscopic (SEM) image on the surface of grouted coal is shown in Figure 14. As illustrated in Figure 14a, there was a primary interface between the coarse-grained coal layer and the fine-grained grout layer. The primary interface was not completely surface contact, but instead comprised irregular point contacts that could result in a relatively weak and discontinuous bonding force. Furthermore, microscopic observations indicated that there was an intermittent secondary interface near the coal layer (Figure 14b). It contained one or more interface branches. Between the primary interface and secondary interface, the intermediate layer like a "transition zone" was generated (shown in Figure 14b–d). Besides, the two mediums considerably differed from each other in microcracks. As shown in Figure 14b, many major cracks were in the coal layer between coal particles and coal matrix, compared with a few minor cracks in the grout layer. This indirectly verified the reason why grout has higher strength and stiffness when it suffers shearing.

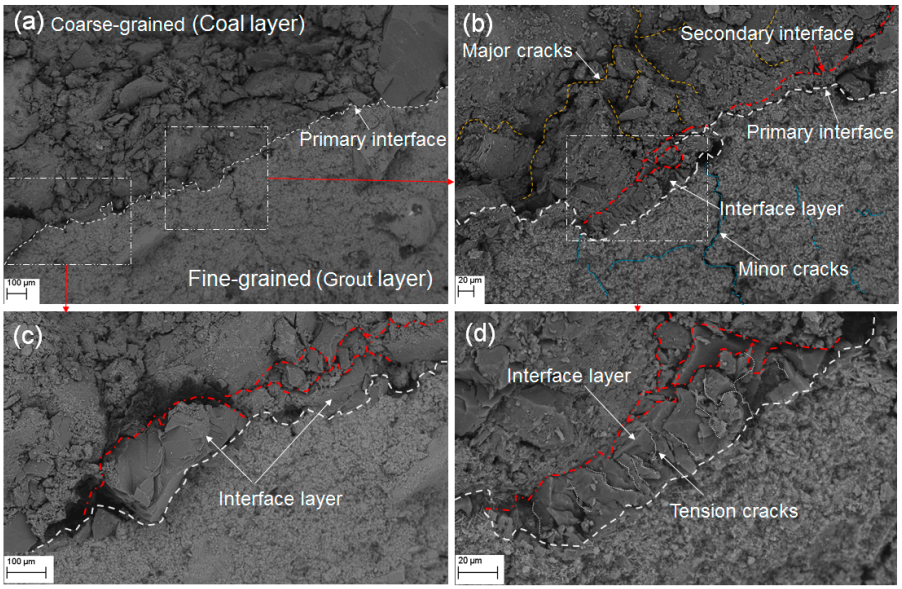

Figure 14. The microscope interface properties of the coal-grout structure. (**a**) A general view of the primary interface separated by the top coarse-grained coal layer and the bottom fine-grained grout layer. (**b**) A close-up of a photomicrograph showing three main parts of the coal-grout interface (primary interface, secondary interface and interface layer). (**c**) A typical interface layer with intact coal grains or coal matrix. (**d**) Another typical interface layer with cracked coal grains by micro-tension.

From Figure 14c,d, two typical statuses of the interface layer were revealed. One is a relatively complete layer consisting of the large coal grains and coal matrix (Figure 14c). Another is a cracked layer subjected to the tension that resulted in many tiny cracks in the coal matrix (Figure 14d). The secondary interface could be viewed as a series of coal failures near the primary interface, which formed after the primary interface. The bonding force between the coal layer and grout layer was created when cement grout solidified. Furthermore, micro shrinkage of cement would occur during this curing process, leading to micro-tension between grout and coal. When the micro-tension exceeded the ultimate tensile stress in coal or the cohesive strength between coal grains and coal matrixes, the different failure patterns in the interface layer would engender. The interface layer of grouted coal observed in this study is different from the interfacial transition zone (ITZ) investigated by [37,38]. ITZ is the interface between cement pastes and aggregates, which has a higher porosity and fills with the deposition of hydration products [39,40]. The "coal-grout interface layer" can be seen as an intermediate layer filled with crushed coal between the grout layer and a relatively stable coal layer. When the coal-grout structure suffered high stress, the irregularly cracked interface layer failed easily, which induced the stress drop and affected the overall stability of grouted coal.

5.2. Macroscopic Failure Characteristics

The failure process of a rock or coal sample can be seen as a successive evolution of cracks at the mesoscopic level [41,42]. As for the coal and grouted coal, the appearance, propagation, and coalescence of mesoscopic cracks resulted in their failure, when they suffered shearing. Figure 15 shows images of typical failure patterns of the specimen after shear tests. As described above, there were three typical failure modes for coal and grouted coal. In Figure 15a, it illustrates a smooth shear plane in pure coal sample, corresponding to the failure type I. The composite failure type II for the grouted coal is depicted in Figure 15b. A relatively rough shear plane was formed. Tension cracks can be found on the surface from both Figure 15a,b. Based on the shear stress-displacement curves for failure I and II, a gentle process by the development and coalescence of cracks in coal and grout can be deduced during the shearing. When grout percentage and/or normal stress increased, the failure of the specimen is shown in Figure 15c, which corresponds to the failure type III.

The coal around the solidified grout was fragmentized. A small part of coal stuck on the surface. The "coal-grout interface layer" described above became weak and crushed when it suffered high stress. In this case, the combination of coal and grout was no longer stable. Hence, the cracks in external coal coalesced and failed, then the fragmentized interface layer induced a stress drop followed by the propagation and coalescence of cracks in the grout. It is characterized by multi-stage failure (or non-simultaneous failure).

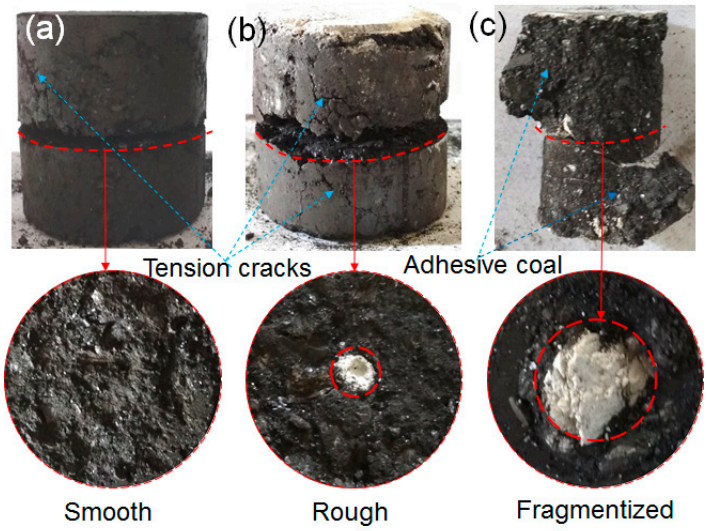

Figure 15. The comparison of typical failure patterns and shear planes for specimens after shear tests. (**a**) Coal failure, type I. (**b**) Coal and grout composite failure, type II. (**c**) Coal failure before grout failure (multi-stage failure), type III.

5.3. Suggestions for Cement Pre-Grouting in Soft Coal Mass

As discussed above, the cement grouting can significantly improve the strength and stiffness of soft coal. The formed cement column can be seen as effective support for compacted surrounding coal mass. The overall mechanical parameters (strength, stiffness, cohesion and friction angle, etc.) of grouted coal can be predicted by the linear regression formulas we proposed in this paper. In practice, according to the effective compacting grouting diameter, the overall strength and stiffness of grouted coal mass in a certain range can be identified. In this case, the safe and economic pre-grouting parameters such as the number of grout holes and the amount of grout can be designed qualitatively instead of designing by experience.

Moreover, the cracked interface layer between coal and cement grout played a negative effect based on the analysis of the microscopic coal-grout structure and the macroscopic failure characteristics of the specimen. The failure is characterized by the sudden stress drop and decline of strength and stiffness. The possible reason is that the relatively large cement grains could not penetrate the coal layer effectively. Some point contacts between cement and coal resulted in a potentially unstable bonding structure. The main function of cement consolidation grouting is to improve strength for large fractures and cracks in coal mass instead of micro-cracks [43]. On the other hand, the shrinkage of cement resulted in a "broken zone" called "coal-grout interface layer". The crushed interface layer affected the overall stability of the coal-grout structure. Cement drying shrinkage significantly affected the durability and integrity of a structure [44,45]. To solve the shrinkage problem, shrinkage-compensating cement can be used to fill the gaps and enhance structural stability over ordinary cement [46,47]. Also, the use of cement grouts containing supplementary cementitious materials (SCMs) is also an effective way to solve the shrinkage [48,49]. Therefore, in the field, ultra-fine cement, the shrinkage-compensating or SCMs cement could be good choices for pre-grouting to further improve the stability of grouted coal mass.

6. Conclusions

In this study, according to the field observation of cement grouting into soft coal mass, a coal-grout structure was presented. Through a series of direct shear tests for coal and grouted coal specimens, the effect of grouting on coal mass was quantitatively revealed. The influence of grouting ratio (d/D of 0. 20, 40, 60%) on the shear behaviors were studied. A set of formulas were proposed for predicting the mechanical parameters of grouted soft coal mass. The failure modes of coal and grouted coal were systematically analyzed. The micromorphology interface of the coal-grout structure and its impact on macroscopic failure properties of the specimens were discussed. Finally, the application of prediction models and some measures for further improving the overall mechanical properties of grouted coal mass were suggested. The main conclusions can be summarized as follows:

Both the peak and residual shear stresses of grouted coal mass increased and the peak shear displacement decreased with the increase of grouting ratio and normal stress. Three failure types were proposed according to the failure time of coal and grout. Different failure modes depended on the grouting ratio and normal stress.

Linear relations between the peak/residual shear stress and grouting ratio were established, which quantitatively verified the effect of cement grouting on soft coal mass. The vital strength parameters (peak/residual cohesion and friction angle) of grouted coal mass can be predicted by the constructed models.

The average shear stiffness of grouted coal increased linearly with the increase in the grouting ratio. Two typical shear stiffness modes in failure "type III" for grouted coal were revealed, signifying that the sudden stress drop reduced the overall stiffness of grouted coal mass evidently.

The "coal-grout interface layer" generated by shrinkage of cement had a negative effect on the stability of the coal-grout structure. Combining the analysis of microscopic bonding properties and macroscopic failure performance of grouted coal, the use of ultra-fine cement, shrinkage-compensating or SCMs cement could be better choices for further stabilizing the soft coal mass.

Author Contributions: Conceptualization by Y.S. and G.L.; methodology, J.H.; investigation, J.Z.; writing—original draft preparation, Y.S.; writing—review and editing, G.L., J.S., J.Z., R.T.; supervision, G.L.; funding acquisition, G.L., R.T. All authors have read and agreed to the published version of the manuscript.

Funding: This research was supported by the projects of "the Fundamental Research Funds for the Central Universities (2021QN1003, 2020ZDPY0221)", "National Natural Science Foundation of China (52104106, 52174089)".

Institutional Review Board Statement: Not applicable.

Informed Consent Statement: Not applicable.

Data Availability Statement: The data presented in this study are available on request from the corresponding author. The data are not publicly available due to privacy.

Acknowledgments: The authors are grateful to Huaibei Mining (Group) Co. Ltd. Special thanks to Zuqi Wang for her encouragements.

Conflicts of Interest: The authors declare no conflict of interest.

References

1. Yang, H.; Zhang, N.; Han, C.; Sun, C.; Song, G.; Sun, Y.; Sun, K. Stability Control of Deep Coal Roadway under the Pressure Relief Effect of Adjacent Roadway with Large Deformation: A Case Study. *Sustainability* **2021**, *13*, 4412. [CrossRef]
2. Yang, H.; Han, C.; Zhang, N.; Sun, Y.; Pan, D.; Sun, C. Long high-performance sustainable bolt technology for the deep coal roadway roof: A case study. *Sustainability* **2020**, *12*, 1375. [CrossRef]
3. Sun, C.; Li, G.; Gomah, M.E.; Xu, J.; Sun, Y. Creep characteristics of coal and rock investigated by nanoindentation. *Int. J. Min. Sci. Technol.* **2020**, *30*, 769–776. [CrossRef]
4. Kang, Y.; Liu, Q.; Xi, H.; Gong, G. Improved compound support system for coal mine tunnels in densely faulted zones: A case study of China's Huainan coal field. *Eng. Geol.* **2018**, *240*, 10–20. [CrossRef]

5. Zolfaghari, A.; Sohrabi Bidar, A.; Maleki Javan, M.R.; Haftani, M.; Mehinrad, A. Evaluation of rock mass improvement due to cement grouting by Q-system at Bakhtiary dam site. *Int. J. Rock Mech. Min. Sci.* **2015**, *74*, 38–44. [CrossRef]
6. Sun, Y.; Li, G.; Basarir, H.; Karrech, A.; Azadi, M.R. Laboratory evaluation of shear strength properties for cement-based grouted coal mass. *Arab. J. Geosci.* **2019**, *12*, 690. [CrossRef]
7. Brantberger, M.; Stille, H.; Eriksson, M. Controlling grout spreading in tunnel grouting—analyses and developments of the GIN-method. *Tunn. Undergr. Sp. Technol.* **2000**, *15*, 343–352. [CrossRef]
8. Fang, Q.; Du, J.; Li, J.; Zhang, D.; Cao, L. Settlement characteristics of large-diameter shield excavation below existing subway in close vicinity. *J. Cent. South Univ.* **2021**, *28*, 882–897. [CrossRef]
9. Mou, B.; Bai, Y. Experimental investigation on shear behavior of steel beam-to-CFST column connections with irregular panel zone. *Eng. Struct.* **2018**, *168*, 487–504. [CrossRef]
10. Sun, J.; Huang, Y.; Aslani, F.; Ma, G. Properties of a double-layer EMW-absorbing structure containing a graded nano-sized absorbent combing extruded and sprayed 3D printing. *Constr. Build. Mater.* **2020**, *261*, 120031. [CrossRef]
11. Sun, J.; Lin, S.; Zhang, G.; Sun, Y.; Zhang, J.; Chen, C.; Morsy, A.M.; Wang, X. The effect of graphite and slag on electrical and mechanical properties of electrically conductive cementitious composites. *Constr. Build. Mater.* **2021**, *281*, 122606. [CrossRef]
12. Sun, J.; Aslani, F.; Wei, J.; Wang, X. Electromagnetic absorption of copper fiber oriented composite using 3D printing. *Constr. Build. Mater.* **2021**, *300*, 124026. [CrossRef]
13. Li, H.Y. Major and minor structural features of a bedding shear zone along a coal seam and related gas outburst, Pingdingshan coalfield, northern China. *Int. J. Coal Geol.* **2001**, *47*, 101–113. [CrossRef]
14. Basarir, H.; Sun, Y.; Li, G. Gateway stability analysis by global-local modeling approach. *Int. J. Rock Mech. Min. Sci.* **2019**, *113*, 31–40. [CrossRef]
15. Sun, Y.; Li, G.; Zhang, J.; Qian, D. Stability Control for the Rheological Roadway by a Novel High-Efficiency Jet Grouting Technique in Deep Underground Coal Mines. *Sustainability* **2019**, *11*, 6494. [CrossRef]
16. Sun, Y.; Zhang, J.; Li, G.; Wang, Y.; Sun, J.; Jiang, C. Optimized neural network using beetle antennae search for predicting the unconfined compressive strength of jet grouting coalcretes. *Int. J. Numer. Anal. Methods Geomech.* **2019**, *43*, 801–813. [CrossRef]
17. Sun, Y.; Zhang, J.; Li, G.; Ma, G.; Huang, Y.; Sun, J.; Wang, Y.; Nener, B. Determination of Young's modulus of jet grouted coalcretes using an intelligent model. *Eng. Geol.* **2019**, *252*, 43–53. [CrossRef]
18. Li, S.; Han, W.W.; Zhang, Q.; Liu, R.; Weng, X. Research on time-dependent behavior of viscosity of fast curing grouts in underground construction grouting. *Chin. J. Rock Mech. Eng.* **2013**, *32*, 1–7.
19. Sun, Y.; Li, G.; Zhang, J. Developing Hybrid Machine Learning Models for Estimating the Unconfined Compressive Strength of Jet Grouting Composite: A Comparative Study. *Appl. Sci.* **2020**, *10*, 1612. [CrossRef]
20. Sun, Y.; Li, G.; Zhang, J. Investigation on jet grouting support strategy for controlling time-dependent deformation in the roadway. *Energy Sci. Eng.* **2020**, *8*, 2151–2158. [CrossRef]
21. Sun, Y.; Li, G.; Zhang, J.; Qian, D. Experimental and numerical investigation on a novel support system for controlling roadway deformation in underground coal mines. *Energy Sci. Eng.* **2020**, *8*, 490–500. [CrossRef]
22. Kikuchi, K.; Igari, T.; Mito, Y.; Utsuki, S. In situ experimental studies on improvement of rock masses by grouting treatment. *Int. J. Rock Mech. Min. Sci.* **1997**, *34*, 138-e1. [CrossRef]
23. Huang, J.; Zhang, Y.; Sun, Y.; Ren, J.; Zhao, Z.; Zhang, J. Evaluation of pore size distribution and permeability reduction behavior in pervious concrete. *Constr. Build. Mater.* **2021**, *290*, 123228. [CrossRef]
24. Huang, J.; Duan, T.; Zhang, Y.; Liu, J.; Zhang, J.; Lei, Y. Predicting the permeability of pervious concrete based on the beetle antennae search algorithm and random forest model. *Adv. Civ. Eng.* **2020**, *2020*, 8863181.
25. Huang, J.; Shiva Kumar, G.; Ren, J.; Sun, Y.; Li, Y.; Wang, C. Towards the potential usage of eggshell powder as bio-modifier for asphalt binder and mixture: Workability and mechanical properties. *Int. J. Pavement Eng.* **2021**, 1–13. [CrossRef]
26. Utsuki, S.; Mito, Y. Development of Grouting Management Support System and its Application to Actual Dam Grouting. In Proceedings of the 47th US Rock Mechanics/Geomechanics Symposium, San Francisco, CA, USA, 23–26 June 2013; OnePetro: Richardson, TX, USA, 2013.
27. Salimian, M.H.; Baghbanan, A.; Hashemolhosseini, H.; Dehghanipoodeh, M.; Norouzi, S. Effect of grouting on shear behavior of rock joint. *Int. J. Rock Mech. Min. Sci.* **2017**, *98*, 159–166. [CrossRef]
28. Nikbakhtan, B.; Osanloo, M. Effect of grout pressure and grout flow on soil physical and mechanical properties in jet grouting operations. *Int. J. Rock Mech. Min. Sci.* **2009**, *46*, 498–505. [CrossRef]
29. Sun, Y.; Li, G.; Zhang, J.; Sun, J.; Xu, J. Development of an Ensemble Intelligent Model for Assessing the Strength of Cemented Paste Backfill. *Adv. Civ. Eng.* **2020**, *2020*, 1643529. [CrossRef]
30. Sun, Y.; Li, G.; Zhang, J.; Xu, J. Failure Mechanisms of Rheological Coal Roadway. *Sustainability* **2020**, *12*, 2885. [CrossRef]
31. Sun, Y.; Li, G.; Zhang, N.; Chang, Q.; Xu, J.; Zhang, J. Development of ensemble learning models to evaluate the strength of coal-grout materials. *Int. J. Min. Sci. Technol.* **2021**, *31*, 153–162. [CrossRef]
32. Bewick, R.P.; Kaiser, P.K.; Bawden, W.F. Shear rupture under constant normal stiffness boundary conditions. *Tectonophysics* **2014**, *634*, 76–90. [CrossRef]
33. Bewick, R.P.; Kaiser, P.K.; Bawden, W.F.; Bahrani, N. DEM simulation of direct shear: 1. Rupture under constant normal stress boundary conditions. *Rock Mech. Rock Eng.* **2014**, *47*, 1647–1671. [CrossRef]

34. Bewick, R.P.; Kaiser, P.K.; Bawden, W.F. DEM simulation of direct shear: 2. Grain boundary and mineral grain strength component influence on shear rupture. *Rock Mech. Rock Eng.* **2014**, *47*, 1673–1692. [CrossRef]
35. Shang, J.; Zhao, Z.; Ma, S. On the shear failure of incipient rock discontinuities under CNL and CNS boundary conditions: Insights from DEM modelling. *Eng. Geol.* **2018**, *234*, 153–166. [CrossRef]
36. Thirukumaran, S.; Indraratna, B. A review of shear strength models for rock joints subjected to constant normal stiffness. *J. Rock Mech. Geotech. Eng.* **2016**, *8*, 405–414. [CrossRef]
37. Barnes, B.D.; Diamond, S.; Dolch, W.L. The contact zone between portland cement paste and glass "aggregate" surfaces. *Cem. Concr. Res.* **1978**, *8*, 233–243. [CrossRef]
38. Zimbelmann, R. A contribution to the problem of cement-aggregate bond. *Cem. Concr. Res.* **1985**, *15*, 801–808. [CrossRef]
39. Monteiro, P.J.M.; Mehta, P.K. The transition zone between aggregate and type K expansive cement. *Cem. Concr. Res.* **1986**, *16*, 111–114. [CrossRef]
40. Scrivener, K.L.; Crumbie, A.K.; Laugesen, P. The Interfacial Transition Zone (ITZ) Between Cement Paste and Aggregate in Concrete. *Interface Sci.* **2004**, *12*, 411–421. [CrossRef]
41. Moradian, Z.; Einstein, H.H.; Ballivy, G. Detection of Cracking Levels in Brittle Rocks by Parametric Analysis of the Acoustic Emission Signals. *Rock Mech. Rock Eng.* **2016**, *49*, 785–800. [CrossRef]
42. Cai, C.; Gao, F.; Li, G.; Huang, Z.; Hou, P. Evaluation of coal damage and cracking characteristics due to liquid nitrogen cooling on the basis of the energy evolution laws. *J. Nat. Gas Sci. Eng.* **2016**, *29*, 30–36. [CrossRef]
43. Kang, H. Support technologies for deep and complex roadways in underground coal mines: A review. *Int. J. Coal Sci. Technol.* **2014**, *1*, 261–277. [CrossRef]
44. Lura, P.; Jensen, O.; Breugel, K. Van Autogenous shrinkage in high-performance cement paste: An evaluation of basic mechanisms. *Cem. Concr. Res.* **2003**, *33*, 223–232. [CrossRef]
45. Bissonnette, B.; Pierre, P.; Pigeon, M. Influence of key parameters on drying shrinkage of cementitious materials. *Cem. Concr. Res.* **1999**, *29*, 1655–1662. [CrossRef]
46. Fukuyama, K.; Higashibata, Y.; Miyauchi, Y. Studies on repair and strengthening methods of damaged reinforced concrete columns. *Cem. Concr. Compos.* **2000**, *22*, 81–88. [CrossRef]
47. Collepardi, M.; Borsoi, A.; Collepardi, S.; Olagot, J.J.O.; Troli, R. Effects of shrinkage reducing admixture in shrinkage compensating concrete under non-wet curing conditions. *Cem. Concr. Compos.* **2005**, *27*, 704–708. [CrossRef]
48. Krishnamoorthy, T.S.; Gopalakrishnan, S.; Balasubramanian, K.; Bharatkumar, B.H.; Rama Mohan Rao, P. Investigations on the cementitious grouts containing supplementary cementitious materials. *Cem. Concr. Res.* **2002**, *32*, 1395–1405. [CrossRef]
49. Chindaprasirt, P.; Homwuttiwong, S.; Sirivivatnanon, V. Influence of fly ash fineness on strength, drying shrinkage and sulfate resistance of blended cement mortar. *Cem. Concr. Res.* **2004**, *34*, 1087–1092. [CrossRef]

sustainability

MDPI

Article

Study on Evolution Mechanism of Structure-Type Rockburst: Insights from Discrete Element Modeling

Chenxi Zhang [1], Diyuan Li [1,*], Shunchuan Wu [2,3], Long Chen [2] and Jun Peng [1]

[1] School of Resources and Safety Engineering, Central South University, Changsha 410083, China; chenxizhang@csu.edu.cn (C.Z.); jun.peng@whu.edu.cn (J.P.)
[2] School of Civil and Resource Engineering, University of Science and Technology Beijing, Beijing 100083, China; wushunchuan@ustb.edu.cn (S.W.); b20190030@xs.ustb.edu.cn (L.C.)
[3] Faculty of Land Resource Engineering, Kunming University of Science and Technology, Kunming 650093, China
* Correspondence: diyuan.li@csu.edu.cn; Tel.: +86-731-8887-9612

Abstract: Taking the "11.28" rockburst occurred in the Jinping II Hydropower Station as the engineering background, the evolution mechanism of structure-type rockburst was studied in detail based on the particle flow code. The results indicate that the failure mechanism of structure-type rockburst includes a tensile fracture induced by tangential compressive stress and a shear fracture caused by shear stress due to overburdened loadings and shear slip on the structural plane. In addition, it is found that the differences between structure-type rockburst and strainburst mainly include (a) the distribution of the local concentrated stress zone after excavation, (b) the evolution mechanism, and (c) the failure locations. Finally, the influence of four factors on the structure-type rockburst are explored. The results show that (1) when the friction coefficient is greater than 0.5, the effect of structural plane is weakened, and the rock near excavation tends to be intact, the structural-type rockburst intensity decreases; (2) the dissipated and radiated energy in structural-type rockburst reduces with rockmass heterogeneity *m*; (3) the lateral pressure coefficient has a significant effect on the intensity of deep rock failure, specifically in the form of the rapid growth in dissipative energy; (4) and the structural-type rockburst is more pronounced at a structural plane length near 90 mm.

Keywords: structure-type rockburst; evolution mechanism; particle flow code; flat-joint model

Citation: Zhang, C.; Li, D.; Wu, S.; Chen, L.; Peng, J. Study on Evolution Mechanism of Structure-Type Rockburst: Insights from Discrete Element Modeling. *Sustainability* **2021**, *13*, 8036. https://doi.org/10.3390/su13148036

Academic Editor: Guang-Liang Feng

Received: 10 May 2021
Accepted: 15 July 2021
Published: 19 July 2021

Publisher's Note: MDPI stays neutral with regard to jurisdictional claims in published maps and institutional affiliations.

Copyright: © 2021 by the authors. Licensee MDPI, Basel, Switzerland. This article is an open access article distributed under the terms and conditions of the Creative Commons Attribution (CC BY) license (https://creativecommons.org/licenses/by/4.0/).

1. Introduction

Globally, there is an increasing demand for clean energy due to national controls on CO_2 emissions [1]. Hydropower is a typically clean energy source that contributes about 16% of global electricity production at all renewable energy sources [2], which plays an important role in maintaining social stability and sustainable development. However, many deep tunnels are designed in hydropower stations, owing to topographical and geological conditions. Therefore, during construction, rockbursts often occur in hard brittle rocks after excavation under high geostress [3], which severely limits the safety and sustainability of site construction.

Rockburst is a failure phenomenon in which the tangential stress in hard brittle surrounding rock exceeds its strength limit due to excavation unloading under high in situ stress. Due to sharp release of elastic energy, rockburst is usually accompanied by spalling of rock debris, dynamic ejection of rock blocks, and different degrees of crackling sound. Both strainburst and spalling are common stress-induced failure phenomena after excavation in brittle rock under high geostress [4]. Strainburst is a violent failure accompanying the ejection of rock fragments and a large release of energy [5]; however, spalling is a static progressive failure in a stable manner with no obvious ejection performance [6], which depends on the magnitude of energy stored in surrounding rock before failure. Structure-type rockburst in this study is the kind of rockburst influenced by the local geological structure

near excavation, e.g., joints, faults, or other structural planes, in the surrounding rock of deep underground engineering [7,8]. The main difference between structure-type rockburst and strainbursts is that the former is obviously impacted by the structural plane, which makes the two distinct in terms of the mechanisms of energy release and the excavation damage processes [5].

In order to effectively prevent and control rockburst, it is extremely important to study the evolution mechanism of rockburst. A large number of laboratory tests had been carried out to study the rockburst. He et al. [9] reproduced the rockburst process in the laboratory, which was divided into four stages, namely the calm period, small grains ejection, rock flakes and/or grains ejection, and entire fracture collapse. He et al. [10] then studied the acoustic emission characteristics of the limestone rockburst process under true triaxial unloading. Chen et al. [11] conducted a series of true triaxial tests to quantitatively study the energy dissipation of rock blocks during the rockburst process. Su et al. [12] studied the characteristics of strainburst with different loading rates under true triaxial conditions. Zhai et al. [13] comparatively analyzed the rupture, fragmentation characteristics, and failure modes of six rock types during the rockburst process. It is worth noting that cuboid rock specimens were used in the above studies, which mainly adopted the method of keeping one face free or unloading σ_3 to simulate the strainburst occurring in the tunnel sidewalls after excavation.

Hu et al. [14] studied the acoustic emission characteristics of rockburst using cubic specimens with a circular hole under biaxial load. Si et al. [15] performed a series of true triaxial tests, in which the cubic specimens with a circular hole were loaded in three directions with different stresses. The results indicated the middle part at both sides of the circular holes was damaged first, then developed radially to the deep part, and finally formed two symmetrical V-shaped notches. Gong et al. [16] further found that the line connecting the centers of the two V-shaped notches was perpendicular to the maximum principal stress direction. Liang et al. [17] discussed the effect of the horizontal load on the energy evolution law of rockburst and revealed the occurrence mechanism of rockburst in the tunnel from the energy point of view. Although cubic specimens with prefabricated holes were used in the above experiments, the simulated phenomenon was also essentially the strainburst.

The experimental evidence for revealing the mechanism and evolution process of strainburst was provided in the above studies. However, structural planes often exist in rock mass, and the influence of structural planes on the failure of rock mass should also be carefully studied [18,19]. Durrheim et al. [20] summarized 21 rockbursts in the deep gold mines of South Africa in detail and believed that regional structures such as faults and rock walls were the main controlling factors for triggering rockburst. Based on field micro-seismic monitoring and numerical simulation, the impact of the structural plane of the tunnel on the location of the rockburst is reported by Hu et al. [21]. Liu et al. [18] investigated the characteristics and evolution process of rockburst controlled by structural planes through field micro-seismic monitoring technology. Moreover, it was reported that several severe rockbursts affected by the structural plane occurred in the Jinping II Hydropower Station. For example, the "11.28" rockburst in the drainage tunnel at a depth of 2330 m caused seven deaths, one injury, and the destruction of a tunnel boring machine [22], resulting in serious economic losses and severe social impact.

Therefore, it is very necessary to study the influence of the structural plane on rockburst. Zhou et al. [8] qualitatively analyzed the mechanism of structure-type rockburst, and structure-type rockburst was divided into fault-slip burst, shear rupture burst, and buckling burst. Based on the rockburst in the diversion tunnel of Jinping II Hydropower Station, they [23] further conducted a series of shear tests to study the effect of the structural plane on rockburst. The results revealed that there were three failure mechanisms of the structural plane under shear stress: slip dislocation, tensile failure, and impact fracture. Zhang et al. [24] explored the failure development of the surrounding rock mass in "11.28" rockburst and "7.14" rockburst of the Jinping II Hydropower Station using FLAC3D soft-

ware. Based on Abaqus 2D simulation, Manouchehrian and Cai [25] found that weak planes around deep underground tunnels might affect rockburst failure when they were in the right position and orientation.

The above-used numerical methods belong to the continuous numerical analysis methods. However, the continuous method could not effectively reproduce the failure process of rockburst [26], because the contact mode among system elements could not continuously vary with the deformation process [27]. In addition, it is difficult to simulate the structure-type rockburst in laboratory tests, especially the excavation process at the ground stress state. Moreover, the study on the effect of structural plane on deep rockmass failure based on laboratory and numeirical shear tests neglected the effect of excavation [23,28].

Therefore, this study numerically further investigates the evolution mechanism of structure-type rockburst using PFC 2D, a well-known discrete element numerical method, taking into account the interaction between the tunnel and the structural plane after excavation. The reasons for using PFC 2D models in this study are as follows: (1) the exposed fault after the "11.28" rockburst event was sub-parallel to the tunnel axis [22]; (2) the distance of the damaged cross-section at the drainage tunnel was long in the "11.28" rockburst (about 25 m) [25]. Therefore, the 2D plane strain models built in this study are reasonable. In addition, the calculation time of the 3D model for PFC is usually longer than that of the 2D model due to excessive particles in the 3D model, so the latter is generally given priority.

2. Generation of Numerical Model

Particle flow code (PFC) is a commercial numerical simulation software in geotechnical engineering developed by Itasca, Minneapolis, MN, USA, counted as one of the discrete element methods (DEMs). Compared with finite element softwares, PFC software has prominent advantages in simulating the discontinuous characteristics of the research object.

2.1. Contact Models

2.1.1. Flat-Joint Model

The flat-joint model (FJM) was first proposed by Potondy [29,30] in 2012. The model is composed of rigid grains, which include disc particles and notional surfaces in two dimensions. The two grains are bonded by flat-joint contact (FJC) to simulate the interface behavior between two notional surfaces. The notional surface is rigidly connected to the corresponding grains. A grain could form several FJCs with other grains, which means one grain could have multiple notional surfaces. Therefore, the effective contact between the grains in an FJC becomes the contact between the notional surfaces. In a two-dimensional (2D) model, the middle surface is a straight line segment, which can be discretized into several small elements with equal length (Figure 1). Each element can be bonded or unbonded. Therefore, the behavior of the middle surface is mainly acted as bonding or unbonding and varied along the contact surface. Interested readers can refer to previous publications for other features of FJM [29,31,32]. The FJM had been proven to be capable of simulating the characteristics of brittle rocks well [26], such as a high ratio of uniaxial compressive strength and tensile strength, large friction angle, and non-linear strength envelope.

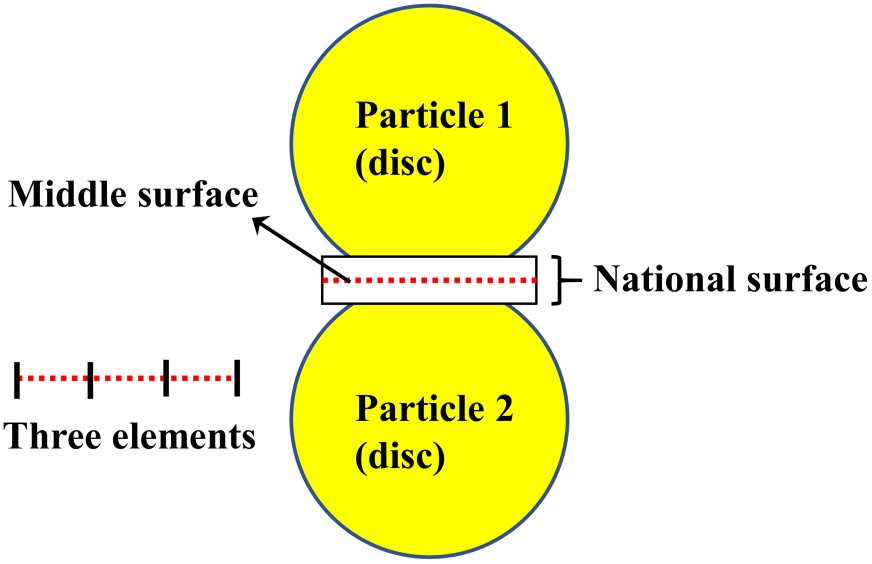

Figure 1. A typical schematic diagram for a 2D flat-joint contact.

2.1.2. Smooth-Joint Model

The SJM can ignore the direction of particle contact to simulate the sliding of a surface. The frictional joint can be simulated by assigning SJM to initial contacts between particles located on both sides of the joint. The smooth-joint contact (SJC) can be regarded as a group of springs, which are evenly distributed on a circular cross section, centered on the contact position, and parallel to the joint surface. If the load exceeds the bond strength, the bond will break, and the associated particles can slide along the surface. The smooth-joint model was often adopted to simulate the shear behavior of faults or joints near the excavation boundary in the surrounding rock [33] and prefabricated fissures in rock specimens [34]. For detailed information about SJM, readers can refer to previous publications [35,36].

2.2. Calibration of Micro-Parameters

The Jinping II Hydropower Station is a typical deep underground project in China, and the maximum buried depth exceeds 2500 m. During the construction period, failure phenomena of deep rock mass, such as rockburst, were commonly observed. Zhang et al. [22] reported that four extremely intense rockbursts occurred in the drainage and headrace tunnels of the Jinping II Hydropower Station in detail. Among them, the most intense rockburst took place on 28 November 2009, at Stake SK9+283-9+322 in the drainage tunnel with a diameter of 7.2 m, which was known as the "11.28" rockburst. More information on the "11.28" rockburst can be found in References [22,24].

Jinping marble is a typical brittle rock, and its mechanical properties have been reported in many studies [31,37–43]. In this study, the Jinping marble is used for parameter calibration, and a set of mechanical properties of Jinping marble, including uniaxial compressive strength (UCS), elastic modulus, Poisson's ratio, and tensile strength (TS), are matched with the simulated values [31,43]. The calibrated micro-parameters are then used to study the evolution mechanism of structure-type rockburst from a mesoscopic viewpoint.

In the parameter calibration, the size of the generated specimens in the PFC is consistent with that used in laboratory tests. For the numerical specimen in uniaxial compression tests, the height (H) of the model is set to be 100 mm, and the ratio of height (H) to diameter (d) is set to be 2. For the numerical specimen in Brazilian splitting tests, the height of the model is set as 25 mm, and the ratio of height to diameter is set to be 0.5. The grain diameter is in the range from 0.7 to 1.16 mm, which obeys uniform distribution, and the ratio of maximum to minimum grain diameter is 1.66. Moreover, the grain density is set to be 2690 kg/m^3. According to the calibration procedures proposed by Wu et al. [31], the

simulated mechanical properties are obtained, which agree well with those in laboratory tests (Table 1). The calibrated micro-parameters are shown in Table 2.

Table 1. Laboratory test results and simulation results.

Category	UCS (MPa)	TS (MPa)	Poisson's Ratio	Elastic Modulus (GPa)
Laboratory test	114.2	6.5	0.26	42.8
FJM results	113.6	5.4	0.26	43.4

Table 2. Micro-parameters in flat-joint model.

Micro-Parameters	Value
Installation gap ratio, g_{ratio}	0.3
Bonded element fraction, φ_B	0.9
Slit element friction, φ_S	0.1
Contact elements, N	2
Effective modulus of both particle and bond, $E_c = \overline{E}_c$(MPa)	35
Ratio of normal to shear stiffness of particle and bond $k_{n1}/k_{s1} = \overline{k}_n/\overline{k}_s$(GPa)	1.5
Bond tensile strength, σ_{b1}(MPa)	8.7
Bond cohesion strength, c_{b1}(MPa)	50.5

Based on field observation of "11.28" rockburst in previous studies, a structural plane with a dip angle of 40°~50°, which was straight and smooth with no filling, was detected near the failure zone [8,22,24,44]. The rock mass beneath the fault collapsed in the rockburst, creating a V-shaped failure zone with a depth of 7 m [22]. In the present study, the dip angle of the structural plane is assigned with a value of 45°. The structural plane is represented by unbonded SJM in the numerical model [36]. Several parameters, including normal stiffness, shear stiffness, and the friction coefficient, are associated with unbonded SJM. According to the results by Duan et al. [34], the shear stiffness of SJC has negligible influence on the simulated UCS and Young's modulus. The normal stiffness has a significant effect on the mechanical behavior, only when the dip angle of joints is smaller than 45°. Because the dip angle of the structural plane is set as 45°, we only consider the effect of the friction coefficient in this study. The micro-parameters of SJC were usually determined on the basis of the rock mechanical properties with inclined pre-existing fracture or different bedding plane inclinations [45,46], which is obviously not suitable for this study due to lack of the mechanical properties of the rockmass at the drainage tunnel. Therefore, the micro-parameters of SJC were calibrated to acquire simulation results that are closer to the observed failure range or locations of the surrounding rock observed in the field after "11.28" rockburst. Micro-parameters used in the smooth-joint model are shown in Table 3. The joint length is assumed to be 90 mm due to the lack of detailed information, and the influence of the joint length on the simulation results will be discussed later.

It needs to be noted that the FJM model is used for all the particles of the rock mass, while the SJM model is only used for the particles of the structural plane.

Table 3. Micro-parameters in smooth-joint model.

Normal Stiffness k_{n2}/GPa	Shear Stiffness k_{s2}/GPa	Friction Coefficient μ	Tensile Strength σ_{b2}/MPa	Cohesion Strength c_{b2}/MPa	Angle of Internal Friction Φ_{r2}
5	5	0.7	0	0	0

2.3. Simulation Procedures

To model the evolution of "11.28" rockburst, a square numerical model is generated (Figure 2). The particle size in the model is the same as that used in numerical specimens for parameter calibration. In previous studies, the dimension of a cubic model for simulating

underground tunnels ranged from 70 to 240 mm [47–49]. In view of the boundary effect and calculation time of the model, the side length of the model in this study is set as 250 mm. A circular hole with a radius of 25 mm is built into the model by directly deleting the particles in the range, which is one-fifth of the horizontal distance between the center of the circular hole and the boundary of the model. A total of 73,333 particles are included in the model. The similarity between the numerical modeling and the actual tunnelling case will be discussed in Section 5.

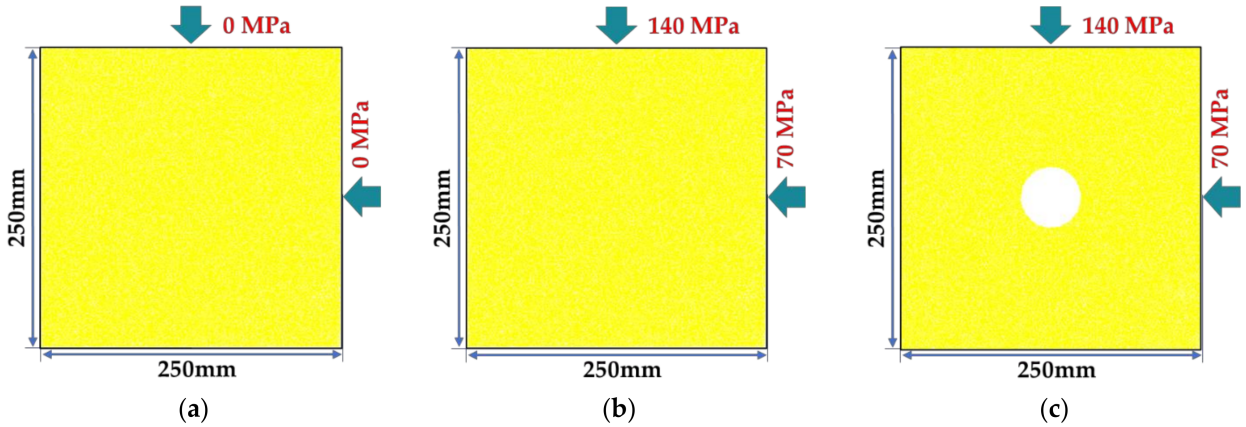

Figure 2. Generated numerical models: (**a**) before stress is applied, (**b**) at initial geostress state, (**c**) after excavation.

After model generation, the unbalanced forces are eliminated, and the overlap between particles is reduced gradually. The FJM is then installed at ball–ball contacts when the distance between two particles is less than installation gap. As shown in Figure 2, the load is firstly applied to the model step by step till the initial geostress is reached (i.e., vertical stress of 140 MPa and horizontal stress of 70 MPa). Then, a circular hole with a diameter of 50 mm was excavated by deleting particles, and the stress in vertical and horizontal directions was kept constant in the servo-controlled loading.

2.4. Energy Balance Calculations

In PFC, based on the law of energy conservation, the meso-scale energy equation can be obtained:

$$W_b = W_e + W_d \tag{1}$$

$$W_d = E_k + E_d + E_s \tag{2}$$

where W_b is the boundary work accumulated, which is generated by the external forces acting on the boundary of numerical model. W_e is strain energy stored in the model. W_d is the dissipative energy, which is the released energy from the surrounding rock after excavation and can be considered a measure of overall damage in rockmass [50,51]. E_k is the kinetic energy of particles. E_s is the slip energy, defined as the total energy dissipated by frictional slip. E_d is the energy dissipated by local damping. The sum of both E_d and E_k, which is the radiated energy from surrounding rock as a result of unstable failure after excavation, can be a measure of rockburst intensity [50,51].

3. Analysis of Simulation Results

3.1. Evolution Mechanism of Strainburst

The simulation results in terms of micro-cracking pattern and force chain of rockburst without a structural plane are shown in Figures 3 and 4, respectively. Because the rockburst zones at the walls of both sides are symmetric, the right side wall is taken as an example to illustrate the evolution process of rockburst.

After excavation, tangential stress concentration gradually occurs in the middle portion of the right side wall. When the model runs to 5000 steps, damage occurs in the surface

and interior of the right wall within a small range, and scattered particles fall off, showing slight spalling failure.

At 15,000 steps, the spalling damage of the right side wall further aggravates and develops unceasingly toward the interior. Due to tensile fracture induced by the tangential stress, the surrounding rock is cut into thin rock plates, which can be considered to be a slight slabbing phenomenon. The thickness of the force chain is positively correlated with the magnitude of contact force among particles, and the black force chain formed in the evolution process of rockburst at the right side wall is regarded as the rock plates.

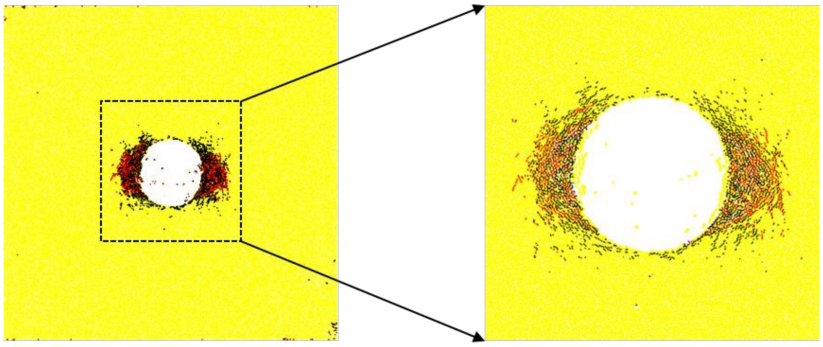

(**a**) Partially enlarged schematic diagram in the model.

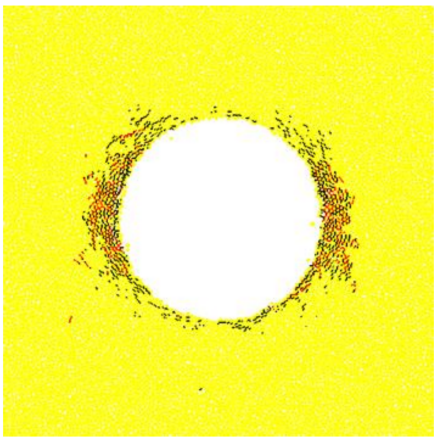

(**b**) 5000 steps

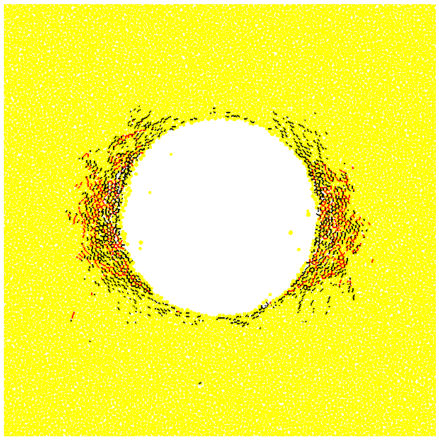

(**c**) 15,000 steps

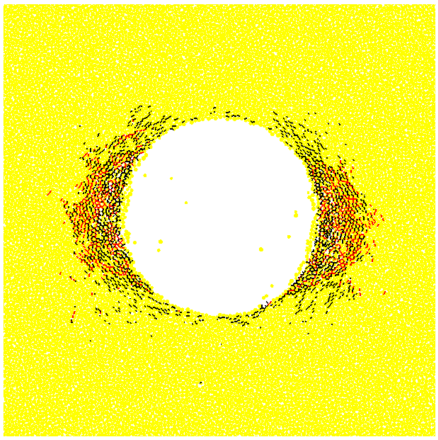

(**d**) 30,000 steps

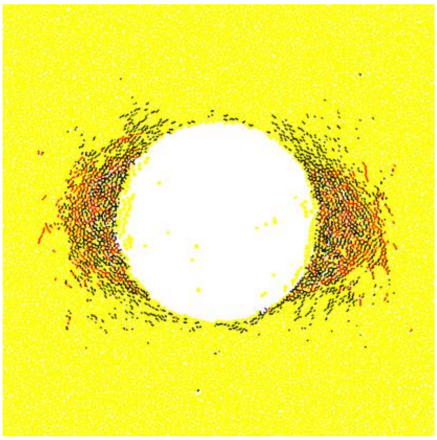

(**e**) 60,000 steps

Figure 3. Micro-cracking patterns at corresponding steps.

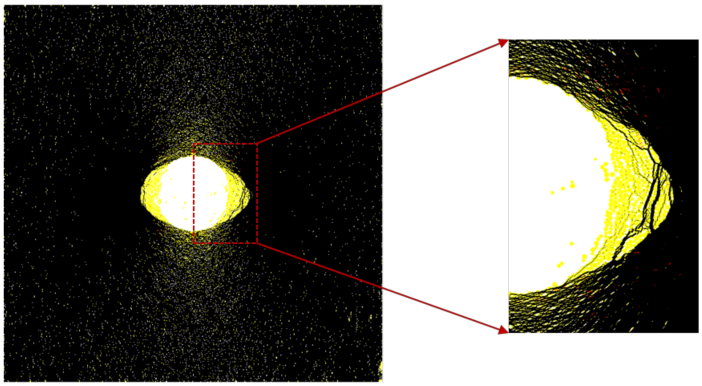

(**a**) Partially enlarged schematic diagram in the model.

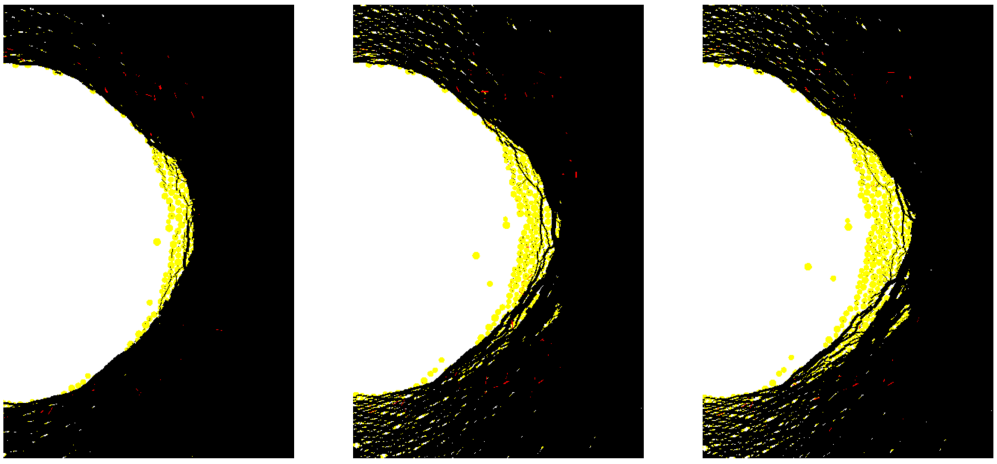

(**b**) 5000 steps (**c**) 15,000 steps (**d**) 20,000 steps

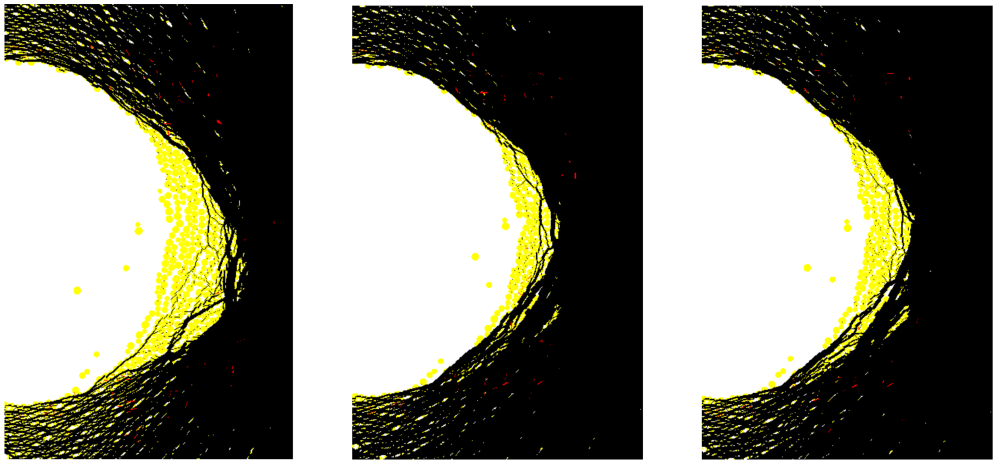

(**e**) 30,000 steps (**f**) 45,000 steps (**g**) 60,000 steps

Figure 4. Force chain diagrams at corresponding steps.

At 20,000 steps, the range of the slabbing failure further extends. Once the bending stress caused by the compressive stress exceeds the bending strength, the rock plates formed previously will break into numerous rock blocks and eject, indicating the occurrence of rockburst.

At 30,000, 45,000, and 60,000 steps, the above rock failure is repeated constantly until it reaches a stable state. It is worth noting that as the fracture propagates to the interior of the surrounding rock, its vertical fracture range is shrinking, forming a typical V-shaped fracture zone. Haimson [52] believed that the failed thin rock plate left hanging cantilevers at the upper and lower ends, which might limit the length of the next spalled

rock fragments. As the failure deepened, spalled rock fragments became shorter, resulting in the decrease in the vertical failure span continuously. The entire process would stop once the rock plates were supported steadily by the remaining cantilever that was previously damaged. The simulation results in this study are quite consistent with the laboratory test results [53] and the field observation results [52].

The surrounding rock in the underground opening is often subjected to high tangential compressive stress but zero or low radial stress, which is similar to uniaxial compressive loading or conventional triaxial loading under low confining pressure. The uniaxial compression state is considered in this study. Based on the stress relations of the circular hole in elastic theory (Equation (3)) [54], the damage range around the tunnel can be estimated. The condition for rock failure is that the axial stress is equal to or larger than the UCS of the rock. Taking the left side wall as an example, the damage range is from -66° to 66°. As shown in Figure 5a,b, the simulation result in the present study agrees well with the analytical result.

$$\sigma_\theta = \frac{(p+q)}{2}\left(1+\frac{a^2}{r^2}\right) - \frac{(q-p)}{2}\left(1+3\frac{a^4}{r^4}\right)\cos 2\theta \tag{3}$$

where σ_θ is tangential stress in the surrounding rock, q is the horizontal load, p is the vertical load, a is the radius of the tunnel, r is the length of the connecting line between a point in the rock mass and the center of the tunnel, which is called the polar radius, and θ is the angle between the polar radius and the horizontal axis.

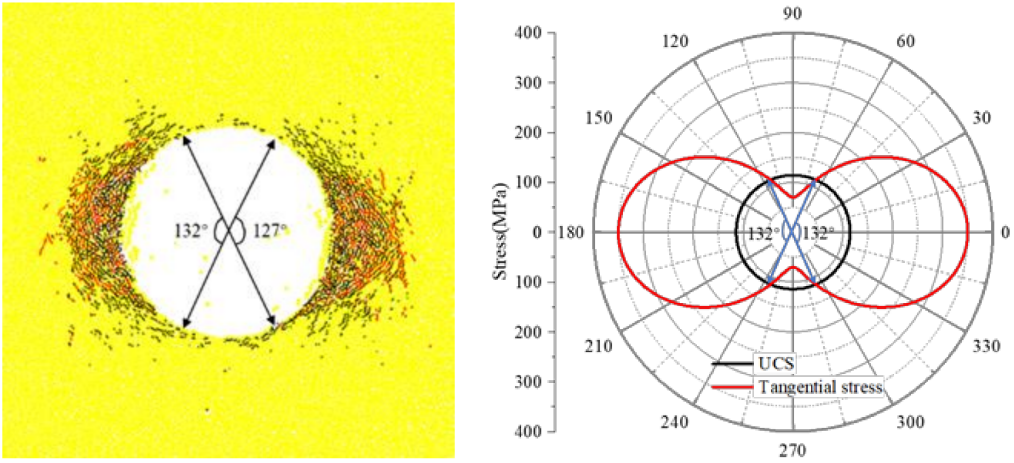

(**a**) (**b**)

Figure 5. Schematic diagram of damage range for the simulation result (**a**) and the analytical result (**b**).

3.2. Evolution Mechanism of Structure-Type Rockburst

The simulation results of the micro-cracking pattern in the model with the structural plane are shown in Figure 6.

At 500 steps, the damage zone first occurs in the Location-1 where it is most vulnerable to excavation. At 5000 steps, with the adjustment of the tangential stress, a lot of tensile and shear cracks generate at the local crack band (Location-4) and the left and right side walls (Location-2 and Location-3). A large damage zone occurs in the interaction zone between the structural plane and the tunnel (Location-1). The local crack band at the left side wall (Location-4) propagates towards the upper left. It is worth noting that the oblique secondary crack band (Location-5) is formed in the upper end of the structural plane. This is because the upper end of the structural plane is far away from the tunnel and is less affected by the tunnel compared with the lower end of the structural plane.

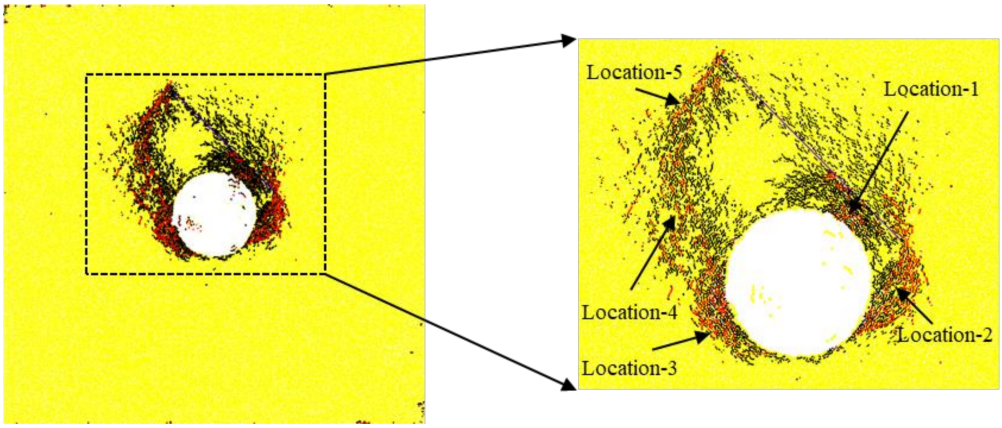

(**a**) Partially enlarged schematic diagram in the model.

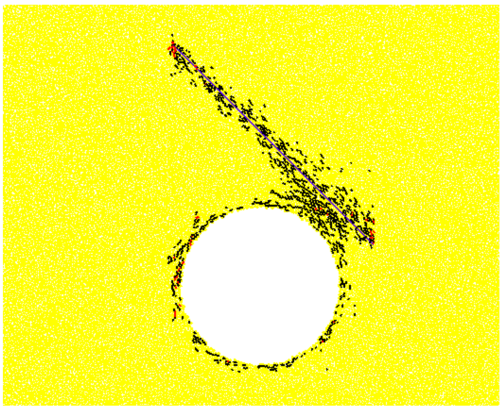

(**b**) 500 steps

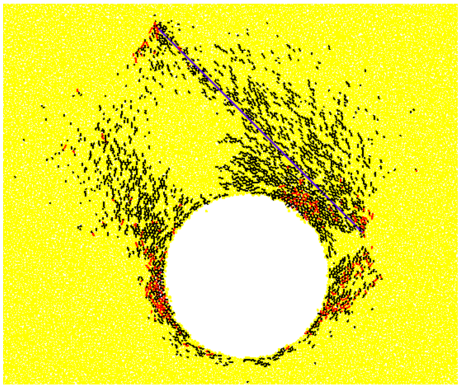

(**c**) 5000 steps

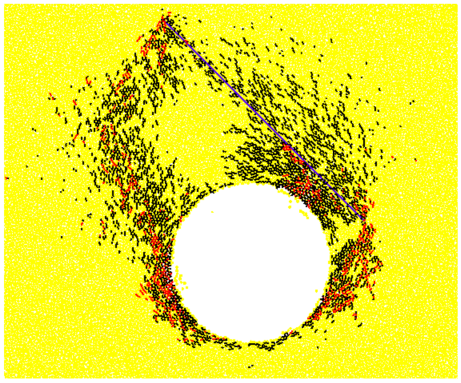

(**d**) 15,000 steps

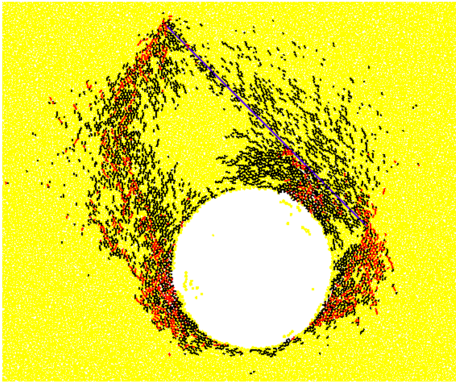

(**e**) 30,000 steps

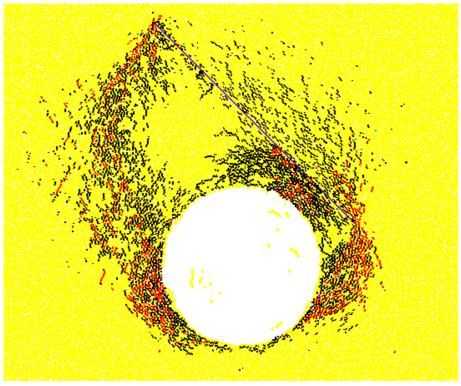

(**f**) 60,000 steps

Figure 6. Micro-cracking patterns at corresponding steps.

At 15,000 steps, the damage degree at Location-1 greatly increases, and the tensile and shear cracks become denser compared with the results of 5000 steps. After the damage reaches a certain degree, small-scale collapse occurs at the right arched shoulder. It is worth noting that rockburst occurs at Location-3 in Figure 6, which is the symmetric position of Location-1. The local crack band (Location-4) develops towards the upper left, and the oblique secondary crack band (Location-5) at the upper end of the structural plane further extends to the lower left.

At 30,000 steps, rockburst occurs in the right and left side walls (Location-2 and Location-3), forming two small-scale V-shaped notches. Tensile cracks caused by tangential compressive stress tend to be accompanied by buckling and slabbing phenomena. The oblique secondary crack band (Location-5) coalesces gradually with the local crack band (Location-4), but the coalescence of the internal cracks in the two bands (Location-4 and Location-5) has not formed yet, indicating that the two bands still have a certain bearing capacity. The interaction zone between the structural plane and the tunnel (Location-1) continues to be damaged until it reaches the structural plane.

At 60,000 steps, ultimate failure occurs in the interaction zone between the structural plane and the tunnel (Location-1). The V-shaped notches on both wall sides continue to develop toward the interior of surrounding rock to form the final V-shaped failure surface. The cracks inside the two crack bands (Location-4 and Location-5) continue to expand, so the rock inside the two crack bands still has part of the bearing capacity. When the gravity of the uncollapsed rock in the enclosed area between two crack bands and the structural plane exceeds the bearing capacity of the rock inside the two crack bands, the uncoalesced parts among the cracks in the two crack bands will be snipped to form a macro fracture band and shear fracture occurs, causing severe rockburst and forming a large V-shaped pit. As shown in Figure 7, the simulation results are in good agreement with the results obtained from field observation [55].

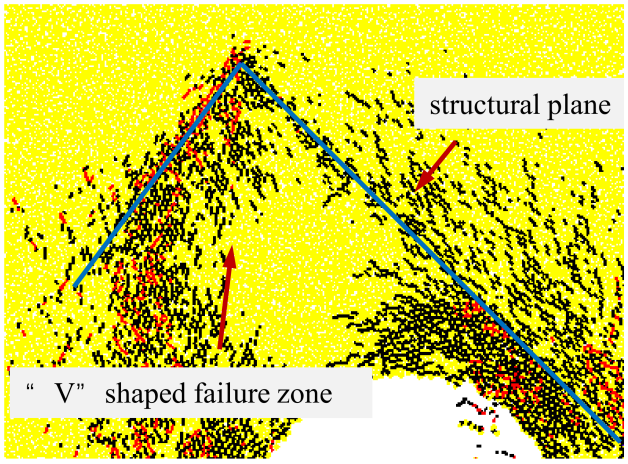

Figure 7. V-shaped failure at PFC numerical result in this study.

In order to obtain slip displacement on the structural plane, we arrange five measuring points (MP1~MP5) to record the histories of slip displacement, as shown in Figure 8. At each measuring point we monitor the displacement of three particles in the hanging wall and footwall, respectively.

It is obvious that slip displacement at MP1, MP2, and MP3 along the structural plane is less affected by excavation compared with that at MP4 and MP5 due to the relative distances from the tunnel, which are 0.01, 0.03, and 0.05 mm, respectively. The slip displacement at MP4 is greater than that at MP5 until 49,200 steps, after which the opposite occurs. This can be attributed to the randomness of particles movement in terms of the magnitude and direction and the effect of contact force concentration at MP5. In general, the slip displacement on the structural plane is approximately positively correlated with the

distance between the measuring point and tunnel, which is consistent with the simulating results from Manouchehrian and Cai [25].

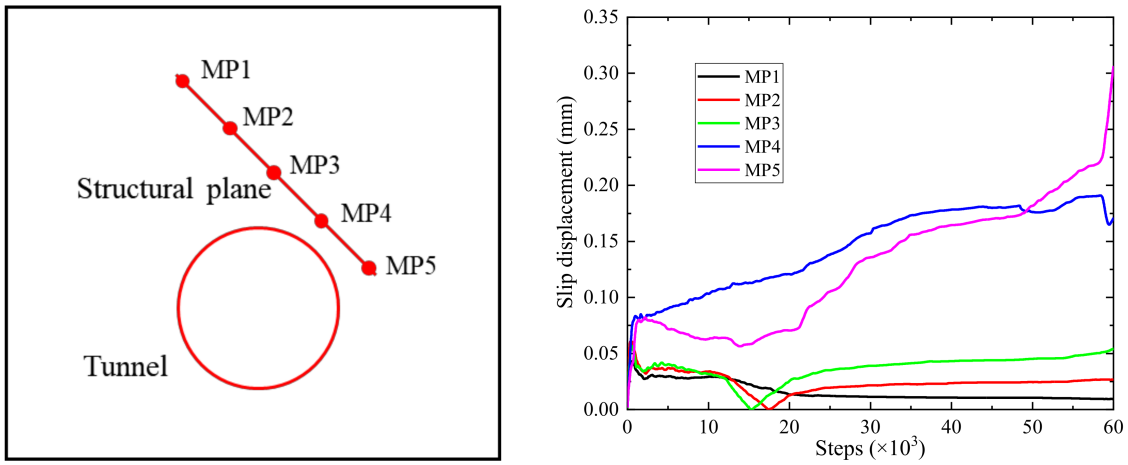

(**a**) (**b**)

Figure 8. Slip displacement on the structure plane. (**a**) Arrangement of measuring points along the structure plane; (**b**) measuring results.

3.3. Comparison between Strainburst and Structure-Type Rockburst

Based on the simulation results in this study, it is found that the main differences between strainburst and structure-type rockburst are as follows:

(1) Figure 9 displays the contact force vector plots for strainburst and structure-type rockburst at 2000 steps after excavation. As shown in Figure 9, the existence of the structural plane directly changes the original in situ stress field, making the stress distribution more complicated after the tunnel excavation. Under high in situ stress, stress concentration zones for structure-type rockburst are formed at various places, i.e., both ends of the structural plane, left and right side walls, and the interaction zone between the structural plane and the tunnel. However, stress concentration zones for strainburst appear at the left and right side walls, which have good symmetry.

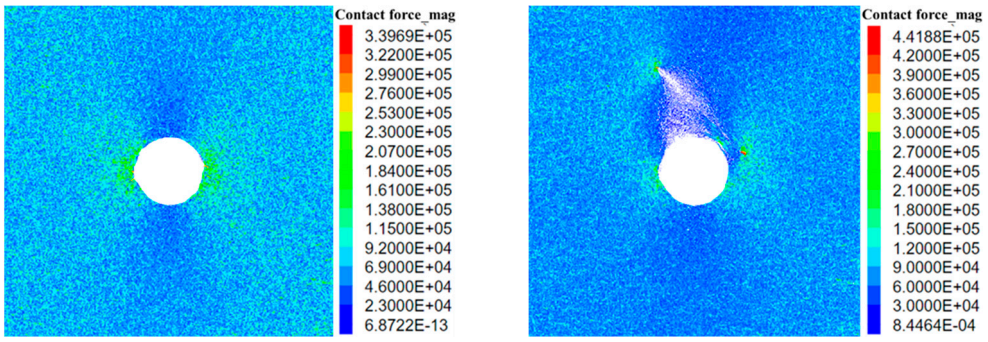

(**a**) (**b**)

Figure 9. Force vector plots for strainburst (**a**) and structure-type rockburst (**b**) at 2000 steps.

(2) The strainburst is mainly caused by the tensile cracking induced by tangential compressive stress, in which buckling and slabbing failure is formed, accompanied by ejection of thin rock blocks. However, the cause and evolution process mentioned above also exists in the structure-type rockburst. Moreover, for structure-type rockburst, the shear fracture in two crack bands (Location-4 and Location-5), due to high in situ stress and shear stress induced by overburdened loadings and shear slip along structural plane, results in a larger-scale rockburst with a large V-shaped pit.

(3) The failure locations for strainburst mainly exist in the middle of both side walls, while the failure locations for structure-type rockburst are closely related to the location of the structural plane.

4. Sensitivity Analysis

4.1. Influence of Structural Plane Roughness

The existence of structural plane has a significant effect on the intensity and failure mode of rockburst [23]. However, the study related to the effect of the structural plane roughness on the rockburst is still limited. Moreover, the results from previous studies showed that the shear strength increased with the increase in friction coefficient μ in the SJM [56,57], and the joint roughness coefficient (JCR) was positively correlated with the shear strength [58].

In this study, the effect of structural plane roughness on the rockburst is investigated. The roughness is represented by the friction coefficient in the SJM. The friction coefficient is assigned with the values of 0.3, 0.5, 0.7, and 0.9 in the present study. The simulation results of the four cases are shown in Figure 10. It is seen intuitively that the width and the density of two crack bands and the range of the V-shaped notch formed at the left and right side walls decrease with the increasing friction coefficient. The structure-type rockburst is not obvious at 0.9 of the friction coefficient because the oblique secondary crack band and the local crack band (Location-4 and Location-5) are not fully penetrated. The above analysis suggests that structure-type rockbursts are more likely to occur at the friction coefficient of less than 0.9.

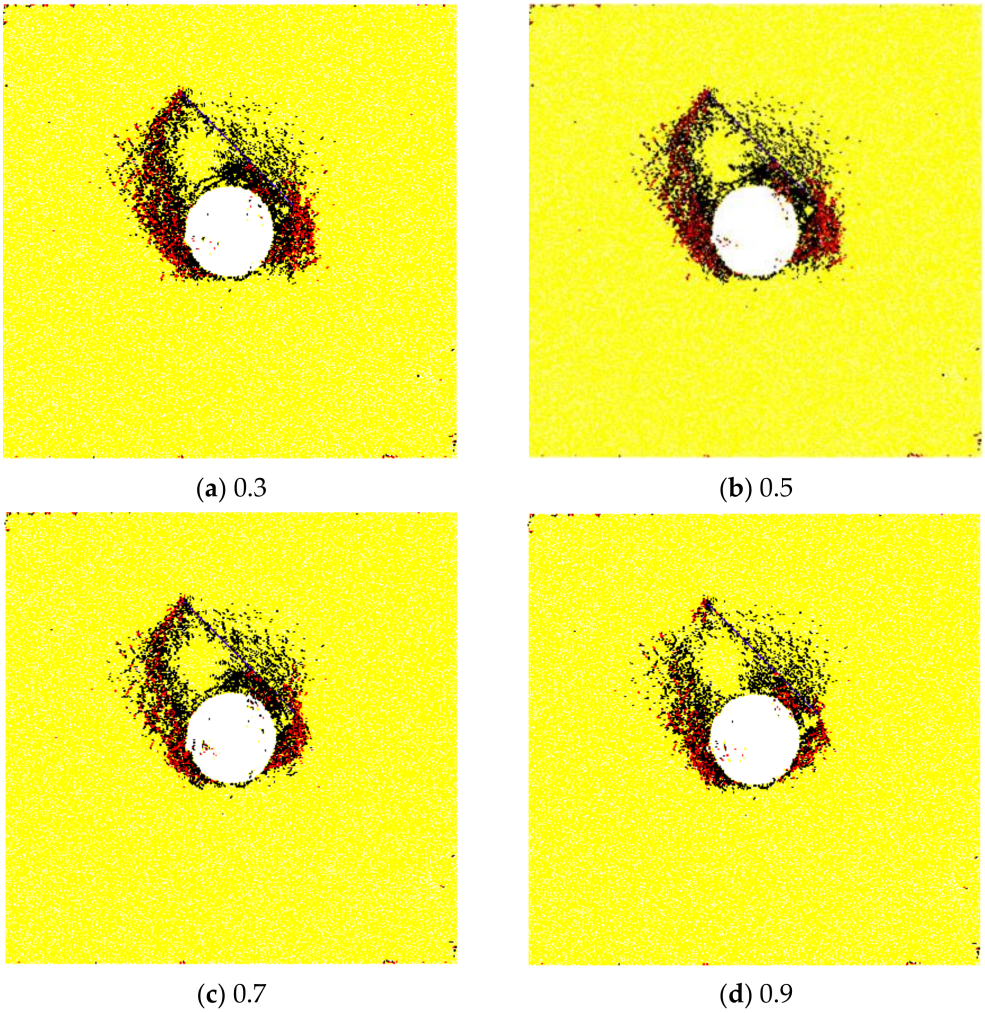

(**a**) 0.3 (**b**) 0.5

(**c**) 0.7 (**d**) 0.9

Figure 10. Micro-cracking patterns of numerical models with different friction coefficients.

Figure 11 shows the variation of the crack number for numerical models with different friction coefficients at 60,000 steps. It is seen that the number of tensile cracks and shear cracks for the model with the friction coefficient of 0.3 is very close to that for the model with the friction coefficient of 0.5. When the friction coefficient is larger than 0.5, the crack number greatly decreases, indicating that the intensity of the overall rockburst weakens.

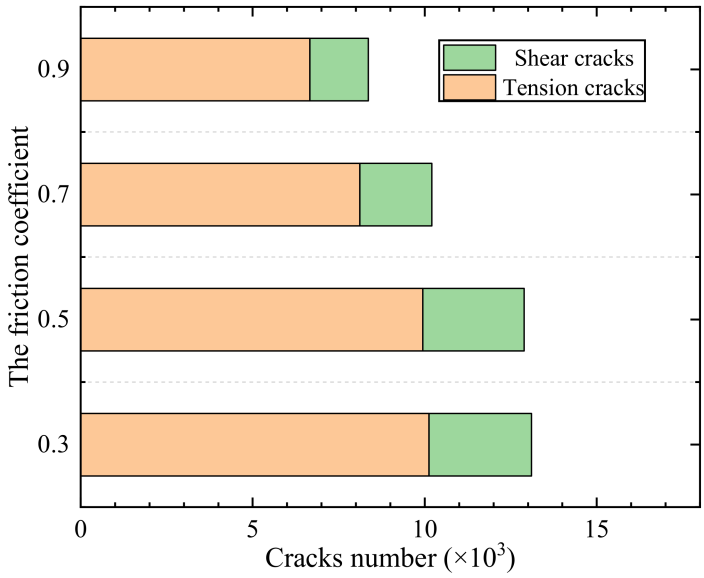

Figure 11. Number of generated cracks for numerical models with different friction coefficients.

It can be seen from Figure 12 that varying the friction coefficient has little to zero impacts on the dissipated and radiated energy after excavation when the friction coefficient is less than 0.5. However, the dissipated and radiated energy decrease when the friction coefficient is larger than 0.5, which is consistent with the variation of the crack number with the friction coefficient. The above analysis shows that the impact of a friction coefficient below 0.5 on the structural-type rockburst intensity and overall damage in surrounding rock is not obvious. When the friction coefficient is greater than 0.5, the effect of the structural plane is weakened, the rock near the structural plane tends to be intact, and the intensity of structural-type rockburst decreases.

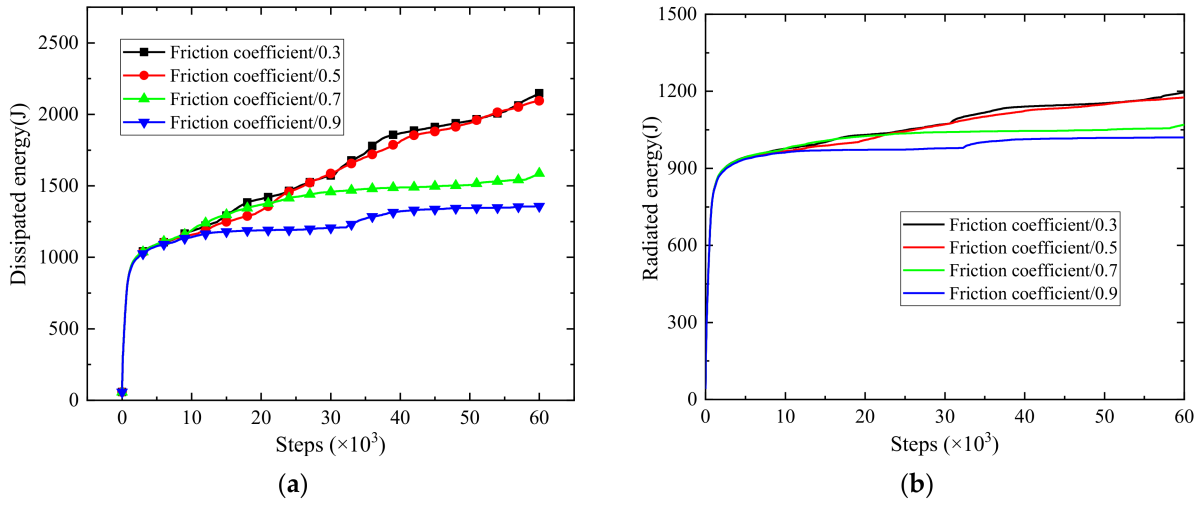

Figure 12. Dissipated energy (**a**) and radiated energy (**b**) in models with different friction coefficients after excavation.

4.2. Influence of Rockmass Heterogeneity

4.2.1. Simulation of Heterogeneity

The heterogeneity in PFC can be considered in two ways. The first one is a direct incorporation of geometric heterogeneity of rock in a grain-based model [59,60]. The second one is an indirect method using statistical distribution models (i.e., Weibull distribution) for micro-parameters [61–63]. In this study, the Weibull distribution is used to describe the heterogeneity of micro-parameters (i.e., cohesion, effective modulus) of the FJM. The probability density function of the Weibull distribution is expressed as

$$\varphi(E) = \frac{m}{E_0} * \left(\frac{E}{E_0}\right)^{m-1} * exp\left[-\left(\frac{E}{E_0}\right)^{m}\right] \tag{4}$$

$$\varphi(c) = \frac{m}{c_0} * \left(\frac{c}{c_0}\right)^{m-1} * exp\left[-\left(\frac{c}{c_0}\right)^{m}\right] \tag{5}$$

where E is the effective modulus, E_0 is the average value of the effective modulus, c is the cohesion, c_0 is the average value of the cohesion, and m is a shape parameter, which can reflect the degree of rock heterogeneity. The smaller the parameter m is, the larger the heterogeneity will be. Taking the effective modulus as an example, the probability density curves under different m values are shown in Figure 13.

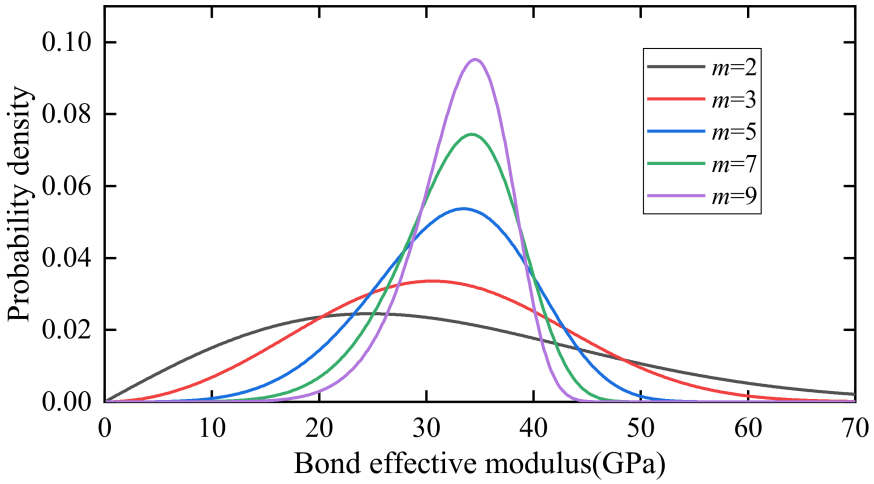

Figure 13. Probability density curves with different m values.

4.2.2. Influence of Cohesion Heterogeneity

The rock macro-mechanical properties are closely related to the micro-parameters in the model, especially the cohesion and effective modulus. The results from previous studies showed that the UCS increased with the increase in cohesion in FJM [64,65]. Hence, the UCS in the model may vary due to the change of the cohesion c_b in grain scale [66].

The parameter m for the cohesion is assigned with 3, 5, 7, and 9 in the study, and the corresponding simulation results are shown in Figures 14–16; it is seen that the variation of the number of shear cracks and tension cracks under different parameters m is basically the same. However, the proportion of the number of shear cracks to the total number of cracks decreases with the increase in parameter m for cohesion.

The shear strength τ_c follows the Coulomb criterion with a tension cut-off for bonded elements in the FJC [29,31], which is expressed as

$$\tau_c = c_b - \hat{\sigma} \tan \varnothing_b \tag{6}$$

where c_b is the cohesion, $\varnothing_b$ is the friction angle, and $\hat{\sigma}$ is the normal stress. The bonded state is broken in shear, and a shear crack is generated when the shear stress $\tau_{max}^{(e)}$ exceeds

the shear strength τ_c. The cohesion c_b will be more discrete as the heterogeneity m decreases, which will make shear strength τ_c more discrete. Therefore, many contacts with the low shear strength distribute non-uniformly in rockmass, which makes it easier for shear cracks to form. Due to the randomness of the cohesion value at assignment for the grains at different positions, the distribution of shear cracks also has the characteristic of scatter.

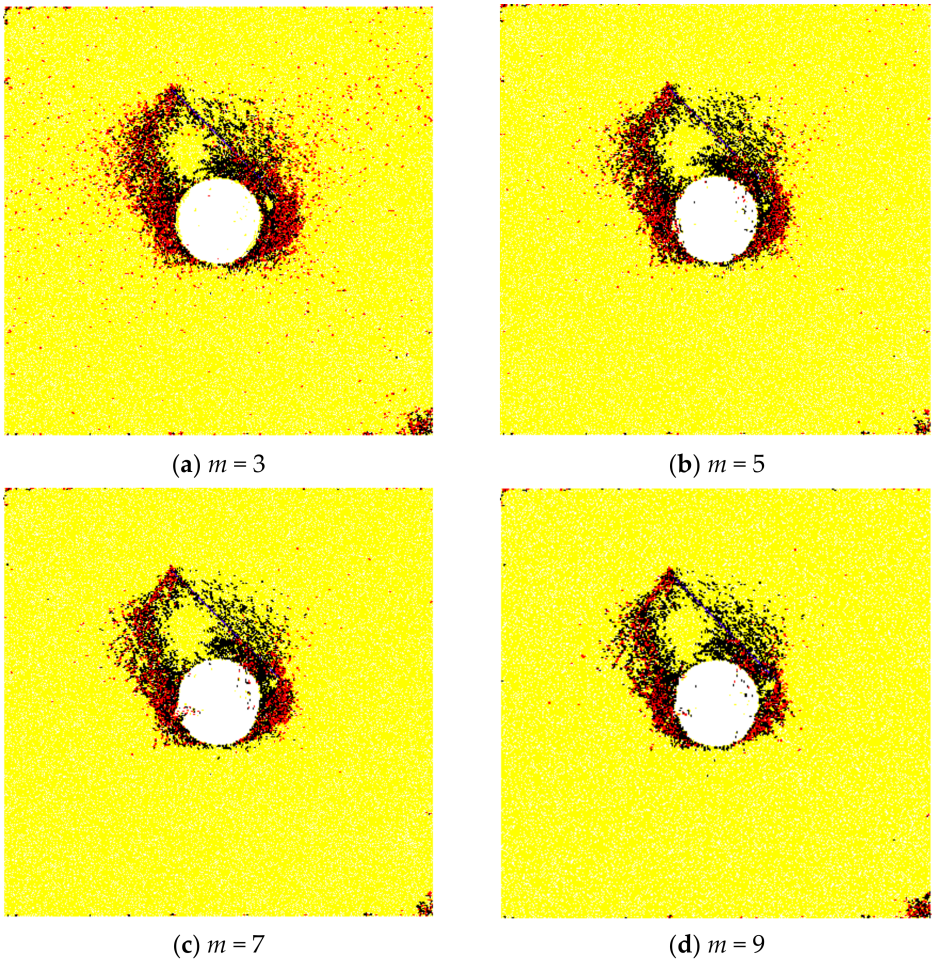

(**a**) $m = 3$ (**b**) $m = 5$

(**c**) $m = 7$ (**d**) $m = 9$

Figure 14. Micro-cracking patterns in models with different m values for cohesion.

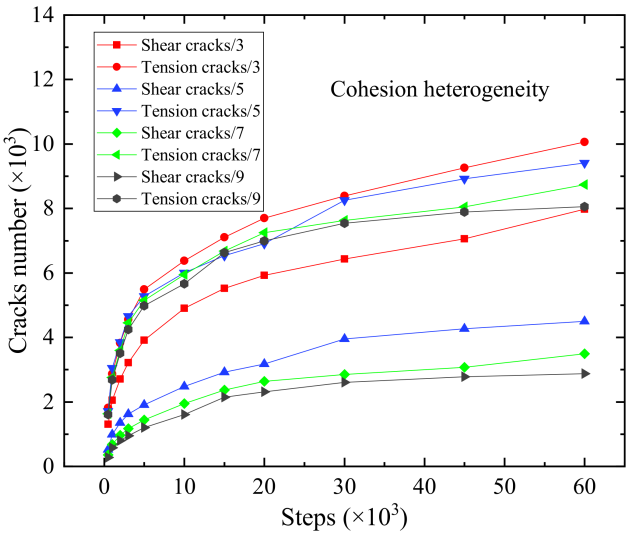

Figure 15. Number of cracks in models with different m values for cohesion.

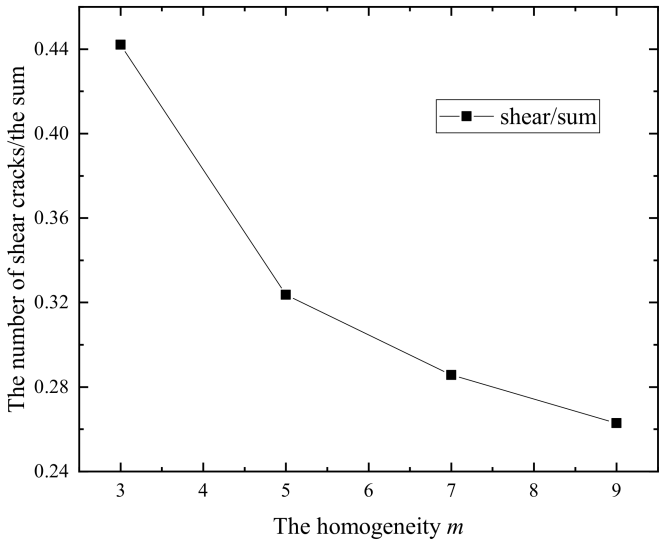

Figure 16. Shear cracks to total cracks ratio.

As shown in Figure 17, dissipated and radiated energy in models decreases with the growth of cohesion heterogeneity m. The energy dissipated for the cases at m of 3, 5, 7, and 9 is 2229.06, 1839.90, 1760.31, and 1543.22 J, respectively, which increase by 40.40%, 15.87%, 10.85%, and −2.82% compared with the 1587.97 J of dissipated energy for homogeneous rockmass. The energy radiated for the cases at m of 3, 5, 7, and 9 are 1237.71, 1142.54, 1113.56, and 1078.71 J, respectively, which increase by 15.67%, 6.78%, 4.07%, and 0.81% compared with the 1070 J of that for homogeneous rockmass. This indicates that the structure-type rockburst intensity and overall damage in surrounding rock decrease and rockmass near excavation tends to be homogeneous with increasing cohesion heterogeneity m.

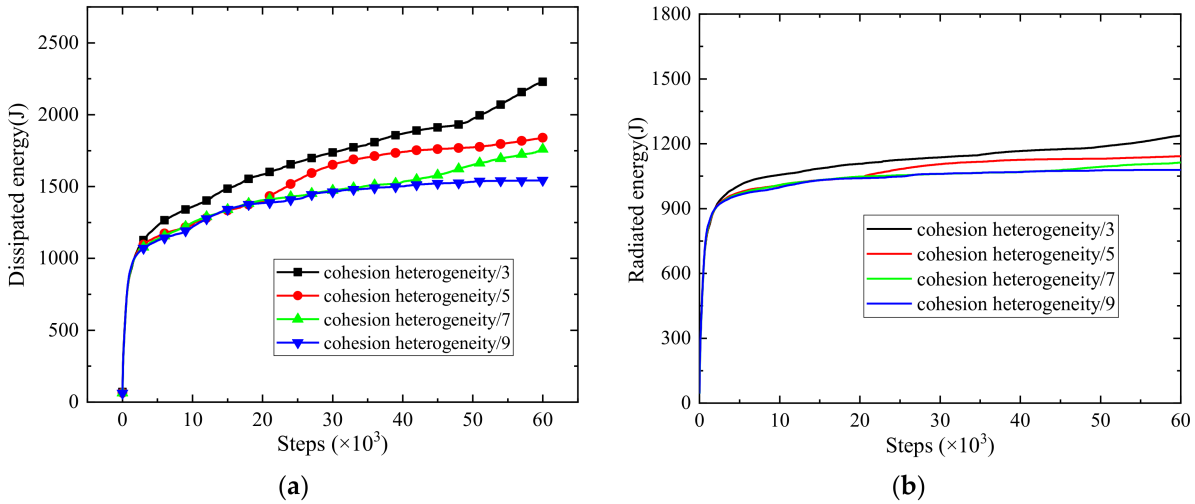

Figure 17. Dissipated energy (**a**) and radiated energy (**b**) in models for different m values of cohesion heterogeneity.

4.2.3. Influence of Effective Modulus Heterogeneity

The simulation results in models with different m for effective modulus are shown in Figures 18 and 19. It can be seen that the overall coalescence of the crack bands in models with different m is basically the same. In addition, due to the strength variation in rockmass under heterogeneous condition, discretized cracks may appear at some positions far away from the tunnel. It is worth noting that the number of cracks is not a completely negative correlation with the parameter m for the effective modulus. The number of cracks at m = 5 is less than that at m = 7. Dai et al. [63] also observed a similar result.

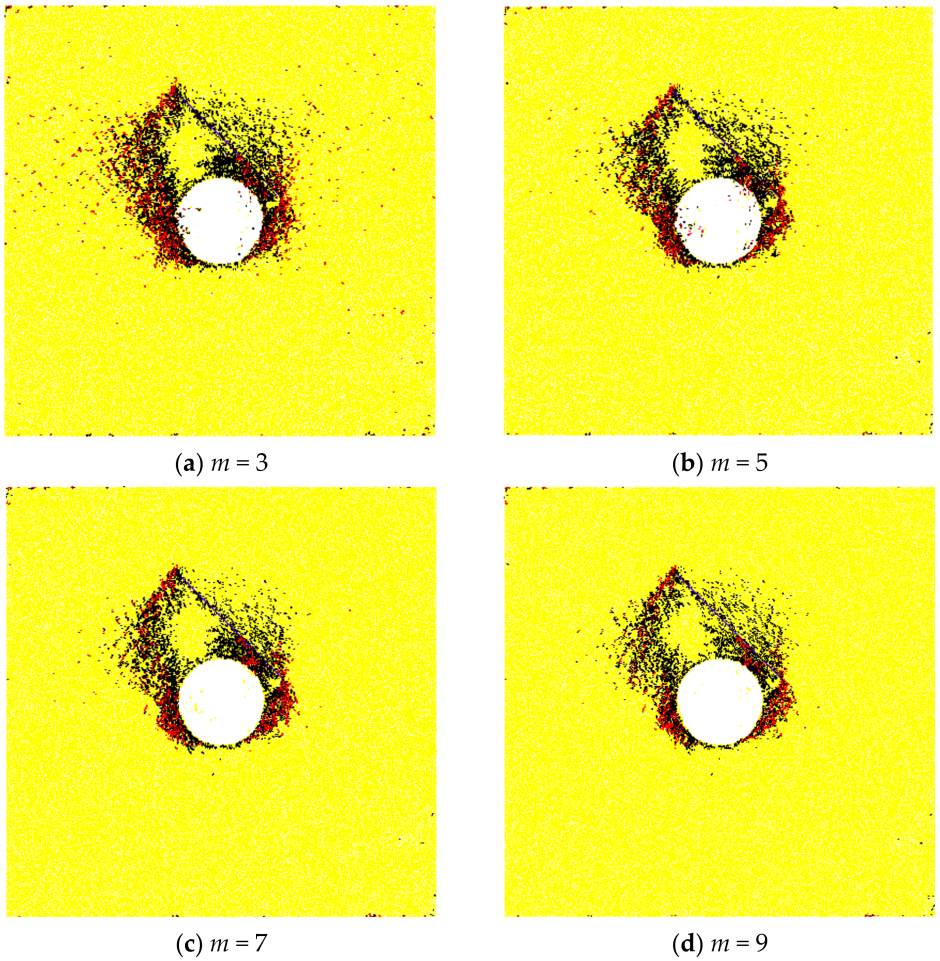

Figure 18. Micro-cracking patterns in models with different m values for effective modulus.

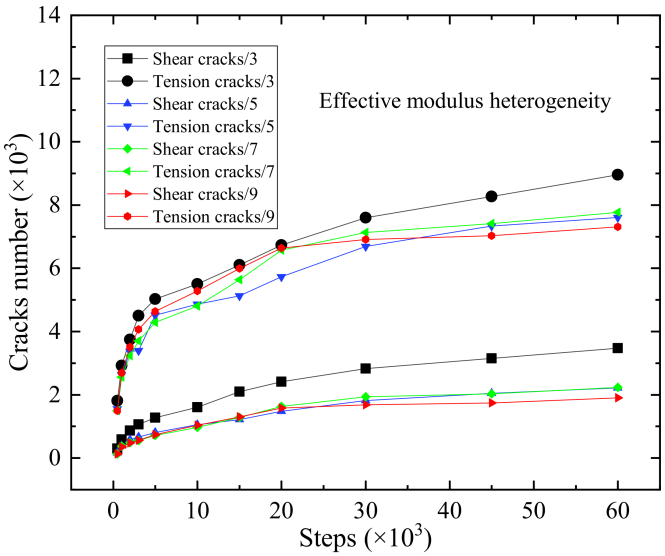

Figure 19. Number of cracks in models with different m values for effective modulus.

As shown in Figure 20, dissipated energy in models after excavation decreases with the growth of modulus heterogeneity m except m = 7, at which dissipated energy is slightly larger than that at m = 5. This is in accordance with the variation of cracks number. The energy dissipated for the cases at m of 3, 5, 7, and 9 are 1995.89, 1638.03, 1675.05, and 1540.44 J, respectively, which increase by 25.70%, 3.15%, 5.48%, and −3.00% compared

with the 1587.97 J of dissipated energy for homogeneous rockmass. The energy radiated for the cases at m of 3, 5, 7, and 9 are 1304.68, 1160.14, 1148.35, and 1102.56 J, respectively, which increase by 21.93%, 8.42%, 7.32%, and 3.04% compared with the 1070 J of that for homogeneous rockmass. This shows the structure-type rockburst intensity and overall damage in surrounding rock decrease in general and rockmass near excavation tends to be homogeneous with the growth of modulus heterogeneity m.

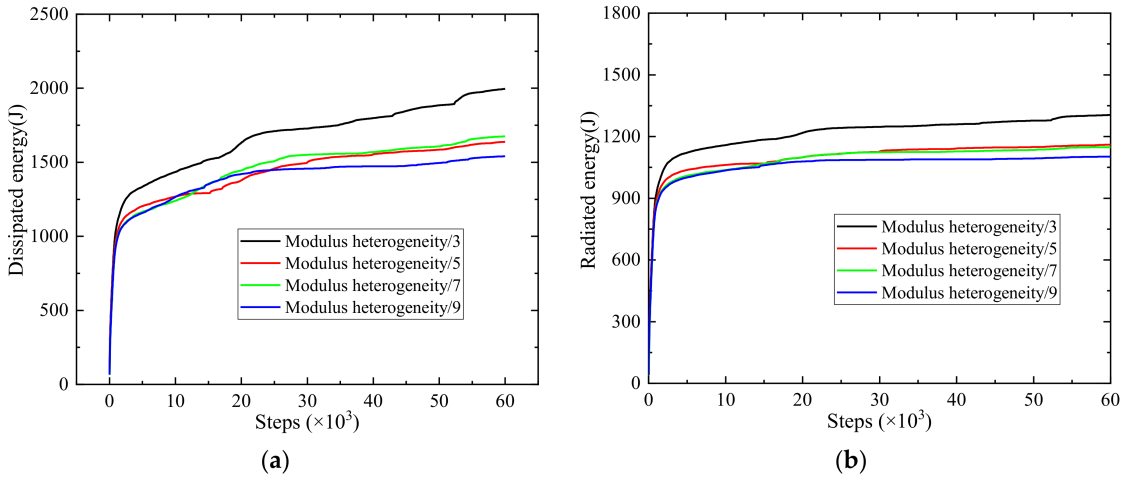

Figure 20. Dissipated energy (**a**) and radiated energy (**b**) in models for different m values of modulus heterogeneity.

4.2.4. Comparison for Influence of Cohesion and Modulus Heterogeneity

It can be found from Figure 21a that the number of shear and tensile cracks in the models with cohesion heterogeneity is significantly higher than that in the models with modulus heterogeneity at the same parameter m, which means that the effect of cohesion heterogeneity on overall damage in surrounding rock is greater than the effect of modulus heterogeneity. In order to compare the impact of two parameters' heterogeneity on rockburst, as shown in Figure 21b, the radiated energy is normalized with the value for homogeneous rockmass. It is obvious that normalized radiated energy in the models with cohesion heterogeneity is always lower than that in the models with modulus heterogeneity, indicating the effect of modulus heterogeneity on the structure-type rockburst intensity is greater than the effect of cohesion heterogeneity.

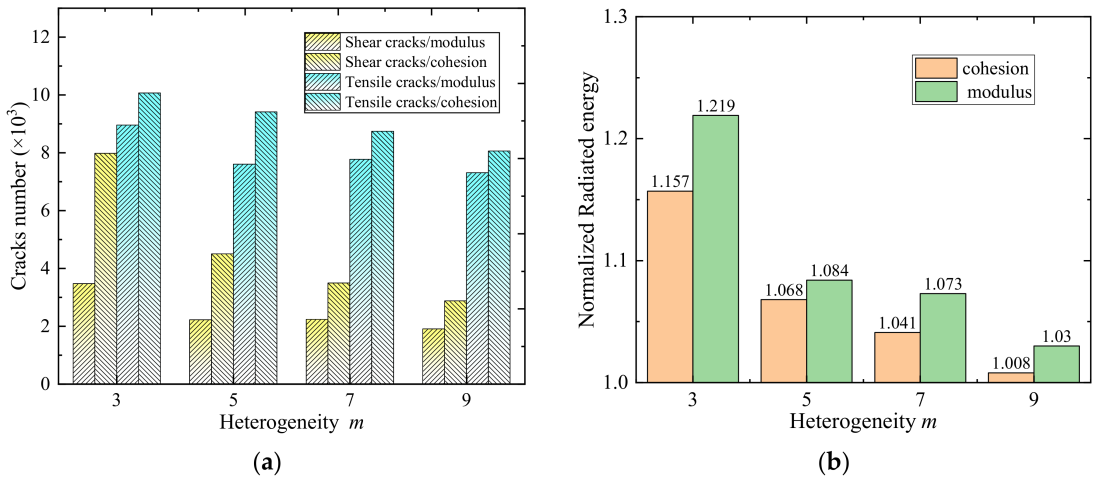

Figure 21. Crack number (**a**) and normalized radiated energy (**b**) of the two micro-parameters under different homogeneity levels.

4.3. Influence of Lateral Pressure Coefficient

In this section, we study the effect of lateral pressure coefficient λ on the simulation results. The lateral pressure coefficient λ is defined as the ratio of vertical in situ stress to horizontal in situ stress. In this study, the vertical in situ stress is kept unchanged (i.e., 140 MPa). The horizontal in situ stress is set to be 35, 70, 105, and 140 MPa, and the corresponding λ is 0.25, 0.5, 0.75, and 1, respectively.

The simulation results for models with different λ are shown in Figure 22. When the λ is 1, the failure zones are formed in the two ends of the structural plane, the interaction zone between the structural plane and the tunnel, and the lower half of the tunnel. It can be seen that the structure-type rockburst is not obvious at λ of 1. The results for models with λ of 0.25, 0.5, and 0.75 are quite different from that for the model with λ of 1. The oblique secondary crack band (Location-5) and the local crack band (Location-4) (see blue arrow in Figure 22) are connected at λ of 0.25, 0.5, and 0.75, which becomes more obvious as λ decreases. Moreover, the width of the failure zones at both side walls decreases with λ owing to the existence of the structural plane and the reduction of horizontal in situ stress. The damage zone at both side walls becomes very small at λ of 0.25 compared with that at λ of 0.5. Therefore, it can be concluded that structure-type rockburst is more pronounced when the λ is close to 0.5.

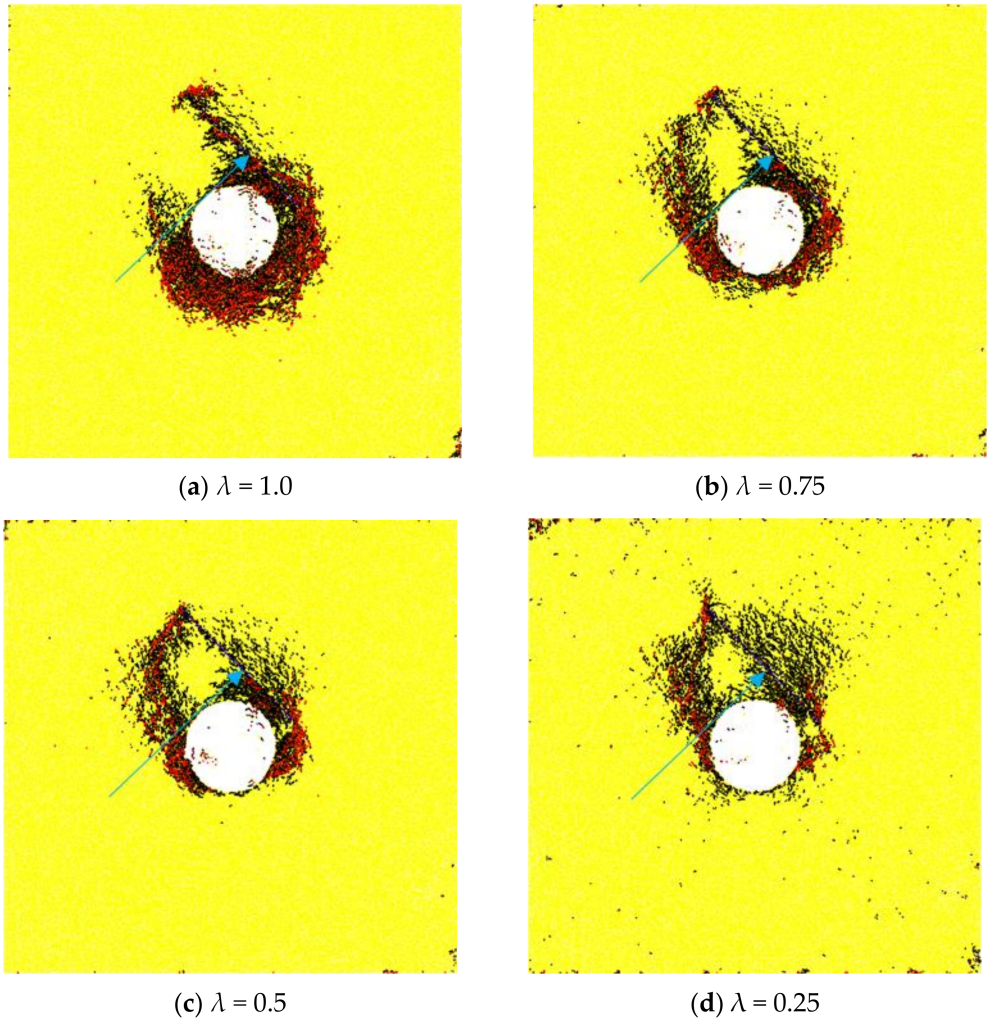

(**a**) λ = 1.0 (**b**) λ = 0.75

(**c**) λ = 0.5 (**d**) λ = 0.25

Figure 22. Micro-cracking patterns in models with different coefficients of lateral pressure.

As shown in Figure 23, the dissipative and radiated energy after excavation rise with lateral pressure coefficient λ. Concretely speaking, the energy dissipated for the cases at λ of 0.25, 0.5, 0.75, and 1 are 1333.59, 1587.97, 2298.68, and 4474.17 J, respectively, which increase by 19.07%, 53.81%, and 175.11%, respectively, compared with that at λ of 0.25, indicating that λ has a very significant effect on the overall damage in surrounding rock. The energy radiated for the cases at λ of 0.25, 0.5, 0.75, and 1 are 949.98, 1069.98, 1351.7, and 2327.76, respectively, which increase by 12.63%, 42.29%, and 145.03%, respectively, compared with that at λ of 0.25, showing λ has a very significant effect on the intensity of rockmass failure. The results show that the elastic strain energy stored in the rock under initial in situ stress eliminates with the decreasing lateral pressure coefficient under constant vertical in situ stress. The dissipative energy during the stress redistribution after excavation reduces obviously, accompanied by the decrease in crack number and radiated energy.

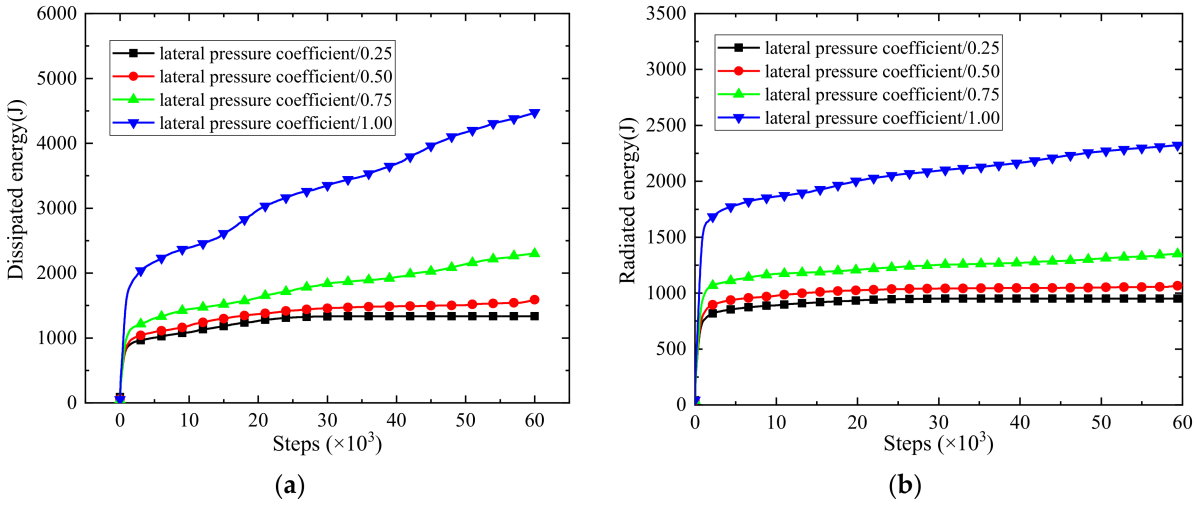

Figure 23. Dissipated energy (**a**) and radiated energy (**b**) in models for different lateral pressure coefficient after excavation.

4.4. Influence of Structural Plane Length

The results in previous sections show that the existence of the structural plane has a significant effect on rock failure in deep ground. However, the effect of structural plane length on rock failure is seldom discussed in previous studies. This section examines the influence of structural plane length on the simulation results. Numerical models with structural plane length ranging from 50 to 130 mm are generated, and the simulation results of different models are shown in Figure 24.

The length of the structural plane in the "11.28" rockburst that occurred in the Jinping II Hydropower Station is not given in the literature. It is found that when the structural plane length is near 90 mm, the simulation results agree with the field observation. If the length of the structural plane is smaller, the damage is mainly concentrated in the interaction zone and both side walls. The oblique secondary crack band and the local crack band are not developed sufficiently, so it is difficult to form a V-shaped failure zone at the tunnel dome. If the length of the structural plane is larger, the damage mainly occurs in the interaction zone and the left side wall. The upper end of the structural plane is less affected by the tunnel, so the V-shaped failure zone at the tunnel dome is hard to form. Therefore, it can be concluded that structure-type rockburst is more pronounced when the structural plane length is close to 90 mm.

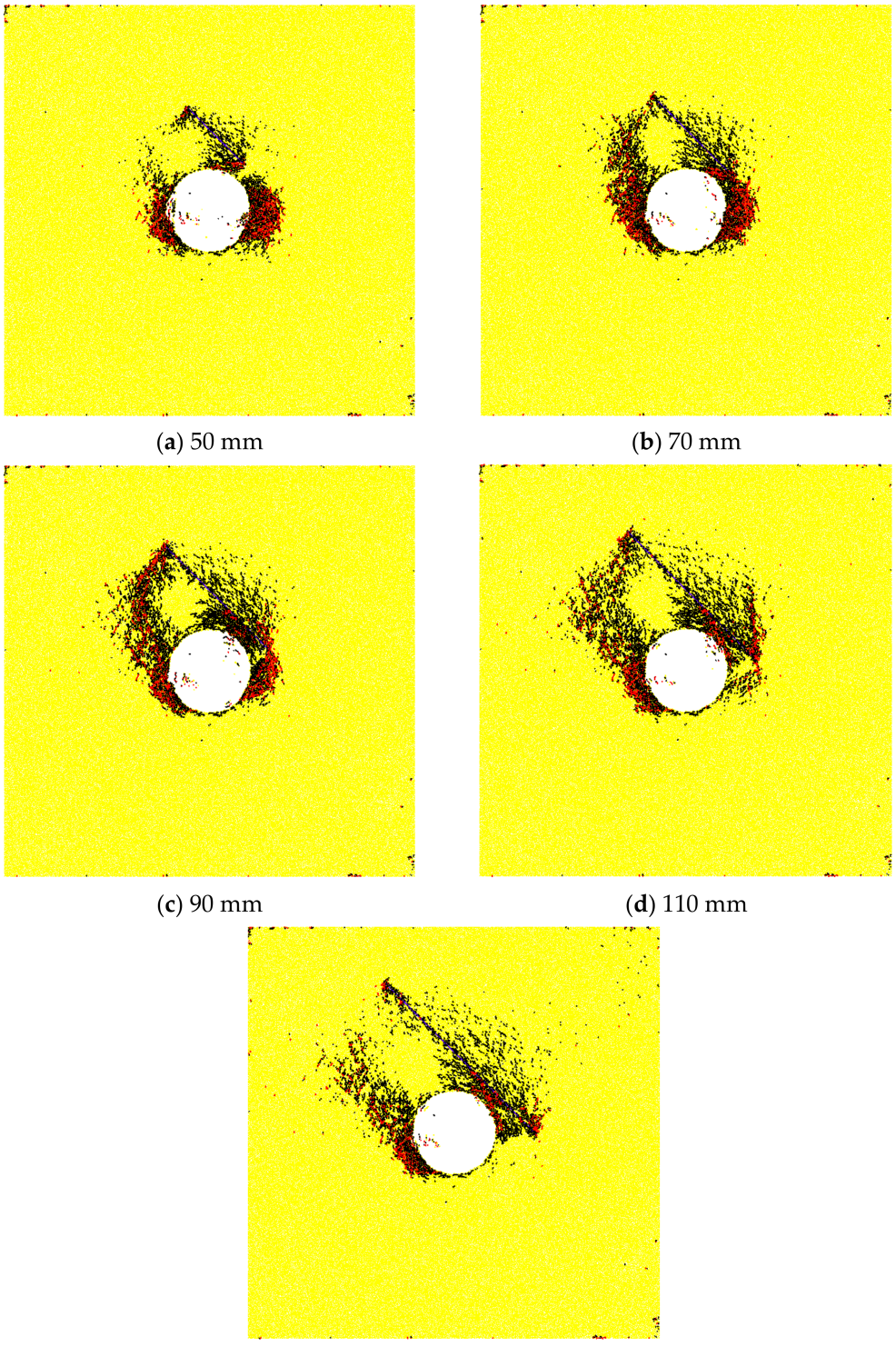

(**a**) 50 mm (**b**) 70 mm

(**c**) 90 mm (**d**) 110 mm

(**e**) 130 mm

Figure 24. Micro-cracking patterns in models with different structural plane lengths.

5. Similarity between the Numerical Modeling and the Actual Tunnelling Case

In order to explore the evolution mechanism of the "11.28" rockburst from the view of DEM, based on the field observations, this problem was considered as the PFC 2D plane strain model at the laboratory scale, e.g., the interaction mechanism between the single joint and the circular hole under high geostress and unloading induced by excavation. In this study, the initial geostress state near the tunnel before excavation was reached and kept constant by the servo mechanism, which is in agreement with the actual tunnelling

case and is difficult to achieve in laboratory tests currently. A more realistic simulation can be carried out by building the models of the same size as the field tunnel to study the failure mechanism of a tunnel near the fault. However, due to ISRM's requirements for specimen size in the uniaxial compressive test [67] and Brazilian split test [68], the particle size used in the micro-parameters calibration is in the range of 0.7~1.16 mm, which is usually consistent with the particle size in the model due to the dependence of mechanical properties for numerical specimens on the particle radius [26,69,70]. However, this also limits the overall size of the model in PFC. The field-scale numerical models based on the particle flow code are still needed to further study the problem in the future.

6. Conclusions

The present numerical study investigates the evolution mechanism of structure-type rockburst using a discrete element modeling approach. The main conclusions are as follows:

(1) For the structure-type rockburst, the failure occurs first in the interaction zone between the structural plane and the tunnel. A small-scale strainburst occurs at both sides of the tunnel before complete failure of rock mass. The secondary crack band develops obliquely downwards and connects with the local crack band that develops upward. The shear slip along the structural plane may happen through the whole loading process. Before the two crack bands penetrate completely, shear fracture occurs in the positions where micro-cracks are incomplete coalescence, causing violent rockburst and V-shaped notch.

(2) The main differences between strainburst and structure-type rockburst mainly include (a) the distribution of local concentrated stress zone, (b) the evolution mechanism, and (c) the failure locations.

(3) For the friction coefficient greater than 0.5, the influence of the structural plane is weakened, the rock near excavation tends to be intact, and the dissipated and radiated energy in model decreases. The structure-type rockburst is more likely to occur when the friction coefficient is less than 0.9.

(4) The dissipated and radiated energy and crack number in structural-type rockburst reduce with increasing cohesion and effective modulus heterogeneity m in rockmass.

(5) The lateral pressure coefficient has a significant effect on the intensity and failure mode of deep rock failure, and the dissipative and radiated energy after excavation rise obviously with lateral pressure coefficient under constant vertical stress. The structural-type rockburst is more pronounced when the structural plane length is close to 90 mm.

Furthermore, this study is based on a two-dimensional plane strain model and intermediate principal stress is not considered. In addition, due to the limitation of the particle size, numerical models at the laboratory scale rather than field scale are built to study the evolution mechanism of structure-type rockburst. Therefore, further research is still needed in the future.

Author Contributions: Conceptualization, C.Z.; methodology, D.L.; writing—original draft, C.Z.; writing—review and editing, S.W., L.C. and J.P.; supervision, S.W.; funding acquisition, D.L. All authors have read and agreed to the published version of the manuscript.

Funding: The study presented in this paper was supported by the Distinguished Youth Science Foundation of Hunan Province of China (No. 2019JJ20028) and the key project of the National Natural Science Foundation of China (No. 41630642).

Institutional Review Board Statement: Not applicable.

Informed Consent Statement: Not applicable.

Data Availability Statement: Not applicable.

Conflicts of Interest: The authors declare no conflict of interest.

References

1. Jiang, T.; Shen, Z.; Liu, Y.; Hou, Y. Carbon Footprint Assessment of Four Normal Size Hydropower Stations in China. *Sustainability* **2018**, *10*, 2018. [CrossRef]
2. Tang, W.; Li, Z.; Tu, Y. Sustainability Risk Evaluation for Large-Scale Hydropower Projects with Hybrid Uncertainty. *Sustainability* **2018**, *10*, 138. [CrossRef]
3. Feng, G.; Xia, G.; Chen, B.; Xiao, Y.; Zhou, R. A Method for Rockburst Prediction in the Deep Tunnels of Hydropower Stations Based on the Monitored Microseismicity and an Optimized Probabilistic Neural Network Model. *Sustainability* **2019**, *11*, 3212. [CrossRef]
4. Martin, C.; Kaiser, P.; McCreath, D. Hoek-Brown parameters for predicting the depth of brittle failure around tunnels. *Can. Geotech. J.* **1999**, *36*, 136–151. [CrossRef]
5. Cai, M.; Kaiser, P. *Rockburst Support Reference Book—Volume I: Rockburst Phenomenon and Support Characteristics*; MIRARCO- Mining Innovation: Sudbury, ON, Canada, 2018; pp. 40–47.
6. Jiang, Q.; Feng, X.T.; Fan, Y.; Fan, Q.; Liu, G.; Pei, S.; Duan, S. In situ experimental investigation of basalt spalling in a large underground powerhouse cavern. *Tunn. Undergr. Space Technol.* **2017**, *68*, 82–94. [CrossRef]
7. Wu, W.; Feng, X.; Zhang, C.; Qiu, S. Classification of failure modes and controlling measures for surrounding rock of deep tunnel in hard rock. *Chin. J. Rock Mech. Eng.* **2011**, *30*, 1782–1801.
8. Zhou, H.; Meng, F.; Zhang, C.; Lu, J.; Xu, R. Effect of structural plane on rockburst in deep hard rock tunnels. *Chin. J. Rock Mech. Eng.* **2015**, *34*, 720–727.
9. He, M.C.; Miao, J.L.; Li, D.; Wang, C.G. Experimental study on rockburst processes of granite specimen at great depth. *Chin. J. Rock Mech. Eng.* **2007**, *26*, 865–876.
10. He, M.C.; Miao, J.L.; Feng, J.L. Rock burst process of limestone and its acoustic emission characteristics under true-triaxial unloading conditions. *Int. J. Rock Mech. Min. Sci.* **2010**, *47*, 286–298. [CrossRef]
11. Chen, Z.Y.; Su, G.S.; Ju, J.W.; Jiang, J.Q. Experimental study on energy dissipation of fragments during rockburst. *Bull. Eng. Geol. Environ.* **2019**, *78*, 5369–5386. [CrossRef]
12. Su, G.S.; Jiang, J.Q.; Feng, X.T.; Jiang, Q.; Chen, Z.Y.; Mo, J.H. Influence of loading rate on strainburst: An experimental study. *Bull. Eng. Geol. Environ.* **2019**, *78*, 3559–3573. [CrossRef]
13. Zhai, S.B.; Su, G.S.; Yin, S.D.; Zhao, B.; Yan, L.B. Rockburst characteristics of several hard brittle rocks: A true triaxial experimental study. *J. Rock. Mech. Geotech.* **2020**, *12*, 279–296. [CrossRef]
14. Hu, X.C.; Su, G.S.; Chen, G.Y.; Mei, S.M.; Feng, X.T.; Mei, G.X.; Huang, X.H. Experiment on rockburst process of borehole and its acoustic emission characteristics. *Rock Mech. Rock Eng.* **2019**, *52*, 783–802. [CrossRef]
15. Si, X.F.; Gong, F.Q.; Luo, Y.; Li, X.B. Experimental simulation on rockburst process of deep three-dimensional circular cavern. *Rock Soil Mech.* **2018**, *39*, 621–634.
16. Gong, F.Q.; Si, X.F.; Li, X.B.; Wang, S.Y. Experimental investigation of strain rockburst in circular caverns under deep three-dimensional high-stress conditions. *Rock Mech. Rock Eng.* **2019**, *52*, 1459–1474. [CrossRef]
17. Liang, P.; Zhang, Y.B.; Tian, B.Z.; Yao, X.L.; Sun, L.; Liu, X.X. Experimental study on energy evolution characteristics in the process of tunnel rock burst. *Chin. J. Rock Mech. Eng.* **2019**, *38*, 736–746.
18. Liu, F.; Tang, C.A.; Ma, T.H.; Tang, L.X. Characterizing rockbursts along a structural plane in a tunnel of the Hanjiang-to-Weihe river diversion project by microseismic monitoring. *Rock Mech. Rock Eng.* **2019**, *52*, 1835–1856. [CrossRef]
19. Sun, S.R.; Sun, H.Y.; Wang, Y.J.; Wei, J.; Liu, J.H.; Kanungo, D.P. Effect of the combination characteristics of rock structural plane on the stability of a rock-mass slope. *Bull. Eng. Geol. Environ.* **2014**, *73*, 987–995. [CrossRef]
20. Durrheim, R.J.; Roberts, M.K.C.; Haile, A.T.; Hagan, T.O.; Jager, A.J.; Handley, M.F.; Spottiswoode, S.M.; Ortlepp, W.D. Factors influencing the severity of rockburst damage in South African gold mines. *J. S. Afr. Inst. Min. Met.* **1998**, *98*, 53–57.
21. Hu, L.; Feng, X.T.; Xiao, Y.X.; Wang, R.; Feng, G.L.; Yao, Z.B.; Niu, W.J.; Zhang, W. Effects of structural planes on rockburst position with respect to tunnel cross-sections: A case study involving a railway tunnel in China. *Bull. Eng. Geol. Environ.* **2020**, *79*, 1061–1081. [CrossRef]
22. Zhang, C.Q.; Feng, X.T.; Zhou, H.; Qiu, S.L.; Wu, W.P. Case histories of four extremely intense rockbursts in deep tunnels. *Rock Mech. Rock Eng.* **2012**, *45*, 275–288. [CrossRef]
23. Zhou, H.; Meng, F.Z.; Zhang, C.Q.; Hu, D.W.; Yang, F.J.; Lu, J.J. Analysis of rockburst mechanisms induced by structural planes in deep tunnels. *Bull. Eng. Geol. Environ.* **2015**, *74*, 1435–1451. [CrossRef]
24. Zhang, C.Q.; Feng, X.T.; Zhou, H.; Qiu, S.L.; Wu, W.P. Rockmass damage development following two extremely intense rockbursts in deep tunnels at Jinping II hydropower station, southwestern China. *Bull. Eng. Geol. Environ.* **2013**, *72*, 237–247. [CrossRef]
25. Manouchehrian, A.; Cai, M. Numerical modeling of rockburst near fault zones in deep tunnels. *Tunn. Undergr. Space Technol.* **2018**, *80*, 164–180. [CrossRef]
26. Xu, X.L.; Wu, S.C.; Gao, Y.T.; Xu, M.F. Effects of micro-structure and micro-parameters on Brazilian tensile strength using flat-joint model. *Rock Mech. Rock Eng.* **2016**, *49*, 3575–3595. [CrossRef]
27. Jing, L. A review of techniques, advances and outstanding issues in numerical modelling for rock mechanics and rock engineering. *Int. J. Rock Mech. Min. Sci.* **2003**, *40*, 283–353. [CrossRef]
28. Hazzard, J.F.; Collins, D.S.; Pettitt, W.S.; Young, R.P. Simulation of Unstable Fault Slip in Granite Using a Bonded-particle Model. *Pure Appl. Geophys.* **2002**, *159*, 221–245. [CrossRef]

29. Potyondy, D.O. A flat-jointed bonded-particle material for hard rock. In Proceedings of the 46th US Rock Mechanics/Geomechanics Symposium, Chicago, IL, USA, 24–27 June 2012.
30. Potyondy, D.O. *PFC 2D Flat Flat-Joint Contact Model*; Technical Memorandum ICG7138-L; Itasca Consulting Group, Inc.: Minneapolis, MN, USA, 2012.
31. Wu, S.C.; Xu, X.L. A study of three intrinsic problems of the classic discrete element method using flat-joint model. *Rock Mech. Rock Eng.* **2016**, *49*, 1813–1830. [CrossRef]
32. Potyondy, D.O. The bonded-particle model as a tool for rock mechanics research and application: Current trends and future directions. *Geosyst. Eng.* **2015**, *18*, 1–28. [CrossRef]
33. Wu, S.; Chen, L.; Cheng, Z. Macro and meso research on the zonal disintegration phenomenon and the mechanism of deep brittle rock mass. *Eng. Fract. Mech.* **2019**, *211*, 254–268. [CrossRef]
34. Duan, K.; Kwok, C.; Pierce, M. Discrete element method modeling of inherently anisotropic rocks under uniaxial compression loading. *Int. J. Numer. Anal. Methods* **2016**, *40*, 1150–1183. [CrossRef]
35. Mas Ivars, D.; Potyondy, D.O.; Pierce, M.; Cundall, P.A. The smooth-joint contact model. In Proceedings of the 8th World Congress on Computational Mechanics/5th European Congress on Computational Methanics and Applied Science and Engineering, Venice, Italy, 30 June–4 July 2008.
36. Hu, W.R.; Kwok, C.; Duan, K.; Wang, T. Parametric study of the smooth-joint contact model on the mechanical behavior of jointed rock. *Int. J. Numer. Anal. Methods* **2018**, *42*, 358–376. [CrossRef]
37. Zhao, J.; Feng, X.T.; Zhang, X.W.; Zhang, Y.; Zhou, Y.Y.; Yang, C.X. Brittle-ductile transition and failure mechanism of Jinping marble under true triaxial compression. *Eng. Geol.* **2018**, *232*, 160–170. [CrossRef]
38. Zhao, X.J.; Chen, B.R.; Zhao, H.B.; Jie, B.H.; Ning, Z.F. Laboratory creep tests for time-dependent properties of a marble in Jinping II hydropower station. *J. Rock. Mech. Geotech.* **2012**, *4*, 168–176. [CrossRef]
39. Zhang, C.S.; Chu, W.J.; Liu, N.; Zhu, Y.S.; Hou, J. Laboratory tests and numerical simulations of brittle marble and squeezing schist at Jinping II hydropower station, China. *J. Rock. Mech. Geotech.* **2011**, *3*, 30–38. [CrossRef]
40. Jiang, Q.; Zhong, S.; Cui, J.; Feng, X.T.; Song, L.B. Statistical characterization of the mechanical parameters of intact rock under triaxial compression: An experimental proof of the Jinping marble. *Rock Mech. Rock Eng.* **2016**, *49*, 4631–4646. [CrossRef]
41. Zheng, Z.; Feng, X.T.; Yang, C.X.; Zhang, X.W.; Li, S.J.; Qiu, S.L. Post-peak deformation and failure behaviour of Jinping marble under true triaxial stresses. *Eng. Geol.* **2020**, *265*, 105444. [CrossRef]
42. Wang, B.; Zhu, J.B.; Wu, A.Q.; Hu, J.M.; Xiong, Z.M. Experimental study on mechanical properties of Jinping marble under loading and unloading stress paths. *Chin. J. Rock Mech. Eng.* **2008**, *27*, 2138–2145.
43. Zhou, H.; Yang, Y.S.; Xiao, H.B.; Zhang, C.Q.; Fu, Y.P. Research on loading rate effect of tensile strength property of hard brittle marble-test characteristics and mechanism. *Chin. J. Rock Mech. Eng.* **2013**, *32*, 1868–1875.
44. Feng, G.L.; Feng, X.T.; Chen, B.R.; Xiao, Y.X.; Zhao, Z.N. Effects of structural planes on the microseismicity associated with rockburst development processes in deep tunnels of the Jinping-II Hydropower Station, China. *Tunn. Undergr. Space Technol.* **2019**, *84*, 273–280. [CrossRef]
45. Duan, K.; Ji, Y.L.; Xu, N.W.; Wan, Z.J.; Wu, W. Excavation-induced fault instability: Possible causes and implications for seismicity. *Tunn. Undergr. Space Technol.* **2019**, *92*, 103041. [CrossRef]
46. Cao, R.H.; Yao, R.B.; Hu, T.; Wang, C.S.; Li, K.H.; Meng, J.J. Failure and mechanical behavior of transversely isotropic rock under compression-shear tests: Laboratory testing and numerical simulation. *Eng. Fract. Mech.* **2021**, *241*, 107389. [CrossRef]
47. Sarfarazi, V.; Haeri, H.; Safavi, S.; Marji, M.F.; Zhu, Z.M. Interaction between two neighboring tunnel using PFC2D. *Struct. Eng. Mech.* **2019**, *71*, 77–87.
48. Zhu, W.C.; Li, Z.H.; Zhu, L.; Tang, C.A. Numerical simulation on rockburst of underground opening triggered by dynamic disturbance. *Tunn. Undergr. Space Technol.* **2010**, *25*, 587–599. [CrossRef]
49. Wang, S.Y.; Sloan, S.W.; Tang, C.A.; Zhu, W.C. Numerical simulation of the failure mechanism of circular tunnels in transversely isotropic rock masses. *Tunn. Undergr. Space Technol.* **2012**, *32*, 231–244. [CrossRef]
50. Khademian, Z.; Ugur, O. Computational framework for simulating rock burst in shear and compression. *Int. J. Rock Mech. Min. Sci.* **2018**, *110*, 279–290. [CrossRef]
51. Khademian, Z.; Ozbay, U. Modeling violent rock failures in tunneling and shaft boring based on energy balance calculations. *Tunn. Undergr. Space Technol.* **2019**, *90*, 62–75. [CrossRef]
52. Haimson, B. Micromechanisms of borehole instability leading to breakouts in rocks. *Int. J. Rock Mech. Min. Sci.* **2007**, *44*, 157–173. [CrossRef]
53. Liu, X.X.; Zhan, S.B.; Zhang, Y.B.; Wang, X.L.; Liang, Z.Z.; Tian, B.Z. The mechanical and fracturing of rockburst in tunnel and its acoustic emission characteristics. *Shock Vib.* **2018**, 1–11. [CrossRef]
54. Li, D.Y.; Zhu, Q.Q.; Zhou, Z.L.; Li, X.B.; Ranjith, P. Fracture analysis of marble specimens with a hole under uniaxial compression by digital image correlation. *Eng. Fract. Mech.* **2017**, *183*, 109–124. [CrossRef]
55. Zhang, C.Q.; Feng, X.T.; Zhou, H.; Qiu, S.L.; Wu, W.P. A top pilot tunnel preconditioning method for the prevention of extremely intense rockbursts in deep tunnels excavated by TBMs. *Rock Mech. Rock Eng.* **2012**, *45*, 289–309. [CrossRef]
56. Bahaaddini, M.; Hagan, P.; Mitra, R.; Hebblewhite, B. Parametric study of smooth joint parameters on the shear behaviour of rock joints. *Rock Mech. Rock Eng.* **2015**, *48*, 923–940. [CrossRef]

57. Lambert, C.; Coll, C. Discrete modeling of rock joints with a smooth-joint contact model. *J. Rock Mech. Geotech.* **2014**, *6*, 1–12. [CrossRef]
58. Huan, J.Y.; He, M.M.; Zhang, Z.Q.; Li, N.; Nascimbene, R. A New Method to Estimate the Joint Roughness Coefficient by Back Calculation of Shear Strength. *Adv. Civ. Eng.* **2019**, 1–11. [CrossRef]
59. Li, X.F.; Li, X.; Li, H.B.; Zhang, Q.B.; Zhao, J. Dynamic tensile behaviours of heterogeneous rocks: The grain scale fracturing characteristics on strength and fragmentation. *Int. J. Impact Eng.* **2018**, *118*, 98–118. [CrossRef]
60. Peng, J.; Wong, L.N.Y.; Teh, C.I. Influence of grain size heterogeneity on strength and microcracking behavior of crystalline rocks. *J. Geophys. Res. Solid Earth* **2017**, *122*, 1054–1073. [CrossRef]
61. Tang, C.A.; Liu, H.; Lee, P.K.K.; Tsui, Y.; Tham, L.G. Numerical studies of the influence of microstructure on rock failure in uniaxial compression—part I: Effect of heterogeneity. *Int. J. Rock Mech. Min. Sci.* **2000**, *37*, 555–569. [CrossRef]
62. Tang, C.A. Numerical simulation of progressive rock failure and associated seismicity. *Int. J. Rock Mech. Min. Sci.* **1997**, *34*, 249–261. [CrossRef]
63. Dai, S.; Gao, W.; Wang, C.; Xiao, T. Damage Evolution of Heterogeneous Rocks Under Uniaxial Compression Based on Distinct Element Method. *Rock Mech. Rock Eng.* **2019**, *52*, 2631–2647. [CrossRef]
64. Wong, T.F.; Wong, R.H.; Chau, K.T.; Tang, C.A. Microcrack statistics, Weibull distribution and micromechanical modeling of compressive failure in rock. *Mech. Mater.* **2006**, *38*, 664–681. [CrossRef]
65. Bahaaddini, M.; Sheikhpourkhani, A.M.; Mansouri, H. Flat-joint model to reproduce the mechanical behaviour of intact rocks. *Eur. J. Environ. Civ. Eng.* **2019**, 1–22. [CrossRef]
66. Chen, P.Y. Effects of microparameters on macroparameters of flat-jointed bonded-particle materials and suggestions on trial-and-error method. *Geotech. Geol. Eng.* **2017**, *35*, 663–677. [CrossRef]
67. Fairhurst, C.; Hudson, J.A. Draft ISRM suggested method for the complete stress-strain curve for intact rock in uniaxial compression. *Int. J. Rock Mech. Min. Sci.* **1999**, *36*, 279–289.
68. International Society for Rock Mechanics. Suggested methods for determining tensile strength of rock materials. *Int. J. Rock Mech. Min. Sci. Geomech. Abstr.* **1978**, *15*, 99–103. [CrossRef]
69. Ding, X.B.; Zhang, L.Y.; Zhu, H.H.; Zhang, Q. Effect of model scale and particle size distribution on PFC3D simulation results. *Rock Mech. Rock Eng.* **2014**, *47*, 2139–2156. [CrossRef]
70. Koyama, T.; Jing, L. Effects of model scale and particle size on micro-mechanical properties and failure processes of rocks—A particle mechanics approach. *Eng. Anal. Bound. Elem.* **2007**, *31*, 458–472. [CrossRef]

sustainability

MDPI

Article

Statistical Assessment of the Effects of Grain-Structure Representation and Micro-Properties on the Behavior of Bonded Block Models for Brittle Rock Damage Prediction

Carlos Efrain Contreras Inga [1,*], Gabriel Walton [1] and Elizabeth Holley [2]

[1] Department of Geology and Geological Engineering, Colorado School of Mines, 1516 Illinois St., Golden, CO 80401, USA; gwalton@mines.edu
[2] Department of Mining Engineering, Colorado School of Mines, 1600 Illinois St., Golden, CO 80401, USA; eholley@mines.edu
* Correspondence: ccontreras@mymail.mines.edu

Abstract: The ability to predict the mechanical behavior of brittle rocks using bonded block models (BBM) depends on the accuracy of the geometrical representation of the grain-structure and the applied micro-properties. This paper evaluates the capabilities of BBMs for predictive purposes using an approach that employs published micro-properties in combination with a Voronoi BBM that properly approximates the real rock grain-structure. The Wausau granite, with Unconfined Compressive Strength (UCS) of 226 MPa and average grain diameter of 2 mm, is used to evaluate the effectiveness of the predictive approach. Four published sets of micro-properties calibrated for granites with similar mineralogy to the Wausau granite are used for the assessment. The effect of grain-structure representation in Voronoi BBMs is analyzed, considering grain shape, grain size and mineral arrangement. A unique contribution of this work is the explicit consideration of the effect of stochastic grain-structure generation on the obtained results. The study results show that the macro-properties of a rock can be closely replicated using the proposed approach. When using this approach, the micro-properties have a greater impact on the realism of the predictions than the specific grain-structure representation. The grain shape and grain size representations have a minor effect on the predictions for cases that do not deviate substantially from the real average grain geometry. However, the stochastic effect introduced by the use of randomly-generated Voronoi grain-structures can be significant, and this effect should be considered in future studies.

Keywords: strength prediction; brittle rock; grain-structure representation; micro-properties; bonded block models; Voronoi tessellation

Citation: Contreras Inga, C.E.; Walton, G.; Holley, E. Statistical Assessment of the Effects of Grain-Structure Representation and Micro-Properties on the Behavior of Bonded Block Models for Brittle Rock Damage Prediction. *Sustainability* **2021**, *13*, 7889. https://doi.org/10.3390/su13147889

Academic Editor: Antonio Caggiano

Received: 22 May 2021
Accepted: 9 July 2021
Published: 14 July 2021

Publisher's Note: MDPI stays neutral with regard to jurisdictional claims in published maps and institutional affiliations.

Copyright: © 2021 by the authors. Licensee MDPI, Basel, Switzerland. This article is an open access article distributed under the terms and conditions of the Creative Commons Attribution (CC BY) license (https://creativecommons.org/licenses/by/4.0/).

1. Introduction

The characterization of rock strength and fracturing processes usually relies on laboratory tests, such as uniaxial compression, triaxial compression and tensile strength tests. The results of multiple laboratory studies have revealed that the fracturing process of brittle rock under compression consists of several stages: (i) crack closure, (ii) linear elastic deformation, (iii) crack initiation and stable crack growth, (iv) crack damage and unstable crack growth and (v) failure and post-peak deformation [1–4]. In some cases, it can be difficult to characterize the fracturing behavior of a rock accurately. Various laboratory studies [5–7] show that individual specimens of the same rock type can exhibit distinct fracturing behavior and associated strength because of rock heterogeneities. Lan et al. [8] classified the sources of heterogeneity of intact rock in three groups: (i) grain-geometry heterogeneity related to variations in the size and shape of the mineral grains, (ii) grain deformability heterogeneity associated with the contrasts among mineral phases in terms of density and elastic properties and (iii) grain-grain contact heterogeneity linked to the variability of the stiffness, length, orientation and distribution of grain-contacts. When

a rock undergoes compressive loading, the heterogeneity of the grain-structure leads to complex micro-mechanical behavior that produces localized stress concentrations within the intact rock, resulting in fracture development [9–11]. Accordingly, grain-structure heterogeneity also controls the macroscopic mechanical response of intact rock [8,9,12].

Multiple experimental studies have investigated the influence of grain-structure heterogeneity on the mechanical response of rock to loading. Numerous individual sets of compressive laboratory tests have identified a potential link between grain size and compressive strength [13–21]. These compressive tests were conducted mainly on granite, limestone and marble, and the results indicate that rock strength tends to decrease as the average grain size increases. Other studies focused on the effect of the mineral composition [20–25] found notable correlations between the unconfined compressive strength of granite and its mica, quartz and feldspar content, as well as the quartz to feldspar ratio. Based on this information, various relationships between grain size, mineral content and rock strength have been postulated [20,21,24,25]. A more recent longitudinal study [26] conducted using mechanical and geological (i.e., grain size and mineral composition) property data for granites compiled from the literature examined the previously proposed correlations and found these correlations to not be apparent in the context of the larger database used for the analysis. This discrepancy between studies was attributed to the potential influence of confounding variables in statistical analyses performed on individual data sets. Accordingly, the experimental literature offers no definitive consensus on the influences of geological characteristics on the mechanical attributes of granites.

Due to continued developments in computer power and numerical techniques, numerical modeling has been increasingly used in recent decades to quantitatively investigate damage and fracturing behavior of brittle rocks. Compared with experimental testing, numerical modeling can be more cost-effective and allows one to simulate conditions that are difficult to achieve in the laboratory [27,28]. Broadly speaking, numerical modeling approaches to simulate brittle rock damage can be classified into three categories: (i) continuum, (ii) discontinuum and (iii) hybrid continuum-discontinuum [29,30]. Continuum methods represent the rock as a single continuous body and define rock damage through constitutive relations and associated failure criteria [29]. Due to these premises, the continuum approach is unable to represent fracture development explicitly, and its results are highly dependent on the assigned constitutive relationship [11,31]. The limitations of continuum methods are partially overcome by discontinuum and hybrid continuum-discontinuum approaches, which can explicitly simulate rock damage development under diverse loading conditions, eliminating the need for pre-defined macroscopic constitutive models [32–34]. Among the discontinuum and hybrid methods, the Discrete Element Method (DEM) and the Finite Discrete Element Method (FDEM) are the most commonly applied approaches for brittle rock mechanical behavior modeling. The DEM simulates rocks as assemblies of discrete particles or blocks able to interact and separate as fractures develop [32,35]. The hybrid FDEM starts from a continuum representation of the rock that allows the progressive development of new fractures and, consequently, new discrete bodies [32].

Discontinuum and hybrid numerical modeling methods, in contrast to continuum methods, can more accurately represent the heterogeneity of crystalline rocks [33]. Various approaches have been developed to represent the grains within an intact rock and their respective contacts. Within the broad category of DEM, the Bonded Particle Model (BPM) and Bonded Block Model (BBM) methods are the most commonly applied. Conventional BPMs represent grains as circular or spherical particles (or balls) bonded at their contacts [30]. BBMs represent grain-structures as collections of blocks where each block represents a grain that can adopt distinct polygonal or polyhedral shapes, and the interfaces between blocks represent the grain-grain contacts. Voronoi tessellations are usually applied to generate the grain-structure for a BBM, since the mathematical process of Voronoi tessellation is the most convenient technique to randomly generate polygonal or polyhedral shapes. Typically, when blocks adopt triangular/tetrahedral shapes, grains

are referred to as trigons. When blocks present four sides or more and are generated using tessellations, they are called Voronoi blocks [32,36,37]. The Grain-Based Model (GBM) approach was introduced in BPMs to improve grain-structure representation by adding a series of grain-boundaries defined by smooth joint elements to a BPM [38]. This approach is referred as PFC-GBM when it is applied using Itasca's PFC software. In contrast to strictly discontinuum modeling methods, the hybrid FDEM approach explicitly models rock elastic deformation, crack initiation and crack propagation [39]. In the conventional approach of the FDEM, grains can adopt irregular shapes by connecting several triangular elements [40]. More recent developments employ the GBM approach to define the grain-structure using Voronoi tessellations (FDEM-GBM), such as IRAZU-GBM [41] or the "grain-based continuum-discontinuum method" (GBCDM) [42]. More details about all these methods can be found in the literature [32,33,37,38,40,41].

Wang and Cai [11,34] pointed out that, compared with other block shape assemblies, polygonal and polyhedral block assemblies have achieved a more realistic representation of the geometrical heterogeneity of the grain-structure within crystalline intact rocks. Based on that premise, Voronoi tessellations, which are increasingly applied to generate polygonal/polyhedral grain-structures [11,31,34,37,41,43], are used in this study for the development of BBMs.

In general terms, the macro-mechanical response of a BBM to loading depends on three factors: (i) numerical model physics, (ii) micro-properties and (iii) grain-structure attributes. The numerical model physics sets criteria and constraints that control the numerical simulation (e.g., explicit time-stepping solution method, damping method, etc.). The term micro-properties is commonly used to describe the grain and grain-grain contact properties of BBMs [9,11,34,37,44–47]. These properties govern the mechanical interactions within the grain-structure (i.e., interaction among grains). The grain-structure attributes define the geometry and distribution of the grains (i.e., size and shape and relative positioning of different grains). Consequently, they control localized stress concentrations within the intact rock. Additionally, the combination of the second and third factors controls the micro-mechanical behavior within the rock structure. Thus, once the model physics is properly defined, the ability to predict the mechanical behavior of a rock using BBMs directly depends on the grain-structure geometry represented in the model and the micro-properties assigned to the grains and contacts of such grain-structure. As stated by Potyondy [48], if one could replicate the grain-structure and the micro-mechanical interactions (i.e., micro-properties) within a model, then that model should reproduce the rock's macro-mechanical behavior. With all that said, if we accept that the model physics as implemented in standard codes is correct and generate a BBM that provides a reasonable representation of the grain-structure of the rock, then we hypothesize that a set of micro-properties for a given mineral assemblage from a prior study should produce a realistic prediction of the macro-properties of the rock. Moreover, such a set of calibrated micro-properties should be generalizable across rocks with similar characteristics.

Most of the micro-properties outlined in the literature are obtained from a calibration process that employs a simulated grain-structure approximation to replicate rock macro-properties obtained in actual laboratory tests. Given the inability to reproduce the exact grain-structure geometry, the resulting calibrated micro-properties do not fully replicate the mechanical interactions between grains. Moreover, some simplification in the representation of the grain-structure could add significant variability to the resulting micro-properties. Conversely, a reasonably realistic representation of the grain structure used for the calibration of micro-properties can provide a more realistic approximation of the micro-mechanical behavior of the rock. The ideal representation of the grain-structure of a rock would replicate the exact grain geometry and grain distribution within the grain-structure. However, as mentioned before, it is not feasible to generate an exact grain-structure replica. Alternatively, a typical approach consists of developing a reasonable approximation of the grain-structure using the Voronoi tessellation technique. This approach randomly generates grain-structure representations that account for the grain size and grain shape, among

other parameters. Even though Voronoi tessellations are increasingly used in numerical modeling, the degree to which Voronoi grain-structure models approximate real grain-structures has not been studied in depth. The effect of the grain-structure representation on the mechanical behavior of rock has been addressed by multiple authors using Voronoi tessellations. Several relevant studies have focused on the effects of grain size and grain size distribution using BBMs [9,37,44,49–53], PFC-GBMs [10,54–57] and FDEM-GBM [42]. The effects of grain shape have also been investigated, mostly using BBMs [46,50,52,58], and recently using FDEM-GBM [42]. The effects of mineral arrangement have been studied using BBM [8,44,51] and PFC-GBM [10,59]. There are few studies on the effects of mineral composition [42,49] and fabric orientation [37]. However, none of these studies accounted for the stochastic nature of Voronoi grain-structures and how it affects the numerical simulation results.

The present study examines the capabilities of BBMs for the prediction of brittle rock mechanical behavior by evaluating a predictive modeling approach that does not require micro-property calibration. Such an approach consists of using previously calibrated micro-properties in combination with a Voronoi model that approximates the grain-structure of a target rock to replicate its macro-mechanical behavior. BBMs representing the grain-structure of the Wausau granite under uniaxial compression were developed to evaluate the effect of the micro-properties on the predictions and the effectiveness of the predictive approach. In addition, a series of Voronoi grain-structures with different grain shapes, grain sizes and mineral arrangements were employed in a sensitivity analyses to assess the influence of the realism of the grain-structure representation on the predictions, as well as to indirectly demonstrate the ability of Voronoi grain-structures to reasonably approximate an actual grain-structure. In addition, the assessments conducted in this study examine the stochastic nature of the model results associated with the randomness of the grain-structure representations generated using Voronoi tessellations.

2. The Wausau Granite

The Wausau granite is a dark red alkali-feldspar granite from Marathon County, Wisconsin [60]. The specimens of Wausau granite for this study (Figure 1) were obtained from a quarry. Three standard thin sections were prepared for thin section petrography and Scanning Electron Microscopy (SEM)-based automated mineralogy. Thin section petrography identified the presence of quartz, biotite, K-feldspar and plagioclase. The specimens were observed to have negligible porosity, as is typical of most granites. The automated mineralogy analyses were performed on a TESCAN-VEGA-3 Integrated Mineral Analyzer (TIMA) model LMU VP-SEM in the Department of Geology and Geological Engineering at the Colorado School of Mines. The TIMA acquires spectral data using four energy dispersive X-ray (EDX) spectrometers set at a beam stepping interval of 15 μm, a beam intensity of 14 and an acceleration voltage of 24 keV. Interactions between the beam and the specimen were modeled through Monte Carlo simulation. The composition of each acquisition point was determined by comparing EDX spectra with spectra held in a look-up table. The assignment makes no distinction between mineral species and amorphous grains of similar chemical composition. Results were output by the TIMA3 software as a spreadsheet giving the area percent of each composition in the look-up table, with compositional assignments grouped appropriately. Table 1 summarizes the mineral modal abundances and grain size distributions for the specimens used in this study. The studies of LaBerge and Myers [61] and Sims et al. [60] identified an exsolution or irregular intergrowth of sodic and potassic feldspars in the Wausau granite. This intergrowth was also identified in this study.

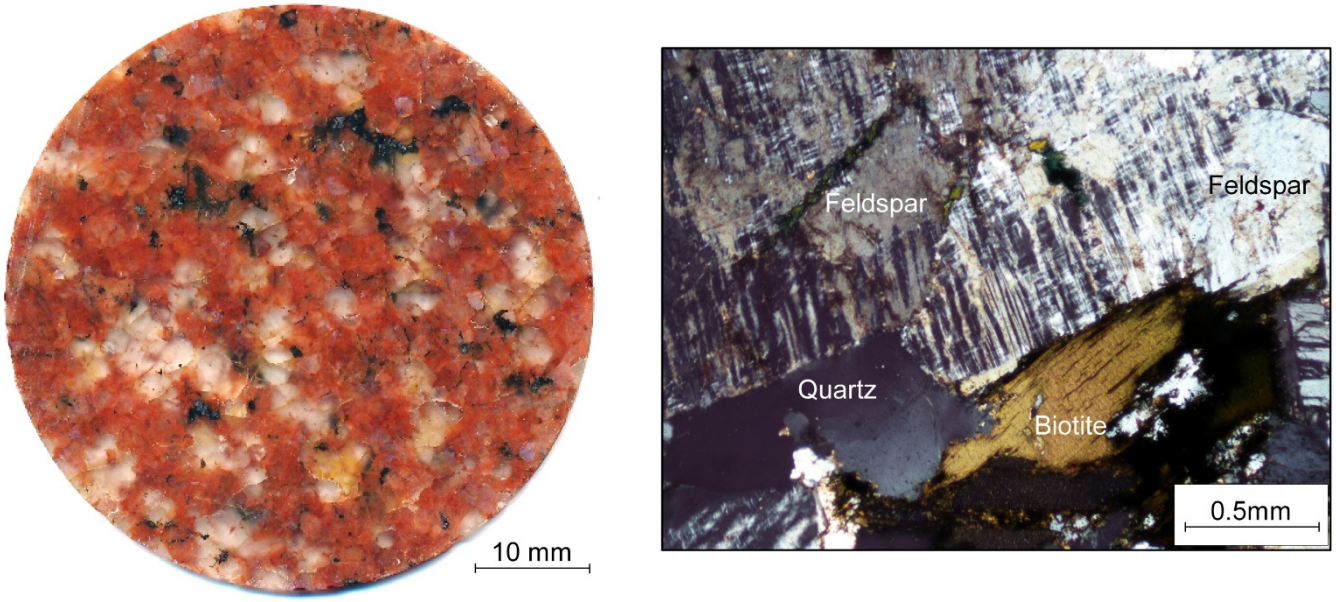

(**a**) (**b**)

Figure 1. (**a**) Disk-shaped specimen and (**b**) thin-section photomicrograph of the Wausau granite under cross-polarized light.

Table 1. Grain size distribution of the Wausau granite.

Mineral	Modal Abundance (%)	Grain Diameter (mm)	
		Mean (μ)	S.D. (σ)
Biotite	3	0.9	0.4
Quartz	32	2.5	1.0
Plagioclase	41	2.0	0.6
K-feldspar	24	2.0	0.6
All grains	100	2.0	0.8

In this case, 11 Uniaxial Compressive Strength (UCS) tests were conducted on cylindrical specimens, which were 51.4 mm in diameter, with a length-to-diameter ratio of 2.5:1. Four of these tests have complete stress-strain information recorded with electric resistance precision strain gauges. A total of four Omega linear strain gauges (two axial and two lateral, 30 mm long) were glued to the middle section of each specimen using epoxy resin. The strain gauges were attached at 90° intervals with the two axial and two lateral strain gauges diametrically opposed from each other.

The UCS test results show that the peak strength of the Wausau granite ranges from 204 MPa to 260 MPa. The crack damage (CD) stress was obtained from the instantaneous tangent modulus curve [62]. Note that it was possible to determine CD for all 11 specimens from the point of non-linearity of the stress-displacement curve recorded by the loading machine (since the absolute displacements are not reflective of the specimen displacements, but the linear/non-linear trends are). The crack initiation (CI) stress was estimated using the crack volumetric strain ($\varepsilon_{v,c}$) curve reversal [3,63], whereas Young's modulus (E_m) and Poisson's ratio (ν_m) were determined directly from the strain-stress curves of those four tests. Table 2 summarizes the experimental mechanical properties obtained from the laboratory tests.

Table 2. Experimentally determined macro-mechanical properties of the Wausau granite.

Property	Number of Tests	Mean (μ)	S.D. (σ)	Median	Minimum	Maximum
Density, ρ_m (kg/m^3)	11	2605	8	2602	2594	2619
Uniaxial Compressive Strength, UCS (MPa)	11	226	21	221	203	260
Crack damage stress, CD (MPa)	11	220	19	219	198	246
Crack initiation stress, CI (MPa)	4	107	9	109	95	115
Young's Modulus, E_m (GPa)	4	70	2	70	66	72
Poisson's Ratio, ν_m	4	0.24	0.02	0.24	0.22	0.27

3. Modeling Strategy and Methods

This study employs an approach that does not require the calibration of model micro-properties. Instead, the mechanical behavior of a rock was replicated using previously calibrated micro-properties. This approach is based on the premise that a BBM that reasonably approximates a rock's actual grain-structure can be used in combination with calibrated micro-properties from a prior study to provide realistic predictions of that rock's macro-properties. The proposed approach is expected to be feasible when applied in rocks with similar mineral constituents. The first portion of the study evaluated which calibrated micro-properties selected from the literature can best approximate the macro-mechanical behavior of the Wausau granite and be utilized for prediction purposes. Four sets of micro-properties were used in this assessment as published in four different studies: Lan et al. [8], Chen and Konietzky [64], Farahmand and Diederichs [45] and Chen et al. [65]. These four sets of micro-properties were previously calibrated to match the macro-response of two types of granites (the Lac du Bonnet granite [8,45,64] and the Kirchberg-II granite [65]) with similar mineral compositions to the Wausau granite. Once the set of micro-properties that provides the best fit between the actual and predicted macro-properties of the Wausau granite was identified, this set was used to assess the model sensitivity to specific aspects of grain-structure representation. In the analyses, the experimentally determined variability of the Wausau granite's macro-properties was considered to evaluate the accuracy of the numerical model predictions.

3.1. BBM Generation Approach

In this study, the grain-structure of intact rock was first generated in 3D using an assembly of Voronoi tessellations, where each tessellation or cell is equivalent to a mineral grain. Mathematically, a Voronoi tessellation is the partition of a n-D space in an assembly of n-D polyhedral entities defined as zones of influence of a particular set of seeds. The entities fill the space without overlaps nor gaps [66]. The resulting Voronoi tessellations (also referred to as Voronoi polyhedrons or Voronoi grains) are convex cells, which intersect along planar faces, straight edges and vertices. The software Neper [67] was employed to generate the 3D grain assemblies. Neper is an open-source software package for polycrystal generation and meshing in 3D or 2D using Voronoi or Laguerre tessellations created from a set of seeds [67]. As opposed to the former, Laguerre tessellations are a generalization of Voronoi tessellations that allow for geometries that are not possible to achieve with Voronoi cells. The Laguerre generalization can be achieved using distinct weighted seeds that make boundaries between cells non-equidistant between seeds [68].

In Neper, the morphological properties of the cells were defined to reproduce the morphology of real mineral grains. Neper allows one to specify grain (or cell) morphological properties using statistical distributions of grain size and grain shape, expressed in terms of mean, standard deviation and distribution type. The grain size is commonly defined in terms of the diameter, d, of a sphere of equivalent volume (or circle of equivalent area in 2D) [67], whereas the grain shape can be described in terms of grain sphericity. A variety of metrics for sphericity have been defined in the literature [42,69,70]. In this study, we adopt the definition of Wadell [69], as this is the definition implemented in Neper. Wadell [69] defines sphericity, s, as the ratio between the area of a sphere of equivalent volume and the

area of the grain. The 2D equivalent of sphericity is called circularity defined as the ratio of the perimeter of a circle of equivalent area and the perimeter of the grain [71].

Since the micro-properties used from the literature were derived through calibration of 2D models, 2D grain structure representations were required for modeling purposes. To obtain 2D representations of the intact rock grain-structure, a set of 2D BBMs was generated by cutting multiple axial sections from the cylindrical 3D grain-structure created in Neper. The axial sections were cut using the software 3DEC [72]. This approach was adopted as an alternative to direct 2D tessellation generators, which in many cases do not allow for sufficient grain shape and grain size heterogeneity to realistically approximate the grain-structure of some rocks. Even though each 2D BBM presents a unique mineral arrangement and unique individual grain morphological characteristics, each group of 2D BBMs is a group of 2D simplifications of the same 3D grain-structure that therefore represent the same average mineral composition, average grain shape and average grain size depicted in the 3D grain-structure.

3.2. BBM Configuration

Six different 3D Voronoi grain-structures were developed in Neper for this study. The 3D Voronoi grain-structures were developed within cylindrical domains. All 3D grain-structures represent cylindrical rock specimens with a diameter of 51.4 mm and a height of 128.5 mm. The morphology of the grains was defined using the diameter and sphericity, as these are used as inputs in Neper [68]. Given that Voronoi grain-structures are stochastically generated, the mineral arrangement or spatial distribution of grains within the specimen domain is random. This is considered an appropriate approximation given Wausau granite's lack of fabric.

The first 3D grain-structure model was designed to represent the actual Wausau granite grain-structure as closely as possible. This 3D grain-structure was established as a baseline for the sensitivity analyses (see Figure 2). This baseline grain-structure represents the average mineral composition, average grain size, grain size distribution and approximate typical grain shape of the Wausau granite. The average mineral composition was defined based on the results of the automated mineralogy. Thin-section microscopy and macroscopic observation were used to constrain the average grain shape within the specimens. The average grain shape was qualitatively assessed to resemble in Neper when using an average grain sphericity (s) equal to 0.8. Such approximate grain sphericity adequately resembles the average circularity measured on disk-shaped specimens of the Wausau granite (average circularity of 0.83, maximum circularity of 0.96 and minimum circularity of 0.55) considering the limitations of the Voronoi tessellation approach (i.e., only convex grains are generated within the model). The average grain shape approximated in Neper is comparable to a prismatic shape rather than a uniformly rounded polyhedron as used in previous studies [44,51,64,65]. The average grain size or grain diameter (d = 2.0 mm) and corresponding size distribution were defined through measurements of the apparent grain size made on specimens of the Wausau granite. These apparent grain size measurements made in 2D specimens properly capture the grain size variability and closely approximate the actual average grain size within the Wausau granite, which lacks fabric and presents an apparently random mineral arrangement. Once the 3D model generated in Neper was imported into 3DEC (but before the cutting of 2D sections), the mineral type was randomly assigned to the blocks within the 3D grain-structure. Each 2D BBM obtained from the 3D grain-structure maintains the mineral type distribution along the axial section from which it was generated. The mineral content proportions (i.e., 24% of k-feldspar, 41% of plagioclase, 32% of quartz and 3% of biotite) and the different size distributions per mineral type were used as constraints. Thus, 100% of the biotite grains have diameters between 0.0 and 2.0 mm; 16%, 68% and 16% of the quartz grains correspond to ranges of 0.0–2.0 mm, 2.0–3.5 mm and 3.5–7.0 mm, respectively; and 100% of the k-feldspar and plagioclase feldspar grains have diameters between 0.0 and 7.0 mm. Note that although some of the feldspars (i.e., k-feldspar and plagioclase) in the Wausau granite are present

as exsolutions, all grains of the feldspar group were modeled as either pure k-feldspar or plagioclase. As both types of feldspars have similar mechanical properties [8,45,64], variations in the k-feldspar to plagioclase proportion within the exsolutions are expected to have a negligible influence on the overall rock mechanical behavior.

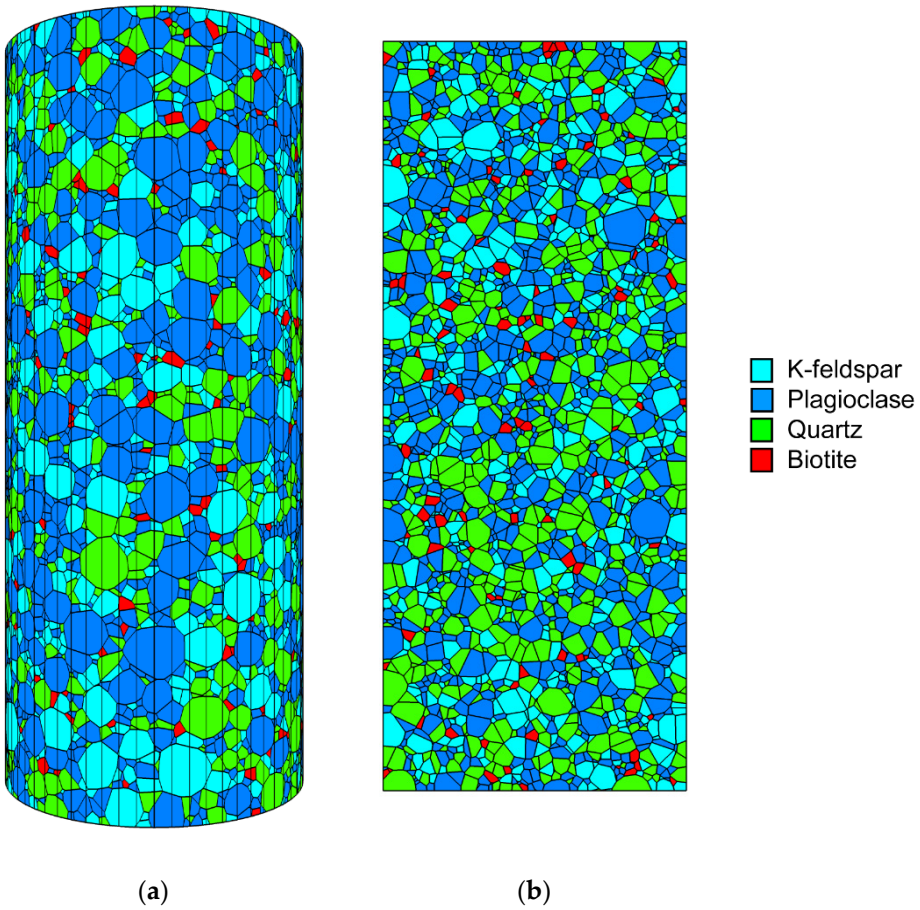

Figure 2. (**a**) Three-dimensional and (**b**) two-dimensional (cross-section) views of the baseline BBM.

In addition to the baseline grain-structure, five additional 3D grain-structures with different grain geometric characteristics were developed for a sensitivity analysis. For the assessment of the grain shape effect, two grain-structures were generated with the same mineral composition, average grain diameter, and grain size variability but different grain shape (i.e., average sphericity). To evaluate the effect of the grain size, three more grain-structures were built with the same mineral composition, grain shape and equivalent grain size variability (i.e., same grain diameter standard deviation) but different average grain diameter. Table 3 summarizes the grain geometric characteristics of each one of the 3D grain-structures. Figure 3 shows a visual comparison of the different BBMs.

Table 3. Geometric characteristics of the 3D Bonded Block Models.

Bonded Block Model	Grain Diameter (mm)		Grain Sphericity, s		Number of Grains	Description
	μ	σ	μ	σ		
BBM-1	2.0	0.8	0.80	0.02	40,700	Baseline (BL) model with moderate average sphericity (s = 0.80) and average grain diameter of 2.0 mm
BBM-2	2.0	0.8	0.85	0.02	40,700	Model with high average sphericity (s = 0.85) and average grain diameter of 2.0 mm
BBM-3	2.0	0.8	0.75	0.02	40,700	Model with low average sphericity (s = 0.75) and average grain diameter of 2.0 mm
BBM-4	1.7	0.8	0.80	0.02	56,800	Model with moderate average sphericity (s = 0.80) and average grain size of 1.7 mm
BBM-5	2.3	0.8	0.80	0.02	29,700	Model with moderate average sphericity (s = 0.80) and average grain size of 2.3 mm
BBM-6	2.9	0.8	0.80	0.02	16,700	Model with moderate average sphericity (s = 0.80) and average grain size of 2.9 mm

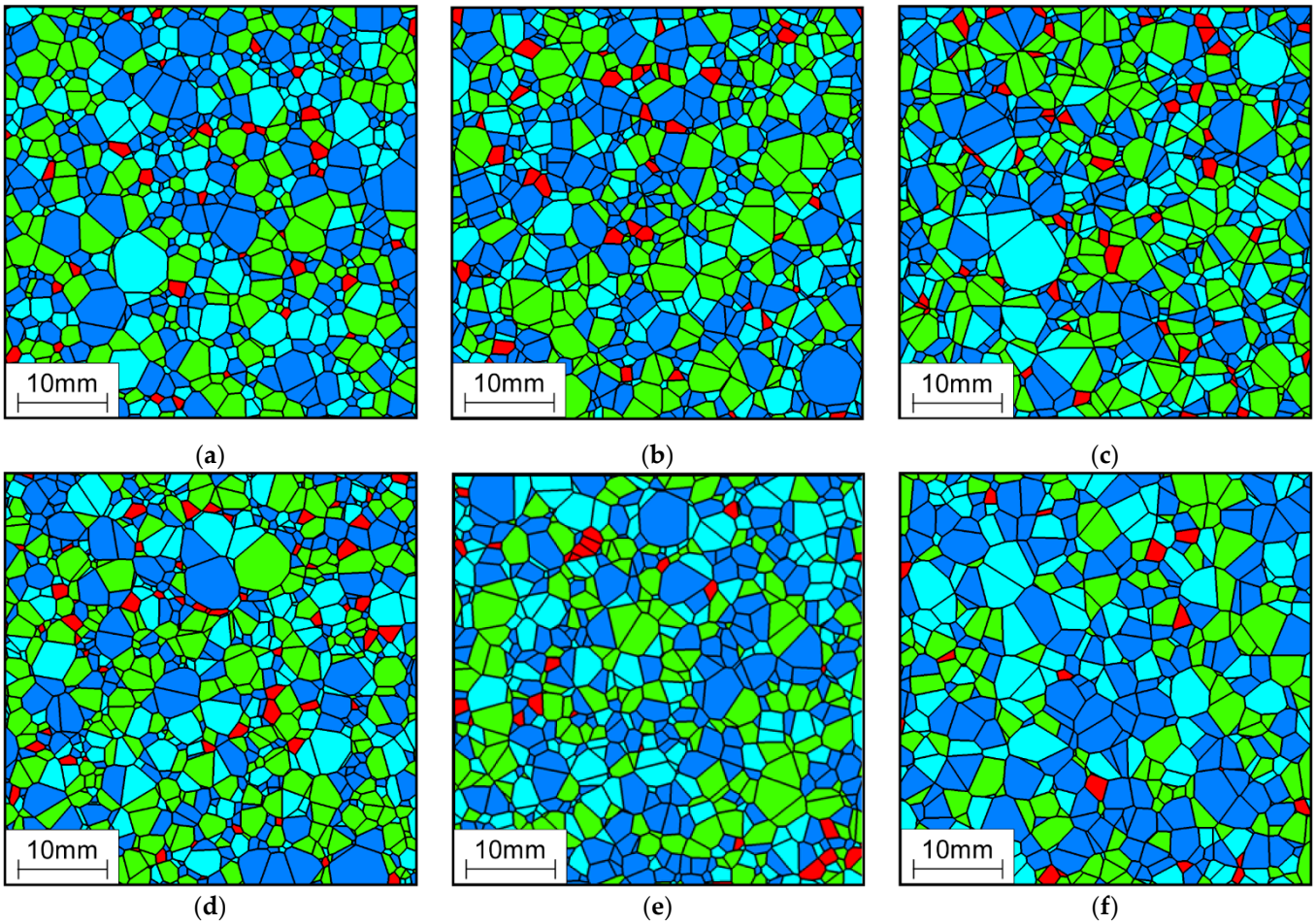

Figure 3. Two-dimensional views of the different 3D BBMs. (**a**) s = 0.85, d = 2.0 mm; (**b**) s = 0.8, d = 2.0 mm [baseline]; (**c**) s = 0.75, d = 2.0 mm; (**d**) s = 0.8, d = 1.7 mm; (**e**) s = 0.8, d = 2.3 mm; and (**f**) s = 0.8, d = 2.9 mm.

To assess the use of previously calibrated micro-properties for prediction purposes, only the baseline grain-structure was employed. In this case, 18 evenly distributed axial sections were cut from the 3D baseline model, and one 2D BBM was created from each axial section. Given that Voronoi BBMs are randomly generated, there is a possibility of obtaining grains with shapes that UDEC is unable to mesh while generating the axial sections. A FISH script in UDEC [73] helped identify such grains which, when projected onto a 2D

section, resulted in a polygon with at least one corner having a highly acute angle (i.e., <5°). If a potentially problematic grain was identified, a new 3D grain-structure was generated with a different seed to obtain a full set of 18 sections. For comparison, four groups of 18 2D BBMs were established, one group for each of the four previously calibrated micro-property sets assessed in this study. The effect of variability in mineralogical arrangement was assessed by comparing the baseline model against four "clones" of itself. Each clone maintains the same original grain-structure geometry of the baseline model but has different randomly assigned mineral types for the grains. As in the previous analysis, 18 2D BBMs were generated from each grain distribution. For the assessment of the grain shape and grain size effects, a total of 90 2D BBMs were used to analyze each specific geometric configuration (18 sections for each of the five alternative 3D grain-structures).

3.3. Constitutive Behavior of Intact Rock and Micro-Property Assignment

The 2D numerical simulations of this study were run in the software UDEC [73]. UDEC allows for simulation of grains within a BBM as rigid, elastic (deformable) or plastic (damageable) bodies [11,33,37]. In the case of elastic or plastic grains, a constitutive relationship can be applied to each grain to model its behavior. The mechanical interaction between two grains along their common contact can be recreated using a joint constitutive model [73].

This study modeled the mineral grains as unbreakable elastic blocks, allowing failure to occur only along the grain-contacts [11,37,49]. The same simplification was applied in previous studies [8,37,45,49,53,64,65]. Since the present study is focused on the prediction of the pre-peak macro-properties of the rock under unconfined conditions only, such a simplification is expected to have a negligible effect on the results of the simulations [43]. The elastic blocks were discretized into a mesh of deformable triangular finite-difference zones. The simulation results are strongly sensitive to the mesh size [74,75]. To minimize the effect of mesh size, a maximum triangular zone edge length of 0.8 mm was applied in all the BBMs. Such a maximum zone edge length ensures that at least 16 zones are generated inside a grain of average size (i.e., a 4-edge grain with the average diameter represented in the model). The resulting average grain edge length to zone edge length ratio is greater than or equal to 2, which agrees with the recommended ratio used in previous studies [43,44] to achieve stable numerical results.

In UDEC, sets of calibrated micro-properties from four different studies [8,45,64,65] were applied to the models. These micro-properties from the literature were originally obtained through an iterative multi-step calibration process in each of the respective studies. Broadly speaking, such a process consists of adjusting the grain and contact micro-properties until a set of micro-properties that replicates the rock's macro-response is identified. The grain micro-properties correspond to an elastic isotropic model with distinct density (ρ), Young's modulus (E) and Poisson's ratio (ν) for each mineral type. The grain-contact micro-properties were modeled using a Coulomb slip-joint constitutive model with residual strength properties. Each grain-contact was assigned a normal stiffness (k_n), shear stiffness (k_s), peak friction angle (φ), peak cohesion (C), peak tensile strength (σ_t) and residual friction angle (φ_r). The residual cohesion (C_r) and residual tensile strength (σ_{tr}) were assumed to be zero in accordance with the previously mentioned four studies. The grain and contact micro-properties used in this study are summarized in Tables 4–11.

Table 4. Grain micro-properties used by Lan et al. [8].

Mineral Type	Bulk Modulus K (GPa)	Shear Modulus G (GPa)	Young's Modulus E (GPa)	Poisson's Ratio ν	Density ρ (g/cc)
K-Feldspar	53.7	27.2	69.8	0.28	2.56
Plagioclase	50.8	29.3	88.1	0.26	2.63
Quartz	37.0	44.0	94.5	0.08	2.65
Biotite	41.1	12.4	33.8	0.36	3.05

Table 5. Contact micro-properties determined by Lan et al. [8].

Contact Type	k_n (GPa/m)	k_s/k_n	C (MPa)	φ (°)	σ_t (MPa)
KF/KF	9.20×10^4	0.67	40.0	27.0	14.4
KF/PL	8.56×10^4	0.67	40.0	27.0	14.4
KF/QZ	1.29×10^5	0.67	40.0	27.0	14.4
KF/BT	1.51×10^5	0.67	40.0	27.0	14.4
PL/PL	9.28×10^4	0.67	40.0	27.0	14.4
PL/QZ	1.24×10^5	0.67	40.0	27.0	14.4
PL/BT	1.49×10^5	0.67	40.0	27.0	14.4
QZ/QZ	2.55×10^5	0.67	40.0	27.0	14.4
QZ/BT	3.13×10^5	0.67	40.0	27.0	14.4
BT/BT	4.70×10^5	0.67	40.0	27.0	14.4

Table 6. Grain micro-properties used by Chen and Konietzky [64].

Mineral Type	Young's Modulus E (GPa)	Poisson's Ratio ν
K-Feldspar	62	0.27
Plagioclase	69	0.23
Quartz	91	0.20
Biotite	35	0.25

Table 7. Contact micro-properties determined by Chen and Konietzky [64].

Contact Type	k_n (GPa/m)	k_s/k_n	C (MPa)	φ, φ_r (°)	σ_t (MPa)
KF/KF	7.75×10^5	1.00	52.0	55.0, 27.5	23.0
KF/PL	7.87×10^5	1.00	54.5	57.0, 28.5	23.5
KF/QZ	8.93×10^5	1.00	57.0	58.5, 29.3	24.5
KF/BT	5.97×10^5	1.00	44.5	51.5, 25.8	21.0
PL/PL	8.00×10^5	1.00	57.0	59.0, 29.5	24.0
PL/QZ	9.06×10^5	1.00	59.5	60.5, 30.3	25.0
PL/BT	6.10×10^5	1.00	47.0	53.5, 26.8	21.5
QZ/QZ	1.01×10^6	1.00	62.0	62.0, 31.0	26.0
QZ/BT	7.16×10^5	1.00	49.5	55.0, 27.5	22.5
BT/BT	4.20×10^5	1.00	37.0	48.0, 24.0	19.0

Table 8. Grain micro-properties used by Farahmand and Diederichs [45].

Mineral Type	Young's Modulus E (GPa)	Poisson's Ratio ν	Density ρ (g/cc)
K-Feldspar	96.8	0.28	2.56
Plagioclase	88.1	0.26	2.63
Quartz	94.5	0.08	2.65
Biotite	33.8	0.36	3.05

Table 9. Contact micro-properties determined by Farahmand and Diederichs [45].

Contact Type	k_n (GPa/m)	k_s/k_n	C (MPa)	φ, φ_r (°)	σ_t (MPa)
KF/KF	2.3×10^5	0.65	110.0	62.0, 5.0	35.0
KF/PL	2.1×10^5	0.65	108.0	61.0, 5.0	32.0
KF/QZ	2.7×10^5	0.65	76.0	53.0, 5.0	28.2
KF/BT	2.3×10^5	0.65	60.0	48.0, 5.0	11.4
PL/PL	2.5×10^5	0.65	112.0	63.0, 5.0	37.0
PL/QZ	2.3×10^5	0.65	80.0	49.0, 5.0	28.2
PL/BT	2.3×10^5	0.65	54.0	45.0, 5.0	22.4
QZ/QZ	2.8×10^5	0.65	130.0	65.0, 5.0	35.0
QZ/BT	2.3×10^5	0.65	57.0	52.0, 5.0	23.4
BT/BT	1.3×10^5	0.65	88.0	55.0, 5.0	25.3

Table 10. Grain micro-properties used by Chen et al. [65].

Mineral Type	Young's Modulus E (GPa)	Poisson's Ratio ν
Feldspar	52	0.19
Quartz	81	0.16
Biotite	25	0.22

Table 11. Contact micro-properties determined by Chen et al. [65].

Contact Type	k_n (GPa/m)	k_s/k_n	C (MPa)	φ, φ_r (°)	σ_t (MPa)
FL/FL	5.71×10^5	1.00	52.0	48.0, 0.48	23.0
FL/QZ	7.17×10^5	1.00	57.0	53.0, 0.53	24.5
FL/BT	4.28×10^5	1.00	44.5	43.0, 0.43	21.0
QZ/QZ	8.63×10^5	1.00	62.0	58.0, 0.58	26.0
QZ/BT	5.74×10^5	1.00	49.5	48.0, 0.48	22.5
BT/BT	2.85×10^5	1.00	37.0	38.0, 0.38	19.0

4. Numerical Simulation

4.1. Numerical Test Setup

In the UCS test simulations, axial load was applied to the specimens via a constant vertical velocity directly to the top and bottom surfaces of the BBM to produce an effective loading velocity, v (i.e., $-v/2$ and $v/2$ applied to the top and bottom surfaces, respectively). By applying loading directly on the surface of the model, a frictionless loading condition is set, avoiding the end effect caused by loading platens [11,34]. The loading velocity and applied damping form have great influence on the modeling results. Thus, the loading rate must be appropriately slow and the damping high enough to ensure quasi-static equilibrium conditions for the model [46]. After a sensitivity analysis, a constant velocity of 0.1 m/s was established as a loading rate below which changes in velocity have limited influence on the model results. The "local" damping mode was set for the simulations in UDEC with the default damping coefficient of 0.8. This form of velocity-proportional damping minimizes any dynamic oscillation arising while failure occurs within the model [9,76]. For a loading rate of 0.1 m/s, UDEC automatically calculates a timestep of around 10–8 s for the models, which leads to a loading step of approximately 10–6 mm/step [11].

The axial and lateral strains were monitored using multiple pairs of control grid points. The strains were calculated by averaging the displacements between each pair of control points using a FISH script [73]. Five pairs of points were arranged for tracking the axial strains, and 11 pairs of points were arranged for tracking the lateral strains in the 2D models. The control grid points were located on the edges of the models. Figure 4 shows the strain tracking configuration for the 2D models. The axial stress was tracked

and calculated by averaging the axial zone stresses (σ_{yy}) measured in all the blocks within the specimens through a FISH script.

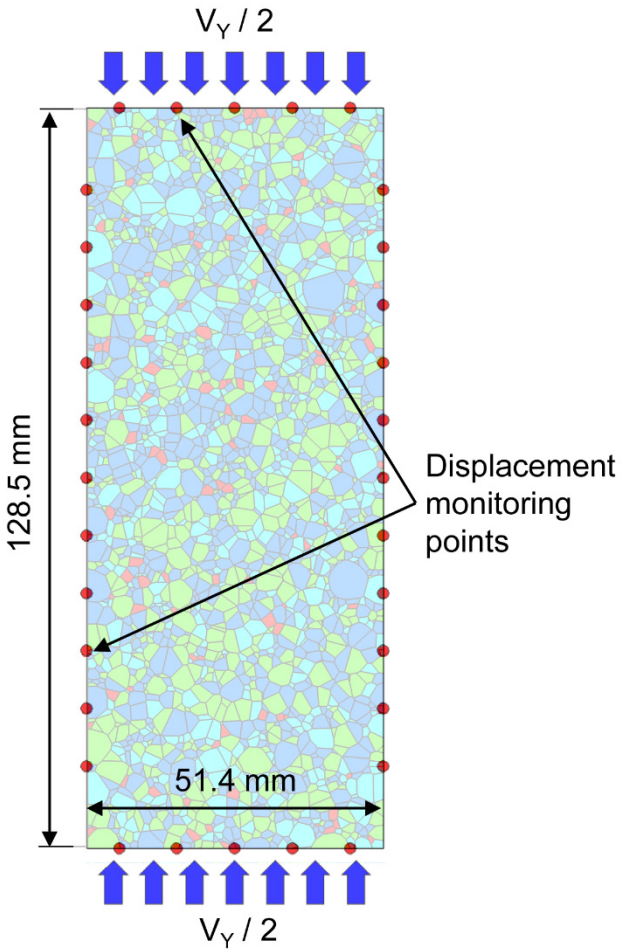

Figure 4. Loading conditions and strain tracking points for UCS test simulations.

4.2. Evaluation of Micro-Properties for Predictive Modeling Purposes

This portion of the study assesses which one of the four previously calibrated sets of micro-properties can best replicate the macro-mechanical behavior of the Wausau granite when applied in combination with a Voronoi model that closely approximates its grain-structure. Figure 5 shows the stress-strain curve for the average UCS experimental results and representative stress-strain curves resulting from models with each one of the four sets of micro-properties. Note that the model curves show the stress-strain behavior resulting from the same grain-structure representation (in this case, axial Section 3 cut from the baseline model). The results of the simulations show that the micro-properties calibrated by Farahmand and Diederichs [45] provide the most accurate prediction of the Wausau granite's macro-properties compared to the other three sets of micro-properties. The lack of any notable initial concave section of the stress-strain curve corresponding to a crack closure phase in the experimental strain-stress curve of the Wausau granite is consistent with the fact that the specimens of this granite have very low porosity. The similarities between the experimental curve and the simulated curves suggest that BBMs can closely resemble the initial section of the strain-stress curves of very low porosity rocks such as granites, which typically have less than 1% primary porosity. In other words, the assumption of zero porosity in the generated grain structure appears to be a reasonable approximation. Due to the very brittle nature of the Wausau granite, the post-peak behavior was not recorded during the UCS tests since the specimens failed violently right after they reached the peak strength. As observed in Figure 5, neither of the simulated curves shows a post-peak

behavior that resembles the experimental results, nor the typical strength drop expected for most brittle rocks loaded under unconfined conditions. In contrast, the curves show a more ductile behavior associated with the increased post-peak grain interlocking resulting from modeling the grains as unbreakable elastic bodies. Accordingly, the post-peak results shown in Figure 5 should not be considered realistic and will not be analyzed in this paper. However, as stated previously, the use of unbreakable elastic grains has negligible effects on the pre-peak simulation results [43] and macro-property predictions.

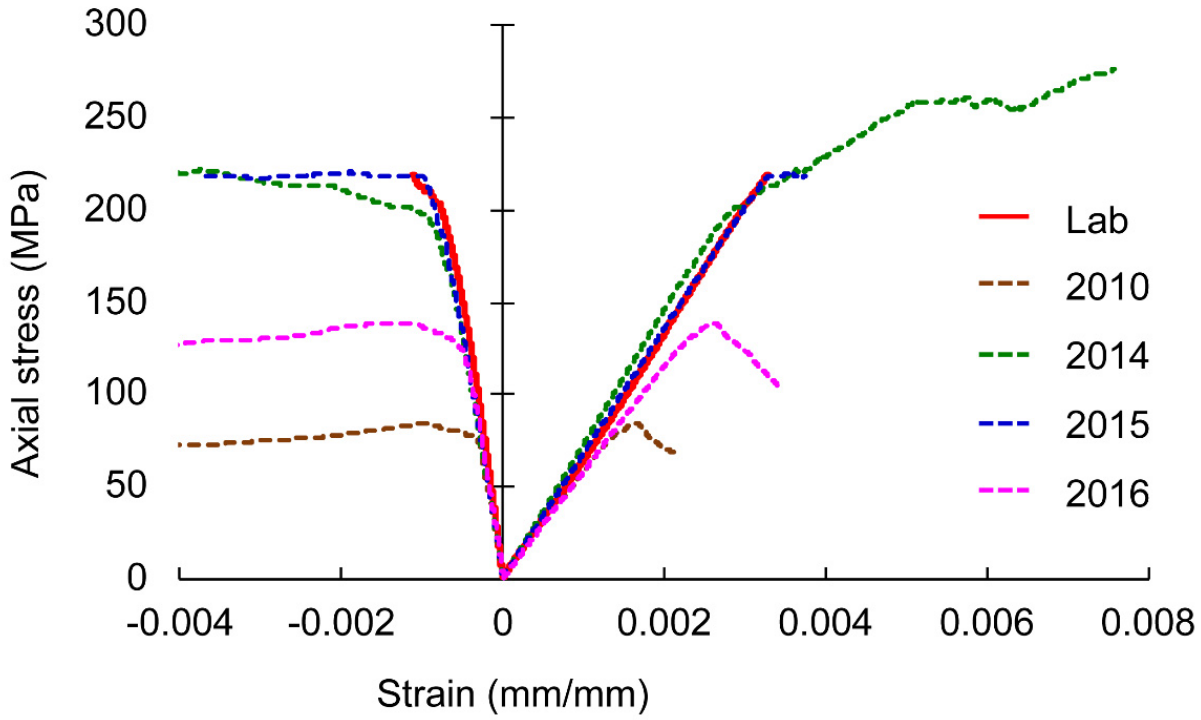

Figure 5. Stress-strain curve for the average UCS experimental results of the Wausau granite (red) and representative UCS test simulations using micro-properties calibrated by Lan et al. [8], Chen and Konietzky [64], Farahmand and Diederichs [45] and Chen et al. [65].

Figure 6 presents the mean and variability (i.e., standard deviation) of the macro-properties (i.e., UCS, crack damage stress, crack initiation stress, Young's modulus and Poisson's ratio) predicted using 18 models for each set of micro-properties. The predicted macro-properties are compared with the actual macro-properties of the Wausau granite obtained in the laboratory, which are also presented in terms of mean and standard deviation.

On average, the micro-properties from Farahmand and Diederichs [45] predict UCS values very close to the average experimental peak strength of the Wausau granite (226 MPa). The micro-properties from Chen and Konietzky [64] produced higher peak strength values with an average of 289 MPa, 28% above the actual average peak strength of the Wausau granite. The sets of parameters from Lan et al. [8] and Chen et al. [65] provided estimations significantly below the real Wausau granite's UCS, around 83 MPa (63% lower) and 139 MPa (38% lower), respectively (see Figure 6a).

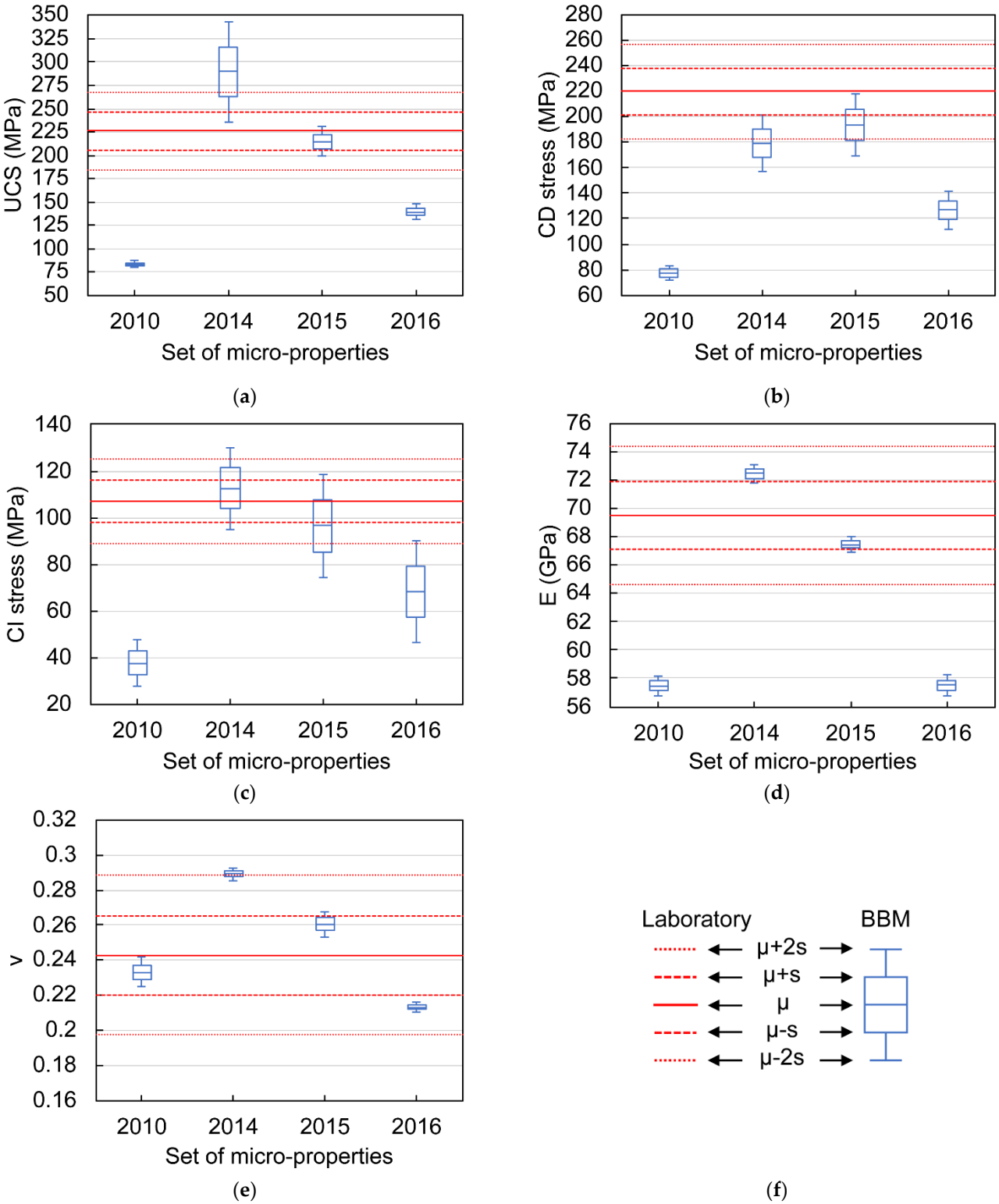

Figure 6. Predicted rock properties obtained by combining the baseline set of 18 2D models with each set of micro-properties, shown on the X-axis by publication year: Lan et al. [8], Chen and Konietzky [64], Farahmand and Diederichs [45] and Chen et al. [65]. (**a**) UCS, (**b**) crack damage stress, (**c**) crack initiation stress, (**d**) Young's modulus and (**e**) Poisson's ratio. (**f**) Chart legend.

The micro-properties from Chen and Konietzky [64] and Farahmand and Diederichs [45] provide the best approximations of the CD and CI stresses. In the case of the CD stress, the Chen and Konietzky [64] micro-parameters result in average values 18% lower than the

actual average CD stress, whereas the set from Farahmand and Diederichs [45] results in values around 198 MPa (10% below the actual average CD stress). For the CI stress, the results from Chen and Konietzky [64] average 113 MPa (5% above the actual CI stress), whereas the results from Farahmand and Diederichs [45] average 97 MPa (10% below). The sets from Lan et al. [8] and Chen et al. [65] produced results well below the real CD and CI stresses. The micro-properties from Lan et al. [8] average 77 MPa (65% below) and 37 MPa (65% below) for the CD stress and CI stress, respectively. The set of Chen et al. [65] produces average CD and CI stress values of 127 MPa (42% below) and 68 MPa (36% below), respectively (see Figure 6b,c).

Regarding the prediction of the Young's modulus (Figure 6d), again, the micro-properties from Chen and Konietzky [64] and Farahmand and Diederichs [45] achieve the best predictions. The results of Chen and Konietzky [64] average 72 GPa, and the results from Farahmand and Diederichs [45] average 67 GPa, 4% above and 3% below the actual average Young's modulus of the Wausau granite, respectively. Both the sets of micro-properties from Lan et al. [8] and Chen et al. [65] predict on average 57 GPa for the Young's modulus, which is 17% lower than the actual value. The four sets of micro-properties produce predictions of the Poisson's ratio that are close to the average value measured in the laboratory (0.24). On average, the predictions differ 4% [8], 19% [64], 7% [45] and 12% [65] from the average actual Poisson's ratio (see Figure 6e). Table 12 summarizes the average values of the predictions.

Table 12. Summary of average predictions obtained from the baseline set of 18 2D models in combination with each set of micro-properties [8,45,64,65].

Micro-Properties	Lab	2010		2014		2015		2016	
	Mean	Mean	Dif. [1]	Mean	Dif. [1]	Mean	Dif. [1]	Mean	Dif. [1]
UCS (MPa)	225.9	83.2	−63	289.5	28	215.5	−5	139.3	−38
CD (MPa)	220.0	77.3	−65	179.4	−18	197.9	−10	126.8	−42
CI (MPa)	107.0	37.7	−65	112.5	5	96.6	−10	68.4	−36
E (GPa)	69.5	57.5	−17	72.5	4	67.5	−3	57.5	−17
ν	0.243	0.233	−4	0.289	9	0.261	7	0.213	−12

[1] Dif. = difference expressed as a percentage of the laboratory mean value.

Discussion on the Capabilities of Published Micro-Properties for Prediction Purposes

Even though the micro-properties from Lan et al. [8], Chen and Konietzky [64] and Farahmand and Diederichs [45] were calibrated for the Lac du Bonnet granite, and the micro-properties from Chen et al. [65] were calibrated to a different granite with very similar characteristics, the values of the published parameters are very different from set to set. Consequently, when these sets of micro-properties were used to predict the macro-properties of the Wausau granite, the resulting parameters showed clear disparities, which are especially noticeable in the predicted UCS, CD and CI values. The differences in the calibration process and simplifications used for the calibration of the micro-properties within the four studies must be considered in order to explain the obtained results.

In the case of Lan et al. [8], the study used specimen models scaled to different sizes to perform the calibration and reduce the required simulation time. A reduced-scale model was used for the calibration of the contact stiffness micro-properties (i.e., normal and shear stiffness), whereas the rest of the contact micro-properties were calibrated using a full-scale model. Contact strength micro-properties (i.e., cohesion, friction angle and tensile strength) were adjusted applying a major simplification: the same values of friction, cohesion and tensile strength were assigned to all the contacts in the models. This suggests that the physics involved in the micro-mechanical behavior of each type of mineral grain is not properly represented. Chen and Konietzky [64], Farahmand and Diederichs [45] and Chen et al. [65] followed iterative multi-step processes to adjust the micro-properties using one single grain-structure model, resulting in unique values of stiffness and strength

contact micro-properties for each type of contact. However, they adjusted the parameters under different test conditions (e.g., UCS tests, triaxial compression strength tests, Brazilian tensile strength tests, direct tensile strength and fracture toughness tests). Chen and Konietzky [64] calibrated the micro-properties based only on UCS, Brazilian tensile strength and fracture toughness test simulations. Therefore, their parameters are able to provide realistic predictions of the rock behavior only under unconfined or low-stress conditions. This explains the unrealistic post-peak behavior shown in the stress-strain curve predicted for the Wausau granite using this set of micro-parameters (see Figure 5). Chen et al. [65] used only triaxial compression test simulations for the calibration, obtaining a set of micro-properties that only provides realistic predictions of the mechanical behavior under confined compression conditions. Figure 5 shows that the set of micro-properties from Chen et al. [65] fails to predict the unconfined peak strength of the Wausau granite accurately. Finally, Farahmand and Diederichs [45] used UCS, triaxial compression strength and Brazilian tensile strength tests for the calibration of the micro-properties covering a broader spectrum of confining stress conditions, which in our view provided the most well-constrained and therefore broadly applicable set of micro-properties for the mineral and contact types considered. It is therefore somewhat unsurprising that these properties provided the best overall prediction of Wausau granite properties. The micro-properties calibrated by Farahmand and Diederichs [45] were used to analyze the effect of mineral arrangement, grain shape and grain size, in the following sections, since they provide the best approximations of the Wausau granite macro-properties.

4.3. Effect of Mineral Arrangement and Voronoi Grain-Structures

The influence of the mineral arrangement was analyzed by comparing five sets of 18 2D BBMs generated from five 3D representations of the Wausau granite. These 3D representations are equivalent between each other in terms of mineral content and grain-structure geometry, but different with regards to mineral type assigned to each grain. In contrast, the influence of randomly-generated Voronoi grain-structures was analyzed through the variations in the predictions within each set of 2D models. Figure 7 shows the distribution of the predicted macro-properties per each one of the sets of 2D BBMs (1, 2, 3, 4 and 5) and the overall distribution. Tables 13 and 14 summarize the results in terms of their means and standard deviations, respectively.

Table 13. Summary of average predictions per mineral arrangement.

Mineral Arrangement	Lab	1 (BL [1])		2		3		4		5		Global Average	
	Mean	Mean	Dif. [2]	Mean	Dif. [2]	Mean	Dif. [2]	Mean	Dif. [2]	Mean	Dif. [2]	Mean	Dif. [2]
UCS (MPa)	225.9	215.5	−5	211.6	−6	217.6	−4	216.6	−4	213.1	−6	214.9	−5
CD (MPa)	220.0	197.9	−10	188.2	−14	194.5	−12	193.3	−12	194.8	−11	193.7	−12
CI (MPa)	107.0	96.6	−10	96.4	−10	99.7	−7	99.3	−7	90.4	−16	96.5	−10
E (GPa)	69.5	67.5	−3	67.5	−3	67.4	−3	67.4	−3	67.6	−3	67.6	−3
ν	0.243	0.261	7	0.260	7	0.262	8	0.262	8	0.259	7	0.259	7

[1] BL = baseline; [2] Dif. = difference expressed as a percentage of the laboratory mean value.

Table 14. Summary of the prediction variability per mineral arrangement.

Mineral Arrangement	Lab	1 (BL [1])		2		3		4		5		Global Average	
	S.D. [2]	S.D. [2]	Dif. [3]	S.D. [2]	Dif. [3]	S.D. [2]	Dif. [3]	S.D. [2]	Dif. [3]	S.D. [2]	Dif. [3]	S.D. [2]	Dif. [3]
UCS (MPa)	20.6	8.4	−59	6.4	−69	4.5	−78	9.8	−53	8.4	−59	7.9	−62
CD (MPa)	18.6	11.2	−40	15.1	−19	10.7	−43	10.3	−45	11.7	−37	12.1	−35
CI (MPa)	9.2	10.2	12	9.0	−2	13.8	51	10.5	14	9.7	6	11.1	21
E (GPa)	2.4	0.2	−91	0.2	−91	0.3	−89	0.2	−91	0.3	−86	0.3	−89
ν	0.023	0.004	−82	0.004	−84	0.003	−85	0.003	−86	0.004	−84	0.004	−84

[1] BL = baseline; [2] S.D. = standard deviation; [3] Dif. = difference expressed as a percentage of the laboratory standard deviation.

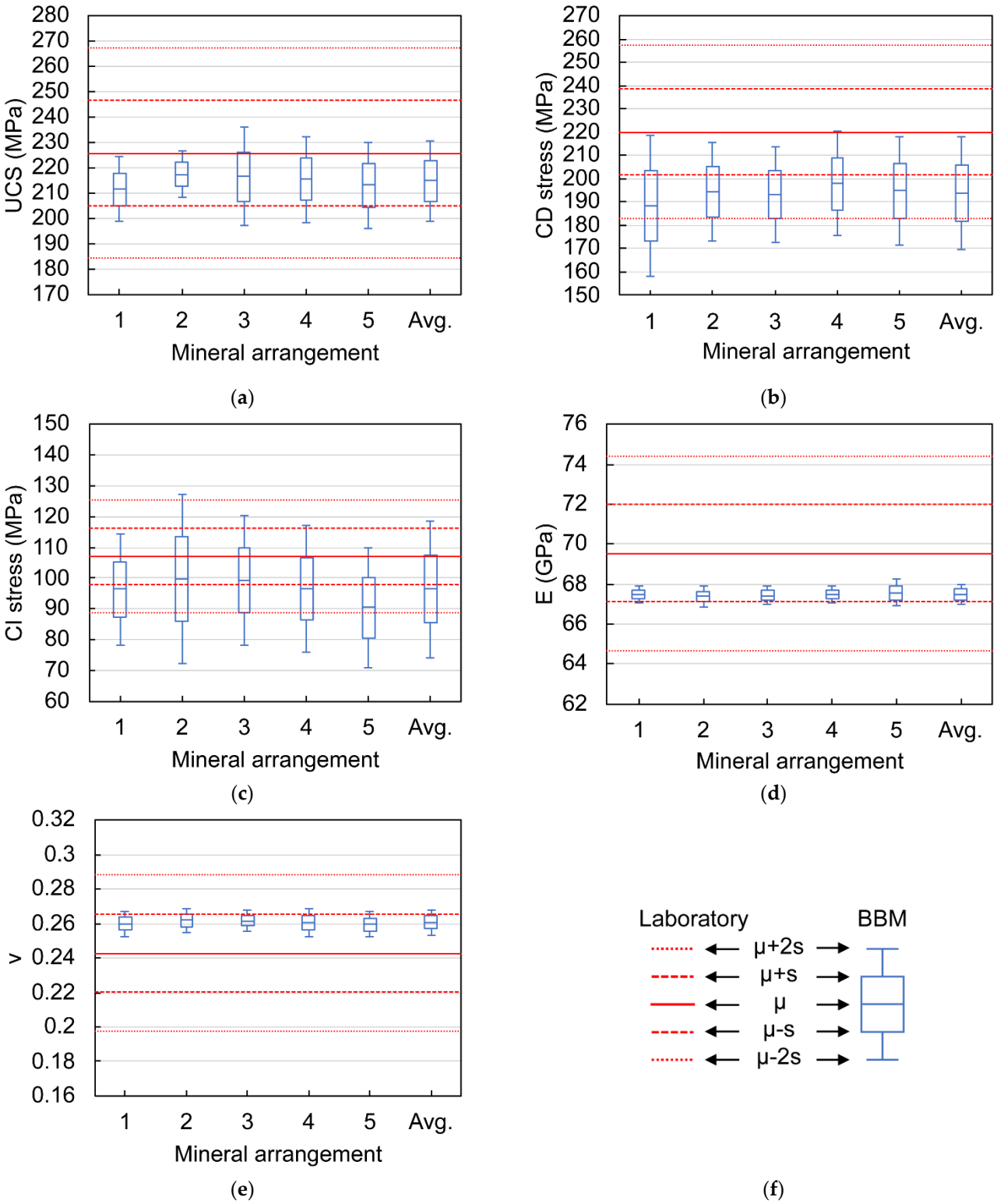

Figure 7. Predicted rock properties for the baseline model (1), each of the four "clone" grain-structures (2, 3, 4 and 5) and the global average for all the simulation results (Avg.). (**a**) UCS, (**b**) crack damage stress, (**c**) crack initiation stress, (**d**) Young's modulus and (**e**) Poisson's ratio. (**f**) Chart legend.

As expected, the different mineral arrangements represented in the BBMs led to a variety of rock macro-property predictions. This indicates that the stochastic effects introduced by mineral arrangement assignment and Voronoi grain-structures significantly affect the prediction results, independently of the mineral content and grain geometric

features represented in the models. Even though the average macro-property predictions for each of the five sets of BBMs closely approximate the average experimental macro-properties (differences less than 16%), the standard deviations of the predictions differ significantly from one another.

Specifically, the UCS, CD stress and CI stress tend to vary more significantly based on differences in stochastic grain structure characteristics than the Young's modulus and Poisson's ratio. This is evident when comparing the distributions of the predictions of each set of 18 BBMs and the overall predictions. In addition, the results of this analysis show that compared to other macro-properties, the standard deviations of the CI stress predictions tend to exceed the experimental variability of the Wausau granite, ranging between 98 and 151% of the observed standard deviation among the five different grain structure cases. The standard deviations of the UCS and CD predictions range from 31 to 47% and 55 to 81% of the experimental standard deviations of these parameters, respectively. In the case of the Young's modulus and Poisson's ratio, the standard deviations range from 9 to 14% and 14 to 18% of the experimental standard deviations, respectively.

The final analysis of this section examined the predictions of macro-properties of the Wausau granite to determine whether these predictions were realistic. This was accomplished by comparing the range of predicted values against the range of laboratory results. Considering all the 90 2D models used in this assessment, the predicted values for the UCS, Young's modulus and Poisson's ratio fall within the observed range of the experimental macro-properties (i.e., $\mu \pm 2\sigma$ interval), whereas the predictions for the CD stress and CI stress are within this experimentally constrained range in 82 and 71% of the simulations, respectively. Therefore, all predictions for the UCS, Young's modulus and Poisson's ratio can be considered reasonable approximations of the true values of these parameters. In contrast, some of the CD stress and CI stress predictions fell below the experimentally constrained range.

4.4. Effect of Grain Shape

In this analysis, the grain shape is expressed in terms of the sphericity parameter used in Neper [67]. Figure 8 shows the comparison of the predicted macro-properties for three different values of sphericity: low sphericity (0.75), moderate sphericity (0.80) and high sphericity (0.85), where the moderate sphericity case was qualitatively assessed to correspond to the most realistic representation of the average grain shape of the Wausau granite. Table 15 summarizes the average predictions for this analysis.

For all analyzed macro-properties, the results indicate a slight influence of the average grain sphericity on the predictions. For UCS, CD stress and CI stress, the predictions tend to show higher values as the sphericity increases. Regarding the UCS predictions (Figure 8a), the average values for low sphericity (209 MPa), moderate sphericity (215 MPa) and high sphericity (242 MPa) are very close to the actual peak strength of the rock, with differences of less than 8%, 5% and 7%, respectively. Note that the influence of sphericity on UCS is non-linear, with the average high sphericity strength prediction being significantly larger than the predictions in the low and moderate sphericity cases. The CD stress (Figure 8b) presents a similar behavior to the UCS. Low sphericity and moderate sphericity predictions average 192 MPa (13% below the real CD stress) and 194 MPa (12% below the real CD stress), whereas the high sphericity prediction reached an average of 213 MPa (3% below the real CD stress). In the case of the CI stress (Figure 8c), the average predictions corresponding to the different degrees of sphericities are all close to the average laboratory value (<15% difference), with the values again increasing with increasing sphericity.

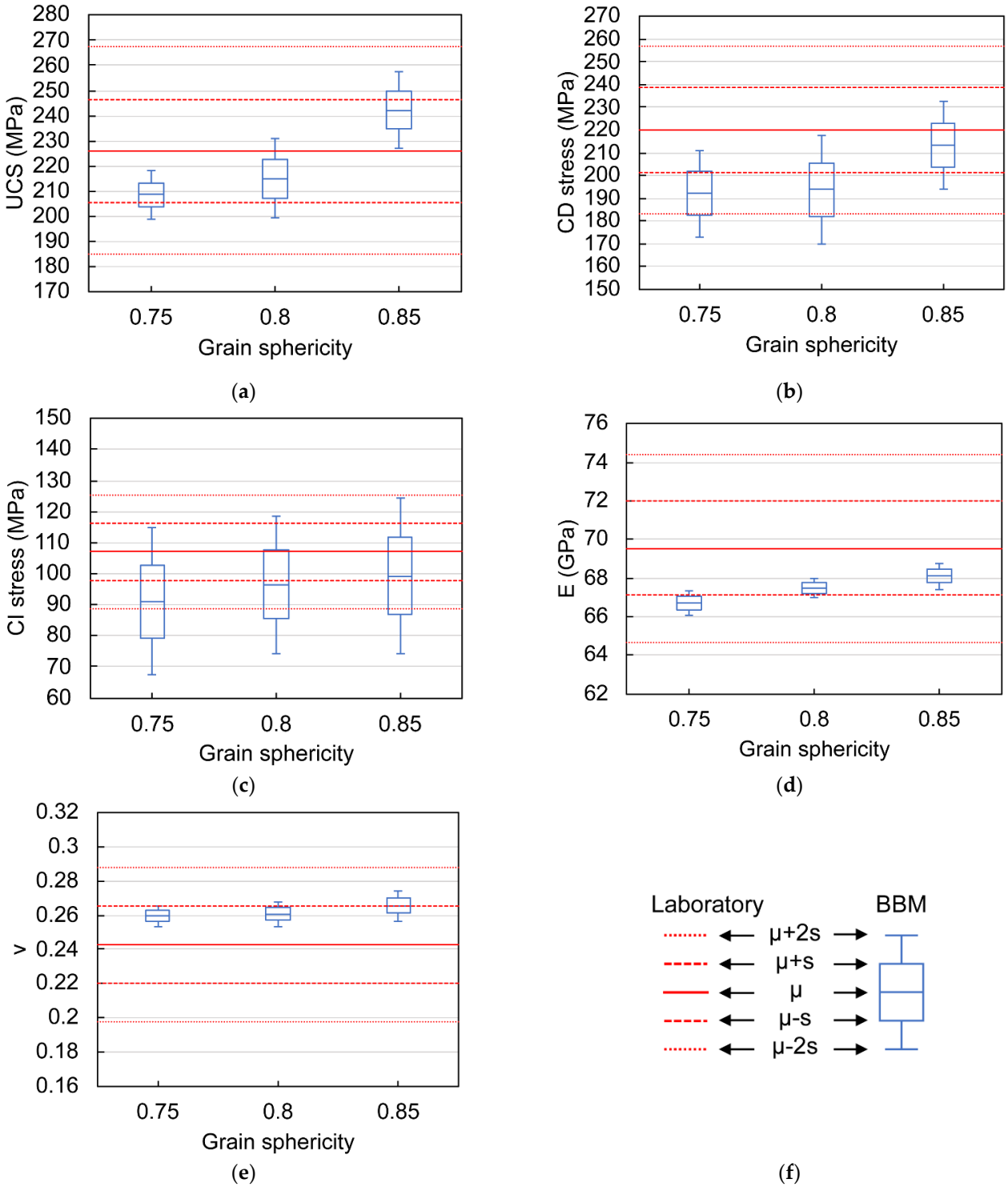

Figure 8. Predicted rock properties per grain sphericity (**a**) UCS; (**b**) crack damage stress; (**c**) crack initiation stress; (**d**) Young's modulus; (**e**) Poisson's ratio. (**f**) Chart legend.

Table 15. Summary of average predictions per grain shape (sphericity).

Grain Shape	Lab	s = 0.75		s = 0.80		s = 0.85	
	Mean	Mean	Dif. [1]	Mean	Dif. [1]	Mean	Dif. [1]
UCS (MPa)	225.9	208.6	−8	214.9	−5	242.2	7
CD (MPa)	220.0	192.1	−13	193.7	−12	213.3	−3
CI (MPa)	107.0	91.1	−15	96.5	−10	99.3	−7
E (GPa)	69.5	66.7	−4	67.5	−3	68.1	−2
ν	0.243	0.260	7	0.261	7	0.265	9

[1] Dif. = difference expressed as a percentage of the laboratory mean value.

The described behavior appears to be associated with the degree of interlocking within the grain structure. As previously described in the studies of Azocar [50], Mayer and Stead [46] and Zhu et al. [58], polyhedral grain shapes tend to provide higher degrees of interlocking within grains that favor tensile failure between grains and lead to higher peak strengths, in contrast to triangular grain shapes that favor shear failure between grains. Correspondingly, in this study, grains with high sphericity are more interlocked, resulting in a higher propensity for tensile failure between grains as opposed to shear failure, since grains with lower sphericity tend to more closely approximate triangular shapes.

The results also show a correlation between the degree of sphericity and the stiffness of the model: the greater the sphericity, the greater the Young's modulus and the Poisson's ratio. Nevertheless, the effects of sphericity on these parameters are relatively minor. The average predictions of Young's modulus (Figure 8d) for the three degrees of sphericity are slightly below the average experimental value (differences up to 4%). The Poisson's ratio predictions (Figure 8e) obtained for the three degrees of sphericity also present averages close to the actual Poisson's ratio of the Wausau granite (differences up to 9%).

These findings differ from a recent study by Xu et al. [52] that indicates that grain sphericity has little or no influence on rock strength or mechanical behavior. Such a difference could be related to the variability of the results associated with the stochastic effect provided by the random nature of Voronoi grain-structures, which has greater potential to influence results when the number of simulations is limited, as in the case of Xu et al. [52].

All the predictions of the UCS, Young's modulus and the Poisson's ratio are within the observed range of the experimental macro-properties. Similarly, the CD stress predictions for high grain sphericity fall within the experimental range. The predictions of CD stress for low and moderate sphericities only fall within that range in around 86 and 82% of the simulations, respectively. The predictions of CI stress are within the experimental CI range only in 47%, 72% and 61% of the simulations for low, moderate and high sphericities, respectively.

4.5. Effect of Grain Size

Four different average grain sizes were analyzed: 1.7 mm, 2.0 mm, 2.3 mm and 2.9 mm, where 2.0 mm is the average grain size measured in specimens of the Wausau granite. Table 16 presents the average mechanical property predictions by grain size.

Table 16. Summary of average predictions per grain size (diameter).

Micro-Properties	Lab	d = 1.7 mm		d = 2.0 mm		d = 2.3 mm		d = 2.9 mm	
	Mean	Mean	Dif. [1]	Mean	Dif. [1]	Mean	Dif. [1]	Mean	Dif. [1]
UCS (MPa)	225.9	224.9	0	214.9	−5	221.4	−2	216.7	−4
CD (MPa)	220.0	202.2	−8	193.7	−12	200.9	−9	198.5	−10
CI (MPa)	107.0	93.5	−13	96.5	−10	94.0	−12	93.7	−12
E (GPa)	69.5	66.9	−4	67.5	−3	68.3	−2	69.7	0
ν	0.243	0.259	7	0.261	7	0.264	9	0.272	12

[1] Dif. = difference expressed as a percentage of the laboratory mean value.

In these results, there is no clear influence of the grain size on the predictions of UCS, CD stress and CI stress (Figure 9a–c) within the 1.7–2.9 mm grain size range. In the case of the UCS, the results for the four grain sizes present average predictions slightly below the actual peak strength of the Wausau granite (differences less than 5%). The average predictions of the CD stress differ by up to 12% from the average experimental value. On average, the predicted values of CI stress are very similar for the four different grain sizes and are between 10 and 13% below the average experimental CI value.

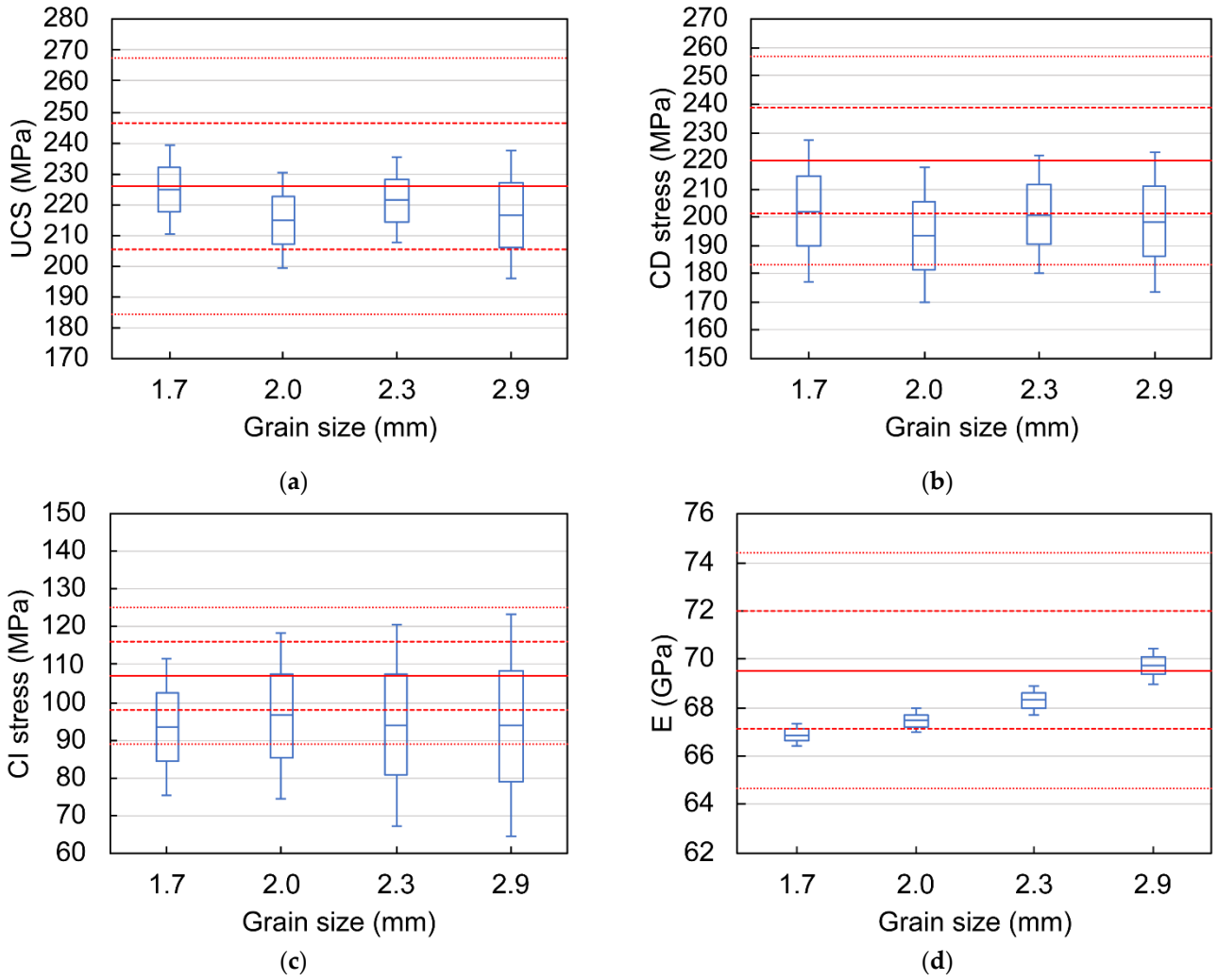

Figure 9. *Cont.*

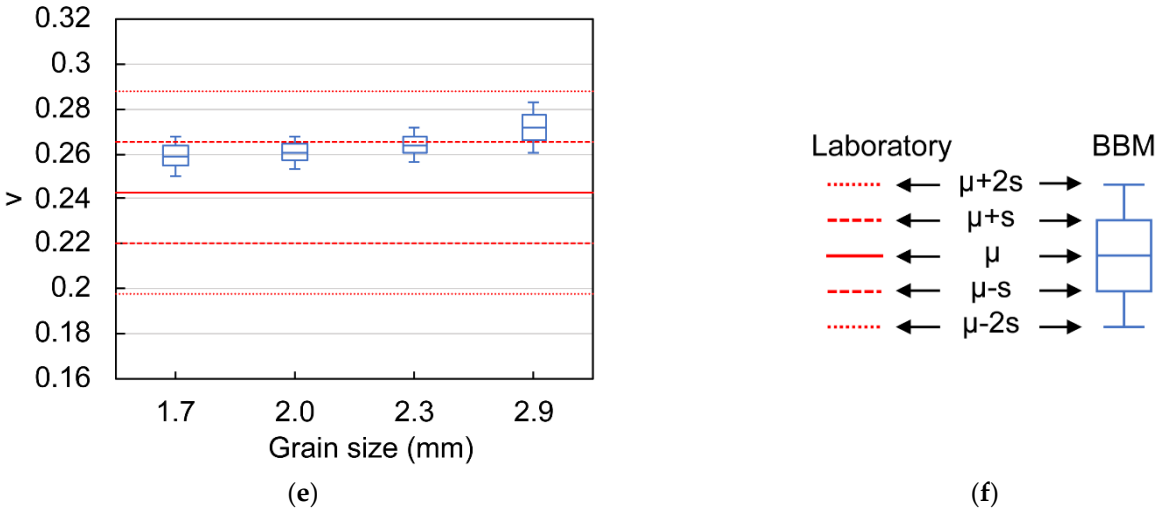

Figure 9. Predicted rock properties per grain size (**a**) UCS; (**b**) crack damage stress; (**c**) crack initiation stress; (**d**) Young's modulus; (**e**) Poisson's ratio. (**f**) Chart legend.

These results are consistent with the findings of some studies [37,49,51] that examined the effect of grain size on the peak strength and CI stress using similar grain diameter ranges (i.e., average diameters below 4.8 mm). Other studies using BBMs [51] that examined greater average grain sizes (i.e., up to 6 mm) reported a slight positive correlation that indicates that compressive strength is dependent on grain size. However, there is a conflict between the described results and the correlations between grain size and UCS identified using laboratory test data [42], as well as for the CI and CD stress thresholds [26]. In the future, additional simulations including a larger range of grain sizes should be conducted for further investigation of the influence of grain size on compressive strength.

An apparent influence of the grain size on the predicted values for the Young's modulus and Poisson's ratio was identified in Figure 9d,e, respectively. In both cases, the predicted average value tends to be higher when the grain size increases. The predictions for the Young's modulus show average values with a difference of less than 4% compared to the average experimental Young's modulus for the four grain size cases. For the Poisson's ratio, the four grain size types predict average values between 7 and 12% above the actual Poisson's ratio of the rock. The dependence of the elastic parameters on grain size is believed to be associated with the decrease in the number of grain-contacts when the grain size increases. When the soft grain-contacts reduce in number, the stiffness of the whole system increases as a result of the relative prevalence of larger stiff grains. The studies of Ghazvinian et al. [37] and Gui et al. [51] also identified a similar trend in the Young's modulus in their analyses.

This analysis also indicates that realistic predictions of the Wausau granite macro-properties can be obtained even if the average grain size varies up to ±45%. This suggests that the variability of the average grain size within a given rock type would not significantly affect the predictions of rock mechanical behavior in a majority of cases.

All the predictions of the UCS, Young's modulus and the Poisson's ratio fall within the observed range of the experimental macro-properties. In contrast, when considering the four different grain sizes, only 82–94% of the CD stress predictions and 44–72% of the CI stress predictions are within the experimental range. Apparently, changes in grain size (within the 1.7–2.9 mm grain size range) do not significantly affect the realism of the predictions.

5. Conclusions

This paper presented an assessment of the capabilities of BBMs for rock mechanical behavior prediction using a predictive modeling approach that does not require micro-property calibration. The effectiveness of the proposed approach was analyzed, and the

influences of the micro-properties and grain geometric features represented in BBMs on the predictions were evaluated. In contrast to previous similar works, this study explicitly accounted for the effects of stochastically generated Voronoi grain-structures on mechanical behavior predictions.

The proposed modeling approach can produce realistic predictions of brittle rock mechanical behavior using previously calibrated micro-properties in combination with a close approximation of the grain-structure of interest. Furthermore, the results obtained using this approach demonstrate that properly calibrated micro-properties can be transferrable from one rock to another. Thus, this approach could potentially be used for predictive modeling of rocks without available laboratory data. However, the applicability of this approach could be limited by the lack of availability of calibrated micro-properties for certain types of rocks and minerals.

The BBM grain-structure used for the calibration of micro-properties has a direct effect on the resulting set of micro-properties. Consequently, the effectiveness of this approach is limited by the realism of the grain-structure representation and simplifications applied in the initial calibration process used to obtain the required micro-properties. Our results demonstrate that micro-properties calibrated using an inadequate approximation of the grain structure will not likely be useful for predictive modeling.

The selection of an appropriate set of calibrated micro-properties is a critical factor in predicting brittle rock strength and can greatly affect the results of a prediction. In this study, the micro-properties calibrated by Farahmand and Diederichs [45] provided the most realistic predictions for the Wausau granite. In the calibration procedure of Farahmand and Diederichs [45], the simulated confining stress conditions and the grain-structure representation appear to be the key factors to obtain a reliable calibration of parameters.

The stochastic nature of Voronoi grain-structures used in BBMs shows an evident influence on the emergent mechanical properties predicted by these models. The variability of the predictions obtained from a set of BBMs that depict the same underlying grain-structure attributes is particularly significant in the case of the UCS, CD stress and CI stress. In addition, for the CD stress and CI stress, some of the predicted values (up to 29% of the predictions) fall outside the observed range of experimental macro-properties. With that said, any one simulation may provide an unrealistic prediction of macroscopic rock properties. Alternatively, the chances of achieving realistic predictions of rock macro-properties are higher when using the average prediction obtained from numerous simulations that stochastically approximate the same grain-structure.

According to the results of this study, the specific representation of the grain shape and grain size has a limited effect on the predictions relative to the variability related to stochastic effects associated with grain structure generation and mineral assignment. The grain sphericity has some influence on the results of the predictions, particularly at later stages of loading. In the case of the Wausau granite, low, moderate and high degrees of sphericity provide realistic estimations of the UCS and CD stress. Among the three sphericities considered, high sphericities (s = 0.85) can lead to significantly higher peak strength and CD stress estimations. The grain size does not show an evident influence on the prediction of the UCS, CD stress and CI stress. Still, grain size clearly impacts the elastic properties (Young's modulus and Poisson's ratio), as identified in previous studies [37,49]. Such an influence does not generate significant differences in the predictions, within the assessed range of average grain sizes (1.7 mm to 2.9 mm). Thus, a BBM created using the Voronoi tessellation method that realistically represents the average grain shape (i.e., sphericity) and properly approximates the average grain size (within a variability of $\pm$45%) could potentially be used in combination with a set of properly calibrated micro-properties to provide realistic predictions of rock mechanical properties for other rock types.

Author Contributions: Conceptualization, C.E.C.I., G.W. and E.H.; methodology, C.E.C.I., G.W. and E.H.; software, C.E.C.I.; validation, C.E.C.I.; formal analysis, C.E.C.I.; investigation, C.E.C.I.; resources, G.W. and E.H.; data curation, C.E.C.I.; writing—original draft preparation, C.E.C.I.; writing—review and editing, C.E.C.I., G.W. and E.H.; visualization, C.E.C.I.; supervision, G.W.;

project administration, G.W.; funding acquisition, G.W. All authors have read and agreed to the published version of the manuscript.

Funding: The research conducted for this study was funded by the National Institute for Occupational Safety and Health (NIOSH) under Grant Number 200-2016-90154.

Institutional Review Board Statement: Not applicable.

Informed Consent Statement: Not applicable.

Data Availability Statement: The data presented in this study are available on request from the corresponding author.

Acknowledgments: The authors extend their gratitude for the financial support. Special thanks to Katharina Pfaff of the automated mineralogy laboratory, Jae Erickson of the thin-section laboratory, and Bruce Yoshioka, Brent Duncan, Omid Frough and Muthu Vinayak of the Earth Mechanics Institute at the Colorado School of Mines for their help during various tests and analyses.

Conflicts of Interest: The authors declare no conflict of interest.

References

1. Bieniawski, Z.T. Mechanism of Brittle Fracture of Rock: Part I—Theory of the Fracture Process. *Int. J. Rock Mech. Min. Sci.* **1967**, *4*, 395–404. [CrossRef]
2. Wawersik, W.R.; Fairhurst, C. A Study of Brittle Rock Fracture in Laboratory Compression Experiments. *Int. J. Rock Mech. Min. Sci. Geomech.* **1970**, *7*, 561–575. [CrossRef]
3. Martin, C.D.; Chandler, N.A. The Progressive Fracture of Lac Du Bonnet Granite. *Int. J. Rock Mech. Min. Sci.* **1994**, *31*, 643–659. [CrossRef]
4. Eberhardt, E.; Stead, D.; Stimpson, B.; Read, R.S. Identifying Crack Initiation and Propagation Thresholds in Brittle Rock. *Can. Geotech. J.* **1998**, *35*, 222–233. [CrossRef]
5. Martin, C.D. The Strength of Massive Lac Du Bonnet Granite around Underground Openings. Ph.D. Thesis, University of Manitoba, Winnipeg, MB, Canada, 1993.
6. Staub, I.; Andersson, J.C.; Magnor, B. *Äspö Pillar Stability Experiment: Geology and Mechanical Properties of the Rock in TASQ*; Svensk Kar: Stockholm, Sweden, 2004.
7. Eberhardt, E. Brittle Rock Fracture and Progressive Damage in Uniaxial Compression. Ph.D. Thesis, University of Saskatchewan, Saskatoon, Saskatchewan, 1998.
8. Lan, H.; Martin, C.D.; Hu, B. Effect of Heterogeneity of Brittle Rock on Micromechanical Extensile Behavior during Compression Loading. *J. Geophys. Res.* **2010**, *115*. [CrossRef]
9. Gao, F.; Stead, D.; Elmo, D. Numerical Simulation of Microstructure of Brittle Rock Using a Grain-Breakable Distinct Element Grain-Based Model. *Comput. Geotech.* **2016**, *78*, 203–217. [CrossRef]
10. Liu, G.; Cai, M.; Huang, M. Mechanical Properties of Brittle Rock Governed by Micro-Geometric Heterogeneity. *Comput. Geotech.* **2018**, *104*, 358–372. [CrossRef]
11. Wang, X.; Cai, M. Modeling of Brittle Rock Failure Considering Inter- and Intra-Grain Contact Failures. *Comput. Geotech.* **2018**, *101*, 224–244. [CrossRef]
12. Mahabadi, O.K. Investigating the Influence of Micro-Scale Heterogeneity and Microstructure on the Failure and Mechanical Behaviour of Geomaterials. Ph.D. Thesis, University of Toronto, Toronto, ON, Canada, 2012.
13. Olsson, W.A. Grain Size Dependence of Yield Stress in Marble. *J. Geophys. Res.* **1974**, *79*, 4859–4862. [CrossRef]
14. Singh, S.K. Relationship among Fatigue Strength, Mean Grain Size and Compressive Strength of a Rock. *Rock Mech. Rock Eng.* **1988**, *21*, 271–276. [CrossRef]
15. Wong, R.H.C.; Chau, K.T.; Wang, P. Microcracking and Grain Size Effect in Yuen Long Marbles. *Int. J. Rock Mech. Min. Sci. Geomech.* **1996**, *33*, 479–485. [CrossRef]
16. Eberhardt, E.; Stimpson, B.; Stead, D. Effects of Grain Size on the Initiation and Propagation Thresholds of Stress-Induced Brittle Fractures. *Rock Mech. Rock Eng.* **1999**, *32*, 81–99. [CrossRef]
17. Fredrich, J.T.; Evans, B. Teng-Fong Wong Effect of Grain Size on Brittle and Semibrittle Strength: Implications for Micromechanical Modelling of Failure in Compression. *J. Geophys. Res.* **1990**, *95*, 10907–10920. [CrossRef]
18. Přikryl, R. Some Microstructural Aspects of Strength Variation in Rocks. *Int. J. Rock Mech. Min. Sci.* **2001**, *38*, 671–682. [CrossRef]
19. Sajid, M.; Coggan, J.; Arif, M.; Andersen, J.; Rollinson, G. Petrographic Features as an Effective Indicator for the Variation in Strength of Granites. *Eng. Geol.* **2016**, *202*, 44–54. [CrossRef]
20. Tuğrul, A.; Zarif, I.H. Correlation of Mineralogical and Textural Characteristics with Engineering Properties of Selected Granitic Rocks from Turkey. *Eng. Geol.* **1999**, *51*, 303–317. [CrossRef]
21. Güneş Yilmaz, N.; Mete Goktan, R.; Kibici, Y. Relations between Some Quantitative Petrographic Characteristics and Mechanical Strength Properties of Granitic Building Stones. *Int. J. Rock Mech. Min. Sci.* **2011**, *48*, 506–513. [CrossRef]

22. Shea, W.T.; Kronenberg, A.K. Strength and Anisotropy of Foliated Rocks with Varied Mica Contents. *J. Struct. Geol.* **1993**, *15*, 1097–1121. [CrossRef]
23. Lajtai, E.Z. Microscopic Fracture Processes in a Granite. *Rock Mech. Rock Eng.* **1998**, *31*, 237–250. [CrossRef]
24. Yesiloglu-Gultekin, N.; Sezer, E.A.; Gokceoglu, C.; Bayhan, H. An Application of Adaptive Neuro Fuzzy Inference System for Estimating the Uniaxial Compressive Strength of Certain Granitic Rocks from Their Mineral Contents. *Expert Syst. Appl.* **2013**, *40*, 921–928. [CrossRef]
25. Keikha, T.; Keykha, H.A. Correlation between Mineralogical Characteristics and Engineering Properties of Granitic Rocks. *Electron. J. Geotech. Eng.* **2013**, *18*, 4055–4065.
26. Cowie, S.; Walton, G. The Effect of Mineralogical Parameters on the Mechanical Properties of Granitic Rocks. *Eng. Geol.* **2018**, *240*, 204–225. [CrossRef]
27. Li, X.F.; Li, H.B.; Zhao, J. 3D Polycrystalline Discrete Element Method (3PDEM) for Simulation of Crack Initiation and Propagation in Granular Rock. *Comput. Geotech.* **2017**, *90*, 96–112. [CrossRef]
28. Li, X.F.; Li, H.B.; Zhao, J. The Role of Transgranular Capability in Grain-Based Modelling of Crystalline Rocks. *Comput. Geotech.* **2019**, *110*, 161–183. [CrossRef]
29. Jing, L. A Review of Techniques, Advances and Outstanding Issues in Numerical Modelling for Rock Mechanics and Rock Engineering. *Int. J. Rock Mech. Min. Sci.* **2003**, *40*, 283–353. [CrossRef]
30. Potyondy, D.O.; Cundall, P.A. A Bonded-Particle Model for Rock. *Int. J. Rock Mech. Min. Sci.* **2004**, *41*, 1329–1364. [CrossRef]
31. Sinha, S.; Walton, G. Application of Micromechanical Modeling to Prediction of In-Situ Rock Behavior. In Proceedings of the 52nd US Rock Mechanics/Geomechanics Symposium, Seattle, WA, USA, 17–20 June 2018.
32. Lisjak, A.; Grasselli, G. A Review of Discrete Modeling Techniques for Fracturing Processes in Discontinuous Rock Masses. *J. Rock Mech. Geotech. Eng.* **2014**, *6*, 301–314. [CrossRef]
33. Zhang, Y.; Wong, L.N.Y. A Review of Numerical Techniques Approaching Microstructures of Crystalline Rocks. *Comput. Geosci.* **2018**, *115*, 167–187. [CrossRef]
34. Wang, X.; Cai, M. A Comprehensive Parametric Study of Grain-Based Models for Rock Failure Process Simulation. *Int. J. Rock Mech. Min. Sci.* **2019**, *115*, 60–76. [CrossRef]
35. Jing, L.; Stephansson, O. Fundamentals of discrete element methods for rock engineering—Theory and applications. In *Developments in Geotechnical Engineering*; Elsevier: Amsterdam, The Netherlands, 2007; pp. 365–398.
36. Jing, L.; Hudson, J.A. Numerical Methods in Rock Mechanics. *Int. J. Rock Mech. Min. Sci.* **2002**, *39*, 409–427. [CrossRef]
37. Ghazvinian, E.; Diederichs, M.S.; Quey, R. 3D Random Voronoi Grain-Based Models for Simulation of Brittle Rock Damage and Fabric-Guided Micro-Fracturing. *J. Rock Mech. Geotech. Eng.* **2014**, *6*, 506–521. [CrossRef]
38. Bahrani, N.; Kaiser, P.K.; Valley, B. Distinct Element Method Simulation of an Analogue for a Highly Interlocked, Non-Persistently Jointed Rockmass. *Int. J. Rock Mech. Min. Sci.* **2014**, *71*, 117–130. [CrossRef]
39. Mahabadi, O.K.; Lisjak, A.; Munjiza, A.; Grasselli, G. Y-Geo: New Combined Finite-Discrete Element Numerical Code for Geomechanical Applications. *Int. J. Geomech.* **2012**, *12*, 676–688. [CrossRef]
40. Munjiza, A. *The Combined Finite-Discrete Element Method*; John Wiley & Sons: Chichester, UK, 2004.
41. Abdelaziz, A.; Zhao, Q.; Grasselli, G. Grain Based Modelling of Rocks Using the Combined Finite-Discrete Element Method. *Comput. Geotech.* **2018**, *103*, 73–81. [CrossRef]
42. Li, X.F.; Li, H.B.; Zhao, J. Transgranular Fracturing of Crystalline Rocks and Its Influence on Rock Strengths: Insights from a Grain-Scale Continuum–Discontinuum Approach. *Comput. Methods Appl. Mech. Eng.* **2021**, *373*, 113462. [CrossRef]
43. Sinha, S.; Walton, G. A Study on Bonded Block Model (BBM) Complexity for Simulation of Laboratory-Scale Stress-Strain Behavior in Granitic Rocks. *Comput. Geotech.* **2020**, *118*, 103363. [CrossRef]
44. Fabjan, T.; Ivars, D.M.; Vukadin, V. Numerical Simulation of Intact Rock Behaviour via the Continuum and Voronoi Tessellation Models: A Sensitivity Analysis. *Acta Geotech. Slov.* **2015**, *12*, 5–23.
45. Farahmand, K.; Diederichs, M.S. A Calibrated Synthetic Rock Mass (SRM) Model for Simulating Crack Growth in Granitic Rock Considering Grain Scale Heterogeneity of Polycrystalline Rock. In Proceedings of the 49th US Rock Mechanics/Geomechanics Symposium, San Francisco, CA, USA, 29 June–1 July 2015; Volume 1.
46. Mayer, J.M.; Stead, D. Exploration into the Causes of Uncertainty in UDEC Grain Boundary Models. *Comput. Geotech.* **2017**, *82*, 110–123. [CrossRef]
47. Gao, F.Q.; Stead, D. The Application of a Modified Voronoi Logic to Brittle Fracture Modelling at the Laboratory and Field Scale. *Int. J. Rock Mech. Min. Sci.* **2014**, *68*, 1–14. [CrossRef]
48. Potyondy, D.O. A Flat-Jointed Bonded-Particle Material for Hard Rock. In Proceedings of the 46th US Rock Mechanics/Geomechanics Symposium 2012, Chicago, IL, USA, 24–27 June 2012; Volume 3, pp. 1510–1519.
49. Nicksiar, M.; Martin, C.D. Factors Affecting Crack Initiation in Low Porosity Crystalline Rocks. *Rock Mech. Rock Eng.* **2014**, *47*, 1165–1181. [CrossRef]
50. Azocar, K. Investigating the Mesh Dependency and Upscaling of 3D Grain-Based Models for the Simulation of Brittle Fracture Processes in Low-Porosity Crystalline Rock. Master's Thesis, Queen's University, Kingston, ON, Canada, 2016.
51. Gui, Y.L.; Zhao, Z.Y.; Ji, J.; Wang, X.M.; Zhou, K.P.; Ma, S.Q. The Grain Effect of Intact Rock Modelling Using Discrete Element Method with Voronoi Grains. *Geotech. Lett.* **2016**, *6*, 136–143. [CrossRef]

52. Xu, T.; Fu, T.F.; Heap, M.J.; Meredith, P.G.; Mitchell, T.M.; Baud, P. Mesoscopic Damage and Fracturing of Heterogeneous Brittle Rocks Based on Three-Dimensional Polycrystalline Discrete Element Method. *Rock Mech. Rock Eng.* **2020**, *53*, 5389–5409. [CrossRef]
53. Kazerani, T.; Zhao, J. Micromechanical Parameters in Bonded Particle Method for Modeling of Brittle Material Failure. *Int. J. Numer. Anal. Methods Geomech.* **2010**, *34*, 1877–1895. [CrossRef]
54. Peng, J.; Yuen Wong, L.N.; Teh, C.I. Influence of Grain Size on Strength of Polymineralic Crystalline Rock: New Insights from DEM Grain-Based Modeling. *J. Rock Mech. Geotech. Eng.* **2021**, 1–12. [CrossRef]
55. Peng, J.; Wong, L.N.Y.; Teh, C.I. Influence of Grain Size Heterogeneity on Strength and Microcracking Behavior of Crystalline Rocks. *J. Geophys. Res. Solid Earth* **2017**, *122*, 1054–1073. [CrossRef]
56. Peng, J.; Wong, L.N.Y.; Teh, C.I. Effects of Grain Size-to-Particle Size Ratio on Micro-Cracking Behavior Using a Bonded-Particle Grain-Based Model. *Int. J. Rock Mech. Min. Sci.* **2017**, *100*, 207–217. [CrossRef]
57. Li, H.; Ma, H.; Shi, X.; Zhou, J.; Zhang, H.; Daemen, J.J.K. A 3D Grain-Based Model for Simulating the Micromechanical Behavior of Salt Rock. *Rock Mech. Rock Eng.* **2020**, *53*, 2819–2837. [CrossRef]
58. Zhu, D.-F.; Tu, S.-H.; Ma, H.; Zhang, X. A 3D Voronoi and Subdivision Model for Calibration of Rock Properties. *Model. Simul. Mater. Sci. Eng.* **2017**, *25*, 085005. [CrossRef]
59. Zhou, J.; Lan, H.; Zhang, L.; Yang, D.; Song, J.; Wang, S. Novel Grain-Based Model for Simulation of Brittle Failure of Alxa Porphyritic Granite. *Eng. Geol.* **2019**, *251*, 100–114. [CrossRef]
60. Sims, P.K.; Schulz, K.J.; Dewitt, E.; Brasaemle, B. *Petrography and Geochemistry of Early Proterozoic Granitoid Rocks in Wisconsin Magmatic Terranes of Penokean Orogen, Northern Wisconsin*; US Government Printing Office: Washington, DC, USA, 1993; pp. 1–31.
61. LaBerge, G.L.; Myers, P.E. Precambrian Geology of Marathon County, Wisconsin. *Wis. Geol. Nat. Hist. Surv. Inf. Circ.* **1983**, *45*, 88.
62. Ghazvinian, E. Fracture Initiation and Propagation in Low Porosity Crystalline Rocks: Implications for Excavation Damage Zone (EDZ) Mechanics. Ph.D. Thesis, Queen's University, Kingston, ON, USA, 2015.
63. Nicksiar, M.; Martin, C.D. Evaluation of Methods for Determining Crack Initiation in Compression Tests on Low-Porosity Rocks. *Rock Mech. Rock Eng.* **2012**, *45*, 607–617. [CrossRef]
64. Chen, W.; Konietzky, H. Simulation of Heterogeneity, Creep, Damage and Lifetime for Loaded Brittle Rocks. *Tectonophysics* **2014**, *633*, 164–175. [CrossRef]
65. Chen, W.; Konietzky, H.; Tan, X.; Frühwirt, T. Pre-Failure Damage Analysis for Brittle Rocks under Triaxial Compression. *Comput. Geotech.* **2016**, *74*, 45–55. [CrossRef]
66. Quey, R.; Dawson, P.R.; Barbe, F. Large-Scale 3D Random Polycrystals for the Finite Element Method: Generation, Meshing and Remeshing. *Comput. Methods Appl. Mech. Eng.* **2011**, *200*, 1729–1745. [CrossRef]
67. Quey, R. *Neper Reference Manual: The Documentation for Neper 3.5.1*. 2019, pp. 1–106. Available online: https://neper.info/docs/neper.pdf (accessed on 27 November 2019).
68. Quey, R.; Renversade, L. Optimal Polyhedral Description of 3D Polycrystals: Method and Application to Statistical and Synchrotron X-Ray Diffraction Data. *Comput. Methods Appl. Mech. Eng.* **2018**, *330*, 308–333. [CrossRef]
69. Wadell, H. Volume, Shape, and Roundness of Quartz Particles. *J. Geol.* **1935**, *43*, 250–280. [CrossRef]
70. Bullard, J.W.; Garboczi, E.J. Defining Shape Measures for 3D Star-Shaped Particles: Sphericity, Roundness, and Dimensions. *Powder Technol.* **2013**, *249*, 241–252. [CrossRef]
71. Wadell, H. Sphericity and Roundness of Rock Particles. *J. Geol.* **1933**, *41*, 310–331. [CrossRef]
72. Itasca Consulting Group Inc. *3DEC Version 5.2: 3 Dimensional Distinct Element Code, User's Guide*, 4th ed.; Itasca Consulting Group Inc.: Minneapolis, MN, USA, 2016.
73. Itasca Consulting Group Inc. *UDEC Version 6.0: Universal Disctinct Element Code, User's Guide*, 4th ed.; Itasca Consulting Group Inc.: Minneapolis, MN, USA, 2014.
74. Cai, J.G.; Zhao, J. Effects of Multiple Parallel Fractures on Apparent Attenuation of Stress Waves in Rock Masses. *Int. J. Rock Mech. Min. Sci.* **2000**, *37*, 661–682. [CrossRef]
75. Chen, S.G.; Cai, J.G.; Zhao, J.; Zhou, Y.X. Discrete Element Modelling of an Underground Explosion in a Jointed Rock Mass. *Geotech. Geol. Eng.* **2000**, *18*, 59–78. [CrossRef]
76. Kazerani, T.; Yang, Z.Y.; Zhao, J. A Discrete Element Model for Predicting Shear Strength and Degradation of Rock Joint by Using Compressive and Tensile Test Data. *Rock Mech. Rock Eng.* **2012**, *45*, 695–709. [CrossRef]

sustainability

MDPI

Review

Bibliometric and Knowledge Network of Global Research on Pile Foundations: A Review of Recent Developments

Aman Tiwari *, Nitin Dindorkar and Suneet Kaur

Maulana Azad National Institute of Technology, Bhopal 462003, India
* Correspondence: aman20tiwari@gmail.com; Tel.: +91-9926394648

Abstract: Foundation on soft soil has always been a challenge for civil engineers and pile foundation is by far the most suitable and comprehensive idea for construction on soft soil. In this study, we produced a comprehensive overview of pile foundation research from 1992 to 2021 by making use of bibliometric analysis. This study was conducted based on the Web of Science Core Collection Database. In this analysis, data were retrieved and then sieved for different parameters to organize the data into various categories by means of Excel and VOS viewer. The objective of the research was to make an explanatory data set in order to help researchers in the pile foundation area. A database of 4803 publications has been retrieved. The analysis results show that the People's Republic of China has yielded the greatest number of publications. Studies in this period are focusing on key factors associated with pile foundations such as soil structure interaction, pile group, settlement, liquefaction, bearing capacity etc. as suggested by the keywords analyzed in these publications. Analysis of the most cited articles in the field of Geotechnical and Geoenvironmental Engineering reveals that the research area has expanded from analyzing axial behavior and strength of pile foundations to analyzing seismic responses, further moving to sustainable structure and artificial intelligence applications in the concerned field in the last 30 years.

Keywords: bibliometric analysis; pile foundation; sustainable structure; VOS viewer; Web of Science

Citation: Tiwari, A.; Dindorkar, N.; Kaur, S. Bibliometric and Knowledge Network of Global Research on Pile Foundations: A Review of Recent Developments. *Sustainability* **2023**, *15*, 11108. https://doi.org/10.3390/su151411108

Academic Editors: Antonio Caggiano, Jian Zhou, Mahdi Hasanipanah and Danial Jahed Armaghani

Received: 16 June 2023
Revised: 6 July 2023
Accepted: 13 July 2023
Published: 17 July 2023

Copyright: © 2023 by the authors. Licensee MDPI, Basel, Switzerland. This article is an open access article distributed under the terms and conditions of the Creative Commons Attribution (CC BY) license (https://creativecommons.org/licenses/by/4.0/).

1. Introduction

1.1. General

Pile foundations are that part of the structure which transmits to, and into, the underlying soil or rock, the loads supported by the foundation and its self-weight. Pile foundations are the structural members used to transmit surface loads down to lower levels in the soil mass. This may be by vertical distribution of the load along the pile shaft or by direct application of the load to a lower stratum through the pile point. Piles are commonly employed in civil and marine engineering. Many studies on pile foundations have focused on the impact of vertical loads from above structures [1,2]. All piles have a combination of bearing and friction forces through which they transfer the load to the soil. It varies from one kind of soil to another. Rehabilitation and repairing of pile foundations is quite a difficult process. Therefore, strength, serviceability, economy, and constructability are all factors that must be taken into consideration while designing the structure [3]. With certain advantages of pile foundation, this field has evolved apparently in the construction area and some of its allied areas. In the early stages of its application, only static and vertical loading was considered. Later on, it has been examined and used for dynamic responses also [4,5]. Geotechnical parameters of soil, such as cohesion, internal friction angle, and many more, exhibit a high degree of variability and uncertainty and cannot be managed using typical deterministic design techniques [6]. Novak was the first to make an attempt to use continuum theory to understand the dynamic response of a single pile [7] and further proceeded with other theories [8]. Pile foundations without superstructures have been increasingly popular in seismic research in recent years [9]. Various methods have been developed for soil structure interaction examinations, such as the Winkler model [10–12] and

the plane strain model [13,14]. Furthermore, group of pile [15,16], combined pile [17,18], hybrid pile [19], pile subjected to lateral loads [20] owing to earthquakes, wind and water currents, traffic pressures, and soil conditions [21,22] and other advanced pile structures were developed after analysis by various researchers. Many of the recent studies on pile foundation are conducted by numerical modeling using various FEM software [23–25].

It is important to evaluate the growth trend in pile foundation research fully and quantitatively, as this can assist academic professionals in making educated decisions about their future studies. Additionally, it is difficult to organize, thoroughly summarize, and quantitatively assess the development trends and characteristics of a particular subject across a vast number of studies conducted over a lengthy period in typical review articles [26]. Pile foundation research, in particular, is an interdisciplinary field that encompasses environmental science [27], marine engineering [28], energy [29], economics, and other fields. Thus, bibliographic analysis is required to provide a full picture of pile foundation research.

In bibliometric analysis, statistical and mathematical methods are used to quantitatively evaluate various ways of distributing knowledge [30]. A research topic or field's intellectual structure and rising trends are presented by summarizing enormous amounts of data. Bibliometrics aims at a particular research area and scrutinizes the documentation produced, work conducted by each country, distribution of authors, changes in keywords, and spatiotemporal dynamics, which suggest the trends and reflect the direction of future research [31]. Thus, bibliometrics is widely used to analyze research publications [32], patents [33], international scientific and technological journals [34], institute and country collaborations [35], and other fields [36].

1.2. Research Focus

Bibliometric studies have the potential to facilitate the connection between scholarly research and the implementation of engineering practices, thereby addressing the gap in technology transfer and knowledge dissemination. Engineers can gain access to crucial knowledge for problem solving in the area of foundation and innovation by comprehending the papers that are most frequently cited and hold significant influence in their respective fields. The utilization of bibliometrics in engineering projects can facilitate the identification of pivotal technologies and methodologies that have exhibited significant influence within the field. This knowledge has the potential to inform and shape the process of pile foundation project planning and implementation, thereby increasing the likelihood of achieving successful outcomes.

2. Procedure of Analysis

The Web of Science Core Collection Database was used to conduct this investigation. Bibliometric analysis and science mapping are made possible with the use of tools such as MS Excel and VOS viewer. Using bibliometrics, the analysis was conducted on research on pile foundation from 1992 to 2021 based on various criteria such as number of publications, authors, collaboration, countries, and so on. The study included the geographical distribution of research areas and extensive analysis of authors, summarizing the trends of research globally in the last three decades. For the purpose of this study, the Science Citation Index (SCI) and the Science Citation Index Expanded (SCI-E) databases of the "Web of Science Core Collection" were used as object databases, and the search criterion is TS = ("PILE FOUNDATION" OR (("PILE *") AND ("FOUNDATION *"))). Records were extracted in a tab delimited file from the Web of Science. For each paper in the database, we scrutinized data based on the affiliations and initials of authors, language of publication, names of periodicals, year of publication, names of publishers, geographical locations, keywords, and the number of citations [37]. The citations and the number of publications may be slightly different because the data were collected at a specific time on 31 January 2022. New journals, issues, or articles may have been added to the index over the time period.

Furthermore, the retrieved database was refined to achieve the number of citations and the H-index of authors. The H-index indicates the authors' research quality and

academic impact. A high H-index signifies high productivity and impact [38]. If two or more researchers, institutions, and/or countries are involved in a collaborative study, their present research patterns can be examined using cooperative network analysis [39]. Finally, research directions for the future are mentioned.

3. Results

3.1. Type of Document

By using the Web of Science database based on research on pile foundation, we have found that a total of 4803 documents are present in the last three decades, which includes articles, review, abstract etc depicted in Figure 1. To be precise, as shown in Table 1 there are 4494 articles, 102 article proceedings papers, 88 early access articles, 70 reviews, 29 editorial materials, and three meeting abstracts.

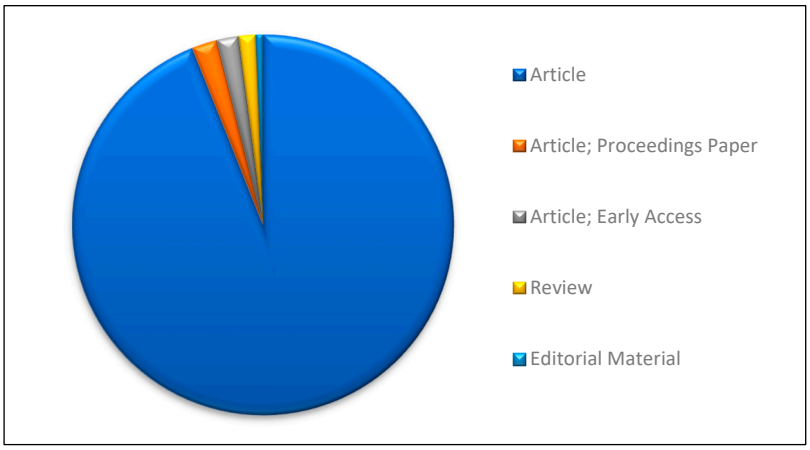

Figure 1. Pie chart representing the weightage of type of documents.

Table 1. Type of documents with number.

Document Type	N	%
Article	4494	93.5
Article, Proceedings Paper	102	2.1
Article, Early Access	88	1.8
Review	70	1.4
Editorial Material	29	0.6

N—number of documents, %—weightage with respect to total documents.

3.2. Features of Document Computed

With only 18 publications in 1991 to 644 publications in 2021, there has been a remarkable research increment (almost 35 times) in the field of pile foundation. Out of the total 4803 articles, there are 90 such articles that do not have any specified publication year. As shown in Figure 2, there is a marginal increase in the number of publications in the first two decades, i.e., 1992–2010, and then there is a thrust in the research area between 2010 and 2021. The length of a single publication in considered years ranges from 11 to 15 pages. As the research has gone wider in the area, so has the number of publications and, apparently the number of citations. The number of citations is one measure of a publication's scientific quality, since it signifies the publication's effect on the linked study area. In 2014, the total citation was 4991, which is the maximum and could be the reason for the rapid increment in the graph in the last decade. The low number of citations for the year 2021 signifies that the studies are new and will be cited in future studies to come. On the other hand, cited references have surged in every ten years, which shows the credibility, novelty, and usefulness of the publications published in previous years. The Table 2 contains the document information.

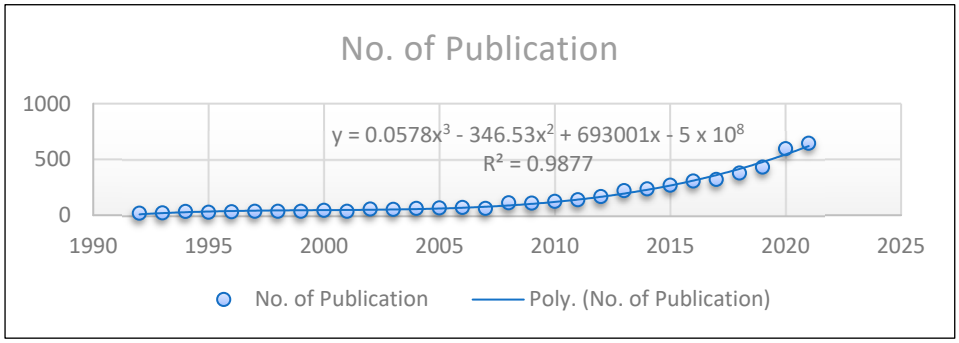

Figure 2. Graph with cumulative publications.

Table 2. Features of document year wise (1992–2021).

Years	P	PG	PG/P	CR	CR/P	TC	TC/P
1992	18	227	13	291	16	418	23
1993	21	267	13	350	17	371	18
1994	33	457	14	539	16	1124	34
1995	26	344	13	582	22	487	19
1996	31	362	12	1025	33	624	20
1997	34	434	13	622	18	1002	29
1998	35	373	11	603	17	916	26
1999	35	494	14	815	23	1184	34
2000	43	484	11	715	17	1529	36
2001	35	462	13	832	24	1674	48
2002	55	696	13	1136	21	1861	34
2003	52	674	13	1140	22	2066	40
2004	60	692	12	1230	21	1803	30
2005	65	932	14	1643	25	1922	30
2006	69	874	13	1431	21	3134	45
2007	61	697	11	1363	22	1728	28
2008	110	1322	12	2638	24	2482	23
2009	108	1380	13	2874	27	3495	32
2010	123	1398	11	3017	25	2846	23
2011	138	1698	12	3356	24	3081	22
2012	166	1964	12	4098	25	3182	19
2013	219	2632	12	5917	27	4362	20
2014	236	3002	13	7125	30	4991	21
2015	268	3334	12	8868	33	4797	18
2016	306	3901	13	9888	32	4388	14
2017	320	4296	13	11,616	36	4049	13
2018	377	5023	13	13,931	37	3759	10
2019	430	6044	14	16,314	38	2771	6
2020	595	8353	14	24,301	41	2444	4
2021	644	9393	15	26,053	40	636	1

P—number of publications, PG—pages, CR—cited references, TC—citations, PG/P—average number of pages, CR/P—average cited references, TC/P—average citations in a paper.

With the above tabled data, we have also performed a regression analysis (Figure 2) where it can be seen that the graph is accelerating in a fair manner, having R^2 value equal to 0.9877. Regression coefficients are estimations of unknown publication factors that characterize the relationship between a predictor and a response variable. R^2 coefficient of determination is a statistical measure of how well regression predictions approach the observed data points in regression. R^2 value of 1 shows that the regression predictions fit the data exactly.

3.3. Subject Category, Journals and Publishers

The data were also categorized and differentiated based on the subject category in which the documents fell. The number of subject categories in which documents were taken is 10, considering significant numbers had a percentage higher than five. Pile foundation research has been conducted extensively in various fields of science, such as geology, material science, civil engineering, oceanography, and many more. Out of the several fields, the 'Geological' engineering field has the maximum number of publications with 2264 publications, followed by 'Geosciences' with 1608, 'Civil' engineering with 1493, 'Construction and Building Technology' with 426 and so on. In Table 3, the 'Geological' engineering category has more than half the publications as compared to the core civil engineering category, which is at third position. The presence of 'Computer Science' in the list reveals the diffusion of software in the field of construction as well. Many of the current studies use various numerical modeling software to analyze and design the structures.

Table 3. Top 10 subject categories with respective number of publications.

Subject Category	TP	R	%
Geological	2264	1	47.14
Geosciences	1608	2	33.48
Civil	1493	3	31.08
Construction and Building Technology	426	4	8.87
Ocean	402	5	8.37
Materials Science	348	6	7.25
Oceanography	323	7	6.72
Mechanical	303	8	6.31
Computer Science	295	9	6.14
Mechanics	264	10	5.50

TP—Total number of publications, R—Ranking as per number of publications, %—Percentage of publication.

While analyzing the documents from 1992 to2021, out of the top 20 journals, "Soil Dynamics and Earthquake Engineering" is featured with a maximum of 294 publications, while "Journal of Geotechnical and Geoenvironmental Engineering" follows the table with 253 publications. Software evolution in the field of construction and allied areas insists researchers to publish articles in the concerned journals, which can be seen in the table having "Computers and Geotechnics" on the third position with more than 200 publications.

"Proceedings of The Institution of Civil Engineers-Geotechnical Engineering" and "Soils and Foundations" have the same rank as they both have the same number of publications, i.e., 133. "Geotechnique" has highest TC/TP ratio (52.6), on the other hand "Journal of Geotechnical and Geoenvironmental Engineering" being on the second rank has a maximum number of citations which is 7711. Table 4 shows the 20 most productive journals, with ranking corresponding to their number of publications. IF represents the impact factor of the respective journal taken from JCR. Impact factor is a measurement of the frequency with which the average article in a journal has been referenced in a specific duration, hence the higher the impact factor, the more the citation of a publication or journal, subsequently reaching a greater extent.

Out of a total of 4803 publications published in a specified duration of three decades, 3666 publications (more than 75%) are published by the top 20 publishers. Publication "Elsevier SCI LTD" is at the top with 763 publications (15.9% of total publications), followed by "ASCE-AMER SOC Civil Engineers" with 591 publications (12.3% of total publications). These two are the only publishers whose percentage of publications is greater than 10% in the pile foundation stream. The rest of the publishers have a lower percentage of publications, ranging from 7 to 1% only. On the contrary, "Elsevier Science BV", being on the 17th position, has the highest ratio (24.31) of citations. Details in Table 5 is showing twenty most active publishers in the field.

Table 4. Top twenty journals that publish pile foundation related studies.

Journal Name	TP (R)	TC	TC/TP	IF
Soil Dynamics and Earthquake Engineering	294 (1)	5573	19.0	3.718
Journal of Geotechnical and Geoenvironmental Engineering	253 (2)	7711	30.5	4.012
Computers and Geotechnics	205 (3)	4124	20.1	4.956
Canadian Geotechnical Journal	169 (4)	3759	22.2	3.725
Ocean Engineering	135 (5)	1433	10.6	3.795
Proceedings of The Institution of Civil Engineers-Geotechnical Engineering	133 (6)	1278	9.6	1.341
Soils and Foundations	133 (6)	2372	17.8	2.436
International Journal of Geomechanics	120 (7)	1396	11.6	3.819
Géotechnique	105 (8)	5518	52.6	4.592
Advances in Civil Engineering	98 (9)	193	2.0	1.924
Marine Georesources and Geotechnology	91 (10)	450	4.9	2.673
Engineering Structures	84 (11)	1180	14.0	4.471
International Journal for Numerical and Analytical Methods in Geomechanics	72 (12)	2279	31.7	4.264
Geomechanics and Engineering	71 (13)	440	6.2	3.223
Soil Mechanics and Foundation Engineering	69 (14)	141	2.0	0.806
Geotechnical Testing Journal	62 (15)	575	9.3	1.469
Acta Geotechnica	60 (16)	774	12.9	5.856
KSCE Journal of Civil Engineering	59 (17)	381	6.5	1.805
Journal of Bridge Engineering	57 (18)	785	13.8	3.066
Bautechnik	52 (19)	135	2.6	0.408

TC—citations, TC/TP—average citations, IF—Impact factor.

Table 5. Twenty most active publishers in the pile foundation field.

Publisher	TP	(%)	TC	TC/TP
Elsevier Sci Ltd.	763	15.9	14,360	18.82
ASCE	591	12.3	12,757	21.59
Pergamon-Elsevier Science Ltd.	335	7.0	7019	20.95
Ice Publishing	265	5.5	4704	17.75
Springer	206	4.3	2131	10.34
Hindawi Ltd.	179	3.7	426	2.38
MDPI	165	3.4	638	3.87
Springer Heidelberg	147	3.1	1018	6.93
Japanese Geotechnical Soc	133	2.8	2372	17.83
Techno-Press	113	2.4	723	6.40
Taylor & Francis Ltd.	102	2.1	688	6.75
Taylor & Francis Inc.	101	2.1	534	5.29
Wiley	96	2.0	1354	14.10
Amer Soc Testing Materials	80	1.7	608	7.60
Elsevier	76	1.6	871	11.46
Canadian Science Publishing, NRC Research Press	72	1.5	1588	22.06
Elsevier Science BV	65	1.4	1580	24.31
Ernst & Sohn	62	1.3	117	1.89
Korean Society of Civil Engineers-KSCE	58	1.2	372	6.41
Canadian Science Publishing	57	1.2	875	15.35

3.4. Author and Language

While examining the author yield in this particular area of research, it has been seen that the author "El Naggar MH" has topped the list with 59 publications, followed by him "Liu HL" has a total of 39 publications. Ratio CP/TP indicates the relation between collaborative and total publication. Table 6 shows that 19 out of 20 top authors have published their articles collaboratively. Surprisingly, there is only a single author (Liang, FY) who has published an individual publication. Many of the authors have published the same number of articles, hence it is not easy and righteous to rank them. Sometimes

the H-index is the proper criterion to identify authors' yield and valuable contribution in a particular field. Based on this criterion, the author "Randolph, MF" has contributed pre-eminently in the field of pile foundation with an H-index of 68. Apart from him, "Ng, CWW", "Gazetas, G", and "Zhang, LM" are some other authors having an H-index of more than or equal to 50. Figure 3 depicts the total publications of each author in the form of the intensity of color in the picture; the dark yellow color indicates a high number of publications. The present picture is obtained with the help of the VOS viewer application.

Table 6. Ten most productive authors of pile foundation related research.

Author	TP	(%)	IP	CP	CP/TP	H-Index
El Naggar, MH	59	1.23	0	59	1	19
Liu, HL	39	0.81	0	39	1	39
Bhattacharya, S	28	0.58	0	28	1	29
Aznarez, JJ	27	0.56	0	27	1	16
Randolph, MF	26	0.54	0	26	1	68
Ling, XZ	26	0.54	0	26	1	19
Ding, XM	26	0.54	0	26	1	20
Maeso, O	25	0.52	0	25	1	17
Wang, KH	24	0.50	0	24	1	16
Huang, MS	24	0.50	0	24	1	30
Jeng, DS	22	0.46	0	22	1	43
Kong, GQ	20	0.42	0	20	1	24
Laloui, L	20	0.42	0	20	1	45
Ng, CWW	19	0.40	0	19	1	50
Ibsen, LB	19	0.40	0	19	1	18
Gazetas, G	19	0.40	0	19	1	50
Liang, FY	18	0.37	1	17	0.95	15
Zhang, LM	18	0.37	0	18	1	51
Zhang, F	18	0.37	0	18	1	26
Sritharan, S	18	0.37	0	18	1	23

TP—Total number of publications, IP—Individual-author publications, CP—Collaboration publications.

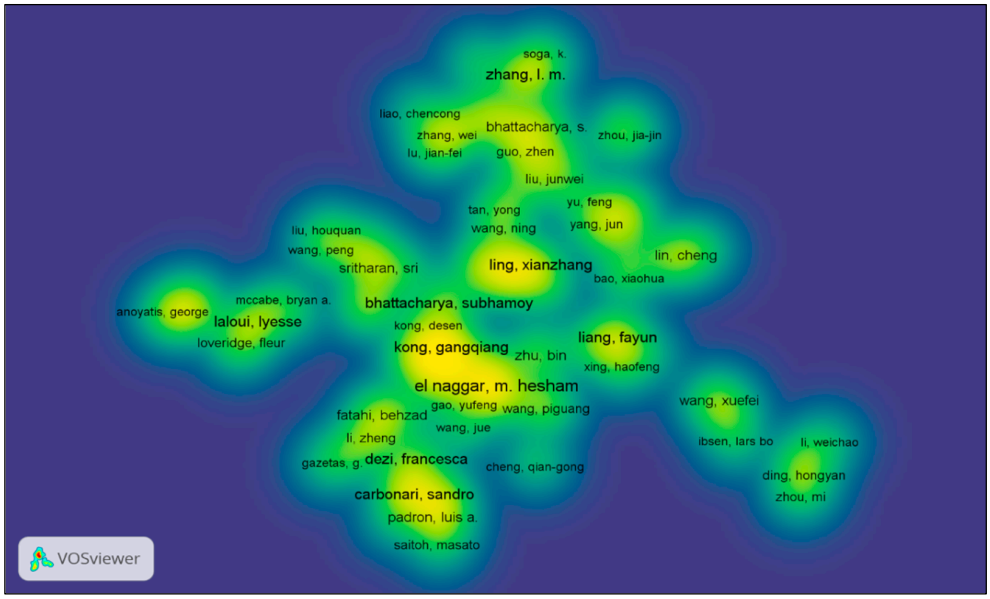

Figure 3. Intensity of authors according to number of publications.

As it is known that English is the most acceptable language across the globe, the maximum number of documents published are in English. Out of 4803 documents, 4683 are in English (approx. 97%), followed by German with 87 documents, 11 in Spanish, six in Turkish and four in Japanese, and a few documents in Portuguese, Croatian, French, Czech,

Polish, Finnish, Chinese, and Russian languages. Top five languages with corresponding number of documents are shown in Table 7 and with a share depiction in Figure 4.

Table 7. Top five languages used in published articles.

Language	N
English	4683
German	87
Spanish	11
Turkish	6
Japanese	4

N—Number of Documents.

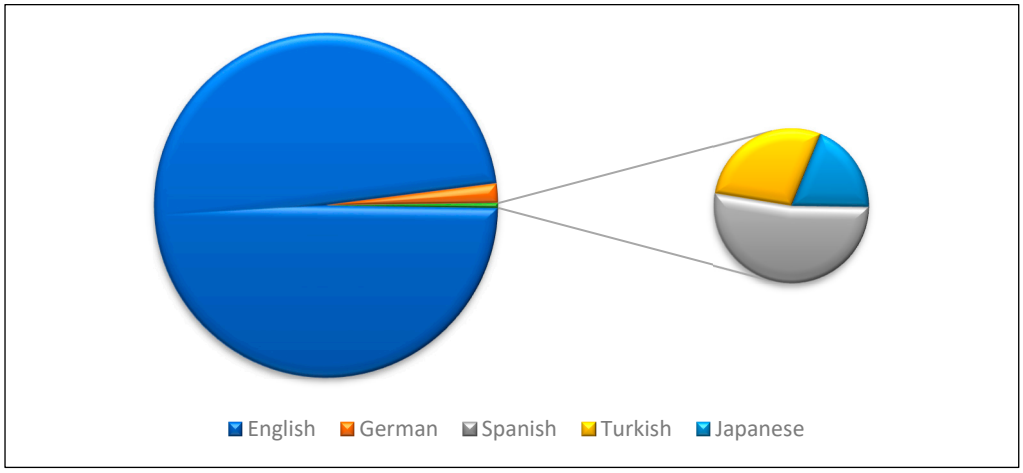

Figure 4. Weightage of languages in overall publications.

3.5. Author Keyword

Author keywords were extracted and segmented for every decade separately to understand the usage and coverage of each keyword in different times, i.e., 1992–2001, 2002–2011, and 2012–2021. In total, we found 2142 keywords from 1992 to 2021, which was for the last three decades considered in this study. 'Pile', being the most widely used word is on the top position all through three decades as certain as it is, while 'pile foundation' improved its position in the second decade, keeping it for the next decade, while also positioning itself as second in the overall analysis. It can be clearly seen that as research on pile foundation increased in the last decade of consideration, similarly, the occurrence of keywords increased exponentially in this period. Word 'Monopile' is practiced interestingly, with 0 in first to 103 in last decade. In Figure 5, each term is represented by a circle on the map. The figure depicts the co-occurrence of a keyword in extracted publications at a minimum of five times. The diameter of the circle shows the number of links between the two keywords. As a result, a wider circle indicates more connections with other keywords. Between two circles, the thickness of the line represents the frequency with which the words are used together. Table 8 shows the usage of each keyword with respect to the different decades, and Figure 6 presents the temporal analysis of these keywords for three decades.

3.6. Ten Most Cited Articles in Pile Foundation Research

Table 9 shows the articles that are most cited in the pile foundation field for the selected duration of this study. The "Energy foundations and other thermo-active ground structures" [40] article is the most cited with a total citation of 684. The article was published in the year 2006 and is still quite useful and relevant for current studies as it is citated 258 times in the last ten years. "Seismic soil-pile-structure interaction experiments and analyses" [41] is the second oldest article in the list and has the second most citations with 441 times, whereas "Axisymmetrical time-domain transmitting boundaries" is the oldest article [42] and "Response of stiff piles in sand to long-term cyclic lateral loading" [43] is

the newest article with 331 and 275 citations, respectively. An analysis of the tabled data reflects that energy related work and dynamics in pile foundations are dominant in these years. Total citation data were collected with respect to all of the databases retrieved from the Web of Science [44–49].

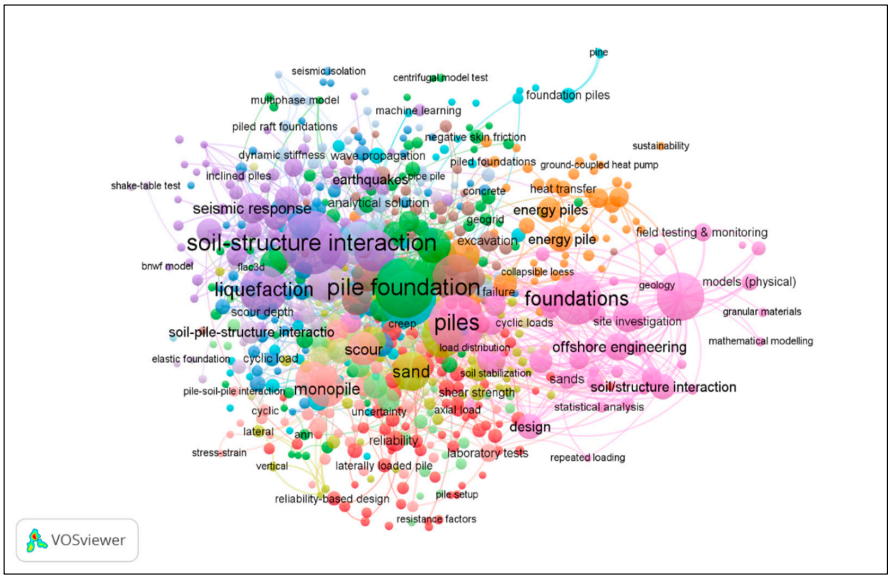

Figure 5. Keyword analysis map.

Table 8. Top ten keywords with temporal differentiation for each decade.

Keywords	1992–2021	1992–2001	2002–2011	2012–2021
Pile	431	48	114	269
Pile foundation	360	16	87	257
Soil structure interaction	292	19	67	206
Foundation	248	17	76	155
Pile group	159	5	46	108
Settlement	153	16	28	109
Liquefaction	152	5	39	108
Sand	125	6	22	97
Bearing capacity	115	9	17	89
Monopile	107	0	4	103

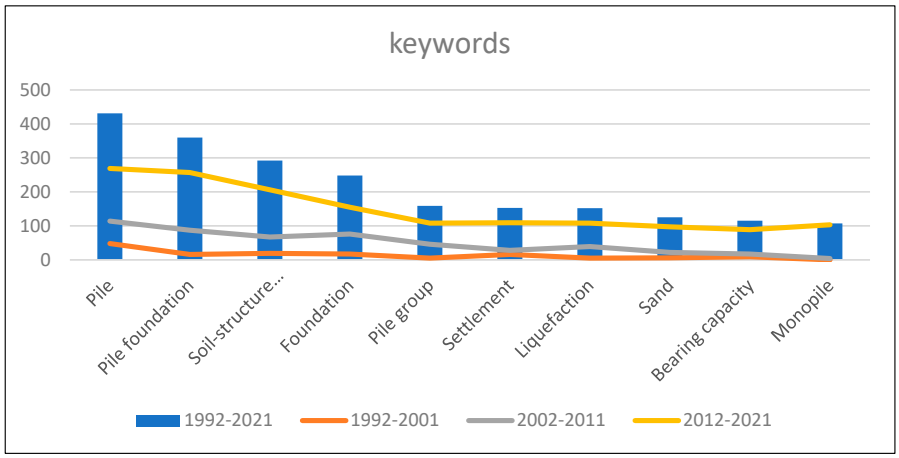

Figure 6. Temporal analysis of keywords.

Table 9. Ten most productive articles.

Article	TC	Citation in Last 10 Years	PY
Energy foundations and other thermo-active ground structures	684	258	2006
Seismic soil-pile-structure interaction experiments and analyses	441	127	1999
Experimental and numerical investigations of the behavior of a heat exchanger pile	413	109	2006
Science and empiricism in pile foundation design	410	176	2003
Energy pile test at Lambeth College, London: Geotechnical and thermodynamic aspects of pile response to heat cycles	385	141	2009
Axisymmetrical time-domain transmitting boundaries	331	34	1994
Piled raft foundations: Design and applications	282	49	2001
Response of stiff piles in sand to long-term cyclic lateral loading	275	138	2010
Behavior of monopile foundations under cyclic lateral load	244	152	2009
A new model and analytical solutions for borehole and pile ground heat exchangers	213	61	2010

TC—Total Citation, PY—Publication Year.

3.7. Countries Involved

The People's Republic of China is leading the way as far as the number of publications is considered, with 1672 total publications in the last three decades, followed by the USA with 739 publications, which is less than half of the earlier one. Though total citation is highest for the country having the highest number of publications, the ratio of citation to publication is led by Australia (TC/TP = 24.30), even if its ranking is fourth out of the top 10 nations worldwide as reflects in Table 10. The data show that analysis on pile foundation is conducted in abundance by Asian countries, since the top 10 countries consist of five Asian countries, and two countries from the European and American continents. If the top two countries are excluded then the rest of the countries have less than 10 percent of publications individually, considering the total publication. Ironically, South Korea spends 4.53% of its GDP on research and development, just managing to be in the table of the top ten productive countries in our concerned area. India, being a developing nation is spending only 0.65% of its GDP on R&D [50,51]. Here, one matter of fact should be brought to attention, which is that 113 countries' data are missing, or can be said that it is not declared in the given data.

While creating a graphical representation on VOS viewer software (version 1.6.17), the minimum number of documents for considering any country is taken as three and the minimum number of citations for a country is taken as five, where out of 91 countries, 68 meet the thresholds. A VOS viewer created network diagram is shown in Figure 7, which designates different countries and collaboration. The size or intensity of the circle represents the quantity of publications of a respective country, and the intensity of the link represents collaboration between the countries.

3.8. Sustainablity in Focus

Recently, sustainability has become an increasingly important factor in all aspects of infrastructure development, but especially in the installation of pile foundations. Eco-friendly procedures that lessen the infrastructure's negative effects on the environment and boost its long-term viability are becoming increasingly important as the need for such projects rises. Significant developments have been made to improve the sustainability of pile foundations. The carbon footprint of building has decreased because to engineers' increased emphasis on eco-friendly materials like recycled steel and concrete [52,53]. Precast piles, another cutting-edge building method, are rising in popularity due to their efficiency

and lower waste output. Environmental issues are taken into account in sustainable pile foundation designs to provide maximum energy efficiency and little impact to local ecosystems. Sustainable approaches included into pile foundation construction not only increase the infrastructure's durability, but also pave the way for a more environmentally friendly and long-lasting future. The most influential journals and publishers that have covered sustainable development in infrastructure projects in the recent past are shown in Table 11. Table 11 shows the journals, their publishers, year of publication and citations of respective papers. It can be seen that after the year 2010 there has been substantial progress in the area of suitable development and its research, which can be inferred by the increasing number of citations also, rising from 21 citations of a paper from "Water Resource Management" journal in 2011 to 68 citations of a paper from "Processes" in 2020.

3.9. Significance of the Analysis

Bibliometric research possesses inherent scientific significance and engineering application value, owing to its distinctive contributions to the realms of academia and practical industries. The evaluation of research impact can be achieved through bibliometric research, which provides a quantitative assessment of the influence of research papers, journals, or individual researchers. Through the examination of citation patterns and other bibliometric indicators, scholars are able to assess the impact and significance of scientific publications, thereby offering valuable insights into the caliber and importance of research output. The assessment of research productivity is facilitated by bibliometrics, which enables the evaluation of researchers, institutions, or countries based on their scientific output. Comparisons and benchmarking are facilitated by this process, thereby assisting funding agencies and policymakers in making well-informed decisions regarding the allocation of research funding.

Bibliometric analyses have the capacity to unveil collaborative networks among researchers and institutions through the process of mapping. The comprehension of how knowledge dissemination and interdisciplinary collaborations contribute to scientific advancements is of utmost importance. Resource allocation is a crucial aspect in engineering disciplines, and bibliometrics plays a significant role in facilitating the efficient distribution of resources. Through the process of identifying areas of active research and prominent researchers, institutions and companies are able to strategically allocate their efforts and investments towards projects that are both relevant and impactful.

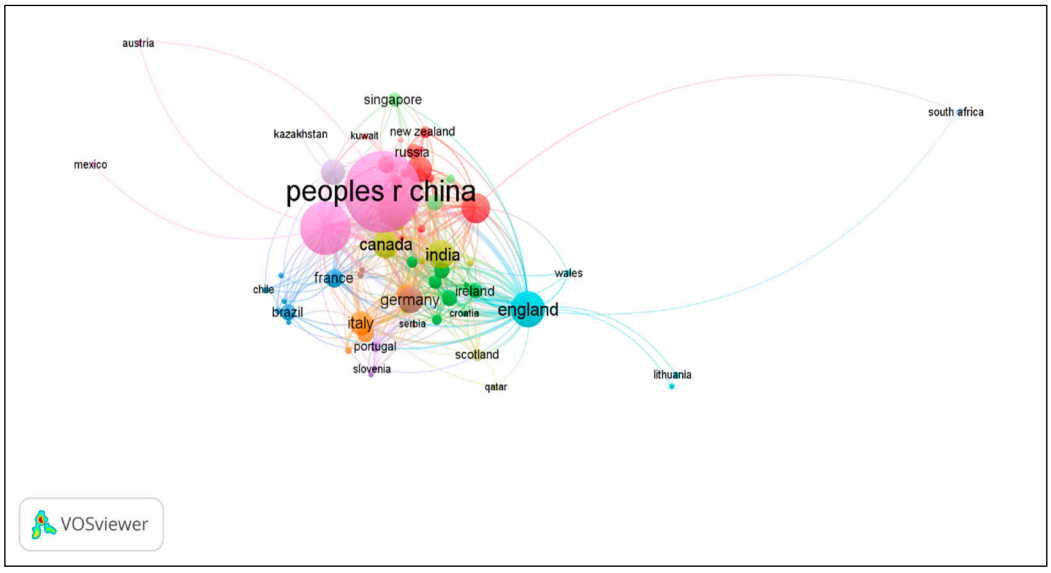

Figure 7. Intensity and collaboration of countries.

Table 10. Ten most productive countries/territories conducting pile foundation related research.

Countries/Regions	TP	TC	TC/TP	%	GDP (in Trillion $)	% of GDP on R&D
People's Republic of China	1672	16,279	9.74	34.81	13.4	2.14
USA	739	12,305	16.65	15.39	20.49	2.83
England	344	6427	18.68	7.16	2.83	1.70
Australia	303	7363	24.30	6.31	1.33	1.87
Japan	247	4685	18.97	5.14	4.97	3.28
India	237	2965	12.51	4.93	2.72	0.65
Canada	212	3510	16.56	4.41	1.71	1.54
Germany	203	2373	11.69	4.23	4.00	3.13
Iran	191	2678	14.02	3.98	0.61	0.83
South Korea	180	2094	11.63	3.75	1.58	4.53

TP—Total number of publications, TC—Total number of citations, TC/TP—Average number of citations in a publication, GDP—Gross domestic production of country.

Table 11. Most promising journals and publishers conducting sustainable pile foundation related research.

S.No.	Source Title	Publisher	Publication Year	Cited Reference Count
1	Applied Acoustics	Elsevier Sci Ltd.	2003	19
2	Water Science and Technology	IWA Publishing	2006	5
3	Water Resources Management	Springer	2011	21
4	Journal Of Water Supply Research and Technology-Aqua	IWA Publishing	2013	24
5	Water Science and Technology	IWA Publishing	2014	25
6	Clean-Soil Air Water	Wiley	2014	25
7	Expert Systems with Applications	Pergamon-Elsevier Science Ltd.	2014	52
8	Materiales De Construccion	Consejo Superior Investigaciones Cientificas-Csic	2015	41
9	Construction And Building Materials	Elsevier Sci Ltd.	2016	10
10	Advances In Applied Ceramics	Taylor & Francis Ltd.	2017	11
11	Journal of Cleaner Production	Elsevier Sci Ltd.	2018	54
12	Proceedings of the Institution of Civil Engineers-Water Management	ICE Publishing	2018	34
13	Processes	MDPI	2020	68
14	Sustainability	MDPI	2021	19
15	Building And Environment	Pergamon-Elsevier Science Ltd.	2021	41

4. Discussion and Conclusions

In the present article, bibliometric analysis has been applied to the pile foundation literature, allowing for a more accurate classification of prior studies, and facilitating the projection of future work in the field. Using bibliometric analysis, one can look at a wide range of patterns in the existing research, including those between authors, collaboration

networks, countries, journals, and keywords. In this article, we present an up-to-date assessment of the research trends in pile foundation based on a bibliometric study of publications published between 1992 and 2021, from a global perspective to a detailed profile.

According to the statistical findings,

1. There has been a huge increase in pile foundation research over the past three decades, with China accounting for nearly 35% of all publications.
2. Research on pile foundations developed rapidly after 2008 and is accelerating exponentially, which shows the severity and importance of pile foundations in modern infrastructure taking place around the globe.
3. As the research on pile foundation has increased in the last decade, every individual area, i.e., soil structure interaction, pile group, settlement, liquefaction, monopile, etc., has been touched extensively by researchers.
4. The People's Republic of China allocates around 2.14% of its GDP for R&D has nearly 35% of total publications, whereas South Korea allocates the highest 4.53% for R&D, out of the top productive countries considered in the study.
5. Based on current trends, it is evident that future research on pile foundation will prioritize sustainable development.
6. It can be mentioned that future studies will be focused on the dynamics of pile foundations and software involvement with artificial intelligence.

The reliance of bibliometric analysis on pile foundation research is predominantly centered on quantitative data. This type of analysis primarily emphasizes citation counts and other quantitative metrics as indicators of the impact of research in this field. Retrospective studies inherently possess a retrospective nature, as they heavily rely on historical data. The present bibliometric analysis can play a crucial role in the identification of emerging research trends and areas of interest within a pile foundation discipline. Through the examination of publication patterns and the identification of co-occurring keywords, scholars can accurately identify domains experiencing rapid expansion or diminishing interest. This analytical approach facilitates a more comprehensive understanding of the present status and prospective trajectories of a particular field.

Author Contributions: Conceptualization, A.T.; methodology, A.T.; software, A.T.; resources, N.D.; data curation, A.T.; writing—original draft preparation, A.T.; writing—review and editing, A.T.; supervision, N.D. and S.K. All authors have read and agreed to the published version of the manuscript.

Funding: This research received no external funding.

Informed Consent Statement: Not applicable.

Data Availability Statement: The data presented in this study is retrieved from the Web of Science database.

Conflicts of Interest: The authors declare no conflict of interest.

References

1. Bea, R.G.; Jin, Z.; Valle, C.; Ramos, R. Evaluation of reliability of platform pile foundations. *J. Geotech. Geoenviron. Eng.* **1999**, *125*, 696–704. [CrossRef]
2. Tang, W.H.; Kulhawy, F.H. Uncertainties in Offshore Axial Pile Capacity. In *Foundation Engineering*; ASCE: Reston, VA, USA, 1989; pp. 833–847.
3. Magade, S.B.; Ingle, R.K. Analysis methods for pile foundation: A critical review of the literature and recommended suggestions. *Innov. Infrastruct. Solut.* **2021**, *6*, 1–11. [CrossRef]
4. Pender, M.J. Aseismic pile foundation design analysis. *Bull. New Zealand Soc. Earthq. Eng.* **1993**, *26*, 49–160. [CrossRef]
5. Vugts, J.H.; Dob, S.L.; Harland, L.A. The extreme dynamic response of bottom supported structures using an equivalent quasi-static design wave procedure. *Appl. Ocean. Res.* **1998**, *20*, 37–53. [CrossRef]
6. Liang, R.Y.; Nusier, B.O.; Malkawi, A.H. A reliability based approach for evaluating the slope stability of embankment dams. *Eng. Geol.* **1999**, *54*, 271–285. [CrossRef]
7. Novak, M. Dynamic stiffness and damping of piles. *Can. Geotech. J.* **1974**, *11*, 574–598. [CrossRef]
8. Zheng, C.; Ding, X.; Sun, Y. Vertical vibration of a pipe pile in viscoelastic soil considering the three-dimensional wave effect of soil. *Int. J. Geomech.* **2016**, *16*, 04015037. [CrossRef]

9. Zhao, M.; Huang, Y.; Wang, P.; Cao, Y.; Du, X. An analytical solution for the dynamic response of an end-bearing pile subjected to vertical P-waves considering water-pile-soil interactions. *Soil Dyn. Earthq. Eng.* **2022**, *153*, 107126. [CrossRef]
10. Di Laora, R.; Mandolini, A.; Mylonakis, G. Insight on kinematic bending of flexible piles in layered soil. *Soil Dyn. Earthq. Eng.* **2012**, *43*, 309–322. [CrossRef]
11. Anoyatis, G.; Di Laora, R.; Mandolini, A.; Mylonakis, G. Kinematic response of single piles for different boundary conditions: Analytical solutions and normalization schemes. *Soil Dyn. Earthq. Eng.* **2013**, *44*, 183–195. [CrossRef]
12. Anoyatis, G.; Lemnitzer, A. Kinematic Winkler modulus for laterally-loaded piles. *Soils Found.* **2017**, *57*, 453–471. [CrossRef]
13. Ke, W.; Zhang, C. A closed-form solution for kinematic bending of end-bearing piles. *Soil Dyn. Earthq. Eng.* **2017**, *103*, 15–20. [CrossRef]
14. Zhang, C.; Deng, P.; Ke, W. Assessing physical mechanisms related to kinematic soil-pile interaction. *Soil Dyn. Earthq. Eng.* **2018**, *114*, 22–26. [CrossRef]
15. Xu, Q.; Zhu, H.; Ma, X.; Ma, Z.; Li, X.; Tang, Z.; Zhuo, K. A case history of shield tunnel crossing through group pile foundation of a road bridge with pile underpinning technologies in Shanghai. *Tunn. Undergr. Space Technol.* **2015**, *45*, 20–33. [CrossRef]
16. Yan, K.; He, J.; Cheng, Q.; Fan, G.; Wang, Z.; Zhang, J. A centrifugal experimental investigation on the seismic response of group-pile foundation in a slope with an inclined weak intercalated layer. *Soil Dyn. Earthq. Eng.* **2020**, *130*, 105961. [CrossRef]
17. Bhaduri, A.; Choudhury, D. Steady-state response of flexible combined pile-raft foundation under dynamic loading. *Soil Dyn. Earthq. Eng.* **2021**, *145*, 106664. [CrossRef]
18. Chanda, D.; Saha, R.; Haldar, S. Behaviour of piled raft foundation in sand subjected to combined VMH loading. *Ocean Engineering.* **2020**, *216*, 107596. [CrossRef]
19. Li, L.; Liu, H.; Wu, W.; Wen, M.; El Naggar, M.H.; Yang, Y. Investigation on the behavior of hybrid pile foundation and its surrounding soil during cyclic lateral loading. *Ocean. Eng.* **2021**, *240*, 110006. [CrossRef]
20. Matlock, H.; Reese, L.C. Generalized solutions for laterally loaded piles. *Trans. Am. Soc. Civ. Eng.* **1962**, *127*, 1220–1248. [CrossRef]
21. Randolph, M.F. The response of flexible piles to lateral loading. *Geotechnique* **1981**, *31*, 247–259. [CrossRef]
22. Rollins, K.M.; Peterson, K.T.; Weaver, T.J. Lateral load behavior of full-scale pile group in clay. *J. Geotech. Geoenviron. Eng.* **1998**, *124*, 468–478. [CrossRef]
23. Khari, M.; Dehghanbandaki, A.; Armaghani, D.J. Physical modelling of bending moments in single piles under combined loads in layered soil. *Geomech. Eng.* **2021**, *25*, 373. [CrossRef]
24. Lv, Y.; Liu, H.; Ng, C.W.; Ding, X.; Gunawan, A. Three-dimensional numerical analysis of the stress transfer mechanism of XCC piled raft foundation. *Comput. Geotech.* **2014**, *55*, 365–377. [CrossRef]
25. Mendonca, A.V.; Paiva, J.B. An elastostatic FEM/BEM analysis of vertically loaded raft and piled raft foundation. *Eng. Anal. Bound. Elem.* **2003**, *27*, 919–933. [CrossRef]
26. Zeng, J.; Qu, J.; Ma, H.; Gou, X. Characteristics and Trends of household carbon emissions research from 1993 to 2019: A bibliometric analysis and its implications. *J. Clean. Prod.* **2021**, *295*, 126468. [CrossRef]
27. Björdal, C.G.; Elam, J. Bacterial degradation of nine wooden foundation piles from Gothenburg historic city center and correlation to wood quality, environment, and time in service. *Int. Biodeterior. Biodegrad.* **2021**, *164*, 105288. [CrossRef]
28. Li, L.; Gong, W.; Li, J. Service life of prestressed high-strength concrete pile in marine environment considering effects of concrete stratification and temperature. *Constr. Build. Mater.* **2020**, *253*, 119233. [CrossRef]
29. Yu, Q.; Yu, H.; Zhou, L.; Meng, A.; Hu, X.; Hou, X. Structural energy transfer to the elevated pile-cap foundation of an offshore wind turbine based on extracted transfer path analysis. *J. Sound Vib.* **2021**, *512*, 116388. [CrossRef]
30. Rahman, M.; Haque, T.L.; Fukui, T. Research Articles Published in Clinical Radiology Journals: Trend of Contribution from Different Countries1. *Acad. Radiol.* **2005**, *12*, 825–829. [CrossRef]
31. Wang, Z.; Zhao, Y.; Wang, B. A bibliometric analysis of climate change adaptation based on massive research literature data. *J. Clean. Prod.* **2018**, *199*, 1072–1082. [CrossRef]
32. Peng, Y.; Lin, A.; Wang, K.; Liu, F.; Zeng, F.; Yang, L. Global trends in DEM-related research from 1994 to 2013: A bibliometric analysis. *Scientometrics* **2015**, *105*, 347–366. [CrossRef]
33. Narin, F. Patent bibliometrics. *Scientometrics* **1994**, *30*, 147–155. [CrossRef]
34. Dastidar, P.G.; Kumar, J.D. Content analysis of documents using neural networks: A study of antarctic science research articles published in international journals. *Adv. Polar Sci.* **2012**, *23*, 41–46. [CrossRef]
35. Mindeli, L.E.; Markusova, V.A. Bibliometric studies of scientific collaboration: International trends. *Autom. Doc. Math. Linguist.* **2015**, *49*, 59–64. [CrossRef]
36. Rajendram, R.; Lewison, G.; Preedy, V.R. Worldwide alcohol-related research and the disease burden. *Alcohol Alcohol.* **2006**, *41*, 99–106. [CrossRef]
37. Zhao, Y.; Jiang, Y.; Zhou, Z.; Yang, Z. Global trends in karst-related studies from 1990 to 2016: A bibliometric analysis. *Alex. Eng. J.* **2021**, *60*, 2551–2562. [CrossRef]
38. Zhai, L.; Yan, X.; Zhu, B. The h l-index: Improvement of h-index based on quality of citing papers. *Scientometrics* **2014**, *98*, 1021–1031. [CrossRef]
39. Powell, W.W.; Koput, K.W.; Smith-Doerr, L. Interorganizational collaboration and the locus of innovation: Networks of learning in biotechnology. *Adm. Sci. Q.* **1996**, *1*, 16–45. [CrossRef]
40. Brandl, H. Energy foundations and other thermo-active ground structures. *Géotechnique* **2006**, *56*, 81–122. [CrossRef]

41. Boulanger, R.W.; Curras, C.J.; Kutter, B.L.; Wilson, D.W.; Abghari, A. Seismic soil-pile-structure interaction experiments and analyses. *J. Geotech. Geoenviron. Eng.* **1999**, *125*, 750–759. [CrossRef]
42. Deeks, A.J.; Randolph, M.F. Axisymmetric time-domain transmitting boundaries. *J. Eng. Mech.* **1994**, *120*, 25–42. [CrossRef]
43. LeBlanc, C.; Houlsby, G.T.; Byrne, B.W. Response of stiff piles in sand to long-term cyclic lateral loading. *Géotechnique* **2010**, *60*, 79–90. [CrossRef]
44. Laloui, L.; Nuth, M.; Vulliet, L. Experimental and numerical investigations of the behaviour of a heat exchanger pile. *Int. J. Numer. Anal. Methods Geomech.* **2006**, *30*, 763–781. [CrossRef]
45. Randolph, M.F. Science and empiricism in pile foundation design. *Géotechnique* **2003**, *53*, 847–875. [CrossRef]
46. Bourne-Webb, P.J.; Amatya, B.; Soga, K.; Amis, T.; Davidson, C.; Payne, P. Energy pile test at Lambeth College, London: Geotechnical and thermodynamic aspects of pile response to heat cycles. *Géotechnique* **2009**, *59*, 237–248. [CrossRef]
47. Poulos, H.G. Piled raft foundations: Design and applications. *Géotechnique* **2001**, *51*, 95–113. [CrossRef]
48. Achmus, M.; Kuo, Y.S.; Abdel-Rahman, K. Behavior of monopile foundations under cyclic lateral load. *Comput. Geotech.* **2009**, *36*, 725–735. [CrossRef]
49. Man, Y.; Yang, H.; Diao, N.; Liu, J.; Fang, Z. A new model and analytical solutions for borehole and pile ground heat exchangers. *Int. J. Heat Mass Transf.* **2010**, *53*, 2593–2601. [CrossRef]
50. The World Bank, Research and Development Expenditure (%GDP). Available online: https://data.worldbank.org/indicator/GB.XPD.RSDV.GD.ZS (accessed on 20 April 2022).
51. World GDP Ranking 2020, Data and Charts. Available online: https://knoema.com/nwnfkne/world-gdp-ranking-2020-gdp-by-country-data-and-charts (accessed on 20 April 2022).
52. Wang, C.; Xiao, J.; Liu, W.; Ma, Z. Unloading and reloading stress-strain relationship of recycled aggregate concrete reinforced with steel/polypropylene fibers under uniaxial low-cycle loadings. *Cem. Concr. Compos.* **2022**, *131*, 104597. [CrossRef]
53. Wang, C.; Wu, H.; Li, C. Hysteresis and damping properties of steel and polypropylene fiber reinforced recycled aggregate concrete under uniaxial low-cycle loadings. *Constr. Build. Mater.* **2022**, *319*, 126191. [CrossRef]

Disclaimer/Publisher's Note: The statements, opinions and data contained in all publications are solely those of the individual author(s) and contributor(s) and not of MDPI and/or the editor(s). MDPI and/or the editor(s) disclaim responsibility for any injury to people or property resulting from any ideas, methods, instructions or products referred to in the content.

sustainability

MDPI

Review

The State of the Art and New Insight into Combined Finite–Discrete Element Modelling of the Entire Rock Slope Failure Process

Huaming An [1], Yuqing Fan [2], Hongyuan Liu [3], Yinyao Cheng [1,3,*] and Yushan Song [1]

[1] Faulty of Public Security and Emergency Management, Kunming University of Science and Technology, Kunming 650093, China; huaming.an@kust.edu.cn (H.A.); yushan.song@stu.kust.edu.cn (Y.S.)
[2] School of Mining Engineering, Guizhou University of Engineering Science, Bijie 551700, China; yuqingfanfan@gmail.com
[3] College of Science and Engineering, University of Tasmania, Hobart, TAS 7001, Australia; hong.liu@utas.edu.au
* Correspondence: yingyao.cheng@utas.edu.au

Abstract: The stability of rock slopes is of significance, as even the slightest slope failure can result in damage to infrastructure and catastrophes for human beings. Thus, this article focuses on the review of the current techniques available for rock slope stability analysis. The rock slope stability techniques can be classified as conventional methods and numerical methods. The advantages and limitations of the conventional method are briefly reviewed. The numerical methods mainly included three types, i.e., continuum methods, discontinuum methods, and the combined/hybrid continuum–discontinuum methods. This article pays more attention to the last type. The combined/hybrid finite–discrete element method (FDEM), which might be the most widely used continuum–discontinuum method, is introduced and we illustrated its abilities in modelling the entire rock slope failure process. The fundamental principles of FDEM, i.e., the contact interaction of the discrete bodies and the transition from continuum to discontinuum, are introduced in detail. The abilities of the FDEM in modelling the rock slope failure process are calibrated by modelling the entire typical rock slope failure process. Then, the application of the FDEM in the analysis of slope stability is introduced and discussed. Finally, the authors give insight into the GPGUP-parallelized FDEM modelling of the high rock slope failure process by the implementation of the strength reduction method (SRM). It is concluded that the FDEM can effectively model the entire rock slope failure process, even without the implantation of any slope modes, and the GPGUP-parallelized FDEM is a promising tool in the study and application of rock slope stabilities.

Keywords: rock slope analysis; limited analysis method; numerical methods; combined/hybrid finite–discrete element method; FDEM

Citation: An, H.; Fan, Y.; Liu, H.; Cheng, Y.; Song, Y. The State of the Art and New Insight into Combined Finite–Discrete Element Modelling of the Entire Rock Slope Failure Process. *Sustainability* **2022**, *14*, 4896. https://doi.org/10.3390/su14094896

Academic Editors: Mahdi Hasanipanah, Danial Jahed Armaghani and Jian Zhou

Received: 17 February 2022
Accepted: 13 April 2022
Published: 19 April 2022

Publisher's Note: MDPI stays neutral with regard to jurisdictional claims in published maps and institutional affiliations.

Copyright: © 2022 by the authors. Licensee MDPI, Basel, Switzerland. This article is an open access article distributed under the terms and conditions of the Creative Commons Attribution (CC BY) license (https://creativecommons.org/licenses/by/4.0/).

1. Introduction

The fast development of modern society results in a variety of geotechnical activities, some of which require the excavation of rock cuts. Those actives, e.g., embayment, open-pit mining, and highway and urban contraction, can form many slopes. Figure 1 gives two typical rock slope examples. Figure 1a illustrates a rock slope with an angle of about 60° for the surface, which is reinforced by tensioned anchors. Figure 1b is a typical rock slope formed due to mining excavation in the Palabora open pit. The slope is 830 m in depth with an overall slope angle of 45–50°. There are also natural rock slopes in addition to the man-made slopes. For instance, the mountains or valleys are generally steep or falter slopes. As highways or railways might be built along valleys, the stability of the slopes, whether man-made or natural, are of significance in terms of protecting the surroundings and avoiding casualties.

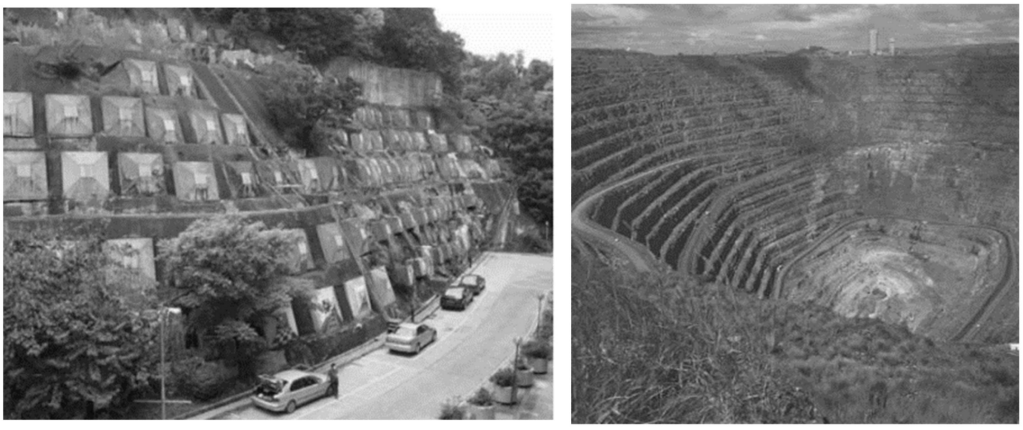

(**a**) (**b**)

Figure 1. Examples of rock slopes (from reference [1]). (**a**) Rock slope in Hong Kong. (**b**) Palabora open-pit mine.

The slope stability is always seen as critical, since even the tiniest slope failure may be costly in terms of monetary damage and human lives. It is essential to understand the geological, geomorphological, and hydrogeological characterization of a slope before the reconstruction of any structure. More importantly, a comprehensive understanding of the impacts of the external factors, e.g., external loading, seismicity, and groundwater, is crucial for preventing and controlling slope instabilities. In addition, the rock characteristics of the slope, e.g., faults, folds, and discontinuities, are significant factors influencing the stabilities of the rock slopes. The stability analysis of the rock slope is always associated with the factor of safety, which is the most well-known performance indicator in slope stability. The factor of the safety of the rock slope is a ratio of the average shear strength of a specific slip face to the average applied shear stress. If the ratio, i.e., the factor of the safety $F = 1$, it represents the "critical equilibrium" or "limiting equilibrium", and this implies that a slope is on the verge of collapse or sliding, or complete failure. In this scenario, the rock slide is imminent along a certain slip surface. If the factor of the safety $F > 1$, the slope is stable and it is not on the verge of sliding. If the factor of the safety $F < 1$, it represents instability, and in this case, the slope design cannot be constructed.

In general, the rock slope has four categories in terms of failure types, i.e., plane failures, wedge failures, toppling failures, and circular failures. Figure 2a illustrates a general sketch of a plane failure (left part) and the plane failure of a rock slope in a mountain (right part). As illustrated in Figure 2a, for a plane failure, there is a structural discontinuity plane where sliding occurs. The angle of the discontinuity plane is smaller than the slope-face angle and it is greater than the fraction angle of the discontinuity surface [2]. Figure 2b illustrates the edge failure of the rock slope. It involves two discontinuities inclined out of the slope face and a rock mass, such as a wedge on them. During the edge failure, the wedge-like rock mass is generated and slides along the two crossing discontinuities that both drop out of the cut slope at an oblique angle to the curt face. Figure 2c shows the toppling failures of rock slopes. Toppling failures are most prevalent in rock masses that have been broken into a series of slabs or columns by a sequence of fractures that run roughly parallel to the slope face and dip sharply into it. Figure 2d illustrates the circular failure of the rock slope, which is named by the failure type—like the arc of a circle. It often occurs in solid mass with large grain sizes. Thus, for the circular failure of the rock slope, the rock mass is generally fragmented and the failure is not predominately controlled by a discontinuity (e.g., plane failure) or two intercrossing discontinuities (e.g., wedge failure).

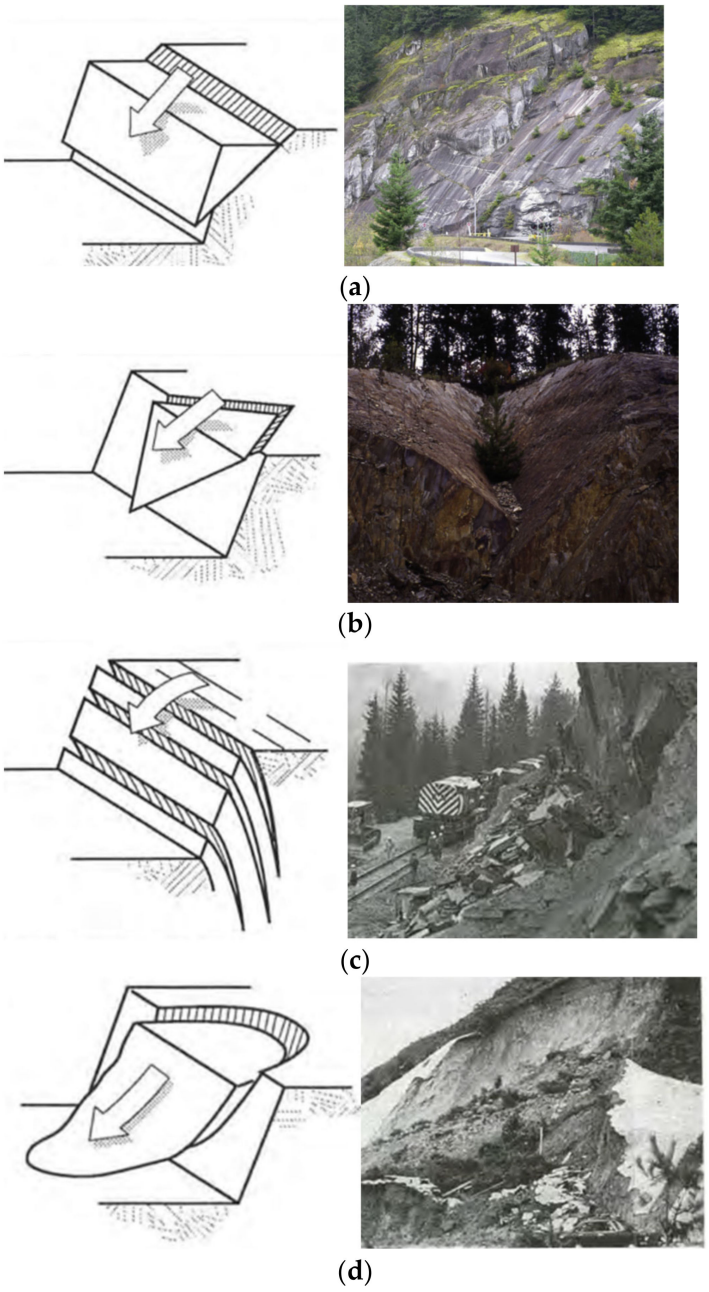

Figure 2. The main failure types for rock slopes (from references [3,4]). (**a**) General plane failure sketch (from references [3,4]). (**b**) Wedge failure sketch (from references [3,4]). (**c**) Toppling failure sketch (from reference [3]). (**d**) Circular failure (from reference [3]).

The rock slope stability analysis is essential for many engineering projects, e.g., road cuts and open-pit mining. The main purposes of the rock slope stability analysis are to determine the stability of the rock slope, to investigate the different support options, and to optimize the slope in terms of reliability. There are many techniques available for performing the analyses, which can be in general classified into the conventional methods and numerical methods. The conventional methods include limit equilibrium techniques and the kinematic method. Limit equilibrium techniques are popular methods for the analysis of the plane or the toppling failure of the rock slope. This technique can provide a factor of safety or it can provide shear strength parameters for a rock slope. There are also lots of computer programs used for slope instability analysis, which are made based on the limit equilibrium concept [5]. The limit equilibrium approach has traditionally been used

to test the stability of rock slopes, which are confined to the analysis of planar or wedge instabilities, while other complicated failure kinematics, such as toppling, are often not addressed by these methodologies.

The numerical methods are significant tools utilized during the slope design stage. As for the numerical techniques, there are mainly two categories, i.e., the continuum method and the discontinuum method. The representative continuum methods for modelling the rock slopes are the finite element method [6], failure-process analysis method (RFPA) [7], numerical manifold method (NMM) [8], and finite difference method (FDM) [9]. Jin, Yin and Yuan (2020) used the smooth-particle finite element method to simulate the rock slope failure process [6]. The smooth-particle finite element method is an updated Lagrangian approach with frequent re-meshing by the Delaunay triangulation method [6]. To employ continuum modelling, the rock mass in the slope is considered as a continuum material. In addition, the finite element method is widely used to study the failure mechanisms of the unsupported conical slope by the implementation of various rock failure models and criteria [10–14], e.g., the anisotropic undrained shear (AUS) model [11] and the Hoek–Brown failure criterion. However, for a real rock slope, there are unavoidable pre-existing planes of weaknesses, e.g., schistosity, joint sets, and faults. Those weaknesses in the rock slope might be the key issues that result in the instability of the rock slope. The continuum technique has limits in explicitly simulating complicated discontinuities, progressive failure, substantial deformation, and complex rock movement during the whole failure process due to the continuum assumptions [15]. There is also a variety of discontinuum methods applied for the simulation of the rock slope failure process. The distinct element method (DEM) [16] might be the most widely used discontinuum method. Jiang and Murakami (2012) employed the distinct-element method to model the full-process slope failure. The particle flow code (PFC) [7] and the discontinuous deformation analysis method (DDA) [17] are widely used to model the slope failure process.

The rock slope failure process is extremely complicated, it involves crack initiation propagation, and coalescence, and rock-bodies movement, rotation, and fragmentation. Neither the continuum method nor the discontinuum method can solve these problems [18]. Thus, a more robust numerical method, taking the advantages of both the continuum method and discontinuum method, is needed to reproduce the full failure process. The continuum–discontinuum method might be the most suitable technique to model the entire rock failure process, as it combines the advantage of the continuum-based methods and the discontinuum-based methods. Many researchers have focused their studies on the continuum–discontinuum modelling of the rock slope failure process [19–23]. Thus, this research reviews the rock slope sliding modelling using the continuum–discontinuum method. As the hybrid finite–discrete element method (FDEM) is one of the most popular approaches to modelling the rock fracture process, and Table 1 lists the representative study on the FDEM modelling of rock slope failure processes, this research introduced the main principles of the hybrid finite–discrete element method. In addition, the calibrated applications of the hybrid finite–discrete element method are introduced and explained in detail to demonstrate the validity and capability of the hybrid finite–discrete element method in modelling the entire rock slope failure process.

Table 1. Summary of FDEM modelling of the rock slope failure process.

Numerical Code	Modelled Results	Reference
Y-Slope	Y-Slope considers the tensile and shear failure. The failure is caused by gravity. By decreasing the strength parameters, the cracks initiate from the toe of the slope and propagate further into the slope. Finally, the cracks form a discontinuity surface. The crack initiation, propagation, colliding, fragmentation, and piling are modelled.	[19]
FDEM realized using ABAQUS/Explicit	The FDEM framework is implemented in the ABAQUS/Explicit. The cohesive zone model (CZM) is employed to model the fracture occurring along the bulk elements boundary. The gravity increase method is implanted in the ABAQUS/Explicit-based FDEM program to model the slope failure process. The failure processes of the laboratory-scale slope with various joint inclination surfaces are modelled.	[20]
Y-Geo based on Munjiza's Y-code	Y-Geo is used to model the evaluation of a rock slide that occurred in Italy in 1997. The modelled results in terms of the runout profiles and evaluation of the slopes agree well with the site observation.	[21]
ELFEN	A modified Mohr–Coulomb elastoplastic model is implemented in ELFEN to model the material softening, and deal with both the tension and shear states. Then, the ELFEN was employed to model the 1991 Randa rockslide. Due to strength degradation, the rock mass breaks into blocks and are modelled using ELFEN.	[23]
Y-2D with Y-GUI	The failure process of the rock avalanche is modelled. The weak interface in the slope was firstly produced, then, the rock avalanche was initiated. A large volume of rock mass started to move, which further fragmented. During the process, the blocks were progressively broken into smaller fragments.	[22]

2. Combined Finite–Discrete Element Method

The continuum–discontinuum method (CDM) is a promising tool for the study of the rock fracture and fragmentation process under static or dynamic loading conditions, e.g., blasting [24–30]. It has been successfully applied in many geotechnical engineering problems associated with the transition from continuum to discontinuum through fracture and fragmentation over the last two decades [31–34]. Compared with the continuum method or discontinuum method, the CDM can not only model the rock damage, fracture initiation, coalescence, and propagation as most of the continuum-based methods do, but it also can model the interaction of the fracture rocks and even the muck-pilling of the rock fragments during a rock blasting process [30]. Many CDM methods have been proposed for overcoming the shortcomings of the continuum-based method or discontinuum method in simulating the entire rock fracture process, e.g., the combination of the boundary element method with the finite element method (BEM/FEM), the combination of the discrete element method with the finite element method (DEM/FEM), and the combination of the discrete element method with the boundary element method (DEM/BEM) [35].

The hybrid/combined finite element method (FDEM) might be the most widely used continuum–discontinuum method. Based on the FDEM, many tools are developed for modelling the entire rock fracture process, e.g., Y-2D [36], Y-GUI [37], Y-GEO [30], Y-Slope [19], Y2D/3D IDE [30], and the commercial software ELFEN [38,39]. Y-slope models the crack initiation, propagation, colliding, fragmentation and pilling process during the rock slope failure process [19]. Y2D/3D IDE has been implemented to model the entire fracture, fragmentation, and muck-pilling process induced by the blast [30], and has also been used to study the excavation damaged zone (EDZ) induced by blasting in deep tunnels [29]. Y-GUI is a graphical user interface developed for Y2D, as Y2D setting up Y2D modes is a time-consuming and error-prone process [22]. The GUI is developed to setup Y-2D modes graphically and minimize the possibility of erroneous input files [22]. Y2D has modelled the slope failure process where rock avalanches occur [22].

As the FDEM has been used in many geotechnical problems, the fundamental principles and FDEM applications have been introduced in detail. For a FDEM mode, it can have one discrete body or many discrete bodies. As illustrated in Figure 4, the discrete body is meshed by three-node finite elements (Figure 4a), and the four-node joint elements (Figure 4b) are embedded among the finite elements. The damage and the deformity of the rock mass are modelled using the three-node finite element, while the fracture initiation and propagation are simulated by the distortion of the four-node joint elements depending on the calculated strains on the finite element of a discrete.

Sun et al. (2022) [19] gave the rock mass with fracture and its equivalent FDEM model meshed by three-node finite element and four-node joint elements, as illustrated in Figure 3. The rock model is meshed using finite elements and the cracks are modelled using the broken joint elements, i.e., crack elements. The stress and strain of the individual body are described using the continuum law. The fracture of the rock, i.e., the transition from continuum to discontinuum, is modelled by the breakage of the joint element among the three-node finite elements. The motion of each node of the discrete body is updated using Newton's second law (Equation (1) [40]).

$$M\frac{\partial^2 X}{\partial t^2} + C\frac{\partial X}{\partial t} = F \tag{1}$$

where M is the mass of the discrete body while C is the damping diagonal matrices, X is the nodal displacement and F is the node force vector.

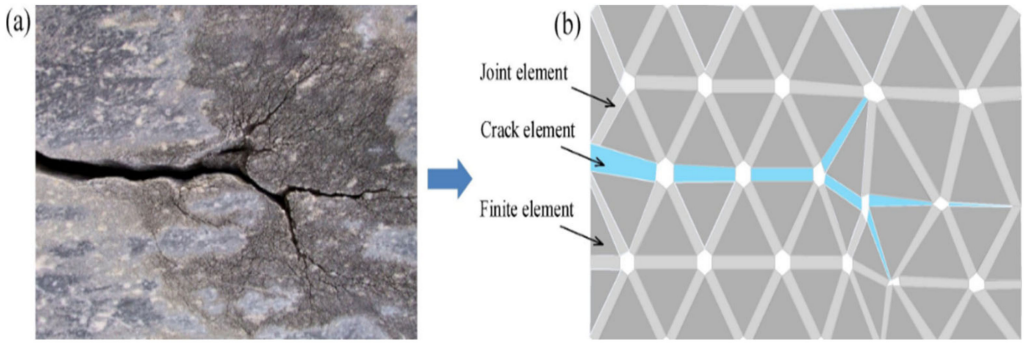

Figure 3. The rock mass with cracks and its equivalent numerical model [19]: (**a**) rock mass (from reference [19]); (**b**) FDEM model (from reference [19]).

Contact detections of the discrete elements or discrete bodies are essential for the FDEM, as there might be thousands or even millions of discrete elements or discrete bodies. Thus, many algorithms for automatic contact detection are proposed [36,42], e.g., the no-binary search, buffer zone, binary tree, and alternating digital tree. After the coupled discrete elements or discrete bodies are detected, the contact forces between the coupled discrete elements or bodies are calculated.

Most of the FDEMs use the penalty method to calculate the contact forces in the tangential and normal directions [26,36]. As illustrated in Figure 5, the two bodies are called the target and contactor, respectively. The penetration of the contactor into the target causes contact force. An infinitesimal contact force due to the penetration can be calculated using Equation (2) [36], while the total contact force due can be calculated using Equation (3) [36].

$$\mathrm{df} = [grad\varphi_c(P_c) - grad\varphi_t(P_t)]dA \tag{2}$$

$$\mathrm{f_c} = \int_{S=E_{t\cap E_c}} (grad\varphi_c(P_c) - grad\varphi_t(P_t))dA \tag{3}$$

where df is the infinitesimal overlap dA force and the φ_c and φ_t are potential functions.

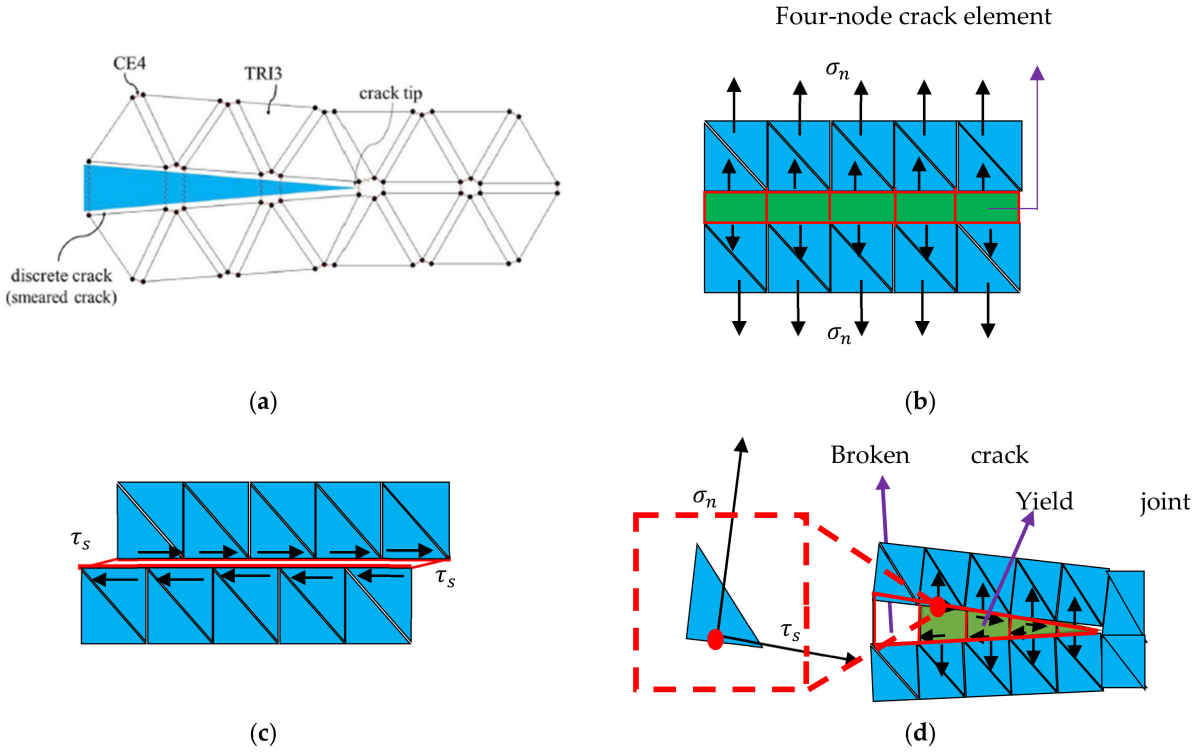

Figure 4. FDEM modelling rock fracture modes [19,25,27,28,41]. (**a**) FDEM model assembled with three-node and four-node elements (from reference [41]); (**b**) tensile failure (from reference [28]); (**c**) shear failure (from reference [27]); (**d**) mixed tensile–shear failure (from reference [25]).

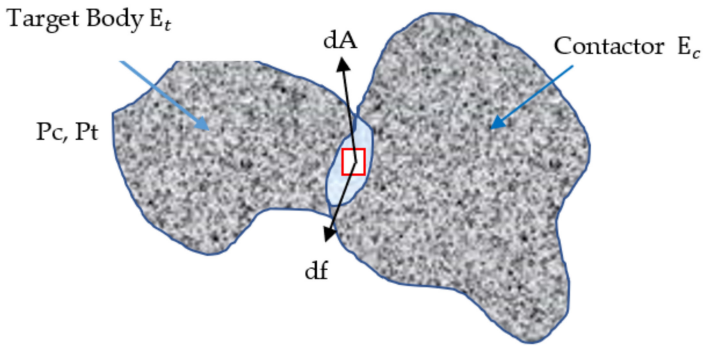

Figure 5. Contact force due to penetration [26].

During the contact interaction, the discrete element or bodies are deformable and the joint elements can be distorted to perform the continuum of the rock mass. The distortion in the vertical and normal direction will finally result in the shear and tensile failure, which perform the transition of the intact rock from continuum to discontinuum through the rock fracture and fragmentation. Bonding stress is induced during the distortion or the separation of the joint elements. Figure 6 gives the relationship between the bonding stresses with the separation of the joint elements in the normal direction (Figure 6a, right), and the vertical direction (Figure 6a, left). The bonding stress in the normal direction can be obtained according to Equation (4) [43]:

$$\sigma_n = \begin{cases} \left[2 \cdot \frac{\delta_n}{\delta_{np}} - \left(\frac{\delta_n}{\delta_{np}}\right)^2\right] \cdot \sigma_t & if \quad 0 \le \delta_n \le \delta_{np} \\ f(D) \cdot \sigma_t & if \quad \delta_{np} \le \delta_n \le \delta_{nu} \\ 0 & if \quad \delta_n \ge \delta_{nu} \end{cases} \tag{4}$$

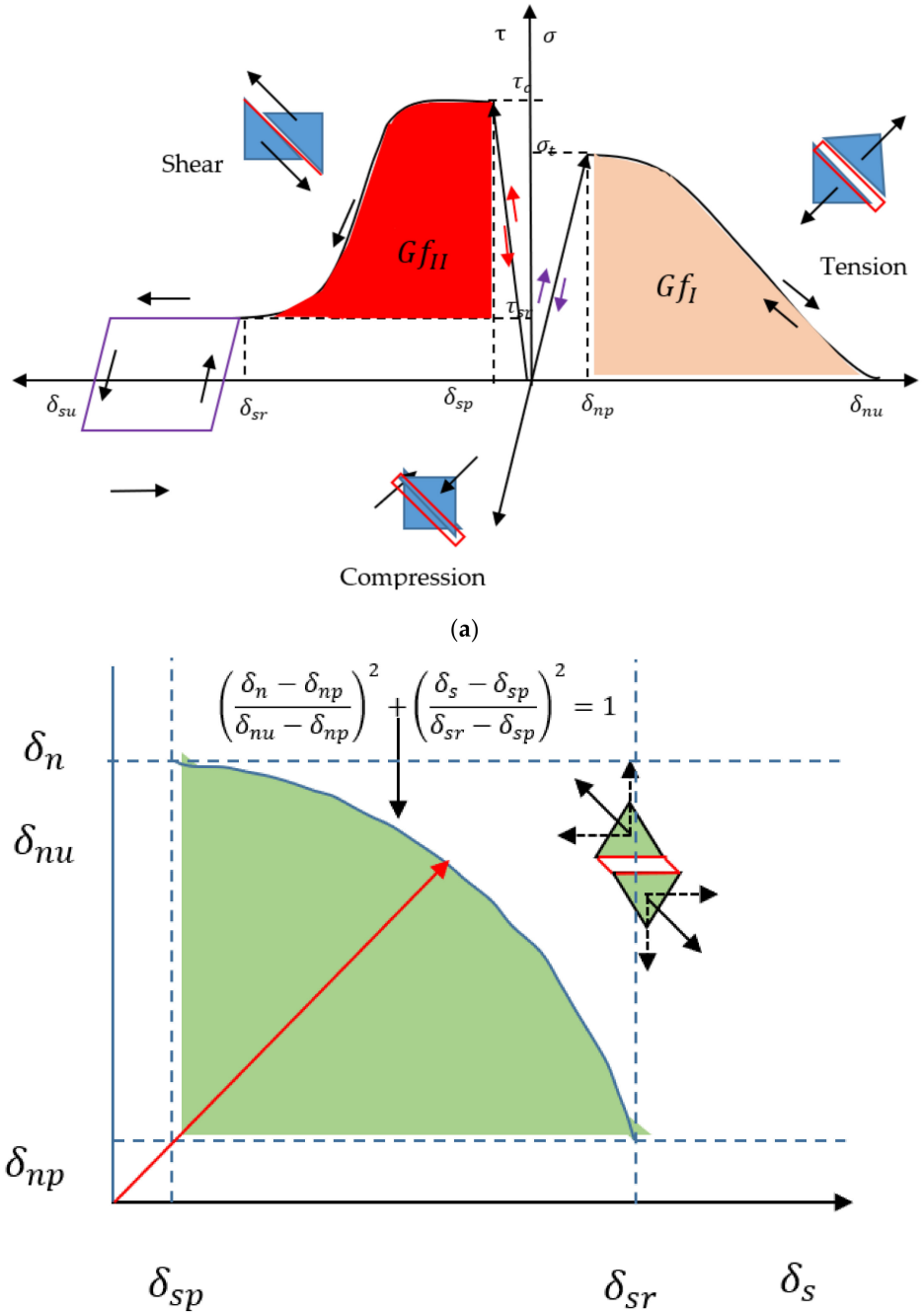

(**a**)

(**b**)

Figure 6. Transition from continuum to discontinuum [24,28]: (**a**) Tension fracture (pure Mode-I fracture (left parts)) and shear fracture (pure Mode-II fracture) (from reference [28]); (**b**) mixed tensile–shear fracture from (from reference [27]).

The tensile fracture or the Mode-I fracture process is governed by the Mode-I fracture energy release, and the value can be calculated as follows (Equation (5) [43]).

$$G_{fI} = \int_{\delta_{np}}^{\delta_{nu}} \sigma_n(\delta_n) d\delta_n \quad (5)$$

where the G_{fI} is the Mode-I fracture energy release rate.

For the shear fracture or the Mode-II fracture process, the sliding of the adjacent finite element and the shear stress relationship is illustrated in the right part of Figure 6a. The shear stress τ increases with the increase of the sliding δ_s and the shear strength corresponds to the sliding displacement of δ_{sp}, which indicates the shear fracture occurs. After that, the boding stress in the tangential direction or the shear stress decreases. As it decreases to a residual stress δ_{sr} according to a mechanical damage model, the shear fracture finishes. The bonding stress in the tangential direction can be expressed as Equation (6) [43] according to the sliding displacement of the adjacent finite elements.

$$\tau = \begin{cases} 2 \cdot \frac{\delta_s}{\delta_{sp}} \cdot \sigma_c & if \quad 0 \le \delta_s \le \delta_{sp} \\ g(D) & if \quad \delta_{sp} \le \delta_s \le \delta_{sr} \\ \sigma_n \cdot tan\left(\varnothing_f\right) & if \quad \delta_s \ge \delta_{sr} \end{cases} \tag{6}$$

where D is the damage variable and $g(D)$ is the function of the damage [44], and $\varnothing_f$ is the joint residual friction angle.

Figure 6b illustrates mixed fracture criteria. When Equation (7) [43] is satisfied, the mixed-Mode I–II occurs.

$$\left(\frac{\delta_n - \delta_{np}}{\delta_{nu} - \delta_{np}}\right)^2 + \left(\frac{\delta_s - \delta_{sp}}{\delta_{sr} - \delta_{sp}}\right)^2 \ge 1 \tag{7}$$

It should be noted that although most of the FDEMs, e.g., Y-FDEM [27] and Y-Slope [19], are implemented based on the open-source combined finite–discrete element libraries Y2D and Y3D originally developed by Munjiza (2004) [36] and Xiang et al. (2009) [45] and programmed using C++ or VC++, the C program is not the only platform for the implementation of the FDEM. Other platforms can be used for the implementation of the FDEM framework. Zhou, Yuan et al. (2016) [20] proposed a cohesive zone model-based on a combined finite–discrete element method to simulate the rock sliding process at the laboratory scale. The Mohr–Coulomb model with a tension and cut-off is impended for the FDEM to model both the tensile and the shear failure. Then, the FDEM is implanted into the ABAQUA to perform the transition from continuum to discontinuum through fracture and fragmentation during the rock slope sliding process.

3. Calibration of Hybrid Finite–Discrete Element Method for Modelling the Rock Slope Failure Process

The FDEM has been calibrated by many typical rock mechanism tests, e.g., the Brazilian tensile strength test [27], uniaxial compressive strength test [28], three-point test [26], and four-point test [24]. Those modelling results indicate that the FDEM can effectively model various fracture types, i.e., tensile, shear, and combination failures. To better indicate the capability of the FDEM in modelling the entire rock failure process of a rock slope, the FDEM has been employed to model the typical rock slope failure process [46], and it is even used for the back analysis of the rock slope in which the failure has occurred [21].

Grasselli, Lisjak et al. (2011) modelled the toppling failure of the rock slope, which is one of the main rock slope failure types [46], to calibrate and show the capabilities of the FDEM method in modelling the entire rock failure process of the rock slope. Figure 7 illustrates the temporal sequence of the failure process and the resultant fragmentation of the toppling failure of the rock slope. As can be seen from Figure 7, the toppling rock slope is comprised of multiple columns and those interact on an inclined plane during the rock-toppling failure process. According to Bray and Goodman (1981) [47], the toppling slope can be divided into three sections, i.e., the stable section, sliding section, and toppling section (Figure 7b). Due to the gravity of the columnar blocks, the failure occurs in the toppling and sliding sections, as illustrated in Figure 7b. The blocks slid on the inclined plane in the sliding sections while the blocks slide and rotate in the toppling section. During the interactions of the blocks, many blocks break into smaller blocks and even fragments (Figure 7c). Finally, more fragments are produced and pile on the toe of the slope during

the gravity of the blocks interacting with the adjacent blocks (Figure 7c). The rock mass on the stable section is not significantly influenced by the slope failure process, as there is no interaction between adjacent blocks and the force along the sliding face induced by gravity is not big enough to cause the blocks to slide, due to the friction on the discontinuity face.

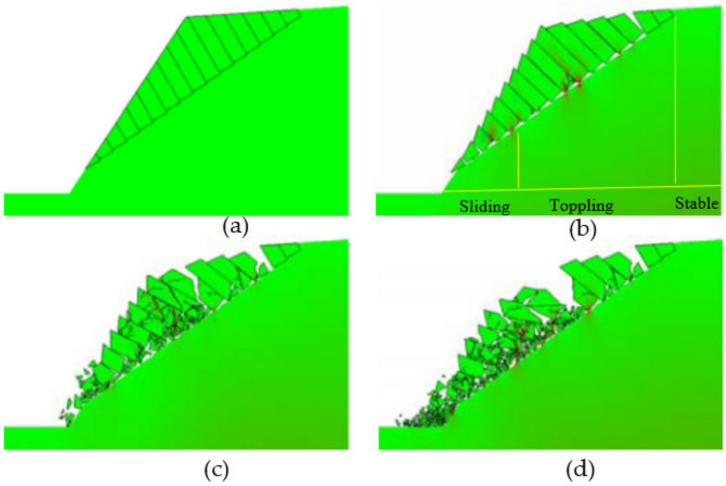

Figure 7. Toppling failure process of the rock slope modelling using FDEM (from reference [46]). (**a**) Initial state; (**b**) sliding along the discontinuity surface; (**c**) interaction between rock blocks; (**d**) piling to the toe of the slope.

Sun, Liu et al. (2022) developed the Y-slope to model the entire failure process of rock slopes from initiation and transportation to deposition [19]. The Y-slope is developed based on the Y-code. The Y-slope considered the shear and tensile failure conditions by the implementation of the strength reduction methods. To calibrate the Y-slope, the equilibrium state of a benchmark is modelled. The stress distribution and displacement distribution are illustrated in Figure 8. It finds that both the stress distribution and the displacement follow a layered distribution, which are similar to the typical results of the rock slope at the equilibrium state obtained from commercial software.

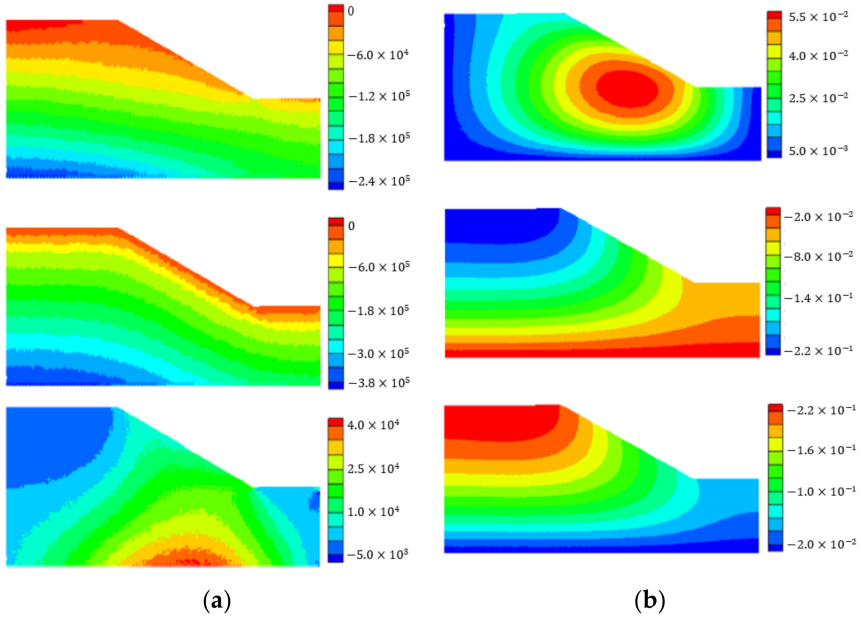

Figure 8. FDEM modelling of stress distribution and displacement destitution of the equilibrium state of a benchmark (from reference [19]). (**a**) Stress distribution; (**b**) displacement distribution.

Thus, the FDEM can model the transition of the rock slope from continuum to discontinuum through the rock fracture initiation, propagation and sliding, or rotation. In addition, it can effectively demonstrate the stress distribution and displacement distribution.

4. Application of the Hybrid Finite–Discrete Element Method in Modelling the Entire Rock Failure Process

Barla, Piovano et al. (2012) simulated two different rock slides observed at the Apletto Mine in Cesana Brianza, Italy [21]. Figure 9 shows the plane view, in which two sections, i.e., Section A and Section B, can be observed. Due to the intensive and persistent rainfall, instability has occurred in Section A. Barla, Piovano et al. (2012) made a back analysis of the side of Section A using FDEM, while the failure process of Section B also is simulated using FDEM.

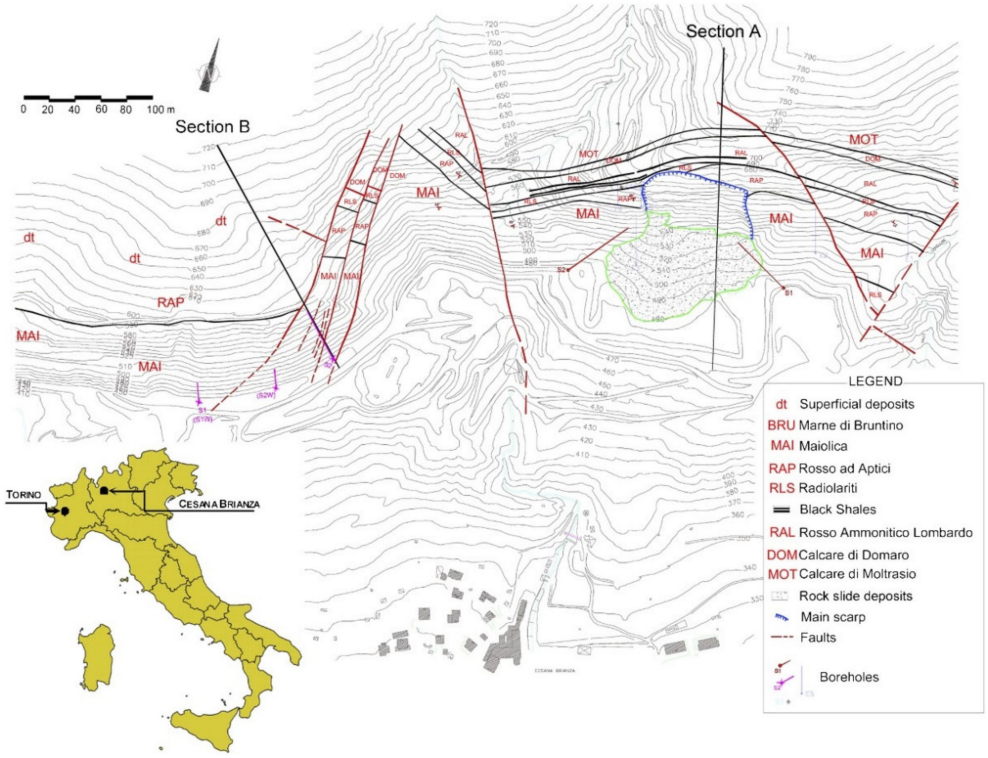

Figure 9. Plane view of the Alpetto Mine in Northern Italy (from reference [21]).

Figure 10 shows the FDEM modelling of the rock slope failure process of Section A of the Alpetto high rock cut slope. Figure 10a-A illustrates the initial state of the cut slope. It can be seen that the bedding plane in the rock mass is approximately parallel to the slope, which results in the formation of thin slabs. The slabs are generated and move along the discontinuity or the sliding surface (Figure 10a-D). During the movement, the slabs turn to fragments due to the interactions of the slabs with the rock slope discontinuity. Finally, the fragments cover the bottom part of the slope. Figure 10b shows the FDEM modelling of the rock slope sliding process of Section B of the Alpetto high rock cut slope. The FDEM modelled two slopes (Section A and Section B) that are both similar to the high steep-slope failure process. The final fractured rock mass covers the bottom of the slope.

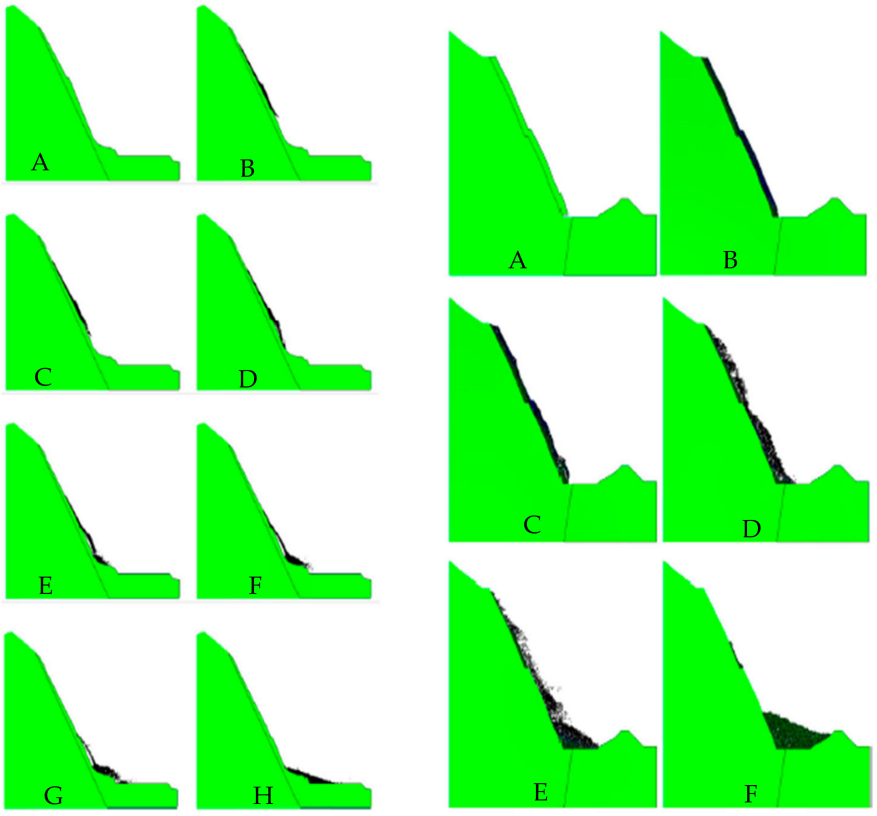

(**a**) (**b**)

Figure 10. FDEM modelling of rock slope sliding process of the Alpetto high rock cut slope (from reference [21]). (**a**) Section A; (**b**) Section B.

5. Discussion

5.1. Discussion on the Numerical Modelling Entire Slope Failure Process

Although many numerical techniques have been applied to model the rock slope failure process [2,6,8,9,18,19,48,49], naturally modelling the entire failure process is still a challenge. The entire rock slope failure process involves continuous displacement and discontinuous interaction. It is also associated with crack initiation, crack propagation, and even the coalescence of the cracks. In the post-failure process, the rock mass may move, rotate, collide, and finally fragment. As it involves continuous behaviours before the failure occurs, and discontinuous behaviour during the post-failure process, an individual continuum or discontinuum method has its limitations in modelling the entire failure process of rock slopes.

Figure 11 illustrates an FDEM method, i.e., Y-slope, which modelled the entire rock slope failure process [19]. Due to the gravity of the rock mass, a crack initiates from the toe of the slope, in which the stress is concentrated (Figure 11a). Then, the crack starts to propagate and reaches the top surface of the slope (Figure 11b–d). Thus, a sliding surface is formed. After that, the rock mass on the sliding surface begins to move along the formed surface (Figure 11e). During the post-failure process, the sliding rock mass rotates, interacts, and collides, which results in massive fragments being produced (Figure 11f). Finally, massive fragments accumulate in the vicinity of the slope toe. The rock slope failure process illustrated in Figure 11 effectively indicates that the FDEM can model the entire slope failure process well, from the continuous behaviours to the discontinuous behaviours.

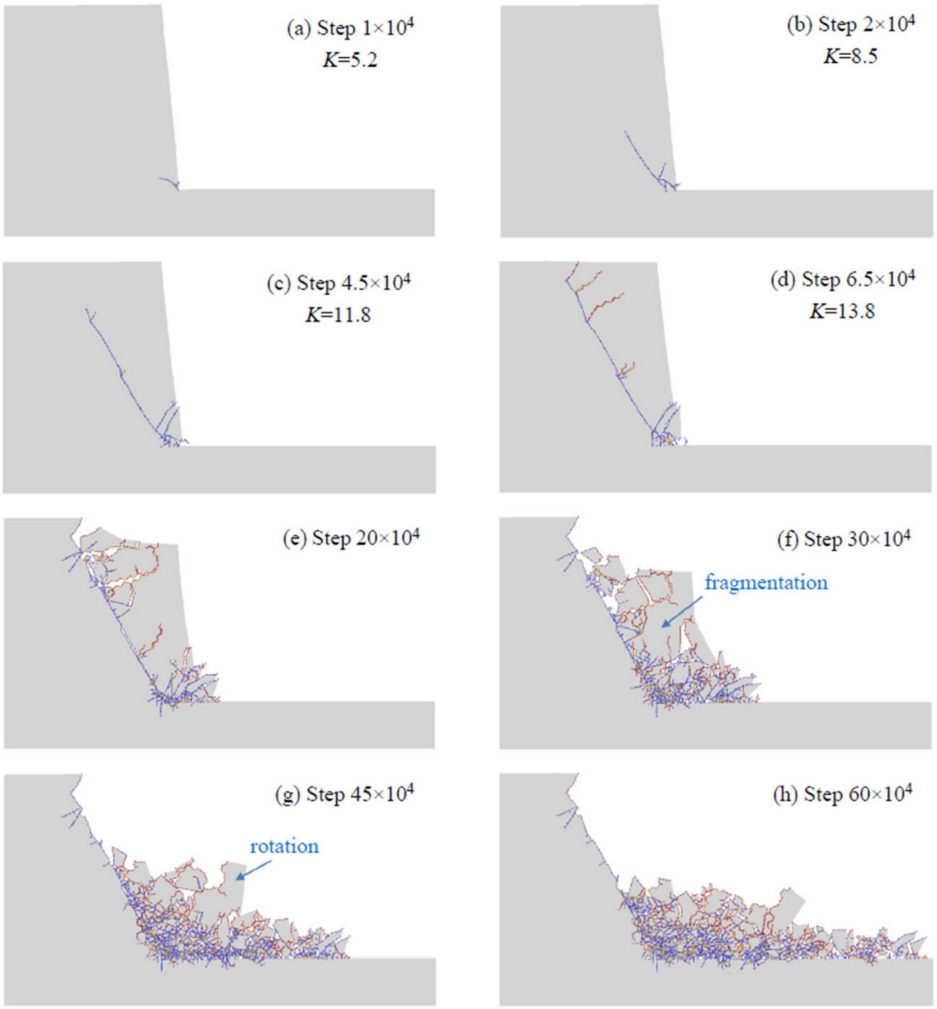

Figure 11. FDEM modelling of the entire rock slope failure process [19].

Figure 12 compares two modelling results for a same toppling failure process. Figure 12a illustrates a toppling failure process modelled using the UDEC, while Figure 12b shows the same failure process modelled using FDEM.

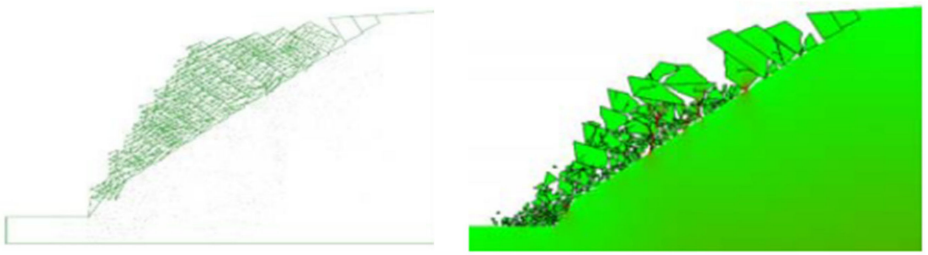

(**a**) (**b**)

Figure 12. Comparison of the slope failure process modelled by: (**a**) the UDEC; (**b**) the FDEM (from reference [46]).

Generally, the modelled results are almost the same in terms of failure formation. As can be seen, the failure initiated from the bottom-three rock blocks, and this caused the instability of the other blocks, except for the two blocks at the top of the sliding discontinuity. Then, the fracture blocks moved along the sliding surface. Thus, the UEDC and the FDEM both can model the toppling failure process well. However, it seems that

FDEM has modelled the fracture initiation and propagation better when compared with the UDEC-obtained results in this case, which shows the advantage of the continuum method.

5.2. Discussion on the Advantages and Limitations of the FDEM in Rock Fracture Modelling

As the FDEM is a combined/hybrid continuum and discontinuum method, it takes the advantages of both the continuum method, e.g., FEM, and discontinuum method, e.g., DDA. The continuum method can model the rock initiation well, as well as propagation and coalescence, including the localization of the failure [18], while the discontinuum is good at modelling the sliding of the rocks along the discontinuous surface, as well as the interaction and rotation of the blocks. Thus, the FDEM can model the entire rock slope sliding process, i.e., crack initiation, propagation, coalescence, and the rock bodies' movements, interactions, and fragmentations. In another word, the FDEM allows for new crack initiation and exiting crack extension, and can model the larger deformation, including rotations.

However, the FDEM also has its limitations. For example, the FDEM requires very specialized input parameters, and the required joint properties are not routinely measured [39]. In addition, the FDEM modelling results are very sensitive to the mesh size and mesh orientation, since the joint element or crack elements are inserted among the finite element boundaries to model the fracture initiation and propagation. Moreover, the FDEM encounters difficulties when simulating failures through intact rock.

Thus, new techniques need to be developed to more naturally model the crack initiation and propagation, and to try to avoid the effects of the mesh size and mesh orientation. Moreover, the crack initiated from the intact rock should be developed as the rock slope sliding process includes not only discontinuous mechanical behaviours but also crack initiation, propagation, and coalescence from intact rock [23,50].

6. New Insight into GPGPU-Parallelized FDEM Modelling of Rock Slope Failure Process

The significance of understanding the mechanism of the rock fracturing process has been widely realized in several fields, e.g., rock slopes and tunnellings, in which the stability is sensitive to the fractures. Numerical methods have been implemented to model the fracture process and the FDEM is considered as a promising tool, as mentioned in the Introduction Section. However, the computing power limited the FDEM, not only with 3D modelling but also in carrying out large-scale 2D modelling with a small mesh size in the past. The recently developed general purpose graphic processing unit (GPGUP) accelerators have dramatically improved this situation. Thus, this section gives a brief insight into the GPGUP-parallelized FDEM in modelling the rock slope failure process.

The FDEM code, i.e., Y-HFDEM, used in this section is originally developed by the authors in reference [51] and has been employed to study the conventional rock mechanism tests [26–28], rock blasting in mining production [25], and tunnelling excavation [29,41]. To overcome the computationally expensive issue of Y-HFDEM, the authors Fukuda et al. (2019–2020) [52,53] recently parallelized it on the basis of the GPGPU using a compute-unified device architecture (CUDA) C/C++. The detailed computing performance analysis shows the GPGPU-parallelized HFDEM 2D/3D IDE code can achieve the maximum speedups of 128.6 [53] and 286 [52] times in the case of the 2D and 3D modellings, respectively. More recently, adaptive efficient contact activation [54], mass scaling, the hyperplane separation theorem, and the semi-adaptive contact activation approach [55] have been implemented by the authors to further speed up the GPGPU-parallelized HFDEM, which paves the way for investigating the large-scale rock slope failure process.

The safety factor (SF) has been introduced in the Introduction Section, which is regarded as the key indicator for the stability of a slope. In addition, the safety factor can be obtained by weakening the rock material until the slope fails using the strength reduction method (SRM) [56,57]. For the modelling of the rock slope failure process using GPGUP-parallelized Y-HFDEM, the strength reduction method (SRM) is implemented in the proposed method. Then, a typical rock high slope is modelled to gain insight into the

GPGUP-parallelized Y-HFDEM on the rock slope stability analysis. Figure 13 illustrates the geometrical mode, the size of which is the same as in Figure 11 of reference [19].

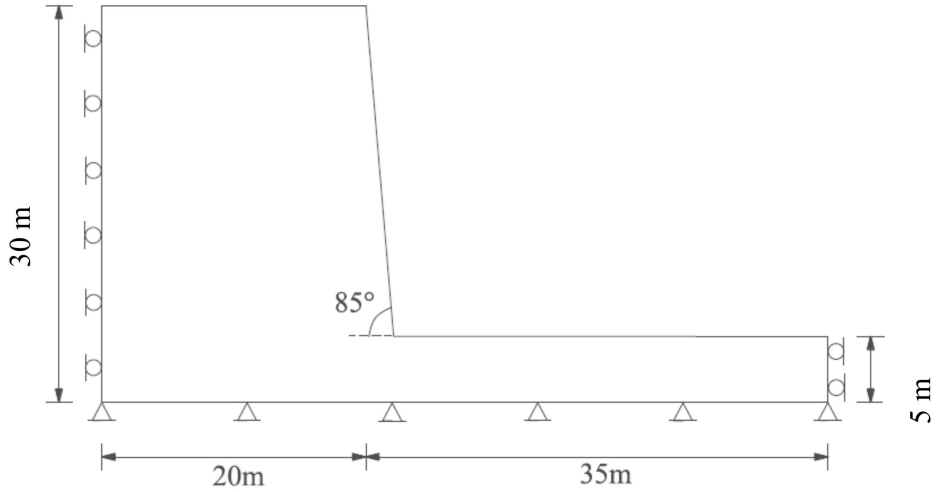

Figure 13. Geometrical model of high rock slope (from reference [19]).

Table 2 gives the input parameters for the FDEM high rock slope model, which are the same as in Figure 11 of reference [19].

Table 2. Input parameters for the FDEM high rock slope model.

Properties	Values
Young's modulus (GPa)	10
Poisson's ratio	0.25
Density (kg/m^3)	2000
Friction angle (degrees)	32
Cohesion (MPa)	1
Tensile strength (MPa)	0.5

The following input parameters in Table 3 are not provided in reference [19] but are chosen following the calibration procedure described by Mohammadnejad et al. (2020) [54].

Table 3. Input parameters for the GPGUP-parallelized Y-HFDEM high rock slope model.

Properties	Values
Mode-I fracture energy (J/m^2)	4
Mode-II fracture energy (J/m^2)	12
Normal contact penalty (GPa)	100
Tangent contact penalty (GPa)	100
Artificial stiffness penalty (GPa)	1000

During the modelling, the gravity of the rock mass is firstly applied to the model and the stress reaches an equilibrium state through implementing a local damping approach. A damping coefficient is incorporated into the constitutive model in the FDEM, which is the so-called critical damping technique, one of the simplest approaches that have been used in many explicit FDEM. However, it was noted that the convergence rate of the critical damping technique is rather poor. Correspondingly, a local damping with a mass scaling technique is implemented into the GPGPU-parallelized HFDEM IDE code following Equation (8).

$$\boldsymbol{M}^{scale}\partial^2\boldsymbol{u}/\partial t^2 = \boldsymbol{f}_{tot} + \alpha\left|\left|\boldsymbol{f}_{tot}\right|\right|sgn(\boldsymbol{v}) \quad (8)$$

where $\boldsymbol{M}^{scale}$ is the scaled lumped mass, $\boldsymbol{f}_{tot}$ is the nodal out-of-balance force, $\boldsymbol{v}$ is the nodal velocity, $|\,|\boldsymbol{f}_{tot}|\,|$ is the absolute value of each component of $\boldsymbol{f}_{tot}$, $sgn(\cdot)$ is the sign function automatically determined by the sign of $(\cdot)$, and α is the local damping coefficient. Please refer to Fukuda et al. (2019) [53] for the implementation of the local damping method in detail. This process is completely different from that implemented in reference [19].

During the process, no fracture is allowed, since cohesive elements have not been inserted. After that, cohesive elements are inserted and static equilibrium is achieved. As the strength reduction method (SRM) is implemented in the proposed method, an iterative process begins. The strength parameters are reduced and re-arranged into the model. Then, a stress equilibrium state will be achieved again. The iterative process will not stop until the slope becomes unstable. Figure 14 illustrates a typical rock slope failure process using the proposed method with the implementation of the SRM. The left part of Figure 14 indicates the stress distribution while the right part shows the fracture initiation and propagation. Figure 14a indicates the stress equilibrium state after the gravity of the rock mass is applied to the model. The stress concentration can be observed at the toe of the slope, where fractures initiate (Figure 14b). Then, the fractures propagate into the slope (Figure 14c) and form a sliding failure surface (Figure 14d). The rock mass slides along the newly formed sliding surface. Due to the sliding, rotation, and colliding, the rock mass breaks into fragments and finally piles at the lower bench of the slope (Figure 14e). Thus, the GPGUP-parallelized Y-HFDEM can effectively model the entire slope failure evolution process due to the implementation of the SRM in the proposed method.

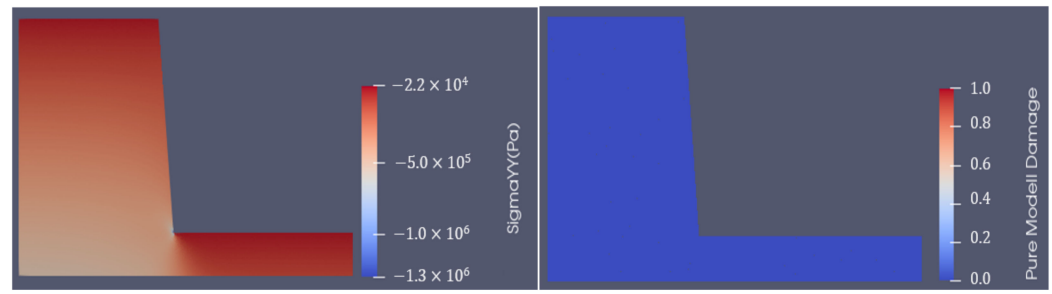

(**a**)

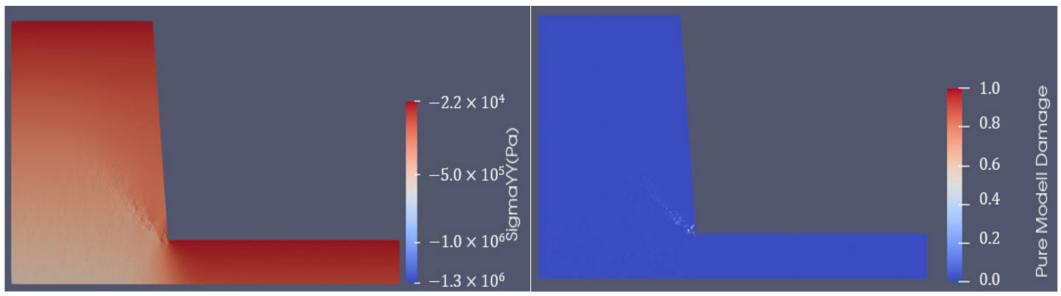

(**b**)

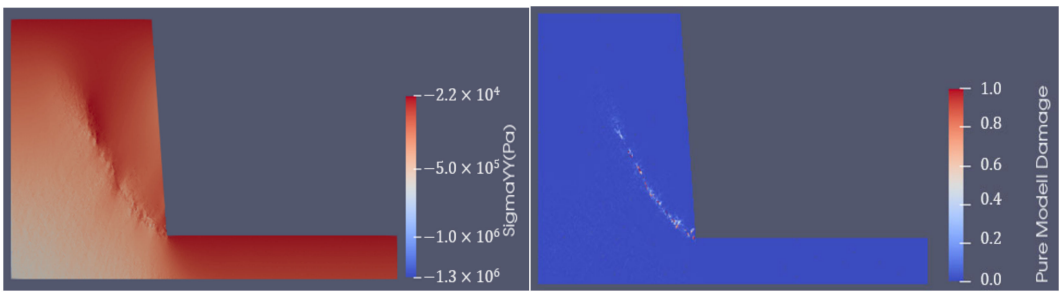

(**c**)

Figure 14. *Cont.*

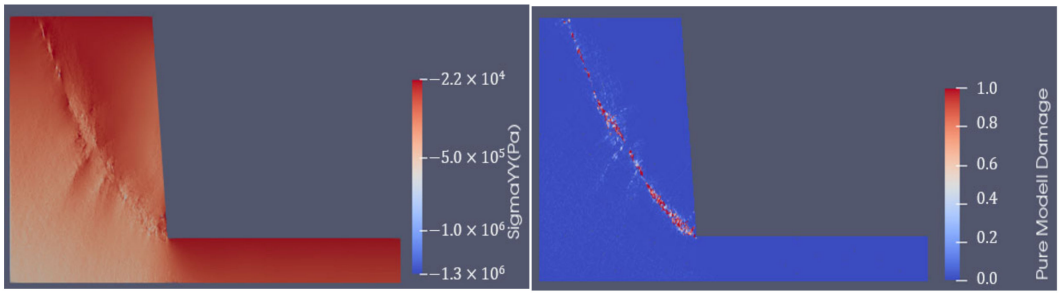

(**d**)

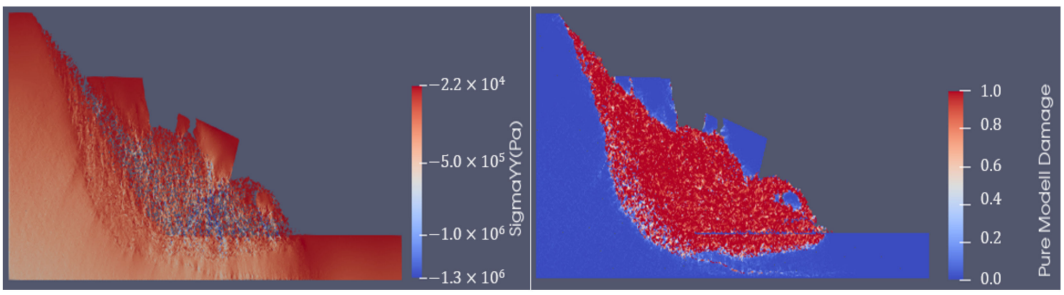

(**e**)

Figure 14. GPGUP-parallelized Y-HFDEM IDE modelling of rock slope failure process. (**a**) Stress equilibrium state; (**b**) 3 s; (**c**) 5 s; (**d**) 10 s; (**e**) 25 s.

7. Conclusions

The stability of rock slopes plays a significant role in many geotechnical engineering projects. To avoid the catastrophes induced by the instability of the rock slopes and to optimize the slopes for reliability, many techniques have been developed, which can be classified into convention methods and numerical methods. The limited analysis method is the most popular and widely used conventional technique, which can provide the factor of the safety of the rock slopes. However, the limited method is mostly limited to analyzing the planar failure and wedge failure, and it is beyond the capability of the limited analysis method for complicated failure types. With the fast development of computation techniques, numerical techniques are employed to analyze the stability of the rock slopes. In general, the numerical techniques mainly include three types, i.e., the continuum method, discontinuum method, and the combined/hybrid continuum–discontinuum method. Both the continuum and discontinuum methods can model the slope failure process. However, due to the material assumptions, i.e., the continuum material or discontinuum material, the continuum or discontinuum methods have limitations in modelling the entire failure process. The continuum–discontinuum methods combined the advantages and avoid the disadvantages of the continuum methods and the discontinuum methods. Thus, a representative continuum–discontinuum method, i.e., the combined/hybrid finite–discrete element method (FDEM), is reviewed, calibrated, and then implemented in the rock slope stability analysis in this article. The fundamental principles of the FDEM are introduced. Compared with continuum methods and discontinuum methods, one of the most distinct is that the FDEM can model the transition from continuum to discontinum. Therefore, the FDEM can model the entire slope sliding process naturally. This research paper gives a detailed explanation of this distinction, i.e., the transition from continuum to discontinuum. In addition, the three fracture modes that make the FDEM able to model the transition from continuum to discontinuum through fracture and fragmentation are introduced. The calibration of the FDEM is essential to show its abilities in rock slope failure modelling. The authors reviewed the typical slope failure process modelled using the FDEM to calibrate the proposed method. The stress and displacement distributions modelled by the FDEM are similar to those obtained by commercial software. Moreover, the FDEM can obtain the fracture initiation, the interaction of the rock bodies, and the rock wedges sliding along the

failure surface. After that, the employment of the FDEM for the back analysis of the rock slope failure and predicting the rock failure using FDEM is given. Finally, the GPGUP-parallelized FDEM with the implementation of the strength reduction method (SRM) is introduced and employed to model the rock slope failure process to gain insight into the recent advance in FDEM techniques. On the basis of the review research, it is concluded that:

- The FDEM can effectively model the entire rock slope failure process from the fracture initiation, wedge sliding, and fragmentation due to the transition from the continuum to discontinuum technique implemented in the FDEM;
- The continuum or the discontinuum methods have their limitations in naturally modelling the entire rock failure process. However, the distinctive character, i.e., the transition from continuum to discontinuum, means that the FDEM can effectively model the natural failure process for the rock slopes, even without any failure modes implemented in the proposed method;
- The GPGUP-parallelized FDEM with the implementation of SRM is a promising technique in the back analysis and prediction of the slope failure process, as it combined the advantages of the continuum methods and discontinuum methods, and it can naturally model the transition for rock from continuum to discontinuum through fracture and fragmentations.

Author Contributions: Conceptualisation, H.L. and H.A.; writing—original draft preparation, H.A., H.L., Y.S. and Y.C.; funding acquisition, Y.F.; writing—review and editing, H.A., Y.S. and H.L.; supervision, H.L. All authors have read and agreed to the published version of the manuscript.

Funding: This work was partly supported by the Start-Up Fund for Talent of Kunming University of Science and Technology (Grant No. KKSY201867017), and funding from the Research Centre for Analysis and Measurement KUST (Analytic and Testing Research Centre of Yunnan, Grant No. 2020T20180040 and 2021M20202139010), Guizhou Provincial Department of Education's Natural Science Research Top-Notch Talents Project (Y[2020]041), and Guizhou High-Level Innovative Talents Training Project (2016, No.21), which are greatly appreciated.

Institutional Review Board Statement: Not applicable.

Informed Consent Statement: Not applicable.

Data Availability Statement: The data used to support the findings of this study are included in the article.

Conflicts of Interest: The authors declare that there are no conflicts of interest regarding the publication of this paper.

References

1. Wyllie, D.C.; Mah, C. *Rock Slope Engineering*; CRC Press: Boca Raton, FL, USA, 2004.
2. Tang, H.; Yong, R.; Ez Eldin, M.A.M. Stability analysis of stratified rock slopes with spatially variable strength parameters: The case of Qianjiangping landslide. *Bull. Eng. Geol. Environ.* **2017**, *76*, 839–853. [CrossRef]
3. Norrish, N.I.; Wyllie, D.C. *Landslides: Investigation and Mitigation. Chapter 15—Rock Slope Stability Analysis*; Transportation Research Board: Washington, DC, USA, 1996.
4. Stead, D.; Wolter, A. A critical review of rock slope failure mechanisms: The importance of structural geology. *J. Struct. Geol.* **2015**, *74*, 1–23. [CrossRef]
5. Abramson, L.W.; Lee, T.S.; Sharma, S.; Boyce, G.M. *Slope Stability and Stabilization Methods*; John Wiley & Sons: Hoboken, NJ, USA, 2001.
6. Jin, Y.-F.; Yin, Z.-Y.; Yuan, W.-H. Simulating retrogressive slope failure using two different smoothed particle finite element methods: A comparative study. *Eng. Geol.* **2020**, *279*, 105870. [CrossRef]
7. Lv, Z.Q.; Wang, B.S.; Zhang, X.X. The PFC2DSimulation of the Slope Stability. In *Advanced Materials Research*; Trans Tech Publications Ltd.: Bäch SZ, Switzerland, 2015; pp. 240–243.
8. Yang, Y.; Xu, D.; Liu, F.; Zheng, H. Modeling the entire progressive failure process of rock slopes using a strength-based criterion. *Comput. Geotech.* **2020**, *126*, 103726. [CrossRef]
9. Shen, J.; Karakus, M. Three-dimensional numerical analysis for rock slope stability using shear strength reduction method. *Can. Geotech. J.* **2014**, *51*, 164–172. [CrossRef]
10. Yodsomjai, W.; Keawsawasvong, S.; Thongchom, C.; Lawongkerd, J. Undrained stability of unsupported conical slopes in two-layered clays. *Innov. Infrastruct. Solut.* **2021**, *6*, 15. [CrossRef]

11. Yodsomjai, W.; Keawsawasvong, S.; Senjuntichai, T. Undrained stability of unsupported conical slopes in anisotropic clays based on anisotropic undrained shear failure criterion. *Transp. Infrastruct. Geotechnol.* **2021**, *8*, 557–568. [CrossRef]
12. Yodsomjai, W.; Keawsawasvong, S.; Likitlersuang, S. Stability of unsupported conical slopes in Hoek-Brown rock masses. *Transp. Infrastruct. Geotechnol.* **2021**, *8*, 279–295. [CrossRef]
13. Li, A.-J.; Lyamin, A.; Merifield, R. Seismic rock slope stability charts based on limit analysis methods. *Comput. Geotech.* **2009**, *36*, 135–148. [CrossRef]
14. Li, A.J.; Merifield, R.S.; Lyamin, A.V. Stability charts for rock slopes based on the Hoek-Brown failure criterion. *Int. J. Rock Mech. Min. Sci.* **2008**, *45*, 689–700. [CrossRef]
15. Jing, L. A review of techniques, advances and outstanding issues in numerical modelling for rock mechanics and rock engineering. *Int. J. Rock Mech. Min. Sci.* **2003**, *40*, 283–353. [CrossRef]
16. Jiang, M.; Murakami, A. Distinct element method analyses of idealized bonded-granulate cut slope. *Granul. Matter* **2012**, *14*, 393–410. [CrossRef]
17. Zhang, Y.; Xu, Q.; Chen, G.; Zhao, J.X.; Zheng, L. Extension of discontinuous deformation analysis and application in cohesive-frictional slope analysis. *Int. J. Rock Mech. Min. Sci.* **2014**, *70*, 533–545. [CrossRef]
18. Tang, S.; Huang, R.; Tang, C.; Liang, Z.; Heap, M. The failure processes analysis of rock slope using numerical modelling techniques. *Eng. Fail. Anal.* **2017**, *79*, 999–1016. [CrossRef]
19. Sun, L.; Liu, Q.; Abdelaziz, A.; Tang, X.; Grasselli, G. Simulating the entire progressive failure process of rock slopes using the combined finite-discrete element method. *Comput. Geotech.* **2022**, *141*, 104557. [CrossRef]
20. Zhou, W.; Yuan, W.; Ma, G.; Chang, X.L. Combined finite-discrete element method modeling of rockslides. *Eng. Comput.* **2016**, *33*, 1530–1559. [CrossRef]
21. Barla, M.; Piovano, G.; Grasselli, G. Rock slide simulation with the combined finite-discrete element method. *Int. J. Geomech.* **2012**, *12*, 711–721. [CrossRef]
22. Mahabadi, O.; Grasselli, G.; Munjiza, A. Y-GUI: A graphical user interface and pre-processor for the combined finite-discrete element code, Y2D, incorporating material heterogeneity. *Comput. Geosci.* **2010**, *36*, 241–252. [CrossRef]
23. Eberhardt, E.; Stead, D.; Coggan, J.S. Numerical analysis of initiation and progressive failure in natural rock slopes—The 1991 Randa rockslide. *Int. J. Rock Mech. Min. Sci.* **2004**, *41*, 69–87. [CrossRef]
24. An, H.; Wu, S.; Liu, H.; Wang, X. Hybrid Finite-Discrete Element Modelling of Various Rock Fracture Modes during Three Conventional Bending Tests. *Sustainability* **2022**, *14*, 592. [CrossRef]
25. An, H.; Song, Y.; Liu, H.; Han, H. Combined Finite-Discrete Element Modelling of Dynamic Rock Fracture and Fragmentation during Mining Production Process by Blast. *Shock. Vib.* **2021**, *2021*, 6622926. [CrossRef]
26. An, H.; Song, Y.; Liu, H. FDEM Modelling of Rock Fracture Process during Three-Point Bending Test under Quasistatic and Dynamic Loading Conditions. *Shock. Vib.* **2021**, *2021*, 5566992. [CrossRef]
27. An, H.; Liu, H.; Han, H. Hybrid finite–discrete element modelling of rock fracture process in intact and notched Brazilian disc tests. *Eur. J. Environ. Civ. Eng.* **2021**, 1–34. [CrossRef]
28. Huaming, A.; Hongyuan, L.; Han, H. Hybrid finite-discrete element modelling of rock fracture during conventional compressive and tensile strength tests under quasi-static and dynamic loading conditions. *Lat. Am. J. Solids Struct.* **2020**, *17*, 1–32.
29. An, H.; Liu, H.; Han, H. Hybrid Finite-Discrete Element Modelling of Excavation Damaged Zone Formation Process Induced by Blasts in a Deep Tunnel. *Adv. Civ. Eng.* **2020**, *2020*, 7153958. [CrossRef]
30. An, H.; Liu, H.; Han, H.; Zheng, X.; Wang, X. Hybrid finite-discrete element modelling of dynamic fracture and resultant fragment casting and muck-piling by rock blast. *Comput. Geotech.* **2017**, *81*, 322–345. [CrossRef]
31. Mohammadnejad, M.; Liu, H.; Chan, A.; Dehkhoda, S.; Fukuda, D. An overview on advances in computational fracture mechanics of rock. *Geosystem Eng.* **2021**, *24*, 206–229. [CrossRef]
32. Bradley, A.L. Investigating the Influence of Mechanical Anisotropy on the Fracturing Behavior of Brittle Clay Shales with Application to Deep Geological Repositories. In Proceedings of the 13th ISRM International Congress of Rock Mechanics, Montreal, QC, Canada, 10–13 May 2015.
33. Zhao, Q.; Lisjak, A.; Mahabadi, O.; Liu, Q.; Grasselli, G. Numerical simulation of hydraulic fracturing and associated microseismicity using finite-discrete element method. *J. Rock Mech. Geotech. Eng.* **2014**, *6*, 574–581. [CrossRef]
34. Lukas, T.; Schiava D'Albano, G.G.; Munjiza, A. Space decomposition based parallelization solutions for the combined finite–discrete element method in 2D. *J. Rock Mech. Geotech. Eng.* **2014**, *6*, 607–615. [CrossRef]
35. Jing, L.; Hudson, J. Numerical methods in rock mechanics. *Int. J. Rock Mech. Min. Sci.* **2002**, *39*, 409–427. [CrossRef]
36. Munjiza, A. *The Combined Finite-Discrete Element Method*; Wiley Online Library: Hoboken, NJ, USA, 2004.
37. Munjiza, A.; Xiang, J.; Garcia, X.; Latham, J.; D'Albano, G.S.; John, N. The virtual geoscience workbench, VGW: Open source tools for discontinuous systems. *Particuology* **2010**, *8*, 100–105. [CrossRef]
38. Vyazmensky, A.; Stead, D.; Elmo, D.; Moss, A. Numerical Analysis of Block Caving-Induced Instability in Large Open Pit Slopes: A Finite Element/Discrete Element Approach. *Rock Mech. Rock Eng.* **2010**, *43*, 21–39. [CrossRef]
39. Styles, T. *Numerical Modelling and Analysis of Slope Stability within Fracture Dominated Rock Masses*; University of Exeter: Exeter, UK, 2009.
40. Tatonea, B.; Grassellia, G. A calibration procedure for two-dimensional laboratory-scale hybrid finite-discrete element simulations. *Int. J. Rock Mech. Min. Sci.* **2015**, *75*, 56–72. [CrossRef]

41. Han, H.; Fukuda, D.; Liu, H.; Salmi, E.F.; Sellers, E.; Liu, T.; Chan, A. Combined finite-discrete element modelling of rock fracture and fragmentation induced by contour blasting during tunnelling with high horizontal in-situ stress. *Int. J. Rock Mech. Min. Sci.* **2020**, *127*, 104214. [CrossRef]
42. Mohammadi, S. *Discontinuum Mechanics: Using Finite and Discrete Elements*; WIT Press: Southampton, UK, 2003.
43. Munjiza, A.; Andrews, K.; White, J. Combined single and smeared crack model in combined finite-discrete element analysis. *Int. J. Numer. Methods Eng.* **1999**, *44*, 41–57. [CrossRef]
44. Liu, H.; Kou, S.; Lindqvist, P.-A.; Tang, C. Numerical studies on the failure process and associated microseismicity in rock under triaxial compression. *Tectonophysics* **2004**, *384*, 149–174. [CrossRef]
45. Xiang, J.; Munjiza, A.; Latham, J.P. Finite strain, finite rotation quadratic tetrahedral element for the combined finite–discrete element method. *Int. J. Numer. Methods Eng.* **2009**, *79*, 946–978. [CrossRef]
46. Grasselli, G.; Lisjak, A.; Mahabadi, O.; Tatone, B. Slope Stability Analysis Using a Hybrid Finite-Discrete Element Method Code (EMDEM). In Proceedings of the 12th ISRM Congress, Beijing, China, 18–21 October 2011.
47. Bray, J.W.; Goodman, R.E. The theory of base friction models. *Int. J. Rock Mech. Min. Sci. Geomech. Abstr.* **1981**, *18*, 453–468. [CrossRef]
48. Zhu, C.; He, M.C.; Karakus, M.; Cui, X.B.; Tao, Z.G. Investigating Toppling Failure Mechanism of Anti-dip Layered Slope due to Excavation by Physical Modelling. *Rock Mech. Rock Eng.* **2020**, *53*, 5029–5050. [CrossRef]
49. Zheng, W.; Zhuang, X.; Tannant, D.D.; Cai, Y.; Nunoo, S. Unified continuum/discontinuum modeling framework for slope stability assessment. *Eng. Geol.* **2014**, *179*, 90–101. [CrossRef]
50. Wong, L.N.Y.; Wu, Z. Application of the numerical manifold method to model progressive failure in rock slopes. *Eng. Fract. Mech.* **2014**, *119*, 1–20. [CrossRef]
51. Liu, H.Y.; Kang, Y.M.; Lin, P. Hybrid finite–discrete element modeling of geomaterials fracture and fragment muck-piling. *Int. J. Geotech. Eng.* **2015**, *9*, 115–131. [CrossRef]
52. Fukuda, D.; Mohammadnejad, M.; Liu, H.; Zhang, Q.; Zhao, J.; Dehkhoda, S.; Chan, A.; Kodama, J.-I.; Fujii, Y. Development of a 3D Hybrid Finite-Discrete Element Simulator Based on GPGPU-Parallelized Computation for Modelling Rock Fracturing Under Quasi-Static and Dynamic Loading Conditions. *Rock Mech. Rock Eng.* **2020**, *53*, 1079–1112. [CrossRef]
53. Fukuda, D.; Mohammadnejad, M.; Liu, H.Y.; Dehkhoda, S.; Chan, A.; Cho, S.H.; Min, G.J.; Han, H.; Kodama, J.; Fujii, Y. Development of a GPGPU-parallelized hybrid finite-discrete element method for modeling rock fracture. *Int. J. Numer. Anal. Methods Geomech.* **2019**, *43*, 1797–1824. [CrossRef]
54. Mohammadnejad, M.; Fukuda, D.; Liu, H.Y.; Dehkhoda, S.; Chan, A. GPGPU-parallelized 3D combined finite-discrete element modelling of rock fracture with adaptive contact activation approach. *Comput. Part. Mech.* **2020**, *7*, 849–867. [CrossRef]
55. Fukuda, D.; Liu, H.; Zhang, Q.; Zhao, J.; Kodama, J.-I.; Fujii, Y.; Chan, A.H.C. Modelling of dynamic rock fracture process using the finite-discrete element method with a novel and efficient contact activation scheme. *Int. J. Rock Mech. Min. Sci.* **2021**, *138*, 104645. [CrossRef]
56. Cheng, Y.M.; Lansivaara, T.; Wei, W.B. Two-dimensional slope stability analysis by limit equilibrium and strength reduction methods. *Comput. Geotech.* **2007**, *34*, 137–150. [CrossRef]
57. Wei, Y.; Jiaxin, L.; Zonghong, L.; Wei, W.; Xiaoyun, S. A strength reduction method based on the Generalized Hoek-Brown (GHB) criterion for rock slope stability analysis. *Comput. Geotech.* **2020**, *117*, 103240. [CrossRef]

MDPI
St. Alban-Anlage 66
4052 Basel
Switzerland
www.mdpi.com

Sustainability Editorial Office
E-mail: sustainability@mdpi.com
www.mdpi.com/journal/sustainability

Disclaimer/Publisher's Note: The statements, opinions and data contained in all publications are solely those of the individual author(s) and contributor(s) and not of MDPI and/or the editor(s). MDPI and/or the editor(s) disclaim responsibility for any injury to people or property resulting from any ideas, methods, instructions or products referred to in the content.

Academic Open
Access Publishing

mdpi.com

ISBN 978-3-0365-9775-1